ANL-7910
Reactor Technology

Argonne National Laboratory

9700 South Cass Avenue
Argonne, Illinois 60439

APPLIED PHYSICS DIVISION ANNUAL REPORT

July 1, 1970, to June 30, 1971

Robert Avery, Division Director
Fred W. Thalgott, Deputy Division Director
Harry H. Hummel, Associate Division Director
W. C. Redman, Associate Division Director
William J. Sturm, Assistant Division Director
Lyman J. Templin, Assistant Division Director

NOTICE

This report was prepared as an account of work sponsored by the United States Government. Neither the United States nor the United States Atomic Energy Commission, nor any of their employees, nor any of their contractors, subcontractors, or their employees, makes any warranty, express or implied, or assumes any legal liability or responsibility for the accuracy, completeness or usefulness of any information, apparatus, product or process disclosed, or represents that its use would not infringe privately owned rights.

January 1972

DISTRIBUTION OF THIS DOCUMENT IS UNLIMITED

DISCLAIMER

This report was prepared as an account of work sponsored by an agency of the United States Government. Neither the United States Government nor any agency Thereof, nor any of their employees, makes any warranty, express or implied, or assumes any legal liability or responsibility for the accuracy, completeness, or usefulness of any information, apparatus, product, or process disclosed, or represents that its use would not infringe privately owned rights. Reference herein to any specific commercial product, process, or service by trade name, trademark, manufacturer, or otherwise does not necessarily constitute or imply its endorsement, recommendation, or favoring by the United States Government or any agency thereof. The views and opinions of authors expressed herein do not necessarily state or reflect those of the United States Government or any agency thereof.

DISCLAIMER

Portions of this document may be illegible in electronic image products. Images are produced from the best available original document.

Foreword

This is the eighth successive issue of the Applied (Reactor) Physics Division Annual Report and, in format, it simulates the preceding report, ANL-7710, and the earlier six reports: ANL-7010, 7110, 7210, 7310, 7410 and 7610. As in the previous reports, it emphasizes work performed by individual members or small groups of members of the Division, rather than integrated programmatic accomplishments. Nevertheless, when reasonable and possible, papers related to a given subject are grouped together within a section.

In order to assist those who may wish to pursue a given subject more extensively, a list of pertinent references is included in each article. A catalog of open literature and report publications and of abstracts prepared by staff of the Applied Physics Division during the reporting period are appended in Section VI to further aid those who may be interested in having additional information concerning work done in this Division.

Table of Contents

SECTION I
FISSION PROPERTIES AND CROSS SECTION DATA

I-1. Fast Neutron Total and Scattering Cross Sections of Palladium 3
A. B. SMITH, P. LAMBROPOULOS, P. GUENTHER and J. WHALEN

I-2. Fast Neutron Total and Scattering Cross Sections of ^{240}Pu 5
A. B. SMITH, P. P. LAMBROPOULOS and J. F. WHALEN

I-3. Measurements of the ^{235}U Fission Cross Section at 552 and 644 keV 7
W. P. POENITZ

I-4. The Fission Cross Section Ratio of ^{238}U to ^{235}U at 2.5 MeV 9
W. P. POENITZ and R. J. ARMANI

I-5. Additional Measurements of the Ratio $\sigma_f(^{239}\text{Pu})/\sigma_f(^{235}\text{U})$ 11
W. P. POENITZ

I-6. Measurement of (n,p) Cross Sections for Titanium, Nickel and Iron by Activation Methods 12
J. W. MEADOWS and D. L. SMITH

I-7. Utilization of Measured and Calculated Titanium Cross Sections in the ENDF/B Evaluated File 14
A. B. SMITH and E. M. PENNINGTON

I-8. Empirical Formula for Interpolation of Tabulated Photon Photoelectric Cross Sections 16
D. L. SMITH

I-9. Thick Target Yield for the Ta(p,n) Reaction 16
J. W. MEADOWS

I-10. Relative Yields of the Neutron Groups from the ^{7}Li$(p,n)^{7}$Be, ^{7}Be* Reactions 17
J. W. MEADOWS

I-11. Note on the Prompt Fission Neutron Spectra of Uranium-235 and Plutonium-239 18
A. B. SMITH

I-12. Polarization in the Elastic Scattering of 2 MeV Neutrons from Intermediate Weight Nuclei 20
S. A. COX

I-13. Spontaneously Fissioning Isomer of ^{236}U 22
J. W. MEADOWS and W. P. POENITZ

I-14. Interpretation, Intercomparison and Evaluation Methods for Neutron Cross Sections 23
W. P. POENITZ

I-15. Independent Study of 2200 m/s Fission Constants 27
A. DEVOLPI

I-16. Theory of Measurement 29
P. A. MOLDAUER

SECTION II
FAST REACTOR PHYSICS

II-1. ZPR-9 Assembly 27: The Fast Test Reactor Engineering Mockup Critical (FTR-EMC) 33
J. W. DAUGHTRY, C. D. SWANSON, A. B. LONG, R. B. POND and G. K. RUSCH

II-2. Fuel and Control Rod Enrichment Experiment in the Fast Test Reactor Engineering Mockup Critical (FTR-EMC) 39
R. B. POND, J. W. DAUGHTRY, C. D. SWANSON and A. B. LONG

II-3. Measured Reaction Rate Distributions in the Fast Test Reactor-Engineering Mockup Critical (FTR-EMC), ZPR-9 Assembly 27 41
A. B. LONG and C. D. SWANSON

II-4. Control Rod and Loop Experiments in ZPR-9 Assembly 26, FTR-3 45
J. W. DAUGHTRY, R. B. POND, C. D. SWANSON and R. M. FLEISCHMAN

II-5. The Shutdown Margin Experiment in FTR-3 50
J. W. DAUGHTRY and R. B. POND

II-6. Planning and Analysis in Support of the Fast Flux Test Facility (FFTF) Critical

Experiments on ZPR-9 56
A. Travelli, A. J. Ulrich and J. C. Beitel
II-7. Analysis of Sample Worth and Reaction Rate Measurements in FTR-3, ZPR-9 Assembly 26 66
C. D. Swanson and P. H. Kier
II-8. Analysis of UO_2 Small-Sample Doppler Measurements in FTR-3, ZPR-9 Assembly 26. 73
P. H. Kier and C. E. Till
II-9. A Calculation of the Isothermal Doppler Effect in FTR 79
P. H. Kier
II-10. Analysis of UO_2 Small-Sample Doppler Measurements in ZPR-3 Assembly 51 82
P. H. Kier
II-11. ZPR-6 Assemblies 6A and 7: Benchmark Specifications for the Two Large Single-Core-Zone Critical Assemblies—^{235}U-Fueled Assembly 6A and Plutonium-Fueled Assembly 7—LMFBR Demonstration Reactor Benchmark Program 86
C. E. Till, L. G. LeSage, R. A. Karam, R. A. Lewis, J. E. Marshall, M. Salvatores and B. A. Zolotar
II-12. Measurements in ZPR-6 Assembly 7 with the High-240 Plutonium Zone 102
E. M. Bohn, L. G. LeSage and J. E. Marshall
II-13. Measurements in the Sodium-Voided, High-240 Plutonium Zone of ZPR-6 Assembly 7 112
E. M. Bohn, J. E. Marshall and J. F. Meyer
II-14. Neutron Spectrum Measurements in ZPR-6 Assembly 7 117
T. J. Yule
II-15. Spectrum Measurement Between the Halves of ZPR-6 Assembly 7 119
T. J. Yule
II-16. Reaction-Rate Measurements in ZPR-6 Assembly 7 123
G. S. Stanford and W. R. Robinson
II-17. Integral Alpha Measurements in ZPR-6 Assembly 7 131
M. M. Bretscher
II-18. Reactivity Worth Measurements of a Simulated B_4C Control Rod Assembly in ZPR-6 Assembly 7 135
E. M. Bohn, L. G. LeSage and J. E. Marshall
II-19. Sodium-Void and Small-Sample Reactivity Worth Measurements in ZPR-6 Assembly 7 141
L. G. LeSage, E. M. Bohn and J. E. Marshall
II-20. Perturbation Denominator Measurements in ZPR-6 Assembly 7 154
M. M. Bretscher
II-21. Doppler Effect Measurements in ZPR-6 Assembly 7 156
L. G. LeSage, E. M. Bohn, R. B. Pond, J. E. Marshall and E. F. Groh
II-22. Analysis of Small-Sample Doppler Measurements in ZPR-6 Assemblies 6 and 7 161
P. H. Kier, M. Salvatores, W. R. Robinson and K. D. Dance
II-23. Analysis of ZPR-6 Assembly 6A 163
R. A. Karam
II-24. Uranium Doppler-Effect Measurements in ZPR-6 Assembly 6A 166
R. B. Pond and J. W. Daughtry
II-25. Initial Plate-Rod Heterogeneity Measurements—LMFBR Demonstration Reactor Critical Experimental Program 169
R. A. Lewis, L. G. LeSage, C. E. Till, J. E. Marshall, E. M. Bohn, M. Salvatores and G. S. Stanford
II-26. The Variable Temperature Rodded Zone (VTRZ) Project 185
K. D. Dance, J. F. Meyer, E. F. Groh and D. M. Smith
II-27. Noise Effects in Rod Drop Analysis 190
E. F. Bennett and I. K. Olson
II-28. A Theoretical Formulation of Analysis of Deterministic Errors in Inverse-Kinetics Measurements of Reactivity in Subcritical Systems 192
D. H. Shaftman
II-29. Inverse-Kinetics Analysis with Implicit Compensation for Approximations of Point-Kinetics 197
D. H. Shaftman
II-30. An Analysis of Subcritical Reactivity Measurements Using Pulsed-Neutron Techniques 198
W. Y. Kato and D. A. Meneley
II-31. Subcriticality Determination by Rod Drop in the FTR-3 Critical Experiments 203
C. E. Cohn
II-32. Subcriticality Determination by Noise Techniques in the FTR Engineering-Mockup

Critical-Experiment Program 207
C. E. COHN
II-33. Inverse Kinetics Techniques Applied to ZPPR Fast Critical Assemblies 208
R. W. GOIN, S. G. CARPENTER, J. M. GASIDLO and R. E. KAISER
II-34. Measurement and Analysis of Space Dependent Parameters in a Demonstration Plant Benchmark Critical 215
R. E. KAISER, W. G. DAVEY, P. I. AMUNDSON, A. L. HESS, R. J. FORRESTER, B. NEWMARK and C. L. BECK
II-35. Critical Mass Evaluation for the Final Plate Version of ZPPR Assembly 2 and Comparison of Reference Loadings 228
R. E. KAISER, A. L. HESS and R. J. NORRIS
II-36. Effects of Sodium Voiding on Reactor Parameters in the Demonstration Plant Benchmark Critical 238
A. P. OLSON, W. G. DAVEY, R. E. KAISER, J. C. YOUNG, R. J. NORRIS and A. L. HESS
II-37. Demonstration Plant Benchmark Central Reactivity Measurements 241
C. L. BECK, W. G. DAVEY, R. E. KAISER, R. J. NORRIS and P. I. AMUNDSON
II-38. Calculated Size Effects for Reactivity Perturbation Samples in ZPPR 247
P. J. COLLINS and R. G. PALMER
II-39. Evaluation of Experimental Uncertainties on Small-Sample Reactivity Measurements in ZPPR Assembly 2 249
S. G. CARPENTER and R. E. KAISER
II-40. Gamma Ray Dose Measurements in the ZPPR Demonstration Benchmark 253
G. G. SIMONS and T. S. HUNTSMAN
II-41. Demonstration Benchmark Control Rod Measurement Program—Part I: Measurements 254
S. G. CARPENTER, J. T. HITCHCOCK, R. W. GOIN and J. C. YOUNG
II-42. Demonstration Benchmark Control Rod Measurements—Part II: Analysis 261
J. P. PLUMMER, R. G. PALMER, G. L. GRASSESCHI and B. NEWMARK
II-43. Tantalum Capture and Plutonium Fission Rates Around Control-Rod Mockups in ZPPR Assembly 2 264
D. W. MADDISON
II-44. Reactivity Doppler Measurements in ZPPR Assembly 2 265
R. E. KAISER, J. M. GASIDLO and W. G. DAVEY
II-45. Kinetics Parameters for ZPPR Assembly 2 271
A. P. OLSON, R. E. KAISER and G. L. GRASSESCHI
II-46. Measured Reaction Rates in ZPR-3 Assemblies 60, 61, and 62 Using Foils 273
D. W. MADDISON
II-47. Neutron Spectra in ZPR-3 Assemblies 62 and 63B 275
G. G. SIMONS and R. J. FORRESTER
II-48. ZPR-3 Assembly 63, A Heterogeneously Loaded, Steel Reflected EBR-II Critical Assembly 280
W. P. KEENEY, R. O. VOSBURGH, J. M. GASIDLO and D. MENEGHETTI
II-49. Further Analyses of Plutonium-Fueled ZPR-3 Benchmark Criticals Using ENDF/B VERSION I 291
A. L. HESS and R. G. PALMER
II-50. Prescription of a Benchmark Model of ZPPR Assembly 2 for Data Testing of ENDF/B 299
A. L. HESS and R. G. PALMER
II-51. Calculations for Fast Reactor Benchmarks with ENDF/B Data 304
E. M. PENNINGTON
II-52. Sensitivity Studies of the Effect of Uncertainty in the $^{238}U(n,\gamma)$ and in the $^{239}Pu(n,f)$ and (n,γ) Cross Sections 309
H. H. HUMMEL
II-53. Comparisons of ENDF/B VERSIONS I, II and II-Modified 310
R. A. KARAM, W. R. ROBINSON, M. SALVATORES and C. E. TILL
II-54. A Study of Methods of Cross Section Error Identification Utilizing Integral Data from Fast Critical Assemblies 313
K. O. OTT, R. B. POND and J. M. KALLFELZ
II-55. ^{239}Pu Self-Shielding Factors as a Function of σ_p Based on ENDF/B VERSION I Data. 315
M. SALVATORES and K. D. DANCE
II-56. Two-Dimensional Fast-Reactor Disassembly Calculations with Space-Time Kinetics. 318
E. L. FULLER, D. A. MENELEY, T. A. DALY, W. T. SHA, A. J. LINDEMAN and G. K. LEAF

II-57. Conservative Analytical Estimates of the Consequences of Failure Propagation in a Hypothetical Accident for a Ceramic-Fueled LMFBR 322
P. J. PERSIANI and M. STEVENSON
II-58. Comparison of Filter Effects in the Design of the Fuel Element Failure Propagation Loop (FEFPL) 331
A. E. MCARTHY
II-59. Gamma-Ray Dose Rates from Radioactive Sodium and Fission Products in the Fuel Element Failure Propagation Loop (FEFPL) 334
A. E. MCARTHY

SECTION III
EXPERIMENTAL TECHNIQUES AND FACILITIES

III-1. Improved Fast Neutron Time-of-Flight System 339
A. B. SMITH, P. GUENTHER and A. ENGFER
III-2. Multi-Detector Time-of-Flight System Software 340
P. GUENTHER
III-3. Total Cross Section Measurements Using Time-of-Flight Methods on the Fast Neutron Generator (FNG) 341
J. F. WHALEN and A. B. SMITH
III-4. Modification of the Peripheral Configuration for On-Line and Off-Line Fast Neutron Generator (FNG) Computer Systems 342
J. F. WHALEN
III-5. Installation of Apparatus for Measurement of $(n,n'\gamma)$ Cross Sections at the Fast Neutron Generator (FNG) Facility 342
D. L. SMITH
III-6. Facility for Measurement of Delayed Neutron Spectra 343
S. A. COX
III-7. Black Neutron Detector 344
W. P. POENITZ
III-8. Neutron Energy Spectrum Measurements in Large, Slightly Subcritical Assemblies by the TOF Method 346
E. BENNETT, C. COHN, R. DOERNER, RAYMOND GOLD, K. PORGES, J. L. SNELGROVE, A. DEVOLPI and B. ZOLOTAR
III-9. ZPR-6 Time-of-Flight Neutron Spectrum Measurement Facility 348
J. L. SNELGROVE and R. C. DOERNER
III-10. On-Line Detection Systems for the Time-of-Flight Neutron Spectrum Measurement Facility 352
K. PORGES, RAYMOND GOLD and J. L. SNELGROVE
III-11. CAMAC Crate Controllers for the SEL-840MP and DDP-24 Computers 355
C. E. COHN and S. J. RUDNICK
III-12. Pulsed-Neutron Time-of-Flight Measurements at Short Flight Paths in a Zero Power Reactor 356
RAYMOND GOLD, K. G. PORGES and J. L. SNELGROVE
III-13. Detector Efficiency Calibration with Monoenergetic Neutrons 357
K. PORGES, I. OLSON, RAYMOND GOLD and J. SNELGROVE
III-14. Thick Target Neutron Yields of Lithium and Beryllium Targets Bombarded with Protons and Deuterons 361
K. PORGES, J. L. SNELGROVE, RAYMOND GOLD, A. DEVOLPI, R. J. ARMANI and C. E. COHN
III-15. High Pressure ^{4}He Gas Scintillator for MeV Neutron Time-of-Flight Measurements .. 362
RAYMOND GOLD, K. G. PORGES and J. L. SNELGROVE
III-16. Improved Computer Method for Polarity Cross Correlation 363
C. E. COHN
III-17. A Polarity Correlation System for Fast Reactor Noise Studies 365
W. K. LEHTO, J. M. LARSON, R. W. GOIN and J. E. HUTTON
III-18. Real-Time Counting Techniques for Determining Absolute Fission Rates and Reaction Rate Distributions in Zero Power Critical Assemblies 373
A. B. LONG
III-19. Integrated System for On-Line Computer Acquisition of Data from ZPR-6 and ZPR-9 377
A. B. LONG
III-20. Technique Improvements in the Use of Boron Chambers for Reaction Rate Measurements 381
T. J. YULE and E. F. BENNETT

III-21. Measurement of Fast Neutron Flux with a Lithium-Drifted Germanium Detector... 385
D. L. SMITH
III-22. Comparison of Absolute Fission and Capture Rates Measured with Foils and Fission Chambers... 387
R. O. VOSBURGH, D. W. MADDISON and R. J. FORRESTER
III-23. Miscellaneous Electronic Techniques... 388
C. E. COHN
III-24. Computerized Accounting System for ZPPR, ZPR-6 and ZPR-9 Non-Fissile Material Inventory... 390
A. B. LONG
III-25. Developments in Analysis of Fast Neutron Data... 391
A. DEVOLPI
III-26. Improving the Efficiency of Computer Output Operations Using Direct-Memory-Access Channels... 392
C. E. COHN
III-27. Ge(Li) Detector Calibration and Data Correction for Small Source-to-Detector Distances and Absolute Standard Source Comparisons... 395
D. W. MADDISON
III-28. Analysis of Automatic Fission Track Scanning Data... 396
RAYMOND GOLD AND C. E. COHN
III-29. Energy Response Calculations for Encapsulated ^{7}LiF Thermoluminescent Dosimeters. 398
G. G. SIMONS
III-30. Evaluation of Thermoluminescent Materials and Techniques for Determining Gamma Heating in Fast Reactors... 401
T. J. YULE
III-31. A Precision Remote Controlled Electrometer for Reactor Power Measurements... 408
J. M. LARSON
III-32. Effectiveness of the Dual Heater Temperature Control System in the ZPPR Reactivity Doppler Mechanism... 414
J. M. GASIDLO, R. E. KAISER, D. P. PRUETT AND J. C. YOUNG
III-33. Zero Power Plutonium Reactor (ZPPR) Roof Filter Test Experience... 417
P. B. MCCARTHY, R. G. MATLOCK AND R. L. CHEEVER
III-34. Relocating the Argonne Fast Source Reactor (AFSR)... 419
R. O. VOSBURGH, R. G. MATLOCK, P. B. MCCARTHY AND R. N. CURRAN
III-35. Fast Neutron Personnel Dosimetry in ZPR-6 and ZPR-9... 422
RAYMOND GOLD, R. J. ARMANI and G. K. RUSCH
III-36. Fast Neutron Dosimetry Study of the Movable Personnel Shields in ZPR-9 Assembly 27... 424
RAYMOND GOLD, R. J. ARMANI and A. DEVOLPI

SECTION IV
REACTOR COMPUTATION METHODS AND THEORY

IV-1. Implementation Strategy for the MC^{2}-2 Code... 429
B. J. TOPPEL
IV-2. Improvements in the Variably Dimensioned MC^{2} Capability of the Argonne Reactor Computation (ARC) System... 437
C. G. STENBERG
IV-3. ETOE-2, A Program for Conversion of ENDF/B to MC^{2}-2... 442
C. G. STENBERG
IV-4. Modifications of the ARC System and Adaptation to the Current IBM Operating System... 446
W. L. WOODRUFF
IV-5. Two-Dimensional Transport Theory Capabilities in the ARC System... 447
H. GREENSPAN, R. H. THOMPSON AND W. L. WOODRUFF
IV-6. User Experience with the ARC System... 448
H. HENRYSON, II and B. J. TOPPEL
IV-7. Studies of Spectral Synthesis in Spatially Dependent Fast-Reactor Dynamics... 453
W. M. STACEY, JR. and J. P. REGIS
IV-8. Studies of Spectral Flux Synthesis... 455
H. GREENSPAN
IV-9. Synthesis Calculations in a Highly Nonseparable Fast Reactor Cell... 458
V. LUCO
IV-10. Single-Channel Continuous-Trial-Function Calculations in a Fast Reactor Con-

figuration 467
V. Luco
IV-11. Solution of the Multigroup Neutron Diffusion Equations by Space-Energy Factorization 475
W. M. Stacey, Jr. and H. Henryson, II
IV-12. An Efficient Method for Evaluating the $J(\beta,\theta,a,b)$ Integral 475
R. N. Hwang
IV-13. An Accurate Method for Evaluating the Overlap Term in the Unresolved Resonance Region 482
R. N. Hwang
IV-14. The Effect of Wide-Scattering Resonances Upon Multigroup Cross Sections 488
W. M. Stacey, Jr.
IV-15. Approximate Treatments of the Effect of Anisotropy Upon Elastic Neutron Moderation 491
W. M. Stacey, Jr.
IV-16. Variational Field Theory 493
W. M. Stacey, Jr.
IV-17. Collision Probability Methods with Anisotropic Scattering 495
W. M. Stacey, Jr.
IV-18. One-Dimensional Space-Time Kinetcis Benchmark Calculations 497
E. L. Fuller
IV-19. The Point Kinetics Algorithm for FX2 503
E. L. Fuller
IV-20. Generalized Perturbation Methods for Sensitivity Analysis of Fast Criticals 508
M. Salvatores
IV-21. Acceleration of External Source Problems in Near-Critical Systems 513
D. A. Meneley
IV-22. Application of the VIM-I Monte Carlo Code to the Analysis of ZPPR Assembly 2 Experiments 515
F. L. Fillmore
IV-23. Monte Carlo Calculations 518
C. N. Kelber
IV-24. Development of Computer Programs for the Statistical Generation of Fast Neutron Reaction Cross Sections 519
P. A. Moldauer

SECTION V
MISCELLANEOUS

V-1. Safety Effects of Light Water Infiltration in the Argonne Research Reactor, CP-5 525
C. N. Kelber
V-2. Physics Analysis for the CP-5 Fuel Study 525
P. J. Persiani and James H. Talboy
V-3. Analysis of Compton Continuum Measurements 527
Raymond Gold and I. K. Olson
V-4. Some Comments on the Power Balance Parameters Q and ϵ as Measures of Performance for Fusion Power Reactors 528
P. Persiani, W. C. Lipinski and A. J. Hatch
V-5. Nonelectrical or Off-Peak Electrical Air Conditioning 533
B. I. Spinrad
V-6. Extension of the Dual Spectrum Fuel Assay Concept 535
C. N. Kelber

SECTION VI
PUBLICATIONS

July 1, 1970, to June 30, 1971

Open Literature 537
Reports 538
Abstracts 538

Section I

Fission Properties and Cross Section Data

In close support of the reactor program, experimental and theoretical studies of neutron interactions with those nuclei found in the structural and fuel components of reactor systems continue to be carried out. This work is performed principally to provide information necessary for optimal reactor physics design. The major portion of the effort is devoted to studies of fast neutron induced processes, especially those which are important in fast reactors. The studies are directed toward neutron elastic and inelastic scattering, neutron induced reactions including capture, and to characteristics of the fission process.

I-1. Fast Neutron Total and Scattering Cross Sections of Palladium[1]

A. B. Smith, P. Lambropoulos, P. Guenther and J. Whalen

Elemental palladium is in a mass region of particular interest from the point of view of understanding the neutron-nucleus interaction and its implication in the applied use of such neighboring nuclei as zirconium, molybdenum and cadmium. Understanding is usually based upon the concept of the nuclear optical model.[2] The predictions of this model are unambiguously comparable with the observed total neutron cross section over a wide energy range and, in the low energy limit, with average resonance properties. The choice of model parameters is particularly sensitive in the region of palladium where the observed fast neutron properties must be reconciled with the extreme minimum in the $\ell = 0$ strength function. Theoretical and experimental studies at Argonne National Laboratory over a number of years have illuminated these uncertainties in this region of the periodic table. The study of the fast neutron properties of palladium reported here is a part of this work.

The total neutron cross sections of palladium were determined from 0.1 to 1.5 MeV at intervals $\lesssim 2$ keV with resolutions of ~ 2 keV. The statistical accuracy of the individual measurements was $\sim 1\%$ and the consistency also of that order. The results are summarized in Fig. I-1-1. Generally, the cross sections varied smoothly with energy with some structure of small magnitude in the hundred keV region. Differential elastic scattering cross sections were determined from incident energies of 0.3 to 1.5 MeV at intervals of $\lesssim 20$ keV and at eight laboratory scattering angles distributed between 25 and 155 deg. The deduced angle-integrated elastic scattering cross sections are outlined in Fig. I-1-1. Neutron cross sections for the excitation of "states" at 320 ± 50, 390 ± 20, 440 ± 20, 450 ± 20, 550 ± 30, 570 ± 20, 830 ± 20 and 940 ± 25 keV were quantitatively measured. Further, cross sections for the excitation of "states" at 650 ± 25, 720 ± 25, 760 ± 25 and 1010 ± 50 keV were qualitatively and/or tentatively determined. The experimental inelastic scattering results are graphically summarized in Fig. I-1-2.

An optical potential was deduced from the experimental results and shown suitable for extrapolation to higher and lower neutron energies. Calculations based upon the selected potential directly and quantitatively describe the measured total neutron cross sections. The selection of potential was sensitive to the elastic angular distributions, though the comparison of calculated and experimental elastic values required the additional concept of a compound nucleus and statistical interactions. The latter processes are reasonably calculable in this energy region of good experimental definition and, as a consequence, may be preferred to higher energy comparisons of calculated and measured elastic scattering where the relation to the optical potential is more direct but the experimental basis often more uncertain due to poorly resolved inelastic contributions to the observed elastic processes. Concurrent with the quantitative description of the fast neutron processes the selected potential provided reasonable estimates of strength functions in a region where S_0 values are at or near a minimum. Average S_0 values were reasonably extrapolated from the available fast neutron base in this experimentally difficult resonance region, free from energy-local perturbations and with results equiva-

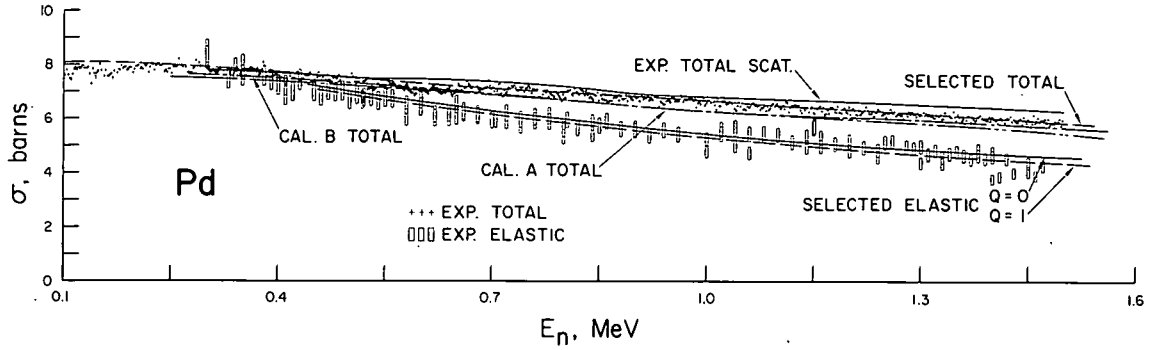

Fig. I-1-1. Measured Neutron Total and Elastic Scattering Cross Sections of Palladium. Data Points Indicate Measured Values. Various Curves Indicate the Results of Calculations as Described in Primary Ref. 2. *ANL Neg. No. 116-915.*

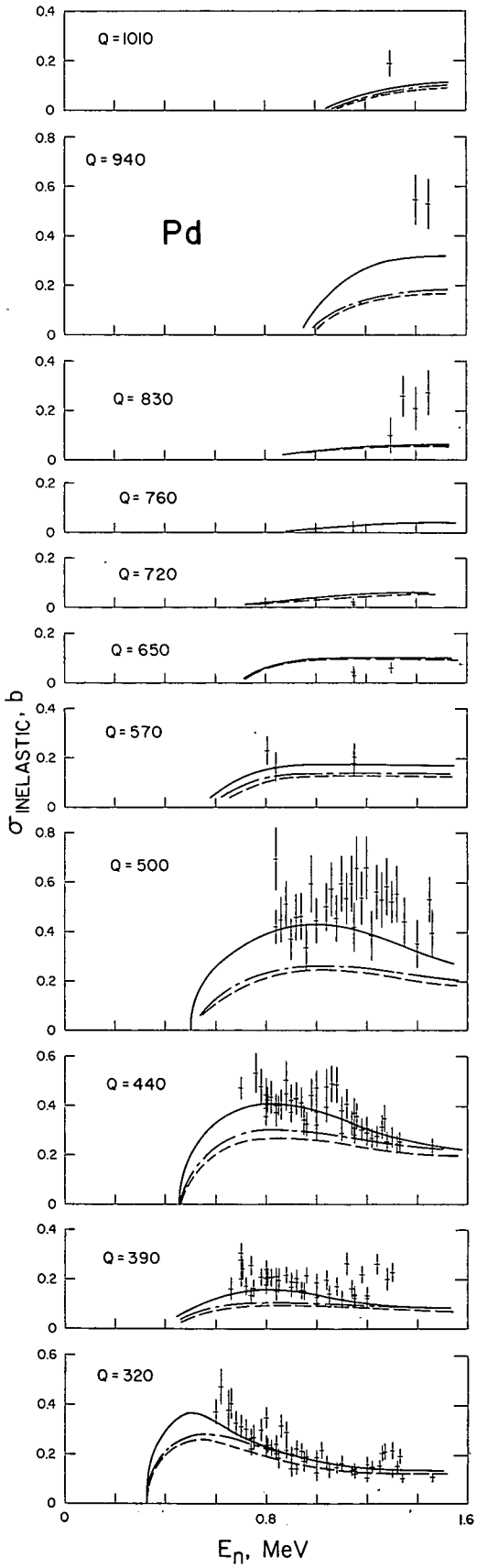

lent to or better than those obtained with potentials often based upon experimental strength function values. It is emphasized that the deduction of a reliable optical potential from fast neutron data requires precise experimental information including total and partial cross sections over an appreciable energy range. Such information is not widely available. Furthermore, attention must be given to the validity of the computational procedures employed if the results are to be meaningful.

References

1. A. Smith, P. Lambropoulos, P. Guenther and J. Whalen, *Palladium and Fast Neutrons*, ANL-7869 (to be published).
2. P. E. Hodgson, *The Optical Model of Elastic Scattering*, (Oxford University Press, London, 1963).

FIG. I-1-2. Measured Inelastic Neutron Excitation Cross Sections of Palladium. The Measured Values are Indicated by Crosses Corresponding to the Noted Reaction Q-values. The Curves are Derived from Calculation as Discussed in Ref. 2. *ANL Neg. No. 116-916.*

I-2. Fast Neutron Total and Scattering Cross Sections of ^{240}Pu[1]

A. B. Smith, P. P. Lambropoulos and J. F. Whalen

The isotope ^{240}Pu is a major constituent of many fast breeding reactors wherein the plutonium fuel may consist of 20 or more percent ^{240}Pu.[2] Thus, fast neutron interactions with this isotope are a consideration in the neutronic design of these systems. Despite this practical importance, experimental knowledge of fast neutron cross sections of ^{240}Pu is sparse and as a consequence evaluated data sets are largely based on nuclear-model estimates. The present work was undertaken in an effort to improve experimental understanding of the fast neutron cross sections of ^{240}Pu by direct measurement of total and scattering cross sections to $\sim$1.5 MeV.

Total Neutron Cross Sections

The measured total neutron cross sections are summarized in Fig. I-2-1. The structure near 530 keV is believed to be a residual artifact due to uncertain corrections for the effects of the large aluminum resonance in this region and to have no physical significance. The errors associated with the results are largely of a systematic nature, and are particularly due to the uncertain transmission-density of the sample.

Elastic Neutron Scattering Cross Sections

The ^{240}Pu differential elastic-scattering cross sections were determined from incident energies of 0.3 to 1.5 MeV in increments $\lesssim$50 keV and at eight scattering angles between $\sim$25 and $\sim$155 deg. The resulting distributions were least-square fitted with the expression

$$\frac{d\sigma}{d\Omega} = \frac{\sigma}{4\pi}\left(1 + \sum_{i=1}^{5} \omega_i P_i\right), \qquad (1)$$

where σ (angle-integrated cross section) and the ω_i coefficients were determined from the fitting procedure, and P_i are Legendre polynomials expressed in the laboratory system. It was estimated that the error in the measured differential values varied from 5 to 10% at forward angles and to as much as 30 to 50% at extreme backward scattering angles. The elastic scattering results are summarized in the format of Eq. (1) in Fig. I-2-2.

Inelastic Neutron Scattering Cross Sections

The inelastic neutron excitation of states at 42 $\pm$ 5, 140 $\pm$ 10, 300 $\pm$ 20, 600 $\pm$ 20 and 900 $\pm$ 50 keV was observed. The corresponding inelastic excitation cross sections are shown in Fig. I-2-3. Furthermore, neutrons corresponding to the excitation of states at energies $\gtrsim$ 1.0 MeV were qualitatively observed but subject to large background effects which made quantitative interpretation unreliable, and therefore the respective cross sections are not reported here.

Calculation and Discussion

The interpretation of the experimental results was primarily based upon optical- and statistical-nuclear models.[3,4] The point of departure was an optical potential of the form

$$V(r) = -Vf(r) - iWg(r) - V_{so}h(r)\,\ell\cdot\sigma, \qquad (2)$$

where $f(r)$ is of the Saxon form, $g(r)$ a Gaussian surface form, and $h(r)$ a Thomas form. The potential parameters were assumed energy-independent over the energy range of the present experiments. Compounds nucleus processes were calculated using the Hauser-Feshbach[4] formula. Fission was introduced by mean- of transmission coefficients and the respective cross

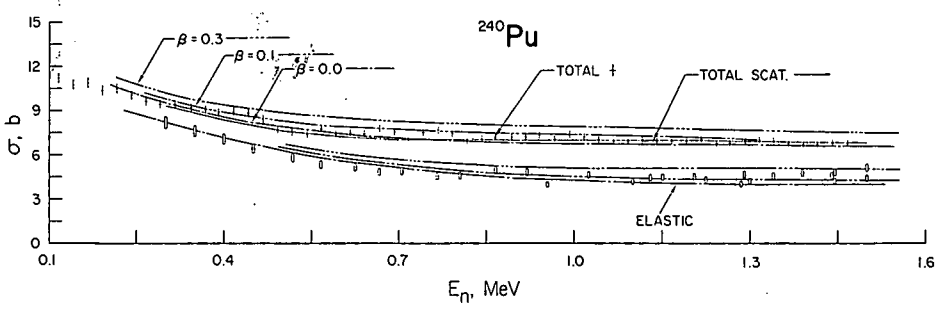

Fig. I-2-1. Measured Total (crosses) and Elastic-Scattering (Boxes) Cross Sections of ^{240}Pu. The Solid Curve Indicates the Total Scattering Cross Section Deduced from the Present Measurements. Dashed Curves Denote the Results of Model Calculations as Described in Ref. 6. *ANL Neg. No. 116-801.*

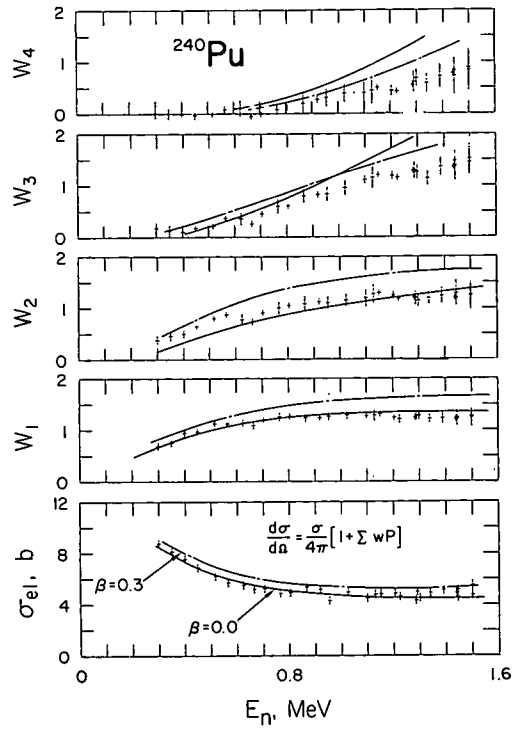

FIG. I-2-2. Differential Elastic-Scattering Cross Sections of ^{240}Pu Expressed in the Format of Eq. (1). Crosses Denote Results Deduced from the Measured Values. Curves are Derived from Calculations (see Ref. 6). *ANL Neg. No. 116-794.*

sections were calculated using the computer program NEARREX.[5] The calculational results were descriptive of experiment as indicated by the various curves shown in Figs. I-2-1 through I-2-3.[6]

Comparison with the ENDF/B Evaluated File

The results of the above experiments are quantitatively compared with the relevant contents of the ENDF/B evaluated file.[7] The measured and evaluated total neutron cross sections are in reasonable agreement over the entire experimental energy range as illustrated in Fig. I-2-4. The discrepancies near 500 keV are not judged significant as they could be attributed to experimental errors. At energies above 1.0 MeV the evaluated results tend to be systematically larger than the measured values but the difference is small—less than 300 mb. Measured and evaluated elastic scattering cross sections differ from one another in both shape and magnitude, as shown in Fig. I-2-4. The evaluated quantities are slightly larger than the measured values near 500 keV and pronouncedly lower at 1.0 MeV and above. At the higher energies the discrepancies are a full barn.

Evaluated cross sections are available for the excitation of states at 43, 142, 296, 599, 863, 903 and 945 keV. These energies are very similar to those measured in the present experiments with the latter three being experimentally observed as a composite state with an average excitation energy of 900 keV. The evaluated and measured inelastic excitation cross sections are compared in Fig. I-2-5. Below 500 keV the evaluated results are in agreement with experimental observation. However, at higher energies they are appreciably larger than the corresponding experimental values.

Generally, it was concluded that the ENDF/B file was reasonably descriptive of the measured total neutron cross sections. In the areas of elastic and inelastic scattering cross sections there were appreciable discrepancies between the measured and evaluated results. These will, of course, be reflected in discrepancies in associated quantities, such as the non-elastic cross section, as internal consistency of the file is mandatory. It is suggested that the observed discrepancies may be

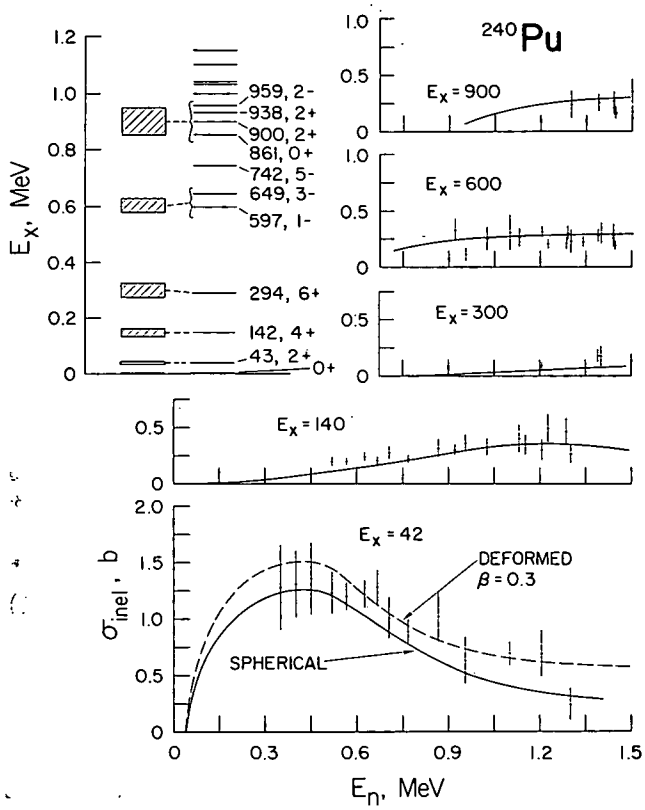

FIG. I-2-3. Inelastic-Neutron Excitation Cross Section of ^{240}Pu. Crosses Indicate Measured Values with Associated Errors for the Excitation of the Individual States. The Insert Correlates the Reported Excited Structure of ^{240}Pu with Th Observed in the Experiments (Boxes). The Energy Dimensio of the Experimental Boxes Indicate the Effective Experiment Resolutions and the Brackets Associate the Experimental Results with the Reported Structure. *ANL Neg. No. 116-802.*

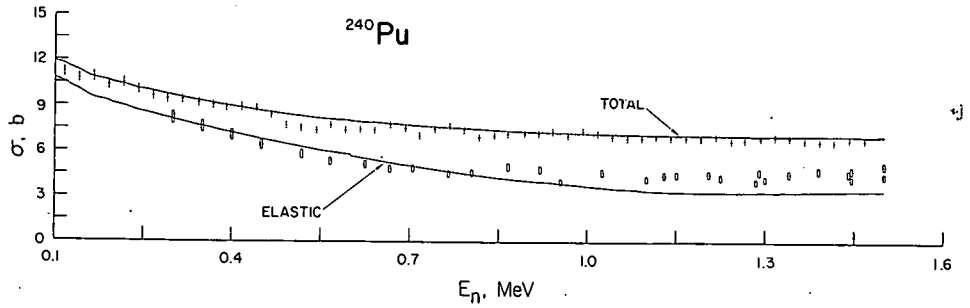

FIG. I-2-4. A Comparison of Measured Total (Crosses) and Elastic-Scattering (Boxes) Cross Sections with Comparable Quantities from ENDF (Curves).[7] *ANL Neg. No. 116-806.*

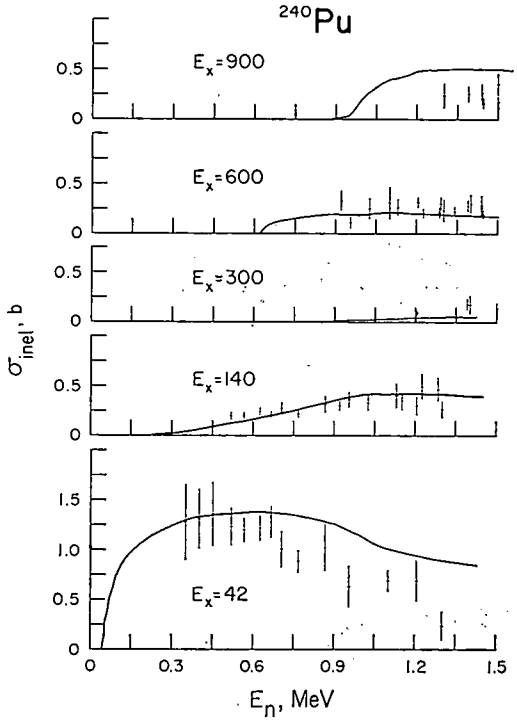

FIG. I-2-5. A Comparison of ENDF Inelastic Excitation Cross Sections[7] with the Respective Experimental Quantities (Crosses). *ANL Neg. No. 116-804.*

due to inappropriate consideration of the fission process in the calculations from which the file was largely deduced.

REFERENCES

1. P. Lambropoulos, J. Whalen and A. B. Smith, *Fast Neutron Total and Scattering Cross Sections of Pu-240 from 0.1 to 1.5 MeV*, Applied Physics Division Annual Report, July 1, 1969, to June 30, 1970, ANL-7710, pp. 11–12.
2. J. E. Marshall, *ZPR-6 Assembly 7*, Reactor Development Program Progress Report, ANL-7742, 6 (1971), Table I.B.3.
3. P. Hodgson, *The Optical Model of Elastic Scattering*, (Oxford University Press, London, 1963).
4. H. Feshbach, C. E. Porter and V. F. Weisskopf, *Model for for Nuclear Reactions with Neutrons*, Phys. Rev. **96**, 44B (1954).
5. Spherical model calculations employed the computer code ABACUS-2: E. Auerbach, *ABACUS-2*, BNL-6562. Compound nucleus calculations employed the computer code NEARRES: P. Moldauer, C. A. Englebrecht and J. Duffy, *NEARREX, Computer Code for Nuclear Reaction Calculations*, ANL-6978 (1964).
6. A. B. Smith, P. P. Lambropoulos and J. F. Whalen, *Fast Neutron Total and Scattering Cross Sections of ^{240}Pu*, Nucl. Sci. Eng. (to be published).
7. Evaluated Nuclear Data File-B (ENDF/B), National Neutron Cross Section Center, Brookhaven National Laboratory.

I-3. Measurements of the ^{235}U Fission Cross Section at 552 and 644 keV

W. P. POENITZ

The fast fission cross section of ^{235}U has been reeatedly measured in the past in many different labratories. It appears that as time passes the results reflect a downward trend of this cross section. In view of the high accuracy requests for this cross section additional measurements are needed since a systematic discrepancy still exists between more recent measurements of $^{235}U(n,f)$ and absolute capture cross sections combined with appropriate ratio measurements. The associated activity method used in the present experi-

ment has been applied by Hanna and Rose,[1] Poenitz,[2] Harris et al.,[3] Menlove and Poenitz,[4] and Knoll and Poenitz[5] for absolute cross section measurements. In the present experiment the $^{51}V(p,n)$ reaction was used to obtain neutrons of about 600 keV. Measurements were carried out in this energy region in order to avoid additional errors due to the energy dependence of the fission cross section. The γ-activity of the residual nuclei, ^{51}Cr, was measured to obtain the absolute neutron flux.

The $^{51}V(p,n)$ reaction was used as a neutron source. Protons were accelerated by a 3 MeV Van de Graaff generator. The target consisted of either a silver or tantalum backing on which metallic vanadium had been evaporated. The target thickness was in the range 10–30 keV. A layer of about 20 keV of silver had been evaporated on top of the vanadium deposit in order to avoid losses of ^{51}Cr by thermal evaporation at runtime. The target has been soldered or glued at the end of a 1 cm diam beam tube made from silver or stainless steel.

The target was positioned in the center of a spherical ionization chamber. The inner sphere of the counter had a diameter of 3 in. and the outer sphere a diameter of 5 in. The spheres were made from 0.025 cm thick silver. A layer of 120 $\mu g/cm^2$ of ^{235}U (99.8 %) had been deposited on the inner sphere by molecular plating. An area of 2.5 % had been lost for construction material and proton beam tube inlet. The mass determination of the fissile material has been obtained by subsequent chemical analysis. Corrections due to extrapolation of the fission spectra to zero pulse height did not exceed 1.5 % due to the high quality of the fissile material. After the end of the run at the accelerator the γ-activity of the targets was measured with a NaI(Tl)-detector. This detector had been calibrated with a large variety of radioactive samples.

Two measurements were carried out at each energy value. Different target arrangements were used in these runs. Additional measurements were carried out with blank targets in order to determine possible neutron background from the proton beam tube. The room background was measured using the $1/r^2$ law and was found to be in the order of 1 %.

Corrections were applied for the total absorption of fission fragments, the back scattering of neutrons from the outer sphere, the increase of the flight path due to neutrons scattered in the inner sphere, inelastic scattering of neutrons in the target material and the counter, and back scattering of neutrons from the construction materials. Due to the basic design of the experiment all of these corrections were small; a total correction of 3.6 % was applied for the effects named above.

The values obtained are:

$$\sigma_f \text{ (522 keV)} = 1.085 \pm 0.043 \text{ b}$$

$$\sigma_f \text{ (644 keV)} = 0.066 \pm 0.042 \text{ b.}$$

The uncertainties were determined by statistical error evaluation using statistical quantities only and then adding systematic uncertainties in a straightforward summation. The present values are in agreement with recent preliminary values by the author,[6] measurements by Gorlov et al.,[7] and Szabo et al.[8] The values are lower by 7–8 % than the smooth curve given by Davey,[9] which is based on the measurements by White.[10]

References

1. R. C. Hanna and B. Rose, *Fast Neuron Capture in ^{238}U and ^{232}Th*, J. Nucl. Energy **8**, 197 (1959).
2. W. P. Poenitz, *The (n,γ) Cross Section of ^{197}Au at 30 and 64 keV Neutron Energy*, J. Nucl. Energy, A/B **20**, 825 (1966).
3. K. K. Harris, H. A. Grench, R. G. Johnson, F. J. Vaughn, J. H. Ferziger and R. Sher, *The $^{197}Au(n,\gamma)^{198}Au$ Cross Section from 13 keV to 683 keV*, Nucl. Phys. **69**, 37 (1965).
4. H. O. Menlove and W. P. Poenitz, *Absolute Radiative Capture Cross Section for Fast Neutrons in ^{238}U*, Nucl. Sci. Eng. **33**, 24 (1968).
5. G. F. Knoll and W. P. Poenitz, *A Measurement of the ^{235}U Fission Cross Section at 30 and 64 keV*, J. Nucl. Energy **21**, 643 (1967).
6. W. P. Poenitz, *Measurement of the ^{235}U Fission Cross Section in the keV Energy Range*, Second Conference on Neutron Cross Sections and Technology, Washington, D. C. 1968, NBS Special Publication 299, Vol. I, 503 (1968), Conf. 680307.
7. G. V. Gorlov, B. M. Goshberg, V. M. Morozov, G. A. Ostroshchenko and V. A. Shigin, *The Fission Cross-Sections of ^{233}U and ^{235}U for Neutrons Having Energies between 3 and 800 keV*, J. Nucl. Energy **12**, 79 (1960).
8. I. Szabo, J. P. Marquette, E. Fort and J. L. Leroy, *Mesure Absolue de la Section Efficace de Fission*, Proc. IAEA Conference on Nuclear Data for Reactors, Helsinki, 1970, CN-26/69.
9. W. G. Davey, *An Analysis of the Fission Cross Sections of ^{232}Th, ^{233}U, ^{234}U, ^{235}U, ^{236}U, ^{237}Np, ^{238}U, ^{239}Pu, ^{240}Pu, ^{241}Pu, and ^{242}Pu from 1 keV to 10 MeV*, Nucl. Sci. Eng. **26**, 149 (1966).
   Also, W. G. Davey, *Selected Fission Cross Sections for ^{232}Th, ^{233}U, ^{234}U, ^{235}U, ^{236}U, ^{237}Np, ^{238}U, ^{239}Pu, ^{240}Pu, ^{241}Pu, and ^{242}Pu*, Nucl. Sci. Eng. **32**, 35 (1968).
10. P. H. White, *Measurements of the ^{235}U Neutron Fission Cross Section in the Energy Range 0.04–14 MeV*, J. Nucl. Energy. A/B **19**, 325 (1965).

I-4. The Fission Cross Section Ratio of ^{238}U to ^{235}U at 2.5 MeV

W. P. Poenitz and R. J. Armani

Introduction

The fission cross section ratio of ^{238}U to ^{235}U is of considerable importance because of the use of ^{238}U as the major breeding material in fast reactors. Additional interest is due to the use of $^{238}U(n,f)$ as a threshold detector in neutron spectral measurements. The accuracy requested by reactor designers for the above ratio is as high at 1%. However, a major discrepancy (as large as 6%) exists between two groups of data. This discrepancy is in the "plateau" range from 2 to 3 MeV between the data by Lamphere[1] and Smirenkin et al.[2] on one hand, and Stein et al.,[3] Smith et al.[4] and Jarvis[5] on the other. In the present experiment, values were measured at 2.5 MeV in order to contribute to a clarification of the "plateau" value of $\sigma_f(^{238}U)/\sigma_f(^{235}U)$. Accurate mass assignment of the fissile materials used in the experiment was emphasized.

Measurements

The fission cross section ratio was derived from the observation of fission fragments detected with a gas scintillation counter. The $^{7}Li(p,n)$ reaction was used as a neutron source. The targets, ranging in energy from 50 to 100 keV, were bombarded with a 2 nsec pulsed and bunched proton beam with a repetition rate of 2×10^6 pulses per sec. The fissile material was deposited on molybdenum backings by electroplating in thicknesses ranging from 30 to 500 μg cm^2. The foils were positioned back-to-back and perpendicular to the 0 deg neutron beam at 10 and 20 cm distances from the target. The time-of-flight technique was used for background suppression. The pulses from the gas scintillation counters were analyzed according to the fission fragment energy and the time-of-flight of the neutrons. This information was stored in an on-line computer.

Measurements were carried out twice for each set of foils, once for the ^{238}U foil facing the target and once for the ^{235}U foil, in order to eliminate effects due to the momentum carried by the incoming neutrons. Effects depending on the foil thickness were checked by measuring the ratio for pairs of foils with 50, 100, 300 and 500 μg/cm^2 deposits of fissile material. Possible background effects on the results were checked by measuring the backgrounds at 10 and 20 cm distances from the target. The corrections for fission events in nuclei other than ^{238}U and ^{235}U were checked by measuring the fission ratio for three sets of foils differing by their isotopic composition.

Four different methods have been applied to obtain the mass ratios. Two of the methods are based on destructive analysis of the foils; thus, each method could not be applied to each pair of foils. It is indicated in Table I-4-I which methods were applied to which pair of foils.

TABLE I-4-I. Description of Foils and Mass Ratio Assignment [Value of $N(^{235}U)/N(^{238}U)$]

Foil Set	Fissile Material	Thickness, μg/cm^2	Isotopic Composition, %				Mass Ratio Assignment (Method and Values)			
			^{235}U	^{238}U	^{234}U	^{236}U	1	2	3	4
I	^{235}U	35	99.857	0.054	0.027	0.062				
	^{238}U	40	0.015	99.985	—	—		0.912		0.893
II	^{235}U	50	98.432	0.106	1.034	0.428				
	^{238}U	50	2.062	96.812	0.991	0.125	1.031	1.043		
	^{235}U	100								
	^{238}U	100					1.020		1.045	
	^{235}U	300								
	^{238}U	300					1.024		1.026	
	^{235}U	500								
	^{238}U	500					0.959		0.959	
III	^{235}U	300	99.564	0.078	0.047	0.311				
	^{238}U	300	0.006	99.993	—	—		1.044		

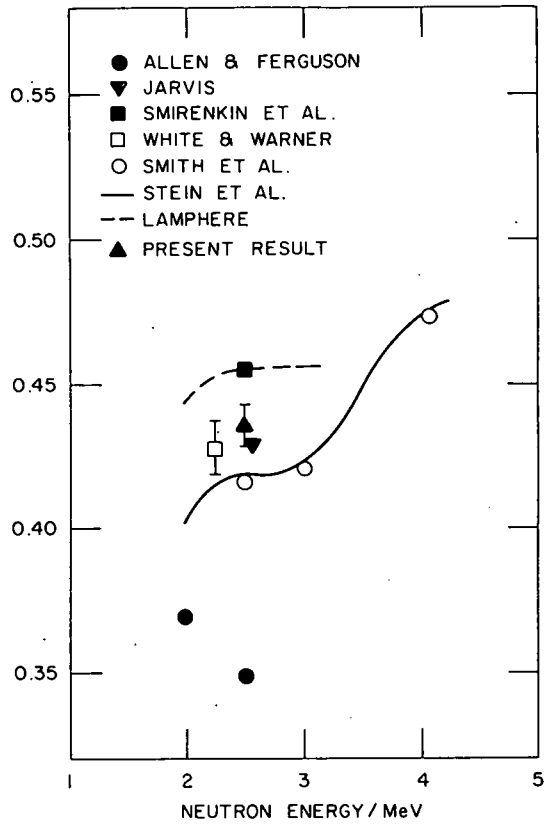

FIG. I-4-1. Comparison of the Present Result of $\sigma_f(^{238}U)/\sigma_f(^{235}U)$ with Other Data. *ANL Neg. No. 116-909.*

METHOD 1

Accurately weighted amounts of U_3O_8 were used to obtain three different solutions of ^{235}U, ^{238}U and ^{234}U, respectively. The ^{234}U solution was used to spike the ^{235}U and ^{238}U solutions such that the total α-activity of each solution was primarily determined by the ^{234}U spike. Foils have been produced from these solutions and their α-activities measured. The ratio of ^{235}U atoms to ^{238}U atoms deposited on the foils were obtained from the α-count rates, the amounts of U_3O_8 put into solution, and the amounts of ^{234}U solution added.

METHOD 2

The deposits were dissolved from the molybdenum backings and an approximately identical, but accurately weighed, amount of a standard ^{233}U was added. The isotopic composition of the mixture was determined by mass spectroscopy. The amounts of ^{235}U and ^{238}U from the foils were obtained from the known amount of ^{233}U and the isotopic composition.

METHOD 3

The deposits were dissolved from the backings. The resulting solutions were compared colorimetrically with a standard uranium solution. Because only the ratio is used for the present experiment, the accuracy of the standard solution does not influence the final result.

METHOD 4

The masses were determined from the known isotopic composition, the measured α-activities of the foils, and the half lifes as given in the literature.

Result and Discussion

The results from nine different measurements, including six different pairs of foils have been combined, yielding a ratio value of 0.436 ± 0.007 at 2.5 MeV. This result is compared with previously reported values in Fig. I-4-1.

The result from the present measurement is between the two extreme limits by Stein et al.,[3] Smith et al.,[4] and Jarvis[5] on the low side and Lamphere[1] and Smirenkin et al.[2] on the high side. The agreement with the result by White and Warner[6] is very good. The accuracy which can be achieved in fission ratio measurements appears to be limited by the uncertainties in the mass assignments. The latter are more likely indicated by discrepancies between different experimental techniques than by the uncertainty claimed for a single method and result.

References

1. R. W. Lamphere, *Fission Cross Sections of Uranium Isotopes 233, 235, 236, and 238 for Fast Neutrons*, Phys. Rev. **104**, 1654 (1956).
2. G. N. Smirenkin, V. G. Nesterov and I. I. Bondarenko, *^{233}U, ^{235}U and ^{239}Pu Fission Cross Sections for 0.3–2.5 MeV Neutrons*, Atomnaya Energiya **13**, 366 (1962).
3. W. E. Stein, R. K. Smith and H. L. Smith, *Relative Fission Cross Section of ^{236}U, ^{238}U, ^{237}Np, and ^{235}U*, Second Conference on Neutron Cross Sections and Technology, Washington, D.C., 1968, NBS Special Publication **299**, 627 (1968).
4. R. K. Smith, R. L. Henkel and R. A. Nobles, *Neutron-Induced Fission Cross Section for ^{233}U, ^{235}U, ^{238}U and ^{239}Pu from 2 to 10 MeV*, Bull. Am. Phys. Soc. **2**, 196 (1957).
5. G. A. Jarvis, *Fission Comparison of ^{238}U and ^{235}U for 2.5 MeV Neutrons*, LA-1571 (1953).
6. P. H. White and G. P. Warner, *The Fission Cross Sections of ^{233}U, ^{235}U, ^{238}U, ^{237}Np, ^{239}Pu, ^{240}Pu and ^{241}Pu Relative to that of ^{235}U for Neutrons in the Energy Range 1–14 keV*, J. Nucl. Energy **21**, 671 (1967).
7. W. D. Allen and A. T. G. Ferguson, *The Fission Cross Sections of ^{233}U, ^{235}U, ^{238}U and ^{239}Pu for Neutrons in the Energy Range 0.080–3.0 MeV*, Proc. Phys. Soc. **A70**, 573 (1957).

I-5. Additional Measurements of the Ratio $\sigma_f(^{239}Pu)/\sigma_f(^{235}U)$

W. P. Poenitz

Several measurements of the fission cross section ratio of ^{239}Pu to ^{235}U have been made.[1-6] The quoted uncertainty of the results is about 3% and the agreement among the various reported values is consistent with this uncertainty over most of the fast neutron energy range. However, two major problems important to fast reactor calculations and design remain unsolved. Below 100 keV the ratios measured by White et al.,[1] and by Allen and Ferguson[7] diverge and differ by about 15% at 40 keV. Measurements by Gilboy and Knoll[8] support the results by White et al.,[1] and the values obtained by Szabo et al.[5] agree very well with those by Allen and Ferguson.[7] Several other measurements[4,9,10] resulted in values between these two extreme limits.

Above 800 keV the new measurements by Savin et al.[6] display some structure in addition to, or different from, that shown in older measurements of Netter[11] and Smirenkin et al.[2] Between 1 MeV and 1.5 MeV the values of Savin et al.[6] display a pronounced maximum and a pronounced minimum while the results of Netter[11] and Smirenkin et al.[2] show a smooth rise in the ratio with increasing energy. Another noticeable feature of Savin's data is a sharp drop of the ratio above 4 MeV.

The present measurements are an extension of a previously reported experiment.[3] A single value has been obtained at the threshold of the $Li(p,n)Be$ reaction. With an average of 30 keV, this point is in the energy range of highest importance for fast power reactors. Additional measurements have been carried out in the higher energy range where attention was given to the possible existence of structure of the type observed by Savin et al.[6]

A detailed description of the experimental procedure has been given in Ref. 3; however, different plutonium and uranium samples have been used in the present experiment. The fissile sample thicknesses were about 35 $\mu g/cm^2$ for uranium (99.856% ^{235}U, 0.062% ^{236}U, 0.054% ^{238}U and 0.028% ^{234}U) and 45 $\mu g/cm^2$ for plutonium (99.843% ^{239}Pu, 0.049% ^{241}Pu, and 1.007% ^{240}Pu). The mass ratio was determined from the known isotopic compositions and the measured activities. The uncertainty of 2.5% for this mass-ratio determination is mainly due to the uncertainties in the ^{234}U contents n the uranium sample and the half lives of ^{235}U and ^{34}U.

Measurements were made with plutonium and uranium foils alternately facing the neutron target and for about equal counting rates. Thus, effects due to scattering in the molybdenum backings and the neutron momentum added to the fission fragments were eliminated. Corrections were applied for the second neutron group of the source reaction, inelastic scattering in the molybdenum backing and the fission counter assembly, in-scattering of lower energetic neutrons from the target-backing, and contributions from fissions other than those of ^{235}U and ^{239}Pu. The extrapolation to zero fission fragment energy has been assumed to be the same for both spectra. An additional effect was found which might have caused the slower rise in the ratio values of previous measurements above 1 MeV compared with the present results. At higher energies a background with about the same time-of-flight spectrum as the fission events was observed which was not eliminated by the coincidence between the two multipliers. This background was reduced by higher threshold settings and estimated from separate measurements using blank molybdenum backings. The major uncertainties of the present results are due to statistics (about 1–2%) and the mass assignment (2.5%).

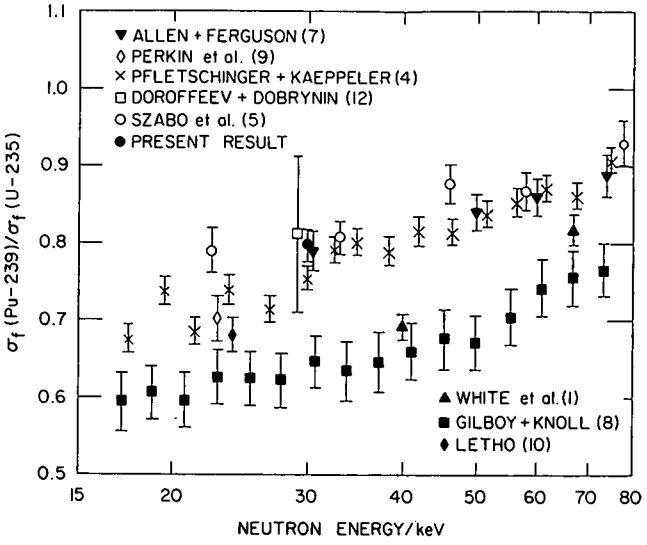

FIG. I-5-1. Comparison of σ_f (^{239}Pu)/σ_f (^{235}U) in the Low keV Energy Range. *ANL Neg. No. 116-824.*

A value of 0.796 ± 0.020 has been obtained for $\sigma_f(^{239}Pu)/\sigma_f(^{235}U)$ at 30 keV. This value is an average of an absolute ratio measurement and a measurement relative to a value of 1.33 at 500 keV obtained by averaging the data given in Refs. 1 through 5 and Ref. 7. Both values were within 1% of their average.

The value obtained at 30 keV is compared in Fig.

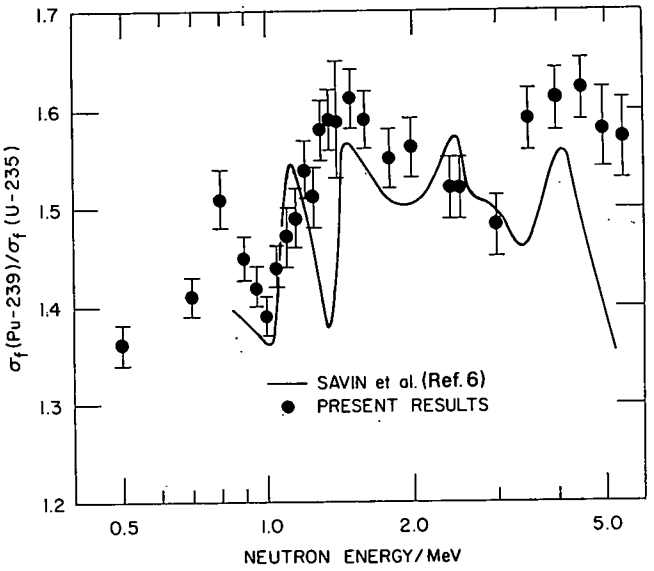

FIG. I-5-2. Comparison of the Present Results with the Structure Observed by Savin et al.[6] *ANL Neg. No. 116-823.*

I-5-1 with data obtained by other experimenters. The present measurement supports the higher values of $\sigma_f(^{239}\text{Pu})/\sigma_f(^{235}\text{U})$ as measured by Allen and Ferguson,[7] Dorofeev and Dobrynin,[12] Pfletschinger and Kaeppeler,[4] and Szabo et al.[5]

In Fig. I-5-2 a comparison is made between the present values and an eye-guide curve through the results by Savin et al.[6] Only the statistical errors of the present measurements have been shown in this figure. No indication has been found for the structure between 1.0 and 1.5 MeV suggested by Savin et al.[6] The present measurements follow in shape essentially those of Netter[11] and Smirenkin et al.[2] With the exception of a few isolated points they agree with those of Nesterov and Smirenkin,[6] White and Warner,[1] Poenitz,[3] Pfletschinger and Kaeppeler,[4] Dorofeev and Dobrynin,[16] and Szabo et al.[5]

REFERENCES

1. P. H. White, Y. G. Hodgkinson and G. Y. Wall, *Measurements of Fission Cross Sections for Neutrons of Energies in the Range 40–500 keV*, Proc. IAEA Symposium on the Physics and Chemistry of Fission, Salzburg, March 22–26, 1965, Vol. I, 219 (1965), SM-60-14.
   Also, P. H. White and G. P. Warner, *The Fission Cross Sections of ^{233}U, ^{235}U, ^{238}U, ^{237}Np, ^{239}Pu, ^{240}Pu and ^{241}Pu Relative to that of ^{235}U for Neutrons in the Energy Range 1–14 MeV*, J. Nucl. Energy **21**, 671 (1967).
2. G. N. Smirenkin, V. G. Nesterov and I. I. Bondarenko, *^{233}U, ^{235}U and ^{239}Pu Fission Cross Sections for 0.3–2.5 MeV Neutrons*, Atomnaya Energiya **13**, 366 (1962).
   Also, V. G. Nesterov and G. N. Smirenkin, *Ratios of Fast Neutron Fission Cross Sections of ^{233}U, ^{235}U, and ^{239}Pu*, Atomnaya Energiya **24**, 185 (1968).
3. W. P. Poenitz, *Measurements of the Ratios of Capture and Fission Neutron Cross Sections of ^{235}U, ^{238}U and ^{239}Pu at 130 to 1400 keV*, Nucl. Sci. Eng. **40**, 383 (1970).
4. L. Pfletschinger and F. Kaeppeler, *A Measurement of the Fission Cross Sections of ^{239}Pu and ^{233}U Relative to ^{235}U*, Nucl. Sci. Eng. **40**, 375 (1970).
5. I. Szabo, J. P. Marquette, E. Fort and J. L. Leroy, *Mesure Absolue de la Section Efficace de Fission*, Proc. IAEA Conference on Nuclear Data for Reactors, Helsinki, 1970, CN-26/69.
   Also, I. Szabo, G. Filippi, J. L. Leroy and J. P. Marquette, *^{235}U and ^{239}Pu Fission Cross Sections from 10 keV to 200 keV*, Third Conference on Neutron Cross Sections and Technology, Knoxville, Tennessee 1971 (to be published).
6. M. V. Savin, Yu. S. Zamytin, Yu. A. Khorhlov and I. N. Paramonova, *Fission Cross Section Ratios of ^{235}U, ^{239}Pu and ^{240}Pu for Fast Neutrons*, International Nuclear Data Committee, INDC(CCP)-8/U, 16 (1970).
7. W. D. Allen and A. T. G. Ferguson, *The Fission Cross Sections of ^{233}U, ^{235}U, ^{238}U and ^{239}Pu for Neutrons in the Energy Range 0.030–3.0 MeV*, Proc. Phys. Soc. **A70**, 573 (1957).
8. W. B. Gilboy and G. H. Knoll, *The Fission Cross Sections of Some Plutonium Isotopes in the Neutron Energy Range 5–150 keV*, Nuclear Research Center Karlsruhe, KFK 450 (1966).
9. J. L. Perkin, P. H. White, P. Fieldhouse, E. J. Axton, P. Cross and J. C. Robertson, *The Fission Cross Sections of ^{233}U, ^{234}U, ^{235}U, ^{236}U, ^{237}Np, ^{240}Pu and ^{241}Pu for 24 keV Neutrons*, J. Nucl. Energy **18**, 423 (1965).
10. W. K. Lehto, *Fission Cross Section Ratio Measurements of ^{239}Pu and ^{233}U to ^{235}U from 0.24 to 24 keV*, Nucl. Sci. Eng. **39**, 361 (1970).
11. F. Netter, *Some Aspects of the Nuclear Fission Process*, thesis, submitted to the University of Paris, Commissariat a l'Energie Atomique, CEA-1913 (1961).
12. G. A. Dorofeev and Y. P. Dobrynin, *Effective Fission Cross Sections of ^{233}U, ^{235}U, ^{239}Pu and ^{240}Pu in the Neutron Energy Range 30 keV–5 MeV*, J. Nucl. Energy **5**, 217 (1957).

I-6. Measurement of (n,p) Cross Sections for Titanium, Nickel and Iron by Activation Methods

J. W. MEADOWS and D. L. SMITH

Cross sections for the $^{47}\text{Ti}(n,p)^{47}\text{Sc}$ ($Q = +0.22$ MeV), $^{58}\text{Ni}(n,p)\,^{58}\text{Co}$ ($Q = +0.40$ MeV) and $^{56}\text{Fe}(n,p)$ ^{56}Mn ($Q = -2.90$ MeV) reactions have been determined by measuring the activity induced in samples

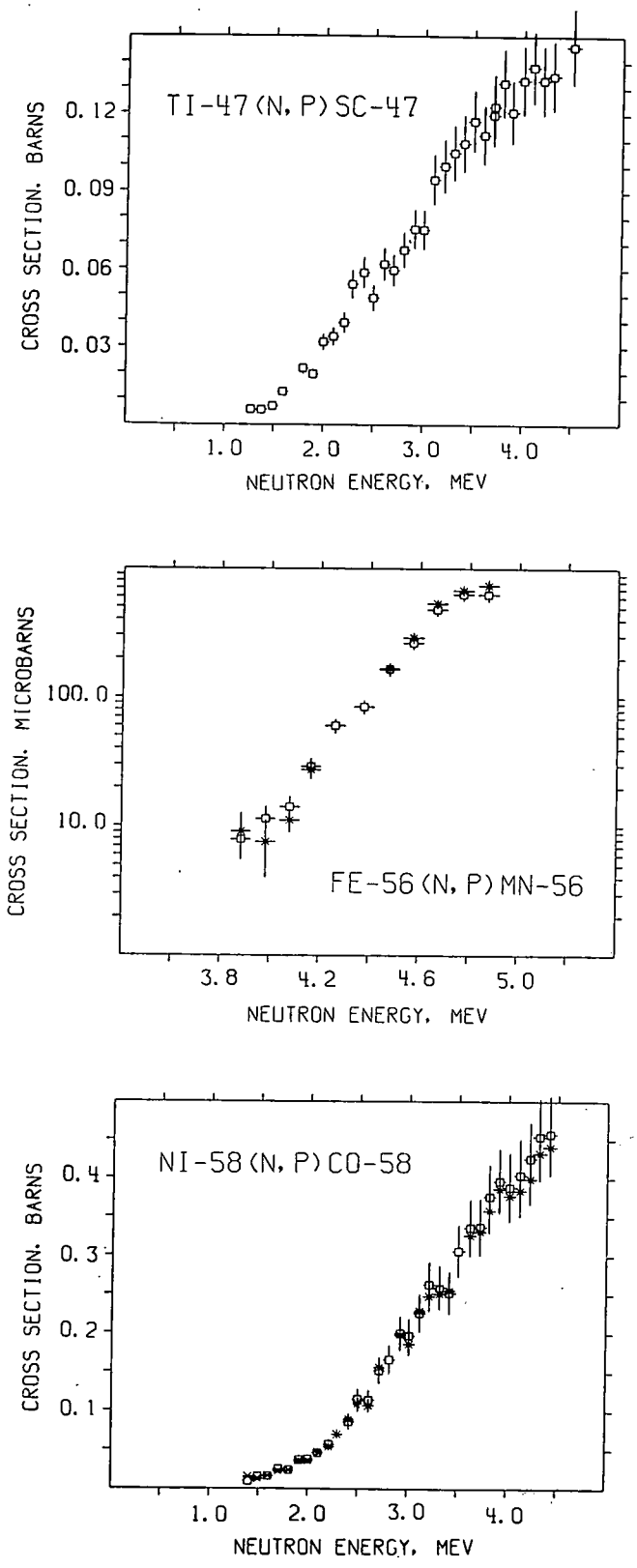

of titanium, nickel and iron irradiated by fast neutrons.

Targets of lithium metal evaporated on tantalum cups were bombarded with proton beams from the Fast Neutron Generator to generate fast neutrons via the $^{7}Li(p,n)^{7}Be$ reaction. The samples used were 1 in. diam metal disks of various thicknesses. These disks were taped to the container of a methane gas ionization chamber used as a fission counter and this assembly was placed within a few inches of the target. The relative neutron exposures for all the samples were deduced from the recorded fissions and the $^{235}U(n,f)$ or $^{238}U(n,f)$ cross sections.

The relative activities of the neutron irradiated samples were measured by detecting the following gamma rays with both lithium-drifted germanium and sodium iodide scintillation detectors:

^{47}Sc: 0.16 MeV gamma ray (3.4 day half life)

^{58}Co: 0. 51 and 0.81 MeV gamma rays (71 day half life)

^{56}Mn: 0.84 MeV gamma ray (2.58 hour half life)

A few of the titanium and nickel samples received long neutron exposures to induce sufficient activities for absolute activity determinations by coincidence counting. The ^{47}Sc activities were measured by β-γ coincidence counting while the ^{58}Co activities were measured by γ-γ (0.51–0.81 MeV) coincidence counting. The activities of all the other samples were then normalized relative to the activities of these "standard" samples. Although no iron samples were calibrated by coincidence counting, the iron sample activities could be related to the nickel sample activities by means of a small correction for the difference in gamma-ray detection efficiencies at 0.81 and 0.84 MeV.

Figure I-6-1 summarizes the results of this work. Corrections for geometric effects and for second-group neutrons from the $^{7}Li(p,n)^{7}Be^{*}$ reaction have been applied to these data; however no corrections for finite sample thicknesses have been determined as yet. These corrections will be small because the neutron transmissions for all the samples exceed 95 percent.

FIG. I-6-1. Cross Sections for the $^{47}Ti(n,p)^{47}Sc$, $^{56}Fe(n,p)^{56}Mn$, and $^{58}Ni(n,p)^{58}Co$ Reactions. Box Data Symbols Represent Measurements Made with a Lithium-Drifted Germanium Detector while Cross Data Symbols Correspond to Measurements Made with a Sodium Iodide Scintillation Detector. *ANL Neg. No. 116-790 Rev. 1.*

I-7. Utilization of Measured and Calculated Titanium Cross Sections in the ENDF/B Evaluated File

A. B. Smith and E. M. Pennington

The Evaluated Nuclear Data File-B (ENDF/B)[1] contains titanium (Material 1016). This evaluation was prepared by E. Pennington and was largely based upon prior evaluated data sets.[2] In order to make available the results of the latest work done at Argonne National Laboratory,[3] to make available other recent experimental values in useful form, and to provide for user requests for basic titanium cross section data, the previous titanium ENDF file was modified and updated to include the most recently measured and calculated values. Modifications were confined to incident energies above 0.1 MeV. Values at all lower incident energies were retained from the original file. The modification emphasized experimental values and used the model calculations to extrapolate the measured quantities where necessary. The file requires internal consistency which is not available in detail from the experimental values, primarily because of the different experimental resolutions employed in the various measurements. Thus, construction of the file requires appreciable extrapolation and interpolation of measurements. Generally, the modification procedures were as follows:

Total Neutron Cross Sections

Total cross section values in the energy range 0.1 to 1.5 MeV were taken explicitly from the recent experimental results determined at Argonne. Above an energy of 1.5 MeV experimental values from Schwartz,[4] Barschall et al.,[5] and Foster and Glasgow[6] were used. Above 10.0 MeV the measured values were extrapolated with model calculations using a carefully selected optical potential normalized to experimental values at lower energies. Where necessary the measured total cross sections were linearly interpolated in energy so as to assure that the energies of the partial cross sections were a sub-set of the total cross section energies. The resulting evaluated total cross section is indicated in Fig. I-7-1.

Elastic Neutron Scattering Cross Sections

The evaluated elastic scattering cross section was calculated directly from the evaluated total cross section and the non-elastic cross section. The non-elastic cross section was constructed from the various partial cross sections and linearly interpolated to the more detailed energies of the total cross section file. In this manner the resulting evaluated elastic cross section retained the detail of the high-resolution total cross section file and maintained internal consistency. When averaged over corresponding energy increments the evaluated elastic scattering cross sections were in good agreement with those recently measured here. The resulting elastic evaluated file is shown in Fig. I-7-1.

The elastic scattering angular distributions were expressed as $f_\ell(E)$ coefficients as defined by the ENDF format. At neutron energies of ≤ 1.5 MeV these coefficients were taken explicitly from the new experimental results. Additional experimental results were used at 3.2 MeV[6] and 4.0 MeV.[7] Model calculations, normalized to available experimental values, were used to interpolate the measurements and extrapolate the $f_\ell(E)$ coefficients to higher energies. The $f_\ell(E)$ values obtained in the above manner provide a good representation of the best available experimental information. However, they are generally based upon measurements made with approximately an order of magnitude poorer resolution than those employed in total cross section studies. Thus $f_\ell(E)$ values will not display as detailed an energy dependence as either the total or elastic cross sections of the file.

Inelastic Neutron Scattering Cross Sections

The inelastic neutron scattering cross sections were assumed entirely due to the even isotopes of titanium (88% abundant). At incident neutron energies of ≤ 1.5 MeV the experimental results of recent work here were explicitly used. Their components plus the cross sections due to the excitation of known states at 2.32, 2.40 and 3.2 MeV were extrapolated to incident neutron energies of $\sim$7.0 MeV using the calculation and the selected potential normalized to the measured values. At higher energies the continuum inelastic distributions and nuclear temperatures of the original evaluation were retained. The resulting partial and total inelastic neutron scattering cross sections are shown in Fig. I-7-2.

Non-Neutron Exit Channels

Radiative capture cross sections and (n,X) reaction cross sections, where $X \neq$ neutron, were retained from the original evaluation without modification since the present experimental results did not directly define these quantities. These non-neutron reaction cross sections were incorporated into the non-elastic cross sections used to obtain the elastic file as described above.

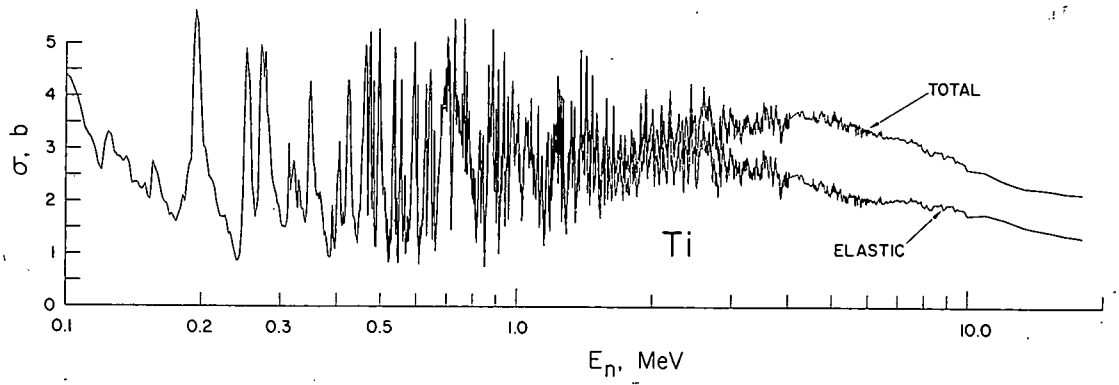

FIG. I-7-1. Evaluated Total and Elastic Scattering Cross Sections of Titanium, 0.1 to 18.0 MeV. *ANL Neg. No. 116-793.*

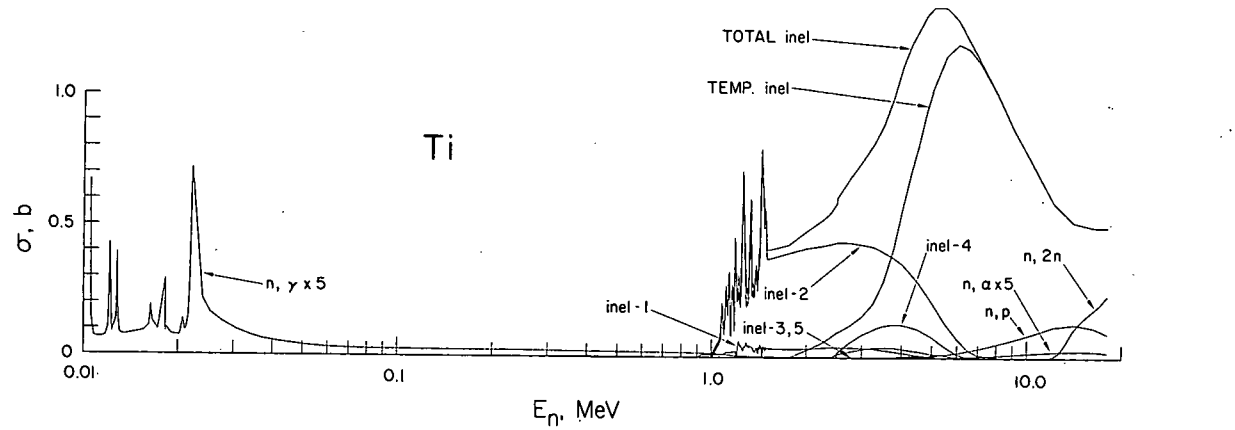

FIG. I-7-2. Evaluated Inelastic Scattering, (n,γ), (n,p), $(n,2n)$ and (n,α) Cross Sections of Titanium, 0.01 to 18.0 MeV. *ANL Neg. No. 116-792.*

Where necessary various partial cross sections were interpolated in energy-magnitude in a linear manner.

The revised and updated ENDF file deduced in the above manner was verified using the check routine CHECKER[1] and the physical content inspected with suitable graphical procedures. The final result is an evaluated file in the widely used ENDF format fully contemporary with available microscopic cross section information and largely meeting the needs of the initial user request.

REFERENCES

1. *Evaluated Nuclear Data File-B (ENDF/B)*, National Neutron Cross Section Center, Brookhaven National Laboratory. The format is defined in BNL-50066.
2. E. Pennington and J. Gajniak, *Compilation of ENDF/B Data for Magnesium, Titanium, Vanadium, Molybdenum and Gadolinium*, ANL-7387 (1968).
3. E. Barnard, J. A. M. DeVilliers, D. Reitmann, P. Moldauer, A. Smith and J. Whalen, *Fast Neutron Total and Scattering Cross Sections of Elemental Titanium*, Applied Physics Division Annual Report, July 1, 1969, to June 30, 1970 ANL-7710, pp. 7–9.
4. R. Schwartz et al., National Bureau of Standards (private communication). Numerical data available from the National Neutron Cross Section Center, Brookhaven National Laboratory.
5. H. Barschall et al., University of Wisconsin (private communication). Numerical data available from the National Neutron Cross Section Center, Brookhaven National Laboratory.
6. D. Glasgow and D. Foster, *Fast Neutron Total Cross Sections of Forty Four Elements*, HW-SA-2875 (1963). Numerical data available from the National Neutron Cross Section Center, Brookhaven National Laboratory.
7. R. Becker, W. Guindon and G. J. Smith, *Elastic Scattering of 3.2 MeV Neutrons from Many Elements*, Nucl. Phys. **89**, 154 (1966).
8. M. Walt and H. Barschall, *Scattering of 1-MeV Neutrons by Intermediate and Heavy Elements*, Phys. Rev. **93**, 1062 (1954).
9. J. Towle, Atomic Weapons Research Establishment (private communication). Numerical data available from the National Neutron Cross Section Center, Brookhaven National Laboratory.

I-8. Empirical Formula for Interpolation of Tabulated Photon Photoelectric Cross Sections

D. L. Smith

Photoelectric absorption is the predominant interaction between photons and matter for low-energy photons with energies exceeding the required threshold for ejection of the most weakly bound electrons of the atoms in the medium. Photoelectric cross sections, which are difficult to measure or calculate, are required for radiation-shielding applications and in the analysis of photon-energy deposition in reactor cores and in nuclear explosion environments.

The available photoelectric cross sections, which are evaluated compilations including both experimental and calculated values, usually appear in tabular form. The user must interpolate to obtain cross sections for energies other than the tabulated values. It has been found that the empirical formula

$$\sigma_T(E_\gamma) = \exp\left[p_1 - \left(\sum_{i=2}^{k} p_i E_\gamma^{i-2}\right) \ln E_\gamma\right] \quad (1)$$

is very useful for interpolation of photon photoelectric cross tabulations. Sets of parameters $\{p_i\}$ which yield good fits of Eq. (1) to tabulated cross sections for various atomic numbers Z and photon energy intervals can be generated by least-squares analysis. The number of adjustable parameters required for a particular fit varies with Z, the photon energy interval, and the desired precision.

A collection of sets of parameters $\{p_i\}$ which provide fits of Eq. (1) to the total photoelectric cross sections compiled recently by Storm and Israel[1] for Z = 1 to 100 and E_γ = 1 keV to 100 MeV has been generated by this procedure. The agreement between the fitted curves and the tabulated values is better than ±3% throughout. This collection is available in Ref. 2.

References

1. E. Storm and H. I. Israel, *Photon Cross Sections from 1 keV to 100 MeV for Elements Z = 1 to Z = 100*, Nucl. Data Tables **A7**, p. 565 (1970).
2. D. L. Smith, *Empirical Formula for Interpolation of Tabulated Photon Photoelectric Cross Sections*, ANL-7796 (1971).

I-9. Thick Target Yield for the Ta(p,n) Reaction

J. W. Meadows

Neutron production in target backings and defining aperatures by the (p,n) reaction can be a significant source of background for proton energies above ~5 MeV. An elementary calculation indicates a thick target neutron yield of ~10^6/sr-μC for 7 MeV protons striking a heavy metal target such as gold or tantalum. This can be compared with the 0 deg yield of a nominal 25 keV lithium target which is only ~2×10^6/sr-μC.

The following experiment was carried out to provide corrections for a specific experiment. However, the results have been recalculated to give neutron yields at 0 deg. Although these results may be in error by as much as 25% due to uncertainties in the solid angle and in the neutron spectrum, they are still useful in estimating the seriousness of this source of background.

The proton target was a clean, new, tantalum cup. Neutrons were detected by a fission ion chamber at 0 deg which subtended an angle of 17 deg and contained 93% ^{235}U (0.196 mg/cm^2) or 99.5% ^{238}U (1.04 mg/cm^2). The incident proton beam was measured with a current integrator and all measurements were normalized to the same total charge.

The experimental results are shown in Fig. I-9-1. The 0-deg neutron yield, shown in Fig. I-9-2, was calculated assuming a constant ^{235}U fission cross section of 1.25 b. Comparison of the ^{235}U and ^{238}U fission rates shown in Fig. I-9-2 indicates that ~75% of the neutrons had energies below 1.5 MeV.

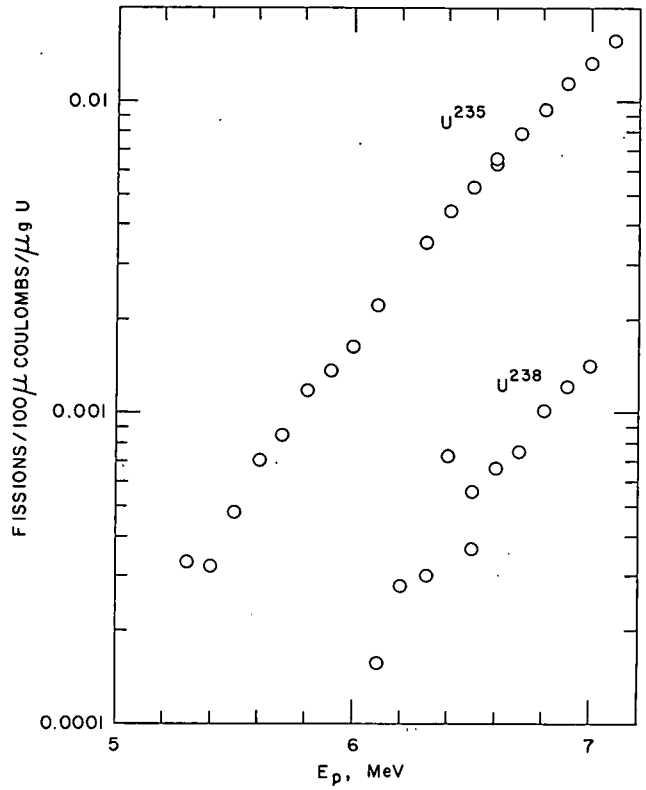

FIG. I-9-1. The Thick Target Yield at 0 Deg for the Ta(p,n) Reaction. *ANL Neg. No. 116-927.*

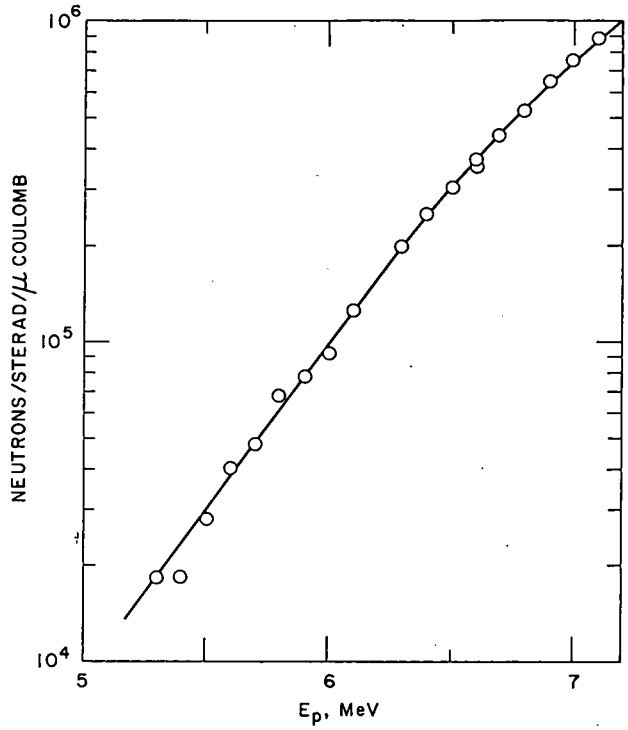

FIG. I-9-2. The Relative ^{235}U and ^{238}U Fission Rates for Neutrons from a Thick Tantalum Target. *ANL Neg. No. 116-926.*

I-10. Relative Yields of the Neutron Groups from the ^{7}Li(p,n)^{7}Be,^{7}Be* Reactions

J. W. MEADOWS

The ^{7}Li(p,n)^{7}Be reaction is a convenient and widely used source of neutrons. Below proton energies of 2.38 MeV the reaction goes only to the ^{7}Be ground state and the neutrons are monoenergetic in the center of mass system. Above 2.38 MeV the reaction can also go to the first excited state of ^{7}Be and yield a second neutron group. However the third neutron group does not appear until 7.07 MeV so the reaction is still useful for monoenergetic experiments providing the relative intensities of the first and second groups are known. Intensity ratios have been measured in this energy range[1,2] but the estimated errors range from ~6% near 3 MeV to ≥15% near 7 MeV. This paper presents some additional measurements. The choice of angles was based on the intended use of the reaction as a neutron source.

The two neutron groups were separated by time-of-flight methods. Neutrons were produced by proton bursts approximately 2 nsec long striking a lithium target and were detected at a distance of ~6 m. The two groups were completely separated over the entire energy range. The target was a thin layer of metallic lithium evaporated onto a tantalum backing. Most of the data were taken with target thicknesses of ~75 keV as measured at the ^{7}Li(p,n)^{7}Be threshold. The average proton beam current was only 1–2 μamps so the targets were stable for long periods. The beam current was monitored by a current integrator and the yields of the several targets were measured at 4 MeV relative to a long counter.

The neutron detector was a hydrogeneous liquid scintillator in a glass container 2.5 cm in diam by 2.0 cm thick. Bias levels were set to reject all neutrons with energies less than 950 keV. The shape of the de-

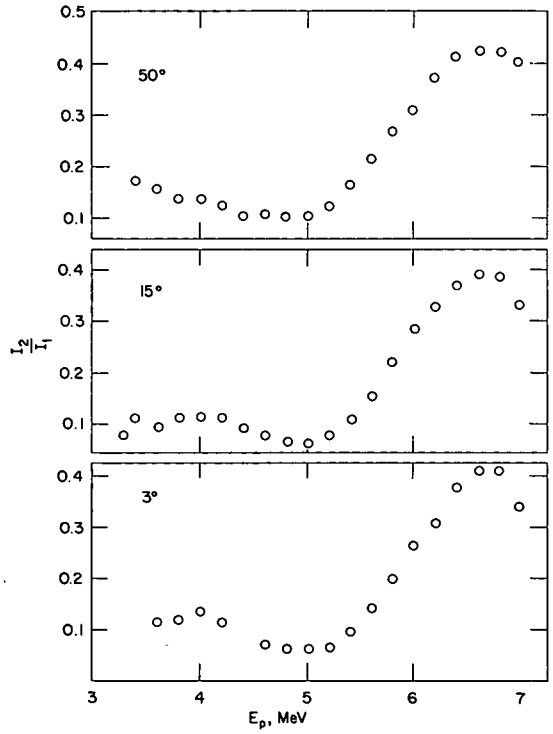

FIG. I-10-1. Ratios of the Yields of the Neutron Groups from the $^7Li(p,n)^7Be$ and $^7Li(p,n)^7Be^*$ Reactions. *ANL Neg. No. 116-848.*

tector response was computed for a single scattering event with a 950 keV bias plus an approximate correction for double scattering. For neutron energies below 2000 keV (3.6 MeV proton energy) the detector response varies rapidly with neutron energy, bias level, and the overall gain of the detector electronics. Data in this region can be considerably in error. Above 2000 keV the detector response is dominated by the shape of the n,p scattering cross section and is relatively insensitive to the above factors. For this reason the detector response contributes very little to the errors in the relative yields of the two neutron groups.

Figure I-10-1 shows the relative yields of the neutron groups (I_2/I_1) at 3, 15 and 50 deg. The error associated with each data point above 3.6 MeV is 5% and

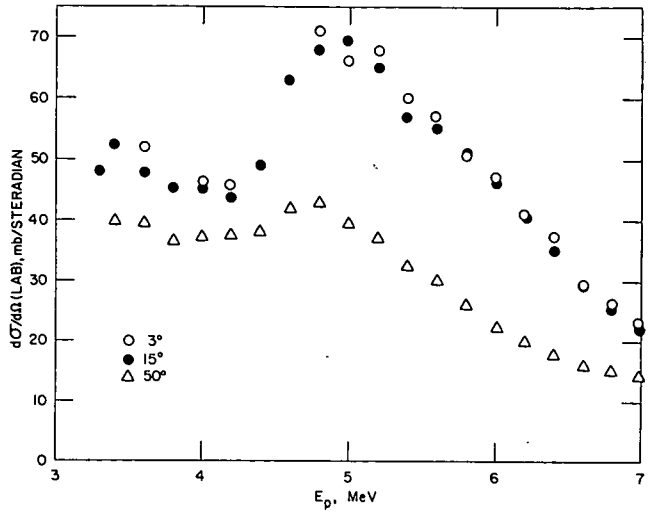

FIG. I-10-2. Differential Cross Sections for the Total Neutron Yield of the $^7Li(p,n)^7Be$ Reaction. *ANL Neg. No. 116-847.*

is largely due to the counting statistics and the background subtraction.

The differential cross sections for total neutron yield are shown in Fig. I-10-2. These results were obtained by normalizing each measurement to the integrated proton current. The results were normalized at 4 MeV to the 0 deg results of Bevington et al.[1] which were normalized to the results of Gabbard et al.[3] at lower energies. The errors due to counting statistics, background subtraction, and normalization are estimated to be $\lesssim 10\%$. In addition the detector response curve can contain a systematic error which may be as large as 10% at 7 MeV.

REFERENCES

1. P. R. Bevington, W. W. Rolland and H. W. Lewis, *Relative Yields of Neutron Groups from the $^7Li(p,n)^7Be$, $^{7*}Be$ Reactions*, Phys. Rev. **121**, 871 (1961).
2. R. R. Borchers and C. H. Poppe, *Neutrons from Proton Bombardment of Lithium*, Phys. Rev. **129**, 2679 (1963).
3. F. Gabbard, P. R. Davis and T. W. Bonner, *Study of the Neutron Reactions $^6Li(n,\alpha)^3H$, $^{19}F(n,\gamma)^{20}F$, and $^{127}I(n,\gamma)^{128}I$*, Phys. Rev. **114**, 201 (1959).

I-11. Note on the Prompt Fission Neutron Spectra of Uranium-235 and Plutonium-239[1]

A. B. SMITH

Some recent macroscopic and spectrum-averaged measurements and some analyses of fast critical experiments indicate an uncertain knowledge of the prompt fission neutron spectrum.[2] It has been suggested that the average energy of the prompt fission neutron spectrum of ^{235}U is $\geq 10\%$ harder than previ-

ously deduced from a number of microscopic measurements[3] and that the average energy of the ^{239}Pu spectrum is appreciably nearer that of the ^{235}U spectrum than indicated by many microscopic measurements. The effect of such fission spectrum uncertainties on fast-reactor parameters has been extensively studied.

The microscopic experiments reported herein had the limited objective of: a) testing the validity of the previously reported microscopic prompt fission neutron spectrum of ^{235}U and providing a basis for comparison with macroscopic results, and b) determining the ratio of the average prompt fission neutron energy of ^{239}Pu to that of ^{235}U. Generally, the experimental rationale was the definition or the resolution of discrepancy rather than a definitive and comprehensive spectral study.

Ratio of Average Fission Neutron Energy of ^{239}Pu to ^{235}U

The relative ratio of the number of ^{239}Pu fission neutrons to those of ^{235}U was determined as a function of fission neutron energy from ~0.3 to ~8.0 MeV. Interpretation of the measured ratios was based upon the assumption that both ^{235}U and ^{239}Pu spectra are of the form

$$N(E) \propto E^n \exp(-E/T), \tag{1}$$

where n is a single constant for ^{235}U and ^{239}Pu and T is a "temperature" that can vary with isotope. It follows from Eq. (1) that

$$\ln R = A + BE, \tag{2}$$

where R is the energy-dependent ratio of ^{239}Pu-to-^{235}U fission neutrons and A and B are constants. Further, B can be expressed as a function of the temperature [T of Eq. (1)] of the ^{235}U and the ^{239}Pu spectra by the form

$$B = \frac{1}{T(235)} \frac{T(235)}{T(239)} - 1, \tag{3}$$

where $T(235)$ and $T(239)$ refer to ^{235}U and ^{239}Pu neutron temperatures, respectively. A and B of Eq. (2) were determined from a least-squares fit to the measured R distributions. Individual datum points were weighted inversely proportional to the square of their respective standard deviations. A typical fit to an experimental distribution is shown in Fig. I-11-1. The average $\bar{B}$ values for a given incident energy and bias group were calculated from the results of all eight detectors and an RMS deviation from the average was determined.

The ratio of temperatures, $T(239)/T(235)$, and average fission-neutron energies, $\bar{E}(239)/\bar{E}(235)$, follows directly from Eq. (3). Using a value of $T(235) = 1.297$ MeV and the $\bar{B}$ values derived from the measurements,

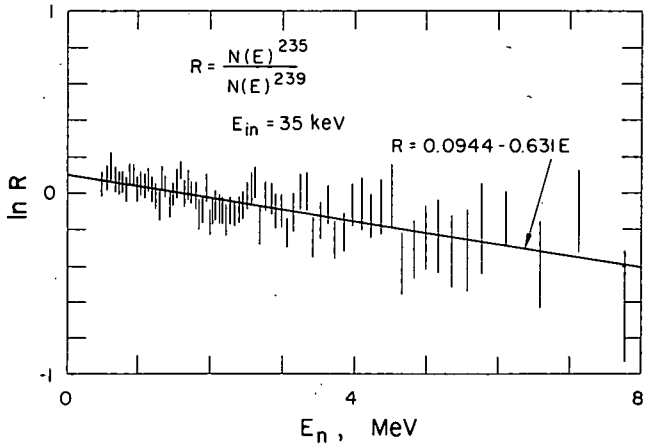

Fig. I-11-1. Linear Fit to the Logarithm of the Measured Relative Ratio of the ^{239}Pu Fission Spectrum to that of ^{235}U. Vertical Bars Indicate Experimental Uncertainties: *ANL Neg. No. 116-434.*

the ratios $\bar{R} = \bar{E}(239)/\bar{E}(235)$ were calculated. Relatively large changes in the reference $T(235)$ value had only a small effect on $\bar{R}$ (a 10% shift in T changes $\bar{R}$ by about 1%). The individual $\bar{B}$ values were further combined, weighted each by the inverse of its RMS deviation to obtain a "grand" average $\bar{B} = -0.0543$. This $\bar{B}$ value leads to $\bar{R} = \bar{E}(239)/\bar{E}(235) = 1.075$ with an estimated uncertainty of 1.5 to 2.0%. No significant dependence of $\bar{R}$ on incident neutron energy was noted over the incident neutron energy range of 35 to 400 keV in the present experiments.

Uranium-235 Fission Neutron Spectrum to Energies of 1.6 MeV

The calibrated response of the detectors was used to deduce the shape of the ^{235}U prompt fission neutron spectrum to fission neutron energies of less than 1.6 MeV. Results typical of a number of measurements are indicated by the solid datum points shown in the upper portion of Fig. I-11-2. A numerical measure of the spectral shape was determined assuming the distributions were of Maxwellian form. Each measured distribution was fitted, by the method of least-squares, with the expression

$$\ln \frac{N(E)}{\sqrt{E}} = \alpha + \beta E, \tag{4}$$

where β is the inverse of the Maxwellian temperature. One such fit is indicated by the curve in the upper portion of Fig. I-11-2. The subjectively weighted average beta value obtained from all the measurements was $\beta = -0.710 \pm 0.070$ MeV^{-1}. With no judgement of quality, the uncertainty was increased by a factor of about 2. There was no observable dependence of beta on incident neutron energy (~35 and ~400 keV inci-

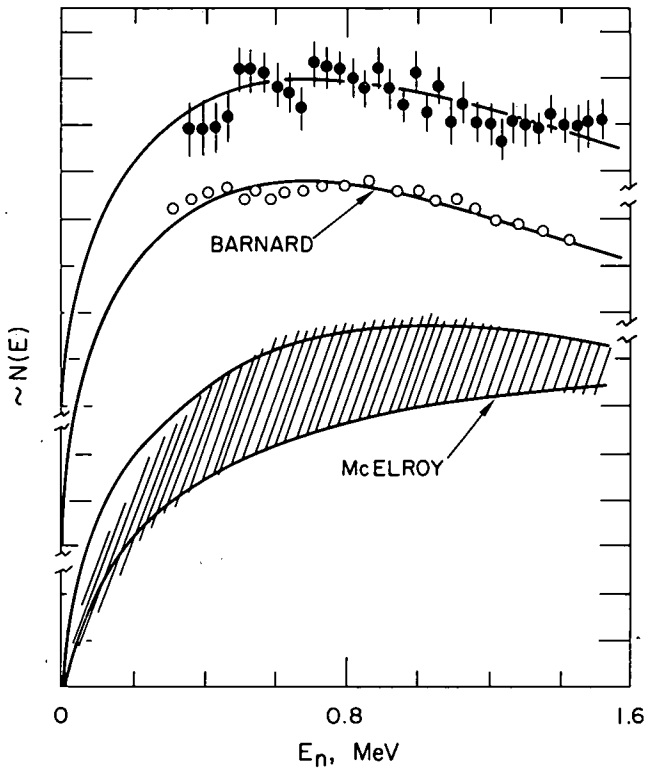

FIG. I-11-2. Uranium-235 Prompt-Fission-Neutron Spectra in the Interval 0.0 to 1.6 MeV. The Solid Datum Points are Illustrative of a Number of Results of the Present Work. The Open Circles Represent the Microscopic Results of Barnard et al.[3] The Shaded Band Indicates the Spectra Implied by McElroy[4] from Macroscopic Fission-Averaged Cross Section Measurements. Solid Curves are the Results of Fitting Maxwellian Distributions to the Respective Values as Described in the Text. Normalization of the Three Distributions is Arbitrary. *ANL Neg. No. 116-474.*

dent neutron energies). The microscopic data of Barnard et al.[4] were interpreted in an identical manner and over the same energy interval as employed in the present work. Their results and the interpretation, indicated by the open datum points and curve in the center of Fig. I-11-2, led to a value of $\beta = -0.737$ MeV^{-1}. The value of beta derived from the Barnard data and that of the present experiment imply temperatures somewhat larger than those usually deduced from a wider energy range. No significance is attached to this difference due to the small energy range employed (~0.3 to 1.6 MeV). The present beta values and associated uncertainties are consistent with an "accepted" microscopic temperature of ~1.297 MeV.

The present results to 1.6 MeV are in contrast to those implied by McElroy[5] from fission-averaged cross section measurements. McElroy arrives at a prompt fission neutron spectrum, indicated by the shaded band in the lower portion of Fig. I-11-2. The deduced beta values corresponding to the maximum and minimum limits of the McElroy band were: $\beta = -0.493$ MeV^{-1} and $\beta = 0.338$ MeV^{-1}, respectively. These macroscopic beta values are not consistent with those derived from the present work, even accepting the largest uncertainties.

REFERENCES

1. A. B. Smith, *Note on the Prompt-Fission-Neutron Spectra of Uranium-235 and Plutonium-239*, Nucl. Sci. Eng. **44**, 439 (1971).
2. J. Grundl, *Fission Neutron Spectra, Macroscopic and Integral Results*, Proc. Conference on Neutron Standards and Flux Normalization, October 21–23, 1970, Argonne, Illinois. AEC Symposium Series #23, pp. 417–436.
3. T. Weidling, *Microscopic Fission Neutron Spectrum Measurements*, Proc. Conference on Neutron Standards and Flux Normalization, October 21–23, 1970, Argonne, Illinois. AEC Symposium Series #23, pp. 437–451.
4. E. Barnard, A. T. G. Ferguson, W. R. McMurray and I. J. Van Heerden, *Time-of-Flight Measurements of Neutron Spectra from the Fission of ^{235}U, ^{238}U and ^{239}Pu*, Nucl. Phys. **71**, 238 (1965).
5. W. McElroy, *Implications of Recent Fission-Averaged Cross Section Measurements*, Nucl. Sci. Eng. **36**, 109 (1969).

I-12. Polarization in the Elastic Scattering of 2 MeV Neutrons from Intermediate Weight Nuclei

S. A. Cox

One of the best methods for describing the interaction of a neutron with a nucleus utilizes the optical model combined with Hauser-Feshbach and coupled channel theory. The optical model includes a number of parameters whose values depend on the specific nucleus. Once this parameter set has been determined the details of the interaction can be calculated with high accuracy. Since the polarization of the scattered neutrons is generally quite sensitive to the particular choice of parameters it can be a valuable aid in their determination.

In a previous report[1] we presented the results of a

comprehensive survey of 29 nuclei representative of most of the periodic table. The incident energy was in the vicinity of 1 MeV. Data were taken at 8 angles using a partially polarized neutron beam emitted at 51 deg from the Li(p,n) reaction. Both the differential scattering across section and polarization were measured at each angle. A scan of a number of optical model parameters was made in order to achieve the best theoretical fit to the data. By demanding that the final parameter set fit both the differential scattering cross section and the polarization some of the ambiguities in the choice of optical model parameters are removed.

In the present experiment data were taken at 2 MeV incident neutron energy. Because of the more complicated structure in the angular distribution of scattering and polarization the data were taken at 16 angles. The experimental procedure was the same as in the previous report except for the addition of some shielding. Also since the Fast Neutron Generator[2] is capable of producing 8 MeV protons, measurements can be made at much higher neutron energies. With the Li(p,n) reaction neutrons emitted at 51 deg can be produced at an energy of 5.6 MeV.

In the previous report it is pointed out that the periodic table separated into three rather distinct regions according to the difficulty or ease with which a good theoretical fit could be achieved. In general for nuclei with A $<$ 80 it is not possible to achieve a good fit to both the differential scattering cross sections and polarization although either one could be fitted separately. In the region from A $\approx$ 80 to A $\approx$ 125 it is relatively easy to obtain a good simultaneous fit to the differential cross section and polarization for all nuclei studied. For nuclei with A $>$ 125 the data again become more difficult to fit.

It is interesting to compare the present data at 2 MeV with the previous data at 0.870 MeV in the three regions just described. In Fig. I-12-1 the results for titanium, cadmium, and gold are given for a neutron energy of 0.870 MeV. Titanium typifies the region below A = 80 where theoretical fits are difficult. Cadmium is a typical example of the intermediate region where fits are easily achieved; and gold represents the region above A = 125 where fits are again more difficult. In Fig. I-12-2 the 2 MeV results are given for the same three elements. The solid and dashed curves in both figures are optical model calculations. In the case of titanium at 0.870 MeV the solid curve represents the best fit to the scattering cross section and the dashed curve the best fit to the polarization data. The optical model parameters required are quite different. For example the real potential depth is 45 MeV for the solid curve and 50 MeV for the dashed curve. A good fit is easily achieved for cadmium. In the case of gold the fit to the polarization is vastly improved by increasing the imaginary well diffuseness parameter from 0.50 (solid curve) to 1.00 F (dashed curve). The fit to the scattering data is only slightly improved.

The optical model curves given in Fig. I-12-2 are obtained using the same parameter sets as for Fig. I-12-1. Only the neutron energy is changed. Several features are immediately apparent. The parameter set which yields a good fit to the titanium differential scattering cross section at 0.870 gives a poor fit at 2.000 MeV. The parameter set which results in a poor fit at 0.870 MeV still gives a poor fit at 2.000 MeV. Both parameter sets give poor fits to the polarization data. There are two reasons why titanium might be difficult to fit. It lies in a region of the periodic table (A = 48) where there is still some resonance structure exhibited in the

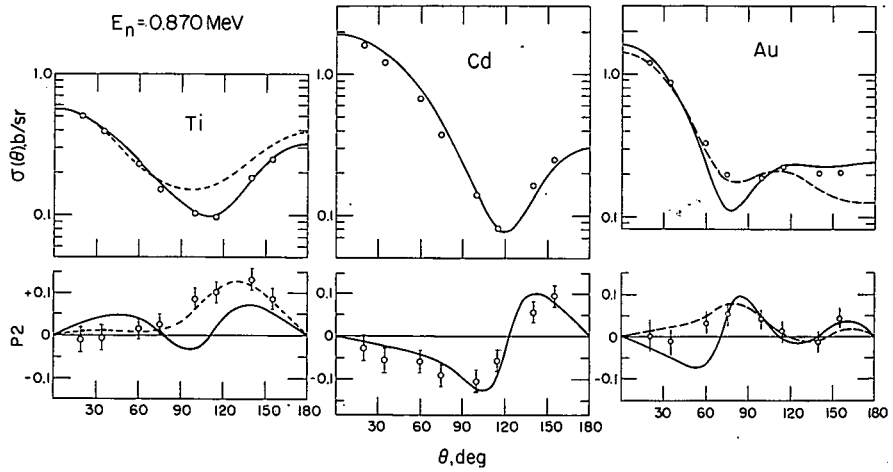

FIG. I-12-1. Differential Elastic Scattering Cross Sections and Polarizing Power Data (Open Circles) Compared With Optical Model-Hauser Feshbach Calculations (Solid Curve) for 0.870 MeV Neutrons Incident on Titanium, Cadmium, and Gold. *ANL Neg. No. 113-2481.*

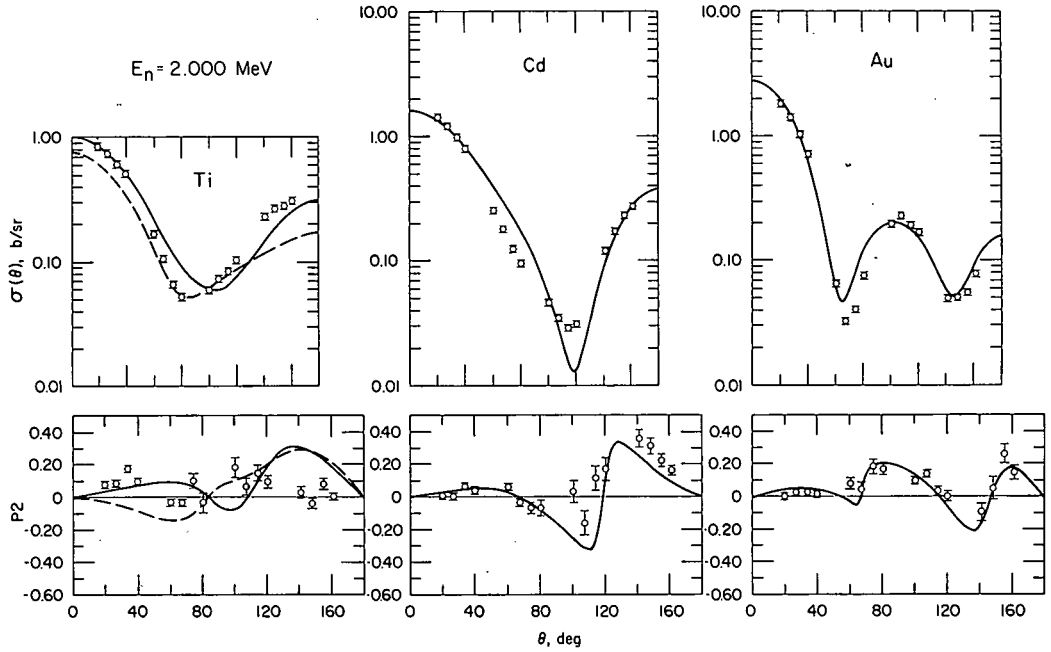

FIG. I-12-2. Differential Elastic Scattering Cross Section and Polarizing Power Data (Open Circles) Compared With Optical Model-Hauser Feshbach Calculations (Solid Curve) for 2.000 MeV Neutrons Incident on Titanium, Cadmium, and Gold. The Optical Model Parameters Are the Same as Those Used for Fig. I-12-1. *ANL Neg. No. 116-920.*

excitation function for the scattering cross sections. In addition the region of the periodic table in the vicinity of A $\approx$ 50 contains many highly deformed nuclei. The combination of both effects would make it especially difficult to obtain a good fit to the data. The situation is more favorable in the cases of cadmium and gold. The parameter sets obtained at 0.870 MeV yield good fits to the differential cross section data and very good fits to the polarization data. Considering the detailed structure in the differential cross section and polarization for gold the fit is remarkably good.

At present, data have been taken at 2.000 MeV for 18 other elements: aluminum, vanadium, cobalt, copper, zinc, selenium, yttrium, zirconium, niobium, molybdenum, silver, indium, tin, antimony, tantalum, tungsten, gold and lead. It is hoped and expected that the analysis of the data for these and other elements at 2.00 MeV and higher energies will result in an improved parameter set for neutron interaction calculations and contribute to an understanding of the neutron-nucleus interaction.

REFERENCE

1. S. A. Cox and E. E. Dowling Whiting, *Polarization in Elastic Neutron Scattering*, Reactor Physics Division Annual Report, July 1, 1968 to June 30, 1969, ANL-7610, pp. 9–14.
2. S. A. Cox, *The Fast Neutron Generator (FNG) Facility*, Applied Physics Division Annual Report, July 1, 1969, to June 30, 1970, ANL-7710, pp. 265–266.

I-13. Spontaneously Fissioning Isomer of ^{236}U

J. W. MEADOWS and W. P. POENITZ

The existence of an isomeric state in ^{236}U which decays by spontaneous fission with a half-life of 85–115 nsec has been proposed by Pilcher and Brooks.[1] From the figure given in that report, at least 1% of the apparent total ^{235}U fission events induced by 30-keV incident neutrons are due to such a spontaneously fissioning isomer of ^{236}U. This amount would be of practical importance in absolute and relative fission cross section experiments, fission neutron spect measurements, and other fission studies that use time-of-flight method for background suppression and spectroscopic purposes. Therefore, direct search for

this isomer has been carried out using a fast-ionization fission chamber with a time resolution of about 3 nsec. The measurement was made at an incident neutron energy of 30 keV using the kinematic collimation of the neutron beam close to the threshold energy of the $^{7}Li(p,n)^{7}Be$ reaction. The general room background was measured by positioning the fission counter outside the neutron beam.

Of a total of 3.7×10^{4} fission events observed in the present experiment, only 15, 8, 12 and 9 fission events were found in 100-nsec intervals, 100, 200, 300 and 400 nsec, respectively, after the prompt-fission peak. The total relative number of events outside the prompt peak was about 0.12%, approximately 75% of which were attributed to the measured room background. Thus, the contribution to observed ^{235}U neutron-induced fission of a possible spontaneously fissioning isomeric state in ^{236}U is less than 3×10^{-2}%. This is one to two orders of magnitude lower than indicated by the work of Pilcher and Brooks[1] and too small to significantly affect fission cross-section measurements using time-of-flight techniques.

Reference

1. J. V. Pilcher and F. D. Brooks, *Spontaneously Fissioning Isomers of Uranium-236 and -239*, Annual Report of Southern Universities Nuclear Institute, SUNI-14, Faure, Republic of South Africa (1970).

I-14. Interpretation, Intercomparison and Evaluation Methods for Neutron Cross Sections

W. P. Poenitz

Introduction

It appears that many of the data evaluations presented in the past use contradictory interpretations of data and various evaluation concepts which may be questioned with regard to their validity. Thus these evaluations, most notably those for ^{238}U, contribute further to the confusion in absolute cross sections. It is the goal of this paper to interpret data on the basis of their experimental origin and to discuss evaluation methods based on this concept. As an example, an evaluation of the absolute cross section data of $^{235}U(n,f)$, $^{238}U(n,\gamma)$, $^{197}Au(n,\gamma)$, and $^{6}Li(n,\alpha)$ and the ratios $\sigma_\gamma(^{197}Au)/\sigma_f(^{235}U)$, $\sigma_\gamma(^{238}U)/\sigma_f(^{235}U)$ and $\sigma_\alpha(^{6}Li)/\sigma_f(^{235}U)$ has been carried out on the basis of these considerations. The energy range from 25–1000 keV has been considered. Some of the cross sections included in this evaluation are of importance to fast reactor systems, the rest are standard cross sections.

A standard cross section is at the present time as poorly established as was, for example, the length standard when it was defined as a forty-thousandth of the circumference of the earth. Every new measurement may change the standard and thus violate the meaning of "standard." Even worse! not only one standard cross section is in use but several, including $n,n)$, $^{10}B(n,\alpha,\gamma)$, $^{6}Li(n,\alpha)$, $^{197}Au(n,\gamma)$ and $^{235}U(n,f)$. Those named have been accepted in recent years as standards justified by their practical use in experiments.[1] Restriction to these cross sections as standards supplies a feasible means of measuring and comparing cross sections of different types of reactions.

Because a standard cross section is determined by many absolute measurements, the interpretation and evaluation of such data becomes a vital part in establishing the standard cross section to be used. These standards influence in turn the selection of cross sections to be used in reactor evaluations and design.

Classification and Interpretation of Data

In order to incorporate a proper set of data in a cross section evaluation, clarification and classification of the available experimental data are needed.

RELATIVE DATA

Cross section values have been measured "relatively" if the ratio between two cross sections has been determined. Such data should be compiled separately to obtain proper ratio values between the two cross sections. If several cross sections have been measured in an experiment using the same experimental technique for all, or if they have been measured relative to the same standard cross section, proper ratios can be extracted for any combination of the two cross sections involved.

ABSOLUTE DATA

Cross section values have been measured "absolutely" if no other cross sections were involved. Exceptions are usually made if thermal cross sections or

resonance parameters are used which are known with an accuracy superior to that in the fast energy range. Those which have been measured relative to the $H(n,n)$ cross section are accepted as equivalent to absolute data. The justification of this lies in the high accuracy with which the hydrogen scattering cross section can be determined by the transmission method. On the other hand there is no justification to consider such data superior to other absolute data because obviously there are difficulties in obtaining proper relative data using the $H(n,n)$ cross section to eliminate the neutron flux.

SHAPE AND MAGNITUDE OF DATA

Absolute cross section data as well as ratio data usually contain two different kinds of information. The "shape" of the cross section or the ratio is the variation of these quantities as a function of energy. The "magnitude" depends on many quantities which are usually common to all measured values. The inevitable conclusion is that a single absolute cross section measurement supplies the same amount of information, as far as the amplitude of the cross section is concerned, as a measurement consisting of many values at different energies. The latter data supply, however, the additional information about the shape of the cross section. The equivalence of a "single-energy-point" measurement and a "many-energy-point" measurement for the magnitude of a quantity is important for a proper compilation of the data. It suggests the evaluation of the shape of a cross section or a ratio separately from its magnitude.

INDEPENDENCE OF DATA

In order to obtain a proper and fair answer in an evaluation of a cross section or a ratio, there has to be assurance that the different input data sets are independent of one another. This rule has been violated in nearly all recent cross section evaluations, especially in those for $^{238}U(n,\gamma)$. If the input data in an evaluation are thus improperly manipulated, the output information will reflect this manipulation and not the present knowledge of a cross section.

Selection of Data and Evaluation Methods

Completely opposing concepts have been used for the selection of input data in cross section compilations. In some evaluations one cross section has been declared as the ultimate in cross section measuring technology and other data have been admitted or eliminated as input data, or have been renormalized to the preferred cross section. In other compilations all existing data have been admitted, unfortunately even those which were superceded by remeasurements in the same laboratories using the same experimental technique. The problem of selecting input data appears to require a different approach. Some rules are more or less obvious: Data should be replaced by re-evaluations of previously published data if such re-evaluated values are available from the experimentors. If an experiment has been repeated in the same laboratory employing the same basic technique, the new data should be used. The rest of the data should be admitted, properly weighted. However, in practical examples it will turn out that some data can be rejected since they are in disagreement with a clear majority of other data by several error bar magnitudes. An example is the older measurements of the fission cross section of ^{235}U which are higher by up to 60% than the values obtained from the present evaluation. To eliminate some of the older data appears to be justified by the observation of a systematic trend of the measured values which reflect certain features of the considered reaction. For example, some of the older measured fission cross sections of ^{235}U and some of the capture cross sections of ^{197}Au appear to be too large. The reason most probably lies in the high thermal cross sections and the high resonance integrals of these materials.

It is surprising that evaluations of cross sections often are based on personal opinion or a belief of an evaluator about certain cross section experiments. Some of the evaluations using dependent input data justified this action by emphasizing the benefit from consistency with other previously selected data. Consistency between different cross sections is a need, especially in reactor calculations;[2] however, there are proper methods to obtain such consistency by means other than to impress one selected cross section on all others. An example of a proper internally consistent evaluation is that employed for σ_f, σ_γ, ν, η, and α data at thermal neutron energy.

An evaluation method should be based on a well-defined mathematical procedure to obtain best-values of a cross section. The evaluation of a single cross section should include all available absolute data which are independent of one another. Inclusion of relative data would require extending the data evaluation to the reference cross section. This means that a simultaneous evaluation of absolute cross sections and their ratios is required. For fast neutron cross sections such simultaneous evaluation has been carried out by Sowerby et al.[3] and Poenitz.[4] An evaluation of data to be used in reactor calculations should include all major cross sections needed in these calculations and th[illegible] ratios. Such evaluation will yield more accurate resu[illegible] if the standard cross sections are included.

The next step after the selection of independent input data properly classified and separated as absolute,

relative, shape, or magnitude data is the assignment of weights to the input data. In some evaluations the squares of the inverse error bars are used as weight. In others, the quoted error bars have been enhanced after considerations of the agreement or disagreement of the given data with data from other laboratories or the experimental techniques employed in their measurement. It has been noted recently that all such measures of the confidence in a set of data are ambiguous.[4] On the other hand they supply some information about the reliability of data and should be combined in a proper way to obtain a weight for the input data in a cross section evaluation.

The quoted error bars reflect the confidence limit according to the different contributions of quantities involved in the computation of the result. It must be emphasized that in most cases the quoted error bars are the 68 % probability limits only, obtained by applying an error evaluation method which is valid for statistical quantities. It would appear improper to interpret data presented by an experimentor so that the true value is expected to be his quoted value or "close" to it, and to label other values as "right" or "wrong," depending on whether agreement or disagreement within error bars has been found.

The age of a set of measured values has been used occasionally as a justification for ignoring the values. This view is opposed by many examples where older measurements appear to be closer to newest results than less recent results. On the other hand, giving newer and older measurements the same weights would mean denying the advances made in the experimental techniques. Therefore, the introduction of a weight containing the age of a measurement appears appropriate; however, too strong a down-weighting of older measurements (such as ignoring them altogether in some compilations) has to be avoided.

The agreement or disagreement of a set of values with other data has been used occasionally to eliminate or admit such values in a cross section evaluation. The ideal goal is to reach an agreement between data measured by several laboratories. It has often been found in the past that such agreement has been reported, though the cross section or ratio values later drifted away from these previously consistent values. On the other hand, it appears appropriate to down-weight data which deviate greatly from a large majority of values which are in agreement. The use of the inverse of the absolute discrepancy appears to be an appropriate measure. Some addition to the discrepancy has to be made to avoid excessively large weights for values which are accidentally identical with the average.

Consideration could be given to the assignment of a weight to the results of an experiment according to the experimental techniques applied. (For example, a time-of-flight measurement would be preferred over a steady-state beam experiment). However, it appears to be tremendously difficult to assign fair measures to such different experimental techniques even for experimentalists who did comparative measurements employing several techniques.

TABLE I-14-I. EVALUATION RESULTS

Energy, keV	$\sigma_\gamma(^{238}U)$	σ_γ(Au)	σ_α(Li)	$\sigma_f(^{235}U)$
25	0.482	0.639	1.002	2.221
30	0.443	0.576	0.922	2.061
40	0.382	0.489	0.800	1.851
50	0.344	0.439	0.733	1.769
65	0.287	0.381	0.665	1.629
80	0.235	0.344	0.638	1.556
100	0.205	0.320	0.636	1.509
120	0.186	0.303	0.657	1.495
150	0.166	0.299	0.847	1.475
200	0.145	0.270		1.342
250	0.129	0.237		1.260
300	0.118	0.207		1.187
400	0.112	0.165		1.133
500	0.111	0.138		1.088
650	0.122	0.110		1.087
800	0.139	0.098		1.116
1000	0.134	0.084		1.169

EVALUATION EXAMPLE

INPUT DATA

The selection of input data followed the considerations given above. In addition, values have not been used if no documentation of the experiment were available.

EVALUATION METHOD

In a first step, the shapes of $\sigma_\gamma(^{197}Au)$, $\sigma_\gamma(^{238}U)$, $\sigma_\alpha(^{6}Li)$, $\sigma_f(^{235}U)$, $\sigma_\gamma(^{197}Au)/\sigma_f(^{235}U)$, $\sigma_\gamma(^{238}U)/\sigma_f(^{235}U)$ and $\sigma_\alpha(^{6}Li)/\sigma_f(^{235}U)$ were evaluated using smooth curves through the original data and the given error bars as weights. In a second step, the amplitudes[5] were adjusted by minimizing the average deviations. The weights were composed from the absolute given error bars, the number of years between the measurements and the present time, plus 5, and the deviation from the unweighted average, plus 2. The numbers 5 and 2 are chosen somewhat arbitrarily.

The resulting adjusted values were used in a simultaneous evaluation including all the above named absolute cross sections and ratios in order to obtain a consistent set of data. The results are given in Table I-14-I. The input data for $^{6}Li(n,\alpha)$ in the resonance region were insufficient and thus lead to no result for this cross section.

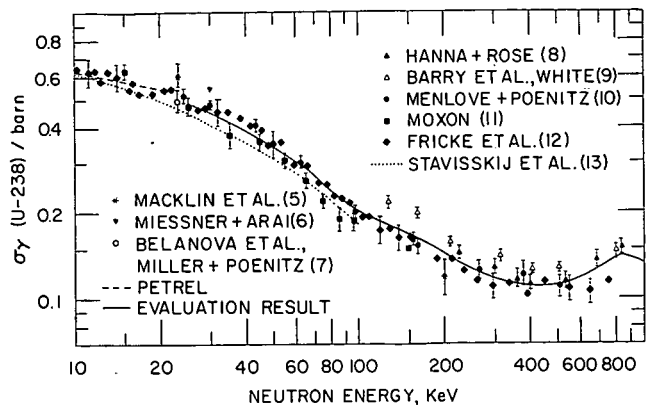

FIG. I-14-1. The Capture Cross Section of ^{238}U. *ANL Neg. No. 116-321 Rev. 1.*

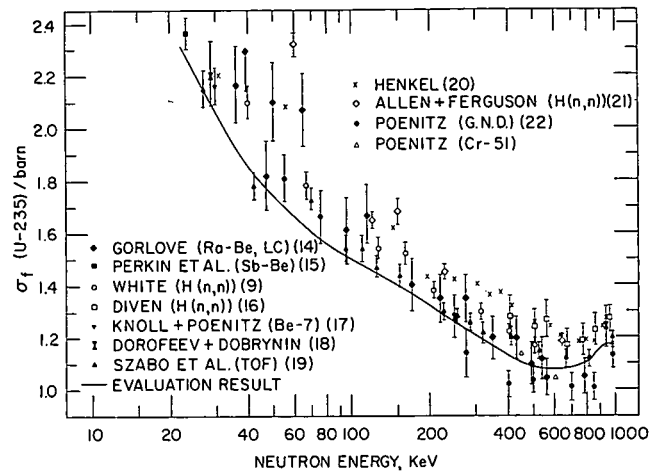

FIG. I-14-2. The Fission Cross Section of ^{235}U. See Paper I-3 for Poenitz' Data on Cr-51. *ANL Neg. No. 116-322 Rev. 1.*

DISCUSSION

The results of the present evaluation compare well with the absolute cross section data from the last 10 years for $\sigma_\gamma(^{197}Au)$ and $\sigma_\gamma(^{238}U)$. Good agreement is also obtained with the $^6Li(n,\alpha)$ data in the energy range 25–150 keV. The evaluation result for ^{235}U is on the low side of the data as a result of the absolute $^6Li(n,\alpha)$, $^{197}Au(n,\gamma)$ and $^{238}U(n,\gamma)$ data. This demonstrates the feed-back of the latter cross sections on $^{235}U(n,f)$ in a simultaneous evaluation of several cross sections. A similar result has been obtained by Sowerby et al.[3] A comparison of the available data for $^{238}U(n,\gamma)$ and $^{235}U(n,f)$ is made in Fig. I-14-1 for which the data were taken from Refs. 5 through 13 and in Fig. I-14-2 for which the data were taken from Refs. 14 through 22 and Paper I-3, respectively.

REFERENCES

1. *Nuclear Standards for Neutron Measurements*, IAEA-107, Vienna (1968).
2. J. M. Kallfelz and W. P. Poenitz, *Fast Reactor Calculations with Consistent Sets for Some Important Neutron Cross Sections*, Reactor Physics Division Annual Report, July 1, 1967 to June 30, 1968, ANL-7410, pp. 191–197.
3. M. G. Sowerby and B. H. Patrick, *A Simultaneous Evaluation of the Fission Cross Sections of ^{235}U, ^{239}Pu and ^{238}U and the Capture Cross Section of ^{238}U in the Energy Range 100 eV to 20 MeV*, IAEA Conference on Nuclear Data for Reactors, IAEA/CN-26/34, Helsinski, 1970.
4. W. P. Poenitz, *Interpretation and Intercomparison of Standard Cross Sections*, EANDC Conference on Neutron Standards and Flux Normalization, Argonne National Laboratory, 1970, USAEC CONF-701002.
5. R. L. Macklin, N. H. Lazar and W. S. Lyon, *Neutron Activation Cross Sections with Sb-Be Neutrons*, Phys. Rev. **107**, 504 (1957).
   Also, W. S. Lyon and R. L. Macklin, "Neutron Activation at 195 keV," Phys. Rev. **114**, 1619 (1959).
6. H. Miessner and E. Arai, *Measurements of Effective Neutron Cross Sections in the keV Region*, KFK 451 (1966).
7. T. S. Belanova, A. A. Vankov, F. F. Mikhailus and Yu. Ya. Stavisskii, *Absolute Measurements of the Absorption Cross Sections of 24 keV Neutrons*, J. Nucl. Energy **20**, 411 (1966)
   Also, L. B. Miller and W. P. Poenitz, *Monte Carlo Interpretation of a ^{238}U Spherical Shell Transmission Experiment at 23 keV*, Nucl. Sci. Eng. **35**, 295 (1969).
8. R. C. Hanna and B. Rose, *Fast Neutron Capture in ^{238}U and ^{232}Th*, J. Nucl. Energy **8**, 197 (1959).
9. J. F. Barry, J. Bunce and P. H. White, *Cross Section for the Reaction $^{238}U(n,\gamma)^{239}U$ in the Energy Range 0.12–7.6 MeV*, J. Nucl. Energy, A/B **18**, 481 (1964).
   Also, P. H. White, *Measurements of the ^{235}U Neutron Fission Cross Section in the Energy Range of 0.04–14 MeV*, J. Nucl. Energy A/B **19**, 325 (1965).
10. H. O. Menlove and W. P. Poenitz, *Absolute Radiative Capture Cross Section for Fast Neutrons in ^{238}U*, Nucl. Sci. Eng. **33**, 24 (1968).
11. M. C. Moxon, Atomic Energy Research Establishment (private communication).
12. M. P. Fricke, D. R. Mathews, S. J. Friesenhahn, A. D. Carlson and J. M. Neill, *Radiative Capture Cross Sections for 1–1000 keV Neutrons*, Proc. Third Conference on Neutron Cross Sections and Technology, University of Tennessee, Knoxville, 1971, CONF-710301, Vol. I, p. 252.
13. Yu. Ya. Stavisskii, B. A. Tolstikov, F. B. Tchelnokov, *Radiative Neutron Capture in ^{238}U*, Second IAEA Conference on Nuclear Data for Reactors, IAEA/CN-26/78, Helsinski, 1971.
14. G. V. Gorlov, B. M. Goshberg, V. M. Morozov, G. A. Ostroshchenko and V. A. Shigin, *The Fission Cross Sections of ^{233}U and ^{235}U for Neutrons having Energies between 3 and 800 keV*, J. Nucl. Energy **12**, 79 (1960).
15. J. L. Perkin, P. H. White, P. Fieldhouse, E. J. Axton, P. Cross and J. C. Robertson, *The Fission Cross Sections of ^{233}U, ^{234}U, ^{235}U, ^{236}U, ^{237}Np, ^{239}Pu, ^{240}Pu and ^{241}Pu for 24 keV Neutrons*, J. Nucl. Energy **19**, 423 (1965).
16. B. C. Diven, *Fission Cross Section of ^{235}U for Fast Neutrons*, Phys. Rev. **105**, 1350 (1957).
17. G. F. Knoll and W. P. Poenitz, *A Measurement of the ^{235}U Fission Cross Section at 30 keV and 64 keV*, J. N Energy **21**, 643 (1967).
18. G. A. Dorofeev and Y. P. Dobrynin, *Effective Fission Cross Sections of ^{233}U, ^{235}U, ^{239}Pu and ^{240}Pu in the Neutron En-*

ergy Range 30 keV–5 MeV, J. Nucl. Energy **5**, 217 (1957).
19. I. Szabo, J. P. Marquette, E. Fort and J. L. Leroy, *Mesure Absolue de la Section Efficace de Fission*, Proc. IAEA Conference on Nuclear Data for Reactors, IAEA/CN-26/69, Helsinki (1970).
20. R. L. Henkel, *Fast Neutron Cross Sections: Corrections to LA-1714 and a Correlation of 3 MeV Values*, LA-2122 (1957).
Also, R. L. Henkel, *Fission Excitation Curves for ^{233}U, ^{235}U, ^{236}U and ^{237}Np*, LA-1495 (1952).
Also, W. D. McNeese, *Preparation in Plutonium Sheet by Extrusion*, LA-2113 (1957).
21. W. D. Allen and A. T. G. Ferguson, *The Fission Cross Sections of ^{233}U, ^{235}U, ^{238}U and ^{239}Pu for Neutrons in the Energy Range 0.030–3.0 MeV*, Proc. Phys. Soc. ***A70***, 753 (1957).
22. W. P. Poenitz, *Measurement of the ^{235}U Fission Cross Section in the keV Energy Range*, Second Conference on Neutron Cross Sections and Technology, Washington, D. C., 1968, NBS Special Publication 299, Vol. I, 503 (1968).

I-15. Independent Study of 2200 m/s Fission Constants

A. DeVolpi

Because of apparent discrepancies in the basic 2200 m/s fission parameters, an independent examination and determination of possible adjustments was performed. Rather significant modifications of the previously "accepted" set of thermal fission constants are proposed on the basis of reduced confidence in α input, adjusted η values, and equal weighting of ν measurements. As a prominent example, the review suggests that, compared with IAEA surveys, the ^{235}U fission cross-section should be 1% higher—585.7 ± 1.8 b—and the neutron yield should be correspondingly lower—2.400 ± 0.007 neutrons/fission.

In studies and experiments associated with breeder reactors, there is a high degree of contingency traceable to the absolute yield[2] of neutrons from spontaneous fission of ^{252}Cf. This dependence arises, in short, from a direct connection between $\nu(^{252}Cf)$ as a reference upon which all values of ν for thermal fission of ^{233}U, ^{235}U, and ^{239}Pu and upon which all values of $\nu(E)$ are referenced.

A long-standing experimental program at Argonne was recently completed with the publication of a multiply-verified value for $\nu(^{252}Cf)$.[1] Prior to this result, there have been published a number of measurements listed with precision of 1% or better, but differing by as much as 3%. The Argonne value falls within this range, but markedly below the weighted average of all experimental data.

It has also been evident that there exist a number of other anomalies in completely unrelated quantities. In particular, there are very accurate measurements of the fission cross section for ^{235}U which are about 1% higher than the IAEA average. To reconcile these major discrepancies where accuracies of ⅓% were previously attributed to the least-squares fitted values, significant revisions can be generated on the basis of a unified analysis. The result is a set of fission parameters with much higher internal consistency.

To some extent the approach was based on a partially-subjective—but different—view towards credibility of some experiments. This reviewer has accepted some of the more recent low measurements of the ^{233}U and ^{234}U half-lives, has eliminated the artificial down-weighting applied to certain absolute measurements of $\nu(^{252}Cf)$, and has reduced the experimental values of some manganese bath results for η. After applying a uniform constraint of $\nu\sigma_f = \eta\sigma_a$, an adjusted set of fission parameters was generated with substantive support from the internal consistency of the revised experimental input data. The effect of these changes upon ^{235}U propagates to both ^{233}U and ^{239}Pu, but these two isotopes have additional ambiguities due to inadequate input data.

Table I-15-I (Table XIV of Ref. 2) summarizes the full results, which are available with complete documentation in an Argonne National Laboratory report.[2]

References

1. A. DeVolpi and K. G. Porges, *Neutron Yield of ^{252}Cf Based on Absolute Measurements of the Neutron Rate and Fission Rate*, Phys. Rev. C1, 683–694 (1970).
2. A. DeVolpi, *Discrepancies and Possible Adjustments in the 2200 m/s Fission Parameters*, ANL-7830 (1971).

TABLE I-15-I. REVISED VALUES FOR 2200-m/s CONSTANTS

	^{233}U				^{235}U		^{239}Pu		
	Experiment	Adjustment A[a]	Adjustment B[a]	Adjustment C[b]	Experiment	Adjusted	Experiment	Adjustment A[c]	Adjustment B[c]
σ_a	575.6 ± 1.6 (0%)[d]	582.5 ± 1.8 (+0.85%)	578.0 (+0.07%)	575.6 (-0.35%)	680.5 ± 2.7 (+0.15%)	683.0 ± 1.9 (+0.66%)	1012.1 ± 6.2 (0%)	1021.6 (+0.86%)	1013.4 ± 4.6 (+0.13%)
σ_f	539.3 ± 4.8 (+1.6%)	537.9 ± 1.9 (+1.4%)	536.5 (+1.1%)	531.9 (+0.25%)	587.4 ± 2.5 (+1.0%)	585.7 ± 1.8 (+0.95%)	742.5 ± 2.8 (+0.26%)	742.5 (+0.26%)	742.5 ± 3.1 (+0.26%)
σ_γ	50.6 ± 3.2 (0%)	44.6 ± 0.9 (-5%)	41.5 (-13%)	43.7 (-7.6%)	- -	97.3 ± 1.1 (-1.0%)	275.5 ± 7.8 (0%)	279.1 (+2.9%)	270.9 ± 2.6 (-1.7%)
α	0.0900 ± 0.0004 (0%)	0.0830 ± 0.0018 (-6.6%)	0.0773 (-14%)	0.0822 (-7.7%)	0.1691 ± 0.0021 (-0.59%)	0.1661 ± 0.0021 (-2.0%)	0.3598 (0%)	0.376 (+2.8%)	0.365 ± 0.004 (+1.4%)
η	2.278 ± 0.008 (-0.44%)	2.265 ± 0.006 (-0.86%)	2.278 (-0.29%)	2.284 (0%)	2.067 ± 0.009 (-0.48%)	2.058 ± 0.006 (-0.68%)	2.100 ± 0.009 (-0.48%)	2.091 (-0.84%)	2.091 ± 0.007 (-0.84%)
ν_t	2.464 ± 0.005 (-1.0%)	2.453 ± 0.007 (-1.4%)	2.454 (-1.3%)	2.472 (-0.6%)	2.393 ± 0.008 (-1.2%)	2.400 ± 0.007 (-0.92%)	2.854 ± 0.008 (-1.0%)	2.877 (-0.10%)	2.854 ± 0.007 (-0.91%)
σ_s[e]	10.5 (+24%)	3.5 (-59%)	8.1 (-4.9%)	10.5 (+24%)	14.3 ± 0.5 (-7.0%)	13.6 ± 1.5 (-5.0%)			

$\nu_t(^{252}Cf)$ = 3.731 ± 0.008 (Experiment) (-0.35%)
= 3.735 ± 0.008 (Adjusted) (-0.94%)

$\sigma_f(^{239}Pu)/(^{235}U)$ = 1.2633 ± 0.0081 (Experiment) (-1.5%)
= 1.2677 ± 0.0081 (Adjusted) (-0.8%)

$\tau_{1/2}(^{233}U)$ = 1.554 ± 0.003 x 10^5 years (Adjustment A) (-2.5%)
= 1.562 ± 0.003 x 10^5 years (Adjustment B) (-2.0%)

$\tau_{1/2}(^{234}U)$ = 2.444 ± 0.005 x 10^5 years (Experiment) (-1.8%)

$\nu_t(^{235}U/^{252}Cf)$ = 0.6414 ± 0.0018 (Experiment) (0%)
= 0.6426 ± 0.0015 (Adjusted) (0%)

$\nu_t(^{239}Pu/^{252}Cf)$ = 0.7648 ± 0.0067 (Experiment) (0%)
= 0.7703 ± 0.0022 (Adjustment A) (+0.85%)

$\nu_t(^{235}U)\sigma_f(^{235}U)$ = 1405.6 (Experiment) (-0.01%)
= 1405.7 (Adjusted) (-0.01%)

$\eta(^{235}U)\sigma_a(^{235}U)$ = 1406.6 (Experiment) (+0.06%)
= 1405.6 (Adjusted) (-0.01%)

$\nu_t(^{233}U)\sigma_f(^{233}U)$ = 1328.8 (Experiment) (+0.71%)
= 1319.5 (Adjustment A) (0%)
= 1316.6 (Adjustment B) (-0.22%)

$\eta(^{233}U)\sigma_a(^{233}U)$ = 1311.2 (Experiment) (-0.63%)
= 1319.4 (Adjustment A) (0%)
= 1316.7 (Adjustment B) (-0.21%)

$\nu_t(^{239}Pu)\sigma_f(^{239}Pu)$ = 2119.1 (Experiment) (-0.81%)
= 2136.2 (Adjustment A) (+0.02%)
= 2119.1 (Adjustment B) (-0.81%)

$\eta(^{239}Pu)\sigma_a(^{239}Pu)$ = 2125.4 (Experiment) (-0.51%)
= 2136.2 (Adjustment A) (+0.02%)
= 2119.0 (Adjustment B) (-0.81%)

	Other Values
$\eta(^{239}Pu)\sigma_a(^{239}Pu)/\eta(^{235}U)\sigma_a(^{235}U)$ = 1.5110 (Experiment) (+0.15%) = 1.5197 (Adjustment A) (+0.03%) = 1.5075 (Adjustment B) (-0.76%)	1.509 ± 0.023 (Magnuson)
$(\eta - 1)(^{239}Pu)\sigma_a(^{239}Pu)/(\eta - 1)(^{235}U)\sigma_a(^{235}U)$ = 1.5333 (Experiment) (+3.6%) = 1.5424 (Adjustment A) (-0.09%) = 1.5300 (Adjustment B) (-0.90%)	
$\eta(^{239}Pu)/\eta(^{235}U)$ = 1.0160 (Experiment) (+0.13%) = 1.0160 (Adjustment A) (-0.16%) = 1.0160 (Adjustment B) (-0.16%)	1.017 (Vidal et al.)
$\eta(^{233}U)/\eta(^{235}U)$ = 1.1021 (Experiment) (-0.05%) = 1.1006 (Adjustment A) (-0.17%) = 1.1069 (Adjustment B) (+0.40%)	1.081 ± 0.005 (Vidal et al.)
$\eta(^{233}U)\sigma_a(^{233}U)/\eta(^{235}U)\sigma_a(^{235}U)$ = 0.9322 (Experiment) (-0.19%) = 0.9386 (Adjustment A) (0%) = 0.9367 (Adjustment B) (-0.20%)	0.934 ± 0.014 (Magnuson)

[a] For ^{233}U Adjustment A, $\nu_t(^{233}U)\sigma_f(^{233}U)$ = 1319.5 (as Hanna et al.); for Adjustment B, the product is 1316.6.
[b] For $\nu_t(^{233}U)\sigma_f(^{233}U)$ = 1314.8.
[c] For ^{239}Pu Adjustment A, $\nu_t(^{239}Pu)\sigma_f(^{239}Pu)$ = 2136.2 (as Hanna et al.); for Adjustment B, the product is 2119.1.
[d] In parentheses are percentage differences comparing Hanna et al. input-experimental and output-adjusted data. (The experiment averages derived in this report are compared with IAEA experimental averages; the adjusted output is compared with the IAEA LSF.)
[e] Rolled metal.

I-16. Theory of Measurement

P. A. Moldauer

Traditionally, the interpretation of a measurement in quantum mechanics has involved a process called "reduction of the state vector." Since this reduction is a nonlinear acausal change which cannot be described by the Schrödinger equation, the question has often been raised whether quantum mechanics is a complete theory which is capable of describing the measurement process.

In the usual notation one can predict the outcome of only one measurement at a time. "Reduction" is then the way by which a previous measurement is made to affect the outcome of a later measurement, leading to the correct correlations between successive measurements. By recasting the notation so that all observations are described in terms of *projection operators* (referring to properties of the measuring apparatus), it has been found possible to describe not only the outcomes of individual measurements, but also all correlations between successive measurements. Moreover it is found that these correlations are correctly predicted by the linear causal time development of the quantum state as described by the Schrodinger equation. Consequently, quantum mechanics describes the measurement process completely without the need for "reduction."

Section II

Fast Reactor Physics

The section on Fast Reactor Physics is concerned with the analyses and measurements of liquid metal fast breeder reactor characteristics and parameters. The measurements are generally made on the critical facilities ZPPR (Zero Power Plutonium Reactor), ZPR-3, ZPR-6 and ZPR-9, and are often performed to check calculated results and hence to evaluate the analytical methods and the nuclear constants used in the calculations. Again, the critical assemblies may be constructed to permit measurements on mockups of liquid metal fast breeder power reactors. The results may possibly be extrapolated to aid in the design of the originally conceived power reactor. The work reported in this section is of value in understanding the fundamentals of the liquid metal fast breeder and in developing analytic methods for predicting with accuracy the performance of such reactors.

II-1. ZPR-9 Assembly 27: The Fast Test Reactor Engineering Mockup Critical (FTR-EMC)

J. W. Daughtry, C. D. Swanson, A. B. Long, R. B. Pond and G. K. Rusch

Introduction

ZPR-9 Assembly 27 is the Fast Test Reactor Engineering Mockup Critical (FTR-EMC). The objectives of the EMC experiments are to verify the neutronics characteristics of the FTR preliminary design and to provide data for fixing final design parameters, such as fuel enrichments and boron loading in control and safety rods, and for assessing power distributions, fixed-shim methods, test loop loading effects, safety characteristics and end-of-life conditions.

The FTR is the main component of the Fast Flux Test Facility (FFTF) which is being built primarily for fast reactor fuel testing. The FTR is to be a plutonium-fueled, sodium-cooled, fast reactor with a core volume of 1034 liters (cold) designed to operate at 400 MW. It is to be made up of hexagonal subassemblies equal in cross sectional area to approximately 4.1 ZPR-9 matrix tubes. This, in itself, constitutes a limitation to the degree of accuracy of the mockup.

Within the constraints imposed by the ZPR-9 matrix and drawers and the available material inventory, the EMC approximates, as closely as possible, the current design of the FTR. In particular, the EMC is very similar to the FTR in fissile mass and in the atom densities and volumes of each region and in the locations of the test loops and control, safety, and shim rods. The length of the ZPR-9 matrix limits the extent of the axial mockup to approximately 47 in. from the midplane of the reactor. Both the size of the matrix and the limited inventory of stainless steel prevent the mockup of the complete radial shield.

The EMC experiments constitute Phase C of the FFTF Critical Experiments Program. They are related to the experiments previously performed in Phases A and B of the same program. However, while the Phase A and B experiments were used to study idealized models of the FTR in clean experiments, the EMC experiments are being performed in an assembly which reproduces as closely as possible the actual configuration anticipated for the FTR.

The purpose of this paper is to provide a detailed description of the assembly including the worths of the ZPR-9 control and safety rods and the temperature coefficient of reactivity.

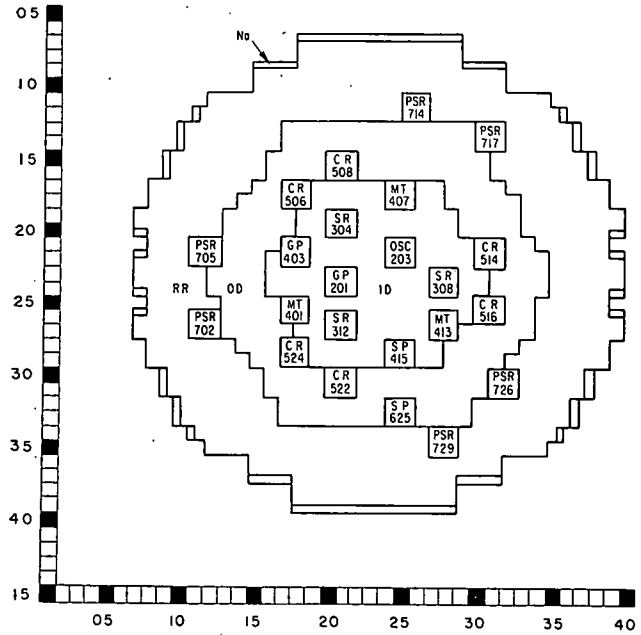

Fig. II-1-1. The FTR-EMC Assembly; Stationary Half of ZPR-9. *ANL Neg. No. 116-744.*

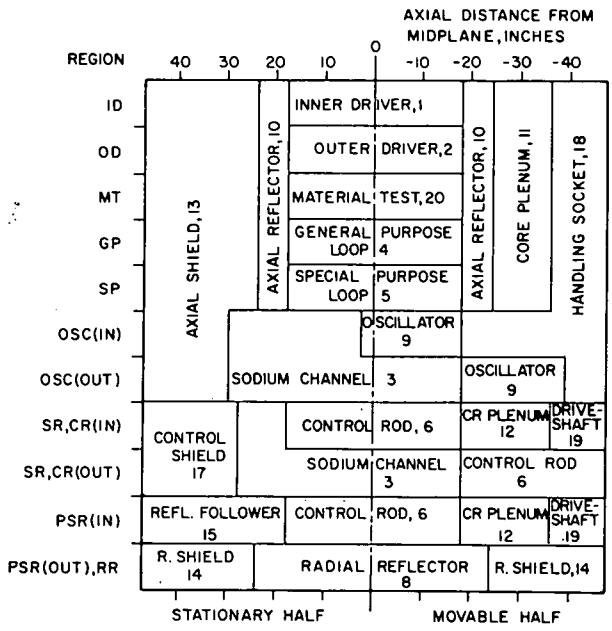

Fig. II-1-2. Axial Subregions of the FTR-EMC. *ANL Neg. No. 116-1054.*

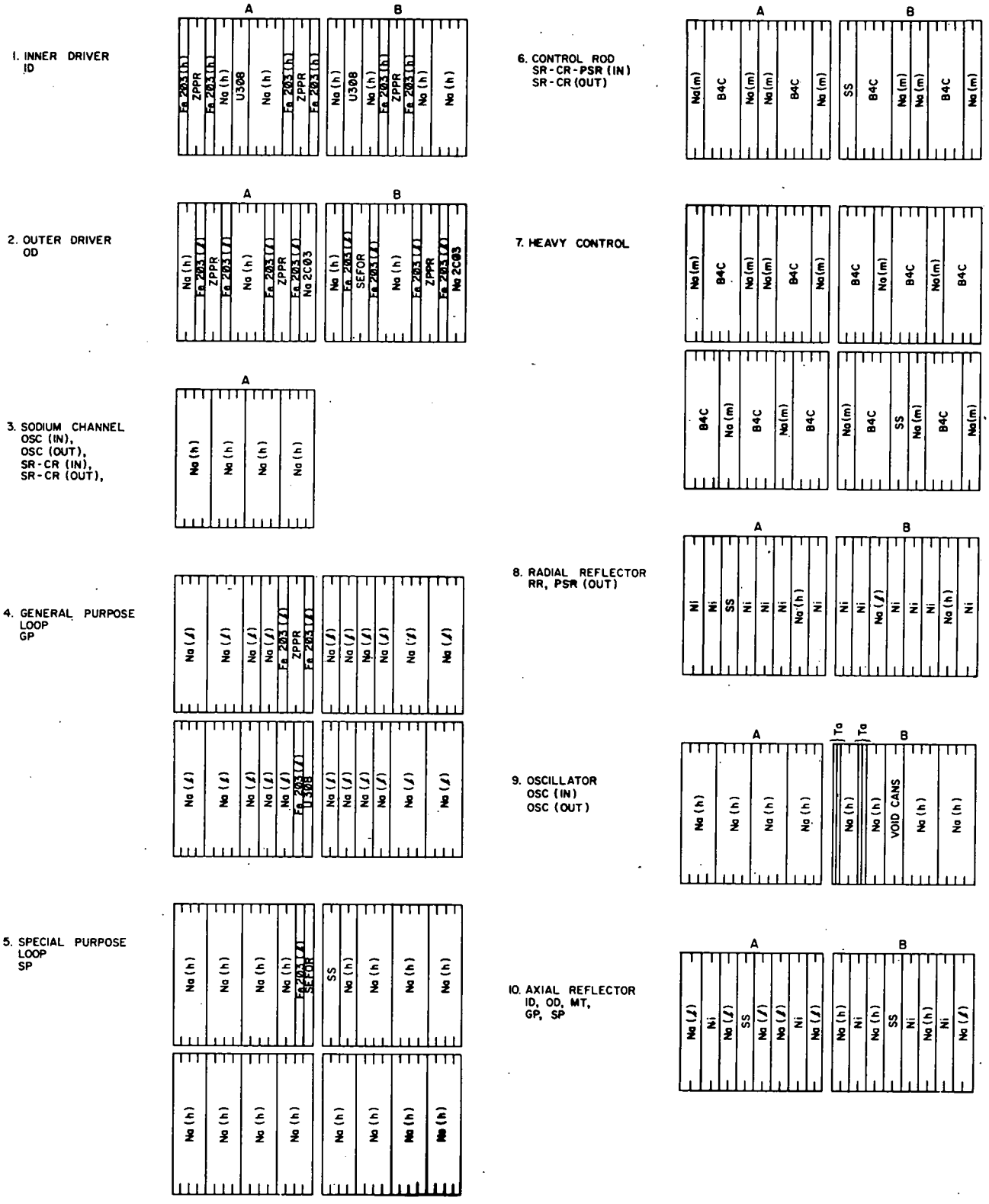

FIG. II-1-3. Plate Arrangements for FTR-EMC Compositions. *ANL Neg. No. 116-1056.*

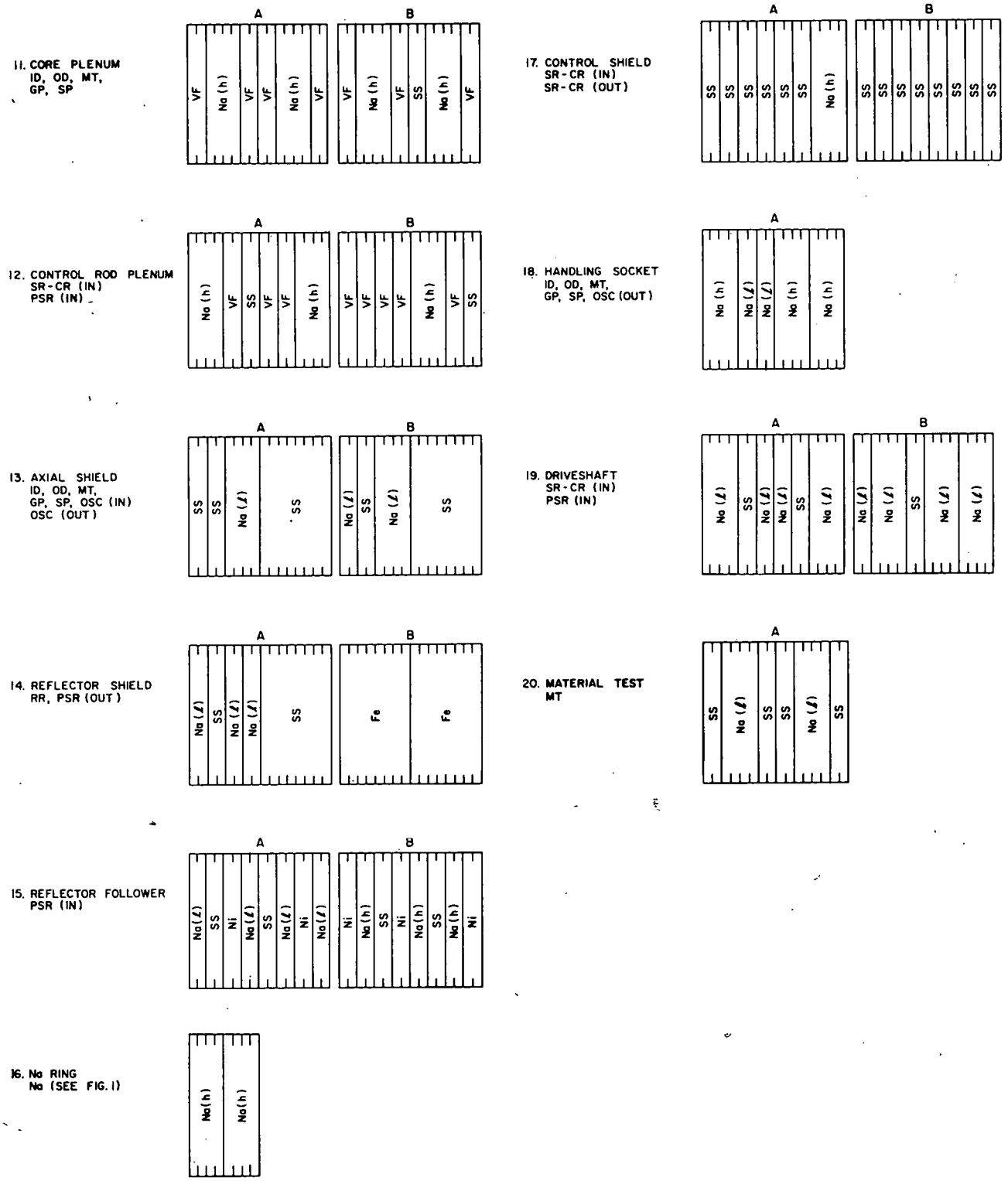

FIG. II-1-3. (cont.) Plate Arrangements for FTR-EMC Compositions. *ANL Neg. No. 116-1057.*

DESCRIPTION OF THE ASSEMBLY

In assembling the EMC in the ZPR-9 facility, the top half of the FTR was mocked up in the movable half of the ZPR-9 matrix. Figure II-1-1 is a diagram representing the front face of the stationary half. This corresponds to a cutaway view at the midplane of the FTR looking vertically down. The various regions of

the assembly are identified by letters: ID (inner driver), OD (outer driver), RR (radial reflector), MT (material test), GP (general purpose loop), SP (special purpose loop), SR (safety rod), OSC (oscillator), CR (control rod), and PSR (peripheral shim rod). Segments of a one inch thick sodium ring surround the reflector.

Each hexagonal subassembly of the FTR is identified by a number which gives the row (or ring) in which that subassembly is located, plus the location in that row. In this numbering scheme the central assembly is designated 101. In the first row surrounding the central subassembly, row 2, there are six subassemblies numbered from 201 to 206. In row 3 there are twelve subassemblies, 301 through 312, and so on. The numbers in Fig. II-1-1 identify each four-matrix-tube array with its corresponding hexagonal subassembly of the FTR. The front face of the movable half is the mirror image of that shown in Fig. II-1-1.

Every region identified in Fig. II-1-1 is divided axially in subregions of various sizes and compositions which are described in Fig. II-1-2. The regions representing the control, safety, and shim rods and the oscillator are shown for both the fully inserted and the fully withdrawn conditions. Each subregion is identified by name and number in Fig. II-1-2. The region identifiers along the left edge of the chart correspond to the letters in Fig. II-1-1.

The plate arrangements for each subregion identified

TABLE II-1-I. As-Built Atom Concentrations for the FTR-EMC[a], 10^{21} atoms/cc

	Inner Driver		Outer Driver	
	A	B	A	B
^{238}Pu	0.001	0.0004	0.001	0.0005
^{239}Pu	1.765	0.887	1.763	1.478
^{240}Pu	0.234	0.118	0.233	0.174
^{241}Pu	0.030	0.014	0.031	0.019
^{242}Pu	0.004	0.002	0.004	0.002
$^{239+241}$Pu	1.795	0.901	1.794	1.497
$^{240+242}$Pu	0.238	0.120	0.237	0.176
^{235}U	0.015	0.009	0.011	0.012
^{238}U	6.647	4.144	5.008	5.117
O	15.792	10.095	13.107	13.107
C	0.031	0.033	1.073	1.072
Na	6.686	10.887	8.766	8.766
Fe	18.007	14.999	17.921	17.644
Cr	2.979	3.205	3.221	3.142
Ni	1.379	1.484	1.491	1.455
Mn	0.234	0.251	0.253	0.246
Mo	0.461	0.239	0.462	0.445

	Sodium Channel	General Purpose Loop
^{238}Pu	—	0.001
^{239}Pu	—	0.220
^{240}Pu	—	0.029
^{241}Pu	—	0.004
^{242}Pu	—	0.0005
$^{239+241}$Pu	—	0.224
$^{240+242}$Pu	—	0.030
^{235}U	—	0.002
^{238}U	—	0.829
O	—	2.412
C	0.031	0.035
Na	18.683	15.783
Fe	10.427	13.049
Cr	2.984	3.377
Ni	1.381	1.563
Mn	0.234	0.265
Mo	0.011	0.068

	Special Purpose Loop	Control Rod
$^{239+241}$Pu	0.058	—
$^{240+242}$Pu	0.005	—
^{235}U	0.001	—
^{238}U	0.252	—
O	0.624	—
C	0.036	9.390
Na	17.238	7.195
Fe	12.606	14.806
Cr	3.488	4.229
Ni	1.615	1.958
Mn	0.274	0.332
Mo	0.032	0.015
^{10}B	—	7.135
^{11}B	—	28.936

	Heavy Control Rod	Radial Reflector	
		A	B
C	11.721	0.040	0.024
Na	5.653	2.090	4.081
Fe	13.076	13.675	8.400
Cr	3.732	3.888	2.378
Ni	1.728	58.045	57.347
Mn	0.293	0.456	0.338
Mo	0.013	0.014	0.008
^{10}B	8.919	—	—
^{11}B	36.170	—	—

	Oscillator	Axial Reflector	
		A	B
C	0.032	0.052	0.047
Na	15.960	10.586	8.198
Fe	10.834	17.365	16.241
Cr	3.100	4.961	4.63[illegible]
Ni	1.435	20.859	29.98[illegible]
Mn	0.243	0.439	0.43[illegible]
Mo	0.011	0.018	0.016
Ta	2.908	—	—

TABLE II-1-I. *Continued*

	Core Plenum		Control Rod Plenum
	A	B	
C	0.035	0.051	0.052
Na	9.256	9.256	6.926
Fe	12.080	17.371	17.722
Cr	3.457	4.971	5.071
Ni	1.600	2.301	2.348
Mn	0.271	0.390	0.398
Mo	0.012	0.018	0.018

	Axial Shield		Radial Reflector Shield	
	A	B	A	B
C	0.131	0.116	0.117	0.020
Na	4.555	6.462	5.929	—
Fe	44.554	39.307	39.793	77.043
Cr	12.749	11.248	11.387	1.950
Ni	5.902	5.207	5.272	0.892
Mn	1.000	0.882	0.893	0.663
Mo	0.045	0.040	0.040	0.007

	Reflector Follower	Sodium Ring
C	0.065	0.031
Na	7.298	18.683
Fe	22.138	10.427
Cr	6.325	2.984
Ni	26.095	1.381
Mn	0.558	0.234
Mo	0.022	0.011

	Control Shield	Handling Socket
C	0.148	0.034
Na	2.320	18.024
Fe	50.166	11.566
Cr	14.355	3.310
Ni	6.646	1.532
Mn	1.126	0.260
Mo	0.051	0.012

	Drive Shaft	Material Test
C	0.059	0.098
Na	14.595	9.177
Fe	19.854	33.162
Cr	5.682	9.489
Ni	2.630	4.393
Mn	0.446	0.744
Mo	0.020	0.033

[a] Letters A and B refer to drawer types.

in Fig. II-1-2 are shown in Fig. II-1-3 according to their code numbers. The plate identification code is as follows:

Fe2O3	iron oxide (Fe_2O_3)
U3O8	uranium oxide (U_3O_8)
Na	sodium in a stainless steel can
Na2CO3	sodium carbonate (Na_2CO_3) in a stainless steel can
B4C	boron carbide (B_4C) in a stainless steel can
SS	stainless steel
Ta	tantalum
Ni	nickel
VF	void frame
Fe	iron
ZPPR, SEFOR	two types of Pu-U-Mo fuel in stainless steel cans.

The letters ℓ, m, and h in parenthesis, refer to different weights of the same type of plate in the ANL inventory (light, medium, and heavy). In addition to the plate angements, Fig. II-1-3 indicates the composition nes and the regions of Figs. II-1-1 and II-1-2 where each plate arrangement is found. Composition 7 (heavy control) does not appear in Figs. II-1-1 or II-1-2. It is a control rod composition with increased B_4C content used during the boron control rod enrichment experiment (see Paper II-2).

The plate arrangements in Fig. II-1-3 are drawn to scale as viewed facing the front of the stationary half drawers. When the same composition is in the movable half it will be the mirror image of that shown. When a composition occurs only in the movable half, the plate arrangements shown in Fig. II-1-3 are as viewed facing the front face of the movable half. The Type A drawers of compositions 1, 2, 8, 10, 13, and 14 are located in the odd-numbered matrix columns.

The as-built atom concentrations of all compositions are listed in Table II-1-I. Table II-1-II gives the dimensions and volumes of the assembly.

EOC and BOL Configurations

During the experiments that have been performed thus far, many configurations (both critical and subcritical) have been assembled. Of these, two are of special interest. These are the end-of-cycle (EOC) configuration and the beginning-of-life (BOL) configuration.

The EOC configuration was built to provide a rough simulation of the FTR at the end of an equilibrium cycle. Referring to Figs. II-1-1 and II-1-2, all six

TABLE II-1-II. Dimensions and Core Volumes of the FTR-EMC

Inner core radius, cm	38.5
Outer core outer radius, cm	60.5
Radial reflector outer radius, cm	90.9
Core height, cm	91.6
Core volume, liters	
Inner core	425.9
Outer core	627.7
Total	1053.6

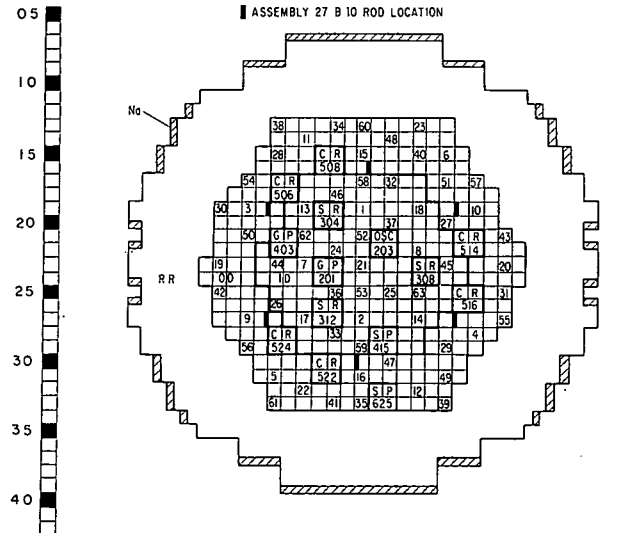

Fig. II-1-4. EOC Configuration of the FTR-EMC Showing Depletion Pattern. *ANL Neg. No. 116-1055.*

TABLE II-1-III. Isotopic Mass Changes due to the Substitution of One Column (¼ × 2 × 36 in.) of Depleted Uranium for One Column of ZPPR Pu-U-Mo Fuel

Isotope	Mass Change, kg
^{238}Pu	−0.00066
^{239}Pu	−0.98032
^{240}Pu	−0.13038
^{241}Pu	−0.01760
^{242}Pu	−0.00216
$^{239+241}$Pu	−0.999792
$^{238+240+242}$Pu	−0.13320
^{235}U	0.00518
^{238}U	2.56842
Fe	−0.24660
Cr	−0.06672
Ni	−0.03772
Mn	−0.00602
Si	−0.00194
Mo	−0.10058

peripheral shim rods were removed [PSR(OUT)], all six control rods were fully withdrawn [CR(OUT)], all three safety rods were fully withdrawn [SR(OUT)], and the oscillator was fully withdrawn [OSC(OUT)]. All material test regions were removed and replaced with inner driver composition. In addition, to simulate burnup, the fertile-to-fissile ratio in the core was increased by replacing some of the fuel with depleted uranium. The numbered matrix tubes in Fig. II-1-4 are the locations of the core fuel depletion. All of the numbered tubes contain Type A inner and outer driver drawers that have two columns of ZPPR Pu-U-Mo fuel. The fuel that was replaced with depleted uranium was the column of ZPPR fuel plates on the left in the drawer loading patterns shown in Fig. II-1-3. The isotopic mass changes resulting from the replacement of one column (1/4 x 2 x 36 in.) are given in Table II-1-III. The EOC configuration is shown in Fig. II-1-4. It had a fissile mass of 485.39 kg of ^{239}Pu + ^{241}Pu and 4.30 kg of ^{235}U and an excess reactivity of 147.5 Ih.

The BOL configuration was a mockup of the FTR at the beginning of an equilibrium fuel cycle. Referring to Figs. II-1-1 and II-1-2, the oscillator was fully withdrawn [OSC(OUT)], all three safety rods were fully withdrawn [SR(OUT)], all six control rods [CR] were 50% (18 in.) inserted, peripheral shim rods 702, 714, and 726 were in [PSR(IN)] and peripheral shim rods 705, 717, and 729 were removed [PSR(OUT)]. All three material test [MT] regions (401, 407 and 413) were in. This configuration had a fissile mass of 530.26 kg of ^{239}Pu + ^{241}Pu and 3.81 kg of ^{235}U and an excess reactivity of 212.3 Ih.

The calculated kinetics parameters for the EOC and BOL configurations are given in Table II-1-IV.

ZPR-9 Control and Safety Rod Worths

Five fuel-bearing dual-purpose control/safety rods were installed in each half of the reactor. All fuel-bearing rods were loaded with inner driver Type A composition; when partially or fully withdrawn, a void was left in the core region. The stroke of this type rod from full-in to full-out is approximately 61 cm.

In addition to the fuel rods there were six ^{10}B poison rods in each half of the reactor. These poison rods contained enriched boron powder and the loading varied significantly from rod to rod. The average was about 160 g of ^{10}B per rod. The active length of the rods was 61 cm and they had a stroke of 76 cm. The ^{10}B rod locations are shown in Fig. II-1-4.

Each of the twenty-two fuel-bearing and ^{10}B rods was calibrated in the EOC configuration by the 1 drop—inverse kinetics method. The locations and me ured worths are given in Table II-1-V. The uncertainty associated with each rod worth is approximately ± 2 Ih.

TABLE II-1-IV. DELAYED NEUTRON PARAMETERS FOR THE EOC AND BOL CONFIGURATIONS

	Decay Constants					
Group / Isotope	1	2	3	4	5	6
$^{239+241}Pu$	0.0129	0.0311	0.134	0.331	1.26	3.21
^{240}Pu	0.0129	0.0313	0.135	0.333	1.36	4.04
^{235}U	0.0127	0.0317	0.115	0.311	1.40	3.87
^{238}U	0.0132	0.0321	0.139	0.358	1.41	4.02
Effective Delayed Neutron Fractions for the BOL Configuration						
$^{239+241}Pu$	6.092-5	4.489-4	3.463-4	5.259-4	1.651-4	5.611-5
^{240}Pu	1.696-6	1.654-5	1.163-5	2.120-5	7.754-6	1.757-6
^{235}U	1.388-6	7.780-6	6.867-6	1.487-5	4.675-6	9.497-7
^{238}U	1.360-5	1.433-4	1.695-4	4.059-4	2.354-4	7.846-5
Prompt neutron lifetime, μsec	0.444					
Effective delayed neutron fraction	2.747×10^{-3}					
Ih/% $\Delta k/k$	1108.15					
Effective Delayed Neutron Fractions for the EOC Configuration						
$^{239+241}Pu$	6.039-5	4.450-4	3.433-4	5.213-4	1.637-4	5.562-5
^{240}Pu	1.610-6	1.569-5	1.104-5	2.012-5	7.358-6	1.667-6
^{235}U	1.717-6	9.623-6	8.493-6	1.839-5	5.783-6	1.175-6
^{238}U	1.576-5	1.661-4	1.964-4	4.703-4	2.727-4	9.091-5
Prompt neutron lifetime, μsec	0.549					
Effective delayed neutron fraction	2.904×10^{-3}					
Ih/% $\Delta k/k$	1070.93					

TEMPERATURE COEFFICIENT

The temperature coefficient of reactivity was measured in the EOC and BOL configurations using a calibrated control rod to determine the excess reactivity at different core temperatures. Day-to-day variations in the operating temperature of the reactor were duplicated by adjusting the cooling controls on the cell air conditioning system while the reactor was critical and while the reactor cooling fans were running. The assembly temperature was found by averaging data from 21 thermocouples positioned throughout the core. The measured temperature coefficient in the EOC configuration was (4.1 ± 0.4) Ih/°C. In the BOL configuration the temperature coefficient was determined to be (3.3 ± 0.3) Ih/°C.

TABLE II-1-V. LOCATION AND WORTH OF FUEL-BEARING AND ^{10}B CONTROL/SAFETY RODS IN THE EOC CONFIGURATION OF THE FTR-EMC

Fuel Bearing Rods		
No.	Location	Worth, Ih
1	M19-25	134
2	M22-29	115
3	M26-25	118
4	M24-17	100
5	M21-21	123
6	S19-25	133
7	S22-29	109
8	S26-25	118
9	S24-17	101
10	S21-21	117
^{10}B Rods		
No.	Location	Worth, Ih
1	M16-23	164
2	M19-30	148
3	M27-30	124
4	M30-23	121
5	M27-16	69
6	M19-16	110
7	S16-23	185
8	S19-30	168
9	S27-30	152
10	S30-23	180
11	S27-16	119
12	S19-16	92

II-2. Fuel and Control Rod Enrichment Experiment in the Fast Test Reactor Engineering Mockup Critical (FTR-EMC)

R. B. POND, J. W. DAUGHTRY, C. D. SWANSON and A. B. LONG

INTRODUCTION

The purpose of this experiment was to provide data to aid in the specification of the fuel and boron enrichments to be used in the Fast Test Reactor (FTR). To obtain the desired information, fuel worths and boron control rod worths were obtained in a series of configurations similar to those anticipated in a typical FTR burnup cycle. This was accomplished by initially loading the ZPR-9 facility with an assembly that simulated the

FTR at the end of an equilibrium fuel cycle (EOC). Then, intermediate stages of burnup were simulated by increasing the fissile fuel density in increments while compensating with various arrays of control rods, peripheral shim rods, and material test subassemblies. The final configuration simulated the FTR at the beginning of an equilibrium fuel cycle (BOL) with a new core and partially-inserted control rods.

Assembly Configurations

A detailed description of the FTR-EMC is given in Paper II-1. Throughout the enrichment experiment, the general purpose and special purpose loops were in the assembly; the oscillator was withdrawn [OSC (out)]; and the safety rods were withdrawn [SR(out)]. The state of each peripheral shim rod [PSR], control rod [CR] and material test subassembly [MT] is given in Table II-2-I. A PSR or MT could be either in place or completely removed; no partial insertion was allowed. When an MT was removed it was always replaced with inner driver [ID] composition. The control rods [CR] could be partially inserted any amount. The only limitation was the piece-size inventory of materials used in loading the control rod drawers. When a control rod was partially or fully-withdrawn, the control rod composition was replaced with sodium channel composition. Table II-2-I also lists the number of tubes of depleted driver composition and the fissile mass in each configuration. The replacement of depleted uranium with fuel followed the numbering system shown in Fig. 4 of Paper II-1 in decreasing order. Thus, in going from SUB1 to IC1 one column of depleted uranium (1/4 x 2 x 36 in.) was removed from the drawers marked 63 through 46 and ZPPR type Pu-U-Mo fuel cans were added.

Experimental Methods

For the critical configurations in this series of measurements, the excess reactivity was measured using ZPR-9 calibrated control rods. These rods were recalibrated in each critical configuration using the inverse kinetics method. For subcritical configurations, the

TABLE II-2-I. Summary of Configurations Assembled during the Enrichment Experiment

Configuration	PSR Position[a]						CR Position[a]						MT Position[a]			No. of Depleted Tubes Present	Fissile Mass		Excess Reactivity at 25°C, Ih	Reactivity Change from Previous Configuration, Ih
	702	705	714	717	726	729	506	508	514	516	522	524	401	407	413		$^{239+241}$Pu, kg	^{235}U, kg		
EOC																63	485.390	4.297	147.5 ± 2.4	
SUB1	I	I	I	I	I	I										63	485.390	4.297	−2074 ± 32	−2222 ± 32
IC1	I	I	I	I	I	I										45	503.352	4.204	13.2 ± 2.4	+2087 ± 32
SUB2								I		I		I				45	503.352	4.204	−1721 ± 15	−1734 ± 15
IC2								I		I		I				26	522.313	4.105	125.9 ± 2.4	+1847 ± 15
SUB3								I[b]		I[b]		I[b]				26	522.313	4.105	−434.6 ± 2.5	−560.5 ± 3.5
SUB4							I[c]	I	I[c]	I	I[c]	I				26	522.313	4.105	−1547 ± 10	−1112 ± 10
IC3							I[c]	I	I[c]	I	I[c]	I				13	535.286	4.038	29.8 ± 2.4	+1577 ± 10
SUB5							I	I	I	I	I	I				13	535.286	4.038	−1673 ± 14	−1703 ± 14
IC4-1							I	I	I	I	I	I				0	548.259	3.970	−272.1 ± 2.5	+1401 ± 14
IC4-2[d]							I	I	I	I	I	I				0	548.259	3.970	−261.7 ± 2.5	+10.4 ± 3.5
SUB6	I		I		I		I	I	I	I	I	I				0	548.259	3.970	−1453 ± 8.7	−1191 ± 9
SUB7	I		I		I		I	I	I	I	I	I		I		0	542.259	3.919	−2302 ± 40	−849 ± 41
SUB8							I	I	I	I	I	I		I		0	542.259	3.919	−1178 ± 5.0	+1124 ± 40
SUB9							I	I	I	I	I	I	I	I	I	0	530.259	3.815	−24.35 ± 60	−1257 ± 60
BOL-A	I		I		I		I[e]	I[e]	I[e]	I[e]	I[e]	I[e]	I	I	I	0	530.259	3.815	212.3 ± 2.4	+2647 ± 60
BOL-B	I		I		I		I[e]	I[e]	I[e]	I[e]	I[e]	I[e]	I	I	I	0	530.259	3.815	−1076 ± 3.8	−1288 ± 4
BOL-C	I		I		I		I[e]	I[e]	I[e]	I[e]	I[e]	I[e]	I	I	I	0	530.259	3.815	−408.1 ± 2.5	+668 ± 5
BOL-D	I	I	I	I	I		I[e]	I[e]	I[e]	I[e]	I[e]	I[e]	I	I	I	0	530.259	3.815	−1204 ± 5.3	−796 ± 6
BOL-E	I		I				I[e]	I[e]	I[e]	I[e]	I[e]	I[e]	I	I	I	0	530.259	3.815	13.6 ± 2.4	+1218 ± 6

[a] I means fully inserted unless otherwise indicated. Blank means fully withdrawn for a CR and removed for a PSR or MT.
[b] B_4C content increased by 25% (Heavy Control Composition).
[c] Inserted 50% (18 in.).
[d] IC4-1 and IC4-2 are identical except for a minor modification to the ZPR-9 fuel-bearing dual purpose rods.
[e] Inserted 61% (22 in.).

subcriticality was measured by the rod drop-inverse kinetics method. Repetitive measurements were made in order to establish a statistical uncertainty for the measured reactivity. The kinetics parameters used in the inverse kinetics analysis of the rod drop and control rod calibration flux profiles are given in Table III of Paper II-1. The EOC parameters were used from EOC through SUB-5 and the BOL parameters were used from IC4 through BOL-E.

During the time that flux data were being accumulated during a rod drop measurement, the reactor temperature profile was recorded so that the results of each measurement could be adjusted to the reference temperature of 25°C using an experimentally determined temperature coefficient of reactivity (−4.1 Ih/°C).

Results of the Experiment and How They Are Used

The measured values of excess reactivity and subcriticality are listed in Table II-2-I for each configuration. Calculated values of k have been obtained for most of the configurations listed. Systematic differences between the calculated and experimental results for the EMC have been used to provide correction factors in calculations of similar FTR configurations.

The last column of Table II-2-I gives the reactivity changes between configurations. Comparisons of these values and corresponding calculated quantities indicate possible problem areas. For example, control rod worths may be calculated accurately, while fuel worths may be calculated poorly.

II-3. Measured Reaction Rate Distributions in the Fast Test Reactor-Engineering Mockup Critical (FTR-EMC), ZPR-9 Assembly 27

A. B. Long and C. D. Swanson

Radial reaction rate distributions of $^{239}Pu(n,f)$, $^{238}U(n,f)$ and $^{10}B(n,\alpha)$ were measured in the Beginning-of-Life (BOL) configuration of the FTR-EMC along a radial traverse hole located approximately 1.75 in. back from the interface of the two reactor halves and extending from matrix position S23-23 (central tube) radially outward to S23-39. The diameter of the traverse hole was 1.125 in. and was formed by substituting diluent material containing holes for regular diluent plate material in the appropriate positions. Because there were no suitable plutonium plates with holes, a 2 x 2 in. void was left in each column of fuel material to permit passage of the traverse hole.

The configuration of the core* for the reaction rate measurement is shown in Fig. II-3-1. In the configuration:

a. The oscillator (OSC 203) is in the withdrawn position.
b. Safety rods SR 304, SR 308, and SR 312 are in the withdrawn position.
c. The Material Test Loops MT 401, MT 407, and MT 413 are inserted.
d. Control rods CR 506, CR 514, and CR 522 are fully withdrawn. CR 508, CR 516, and CR 524 are fully inserted.
e. Peripheral shim rods PSR 702, PSR 714, and PSR 726 are inserted.
f. The autorod is mounted in matrix position 23-14.
g. Plates with holes are loaded into drawers S23-21 through S23-39.

Other regions identified in Fig. II-3-1 are the inner driver (ID), outer driver (OD), radial reflector (RR), general purpose loop (GP), and special purpose loop (SP).

* Abbreviations are defined in Paper II-1.

Experimental Technique

The experimental method used to record and correct the $^{239}Pu(n,f)$, $^{238}U(n,f)$ and $^{10}B(n,\alpha)$ reaction rate data is documented in Paper III-18 and Ref. 1. The fission counters and ^{10}B counter used for the traverses were the same as those used in Refs. 1 and 2. In a particular traverse, the counter was placed at the end of the radial sample changer tube (without any stainless steel plugs) and traversed through the void hole using the radial sample changer mechanism. A reduction in the background of the ^{10}B spectrum was achieved in those measurements by using A-CO_2 gas in the counter, thus reducing proton recoils (see Papers III-18 and III-20).

The data were recorded in these measurements "on-line", using the SEL-840 computer, and immediately corrected for dead-time and background as described in Papers III-18 and III-19. New Ortec Model 486 Amplifier Pulse Height Analyzers were used giving a constant dead-time of 1.8 μsec per pulse.

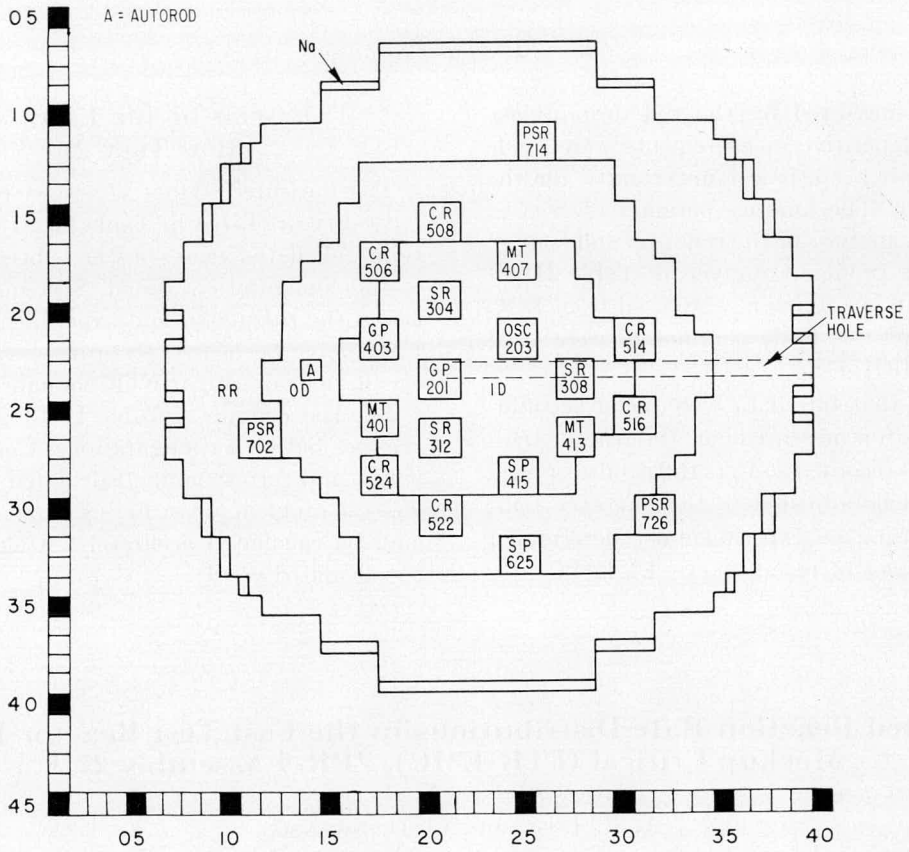

FIG. II-3-1. The EMC Configuration for Radial Reaction Rate Distribution Measurements. *ANL Neg. No. 116-972.*

TABLE II-3-I. RADIAL REACTION RATE DISTRIBUTIONS MEASURED NEAR THE CORE MID-PLANE IN THE BOL CONFIGURATION OF THE FTR-EMC

Relative Reaction Rates				
Position,[a] in.	$^{239}Pu(n,f)$	$^{10}B(n,\alpha)$	Position,[a] in.	$^{238}U(n,f)$
0.00	910.2 ± 4.7	854.1 ± 4.6	0.00	103.76 ± 1.15
2.18		867.6 ± 13.1	2.18	98.27 ± 1.33
2.22	912.5 ± 6.8		2.54	97.17 ± 0.96
4.36	902.0 ± 5.1	846.8 ± 14.7	4.72	94.33 ± 1.40
6.53	872.6 ± 4.6	833.7 ± 8.3	6.89	89.09 ± 1.06
8.71	830.8 ± 5.1	799.2 ± 7.5	9.07	84.00 ± 1.11
10.89	791.2 ± 4.4	747.9 ± 8.3	11.25	80.66 ± 1.29
13.07	718.6 ± 4.0	669.9 ± 4.0	13.43	77.34 ± 1.42
15.24	652.1 ± 3.2	605.1 ± 7.3	14.52	73.85 ± 1.36
17.42	594.2 ± 3.6	558.5 ± 3.4	16.69	68.98 ± 1.51
19.60	547.9 ± 4.0	523.7 ± 1.5	17.79	66.75 ± 1.32
21.78	513.8 ± 2.6	537.9 ± 7.8	19.96	61.95 ± 1.50
22.86	517.2 ± 3.8		22.14	53.50 ± 1.27
23.95	541.6 ± 3.3	680.3 ± 35.7	24.32	37.86 ± 1.16
25.04	602.8 ± 4.1	823.8 ± 2.9	26.49	18.69 ± 0.62
26.13	708.9 ± 4.1	1037.5 ± 3.5	28.67	8.84 ± 0.23
27.21	755.7 ± 5.1		30.85	4.33 ± 0.25
28.30	753.4 ± 4.0	1237.5 ± 44.2	33.03	2.15 ± 0.13
29.40		1136.0 ± 2.3	35.20	1.06 ± 0.07
30.48	601.1 ± 4.1	1001.9 ± 1.8	37.38	0.56 ± 0.03
32.66	397.7 ± 2.9	675.9 ± 2.6	39.56	0.48 ± 0.08
34.84	224.1 ± 2.0	366.4 ± 2.8		
37.02	136.8 ± 1.4			

[a] Radial distance along Row 23 from the axis of the assembly which is at the center of matrix tube 23-23.

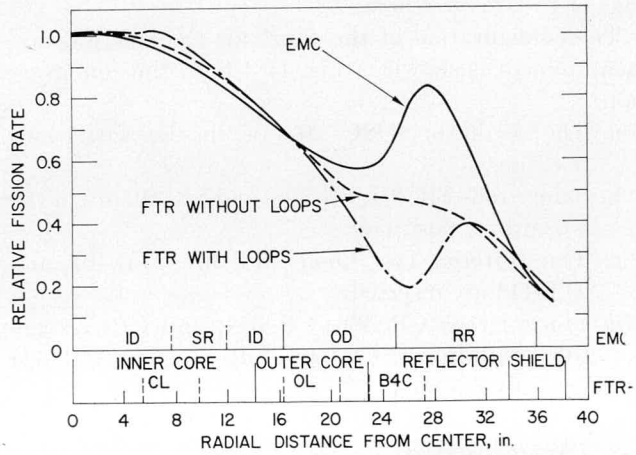

FIG. II-3-2. A Comparison of $^{239}Pu(n,f)$ Radial Reaction Rate Traverses in the EMC and FTR-3 Assemblies. *ANL Neg. No. 116-971.*

Results

The results of the $^{239}Pu(n,f)$, $^{238}U(n,f)$ and $^{10}B(n,\alpha)$ radial reaction rate distributions are listed in Table II-3-I and plotted in Figs. II-3-2 through II-3-4. Results from radial traverses in the FTR-3 assembly are included in these figures for comparison. The data from all traverses are normalized to 1.0 at the core center. The initial FTR-3 traverses[1] were done in the configuration shown in Fig. II-3-5. The FTR-3 traverses through simulated loops and a B_4C control zone[2] were done in the configuration shown in Fig. II-3-6. The closed loop contained 19 % of the fuel density of the FTR-3 inner

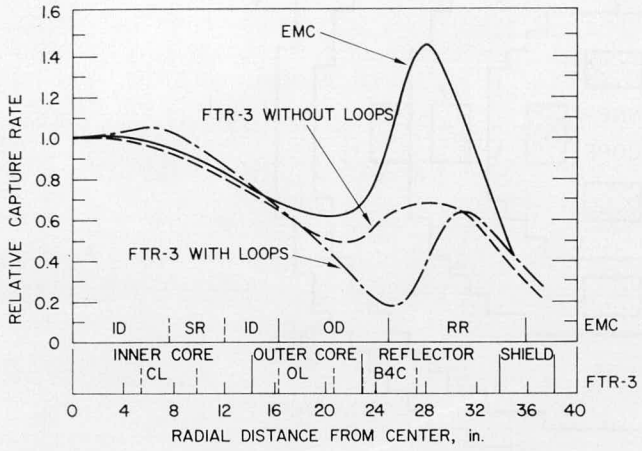

Fig. II-3-3. A Comparison of $^{10}B(n,\alpha)$ Radial Reaction Rate Traverses in the EMC and FTR-3 Assemblies. *ANL Neg. No. 116-970.*

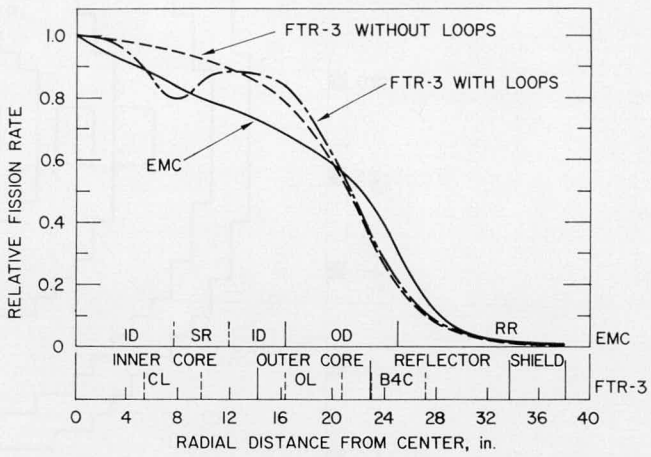

Fig. II-3-4. A Comparison of $^{238}U(n,f)$ Radial Reaction Rate Traverses in the EMC and FTR-3 Assemblies. *ANL Neg. No. 116-973.*

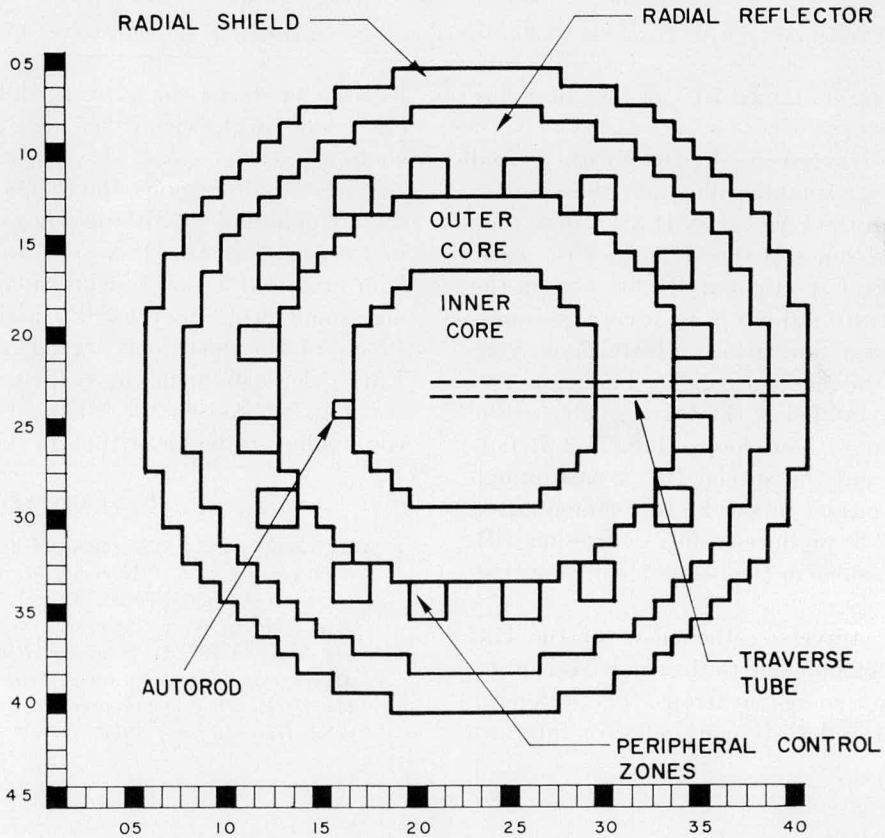

Fig. II-3-5. FTR-3 Configuration without Loops for Radial Reaction Rate Distribution Measurements. *ANL Neg. No. 116-526 Rev. 1.*

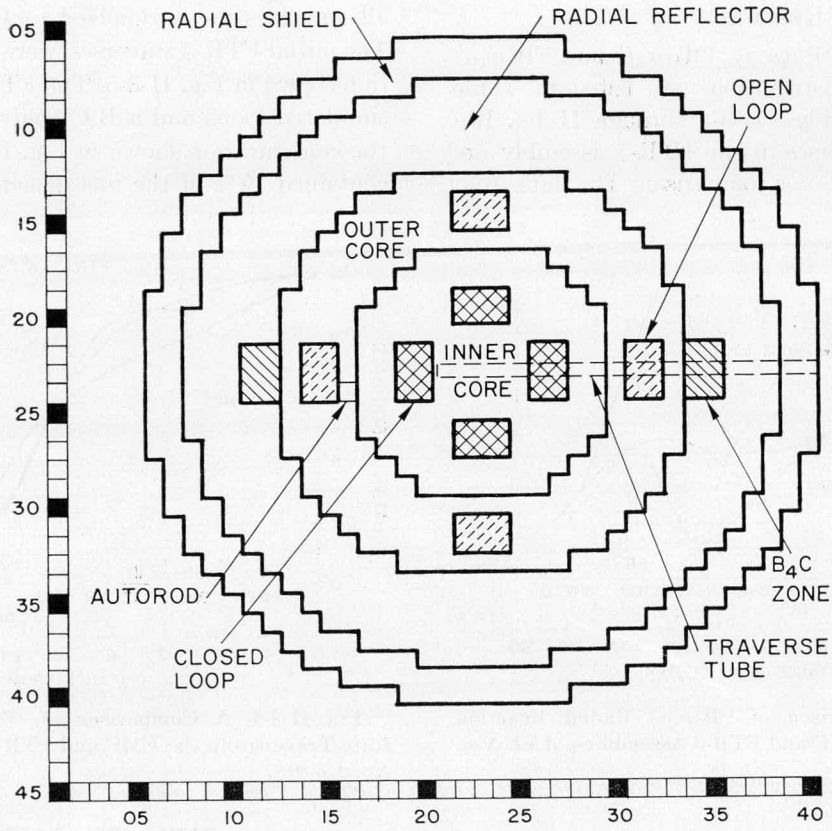

FIG. II-3-6. FTR-3 Configuration with Loops for Radial Reaction Rate Distribution Measurements. *ANL Neg. No. 116-1052.*

core and the open loop contained 70 % of the outer core density.

The reaction rate traverse results for $^{239}Pu(n,f)$ and $^{10}B(n,\alpha)$ in the three assemblies illustrate the effect of B_4C control zones. In the EMC (Fig. II-3-1) there were no peripheral control zones in the vicinity of the traverse hole and CR 514, CR 416, and SR 308 were in the withdrawn position with sodium in their core positions. The ^{239}Pu and ^{10}B reaction rates for EMC have very prominent peaks in the reflector regions. The peripheral control zones above and below the traverse hole in the FTR-3 configuration without loops (Fig. II-3-5) flattened these peaks, and the special B_4C zone through which the traverse passed in the FTR-3 configuration with loops (Fig. II-3-6) produced a flux depression with corresponding depressions in the reaction rate traverses for ^{239}Pu and ^{10}B.

For the $^{238}U(n,f)$ traverses, the effect of the B_4C control zones was negligible due to the small ^{10}B capture cross section for high energy neutrons. The difference between the FTR-3 and EMC core-reflector interface location produced the outward shift of the EMC traverse results in the vicinity of the B_4C peripheral control zones.

With the core regions, the effects of spectral softening due to loops and/or withdrawn control rods are evident in the reaction rate traverses. In FTR-3, the closed loop produced a severe depression in the ^{238}U traverse and small peaks in the ^{239}Pu and ^{10}B traverses. The effects of the open loop are not as apparent.[2] In the EMC, the sodium in the oscillator, SR 308, CR 514, and CR 516 caused the $^{238}U(n,f)$ reaction rate in the core regions to be lower than in the FTR-3 core.

REFERENCES

1. A. B. Long and C. D. Swanson, *Measured Reaction Rate Distributions in ZPR-9 Assembly 26, FTR-3*, Applied Physics Division Annual Report, July 1, 1969 to June 30, 1970, ANL-7710, p. 65.
2. A. B. Long and C. D. Swanson, *Reaction Rate Distribution Measurements During Loop Experiments, ZPR-9 Assembly 27*, Reactor Development Program Progress Report, ANL-7776 (January 1971).

II-4. Control Rod and Loop Experiments in ZPR-9 Assembly 26, FTR-3

J. W. Daughtry, R. B. Pond, C. D. Swanson and R. M. Fleischman*

Introduction

The FTR-3 critical experiments were performed in the ZPR-9 facility to provide physics information in support of the nuclear design of the Fast Test Reactor (FTR). FTR-3 had a two zone PuO_2-UO_2 core and a ring of sixteen simulated B_4C control rods surrounding the core zones. Whenever possible, quarter core symmetry was maintained to simplify the analysis. A detailed description of FTR-3 is given in Ref. 1.

One phase of the program of experiments in FTR-3 was a study of control rod and test loop effects. The control rod measurements were intended to provide

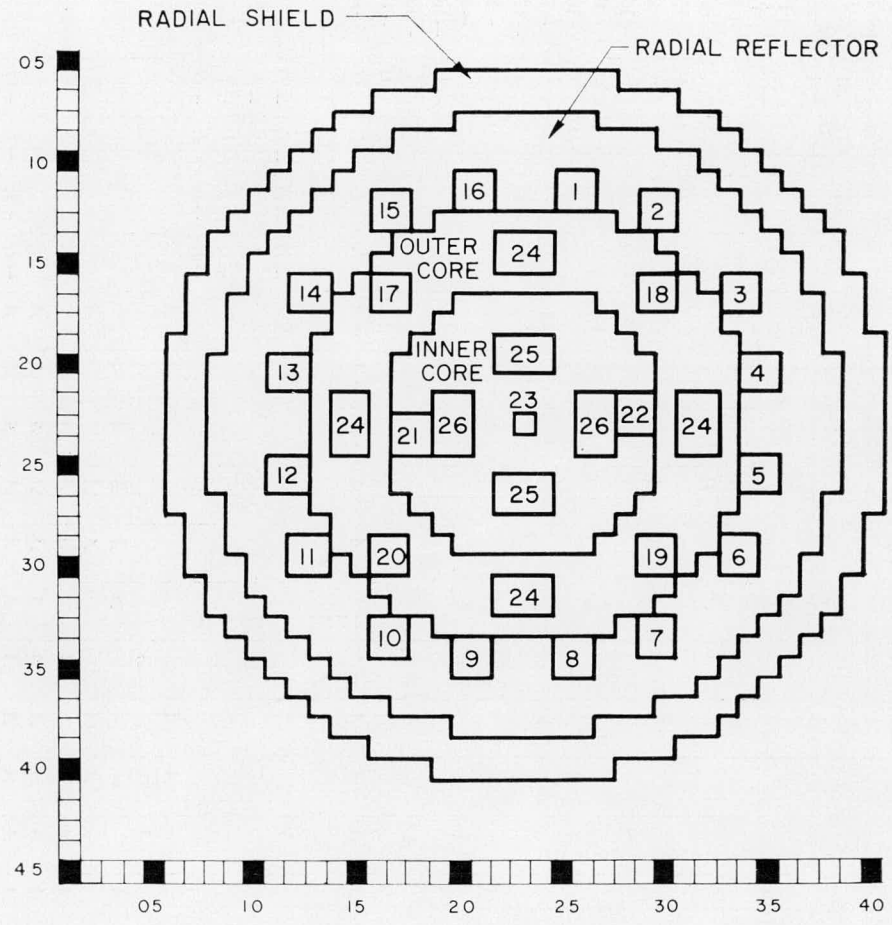

Fig. II-4-1. FTR-3 Assembly Diagram Showing The Locations of Composition Changes In The Control Rod and Loop Experiments. *ANL Neg. No. 116-1028.*

the outer core zone. Its axial and radial reflectors were a nickel-sodium-stainless-steel composition. The total core volume was 1045 liters with a fissile mass of 541 kg of $^{239}Pu + {}^{241}Pu + {}^{235}U$. FTR-3 was not intended to be an accurate mockup of the FTR, but rather, a simplified model in which gross heterogeneities such as ›ps and control rod channels were homogenized into

* WADCO Corporation, a Subsidiary of Westinghouse Electric Corporation, Richland, Washington.

data on B_4C and tantalum as control materials. Simulated control rods were introduced in both core zones as well as at the core-reflector boundary. The reactivity worths of various arrays of control rods were measured to investigate interaction effects, such as rod shadowing and flux tilting. Simulated open and closed loops were introduced in order to obtain more information relative to large in-core perturbations. This paper reports the results of these control rod and loop experiments.

TABLE II-4-I. k_{ex} AND LOADING EXCHANGE WORTHS FOR LOADINGS 71–87

Loading No.	Loading Exchange Zone																				k_{ex} @ 30°C, Ih	σ, Ih	Exchange Worth, Ih	σ, Ih
	1	2	3	4	5	6	7	8	9	10	11	12	13	14	15	16	17	18	19	20				
71																					+50.9	4.0		
72[a]													*B*								+96.9	4.0	+46.0	5.7
73													*B*								+148.3	4.0	+51.4	5.7
74													−*B*								+55.5	4.0	−92.8	5.7
75																	−*C*	−*C*	−*C*	−*C*	−1569	45	−1624.5	45.2
76				*A*	*A*							*A*	*A*								−217.8	5.3	+1351.2	45.3
77																	−*D*				−1073	80	−855.2	80.2
78	| *A*							| *A*	*A* |							*A* |					−660.0	20.2	+413.0	82.5
79																			−*D*		−1675	146	−1015.0	147.4
80	*A* |							*A* |	| *A*							| *A*				−716.0	35.2	+959.0	150.2
81																		−*D*			−1757	163	−1041.0	166.8
82			*A*			*A*					*A*			*A*							−875.3	32.9	+881.7	166.3
83		*A* |					*A* |			| *A*				| *A*						−449.7	11.3	+425.6	34.8
84																				−*D*	−1675	146	−1225.3	146.4
85		| *A*						| *A*		*A* |					*A* |					−1276	89	+399.0	171.0
86																				*B*	−941.0	39.8	+335.0	97.5
87	−*A*	−*A*	−*A*	−*A*	−*A*	−*A*	−*A*	−*A*	−*A*	−*A*	−*A*	−*A*	−*A*	−*A*	−*A*	−*A*	*L*	*L*	*L*	*O*	+50.7	4.0	+991.7	40.0
													B										97.4	5.7
																	−*D*	−*D*	−*D*	−*D*			−4136.5	278.2
																				−*F*			+890.3	175.9
																	−*L*	−*L*	−*L*	−*L*			−5761.0	281.9
																	−*L*	−*L*	−*L*	−*O*			−5426.0	298.3
	A							*A*	*A*							*A*							+1372.0	171.4
		A					*A*			*A*					*A*								+824.6	174.5
			A	*A*	*A*	*A*					*A*	*A*	*A*	*A*									+2232.9	172.4
	A			*A*	*A*			*A*	*A*			*A*	*A*			*A*							+2723.2	177.3
		A	*A*	*A*	*A*	*A*	*A*			*A*	*A*	*A*	*A*	*A*	*A*								+3057.5	245.3
	A	*A*	*A*	*A*	*A*	*A*	*A*	*A*	*A*	*A*	*A*	*A*	*A*	*A*	*A*	*A*							+4429.5	299.2
	A	*A*	*A*	*A*	*A*	*A*	*A*	*A*	*A*	*A*	*A*	*A*	*A*	*A*	*A*	*A*	−*L*	−*L*	−*L*	−*O*			−996.5	422.5

[a] Partial substitution: Loading 72, stationary half only; Loading 73, moveable half only.

Experimental Details

Figure II-4-1 is a diagram showing all simulated control rod and test loop positions for this series of measurements. The zones numbered 1–16 were peripheral control rod locations, numbers 17–23 were in-core control rod locations, the four zones numbered 24 were simulated open loops and the four zones numbered 25 and 26 were simulated closed loops. The length of the control rod and loop loadings was 36 in., which was the same as the core height. Twelve inches of radial reflector composition was loaded at each end of the peripheral control rods and twelve inches of axial reflector composition was loaded at each end of the in-core control rods and loops. Atom densities and drawer loading diagrams are given in Ref. 1 for each region of FTR-3.

Beginning with the FTR-3 reference configuration in Loading 71, having B_4C control composition in zones 1 through 16 and core composition in all other numbered zones of Fig. II-4-1, a series of configurations was assembled by changing the loading in the numbered zones in Fig. II-4-1. The excess reactivity or subcriticality of each configuration was measured.

The excess reactivities of all critical configurations were determined from the positions of calibrated ZPR-9 control rods. These rods were recalibrated in each critical configuration using the inverse kinetics method.[2] In each subcritical configuration the subcriticality was measured by the rod drop-inverse kinetics method.[3] The rod drop measurements were repeated until the desired precision was obtained.

Each measured reactivity, critical or subcritical, was adjusted to a reference temperature of 30°C using an experimentally determined temperature coefficient of reactivity (-3.39 ± 0.04) Ih/°C.[1] The uncertainty in the measured reactivities due to the uncertainty in the temperature coefficient of reactivity was small (less than 0.25 Ih) since the temperature adjustment never exceeded 5.5°C.

The results obtained in this series of measurements are given in Tables II-4-I through II-4-IV. Each configuration is listed by its loading number. The letters identify the loading change from the previous configuration and are defined in Table II-4-V. In some loadings only part of a zone was modified. This is indicated in the tables. For example, in Loading 72 only the stationary half of zone 13 was modified. In Loading 73 the moveable half of zone 13 was modified. The symbol A| means that radial reflector composition was substituted for B_4C control composition in the left half of the zone; $\underline{A}$ means that this same composition change was made in the top half of the zone; etc. A minus sign before the letters in Tables II-4-I through II-4-IV means the reverse of the composition change defined in Table II-

TABLE II-4-II. k_{ex} and Loading Exchange Worths for Loadings 88–100

Loading No.	Loading Exchange Zone															k_{ex} @ 30° C, Ih	σ, Ih	Exchange Worth, Ih	σ, Ih
	2	3	4	5	6	7	10	11	12	13	14	15	21	22	23				
88													$-E$	$-E$		-869.3	41.0	-920.0	41.2
89									A	A						-209.4	4.7	$+659.9$	41.3
90			$A\|$	$A\|$												$+145.8$	4.0	$+355.2$	6.2
91														$-D$		-2074	103	-2219.8	103.1
92		A	$\|A$	$\|A$	A			A			A					-838.7	30.0	$+1235.3$	107.3
93	A					A	A					A				$+159.2$	4.0	$+997.9$	30.3
94													$-F$			-1745	84	-1904.2	84.1
95													$-B$			-2868	162	-1123.0	182.5
96	$-A$	$-A$	$-A$	$-A$	$-A$	$-A$	$-A$	$-A$	$-A$	$-A$	$-A$	$-A$	G	G		$+49.4$	4.0	$+2917.4$	162.0
97															$-E$	-140.6	4.5	-190.0	6.0
98															$-F$	-986.0	18	-845.4	18.6
99															$-B$	-1472	65	-486.0	67.4
100													$-E$	$-E$	G	-942.1	12.8	$+529.9$	66.2
															G			$+1449.9$	80.0
													$-D$					-3027.2	200.9
															$-D$			-1331.4	69.9
															$-M$			-1035.4	19.6
													$-G$	$-G$				-6167.0	229.6
															$-G$			-1521.4	70.2
													$-E$	$-E$				-991.5	96.5
		A	A	A	A			A	A	A	A							$+2250.4$	115.1
	A	A	A	A	A	A	A	A	A	A	A	A						$+3248.3$	119.1
	A	A	A	A	A	A	A	A	A	A	A	A	$-G$	$-G$				-2918.7	258.6

TABLE II-4-III. k_{ex} AND LOADING EXCHANGE WORTHS FOR LOADINGS 101–114

Loading No.	Loading Exchange Zone																		k_{ex} @ 30°C, Ih	σ, Ih	Exchange Worth, Ih	σ, Ih
	1	2	3	4	5	6	7	8	9	10	11	12	13	14	15	16	21	22				
101			*B*			*B*					*B*			*B*					−619.6	34.6	+322.5	36.9
102		*B*					*B*			*B*					*B*				−305.5	7.7	+314.1	35.4
103																	−*I*	−*I*	−2004	81.8	−1698.5	82.2
104		*H*					*H*			*H*					*H*				−1346	29.4	+658.0	86.9
105			*H*			*H*					*H*			*H*					−768.8	14.3	+577.2	32.7
106		−*H*	−*H*			−*H*	−*H*			−*H*	−*H*			−*H*	−*H*				−2055	125	−1286.2	125.8
107				*A*	*A*							*A*	*A*						−715.5	14.1	+1339.5	125.8
108																	−*J*	−*J*	−1584	29	−868.5	32.2
109	*A*							*A*	*A*							*A*			−94.9	4.0	+1489.1	29.3
110																	−*K*	−*K*	−915.8	31.0	−820.9	31.3
111			*H*																−735.5	14.7	+180.3	34.3
112						*H*													−541.2	4.9	+194.3	15.5
113											*H*			*H*					−178.7	4.4	+362.5	6.6
114	−*A*	−*B*	−*A*	−*A*	−*A*	−*A*	−*B*	−*A*	−*A*	−*B*	−*A*	−*A*	−*A*	−*A*	−*B*	−*A*	*M*	*M*	+44.7	4.0	+223.4	5.9
																	−*N*	−*N*			−1689.4	44.9
																	−*F*	−*F*			−3387.9	93.7
																	−*P*	−*P*			−2567.0	88.3
																	−*M*	−*M*			−4307.9	102.3
		B	*B*			*B*	*B*			*B*	*B*			*B*	*B*						+636.6	51.1
		H	*H*			*H*	*H*			*H*	*H*			*H*	*H*						+1235.2	92.8
			H			*H*					*H*			*H*							+737.1	38.2
			H			*H*															+374.6	37.6
		A					*A*			*A*					*A*						+972.1	93.8
			A			*A*					*A*			*A*							+899.7	49.3
		A	*A*			*A*	*A*			*A*	*A*			*A*	*A*						+1871.8	106.0
	A			*A*	*A*			*A*	*A*			*A*	*A*			*A*					+2828.6	129.2
	A	*A*	*A*	*A*	*A*	*A*	*A*	*A*	*A*	*A*	*A*	*A*	*A*	*A*	*A*	*A*					+4700.4	167.1
	A	*B*	*A*	*A*	*A*	*A*	*B*	*A*	*A*	*B*	*A*	*A*	*A*	*A*	*B*	*A*					+4042.4	142.7
	A	*B*	*A*	*A*	*A*	*A*	*B*	*A*	*A*	*B*	*A*	*A*	*A*	*A*	*B*	*A*	−*M*	−*M*			−265.5	175.6

TABLE II-4-IV. k_{ex} AND LOADING EXCHANGE WORTHS FOR LOADINGS 115–119

Loading No.	Loading Exchange Zone															k_{ex} @ 30°C, Ih	σ, Ih	Exchange Worth, Ih	σ, Ih
	1	2	4	5	7	8	9	10	12	13	15	16	24	25	26				
115													$-Q$			-832.3	11.9	-877.0	12.6
116	| A		$\underline{A}$	$\bar{A}$		| A	A |		$\bar{A}$	$\underline{A}$		A |				-5.8	4.1	$+826.5$	12.6
117														$-R$		-1414	37	-1408.2	37.2
118		A			A			A			A					-366.8	4.0	$+1047.2$	37.2
119															$-R$	-1922	68	-1555.2	68.1
														$-R$	$-R$			-2963.4	77.6

TABLE II-4-V. DEFINITIONS OF SYMBOLS USED TO IDENTIFY CHANGES IN COMPOSITION

Symbol[a]	Composition Removed	Composition Added	Symbol[a]	Composition Removed	Composition Added
A	B_4C Control	Radial Reflector	J	Ta (50/50)	Ta (25/75)
B	B_4C Control	Ta Control	K	Ta Control	Ta (50/50)
C	Safety Rod Channel	Outer Core	L	B_4C Control	Outer Core
D	B_4C Control	Safety Rod Channel	M	Ta Control	Inner Core
E	Safety Rod Channel	Inner Core	N	Ta Control	Ta (25/75)
F	Ta Control	Safety Rod Channel	O	Ta Control	Outer Core
G	B_4C Control	Inner Core	P	Ta (50/50)	Safety Rod Channel
H	Ta Control	Radial Reflector	Q	Open Loop	Outer Core
I	Ta (25/75)	Safety Rod Channel	R	Closed Loop	Inner Core

[a] A minus sign before a letter in Tables II-4-I through II-4-IV means the reverse of the composition change defined here.

TABLE II-4-VI. FTR-3 REGION AND ZONE COMPOSITIONS, 10^{21} atoms/cm^3

Isotope or Element	Inner Core		Outer Core	Closed Loop	Open Loop	B_4C Control	Ta (control)	Ta (50/50)	Ta (25/75)	Safety Rod Channel	Radial Reflector	Axial Reflector	Radial Shield
	Type A	Type B											
Mo	0.2340	0.0123	0.4412	0.0357	0.3324	0.0105	0.0077	0.0086	0.0088	0.0097	0.0078	0.0079	0.036
Na	9.1731	11.208	8.7013	9.3880	9.5310	4.1257	4.194	8.812	13.853	18.470	6.7544	9.2102	6.754
C	0.0257	0.0356	1.0686	0.0716	1.0778	14.043	0.022	0.025	0.026	0.028	0.1646	0.0231	0.105
Fe	13.363	13.234	15.906	26.595	17.634	11.320	8.261	9.247	9.533	10.519	8.4575	8.5898	39.022
Cr	2.7593	3.8193	3.1571	7.6726	4.1332	3.2536	2.383	2.668	2.750	3.035	2.432	2.4614	11.258
Ni	1.3166	1.8224	1.5064	3.6610	1.9722	1.5525	1.137	1.273	1.312	1.448	48.072	38.1013	5.372
Mn	0.2026	0.2804	0.2318	0.5634	0.3035	0.2389	0.175	0.196	0.202	0.223	0.2864	0.2789	0.827
Ta							33.428	21.801	11.627				
B-10						10.698							
B-11						43.387							
B						54.085							
Al		0.1109											
O	14.454	8.7577	12.717		10.236								
Pu-238	0.0006		0.0006		0.0003								
Pu-239	0.8814	1.0690	1.4669	0.1877	1.0276								
Pu-240	0.1167	0.0510	0.1723	0.0178	0.1141								
Pu-241	0.0181	0.0049	0.0227	0.0015	0.0136								
Pu-242	0.0019	0.0001	0.0022	0.0001	0.0013								
Pu-239 + Pu-241	0.8995	1.0739	1.4896	0.1892	1.0412								
'u-240 + Pu-242	0.1186	0.0511	0.1745	0.0179	0.1154								
'u	1.0187	1.1250	1.6647	0.2071	1.1569								
U-235	0.0125	0.0069	0.0125	0.0019	0.0097								
U-238	5.7811	3.2769	5.9000	0.8279	4.6547								
U	5.7936	3.2838	5.9125	0.8298	4.6644								

4-V. Wherever inner core composition is specified, Type A composition is loaded into even numbered matrix columns and Type B in odd numbered columns. Atom densities are given in Table II-4-VI for each composition mentioned in Table II-4-V.

The initial or reference FTR-3 configuration, Loading 71, had the following compositions in the numbered zones of Fig. II-4-1:

a. zones 1–16 contained B_4C control composition,
b. zones 17–20 and 24 contained outer core composition,
c. zones 21–23 and 25–26 had inner core composition.

The assembly was returned to this reference configuration in Loadings 74, 87, 96, and 114.

Results of Reactivity Measurements

Tables II-4-I through II-4-IV give the measured k_{ex} for each configuration adjusted to 30°C. The value of σ given with each k_{ex} is the combination of a 70% confidence interval (based on repetitive reactivity measurements) plus a ± 4 Ih uncertainty in physically reproducing each configuration. The list of exchange worths gives the reactivity worth associated with each loading change.

At the bottom of each table is a list of exchange worths obtained indirectly as combinations of the loading changes given in the top part of the table. The worth of any given loading change depends on the configuration of the assembly prior to the change. The procedure of adding up the results of partial changes to infer the worth of composite changes, as done here, neglects this dependence. However, a survey of the results given in Tables II-4-I through II-4-IV shows that within the accuracy of these measurements the worths of the loading changes that were made were essentially independent of the configuration of the other control rods and loops in the assembly.

Many of the configurations reported here have been analyzed by WARD and WADCO to determine their calculational ability in predicting experimental results and to obtain bias factors for fuel, boron, and tantalum to be used in FTR design calculations.[4]

References

1. J. W. Daughtry, R. B. Pond, C. D. Swanson and R. M. Fleischman, *ZPR-9 Assembly 26, FTR-3*, Reactor Physics Division Annual Report, July 1, 1969, to June 30, 1970, ANL-7710, pp. 58–63.
2. C. E. Cohn and J. J. Kaganove, *Digital Method for Control Rod Calibration*, Trans. Am. Nucl. Soc. **5**, 388 (1962).
3. C. E. Cohn, *Experience with Subcriticality Determination by Rod Drop in the FTR-3 Critical Experiments*, Trans. Am. Nucl. Soc. **14**, 29 (1971).
4. S. Ramchandron and R. A. Bennett, *Analysis of Fuel Worth, B_4C, and Ta Control Worth Experiments in the ZPR-9/FTR-3 Critical*, Trans. Am. Nucl. Soc. **14**, 26 (1971).

II-5. The Shutdown Margin Experiment in FTR-3

J. W. Daughtry and R. B. Pond

Introduction

In order to preclude a shutdown or refueling reactivity accident in the Fast Test Reactor (FTR), it is important to have a reliable method for continuously monitoring the reactivity status of the reactor under shutdown conditions, expecially during refueling operations, during control, safety, or shim rod reloading, and during fuel test loop loading. The requirement on the accuracy of the shutdown reactivity for the FTR is $\pm 20\%$ at about \$30 subcritical. One system that has been proposed to provide the desired information uses a digital computer to convert subcritical count rate data to reactivity. This requires a calibration within a few dollars of critical using a method such as noise analysis, pulsed neutron, or rod drop-inverse kinetics.

An experiment was conducted in the FTR-3 assembly on ZPR-9 to evaluate the proposed system for monitoring the shutdown margin and to compare various subcriticality measurement methods for their suitability in making the near-critical calibration. To obtain the desired information, a series of configurations was assembled on ZPR-9 spanning the reactivity range from critical to about \$30 subcritical. Neutron count rate data were recorded with a number of detectors in each configuration. Subscriticality measurements were made by several methods; each method was used as far subcritical as possible.

There were three general types of subcriticality measurements: (1) rod drop, (2) noise analysis, and (3) asymmetric source.

Two groups of visiting experimenters were involved in this series of measurements. One group from Oak Ridge National Laboratory (ORNL): N. J. Ackerman,

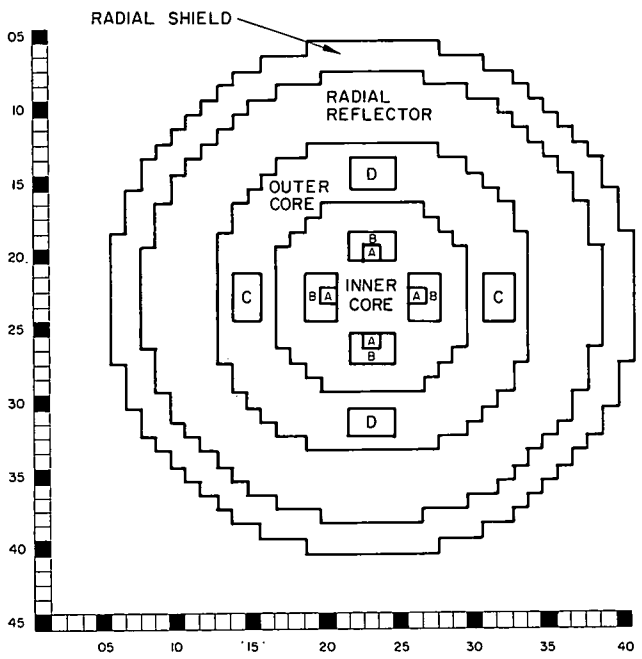

FIG. II-5-1. Initial Configuration for the Shutdown Margin Experiment. *ANL Neg. No. 116-1066.*

A. R. Buhl and R. C. Kryter were responsible for the asymmetric source measurements and the noise measurements by the cross power spectral density (CPSD) technique. The other group, from the University of Washington and under contract with WADCO: R. W. Albrecht and G. M. Hess were responsible for the noise measurements by the polarity spectral coherence (PSC) technique.

INITIAL REACTOR CONFIGURATION

Figure II-5-1 shows the matrix loading pattern for FTR-3 loading 125 which was the initial configuration for the shutdown margin experiment. The zones marked by letters in Fig. II-5-1 are the locations of simulated FTR open and closed loops in FTR-3. The drawers labeled A in the inner core region contained closed loop Type A drawers. The remainder of the drawers in the inner core loops, labeled B, contained closed loop Type B drawers. The zones labeled C contained safety rod channel composition, and the zones labeled D contained open loop composition. Atom densities for these compositions are given in Table II-5-I. The remainder of the assembly (radial shield, radial reflector, outer core, inner core and the axial configuration) is described in detail in Ref. 1.

Neutron detectors were installed in the assembly at various locations for this series of experiments. Table II-5-II lists the detector types and locations. Except as noted, all detectors were inserted into drawers in the radial reflector region so that one end of the detector was at the midplane of the assembly. The installation of the detectors required the removal of reflector composition from the drawers. Space in the drawers not occupied by the detectors, leads, etc. was filled with nickel and sodium cans in approximately equal volumes.

The ZPR-9 poison rods were used to adjust the subcriticality of the assembly for some of the measure-

TABLE II-5-I. ATOM DENSITIES OF SIMULATED LOOPS IN THE INITIAL CONFIGURATION FOR THE SHUTDOWN MARGIN EXPERIMENT, 10^{21} atoms/cc

Isotope or Element	Closed Loop, Type A	Closed Loop, Type B	Safety Rod Channel	Open Loop
^{238}Pu	—	—	—	0.0003
^{239}Pu	0.5631	—	—	1.0276
^{240}Pu	0.0535	—	—	0.1141
^{241}Pu	0.0044	—	—	0.0136
^{242}Pu	0.0003	—	—	0.0013
^{235}U	0.0057	—	—	0.0097
^{238}U	2.4836	—	—	4.6547
Mo	0.0582	0.0244	0.0097	0.3324
Na	9.1730	9.4957	18.470	9.5310
C	0.0732	0.0708	0.028	1.0778
O	—	—	—	10.236
Fe	27.192	26.297	10.519	17.634
Cr	7.8448	7.5866	3.035	4.1332
Ni	3.7432	3.6200	1.448	1.9722
Mn	0.5760	0.5571	0.223	0.3035

TABLE II-5-II. NEUTRON DETECTORS USED IN THE SHUTDOWN MARGIN EXPERIMENT

Location	Type		Using Organization
M14-15 M15-14	^{3}He neutron detectors		WADCO
S22-36 S24-10 S31-14 S14-31 S15-32	^{235}U fission counters		ORNL
M31-32 M32-31	Nuclear Enterprises glass scintillators NE905 containing ^{6}Li		
S13-13 S13-33[a] M32-32	WE6376	Westinghouse ^{235}U fission counters	ANL
S27-19[a]	WX42445A		
M23-23[a]	^{10}B ion chamber, SP5		

[a] Distance from midplane of assembly to nearest end of detector:

S13-33	45.7 cm
S27-19	62.0 cm
M23-23	62.0 cm

TABLE II-5-III. ^{10}B Rod Locations

Rod Number	Matrix Location[a]	Radius, cm
1	M19-16	42.9
2	M27-16	42.9
3	M30-23	38.7
4	M27-30	42.9
5	M19-30	42.9
6	M16-23	38.7
7	S19-16	42.9
8	S27-16	42.9
9	S30-23	38.7
10	S27-30	42.9
11	S19-30	42.9
12	S16-23	38.7

[a] S ≡ stationary half, M ≡ movable half.

TABLE II-5-IV. Loading Changes Performed for the Shutdown Margin

Loading No.	Zone[a]	Changes from Previous Configuration	
		Composition Removed	Composition Added
125		Initial Configuration	
126	G	Radial Reflector	B_4C Control
	H	Radial Reflector	B_4C Control
127	L	Install Source Transfer Tube	
128	G	B_4C Control	Radial Reflector
	N	Radial Reflector	B_4C Control
	N	B_4C Control	Radial Reflector
129	M	Radial Reflector	B_4C Control
	G	Radial Reflector	B_4C Control
130	K	Closed Loop, Type B	B_4C Control
	P	Radial Reflector	B_4C Control
131	Q	Radial Reflector	B_4C Control
	I	Closed Loop, Type B	B_4C Control
132	J	Closed Loop, Type B	B_4C Control
133	R	Inner Core	Safety Rod Channel
134	Q	B_4C Control	Radial Reflector

[a] Locations of zones are shown in Fig. II-5-2.

ments. The poison rods contained boron powder, an average of about 160 g of ^{10}B per rod; however, the boron loading varied somewhat from rod to rod. Table II-5-III gives the matrix location and approximate radial distance of each rod from the central axis of the assembly which was at the center of matrix tube 23-23. The average worths of the rods were about 140 Ih at the 38.7 cm radius and 120 Ih at the 42.9 cm radius.

Two calibrations were made in loading 125 to provide known reactivity increments for later use in this experiment. The worth of ^{10}B rod No. 3 was 163 Ih. The combined worth of ^{10}B rods Nos. 6 and 12 was 264 Ih.

The excess reactivity of the initial configuration for the shutdown margin experiment, FTR-3 loading 125, was determined to be (136.3 ± 4.0) Ih at 30°C. The fissile mass was 488.0 kg of $^{239+241}Pu$ plus 4.2 kg of ^{235}U.

Loading Changes

From the initial configuration described in the previous section of this report, a series of loading changes were made which provided a variety of subcritical configurations in which count rates were recorded and subcriticality measurements were made when possible. The different configurations achieved are described in Table II-5-IV and Fig. II-5-2. The changes listed in the table are cumulative. The only change made in loading 127 was the extension of the source transfer tube through the radial shield and radial reflector to the edge of the outer core zone. The transfer tube was in the stationary half of the reactor, approximately four inches from the midplane. In order to extend the source tube to the edge of the core, 2 in. of radial reflector material was removed from drawers S23-08 through S23-12. The subcriticality of the assembly was measured before and after the source tube was installed. The reactivity change was less than the uncertainty in the measurements; therefore, the inverse kinetics data from loadings 126 and 127 have been grouped together.

Figure II-5-2 represents the stationary half of ZPR-9

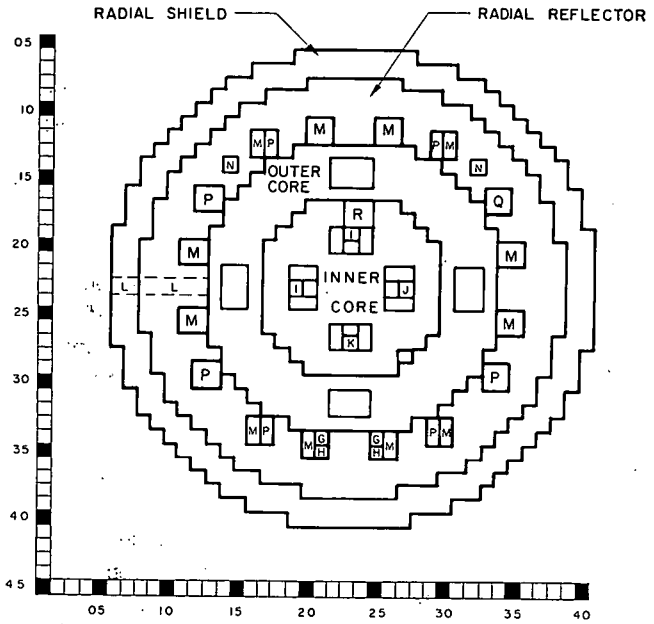

Fig. II-5-2. Matrix Loading Diagram Showing Locations of Zones Reloaded during the Shutdown Margin Experiment. *ANL Neg. No. 116-526.*

during this experiment. The movable half was the mirror image except for the source transfer tube.

Methods and Equipment Used

COUNT RATE DATA

Neutron count rates were recorded from four ^{235}U fission counters in each configuration assembled. The fission counters were located in the reflector regions of the assembly as indicated in Table II-5-II (ANL detectors). In addition, the current levels were recorded from four sets of ^{10}B ion chambers: CH3, SP5, SP10, and SP11. CH3 was a single uncompensated ^{10}B ion chamber, SP10 was a bank of three compensated ^{10}B ion chambers, and SP11 was a bank of four uncompensated ^{10}B ion chambers all located above the reactor matrix near the midplane of the assembly. SP5 was a single, smaller ^{10}B ion chamber located within the reactor matrix at M23-23 in the axial reflector. The end of the detector nearest the core was approximately 6.4 in. from the core or 24.4 in. from the midplane of the assembly.

ROD DROP

The rod drop-inverse kinetics method is described in Ref. 2. Flux data from SP5 and SP11 were recorded simultaneously during each rod drop. The flux profiles were analyzed by the inverse kinetics methods, giving measured values of subcriticality before and after each drop. The kinetics parameters used in the analysis are listed in Table II-5-V. The reactor temperature was monitored during each measurement and the results were adjusted to a reference temperature of 30°C using the measured temperature coefficient of reactivity (3.39 Ih/°C).[1]

NOISE ANALYSIS

Two noise analysis techniques were used in this experiment. The ORNL technique (CPSD) is described in Ref. 3. The WADCO technique (PSC) is described in Ref. 4. The primary detectors for the CPSD measurements were two ^{235}U fission counters located in the stationary half near the midplane of the assembly in matrix tubes 14-31 and 15-32. For the PSC measurements a pair of ^{3}He neutron detectors was located in matrix tubes 14-15 and 15-14 in the movable half near the midplane of the assembly. For some of the experiments the ORNL and WADCO experimenters exchanged signal leads from their neutron detectors so they could attempt noise measurements with different types of detectors. A third pair of detectors was used for some measurements by ORNL. These were ^{6}Li glass scintillators located in the movable half matrix positions 31-32 and 32-31, again near the midplane of the assembly.

ASYMMETRIC SOURCE

The asymmetric source method for measuring subcriticality is described in Ref. 5. A ^{252}Cf source was used for these measurements. The source was 410 ± 20 μg of ^{252}Cf. It was stored in a container of borax and parafin outside the ZPR-9 matrix when not in use. The increase in the count rates and ion chamber currents due to the Cf source were found to be negligible when the source was in the storage container. The source could be transferred remotely from the storage container to the edge of the core. When fully inserted in the reactor the source position was in the stationary-half radial reflector (26 ± 1/8) in. radially from the center of the core and 4 in. axially from the midplane of the core.

TABLE II-5-V. Calculated Kinetics Parameters for ZPR-9 Assembly 26, Loading 125

Isotope	Effective Delayed Neutron Fractions by Groups					
	1	2	3	4	5	6
^{235}U	1.683298-06	9.598775-06	8.408743-06	1.842206-05	5.784307-06	1.178793-06
^{238}U	1.476299-05	1.577476-04	1.850646-04	4.483523-04	2.599266-04	8.664219-05
^{239}Pu	6.252933-05	4.692747-04	3.596905-04	5.532876-04	1.737376-04	5.880351-05
^{240}Pu	1.640600-06	1.426740-05	9.633773-06	1.893038-05	7.151476-06	1.442314-06
^{241}Pu	1.277647-06	9.589982-06	7.350326-06	1.130654-05	3.550361-06	1.201661-06
	Decay Constants by Groups					
^{235}U	0.0127	0.0317	0.115	0.311	1.40	3.87
^{238}U	0.0132	0.0321	0.139	0.358	1.41	4.02
^{239}Pu	0.0129	0.0311	0.134	0.331	1.26	3.21
^{240}Pu	0.0129	0.0313	0.135	0.333	1.36	4.04
^{241}Pu	0.0129	0.0311	0.134	0.331	1.26	3.21

Note: $\beta_{eff} = 2.962238 \times 10^{-3}$; Ih/% $\Delta k/k = 1036.539$; $\ell_p = 7.451128 \times 10^{-7}$ sec; \$1 = 307.048 Ih.

TABLE II-5-VI. Subcritical Neutron Flux Data Recorded During the Shutdown Margin Experiment

Loading No.	Date 11/ /70	Temp, °C	^{252}Cf Source	^{10}B Rods In[a]	Fission Chamber Count Rate, cpm				Ion Chamber Current, amp			
					M32-32	S13-13	S27-19	S13-33	M23-23, SP5	SP11	SP10	CH3
126	10	23.98	Out	None	344,358	262,981	239,433	157,806	1.209×10^{-10}	1.323×10^{-8}	1.728×10^{-9}	3.930×10^{-9}
126	10	23.95	Out	6, 12	200,059	152,176	142,393	94,087	6.900×10^{-11}	7.487×10^{-9}	9.779×10^{-10}	2.213×10^{-9}
127	12	24.67	In	None	1,752,079	1,252,329	1,215,975	752,810	6.371×10^{-10}	5.855×10^{-8}	9.069×10^{-9}	2.315×10^{-8}
127	12	23.70	In	6, 12	1,037,858	794,623	744,008	454,232	3.702×10^{-10}	3.354×10^{-8}	5.185×10^{-9}	1.344×10^{-8}
127	12	23.05	Out	6, 12	200,247	152,429	139,596	93,322	6.362×10^{-11}	6.315×10^{-9}	9.846×10^{-10}	2.221×10^{-9}
127	12	23.02	Out	3[a]	184,401	141,411	129,028	86,793	5.828×10^{-11}	5.834×10^{-9}	9.093×10^{-10}	2.055×10^{-9}
127	13	23.70	Out	6, 12	199,897	152,489	140,105	93,322	6.400×10^{-11}	6.334×10^{-9}	1.002×10^{-9}	2.231×10^{-9}
127	13	23.16	Out	3, 6, 12	161,973	125,634	114,513	76,765	5.158×10^{-11}	5.199×10^{-9}	8.219×10^{-10}	1.831×10^{-9}
128	13	23.33	In	None	2,487,559	1,035,349	1,672,059	863,101	8.940×10^{-10}	7.726×10^{-8}	1.914×10^{-8}	3.066×10^{-8}
128	13	22.97	Out	None	494,589	211,478	336,005	185,398	1.676×10^{-10}	1.500×10^{-8}	2.253×10^{-9}	5.174×10^{-9}
128	16	24.64	In	2, 4, 6, 8, 10, 12	605,478	310,943	451,901	221,427	2.173×10^{-10}	1.885×10^{-8}	2.899×10^{-9}	7.153×10^{-9}
128	16	24.25	Out	2, 4, 6, 8, 10, 12	119,026	53,891	82,219	44,533	3.764×10^{-11}	3.592×10^{-9}	5.589×10^{-10}	1.280×10^{-9}
128	17	35.58	Out	None	426,967	182,312	282,028	150,580	1.410×10^{-10}	1.266×10^{-8}	1.909×10^{-9}	4.366×10^{-9}
128	17	30.15	Out	6, 12	242,976	105,581	161,953	84,989	7.990×10^{-11}	6.877×10^{-9}	1.069×10^{-9}	2.433×10^{-9}
128	17	25.40	Out	2, 4, 6, 8, 10, 12	119,454	54,354	81,559	44,687	3.743×10^{-11}	3.567×10^{-9}	5.553×10^{-10}	1.272×10^{-9}
128	17	24.95	Out	2, 4, 6, 8, 10, 12	103,688	47,883	71,308	39,546	3.242×10^{-11}	3.145×10^{-9}	4.893×10^{-10}	1.123×10^{-9}
129	18	27.69	Out	None	28,403	20,902	24,353	13,462	1.130×10^{-11}	8.575×10^{-10}	1.368×10^{-10}	2.962×10^{-10}
129	18	28.35	Out	1, 2, 4, 5, 7, 8, 10, 11	22,206	16,286	18,775	10,396	8.814×10^{-12}	6.764×10^{-10}	1.081×10^{-10}	2.351×10^{-10}
129	18	29.00	Out	3, 6, 12	26,163	18,911	22,109	12,110	1.008×10^{-11}	7.709×10^{-10}	1.229×10^{-10}	2.657×10^{-10}
130	19	29.03	In	None	73,868	102,244	93,152	39,777	3.572×10^{-11}	2.781×10^{-9}	4.271×10^{-10}	1.247×10^{-9}
130	19	28.47	Out	None	21,258	16,893	18,628	11,195	9.399×10^{-11}	7.034×10^{-9}	1.124×10^{-10}	2.426×10^{-9}
130	19	26.30	Out	1, 2, 4, 5, 7, 8, 10, 11	17,247	13,707	15,114	9,029	6.734×10^{-11}	5.815×10^{-9}	9.300×10^{-11}	2.017×10^{-10}
130	19	25.37	In	1, 2, 4, 5, 7, 8, 10, 11	51,490	80,194	68,736	27,928	2.549×10^{-11}	2.078×10^{-9}	3.160×10^{-10}	1.008×10^{-9}
131	20	25.59	In	None	25,648	43,696	53,389	15,978	1.740×10^{-11}	1.296×10^{-9}	1.935×10^{-10}	7.308×10^{-10}
131	20	25.60	Out	None	8,956	6,457	10,357	5,349	4.652×10^{-12}	3.551×10^{-10}	5.682×10^{-11}	1.257×10^{-10}
132	23	24.03	In	None	21,983	42,084	50,130	14,147	1.540×10^{-11}	1.182×10^{-9}	1.748×10^{-10}	6.959×10^{-10}
132	23	24.61	Out	None	7,856	6,057	9,442	4,750	4.062×10^{-12}	3.197×10^{-10}	5.127×10^{-11}	1.153×10^{-10}
133	24	26.35	In	None	21,571	40,915	48,581	12,926	1.476×10^{-11}	1.113×10^{-9}	1.633×10^{-10}	6.702×10^{-10}
133	24	26.70	Out	None	7,860	5,639	8,998	4,389	3.869×10^{-12}	2.996×10^{-10}	4.780×10^{-11}	9.880×10^{-11}
134	24	28.32	In	None	22,467	41,402	48,801	15,587	1.508×10^{-11}	1.215×10^{-9}	1.820×10^{-10}	6.807×10^{-10}
134	24	28.88	Out	None	8,167	5,813	9,132	5,374	3.962×10^{-12}	3.401×10^{-10}	5.474×10^{-11}	1.121×10^{-10}
134	25	29.29	Out	None	8,067	5,780	9,164	5,354	3.972×10^{-12}	3.359×10^{-10}	5.433×10^{-11}	1.007×10^{-10}

[a] ^{10}B rod No. 3 partially inserted; estimated subcriticality at 23.02°C is 447.3 Ih.

Results

COUNT RATE DATA

Table II-5-VI lists the subcritical flux data recorded during the shutdown margin experiment. Included are ion chamber currents from CH3, SP5, SP10, and SP11 and count rates from the four ANL fission chambers listed in Table II-5-II. At the left of the table the configuration is identified by loading number and date. Also shown is the average core temperature, the location of the ^{252}Cf source (either "OUT" of the assembly and stored in the shielding container or "IN" the assembly at 26 in. from the center of the core), and the identification numbers of all ZPR-9 ^{10}B rods that were in the core when the data were recorded.

Each number listed for the fission counters is the average of ten one minute counts with no dead time corrections. The average ion current for each configuration was determined by obtaining the integrated average current for ten second intervals and taking the average of ten of these observations.

ROD DROP DATA

The results obtained by the rod drop-inverse kinetics method are presented in Table II-5-VII. In order to obtain additional subcritical states without making time-consuming loading changes, it was convenient to insert selected ZPR-9 ^{10}B rods. Column 4 in Table II-5-VII shows which ^{10}B rods were in the reactor prior to

TABLE II-5-VII. Results of Rod Drop—Inverse Kinetics Measurements of Subcriticality in FTR-3 Loadings 126–128

Loading No.	Data Tape No.	^{10}B Rods Dropped[a]	^{10}B Rods In[a]	Data Channel	Temp. T, °C	Measured Subcritical Reactivities in Inhours				Worth of Rods Dropped, Ih
						Initial, at T	Final, at T	Initial, at 30°C	Final, at 30°C	
126	11/10/70-1/1	6, 12	None	Sp 11	23.9	391.8	689.4	412.5	710.1	297.6
	-1/2	6, 12	None	Sp 5	23.9	384.3	675.0	405.0	695.7	290.7
	-2/1	6, 12	None	Sp 11	24.0	396.4	686.5	416.7	706.8	290.1
	-2/2	6, 12	None	Sp 5	24.0	366.1	636.3	386.4	656.6	270.2
127	11/12/70-1/1	6, 12	None	Sp 11	24.3	394.8	689.8	414.1	709.1	295.0
	-1/2	6, 12	None	Sp 5	24.3	381.4	659.6	400.7	678.9	278.2
						Averages		405.9 ± 4.6	692.9 ± 8.7	287.0 ± 4.3
127	11/13/70-1/1	3	6, 12	Sp 11	23.7	653.9	794.6	675.3	816.0	140.7
	-1/2	3	6, 12	Sp 5	23.7	590.2	730.8	611.6	752.2	140.6
	-2/1	3	6, 12	Sp 11	23.5	612.7	747.6	634.7	769.6	134.9
	-2/2	3	6, 12	Sp 5	23.5	654.9	811.8	676.9	833.8	156.9
	-3/1	3	6, 12	Sp 11	23.3	622.3	756.3	645.0	779.0	134.0
	-3/2	3	6, 12	Sp 5	23.3	611.8	756.9	634.5	779.6	145.1
						Averages		646.3 ± 10.4	788.4 ± 12.5	142.0 ± 3.4
128	11/17/70-1/1	6, 12	None	Sp 11	34.6	333.4	608.3	317.8	592.7	274.9
	-1/2	6, 12	None	Sp 5	34.6	327.7	596.5	312.1	580.9	268.8
	-2/1	6, 12	None	Sp 11	33.5	330.4	607.2	318.5	595.3	276.8
	-2/2	6, 12	None	Sp 5	33.5	321.8	592.7	309.9	580.8	270.9
	-3/1	6, 12	None	Sp 11	32.9	325.7	604.9	315.9	595.1	279.2
	-3/2	6, 12	None	Sp 5	32.9	311.3	575.9	301.5	566.1	264.6
						Averages		312.6 ± 2.6	585.2 ± 4.7	272.5 ± 2.2
128	11/17/70-4/1	2, 4, 8, 10	6, 12	Sp 11	28.3	548.9	1092.0	554.7	1097.8	543.1
	-4/2	2, 4, 8, 10	6, 12	Sp 5	28.3	547.0	1119.3	552.8	1125.1	572.3
	-5/1	2, 4, 8, 10	6, 12	Sp 11	27.1	557.1	1107.4	566.9	1117.2	550.3
	-5/2	2, 4, 8, 10	6, 12	Sp 5	27.1	540.2	1118.0	550.7	1127.8	577.1
	-6/2	2, 4, 8, 10	6, 12	Sp 5	26.0	555.2	1135.6	568.8	1149.2	580.4
	-7/2	2, 4, 8, 10	6, 12	Sp 5	25.4	513.3	1064.0	528.9	1079.6	550.7
						Averages		553.8 ± 5.9	1116.1 ± 10.0	562.3 ± 6.6

[a] See Table II-5-III for ^{10}B rod locations.

the rod drop measurement. If "none" is indicated, the assembly was in its most reactive configuration.

Table II-5-VII gives the reactor temperature at the time of each rod drop, the initial and final subcriticalities at that temperature, and the initial and final subcriticalities corrected to 30°C. The last column of Table II-5-VII gives the measured worth of the rod or rods dropped. There appears to be a discrepancy of about 5 % between the results obtained for the same configuration depending upon whether it is the initial or final configuration of the rod drop.

Further examination of Table II-5-VII indicates the possibility of small differences in the results obtained with the two data channels. Since SP11 was located on top of the reactor matrix and SP5 was located in the axial reflector, deviations from the point kinetics model could produce different flux profiles at the two detector locations. It is encouraging that the differences observed were quite small.

NOISE AND ASYMMETRIC SOURCE DATA

The data obtained by the ORNL and WADCO experimenters were analyzed by the respective groups and have been reported elsewhere. Specifically, the results of the CPSD noise analysis technique were reported in Ref. 6 by ORNL. The results of the PSC noise analysis were reported in Ref. 7 by WADCO. The asymmetric source measurements were reported in Ref. 8 by ORNL.

References

1. J. W. Daughtry, R. B. Pond, C. D. Swanson and R. M. Fleischman, *ZPR-9 Assembly 26, FTR-3*, Reactor Physics Division Annual Report, July 1, 1969, to June 30, 1970, ANL-7710, pp. 58–63.
2. C. E. Cohn, *Experience with Subcriticality Determination by Rod Drop in the FTR-3 Critical Experiments*, Trans. Am. Nucl. Soc. **14**, 29 (1971).
3. T. Nomura, S. Gotoh and K. Yamaki, *Reactivity Measurements by the Two-Detector Cross-Correlation Method and Supercritical Reactor-Noise Analysis*, Neutron Noise, Waves and Pulse Propagation, AEC Symp. Ser. 9, CONF-660206 (May 1967).
4. W. Seifritz, *The Polarity Correlation of Reactor Noise in the Frequency Domain*, Nucl. Appl. Technol. **7**, 513 (1969).
5. J. F. Waller and A. F. Henry, *The Asymmetric Source Method of Measuring Reactor Shutdown*, Nucl. Sci. Eng. **32**, 332 (1968).
6. R. C. Kryter, N. J. Ackerman, Jr. and A. R. Buhl, *Measurement of Subcriticality in Large Fast Reactors by Combining Noise and Multiplication Techniques*, Trans. Am. Nucl. Soc. **14**, 45 (1971).
7. R. W. Albrecht and G. M. Hess, *A Comparison of Inverse Kinetics and Polarity Spectrum Reactivity Measurements in FTR-3*, Trans. Am. Nucl. Soc. **14**, 45 (1971).
8. A. R. Buhl, N. J. Ackerman, Jr. and R. C. Kryter, *An Evaluation of the Asymmetric Source Technique for Determining Subcritical Reactivity in Fast Reactors*, Trans. Am. Nucl. Soc. **14**, 45 (1971).

II-6. Planning and Analysis in Support of the Fast Flux Test Facility (FFTF) Critical Experiments on ZPR-9

A. Travelli, A. J. Ulrich and J. C. Beitel

Introduction

The Applied Physics Division is active in planning and evaluating a series of critical experiments in a continuing effort to provide physics information needed for the design of the Fast Test Reactor (FTR), which is an integral part of the Fast Flux Test Facility (FFTF). These planning and evaluating activities are carried out in close cooperation with the WADCO Corporation (the FTR program manager), which is a subsidiary of Westinghouse Electric Corporation in Richland, Washington and with the Advanced Reactor Division of Westinghouse Electric Corporation (the reactor designer) Waltz Mill, Pennsylvania.

During the current reporting period the activities were concerned with (1) completion of a series of experiments planned to investigate basic physics design problems associated with FTR in relatively clean and idealized geometries[1-3] (Phase B), and (2) the initiation of engineering mockup experiments which are directed toward finalizing important design parameters (Phase C). The Phase B experiments were performed in FTR-3 Assembly 26 and the Phase C experiments were performed in the Engineering Mockup Critical (EMC) Assembly 27, both on the ZPR-9 critical facility.

A detailed description of FTR-3 is contained in Ref. 1. An analytical study of kinetics parameters of one of the FTR-3 assemblies appears in a later section of this article.

The FFTF Engineering Mockup Critical, ZPR-9/FTR-EMC

The reference map (Fig. II-6-1) of the FTR at the beginning of life (BOL) as of February 1971 served as

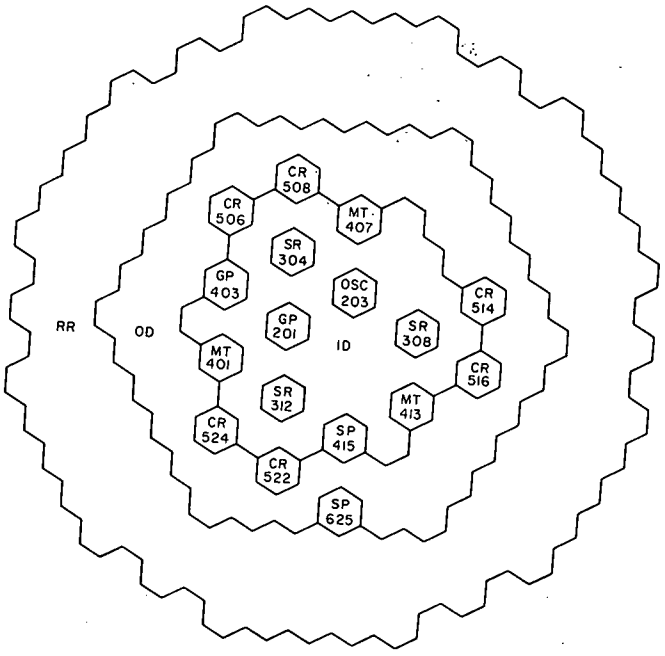

FIG. II-6-1. Reference FTR Map, February 1971. *ANL Neg. No. 116-1079.*

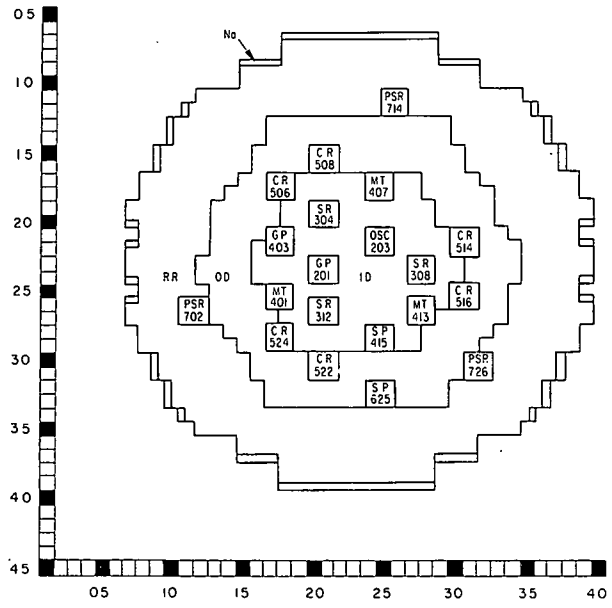

FIG. II-6-2. FTR Engineering Mockup Critical (EMC) BOL-C. *ANL Neg. No. 116-744.*

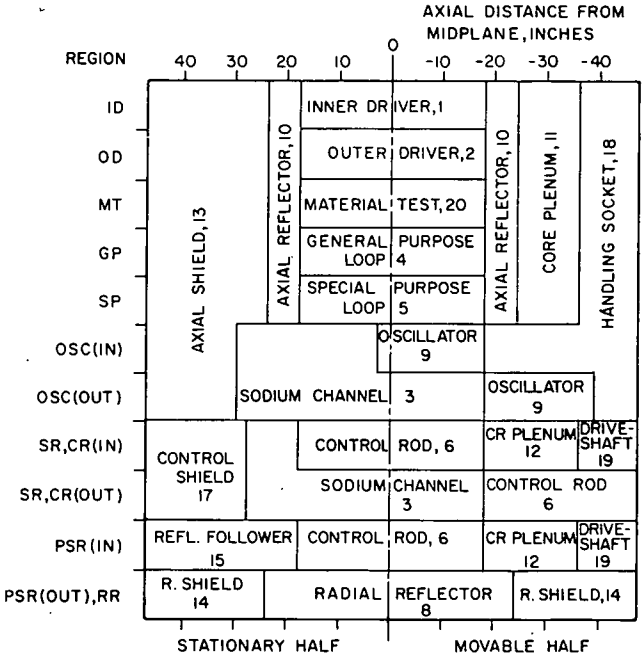

FIG. II-6-3. Axial Compositions of Various Regions of the EMC-BOL-C. *ANL Neg. No. 116-958.*

the basis for the design of FTR-EMC Assembly 27 on ZPR-9 (see Paper II-1). The rows (or rings) of hexagonal subassemblies are numbered from 101 through 930, the first digit being the row number and the other digits giving the order within the row. Not all subassemblies are outlined or numbered in Fig. II-6-1. The figure identifies with letters various types of regions: ID (inner driver), OD (outer driver), RR (radial reflector), MT (materials test), GP (general purpose loop), SP (special purpose loop), SR (safety rod), OSC (oscillator) and CR (control rod).

The FTR-EMC involves many loading configurations, most of which are transitional steps between particular configurations which simulate conditions of the FTR that are of interest for design, safety or operational reasons. Simulation of the first core at BOL is, of course, an important area of the program.

One loading of special interest in the BOL series is BOL-C, which corresponded closely to the BOL configuration of the FTR. The BOL-C was near critical, had the six row-five control rods (CR) inserted 55% into the core, and had three peripheral shim rods (PSR) located at the edge of the core in the radial reflector. Figure II-6-2 shows the map of the ZPR-9 stationary half at the core midplane when the reactor was loaded with this configuration. The figure identifies e PSR regions. Equivalent subassemblies are numred like the corresponding subassemblies of Fig. II-6-1. No radial shield was represented, but segments of a 1.0 in. thick sodium ring surrounded the reflector.

Every region identified in Fig. II-6-2 was divided axially into subregions of various sizes and composition which are described in Fig. II-6-3, both for the inserted and for the withdrawn position, whenever applicable. In the EMC-BOL-C configuration, the three peripheral shim rods at locations 702, 714 and 726 were fully inserted; the oscillator and the three safety rods were fully withdrawn; the in-core control rods 508, 516 and 524 were inserted 22 in. and the in-core control rods 506, 514 and 522 were inserted 18 in., resulting in the

average insertion of 20 in. (55%) specified for the FTR-BOL. Whenever a control rod was partially inserted, the size of the control rod and of the regions which were contiguous to the rod within the same matrix tubes in the movable half were left unchanged; this means that all of the boundaries of these regions were shifted by the length of the rod insertion, while all other boundaries within the same matrix tubes in the stationary half were left unchanged. The name and code number of the compositions used in the various subregions are also indicated in Fig. II-6-3.

The preliminary atom concentrations of all compositions in the EMC-BOL-C are listed in Table II-6-I, where they are compared with the concentrations of the hot FTR-BOL.

Preparation of a Cross Section Set for Analysis of the FTR-EMC

A 29-group cross section set, designated 29007, was prepared from ENDF/B nuclear data, VERSION I revised Category 1, for computational analysis of the FTR-EMC. The energy-group structure of set 29007 is the same as that of set 29004.2.[2] Inner and outer core 29-group cross sections were obtained by averaging in a 2100-group fundamental mode MC²[4] flux spectrum at criticality for the inner and outer core compositions, respectively. The two-region heterogeneous treatment of MC² was used to obtain cross sections for the isotopes present in the fertile and fissile plates (see Paper II-1) in the inner and outer core. Cross sections for the other isotopes in the inner and outer core were obtained through the homogeneous treatment. Because of the great simlarity in the average compositions of the inner and outer cores of FTR-3 with the inner and outer cores of the FTR-EMC, the cross sections for some isotopes in certain fissile and fuel plates of FTR-EMC were assumed to be the same as those previously calculated for the same plates of FTR-3. Radial and axial reflector cross sections were averaged in the 2100-group flux spectrum for the radial and axial reflector compositions, respectively, with zero buckling and using the homogeneous treatment.

TABLE II-6-I. Preliminary Atom Concentrations of the EMC-BOL-C and Corresponding Hot FTR-BOL Values, 10^{21} atoms/cc

Isotope or Element	EMC	FTR	EMC	FTR
	1. Inner Driver		2. Outer Driver	
$^{239+241}$Pu	1.357	1.381	1.645	1.660
$^{240+242}$Pu	0.180	0.188	0.207	0.226
^{235}U	0.012	0.040	0.011	0.037
^{238}U	5.411	5.605	5.063	5.303
O	13.152	14.210	13.010	14.236
C			1.053	
Na	8.889	9.098	8.834	9.098
Fe	16.756	13.336	17.706	13.336
Cr	3.084	3.580	3.170	3.580
Ni	1.364	2.239	1.401	2.239
Mn	0.234		0.241	
Mo	0.355	0.286	0.456	0.286
Si		0.393		0.393
O + 0.87C			13.926	14.236
Isotope or Element	3. Sodium Channel		4. General Purpose Loop	
$^{239+241}$Pu			0.224	0.235
$^{240+242}$Pu			0.030	0.032
^{235}U			0.002	0.038–0.068
^{238}U			0.829	0.924–0.895
O			2.412	2.423
C	0.031		0.035	
Na	18.683	20.160	15.783	15.973
Fe	10.427	5.564	13.049	12.516
Cr	2.984	1.494	3.377	3.360
Ni	1.381	0.934	1.563	2.101
Mn	0.234		0.265	
Mo	0.011	0.119	0.073	0.268
Si		0.164		0.369

Isotope or Element	EMC	FTR	EMC	FTR
	5. Special Purpose Loop		6. Control Rod	
$^{239+241}$Pu	0.058	0.045		
$^{240+242}$Pu	0.005	0.006		
^{235}U	0.001	0.023–0.050		
^{238}U	0.252	0.132–0.159		
O	0.625	0.458		
C			9.371	9.143
Na	17.373	17.423	7.364	7.276
Fe	12.780	11.643	14.842	15.905
Cr	3.510	3.126	4.220	4.269
Ni	1.543	1.955	1.868	2.670
Mn	0.267		0.440	
Mo	0.037	0.249	0.020	0.341
Si		0.343		0.468
^{10}B			7.132	7.314
^{11}B			28.925	29.259
Isotope or Element	7. Heavy Control		8. Radial Reflector	
C	11.733			
Na	5.653		3.156	2.912
Fe	12.200		11.187	6.815
Cr	3.481		3.159	13.309
Ni	1.612		57.327	56.094
Mn	0.273		0.389	
Mo	0.012		0.014	0.02[a]
Si				0.03
^{10}B	8.919			
^{11}B	36.170			
Fe + Cr			14.346	20.124

TABLE II-6-I.—*Continued*

Isotope or Element	EMC	FTR	EMC	FTR
	9. Oscillator		10. Axial Reflector	
C	0.032			
Na	15.960	17.193	9.177	9.098
Fe	10.834	9.963	16.889	15.480
Cr	3.100	2.675	4.805	8.632
Ni	1.435	1.673	25.434	24.029
Mn	0.243		0.425	
Mo	0.011	0.213	0.021	0.286
Si		0.293		0.393
Ta	2.908	2.573		
W		0.286		
Ta + W	2.908	2.859		
Fe + Cr			21.694	24.112
Isotope or Element	11. Core Plenum		12. Control Rod Plenum	
C			0.052	
Na	9.318	9.098	6.926	7.276
Fe	14.940	13.334	17.722	15.905
Cr	4.263	3.579	5.071	4.269
Ni	1.577	2.239	2.348	2.670
Mn	0.321		0.398	
Mo	0.018	0.286	0.018	0.341
Si		0.393		0.468
Isotope or Element	13. Axial Shield		14. Radial Reflector Shield	
Na	5.567	5.286	2.987	2.911
Fe	43.018	42.514	60.143	48.065
Cr	12.364	11.412	6.780	12.902
Ni	5.796	7.138	3.131	8.070
Mn	0.915		0.568	
Mo	0.044	0.910	0.026	1.029
Si		1.252		1.415
Fe + Cr + Ni	61.178	61.064	70.054	69.037

Isotope or Element	EMC	FTR	EMC	FTR
	15. Reflector Follower		16. Sodium Ring	
C	0.065		0.031	
Na	7.298	7.276	18.683	22.4
Fe	22.138	18.322	10.523	
Cr	6.325	9.964	3.011	
Ni	26.095	27.230	1.394	
Mn	0.558		0.236	
Mo	0.022	0.341	0.011	
Si		0.468		
Fe + Cr	28.463	28.286		
Isotope or Element	17. Control Shield		18. Handling Socket	
C	0.148			
Na	2.320	2.554	17.915	17.920
Fe	50.166	49.297	11.409	11.129
Cr	14.355	13.233	3.230	2.987
Ni	6.646	8.277	1.396	1.869
Mn	1.126		0.247	
Mo	0.051	1.055	0.016	0.238
Si		1.452		0.328
Isotope or Element	19. Drive Shaft		20. Material Test	
C	0.059		0.098	
Na	14.595	14.560	9.177	9.098
Fe	19.854	19.475	33.162	31.836
Cr	5.682	5.228	9.489	8.546
Ni	2.630	3.270	4.393	5.345
Mn	0.446		0.744	
Mo	0.020	0.417	0.033	0.682
Si		0.574		0.938

Preliminary Analysis of EMC-BOL-C

The reactivity of the EMC-BOL-C was precalculated in a series of steps similar to those used to calculate the critical mass of FTR-3.[1] As stated earlier, the six in-core control rods were to be 55 % inserted. This complication in geometry could have been adequately handled in a three dimensional analytical model. However, because of computer cost and time limitations, the use of such a model would have required a drastic reduction from 29 broad neutron-energy groups and a small number of mesh points. The problems considered in the calculations were restricted to one and two dimensions in order to avoid the above limitations.

The determination of reactivity of the EMC-BOL-C was based primarily on two diffusion theory calculations in *xy* geometry using the DIF2D[5] code and cross section set 29007. The bank of row-five control rods was fully withdrawn in the first calculation and fully inserted in the second calculation. The desired reactivity was determined by interpolation between the reactivities calculated for these two problems to account for the partial insertion of the bank of row-five rods. The axial bucklings for the two *xy* problems were derived from two diffusion theory problems in *rz* geometry, one with the rods fully withdrawn and the other with rods fully inserted.

The reactor was represented in the *rz* problems as a series of annular regions which corresponded to the various subassembly rows, and which were subdivided axially in various parts to reproduce the axial structure of the reactor. The reactor materials were homogenized within each truncated annulus. The part of the row-five annulus which extended over the length of the core contained control rods and outer driver homogenized

together. In this composition the ^{10}B concentration required adjustment so that the worth of the annulus would be the same as the worth of the row-five rods. Similar adjustment of ^{10}B concentration was required in the row-seven truncated annulus which contained the peripheral shim rods and radial reflector.

The adjustment of the ^{10}B concentration in the row-five annulus when the rods were fully inserted was performed in a one-dimensional radial problem in diffusion theory using DIF1D[5] and cross section set 29007. The ^{10}B concentration was multiplied by a factor, α_5, which was varied until the value of k was equal to that obtained in a representation of the assembly at the midplane in $r\theta$-geometry. The result was $\alpha_5 = 0.6088$. The latter representation treated as individual homogenized regions those regions of the reactor which included, respectively, the four innermost subassembly rows, the subassemblies of row-five except the six row-five control rods, the row-five control rods, the subassemblies of row-six, and the radial reflector. A value of 5.33×10^{-4} cm^{-2} was assumed for the region- and group-independent axial buckling, B_z^2, to be used in these problems. In a similar procedure, the ^{10}B concentration in the row-seven annulus was adjusted by determining a variable multiplier, α_7, which was found to be 0.2400.

Having obtained adjusted ^{10}B concentrations for the annulii of rows five and seven to account for the self-shielding of the rods, a series of five rz-calculations were run, simulating row-five rod positions at 0, 25, 50, 75 and 100 % insertion, respectively. This procedure is based on the assumption that the self-shielding of the rods is essentially independent of the degree of their insertion.

The calculations for various degrees of row-five rod insertion were run with a seven-group set of cross-sections in order to reduce the expense involved. The set was prepared as follows. An auxiliary radial problem in diffusion theory simulating the EMC-BOL-C was solved by the MACH-1[6] code using cross-section set 29007 to give approximate neutron fluxes over each region of interest. The values of k_{eff}, α_7, and B_z^2 were assumed on the basis of previous experience. The boron self-shielding in row-five annulus (α_5) was varied to produce criticality. The calculated fluxes were used to average the 29-group cross sections within the seven-group structure and over each region. Each of the seven groups of the coarser structure contained four of the twenty-nine groups of the finer structure with the exception of the lowest-energy coarse group, which contained five fine groups. Inner core cross sections were averaged by weighting with the radial flux of the inner core (rows one through four); row-five control rods and ^{10}B were averaged with the flux of row five; outer driver cross sections were averaged with the flux of rows five and six; row-seven control rods and ^{10}B were averaged with the flux of row seven; and the radial fluxes in row seven, eight and nine were used to average the cross sections of the radial and axial reflectors. The seven-group set was designated 29701 and was used in the series of five rz problems which were run with varying insertion of the bank of row-five control rods.

The calculations yielded a series of five reactivities, corresponding to different fractional insertions of the rods. The five values were then fitted with a fourth order polynomial of the fractional insertion, and the change in reactivity for 55 % insertion of the rods was determined to be 54 % of the change in reactivity corresponding to a full rod insertion.

Each of the two solutions obtained in rz geometry with seven groups for control rods fully inserted and for control rods fully withdrawn also yielded group- and radially-dependent axial bucklings for use in the corresponding xy-problems. The average values of the axial buckling were calculated for each of the seven groups in those regions of the rz problem which corresponded (a) to the subassemblies of the inner core (rows 1 through 4), (b) to row five, (c) to row six, (d) to row seven, (e) to row eight, and (f) to row nine. These values were then used in the corresponding regions of the xy calculation. In particular, the result of (a) was used over the inner core region, (b) was used over the row-five control rod positions, the average of (b) and (c) was used in the remainder of the outer core, (d) was used in the row-seven control rod positions, and the average of (d), (e) and (f) was used in the remainder of the radial reflector. The region-dependent axial bucklings for the xy calculations, which were derived in this manner for each of the seven groups of the somewhat coarse structure of set 29701, were used for each of the corresponding four or five energy groups of the finer structure of set 29007, which included 29 groups.

The 29-group xy calculations done with these bucklings and with the preliminary atom concentrations from Table II-6-I for the EMC-BOL-C with three PSR in place yielded a value of k equal to 1.0231 when the row-five rods were fully withdrawn and to 0.9478 when the rods were fully inserted. The worth of the bank of six row-five rods was therefore calculated to be 0.07527, and the k_{eff} corresponding to 55 % insertion of the rods was inferred to be 0.9824. In this preliminary evaluation it was assumed that experimental criticality would correspond to the same value of k which had been calculated for FTR-3; this was t critical assembly with the greatest similarity to EMC-BOL-C and whose calculations had been performed using the same basic cross section data and similar

methods. The value of k_{eff} which had been calculated for the critical FTR-3 configuration was 0.9831. On this basis the EMC-BOL-C was predicted to be subcritical, with $\rho = -0.0007$.

Experimentally, the EMC-BOL-C assembly had a reactivity of −0.0036S. However, the fissile mass in the experiment was 1.867 kg of $^{239+241}$Pu less than that assumed in the calculation. The difference was due to the fact that preliminary concentrations had been used in the calculations instead of the then-unavailable as-built concentrations. Correcting for this difference increases the experimental reactivity to −0.00182. Thus, the predicted reactivity disagrees with the experimental value by 0.0011.

Comparison of Computed and Experimental Central Reaction Rate Ratios

Central reaction ratio measurements have been reported for assemblies ZPR-3/51,[7] ZPR-3/56B,[8] ZPPR/FTR-2[9] and ZPR-9/FTR-3[10] of the FFTF critical experiments program. The assemblies are described in Refs. 1–3. Computed central reaction ratios are compared to the experimental values in Table II-6-II.

The cross section sets used in the computations were taken from set 29006[1] for FTR-3, from set 29004.2 for FTR-2 and ZPR-3/56B, and from set 29005 for ZPR-3/51.

Set 29005 has the same 29-energy group structure as the other two sets, and is also based on ENDF/B VERSION I cross section data. The core cross sections were averaged in the fundamental mode spectrum for the core composition at criticality by the MC² code. The cross sections of fissile and fertile core isotopes were averaged using the two-region heterogeneous treatment of MC². Radial and axial reflector cross sections were averaged in the spectrum of the radial and axial reflector compositions, respectively, with zero buckling and using the homogeneous treatment of MC².

The reaction rates were computed using central fluxes from diffusion theory for each assembly. The FTR-3 central flux was obtained from a representation in $r\theta$ geometry using the DIF2D Code, where the axial leakage was simulated by a DB_z^2 absorber. The FTR-2 and ZPR-3/51 central fluxes were solutions of cylindrical problems using the MACH-1 code which again simulated the axial leakage by a DB_z^2 absorber. In the case of ZPR-3/56B the central flux was taken from a diffusion theory fundamental-mode calculation.

It would have been most desirable to compute the action rates using cross sections with resonance self-shielding corrections for the spectrum intercepted by the counters of foils. In lieu of those cross sections the most applicable cross sections available were employed.

TABLE II-6-II. Central Reaction Rates Relative to ^{235}U Fission Rates

Reaction	Ratio by		C/E
	Experiment	Calculation	
FTR-3			
^{239}Pu fission	0.984 ± 0.022	0.890	0.904
^{240}Pu fission	0.256 ± 0.006	0.184	0.719
^{238}U fission	0.0250 ± 0.0006	0.0224	0.896
^{238}U fission[a]	0.0234 ± 0.0013	0.0224	0.957
^{238}U capture[a]	0.161 ± 0.009	0.135	0.839
FTR-2			
^{239}Pu fission	0.973 ± 0.010	0.918	0.943
^{240}Pu fission	0.227 ± 0.002	0.212	0.934
^{238}U fission	0.0294 ± 0.0003	0.0273	0.929
ZPR-3/56B			
^{239}Pu fission	1.028 ± 0.010	0.922	0.897
^{240}Pu fission	0.282 ± 0.003	0.214	0.758
^{238}U fission	0.0309 ± 0.0003	0.0274	0.888
ZPR-3/51			
^{239}Pu fission	1.003 ± 0.010	0.948	0.945
^{240}Pu fission	0.240 ± 0.002	0.234	0.975
^{238}U fission	0.0309 ± 0.0003	0.0300	0.971

[a] Measured by radiochemistry. All other measurements were made by detectors.

The cross sections used to compute reaction rates in the FTR-3 assembly were as follows: uranium isotopes—cross sections appropriate for the uranium in the ZPPR fuel plate in the inner core; plutonium isotopes—cross sections appropriate for plutonium of the inner core homogenized with all of the inner core material except for the U_3O_8 plates. All other reaction cross sections were appropriate (in the sense of MC²) for the fuel plates in the case of plutonium isotopes, or for the fertile plates in the case of uranium isotopes.

Calculations of the Infinite Dilution Worth of ^{10}B in ZPR-3/56B

Five measurements of the worth of boron in the center of ZPR-3 Assembly 56B are reported in Ref. 11. The infinite dilution worth of ^{10}B was inferred from these measurements through computation by determining the self-shielding factor of the samples, F, defined as the ratio of the worth of the ^{10}B in the sample and the infinite dilution worth of ^{10}B.

Recent methods have been developed[12,13] to study self-shielding problems of this type in fast reactors by considering accurately the sample geometry in an approximate transport calculation. This section describes another method which has been used with success to analyze the results of ZPR-3/56B experiments, and which uses accurate transport calculations for an approximate sample geometry. The method was particularly suited to the analysis of the ZPR-3/56B experi-

ments which used hollow cylindrical samples difficult to handle with the other methods.

The first step of this method consists of identifying a hollow spherical sample with the same weight and the same first two chord moments[14] as the sample in question, and in assuming that it also has the same worth. The assumption stems from early thermal reactor work[15] according to which two purely absorbing samples have the same self-shielding factor if the same function

$$f(\Sigma) \equiv \frac{\int dA \int d\Omega(\boldsymbol{n}\cdot\Omega)[1 - e^{-\Sigma\ell(A,\Omega)}]}{\int dA \int d\Omega(\boldsymbol{n}\cdot\Omega)\Sigma\ell(A,\Omega)}$$

is valid for both of them. In this notation, Σ is the microscopic absorption cross section of the sample, dA its surface element, and Ω the vector perpendicular to dA and directed toward the inside of the sample. It can be shown through suitable analytical manipulations that two samples with the same first two chord moments satisfy this condition satisfactorily. In particular, the two $f(\Sigma)$ curves then have the same value and the same slope at $\Sigma = 0$, tend to the same asymptotic expression as $\Sigma \to \infty$, and are reasonably close to each other for all other values of Σ.

The self-shielding factor can then be calculated with relative ease in spherical geometry. A high-order transport (S_{16}) calculation yields the energy-dependent depression of the flux in the sample, and the value of F is derived from perturbation calculations.

Four of the measurements were performed on three cylindrical samples at the center of the reactor in the radial traverse tube and one on a cylindrical sample, also at the center of the reactor but in the axial traverse tube. The inner core plate loading was locally and differently perturbed to accommodate each of these two traverse tubes.

The samples were all 4.2875 cm high. A computer code was developed to calculate the chord moments in the cylindrical geometry and to identify the equivalent spheres.

The group-wise self-shielding factor, f, the ratio of the average flux within the spherical annular sample position with sample material present to that with the sample material not present, was calculated for each of the 29 energy groups of set 29004. The average fluxes for each group with and without sample material present were obtained from spherical S_{16} calculations using the SNARG-1D code.[16]

The perturbation worth for ^{10}B at the center of ZPR-3 Assembly 56B was computed in diffusion theory using the MACH-1 code. The perturbation worth component associated with each group was then multiplied by the f calculated for that group and the products were summed to give the computed perturbation worth corrected for self-shielding. This method assumed that the adjoint flux for each group over the sample volume with and without the sample in place is almost the same when calculated in diffusion theory or in the S_{16} approximation. It also assumes that the leakage component of the sample worth is negligible. The self-shielding factor, F, for each sample was taken to be the ratio of the perturbation worth of ^{10}B to that without the self-shielding correction. The results appear in Table II-6-III. The values of the infinite-dilution ^{10}B worth obtained from the various samples for the radial traverse tube (samples 1, 2 and 3) fall well within their experimental error from their weighted average, 6926 ± 13 Ih/kg, (the value calculated from perturbation theory was 7209 Ih/kg). This indicates that very small errors, if any, were introduced by the evaluation of the self-shielding factors. A consistent agreement of this type, if it were to be found also in other experiments to be evaluated in the future, would not only confirm the validity of the method but possibly also simplify the experimental procedures.

An estimate of the effect of different plate loadings surrounding the sample is obtained by comparing the

TABLE II-6-III. Experimental Sample Sizes and Worths, Calculated Self-Shielding Factors, and Inferred Infinite-Dilution ^{10}B Worths

Sample No.	1	2	3	4[b]
B-10 weight, g	0.8641	0.5906	0.3470	0.5906
Outer radius of cylindrical sample, cm	0.25400	0.49657	0.49657	0.49657
Inner radius of cylindrical sample, cm	0	0.44577	0.47117	0.44577
Outer radius of equivalent sphere, cm	0.75945	1.08987	1.08987	1.08987
Inner radius of equivalent sphere, cm	0.699039	1.05926	1.07530	1.05926
Experimental B-10 worth, Ih/kg	−6158 ± 18	−6598 ± 17[a]	−6736 ± 39	−6691 ± 34
Self-shielding factor, F	0.89133	0.95153	0.96836	0.95153
Infinite dilution B-10 worth, Ih/kg	−6909 ± 20	−6934 ± 18[a]	−6956 ± 40	−7032 ± 36

[a] Average worth from two measurements.

[b] The same sample as sample 2, but measured at the center of the reactor in an axial traverse tube rather than in a radial traverse tube, in which the others were measured.

result for sample 4 with that of sample 2. The difference is small (1.4%) but measurable, and is due to plate heterogeneity effects which were not taken into account in the calculations. In addition, there may be small systematic errors due to the calibration of the autorod.[11]

Calculation of the ^{238}U (n,f) Radial Traverse in ZPPR/FTR-2, Taking Heterogeneity into Account

A calculation of the radial dependence of the ^{238}U fission rate near the axial mid-plane in ZPPR/FTR-2 has been reported previously.[1] The neutron flux was obtained using the 29-group cross section set 29004.2 and the SNARG-1D code, with one-dimensional cylindrical-transport theory in the S_4 approximation. The 29-group cross sections of fissile and fertile isotopes included the heterogeneity effect due to resonance self-shielding according to the two region treatment of MC^2. The calculation of this effect was modeled for the plate arrangement in the cell of the ZPPR/FTR-2 core.

Calculation of the ^{238}U fission rate as a function of position in a central cell with the plate arrangement of the core of ZPR-3/56B was also reported previously.[2] This computation with cross section set 29004.2 included the effect of geometric self-shielding on the fission rate. The SNARG-1D code in the DS_{14} approximation and the modified single-Gaussian quadrature[17] was used in the calculation.

Since the plate arrangement of the cores of 56B and of FTR-2 were the same, the intracellular variation of fission rate in Ref. 2 could be combined with the radial variation of Ref. 1. The calculated fission rate from Ref. 2 was averaged over the active length of the experimental fission counter for each position in the central cell and divided by the rate for the counter position corresponding to the center of the core. The calculated radial variation of the fission rate from Ref. 1 was then multiplied by the value of this ratio which was proper for the cellular location of each computed radial point within the core.

In the peripheral B_4C control ring and in the reflector, the reaction rate calculation used the 29-group cross sections obtained from a 2100 group fundamental mode MC^2 flux averaging for the homogenized reflector composition with zero buckling. The resulting radial ^{238}U fission rate traverse is compared with the experimental measurement[18] in Fig. II-6-4.

The agreement between the experimental and computational results plotted in Fig. II-6-4 is very much better than that reported in Ref. 1. The improvement is due in part to the removal of a plotting error which had resulted in misplacing the experimental points in Ref. 1, and, in part, to the fact that the new calculation takes into account the broad-group heterogeneity effect

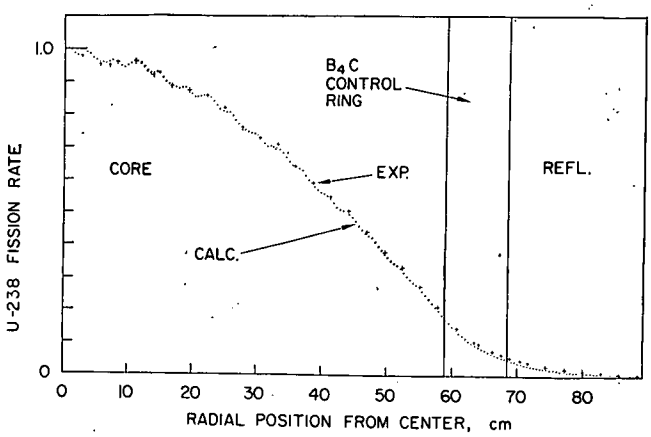

Fig. II-6-4. Comparison of Experimental and Calculated Values of the Radial U^{238} Fission-rate Distributions in the FTR-2 Assembly on ZPPR. *ANL Neg. No. 116-964.*

on the ^{238}U traverse. As a result, the oscillations of the reaction rate over the cells are reflected in the calculations and agree almost perfectly with the corresponding oscillations measured in the course of the experiments.

Calculation of Kinetics Parameters of the Initial Configuration for Subcritical Reactivity Measurements in FTR-3

During the FTR-3 experiments, a series of loadings were devoted to the study of techniques for measuring subcritical reactivity in a far-subcritical reactor (see Paper II-5). In preparation for these experiments the sixteen peripheral B_4C control rods were removed in steps and replaced by radial reflector. At each step the increase in reactivity was compensated by reducing the reactivity of the core by fuel removal at several locations which simulated open and closed loops. The resulting assembly, loading 125, is illustrated in Fig. II-6-5 and was called the Initial Configuration for Subcritical Reactivity Measurements, and had a slightly positive reactivity of 136.3 Ih. The peripheral B_4C rods were again replaced in steps in subsequent loadings producing the desired subcritical states required in the experiments.

The compositions present in regions A, B, C and D of Fig. II-6-5 are closed loop type A, closed loop type B, safety rod channel, and open loop composition, respectively. The atom concentrations in those compositions are given in Table II-6-IV. The volume-equivalent cylindrical dimensions of FTR-3 are shown in Fig. II-6-6. The atom concentrations present in the other regions of loading 125 shown in Figs. II-6-5 and II-6-6 are given in Table II-6-V.

In order to calculate the kinetics parameters for this assembly, the neutron flux distribution was obtained in two-dimensional rz geometry and in 29-group diffusion theory by means of the DIF2D code of the ARC

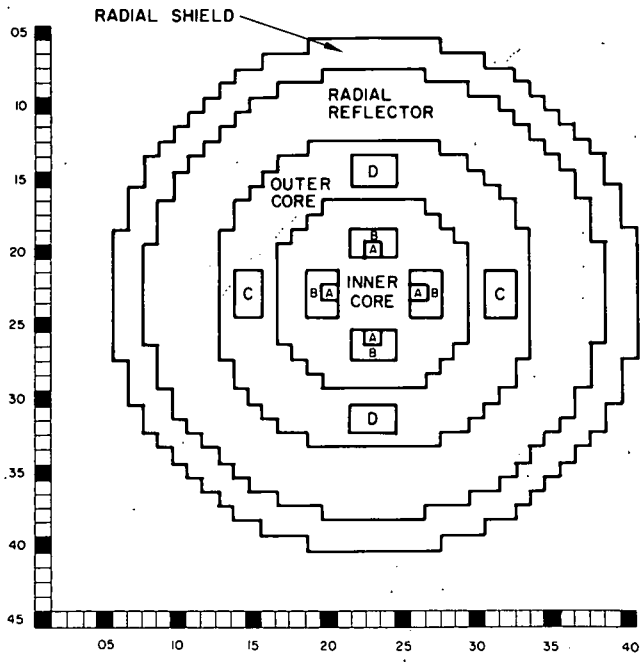

FIG. II-6-5. Initial Configuration for Subcritical Reactivity Measurements in FTR-3. *ANL Neg. No. 116-963.*

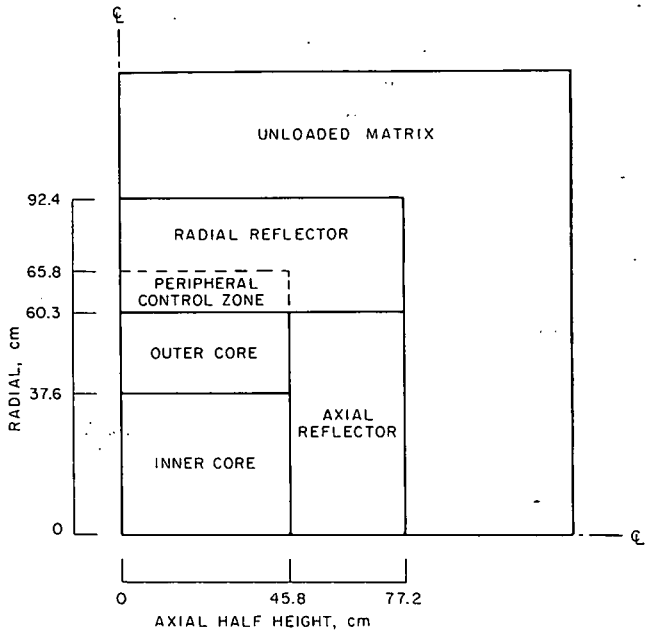

FIG. II-6-6. Side View of FTR-3 in ZPR-9. *ANL Neg. No. 116-553.*

TABLE II-6-IV. AS-BUILT ATOM DENSITIES FOR OPEN AND CLOSED LOOPS, 10^{21} atoms/cc

Isotope or Element	Closed Loop		Open Loop	Safety Rod Channel
	Type A	Type B		
^{238}Pu	—	—	0.0003	
^{239}Pu	0.5631	—	1.0276	
^{240}Pu	0.0535	—	0.1141	
^{241}Pu	0.0044	—	0.0136	
^{242}Pu	0.0003	—	0.0013	
$^{239+241}$Pu	0.5675	—	1.0412	
$^{240+242}$Pu	0.0538	—	0.1154	
Pu	0.6213	—	1.1569	
^{235}U	0.0057	—	0.0097	
^{238}U	2.4836	—	4.6547	
U	2.4893	—	4.6644	
Mo	0.0582	0.0244	0.3324	0.0097
Na	9.1730	9.4957	9.5310	18.47
C	0.0732	0.0708	1.0778	0.028
O	—	—	10.236	—
Fe	27.192	26.297	17.634	10.52
Cr	7.8448	7.5866	4.1332	3.035
Ni	3.7432	3.6200	1.9722	1.448
Mn	0.5760	0.5571	0.3035	0.223

TABLE II-6-V. FTR-3 ATOM DENSITIES, 10^{21} atoms/cc

Isotope or Element	Inner Core Avg.[a]	Outer Core	Outer Core Drawer Next to ^{10}B Rods	Radial Reflector	Axial Reflector	Radial Shield
^{238}Pu	0.0003	0.0006	0.0006	—	—	—
^{239}Pu	0.9822	1.4669	1.4466	—	—	—
^{240}Pu	0.0814	0.1723	0.1704	—	—	—
^{241}Pu	0.0110	0.0227	0.0225	—	—	—
^{242}Pu	0.0009	0.0022	0.0022	—	—	—
$^{239+241}$Pu	0.9932	1.4896	1.4691	—	—	—
$^{240+242}$Pu	0.0823	0.1745	0.1726	—	—	—
^{235}U	0.0095	0.0125	0.0114	—	—	—
^{238}U	4.4359	5.9000	4.9970	—	—	—
Mo	0.1149	0.4412	0.4338	0.0078	0.0079	0.036
Na	10.266	8.7013	6.2784	6.7544	9.2102	6.754
C	0.0310	1.0686	1.0684	0.1646	0.0231	0.105
O	11.394	12.717	8.0809		—	—
Fe	13.294	15.906	14.124	8.4575	8.5898	39.022
Cr	3.3287	3.1571	3.1204	2.432	2.4614	11.258
Ni	1.5883	1.5064	1.4889	48.072	38.1013	5.372
Mn	0.2444	0.2318	0.2291	0.2864	0.2789	0.827
Al	0.0596	—	—	—	—	—

[a] 112 Type A drawers and 130 Type B drawers.

system. The various regions of the core were represented by a succession of concentric cylinders, each of which contained the same materials as the corresponding regions of the core. Six such cylindrical regions were used to represent the core.

The neutron cross sections used in the calculation corresponded to a modification of Set 29006, in which the broad-group heterogeneity effect due to the plate loading patterns in the cells of the FTR-3 core were taken into account by means of the MODXSS[19] code. The modified cross section set was labeled "Set MD-29006." The delayed neutron data concerned six families

of delayed neutrons and described their respective yields,[20] decay constants,[20] and energy distributions.[21]

A separate calculation for the same assembly was run in one-dimensional cylindrical geometry. The purpose of the one-dimensional calculation was to assess the effect of the axial reflector and the extent to which this more economical type of calculation may be used to determine kinetics parameters in FFTF-like assemblies.

The one-dimensional calculation was run through the DIF1D code of the ARC system with the same cross sections, compositions, radial mesh spacings and delayed neutron data as the two-dimensional calculation. The region- and group-independent buckling (5.4075 10^{-4} cm^2) was determined so that the effective multiplication constant (0.991760) would also be the same in the two problems. In the one-dimensional problem, the flux and the fission cross section were assumed to vanish respectively, at the extrapolated axial boundary of the core (67.549 cm from the reactor midplane) and at the physical axial boundary of the core (45.801 cm from the reactor midplane).

Table II-6-VI describes the results of the calculations. One-dimensional and two-dimensional calculations agree very well with each other in the values of the perturbation denominator, in the effective delayed neutron fraction, and in the inhours per percent reactivity. Therefore, one-dimensional calculations appear to be adequate for most static calculations. However, the internal 1/v product is underestimated by approximately 13 % in the one-dimensional calculation, causing a similar bias in the values of the neutron generation time, of the prompt neutron lifetime, and of the inverse rolloff angular velocity. The underestimate is a direct consequence of the inability of the one-dimensional calculations to take properly into account the significant neutron population in the axial reflector.

The value of the inverse rolloff angular velocity obtained from the two-dimensional calculation (247.28 μsec) is in excellent agreement with the corresponding experimental value (252 $\pm$ 6 μsec) measured by ORNL personnel.[22]

TABLE II-6-VI. KINETICS PARAMETERS OF THE INITIAL CONFIGURATION IN FTR-3 AS OBTAINED FROM ONE-DIMENSIONAL AND TWO-DIMENSIONAL CALCULATIONS

Parameter	*R* Calculation	*RZ* Calculation
Effective multiplication constant, k_{eff}	0.991760	0.991760
Perturbation denominator, $PD = \langle \phi^* \mid \chi^p \Sigma_f \mid \phi \rangle$	1.844777×10^{-5}	1.847618×10^{-5}
Internal $1/v$ product, $IP = \langle \phi^* \left\| \frac{1}{v} \right\| \phi \rangle$	1.196290×10^{-11}	1.347272×10^{-11}
Neutron generation time, $\Lambda = IP/PD$, sec	6.484739×10^{-7}	7.291940×10^{-7}
Prompt neutron lifetime, $\ell_p = k_{eff}\,\Lambda$, sec	6.431304×10^{-7}	7.231854×10^{-7}
Effective delayed neutron fraction, β_{eff}	0.00297056	0.00294884
Inverse rolloff angular velocity, $\alpha = \Lambda/\beta_{eff}$, sec	218.30×10^{-6}	247.28×10^{-6}
Inhours per percent reactivity	1036.517	1040.638

REFERENCES

1. A. Travelli, A. J. Ulrich and J. C. Beitel, *Analytical Studies in Support of the Fast Flux Test Facility (FFTF) Critical Experiments on ZPPR and ZPR-9*, Applied Physics Division Annual Report, July 1, 1969 to June 30, 1970, ANL-7710, pp. 77–97.
2. A. Travelli, A. J. Ulrich, D. Meneghetti and J. C. Beitel, *Calculational Studies in Support of the Fast Flux Test Facility (FFTF) Critical Experiments on ZPR-3 and ZPPR*, Reactor Physics Division Annual Report, July 1, 1968 to June 30, 1969, ANL-7610, pp. 115–137.
3. D. Meneghetti, A. J. Ulrich, P. J. Persiani and J. C. Beitel, *Calculational Studies in Support of the Fast Flux Test Facility (FFTF) Critical Experiments on ZPR-3*, Reactor Physics Division Annual Report, July 1, 1967 to June 30, 1968, ANL-7410, pp. 221–227.
4. B. J. Toppel, A. L. Rago and D. M. O'Shea, *MC²*, *A Code to Calculate Multigroup Cross Sections*, ANL-7318 (1967).
5. B. J. Toppel, *The Argonne Reactor Computational (ARC) System*, ANL-7332 (1967).
6. D. A. Meneley, L. C. Kvitek and D. M. O'Shea, *Mach-1, a One-Dimensional Theory Package*, ANL-7223 (1966).
7. W. G. Davey and R. L. McVean, *ZPR-3 Operations and Analysis, Mockup Studies*, Reactor Development Program Progress Report, ANL-7460, 22 (1968).
8. W. G. Davey and R. L. McVean, *ZPR-3 Operations and Analysis, Mockup Studies*, Reactor Development Program Progress Report, ANL-7577, 35 (1969).
9. W. P. Keeney, *ZPR-3 and ZPPR Operations and Analysis, Mockup Critical Experiments*, Reactor Development Program Progress Report, ANL-7655, 42 (1969).
10. A. B. Long and C. D. Swanson, *Central Reaction Ratios in ZPR-9 Assembly 26, FTR-3*, Applied Physics Division Annual Report, July 1, 1969 to June 30, 1970, ANL-7710, pp. 63–65.
11. W. G. Davey and R. L. McVean, *ZPR-3 Operations and Analysis, Mockup Studies*, Reactor Development Program Progress Report, ANL-7577, 19, 20, 33, (1969).
12. R. A. Karam, K. D. Dance, T. Nakamura and J. E. Marshall, *Analysis of Central Reactivity Worths in Fast Critical Assemblies*, Nucl. Sci. Eng. **40**, 414 (1970).
13. P. E. McGrath and W. K. Foell, *Integral Transport Theory Analysis of Small-Sample Reactivity Measurements*, Trans. Am. Nucl. Soc. **12**, 188 (1969).
14. A. M. Weinberg and E. P. Wigner, *The Physical Theory of Neutron Chain Reactors*, pp. 713–718 (1958).
15. J. Dwark, P. L. Hoffmann, H. Hurwitz, Jr. and E. J. Clancy, *Self-Shielding Factors for Infinitely Long Hollow Cylinders*, KAPL-1262, (January 1955).
16. G. J. Duffy, H. Greenspan, S. D. Sparck, J. V. Zapatka and

1	TRANSFER TUBE 1.062" O.D., 0.010" WALL	304 SS
2	TRANSFER TUBE 1.000" O.D., 0.010" WALL	304 SS
3	PERTURBATION CAPSULE HOUSING 0.42" O.D., 0.010" WALL	304 SS
4	PERTURBATION CAPSULE	
5	PERTURBATION CAPSULE INNER TUBE 0.36" O.D., 0.010" WALL	304 SS
6	PERTURBATION CAPSULE END PLUG	304 SS

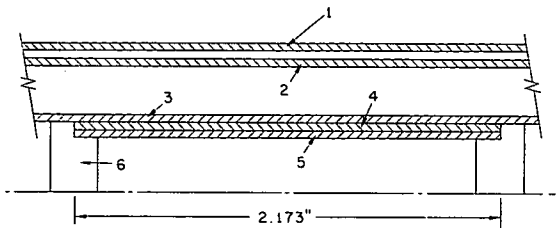

FIG. II-7-1. Immediate Environment of a Perturbation Sample. *ANL Neg. No. 116-977.*

TABLE II-7-II. CALCULATED PERTURBATIONS IN THE REAL AND ADJOINT FLUXES DUE TO TRANSFER TUBE AND SAMPLE HOLDER

gp	ϕ/ϕ_∞	$\phi^*/\phi_\infty{}^*$	$\frac{\phi}{\phi_\infty}\times\frac{\phi^*}{\phi_\infty{}^*}$	*gp*	ϕ/ϕ_∞	$\phi^*/\phi_\infty{}^*$	$\frac{\phi}{\phi_\infty}\times\frac{\phi^*}{\phi_\infty{}^*}$
1	0.9254	0.9419	0.8716	15	0.9866	0.9806	0.9675
2	0.9309	0.9506	0.8849	16	1.0022	0.9770	0.9791
3	0.9406	0.9539	0.8972	17	0.9692	0.9706	0.9406
4	0.9511	0.9542	0.9076	18	0.9740	0.9768	0.9513
5	0.9517	0.9499	0.9040	19	0.9832	0.9778	0.9613
6	0.9548	0.9533	0.9103	20	0.9907	0.9794	0.9703
7	0.9608	0.9581	0.9206	21	1.0004	0.9792	0.9796
8	0.9580	0.9588	0.9185	22	0.9900	0.9792	0.9695
9	0.9676	0.9682	0.9368	23	1.0012	0.9787	0.9798
10	0.9702	0.9693	0.9404	24	0.9982	0.9781	0.9764
11	0.9698	0.9698	0.9404	25	1.0054	0.9695	0.9748
12	0.9797	0.9757	0.9559	26	1.0148	0.9780	0.9924
13	0.9629	0.9685	0.9326	27	1.0131	0.9754	0.9881
14	0.9834	0.9783	0.9621	28	1.0040	0.9725	0.9764

transfer tube that contains the sample. The ratios of perturbed-to-unperturbed fluxes, ϕ^*/ϕ_∞^* and ϕ/ϕ_∞, was taken to be the ratio of the flux at the position of the sample to the flux at the boundary of the cell.

The effect of these flux perturbations, which are given in Table II-7-II, on the computed central worths is easily obtained only for those samples for which the dominant reactivity effect is the change in absorption cross section. For these samples (tantalum and enriched-boron) a good estimate of the effect of the immediate environment is obtained by multiplying the group-wise reactivity from the perturbation calculations by the product of perturbed-to-unperturbed flux ratios. When this was done, there resulted a 2.9% reduction in the worth of the tantalum sample and a 5.2% reduction in the worth of the enriched boron sample. For the fissile samples, this effect would be slightly larger because the fission source term involved the high-energy adjoint fluxes which are more highly perturbed than the low-energy adjoint fluxes (the absorption effect is mainly at low energies). Therefore, although including the immediate environment of the sample in the calculation tends to reduce the discrepancies between calculation and measurement, the discrepancies cannot be attributed to this effect.

ANALYSIS OF RADIAL WORTH TRAVERSES

Radial worth measurements were made for three samples: enriched boron, plutonium (11% 240) and depleted uranium. The measurements were made in a radial direction midway between peripheral control drawers as shown in Fig. II-7-2. The worth traverse

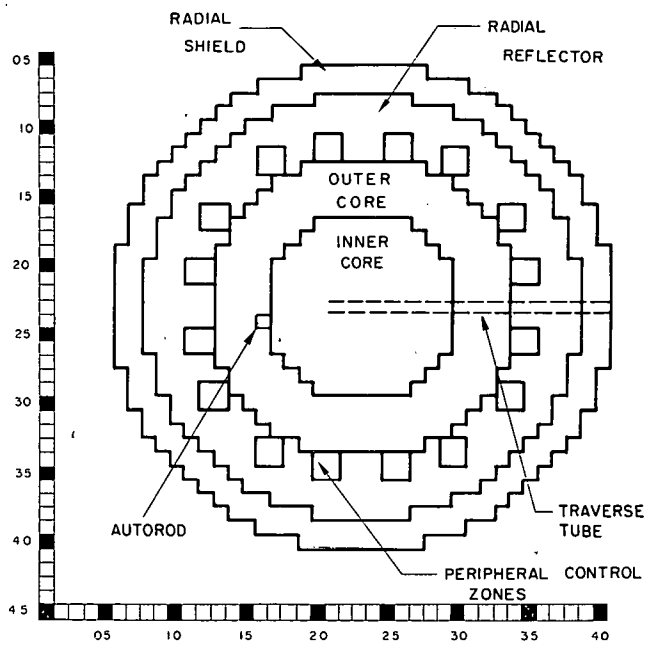

FIG. II-7-2. FTR-3 Configuration for Radial Sample Worth and Reaction Rate Traverses. *ANL Neg. No. 116-526 Rev. 1.*

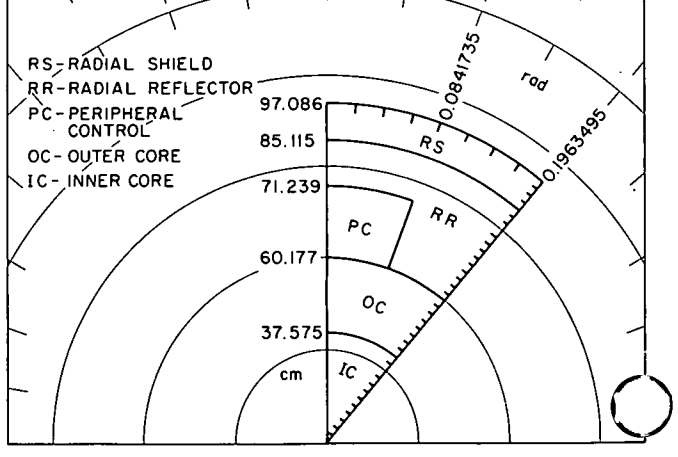

FIG. II-7-3. Representation of FTR-3 in R-θ Configuration. *ANL Neg. No. 116-966.*

measurements were analyzed using two-dimensional diffusion-perturbation theory in $r\theta$ geometry. Real and adjoint fluxes were computed for the reactor representation shown in Fig. II-7-3 in which a section of the reactor is divided into 37 radial intervals and 8 azimuthal intervals. Symmetry was assumed at both azimuthal boundaries shown in the figure. A buckling search, which yielded a critical extrapolated transverse height of 134 cm, was made so that fluxes of a critical system could be used.

The sample worths were computed in the same manner as the center worths; namely, as the difference between the worths of the sample-plus-stainless-steel and stainless steel. As for the central worth analyses, the sample cross sections were based on the assumption of infinitely-thin samples and an inner core spectrum. A comparison of the computed and measured worth traverses is given in Figs. II-7-4 through II-7-6. Both the computed and measured worths are normalized to unity at the center.

It is seen that for all three samples there is good agreement between calculation and experiment in the inner core region and the inner portion of the outer core region. However, near the core-reflector interface the calculations for the boron and plutonium samples yield the start of a depression that was not measured. For the depleted uranium sample, the calculation correctly predicts the change in sign of the worth in the reflector and shield. For the plutonium sample, the graph also contains the worths as calculated with the rz representation of the core, in which the peripheral control drawers are represented as an annular region. As may be expected, this curve dips far too much at the core-reflector interface. This illustrates the importance of the geometric representation of the assembly in calculating accurate worth traverses. Although the $r\theta$ representation is far superior to the rz representation for these measurements, it is not an ideal representation of a square matrix. Near the core-reflector interface in the proximity of the peripheral control drawers, the flux is a sensitive function of space and energy, which may not be well represented in our calculations. Another possible source of error in the calculations for the inner core and reflector regions is the use of sample cross sections that were derived with an inner core spectrum. In the analysis of reaction rate traverses in FTR-2,[7] better agreement between theory and experiment in the reflector was attained when the cross sections for the foils were derived using the reflector spectrum.

It is of interest to compare the shape of worth traverses in the core with that of the ^{238}U Doppler effect to determine if an estimate of the Doppler effect can be deduced from sample worth traverse data. The spatial dependence of the Doppler effect was obtained from a

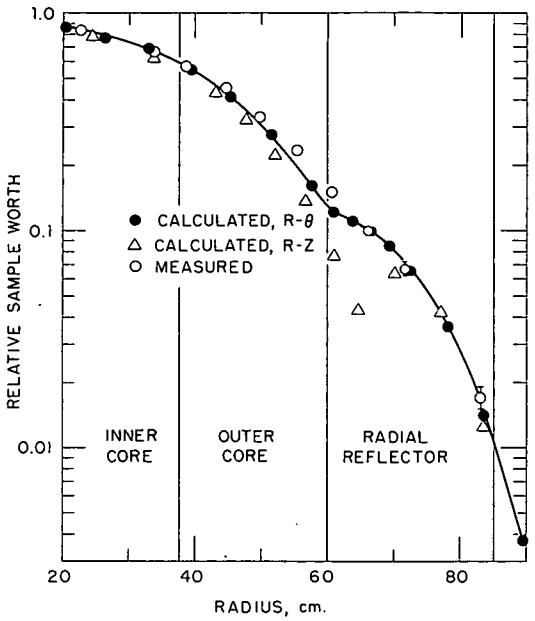

FIG. II-7-4. Comparison of Measured and Calculated Worth Traverse, Plutonium Sample P-11. *ANL Neg. No. 116-968.*

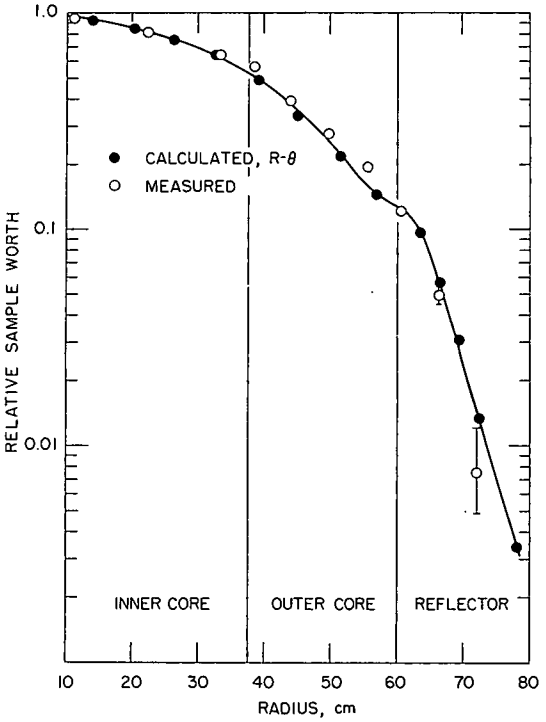

FIG. II-7-5. Comparison of Measured and Calculated Worth Traverse, Enriched Boron Sample B-7. *ANL Neg. No. 116-967.*

perturbation run in which the effective Doppler change in ^{238}U capture cross sections (see Paper II-8) to 1070°K was imposed throughout the core. These cross sections included the effects of hot-sample, cold-core resonance

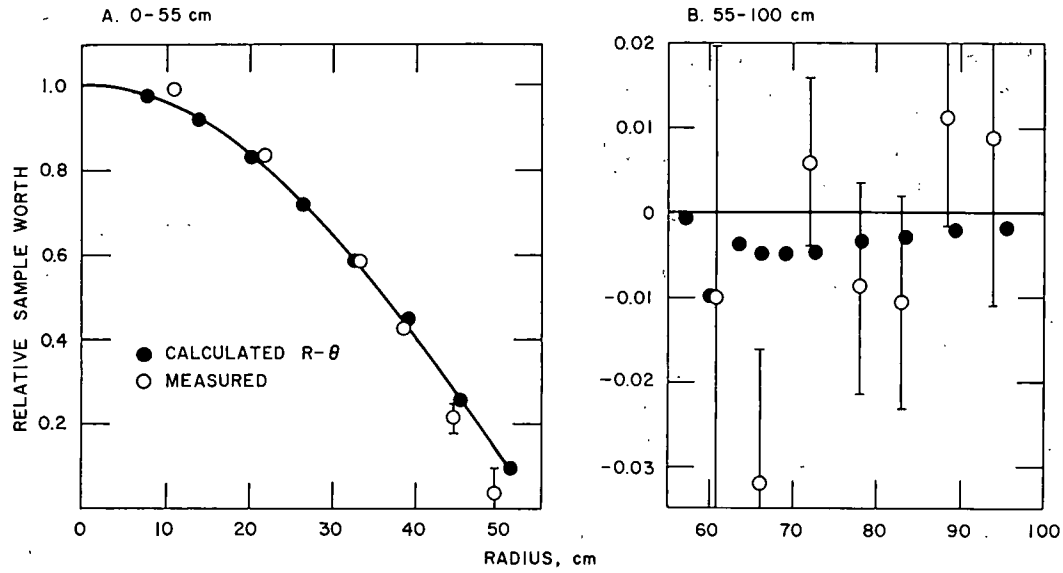

FIG. II-7-6. Comparison of Measured and Calculated Worth Traverse, Depleted Uranium Sample MB-25. *ANL Neg. No. 116-979.*

TABLE II-7-III. RELATIVE WORTHS OF BORON, URANIUM, AND PLUTONIUM SAMPLES IN RADIAL TRAVERSES IN FTR-3 AS CALCULATED IN R-θ GEOMETRY

r, cm	ρ/ρ0				
	Boron	Uranium	Plutonium	Tantalum	^{238}U Doppler
0	1.0	1.0	1.0	1.0	1.0
7.828	0.97765	0.97517	0.98030	0.97651	0.97648
14.09	0.92644	0.91835	0.93292	0.92259	0.92238
20.35	0.84848	0.83200	0.86293	0.84025	0.83936
26.62	0.74680	0.71955	0.77360	0.73228	0.72961
32.88	0.62492	0.58481	0.66998	0.60202	0.59553
39.11	0.48327	0.45069	0.55258	0.45250	0.43500
45.25	0.33933	0.25695	0.41388	0.30534	0.29609
51.39	0.21801	0.09580	0.27700	0.19325	0.19451
57.04	0.14296	−0.00063	0.17077	0.14206	0.14019
60.87	0.12853	−0.00966	0.12139	0.16666	
63.63	0.09455	−0.00371	0.11038	0.13835	
66.40	0.05645	−0.00486	0.09908	0.08506	
69.16	0.03088	−0.00486	0.08465	0.04620	
72.62	0.01339	−0.00467	0.06534	0.01888	
78.17	0.00338	−0.00343	0.03600	0.00385	
83.5	0.000714	−0.00258	0.01414	0.00038	
89.6	0.000089	−0.00191	0.00369	−0.00017	
95.6	−0.000053	−0.00155	0.000225	−0.00025	

interaction and the flux perturbations introduced by the Doppler drawer and its surrounding steel buffer.

From Table II-7-III, in which the calculated worth traverses are summarized, it is seen that the shape of the Doppler worth is approximated very well by tantalum and well by boron. Our real interest lies in comparing measured Doppler worth traverses with measured sample worth traverses. Since there are discrepancies between measured and computed worth traverses [for the position-dependent ^{238}U small-sample Doppler measurements in ZPR-3 Assembly 51 there are sizeable discrepancies, (see Paper II-10)] one should not give too much weight to the close agreement between the calculated worth traverses.

ANALYSIS OF REACTION RATE MEASUREMENTS

Radial traverses at the core midplane and central axial traverses were calculated for the ^{239}Pu(n,f), ^{238}U(n,f), and ^{10}B(n,α) reaction rates. The reaction rate traverse experiment is described in Ref. 8. Central reaction rate ratios for ^{239}Pu fission, ^{240}Pu fission, ^{238}U fission, and ^{238}U capture relative to ^{235}U fission were also calculated. A fission counter was used to measure all reaction rate ratios[9] except for $^{238}U_c/^{235}U_f$ which was determined by foil irradiation. The $^{238}U_f/^{235}U_f$ ratio was determined by both methods for comparison.

FTR-3 reaction rate traverse and central reaction rate ratio calculations were previously reported by Travelli et al.[7,10] However, the calculations reported here involve three additional methods that were not used in the previous calculations:

1. The cross sections used to calculate fluxes were spatially weighted within the cell (with the MODXSS code).
2. Infinitely-dilute cross sections were used for the "foil" isotopes.
3. The effect of the flux perturbation due to the stainless steel in the traverse tube and detector was investigated using the flux perturbation factors calculated for the sample worth analysis.

Infinitely-dilute cross sections were thought to be appropriate for the calculations because the foils used in the measurements were very thin (for ^{239}Pu and ^{238}U the

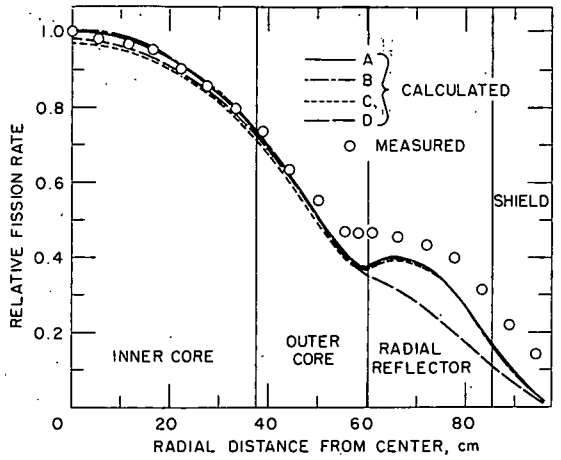

FIG. II-7-7. Comparison of Measured and Calculated $^{239}Pu(n,f)$ Radial Reaction Rate Traverse. Calculations were Obtained as Follows: A, with Infinitely Dilute Cross Sections Averaged in the Inner Core Spectrum; B, with Infinitely Dilute Cross Sections Averaged in the Reflector Spectrum; C, as in A with Corrections Applied for the Stainless Steel in the Traverse Tube; and D, with Inner Core Cross Sections. *ANL Neg. No. 116-976.*

fissionable material was electrolytically deposited to a thickness of 20 $\mu g/cm^2$ on a stainless steel disk). The infinitely-dilute cross sections generated for the sample worth calculations were used. These cross sections were averaged in the spectrum of the inner core. In addition, infinitely-dilute ^{239}Pu cross sections averaged in the spectra of the axial and radial reflectors were used to determine the effect of spectral weighting of cross sections on the reaction rates in the reflector regions. Finally, to determine the possible effect of self-shielding, ^{239}Pu cross sections for the inner core composition (σ_p = 127 b) were used for comparison with results using infinitely-dilute cross sections.

Although no specific calculation of the effect of the stainless steel environment of the traverse foils was done, the perturbation factors calculated for the sample worth analysis are sufficient to give an indication of the effect. This is most valid for the radial traverse calculation since the same transfer tube was used for both worth and reaction rate measurements. The perturbation factors were also applied to the reaction rate ratio calculations even though the only stainless steel present was in the detector itself.

Results of the reaction rate traverse calculations are shown in Figs. II-7-7 through II-7-12 along with the experimental results. The two-dimensional $r\theta$ fluxes generated for the sample worth calculations were used for the radial calculations. The fluxes used were appropriate for a traverse midway between two peripheral control rods as shown in Fig. II-7-2. Fluxes from a two-dimensional diffusion theory problem in rz geometry were used for the axial calculations. The peripheral control zones were represented by an annular region outside the core.

The calculated reaction rates using infinitely-dilute cross sections averaged in the spectrum of the inner core were normalized to 1.0 at the core center, as were the measured rates. All other calculated traverses used the same fluxes and were not renormalized to 1.0 at the center. Therefore, the differences between various traverse calculations reflect differences in the cross sections used and are independent of normalization.

The radial and axial calculations for ^{239}Pu (Figs. II-7-7 and II-7-10) illustrate all of the effects discussed above. Calculations using infinitely-dilute cross sections averaged in the spectrum of the inner core are in good agreement with measured values well within the core regions. Agreement is poor at the core-reflector interface and in the reflector region where the reaction rates are underpredicted.

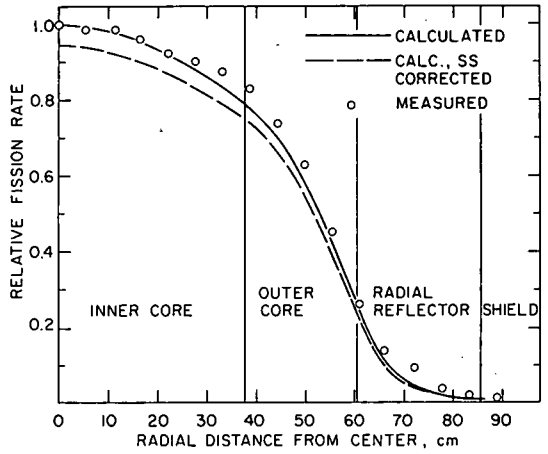

FIG. II-7-8. Comparison of Measured and Calculated $^{238}U(n,f)$ Radial Reaction Rate Traverse. *ANL Neg. No. 116-969.*

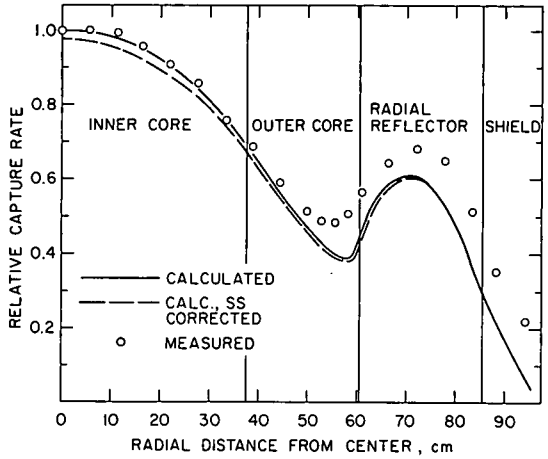

FIG. II-7-9. Comparison of Measured and Calculated $^{10}B(n,\alpha)$ Radial Reaction Rate Traverse. *ANL Neg. No. 116-975.*

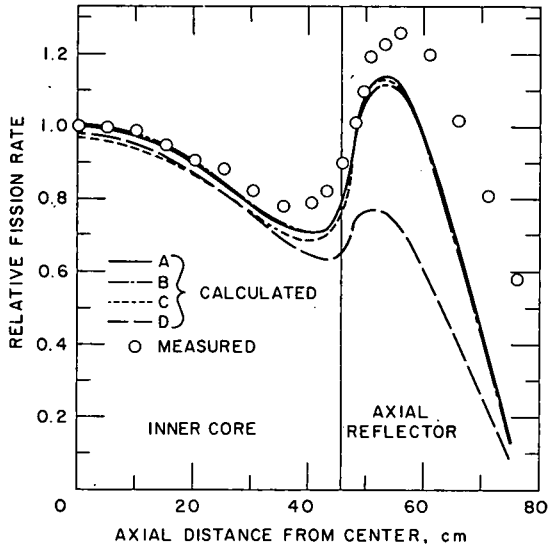

FIG. II-7-10. Comparison of Measured and Calculated $^{239}Pu(n,f)$ Axial Reaction Rate Traverse. Calculations were Obtained as Follows: A, with Infinitely Dilute Cross Sections Averaged in the Inner Core Spectrum; B, with Infinitely Dilute Cross Sections Averaged in the Reflector Spectrum; C, as in A with Corrections Applied for the Stainless Steel in the Traverse Tube; and D, with Inner Core Cross Sections. *ANL Neg. No. 116-978.*

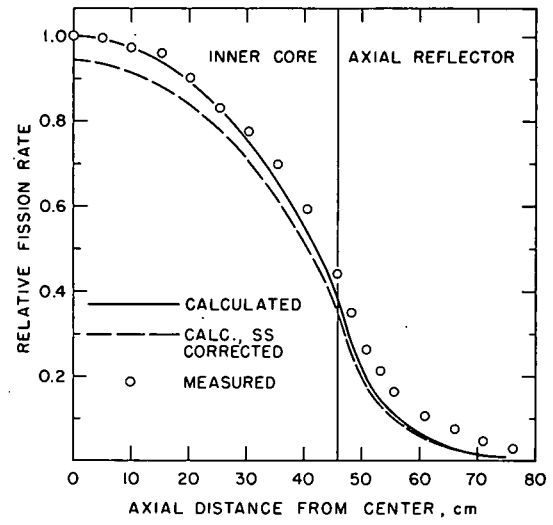

FIG. II-7-11. Comparison of Measured and Calculated $^{238}U(n,f)$ Axial Reaction Rate Traverse. *ANL Neg. No. 116-974.*

Using infinitely-dilute cross sections averaged in the reflector spectrum had negligible effect on the calculated traverse, even in the reflector region. However, self-shielded cross sections appropriate for ^{239}Pu in the inner core composition gave significantly lower reaction rates in the reflector than infinitely-dilute cross sections. Thus differences between reaction rate calculations in the reflector regions were due almost completely to differences in self-shielding with insignificant effects due to spectral averaging of cross sections.

The effect of a stainless steel environment around the foils is shown on all the traverse figures. It amounted to a 2 to 6% reduction in the central reaction rate with similar or smaller differences along the traverse. The correction did not significantly affect the shape of the traverse nor did it account for the discrepancies between calculation and measurement at the core-reflector interface or in the reflector.

It may be concluded that infinitely-dilute cross sections are the most appropriate for reaction rate calculations of this type. It made little difference whether core or reflector spectrum averaging was used. While self-shielded core cross sections gave equivalent results in the core regions, they gave poorer results in the reflector regions. No matter what cross sections were used, however, the reaction rates in the reflector regions were underpredicted, an indication that the calculational model was not representing the flux in the reflector regions properly. The stainless steel corrections did not affect the traverse calculations enough to make more detailed or specific calculations of this effect necessary.

A comparison of calculated and measured central reaction rate ratios is given in Table II-7-IV. The calculations were done with the $r\theta$ fluxes previously described. The calculated results were the same for infinitely dilute and self-shielded core cross sections for the $^{240}Pu_f$ and $^{238}U_f$ to $^{235}U_f$ ratios while the $^{239}Pu_f/^{235}U_f$ ratio was 2.3% lower with the self-shielded set. Similar results are expected based on the traverse results which showed the two sets to be equally as good in the core region. However, the $^{238}U_c/^{235}U_f$ ratio using core cross sections was 23% lower than the ratio with infinitely dilute cross sections, indicating the strong dependence of $^{238}U_c$ cross sections on resonance self-shielding. The infinitely dilute

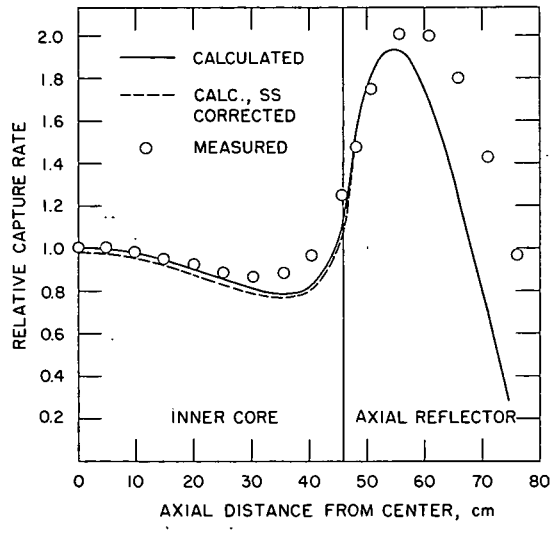

FIG. II-7-12. Comparison of Measured and Calculated $^{10}B(n,\alpha)$ Axial Reaction Rate Traverse. *ANL Neg. No. 116-980.*

TABLE II-7-IV. Comparison of Calculated and Measured Central Reaction Rate Ratios in FTR-3

Ratio and Measurement Technique	Calculation				
	Experiment	Dilute Cross Sect.	Core Cross Sect.	Dilute Cross Sect. SS Corrected	Travelli Calc.[12]
$^{239}Pu_f/^{235}U_f$ by detector	0.984 ± 0.022	0.890	0.869	0.887	0.890
$^{240}Pu_f/^{235}U_f$ by detector	0.256 ± 0.006	0.184	0.184	0.180	0.184
$^{238}U_f/^{235}U_f$ by detector	0.0250 ± 0.0006	0.0227	0.0227	0.0221	0.0224
$^{238}U_f/^{235}U_f$ by radiochemistry	0.0234 ± 0.0013	0.0227	0.0227	0.0221	0.0224
$^{238}U_c/^{235}U_f$ by radiochemistry	0.161 ± 0.009	0.177	0.137	0.178	0.135

cross sections overpredicted the ratio by 10 % while the core cross sections underpredicted the ratio by 15 %.

Corrections for stainless steel produced only small (0.3 to 2.6 %) differences in the ratios. Recall that the stainless steel correction factors were calculated for the sample worth measurements which involved a much greater perturbation to the reactor than the detector used for the ratio measurements. Therefore the effect of stainless steel was probably even smaller than indicated here.

The previous reaction rate ratio calculations by Travelli and Ulrich[10] are included in Table II-7-IV for comparison.

References

1. J. W. Daughtry, R. B. Pond, C. D. Swanson and R. M. Fleischman, *ZPR-9 Assembly 26, FTR-3*, Applied Physics Division Annual Report, July 1, 1969, to June 30, 1970, ANL-7710, pp. 58–63.
2. B. J. Toppel, A. L. Rago and D. M. O'Shea, *MC², A Code to Calculate Multigroup Cross Sections*, ANL-7318 (1967).
3. K. D. Dance, *An Equivalence-Theory Capture Cross Section Code for Plate-Type Cells*, Reactor Physics Division Annual Report, July 1, 1967 to June 30, 1968, ANL-7410, pp. 434–435.
4. K. D. Dance, Argonne National Laboratory (private communication).
5. B. J. Toppel, Ed., *The Argonne Reactor Computation (ARC) System*, ANL-7332 (1967).
6. P. J. Collins and R. G. Palmer, *Calculated Size Effects for Reactivity Samples in ZPPR*, Trans. Am. Nucl. Soc. **14**, 846 (1971).
7. A. Travelli, A. J. Ulrich and J. C. Beitel, *Analytical Studies in Support of the Fast Flux Test Facility (FFTF) Critical Experiments on ZPPR and ZPR-9*, Applied Physics Division Annual Report, July 1, 1969, to June 30, 1970, ANL-7710, pp. 77–97.
8. A. B. Long and C. D. Swanson, *Measured Reaction Rate Distributions in ZPR-9 Assembly 26, FTR-3*, Applied Physics Division Annual Report, July 1, 1969, to June 30, 1970, ANL-7710, pp. 65–70.
9. A. B. Long and C. D. Swanson, *Central Reaction Ratios in ZPR-9 Assembly 26, FTR-3*, Applied Physics Divison Annual Report, July 1, 1969, to June 30, 1970, ANL-7710, pp. 63–65.
10. A. Travelli and A. J. Ulrich, *Comparison of Computed and Experimental Central Reaction Rate Ratios*, Reactor Development Program Progress Report, ANL-7798, March 1971, pp. 95–98.

II-8. Analysis of UO_2 Small Sample Doppler Measurements in FTR-3, ZPR-9 Assembly 26

P. H. Kier and C. E. Till

Introduction

The UO_2 small-sample Doppler measurements in ZPR-9 (Zero Power Reactor) Assembly 26, the third in a series of critical assemblies associated with the FTR (Fast Test Reactor) Program,[1] have been analyzed in great detail to yield information on the comparative accuracy of several computational formulations. Details of the experiment are given by Pond et al. in Ref. 2. The natural UO_2 sample was 1 in. in diam, 12 in. long and contained 1116g of uranium. The sample was placed in the oscillator drawer, shown in Fig. II-8-1, which was located in the central matrix location of the assembly. In the 16 front drawers surrounding the oscillator drawer, U_3O_8 plates were replaced by stainless steel to provide an additional ¼ in. thick steel region between the sample and the inner core. This region, which will be referred to as the buffer, is shown in the drawing of the modified inner core zone, Fig. II-8-2.

Calculational Models

A perturbation formulation was used to compute the Doppler reactivity effect of the change in temperature of the UO_2 sample. This formulation is based on the assumption that the Doppler effect arises solely from the change in capture in ^{238}U, that is,

$$\Delta k/k^2 = \frac{N^{28}}{D} \int \delta\sigma_c^{28} \phi^{\infty} \phi^{*\infty} \, dV \qquad (1)$$

where D is the perturbation denominator and ϕ^{∞} and $\phi^{*\infty}$ are the unperturbed real and adjoint fluxes. That is, ϕ^{∞} and $\phi^{*\infty}$ are the fluxes when the center of the assembly contains inner core fuel drawers. Since the unperturbed fluxes are used in Eq. (1), the flux perturbations introduced by the oscillator drawer and stainless steel buffer should be incorporated into $\delta\sigma_c^{28}$, the effective Doppler change in the capture cross section of ^{238}U.

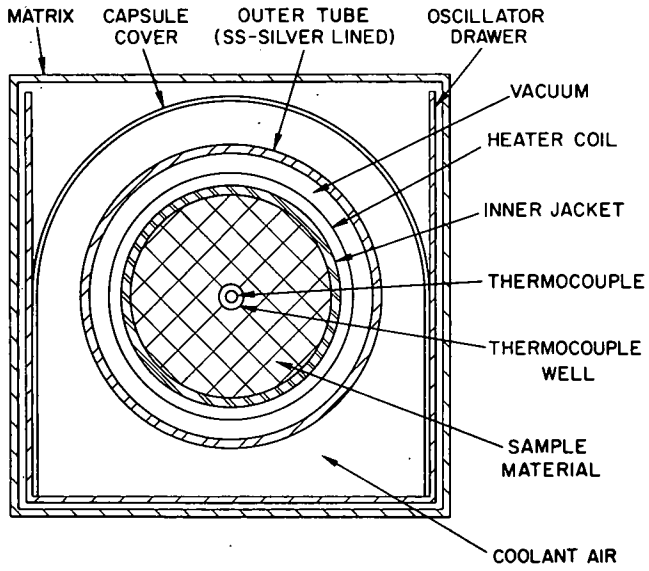

Fig. II-8-1. Cross Sectional View of the Oscillator Drawer and Doppler Capsule. *ANL Neg. No. 116-417.*

The expression for $\delta\sigma_c^{28}$ should also include the hot-sample cold-core resonance interaction effect. Not only is the Doppler change in ^{238}U capture cross sections in the sample affected by ^{238}U in the core remaining cold but also the uranium cross sections in the portion of core adjacent to the sample are affected by the change in temperature of the sample.[3] The primary function of the stainless steel filter is to reduce the magnitude of this effect. The RABBLE code,[4] which is based on an integral transport formulation, can explicitly include the environment when computing cross sections for uranium in the sample, and therefore it provides a means of including the hot-sample cold-core resonance interaction effect.

An expression for $\delta\sigma_c^{28}$ that includes both the perturbation in the fluxes introduced by the presence of the oscillator drawer and the hot-sample cold-core resonance interaction effect is

$$\delta\sigma_c^{28} = \delta\sigma^s(\bar{\phi}_h^s \bar{\phi}_c^{s*}/\phi^{\infty}\phi^{*\infty}) + \delta\sigma^{c1}(\bar{\phi}_h^c \bar{\phi}_c^{c*}/\phi^{\infty}\phi^{*\infty}), \qquad (2)$$

where

$\delta\sigma^s$ is the Doppler change in the capture cross section section of ^{238}U in the sample

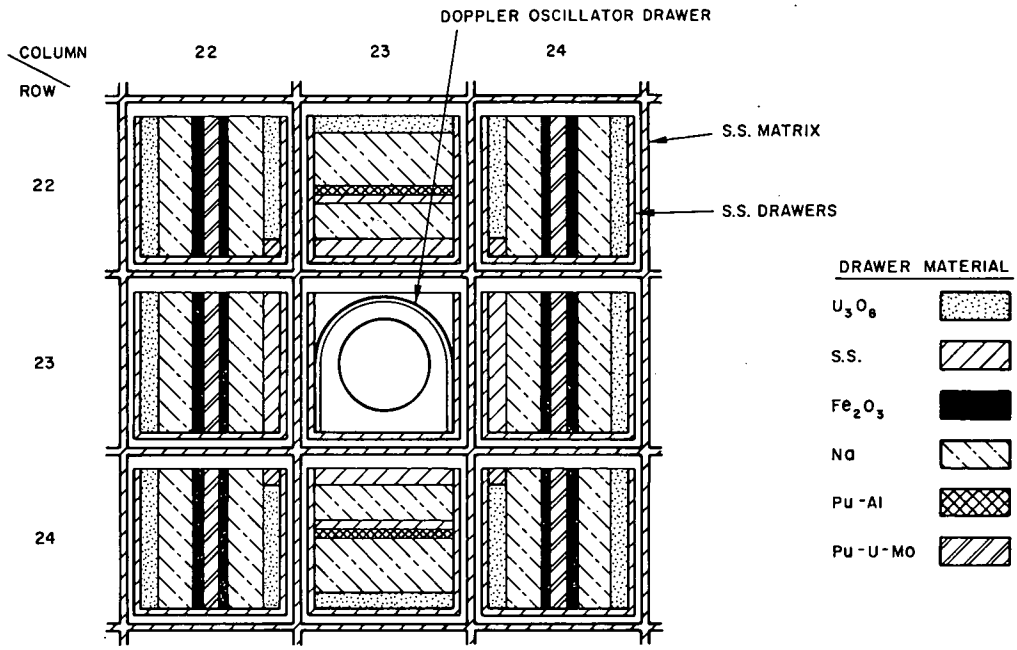

Fig. II-8-2. Modified Core Surrounding Doppler-Oscillator Drawer. *ANL Neg. No. 116-418.*

$\delta\sigma^{c1}$ is the change in the capture cross section section of ^{238}U in the adjacent core per ^{238}U atom in the sample arising from the temperature change of the sample

$\bar{\phi}_h^s$ and $\bar{\phi}_h^c$ are the average perturbed real flux in the hot sample and the adjacent core respectively

$\bar{\phi}_c^{s*}$ and $\bar{\phi}_c^{c*}$ are the average perturbed adjoint flux in the cold sample and adjacent core respectively.

In Eq. (2), the flux perturbation effect is accounted for by the presence of the ratios of perturbed to unperturbed flux and the hot-sample cold-core resonance interaction effect is accounted for by the presence of the adjacent core term and implicitly by the use of RABBLE to generate group cross sections.

The ratio of perturbed to unperturbed fluxes were obtained from S_8 transport computations for a cylindrical cell centered upon the Doppler oscillator drawer. This cell, which is described in Table II-8-I, was sufficiently large that the flux in the thin outer region was taken to be the unperturbed flux.

To assess the magnitude of these two effects, the small sample Doppler effect was computed with use of three prescriptions for $\delta\sigma_c^{28}$. In order of increasing sophistication, these prescriptions were:

1. $\delta\sigma_c^{28}$ was taken as the difference between two MC²[5] derived cross sections. Because MC² cannot include the environment when computing resonance cross sections for the sample, neither the flux perturbation effect nor the hot-sample cold-core resonance interaction effect was included.
2. $\delta\sigma_c^{28}$ was taken as the difference between RABBLE derived cross sections with contributions from the sample ($\delta\sigma^s$) and the adjacent core ($\delta\sigma^c$). This prescription accounts for the hot-sample cold-core resonance interaction effect but not the flux perturbation effect.
3. $\delta\sigma_c^{28}$ was computed by use of Eq. (2). Here the components from the sample and the adjacent core were weighted by the appropriate products of flux ratios. This prescription accounts for both the hot-sample cold-core resonance interaction effect and the flux perturbation effect.

Calculational Details

The calculations were made with use of a 30 group cross section set. Groups 1–24 were ½ lethargy units wide, groups 25–29 were 1 lethargy unit wide and group was the thermal group. There were contributions to the Doppler effect from groups 11–27, which covers an energy range from 67 keV to 5 eV. The cross section set that was used in the diffusion and perturbation computations, which is described in greater detail in Paper II-7, was used in the analysis of other measurements in FTR-3. Separate MC² runs were made to derive cross sections for the inner core, outer core, peripheral control, radial reflector, radial shield and axial reflector regions. The cross sections for the inner core and outer core regions were then corrected for resonance shielding and cell heterogeneities. The computations were for elevated sample temperatures of 782 and 1069°K and for a base temperature of 293°K. ENDF/B VERSION I data were used in all computations.

TABLE II-8-I. Cell Used in Transport Calculations of the Flux Perturbations Introduced by the Oscillator Drawer and Buffer

Region	Material	Outer Radius, cm	Mesh Points
Sample	UO_2	1.27	5
Oscillator drawer	SS	3.32	8
Buffer	SS	4.05	3
Adjacent core	Inner core	9.35	14
Inner core	Inner core	24.725	41
Boundary	Inner core	25.1	1

TABLE II-8-II. Cell Used in Rabble Calculation of Cross Sections for FTR-3

Region	Material	Outer Radius, cm	Mesh Points
Sample	UO_2	1.27	2
Oscillator drawer	SS	3.32	2
Buffer	SS	4.05	1
Adjacent core	Inner core	9.35	4
Inner core	Inner core	14.00	3

MC² problems were run to obtain Doppler cross section changes for use in prescription 1. To obtain resonance cross sections, the pin cell geometry option was used with the central region being the UO_2 sample and the annular region being the homogenized buffer and oscillator drawer. The fine group (¼ lethargy unit) spectrum characteristic of the inner core was used to collapse to broad group cross sections. Thus, the MC² derived sample cross sections for ^{238}U have proper resonance self-shielding, except for the hot-sample cold-core resonance interaction effect, and a gross spectrum characteristic of the inner core.

RABBLE runs, which included the inner core explicitly, were made to derive ^{238}U cross sections for use in prescriptions 2 and 3. The cell used in these calculations is described in Table II-8-II. The cell had five regions: the sample, the homogenized oscillator drawer, the stainless steel buffer, the adjacent core and the inner core. Both the adjacent core and inner core regions contained homogenized inner core material. The oscillator

TABLE II-8-III. Comparison of MC² and Rabble Capture Cross Sections for ^{238}U in the UO_2 Sample, b

Group	E_{max}, eV	E_{min}, eV	σ_c (293°K)	
			MC²	RABBLE
11	67,379	40,867	0.33225	—
12	40,867	24,787	0.44027	—
13	24,787	15,034	0.55583	0.58694
14	15,034	9,118.8	0.67340	0.69210
15	9,118.8	5,530.8	0.78099	0.76881
16	5,530.8	3,354.6	0.84205	0.86955
17	3,354.6	2,034.6	0.97634	0.96187
18	2,034.6	1,234.1	0.91751	0.90081
19	1,234.1	748.52	1.12450	1.10800
20	748.52	454.00	1.00170	0.97411
21	454.00	275.36	0.93080	0.89400
22	275.36	167.02	1.18558	1.34310
23	167.02	101.30	1.06618	1.78590
24	101.30	61.442	2.19957	1.91900
25	61.442	37.266	0.43319	0.61509
26	37.266	13.709	5.32351	6.52860
27	13.709	5.0439	0.89768	2.41990

drawer region and buffer region were taken to be 29.5 and 83.6 v/o 304 SS, respectively. The atom fractions in 304 SS were taken as Fe/Cr/Ni/Mn/C/Mo = 68.92/19.88/9.49/1.46/0.18/0.06.

The RABBLE problems were run with the sample at three temperatures while the other regions were maintained at the base temperature. A transverse buckling of 0.00103 was assumed. These calculations covered groups 13–27 and thus extended up to 24.8 keV. Since the resonances of ^{238}U are resolved only up to 4 keV, it was necessary to use the RANDOM code[6] to generate by random selection s-wave and p-wave ladders with good statistics between 4 and 24.8 keV.

In Table II-8-III are given the group cross sections for ^{238}U in the sample at 293°K as generated by MC² and by RABBLE. Contributions to the Doppler effect from groups 11 and 12 are sufficiently small that it was considered to be unnecessary to cover these groups in the RABBLE calculation. Above 300 eV there is good agreement between the MC² and the RABBLE derived cross sections. At lower energies, where the Narrow Resonance (NR) approximation used by MC² becomes tenuous, the discrepancies are larger.

An important part of the Doppler effect calculation is the use of accurate real and adjoint flux distributions throughout the reactor so that the perturbation denominator is computed accurately. For this reason two-dimensional diffusion and perturbation calculations were made. The reactor was represented in *rz* geometry as shown in Fig. II-8-3, where each hash mark represents a mesh point. The volume occupied by the Doppler sample is enclosed by the dotted lines. The perturbation calculations of the small-sample Doppler effect were run in the following manner. A dummy isotope with zero cross sections and the concentration of ^{238}U in the sample was added to the inner core and the outer core compositions. Also the volume occupied by the sample was made a discrete region to which the inner core composition was assigned. The perturbation was represented by giving the dummy isotope capture cross sections equal to $\delta\sigma_c^{28}$. In this way we obtained the small-sample Doppler effect from the reactivity contribution from the sample region and also a map of the Doppler worth in the inner core and outer core regions. The $\delta\sigma_c^{28}$ for the three prescriptions for elevated temperatures of 782 and 1069°K are given in Tables II-8-IV and II-8-V, respectively.

Results

Comparison of the calculated small-sample Doppler effect in ^{238}U with the measured values is noted in Table II-8-VI. In relating reactivity to period, the same conversion factor, 1064 Ih/$\%\Delta k/k$, was used as in the pre-analysis of the assembly. From this table we see excel-

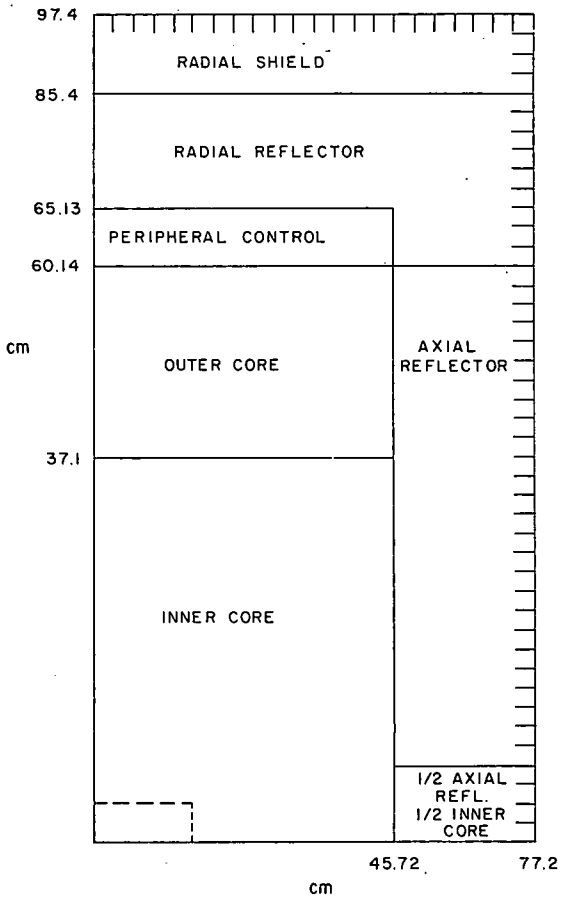

Fig. II-8-3. Representation of FTR-3 in 2-D Computations. *ANL Neg. No. 900-1306.*

TABLE II-8-IV. COMPARISON OF THE CHANGE IN THE GROUP CAPTURE CROSS SECTION OF ^{238}U AS THE TEMPERATURE OF THE UO_2 SAMPLE IS RAISED FROM 293 TO 782°K, b

Group	MC²	RABBLE			RABBLE-S_n		
		Sample	Core[a]	Total	Sample	Core[a]	Total
11	0.00180	0.00180	0.0	0.00180	0.00170	0.0	0.00170
12	0.00698	0.00698	0.0	0.00698	0.00698	0.0	0.00679
13	0.01271	0.01165	0.00049	0.01214	0.01023	0.00084	0.01070
14	0.02341	0.02323	0.00086	0.02409	0.02232	0.00084	0.02316
15	0.04187	0.03767	0.00098	0.03865	0.03635	0.00097	0.03732
16	0.06035	0.06647	0.00135	0.06782	0.08309	0.00143	0.08452
17	0.09522	0.09303	0.0	0.09303	0.07564	0.0	0.07564
18	0.11836	0.12599	0.0	0.12599	0.10422	0.0	0.10422
19	0.19145	0.20550	0.0	0.20550	0.18272	0.0	0.18272
20	0.24129	0.25489	−0.00120	0.25369	0.25532	−0.00120	0.25412
21	0.23162	0.24680	−0.00240	0.24440	0.22878	−0.00236	0.22642
22	0.26061	0.27990	−0.00370	0.27620	0.27089	−0.00398	0.26691
23	0.23838	0.31420	−0.01597	0.29823	0.42564	−0.01833	0.40731
24	0.26843	0.30230	−0.02700	0.27530	0.34068	−0.03043	0.31045
25	0.00707	0.01333	−0.00036	0.01297	0.02038	−0.00042	0.01996
26	0.15410	0.28730	0.05774	0.34505	0.36227	0.07185	0.43412
27	0.02294	0.05690	−0.01597	0.04093	0.08202	−0.01989	0.06213

[a] Per ^{238}U atom in the sample.

TABLE II-8-V: COMPARISON OF THE CHANGE IN THE GROUP CAPTURE CROSS SECTION OF ^{238}U AS THE TEMPERATURE OF THE UO_2 SAMPLE IS RAISED FROM 293 TO 1069°K, b

Group	MC²	RABBLE			RABBLE-S_n		
		Sample	Core[a]	Total	Sample	Core[a]	Total
11	0.00224	0.00224	0.0	0.00224	0.00212	0.0	0.00212
12	0.00874	0.00874	0.0	0.00874	0.00851	0.0	0.00851
13	0.01603	0.01430	0.00061	0.01491	0.01258	0.00058	0.01316
14	0.02986	0.02933	0.00110	0.03043	0.02819	0.00108	0.02927
15	0.05406	0.04841	0.00147	0.04988	0.04670	0.00145	0.04815
16	0.08019	0.08677	0.00209	0.08886	0.10837	0.00221	0.11058
17	0.12629	0.12243	0.00123	0.12366	0.09942	0.00125	0.10067
18	0.15906	0.16989	0.00123	0.17112	0.14029	0.00120	0.14149
19	0.26175	0.28250	0.00123	0.28373	0.25036	0.00120	0.25156
20	0.33214	0.35259	−0.00123	0.35136	0.35157	−0.00124	0.35034
21	0.31532	0.34440	−0.00123	0.34317	0.31754	−0.00120	0.31634
22	0.37544	0.41100	−0.00737	0.40363	0.39513	−0.00794	0.38719
23	0.32123	0.45080	−0.02211	0.42869	0.60588	−0.02533	0.58055
24	0.40178	0.43860	−0.03686	0.40174	0.49122	−0.04147	0.44975
25	0.01319	0.02482	−0.00061	0.02421	0.03780	−0.00071	0.03709
26	0.23951	0.44750	0.09092	0.35658	0.56065	0.11306	0.67371
27	0.03475	0.09070	−0.02580	0.06490	0.13619	−0.03310	0.10309

[a] Per ^{238}U atom in the sample.

TABLE II-8-VI. COMPARISON OF EXPERIMENTAL WITH CALCULATED DOPPLER EFFECTS FOR UO_2 SAMPLE IN FTR-3, Ih/kg U

	$\Delta T = 293 \rightarrow 782$°K		$\Delta T = 293 \rightarrow 1069$°K	
	$\Delta k/k$	C/E	$\Delta k/k$	C/E
Experimental [a]	−1.0042 ± 0.0043	—	−1.3689 ± 0.0038	—
MC², $\Delta\sigma$	−0.9821	0.978	−1.3170	0.962
RABBLE, $\Delta\sigma$	−1.0265	1.022	−1.4042	1.026
RABBLE-S_n, $\Delta\sigma$	−0.9794	0.975	−1.3197	0.964

TABLE II-8-VII. Real and Adjoint Flux Ratios from S_8 Transport Calculations

Group	Real Ratio, 1069°K		Adjoint Ratio, 293°K	
	Sample	Revised Core	Sample	Revised Core
11	0.994	0.994	0.953	0.983
12	1.027	1.008	0.948	0.982
13	0.930	0.971	0.946	0.981
14	1.029	1.006	0.934	0.977
15	1.054	1.015	0.915	0.972
16	1.371	1.093	0.911	0.972
17	0.891	1.047	0.912	0.973
18	0.900	1.006	0.918	0.973
19	0.982	1.005	0.903	0.970
20	1.095	1.034	0.911	0.972
21	1.054	1.021	0.875	0.962
22	1.355	1.125	0.710	0.957
23	1.516	1.179	0.886	0.972
24	1.322	1.166	0.847	0.964
25	1.865	1.229	0.816	0.956
26	1.637	1.291	0.765	0.963
27	1.838	1.334	0.817	0.962

TABLE II-8-VIII. Group-Wise Contributions to Doppler Effect as Calculated with Rabble-S_n Corrected ^{238}U Capture Cross Sections

Group	E_{min}, eV	$\Delta T = 293 \rightarrow 782$°K	$\Delta T = 293 \rightarrow 1069$°K
11	40,867	0.010425	0.009648
12	24,787	0.032288	0.030031
13	15,034	0.045731	0.041739
14	9,118.8	0.071501	0.067060
15	5,530.8	0.069121	0.066181
16	3,354.6	0.098317	0.095458
17	2,034.6	0.031734	0.031343
18	1,234.1	0.140760	0.141815
19	748.52	0.173378	0.177140
20	454.00	0.166814	0.170668
21	275.36	0.067196	0.069671
22	167.02	0.047176	0.050781
23	101.30	0.034290	0.036270
24	61.442	0.010800	0.011611
25	37.266	0.000108	0.000149
26	13.709	0.000366	0.000421
27	5.0439	0.000006	0.000007

lent agreement between calculation and experiment as the discrepancies are less than 4 % for all three prescriptions. By comparison of the results for MC² and RABBLE derived cross sections, it is seen that the calculated hot-sample cold-core resonance interaction effect augments the Doppler effect by about 4 %. This is in agreement with the detailed study at the small-sample Doppler effect in ZPR-9 Assembly 18.[3] In contrast, by comparing the results for RABBLE and RABBLE-S_n derived cross sections it is seen that the flux perturbation effect reduces the Doppler effect by about 4 %.

It would be unwarranted to generalize this cancellation of the two effects to other assemblies. For example, in Assembly 18 the flux perturbation effect augmented the Doppler effect by about 10 %. Table II-8-VII gives the perturbed-to-unperturbed flux ratios for the Doppler calculation between 293 and 1069°K. It is seen that the adjoint ratio is consistently less than unity, while the real ratio fluctuates about unity for the higher energy groups and then becomes greater than unity for the lower energy groups. The flux ratios exhibit the same characteristics in Assembly 18, except that the adjoint ratios are closer to unity and the real flux ratio in group 16 is appreciably greater. Assembly 18 and FTR-3 differed in that Assembly 18 had a small, concentrated uranium-fueled core while FTR-3 had a large, dilute plutonium-fueled core. It appears that we are seeing more of a 'flux-trap" effect in the test zone in Assembly 18 than in the more dilute FTR-3.

In Table II-8-VIII, the relative contributions to the Doppler effect by group is given for $\delta\sigma_c^{28}$ obtained from prescription 3. It is seen that nearly half of the Doppler effect comes from the three groups that cover the energy interval 2034 keV to 454 eV. The diffusion calculations from which the flux distributions were obtained yield a rough check of the methods that were used to construct the cross section set by giving the multiplication constant, k. These diffusion calculations yielded $k = 0.983$, which is consistent with the analysis of ZPR-6 Assembly 5 when similar methods were used.[7]

Material worths at the center of FTR-3 were also measured and have been analyzed (see Paper II-7). The worth of the fissile samples were overpredicted by 25–30 %, which is similar to that found for all previous plutonium-fueled assemblies of this general type. This general pattern of overprediction of fuel worths, however, tends to reduce the confidence one could place in the excellent agreement between the calculation and measurement of the central small-sample Doppler effect. For example, for the Doppler effect C/E is about 30 % smaller than for the fissile sample worths. This is similar to the 35 % underestimate of Doppler-to-fuel worth ratio found for uranium-fueled systems,[8] although for those systems the Doppler effect was underestimated by some 25 %. As previous reviews[9] have indicated, until some general pattern of agreement is established between the bulk of reactivity perturbation calculations and measurements, any single comparison, such as the Doppler effect comparison of this paper, must be considered in the frame-work of apparent systematic bias in the whole class of measurements.

References

1. J. W. Daughtry, R. B. Pond, C. D. Swanson and R. M. Fleischman, *ZPR-9 Assembly 26, FTR-3,* Applied Physics Division Annual Report, July 1, 1969 to June 30, 1970, ANL-7710, pp. 58–63.
2. R. B. Pond, J. W. Daughtry, C. E. Till, E. F. Groh, C. D. Swanson and P. H. Kier, *Plutonium and ^{238}U Doppler Measurements in ZPR-9 Assembly 26, FTR-3,* Applied Physics Division Annual Report, July 1, 1969 to June 30, 1970, ANL-7710, pp. 73–77.
3. R. A. Lewis and T. W. Johnson, *Sensitivity of Small-Sample Doppler-Effect Measurements to Environment,* Reactor Physics Division Annual Report, July 1, 1967 to June 30, 1968, ANL-7410, pp. 96–103.
4. P. H. Kier and A. A. Robba, *RABBLE, A Program for Computation of Resonance Absorption in Multiregion Reactor Cells,* ANL-7326 (1967).
5. B. J. Toppel, A. L. Rago and D. M. O'Shea, *MC², A Code to Calculate Multigroup Cross Sections,* ANL-7318 (1967).
6. G. L. Grasseschi and V. C. Rogers, Argonne National Laboratory (private communication).
7. R. A. Karam, J. E. Marshall and K. D. Dance, *Analysis of Heterogeneity and Sodium-Void Effects in a 2700-Liter Uranium Carbide Fast Core, ZPR-6 Assembly 5,* Nuc. Sci. Eng. **43,** 5 (1971).
8. C. E. Till, W. G. Davey, R. A. Lewis and R. G. Palmer, *The Argonne National Laboratory Critical Experiment Program,* Proc. BNES Conference on the Physics of Fast Reactor Operation and Design, London June 23–26, 1969, pp. 40–49.
9. C. E. Till and W. G. Davey, *Investigation of Sodium-Voiding Reactivities and Other Safety Parameters in Fast Critical Assemblies,* Trans. Am. Nucl. Soc. **13,** 719 (1970).

II-9. A Calculation of the Isothermal Doppler Effect in FTR

P. H. Kier

Introduction

An isothermal Doppler effect in FTR (Fast Test Reactor) has been calculated for a core configuration based on beginning of equilibrium (BOE) cycle conditions of an average core burnup of 15 MWd/kg and a scatter refueling fuel distribution. All peripheral control subassemblies were fully inserted and three Row 5 control subassemblies were partly inserted. This configuration was represented in *rz* geometry with the reactor divided into 16 zones as shown in Fig. II-9-1. Zones 1–6 represent the core homogenized by ring. In Zone 16, the three partly inserted control subassemblies are homogenized with ring 5 fuel subassemblies. Zone 7 represents homogenized peripheral control, fixed shim, and radial reflector subassemblies. Zones 8, 11, 14, and 15 represent the axial reflector, upper plenum, outer radial reflector and radial shield regions, respectively. The withdrawn control rods are included in Zones 9, 10, 12 and 13. The description of the types of subassemblies in the fuel-bearing zones is given in Table II-9-I. The compositions of the fuel-bearing zones and non-fuel-bearing zones are given in Table II-9-II and Table II-9-III, respectively.

Calculational Model

The Argonne Reactor Computation (ARC) System[1] was used for all computations. Isotopic broad group cross sections were generated with use of the MC²[(2)] module and ENDF/B VERSION 1 data. Then the two-dimensional diffusion module was used to compute the real and the adjoint flux distributions which were then used in the two-dimensional perturbation module to compute the reactivity effect of changing the temperature of the isotopes of uranium and plutonium from 1180 to 2180°K. The cross section set had 30 broad groups. Groups 1–26 were one-half lethargy unit wide, groups 27–29 were one lethargy unit wide, and group 30 was the thermal group.

Several MC² problems were run to generate isotopic

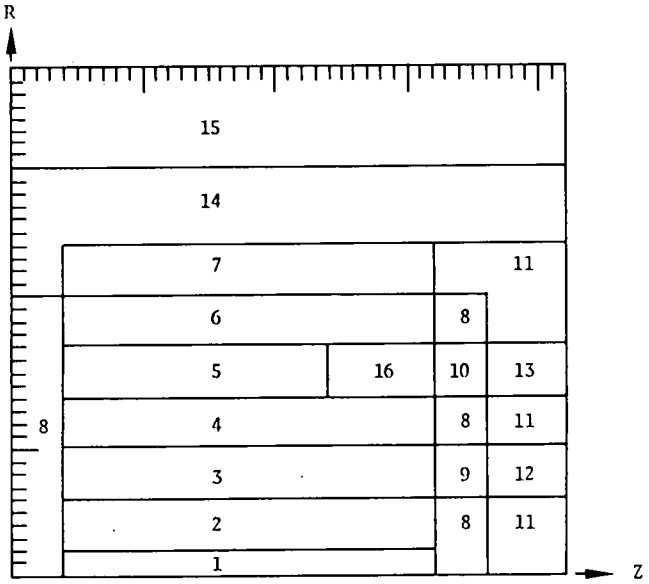

Fig. II-9-1. Representation of FTR in 2-D Calculations. *ANL Neg. No. 116-961.*

TABLE II-9-I. Subassemblies Assigned to the Fuel Bearing Zones

Type	MWd/kg	Subassemblies Per Zone						
		1	2	3	4	5	6	16
Inner driver, i.d.	0		1	3	5			
	15		1	3	5			
	30	1	1	3	5			
Outer driver, i.d.	0					6	9	6
	15					7	9	7
	30					7	9	7
Special-purpose closed loop					1		1	
General-purpose closed loop			1		1			
Open loop, i.d.	15		1		1			
Open loop, o.d.	15						2	
Safety rod sodium channel				3				
Control rod sodium channel						4		1
Oscillator			1					
B_4C control rods								3
Total		1	6	12	18	24	30	24

cross sections. Two runs were made for the driver regions, using the average concentrations of the inner and outer driver regions for beginning of cycle conditions. To obtain proper resonance shielding, a two-region cell centered on a fuel pin was used in the calculation of resonance cross sections. The center region was the meat of the fuel pin with a radius of 0.246 cm. The annular region (0.3924 cm outer radius) was 73.6 v/o sodium and 24.6 v/o stainless steel cladding. To obtain the fundamental mode spectrum that was used to collapse to broad group cross sections, concentrations characteristic of the homogenized subassemblies (including the duct tube) were used. The two MC² runs differed only in the temperature of the isotopes in the fuel pin; in one run the temperature was 1180°K and in the other 2180°K.

An MC² problem was run to derive cross sections for the seven fixed shim subassemblies that form part of the peripheral control. Each fixed shim subassembly contains 19 stainless-steel-clad rods of an alloy 90 v/o tantalum and 10 v/o tungsten. To obtain proper resonance shielding for ^{181}Ta and the isotopes of tungsten, a two-region cell centered on an absorber rod was used in the calculation of resonance cross sections. The center region was the meat of the absorber with a radius of 1.01 cm and the annular region, 1.441 cm outer radius, was 60 v/o sodium and 40 v/o stainless steel. To collapse to broad group cross sections, the fundamental mode spectrum characteristic of the tantalum subassemblies was not used because to do so would grossly exaggerate the attenuation of the flux. Rather, fine group fluxes (the flux groups were $\frac{1}{8}$ lethargy units wide) characteristic of the fundamental mode spectrum in the driver regions was used to collapse to broad group cross sections for tantalum and tungsten.

The other part of the peripheral control and the in-core control are supplied by boron carbide subassemblies. It would be logical that the treatment of a boron carbide subassembly would be similar to that of a tantalum subassembly. The shielding in the boron carbide rods would be accounted for and the gross spectrum would not have exaggerated attenuation. However, because boron is not a resonant material, the boron carbide subassemblies cannot be treated in this way in MC². Cross sections were obtained from a homogeneous MC² run in which there was assumed to be no leakage, a procedure that introduces two compensating errors. Because the surroundings that feed neutrons into the boron carbide subassembly are neglected, the attenuation of the flux within each broad group is overestimated. Because the (n,α) reaction in ^{10}B has an inverse speed dependence, this effect would cause the broad group cross section to be underestimated. However, the

TABLE II-9-II. Atom Densities in Fuel-Bearing Zones, 10^{24} atoms/cm³

	Zone 1	Zone 2	Zone 3	Zone 4	Zone 5	Zone 6	Zone 16
^{235}U	0.318 -4	0.304 -4	0.269 -4	0.370 -4	0.292 -4	0.357 -4	0.292 -4
^{238}U	0.5497 -2	0.3379 -2	0.41884 -2	0.5023 -2	0.44193 -2	0.51334 -2	0.44193 -2
^{239}Pu	0.12869 -2	0.9244 -3	0.10137 -2	0.12173 -2	0.13627 -2	0.15854 -2	0.13627 -2
^{240}Pu	0.2215 -3	0.1439 -3	0.1557 -3	0.1867 -3	0.2034 -3	0.2357 -3	0.2034 -3
^{241}Pu	0.114 -4	0.380 -5	0.4280 -5	0.510 -5	0.39 -5	0.42 -5	0.39 -5
F.P.	0.2695 -3	0.90 -4	0.1012 -3	0.1199 -3	0.934 -4	0.1032 -3	0.934 -4
O	0.14426 -1	0.10027 -1	0.1082 -1	0.12986 -1	0.12403 -1	0.13986 -1	0.12043 -1
Na	0.9098 -2	0.12065 -1	0.1183 -1	0.9942 -1	0.10919 -1	0.9375 -2	0.9295 -2
SS	0.20133 -1	0.17915 -1	0.1712 -1	0.19922 -1	0.18122 -1	0.20048 -1	0.2026 -1
^{10}B							0.925 -3
^{11}B							0.3699 -2
C							0.1156 -2

TABLE II-9-III. ATOM DENSITIES IN NON-FUEL-BEARING ZONES, 10^{24} atoms/cm^3

	Zone 7	Zone 8	Zone 9	Zone 10	Zone 11	Zone 12	Zone 13	Zone 14	Zone 15
Na	0.6462 -2	0.9098 -2	0.8581 -2	0.8840 -2	0.9098 -2	0.8581 -2	0.884 -2	0.2912 -2	0.1210 -2
SS[a]	0.80894 -2	0.2103 -1	0.2139 -1	0.2076 -1	0.2013 -1	0.2139 -1	0.2076 -1	0.1925 -2	0.7936 -1
^{10}B	0.1154 -2	—	0.1850 -2	0.925 -3	—	0.185 -2	0.925 -3	—	—
^{11}B	0.6575 -2	—	0.7398 -2	0.3699 -2	—	0.7398 -2	0.3699 -2	—	—
C	0.20547 -2	—	0.23115 -2	0.1156 -2	—	0.23115 -2	0.1156 -2	—	—
Ta-10W[b]	0.3948 -2	—	—	—	—	—	—	—	—
Inconel[c]	0.44013 -1	0.29425 -1	0.22069 -1	0.2575 -1	—	—	—	0.7545 -1	—

[a] Atom fractions of Stainless Steel: Fe 0.6721, Cr 0.1805, Ni 0.1129, Mo 0.0345.
[b] Atom fractions of tantalum-10% tungsten: Ta 0.9015, W 0.0985.
[c] Atom fractions of Inconel: Fe 0.0740, Cr 0.1743, Ni 0.7455, Mo 0.0021, Si 0.0041.

TABLE II-9-IV. CONTRIBUTIONS TO DOPPLER EFFECT IN FTR BY ISOTOPE USING ENDF/B VERSION 1 DATA—TEMPERATURE CHANGE FROM 1180 TO 2180°K

Isotope	$\Delta k/k$, %	$\alpha^{(a)}$
^{238}U	−0.29795	−0.00485
^{239}Pu	0.05729	
Total[b]	−0.24018	−0.00391

[a] $(1/k)\ (dk/dT) = \alpha/T$.
[b] Includes contributions from ^{240}Pu and ^{235}U.

subassembly was treated as being homogeneous. Hence, the shielding of the boron carbide rods was neglected, thereby causing the cross section to be overestimated. Thus, the two errors introduced by the calculational model tend to cancel.

Another MC^2 problem was run to obtain cross sections in the radial reflector region. This was a homogeneous run with no leakage. From these five MC^2 problems, cross sections for the constituents of steel were generated for three spectra: driver, radial reflector, and boron carbide subassembly. Steel cross sections derived in the driver spectrum were used in Zones 1–6, 11, and 16; steel cross sections derived in the reflector spectrum were used in Zones 8, 10, 14, and 15; and steel cross sections derived in the boron carbide spectrum were used in Zones 7, 9, 12, and 13.

RESULTS

The results of the perturbation calculations for the isothermal Doppler effect obtained by raising the temperature of the fuel from 1180 to 2180°K are given in Table II-9-IV. The reactivity effect of this temperature change was found to be −0.24018 $\%\Delta k/k$. With the assumption that the Doppler effect has an inverse temperature dependence (i.e., $dk/dT = \alpha k/T$), the resulting Doppler coefficient, α, was −0.00391. In interpreting this result it must be remembered that the data for ^{239}Pu in ENDF/B VERSION 1 is highly suspect of being in error because they yield a strongly positive Doppler effect in contrast with recent experiments in which a small and probably negative Doppler effect in plutonium samples was measured[3] (see Paper II-22).

To substantiate that the relatively small Doppler coefficient results from the overly positive contribution from ^{239}Pu, separate perturbation calculations were made to obtain the contributions from ^{239}Pu and ^{238}U. It was found that ^{239}Pu did give a significant positive contribution to the Doppler coefficient, +0.05729 $\%\Delta k/k$, and that the ^{238}U contribution alone yields a Doppler coefficient of −0.00485. Upon comparing the total Doppler effect with the contributions of ^{238}U and ^{239}Pu it is seen that the contributions from ^{235}U and ^{240}Pu are negligible. It appears, therefore, that, if on the basis of experiment the contribution to the Doppler effect from ^{239}Pu is ignored, the Doppler effect in FTR is well approximated by the Doppler effect in ^{238}U.

REFERENCES

1. B. J. Toppel, Ed, *The Argonne Reactor Computation (ARC) System*, ANL-7332 (1967).
2. B. J. Toppel, A. L. Rago and D. M. O'Shea, *MC^2, A Code to Calculate Multigroup Cross Sections*, ANL-7318 (1967).
3. R. B. Pond, J. W. Daughtry, C. E. Till, E. F. Groh, C. D. Swanson and P. H. Kier, *Plutonium and ^{238}U Doppler Measurements in ZPR-9 Assembly 26, FTR-3*, Applied Physics Division Annual Report, July 1, 1969 to June 30, 1970, ANL-7710, pp. 73–77.

II-10. Analysis of UO_2 Small-Sample Doppler Measurements in ZPR-3 Assembly 51

P. H. Kier

Introduction

ZPR-3 Assembly 51 was the first assembly in the Fast Test Reactor (FTR) critical program. It had a one-region, plutonium-fueled core, a nickel inner radial reflector, a nickel axial reflector and an iron outer radial reflector as shown in Fig. II-10-1[1]. Table II-10-I gives the compositions of these regions. Doppler measurements with a natural UO_2 sample, 6 in. in length and ½ in. in diam, were made at three elevated temperatures (500, 800 and 1100°K) at three positions in the core to yield information on the spatial dependence of the Doppler effect. The three matrix positions were at the center of the core (P-16), at the core between the center and the inner reflector (P-12), and at the core adjacent to the inner reflector (P-10).

The Doppler effect was measured at P-16 with both a nickel and a stainless steel buffer but since nickel provided greater neutronic buffering, only the nickel buffer was used in the two off-center measurements. The buffer region was a square annulus, 5.08 cm in outer dimension by 0.95 cm thick, which contained either nickel or stainless steel plates. The nickel plates had a linear density of 131.93 gm/cm for a cross sectional area of 15.121 cm² and the stainless steel plates had a linear density of 110.14 gm/cm for a cross sectional area of 14.516 cm².[2] The details of the oscillator rod are given in Fig. II-10-2.[3]

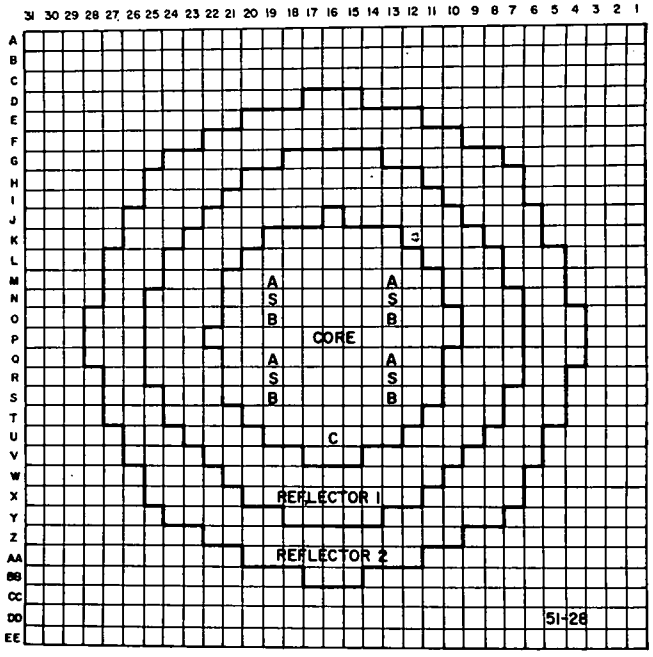

Fig. II-10-1. Reference Core for Assembly 51. *ANL-ID-103-2694.*

Calculational Model

The calculational model used one-dimensional perturbation theory and the assumption that Doppler effect arises solely from the Doppler change in the capture cross section of ^{238}U, that is,

$$\frac{\Delta k}{k^2} = \frac{N^{28}}{D} \int_{sample} dV \int \delta\sigma_c^{28} \phi\phi^* \, dE, \qquad (1)$$

where D is the perturbation denominator, N^{28} is the atom density of ^{238}U, $\delta\sigma_c^{28}$ is the Doppler change in the capture cross section of ^{238}U and ϕ and ϕ^* are the real and adjoint fluxes. Because the sample, oscillator rod, and buffer are neutronically quite different from the core, the fluxes in the vicinity of the sample vary rapidly and should therefore be obtained from transport calculations. Let us define ϕ_∞ and ϕ_∞^* as the real and adjoint flux distributions in the system when the drawer containing the sample contains core material. Then Eq. (1) can be rewritten as

$$\frac{\Delta k}{k^2} = \frac{N^{28}}{D} \int_{sample} dV \int \delta\sigma_c^{28} \phi_\infty\phi_\infty^* \cdot[\phi^*/\phi_\infty^* \times \phi/\phi_\infty] \, dE. \qquad (2)$$

The unperturbed fluxes, ϕ_∞ and ϕ_∞^*, are relatively slowly varying functions of space and are obtained, therefore, from diffusion calculations. For the center position, P-16, the ratios of perturbed-to-unperturbed fluxes were computed from one-dimensional S_8 transport problems for the cell described in Table II-10-II. A perturbed-to-unperturbed flux ratio was taken as the ratio of the average flux in the sample to the flux in the boundary region. For the off-center measurements two-dimensional transport calculations would be required to obtain the perturbed-to-unperturbed flux ratios. Because of their great expense, these two-dimensional transport calculations were not done and consequently, it was assumed that these flux ratios are independent of the location where the Doppler effect was measured.

The calculations were made with use of a 29 group cross section set that utilized ENDF/B VERSION I data. Groups 1–24 were ½ lethargy unit wide and groups 25–29 were one lethargy unit wide.

TABLE II-10-I. ATOM DENSITIES IN ASSEMBLY 51 COMPOSITIONS, 10^{24}/cm^3

Isotope	Core	Inner Rad. Reflector	Outer Rad. Reflector	Axial Reflector	Nickel[a] Buffer	Steel[a] Buffer	Osc. Rod	Doppler Sample
^{239,241}Pu	0.001736							
^{240,242}Pu	0.000172							
^{235}U	0.000015							0.000110
^{238}U	0.007005							0.015312
Mo	0.000328							
Na	0.009253	0.004143		0.010321				
C	0.003113		0.000561					
O	0.01279							0.030846
Al	0.000055							
Fe	0.01564	0.007529	0.074860	0.010426	0.008077	0.050225	0.019075	0.002875
Cr	0.003666	0.001860	0.001153	0.002583	0.001984	0.012489	0.004743	0.000715
Ni	0.001604	0.056338	0.000494	0.028926	0.063459	0.005468	0.002077	0.000313
Mn	0.000153	0.000227	0.000560	0.000182	0.000251	0.000522	0.000198	0.000030
Si	0.000180	0.000091	0.000055	0.000126	0.000097	0.000612	0.000198	0.000035

[a] Includes SS in core drawer and matrix tube.

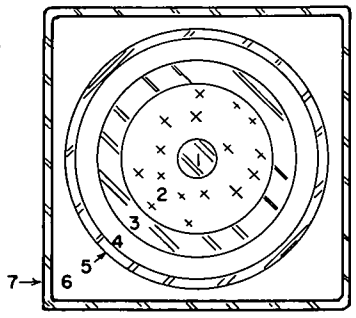

FIG. II-10-2. Cross Section of Oscillator Rod through Doppler Sample. *ANL-ID-103-2998.*

Isotopic cross sections for the core region were obtained from a homogeneous MC²[4] run. The homogeneous uranium and plutonium cross sections were then corrected for resonance self-shielding. To account for cell heterogeneities, the isotopic cross sections were finally weighted by the intracell plate-averaged fluxes obtained from an S_{16} transport calculation for the two-drawer cell. Isotopic cross sections for the inner radial reflector and the axial reflector were obtained from separate homogeneous MC² runs in which there was assumed to be no leakage. Isotopic cross sections for the outer reflector were assumed to be the same as for the axial reflector region.

The Doppler changes in the capture cross sections of ^{238}U in the sample were obtained from heterogeneous MC² problems with uranium temperatures of 293, 500, and 1100°K. In the pin cell that was used to obtain the self-shielded resonance cross sections, the sample was the fuel pin and the oscillator rod and nickel buffer were homogenized together to form the annular region. The fine group (¼ lethargy) fluxes characteristic of the fundamental mode spectrum in the core were used to collapse to broad group cross sections. The ^{238}U cross sections in the sample at 293°K and the Doppler changes in these cross sections are given in Table II-10-III.

RESULTS

For a circularized representation of Assembly 51, a buckling search diffusion calculation was made to obtain the critical extrapolated height of the unperturbed system. For this extrapolated height (114 cm) the real and the adjoint flux distributions were computed. Then three perturbation problems were run in which sample material replaced core material at mesh points corresponding to the three matrix locations. The

TABLE II-10-II. DESCRIPTION OF CELL USED IN S_8 TRANSPORT CALCULATIONS OF FLUX PERTURBATIONS INTRODUCED BY DOPPLER SAMPLE DRAWER

Region	Composition	Radius, cm
Sample	Homogenized sample and thermocouple	0.635
Filter	Homogenized capsule, heater, vacuum can, enclosure tube, guide tube and vacuum	1.709
Buffer	Homogenized buffer (Ni or SS), core drawer and matrix tube	3.126
Rev. Core	Core	9.378
Core	Core	21.46
Boundary	Core	21.88

perturbations differed only in the temperature of ^{238}U, i.e., in the ^{238}U cross sections. By subtracting the reactivity effect for room temperature uranium from the reactivity effect for the elevated temperatures, the Doppler effects, uncorrected for the flux perturbations, were obtained. These are given by group in Table II-10-IV. From comparison of the groupwise contributions at the three locations, the softening of the calculated spectrum as the inner radial reflector is approached can be readily inferred.

TABLE II-10-III. ^{238}U Capture and Doppler Changes in Capture Cross Sections in the 1/2 in Diameter UO_2 Sample

Group	E_{max}, eV	E_{min}, eV	σ(293°K)	$\delta\sigma$(500°K)	$\delta\sigma$-(1100°K)
11	67379	40867	0.33276	0.00060	0.00127
12	40867	24787	0.44459	0.00238	0.00512
13	24787	15034	0.56571	0.00447	0.00979
14	15034	9118.8	0.69367	0.00869	0.01943
15	9118.8	5530.8	0.82202	0.01676	0.03850
16	5530.8	3354.6	0.91005	0.02694	0.06367
17	3354.6	2034.6	1.08404	0.04660	0.11358
18	2034.6	1234.1	1.06955	0.06217	0.15723
19	1234.1	748.52	1.36768	0.10779	0.28336
20	748.52	454.00	1.32344	0.14586	0.38867
21	454.00	275.36	1.23002	0.13627	0.35473
22	275.36	167.02	1.65851	0.19852	0.58996
23	167.02	101.30	1.89464	0.16652	0.47092
24	101.30	61.442	2.33551	0.21222	0.61514
25	61.442	37.266	0.47147	0.00404	0.02137
26	37.266	13.709	5.04957	0.12110	0.45397
27	13.709	5.0439	1.48534	0.03209	0.11383

TABLE II-10-IV. Unnormalized Calculated Group-Wise Contribution to Doppler Effect Uncorrected for Perturbation Introduced by Doppler Drawer, $-10^{-7}\ \Delta k/k$

Group	P-12		P-10		P-16	
	500°K	1100°K	500°K	1100°K	500°K	1100°K
11	0.2067	0.4420	0.1126	0.2409	0.3508	0.7502
12	0.6223	1.3408	0.3257	0.7017	1.0410	2.2430
13	0.9724	2.1268	0.3952	0.8643	1.6701	3.6529
14	1.3382	2.9911	1.0818	2.4181	2.2381	5.0025
15	1.5354	3.5279	1.0725	2.4643	2.5068	5.7599
16	1.5768	3.7260	1.1623	2.7466	2.5139	5.9404
17	1.0639	2.5928	1.1898	2.8997	1.6814	4.0978
18	3.8520	9.7425	3.3419	8.4522	5.6563	14.3057
19	4.3728	11.4949	3.9792	10.4602	6.0258	15.8401
20	4.0852	10.8857	5.3082	14.1446	5.0401	13.4300
21	1.91673	4.9895	2.8333	7.3754	2.0893	5.4388
22	1.4780	4.3920	2.3110	6.8678	1.4267	4.2398
23	0.5807	1.7900	1.7072	4.8281	0.4510	1.2754
24	0.5126	1.4860	2.4751	7.1747	0.2231	0.6467
25	0.0019	0.0102	0.0043	0.0225	0.0007	0.0036
26	0.0506	0.1895	0.4842	1.8557	0.0034	0.0128
Total	24.1664	61.7277	27.7845	73.5169	32.9186	82.6397

TABLE II-10-V. Comparison of Real and Adjoint Perturbed-to-Unperturbed Flux Ratios for Nickel and Stainless Steel Buffers

Group	Nickel			Stainless Steel		
	ϕ^*/ϕ^*_∞	ϕ/ϕ_∞	$\frac{(\phi^*/\phi^*_\infty)}{(\phi/\phi_\infty)}$	ϕ^*/ϕ^*_∞	ϕ/ϕ_∞	$\frac{(\phi^*/\phi^*_\infty)}{(\phi/\phi_\infty)}$
11	0.9491	1.0769	1.0221	0.9467	0.9730	0.9211
12	0.9546	0.8515	0.8128	0.9453	1.0293	0.9730
13	0.9498	0.4526	0.4298	0.9440	0.9166	0.8652
14	0.9392	1.9378	1.8200	0.9426	1.0289	0.9698
15	0.9512	1.3632	1.2968	0.9271	1.0625	0.9850
16	0.9351	1.9700	1.8421	0.9275	1.3529	1.2548
17	0.9411	1.2450	1.1717	0.9276	0.9318	0.8644
18	0.9429	1.1384	1.0734	0.9275	0.9682	0.8980
19	0.9453	1.3053	1.2340	0.9094	1.0466	0.9518
20	0.9315	1.5018	1.3989	0.9312	1.1863	1.1047
21	0.9288	1.6321	1.5160	0.9282	1.1672	1.0834
22	0.8848	2.0074	1.7762	0.9014	1.5871	1.4307
23	0.9095	2.4753	2.2512	0.9252	1.7631	1.6311
24	0.8509	2.3430	1.9937	0.8810	1.6456	1.4498
25	0.7868	3.3787	2.6584	0.8409	2.1381	1.7980
26	0.8378	3.3346	2.7938	0.8650	2.0004	1.7304

The reactivities computed with use of diffusion theory fluxes must be corrected for the flux perturbations introduced by the Doppler drawer, which were obtained from S_8 transport calculations.[5] The perturbed-to-unperturbed flux ratios with both buffers are given in Table II-10-V, with 1100°K uranium cross sections used in obtaining the real flux ratios (when 500°K uranium cross sections were used, the results differed by less than 1%). For both buffers, the perturbed adjoint flux is depressed in the sample and the perturbed real flux is generally larger in the sample. However, the increases in the real flux in the sample are significantly greater when the buffer is nickel.

The corrected Doppler effects obtained by multiplying the uncorrected results (Table II-10-IV) by the product of flux ratios (Table II-10-V) are given in Table II-10-VI. For the steel buffer in P-16, the flux perturbation effect increases the Doppler effect by about 3%. This result is consistent with the results for ZPR-9 Assemblies 18 and 26. In Assembly 18, a small uranium-fueled core, this effect increased the Doppler effect by about 10%,[6] while in Assembly 26, a large plutonium-fueled core, this effect reduced the Doppler effect by 4% (see Paper II-8). It appears that for small, concentrated cores, the scattering material in the buffer introduces a 'flux trap' effect at low energies that augments the Doppler worth of the sample.

The flux perturbation effect for the nickel buffer is much greater than that for the steel buffer and ranges from 32% for measurements at location P-16 to 51% for measurements at P-10. Because the flux perturbation effect preferentially augments the Doppler worth at low energies and because the spectrum is softer

near the periphery of the core, the net effect is greater near the periphery than at the center.

The measured computed Doppler effects are compared in Table II-10-VII. To account for the Doppler sample not extending through the entire transverse height of the reactor, the computed reactivities are multiplied by the factor

$$f = \frac{\int_0^a (\cos \pi x/2H)^2 \, dx}{\int_0^H (\cos \pi x/2H)^2 \, dx} = \frac{a}{H} + \frac{1}{\pi} \sin \frac{\pi a}{H}, \quad (3)$$

where $2H$ is the extrapolated transverse height and $2a$ is the length of the sample, 15.24 cm. In computing f we used $2H = 118$ cm, which was the critical extrapolated height obtained from a buckling search with the Doppler drawer rather than with a core drawer in the center matrix position. To convert from reactivity to period the factor 1103 Ih/% $\Delta k/k$ was used. This value was obtained from two-dimensional rz real and adjoint fluxes.

From Table II-10-VII, we see that the agreement between calculation and measurement varies greatly with the position of the measurement. For the measurements at P-16, the calculations underpredict the Doppler effect by 8–22%; at P-12, the calculations overpredict the Doppler effect by 6–10%; at P-10, the calculations overpredict the Doppler effect by about 60%. It is evident that the spatial distribution of the Doppler effect is not predicted accurately. The results can be partially explained if the calculated spectrum is too hard at the center and too soft at the periphery of the core. The results for P-16 indicate that the spectrum is too hard there because the discrepancy for the measurement to 1100°K is appreciably greater than that for the measurement to 500°K. From Table II-10-III, it is seen that the Doppler change in capture cross section tends to saturate more at high energies than at low energies. The calculations indicate excessive saturation in the Doppler change in cross sections or that the spectrum is too hard.

In location P-10, in the core adjacent to the nickel reflector, the flux spectrum is changing rapidly so that it is not surprising that the calculated spectrum is inaccurate. However, at this location another effect becomes important. The calculation of the flux perturbation effect introduced by the Doppler drawer was based on the assumption that it is surrounded by core. However, at location P-10 there is as much nickel reflector in the vicinity of the sample as there is core and, as may be seen by comparing the results of the nickel and steel buffers, the small-sample Doppler effect is strongly dependent on the immediate environment of the sample. Our assumption appears to overpredict the augmentation of the Doppler worth from the flux perturbation effect in position P-10. The overprediction, which would be preferentially larger at low energies, coupled with a prediction of too soft a spectrum, could explain the large overprediction of the Doppler effect at location P-10.

TABLE II-10-VI. Percentage Increase in Calculated Doppler Effect from Perturbation Introduced by Doppler Drawer

Location	Buffer	Temp, °K	% Increase
P-16	SS	500	2.8
		1100	3.2
P-16	Ni	500	32.8
		1100	33.3
P-12	Ni	500	36.9
		1100	37.9
P-10	Ni	500	51.6
		1100	51.5

TABLE II-10-VII. Comparison of Measured and Calculated Small-Sample Doppler Effects in Assembly 51, Ih

Location	Buffer	Temp, °K	Exp ρ	Calc ρ	C/E
P-16	SS	500	−0.1019 ± 0.0039	−0.0954	0.9362
		1100	−0.3068 ± 0.0044	−0.2401	0.7826
P-16	Ni	500	−0.1315 ± 0.0053	−0.1230	0.9354
		1100	−0.3857 ± 0.0054	−0.3100	0.8037
P-12	Ni	500	−0.0846 ± 0.0058	−0.0932	1.10
		1100	−0.2258 ± 0.0057	−0.2392	1.06
P-10	Ni	500	−0.0728 ± 0.0044	−0.1186	1.63
		1100	−0.1989 ± 0.0037	−0.3137	1.58

References

1. A. Travelli, A. J. Ulrich, D. Meneghetti and J. C. Beitel, *Calculational Studies in Support of the Fast Flux Test Facility (FFTF) Critical Experiments on ZPR-3 and ZPPR*, Reactor Physics Division Annual Report July 1, 1968 to June 30, 1969, ANL-7610, pp. 115–137.
2. P. I. Amundson, Argonne National Laboratory (private communication).
3. A. M. Broomfield, A. L. Hess, P. I. Amundson, Q. L. Baird, E. F. Bennett, W. G. Davey, J. M. Gasidlo, W. P. Keeney, J. K. Long and R. L. McVean, *ZPR-3 Assemblies 48, 48A, and 48B, The Study of a Dilute Plutonium-Fueled Assembly and its Variants*, ANL-7759 (1970).
4. B. J. Toppel, A. L. Rago and D. M. O'Shea, *MC²*, *A Code to Calculate Multigroup Cross Sections*, ANL-7318 (1967).
5. L. T. Bryant, G. J. Duffy, H. Greenspan, H. Henryson, II and G. K. Leaf, *The ARC System One-Dimensional Transport Theory Capability, SNARC 1D*, ANL-7717 (1971).
6. R. A. Lewis and T. W. Johnson, *Sensitivity of Small-Sample Doppler Effect Measurements to Environment*, Reactor Physics Division Annual Report, July 1, 1967 to June 30, 1968, ANL-7410, pp. 96–103.

II-11. ZPR-6 Assemblies 6A and 7: Benchmark Specifications for the Two Large Single-Core-Zone Critical Assemblies—^{235}U-Fueled Assembly 6A and Plutonium-Fueled Assembly 7—LMFBR Demonstration Reactor Benchmark Program

C. E. Till, L. G. LeSage, R. A. Karam, R. A. Lewis, J. E. Marshall, M. Salvatores* and B. A. Zolotar

Introduction

The purpose of this paper is to specify in final form the characteristics of the two large uniform fast critical assemblies, ZPR-6 Assemblies 6A and 7, in a form suitable for data testing.

These two assemblies were designed to be as identical as possible, the only significant difference being the fuel isotope—^{235}U in Assembly 6A and plutonium in Assembly 7. They are large, single-zone assemblies with few complications. The unit-cell is particularly simple and symmetric. The core geometry has an L/D in the neighborhood of unity, and the blankets are uniform depleted uranium. The core compositions simulate a typical LMFBR. The fuel is oxide. The fuel volume fraction in either assembly is about 33%, based on 85% theoretical density (TD) oxide (ρ = 9.32 g/cc). The sodium volume fraction, based on hot sodium at 0.84 g/cc, is 42% in either assembly. The steel volume fractions are 20%. The overall properties of the assemblies are summarized in Table II-11-I.

These two assemblies give two integral data points toward the end of the scale of assembly compositions with soft spectra and characteristics typical of current LMFBR design. They should give diagnostic information on the suitability of ENDF/B cross section data for fast reactor design that is unparalleled by other assemblies currently available.

The reader should also be aware that the two assemblies, ZPR-6 Assemblies 6A and 7, in this paper represent one part of an overall program based on these same basic compositions. They are part of the Demonstration Reactor Benchmark Program.[1] ZPPR Assembly 2 studies the effects of two-core zones of a more realistic LMFBR height and an oxide blanket. The inner core zone of Assembly 2 is the same composition as Assembly 7, and the outer core zone has similar volume fractions but a 50% increase in plutonium content. ZPPR Assembly 3 is planned to be of the same compositions, but to concentrate on the effects of control rod patterns and compositions. The ZPR inventory of oxide pins and sodium-containing calandria were also specified to be identical with the compositions and volume fractions of Assemblies 6A and 7. Thus the main studies of the effects of plate-pin translations and the Variable Temperature Rodded Zone Program planned for ZPR-6 are based on the same compositions. Finally, the inventory of plutonium fuel of high ^{240}Pu content was also specified to hold the fertile-to-fissile ratio constant as plates of high ^{240}Pu fuel are substituted for those of normal ZPR plutonium composition. Thus the various complications due to geometry, both of the unit-cell and of the reactor itself, the effects of plutonium fuel of realistic higher isotopic content, and the effects of temperature on the reactor properties will all be studied as part of this program. This paper, however, concentrates on the simplest first stage: the properties of a simple critical assembly of one core composition and the change in its properties with a change in the main fuel isotope from ^{235}U to plutonium.

Most of the results from Assemblies 6A and 7 have been reported previously.[2,3] In some cases small discrepancies exist between this paper previously reported values. In all cases of disagreement, the values reported in this paper supersede any previously reported values.

Assembly Critical Masses and Dimensions

The plate unit-cell for both assemblies is shown in Fig. II-11-1. The unit-cell is a single drawer with a 1/4 in. thick fuel element at the center of the drawer and a symmetric succession of 1/8 in. Fe_2O_3, 1/2 in. sodium, and 1/4 in. U_3O_8 plates on each side of the fuel plate. For Assembly 7, the 1/4 in. fuel plate is simply the normal ZPR plate-type plutonium fuel, an alloy of 69.5 w/o uranium, 28 w/o plutonium, and 2.5 w/o molybdenum, clad in stainless steel. For Assembly 6A, the 1/4 in. fuel section is made up of 1/16 in. enriched uranium, 1/8 in. depleted uranium, and 1/16 in. stainless steel plates.

There may be some confusion in the mind of the reader as to the relationship of Assembly 6A to Assembly 6. The results of Assembly 6 are reported in Ref. 4 Assembly 6 was an earlier version of Assembly 6A constructed when the inventory of ^{235}U fuel was insufficient to construct a full-scale uniform composition core. Some zoning was therefore done to allow the

* Comitato Nazionale per L'Energia Nucleare, Casaccia, Italy.

TABLE II-11-I. APPROXIMATE COMPARISON OF OVERALL PROPERTIES OF ASSEMBLIES 6A AND 7

	Assembly 6A	Assembly 7
Fissile element type	^{235}U	Pu
Fuel type	Oxide	Oxide
Core type	Single zone	Single zone
Fuel volume fraction	0.33	0.33
Sodium volume fraction	0.42	0.42
Steel volume fraction	0.20	0.20
Void volume fraction	0.05	0.05
Fertile-to-fissile atom ratio	5.05	6.45
Blanket	Depleted U	Depleted U
L/D	0.84	0.95
Volume, liters	4000	3100

assembly to reach criticality. For Assembly 6A, more fuel was available and although some compromises from a strictly uniform core were necessary even in Assembly 6A construction, they were considerably fewer than in Assembly 6. Assembly 6A was therefore designed to be the reference benchmark assembly for this composition, and where a small nonuniformity in the loading existed near the edge of the core of Assembly 6A, measurements were made specifically to experimentally adjust the core to its completely uniform equivalent.

We now describe in detail the geometry and loading of the as-built reference cores, then list and describe the various corrections made to the latter to translate to a uniform two-dimensional cylindrical core with zero-excess reactivity. This will then serve as the model for definition of a uniform spherical model for data testing, which will be described in a later section.

THE AS-BUILT REFERENCE ASSEMBLIES

Figures II-11-2 and II-11-3 give the exact as-built geometries for the two assemblies. It is stressed that the dimensions on these figures are those for the as-built system and must not be confused with the dimensions for the final two-dimensional cylindrical model. The latter includes a number of corrections which will be described below. The as-built figures are shown so that the reader may note the degree of correspondence between the configuration actually built and the two-dimensional model defined for calculation. The fissile loadings for the as-built reference cores are given in line 1 of Table II-11-II.

THE REACTIVITY CORRECTIONS

Excess Reactivity

The as-built cores contain a certain amount of excess reactivity built in for operational purposes. Line 2a of Table II-11-II lists the values for each assembly, corrected to an average core temperature of 20°C.

Edge Smoothing Correction

Line 2b of Table II-11-II gives the correction made to convert the irregular radial boundaries of the assemblies as shown in Figs. II-11-2a and II-11-2b to an equivalent area cylindrical system. The correction was calculated by summing the (mass) × (reactivity gradient) × (difference in radius) for each small triangular section inside or outside the equivalent-area cylindrical boundary. This is a relatively small correction in these assemblies because of their large size. The calculated gradient of the worth of the core material at the core-blanket radial interface, normalized to the measured edge drawer worth, was used for the value of the reactivity gradient. The difference in radius values were obtained by graphical integration.

Interface Gap Correction

In the past a correction has sometimes been listed for the effect of a possible interface void gap between the two halves of the ZPR machines. We specifically have taken this correction to be zero for these assem-

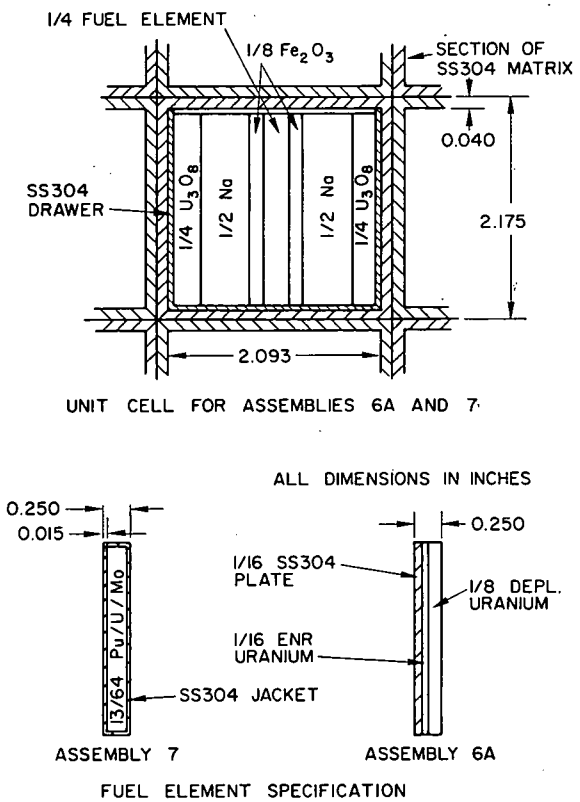

FIG. II-11-1. Cross Section of Unit-Cell Showing Matrix and Plate Loaded Drawer, ZPR-6 Assemblies 6A and 7. *ANL Neg. No. 116-888.*

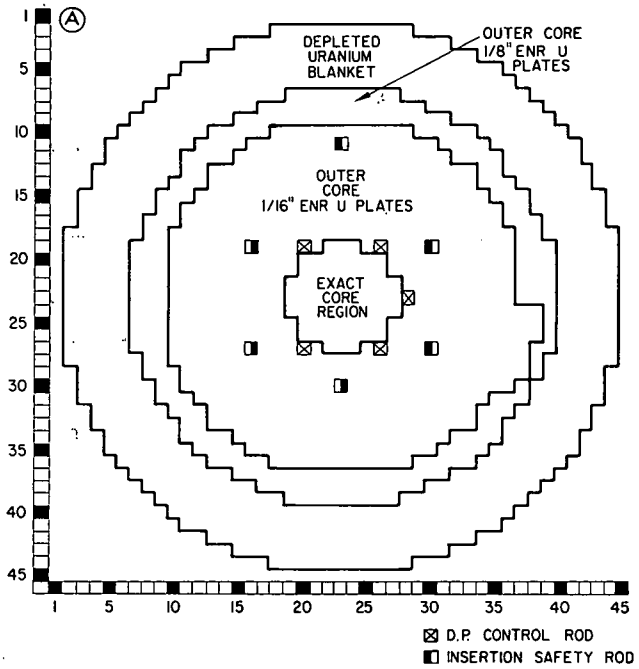

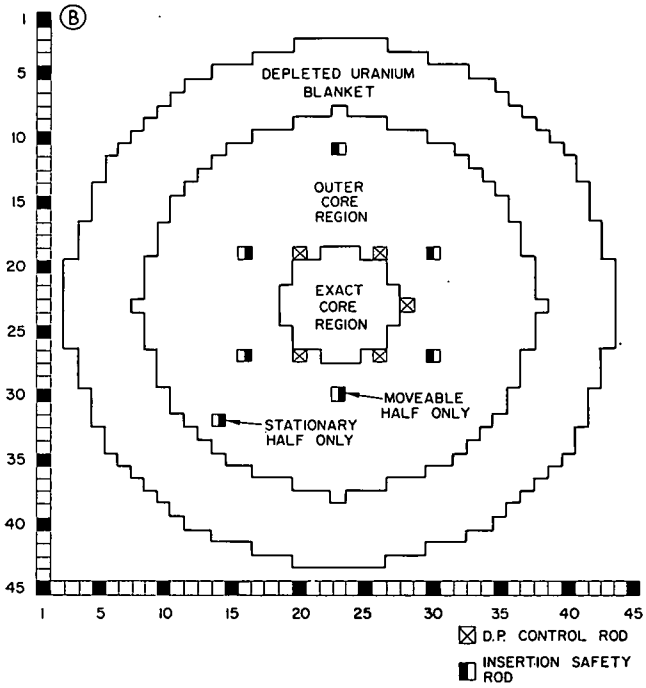

FIG. II-11-2a. Radial Cross Section for 75.1 Ih Excess Reactivity, As-Built ZPR-6 Assembly 6A. *ANL Neg. No. 116-890.*

FIG. II-11-2b. Radial Cross Section for 96.2 Ih Excess Reactivity, As-Built ZPR-6 Assembly 7. *ANL Neg. No. 116-889.*

blies. The gap worth is known only to be small. The precise value of the gap at the time of the reference measurement is not known, and in any case is very difficult to determine. Experience with the assemblies, however, indicate that the gap values range from 0–10 mils, typically, with measured gap worths in the range of 0.8 Ih/mil. The correction has therefore been assigned the value of zero, with a possible error of a few inhours associated with this.

Uniform Core Correction

As shown in Fig. II-11-2a, the as-built reference version of Assembly 6A included an outer core region that was fueled with ⅛ in. thick ZPR enriched uranium plates rather than the 1/16 in. thick plates used for

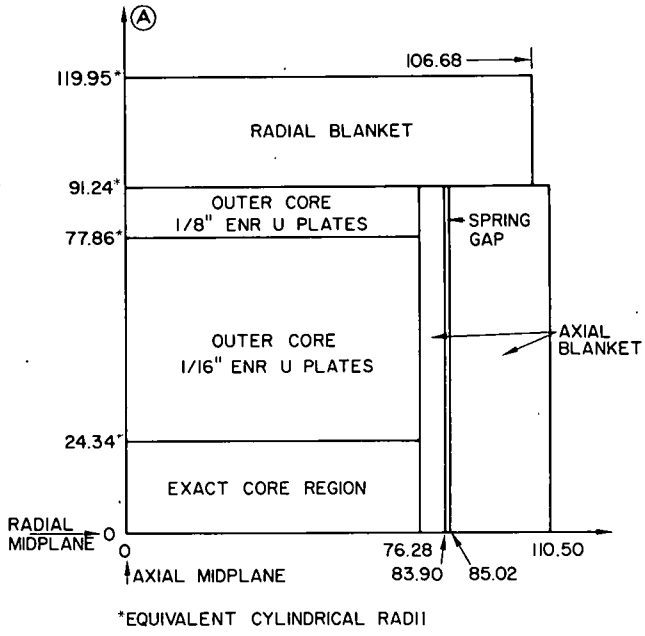

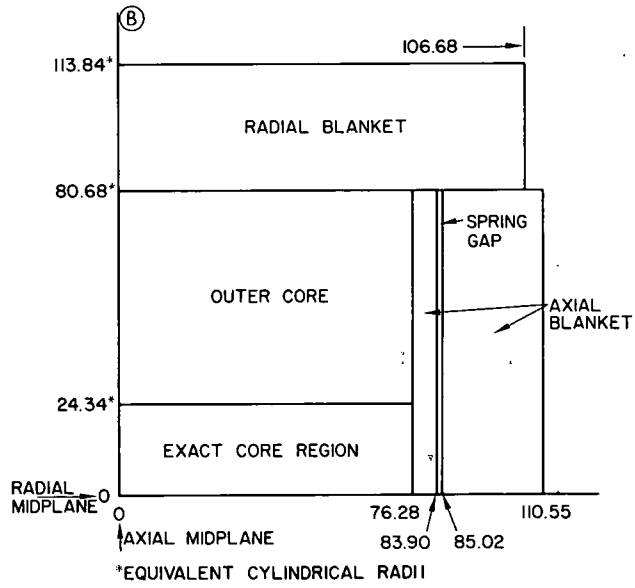

FIG. II-11-3a. Axial Cross Section for 75.1 Ih Excess ... activity, As-Built ZPR-6 Assembly 6A. *ANL Neg. No. 116-892.*

FIG. II-11-3b. Axial Cross Section for 96.2 Ih Excess Reactivity, As-Built ZPR-6 Assembly 7. *ANL Neg. No. 116-891.*

the bulk of the loading (which has the unit-cell shown in Fig. II-11-1). The fissile density per drawer was preserved by halving the number of plates used per drawer; however, the reactivity worth of a drawer containing the ⅛ in. thick plates was slightly greater than that of the 1/16 in. plate drawers because of the somewhat different degree of heterogeneity. The actual drawer loadings and the measurements that were made to correct the actual core loading to an equivalent all-1/16 in. type drawer loading are discussed in Ref. 3. In brief, however, the technique used was to measure in several steps the reactivity associated with replacing the ⅛ in. fuel drawers with 1/16 in. fuel drawers in a quadrant of the core. The results were then extrapolated the further 270° to give the full-core value. This value is listed as the uniform core reactivity correction in line 2d of Table II-11-II. It is simply the reactivity change caused by the substitution of one type of fuel for the other over the entire outer region, and its value is 86.9 Ih. However, in addition to the reactivity change that results from replacing ⅛ in. fuel drawers with 1/16 in. fuel drawers, a small change in the actual critical mass present also takes place because the fissile weights in the two drawer types are not exactly the same. This change in critical mass is listed in line 3a of Table II-11-II. It must also be included in the correction.

TABLE II-11-II. CRITICAL MASSES FOR ZPR-6 ASSEMBLIES 6A AND 7

	Assembly	
	6A	7
1. Fissile loading of as-built reference core[a]		
^{235}U	1784.4 kg	15.3 kg
$^{239}Pu + ^{241}Pu$	0	1118.1 kg
2. Reactivity corrections[b]		
a. Excess reactivity of as-built reference core	−75.1 Ih	−96.2 Ih
b. Edge smoothing correction	−3.3 Ih	−15.2 Ih
c. Interface gap correction	0	0
d. Uniform core correction	+86.9 Ih	0
e. Net reactivity correction	+8.5 Ih	−111.4 Ih
3. Fissile mass adjustments between as-built reference core and zero-excess reactivity uniform core due to:		
a. Loading from as-built reference core to uniform core		
^{235}U	+5.4 kg	0
b. Net reactivity correction[c]		
^{235}U	+3.7 kg	−0.1 kg
$^{239}Pu + ^{241}Pu$	0	−10.6 kg
4. Corrected zero-excess reactivity critical mass for uniformly loaded core at 20°C		
^{235}U	1793.5 kg	15.2 kg
$^{239}Pu + ^{241}Pu$	0	1107.5 kg
Total fissile[d]	1793.5 kg	1122.7 kg

[a] The as-built reference cores are shown in Figs. II-11-2 and II-11-3.

[b] $1\%\ \delta k/k$ = 458 Ih for Assembly 6A, $1\%\ \delta k/k$ = 1034 Ih for Assembly 7.

[c] Values based on edge drawer worth in Assembly 6A of 2.3 Ih/kg ^{235}U and in Assembly 7 of 10.4 Ih/kg fissile.

[d] The total uncertainty in this mass is estimated to be ±10 kg or less.

THE CORRECTED ZERO-EXCESS REACTIVITY CRITICAL MASS FOR UNIFORMLY LOADED ASSEMBLIES AT 20°C

The sum of the reactivity corrections is listed in line 2e of Table II-11-II. These values are converted to fissile masses using measured edge drawer worths. The value in Assembly 6A is 2.3 Ih/kg of ^{235}U and in Assembly 7 is 10.4 Ih/kg of fissile material. The result is shown in line 3b.

The region at the center of each assembly designated as the "exact core region" in Figs. II-11-2 and II-11-3 is simply a region in which the material concentrations are more accurately known than in the rest of the core. The nominal loading of the drawers in this region is exactly the same as that for the drawers in the rest of the core. However, in the "exact core region" the exact weight of each individual piece of fuel or diluent loaded into the region was recorded and, in some cases, pieces with weights slightly above or below the average piece weight for the group of materials were selectively loaded into these drawers. The purpose was to construct a plate region with very well-known concentrations corresponding to the concentrations given by the pin-calandria combination to be used in later experiments. As will be noted in the next section, some minor concentration differences exist between the exact region and the rest of the core. The differences are generally due simply to a more exact knowledge of the weights in this region and they should have no significant effect on the analysis of the assemblies.

The dimensions of both the as-built cores corresponding to Figs. II-11-2 and II-11-3, and finally, the zero-excess reactivity, uniformly loaded cylindrical versions of ZPR-6 Assembly 6A and 7 are given in Table II-11-III.

SPECIFICATION OF THE HOMOGENEOUS ATOM DENSITIES

We have made a particular effort in this document to carefully define the actual compositions of the two assemblies and the precisions to which the compositions

TABLE II-11-III. Dimension for "As-Built" Cores and the Zero-Excess Reactivity, Uniformly Loaded, Cylindrical Versions of ZPR-6 Assemblies 6A and 7

	Assembly			
	6A		7	
	As-Built 75.1 Ih Excess Core)	Zero-Excess Core (Reference Uniform Core)	As-Built 96.2 Ih Excess Core	Zero-Excess Core (Reference Uniform Core)
Outer core radius, cm	91.24	91.34	80.68	80.30
Radius of 1/16 in. fuel plate region (6A only), cm	77.86	—	—	—
"Exact Core" region radius, cm	24.34	24.34	24.34	24.34
Core height, cm	152.56	152.56	152.56	152.56
Radial blanket thickness, cm	28.71	28.61	33.16	33.54
Axial blanket thickness, cm	34.22	34.22	34.27	34.27
Core volume, liters	3990	3999	3120	3090

are known. An effort was also made to assure that the data for both assemblies were treated in exactly the same manner.

The steps taken were the following: For both assemblies, the reference critical loadings—Loading 6 for Assembly 6A and Loading 12 for Assembly 7—were inventoried. The number of each type of fuel and diluent plate in each assembly was listed. (Table II-11-XV summarizes this information.) The mean weight and compositions of each piece type was then established (Tables II-11-XVI and II-11-XVII) and the sources from which the knowledge of this physical, chemical, and isotopic data were drawn were evaluated (Table II-11-XVIII). This inventory information is given in detail below, Inventory and Composition of Materials of Assemblies 6A and 7.

The weight of each isotope in each region was established in this way. Then from a knowledge of the number of matrix positions occupied by the core and the blanket, and definition of the (matrix position) unit-cell volume, the densities of each isotope in each region were defined. The unit-cell volumes were defined from the following considerations.

For both assemblies, the stainless steel drawers in which the core materials were loaded were 33.442 in. in inside length, with a 0.032 in. wall thickness. The core material extended 30.000 in. from the inside front face of the front drawer. The core half-height for both assemblies was therefore 30.032 in.

For the axial blanket in both assemblies, depleted uranium plates and blocks extended from 30.000 in. to 33.000 in. in the drawer. The remaining 0.442 in. was occupied by a light stainless steel spring, which in effect creates a small void region. A further 10.000 in. of depleted uranium block followed this, to complete the axial blanket. In Assembly 7, this was contained in a 12.000 in. inside length, 0.020 in. thick wall stainless steel back drawer, while in Assembly 6A the material was placed directly in the matrix tube without the back drawer.

For both assemblies, the radial blankets were constructed by placing depleted uranium blocks directly in the matrix tubes without drawers. Thus the following axial region heights were defined:

1. Core half-height (both assemblies)	30.032 in.	(0.032 + 30.000 in.)
2. Axial blanket for Assembly 6A	13.374 in.	(3.442 + 0.032 + 10.000 in.)
Front drawer loading	3.000 in.	
Spring gap	0.474 in.	(0.442 + 0.032 in.)
Back drawer loading	10.000 in.	
3. Axial blanket for Assembly 7	13.394 in.	(3.442 + 0.032 + 0.020 + 10.000 in.)
Front drawer loading	3.000 in.	
Spring gap	0.494 in.	(0.442 + 0.032 + 0.020 in.)
Back drawer loading	10.000 in.	
4. Radial blanket half-height (both assemblies)	42.000 in.	

Consequently, the core and blanket unit-cell volumes are:

1. Core (both assemblies)	$(30.032)(2.175)^2 = 142.07$ in.^{3} or 2329.1 cm^3
2. Axial blanket (Assembly 6A)	$(13.374)(2.175)^2 = 63.267$ in.^{3} or 1036.8 cm^3
3. Axial blanket (Assembly 7)	$(13.394)(2.175)^2 = 63.362$ in.^{3} or 1038.3 cm^3
4. Radial blanket (both assemblies)	$(42.000)(2.175)^2 = 198.69$ in.^{3} or 3255.9 cm^3

For each region the density of each element of isotope is simply:

$$\frac{\text{Isotope wt., g}}{\text{Region volume, cm}^3} \times \frac{\text{Avagadro No.}}{\text{Isotopic atomic weight}}.$$

Atomic weights are normalized to ^{12}C as indicated on the 1969 AEC nuclides chart (Battelle) and the physical ^{12}C scale consistent value for Avagadros No. of 6.023×10^{23} atoms/mole.

Table II-11-IV lists the results. The mean atom densities are given for each region for both assemblies. Consistency checks were made to assure that the listed

TABLE II-11-IV. MEAN ATOM DENSITIES FOR THE ZERO-EXCESS, UNIFORM CYLINDRICAL MODEL OF ASSEMBLIES 6A AND 7, 10^{21} atoms/cc

	Assembly 6A				Assembly 7			
	Exact Core	Outer Core	Axial Blanket	Radial Blanket	Exact Core	Outer Core	Axial Blanket	Radial Blanket
Outer radius, cm	24.34	91.34	—	119.95	24.34	80.30	—	113.84
^{238}Pu	—	—	—	—	0.00033	0.00049	—	—
^{239}Pu	—	—	—	—	0.8867	0.8879	—	—
^{240}Pu	—	—	—	—	0.1177	0.1178	—	—
^{241}Pu[a]	—	—	—	—	0.0133	0.0152	—	—
^{242}Pu	—	—	—	—	0.00141	0.00177	—	—
^{234}U	0.011	0.011	0.00040	0.00040	0.00006	0.00006	0.00040	0.00040
^{235}U	1.153	1.149	0.0836	0.0866	0.0126	0.0126	0.0834	0.0866
^{236}U	0.0056	0.0056	0.0020	0.0020	0.00030	0.00030	0.0020	0.0020
^{238}U	5.801	5.784	38.65	40.06	5.777	5.802	38.59	40.06
^{241}Am[a]	—	—	—	—	0.0030	0.0028	—	—
Mo	0.011	0.011	0.0040[b]	0.0034[b]	0.2357	0.2382	0.0046[b]	0.0034[b]
Na	9.2904	9.202	—	—	9.2904	9.132	—	—
O[c]	13.90	14.74	0.026[b]	0.022[b]	13.98	14.82	0.030[b]	0.021[b]
Fe[d]	13.42	13.99	4.931	4.197	12.97	13.53	5.652	4.197
Ni	1.291	1.264	0.5977	0.5082	1.240	1.212	0.6910	0.5082
Cr	2.842	2.841	1.378	1.172	2.709	2.697	1.579	1.17
Mn	0.221	0.222	0.107	0.0897	0.212	0.213	0.123	0.0897

[a] ^{241}Pu decay to ^{241}Am corrected to 9/15/71.

[b] Arising from SS304 impurities.

[c] Includes ~0.005% due to SS304 and Pu/U/Mo fuel impurities.

[d] Includes ~0.0088% due to heavy (atomic wt. ≥ Si) SS304 impurities and Pu/U/Mo fuel impurities.

Note: The number of digits in each density is a measure of the compositional precision. Nominally, the rightmost digit bounds the density according to a 2σ or 93% confidence interval.

atom densities were consistent with both the dimensions of Table II-11-III and the masses, for example, of Table II-11-II.

The precision to which the atom densities can be defined is generally controlled by the precision to which the total region weight of any particular isotope is known. Since the total region weights are made up of a very large number of pieces, they are in general reasonably well-known. For most of the materials, simple statistical considerations indicate that the total weights may be known to precisions approaching five digits. The atomic weights used were uniformly taken to five significant digits; e.g., ^{235}U at 235.04. The intent of the tabulation in Table II-11-IV is that the atom densities can probably be taken as being precise to the number of digits shown.

DEFINITION OF THE ONE-DIMENSIONAL SPHERICAL MODEL

For both assemblies spherical models were defined by defining a two-dimensional finite cylindrical model each assembly and then defining the one-dimensional spherical model as a sphere having the same k_{eff} as the two-dimensional cylinder.

THE TWO-DIMENSIONAL FINITE CYLINDRICAL MODEL

The dimensions of the two-dimensional model were simply those of the zero-excess Reference Uniform Core, as listed in Table II-11-III. One simplification was made. The radial blanket height was defined to be 221.0 cm, the same as core plus axial blanket heights. The atom densities were those given in Table II-11-IV.

In the calculational model, each axial and radial region was given the dimensions shown in Table II-11-III, with the single exception noted above. Some simplification was also made in the isotopic compositions by combining some of the minor constituents shown in Table II-11-IV. For both cases, ^{234}U and ^{236}U were included in the ^{238}U concentration. In Assembly 6A, molybdenum was included in the iron. In Assembly 7, ^{238}Pu and ^{242}Pu were included in the ^{240}Pu concentration and ^{241}Am was included in the ^{238}U concentration.

Two-dimensional (r,z) diffusion theory calculations were made for both assemblies to serve as the two-dimensional model. The cross sections used in the calculation were homogeneous-option MC^2-generated using ENDF/B VERSION I data. The cross section generation method is described in somewhat more

TABLE II-11-V. SPHERICAL MODELS OF ASSEMBLIES 6A AND 7 MEAN ATOM DENSITIES, 10^{21} atoms/cc

Assembly	Region	^{239}Pu	^{240}Pu	^{241}Pu	^{235}U	^{238}U	Mo	Na	O	Fe	Ni	Cr	Mn
6A	Core	—	—	—	1.153	5.8176	—	9.2904	13.90	13.431	1.291	2.842	0.221
	Blanket	—	—	—	0.0855	39.5508	—	—	0.023	4.4669	0.5407	1.247	0.0960
7	Core	0.88672	0.11944	0.0133	0.01259	5.78036	0.2357	9.2904	13.98	12.97	1.240	2.709	0.212
	Blanket	—	—	—	0.0856	39.6179	0.0038	—	0.024	4.637	0.5635	1.295	0.0998

TABLE II-11-VI. SPHERICAL MODELS OF ASSEMBLIES 6A AND 7 CRITICAL DIMENSIONS

	Assembly 6A	Assembly 7
Core radius, cm	95.67	88.16
Blanket thickness, cm	30.65	33.81

detail in the next section. The diffusion theory code used was DIF-2D in the ARC system.

SPECIFICATION OF THE ONE-DIMENSIONAL SPHERICAL MODEL

The homogeneous spherical models were defined by first determining a blanket thickness, and then searching for a core radius giving a spherical reactor with the same k_{eff} as the homogeneous two-dimensional cylinder.

The blanket dimensions and compositions were defined as the weighted average of the axial and radial blanket dimensions and compositions as given in Tables II-11-III and II-11-IV. The weighting was done on the basis of the relative leakages into the axial and radial blankets (as given by the two-dimensional calculations).

The spherical model core compositions were defined to be those of the "exact core" composition of the two-dimensional model. It is these compositions that are most accurately known and it was also these compositions that made up the environment in which the central measurements such as central reactivities and reaction rates, which form a part of the benchmark comparisons, were made.

The resulting spherical models are defined by Tables II-11-V and II-11-VI. The atom densities are given in Table II-11-V and the dimensions are given in Table II-11-VI. These are the compositions and dimensions that should be used for benchmark comparisons.

EVALUATION OF HETEROGENEITY CORRECTIONS

THE BASE HOMOGENEOUS CALCULATION

The homogeneous composition cross sections used in the previous section were defined on the following basis. A broad group structure using 27 groups was selected, consisting of 21 groups with a lethargy width of 0.50, followed by 4 groups of 1.0, 1 group of 2.0, and finally a thermal group. The broad group cross sections were generated for the homogeneous compositions of the "exact core" regions of Table II-11-V. The MC[2] code was used with the following options: (a) 30 ultra-fine groups per fine group of lethargy width 0.25; (b) consistent P_1 approximation with isotopic scattering; (c) $\phi(E)$ = constant for a fine-group weighting.

THE HETEROGENEITY CALCULATION

First, in-plate capture and fission resonance cross sections for each absorber plate were obtained from equivalence theory[5] and the two-sided E_3 formulation of Meneghetti[6] for the Dancoff effect. Heterogeneous unit-cell cross sections were then calculated using broad group flux shapes determined by the integral transport code CALHET.[7] This averaging procedure amounts to preserving the reaction rates in the homogenization process.

In the reduction of the actual unit-cell to the slab geometry unit-cell calculational model, the following approximations were made. Horizontal stainless steel of the matrix and drawer was smeared homogeneously through the cell. The voids between the drawers, plates and matrix tubes were accounted for by reducing the plate densities appropriately while preserving the overall dimensions.

THE HETEROGENEITY RESULTS FOR ASSEMBLIES 6A AND 7

Table II-11-VII lists the heterogeneity results. The homogeneous k_{eff} given by the two-dimensional, and by definition, the one-dimensional calculation, is given in line 1. These correspond to a physical model that has the core materials simply ground-up into a homogeneous mixture.

Line 2 of Table II-11-VII gives the effects on reactivity of the inclusion of resonance self-shielding appropriate to the plate configurations. Separate calculations were made to display the individual effect heterogeneous resonance self-shielding on each of the main heavy isotopes. It will be noted that the effects are not large, and are to some degree self-cancelling.

Line 3 of Table II-11-VII gives the effect on reactivity of the spatial fine-structure of the flux. It will be noted that in both assemblies the self-multiplication effects in the fuel tend to dominate, with the larger effect in Assembly 7 where the higher fission-energy fission cross sections and ν of plutonium lead to greater self-multiplication in the fissile plate.

Line 4 gives the total reactivity effect due to unit-cell heterogeneity. The effects are not greatly different in the two assemblies—both are of the order of 1 % in k, with the slightly larger effect in the plutonium-fueled Assembly 7.

Finally, the k_{eff} values calculated for the heterogeneous compositions are given in line 5 of Table II-11-VII. Line 5a gives the result for the one-dimensional spherical model using the heterogeneous cross sections. All the intermediate Δk_{eff} numbers shown were calculated using the one-dimensional model as well, and in each case the difference was taken between the one-dimensional k_{eff} calculation with the homogeneous cross sections and a one-dimensional k_{eff} calculation with the set of heterogeneous cross sections appropriate to the effect under investigation. Line 5b represents an interesting cross-check. The two-dimensional calculations were rerun using the heterogeneous cross sections and the listed value of k_{eff} was obtained. As will be noted, no significant difference is found. This indicates that the use of the homogeneous one-dimensional spherical calculations with the correction to k_{eff} for heterogeneity simply added to the homogeneous k_{eff} is a perfectly satisfactory approximation for assemblies of this size. While the precise magnitude of the heterogeneity correction will change as cross section sets and methods change, the generality of the foregoing statement should hold for these assemblies. Thus in reestablishing a heterogeneity correction, even to higher precision, at some later date it should only be necessary to carry out the one-dimensional computation.

TABLE II-11-VII. HETEROGENEITY EFFECTS

	Assembly 6A	Assembly 7
1. Homogeneous k_{eff}[a,b]	0.9819	0.9615
2. Δk_{eff} due to heterogeneous resonance self-shielding[a]		
a. ^{238}U	0.0061	0.0053
b. ^{235}U	−0.0013	—
c. Pu + Mo	—	−0.0029
3. Δk_{eff} due to spatial heterogeneity[a]	0.0047	0.0111
4. Δk_{eff} due to the total heterogeneity effect[a]	0.0095	0.0135
5. Heterogeneous k_{eff}		
a. 1D diffusion theory	0.99139	0.97499
b. 2D diffusion theory	0.9914	0.9750

[a] One-dimensional diffusion theory.
[b] Two-dimensional diffusion theory.

The Unit-Cell Reaction Rates

Detailed unit-cell measurements of the capture and fission in ^{238}U and fission in ^{235}U and ^{239}Pu (Assembly 7 only) were made in these assemblies. Activation foils of ^{238}U, ^{235}U, and ^{239}Pu were used to measure the rates within the fuel and U_3O_8 plates, such that the actual cell-average values of the reaction rates could be obtained. To be clear, these unit-cell reaction rate values correspond to the reactions actually taking place in the unit-cell in the assembly, and not, for example, to a cell average defined as the value of the flux at every point in the cell multiplied by the cross section of the foil material in question. Some authors have referred to the latter as the unit-cell reaction rate. As we will use the term here, we mean it to refer to the flux and volume weighted reaction rates as they actually take place in the unit-cell. That is, the per atom unit-cell reaction rate ratios convert to the actual ratios of the number of reactions taking place in the cell simply through the multiplication of the former ratios by the relevant atom density ratios.

Such measurements were done on both Assemblies 6A and 7. At this point in time only the measurements on Assembly 7 have been reduced. On Assembly 7, however, measurements were also made of the reaction rates in pin-geometry. (This is possible using the ZPR inventory of pins of this composition and sodium-filled calandria.) These measurements have also been reduced and both the pin and the plate measurements will be listed here.

To relate the plate- and pin-geometry measurements on Assembly 7 to the values for a truly homogeneous composition, unit-cell calculations of the reaction rates were carried out for the three unit-cell geometries. Calculations were also made for the unit-cell of Assembly 6A so that the 6A reaction rates could be linked to the Assembly 7 measurements as a temporary expedient at this point in time before the 6A experiment reaction rate results are available.

The Unit-Cell Reaction Rate Measurements in Assembly 7

The details of the techniques used for counting the activated foils and reducing the data to absolute reaction rates are identical with those used in Ref. 8. The absolute calibrations were effected three separate and independent ways: (1) by absolute fission chambers with identical foils on their faces to those used in the unit-cell measurements, with the fission chambers placed in the reactor at the same spectral position;

TABLE II-11-VIII. COMPARISON OF UNIT-CELL REACTION-RATES, MEASURED AND CALCULATED

	Calculated Unit-Cell					Measured Unit-Cell (1σ = 2%)	
	Homogeneous	Pin Geometry		Plate Geometry		Pin Geometry	Plate Geometry
		Normal Unit-Cell	Experiment Unit-Cell	Normal Unit-Cell	Experiment Unit-Cell	Experiment Unit-Cell	Experiment Unit-Cell
$^{28}c/^{49}f$	0.1666	0.1642	0.1642	0.1636	0.1641	0.1433	0.1430
$^{28}f/^{49}f$	0.02343	0.02357	0.02342	0.02383	0.02305	0.02470	0.02338
$^{25}f/^{49}f$	1.141	1.145	1.146	1.159	1.145	1.054	1.065

(2) by thermal irradiation of identical foils in the ATSR thermal column; and (3) by absolute radiochemical analysis of some of the foils that were actually used in the unit-cell measurement. The degree of agreement between the various calibration methods lends unusually high confidence to the measured results.

The pin-geometry measurements are reported in Paper II-25. More detail on the reaction rate measurement methods is also to be found in this memo.

Five different unit-cell geometry calculations were made for Assembly 7. The results of the calculations and the measurements are shown in Table II-11-VIII. The homogeneous ratios are simply those from the calculations of the one-dimensional spherical model. The pin-geometry calculations were appropriate to the unit-cell of the pin-calandria combination. The column denoted "Normal Unit-Cell" refers to the values for a large array of such cells. The "Experiment Unit-Cell" column gives the values for the actual experimental geometry in which the array was a 5 x 5 square, 25-matrix position zone at the center of Assembly 7, and the small flux perturbation introduced by the change in the unit-cell geometry had not quite died out at the center of the pin-geometry zone.

For the plate-geometry unit-cell the column entitled "Normal Unit-Cell" was simply that of Fig. II-11-1. The "Experiment Unit-Cell" was the analytical representation of the actual unit-cell in which the foil measurements were made. This differs somewhat from the normal unit-cell loading of Fig. II-11-1 in that two "half-thickness" Pu-U-Mo fuel plates were used instead of the normal ¼ in. thick plate. This was to allow foils to be placed at the center of the fuel column to enable an integration to be made of the reaction rates through the fuel plate. Each of the half-thickness plates had 0.015 in. stainless steel cladding and a 0.095 in. core thickness. The effect of this substitution for the normal fuel plate was to reduce the amount of fuel present in the unit-cell in which the foils were placed. The actual experimental loading, therefore, had approximately 33% less Pu-Mo, 15% less ^{238}U, and 7.5% more stainless steel than the reference unit-cell. The calculated effects of these differences are shown in comparison of the two columns under the plate-geometry heading of Table II-11-VIII.

The cross sections used for the calculations were the following: For the homogeneous case, as previously stated, the cross sections are simply those of Section 4; for the "normal unit-cell" in the plate geometry case the cross sections used were simply those of Section 5; for the "experiment unit-cell" in the plate-geometry case special cross sections were generated with the appropriate resonance self-shielding for ^{238}U and ^{239}Pu; for the pin-geometry unit-cell, both "normal" and "experiment", the cross sections were generated for the appropriate cylindrical geometry; for all the pin and plate cases, once the resonance corrections were made the CALHET code was used to re-average over the flux fine structure. The effect of this, as previously stated, is to preserve the reaction rate in the homogenization process. The pin-geometry "experiment unit-cell", refers to a calculation made with the 5 x 5 unit-cell region imbedded in Assembly 7.

It can be seen that the general conclusion, perhaps somewhat surprisingly, is that the effects of heterogeneity in these assemblies are small.

THE HOMOGENEOUS UNIT-CELL REACTION RATES FOR ASSEMBLY 7

The information from Table II-11-VIII was used to extrapolate both the pin- and plate-geometry measured results to homogeneous values. The average of the two extrapolations was taken for each ratio and this number is given in Table II-11-IX as the measured homogeneous unit-cell reaction rate. These are the numbers that should be used as the benchmark homogeneous reaction rates.

For orientation to ENDF/B VERSION I the calculated values using this set of cross sections are also shown in Table II-11-IX and the ratio of calculation to experiment is shown as well.

REACTION RATES IN ASSEMBLY 6A

Because the Assembly 6A measurements have not yet been reduced, a calculated comparison of the unit-cell reaction rates for both assemblies is given in Table II-11-X.

This table will allow an estimation of the degree of error in these assemblies introduced by the homogeneous approximation normally used in benchmark calculations. As will be noted, the effects are small. Further, by linking through the experimental results for Assembly 7 given in Tables II-11-VIII and II-11-IX, the probable experimental results for Assembly 6A may also be estimated.

Central Reactivity Worths and Normalization Integrals

REACTIVITY WORTHS

Two conceptually different types of central reactivity worth measurements were made in both Assemblies 6A and 7. The first type was made in a small central cavity; the second type comprised measurements made on plates of the core constituents in the actual plate geometry of the unit-cell. The first type is the most common type of central reactivity worth measurement, while the second type is more amenable to a precise analytical description of the experimental geometry.

The central cavity worth measurements were made using different sample changing equipment in the two assemblies. For Assembly 6A, an axial sample changer was used[9] while in Assembly 7 a radial access sample changer was used.[10] For both, however, the cavity in which the samples were placed was about 1 in. wide by 2 in. high. For the axial changer the other dimension is also 2 in., while in the radial sample changer the cavity extends horizontally to the edge of the assembly. Previous experience has always indicated that no difference in the experimental results is to be expected because of the presence of this potential streaming path when the measurements are made at the center of the assembly, as these measurements were.

The experimental results for both assemblies are given in Table II-11-XI. Correction factors to account for self-shielding in the finite size samples are listed for certain key isotopes. These correction factors were based on calculation, but where possible, they were also experimentally verified. For many isotopes no correction factor is listed. This simply means that no evaluation of the correction factor has been made, and does not indicate that the correction factor should be taken as unity.

A few calculated worths are also given in Table II-11-XI. These were by-products of the calculations described in earlier sections of this paper. They therefore use ENDF/B VERSION I data. They are an example of the results of using the spherical homogeneous model with homogeneous sample cross sections and first-order perturbation theory. They are included as an example of results typical of benchmark testing.

TABLE II-11-IX. Assembly 7 Homogeneous Unit-Cell Reaction Rates, per Atom

	Measured (Extrapolated from Both Pin- and Plate-Geometry)	Calculated	C/E (ENDF/B VERSION I)
$^{28}c/^{49}f$	0.1453 ± 0.002	0.1666	1.15
$^{28}f/^{49}f$	0.02424 ± 0.0005	0.02343	0.97
$^{25}f/^{49}f$	1.0554 ± 0.01	1.141	1.08

TABLE II-11-X. Comparison of Calculated Unit-Cell Reaction Rate Ratioed to ^{235}U for Both Assemblies

	Assembly 6A		Assembly 7	
	Homogeneous	Plate	Homogeneous	Plate
$^{28}c/^{25}f$	0.147	0.145	0.146	0.141
$^{28}f/^{25}f$	0.0213	0.0216	0.0205	0.0206
$^{49}f/^{25}f$	—	—	0.8764	0.8628

The second type of central reactivity worth measurement was that of the individual plate materials in the unit cell. In these measurements, as small an amount of the plate is removed as is consistent with obtaining a sufficiently large signal. The measurements represent a good approximation to a calculation using perturbation theory in slab geometry. Table II-11-XII lists the results. The column headed "Environment" gives the position in the unit-cell in which the measured isotope was added or subtracted. Thus, for example, ^{239}Pu in the Pu/U/Mo plate environment corresponds to a measurement in which a small disc sample of ^{239}Pu was placed in a hole in the Pu/U/Mo fuel plate. Sodium in the sodium-plate environment corresponds to removal of the sodium plate and replacement with an empty can.

For both assemblies these measurements were done using an axial oscillator drawer. Two inch long samples of unit-cell (loaded into thin-walled 2 in. cubical boxes) were used for the measurement. The worths were obtained by measuring the worth of a fully-loaded unit-cell box, then altering the amount of the material to be measured and re-measuring the worth of the box.

For detailed analytical work, these measurements are

TABLE II-11-XI. CENTRAL REACTIVITY WORTHS MEASURED IN A CENTRAL CAVITY

Isotope	Isotopic Sample Weight, g	Measured Worth and 1σ Imprecision,[a] Ih/kg of Isotope	Small Sample Correction Factor and 1σ Imprecision[b]	Calculated Worth,[c] Ih/kg
	ZPR-6 Assembly 6A			
^{239}Pu	41.23	59.5 ± 1.4[d]	0.96 ± 0.01[e]	63.85
^{235}U	4.20	41.80 ± 0.48[f]	0.995[g]	49.90
^{238}U	1151.49	−3.29 ± 0.01[h]	—	−4.50
^{10}B	29.29	−820.41 ± 0.34	1.5 ± 0.1[i]	−1211.85
Ta	833.69	−12.50 ± 0.01	—	−20.32
Na	51.38	0.160 ± 0.040	—	0.102
C	101.98	3.863 ± 0.020	—	—
Fe	20.6	0.83 ± 0.15[j]	—	—
Ni	20.6	1.84 ± 0.20[j]	—	—
	ZPR-6 Assembly 7			
^{239}Pu	3.445	159.1 ± 1.3[k]	0.98 ± 0.01[i]	211.0
^{235}U	2.874	133.3 ± 2.0[f]	1.00 ± 0.02[l]	178.9
^{238}U	19.033	−10.91 ± 0.46[h]	—	−13.34
^{10}B	0.1103	−2868.7 ± 57.3[m]	1.02[n]	−3609
Ta	18.647	−43.07 ± 0.41	1.543[g]	−69.48
Na	17.044	−6.205 ± 0.315	—	−6.46
C	33.441	−12.19 ± 0.21	—	—
Al	53.067	−6.717 ± 0.168	—	—
Fe	33.277	−4.270 ± 0.156	—	—
Ni	37.916	−6.467 ± 0.185	—	—
Cr	26.999	−4.537 ± 0.370	—	—
Mo	43.398	−15.39 ± 0.11	—	—

[a] ZPR-6 ASSEMBLY 6A: 1% $\delta k/k \approx$ 458 Ih; ZPR-6 ASSEMBLY 7: 1% $\delta k/k \approx$ 1034 Ih.
[b] Ratio of zero size worth to finite size worth.
[c] ENDF/B VERSION I, homogeneous spherical model calculation.
[d] Obtained from worth of plutonium sample (72 w/o ^{239}Pu/Pu) measured in Assembly 6A and worths measured as a function of ^{239}Pu content in Assembly 7.
[e] Obtained from extrapolation of Assembly 7 results.
[f] Obtained from worth of enriched uranium sample (93.20 w/o ^{235}U, 6.80 w/o ^{238}U).
[g] Calculated including spatial and resonance self-shielding.
[h] Obtained from worth of depleted uranium sample (0.22 w/o ^{235}U, 99.78 w/o ^{238}U).
[i] Calculated and verified by experiment.
[j] Obtained from worth of SS304 sample in ZPR-6 Assembly 6A and iron, nickel, and SS304 samples in Assembly 6.
[k] Obtained from worth of plutonium sample (99 w/o ^{239}Pu/Pu).
[l] Indicated by experiment.
[m] Obtained from worth of natural boron sample (19.9 w/o ^{10}B/B).
[n] Calculated including spatial self-shielding.

probably the most useful because their geometries are more precisely describable than are those of the type measured in the cavity. However, utilization of the unit-cell worth measurements requires detailed unit-cell calculations and this is unlikely for most data testing.

For usual benchmark data testing, the worths measured in the cavity and listed in Table II-11-XI are the appropriate numbers to be used. Sample size correction should be applied before the data are compared with first-order perturbation theory calculations. Where the correction factors are listed in Table II-11-XI they can be used with the uncertainties listed. Where no correction factor is listed, the user must make his own evaluation.

NORMALIZATION INTEGRALS

The normalization integrals (denominator of the perturbation expression) have been measured in Assemblies 6A and 7 by the techniques described in Ref. 11. This measurement actually involves an inference of the value of

$$\frac{(\nu\Sigma_f\phi\phi_f^*)_{r=0}}{\int \nu\Sigma_f\phi\phi_f^*\, dV}$$

TABLE II-11-XII. CENTRAL WORTHS FROM SAMPLES MEASURED IN UNIT-CELL PLATE ENVIRONMENT

Material	Weight, g	Environment	Measured Worth, Ih/kg
Assembly 7[a]			
^{239}Pu	1.919	Pu/U/Mo plate	171.5 ± 5.2
Pu/U/Mo[b]	21.155	Pu/U/Mo plate	33.1 ± 0.5
^{238}U	14.43	Pu/U/Mo plate	−8.72 ± 0.72[c]
^{238}U	121.12	U_3O_8 plate	−8.96 ± 0.08[c]
Na	42.90	Na plate	−6.68 ± 0.23
U_3O_8	60.68	U_3O_8	−9.27 ± 0.16
Fe_2O_3	32.74	Fe_2O_3 plate	−6.09 ± 0.31
SS304	46.95	Pu/U/Mo SS304 cladding	−5.27 ± 0.21
SS304	46.77	Vertical matrix	−5.44 ± 0.21
SS304	46.29	Horizontal matrix	−4.45 ± 0.22
Fe	58.05	Fe_2O_3	−4.41 ± 0.17
Fe	38.43	Horizontal matrix SS304	−4.73 ± 0.26
Ni	38.66	Horizontal matrix SS304	−6.85 ± 0.26
Assembly 6A			
^{235}U	4.336	Enriched uranium plate	47.90 ± 0.69
SS304	11.586	SS304 plate	−1.424 ± 0.216
Fe_2O_3	23.52	Fe_2O_3	−0.400 ± 0.055
U_3O_8	95.755	U_3O_8 plate	−2.884 ± 0.011
^{238}U	50.3	Depleted uranium plate	−3.50 ± 0.02[c]
Na	42.912	Na plate	+0.137 ± 0.019

[a] See ZPR-TM-45 for details of measurement.

[b] The composition of the Pu/U/Mo material was 28.25 w/o Pu, 69.25 w/o depleted U and 2.50 w/o Mo. The plutonium composition was 86.5 w/o ^{239}Pu, 11.5 w/o ^{240}Pu, 1.81 w/o ^{241}Pu and 0.2 w/o ^{242}Pu.

[c] Obtained from worth of depleted uranium sample containing 99.78 w/o ^{238}U and 0.22 w/o ^{235}U.

from measurements at the reactor center ($r = 0$) of the apparent reactivity of a known ^{252}Cf source (S^{252}) at a power level at which the reactor neutron production rate $\overline{\nu F_0}$ is known (also at $r = 0$). That is, from

$$\left(\frac{\Delta k}{k}\right)^{252} = \frac{S^{252}}{\overline{\nu F_0}} \frac{(\nu\Sigma_f \phi\phi^*)_{r=0}}{\int \nu\Sigma_f \phi\phi_f^* \, dV}.$$

$(\Delta k/k)^{252}$ is a measured value, essentially of a period, S^{252} is known from a previous calibration, and $\bar{F}_0$ is obtained from central absolute fission rate measurements. $\bar{\nu}$ and a correction to ϕ_f^* (for the difference between the fission neutron adjoint averaged over the core fission neutron spectrum and the ^{252}Cf fission spectrum) are calculated but uncertainties in these quantities do not strongly affect the final precision.

The calculated and measured values are given in Table II-11-XIII. The calculations are for the homogeneous spherical model with ENDF/B VERSION I cross sections.

As has been pointed out from time-to-time in the past[12,13] the effect of correcting central worth calculations by multiplying through by the ratio of the calcul-to-experimental normalization integrals is to re- e any dependence of the calculated central worth on reactor geometry, delayed neutron fractions, or anything else except the properties of the reactor composition as reflected in the energy variation of the central fluxes and adjoints, and the cross sections of the sample itself. This is illustrated in Table II-11-XIV

TABLE II-11-XIII. NORMALIZATION INTEGRALS

	Assembly 6A	Assembly 7
Calculated	9.094×10^5	7.328×10^5
Experiment	$(10.86 \pm 0.14)^a \times 10^5$	$(9.48 \pm 0.35) \times 10^5$
Experiment / Calculated	1.19 ± 0.01	1.29 ± 0.05

[a] This is a revised value from that previously published[2] due to a probable error in the ^{252}Cf source assignment.

TABLE II-11-XIV. "FUEL" CENTRAL WORTHS

	Assembly 6A ^{235}U Worth, Ih/kg	Assembly 7 ^{239}Pu Worth, Ih/kg
Calculated	49.90	211.0
Experiment	41.59[a] ± 0.49	155.9[a] ± 1.3
Calculated / Experiment	1.20 ± 0.01	1.35 ± 0.01

[a] Includes small sample correction factor given in Table II-11-IX.

TABLE II-11-XV. MATERIALS INVENTORY FOR THE AS-BUILT, INITIAL-CRITICALITY CONFIGURATIONS OF ASSEMBLIES 6A AND

Material		Assembly 6A, Loading 6, 75.1 Ih Excess				Assembly 7, Loading 12, 96.2 Ih Excess			
Type	Nominal Size, in.	I.C.[a]	O.C.[a]	A.B.[a]	R.B.[a]	I.C.	O.C.	A.B.	R.B.
Pu/U/Mo DOW	1/4 x 2 x 4	—	—	—	—	0	819	—	—
	5	—	—	—	—	732	305	—	—
	6	—	—	—	—	0	727	—	—
	7	—	—	—	—	0	699	—	—
	8	—	—	—	—	0	686	—	—
Pu/U/Mo NUMEC	1/4 x 2 x 4	—	—	—	—	0	1090	—	—
	5	—	—	—	—	0	354	—	—
	6	—	—	—	—	0	6	—	—
	7	—	—	—	—	0	666	—	—
	8	—	—	—	—	0	768	—	—
Enriched uranium	1/16 x 2 x 2	0	7545	—	—	—	—	—	—
	3	1220	6270	—	—	—	—	—	—
	1/8 x 2 x 2	0	1528	—	—	—	—	—	—
	3	0	1290	—	—	—	—	—	—
Depleted uranium	1/16 x 2 x 3	0	2040	0	0	—	—	—	—
	1/8 x 2 x 2	0	0	13712	0	—	—	9226	0
	3	1220	14900	0	0	—	—	1152	0
	1 x 1 x 1	0	0	0	0	—	—	400	0
	2 x 2 x 2	0	0	1714	1216	—	—	1268	1330
	5	0	0	3428	9728	—	—	2636	10640
U_3O_8	1/4 x 2 x 2	3660	47760	—	—	3660	36540	—	—
Na cans (yellow)	1/2 x 2 x 6	1220	0	—	—	1220	0	—	—
	7	0	1936	—	—	0	1000	—	—
	8	0	1936	—	—	0	1000	—	—
Na cans (black)	1/2 x 2 x 2	0	200	—	—	0	0	—	—
	7	0	4832	—	—	0	3848	—	—
	8	0	4032	—	—	0	3848	—	—
Fe_2O_3	3/32 x 2 x 3	2440	0	—	—	2440	200	—	—
	1/8 x 2 x 2	0	19560	—	—	0	7500	—	—
	3	0	18800	—	—	0	19160	—	—
SS304 plates	1/16 x 2 x 1	0	640	—	—	—	—	—	—
	2	0	2760	—	—	—	—	—	—
	3	1200	13880	—	—	—	—	—	—
SS304 front drawers	2 x 2 x 33.4	122	1592	—	—	122	1218	—	—
SS304 back drawers	2 x 1/2 x 12	—	—	—	—	—	—	1318	0
SS304 matrix tubes	2 x 2 x 48	122	1592	—	1216	122	—	1218	1330
SS1095 springs	3/32 x 2 x 2	0	0	1692	0	0	0	1318	0

[a] I.C. ≡ Inner core or exact region, O.C. ≡ Outer core, A.B. ≡ Axial blanket, R.B. ≡ Radial blanket (Note: R.B. extends the full axial height).

TABLE II-11-XVI. MEAN WEIGHT COMPOSITION OF URANIUM AND PLUTONIUM PLATES IN ASSEMBLIES 6A AND 7[a], g

Component	Pu/U/Mo Metal Alloy (DOW)					Pu/U/Mo Metal Alloy (NUMEC)				
	¼ x 2 x 4 in.	¼ x 2 x 5 in.	¼ x 2 x 6 in.	¼ x 2 x 7 in.	¼ x 2 x 8 in.	¼ x 2 x 4 in.	¼ x 2 x 5 in.	¼ x 2 x 6 in.	¼ x 2 x 7 in.	¼ x 2 x 8 in.
^{238}Pu	0.05	0.05	0.08	0.08	0.09	0.07	0.09	0.11	0.13	0.15
^{239}Pu	107.88	136.56	164.44	193.00	222.00	106.99	135.38	163.46	191.32	220.14
^{240}Pu	14.39	18.20	21.96	25.73	29.62	14.21	17.97	21.75	25.47	29.31
^{241}Pu[b]	1.78	2.06	2.85	2.97	3.49	1.96	2.48	3.02	3.57	4.06
^{242}Pu	0.21	0.22	0.34	0.33	0.40	0.23	0.29	0.36	0.43	0.49
^{234}U	0.0030	0.0038	0.0046	0.0054	0.0062	0.0030	0.0038	0.0046	0.0054	0.0062
^{235}U	0.665	0.841	1.02	1.19	1.37	0.667	0.843	1.02	1.19	1.37
^{236}U	0.015	0.019	0.023	0.027	0.031	0.015	0.019	0.023	0.027	0.31
^{238}U	301.27	380.80	461.91	539.06	619.93	301.96	382.12	461.92	540.51	621.39
Mo	11.08	13.90	16.97	19.68	22.97	10.97	13.87	16.76	19.62	22.55
^{241}Am	0.36	0.45	0.55	0.64	0.74	0.36	0.46	0.55	0.65	0.75
U, Pu[c]	0.45	0.56	0.68	0.79	0.91	0.45	0.57	0.69	0.81	0.93
Imps.										
O	—	—	—	—	—	—	—	—	—	—
Fe^{+}[d]	30.74	36.08	42.41	47.75	54.31	30.54	35.41	41.67	47.44	53.68
Ni	4.641	5.448	6.403	7.211	8.201	4.611	5.403	6.292	6.163	8.105
Cr	8.210	9.636	11.33	12.75	14.51	8.156	9.456	11.13	12.67	14.34
Mn	0.740	0.869	1.02	1.15	1.31	0.735	0.862	1.00	1.14	1.29
Data source[e]	A	A	A	A	A	A	A	A	A	A

Component	Enriched Uranium Metal				Depleted Uranium Metal						U_3O_8
	1/16 x 2 x 2 in.	1/16 x 2 x 3 in.	⅛ x 2 x 2 in.	⅛ x 2 x 3 in.	1/16 x 2 x 3 in.	⅛ x 2 x 2 in.	⅛ x 2 x 3 in.	1 x 1 x 1 in.	2 x 2 x 2 in.	2 x 2 x 5 in.	¼ x 2 x 2 in.
^{234}U	0.67	1.01	1.31	2.01	0.0011	0.0015	0.0022	0.0030	0.024	0.061	0.0010
^{235}U	68.62	103.65	134.21	206.19	0.238	0.315	0.472	0.637	5.22	13.1	0.213
^{236}U	0.32	0.49	0.63	0.97	0.0055	0.0075	0.011	0.015	0.012	0.31	0.0050
^{238}U	4.04	6.09	7.74	11.92	111.97	148.07	222.58	299.9	2443.8	6136.7	101.24
O	—	—	—	—	—	—	—	—	—	—	18.18
Data source[e]	B	B	B	B	B	B	B	B	B	B	C

[a] The small mass differences between this table and the data supplied by the Special Materials and Services Division is explained in detail in the ZPR/ZPPR Reactor Materials Inventory Manual (to be published).

[b] ^{241}Pu decay to ^{241}Am corrected to September 15, 1971.

[c] Typically, 70 w/o heavy elements (atomic no. > Si) and 30 w/o light elements.

[d] Fe^{+} = Fe + SS impurities (see Table II-11-XVII).

[e] See Table II-11-XVIII.

where the "fuel central worths" are listed for both assemblies.

It may also be noted that without any such corrections the fuel worth is overpredicted by about 20% in the uranium-fueled Assembly 6A and about 35% in the plutonium-fueled Assembly 7. These discrepancies are similar to those observed in past ^{235}U and ^{239}Pu fueled assemblies. No significant improvement was found, therefore, in these large assemblies. For the moment this discrepancy appears to remain about the same as it was in the smaller assemblies of the past.

Inventory and Composition of Materials of Assemblies 6A and 7

The inventory of all assembly components, exlcuding poison rods and hardware for Assemblies 6A and 7, is summarized in Table II-11-XV. In both cases the assembly configurations at initial criticality (Loading 6 for Assembly 6A and Loading 12 for Assembly 7) are the most appropriate for inventory determinations. Although the Table II-11-III homogeneous atom densities are actually based on these as-built excess-reactivity systems, the atom density effect of removing the necessary edge drawers to define the uniform-zero-excess model is negligible; for example, for ^{239}Pu the change occurs in the sixth figure and is outside the limits of significance.

Tables II-11-XVI and II-11-XVII summarize the nominal size and mean isotopic weight compositions for all assembly components. The standard deviations in the mean weights were not indicated but will be delineated in the upcoming Reactor Materials Inventory Manual. The chemical impurities in the Pu/U/Mo metal fuel and in SS304 were treated as follows:

Pu/U/Mo impurities are considered to be all identifiable elements other than plutonium, uranium, molybdenum, and americium. SS304 impurities are all elements other than iron, nickel, chromium and mangenese. Proper mass normalization was accomplished by defining for the Pu/U/Mo,

$$\text{w/o U} = 100.00 - (\text{w/o Pu} + \text{w/o Mo} + \text{w/o Am} + \text{w/o Total Impurities}),$$

and for the SS304 sources,

$$\text{w/o Fe} = 100.00 - (\text{w/o Ni} + \text{w/o Cr} + \text{w/o Mn} + \text{w/o Total Impurities}).$$

Then, the total weight of impurities was examined for elements already defined; for example, the molybdenum was transferred from SS304 impurities to the molybdenum column. Finally, the remaining weight of

TABLE II-11-XVII. Mean Weight Composition of Non-Fuel Materials in Assemblies 6A and 7, g

Material		Component						Data Source[b]
Type	Nominal Size, in.	Na	O	Fe+[a]	Ni	Cr	Mn	
Na cans (yellow)	½ x 2 x 6	82.560	—	42.72	6.539	11.30	0.891	D
	½ x 2 x 7	96.72	—	49.69	7.605	13.15	1.04	D
	½ x 2 x 8	110.98	—	55.47	8.490	14.67	1.16	D
Na cans (black)	½ x 2 x 2	24.46	—	17.31	2.374	4.541	0.376	E
	½ x 2 x 7	95.56	—	50.48	6.923	13.25	1.10	E
	½ x 2 x 8	107.41	—	57.20	7.845	15.01	1.24	E
Fe_2O_3	⅜₈ x 2 x 3	—	15.50	36.06	—	—	—	F
	⅛ x 2 x 2	—	12.14	28.25	—	—	—	G
	⅛ x 2 x 3	—	18.10	42.11	—	—	—	G
SS304 plates	1/16 x 2 x 1	—	—	11.10	1.523	2.913	0.241	H
	1/16 x 2 x 2	—	—	21.64	2.968	5.678	0.471	H
	1/16 x 2 x 3	—	—	32.22	4.420	8.455	0.701	H
SS304 front drawers	2 x 2 x 33.4	—	—	584.3	75.56	153.6	13.2	I
SS304 back drawers	2 x ½ x 12	—	—	63.02	8.522	16.35	1.34	J
SS304 matrix tubes	2 x 2 x 48	—	—	1460.0	185.1	378.3	30.6	K
SS1095 springs	⅜₂ x 2 x 2	—	—	12.51	—	—	0.05	L

[a] Fe+ = Fe + SS impurities. Impurities = SS − (Fe + Ni + Cr + Mn). SS304 impurities are typically composed of ~90 w/o heavy elements (atomic no. ≥ Si) and ~10 w/o light elements.

[b] See Table II-11-XVIII.

TABLE II-11-XVIII. REFERENCES FOR PHYSICAL, CHEMICAL, AND ISOTOPIC DATA ON ZPR MATERIALS[a]

Data Source	Description
A	ANL, Special Materials and Services Division, SPM, (1/19/71, M. Nelson), summary of vendor-supplied plate and melt data. Modifications as follows (Applied Physics Division, J. E. Marshall, Materials Inventory Coordinator): 1. ^{241}Am at fabrication (t = 0) from ANL-PSD overcheck program. 2. ^{241}Pu decay at 9/15/71, hand corrected. 3. Total impurities separated using ANL-PSD overcheck analysis. 4. SS304 analysis from jacket materials vendor. 5. Depleted uranium taken "by difference"; i.e., at t = 0, DU = 100 w/o − (w/o Pu + w/o Mo + w/o total impurities + w/o Am).
B	ZPR-6 Memo No. 40, Revised (9/26/67, G. Main). Modifications as follows (J. E. Marshall): 1. The ^{234}U and ^{236}U content of DU was assigned the mean weight percent values from the Pu/U/Mo plate data 2. The w/o ^{235}U/Du taken from a sampling of new SPM data.
C	J. E. Marshall; sample of 600 plates (without coating) from 1/1/71 to 6/1/71. Isotopic content from SPM (J. Frogge) and Pu/U/Mo plate data (^{234}U and ^{236}U only).
D	Vendor supplied can weights compiled by C. D. Swanson. SS304 chemistry from can fabricator (J. E. Marshall).
E	ZPR-6 Memo No. 40, Revised (9/26/67, G. Main). SS304 analysis not available so abundance-weighted mean core SS304 chemistry was assigned.
F	J. E. Marshall; exact weight of I.C. plates. Chemistry from R. Palmer (AP-West), 9/2/69.
G	J. E. Marshall; samples of 200–300 plates. Chemistry assumed to be the R. Palmer (Re: Data Source F) values.
H	ZPR-6 Memo No. 40, Revised (9/26/67, G. Main). SS304 analysis—special job for J. E. Marshall, 2/71.
I	J. E. Marshall; 50 drawer T. C. sample. Special chemistry analysis for J. E. Marshall, 1/71.
J	J. E. Marshall; 50 drawer T. C. sample. Vendor-supplied chemistry on sheet stock.
K	J. E. Marshall; compilation of vendor-supplied data from 1958 to 1969 (L. R. Dates).
L	J. E. Marshall; 20 spring sample. No. SS1095 analysis was available—used SAE Handbook mid-range values.

[a] For more detail see the ZPR/ZPPR Reactor Materials Inventory Manual (to be published).

Note: Du ≡ Depleted material; AP ≡ Applied Physics Division.

impurities was assigned according to the following rule: The weight of all elements with atomic weights less than that of silicon was transferred to the oxygen column, with atomic weights equal to or greater than silicon to the iron column. Thus, the unassigned impurity mass was conserved and the atom densities of oxygen and iron were very slightly increased as a result. Table II-11-III includes the results of this impurity breakdown while Table II-11-XVI depicts the relative mass effect of the impurities.

Finally, Table II-11-XVIII contains a summary of the source or reference for the composition data. The references are keyed to Tables II-11-XVI and II-11-XVII by alphabetic characters.

REFERENCES

1. C. E. Till and W. G. Davey, *The Demonstration Reactor Benchmark Critical Assemblies Program*, Trans. Am. Nucl. Soc. **13**, 293 (1970).
2. R. A. Karam, W. R. Robinson, G. S. Stanford and G. K. Rusch, *ZPR-6 Assembly 6A, A 4000-Liter UO_2 Fast Core*, Applied Physics Division Annual Report, July 1, 1969, to June 30, 1970, ANL-7710, pp. 175–183.
3. L. G. LeSage, E. M. Bohn, J. E. Marshall, R. A. Karam, C. E. Till, R. A. Lewis and M. Salvatores, *Initial Experimental Results from ZPR-6 Assembly 7, The Single Zone Demonstration Reactor Benchmark Assembly*, Trans. Am. Nucl. Soc. **14**, 17 (1971).
4. R. A. Karam, L. R. Dates, W. Y. Kato, J. E. Marshall, T. Nakamura and G. K. Rusch, *A 4000-Liter Uranium Oxide Fast Core, ZPR-6 Assembly 6*, Reactor Physics Division Annual Report, July 1, 1967 to June 30, 1968, ANL-7410, pp. 75–86.
5. K. D. Dance, *An Equivalence-Theory Cross Section for Plate-Type Cells*, Reactor Physics Division Annual Report, July 1, 1967 to June 30, 1968, ANL-7410, pp. 434–435.
6. D. Meneghetti, *Calculational Studies of Sodium-Void Reactivity Variations Due to Thin Slab Heterogeneities in Fast Critical Assemblies*, Proc. International Conference on Fast Critical Assemblies and Their Analysis, October 10–13, 1966, Argonne, Illinois, ANL-7320, pp. 377–386.
7. F. L. Fillmore and B. D. Felten, *The CALHET Heterogeneous Perturbation Theory Code and Applications to ZPR-3-48*, AI-67-91 (1967).
8. C. E. Till, J. M. Gasidlo, E. F. Groh, L. G. LeSage, W. R. Robinson and G. S. Stanford, *Null-Reactivity Measurements of Capture/Fission Ratio in ^{235}U and ^{239}Pu*, Nucl. Sci. Eng. **40**, 132 (1970).
9. R. A. Karam, K. D. Dance, T. Nakamura and J. E. Marshall, *Analysis of Central Reactivity Worths in Fast Critical Assemblies*, Nucl. Sci. Eng. **40**, 414 (1970)
10. L. G. LeSage, E. F. Groh and W. R. Robinson, *An Investigation of the Properties of Zoned Systems*, Reactor Physics Division Annual Report, July 1, 1967 to June 30, 1968, ANL-7410, pp. 145–151.
11. R. A. Karam, *Measurements of the Normalization Integral and the Spatial Distribution of the Importance of Fission Neutrons*, Nucl. Sci. Eng. **37**, 192 (1969).
12. W. C. Redman and M. M. Bretscher, *Experimental Determination of the Perturbation Denominator in Fast Critical Assemblies*, Nucl. Sci. Eng. **44**, 450 (1971).
13. L. G. LeSage, C. E. Till and G. S. Stanford, *Comparison of Measured and Calculated Null Compositions, Central Reaction Ratios, and Reactivity Worths in ZPR-9 Assemblies 24 and 25 and ZPR-3 Assembly 55*, Trans. Am. Nucl. Soc. **13**, 93 (1970).

II-12. Measurements in ZPR-6 Assembly 7 with the High-240 Plutonium Zone

E. M. Bohn, L. G. LeSage and J. E. Marshall

A. Introduction

The results of measurements in the high-240 plutonium (H240) zone of ZPR-6 Assembly 7 are presented in this report. The measurements include small sample reactivity worths, ^{238}U Doppler reactivity worth, central region sodium voiding worth, and fission rate ratios.

Assembly 7 is a large, dilute, single-zoned, PuO_2 fueled critical assembly constructed in ZPR-6 as part of the Demonstration Reactor Benchmark Program.[1] A complete description of the uniform reference version of Assembly 7 may be found in Paper II-11. The results of measurements in the uniform reference version of Assembly 7 are given in Papers II-19, II-25, II-18, and II-21. The results of measurements in the sodium-voided, high-240 plutonium zone in Assembly 7 are reported in Paper II-13.

The H240 zone was constructed at the center of Assembly 7 by replacing regular plutonium fuel containing 12 w/o ^{240}Pu with plutonium fuel containing 27 w/o ^{240}Pu. Experimental studies in this H240 zone are important for two reasons: the composition of the H240 zone matches more closely the actual composition of LMFBR cores currently under design consideration, and, by comparing measurements in the uniform reference core of Assembly 7 with measurements in the H240 zone, some of the effects of fuel burnup (which is characterized by a buildup of ^{240}Pu) may be assessed.

Five basic experiments were included in the H240 experimental program: small sample reactivity worth measurements at the center of the H240 zone and radially through the core, perturbation denominator measurement, ^{238}U Doppler reactivity worth measurement, sodium void measurement, and fission rate and ratio measurements.

The small sample reactivity worths and perturbation denominator measurement provide information about the real and adjoint flux spectrum in the H240 zone and serve as a test of the calculation of these spectra and as a test of the cross sections of some of the materials used in the measurements. The ^{238}U Doppler worth and sodium void worth are two of the most important safety reactivity coefficients in an LMFBR. The results of the fission ratio measurements when compared with calculated fission ratios offer a means of evaluating the fission cross sections of core materials.

B. Description of Assembly 7 with the H240 Zone

The uniform reference version of Assembly 7 has a one-drawer unit-cell loading pattern consisting of two ¼ in. thick plates of U_3O_8, two ½ in. wide stainless steel cans containing sodium, two ⅛ in. thick plates of Fe_2O_3, and a ¼ in. thick plutonium fuel plate canned in stainless steel. The plutonium fuel is a Pu/U/Mo alloy: 28 w/o Pu, 69.5 w/o U, and 2.5 w/o Mo.[2] The isotopic composition of the plutonium in the fuel plate is 88% (^{239}Pu + ^{241}Pu) and 12% ^{240}Pu.[2]

The unit-cell loading pattern in the H240 zone is exactly the same as in the uniform reference version of Assembly 7, except that the fuel plate has been replaced with a high ^{240}Pu fuel plate containing a Pu/U/Mo alloy of 36 w/o Pu, 61.5 w/o U, and 2.5 w/o Mo.[2] The isotopic composition of the plutonium in the high ^{240}Pu fuel plate is 73% (^{239}Pu + ^{241}Pu) and 27% ^{240}Pu.[2]

The single drawer unit cell loadings for the regular uniform reference core and the H240 zone of Assembly 7 are shown in Fig. II-12-1.

The H240 zone was constructed in Assembly 7 by replacing the regular plutonium fuel plates with high ^{240}Pu fuel plates along the entire height of the core (60 in.) in a central region including 61 drawers in each reactor half. The H240 zone contains approximately 100 kg of high ^{240}Pu fuel and has an effective radius of 24.34 cm. The radial and axial cross sections of Assembly 7 with the H240 zone are shown in Figs. II-12-2 and II-12-3, respectively.

The atom densities in each region of Assembly 7 with the H240 zone are given in Table II-12-I. The ^{241}Pu concentration in Table II-12-I has been adjusted for the

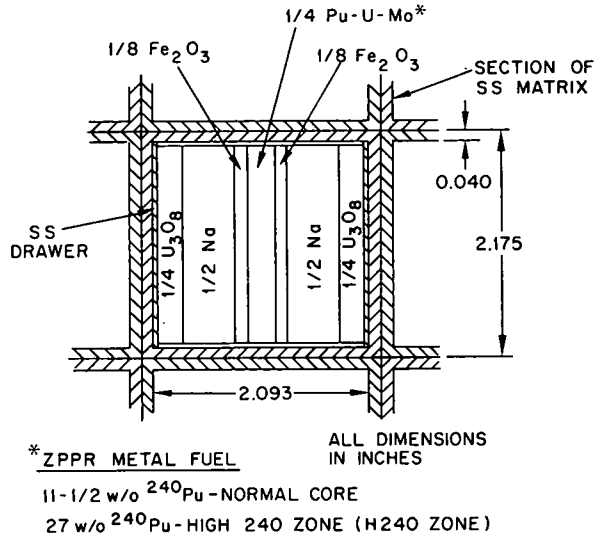

Fig. II-12-1. One-Drawer Unit-Cell Loadings in ZPR-6 Assembly 7. Pu/Al Core Drawers (see Figs. II-12-2 and II-12-3) not shown. They contain a ⅛ in. Pu/Al Fuel Plate (1 w/o Al) and a ⅛ in. Depleted Uranium Plate in Place of the ¼ in. Pu/U/Mo Fuel Plate.) *ANL Neg. No. 116-992.*

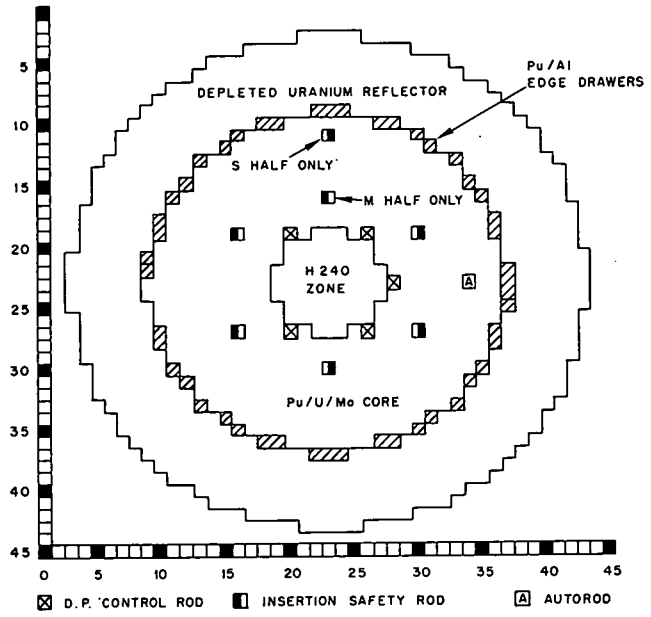

FIG. II-12-2. Radial Cross Section of ZPR-6 Assembly 7 with the H240 Zone. Excess Reactivity of this Core is ~60 Ih. *ANL Neg. No. 116-994.*

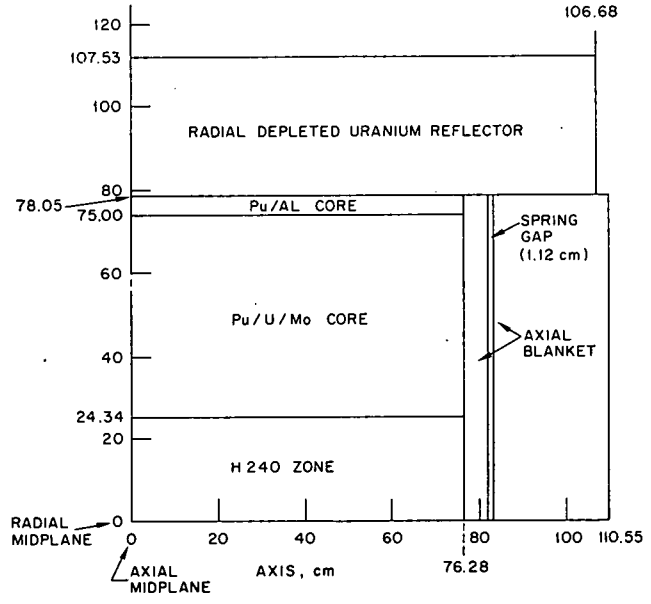

FIG. II-12-3. Axial Cross Section of ZPR-6 Assembly 7 with the H240 Zone. Excess Reactivity of this core is ~60 Ih. *ANL Neg. No. 116-991.*

decay of ^{241}Pu to ^{241}Am from the date of fuel fabrication to 5/1/71, the starting date of the H240 measurements, using a half-life of 13.2 years.

The fertile-to-fissile ratio in both the uniform reference version of Assembly 7 and in the H240 zone is 6.5. In the H240 zone, the increase in ^{240}Pu content is offset by a decrease in ^{238}U content in the fuel plates.

The kinetics parameters of Assembly 7 with the H240 zone are only slightly different from those of the uniform reference version of Assembly 7. The effective delayed neutron fraction, β_{eff}, is 3.20×10^{-3}, and there are 1027 Ih/$\%\Delta k/k$. Compared with the uniform reference version of Assembly 7, β_{eff} has increased by 1%. The small increase in β_{eff} is due to the presence of the higher mass isotopes of plutonium with their associated higher delayed neutron yields per fission.

C. Small Sample Reactivity Worth Measurements

The reactivity worths of several small samples were measured at the center of the H240 zone and radially on the axial midplane of the core. The radial sample changer and fine-autorod system were used for these measurements. A detailed description of the radial sample changer, the fine-autorod, and the technique of reactivity measurement in Assembly 7 is given in Paper II-19.

The results of the measurements at the center of the H240 zone are given in Table II-12-II. Several plutonium samples with varying ^{240}Pu content were measured. For each of the plutonium compositions, at least two samples which differed in weight, were measured; the results of these measurements indicate that the self-shielding effect in these samples is small (<1% in almost every case). Similar results were obtained at the center of the uniform version of Assembly 7 (see Paper II-19).

The ratio of the central worths measured in the H240 zone to those measured in the reference core are given in Table II-12-II. For all samples, the average ratio of specific worths (Ih/kg) is 1.11. The calculated real and adjoint spectra in the reference core and H240 zone differ very little over almost the entire energy range important for most of the reactivity samples. Thus, the average ratio of worths primarily indicates the difference in the perturbation denominator of the reference core and the core with the H240 zone. (See below, Perturbation Denominator, for a complete discussion of this point.)

The measured central worths are compared with calculated central worths in Table II-12-III. The central worths were calculated using first-order perturbation theory and real and adjoint fluxes from a 1-D diffusion calculation. The cross sections used to compute the real and adjoint spectra were generated from ENDF/B-1 cross section data in a heterogeneous MC²[4] run (resonance self-shielding computed for the plate-type unit-cell using equivalence theory) and weighted by the spatial distribution of fluxes within the unit-cell.[5] The spatial distribution of fluxes within the unit-cell was calculated using the CALHET[6] code. The perturbation sample cross sections were taken from a homogeneous MC² run (no spatial resonance self shielding in the unit-cell included).

The calculated-to-experimental (C/E) ratio of central worths, excluding sodium, averages about 1.28. Most of this discrepancy between measured and calculated

TABLE II-12-I. Atom Densities for Assembly 7 with the H-240 Zone,[a] 10^{21} atoms/cc

Region	^{238}Pu	^{239}Pu	^{240}Pu	^{241}Pu[b]	^{242}Pu	^{234}U	^{235}U	^{236}U	^{238}U	^{241}Am[b]	Mo	Na	O[c]	Fe[d]	Ni	Cr	Mn	Al
H-240	0.00114	0.8370	0.3212	0.0593	0.0174	0.00006	0.0122	0.00029	5.585	0.0067	0.2297	9.288	13.84	12.91	1.235	2.701	0.221	
Pu/U/Mo core	0.00049	0.8879	0.1178	0.0146	0.00177	0.00006	0.0126	0.00030	5.802	0.0034	0.2382	9.132	14.82	13.53	1.212	2.697	0.213	
Pu/Al core[e]	<0.0001	1.063	0.0499	0.0049	0.0005	0.00006	0.0126	0.00030	5.717	<0.001	0.242	9.132	14.82	13.15	1.481	2.675	0.21	0.101
Axial blanket[f]						0.00040	0.0834	0.0020	38.59		0.0046[g]		0.030[g]	5.652	0.6910	1.579	0.123	
Radial blanket[f]						0.00040	0.866	0.0020	40.06		0.0034[g]		0.021[g]	4.197	0.5082	1.172	0.0897	

[a] The number of digits in each density is a measure of the compositional precision. Nominally, the right most digit bounds the density according to a 2σ or 93% confidence interval.

[b] $^{241}\text{Pu} \xrightarrow{\beta} {}^{241}\text{Am}$ decay corrected to May 1, 1971.

[c] Includes $\sim 0.001 \times 10^{21}$ atoms/cc due to SS304 and Pu/U/Mo fuel impurities.

[d] Includes $\sim 0.001 \times 10^{21}$ atoms/cc due to heavy (atomic weight $\geq$ Si) SS304 impurities and Pu/U/Mo fuel impurities.

[e] The compositional data available for the Pu/Al plates is not as complete as that for the Pu/U/Mo fuel.

[f] The axial blanket material was loaded into special stainless steel backdrawers. The radial blanket material was loaded directly into the matrix tubes. In addition, the axial blanket atom concentrations include the spring gap materials and volume. (See Fig. II-12-3).

[g] Arising from SS304 impurities.

TABLE II-12-II. SMALL SAMPLE REACTIVITY WORTHS MEASURED AT THE CENTER OF ASSEMBLY 7 WITH THE H240 ZONE

Sample[a]	Sample Ident.[a]	Sample Weight, g	Specific Worth,[b] Ih/kg (1027 Ih/% $\delta k/k$)	Ratio of Measured Worths in H240 Zone To Reference Core[c]
Pu (1 w/o ^{240}Pu)	MB06	3.524	172.1 ± 2.2	1.13
	MB10	9.956	174.2 ± 0.6	1.10
	MB11	21.409	177.1 ± 0.3	1.11
Pu (11.5 w/o ^{240}Pu)	Pu-7	2.706	158.2 ± 1.0	1.09
	Pu-11	15.122	159.7 ± 0.2	1.10
Pu (22 w/o ^{240}Pu)	Pu-13	3.031	142.6 ± 2.1	1.13
	Pu-17	13.939	142.1 ± 0.3	1.11
Pu (45 w/o ^{240}Pu)	Pu-19	3.442	108.0 ± 1.5	1.08
	Pu-23	13.923	108.4 ± 0.2	
Enriched U	U-235(L)	3.084	131.5 ± 2.1	1.10
Depleted U	U-238(L)	25.988	−10.80 ± 0.25	1.14
Ta	Ta(L)	8.697	−64.4 ± 1.1	1.11
Boron (Nat.)	B(L)	0.5553	−633 ± 16	1.11
SS304		43.827	−5.34 ± 0.19	1.09
Na	Na(L2)	17.044	−7.00 ± 0.48	1.13
C	C(L)	33.441	−13.87 ± 0.18	1.09

[a] A complete description of each sample, including dimensions and composition, may be found in Tables II-19-V and II-19-VI.

[b] These values are the net specific worths, i.e.—the worth of stainless steel cladding and sample holders has been accounted for using the measured worth of stainless steel. The uncertainty in each measurement was computed as described in Ref. 3 and includes the uncertainty in each sample measurement and the uncertainty in the stainless steel cladding and holder worth.

[c] The measured values in the regular core were taken from Table II-19-V and are the "central matched plate zone" values.

values is due to the difference between measured and calculated perturbation denominators as indicated in the last column of Table II-12-III where "adjusted" C/E ratios are given. In this column, the calculated worth has been multiplied by the ratio of the calculated-to-measured perturbation denominator. With the exception of sodium, the calculated and measured central worths appear to be in good agreement.

The perturbation denominator was measured as described in Ref. 13. The method involved the measurement of the apparent worth of a ^{252}Cf source at the center of the core and measurements of the fission rate in a unit cell of core material at the center of the core.[8] The ratio of the calculated-to-measured perturbation denominator in Assembly 7 with the H240 zone is 0.78 ± 0.05. This ratio is essentially the same as that obtained for the uniform, reference core of Assembly 7, namely 0.79 ± 0.03.[7]

A discussion of the measurement of the perturbation denominator and the use of this quantity as an aid in the interpretation of reactivity measurements may be found below, in the section entitled Perturbation Denominator.

The reactivity worths of several samples were measured as a function of distance from the center of the core the reactor midplane. The results of the radial reactivity worths are given in Table II-12-IV and are graphically displayed in Figs. II-12-4 through II-12-7. The results of calculated radial worths are also included in Figs. II-12-4 through II-12-7. The calculated worths have been adjusted by the ratio of the calculated-to-measured perturbation denominator (see Perturbation Denominator) and include sample self-shielding factors in the case of the plutonium and boron samples.

Agreement between calculated and measured radial worths appears to be good for the fissile samples (plutonium and uranium) and for boron. For the ^{238}U sample, the shape is well represented by the calculated curve, but the calculated worth is consistently greater (more negative) than the measured value. A sample self-shielding factor has not been included in the calculated ^{238}U sample worth.

Agreement between calculated and measured radial worths for the scattering materials (sodium and stainless steel) is not good, especially in the case of sodium. For scattering materials, the spectral component of the calculated reactivity worth is important. The spectral component of reactivity is sensitive to the difference between calculated group adjoint fluxes. Thus, for sodium and stainless steel, small errors in the calculated spatial distribution of adjoint group fluxes may be reflected in significant disagreement between calculated and measured radial reactivity worths.

D. CENTRAL REGION SODIUM VOID WORTH

Sodium was voided from a small region at the center of the H240 zone. The voided region included the first six inches of the central nine drawers (3x3 drawer array) in each reactor half. The two ½ in. sodium filled cans

in each of these drawers (see Fig. II-12-1) were replaced with empty stainless steel cans.

The total excess reactivity of the core was measured before and after the sodium voiding. The excess reactivity measurements have been corrected with the measured temperature coefficient of reactivity (3.23 ± 0.1) Ih/°C and ^{241}Pu decay coefficient of reactivity (0.62 ± 0.08)Ih/day characteristic of Assembly 7 with the H240 zone. An uncertainty in the separation of the reactor table halves ("table closure") of ± 2 Ih was assumed. (A complete description of the technique employed in this type of reactivity measurement may be found in Paper II-19.)

The results of the sodium-voiding measurement are summarized in Table II-12-V. The sodium void worth in the central region of the H240 zone was found to be (6.24 ± 0.9)Ih/kg of sodium. This result includes a small correction (~0.01 Ih) to account for the slight mismatch in the amount of stainless steel between the sodium filled and empty stainless steel cans. The measured worth of stainless steel in the sodium-voided high ^{240}Pu zone was used (see Paper II-13).

Also included in Table II-12-V is a summary of the central small-region sodium void measurement in the regular uniform reference version of Assembly 7 (see Paper II-19). The region of voiding is exactly the same as that described above. The sodium void worth is (6.94 ± 0.6)Ih/kg at the center of the uniform reference core.

The ratio of the central small-region sodium-vo measurement in the H240 zone of Assembly 7 to tl same measurement in the uniform version of Assembly 7 is 0.90 ± 0.15. When the correction for the perturbation denominator ratio is applied, this ratio becomes

TABLE II-12-III. Comparison of Measured and Calculated Small Sample Reactivity Worths at the Center of Assembly 7 with the H240 Zone

Sample	Measured Specific Worth, Ih/kg (1027 Ih/% $\delta k/k$)	Calculated Worth,[a] Ih/kg	C/E	Adjusted C/E[b]
^{239}Pu	177.7 ± 2.2[c]	229.5[d]	1.29	1.01
^{235}U	141.7 ± 2.1[e]	188.7	1.33	1.04
^{238}U	−11.12 ± 0.25[e]	−14.85	1.34	1.05
Ta	−64.4 ± 1.1	−79.28	1.23	0.96
^{10}B	−3184 ± 80	−3873[f]	1.22	0.95
SS304	−5.34 ± 0.19	−6.82	1.28	1.00
Na	−7.00 ± 0.48	−7.26	1.04	0.81
C	−13.87 ± 0.18	−17.85	1.29	1.01

[a] 1-D diffusion theory, first-order perturbation calculations using homogeneous cross sections for the samples; i.e., cross sections from a homogeneous MC² run.

[b] C/E values have been multiplied by 0.78, the ratio of the calculated-to-measured perturbation denominator.

[c] This value was deduced by correcting the measured Pu (1 w/o ^{240}Pu) worth of sample MB-10 with a calculated ^{240}Pu worth.

[d] A small experimentally determined self-shielding factor (1.03) has been included in this value.

[e] This value was deduced by comparing the measured worths for enriched and depleted uranium.

[f] A small experimentally determined self-shielding factor (0.98) has been included in this value.

TABLE II-12-IV. Small Sample Radial Reactivity Worth Traverses in Assembly 7 with the H240 Zone

Sample[a]	Sample Ident.[a]	Sample Weight, g	Radius,[b] cm	Specific Worth,[c] Ih/kg (1027 Ih/% $\delta k/k$)
Pu (1 w/o ^{240}Pu)	MB10	9.956	0	174.2 ± 0.6
			11.0	167.7 ± 0.4
			22.1	149.7 ± 0.3
			33.1	118.9 ± 0.4
			49.7	70.1 ± 1.0
Enriched U	U-235(L)	3.084	0	131.5 ± 2.1
			11.0	124.4 ± 1.4
			22.1	109.3 ± 0.6
			33.1	88.7 ± 1.3
			49.7	57.7 ± 3.6
Depleted U	U-238(L)	25.988	0	−10.80 ± 0.25
			11.0	−9.84 ± 0.13
			22.1	−8.21 ± 0.18
			33.1	−6.70 ± 0.22
			49.7	−2.48 ± 0.40
Boron (Nat)	B(L)	0.5553	0	−633 ± 16
			11.0	−604 ± 10
			22.1	−527 ± 7
			33.1	−410 ± 8
			49.7	−270 ± 22
NA	NA(L2)	17.044	0	−7.00 ± 0.48
			11.0	−6.19 ± 0.52
			22.1	−3.46 ± 0.37
			33.1	−1.08 ± 0.17
			49.7	+2.81 ± 0.91
SS304		43.83	0	−5.34 ± 0.19
			11.0	−4.94 ± 0.07
			22.1	−3.75 ± 0.02
			33.1	−2.08 ± 0.03
			49.7	+0.26 ± 0.21

[a] A complete description of each sample, including dimensions and composition, may be found in Tables II-19-V and II-19-VI.

[b] Distance from the center of the core along the axial midplane of the core.

[c] These values are the net specific worths; i.e., the worth of stainless steel cladding and sample holders has been accounted for using the measured worth of stainless steel at each radial point. The uncertainty in each measurement was computed as described in Ref. 3 and includes the uncertainty in each sample measurement and the uncertainty in the stainless steel cladding and holder worth.

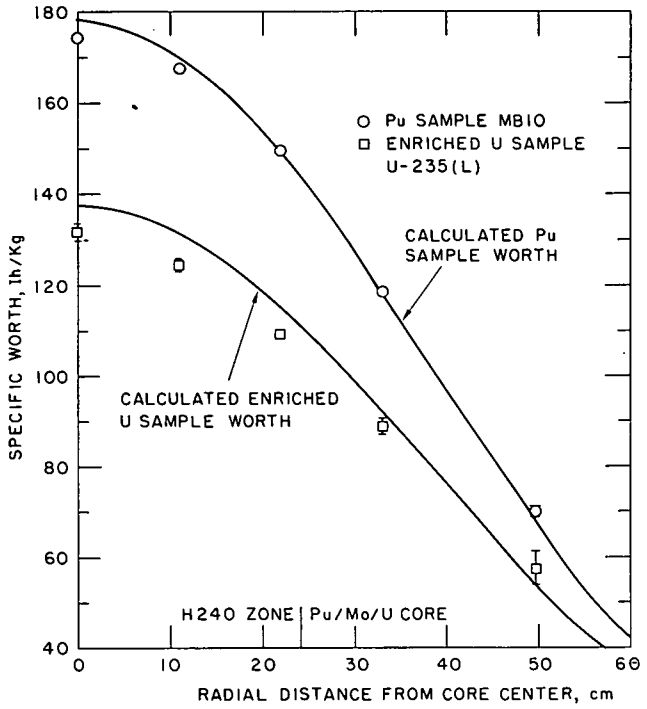

FIG. II-12-4. Radial Reactivity Traverse in ZPR-6 Assembly 7 with the H240 Zone. *ANL Neg. No. 116-995.*

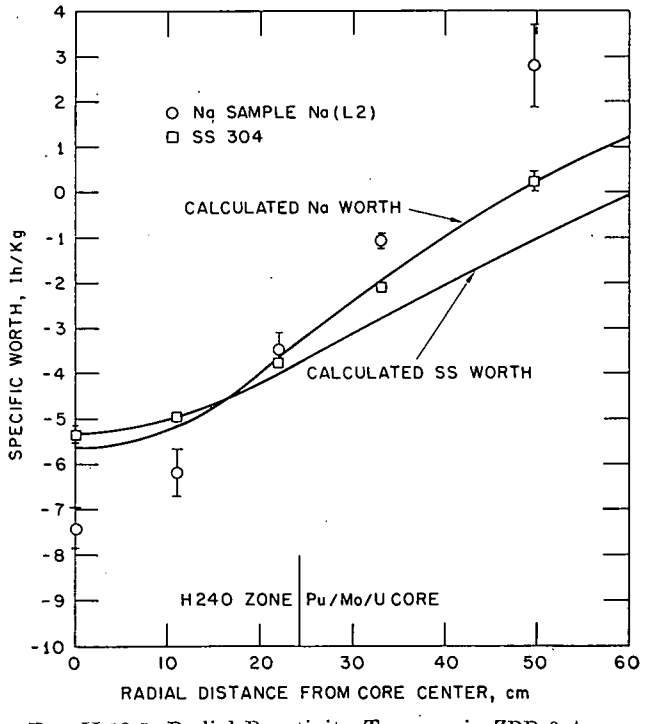

FIG. II-12-5. Radial Reactivity Traverse in ZPR-6 Assembly 7 with the H240 Zone. *ANL Neg. No. 116-998.*

0.80 ± 0.13 (see Eq. 5 of Perturbation Denominator). The ratio of the central small-sample sodium worth in the H240 zone to the same measurement in the uniform version of Assembly 7 (see Table II-12-II) is 1.13 ± 0.10, and this ratio, corrected for the perturbation denominator is 1.01 ± 0.09. The results of the central small-region sodium void worth measurements and the central small sample sodium worth measurements do not disagree by virtue of the rather large uncertainties in the measurements.

The small-region sodium worth of −6.24 ± 0.9 and the small-sample sodium worth of −7.00 ± 0.48 in the H240 zone are also in agreement in the sense that they have overlapping uncertainties. Agreement between these two values is not necessarily expected, however, since there are significant heterogeneity differences between the two measurements.

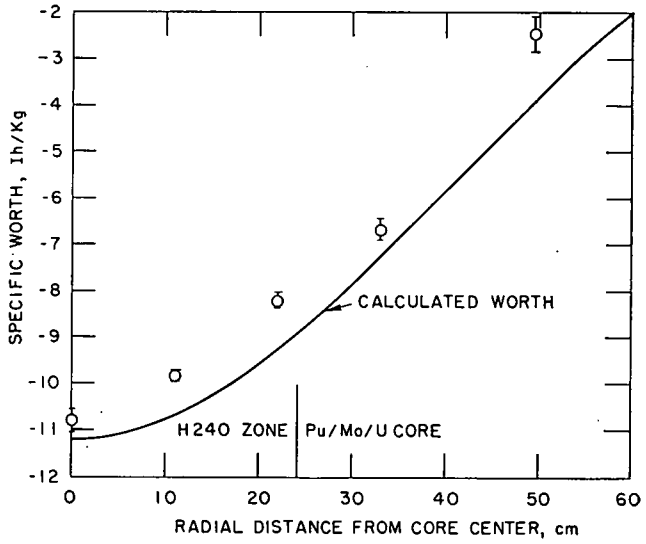

FIG. II-12-6. Depleted Uranium Radial Reactivity Traverse in ZPR-6 Assembly 7 with the H240 Zone. *ANL Neg. No. 116-993.*

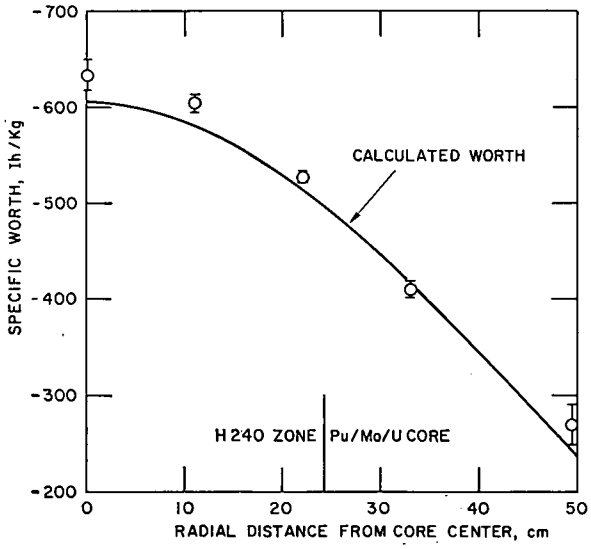

FIG. II-12-7. Boron Radial Reactivity Traverse in ZPR-6 Assembly 7 with the H240 Zone, Sample B(L), Natural Boron. *ANL Neg. No. 116-996.*

TABLE II-12-V. CENTRAL REGION SODIUM VOID WORTHS

Core Environment	Dimension of Core Region which was Voided of Sodium, in.	Amount of Sodium Voided, kg	Net Change in Stainless Steel, kg	Measured Reactivity Change Relative to Sodium Filled Region, Ih	Sodium Void Coefficient[a] Ih/kg
Assembly 7 with the H240 zone[b]	6.52 x 6.52 x 12.0 (This region includes the first six inches of the central nine drawers in each reactor half; S/M 22-22, 22-23, 22-24, 23-22, 23-23, 23-24, 24-22, 24-23, 24-24)	2.972 ± 0.014	+0.009	+18.5 ± 2.7	6.24 ± 0.90
Uniform Reference Version of Assembly 7[c]	(Same as above)	2.972 ± 0.014	+0.004	+20.6 ± 1.8	6.94 ± 0.60

[a] A small correction to account for the slight mismatch in the amount of stainless steel between the sodium filled and empty stainless steel cans is included in these results.

[b] 1% $\Delta k/k$ = 1027 Ih, $\beta_{eff} = 3.20 \times 10^{-3}$.

[c] 1% $\Delta k/k$ = 1033 Ih, $\beta_{eff} = 3.18 \times 10^{-3}$. The results here have been taken from Table II-19-II.

E. ^{238}U Doppler Worth Measurement

The ^{238}U Doppler reactivity worth was measured at the center of the H240 zone. A sample of natural uranium oxide was heated to temperatures ranging from room temperature to 1050°K. The change in the reactivity worth of the sample with a change in the temperature of the sample was measured using the Doppler oscillator equipment and a calibrated autorod. A description of the Doppler measurement technique and references pertaining to the subject are given in Paper II-21. The UO_2 Doppler sample NI containing 1108.88 g of ^{238}U and 7.99 g of ^{235}U was used. It is a freely expanding sample, 1 in. in diam and 12 in. long. The experimental results are given in Table II-12-VI. The reactivity worths have been corrected for the small (<1%) differential nonlinearity of the fine autorod.[6] The uncertainty in the reactivity worths at each temperature reported in Table II-12-VI includes only the uncertainty in the average difference between "sample-in" and "sample-out" autorod integrations at each temperature.

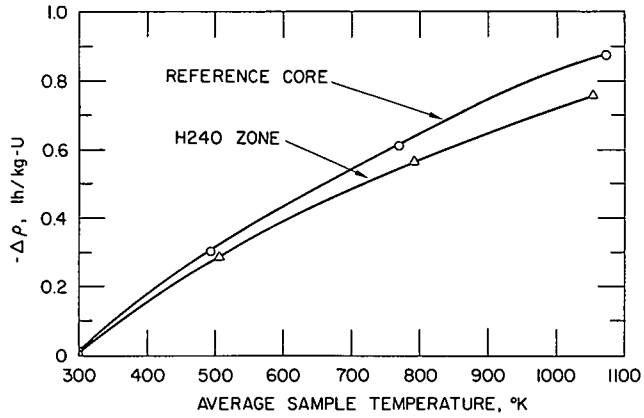

FIG. II-12-8. ^{238}U Doppler Worth Measured at the Center of the Uniform Reference Version of ZPR-6 Assembly 7 and ZPR-6 Assembly 7 with the H240 Zone. *ANL Neg. No. 900-1224 Rev. 1.*

TABLE II-12-VI. CENTRAL DOPPLER REACTIVITY WORTHS FOR NATURAL URANIUM OXIDE MEASURED IN ZPR-6 ASSEMBLY 7 AND IN THE H240 ZONE IN ASSEMBLY 7

Uniform, Reference Version of ZPR-6 Assembly 7[a]		H240 Zone in ZPR-6 Assembly 7[b]	
Temperature,[c] °K	Reactivity Worth,[d] Ih/kg of U	Temperature,[c] °K	Reactivity Worth,[d] Ih/kg of U
293	0 ± 0.010	297	0 ± 0.003
494	−0.300 ± 0.003	507	−0.323 ± 0.003
771	−0.608 ± 0.002	792	−0.643 ± 0.006
1075	−0.871 ± 0.009	1054	−0.860 ± 0.003

[a] 1% $\Delta k/k$ = 1033 Ih, $\beta_{eff} = 3.18 \times 10^{-3}$. The results here have been taken from Table II-21-II.

[b] 1% $\Delta k/k$ = 1027 Ih, $\beta_{eff} = 3.20 \times 10^{-3}$.

[c] The temperature reported here is the average of the five thermocouples located along the length of the sample. There is a 1% uncertainty in the average temperature.

[d] The uncertainty in the change in reactivity worth at each temperature includes only the uncertainty in the average difference between "sample-in" and "sample-out" autorod integration at each temperature.

Also included in Table II-12-VI are the results of the ^{238}U Doppler measurement, using the same Doppler sample, NI, at the center of the uniform, reference version of Assembly 7 (see Paper II-21). The Doppler worths measured in both cores are displayed in Fig. II-12-8 where the measurements in the H240 zone have been normalized (adjusted with the ratio of perturbation denominators) to the measurements in the uniform reference core. The ^{238}U Doppler worth is approximately 12% less in the H240 zone along the entire range of temperatures. This result is an indication of the small amount of spectral hardening in the H240 zone in the region of the ^{238}U Doppler resonances (below 10 keV).

TABLE II-12-VII. Fission Rate Ratios in the H240 Zone of ZPR-6 Assembly 7

Fission Foil	Detector Drawer Location,[a] Row-Col.	Measured Fission Rate Relative to ^{239}Pu[b]	Calculated Fission Rate Relative to ^{239}Pu
^{239}Pu	M25-22	1.00	
^{240}Pu	M24-25	0.1930 ± 0.0024	0.1914
^{238}U	M21-24	0.0236 ± 0.00058	0.0230
^{235}U	M22-21	1.0308 ± 0.0243	1.150

[a] All drawer locations are such that the fission foil is located 12.35 cm radially from the center of the core.

[b] Uncertainties include the uncertainties in weights of isotopes on the foils, count rates, and the fission fragment low energy spectrum cut-off loss. The fission ratios are given here as ratios of the measured fission rates per atom of fissile isotope.

F. Fission Rate Ratios and Traverses

Fission rates in ^{239}Pu, ^{240}Pu, ^{241}Pu, ^{235}U, and ^{238}U were measured near the center of the core with four thin-walled Kirn-type fission flow counters.[10] Each counter contained a foil with a thin (~20 $\mu g/cm^2$) deposit of the fissioning isotope. The detectors were placed near the center of the core in the H240 zone. The detectors were loaded into fuel drawers in a two inch cavity six inches back from the axial reactor midplane so that the fission foil was located 18.1 cm from the drawer front (axial reactor midplane) and 12.4 cm radially from the center of the core. The location of fuel drawers containing detectors is given in Table II-12-VII. The fission ratios, measured relative to the ^{239}Pu fission rate, are also given in Table II-12-VII. (The results of the ^{241}Pu measurement have not yet been analyzed.) In forming the ratios in Table II-12-VII, complete symmetry of flux has been assumed; i.e., the neutron flux is assumed to be the same at each detector location.

The fission ratios have been corrected for the fission fragment low-energy spectrum cut-off and for contributions to the measured fission rates from other fissioning isotopes present on the foil deposit. The fission ratios given in Table II-12-VII are ratios of the measured fission rates per atom of fissile isotope. The weights of the fissile isotopes present on each foil were determined as described in Ref. 11, using an α-counting technique.

Also included in Table II-12-VII are the results of calculated fission ratios. The method of calculation is as described in Section C. The cross sections for the fissile isotopes on the foils were taken from a homogeneous MC² run. The agreement between measured and culated fission ratios appears to be good for the $^{?}Pu/^{239}Pu$ and $^{238}U/^{239}Pu$ fission ratios but the $^{235}U/^{239}Pu$ fission ratio is calculated 11 % too high. This type of comparison between calculated and measured fission ratios could be a result of calculating the high energy flux (>0.2 MeV) too low, or, in part, a result of poor ^{235}U fission cross section data.

In addition to the ratios near the center of the core, radial fission rate traverses were obtained for ^{239}Pu, ^{235}U, and ^{238}U. A small (~1 in. diam.) fission flow-counter was inserted into the sample tube of the radial sample changer.[12] The radial sample changer was positioned such that the sample tube extended radially along row 23 from the core center to the outside edge of the radial blanket at the reactor midplane (see Paper II-19 for a description of the radial sample changer as it was used in Assembly 7). The fission detector was positioned at several locations along the core radius, and the fission rate was recorded at each location. The results are shown in Figs. II-12-9 through II-12-11.

All fission foils contained thin (~20 $\mu g/cm^2$) deposits of the fissioning material. The compositions of the foil deposits were as follows:[13] ^{235}U foil—0.6646 μg ^{234}U, 63.265 μg ^{235}U, 0.275 μg ^{236}U, and 0.068 μg ^{238}U; ^{239}Pu foil—57.467 μg ^{239}Pu, 0.588 μg ^{240}Pu, and 0.029 μg ^{241}Pu; ^{238}U foil—78.585 μg ^{238}U and 0.011 μg ^{235}U.

The fission count obtained at each radial position was corrected for the fission fragment low-energy spectrum loss. The correction factors, which are dependent upon the radial location of the detector, were determined by recording fission fragment spectra at several radial locations.

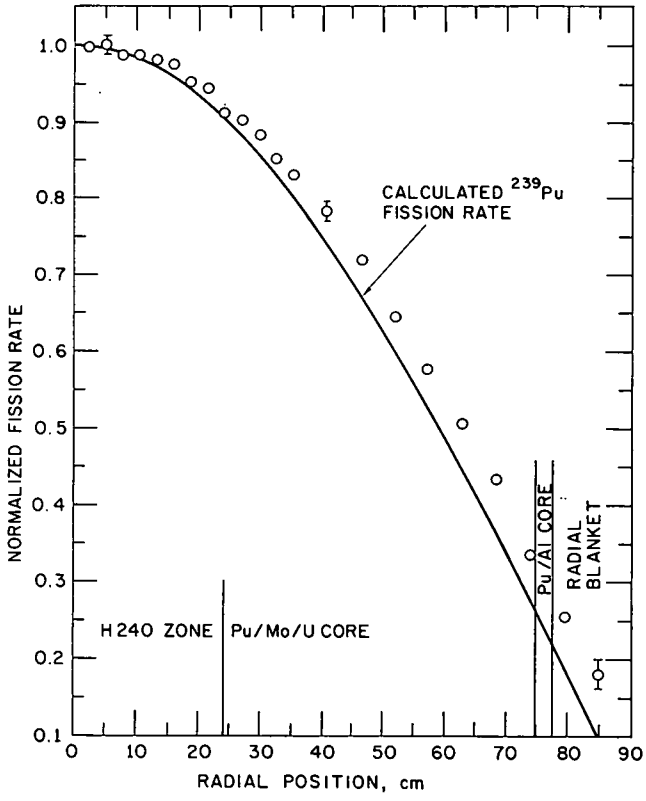

Fig. II-12-9. ^{239}Pu Fission Rate Traverse in ZPR-6 Assembly 7 with the H240 Zone. *ANL Neg. No. 116-987.*

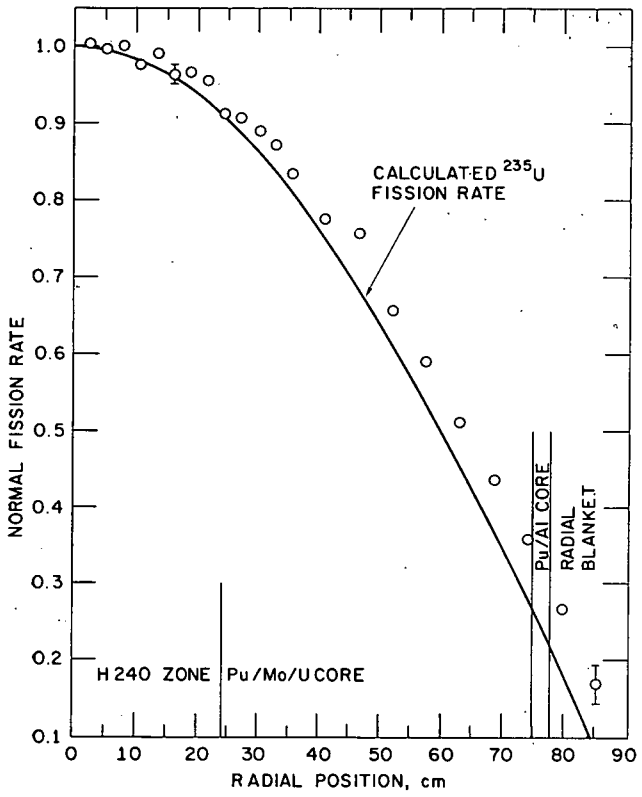

FIG. II-12-10. ^{235}U Fission Rate Traverse in ZPR-6 Assembly 7 with the H240 Zone. *ANL Neg. No. 116-990.*

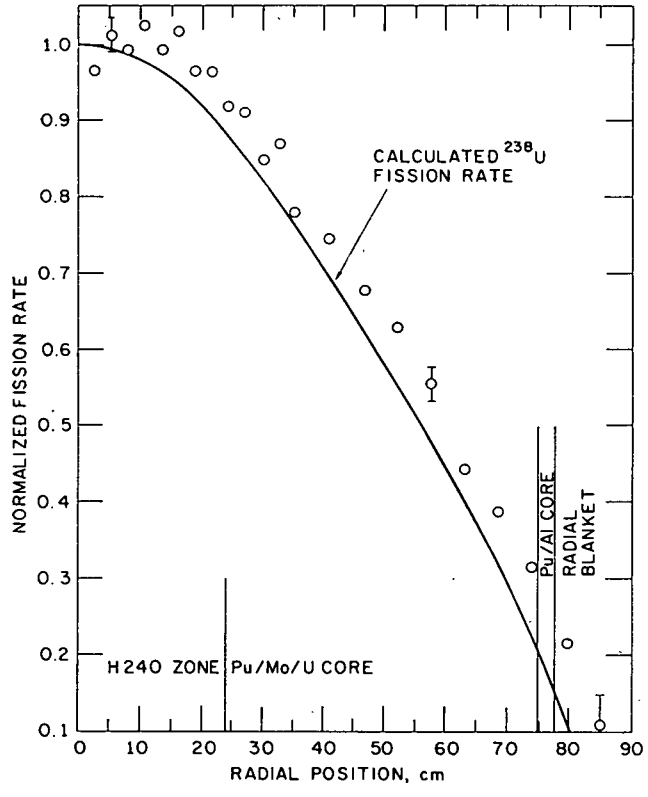

FIG. II-12-11. ^{238}U Fission Rate in ZPR-6 Assembly 7 with the H240 Zone. *ANL Neg. No. 116-999.*

Included in Figs. II-12-9 through II-12-11 are the results of calculated relative radial fission rates obtained as described above for the fission ratios. The calculated fission rates have been normalized to the measured rates near the center of the core. In each case, the calculated fission rate distribution exhibits a greater flux gradient than the measured fission rates.

The scattering of the ^{238}U fission rates (Fig. II-12-11) near the center of the core is due to the unit-cell heterogeneity effects because the fission chamber is located, alternately, near a U_3O_8 plate and near a fuel plate.

G. Perturbation Denominator

The perturbation denominator was measured as described in Ref. 7. The method involved the measurement of the apparent worth of a ^{252}Cf source at the center of the core and measurements of the fission rate in a unit cell of core material at the core center.[8] The perturbation denominator measurements are made primarily for the purpose of adjusting other measured and calculated worth values so that more meaningful comparisons can be made, as discussed below. This discussion is, of course, based on a first-order perturbation theory model.

Comparison of Measured and Calculated Central Sample Worths

A discrepancy between measured and calculated central worths may be due to several different causes, such as incorrect effective sample cross sections, inaccurate calculated real and adjoint flux spectra at the sample location, an incorrect calculation of perturbation denominator, incorrect values of β_{eff}, or experimental error. An adjusted calculated worth, ρ_{AC}, can be defined as

$$\rho_{AC} = \rho_c \frac{PD_c}{PD_m}, \qquad (1)$$

where ρ_c is the calculated worth and PD_c and PD_m are the calculated and measured centrally normalized perturbation denominators. A discrepancy between the measured and adjusted calculated central worths cannot be caused by either an incorrect perturbation denominator calculation or by incorrect β_{eff} values, since these causes are eliminated when the calculation is adjusted, as will be discussed below. Therefore, a discrepancy between an adjusted calculated worth and a correct measured worth must be due either to the effective sample cross sections or to the calculated real and adjoint fluxes at the sample location; that is, the discrepancy must be due to the calculated perturba
numerator.

The elimination of the perturbation denominator and the β_{eff} values as causes for discrepancies between the measured and adjusted-calculated worths can be shown

as follows. The measured perturbation denominator, PD_m, is inversely proportional to the measured apparent worth of a ^{252}Cf source;[7] that is

$$PD_m = \frac{C}{\sum \frac{\beta_i}{1 + \lambda_i T_{Cf}}}, \quad (2)$$

where the β_i are the delayed neutron fractions and T_{Cf} is the reactor period associated with the apparent reactivity due to the insertion of the ^{252}Cf source into the critical reactor. The constant, C, is a function of only material properties at the exact location where the source is inserted, primarily the source strength and the local core fission rate.

The measured sample worth, ρ_s, can also be written in terms of its associated reactor period, T_s, as follows:

$$\rho_s = \sum_i \frac{\beta_i}{1 + \lambda_i T_s}. \quad (3)$$

If equations (1), (2), and (3) are combined, an expression for the ratio of the adjusted calculated worth to the measured worth is obtained:

$$\frac{\rho_{AC}}{\rho_s} = \frac{PN_c}{C} \frac{\sum_i \frac{\beta_i}{1 + \lambda_i T_{Cf}}}{\sum_i \frac{\beta_i}{1 + \lambda_i T_s}}. \quad (4)$$

where the calculated perturbation numerator, PN_c, has been substituted for the product $\rho_c \cdot PD_c$. It can be seen that the ratio, ρ_{AC}/ρ_s, is independent of the calculated perturbation denominator. Equation (4) is also essentially independent of the β_is for the range of reactivities used in these measurements. The ratio is dependent only on the calculated local perturbation numerator and measured quantities. This statement must be qualified somewhat since the constant C does contain a small local calculated correction, but its effect is insignificant.

COMPARISON OF WORTH MEASUREMENTS MADE IN DIFFERENT CORES

When the central worth of a given sample is measured in two different cores its worth value will, in general, change. The change may be due entirely or in part to any of the following causes:

a. Change in the local real and adjoint flux spectra,
b. Change in the effective sample cross section due to flux changes in heterogeneity,
c. Change in the normalization of the measurement as manifested by a change in the perturbation denominator,
d. Experimental errors.

Items a and b together constitute a change in the perturbation numerator, and it is the change in this quantity that is usually of interest. It is possible to separate the perturbation numerator change from the total worth change if the ratio of the centrally normalized perturbation denominators for the two cores is measured. The result, which is listed here as the perturbation numerator ratio, PN_m^1/PN_m^2, for cores 1 and 2, is

$$\frac{PN_m^1}{PN_m^2} = \frac{\rho_1}{\rho_2} \frac{PD_m^1}{PD_m^2}, \quad (5)$$

where the ρ_i are the measured worths and the PD_m are the measured perturbation denominators. It is of course assumed that the worth changes are not due to experimental errors (item d). The perturbation numerator ratio, measured indirectly as indicated by Eq. (5), is therefore a function only of the local fluxes and adjoints and the effective sample cross sections.

APPLICATION OF PD MEASUREMENTS TO H240 CORE WORTH RESULTS

For Assembly 7 with the H240 zone the ratio of the calculated-to-measured perturbation denominators was 0.78 ± 0.05. For the uniform version of Assembly 7 the calculated-to-measured perturbation denominator ratio was 0.79 ± 0.03 (see Ref. 7). These results are utilized elsewhere in this paper when comparing the measured central worths, sodium-void coefficients and Doppler worths with the corresponding calculations.

The ratio of the measured perturbation denominator in the reference uniform version of Assembly 7 to that for Assembly 7 with the H240 zone was 1.13 ± 0.05. Therefore, the worth of a sample measured at the center of the H240 zone should be 13% greater than the worth of the same sample measured at the center of the uniform version of Assembly 7, provided of course that the perturbation numerators are the same for the two cases.

The average of the measured central small-sample worths, ρ_{H240}/ρ_{REF}, is 1.12 when expressed in δk units. (This value was obtained from the ratio 1.11 listed in Section C, for the worths expressed in inhour units.) The good agreement between the average of the small-sample worth ratios and the perturbation denominator ratio is evidence of two things. First, the average of the worth ratios gives a good indication of the perturbation denominator ratio for two assemblies in which the spectra are not too different. Second, the change in the average of the worths, and also in most of the individual worths as indicated in Table II-12-II, is due almost entirely to the change in the perturbation denominators. These two conclusions are, of course, not independent of each other.

REFERENCES

1. C. E. Till and W. G. Davey, *The Demonstration Reactor Benchmark Critical Assemblies Program*, Trans. Am. Nucl. Soc. **13**, 293 (1970).

2. W. Y. Kato et al., *Final Safety Analysis Report on the Use of Plutonium in ZPR-6 and -9*, ANL-7442 (1970).
3. E. F. Bennett and R. L. Long, *Precision Limitation in the Measurement of Small Reactivity Changes*, Nucl. Sci. Eng. **17**, 425–432 (1963).
4. B. J. Toppel, A. L. Rago and D. M. O'Shea, *MC²*, *A Code to Calculate Multigroup Cross Sections*, ANL-7318 (1967).
5. A. R. Olson and N. C. Paik, *Heterogeneity and Criticality Studies on the Zero Power Plutonium Reactor (ZPPR) Assembly 2, a Demonstration Reactor Benchmark Critical*, Applied Physics Division Annual Report, July 1, 1969, to June 30, 1970, ANL-7710, pp. 146-155.
6. F. L. Fillmore and B. D. Felten, *The CALHET Heterogeneous Perturbation Theory Code and Application to ZPR-3-48*, AI-67-91 (1967).
7. L. G. LeSage, *Measurement of the Perturbation Denominator for ZPR-6 Assembly 7*, Reactor Development Program Progress Report, ANL-7825, pp. 7.4–7.6 (1971).
8. R. A. Karam, *Measurement of Normalization Integral and Spatial Distribution of the Importance of Fission Neutrons*, Nucl. Sci. Eng. **37**, 192 (1969).
9. L. G. LeSage, C. E. Till and G. S. Stanford, *Comparison of Measured and Calculated Null Compositions, Central Reaction Ratios, and Reactivity Worths in ZPR-9 Assemblies 24 and 25 and ZPR-3 Assembly 55*, Trans. Am. Nucl. Soc. **13**, 93 (1970).
10. F. S. Kirn, *Neutron Detectors with an Absolute Fission Counter*, Proc. IAEA Symposium on Neutron Detection, Dosimetry and Standardization, Harwell, England (1962), IAEA2, p. 247.
11. R. J. Armani, *Absolute Determination of Fission Rates in 235-U and 238-U and Capture Rates in 238-U by Radiochemical Techniques*, Proc. IAEA Symposium on the Standardization of Radionuclides, 1967, Vienna.
12. A. B. Long and C. D. Swanson, *Measured Reaction Rate Distributions in ZPR-9 Assembly 26, FTR-3*, Applied Physics Division Annual Report, July 1, 1969, to June 30, 1970, ANL-7710 pp. 65–70.
13. R. J. Armani, Argonne National Laboratory (private communication).

II-13. Measurements in the Sodium-Voided, High-240 Plutonium Zone of ZPR-6 Assembly 7

E. M. Bohn, J. E. Marshall and J. F. Meyer

A. Introduction

The sodium-voided high-240 plutonium (VH240) zone was constructed in ZPR-6 Assembly 7 by removing sodium from a central region of the high-240 plutonium (H240) zone. A description of the H240 zone in Assembly 7 and the results of measurements in the H240 zone are given in Paper II-12. The program of experiments in the VH240 zone consisted of three measurements: reactivity worth of voiding sodium from the H240 zone, small-sample central worth, and the ^{238}U Doppler reactivity worth.

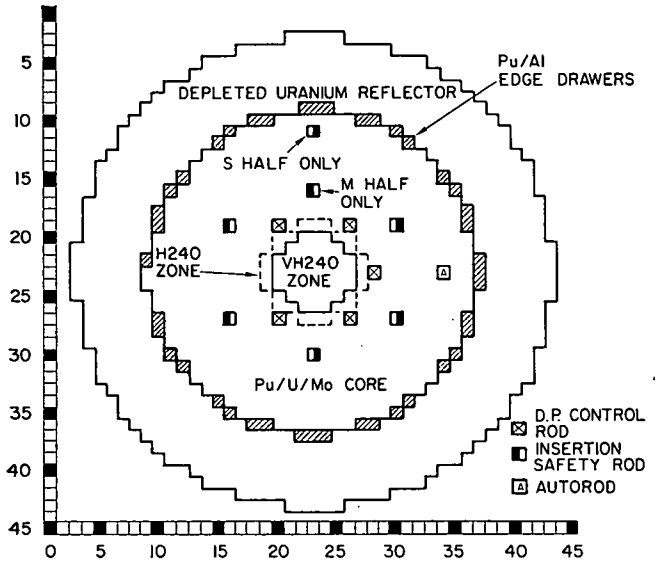

Fig. II-13-1. Radial Cross Section of ZPR-6 Assembly 7 with the VH240 Zone. Excess Reactivity of this Core is ~75 Ih. *ANL Neg. No. 900-1227.*

The sodium-void worth and ^{238}U Doppler worth are of primary concern in the study of liquid metal (sodium) fast breeder reactors. The behavior of the ^{238}U Doppler worth in a sodium voided environment is especially important for the study of loss-of-coolant conditions in an LMFBR.

The small-sample central worth measurements characterize the environment of the VH240 zone in terms of the real and adjoint neutron flux spectra and are therefore useful as calculational and cross section tests.

B. Description of the VH240 Zone in Assembly 7

The sodium-voided high-240 plutonium zone (VH240) was constructed by removing sodium from the H240 zone along the entire height of the core in a central region out to a radius of 19 cm. Radial and axial cross sections of Assembly 7 with the VH240 zone are shown in Figs. II-13-1 and II-13-2.

The removal of sodium from the central region was accomplished by replacing the two columns of ½ in. thick sodium-filled stainless steel cans in each drawer (see Fig. II-12-1) with empty stainless steel cans. The atom concentrations in each region of Assembly 7 with the VH240 zone were the same as those given in Table

II-12-I, except that in the VH240 zone the concentration of sodium was zero (i.e., the atom concentrations of all materials except sodium were the same in the VH240 and H240 regions).

The kinetics parameter of Assembly 7 with the VH240 zone have changed very little compared with the core containing the H240 zone. The effective delayed neutron fraction is calculated to be 3.21×10^{-3} and the calculated inhours per percent reactivity conversion factor is 1026 Ih/% $\Delta k/k$.

The size of the VH240 zone was made as large as was practicable; however, from a physics standpoint, the flux spectrum was not exactly representative of a completely asymptotic sodium-voided spectrum. Reactivity worth calculations for samples at the center of the VH240 zone and at the center of a hypothetical fully sodium-voided core may be compared to estimate the degree that the flux at the center of the VH240 zone approaches the asymptotic flux. The worth of sodium at the center of the VH240 zone is calculated to be 13% different from its worth at the center of a fully sodium-voided core. Similarly, the worths of ^{239}Pu and ^{10}B are calculated to be 3 and 8% different from their worths at the center of a fully sodium-voided core. The ^{238}U Doppler worth is computed to be 30% greater than the worth in a fully voided core. The ratio of the fission rate in ^{238}U to that in ^{239}Pu is predicted to be 2% less in the VH240 zone.

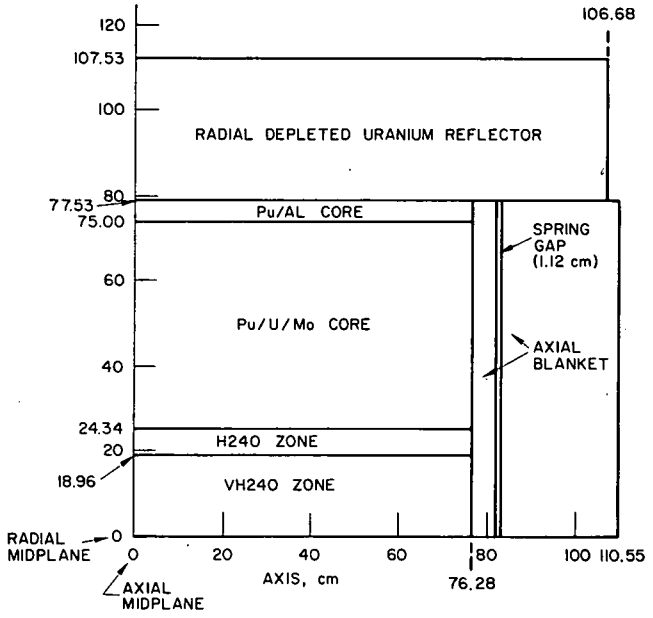

FIG. II-13-2. Axial Cross Section of ZPR-6 Assembly 7 with VH240 Zone. Excess Reactivity of this Core is ~75 Ih. *ANL Neg. No. 900-1216 Rev. 1.*

C. Sodium Voiding Measurements

The reactivity worth of voiding sodium from the central regions of the H240 zone was measured during the transformation of the H240 zone to the VH240 zone. The central portion of the H240 zone was voided of sodium in two steps. The excess reactivity of the core was determined before and after each step. (A complete discussion of the measurement technique may be found in Paper II-19. The results of these two measurements, along with the results of the central small-region sodium voiding measurement reported in Paper II-12, are summarized in Table II-13-I and Fig. II-13-3.

In Fig. II-13-3, a one-quarter axial cross section of the core is shown with the regions that were voided of sodium during each measurement. In region 1, sodium was voided from the first six inches of each of the drawers in the central nine drawers (3 x 3 drawer array) of each reactor half. The resulting sodium-void coefficient is $+6.24 \pm 0.91$ Ih/kg.

During the second sodium-voiding measurement,

TABLE II-13-I. Worth of Sodium Voiding in the H240 Zone

Regions Voided of Sodium (see Fig. II-13-3)	Number of Drawers Voided per One-Half Zone	Depth of Void in Drawer (from midplane),[a] in.	Amount of Sodium Voided, kg	Net Change in Stainless Steel, kg	Measured Reactivity Change Relative to Full H240 Zone,[b] Ih	Measured Na-Void Coefficient,[c] Ih/kg	Calculated Na-Void Coefficient, Ih/kg
Region 1	9	6	2.972 ± 0.014	+0.009	18.5 ± 2.7	6.24 ± 0.91[d]	6.68[e]
Regions 1 and 2	9	30	14.860 ± 0.070	+0.043	35.6 ± 6.9	2.67 ± 0.44	2.76[f]
Regions 1, 2, and 3	37	30	59.44 ± 0.27	+0.170	155.0 ± 7.1	2.62 ± 0.12	

[a] The core half-height is 30.032 in. and the inside length of one drawer is 30 in. Thus, 30 in. sodium voiding in each half represents full core height voiding.

[b] Uncertainty in each measurement reported here includes uncertainties in control rod calibrations, table closure, temperature and ^{241}Pu decay corrections.

[c] The net change in stainless steel has been accounted for in this result. The experimental value for stainless steel worth from Table II-13-II was used.

[d] This result is taken from Table II-12-V.

[e] 1-D diffusion theory, first-order perturbation calculation using the w/Na cross sections in region 1.

[f] Calculation based on the difference between the calculated k of Assembly 7 with the H240 zone and the k of the same core with sodium voided from regions 1 and 2 in Fig. II-13-3. The w/o Na cross sections were used in the voided zone.

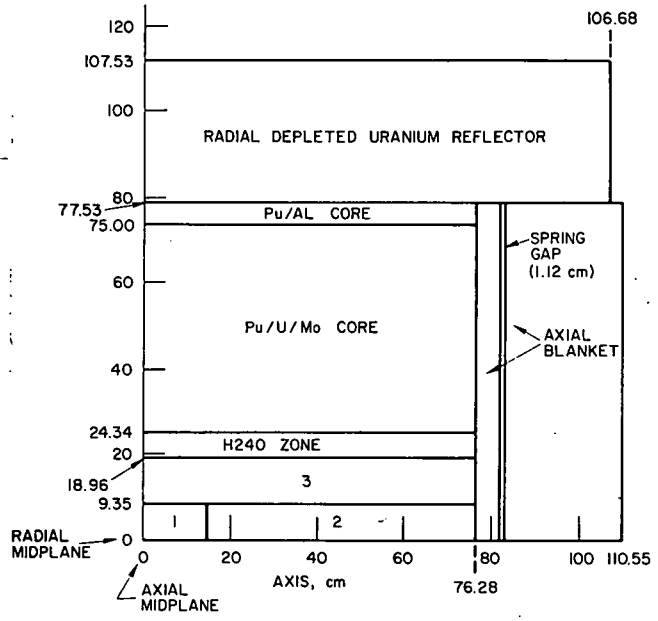

FIG. II-13-3. Axial Cross Section of One-half of ZPR-6 Assembly 7 with the H240 Zone. Sodium was Voided from Region 1 (Voiding Experiment 1) from Regions 1 and 2 (Voiding Experiment 2), and from Regions 1, 2, and 3 (Voiding Experiment 3). *ANL Neg. No. 900-1222 Rev. 1.*

sodium was voided along the entire core height in the central nine drawers of each reactor half (region 1 plus region 2 in Fig. II-13-3). The sodium-void worth obtained is $+2.67 \pm 0.44$ Ih/kg.

In the third sodium voiding measurement, sodium was voided along the entire core height in the central 37 drawers in each reactor half (regions 1, 2 and 3 in Fig. II-13-3). This measurement gives the worth of the VH240 zone relative to the full H240 zone, 155 ± 7 Ih. The specific sodium void worth is found to be $+2.62 \pm 0.12$ Ih/kg.

The results of calculations for the first two voiding measurements are given in Table II-13-I. These calculations are based on one-dimensional diffusion theory and employ cross sections generated from ENDF/B VERSION-I data. The method of calculation and cross section generation is discussed more fully in Paper II-12. In addition to cross sections characteristic of the core with sodium (w/Na cross sections), cross sections characteristic of a fully sodium-voided core (w/o Na cross sections) were also generated.

For the sodium voiding measurement in region 1 of Fig. II-13-3, the calculated sodium void coefficient is 6.68 Ih/kg. This value was obtained from a first-order perturbation calculation using the w/Na cross sections to calculate the real and adjoint flux spectrum. The perturbed sodium cross section was also from the w/Na set, weighted by the spatial flux distribution in the unit-cell. Although agreement between the calculated and measured values appears to be good, there is an indication that the perturbation denominator may be calculated ~20% too low (see Section D).

For the sodium voiding measurement in regions 1 and 2 of Fig. II-13-3 (the full core height voiding) the calculated sodium void worth is 2.92 Ih/kg. The calculated value is based on the difference between the calculated k of Assembly 7 with the H240 zone and the k of the same core with sodium voided from regions 1 and 2. The w/o Na cross sections were used in the sodium voided zone. In the voided zone, an axial extrapolated height of 201 cm was assumed. This value for the extrapolated height is based on the measured extrapolated height in the regular core of Assembly 7 (190 cm) adjusted by the ratio of the measured extrapolated heights, without sodium to with sodium, in ZPR-6 Assembly 6.[1]

The calculated value appears to agree well with the measured value; however, agreement may be fortuitous. The axial shape of the sodium void worth function is determined by the spectral component of reactivity (positive worth) near the center of the core and by the leakage component of reactivity (negative worth) near the core boundary. The integral of the sodium void worth function over the entire core height is proportional to the full core height sodium voiding worth. It is possible to calculate the magnitude of the sodium void worth poorly as a function of position along the axis, yet obtain a total integral sodium void worth that agrees well with the measured worth; that is, the positive and negative components of reactivity may be calculated too low, but the sum of the components is invariant. An example of this type of behavior may be found in Fig. II-13-5 of Paper II-12.

D. Small-Sample Central Reactivity Worth Measurements

The reactivity worths of several small samples were measured at the center of the VH240 zone. The radial sample changer and fine-autorod system were used for these measurements (see Paper II-19). The results of the measurements are given in Table II-13-II.

The ratio of the central worths measured in the VH240 zone to those measured in the H240 zone are also given in Table II-13-II. The ratios vary considerably in magnitude and indicate that the spectrum in the VH240 zone is harder than that in the H240 zone. The degree of spectrum hardening may be more clearly demonstrated by adjusting these ratios so that only the perturbation numerator part of the reactivity worths are compared. The ratio of the perturbation denominator in the VH240 zone to the perturbation denominator in the H240 zone is used for this purpose (see Paper II-12). The calculated ratio of the perturbation denominators is 1.04.

The adjusted central worth ratios for the fissile

TABLE II-13-II. SMALL-SAMPLE REACTIVITY WORTHS MEASURED AT THE CENTER OF ASSEMBLY 7 WITH THE VH240 ZONE

Sample[a]	Sample—Identification[a]	Sample Weight, g	Specific Worth[b], Ih/kg (1026 Ih/% $\Delta k/k$)	Ratio of Measured Worths in VH240 Zone to H240 Zone[c]
Pu (1 w/o ^{240}Pu)	MB-10	9.956	165.7 ± 0.8	0.95
	MB-11	21.409	167.0 ± 0.4	0.94
Pu (11.5 w/o ^{240}Pu)	Pu-11	15.122	152.3 ± 0.5	0.95
Pu (22 w/o ^{240}Pu)	Pu-17	13.939	135.6 ± 0.4	0.95
Pu (45 w/o ^{240}Pu)	Pu-23	13.923	103.7 ± 0.4	0.96
Enriched U	^{235}U (L)	3.084	119.2 ± 2.1	0.91
Depleted U	^{238}U (L)	25.988	−8.94 ± 0.25	0.83
Ta	Ta (L)	5.772	−72.6 ± 1.3	1.13
Boron (NAT)	B (L)	0.5553	−533 ± 12	0.84
SS304		43.809	−5.57 ± 0.11	1.04
Na	Na (L2)	17.044	−7.73 ± 0.39	1.10

[a] A complete description of each sample, including dimension and composition, may be found in Tables II-19-V and II-19-VI.

[b] These values are the net specific worths, i.e., the worth of stainless steel cladding and sample holder has been accounted for using the measured worth of stainless steel. The uncertainty in each measurement was computed as described in Ref. 2 and includes the uncertainty in each sample measurement and the uncertainty in the stainless steel cladding and holder worth.

[c] The measured values of the H240 zone were taken from Table II-12-II.

TABLE II-13-III. COMPARISON OF MEASURED AND CALCULATED SMALL-SAMPLE REACTIVITY WORTHS AT THE CENTER OF ASSEMBLY 7 WITH THE VH240 ZONE

Sample	Measured Specific Worth, Ih/kg (1026 Ih/% $\Delta k/k$)	Calculated Worth,[a] Ih/kg		C/E		Adjusted C/E[b]	
		w/Na Cross Sections	w/o Na Cross Sections	w/Na Cross Sections	w/o Na Cross Sections	w/Na Cross Sections	w/o Na Cross Sections
^{239}Pu	169.1 ± 0.8[c]	223.3[d]	219.7[d]	1.32	1.30	1.04	1.03
^{235}U	128.4 ± 2.1[e]	178.4	175.9	1.39	1.37	1.10	1.08
^{238}U	−9.23 ± 0.25[e]	−12.94	−12.80	1.40	1.39	1.11	1.10
Ta	−72.6 ± 1.3	−57.43	−55.96	0.79	0.77	0.63	0.61
^{10}B	−2681 ± 60	−3084[f]	−3054[f]	1.15	1.14	0.91	0.90
SS304	−5.57 ± 0.11	−7.22	−7.00	1.30	1.26	1.02	0.99
Na	−7.73 ± 0.39	−7.62	−8.58	0.99	1.11	0.78	0.88

[a] 1-D diffusion theory, first-order perturbation calculations using homogeneous cross sections for the samples, i.e., cross sections from a homogeneous MC^2 run.

[b] C/E values have been multiplied by 0.79, the estimated ratio of the calculated-to-measured perturbation denominator. The estimate of the ratio is based on the calculated-to-measured ratios in the reference core of Assembly 7 and in Assembly 7 with the H240 zone.

[c] This value was deduced by correcting the measured plutonium (1 w/o ^{240}Pu) worth of sample MB-10 with a calculated ^{240}Pu worth.

[d] A small experimentally determined self-shielding factor (1.03) has been included in this value.

[e] This value was deduced by comparing the measured worths for enriched and depleted uranium.

[f] A small experimentally determined self-shielding factor (0.98) has been included in this value.

samples are near unity: 0.99 for the plutonium samples, 0.95 for the enriched uranium sample. This is a consequence of the relative constancy of the fission cross sections of these samples in the energy range of importance in both the H240 and VH240 zones. For the absorber materials, boron and ^{238}U, the adjusted central worth ratios are 0.87 and 0.86, demonstrating the relative depletion of low energy flux in the VH240 zone. The adjusted worth ratios of the scattering materials, sodium and stainless steel, are 1.14 and 1.08, respectively, indicating that the real flux in the VH240 zone has shifted to a higher energy region where the slope of the adjoint spectrum is greater.

The adjusted central worth ratio for tantalum is 1.18. Since tantalum is primarily a low-energy absorber, this result is unexpected.

The measured central worths are compared with calculated central worths in Table II-13-III. The calculations are based on first-order perturbation theory using ENDF/B VERSION-I data and central real and adjoint

TABLE II-13-IV. Central Doppler Reactivity Worth of Natural Uranium Oxide Measured in ZPR-6 Assembly 7 with the VH240 Zone

Temperature,[a] °K	Reactivity Worth,[b] Ih/kg of U
301	0 ± 0.007
505	−0.184 ± 0.003
760	−0.358 ± 0.004
1034	−0.504 ± 0.003

[a] The temperature reported here is the average of the five thermocouples located along the length of the sample. There is a 1% uncertainty in the average temperature.

[b] 1% $\Delta k/k$ = 1026 Ih, $\beta_{eff} = 3.21 \times 10^{-3}$.

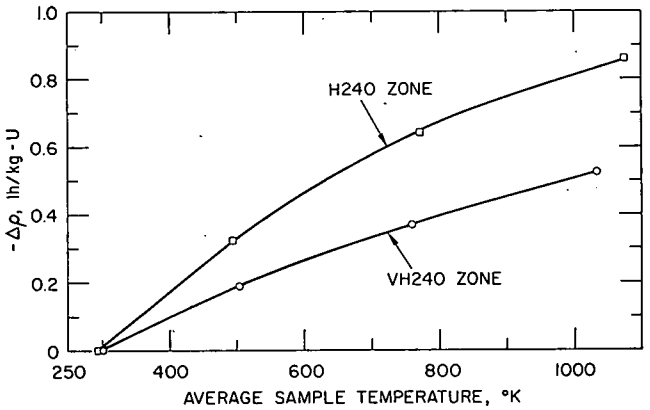

Fig. II-13-4. ^{238}U Doppler Worth Measured at the Center of Assembly 7 with the H240 and VH240 Zones. *ANL Neg. No. 116-997.*

fluxes from a 1-D diffusion calculation. The method of calculation and cross section generation is discussed in Paper II-12.

Since the size of the VH240 zone is such that the flux spectrum at the center of the core is not completely asymptotic in the sense of a fully sodium-voided environment (see Section B), two sets of calculations have been made: one set using the w/Na cross sections and one set using the w/o Na cross sections. The central worth measurements are compared with both sets of calculations in Table II-13-III. Except for sodium, both sets of calculations give nearly the same comparison with the measured worths. The C/E ratios vary over a wide range of values; this behavior cannot be explained by a discrepancy between the calculated and the actual perturbation denominator of the core.

The perturbation denominators of the uniform reference core of Assembly 7[3] and Assembly 7 with the H240 zone (see Paper II-12) were measured. The calculated-to-measured perturbation denominator was found to be 0.79 for the uniform reference core of Assembly 7 and 0.78 for Assembly 7 with the H240 zone. There was no measurement of the perturbation denominator of the core with the VH240 zone; however, a calculated-to-measured perturbation denominator ratio of 0.79 will be assumed for this core. In Table II-13-III, the C/E ratios have been adjusted with this assumed ratio to obtain the "adjusted C/E" ratios. These adjusted ratios are a measure of the agreement (or disagreement) between calculated and measured perturbation numerators.

Some of the adjusted ratios (^{239}Pu, SS304, and sodium) exhibit the same behavior as was found previously for measurements in the H240 zone (see Paper II-12). The adjusted ratios for ^{235}U, ^{238}U, and ^{10}B indicate a 10% disagreement between calculated and measured perturbation numerator worths; this is approximately twice the degree of disagreement found for measurements in the H240 zone. The large disagreement between calculated and measured tantalum worths is unexplained at this point.

E. ^{238}U Doppler Worth Measurement

The ^{238}U Doppler reactivity worth was measured at the center of the VH240 zone. The same natural uranium oxide sample used in the H240 zone measurements (see Paper II-12) were used here. A description of the Doppler measurement technique and references pertaining to the subject are given in Paper II-21. The results of the measurement are given in Table II-13-IV and are plotted in Fig. II-13-4 along with the results obtained in the H240 zone.

In Fig. II-13-4, the VH240 results have been normalized to the H240 results with the ratio of calculated perturbation denominators (see Section D). The ^{238}U Doppler worth in the VH240 zone is about 40% less (in absolute value) than in the H240 zone.

Similar results for the ^{238}U Doppler worth were obtained in ZPR-6 Assembly 6A with and without sodium (see Paper II-24).

References

1. R. A. Karam, W. R. Robinson, G. S. Stanford and G. K. Rusch, *ZPR-6 Assembly 6A, A 4000-Liter UO_2 Fast Core*, Applied Physics Division Annual Report, July 1, 1969, to June 30, 1970, ANL-7710, pp. 175–183.
2. E. F. Bennett and R. L. Long, *Precision Limitations in the Measurement of Small Reactivity Changes*, Nucl. Sci. Eng. **17**, 425–432 (1963).
3. L. G. LeSage, *Measurement of the Perturbation Denominator for ZPR-6 Assembly 7*, Reactor Development Progra Progress Report, ANL-7825, 7.4–7.6 (1971).

II-14. Neutron Spectrum Measurements in ZPR-6 Assembly 7

T. J. Yule

Introduction

The central neutron spectrum was measured in ZPR-6 Assembly 7 (see Paper II-11) using proton-recoil proportional counters. The energy range of the measurement is from 1 keV to 2 MeV. The measured central neutron spectrum is compared with a calculated fundamental-mode spectrum and the influence of heterogeneity effects is considered.

Specifics of Measurement

The techniques and analyses of fast reactor neutron spectroscopy with proton-recoil proportional counters are discussed in detail elsewhere.[1] This particular measurement is part of a series[2] of measurements which have used small counters with improved electronics and which have incorporated corrections for all known sources of systematic error—electric-field distortion, W variation, carbon-recoil contributions, and wall-and-end effects.

A methane-filled or hydrogen-filled counter in a standard fuel drawer was inserted into position 23-22 in the moveable half. During the measurement the neutron sources and fuel-loaded control drawers were withdrawn from the core and the boron-loaded drawers were inserted. This configuration was approximately 2% $\Delta k/k$ subcritical. In one measurement plate material was placed around the probe and in that portion of the drawer not occupied by the preamplifier and cables. Figure II-14-1 shows a sectional view of the loading around the probe. Another measurement was made without the simulated loading to determine local heterogeneity effects.

Measured and Calculated Spectra

The measured central spectrum in which the drawer had a simulated loading and a calculated spectrum are shown in Fig. II-14-2. The predicted spectrum (indicated by the continuous line) was calculated using ENDF/B-VERSION I nuclear data and the MC² code.[3] The calculation assumes a fundamental-mode model in the P_1 approximation. The plate loading of the fuel was approximately considered by using the heterogeneous MC² option which employs the modified Bell approximation to account for self-shielding in the el. The calculation was normalized so that the integral of the flux over the energy range of the experimental points equaled the corresponding integral for the experimental data. This method of normalization is rather arbitrary; it might be more satisfactory to employ a normalization which forces measured and calculated fission rates or some other spectral index to be equal. The continuous curve is the result of smoothing the MC² points, which are calculated for $\frac{1}{120}$ lethargy intervals, with a Gaussian window whose width corresponds to the experimental resolution.

In general, the agreement between the measured spectrum and calculated spectrum is good. However, there are some regions of significant disagreement. There is systematic disagreement in the positions of the measured and calculated resonance dips for energies above 100 keV. There is an indication that the disagreement is brought about by an excessive amount of contaminants in the methane filling.[1] There are also significant differences in the neighborhood of the large resonances, especially the large iron resonance at about 30 keV. It is not easy to explain the discrepancies in terms of experimental resolution or instrumental distortion. As is discussed below, heterogeneity effects cannot account for such large differences.

Heterogeneity Effects

It is possible to distinguish between two types of heterogeneity effects. There are local heterogeneity effects introduced by the fact that the counter is viewing only a particular region of a cell and there are nonlocal effects introduced by the use of a plate loading. The differences between the spectrum seen by the counter and the homogeneous fundamental-mode calculation of the spectrum must be known in order to compare the measured and calculated spectrum. In an attempt to examine the extent of local heterogeneity effects, a measurement was made with and without a

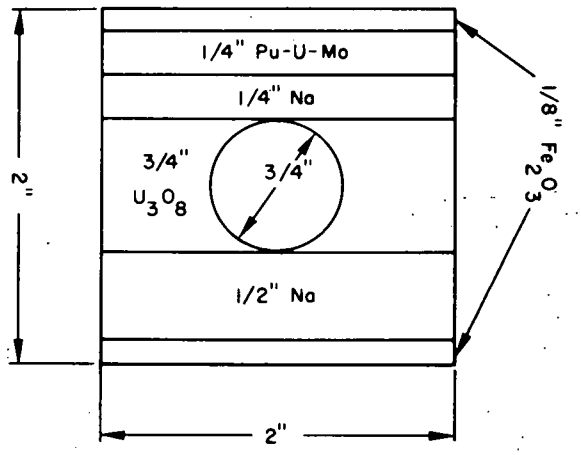

Fig. II-14-1. Cross-Sectional View of Material Placement Around Proton-Recoil Probe for the ZPR-6 Assembly 7 Measurement. All Dimensions are in Inches. *ANL Neg. No. 116-1023.*

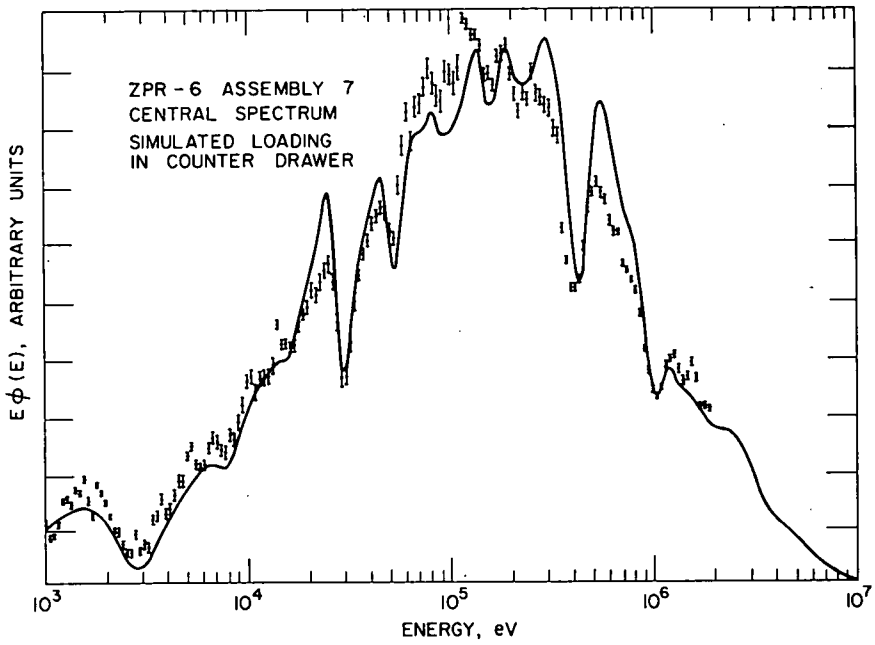

FIG. II-14-2. Central Neutron Spectrum in ZPR-6 Assembly 7 in a Drawer with a Simulated Loading Together with a Smoothed Fundamental Mode Calculation. *ANL Neg. No. 116-1022.*

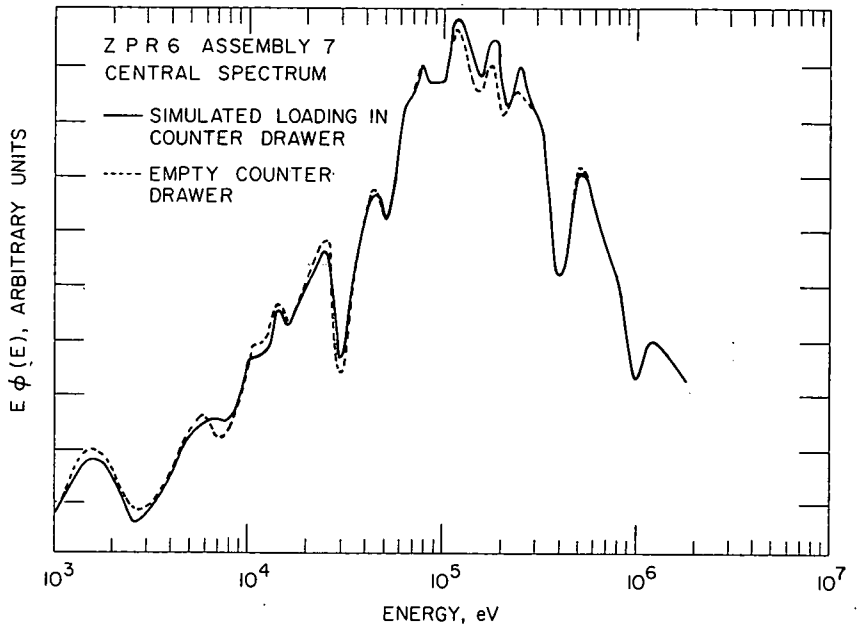

FIG. II-14-3. Central Neutron Spectrum in ZPR-6 Assembly 7 with and without a Simulated Loading in the Counter Drawer. *ANL Neg. No. 116-319 Rev. 1.*

simulated loading of reactor material in the counter drawer. In the simulated loading an attempt was made to keep iron away from the counter. A comparison of the two measurements is shown in Fig. II-14-3. The uncertainties are about the same as those shown in Fig. II-14-2. For the most part, the differences are not significant but there are some small differences near the large iron resonance. In an empty drawer the counter can look directly at the stainless steel matrix and drawer. Having the sodium next to the counter changes the flux near the sodium resonance.

With respect to the effect of non-local heterogenei on the spectrum, there are indications that its influer is small. Two-thousand group heterogeneous unit-cell calculations for cores similar to the one considered here indicated only small differences near the scattering

resonances between homogeneous and heterogeneous spectra.[4] In regions of strong capture and fission resonances the differences can be striking.

Conclusion

The spectrum measurement in ZPR-6 Assembly 7 is rather representative of the measurements made during the last few years in large, dilute fast reactors. The ability to predict the detailed flux variation in the vicinity of some large scattering resonances is not very good. The discrepancies are thought to be outside experimental error and cannot be entirely accounted for by heterogeneity effects.

Efforts are currently being directed toward improving the low- and high-energy limits of the proton-recoil technique. Measurements in the future will attempt to make use of the ability of this method to provide accurate absolute fluxes. Suitable reaction rate measurements will be made in conjunction with the neutron spectrum measurement.

References

1. E. F. Bennett and T. J. Yule, *Techniques and Analyses of Fast Reactor Neutron Spectroscopy with Proton-Recoil Proportional Counters*, ANL-7763 (1971).
2. T. J. Yule and E. F. Bennett, *Measured Neutron Spectra in a Number of Uranium- and Plutonium-Fueled Reactor Assemblies*, Nucl. Sci. Eng. **46**, 236 (1971).
3. B. J. Toppel, A. L. Rago and D. M. O'Shea, *MC²*, *A Code to Calculate Multigroup Cross Sections*, ANL-7318 (1967).
4. P. Govaerts, C. E. N., Cadarache (private communication).

II-15. Spectrum Measurement Between the Halves of ZPR-6 Assembly 7

T. J. Yule

Introduction

When a large reactor is fueled with plutonium, the spontaneous neutron source from ^{240}Pu may lead to significant neutron doses in the vicinity of the reactor, even when the reactor is far subcritical. In the case of a split-table machine, doses may be quite high since it is possible to directly view the core when the halves are separated. Since personnel are required to work between the halves during loading and during the setup of experimental apparatus, it is imperative that the dose be determined with sufficient accuracy.

The neutron spectrum is that of a degraded fission source. For such a spectrum it is difficult to accurately determine the dose with standard neutron rem counters.[1] Figure II-15-1 shows the response of a small $^{6}LiI(Eu)$ scintillator placed in the center of a 10 in. diam polyethylene sphere (the familiar bowling ball detector).[2] Since a degraded fission spectrum extends over regions of rather large differences between the RBE dose and instrument response, measurements with such an instrument are difficult to interpret. It is possible to use different diameter spheres[3] and combine the results to determine with about 15 % accuracy the dose for neutron energies between 10 keV and 10 MeV. There is also available another type of rem counter with an improved response based on the same moderating technique.[4] The counter has a cylindrical design with a BF_3 proportional counter surrounded by an inner polyethylene cylinder. A thin layer of boron plastic fits over the inner cylinder with holes drilled in the plastic to adjust the neutron sensitivity as a function of energy. There is also an outer polyethylene cylinder. An accuracy of 10 % is obtained in the energy interval from 40 keV to 10 MeV and at thermal energies. Besides differences between instrumental response and RBE dose, the counters described above must be calibrated against a standard.

The dose determination described here employs proton-recoil proportional-counter techniques, which were developed for in-core neutron spectroscopy.[5] Although such a measurement is considerably more time consuming and difficult than one with a rem counter, one may place a rather high degree of confidence in the

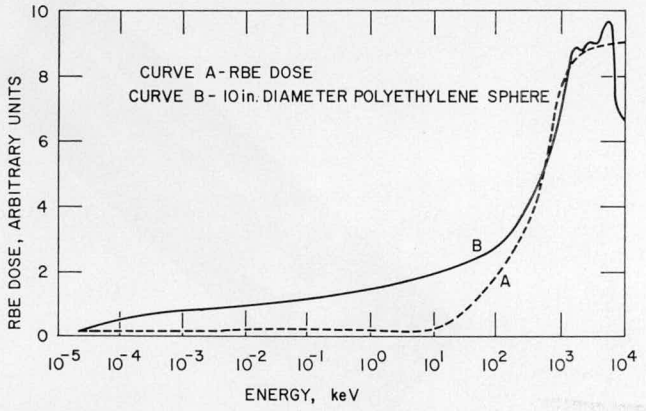

Fig. II-15-1. Response of a $^{6}LiI(Eu)$ Scintillator Placed in the Center of a 10 in. Diam Polyethylene Sphere Compared with the Calculated Thick Tissue RBE Dose for Monoenergetic Neutrons. (See Ref. 2). *ANL Neg. No. 116-880.*

result. Furthermore, such a measurement provides a standard for the testing of other dosimetry techniques in this environment (see Paper III-35). The proton-recoil counters are used to measure the spectrum; the measured spectrum and the RBE curve are employed to determine the dose. Since the n-p scattering cross section is well known and the number of hydrogen atoms in a particular counter is easily determined, an absolute measurement of the spectrum is realized. Such absolute measurements have recently been carried out in the high-dose irradiation cell of the JANUS reactor—a facility for the investigation of biological effects of fast neutrons.[6]

Specifics of the Measurement

The spectrum was measured between the halves of ZPR-6 Assembly 7 with the halves fully separated. Assembly 7 is a large, dilute plutonium-oxide-fueled core with a single-drawer unit cell blanketed on all sides by depleted uranium (see Paper II-11). The core volume is approximately 3500 liters and contains about 1300 kg of plutonium.

The same techniques were employed for the spectrum measurement between the halves as for in-core measurements.[5] However, considerably larger detectors were used in the present measurements to increase the sensitivity. The proton-recoil spectrum above 100 keV was measured with a 1 in. diam methane-filled detector with a 3 in. sensitive length filled to 90 psia. The proton-recoil spectrum below 100 keV was measured with a 1 in. diam hydrogen-filled detector with a 6 in. sensitive length filled to 80 psia. The methane-filled counter has 0.230×10^{23} hydrogen atoms in the sensitive volume and the hydrogen-filled counter has 0.222×10^{23}. A lead sleeve 0.020 in. thick was placed around a detector to reduce soft photon interactions in the walls of the detector. Figure II-15-2 shows the methane-filled detector together with a preamplifier mounted in a thin-walled stainless steel drawer. The drawer, which was supported with a light aluminum stand, was placed on the reactor axis midway between the halves. The distance between the separated halves was 5 ft. The maximum count rate of about 5000 counts/sec occurred with the hydrogen-filled counter. The complete scan of

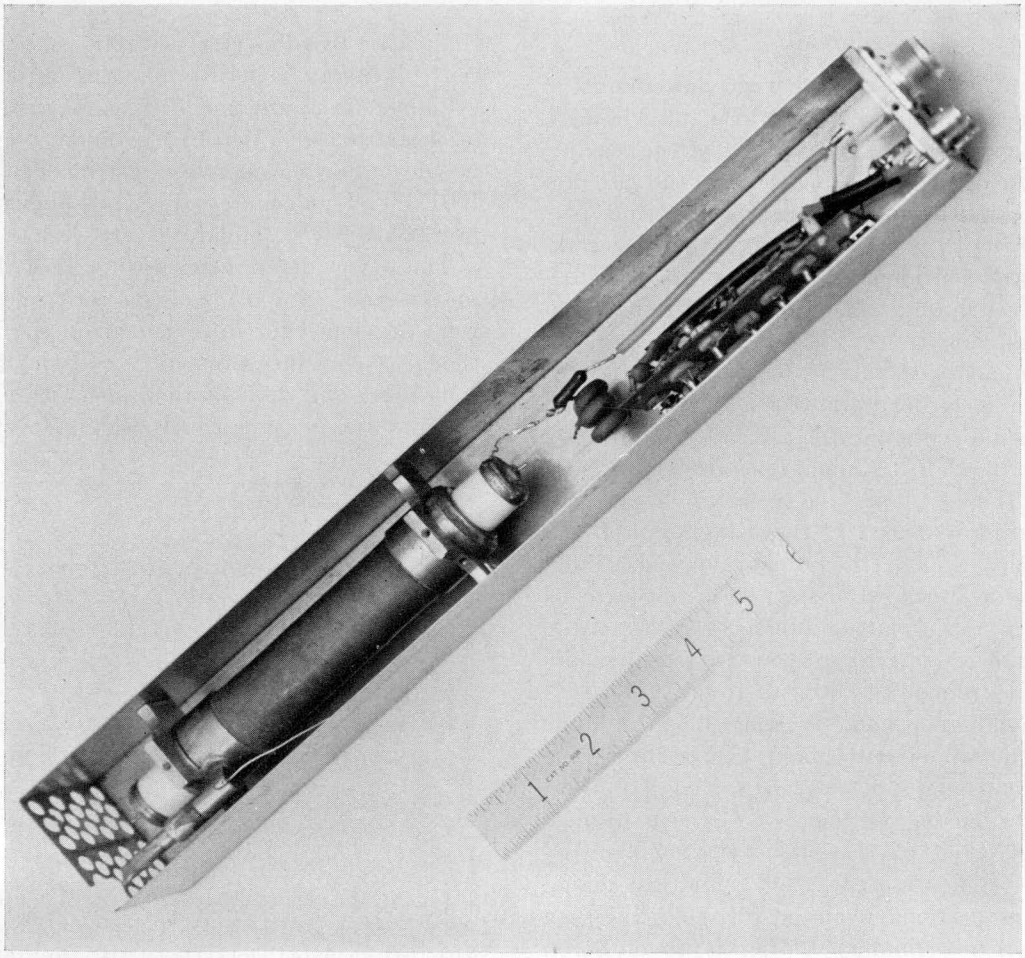

Fig. II-15-2. Methane Detector and Preamplifier Used for the Spectrum Measurement. *ANL Neg. No. 900-405.*

the proton-recoil spectrum was accomplished in about 8 hours.

Analysis of Present Measurement

The measured neutron spectrum is shown in Fig. II-15-3. The oxygen resonances at about 450 keV and 1 MeV are clearly seen. The iron resonance at about 30 keV is also apparent. For an in-core measurement the statistics are usually better and the low energy data extends to 1 keV.

The neutron-to-gamma ratio was such that it was not necessary to match distributions from a pure gamma field in determining the proton-recoil distribution. No corrections were made for electric field distortions or variation of W—the energy loss per ion pair with energy.[5] Electric field corrections and W corrections only significantly alter the spectrum shape at energies less than 10 keV—a region which contributes little to the dose. There is some uncertainty introduced by electric field effects in determining the absolute value of the flux. The electrical volume of the detector is not the same as the mechanical volume defined by the field tubes because of bowing of the field lines near the ends. For the methane counter this difference may be 3 to 4 % and about half as much for the hydrogen counter.

No corrections were made for wall-and-end effects or carbon recoils.[5] It has been found that these corrections are not significant for spectral shapes similar to the one under consideration.

The neutron flux derived from the methane-filled counter data might be assigned an absolute uncertainty of about 10 %. The uncertainty in the neutron flux derived from data obtained with the hydrogen-filled counter is mostly that associated with statistics for energies greater than 10 keV; the uncertainty might be as high as 7 %.

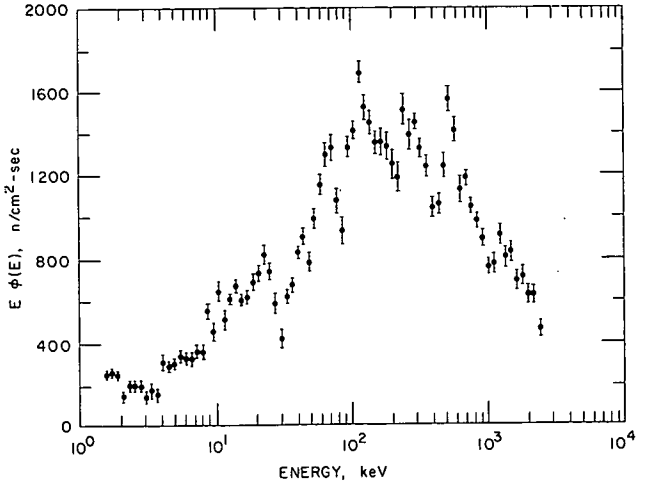

Fig. II-15-3. Measured Neutron Spectrum between the Halves for ZPR-6 Assembly 7. *ANL Neg. No. 116-878.*

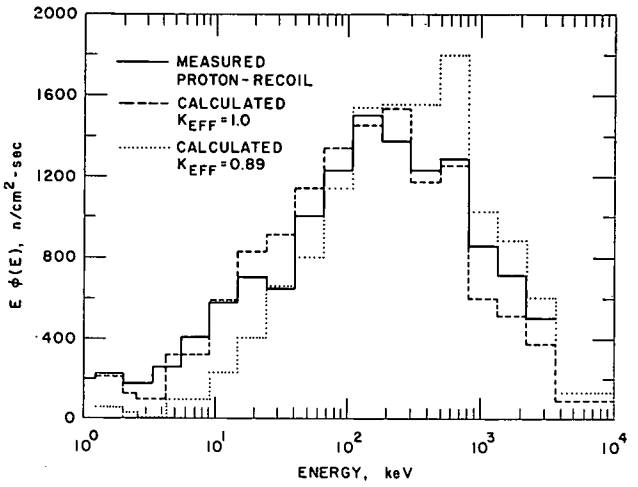

Fig. II-15-4. Group-Averaged Measured Neutron Spectrum between the Halves for ZPR-6 Assembly 7 and Calculated Spectra. *ANL Neg. No. 116-882.*

In Fig. II-15-4 the measured neutron spectrum averaged over half lethargy widths is compared with calculated broad-group spectra. The histograms are normalized to have equal areas within the experimentally measured energy range. The absolute scale applies only to the experimental data; the calculations yield only spectral shapes. The spectrum for $k_{eff} = 1$ is the central spectrum when the halves are together. This spectrum is considerably softer than the measured one. The neutron leakage is greater when the halves are apart. The spectrum for $k_{eff} = 0.89$ is that at the inner boundary calculated with diffusion theory for a cylindrical slab corresponding to a single half. At high energies the agreement is seen to be considerably better than for the spectrum for $k_{eff} = 1$. At lower energies the spectrum for $k_{eff} = 0.89$ is too hard. A transport calculation in which both halves are taken into account would be expected to yield a more reliable prediction of the spectrum between the halves.

To determine the dose and fission rates it is necessary to extrapolate the measured spectrum to higher energies and to lower energies. One is interested in determining fission rates in order to relate the present spectrum measurement to fission rate measurements made with track recorders (see Paper III-35). The high energy extrapolation is straightforward. Since the flux above a few MeV is almost entirely governed by statistical processes, one might expect that using a function of the form $\exp(a + bE)$ would be satisfactory. It has been shown that this form provides a reasonable fit to MC[2] predicted spectra above a few MeV. This form is used in the SIGBAR program, which computes average fission cross sections in fast neutron spectra.[7] In the present case the five highest energy points were fitted by least-squares to the above functional form; this fit

provides the extrapolation above 2.5 MeV. Since the shape of the measured spectrum at high energies is somewhat sensitive to wall-and-end effect corrections, which were not made, and since there is some problem with energy calibration in methane counters when the track length of the recoils become long, the flux extrapolated to 10 MeV has an average uncertainty of about 30%—the uncertainty is somewhat less at lower energies and greater at higher energies.

The extrapolation to lower energies is somewhat more difficult. Extrapolation based on a fit to a simple function over the low energy range of the measurement is unacceptable. From Fig. II-15-4 it is seen that the calculated spectrum for $k_{eff} = 1$ is fairly close to the measured spectrum at lower energies. This spectrum is used for the low-energy extrapolation.

DOSE

The dose was determined by averaging the measured spectrum over half lethargy widths and using the conversion curve shown in Fig. II-15-5 to transform flux to dose.[8] A value of 385 ± 50 mrem/hr was obtained. Contributions to the dose from neutrons below the measurement limit of 1.68 keV are insignificant. Approximately 20% of the dose comes from neutrons above the measurement limit. Figure II-15-6 shows the integrated dose from neutrons above an energy cutoff as a function of the cutoff energy. Almost 85% of the dose comes from neutrons above 250 keV.

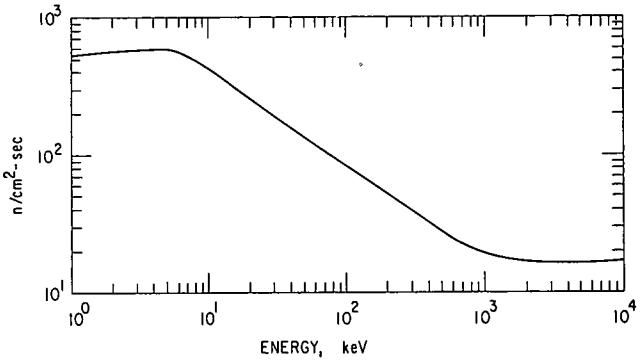

FIG. II-15-5. Incident Flux of Neutrons to Deliver 0.1 Rem/40h as a Function of Neutron Energy (See Ref. 8). *ANL Neg. No. 116-881.*

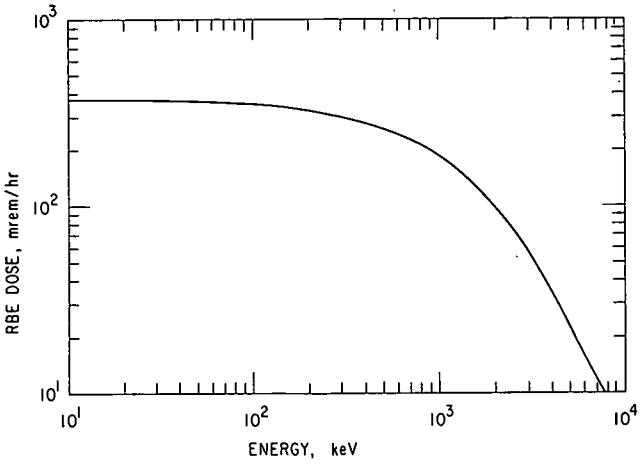

FIG. II-15-6. RBE Dose for the Measured Spectrum from Neutrons above a Cutoff Energy as a Function of the Cutoff Energy. *ANL Neg. No. 116-879.*

TABLE II-15-I. FISSION RATES FOR THE MEASURED SPECTRUM BETWEEN THE HALVES OF ZPR-6 ASSEMBLY 7

Fissile Material	Range	$\phi\sigma_{fiss}$[a]	Per Cent Contribution
Thorium	Measurement limits	6.42E 01	64
	Above 2.5 MeV	3.66E 01	36
	Total	1.01E 02	100
^{238}U	Measurement limits	3.05E 02	68
	Above 2.5 MeV	1.41E 02	32
	Total	4.46E 02	100
^{235}U	Below 1.7 keV	2.40E 03	16
	Measurement limits	1.27E 04	82
	Above 2.5 MeV	3.00E 02	2
	Total	1.54E 04	100

[a] Flux is in n/cm²-sec and the cross section is in barns.

FISSION RATE

Fission rates for thorium, ^{238}U and ^{235}U were determined using the program SIGBAR, except for the low-energy contribution to ^{235}U where the low energy extrapolation indicated above was used. Table II-15-I contains the results together with an indication of contributions from energy regions in which the spectrum was extrapolated. It would take a considerable effort to determine accurately the uncertainties associated with the fission rates. The uncertainties are not less than 20%.

REFERENCES

1. E. Tochilin and B. W. Shumway, *Dosimetry of Neutrons and Mixed n + γ Fields;* F. H. Attix and E. Tochilin, Eds., *Radiation Dosimetry,* (Academic Press, New York, 1969) 2nd Ed., Vol. III, pp 247-308.
2. D. E. Hankins, *A Neutron Monitoring Instrument Having a Response Approximately Proportional to Dose Rate from Thermal to 7.0 MeV,* LA-2717 (1962).
3. D. Nachtigall and F. Rohloff, *Sphere Techniques for Measurement of Flux Density and Dose Rates of Thermal, Intermediate and Fast Neutrons,* Nukleonik **6,** 330 (1964).
4. I. Ö. Andersson and J. Braun, *A Neutron Rem Counter,* Nukleonik **6,** 237 (1964).
5. E. F. Bennett and T. J. Yule, *Techniques and Analyses Fast Reactor Neutron Spectroscopy with Proton-Recoil Proportional Counters,* ANL-7763 (1971).
6. E. F. Bennett and T. J. Yule, *A Neutron Spectrum Map of the JANUS Irradiation Facility Using Proton-Recoil Pro-*

portional Counters, Reactor Physics Division Annual Report, July 1, 1969 to June 30, 1970, ANL-7710, pp. 350–359.
7. R. Gold and I. K. Olson, *SIGBAR—A Program for Computing Average Fission Cross Sections in Fast Neutron Spectra*, Reactor Physics Division Annual Report, July 1, 1968 to June 30, 1969, ANL-7610, pp. 535–536.
8. *Protection Against Neutron Radiation up to 30 Million Electron Volts*, Natl. Bur. Standards (U. S.), Handbook, Vol. 63 (1957).

II-16. Reaction-Rate Measurements in ZPR-6 Assembly 7

G. S. Stanford and W. R. Robinson

Introduction

As part of the complete characterization of Assembly 7 as a Benchmark Critical Assembly,[1] several reaction rate measurements have been made. The measurement of reaction rates provides a sensitive test of the nuclear data which are being used for current LMFBR Demonstration Plant design. The measurements reported here were planned to yield a detailed accounting of the neutron inventory throughout the assembly. Two types of reaction rate measurements have been employed: detailed foil irradiations throughout the assembly, and absolute fission chamber counting at a location in the assembly.

Description of Foil Irradiation Measurements

In order to establish a complete mapping of the reaction rate ratios $^{28}c/^{49}f$ and $^{28}f/^{49}f$ (f and c refer to the fission and capture rates per atom, and 28 and 49 refer to ^{238}U and ^{239}Pu, respectively) throughout the assembly, two types of foil irradiation measurements were made: detailed irradiations in a unit cell and axial and radial traverse through the core.

Detailed irradiations in a unit cell of core material

Irradiations at positions between the plates in a unit cell were made in order to obtain cell-averaged reaction-rate ratios. Thin metallic foils of ^{239}Pu, ^{238}U, and ^{235}U, described in Table II-16-I, were used. These foils were placed between plates of a unit-cell loading contained in a 2 x 2 x 2 in. stainless steel box (10-mil thick stainless steel walls). Three foil loading patterns within the boxes were employed. The locations of foils for each loading pattern, designated as Box Type A, Box Type B, and Box Type C, are shown in Figs. II-16-1 rough II-16-3.

In order to keep the foils in position within the unit cell, a small amount of high-vacuum silicone grease (<1 mg) was used to stick the foils to the plates. In addition, 1 mil thick aluminum was placed between the foils and the U_3O_8 plates to prevent fission-product transfer.

Three reactor runs were required to complete all necessary irradiations. The foil box types and locations in the reactor for each irradiation are described in Table II-16-II and Fig. II-16-4.

Axial and radial foil irradiation traverses in the core

Axial and radial foil irradiation traverses were made in order to account for the spatial distribution of the important reaction rates throughout the assembly. The thin metallic foils of ^{239}Pu and depleted uranium described in Table II-16-I were placed between plates of a drawer along the entire length of the drawer. Three types of foil traverse drawers, Type AA, Type BB, and Type CC, described in Table II-16-III, were used.

In each type of traverse drawer, ^{239}Pu and depleted uranium foils were located at six-inch intervals along the entire length of the drawer. The foils in each drawer were wrapped in 1 mil thick aluminum and centered vertically between rows of plates. In Type AA and Type BB foil traverse drawers, depleted uranium and ^{239}Pu foils were placed between a row of Fe_2O_3 plates and the fuel plates. In Types AA, BB, and CC foil traverse drawers depleted uranium foils were placed between a row of U_3O_8 plates and sodium cans.

The type of foil traverse drawer and the location of

TABLE II-16-I. Description of Activation Foils Used in Assembly 7

Material	Foil Shape	Size, in.	Nominal Thickness, mils
Enriched uranium	Disk	0.322 diam	4.4
Natural uranium	Disk	0.625 diam	5
Depleted uranium	Disk	0.625 diam	5.5
	Rectangle	¼ x ½	5.5
Plutonium	Disk	0.12 diam	3.0
	Disk	0.4 diam	0.5

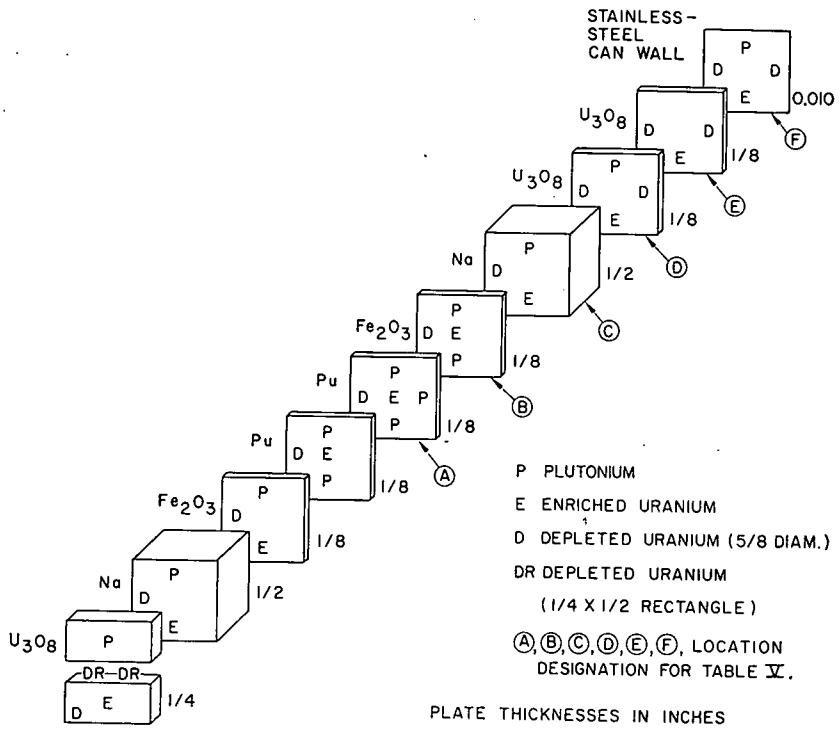

FIG. II-16-1. Foil Locations in Box Type A. *ANL Neg. No. 116-1048.*

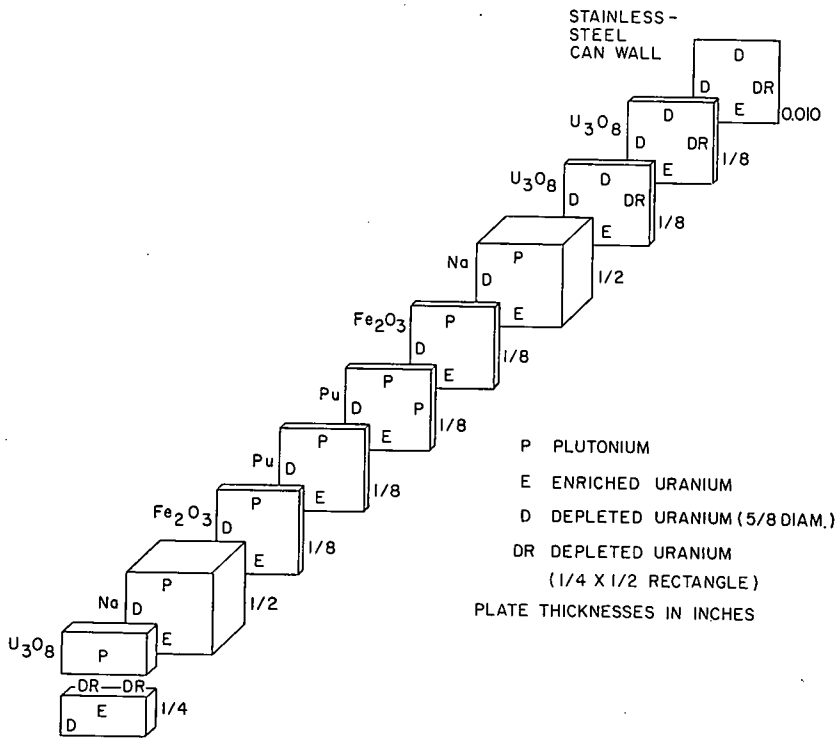

FIG. II-16-2. Foil Locations in Box Type B. *ANL Neg. No. 116-1049.*

the foils within the drawer are given in Table II-16-IV. The locations of the foil traverse drawers in the reactor during each irradiation are described in Table II-16-IV and Fig. II-16-4.

In addition to the unit cell and traversing foil irradiations, foils were simultaneously irradiated at the face of absolute fission chambers in Assembly 7 and in the thermal column of the Argonne Thermal Source

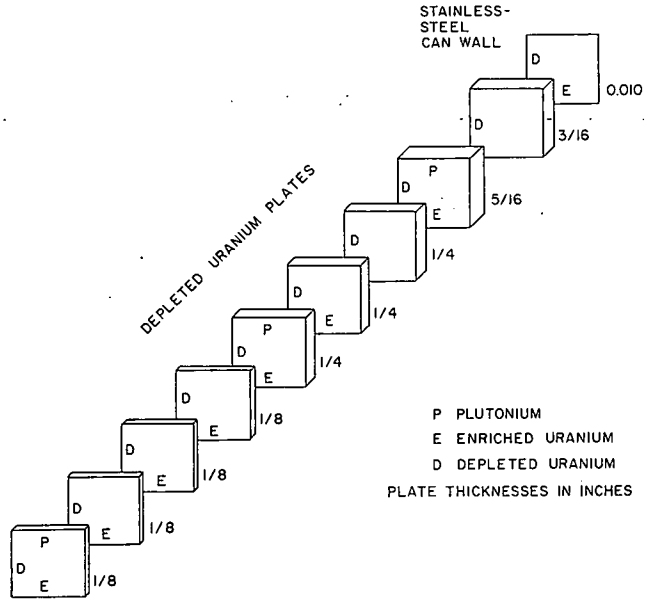

FIG. II-16-3. Foil Locations in Box Type C. *ANL Neg. No. 166-1051.*

TABLE II-16-II. LOCATION OF UNIT-CELL FOIL IRRADIATION BOXES IN ZPR-6 ASSEMBLY 7

Irradiation	Type of Foil Box[a]	Box Location		
		Matrix Position[b]	Distance from Reactor Mid-plane,[c] in.	Designation in Fig. II-16-4[(c)]
1	A	S23-37	0–2	a
	A	S23-37	28–30	b
	B	S30-23	0–2	c
	C	S23-38	0–2	d
	C	S23-38	28–30	e
2	A	S23-23	0–2	f
	A	S23-23	28–30	g
	B	S23-23	14–16	h
	B	S23-23	26–28	i
	C	S23-23	30–32	j
3	A	S23-23	0–2	g

[a] See Figs. II-16-1 through II-16-3.

[b] "S" Stands for stationary reactor half. See Fig. II-16-4. for these locations, which correspond to a, b, ···, j designation of last column of table.

[c] Each foil box is 2 x 2 x 2 in. Thus, a foil box located at the front of a drawer (front face of a drawer is at the reactor midplane) occupies the first two inches (0–2) from the reactor midplane.

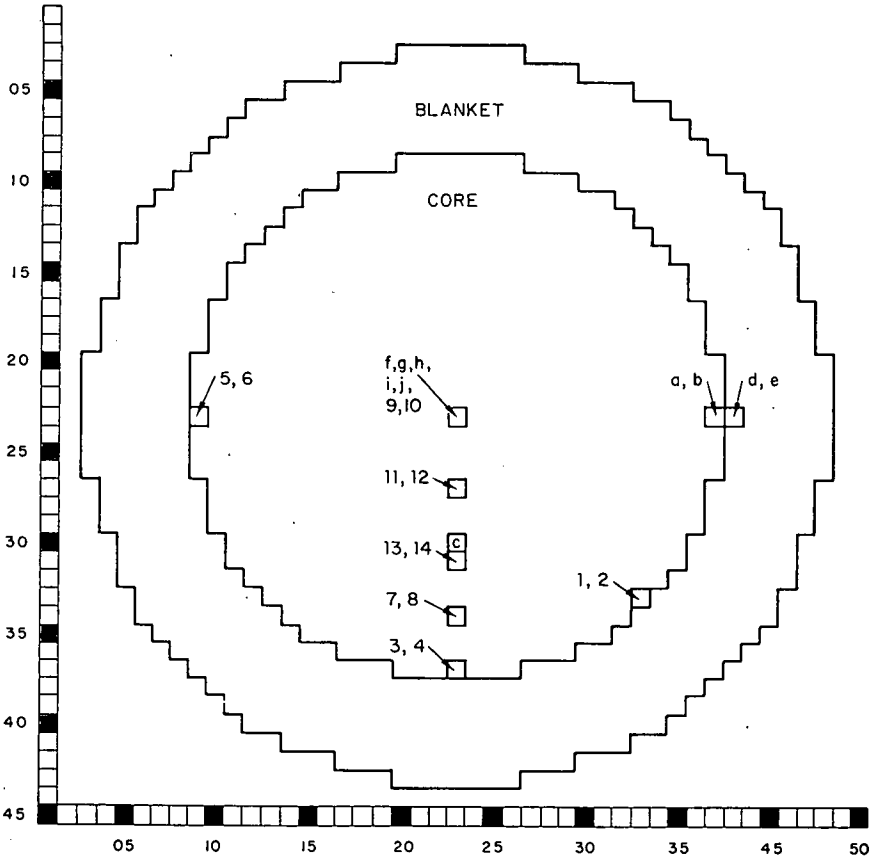

FIG. II-16-4. Radial Cross Section of ZPR-6 Assembly 7 Showing Locations of Unit-Cell Foil Irradiation Boxes (a, b, ···, j) and Foil Irradiation Traverses (1, 2, ···, 14). Refer to Tables II-16-II through II-16-IV for a Complete Description of the Foil Irradiation Boxes a through j and Foil Traverses 1 through 14. *ANL Neg. No. 116-1050.*

Reactor (ATSR). These auxiliary irradiations were used to calibrate the foil counting system and to aid in the determination of absolute reaction rates.

Reduction of Foil Irradiation Data

The gamma activity of the irradiated foils was counted with NaI(Tl) scintillator detectors in an automated foil counting system.[2] Fission rates were determined by counting fission-product gammas above 550 keV. The capture rate in the ^{238}U foils was determined by counting the ^{239}Np gamma activity at 100 keV using a coincidence technique.[3] The fission-product counting was performed first, and followed by coincidence counting of the depleted uranium foils.

The gamma-counting data were then processed using the computer codes NURF and COMBO.[4,5] In these codes the data are corrected for decay rates, counting system deadtime, background radiations, and, in the case of the ^{239}Np coincidence counting, accidental coincidences and gamma-ray self-absorption. From these codes the relative reaction rates per unit mass of foil material were obtained. These relative reaction rates were then corrected for the activity due to contaminating isotopes in the foils to yield relative reaction rates per unit mass of the principal isotope (^{239}Pu, ^{238}U, ^{235}U) for each foil.

Several additional correction factors were employed, including calculated self-shielding corrections for the foils irradiated in the thermal column of ATSR, and experimentally determined corrections for the variation in gamma-detection efficiency with foil size.

The relative reaction rates were converted to absolute reaction rates using three techniques: simultaneous irradiations in a reference thermal spectrum,[6] simultaneous irradiations at the faces of absolute fission counters located in the assembly, and radiochemical analysis of irradiated foils.[7]

TABLE II-16-III. Foil Positions in Foil Irradiation Traverse Drawers

Traverse Type	Type Material[a]	Distance from Reactor Centerplane, in.
AA	Pu	0.5
	Pu	0.875
	D.U.	1.5
	Pu	6.5
	Pu	6.875
	D.U.	7.5
	Pu	12.5
	D.U.	13.5
	Pu	18.5
	Pu	18.875
	D.U.	19.5
	Pu	24.5
	Pu	24.875
	D.U.	25.5
	Pu	28.5
	Pu	28.875
	D.U.	29.5
BB	Pu	0.5
	D.U.	1.5
	Pu	6.5
	D.U.	7.5
	D.U.	13.5
	Pu	18.5
	D.U.	19.5
	Pu	24.5
	D.U.	25.5
	Pu	28.5
	D.U.	29.5
CC	D.U.	1.5
	D.U.	7.5
	D.U.	13.5
	D.U.	19.5
	D.U.	25.5
	D.U.	29.5

[a] Pu is plutonium and D.U. is depleted uranium.

TABLE II-16-IV. Location and Type of Each Foil Irradiation Traverse

Irradiation	Type of Traverse[a]	Traverse Location		
		Matrix Position[b]	Adjacent Plate Materials	Designation in Fig. II-16-4[(b)]
1	BB	S33-33	Pu & Fe_2O_3	1
	CC	S33-33	U_3O_8 & Na	2
	BB	S37-23	Pu & Fe_2O_3	3
	CC	S37-23	U_3O_8 & Na	4
2	AA	M23-09	Pu & Fe_2O_3	5
	CC	M23-09	U_3O_8 & Na	6
	BB	S34-23	Pu & Fe_2O_3	7
	CC	S34-23	U_3O_8 & Na	8
3	AA	M23-23	Pu & Fe_2O_3	9
	CC	M23-23	U_3O_8 & Na	10
	BB	S27-23	Pu & Fe_2O_3	11
	CC	S27-23	U_3O_8 & Na	12
	BB	S31-23	Pu & Fe_2O_3	13
	CC	S31-23	U_3O_8 & Na	14

[a] Refer to Table II-16-III for a description of AA, BB, and CC type traverses.

[b] "S" and "M" stand for stationary and movable reactor half, respectively. See Fig. II-16-4 for these locations, which correspond to 1, 2, ···, 14 designation in last column of table.

Results of Foil Irradiation Measurements

The reaction rate ratios measured at the center of the assembly (location f, described in Table II-16-II and Fig. II-16-4) are given in Table II-16-V. All reaction-rate ratios reported are for reaction rates per atom

TABLE II-16-V. REACTION RATE RATIOS AT THE CENTER OF ZPR-6 ASSEMBLY 7[a]

Ratio	Location in the Unit-Cell[b,c]						Cell Average[d]	Face of The Fission Chambers[c,e]
	Between Two ⅛ in. Fuel Plates (A)	Between Fuel & Fe_2O_3 Plates (B)	Between Fe_2O_3 Plate & Na Can (C)	Between Na Can & U_3O_8 Plate (D)	Between Two ⅛ in. U_3O_8 Plates (E)	Between U_3O_8 Plate & Matrix (F)		
$^{25}f/^{49}f$	1.0540	1.0499	1.0513	1.0585	—	1.0546	1.0645	1.0502
$^{28}f/^{49}f$	0.02614	0.02465	0.02309	0.02221	—	0.02185	0.02338	0.02191
$^{28}c/^{49}f$	0.1412	0.1515	0.1556	0.1522	—	0.1484	0.1430	0.1629
$^{28}f/^{25}f$	0.02480	0.02348	0.02196	0.02098	0.02076	0.02072	0.02202	0.02086
$^{28}c/^{25}f$	0.1342	0.1446	0.1476	0.1438	0.1322	0.1406	0.1343	0.1551

[a] All ratios are reported on a per atom basis. Although these results are preliminary in nature, they are expected to be within 1% of any final corrected values which may appear later.

[b] Refer to Fig. II-6-1 for the locations designated (A), (B), ⋯ , (F).

[c] The absolute errors in these ratios are: $^{25}f/^{49}f \pm 2.5\%$, $^{25}f/^{49}f \pm 1.5\%$, $^{28}c/^{49}f \pm 2.0\%$, $^{28}f/^{25}f \pm 2.5\%$, $^{28}c/^{25}f \pm 2.5\%$. The relative error among the values reported at all locations for each ratio is $\pm 0.5\%$.

[d] The absolute errors in these ratios are the same as given in c. Relative to the values reported at all locations for a ratio, these values are uncertain by $\pm 1\%$.

[e] The fission chambers were not located at the center of the core, but were close enough to the center so that the neutron spectrum was essentially the same as the central spectrum. Because the chambers and foils were contained in a 2 x 2 x 2 in. void, the ratios measured at the fission chambers would not be expected to be the same as the cell-average ratios.

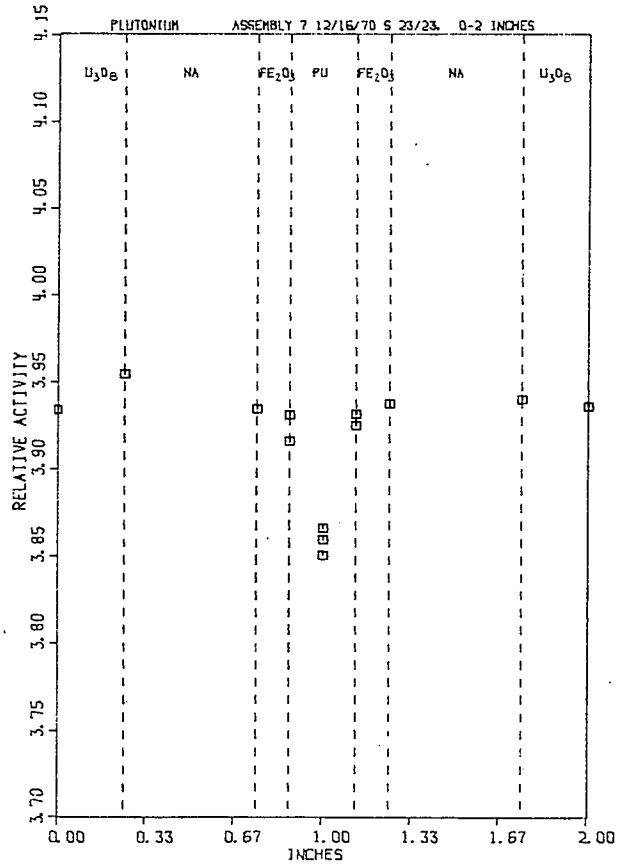

FIG. II-16-5. Relative Fission Rates Measured with ^{239}Pu Foils in the Unit Cell Plate Loading at the Center of ZPR-6 Assembly 7. *ANL Neg. No. 116-1008.*

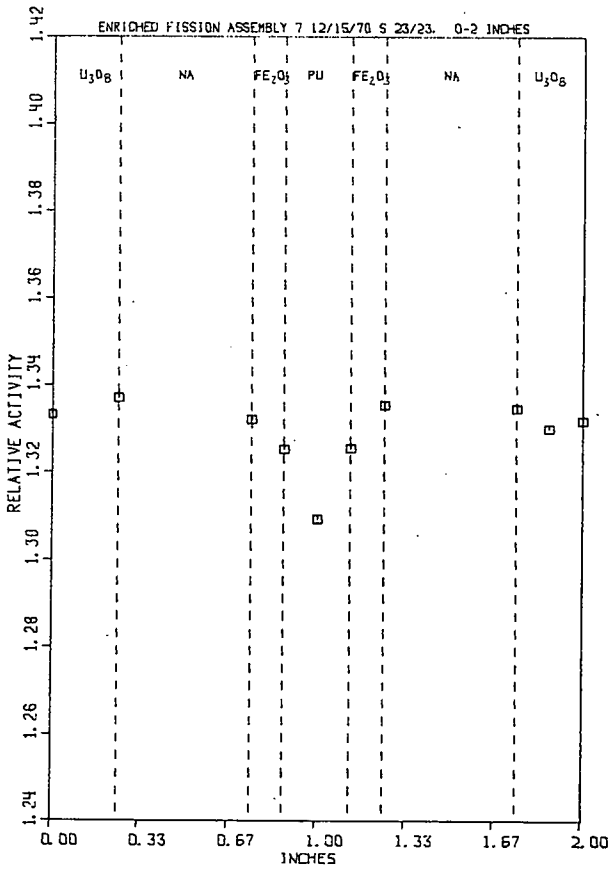

FIG. II-16-6. Relative Fission Rates Measured with ^{235}U Foils in the Unit Cell Plate Loading at the Center of ZPR-6 Assembly 7. *ANL Neg. No. 116-1005.*

of each isotope. Two types of reaction-rate ratios have been determined: ratios at the actual locations of the foils within the unit cell plate loading, and cell-averaged ratios. The cell-averaged ratios were determined using the results of the reaction-rate measurements at all locations within the unit cell and then averaging these rates over the constituents of the unit-cell plate loading. Several subsidiary experiments, including irradiation of foils at locations within a simulated fuel plate and a depleted uranium plate, were necessary to obtain volume-averaging factors.

The reaction-rate ratios are based on the absolute reaction rates which have been determined for each foil type and location. The uncertainties reported in Table II-16-V are due mainly to the uncertainty in the conversion of the relative reaction rates to absolute reaction rates. It is the accuracy in the determination of the mass of fissionable material in the absolute fission chambers that limits the precision of the absolute fission rates assigned to each foil.

The relative reaction rates measured at locations within the unit-cell plate loading at the center of Assembly 7 are shown in Figs. II-16-5 through II-16-8.

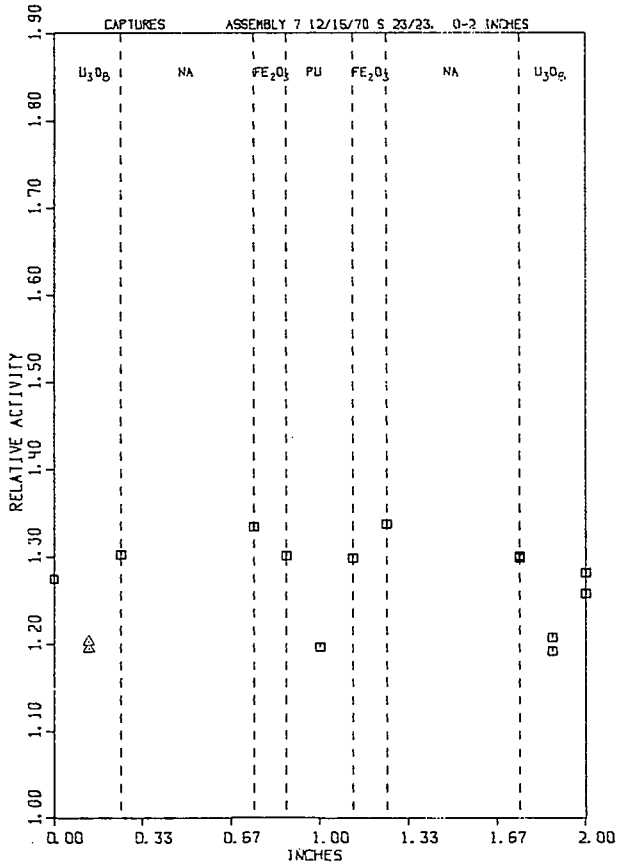

FIG. II-16-7. Relative Capture Rates Measured with ^{238}U Foils in the Unit Cell Plate Loading at the Center of ZPR-6 Assembly 7. *ANL No. 116-1004.*

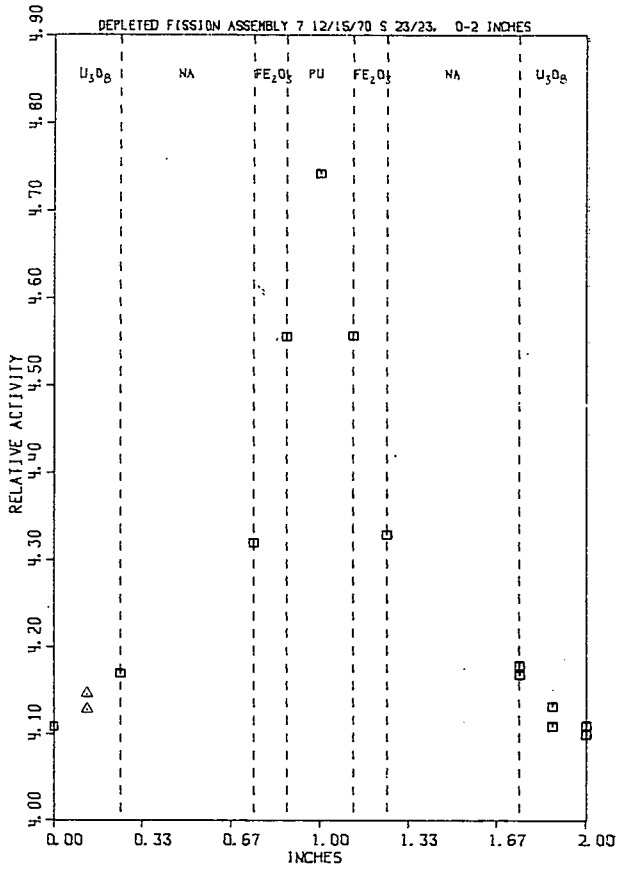

FIG. II-16-8. Relative Fission Rates Measured with Depleted Uranium Foils in the Unit Cell Plate Loading at the Center of ZPR-6 Assembly 7. *ANL Neg. No. 116-1009.*

All these results pertain to the foil-irradiation-box location designated f in Table II-16-II and Fig. II-16-4. The relative fission rate in ^{239}Pu is shown in Fig. II-16-5, the relative fission rate in ^{235}U is shown in Fig. II-16-6, and the relative capture and fission rates in depleted uranium are given in Figs. II-16-7 and II-16-8, respectively. In Figs. II-16-7 and II-16-8 the triangular points represent the rectangular depleted uranium foils that were sandwiched horizontally between ¼ x 1 x 2 in. U_3O_8 plates (see Figs. II-16-1 and II-16-2).

The relative reaction rates determined from the axial foil-irradiation traverses have been fitted with a cosine function using the method of least squares. A typical axial traverse and cosine curve are shown in Fig. II-16-9. In these fits, the reaction rates measured close to the reflector have been omitted. A complete summary of the extrapolated core heights determined for each traverse and foil type is given in Table II-16-VI.

The results of the axial foil irradiation traverses i several matrix drawers located at different positior radially in the core were combined to obtain radial reaction rate traverses. These traverses have been fitted with a Bessel (J_0) function using the method of

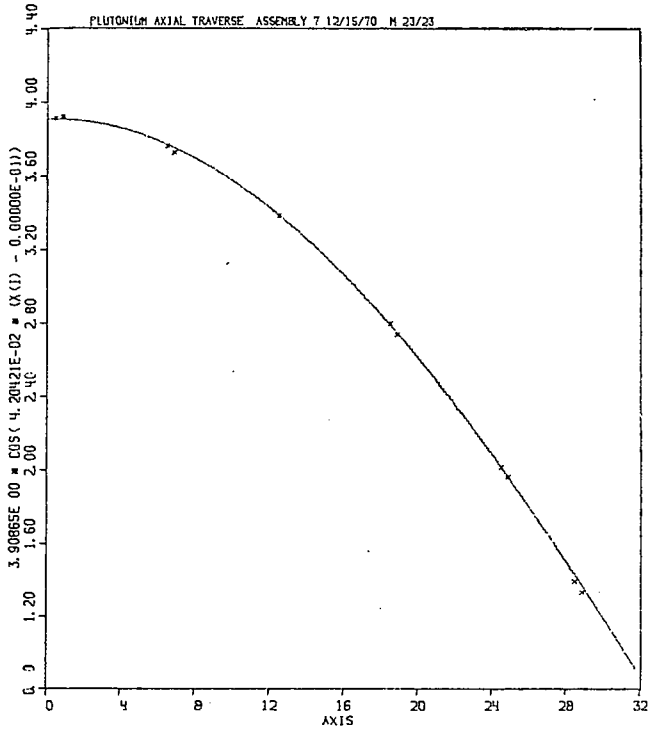

FIG. II-16-9. Cosine Fit to ^{239}Pu Axial Foil Traverse. *ANL Neg. No. 116-1007.*

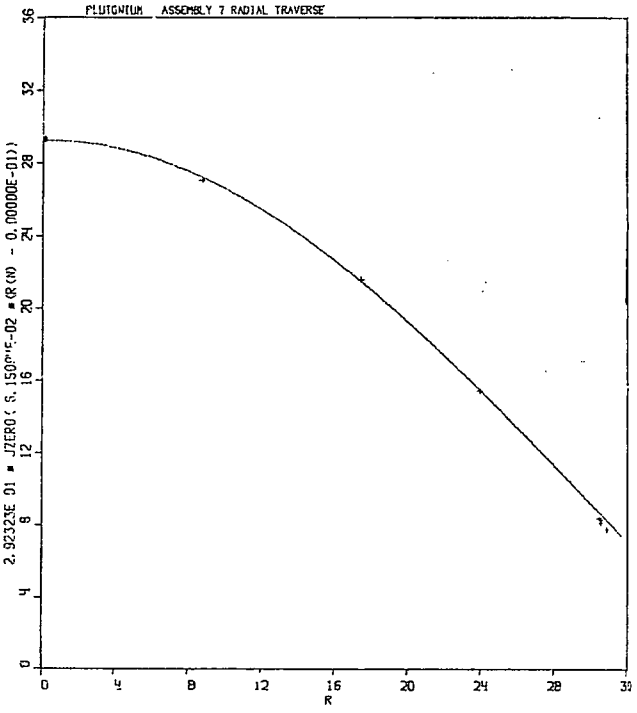

FIG. II-16-10. J_0 Fit to ^{239}Pu Radial Foil Traverse. *ANL Neg. No. 116-1006.*

TABLE II-16-VI. EXTRAPOLATED CORE HEIGHT DETERMINED FROM LEAST SQUARES COSINE FITS OF RELATIVE REACTION RATES MEASURED BY FOIL IRRADIATIONS IN ZPR-6 ASSEMBLY 7[a]

Reaction	Drawer Containing Traverse[b]						
	M23-23	S27-23	S31-23	S34-23	S37-23	M23-09	S33-33
	Radial Position of Traverse, cm						
	0	22.1	44.2	60.8	77.3	77.3	79.3
Depleted U Fissions[c]							
Between Pu & Fe_2O_3	184.24 ±0.35	184.00 ±0.50	184.15 ±1.38	184.14 ±1.51	184.37 ±2.05	183.44 ±1.15	183.57 ±1.27
Between Na & U_3O_8	184.93 ±0.49	183.86 ±0.31	184.20 ±1.13	183.08 ±0.86	182.40 ±1.17	182.15 ±1.10	182.35 ±1.06
Average	184.58	183.93	184.18	183.61	183.38	182.78	182.96
^{238}U Captures[c]							
Between Pu & Fe_2O_3	190.23 ±0.53	189.81 ±0.59	188.70 ±0.52	188.03 ±0.77	186.96 ±0.32	187.68 ±1.00	188.52 ±0.70
Between Na & U_3O_8	190.87 ±0.38	190.31 ±0.60	188.32 ±0.88	189.25 ±0.56	187.22 ±0.94	187.25 ±0.84	188.25 ±0.95
Average	190.55	190.06	188.51	188.64	187.09	187.47	188.39
Pu Fissions[c]							
Between Pu & Fe_2O_3	189.80 ±0.26	189.41 ±0.75	188.49 ±2.69	186.62 ±0.54	187.21 ±2.67	187.89 ±0.60	186.92 ±1.14

[a] Data from foils less than 10 cm from the axial reflector have been excluded. All distances are in cm.
[b] Refer to Table II-16-IV and Fig. II-16-4.
[c] The quoted errors are from the least squares fitting process.

TABLE II-16-VII. EXTRAPOLATED CORE RADIUS DETERMINED FROM LEAST SQUARES BESSEL (J_0) FITS OF RELATIVE REACTION RATES MEASURED BY FOIL IRRADIATIONS IN APR-6 ASSEMBLY 7[a]

Reaction	Axial Position of Uranium Traverse,[b] cm					
	3.8	19.1	34.3	49.5	64.8	72.4
Depleted U Fissions						
Between Pu & Fe_2O_3	97.93 ±0.04	96.29 ±0.46	96.39 ±0.62	98.49 ±0.63	96.66 ±0.32	95.19 ±0.49
Between Na & U_3O_8	98.09 ±0.31	96.85 ±0.29	97.39 ±0.42	97.66 ±0.64	96.40 ±0.19	94.89 ±0.58
Average	98.01	96.57	96.89	98.08	96.53	95.04
^{238}U Captures						
Between Pu & Fe_2O_3	100.03 ±0.82	101.36 ±0.58	100.08 ±0.81	99.70 ±0.10	99.07 ±0.71	97.04 ±0.88
Between Na & U_3O_8	100.48 ±0.92	100.67 ±0.99	100.25 ±0.60	99.63 ±0.69	99.38 ±0.74	97.46 ±0.70
Average	100.26	101.02	100.17	99.67	99.23	97.25
	Axial Position of Plutonium Traverse,[b] cm					
	1.3	16.5	47.0	62.2	72.4	
Pu Fissions						
Between Pu & Fe_2O_3	99.29 ±0.35	98.76 ±0.86	98.10 ±0.27	97.35 ±0.32	97.16 ±0.20	

[a] Data from foils less than 7.5 cm from the radial reflector have been excluded. The quoted errors are from the least squares fitting process. All distances are in cm.

[b] Distance from reactor midplane.

TABLE II-16-VIII. FISSION RATIOS MEASURED RELATIVE TO ^{239}PU IN ZPR-6 ASSEMBLY 7

Detector Drawer Location in Movable Half		Fission Foil in Counter	Fission Ratios[a] Per Atom	Calculated Fission Ratios[b] Per Atom
Column	Row			
19	24	^{239}Pu	1.0000	1.0000
22	27	^{238}U	0.0215 ± 0.0002	0.0217
25	27	^{240}Pu	0.1850 ± 0.0027	0.1839
27	24	^{235}U	1.0474 ± 0.0227	1.162

[a] Fission ratios have been corrected for fission fragment low-energy spectrum cut-off, position relative to ^{239}Pu detector, and count rates due to contaminating fissioning isotopes on each foil.

[b] Calculations were made with homogeneous cross sections (i.e., cross section from MC², not weighted by unit cell fluxes). Fission ratios were computed at a point on the reactor midplane corresponding to the radial position of each fission chamber drawer. The foils on the fission chambers were actually located 7⅛ in. from the reactor midplane.

least squares. A typical radial traverse and fit are shown in Fig. II-16-10. In these fits the reaction rates measured close to the reflector have been omitted. A complete summary of the extrapolated core radii determined for each traverse and foil type is given in Table II-16-VII.

FISSION RATIOS MEASURED WITH FISSION CHAMBERS

Four thin-walled Kirn-type fission flow counters[8] placed near the center of the core were used to measure fission rates in ^{239}Pu, ^{240}Pu, ^{235}U, and ^{238}U. Each counter was loaded in a regular fuel drawer in a two-inch cavity six inches from the axial reactor midplane, so that the fission foil was located 7⅛ in. from the drawer front (axial reactor midplane). The drawer location of each detector is given in Table II-16-VIII. All fission foils contained thin (~20 $\mu g/cm^2$) deposits of the fissioning isotope. The fission ratios obtained from several sets simultaneous count rates are listed in Table II-16-VI.

The fission ratios have been corrected for the fission fragment low-energy spectrum cutoff by using a flat

extrapolation from the valley between the alpha and fission fragment pulse height distributions to the zero energy channel. All detectors, except the ^{240}Pu detector, were located the same distance from the core center. A small position correction factor ($\sim$1.0%) was computed and applied to the ^{240}Pu fission rate in order to compare the ^{240}Pu fission rate directly with the ^{239}Pu fission rate. The fission rates recorded for each foil were also corrected for counts from other fissioning isotopes present on the foil deposit. In every case this correction was small ($<$1.0%) except for the ^{240}Pu foil, for which 8% of the fissions were due to isotopes other than ^{240}Pu. The weights of the fissioning isotopes present on each foil were determined as described in Ref. 9, using an α-counting technique.

The uncertainties in the fission ratios given in Table II-16-VIII include, in order of importance, contributions from the uncertainties in weights of isotopes on the foils, count rates, and the fission fragment low-energy spectrum cutoff loss.

The effects of deadtime in the counting system were investigated by measuring each fission ratio at several power levels. No correlation with power level was found, indicating that deadtime corrections to the measured count rates are unnecessary.

Fission rates per atom relative to ^{239}Pu were calculated at the radial positions of the detectors with homogeneous cross sections. The homogeneous cross sections have been weighted in the MC^2 code by the spectrum characteristic of a homogeneous mixture of core material.

The results of the calculations are given in Table II-16-VIII. Excellent agreement, within experimental error, is obtained for both the ^{238}U and ^{240}Pu fission rate relative to the ^{239}Pu fission rate. The calculated ^{235}U fission rate ratio is 11% greater than the measured value.

References

1. C. E. Till and W. G. Davey, *The Demonstration Reactor Benchmark Critical Assemblies Program*, Trans. Am Nucl. Soc. **13**, 293 (1970).
2. K. E. Plumlee and M. T. Wiggins, *Automatic Foil Activity Counting Facility and Data-Reduction Program* ANL-6628 (1962).
3. R. Sher, *Gamma-Gamma Coincidence Method for Measuring Resonance Escape Probability in ^{238}U Lattice*, Nucl. Sci. Eng. **7**, 479f (1960).
4. G. S. Stanford, *The Codes NURF, COMBO, and TWOSORCE for Processing Foil Counting Data*, ANL-7356 (1967).
5. G. S. Stanford, *New Features in the NURF Foil-Data Program*, Applied Physics Division Annual Report, July 1, 1969, to June 30, 1970, ANL-7710, p. 450.
6. A. R. Boynton, Q. L. Baird, K. E. Plumlee, W. C. Redman, W. R. Robinson and G. S. Stanford, *High Conversion Critical Experiments*, ANL-7203 (1967).
7. R. J. Armani, *Absolute Determination of Fission Rates in ^{235}U and ^{238}U and Capture Rates in ^{238}U by Radiochemical Techniques*, Proc. IAEA Symposium on Standardization of Radionuclides, IAEA, Vienna (1967), p. 613.
8. F. S. Kirn, *Neutron Detectors With an Absolute Fission Counter*, Symposium on Neutron Detection, Dosimetry and Standardization, Harwell, England, IAEA 2, p. 247 (1962).
9. R. J. Armani, *Preparation of ^{239}Pu and ^{241}Pu Isotopes for Capture-to-Fission Measurements in the Experimental Boiling Water Reactor*, Reactor Physics Division Annual Report, July 1, 1966 to June 30, 1967, ANL-7310, p. 379.

II-17. Integral Alpha Measurements in ZPR-6 Assembly 7

M. M. Bretscher

Method

Spectrum-averaged capture-to-fission ratios ($\bar{\alpha}$) have been measured at the center of the core of ZPR-6 Assembly 7 for ^{239}Pu, ^{235}U and ^{238}U by the reactivity-reaction rate technique.[1,2] Derived from first order perturbation theory, the equation which forms the basis of the method is

The measured quantities are

$\rho(A)$, $\rho \equiv$ relative reactivities of a ^{6}Li absorber and the fissile sample, respectively

$\rho'(\mathrm{Cf})$, $S \equiv$ apparent reactivity of a ^{252}Cf spontaneous fission source of strength S

$R_a(A)$, $R_f \equiv$ absolute reaction rates for absorption in ^{6}Li and for fission in the sample, respectively.

$$(1 + \bar{\alpha}) = \frac{R_a(A)\{(\rho/R_f)[1 - (\rho_s/\rho)] - (\bar{\nu}/S)\rho'(\mathrm{Cf})\bar{\phi}_f^*/\bar{\phi}_f^*(\mathrm{Cf})\}\bar{\phi}_a^*(A)/\bar{\phi}_a^*}{\rho(A)\{1 - [\rho_s(A)/\rho(A)]\}}. \quad (1)$$

The other terms in Eq. (1) are calculated from fundamental nuclear data and are defined as follows:

$[1 - \rho_s(A)/\rho(A)]$, $[1 - (\rho_s/\rho)]$
≡ correction terms for the scattering contribution to the measured reactivity in the ^{6}Li absorber and the fissile sample, respectively

$\bar{\phi}_f^*/\bar{\phi}_f^*(\mathrm{Cf})$, $\bar{\phi}_a^*(A)/\bar{\phi}_a^*$
≡ correction terms for differences in neutron importance for neutrons from induced fission in the sample and from spontaneous fission in the source and for neutrons absorbed in ^{6}Li and in the fissile material, respectively

$\bar{\nu}$ ≡ the average number of neutrons per fission in the fissile sample.

Eq. (1) is valid for measurements made at the center of the core provided $R_a(A)$, R_f and $\rho'(\mathrm{Cf})$ are normalized to a common power level.

Measurements

The plutonium, enriched uranium, and depleted uranium samples used for reactivity measurements were in the form of hollow cylinders with wall thicknesses of 5, 15, and 30 mils. They are more fully described in Ref. 3. The metallic lithium samples, containing 99.2 % ^{6}Li, were solid cylinders 0.309 in. diam and 1.75 in. long and were clad in 20 mil aluminum. Reference 1 describes the ^{252}Cf spontaneous fission source and the methods used to measure relative reactivities and absolute reaction rates. To correct for decay, a ^{252}Cf half-life of 2.621 ± 0.006 yr[4] was used. In addition to the cylindrical samples, the specific reactivity of a Pu-U-Mo fuel plate, typical of those used in the core of Assembly 7, was determined (see Paper II-19). The composition of the Pu-U-Mo material was 28.25 w/o Pu, 69.25 w/o depleted U and 2.5 w/o Mo. The plutonium composition was 86.5 w/o ^{239}Pu, 11.5 w/o ^{240}Pu, 1.81 w/o ^{241}Pu, and 0.2 w/o ^{242}Pu.

All the activation samples were mounted in a special holder 10 in. long, positioned at the reactor center in the oscillator tube of the radial sample changer, and irradiated simultaneously. Six enriched uranium foils (0.25 in. diam and 0.005 in. thick) and six small plutonium breeding gain foils[5] (each containing approximately 13 mg Pu) were equally spaced along a 2 in. length at the reactor center. Two ^{6}Li samples were supported end-to-end on each side of this central foil package and were followed by a depleted uranium foil of the same dimensions as the reactivity sample. Enriched uranium monitor foils were located at various positions along the 10 in. holder for the purpose of relating all the activations to the core center. In a drawer located two matrix positions off-center, the ¼ in. thick plutonium fuel plate at the front of the drawer was replaced with two ⅛ in. fuel plates. Plutonium breeding gain foils were placed on each side of these thin plates to get a measure of the fission rate averaged over the ¼ in. plate thickness. Monitor foils of plutonium and enriched uranium were also placed adjacent to fission counters and solid state track recorders (SSTRs) to relate these fission rate measurements to the central location.

Following the irradiation all the monitor foils were gamma counted. Fission rates for the six plutonium and six enriched uranium foils and the depleted uranium sample were measured radiochemically by determining the absolute ^{99}Mo fission product activity. The ^{99}Mo fission yields used in these analyses are given in Ref. 2. Table II-17-I lists the central isotopic specific fission rates measured by radiochemistry techniques, Kirn-type fission-flow counters,[6] and SSTRs.[7] Note that the absolute fission rates measured with the fission-flow counters are consistently lower than the radiochemistry results by about 7 %. The origin of this systematic discrepancy is currently being investigated. In the present analysis of the capture-to-fission ratios the fission counter data have been omitted since these fission rates lead to unusually small values of alpha.

The results of the reactivity and reaction rate measurements together with the californium data are summarized in Table II-17-II. The precision of the reactivity measurements is not as good as it was in the previous alpha determinations.[1,2] These larger errors are a result of the combined effects of reactor drift, which was more pronounced in this plutonium core than in the previous uranium cores, and a massive (~147 g) stainless steel plug used in the measurements to hold the sample in the rabbit. Errors in the reaction rates include estimates of the uncertainties in the fission yields and the calibration of the National Bureau of Standards (NBS) tritiated water standard used in the

TABLE II-17-I. Measured Isotopic Specific Fission Rates

Isotope	Fissions/g-sec		
	Radiochemistry	Fission Counter	SSTR
^{239}Pu	(3.560 ± 0.062)10^7	(3.321 ± 0.032)10^7	(3.526 ± 0.096)10^7
^{235}U	(3.764 ± 0.071)10^7	(3.524 ± 0.078)10^7	
^{238}U	(7.846 ± 0.210)10^5	(7.271 ± 0.160)10^5	

TABLE II-17-II. Measured Isotopic Specific Reactivities and Fission and Absorption Rates

Isotope	Sample Thickness, in.	ρ, Ih/g	R_f or R_a(^{6}Li), Reactions/g-sec
^{239}Pu	0.000		(3.543 ± 0.057)10^7
^{239}Pu	0.005	0.1560 ± 0.0028	
^{239}Pu	0.015	0.1613 ± 0.0014	
^{239}Pu	0.030	0.1630 ± 0.0005	
^{239}Pu	Fuel plate	0.1559 ± 0.0013	(3.523 ± 0.057)10^7
^{235}U	0.005	0.1269 ± 0.0019	(3.764 ± 0.071)10^7
^{235}U	0.015	0.1294 ± 0.0007	
^{238}U	0.015	−0.01150 ± 0.00062	(7.846 ± 0.210)10^5
^{6}Li	0.309	−1.9377 ± 0.0110	(8.194 ± 0.055)10^8

Note: ρ'(Cf) = 0.01495 ± 0.00012 Ih; S(Cf) = (5.663 ± 0.016)10^6 n/sec; radiochemical $^{238}\bar{\alpha}$ = 6.709 ± 0.181.

TABLE II-17-III. Homogeneous Atom Densities for ZPR-6 Assembly 7

	Exact Core	Pu/U/Mo Core	Pu/Al Core	Radial Blanket	Axial Blanket
Outer Radius, cm	24.34	75.00	79.92	113.84	
Isotope	Atomic Concentrations, 10^{21} atoms/cm^3				
^{238}Pu	0.00033	0.00049	<0.0001		
^{239}Pu	0.8867	0.8879	1.063		
^{240}Pu	0.1177	0.1178	0.0499		
^{241}Pu[a]	0.0128	0.0146	0.0049		
^{242}Pu	0.00141	0.00177	0.0005		
^{234}U	0.00006	0.00006	0.00006	0.00040	0.00040
^{235}U	0.0126	0.0126	0.0126	0.0866	0.0834
^{236}U	0.00030	0.00030	0.00030	0.0020	0.0020
^{238}U	0.5777	5.802	5.717	40.06	38.59
^{241}Am[a]	0.0036	0.0034	<0.001		
Mo	0.2357	0.2382	0.242	0.0034	0.0046
Na	9.2904	9.132	9.132		
O	13.98	14.82	14.82	0.021	0.030
Fe	12.97	13.53	13.15	4.197	5.652
Ni	1.240	1.212	1.481	0.5082	0.6910
Cr	2.709	2.697	2.675	1.172	1.579
Mn	0.212	0.213	0.21	0.0897	0.123
Al			0.101		

[a] ^{241}Pu decay to ^{241}Am corrected to May 1, 1971.

^{6}Li absorption rate determinations. A tritium half-life of 12.302 ± 0.040 yr[8] was used in the evaluation of $R_a(A)$. For ^{239}Pu, R_f was based on the average of the radiochemistry and SSTR measurements. The ^{238}U
pture rate was measured radiochemically and com-
ned with the fission rate to give the ^{238}U capture-to-
nssion ratio shown at the bottom of Table II-17-II. The apparent reactivity of the ^{252}Cf source was evaluated at the same power level used in the irradiation of the plutonium, enriched and depleted uranium, and lithium samples.

Calculated Quantities

Assembly 7 of ZPR-6 is a large, dilute, plutonium-oxide-fueled, single-zone core. Regional radii and average homogeneous atom densities are shown in Table II-17-III. Central flux and adjoint distributions (Table II-17-IV) were calculated in the 1-D diffusion approximation using multigroup cross sections gen-

TABLE II-17-IV. Calculated Central Flux and Adjoint Distributions

Group	Lower Energy Boundary, keV	Lethargy Interval	Real Flux	Adjoint Flux
1	6065	0.50	0.274	4.843
2	3679		1.116	4.225
3	2231		2.743	4.187
4	1353		3.889	3.844
5	820.8		4.833	3.463
6	497.9		9.434	3.365
7	302.0		8.986	3.263
8	183.2		12.619	3.173
9	111.1		11.054	3.077
10	67.38		10.096	2.974
11	40.87		8.389	2.884
12	24.79		6.805	2.850
13	15.03		6.038	2.868
14	9.119		4.415	2.942
15	5.531		2.660	3.045
16	3.355		1.638	3.210
17	2.035		0.569	3.341
18	1.234		1.737	3.411
19	0.749		1.205	3.573
20	0.454		0.768	4.144
21	0.275	↓	0.353	4.338
22	0.101	1.00	0.326	4.849
23	0.0373		0.0498	5.561
24	0.0137		0.00251	2.267
25	0.00504		0.00010	5.558
26	0.00068	2.00	0.00000	3.868

TABLE II-17-V. Calculated Quantities

Isotope	Thickness, in.	$1 - (\rho_s/\rho)$	$\bar{\phi}_f^*/\bar{\phi}_f^*$ (Cf)	$\bar{\phi}_a^*$(^{6}Li)/$\bar{\phi}_a^*$	$\bar{\nu}$
^{239}Pu	0.000	1.0061	0.9917	0.9725	2.9241
^{239}Pu	0.005	1.0066	0.9917	0.9721	2.9277
^{239}Pu	0.015	1.0074	0.9918	0.9714	2.9330
^{239}Pu	0.030	1.0084	0.9918	0.9702	2.9398
^{239}Pu	Fuel plate	1.0071	0.9917	0.9781	2.9314
^{235}U	0.000	1.0101	0.9856	0.9817	2.4564
^{235}U	0.005	1.0110	0.9856	0.9827	2.4589
^{235}U	0.015	1.0124	0.9856	0.9837	2.4625
^{238}U	0.015	0.7569	0.9891	0.9949	2.8195
^{6}Li	0.309	0.9824			

TABLE II-17-VI. ^{239}Pu CAPTURE-TO-FISSION RATIOS

Thickness, in.	ENDF/B Cross Sections		ORNL-RPI Cross Sections	
	Calculated	Measured	Calculated	Measured
0.000	0.255	(0.374 ± 0.062)[a]	0.327	(0.370 ± 0.062)[a]
0.005	0.250	0.353 ± 0.062	0.320	0.348 ± 0.062
0.015	0.244	0.294 ± 0.056	0.310	0.288 ± 0.056
0.030	0.235	0.278 ± 0.054	0.298	0.272 ± 0.053
Fuel plate	0.240	0.355 ± 0.055	0.304	0.348 ± 0.055

[a] By extrapolation of ρ to zero thickness.

erated from ENDF/B VERSION I data and corrected for plate heterogeneity effects. Following the procedures described in Ref. 2, $\bar{\nu}$ and the correction factors for scattering reactivity effects and differences in neutron importance were evaluated on the basis of the theoretical real and adjoint spectra (Table II-17-IV). These calculated parameters are given in Table II-17-V.

RESULTS AND DISCUSSION

The reactivity-reaction rate integral alpha values for ^{239}Pu, ^{235}U and ^{238}U were evaluated from Eq. (1) using the data of Tables II-17-II and II-17-V. Reactivities were measured for several sample thicknesses and these results were extrapolated to zero thickness and then substituted into Eq. (1) to obtain the infinitely dilute alpha values. Unlike the alpha measurements made in other fast reactor cores,[1,2] the fission rates were determined for only one sample thickness. Except for the case of the fuel plate, where the ^{239}Pu fission rate was averaged over the plate width, the results presented in Tables II-17-VI and II-17-VII were evaluated on the somewhat unrealistic assumption that the measured fission rate is independent of sample thickness. Since the neutron spectrum in Assembly 7 is harder than that in ZPR-3 Assembly 57, the fission rates are expected to fall off with sample thickness less rapidly than in the previous case.[2] However, the measured alpha values probably decrease a little more rapidly with increasing sample thickness than shown in Tables II-17-VI and II-17-VII because of self-shielding effects on the fission rates.

As expected, the plutonium alpha values are significantly larger than those calculated from ENDF/B VERSION I. For purposes of comparison, the data were re-evaluated on the basis of the recent ORNL-RPI ^{239}Pu differential cross section measurements.[9] The ^{239}Pu multigroup cross sections were modified in the 0.1 to 30 keV range to incorporate this ORNL-RPI data. Using these modified cross sections the central flux and adjoint distributions were re-evaluated to determine a new set of calculated quantities of the type shown in Table II-17-V. Alpha values based on the correction terms calculated from the ORNL-RPI data are also shown in Tables II-17-VI and II-17-VII. The measured alpha values are better predicted by ORNL-modified cross sections than by ENDF/B VERSION I.

The sensitivity of the reactivity-reaction rate integral alpha values to errors in both measured and calculated quantities is illustrated in Table II-17-VIII. For example, a 1% increase in the ^{6}Li absorption rate increases $^{239}\bar{\alpha}$, $^{235}\bar{\alpha}$, and $^{238}\bar{\alpha}$ by 3.8, 4.8 and 1.1%, respectively. A 1% decrease in the ^{239}Pu fission rate decreases $^{239}\bar{\alpha}$ by 5.2%. The results are very sensitive to the value used for $\bar{\nu}$. If $\bar{\nu}$ is increased by 1%, $^{239}\bar{\alpha}$ increases by 9.0% and $^{235}\bar{\alpha}$ by 10%. The errors assigned to the various quantities and their corresponding uncertainties in alpha are shown in Table II-17-IX. These results apply to the 5 mil ^{239}Pu and ^{235}U samples. For the thicker samples the errors in ρ are somewhat smaller. The error in the

TABLE II-17-VIII. ALPHA SENSITIVITIES

A 1.0% Increase In	Causes Percent Increase In $\bar{\alpha}$		
	$^{239}\bar{\alpha}$	$^{235}\bar{\alpha}$	$^{238}\bar{\alpha}$
$\dfrac{R_a(^6\text{Li})\bar{\phi}_a^*(^6\text{Li})/\bar{\phi}_a^*}{\rho(^6\text{Li})\{1-[\rho_s(^6\text{Li})/\rho(^6\text{Li})]\}}$	3.84	4.76	1.14
$(\bar{\nu}/S)\rho'(^{252}\text{Cf})\bar{\phi}_f^*/\bar{\phi}_f^*(^{252}\text{Cf})$	9.00	10.10	0.45
$[1-(\rho_s/\rho)](\rho/R_f)$	−5.21	−5.38	0.68

TABLE II-17-VII. URANIUM CAPTURE-TO-FISSION RATIOS

Isotope	Thickness, in.	ENDF/B Cross Sections		ORNL-RPI Cross Sections	
		Calculated	Measured	Calculated	Measured
^{235}U	0.000	0.309	(0.277 ± 0.050)[a]	0.305	(0.293 ± 0.051)[a]
^{235}U	0.005	0.306	0.265 ± 0.051	0.302	0.280 ± 0.052
^{235}U	0.015	0.300	0.241 ± 0.047	0.297	0.252 ± 0.047
^{238}U	0.015	6.957	(6.944 ± 0.298)[b]	6.858	(6.704 ± 0.284)[b]

[a] By extrapolation of ρ to zero thickness.

[b] Radiochemical $^{238}\bar{\alpha}$ = 6.709 ± 0.181.

TABLE II-17-IX. ERRORS

Quantity	Percent Error	Percent Error In		
		$^{239}\bar{\alpha}$	$^{235}\bar{\alpha}$	$^{238}\bar{\alpha}$
R_a(^{6}Li)	0.67	2.57	3.19	0.76
R_f : 239, 235, 238	1.61, 1.89, 2.67	8.38	10.16	1.81
S(^{252}Cf)	0.29	2.61	2.93	0.13
ρ(^{6}Li)	0.57	2.17	2.70	0.64
ρ: 239, 235, 238	1.80, 1.53, 5.43	9.35	8.23	3.68
ρ'(^{252}Cf)	0.78	7.00	7.85	0.35
$\bar{\nu}$: 239, 235, 238	1.00, 1.00, 1.00	9.00	10.10	0.45
	Combined Error	17.5	19.0	4.26

^{6}Li absorption rate includes an estimate of 0.5% uncertainty in the calibration of the NBS tritiated water standard. Uncertainties of 0.9, 1.8 and 2.4% in the ^{99}Mo fast fission yields for ^{239}Pu, ^{235}U and ^{238}U, respectively, contribute most of the errors in R_f. Although no errors have been assigned to the calculated correction factors, an uncertainty of 1.0% in $\bar{\nu}$ has been assumed.

It was mentioned earlier that the fission rates measured with the fission flow detectors led to unusually low values of alpha. For the case of the 5 mil samples, the ^{239}Pu capture-to-fission ratio is reduced from 0.353 to 0.229 and for ^{235}U from 0.265 to 0.167 if the fission flow counter data are used for R_f.

SUMMARY

Integral capture-to-fission ratios have been measured in ZPR-6 Assembly 7 by the reactivity-reaction rate method. The measurements include a determination of $^{239}\bar{\alpha}$ characteristic of the Pu-U-Mo fuel plates in the core. For both ^{235}U and ^{238}U the measured capture-to-fission ratios are in reasonable agreement with values calculated from ENDF/B VERSION I. In the case of ^{239}Pu, however, the results are significantly larger than the ENDF/B predictions and are best described by the ORNL-RPI differential data.[9] Unfortunately, the alpha values for ^{239}Pu and ^{235}U are very sensitive to uncertainties in $\bar{\nu}$, the average number of neutrons per fission, and the measured fission rates and reactivities for the fissile samples. Consequently, the errors in these capture-to-fission ratio determinations are quite large.

REFERENCES

1. M. M. Bretscher and W. C. Redman, *Low Flux Measurements of ^{239}Pu and ^{235}U Capture-to-Fission Ratios in a Fast Reactor Spectrum*, Nucl. Sci. Eng. **39**, 368 (1970).
2. M. M. Bretscher, J. M. Gasidlo and W. C. Redman, *A Comparison of Measured and Calculated ^{239}Pu, ^{235}U, and ^{238}U Integral Alpha Values in a Soft Spectrum Fast Critical Assembly*, Nucl. Sci. Eng. **45**, 87 (1971).
3. M. M. Bretscher, J. M. Gasidlo and W. C. Redman, *^{239}Pu, ^{235}U and ^{238}U Capture-to-Fission Ratios in ZPR-3 Assembly 57 Measured by the Reactivity-Reaction Rate Method*, Applied Physics Division Annual Report, July 1, 1969 to June 30, 1970, ANL-7710, pp. 112–121.
4. A. DeVolpi and K. G. Porges, *^{252}Cf Half-Life by Neutron Counting: Revision*, Inorg. Nucl. Chem. Letters **5**, 699 (1969).
5. A. B. Shuck, A. G. Hins, W. R. Burt and R. A. Beatty, *Breeding-Gain Specimens for EBR-I Core IV*, ANL-6659 (1963).
6. Reactor Development Program Progress Report, ANL-7765, 11 (December 1970).
7. R. Gold, R. J. Armani and J. H. Roberts, *Absolute Fission Rate Measurements with Solid State Track Recorders*, Nucl. Sci. Eng. **34**, 13 (1968).
8. R. Sher, *Half-Lives of ^{3}H and ^{238}Pu*, BNL-50233 (1970).
9. R. Gwin et al., *Simultaneous Measurement of the Neutron Fission and Absorption Cross Sections of ^{239}Pu Over the Energy Region 0.02 eV to 30 keV*, Nucl. Sci. Eng. **45**, 25 (1971).

II-18. Reactivity Worth Measurements of a Simulated B_4C Control Rod Assembly in ZPR-6 Assembly 7

E. M. BOHN, L. G. LESAGE and J. E. MARSHALL

INTRODUCTION

ZPR-6 Assembly 7 is a large, dilute, single-zone PuO_2 fueled critical assembly that has been constructed as part of the Demonstration Reactor Benchmark Program.[1] A complete description of Assembly 7 may be found elsewhere[2] (also, see Paper II-11). Sodium-void and small-sample reactivity worth measurements in Assembly 7 are reported in Paper II-19, measurements in a central rodded zone in Assembly 7 are reported in Paper II-25, and measurements in a central high-240 plutonium zone and sodium-voided high-240 plutonium zone are reported in Papers II-12 and II-13. Measurements of the reactivity worth of a single, simulated, LMFBR-type, B_4C control rod assembly loaded at the center of ZPR-6 Assembly 7 are reported here.

The simulated control rod consists of a single ZPR-6

drawer containing 63 v/o sodium (canned in stainless steel) and 37 v/o B_4C (natural boron). This simulated control rod loaded along the entire axial height of the core and blanket regions of the assembly represents the "control in" control rod assembly configuration. The "control out" configuration is obtained by replacing the B_4C in the simulated control rod with sodium.

The effects of adding BeO around the B_4C control rod assembly for both the "control in" and "control out" configurations has also been investigated.

The reactivity worths of the simulated control rod assembly configurations were determined using three methods of subcriticality measurement: analysis of rod drops with an inverse kinetics code, analysis of rod drops with a prompt-jump technique, and the inverse count rate-multiplication technique.

Description of the Simulated B_4C Control Rod Configurations

Each of the four control rod configurations ("control in" and "control out", both with and without BeO) are described below.

Simulated B_4C control rod configuration

The simulated B_4C control rod consists of 63 v/o sodium (canned in stainless steel) and 37 v/o B_4C (natural boron). The unit cell drawer loading pattern for this rod, illustrated in Fig. II-18-1, contains five ¼ in. thick sodium cans and six ⅛ in. thick $B_4^{NAT}C$ plates. The control rod is shown in Fig. II-18-1 as it appears when loaded at the center of Assembly 7.

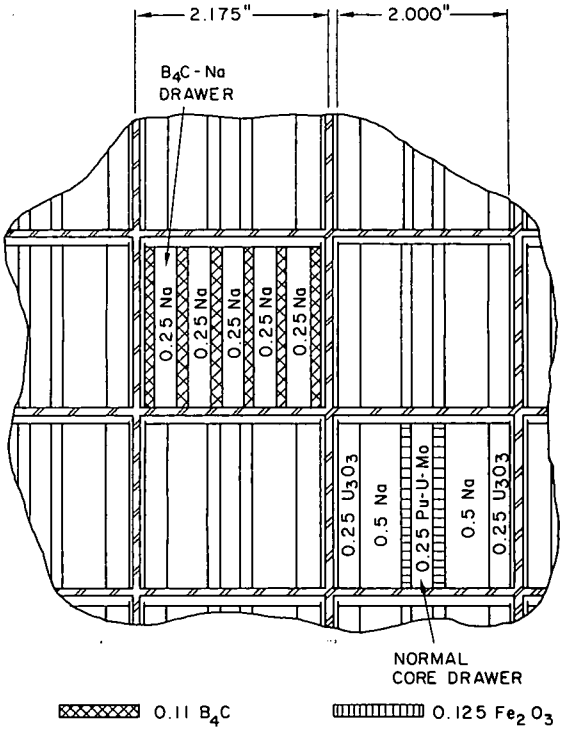

Fig. II-18-1. Cutaway View of the Radial Cross Section of ZPR-6 Assembly 7, Showing the B_4C Control Rod Configuration Loaded at the Center of the Core. *ANL Neg. No. 116-989.*

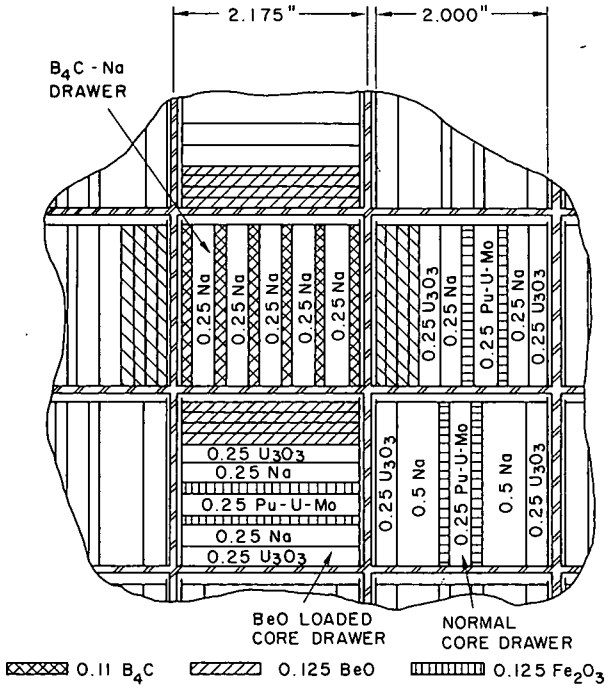

Fig. II-18-2. Cutaway View of the Radial Cross Section of ZPR-6 Assembly 7 Showing the B_4C-BeO Control Rod Configuration Loaded at the Center of the Core. *ANL Neg. No. 116-988.*

Simulated B_4C-BeO control rod configuration

BeO was loaded around the B_4C control rod described above to form the B_4C-BeO control rod configuration. A ½ in. thick column of ⅛ in. thick BeO plates was loaded into the drawers adjacent to the B_4C control rod drawer. The B_4C-BeO control rod configuration as loaded at the center of Assembly 7 is shown in Fig. II-18-2.

Sodium channel configurations

The "control out" configurations corresponding to the simulated B_4C and B_4C-BeO control rod configurations described above were obtained by replacing the B_4C with sodium along the entire length of the control rod. The drawer loading patterns for the sodium channel and the Na-BeO channel are the same as in Figs. II-18-1 and II-18-2, respectively, with all B_4C replaced by sodium.

The atom densities in the simulated control rod assembly are given in Table II-18-I for each "region"

TABLE II-18-I. HOMOGENEOUS COMPOSITIONS IN THE SIMULATED CONTROL ROD ASSEMBLY REGIONS,[a] 10^{21} atoms/cc

Region	Na	B-10	B-11	C	Be	O	Fe+[(d)]	Ni	Cr	Mn
Na Channel	17.97	—	—	—	—	—	9.54	1.46	3.19	0.190
B_4C-Na Channel	10.15	3.80	14.2	4.76	—	—	10.3	1.34	2.90	0.210
BeO Ring	—	—	—	—	53.2	53.2	6.67	0.804	1.86	0.135

[a] The sodium channel and B_4C-Na channel occupy one drawer in the reactor matrix (i.e., one unit cell in volume); see Figs. II-18-I and II-18-2. The area of one drawer (including matrix) is 30.5201 cm^2. Thus, when loaded at the center of the core, the effective circular radius of the control rod channel is 3.117 cm. The BeO loaded in the drawers around the control rod channel (see Fig. II-18-2) occupies an annular volume around the control rod channel with inner radius 3.117 cm and outer radius 4.448 cm.

The concentrations for each region of the control rod assembly include SS304 contributions from the drawer and matrix.

[b] Fe+ ≡ Fe + (SS304-Fe-Ni-Cr-Mn).

of the control rod configuration. Three regions have been defined: the B_4C-Na channel, the sodium channel, and the BeO ring. The atom concentrations in the simulated B_4C control rod configurations are just those listed for the B_4C-Na channel. The atom concentration in the simulated B_4C-BeO control rod configuration are given for two "regions" of the control rod configuration: the B_4C-Na channel and the BeO ring around the B_4C-Na channel.

THE REFERENCE CORE: ZPR-6 ASSEMBLY 7, LOADING 79

The reference core loading for the control rod measurements was Loading 79 of Assembly 7. The core is described in Figs. II-18-3 and II-18-4. The atom densities in each region of the core are given in Table II-18-II.

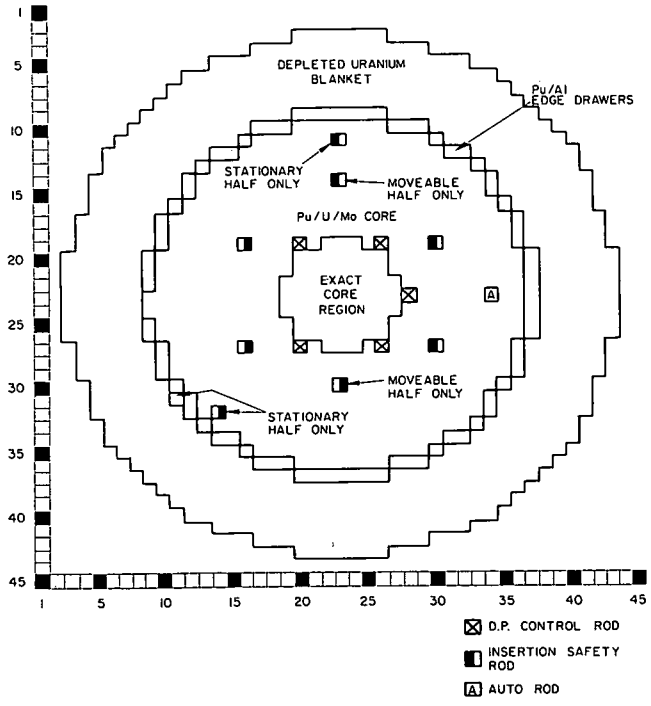

FIG. II-18-3. Radial Cross Section of ZPR-6 Assembly 7, Loading 79. *ANL Neg. No. 116-925.*

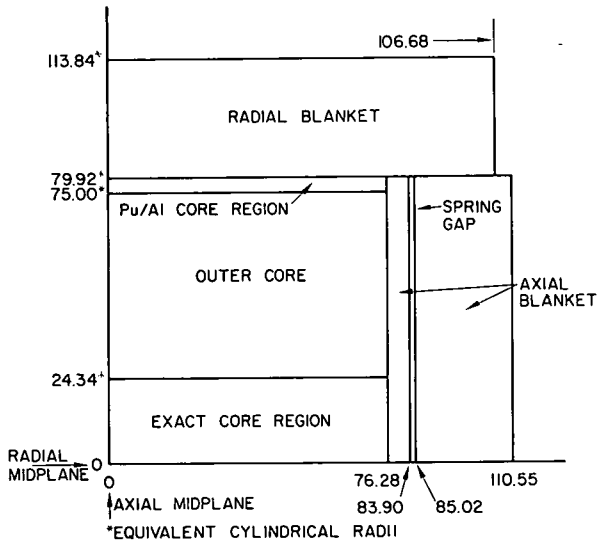

FIG. II-18-4. Axial Cross Section of ZPR-6 Assembly 7, Loading 79. *ANL Neg. No. 116-924.*

The excess reactivity of this core was carefully measured and found to be (72.3 ± 2.2) Ih. The precision in the excess reactivity measurement is limited by the uncertainty in the reactor tables separation when the reactor halves are brought together ("table closure" uncertainty). The uncertainty due to table closure has been conservatively estimated as ±2 Ih.*

REACTIVITY WORTH MEASUREMENTS

Each of the simulated control rod configurations described above was loaded at the center of the reference core displacing the center fueled drawers in each reactor half. The subcriticality of the core was measured

* The contribution to the uncertainty due to table closure has been estimated or measured from time-to-time during the Assembly 7 program. Earlier estimates used ±0.5 Ih. Depending upon the exact sequence of table closure operations used, the table closure uncertainty may vary from ±0.5 to ±2.0 Ih.

TABLE II-18-II. Atom Densities for ZPR-6 Assembly 7, Loading 79,[a] 10^{21} atoms/cc

Region	^{238}Pu	^{239}Pu	^{240}Pu	^{241}Pu[b]	^{242}Pu	^{234}U	^{235}U	^{236}U	^{238}U	^{241}Am[b]	Mo	Na	O[c]	Fe[d]	Ni	Cr	Mn	Al
Exact core	0.00033	0.8867	0.1177	0.0128	0.0014	0.00006	0.0126	0.00030	5.777	0.0036	0.2357	9.290	13.98	12.97	1.240	2.709	0.212	
Pu/U/Mo core	0.00049	0.8879	0.1178	0.0146	0.00177	0.00006	0.0126	0.00030	5.802	0.0034	0.2382	9.132	14.82	13.53	1.212	2.697	0.213	
Pu/Al core[e]	<0.0001	1.063	0.0499	0.0049	0.0005	0.00006	0.0126	0.00030	5.717	<0.001	0.242	9.132	14.82	13.15	1.481	2.675	0.21	0.101
Axial blanket[f]						0.00040	0.0834	0.0020	38.59		0.0046[g]		0.030[g]	5.652	0.6910	1.579	0.123	
Radial blanket[f]						0.00040	0.866	0.0020	40.06		0.0034[g]		0.021[g]	4.197	0.5082	1.172	0.0897	

[a] The exact core and Pu/U/Mo core have the same unit cell loading pattern and are essentially equivalent. The so-called "exact core" region is one in which the weights of all drawer materials have been carefully recorded in order to minimize the uncertainties associated with average plate weights and to aid in the comparison of experimental results between this core and an earlier core containing fuel pins in calandria cans in the exact core region (see Paper II-25).

[b] ^{241}Pu β ^{241}Am decay corrected to May 1, 1971.

[c] Includes $\sim 0.001 \times 10^{21}$ atoms/cc due to SS304 and Pu/U/Mo fuel impurities.

[d] Includes $\sim 0.001 \times 10^{21}$ atoms/cc due to heavy (atomic weight $\geq$ Si) SS304 impurities and Pu/U/Mo fuel impurities.

[e] The compositional data available for the Pu/Al plates are not as complete as those for the Pu/U/Mo fuel.

[f] The axial blanket material was loaded into special stainless steel backdrawers. The radial blanket material was loaded directly into the matrix tubes. In addition, the axial blanket atom concentrations include the spring gap materials and volume. (See Fig. II-18-2.)

[g] Arising from SS304 impurities.

TABLE II-18-III. RESULTS OF SUBCRITICALITY MEASUREMENTS OF THE SIMULATED CONTROL ROD CONFIGURATIONS IN ZPR-6 ASSEMBLY 7,[a] Ih

Simulated Control Rod Configuration	Subcriticality Measurement Technique		
	Rod Drops Analyzed by:		Multiplication
	Inverse Kinetics	Prompt-Jump Method	
Sodium channel	−35.4 ± 2.3	—	−34.2 ± 2.4
B_4C control rod	−457 ± 19	−460 ± 17	−450 ± 11
B_4C-BeO control rod[b]	−593 ± 37	−569 ± 13	−594 ± 21
Na-BeO channel[b]	−54.3 ± 2.2	−59 ± 3	−59.4 ± 2.1
B_4C-BeO in stationary reactor half, Na-BeO in movable reactor half	−340 ± 5	−339 ± 5	−329 ± 12

[a] Each control rod configuration was loaded at the center of Assembly 7, Loading 79, displacing the center fueled drawers in each reactor half. The excess reactivity of Loading 79, with the center fuel drawers, was (72.3 ± 2.2) Ih. Reactivity worths relative to Loading 79 are given in Table II-18-IV. There are 1033 Ih per percent $\delta k/k$ and $\beta_{eff} = 3.18 \times 10^{-3}$.

[b] Sodium was displaced from the four drawers adjacent to the center drawer to accommodate the ½ in. BeO loading (see Fig. II-18-2). The contributions to the measured reactivity change due to loss of sodium is estimated (from other measurements) to be +5 Ih.

using three methods: analysis of rod drops by an inverse kinetics code to determine the initial subcriticality of the core (see Paper II-32), analysis of rod drops using a prompt-jump formulation to determine the initial subcriticality, and the inverse count rate-multiplication technique. The inverse count rate-multiplication technique made use of the reactor flux monitoring channels 3 and 4 which were calibrated by inverse kinetics for count rate versus subcriticality at a near critical power level (−7 Ih) in the reference core.

The results of the subcriticality measurements are given in Table II-18-III. In addition to the four simulated control rod configurations described above, an additional configuration has been included (measurement 5 in Table II-18-III). In this additional measurement, the B_4C-BeO configuration was loaded into the stationary reactor half and the Na-BeO configuration was loaded into the movable reactor half. This combination configuration simulates a control rod inserted exactly half way into the core.

The results given in Table II-18-III have been corrected for temperature and ^{241}Pu decay to the state of the reference core, using measured temperature and ^{241}Pu decay reactivity coefficients.

The precisions reported for each measurement in Table II-18-III include estimated uncertainties due to table closure, temperature and ^{241}Pu decay corrections, and estimated precisions associated with each measurement technique. In the case of inverse kinetics, the estimated uncertainty in the technique is the standard deviation of the results obtained from a number of rod drops. For the prompt-jump technique, two rod drops were analyzed for each experiment; the estimated uncertainty in this case is the average deviation from the average subcriticality obtained from the two rod drops. The results reported for the multiplication techniques are an average of the subcriticality obtained with the flux monitoring channels 3 and 4 for each experiment. A 5% random uncertainty was estimated for the result obtained from each of the two channels.

The three measurement techniques are in good agreement for any one control rod configuration.* There appears to be no bias in any of the three methods; that is, one method does not consistently give a high or low value among the set of three values for each control rod configuration.

RELATIVE REACTIVITY WORTHS OF THE SIMULATED CONTROL ROD CONFIGURATIONS

The reactivity worth of each control rod configuration relative to the reference core, (Loading 79 with fuel drawers loaded at the center in S/M 23-23) is given in Table II-18-IV. Also given in Table II-18-IV are the reactivity worths relative to the sodium and Na-BeO channels. These latter two comparisons permit an inference of the "control in" relative to the "control out" worth of a simulated control rod.

The B_4C control rod "control in" configuration is worth about −420 Ih ($1.28) compared with the "control out" configuration. Similarly, the B_4C-BeO "control in" configuration is worth about −537 Ih ($1.63) relative to the "control out" configuration. The BeO enhances the worth of the B_4C control rod channel by a factor of 1.28.

For the "control out" configurations, the sodium channel is worth −107 Ih ($0.33) and the Na-BeO configuration is worth about −128 Ih ($0.39). The BeO increases the negative worth of the "control out" configuration by 21 Ih.

The B_4C-BeO control rod inserted half-way into the core (B_4C-BeO in the stationary half, Na-BeO in the movable half) is worth about 53% of the B_4C control rod "full in."

* It should be pointed out that the three techniques are not completely independent. Both methods of rod drop analysis make use of the point reactor kinetics equations and the same rod drop data. The multiplication technique relies on a calibration near critical by the inverse kinetics code.

TABLE II-18-IV. REACTIVITY WORTHS OF THE SIMULATED B_4C CONTROL ROD CONFIGURATIONS IN ZPR-6 ASSEMBLY 7

Simulated Control Rod Configuration	Reactivity Worth (Ih) Relative to:								
	S/M 23-23 Fuel Drawers (Loading 79)			Sodium Channel			Na-BeO Channel		
	Rod Drops Analyzed by:		Multiplication	Rod Drops Analyzed by:		Multiplication	Rod Drops Analyzed by:		Multiplication
	Inverse Kinetics	Prompt Jump		Inverse Kinetics	Prompt Jump		Inverse Kinetics	Prompt Jump	
Sodium channel	−107.7 ± 3.2	[a]	−106.5 ± 3.3				−18.9 ± 3.2		−25.2 ± 3.2
B_4C control rod	−529.3 ± 19.1	−532.3 ± 17.1	−522.3 ± 11.2	−421.6 ± 19.1	[a]	415.8 ± 11.3	−402.7 ± 19.1	−401 ± 17.3	−390.6 ± 11.2
B_4C-BeO control rod	−665.3 ± 37.1	−641.3 ± 13.2	−666.3 ± 21.1	−557.6 ± 37.1	[a]	559.8 ± 21.1	−538.7 ± 37.1	−510 ± 13.3	−534.6 ± 21.1
Na-BeO Channel	−126.6 ± 3.1	−131.3 ± 3.7	−131.7 ± 3.0	−18.9 ± 3.0	[a]	−25.2 ± 3.2			
B_4C-BeO in stationary reactor half, Na-BeO in movable reactor half	−412.3 ± 5.5	−411.3 ± 5.5	−401.3 ± 12.2	−304.6 ± 5.5	[a]	−294.8 ± 12.2	−285.7 ± 5.5	−280.7 ± 5.8	−269.6 ± 12.2

[a] Data not available.

REFERENCES

1. C. E. Till and W. G. Davey, *The Demonstration Reactor Benchmark Critical Assemblies Program*, Trans. Am. Nucl. Soc. **13**, 293 (1970).

2. L. G. LeSage, E. M. Bohn, J. E. Marshall, R. A. Karam, C. E. Till, R. A. Lewis and M. Salvatores, *Initial Experimental Results from ZPR-6 Assembly 7, The Single Zone Demonstration Reactor Benchmark Assembly*, Trans. Am. Nucl. Soc. **14**, 17 (1971).

II-19. Sodium-Void and Small-Sample Reactivity Worth Measurements in ZPR-6 Assembly 7

L. G. LeSage, E. M. Bohn and J. E. Marshall

I. Introduction

This report describes the reactivity worth measurements that have been made in the uniformly loaded version of ZPR-6 Assembly 7 and in the rodded zone which was temporarily installed at the center of ZPR-6 Assembly 7. The measurements include central small- and large-sample sodium void, radial and axial small-sample sodium void, radial subassembly-size sodium void, small-sample central worths for both cylindrical and plate type samples and radial small-sample worth traverses.

ZPR-6 Assembly 7 is a large, uniform, mixed plutonium-uranium oxide critical assembly, constructed as part of the Demonstration Reactor Benchmark Critical Assembly Program.[1] Assembly 7 has been described in Ref. 2 and Paper II-11. A description of the central rodded zone and the rodded zone measurements is included in Paper II-25.

Central zones with a ^{240}Pu content roughly 2.5 higher than normal, both with sodium and sodium-voided (i.e., the H240 and VH240 zones), have also been installed in Assembly 7. Results of the reactivity worth measurements in the H240 and VH240 zones, which are not included in the paper, are reported in Papers II-12 and II-13. Subcritical central control-rod reactivity measurements have also been made in Assembly 7. These results are also not included since they are contained in Paper II-18.

The primary purposes of the Assembly 7 central worth measurements were (1) to obtain direct measurements of important worths in a typical LMFBR spectrum, (2) for comparison with calculation as a test of cross section data and analytical techniques, (3) for purposes of normalization between various assemblies, pecially between Assembly 7 and ZPPR Assembly [1]) and between Assembly 7 and ZPR-6 Assembly 6A (see Paper II-11), and (4) for use in correcting slight composition mismatches between the rodded zone in Assembly 7 and the matching plate zone. The spatial worth traverses also provided direct measurements of the important worths as a function of position in typical LMFBR spectra and provided tests of the spatial variations of the cross sections and real and adjoint fluxes.

II. Description of Experiments

The reactivity measurements were made by two different techniques. The 3 x 3-drawer central sodium void and the subassembly-size sodium-void measurements were made by a technique involving the careful measurement of the total assembly excess reactivity both before and after the removal of the sodium. All of the other reactivity measurements were made using either the axial or the radial sample changers and a calibrated autorod. A description of each of these experimental techniques is given in this section.

A. Measurement of Assembly Excess Reactivity

In the excess reactivity technique, the total excess reactivity of the assembly is measured both before and after a material change in the core. With regard to this experimental technique, the term "excess reactivity of the core" means the excess reactivity that would be present if all of the fuel and boron rods and the autorod were moved to their most reactive positions and the reactor temperature was adjusted to a reference level. The difference in the excess reactivity between the two configurations, corrected for ^{241}Pu decay, is taken as the reactivity associated with the material change. This technique is used either when the size of the perturbed region is larger than the maximum size sample that can be handled by one of the sample changers or the reactivity change is larger than the worth of the autorod. A detailed description of this type of reactivity measurement is also given in Paper II-25 where the measurement of the reactivity difference between the matched plate and rodded zones is discussed.

Both the central 3 x 3-drawer by 12-in. sodium-void measurements and the subassembly-size sodium-void

measurements reported here were made by this method. The sequence of operations was as follows:

1. The excess reactivity of the core was measured.
2. The assembly was shut down and the sodium-filled stainless steel cans were replaced with matched empty cans.
3. The excess reactivity of the core with the sodium-voided region installed was measured.
4. The assembly was shut down and the matched empty cans were replaced with the original sodium-filled cans.
5. The excess reactivity of the reference core was again measured.

It was necessary to wait about 1½ h after the assembly halves were driven together for the temperatures in the core to stabilize adequately for accurate measurements. The power was held constant with the autorod during the measurement, the core axial temperature profile was measured, the positions of all fuel rods were recorded, and the average autorod position was obtained from an integration of the rod-position analog signal. The measured excess reactivity consisted of the following components:

1. The available reactivity contained in the withdrawn fuel rods. These rods were calibrated using an inverse kinetics code.
2. The available reactivity contained in the partially withdrawn autorod. The autorod was also calibrated using an inverse kinetics code. The average autorod position during a specified time interval was obtained from integration of a voltage proportional to autorod position.
3. Corrections were made for core temperature differences and for decay of ^{241}Pu among the different measurements. An attempt was made to hold the core temperature to within about 1°C for each of the measurements so that the temperature correction was relatively small. The measured temperature coefficient of reactivity was (-4.05 ± 0.05)Ih/°C and the coefficient of ^{241}Pu decay was -0.33Ih/day.

The temperature coefficient of reactivity and rod calibrations using the inverse kinetics code are discussed in Ref. 3 and Paper II-32.

The imprecision of the excess reactivity measurements is determined by (1) the precisions of the fuel rod calibrations, the temperature coefficient, and the ^{241}Pu decay coefficient and (2) the scatter in the results due to non-reproducibility in the assembly table closure and fuel rod positions between different start-ups. A 1σ uncertainty of 0.5 Ih was estimated for the combined uncertainties of the fuel rod calibrations, the temperature coefficient, and the ^{241}Pu decay coefficient. A 1σ uncertainty of 0.5 Ih was estimated for the combined uncertainties due to table closure and rod positions (which will be referred to as "table closure") based on repeated measurements of the core excess reactivity when no material change was made in the core. However, recent measurements made with the H240 zone installed in Assembly 7 have indicated a 2 Ih 1σ imprecision associated with table closure. It is not known whether there has been some fundamental change in the ZPR-6 facility to account for this change in the table closure value or whether the good agreement in the earlier results was simply fortuitous. Until this point is resolved, the total 1σ imprecision in the excess reactivity measurement resulting from table closure will be taken as 2 Ih.

B. AXIAL SAMPLE-CHANGER MEASUREMENTS

The axial sample-changer (ASC) consists of a specially fitted core drawer, more than twice as long as the core height, with remotely-actuated motor-driven devices to insert and withdraw samples from a multi-sample magazine and to move the drawer along the axial centerline of the assembly. A description of the ASC, including a picture of the oscillator drawer, is given in Ref. 4. The oscillator drawer was loaded with regular plate-core materials except for a sample position which could handle samples 2 x 2 x z-in, where z, the axial dimension, could vary from ⅛ inch to 2-in. The sample-changer device was located behind the axial blanket, and the samples were oscillated from this location to the core center or to any other selected position on the axial centerline.

Two types of samples were measured in the ASC. The simplest were 2 x 2 x 1 in. blocks of pure material (some canned in stainless steel and some bare) which were positioned in the sample cavity with the 1-in. dimension in the z direction. The other samples consisted of plates of the regular core materials contained in thin-walled 2 x 2 x 2 in. stainless steel boxes. The plates were arranged in the boxes similar to the arrangement in the nominal unit-cell drawer loading (see Figs. II-19-1 and II-19-2).

The unit-cell plate samples were used to measure the worths of the individual core constituent materials in their normal plate environment. The procedure was to measure the worth of a plate loaded sample box, then remove part of one of the materials from the sample box and remeasure the box worth. The worths of each of the core constituent materials were measured in this manner. The procedure used to make a sample worth measurement with the ASC is outlined below:

1. The sample was inserted into the oscillator drawer and the drawer and sample were driven into the core.

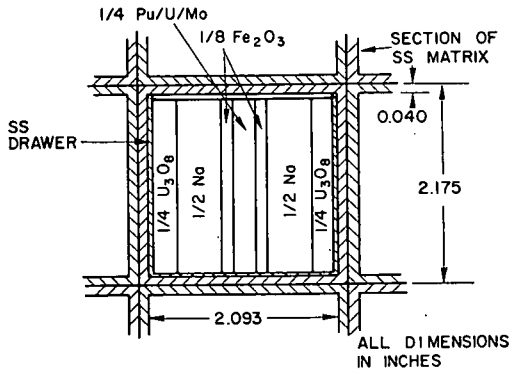

FIG. II-19-1. Cross Section of Unit-Cell Showing Matrix and Plate Loaded Drawer, ZPR-6 Assembly 7. *ANL Neg. No. 116-1034.*

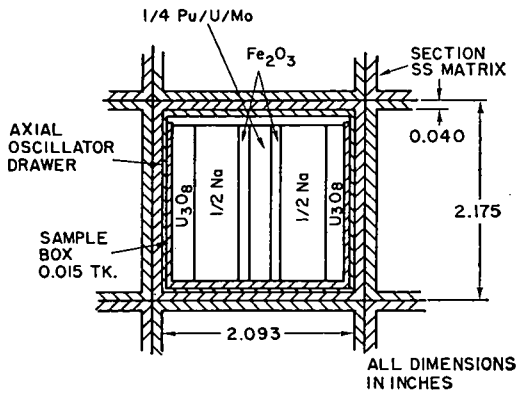

FIG. II-19-2. Cross Section of Central Matrix Tube Containing Axial Oscillator Drawer and Sample Box, ZPR-6 Assembly 7. *ANL Neg. No. 116-1035.*

2. A waiting time of 1 to 2 min was allowed for reactor stabilization.
3. The average autorod position was obtained from an autorod integration measurement. The integration times varied from 2 to 5 min.
4. The oscillator drawer was driven out of the core, the sample was removed, and the oscillator drawer was driven back into the core.
5. A waiting time of 1 to 2 min was allowed for reactor stabilization.
6. The average autorod position was again obtained from a 2 to 5 min autorod integration measurement.
7. The oscillator drawer was driven out of the core. The cycle was repeated starting at step 1.

In order to improve accuracy and to eliminate the effects of first and second order reactor drifts, the cycle is generally repeated several times. The worth of the sample is inferred from the difference in the average position of the calibrated autorod between the sample-in and sample-out integrations. The operation of a somewhat similar ASC is also described in detail in Ref. 5. The calculation of the measurement precision and the drift cancellation are discussed in Ref. 6.

A 1σ imprecision of 0.005 Ih was typical for a total ASC measurement time of about 30 min. This value does not include the uncertainty in the autorod calibration which will be discussed in section IID. In general, however, the reactivity results obtained from sample changer and calibrated autorod measurements have a much better precision than the results obtained from core-excess-reactivity measurements.

C. RADIAL SAMPLE CHANGER

The radial sample changer (RSC) consists of a long ouble-walled thin stainless steel sample tube, installed in a slot located along the radial midplane of the assembly, with remotely actuatable devices to insert and withdraw samples from an eight-sample cylindrical

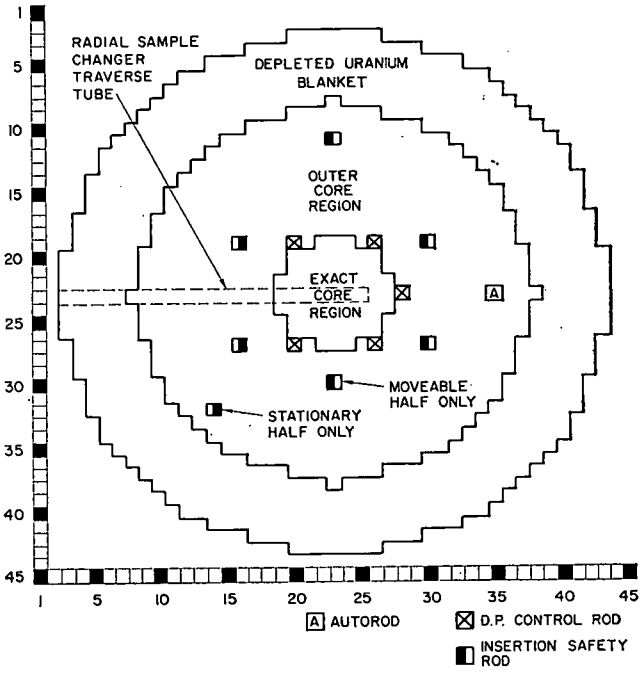

FIG. II-19-3. Radial Cross Section of ZPR-6 Assembly 7 Showing Position of Radial Sample Changer Tube. *ANL Neg. No. 116-1032.*

magazine and to pneumatically oscillate the sample between the cylinder and the end of the sample tube. The RSC tube can be positioned remotely so that the samples are driven into the center of the core or to any selected position along the core radius at the axial midplane. The radial hole for the RSC tube is made by pushing each drawer back 1-in. along a horizontal row in the stationary half (row 23) so that the cross section of the hole is 1-in. wide and 2 in. high.

The location of the RSC tube and also that of the calibrated autorod in Assembly 7 are shown in Fig. II-19-3. Figure II-19-4 is a vertical cross section showing the RSC tube and sample and the surrounding matrix

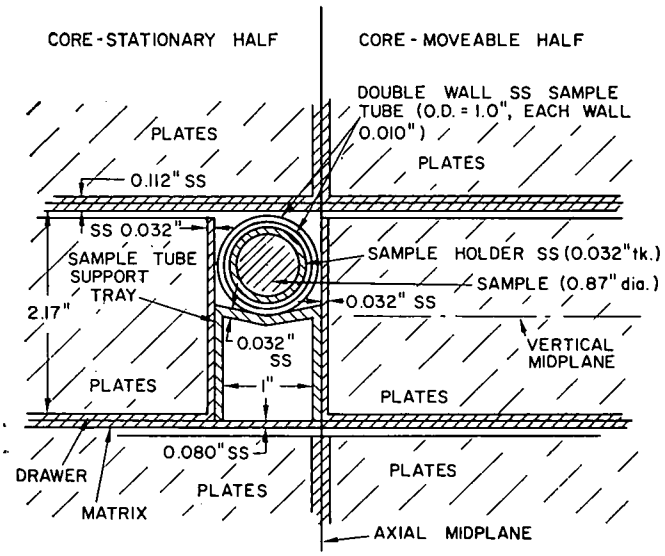

FIG. II-19-4. Vertical Section of ZPR-6 Assembly 7, Showing Arrangement of the Sample and Radial Sample Changer Tube in the Assembly. *ANL Neg. No. 116-1038.*

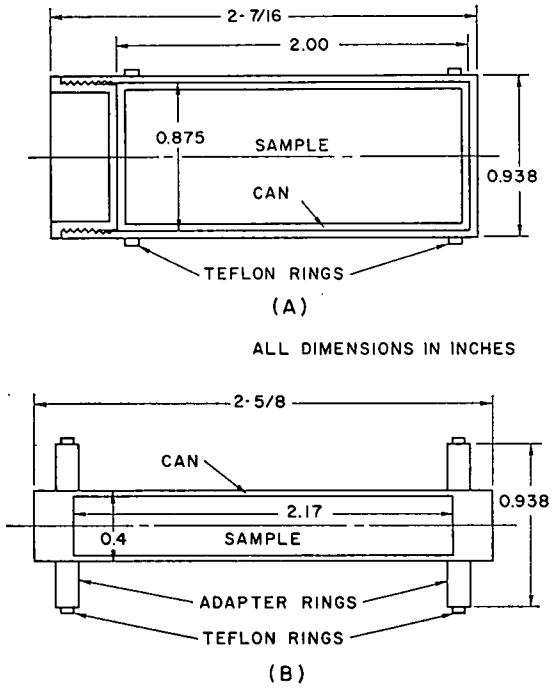

FIG. II-19-5. Axial Section Drawings of the Argonne-East and Argonne-West Type Samples for the Radial Pneumatic Sample Changer. *ANL Neg. No. 116-1039.*

and drawers. A more complete description of the RSC construction and operation is given in Ref. 7.

When the RSC is used, only the samples are oscillated and there is no oscillator drawer movement as with the ASC. Because the travel times are much shorter, wait times of 0.5–1.0 min and integration times of 1–2 min are adequate. Otherwise, the operation of the RSC is the same as the operation of the ASC. The reactivity change associated with oscillating the sample into and out of the core is measured by the calibrated autorod. The precision of the RSC measurements are about the same as the ASC measurements for similar measurement times.

Two types of samples, referred to as Argonne-East and Argonne-West types, were used in the RSC; and drawings of each sample are shown in Fig. II-19-5. The sample holder devices are also shown. The Argonne-East-type samples were cylinders 0.87 in. in diameter and 2 in. long; some of the samples were canned in stainless steel, some were bare, some were solid cylinders, and some were annulus-shaped (hollow cylinders). The Argonne-West type samples were either solid cylinders or annulus-shaped, 2.17 in. long and of various diameters. All the Argonne-West samples were canned in stainless steel. Detailed descriptions of all the samples are given later in this report.

D. CALIBRATED AUTOROD

The Autorod (AR) system consists of a tapered polyethylene blade extending axially through both assembly halves, a servo-drive mechanism, and an analog rod-position-indication system attached to a rod-position integrator. The system is controlled to automatically hold the assembly power level at a constant preset value. The tapered polyethylene blade has the property that the value of $\Delta\rho/\Delta x$, where ρ is reactivity and x is the axial position of the blade, is nearly constant with x. The reactivity signal associated with a sample insertion is proportional to the change in autorod average position. The average autorod position is obtained by integrating, over a preset time interval, the output from a potentiometer whose voltage is proportional to rod position.

The integral worth of the autorod was measured in these experiments by running the rod between the full-in and full-out positions and measuring the reactivity change with an inverse kinetics code. An integral worth value of (6.737 ± 0.034)Ih was obtained from repeated measurements where the imprecision is the standard deviation resulting from the scatter in the measured values. The reactivity results contained in this report do not include the uncertainty in the autorod calibration in their quoted precisions. This additional uncertainty should be included when comparing measured and calculated reactivities, but it should not be considered when comparing two reactivities measured with the same autorod. The inverse kineti method and the code used for calibrating the autor are discussed in Paper II-32. No additional code-related uncertainty has been assigned to the autorod calibration.

A check of the constancy of $\Delta\rho/\Delta x$ with autorod position was made by measuring the worth of a small sample (worth about 10% of the total autorod worth) with the autorod insertion adjusted to various values along its entire length. The results, which are given in Table II-19-I, indicate that $\Delta\rho/\Delta x$ may vary by 2 or 3% over the length of the autorod. In the final data reduction the autorod worth was not assumed linear. A third order fit was made to the data points in Table II-19-I to obtain the autorod calibration curve. The error associated with the $\Delta\rho/\Delta x$ calibration curve was negligible.

E. REFERENCE CORE CONFIGURATION

With two exceptions, discussed below, the actual loading of Assembly 7 for the reactivity measurements was almost identical (±3 kg fissile material) to the "as-built" Reference Core defined in Paper II-11. The core radial cross sections shown in Figs. II-19-3, II-19-6 and II-19-7 are the same as shown in Fig. 2A of Paper II-11.

The reactivity measurements made in the central rodded zone in Assembly 7 were one exception. The rodded zone, which is shown in Fig. II-19-6 of this paper is described in detail in Paper II-25.

The other exception was the measurements made in the central matched-plate zone. There were actually two changes in the core for these measurements, neither of which had any apparent affect on the central reactivity measurements, since, as will be discussed later in this report, the central worth measurements in the matched-plate zone were in very good agreement with similar measurements in the original plate core. The

TABLE II-19-I. Apparent Worth of Small Sample at Different Autorod Positions Assuming that the Differential Rod Worth is Independent of Position

AR position,[a] Percent Travel From Full Out	Apparent Worth of Ta and SS Sample,[b] Ih
10	0.694
15	0.703
21	0.692
26	0.702
32	0.693
37	0.698
45	0.684
52	0.692
60	0.678
67	0.677
74	0.680
82	0.685
89	0.683

[a] The Ta and SS sample was worth about 10% of the autorod total worth so that at 15%, for example, the autorod moved between 10% and 20% insertion when the sample was oscillated.

[b] The standard deviation of these values was about 0.005 Ih.

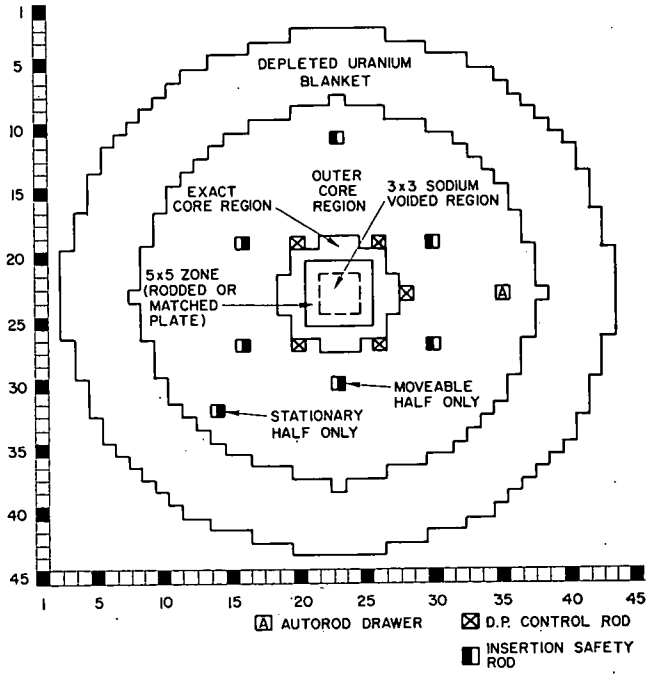

Fig. II-19-6. Radial Cross Section of ZPR-6 Assembly 7 Showing the Locations of the Exact Core Region, the 5 x 5 Rodded and Matched Plate Zones, and the 3 x 3 Sodium-Voided Region. *ANL Neg. No. 116-1042.*

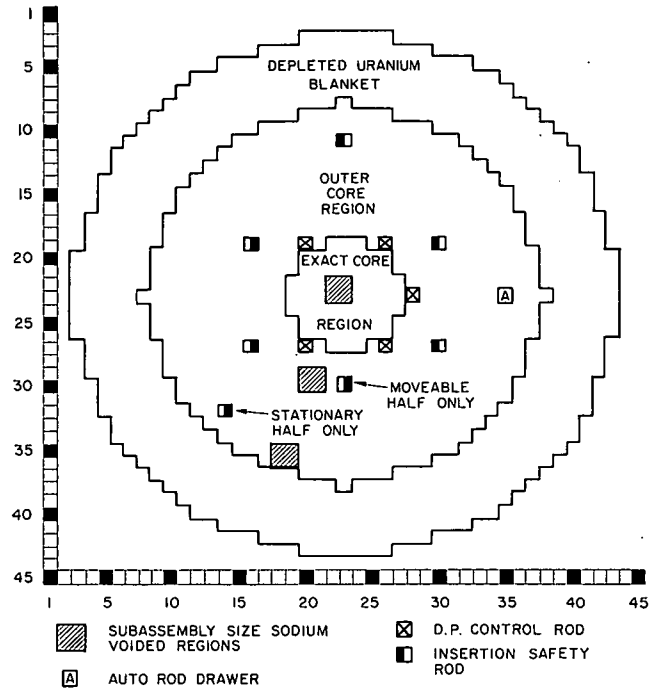

Fig. II-19-7. Radial Cross Section of ZPR-6 Assembly 7 Showing Locations of Subassembly-Size Sodium-Voided Regions. *ANL Neg. No. 116-1031.*

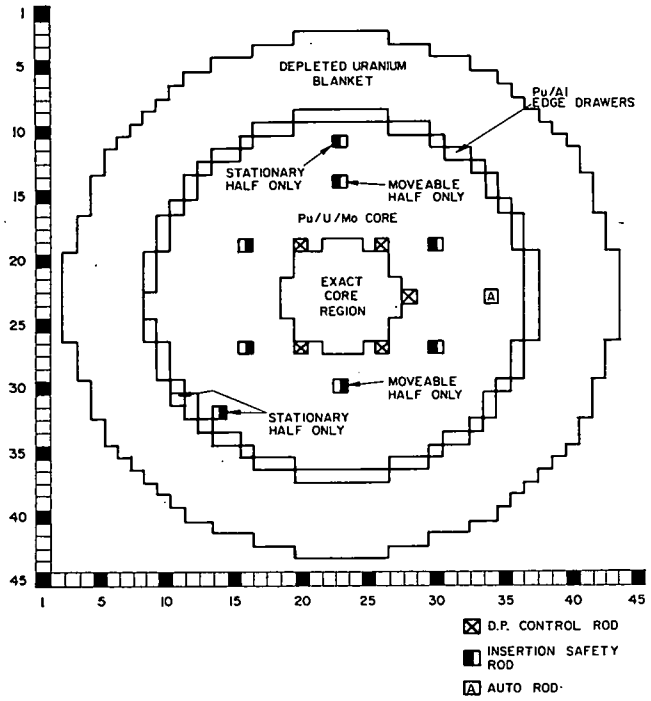

FIG. II-19-8. Radial Cross Section of ZPR-6 Assembly 7 Showing the Locations of the Drawers Loaded with the Pu/Al Fuel Plates. *ANL Neg. No. 116-925 Rev. 1.*

first change—the inclusion of the matched-plate zone as defined in Paper II-25—was effectively no change since the matched-plate zone was the same as the regular plate core except for very slight weight differences in some of the plates. The other change involved the replacement of some of the regular Assembly 7 core drawers near the radial edge of the assembly with drawers containing Pu/Al fuel. The new drawer loading was as shown in Fig. II-19-1 except that the ¼-in. Pu/U/Mo column was replaced with a ⅛-in. column of Pu/Al fuel and a ⅛-in. column of depleted uranium. A total of 168 of the regular Assembly 7 drawers (84 per half) were removed, and, because the fissile weight per drawer was 20 % greater in the Pu/Al drawers, only 145 Pu/Al drawers were added. Figure II-19-8 is a radial cross section of the core with the Pu/Al drawers installed. Calculations indicated that there was no change in either the central spectra or the perturbation denominator as a result of the Pu/Al addition, and the central worth measurements tended to confirm this conclusion.

III. Reactivity Results

The results of the reactivity worth measurements in Assembly 7 are included in Tables II-19-II through II-19-VIII and Figs. II-19-9 through II-19-14. Each of the tables and figures are discussed below.

A. Table II-19-II: Central In-Cell Sodium Void

The results of the central sodium-void measurements in the pin and plate environments are included. The experimental techniques used for these measurements are discussed in Section IIA and IIB. The results are the same as those listed in Paper II-25 and are listed here for the sake of completeness. The location of the 5 x 5 drawer rodded zone and the 3 x 3 drawer sodium-voided regions (both rodded and plate) are shown in Fig. II-19-6. The 5 x 5-drawer rodded zone extended 12-in. from the midplane into each half (i.e. the total length was 24 in.). The results listed in this table are for sodium in its normal plate or rodded environments.

TABLE II-19-II. Comparison of Central Sodium-Void Coefficient Measurements in Plate and Pin Environments, ZPR-6 Assembly 7

Core Environment	Sample Type	Dimension of Core Region Which Was Voided of Sodium	Mass of Sodium Voided, kg	Void Worth,[a] Ih	Specific Worths of Void,[d] Ih/kg (±1 σ)
Plate core	Plate drawers	9 unit cells 6 in. in each half (6.52 x 6.52 x 12.0-in.)	2.972	+20.64[b]	+6.94 ± 0.6
Pin zone	Pin calandria	9 unit cells 6 in. in each half (6.52 x 6.52 x 12.0-in.)	2.968	+19.03[b]	+6.41 ± 0.6
Plate core	Plate sample box	1 unit cell 1 in. in each half (2.17 x 2.17 x 2.0-in.)	0.0429	+0.297[c]	+6.69 ± 0.2
Pin zone	Pin calandria	1 unit cell 6 in. in each half (2.17 x 2.17 x 12.0-in.)	0.3305	+2.221[c]	+6.72 ± 0.07
Pin zone	Pin calandria	1 unit cell 3 in. in each half (2.17 x 2.17 x 6.0-in.)	0.1659	+1.132[c]	+6.82 ± 0.2

[a] 1% $\delta k/k \approx$ 1030 Ih. Total β_{eff} = 0.00319. Prompt neutron lifetime, $\ell_p = 5.48 \times 10^{-7}$ sec.
[b] Reactivity worth determined from change in core excess reactivity before and after voiding.
[c] ASC measurements. Reactivity worths measured by autorod.
[d] Note that it is the sodium-void worth and not the sodium worth that is listed in this table.

TABLE II-19-III. MEASUREMENTS OF SODIUM-VOID COEFFICIENT IN SUBASSEMBLY SIZE REGION IN ZPR-6 ASSEMBLY 7

Location of Voided Region[a]	Drawers Voided in Both Halves		Dimensions of Voided Region[b]	Average Radius of Voided Region, cm	Mass of Sodium Voided, kg	Void Worth,[c] Ih	Specific Worth of Void,[d,e] Ih/kg ($\pm 1\ \sigma$)
	Row	Column					
Assembly center	22	22	Four drawers per half (4.35 x 4.35 x 60.0-in.)	3.91	6.602	+17.44	+2.64 ± 0.30
	22	23					
	23	22					
	23	23					
Midway between center and radial reflector	29	20		43.70	6.443	+1.36	+0.21 ± 0.30
	29	21					
	30	20					
	30	21					
Adjacent to the radial reflector	35	18		73.42	6.529	−11.58	−1.77 ± 0.30
	35	19					
	36	18					
	36	19					

[a] See Fig. II-19-7 for locations of sodium-voided drawers.
[b] In each case, a region 2 x 2 drawers and extending the full axial height of the core was voided.
[c] The reactivity worths were determined from the change in core excess reactivity before and after voiding.
[d] See footnote a, Table II-19-II.
[e] Note that it is the sodium-void worth and not the sodium worth that is listed in this table.

TABLE II-19-IV. CENTRAL REACTIVITY WORTH MEASUREMENTS IN ZPR-6 ASSEMBLY 7 MEASURED IN THE UNIT-CELL PLATE ENVIRONMENT

Material	Weight, g	Location in Unit-Cell of the Perturbed Material	Total Worth,[c] Ih	Specific Worth,[d] Ih/kg ($\pm 1\ \sigma$)
^{239}Pu[a]	1.919	Placed in ½ in. diam hole in Pu/U/Mo plate	0.324	168.7 ± 2.9
Pu/U/Mo[b]	21.155	Placed in ½ in. diam hole in Pu/U/Mo plate	0.694	32.8 ± 0.4
Depl. U	14.46	Placed in ½ in. diam hole in Pu/U/Mo plate	0.123	−8.54 ± 0.44
Depl. U	121.39	Adjacent to ⅛ in. U_3O_8 plate	−1.038	−8.55 ± 0.09
Na	42.90	Both sodium cans replaced by void cans	−0.287	−6.68 ± 0.15
U_3O_8	60.68	¼ in. U_3O_8 plate replaced by ⅛ in. U_3O_8 plate	−0.556	−9.16 ± 0.13
Fe_2O_3	32.74	⅛ in. Fe_2O_3 plate replaced by void	−0.199	−6.07 ± 0.28
SS304	46.95	1/16 in. SS adjacent to Pu/U/Mo plate	−0.246	−5.25 ± 0.20
SS304	46.77	1/16 in. SS adjacent to vertical matrix	−0.252	−5.38 ± 0.37
SS304	46.29	⅛ in. SS adjacent to horizontal matrix	−0.203	−4.39 ± 0.24
Fe	58.05	⅛ in. Fe plate at position of Fe_2O_3 plate	−0.255	−4.40 ± 0.17
Fe	38.43	0.075 in. Fe adjacent to vertical matrix	−0.179	−4.65 ± 0.21
Ni	38.66	0.075 in. Ni adjacent to vertical matrix	−0.265	−6.85 ± 0.21

[a] The value for ^{239}Pu was derived from the measurement of a plutonium sample containing 99% ^{239}Pu.
[b] The composition of the Pu/U/Mo material was 29.4 wt% Pu, 68.1 wt% depleted U, and 2.5 wt% Mo. The plutonium composition was 85.0 wt% ^{239}Pu, 12.8 wt% ^{240}Pu, 2.0 wt% ^{241}Pu, and 0.2 wt% ^{242}Pu.
[c] ASC measurements. Worths measured by autorod.
[d] See footnote a, Table II-19-II.

Two conclusions are apparent from Table II-19-II:) the sodium coefficient is essentially the same for the 3 x 3 drawer region and the single unit-cell region and (2) the sodium coefficient is essentially the same for the plate and rodded environments.

B. TABLE II-19-III: SUBASSEMBLY-SIZE SODIUM VOID

This table lists the results of the "subassembly-size" sodium-void measurements. The regions voided were 2 drawers x 2 drawers in cross section (4 unit cells) and extended for the full 60-in. axial dimension of the core.

TABLE II-19-V. CENTRAL REACTIVITY WORTH MEASUREMENTS IN ZPR-6 ASSEMBLY 7 FOR SMALL CYLINDRICAL SAMPLES USING THE RADIAL SAMPLE CHANGER

No.	Sample[a]	Sample Wt., g	Sample Description				Specific Worth, Ih/kg[d,e] (±1 σ)		
			Geometry[b]	Length, cm	Outside Diameter, cm	Effective Wall Thickness,[c] cm	Normal Plate Core	Central Matched Plate Zone	Central Rodded Zone
1	Pu (1 w/o ^{240}Pu)	3.524	A	3.18	2.13	0.013	158.7 ± 2.3	152.7 ± 2.8	
2	↓	9.956	↓	↓	↓	0.038	157.9 ± 0.3	157.8 ± 0.3	153.8 ± 0.6
3	↓	21.409	↓	↓	↓	0.076		159.5 ± 0.5	
4	Pu (11.5 w/o ^{240}Pu)	2.706	↓	5.52	0.99	0.013	136.5 ± 1.7	144.7 ± 2.7	
5	↓	8.853	↓	↓	↓	0.038		143.2 ± 0.6	
6	↓	15.122	↓	↓	↓	0.063		145.4 ± 0.7	
7	Pu (22 w/o ^{240}Pu)	3.031	↓	↓	↓	0.013		126.4 ± 2.3	
8	↓	8.510	↓	↓	↓	0.038		129.0 ± 1.0	
9	↓	13.939	↓	↓	↓	0.063		128.3 ± 0.5	
10	Pu (45 w/o ^{240}Pu)	3.442	↓	↓	↓	0.013		99.6 ± 2.2	
11	↓	8.508	↓	↓	↓	0.038		97.9 ± 0.9	
12	Enr. U.	3.084	↓	5.00	2.13	0.005	123.6 ± 2.0	119.2 ± 1.0	119.7 ± 2.3
13	Enr. U.	5.231	↓	4.45	↓	0.009		117.5 ± 1.8	
14	Enr. U.	15.775	↓	4.45	↓	0.028		119.8 ± 0.6	
15	Depl. U.	19.074	↓	4.45	↓	0.035		−11.17 ± 0.62	
16	Depl. U.	25.988	↓	5.00	↓	0.041	−9.51 ± 0.32	−9.48 ± 0.10	−9.02 ± 0.19
17	Depl. U.	38.163	↓	4.45	↓	0.069		−9.58 ± 0.34	
18	Ta	8.698	↓	5.08	2.21	0.015	−58.0 ± 1.5	−58.1 ± 1.1	−54.9 ± 0.9
19	Ta	18.647	C	5.52	0.99		−43.1 ± 0.4		
20	Boron	0.5553	↓	5.00	0.125		−570 ± 12	−570 ± 7	−590 ± 12
21	Ni	37.916	↓	5.52	0.99		−6.47 ± 0.19		−6.07 ± 0.24
22	Fe	33.277	↓	↓	↓		−4.27 ± 0.16		−3.97 ± 0.27
23	Cr	26.999	↓	↓	↓		−4.54 ± 0.37		−4.04 ± 0.42
24	SS304	34.506	H	↓	↓		−5.03 ± 0.14	−4.89 ± 0.06	−4.62 ± 0.09
25	SS304	20.966	↓	↓	↓				
26	Mo	43.398	C	5.52	0.99		−15.39 ± 0.11		
27	Al	53.067	↓	5.08	2.21			−6.83 ± 0.17	
28	Na	17.044	↓	↓	2.13		−4.73 ± 0.49	−6.21 ± 0.32	−5.40 ± 0.26
29	C	33.441	↓	↓	2.21		−12.19 ± 0.21	−12.67 ± 0.27	−12.54 ± 0.27
30	Li-6	0.9736	↓	4.45	0.78			−1920 ± 11	

[a] Additional information on the samples is given in Table II-19-7.

[b] A ≡ annulus (hollow cylinder), C ≡ solid cylinder, H ≡ empty sample holder—generally annular geometry with solid ends (see Fig. II-19-5).

[c] The effective wall thicknesses for all the plutonium samples are measured values. The values listed for the uranium and tantalum samples were calculated using published density values.

[d] All measurements were made using the RSC and the calibrated autorod.

[e] See footnote a, Table II-19-II.

The four unit-cell region has the same cross sectional area as a hexagon with a flat-to-flat dimension of 4.67 in. so that the size of the region voided is fairly typical of an LMFBR subassembly. The radial location of the voided regions are shown in Fig. II-19-7.

The results indicate a positive sodium-void coefficient at the center, a nearly zero coefficient near the half-radius position and a negative sodium-void coefficient near the edge of the core. These results have generally the same radial shape as the small-sample, radial, sodium-worth measurements discussed in Section IIIG. In addition, the central subassembly-size sodium-void result is predicted fairly well by the small-sample axial sodium worth measurement also discussed in Section IIIG.

C. TABLE II-19-IV: CENTRAL UNIT-CELL PLATE WORTHS

The worths of the cell constituent materials measured in their normal plate enviroments are listed in this table. The technique for these measures is described in Section IIB. More than one measurement is listed for depleted uranium, iron, and stainless steel since these materials are included at more than one location in the unit cell. The normal-core unit-cell and the ASC experimental unit-cell are shown in Figs. II-19-1 and II-19-2. Since the experimental unit cell was about ⅛

TABLE II-19-VI. MATERIAL AND COMPOSITION DATA FOR RADIAL SAMPLE-CHANGER SAMPLES

No.	Sample			Sample Cladding		Weights of Isotopic Constituents[a,b]											
	Ident. No.	Material	Wt., g	Material	Wt., g	Iso.	Wt., g	Iso.	Wt., g	Iso.	Wt., g	Iso.	Wt., g	Iso.	Wt., g	Iso.	Wt., g
1	MB06	Pu (1 w/o ^{240}Pu)	3.524	SS304	13.218	^{239}Pu	3.445	^{240}Pu	0.035	^{241}Pu	0.002	Al	0.042				
2	MB10	↓	9.956	↓	13.485	↓	9.732	↓	0.100	↓	0.005	↓	0.119				
3	MB11	↓	21.409	↓	13.577	↓	20.926	↓	0.214	↓	0.011	↓	0.257				
4	Pu-7	Pu (11.5 w/o ^{240}Pu)	2.706	↓	10.703	↓	2.306	↓	0.306	↓	0.056	^{242}Pu	0.004	^{241}Am	0.004	Al	0.030
5	Pu-9	↓	8.853	↓	10.351	↓	7.543	↓	1.002	↓	0.182	↓	0.014	↓	0.013	↓	0.097
6	Pu-11	↓	15.122	↓	10.725	↓	12.885	↓	1.712	↓	0.311	↓	0.025	↓	0.022	↓	0.166
7	Pu-13	Pu (22 w/o ^{240}Pu)	3.031	↓	10.369	↓	2.194	↓	0.658	↓	0.115	↓	0.017	↓	0.009	↓	0.038
8	Pu-15	↓	8.510	↓	10.529	↓	6.159	↓	1.846	↓	0.322	↓	0.049	↓	0.026	↓	0.108
9	Pu-17	↓	13.939	↓	10.584	↓	10.088	↓	3.024	↓	0.527	↓	0.080	↓	0.043	↓	0.177
10	Pu-19	Pu (45 w/o ^{240}Pu)	3.442	↓	10.672	↓	1.377	↓	1.421	↓	0.407	↓	0.146	↓	0.044	↓	0.041
11	Pu-21	↓	8.508	↓	10.665	↓	3.405	↓	3.512	↓	1.005	↓	0.360	↓	0.109	↓	0.102
12	U-235(L)	Enr. U	3.084	↓	8.924	^{235}U	2.876	^{238}U	0.167	^{234}U	0.028	^{236}U	0.014				
13	MB20	↓	5.231	↓	13.907	↓	4.877	↓	0.283	↓	0.048	↓	0.023				
14	MB21	↓	15.775	↓	13.729	↓	14.709	↓	0.853	↓	0.143	↓	0.069				
15	MB24	Depl. U	19.074	↓	13.807	^{238}U	19.034	^{235}U	0.040								
16	U-238(L)	↓	25.988	↓	8.953	↓	25.933	↓	0.055								
17	MB25	↓	38.163	↓	13.859	↓	38.083	↓	0.080								
18	TA(L)	Ta	8.698														
19	TA-2	Ta	18.647														
20	B(L)	Boron	0.5553	SS304	8.489	^{10}B	0.1104	^{11}B	0.4449								
21	Ni-1	Ni	37.916														
22	Fe-1	Fe	33.277														
23	Cr-3	Cr	26.966														
24		SS304	34.506			Fe	24.0	Cr	6.3	Ni	3.3	Mn	0.5				
25		↓	20.966			↓	14.5	↓	3.8	↓	2.0	↓	0.3				
26	Mo-1	Mo	43.398														
27	AL(L3)	Al	53.067														
28	NA(L2)	Na	17.044	SS304	9.135												
29	C(L)	C	33.441														
30		Li-6	0.9936	Al	4.806												

[a] The weights of the isotopic constituents are not given for samples containing only one isotope.
[b] All ^{241}Pu and ^{241}Am weights corrected to 4/1/71.

TABLE II-19-VII. COMPARISON OF MEASURED AND CALCULATED CENTRAL WORTHS, ZPR-6 ASSEMBLY 7

Isotope[a]	Weight, g	Measurement Technique[b]	Worth, Ih/kg		Calculation / Experiment	[Calculation / 1.27] / Experiment
			Measurement	Calculation[c]		
^{239}Pu	1.919	ASC	169	205	1.21	0.95
^{238}U (F)[d]	14.46	↓	−8.5	−12.5	1.47	1.16
^{238}U (U)[d]	121.39	↓	−8.5	−13.6	1.58	1.24
Fe	[e]	↓	−4.5	−5.4	1.20	0.94
Ni	38.66	↓	−6.8	−6.0	0.88	0.69
Na	42.90	↓	−6.7	−6.0	0.90	0.71
^{239}Pu	9.732	RSC	159	205	1.29	1.02
^{235}U	2.876	↓	131	175	1.34	1.06
^{238}U	25.93	↓	−9.8	−13.8	1.41	1.11
Ta	8.698	↓	−58	−78	1.34	1.06
Boron	0.5553	↓	−570	−749	1.31	1.03
Fe	33.277	↓	−4.3	−5.4	1.26	0.99
Ni	37.916	↓	−6.5	−6.1	0.94	0.74
Cr	26.999	↓	−4.5	−7.6	1.69	1.33
Na	17.044	↓	−6.2	−6.1	0.98	0.77
C	33.441	↓	−12.4	−15.8	1.27	1.00

[a] Values for ^{239}Pu, ^{235}U and ^{238}U were derived from plutonium, enriched uranium and depleted uranium measurements.

[b] ASC—measurements made using axial sample changer and plate type samples in a unit-cell environment; RSC—measurements made using radial sample changer and cylindrical samples.

[c] First order perturbation theory calculations using 1-D diffusion theory calculated fluxes. For the ASC (unit-cell) calculation cross sections corrected for plate heterogeneity were used in the perturbation calculation. For the RSC calculations cross sections obtained from a homogeneous MC^2 calculation were used in the perturbation calculation. Cross sections corrected for plate heterogeneity were used in the diffusion flux calculations.

[d] ^{238}U (F) is for the ^{238}U in the Pu/U/Mo plate and ^{238}U (U) is for the ^{238}U in the U_3O_8 plates.

[e] Measurement quoted is for the average of two measurements. See Table II-19-IV for individual weights.

TABLE II-19-VIII. LARGE-SAMPLE WORTH MEASUREMENTS USING AXIAL SAMPLE CHANGER

Sample	Sample Wt, g	Sample Dimensions, cm	Worth,[e] Ih/kg
Pu[a]	10.857	5.08 × 5.08 × 0.32	153.8
Na[b]	51.38	5.08 × 5.08 × 2.54	−6.17
SS304[c]	49.17	↓	−4.93
C	103.0	↓	−12.2
Be[b]	114.31	↓	−11.4
^{239}Pu[d]	10.33	—	160.2

[a] The weights in the plutonium sample were: ^{239}Pu-10.33 g, ^{240}Pu-0.497 g, ^{241}Pu-0.0282 g.

[b] The sodium and beryllium samples were canned in SS.

[c] The SS304 sample was an empty sample can with the outside dimensions listed in the third column.

[d] This value was derived from the plutonium worths using the calculated worths of ^{240}Pu and ^{241}Pu.

[e] The standard deviation for these measurements is approximately 2%. Also see footnote a, Table II-19-II.

in. narrower than the normal 2 in. core unit cell, it was necessary to use slightly thinner Fe_2O_3 and U_3O_8 pieces in the experiments. These measurements were made for two purposes:

1. They were used to correct for small composition mismatches between the rodded and matched-plate zones. This correction was necessary in order to determine the reactivity difference between the rodded and plate zones due entirely to the configurational difference.
2. Since the configuration of the unit-cell measurements is well defined and the heterogeneity calculation reasonably straightforward, the results are valuable for comparison with calculation. The normal plate-type unit-cell heterogenity calculations use equivalence theory in the resonance region and transport theory fluxes for spatial and energy weighting.

D. TABLES II-19-V AND II-19-VI: CENTRAL RADIAL SAMPLE CHANGER WORTHS

Table II-19-V lists the results of the central worth measurements using the radial sample changer (RSC) and small cylindrical samples as described in Section IIC. Figure II-19-3 shows the location of the RSC tube in the core, Fig. II-19-5 includes drawings of the RSC samples, and Fig. II-19-4 shows a cross section of the RSC tube and sample and the surrounding matrix and drawers. As can be seen from the figures, the RSC samples are positioned in the core in a small cavity with their axis perpendicular to the plates. The samples are essentially one unit-cell in length so that the samples span the unit cell when they are in the core and, in a

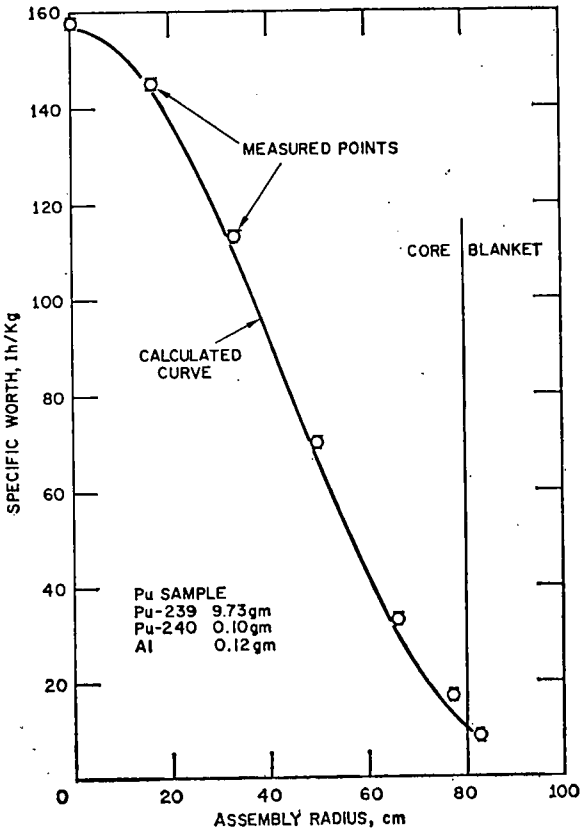

FIG. II-19-9. Measured and Calculated Radial Worth Shapes for a Small Cylindrical Plutonium Sample. *ANL Neg. No. 116-1040.*

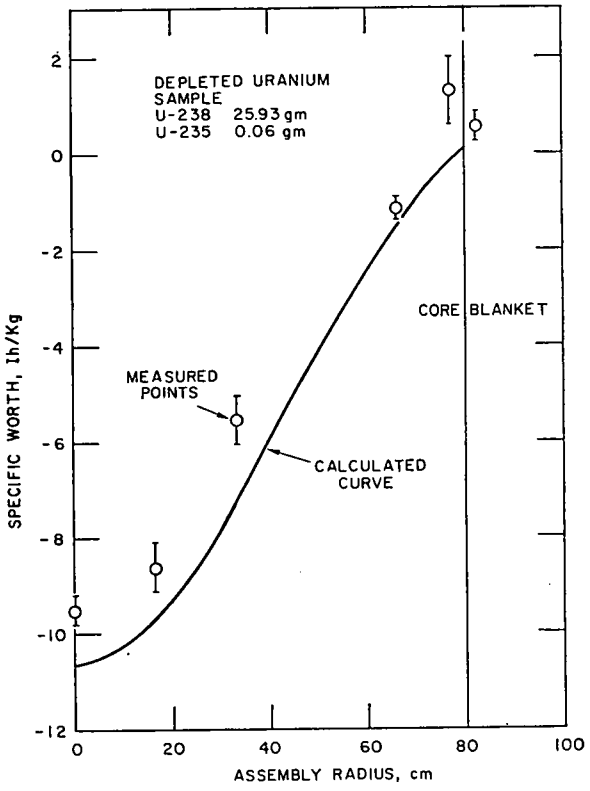

FIG. II-19-11. Measured and Calculated Radial Worth Shapes for a Small Cylindrical Depleted Uranium Sample. *ANL Neg. No. 116-1041.*

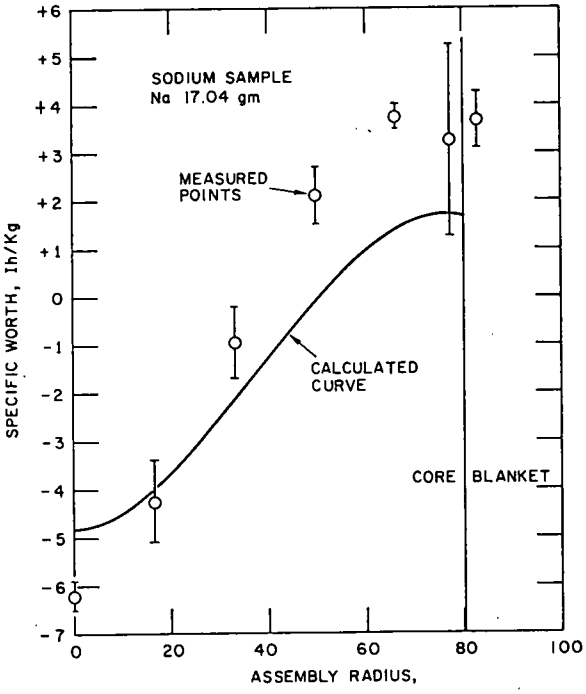

FIG. II-19-10. Measured and Calculated Radial Worth Shapes for a Small Cylindrical Sodium Sample. *ANL Neg. No. 116-1037.*

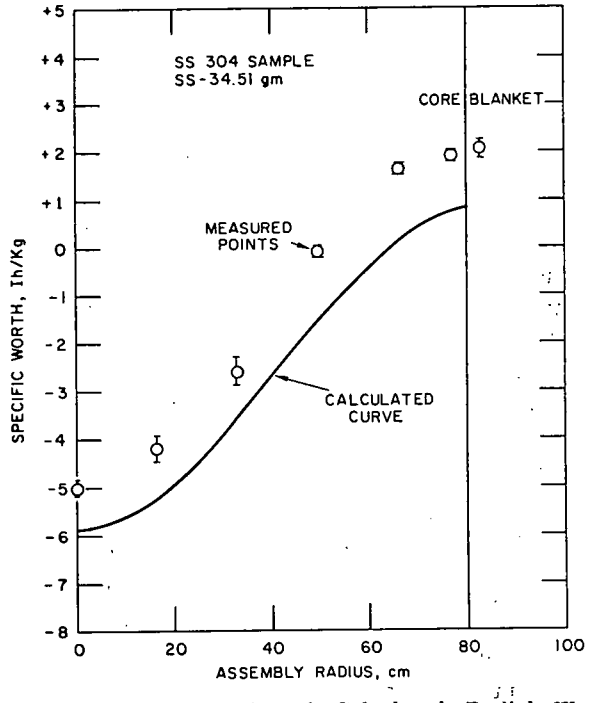

FIG. II-19-12. Measured and Calculated Radial Worth Shapes for a Small Cylindrical 304 Stainless Steel Sample. *ANL Neg. No. 116-1038.*

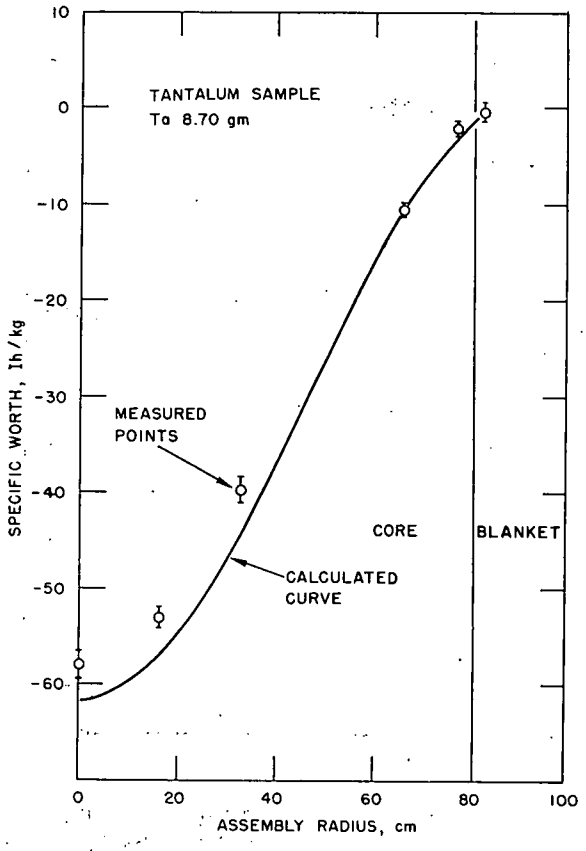

FIG. II-19-13. Measured and Calculated Radial Worth Shapes for a Small Cylindrical Tantalum Sample. *ANL Neg. No. 116-1086.*

very approximate sense, they should give a cell-averaged worth.

Table II-19-V contains a geometrical description of each sample. Detailed information on the weights of all the isotopes in each sample are given in Table II-19-VI.

The reactivity results are given in Table II-19-V for measurements in the normal-plate core and in the central matched-plate and rodded zones. Some of these results have been included in Paper II-25. They are also listed here for completeness.

Since there were no significant differences between the normal-plate core and the matched-plate zone, it was expected that there would be no differences in the reactivity worths measured in the two zones. The matched-plate zone measurements provide a good test of the reproducibility of the RSC worth measurements, and, in general, the agreement between the worths measured in the two environments is very good. There are two discrepancies: measurement 4, the 2.706 g plutonium sample (11.5 w/o Pu-240) and measurement 28, the sodium sample. The plutonium discrepancy, which is small, is less than 6% for measurements with imprecisions of about 2% so that it is not inconceivable that this discrepancy is due simply to unfavorable statistics. In the case of sodium, the second measurement in the matched-plate zone (-6.21 ± 0.32)Ih/kg is considered the better value, since it has the smaller standard deviation and since the result agrees better with the sodium results in Tables II-19-II and II-19-VIII. The agreement with the result in Table II-19-VIII is especially significant, since the sample configurations for the two measurements were nearly the same. The reason for the one lower sodium result in the normal-plate core is not understood.

There are several results in Table II-19-V which give information on the variation of sample worth with sample size. The results seem to indicate that the plutonium and enriched uranium worths were not strong functions of size while the tantalum worth was a strong function of size. The results for depleted uranium were inconclusive. Self-shielding factors, some calculated and some inferred from measurements, for a few of these samples are included in Paper II-11.

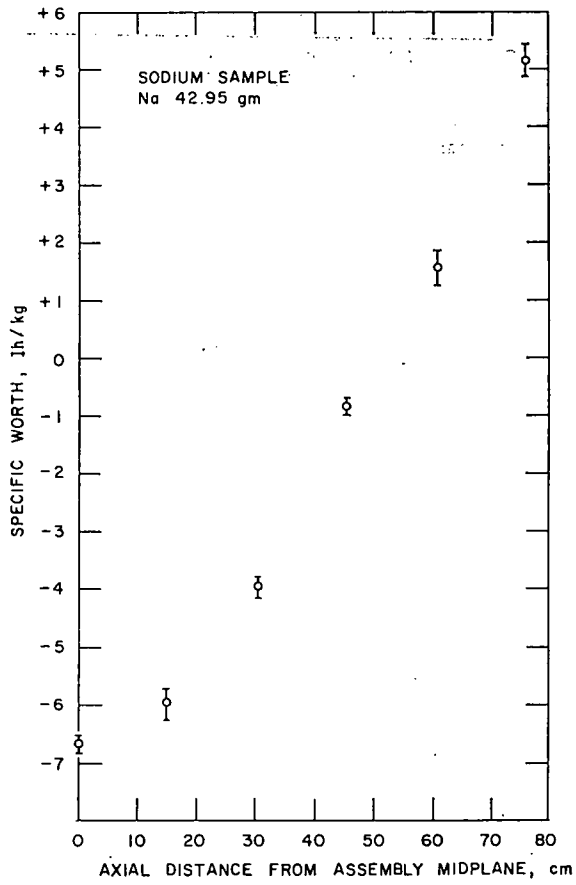

FIG. II-19-14. Measured Axial Worth of a Small Plate-Type Sodium Sample. *ANL Neg. No. 116-1048.*

E. TABLE II-19-VII: COMPARISON OF MEASURED AND CALCULATED WORTHS

Some of the measured values from Tables II-19-IV and II-19-V are compared in this table with calculated worths. The worths listed for ^{239}Pu, ^{235}U and ^{238}U were derived from the plutonium and the enriched and depleted uranium measurements. Calculated worths for ^{240}Pu and ^{241}Pu were needed to deduce the ^{239}Pu worth, but the derived ^{239}Pu value was very insensitive to variations in the calculated ^{240}Pu and ^{241}Pu values.

The calculations were made using first order perturbation theory and fluxes from a 27-broad-group one-dimensional (cylindrical) diffusion theory calculation. The cross sections[8] used in both the flux calculation and the perturbation calculations were generated by the MC^2 code using ENDF/B VERSION I data. The cross sections used in the diffusion calculation and for the unit-cell plate-sample perturbation calculations were corrected for spatial self-shielding using slab geometry equivalence theory and the individual plate cross sections were re-weighted with fluxes from a 27-group transport unit-cell calculation, giving flux and volume-weighted homogenized unit-cell cross sections. The perturbation calculations appropriate to the radial sample changer measurements (cylindrical samples) used cross sections directly from a homogeneous MC^2 calculation. These cross sections, therefore, contain no self-shielding corrections or spatial flux weighting.

The best comparisons between measurement and calculation should be for the unit-cell worths measured with the axial sample changer, since a heterogeneity correction was included. However, the differences between the worths measured in the unit cell using the ASC and the RSC measurements are not great (10 % or less).

The ratio of the calculated to experimental worths are also given in Table II-19-VII. Most of the C/E values lie between 1.20 and 1.40, suggesting a systematic bias between the measurements and calculations. A perturbation denominator measurement[9] was made for Assembly 7 which predicted C/E values of 1.27 based on the discrepancy between measured and calculated perturbation denominators. This discrepancy may be due to errors in the β_{eff} values, the spatial calculation of the core, the autorod calibration or possibly other experimental errors. If the calculated values are divided by 1.27, then the comparison between the calculations and the measurements is independent of the β_{eff} values, the spatial calculation, and any uncertainty in the autorod calibration;* this comparison is given in the final column in Table II-19-VII. It can be seen in Table II-19-VII that the agreement is fairly good between calculation and measurement if the ratio of the calculated and measured perturbation denominators is used to correct the calculated data. This indicates that a large part of the disagreement between the measured and calculated values in Assembly 7 is due to normalization problems. In particular the normalized C/E values for ^{239}Pu are 1.02 and 0.95.

* A more complete discussion of this point is included in Paper II-12.

F. TABLE II-19-VIII: CENTRAL AXIAL SAMPLE-CHANGER WORTHS

The values listed in this table are for samples with nominal outside dimension of 2 x 2 x 1-in. measured in the ASC as described in Section IIB. The 1/8-in. thick plutonium sample was installed in a 2 x 2 x 1-in. stainless steel box for the measurement. The samples were positioned in the drawer perpendicular to the plates so that the samples spanned the unit-cell in a manner similar to the RSC samples.

The results for ^{239}Pu, SS304, sodium and carbon are in very good agreement with the RSC values. Beryllium was not measured in the RSC. The close agreement between the specific worth values listed in this table and those measured by the RSC, for both sodium and carbon, is an indication that these worths are not strong functions of sample size, since the samples measured in the ASC were approximately a factor of three larger than those measured in the RSC.

G. FIGS II-19-8 THROUGH II-19-13: RADIAL AND AXIAL WORTH TRAVERSES

The measured small-sample radial and axial sodium worths and the radial plutonium (99 % ^{239}Pu), depleted uranium, stainless steel, and tantalum worths are included in these figures. The radial worth traverses (including sodium) were all measured with the RSC; the axial sodium traverse was measured using the ASC and the plate-loaded sample boxes. The environment for the off-center radial worth measurements included partial voids at each end of the sample. The possible effect of these voids on the off-center worths was investigated in Ref. 8 and found to be relatively small. The environment of the off-center axial measurements was the same as for the central axial measurements except for the point at 30-in. At 30 in. the ASC drawer was loaded with blanket material on one side of the sample and core material on the other side to match the surrounding core loading. For both the radial and axial measurements the sample lengths were 2-in. (5.08 cm). The data points in Figs. II-19-9 through II-19-14 are plotted at the sample midpoints. The error flags plotted on the figures are for one standard deviation.

Calculated radial plutonium, sodium, depleted uranium, tantalum, and stainless steel curves are also included. The calculated curves have been adjusted with the calculated-to-measured perturbation denominator ratio (i.e. the calculated worths were divided by 1.27 as described in Section IIIF) so that the shapes can be better compared. The calculations were the same as those described in Section IIIE.

The calculated radial shape is in fairly good agreement with the measurements for the plutonium, tantalum, and depleted uranium curves. The discrepancy is somewhat greater for the stainless steel calculation and it is greatest for the sodium radial shape.

The measurements indicate that the sodium coefficient for complete core voiding was significantly more negative than predicted by these calculations. The leakage component of the sodium worth is apparently being underpredicted near the edge of the core. It should be emphasized, however, that these were rather simple calculations and that the primary purpose of this paper is to present the experimental data.

H. NORMALIZATION TO ZPPR ASSEMBLY 2

The reactivity normalization between Assembly 7 and ZPPR Assembly 2 can be inferred from the reactivity measurements of the same or nearly identical samples made in the two assemblies. Since the core composition in Assembly 7 is identical with the inner zone composition in Assembly 2, the central spectra in the two assemblies should be nearly the same, and there is no significant spectral correction to the normalization. The results were compared for some of the small Argonne-West-type cylindrical samples used in the radial sample changer. The measurements in Assembly 7 were made on the axial centerline of the core and 0.5 in. from the midplane. The Assembly 2 measurements were made on the axial centerline and 3 in. from the midplane, so the normalization quoted is actually between these two locations and not between the exact center of the two assemblies, although the difference is very small.

For thirteen samples (8 plutonium samples and Ta-2, Fe-1, Mo-1, Ni-1 and Cr-3) the average ratio of the worths in inhours was 1.377 ± 0.023 where the imprecision is one standard deviation. The ZPPR Assembly 2 results are from Paper II-37, and the Assembly 7 results used were from Table II-19-V. The ratio of the worths in δk units, which should also be the inverse of the ratio of the perturbation denominators for the cores (normalized at the core centers) was 1.358 ± 0.023, based on 1030 Ih/% $\delta k/k$ for Assembly 7 and 1016 Ih/% $\delta k/k$ for ZPPR Assembly 2.

The reactivity normalization between ZPR-6 Assemblies 6A and 7 is included in Paper II-11.

REFERENCES

1. C. E. Till and W. G. Davey, *The Demonstration Reactor Benchmark Critical Assemblies Program*, Trans. Am. Nucl. Soc. **13**, 293 (1970).
2. L. G. LeSage, E. M. Bohn, J. E. Marshall, R. A. Karam, C. E. Till, R. A. Lewis and M. Salvatores, *Initial Experimental Results from ZPR-6 Assembly 7, The Single Zone Demonstration Reactor Benchmark Assembly*, Trans. Am. Nucl. Soc. **14**, 17 (1971).
3. L. LeSage and E. Bohn, *Temperature Characteristics of ZPR-6 Assembly 7*, ANL-7753, 17–21 (1970).
4. R. A. Karam, K. D. Dance, T. Nakamura and J. E. Marshall, *Analysis of Central Reactivity Worths in Fast Critical Assemblies*, Nucl. Sci. Eng. **40**, 414 (1970).
5. L. G. LeSage and W. R. Robinson, *ZPR-9 Assembly 25: Description and Experimental Results*, Applied Physics Division Annual Report, July 1, 1969 to June 30, 1970, ANL-7710, pp. 165–173.
6. E. F. Bennett and R. L. Long, *Precision Limitations in the Measurement of Small Reactivity Changes*, Nucl. Sci. Eng. **17**, 425 (1963).
7. L. G. LeSage, E. F. Groh and W. R. Robinson, *An Investigation of the Properties of Zoned Systems*, Reactor Physics Division Annual Report, July 1, 1967 to June 30, 1968, ANL-7410, p. 145.
8. A. P. Olson and Nam Chin Paik, *Heterogeneity and Criticality Studies on the Zero Power Plutonium Reactor (ZPPR) Assembly 2, a Demonstration Reactor Benchman Critical*, Applied Physics Division Annual Report, July 1, 1969, to June 30, 1970, ANL-7710, pp. 146–155.
9. L. G. LeSage, *Measurement of the Perturbation Donominator for ZPR-6 Assembly 7*, ANL-7825, 74–76 (1971).

II-20. Perturbation Denominator Measurements in ZPR-6 Assembly 7

M. M. BRETSCHER

METHOD AND EXPERIMENTAL RESULTS

Within the approximations of first order perturbation theory, the denominator of the expression for the reactivity of a small sample inserted into a reactor is just the importance-weighted neutron production rate in the entire reactor. It has been shown[1] that seve independent experimental determinations of this "perturbation denominator" can be obtained from the data needed in capture-to-fission ratio measurements by the reactivity-reaction rate method.[2]

TABLE II-20-I. QUANTITIES FOR EXPERIMENTAL DETERMINATION OF PERTURBATION DENOMINATOR

Measured		Calculated	
Quantity	Value	Quantity	Value
S(Cf), n/sec	$(5.663 \pm 0.016)10^6$	$\bar{\phi}_f^*$(Cf)	3.8124
ρ'(Cf), Ih	$(1.495 \pm 0.012)10^{-2}$	$\bar{\phi}_a^*$(^{6}Li)	3.2422
ρ(^{6}Li), Ih/g	-1.9377 ± 0.0110	$\bar{\phi}_f^*$(^{238}U)	3.7710
ρ(^{238}U), Ih/g	$-(1.150 \pm 0.062)10^{-2}$	$\bar{\phi}_a^*$(^{238}U)	3.2587
R_a(^{6}Li), abs/g-sec	$(8.194 \pm 0.055)10^8$	$\bar{\nu}$(^{238}U)	2.8195 ± 0.0282
R_f(^{238}U), fiss/g-sec	$(7.846 \pm 0.210)10^5$	$[1 - (\rho_s/\rho)]$(^{6}Li)	0.9824
$\bar{\alpha}$(^{238}U)	6.709 ± 0.181	$[1 - (\rho_s/\rho)]$(^{238}U)	0.7569

As shown,[3] the perturbation denominator, D, can be measured with a spontaneous fission source (^{252}Cf), a non-fissionable absorber (^{6}Li in this case), and a fissionable material (^{238}U) for which an independent measurement of the capture-to-fission ratio is available. The appropriate expressions are

$$D_S(^{252}\text{Cf}) = S\bar{\phi}_f^*(\text{Cf})/\rho'(\text{Cf})$$

$$D_A(^6\text{Li}) = -\frac{R_a(A)\bar{\phi}_a^*(A)}{\rho(A)\{1 - [\rho_s(A)/\rho(A)]\}}$$

$$D_F(^{238}\text{U}) = \frac{R_f[\bar{\phi}_f^*\bar{\nu} - \bar{\phi}_a^*(1 + \bar{\alpha})]}{\rho[1 - (\rho_s/\rho)]}.$$

See Paper II-17 for a definition of the symbols used in these equations and the numerical values of the measured (Table II-17-II) and calculated (Table II-17-V) parameters in ZPR-6 Assembly 7. For easy reference, these numerical values are repeated in Table II-20-I below. Importance terms have been evaluated using a normalized adjoint distribution such that $\sum_i \phi_i^* = 100.0$ at the center of the reactor. Using the above equations and the data presented in Table II-20-I, experimental values of the perturbation denominator have been calculated. The results are given in Table II-20-II. Note that for ^{238}U radiochemistry techniques where used to measure both the capture and fission rates, the ratio of which gives $\bar{\alpha}$(^{238}U).

The weighted mean, $\bar{D}$, of the three values for the perturbation denominator is given at the bottom of Table II-20-II. In evaluating the standard error of the weighted mean, $[\sum w_i(\bar{D} - D_i)^2/\{(n-1)\sum w_i\}]^{1/2}$, the weights w_i were chosen to be inversely proportional to the square of the errors given in Table II-20-II. Thus, systematic uncertainties in the calculated neutron importance and scattering corrections have not been included in the weights.

TABLE II-20-II. EXPERIMENTAL VALUES OF THE PERTURBATION DENOMINATOR, 10^9

Method	Result
D_S(^{252}Cf)	1.444 ± 0.012
D_A(^{6}Li)	1.396 ± 0.012
D_F(^{238}U)	1.294 ± 0.095
$\bar{D}$(Mean)	1.419 ± 0.019

COMPARISON WITH CALCULATIONS

The numerical values of the perturbation denominator given in Table II-20-II are normalized to the reactor power level at which the reaction rates and ρ'(CF) were measured. To compare the experimental values with conventional calculations, a renormalization is required. The usual normalization is obtained by dividing the perturbation denominator by the product of the real (S) and adjoint (S^*) sources at the center of the core. In this normalization a term is included to convert the experimental reactivities expressed in inhours to units of $(\Delta k/k)$. Thus, normalization of the measured perturbation denominator requires division by a normalization factor given by

$$NF = \frac{S(r = 0)S^*(r = 0)}{\text{Ih}/(\Delta k/k)}.$$

In terms of the central fission rates,

$$S(r = 0) = \sum_i (\nu\Sigma_f)_i\phi_i(0) = \frac{1}{N_0}\sum_j (\bar{\nu}R_f NA)_j,$$

where the last sum is over the fissionable isotopes in the core and where

$R_f \equiv$ central fission rate in fissions/g-sec
$N \equiv$ atom density
$A \equiv$ atomic weight
$\bar{\nu} \equiv$ average number of neutrons per fission
$N_0 \equiv$ Avogadro's number.

Also,

$$S^*(r = 0) = \sum_i \chi_i\phi_i^*(0) \equiv \bar{\phi}_f^*(\text{core}).$$

The appropriate fission rates and atom densities needed in the evaluation of $S(r = 0)$ are given in Tables II-17-I and II-17-III of Paper II-17. $^{240}R_f$ was obtained from the measured ^{240}Pu/^{239}Pu fission ratio, (0.1861 ± 0.0018), and the radiochemistry value of $^{239}R_f$. However, calculated fission ratios were used for ^{241}Pu and ^{242}Pu.

TABLE II-20-III. Comparison of Measured and Calculated Values of the Perturbation Denominator

Quality	Value
$\bar{D}$	$(1.419 \pm 0.019)10^9$
$S(0)$	$(4.367 \pm 0.074)10^7$
$S^*(0) \equiv \bar{\phi}_f^*$(core)	3.781
$\mathrm{Ih}(\Delta k/k)$	1.032×10^5
NF	$(1.600 \pm 0.027)10^3$
$\bar{D}/NF$, normalized mean (M)	$(8.870 \pm 0.190)10^5$
Calculated (C)	7.572×10^5
Ratio, C/M	0.8536 ± 0.0183

The calculated and measured values of the normalized perturbation denominator are compared in Table II-20-III. Multigroup cross sections generated from ENDF/B VERSION-I and corrected for plate heterogeneity were used in a one-dimensional cylindrical diffusion calculation[4] to obtain the calculated value of the perturbation denominator. This calculation also gave a value of 0.981 for k_{eff} for the "as-built" Assembly 7.

The measured perturbation denominator is about 17 % larger than the calculated value. This result is consistent with the observation[5] that for a wide variety of fast reactors calculated central reactivity worths for strongly reactive materials are overestimated by an average of 17 %.

An earlier measurement[6] of the Assembly 7 perturbation denominator (based on ^{252}Cf) reported a value of $(9.48 \pm 0.35)10^5$. The normalization factor used to obtain this result was based on absolute fission rates measured with fission flow counters. In connection with capture-to-fission ratio measurements made in Assembly 7 (see Paper II-17) it was pointed out that fission rates obtained with the flow counters were consistently lower, by about 7 %, than those measured by radiochemistry techniques. Within experimental errors, the two methods gave the same values for the fission ratios. The normalization factor listed in Table II-20-III was evaluated on the basis of the radiochemistry fission rates since these led to the most consistent set of alpha values. If the fission counter data are used, however, the experimental value for the perturbation denominator becomes $(9.47 \pm 0.19)10^5$ which is in good agreement with the earlier measurement. The origin of the systematic discrepancy in fission rates is under current investigation.

References

1. W. C. Redman and M. M. Bretscher, *Experimental Determination of the Perturbation Denominator in Fast Critical Assemblies*, Nucl. Sci. Eng. **44**, 450 (1971).
2. W. C. Redman, *Pile Oscillator Determination of Capture-to-Fission Ratio*, TID-17738.
3. M. M. Bretscher and W. C. Redman, *Low Flux Measurements of ^{239}Pu and ^{235}U Capture-to-Fission Ratios in a Fast Reactor Spectrum*, Nucl. Sci. Eng. **39**, 368 (1970).
4. D. A. Meneley, L. C. Kvitek and D. M. O'Shea, *MACH-1, A One-Dimensional Diffusion Theory Package*, ANL-7223 (1966).
5. H. Morewitz et al., *Annual Technical Progress Report, LMFBR Physics Programs, FY 1970*, AI-AEC-12969, p. 24 (August 1970).
6. Reactor Development Program Progress Report, ANL-7825, p. 7.4 (April–May 1971).

II-21. Doppler Effect Measurements in ZPR-6 Assembly 7

L. G. LeSage, E. M. Bohn, R. B. Pond, J. E. Marshall and E. F. Groh

Introduction

The results of the central Doppler effect measurements in the uniform version of ZPR-6 Assembly 7 are contained in this report. Results are reported for the following samples: Natural UO_2 (in two environments), $^{239}PuO_2$, $^{235}UO_2$, $^{233}UO_2$ and three mixtures of natural UO_2 and $^{239}PuO_2$ of varying compositions. These measurements include the first experimental studies of the effect of $^{238}U/^{239}Pu$ resonance interaction on the Doppler effect and the first ^{233}U Doppler effect measurements.

ZPR-6 Assembly 7, which is a large single-core-zone plutonium-uranium oxide critical assembly constructed as part of the LMFBR Demonstration Reactor Benchmark Critical Assembly Program, is described in Ref. 1 and Paper II-11. The configuration of the core for the Doppler effect measurements is described in the next section. Other reactivity measurements in Assembly 7 are described in Papers II-19 and II-25, and additional Doppler measurements in central zones containing plutonium with a higher concentration of ^{240}Pu (both with sodium and sodium voided) are reported in Papers II-12 and II-13.

Reference Core

The atomic concentrations in each core region are given in Table II-21-I and the approximate radial and

TABLE II-21-I. ATOM DENSITIES FOR ZPR-6 ASSEMBLY 7, LOADING 79,[a] 10^{21} atoms/cc

Region	^{238}Pu	^{239}Pu	^{240}Pu	^{241}Pu[b]	^{242}Pu	^{234}U	^{235}U	^{236}U	^{238}U	^{241}Am[b]	Mo	Na	O[c]	Fe[d]	Ni	Cr	Mn	Al
Exact Core	0.00033	0.8867	0.1177	0.0128	0.0014	0.00006	0.0126	0.00030	5.777	0.0036	0.2357	9.290	13.98	12.97	1.240	2.709	0.212	
Pu/U/Mo Core	0.00049	0.8879	0.1178	0.0146	0.00177	0.00006	0.0126	0.00030	5.802	0.0034	0.2382	9.132	14.82	13.53	1.212	2.697	0.213	
Pu/Al Core[e]	<0.0001	1.063	0.0499	0.0049	0.0005	0.00006	0.0126	0.00030	5.717	<0.001	0.242	9.132	14.82	13.15	1.481	2.675	0.21	0.101
Axial Blanket[f]						0.00040	0.0834	0.0020	38.59		0.0046[g]		0.030[g]	5.652	0.6910	1.579	0.123	
Radial Blanket[f]						0.00040	0.0866	0.0020	40.06		0.0034[g]		0.021[g]	4.197	0.5082	1.172	0.0897	

[a] The exact core and Pu/U/Mo core have the same unit-cell loading pattern and are essentially equivalent. The so-called "exact core" region is one in which the weights of all drawer materials have been carefully recorded in order to minimize the uncertainties associated with average plate weights and to aid in the comparison of experimental results between this core and an earlier core containing fuel pins in calandria cans in the exact-core region (see Paper II-25).

[b] $^{241}\text{Pu} \xrightarrow{\beta} {}^{241}\text{Am}$ decay corrected to May 1, 1971.

[c] Includes $\sim 0.001 \times 10^{21}$ atoms/cc due to SS304 and Pu/U/Mo fuel impurities.

[d] Includes $\sim 0.001 \times 10^{21}$ atoms/cc due to heavy (atomic weight $\geq$ Si) SS304 impurities and Pu/U/Mo fuel impurities.

[e] The compositional data available for the Pu/Al plates is not as complete as that for the Pu/U/Mo fuel.

[f] The axial blanket material was loaded into special stainless steel backdrawers. The radial blanket material was loaded directly into the matrix tubes. In addition, the axial blanket atom concentrations include the spring gap materials and volume (see Fig. II-21-2).

[g] Arising from SS304 impurities.

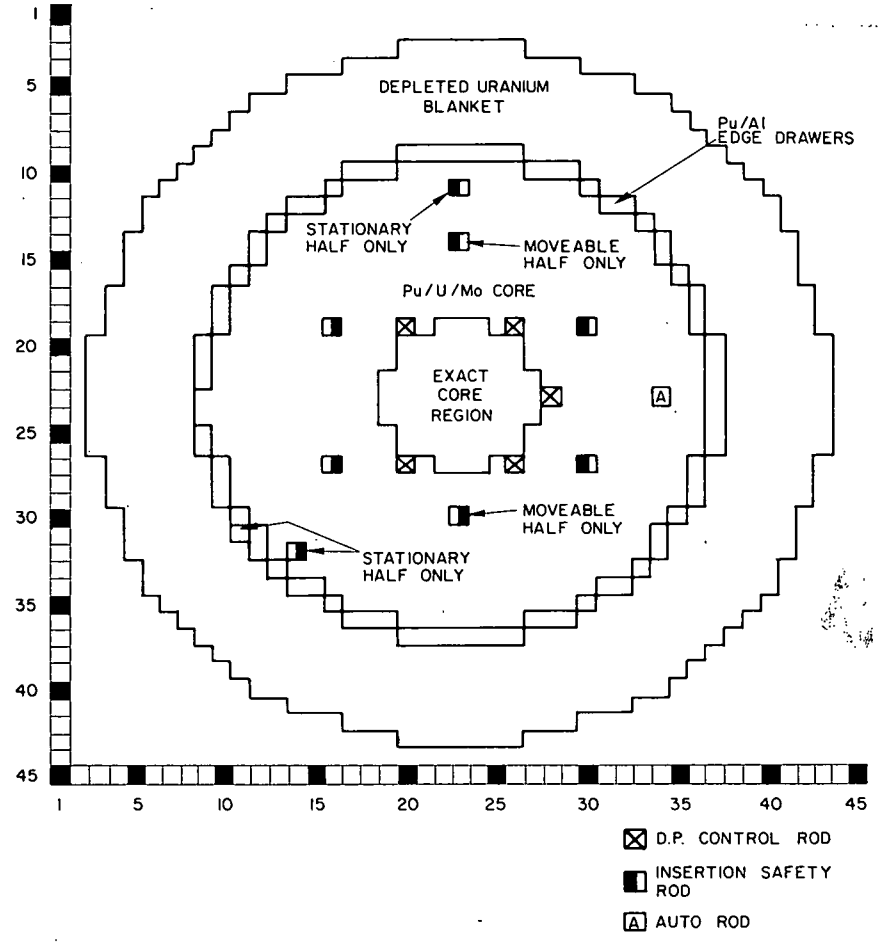

FIG. II-21-1. Radial Cross Section of ZPR-6 Assembly 7, Loading 79. *ANL Neg. No. 116-925.*

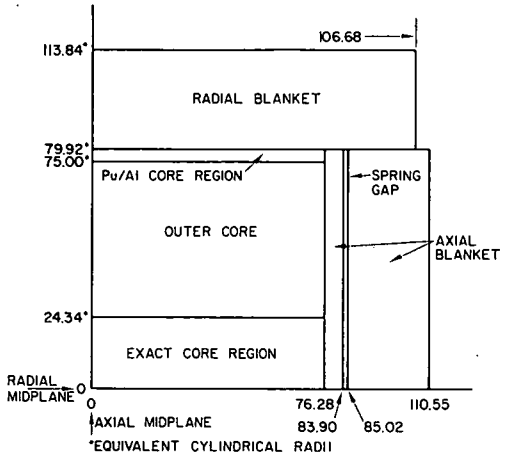

FIG. II-21-2. Axial Cross Section of ZPR-6 Assembly 7, Loading 79. *ANL Neg. No. 116-924.*

axial cross sections of the reactor at the time of the Doppler effect measurements are shown in Figs. II-21-1 and II-21-2. This configuration is slightly different from the reference clean configuration shown in Ref. 1 as a result of the substitution of drawers containing Pu/Al fuel for the normal Pu/U/Mo-fueled drawers near the core-blanket interface. Because the fissile plutonium weight in the Pu/Al drawers was about 20% greater than in the Pu/U/Mo drawers, there are 12 fewer drawers per half shown in Fig. II-21-1 than in the figure in Ref. 1. The total fissile loading of the core remained nearly constant, and, for purposes of central measurements, the core with the Pu/Al drawers was identical with the uniform version of Assembly 7 because both the central spectra and the perturbation denominators were the same for the two cores. Central worth measurements were made for a number of materials in both cores and the measured worth values were the same. These measurements are discussed in Paper II-19. Calculations also indicated the equivalence of the two cores.

The core shown in Figs. II-21-1 and II-21-2 is the clean configuration without the central Doppler drawer installed. The fissile loading of this core was 1136 kg. The fissile loading of the assembly with the Doppler drawer installed varied from 1119 to 1145 kg among the various Doppler measurements as a result of the different reactivity worths of the Doppler samples and Doppler oscillator drawer. The largest critical fissile

loading corresponded to the natural UO_2 Doppler samples and the smallest corresponded to the fissile Doppler samples. The fissile inventory and associated outer core radii for each Doppler measurement are given in Table II-21-II.

Doppler Measurements

The Doppler-effect experimental equipment, the Doppler samples, and the experimental techniques used at ANL have been described in Refs. 2 through 4, and therefore they will not be discussed in this paper.

TABLE II-21-II. Central Doppler Reactivity Worth Measurements in ZPR-6 Assembly 7

Sample No.	Sample Material[a,b]	Core Configuration		Sample Environment	Average Sample Temperature,[d] °K	Reactivity Change,[e,f] Ih/kg of Heavy Metal
		Total Fissile Loading[c], kg	Outer Radius, cm			
N1	Natural UO_2	1145	80.19	Normal plate core	293	0
					494	−0.300 ± 0.011
					771	−0.608 ± 0.010
					1075	−0.871 ± 0.010
N1	Natural UO_2	1145	80.19	¼ in. thick SS filter region around sample.	293	0
					491	−0.299 ± 0.004
					751	−0.597 ± 0.006
					1038	−0.849 ± 0.005
INC-5	PuO_2	1129	79.71		345	0
					588	−0.110 ± 0.011
					798	−0.200 ± 0.011
					1069	−0.341 ± 0.011
HE-8	Enriched UO_2	1127	79.65		294	0
					515	0.197 ± 0.008
					797	0.332 ± 0.013
					1051	0.397 ± 0.008
INC-20	$(^{233}U)O_2$	1119	79.40		322	0
					514	0.182 ± 0.017
					786	0.309 ± 0.019
INC-12	0.67 PuO_2/0.33 U (Nat.)O_2	1132	79.80		344	0
					588	−0.157 ± 0.008
					798	−0.268 ± 0.007
					887	−0.312 ± 0.008
INC-14	0.50 PuO_2/0.50 U (Nat.)O_2	1137	79.95		313	0
					526	−0.172 ± 0.008
					723	−0.299 ± 0.008
					836	−0.358 ± 0.010
					919	−0.411 ± 0.014
INC-26	0.33 PuO_2/0.67 U (Nat.)O_2	1137	79.95		313	0
					524	−0.228 ± 0.009
					798	−0.463 ± 0.009
					856	−0.503 ± 0.008
					902	−0.533 ± 0.008

[a] All samples were the freely-expandable type.

All samples were 1 in. diam and 12 in. long.

This value includes the loading corresponding to the critical mass plus a small excess reactivity (generally equivalent to 3 to 7 kg of fissile material).

[d] Sample temperatures were measured at five axial positions. The precision in average sample temperatures was ±1%.

[e] 1% $\Delta k/k$ = 1030 Ih. Total β_{eff} = 0.00319. Prompt neutron lifetime, $\ell_p = 5.48 \times 10^{-7}$ sec.

[f] The reactivity change values are the result of both the Doppler effect and sample thermal expansion.

TABLE II-21-III. Doppler Sample Composition Data, ZPR-6 Assembly 7

Sample No.	Sample Material	Sample Composition,[a] gm
N1	Natural UO_2	^{238}U 1108.88, ^{235}U 7.99, O 149.42
INC-2	PuO_2	^{239}Pu 793.48, ^{240}Pu 105.83, ^{241}Pu 17.88, O 117.71
He-8	Enriched UO_2	^{235}U 891.87, ^{238}U 10.12, ^{234}U 9.37, ^{236}U 1.88, O 124.30
INC-20	$(^{233}U)O_2$	^{233}U 785.85, ^{234}U 9.67, ^{238}U 3.44, O 138.15
INC-12	0.67 PuO_2/0.33 U (Nat.)O_2	^{239}Pu 511.46, ^{240}Pu 68.22, ^{241}Pu 11.53, ^{238}U 296.34, ^{235}U 0.62, O 114.00
INC-14	0.50 PuO_2/0.50 U (Nat.)O_2	^{239}Pu 387.71, ^{240}Pu 51.71, ^{241}Pu 8.74, ^{238}U 433.04, ^{235}U 0.91, O 117.40
INC-26	0.33 PuO_2/0.67 U (Nat.)O_2	^{239}Pu 268.87, ^{240}Pu 35.86, ^{241}Pu 6.06, ^{238}U 625.78, ^{235}U 1.31, O 124.79

[a] Composition data are from Ref. 10. Compositions corrected for ^{241}Pu decay to date of Doppler measurements (March 1971).

All the Doppler samples measured in Assembly 7 were the 1 in. diam freely-expandable type. With the exception of the first natural UO_2 measurement, a ¼ in. thick stainless steel (304) filter region was installed around the Doppler samples in order to decouple the resonances in the sample from the corresponding resonances in the surrounding core material. Figure II-6-3 of Ref. 4 is a cross-section drawing showing the Doppler sample, the stainless steel filter, and surrounding core drawers. Figure II-6-2 of Ref. 4 is a detailed cross section of the Doppler drawer and sample. For the first natural UO_2 Doppler measurement, the stainless steel filter was not installed, and the surrounding core drawers were all loaded in the normal manner.

The results of the Doppler measurements are tabulated in Table II-21-II, and the composition data for the samples, obtained from Ref. 5, are included in Table II-21-III. Since the samples were the freely-expandable type, the reactivity results listed in Table II-21-II are due to both the Doppler effect and sample thermal expansion. The quoted 1σ imprecisions of the measurements include only those due to the dispersion in the experimental data. An additional experimental 1σ uncertainty of 0.5 to 1.0% due to the autorod calibration should be included when making comparisons between these measurements and calculations. The autorod calibration is discussed in Paper II-19.

Discussion of Results

Since the Doppler results listed in this report have not been corrected for the thermal expansion, the discussion will be brief. The expansion calculations, a comparison of the measurements with calculation, and a more complete discussion of the results is included in Paper II-22.

Previous measurements have shown that the expansion effect in the natural UO_2 samples is negligible so that the results for these samples are due entirely to the Doppler effect. Since the ^{238}U Doppler effect is in general larger in magnitude than the ^{235}U Doppler effect, the results for the natural UO_2 samples are due almost completely to the ^{238}U Doppler effect. The strongly negative ^{238}U Doppler coefficient in a typical dilute PuO_2 LMFBR spectrum is, of course, indicated by these results. It should also be noted that the measured ^{238}U Doppler effect was the same with and without the inclusion of the stainless steel filter as expected.[6]

References

1. L. G. LeSage, E. M. Bohn, J. E. Marshall, R. A. Karam, C. E. Till, R. A. Lewis and M. Salvatores, *Initial Experimental Results from ZPR-6 Assembly 7, The Single Zone Demonstration Reactor Benchmark Assembly*, Trans. Am. Nucl. Soc. **14**, 17 (1971).
2. C. E. Till, R. A. Lewis and E. F. Groh, *^{235}U Doppler Effect Measurement Data and Techniques*, Reactor Physics Division Annual Report, July 1, 1966 to June 30, 1967, ANL-7310, pp. 151–158.
3. C. E. Till, R. A. Lewis and R. N. Hwang, *ZPR-6 Doppler Measurements and Comparisons with Theory*, Proc. International Conference on Fast Critical Experiments and Their Analysis, October 10–13, 1966, ANL-7320, pp. 319–333.
4. R. B. Pond, J. W. Daughtry, C. E. Till, E. F. Groh, C. D. Swanson and P. H. Kier, *Plutonium and ^{238}U Doppler Measurements in ZPR-9 Assembly 26, FTR-3*, Applied Physics Division Annual Report, July 1, 1969 to June 30, 1970, ANL-7710, pp. 74–77.
5. J. E. Ayer, C. F. Konicek, F. E. Soppet and E. J. Petkus, *The Manufacture of Vibratorily Compacted Fuel Elements for Doppler-Coefficient Measurements*, ANL-7647 (1970).
6. R. A. Lewis and T. W. Johnson, *Sensitivity of Small-Sample Doppler Effect Measurements to Environment*, Reactor Physics Division Annual Report, July 1, 1967 to June 30, 1968, ANL-7410, pp. 96–103.

II-22. Analysis of Small-Sample Doppler Measurements in ZPR-6 Assemblies 6 and 7

P. H. Kier, M. Salvatores,* W. R. Robinson and K. D. Dance

Introduction

The small-sample Doppler measurements in ZPR-6 Assembly 6[1] and Assembly 7 (see Paper II-21) have been analyzed. In Assembly 6, the Doppler effect was measured for natural UO_2 and ^{235}U-enriched UO_2 samples. In Assembly 7, the Doppler effect was measured for natural UO_2, ^{235}U-enriched UO_2, ^{233}U-enriched UO_2, PuO_2, and three mixed UO_2-PuO_2 samples. The detailed compositions of these samples, which were 1 in. in diam and 12 in. long, are given in Table II-22-I.

Calculational Methods

First-order perturbation theory was used to compute the reactivity effect of the Doppler change in the capture and fission cross sections associated with a temperature change from 293 to 1070°K. The real and adjoint fluxes used in these calculations were obtained from one-dimensional, spherical diffusion calculations in which the stainless steel buffer and oscillator drawer were not present. Thus, in the basic model, the perturbation in the real and adjoint fluxes introduced by the experimental apparatus is not included, although auxiliary transport computations were made to assess the magnitude of this effect.

For all isotopes except ^{233}U, the MC² code[2] was used to generate cross sections. Fine group (¼ lethargy unit) resonance cross sections at the two temperatures were generated for a two-region cell in which the Doppler sample was surrounded by an annular region containing the steel in the buffer and the oscillator drawer. The resulting fine group, Doppler cross section changes were weighed by the fundamental-mode fine group fluxes for the core of the appropriate assembly to obtain the cross section changes used in the perturbation computations. MC² problems were run for the natural UO_2, ^{235}U-enriched UO_2, and PuO_2 samples. The MC² libraries contain ENDF/B data; however, the ENDF/B data for ^{233}U does not have resonance information, so MC² could not be used to compute Doppler cross section changes. For ^{233}U, the data compiled by Boroughs et al.,[3] was used in Hwang's[4] modification of the ERIC code,[5] which treats resonance overlapping effects somewhat more accurately than MC².

For all samples except the natural UO_2 sample, N-1, the measured reactivity has a significant component from thermal expansion of the sample. Till's perturbation formulation[6] was used to compute the reactivity effect of change in the radius and density of the sample. The expansion properties of the vibratory compacted samples are not well known. It was assumed, therefore, that the samples expand as their inconel jackets, which was taken as 8 mil/in.

The computations were made with 27 broad groups. Groups 1-21 were one-half lethargy units wide, Groups 22-25 were one lethargy unit wide, Group 26 was two lethargy units wide, and Group 27 was the thermal group.

Results

The results of the analysis are given in Table II-22-I with ENDF/B VERSION-II Revised data for ^{235}U, ^{238}U and ^{239}Pu and VERSION-II data for ^{240}Pu and ^{241}Pu. The calculated expansion effects were subtracted from the gross measurement to yield the measured Doppler effect. Period/reactivity conversion factors of 458 and 1035 Ih/$\%\Delta k/k$ were used for Assemblies 6 and 7, respectively.

The calculated Doppler effect in the mixed PuO_2-UO_2 samples were obtained from proration of the values for the pure samples. This proration could possibly introduce errors because the scattering cross section per absorber atom is larger in the mixed samples than in the pure samples. Equivalence theory computations for ^{238}U with scattering cross sections per ^{238}U atom appropriate for samples N-1, INC-12, INC-14 and INC-26 were made. It was found that as the scattering cross section per absorber atom increased, that is, greater

TABLE II-22-I. Composition of Samples used in Doppler Measurements, g

Isotope	Sample						
	He-8	INC-5	INC-12	INC-14	INC-26	N-1	INC-20
^{16}O	124.30	117.71	114.00	117.40	124.79	149.42	138.15
^{239}Pu	—	793.48	511.46	387.71	268.87	—	—
^{240}Pu	—	105.83	68.22	51.71	35.86	—	—
^{241}Pu	—	22.44	14.47	10.97	7.60		
^{235}U	891.87	—	0.62	0.91	1.31	7.99	—
^{238}U	10.12	—	296.34	433.04	625.78	1108.88	3.44
^{233}U	—	—	—	—	—	—	785.85
^{234}U	9.37	—	—	—	—	—	9.67
^{236}U	1.88	—	—	—	—	—	—

* Comitato Nazionale per L'Energia Nucleare, Casaccia, Italy.

TABLE II-22-II. Comparison of Measured and Computed Small-Sample Doppler Effects in ZPR-6 Assemblies 6 and 7 f... T = 293 to 1069°K, Ih/kg (U + Pu)

Sample	Composition	Assembly	Calculation		Measurement	
			Expansion	Doppler	Gross	Doppler
He-8	$^{235}UO_2$	6	−0.0206	0.1688	0.058	0.079
		7	−0.0092	1.024	0.400	0.409
INC-5	PuO_2	7	−0.263	0.4138	−0.346	−0.083
INC-12	$PuO_2/UO_2 = 2$	7	−0.097	−0.0211	−0.385	−0.287
INC-14	$PuO_2/UO_2 = 1$	7	−0.049	−0.2312	−0.442	−0.393
INC-26	$UO_2/PuO_2 = 2$	7	−0.031	−0.5270	−0.617	−0.586
N-1	UO_2	6	—	−0.253	−0.353	−0.353
		7	—	−0.902	−0.884	−0.871
INC-20	$^{233}UO_2$	7	−0.164	3.192	0.359	0.523

TABLE II-22-III. Comparison of the Doppler Effect in ZPR-6 Assembly 7 for ^{239}Pu and ^{235}U as Calculated with Different Sets of ENDF/B Data

Isotope	Reactivity, Ih/kg		
	VERSION 1	VERSION 2	VERSION 2 Revised
^{239}Pu	1.736	0.919	0.591
^{235}U	—	0.788	1.211

dilution, the Doppler change in cross section decreased at high energy and increased at low energy such that the net change in the Doppler effect in ^{238}U was less than 4% in the spectrum of Assembly 7. Also it was impossible to attain temperatures above 950°K in the mixed PuO_2-UO_2 samples. Therefore, the gross measured reactivities given in Table II-22-II for these samples are extrapolations. However, as the plots of the measured reactivity versus temperature are nearly linear above 700°K, the extrapolations may be expected to be quite accurate.

In agreement with recent measurements[7] in ZPR-9 Assembly 26, the measured Doppler effect in plutonium (11.5 w/o ^{240}Pu, 2.4 w/o ^{241}Pu) was small and apparently negative. As the thermal expansion of the samples are not known accurately, there are significant uncertainties in the computed expansion effect and, therefore, in the measured Doppler effect. However, since the measured Doppler effect for the mixed samples is nearly a proration of the pure sample values, we have an indication that the expansion effects are computed fairly accurately.

The results for ^{238}U, sample N-1, are also consistent with experience with close agreement between theory and experiment for the plutonium-fueled Assembly 7 (see Paper II-8) and larger discrepancies for the uranium-fueled Assembly 6.[8] There is generally poor agreement between the measured and calculated Doppler effect in fissile samples with calculations yielding significantly more highly positive effects. Even so, for sample INC-26, which has a composition which approaches that of a fast reactor fuel, there is only a 10% discrepancy between theory and experiment. The basic resonance data have a great effect on the calculated Doppler effect. The Doppler effect for ^{239}Pu was computed with three sets of ENDF/B data: VERSION-I, VERSION-II and VERSION-II Revised. The Doppler effect for ^{235}U was computed with two sets: VERSION-II and VERSION-II Revised. MC^2 was used to derive group cross sections from the basic data except for the ^{239}Pu VERSION-I case for which Hwang's modification of ERIC was used. The results of these comparisons are given in Table II-22-III, from which the great influence of the basic data is apparent.

These calculations neglected both the hot-sample cold-core resonance interaction effect and the effect of the stainless steel buffer and oscillator drawer on the central real and adjoint fluxes. Calculations of the hot-sample cold-core resonance interaction effect indicate that it is a small effect for buffered samples and augments the Doppler effect by about 4%[9] (also see Paper II-8).

The perturbations in fluxes introduced by the test region has a relatively small effect on the measured Doppler effect for ^{238}U samples (less than 10%), but whether it increases or decreases, the measured value depends upon the core. For small, concentrated cores, the flux perturbation effect increases the measured Doppler effect because the test region acts as a flux trap at low energies; for large, dilute cores, the flux perturbation effect tends to reduce the measured Doppler effect. To assess the flux perturbation effect for the natural UO_2 sample, two one-dimensional S_8 transport calcu tions were made. The configuration was identical w that used in similar calculations for ZPR-9 Assembly 26 (see Paper II-8). The calculations yielded ϕ_h/ϕ_∞, the

ratio of the real flux in the hot sample to the unperturbed real flux and ϕ_c^*/ϕ_∞^*, the ratio of the adjoint flux in the cold sample to the unperturbed adjoint flux. The Doppler effect with the flux perturbation effect included was obtained by multiplying the previous groupwise contributions by $\phi_h/\phi_\infty \times \phi_c^*/\phi_\infty^*$. For ^{238}U, the effect was calculated to reduced the Doppler effect by 6.5% in Assembly 6 and 5.5% in Assembly 7. Thus, the two effects that were neglected tended to cancel.

References

1. J. W. Daughtry and R. A. Lewis, *Uranium Doppler Measurements in ZPR-6 and -9 Oxide Cores*, Reactor Physics Division Annual Report, July 1, 1968 to June 30, 1969, ANL-7610, pp. 193–197.
2. B. J. Toppel, A. L. Rago and D. M. O'Shea, *MC²*, *A Code to Calculate Multigroup Cross Sections*, ANL-7318 (1967).
3. G. L. Boroughs, C. W. Craven, Jr., and M. K. Drake, *A Set of Evaluated Nuclear Data for ^{233}U*, GA-8854 (1968).
4. R. N. Hwang, *Application of Statistical Theory and Multi-level Formalism to Doppler Effect Analysis—I*, Nucl. Sci. Eng. **36**, 67 (1969).
5. H. M. Sumner, *ERIC-2, A FORTRAN Program to Calculate Resonance Integrals and From Them Effective Capture and Fission Cross Sections*, AEEW-R323 (1964).
6. C. E. Till, *Fissile Doppler Effect Measurement of the Effects of Thermal Expansion*, Reactor Physics Division Annual Report, July 1, 1966 to June 30, 1967, ANL-7310, pp. 143–151.
7. R. B. Pond, J. W. Daughtry, C. E. Till, E. F. Groh, C. D. Swanson and P. H. Kier, *Plutonium and ^{238}U Doppler Measurements in ZPR-9 Assembly 26, FTR-3*, Applied Physics Division Annual Report, July 1, 1969, to June 30, 1970, ANL-7710, pp. 73–77.
8. C. E. Till, W. G. Davey, R. A. Lewis and R. G. Palmer, *The ANL Critical Experiment Program*, Proc. BNES Conference on the Physics of Fast Reactor Operation and Design, London, June 23–26, 1969, pp. 40–49.
9. R. A. Lewis and T. W. Johnson, *Sensitivity of Small-Sample Doppler-Effect Measurements to Environment*, Reactor Physics Division Annual Report, July 1, 1967 to June 30, 1968, ANL-7410, pp. 96–103.

II-23. Analysis of ZPR-6 Assembly 6A

R. A. Karam

Introduction

Anisotropic effects in relatively small fast reactors where the spectrum is hard were investigated by Bell et al.[1] In this paper, anisotropic effects on the flux fine structure in the unit-cell, on the critical size, and on the spatial activation distribution were calculated for ZPR-6 Assembly 6A, the demonstration plant benchmark critical. This assembly is a 4000-liter UO_2 fast critical in which the neutron spectrum is relatively soft.

Description of Assembly 6A

A complete description of Assembly 6A is given in Paper II-11. Only those parameters used in the calculations are reported in this paper.

The single drawer, plate unit-cell of Assembly 6A is shown in Fig. II-23-1. The as-built dimensions of the assembly are shown in Fig. II-23-2 where it may be noted that the core comprised three regions. The central region was designated as the "exact core region" simply because the weights of all the plates, carefully selected to match the pin-calandria compositions, were accutely known. The surrounding region had the same loading pattern and composition as the "exact core region", except in this region average weights of plates, rather than the actual weights of individual plates, were used to determine the atom density. The core outer region was fueled with 1/8 in. thick enriched plates rather than with the 1/16 in. thick plates used in the rest of the core. The 1/8 in. thick plates, 2 or 3 in. long, were staggered with 1/8 in. thick SS plates of equal length (i.e. the number of 1/8 in. thick plates in a drawer was equal to half the number of 1/16 in. thick plates) in order to maintain the same fissile atom density throughout the core. The reactivity difference between

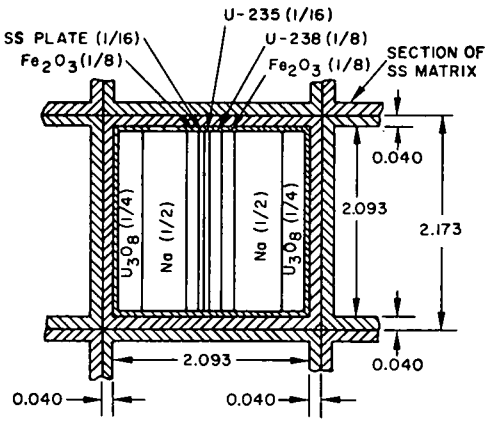

Fig. II-23-1. ZPR-6 Assembly 6A Unit Cell. *ANL Neg. No 116-488 Rev. 1.*

the two types of drawers was measured by substituting the drawers with 1/16 in. thick plates for the drawers with 1/8 in. thick plates in consecutive steps each of which comprised a 15-deg sector. The sector substitution continued until a full quadrant was converted to the composition and configuration of the uniform core. The results were then extrapolated to obtain the critical mass of a clean fully-uniform core. The derived cylindrical radius of the just-critical uniform core was 91.34 cm. The corresponding critical mass was 1793.5 kg of ^{235}U with an uncertainty of 10 kg. The atom densities of the uniform core are given in Table II-23-I.

Calculation

Cross section sets for Assembly 6A were generated, using ENDF/B-I, in the manner described in Ref. 2. (Comparison of the effects of ENDF/B-I, -II, and -II

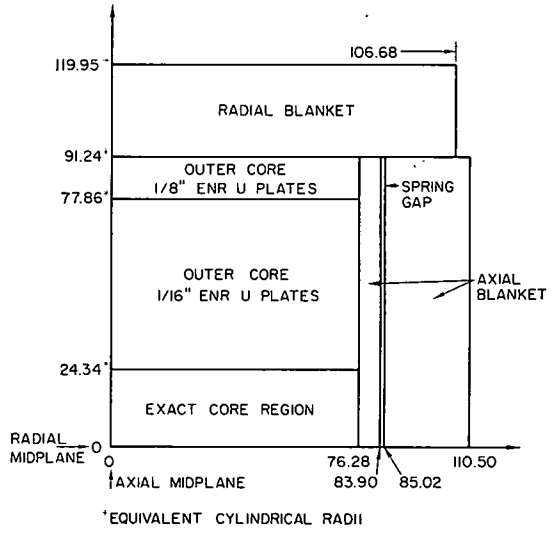

Fig. II-23-2. Block Diagram of the As-Built Assembly 6A. *ANL Neg. No. 116-1044.*

TABLE II-23-I. Atomic Densities in the Uniform Assembly 6A, (a) 10^{24} atoms/cc

Isotope	Exact Core Region	Outer Core Region	Blanket
Na	0.009294	0.009142	—
O	0.01380	0.01465	—
Fe	0.013535	0.01410	0.004224
Ni	0.001229	0.001365	0.0005086
Cr	0.002842	0.002796	0.001176
^{238}U	0.005796	0.005796	0.04008
^{235}U	0.001154	0.001151	0.0008270
Mn	0.0002174	0.0002174	0.00008997

[a] A more complete isotopic analysis of Assembly 6A is reported in Paper II-11. In some cases the atom densities differed slightly from those reported in Paper II-11. For benchmark testing it is recommended that the atom densities in Paper II-11 be used.

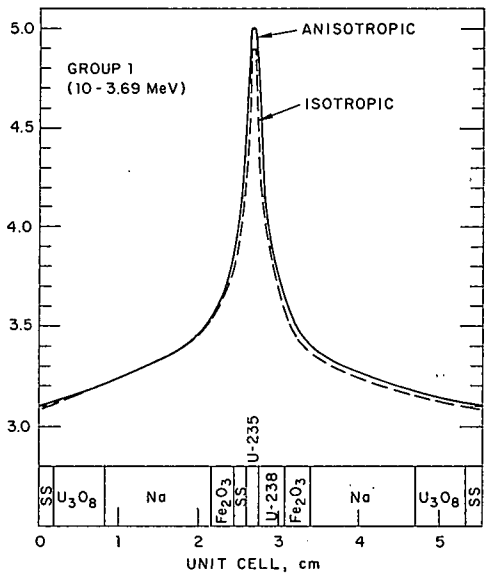

Fig. II-23-3. Comparison of the Unit-Cell Flux Distribution (Group 1: 10–3.69 MeV) as Obtained with the P_1 (Anisotropic) and the Transport Approximations. *ANL Neg. No. 116-1045.*

MODIFIED on the physics parameters of Assembly 6A is reported in Paper II-53. Briefly, two MC² calculations were performed to generate two 25-group cross section sets: one for the homogeneous compositions of Assembly 6A and one for the homogeneous compositions of the blanket ($B^2 = 0$). In both cases the anisotropic option (P_1 only) was used. It should be noted, however, that only isotropic scattering is provided for ^{235}U and ^{238}U in the MC² code. The set for the blanket was used in the final calculations without any further adjustments. The set for the core was corrected for resonance spatial self-shielding in ^{235}U and ^{238}U and weighted with the flux fine structure of the unit-cell.

Results

UNIT-CELL

The k_{eff} of the unit-cell calculated with 1-D, S_n ($n = 16$) and the anisotropic option was 1% greater than that calculated in the same manner with the transport approximation. This difference in k_{eff} disappeared, however, when the transverse dimension in each method was made infinite; this indicated that the decrease in leakage associated with the use of Σ_{total} instead of $\Sigma_{transport}$ was responsible for the difference in k_{eff}.

The unit-cell neutron spectra and the reaction rati $\sigma_f^{28}/\sigma_f^{25}$, $\sigma_c^{28}/\sigma_f^{25}$, calculated with the two methods w essentially the same. Yet there was a small differenc in the spatial distribution of the flux in some energy groups (see Fig II-23-3 for a typical example).

TABLE II-23-II. k_{eff} Comparisons of the As-Built Assembly 6A Using the Anisotropic P_1 and the Transport Approximations

	k_{eff}[a] (ENDF/B-VERSION I)		
	Homogeneous Set	Resonance Self-Shielded Set	Space and Resonance Self-Shielded Set
$l = 1$	0.9915	0.9993	1.0026
$l = 0$	0.9858	—	0.9970

[a] Calculated with 1-D, S_n ($n = 4$) code and the measured extrapolated height.

k_{eff} of the as-built system

The k_{eff} of the as-built system (see Fig. II-23-2) was computed with the MC²-generated homogeneous set, with the resonance self-shielded set, and with the resonance self-shielded and broad group, spatially-averaged set. The measured extrapolated half-height (95.12 cm) was used in a 1-D, S_n ($n = 4$) code to calculate the k_{eff} of the system with the various sets. The results are given in Table II-23-II where it may be seen that the difference in k_{eff} between the anisotropic P_1 and the transport approximations is about 0.5%. Again it should be emphasized that this difference is primarily due to the inherent difference in the transverse leakage associated with Σ_{total} and $\Sigma_{transport}$.

Spatial activation distribution

Discrepancies between the measured and calculated activation distributions in fast reactors have been observed for some time.[3–5] The sources of these discrepancies contribute to errors in the perturbation denominator and hence to reactivity coefficients,[6] to errors in the critical size, and to errors in the power distribution. The contribution to the discrepancies due to anisotropic effects were investigated, for the first time, on a system as large as Assembly 6A. The calculations were performed along the axial height of the cylindrical assembly. The axial height was chosen because along this dimension the boundary between the core region and the blanket region is well defined. The same is not true for the radial dimension which is approximated with square unit-cells. Additionally, the fuel column position in a unit-cell at or near the radial core-blanket interface affects the flux distribution.

The activation distributions were calculated for the as-built core using 1-D codes and the measured extrapolated radius. The extrapolated radius was determined by fitting to a J_0 function the measured foil activity from the core center to 20 cm from the core-blanket interface. The neutron flux used to obtain the activation distributions correspond to the k_{eff} of the as-built system. The measured points were obtained with foils placed next to the ^{235}U column in the unit-cell. In the blanket region the foils were placed on top of the depleted uranium blocks. The accuracy of the relative activities of the foils was 0.5–1.0%.

The calculated and measured ^{235}U fission-rate distributions as a function of core height are shown in Fig. II-23-4. The solid line was obtained with the heterogeneous core fluxes using S_4 and the anisotropic option; foil fission cross sections were those of ^{235}U and ^{238}U in the core for the core region and those of ^{235}U and ^{238}U in the blanket for the blanket region. Essentially the same distribution was obtained with the transport approximation calculation and nearly the same distribution was obtained with diffusion theory calculations.

The measured and calculated ^{238}U fission rates are shown in Fig. II-23-5. Foil fission cross sections were

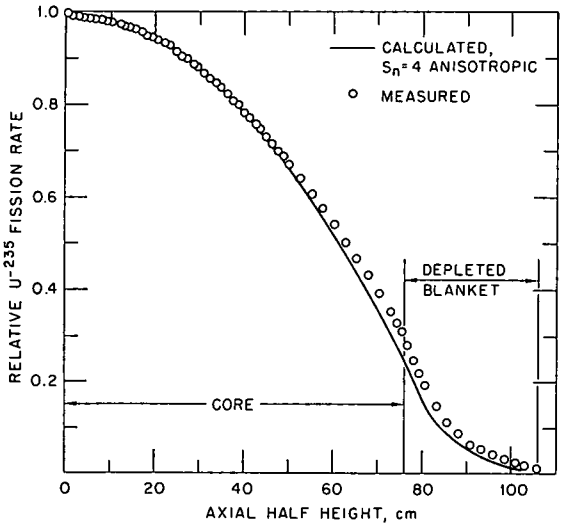

Fig. II-23-4. Measured and Calculated ^{235}U Fission Rate Distribution, ZPR-6 Assembly 6A. *ANL Neg. No. 116-716.*

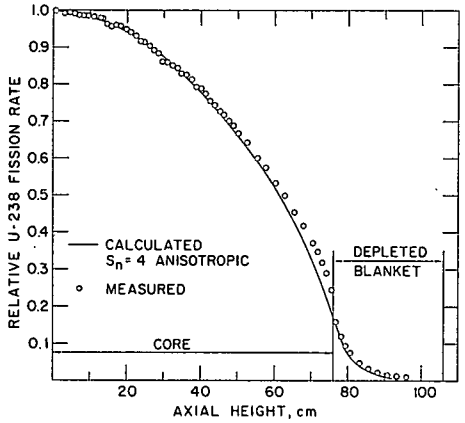

Fig. II-23-5. Measured and Calculated ^{238}U Fission Rate Distribution, ZPR-6 Assembly 6A. *ANL Neg. No. 116-717.*

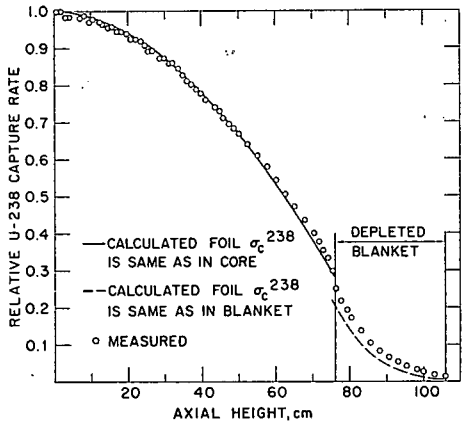

FIG. II-23-6. Measured and Calculated ^{238}U Capture Rate Distribution, ZPR-6 Assembly 6A. *ANL Neg. No. 116-715.*

those characteristic of the core and blanket regions respectively. Again, very little difference between the P_1 and the transport approximations was found. In fact, a diffusion calculation gave essentially the same distribution.

The measured and calculated ^{238}U capture distributions are shown in Fig. II-23-6. Foil cross-sections were also those characteristic of the core and blanket regions respectively. Again very little difference in the calculated distributions was found among the three methods. Yet the difference between calculation and measurement persisted.

Discussion and Conclusions

The discrepancies between the measured and calculated distributions indicate that the calculated buckling is greater than measurements indicate it should be. This is true for both the ^{235}U and ^{238}U fission distributions. If it is postulated that the ENDF/B-I inelastic cross section of ^{238}U is high, then it would be expected that the ^{238}U fission rate would be low near a depleted uranium blanket. Concurrently, however, it would be expected that the ^{235}U fission rate would be high since the ^{235}U broad group cross sections increase as the neutron energy decreases. Figure II-23-4 shows that the calculated ^{235}U fission rate decreases as a function of z faster than the measured points, and consequently the postulated increase does not materialize. Figure II-23-6 shows that the calculated ^{238}U capture rate in the blanket, when normalized to unity at the core center, is significantly lower than the measured rate. These results indicate that either the actual neutron spectrum is harder at the high-energy end and, at the same time, softer at the low energy end, than the calculated spectrum or, if the calculated spectrum is adequate, then the codes inadequately predict the buckling of the neutron flux. There is a possibility that both the spectrum and the buckling prediction are in error. An obvious refinement in the analysis is, of course, the generation of space-dependent cross sections. It would indeed be valuable to repeat these calculations with space-dependent cross sections.

A rough estimate of the effect of the error in the calculated shape of the power distribution on the critical size may be made by using the measured extrapolated radial and axial dimensions to calculate k_{eff} of the equivalent bare core, i.e. a one region reactor. The k_{eff} calculated in this manner was 1 % greater than that obtained using the as-built core and blanket system with the measured extrapolated height.

References

1. G. T. Bell, G. E. Hansen and H. A. Sandmeier, *Multitable Treatments of Anisotropic Scattering in SN Multigroup Transport Calculation*, Nucl. Sci. Eng. **28**, 376 (1967).
2. R. A. Karam, J. E. Marshall and K. D. Dance, *Analysis of Heterogeneity and Sodium-Void Effects in a 2700 Liter Uranium Carbide Fast Core, ZPR-6 Assembly 5*, Nucl. Sci. Eng. **43**, 5–26 (1971).
3. M. Edelmann et al., *Physics Measurements in SNEAK Facility on Steam Cooled Fast Reactor Systems with Uranium and Plutonium Fuel*, Proc. Inter. Conference on the Physics of Fast Reactor Operation and Design, London, 1969, pp. 113–137.
4. M. L. Batch and R. E. Mueller, *Physics Measurements in the Fermi Reactor*, ibid, pp. 336–345.
5. L. LeSage, Argonne National Laboratory (private communication).
6. R. A. Karam, *Measurement of the Normalization Integral and the Spatial Distribution of the Importance of Fission Neutrons*, Nucl. Sci. Eng. **37**, 192–197 (1969).

II-24. Uranium Doppler-Effect Measurements in ZPR-6 Assembly 6A

R. B. Pond and J. W. Daughtry

Introduction

Assembly 6A[1] was a reconstructed version of Assembly 6,[2] a 4000-liter uranium oxide fast critical. Assembly 6 preceded and Assembly 6A followed th year long shutdown of the ZPR-6 facility (1968–1969) while modifications were being made to permit plu-

tonium fuel usage in both the ZPR-6 and -9 facilities. Assemblies 6 and 6A were nearly identical in physical characteristics but had slightly different radial isotopic compositions due to material inventory restrictions and specific design requirements of Assembly 6A. The program of measurements in Assembly 6A was primarily intended to provide various reference and normalization measurements for the Variable Temperature Rodded Zone[3] (VTRZ) Program and for rod-versus-plate heterogeneity study configurations. The uranium Doppler-effect measurements are reported here. Other measurements such as spectrum, critical size, reaction rates and central reactivity worths have been reported in Refs. 1 and 4.

Central ^{238}U Doppler-effect measurements were made in two configurations of Assembly 6A. The first was a repeat of a similar measurement made in Assembly 6 and the second was an identical measurement but in a sodium-voided environment. In the latter case, the central region of radius 39.4 cm was completely voided of sodium. (Approximately 39 v/o of the Assembly 6 and 6A core was sodium and the outer core radius of the assemblies was approximately 90.7 cm.) Empty stainless steel cans were used to replace the stainless steel canned sodium removed in order to preserve the overall stainless steel composition. Calculations indicated that this size zone was sufficient to produce the asymptotic full-core sodium-voided-spectrum at the Doppler measurement position.

The Doppler equipment used in the Assembly 6A experiments was somewhat different from that used in the Assembly 6 experiments. The equipment was designed specifically for high-temperature Doppler-effect measurements[5] and for making measurements in the VTRZ. The high-temperature Doppler measurements require large cooling-air capacity to remove heat loss from the high-temperature Doppler samples. The VTRZ measurements will require special equipment because of the split-construction design of the VTRZ.

The basic Doppler-effect measurement technique was the same in Assemblies 6 and 6A; i.e., the sample oscillation-reactivity difference technique. In order to compare similar Doppler-effect measurements made in Assemblies 6 and 6A, a description of the Doppler apparatus used in each measurement is discussed below.

Doppler Measurement Technique

The Doppler measurement method used at ANL is the sample oscillation-reactivity difference technique. In this technique, the reactivity difference between a Doppler sample and a reference is periodically measured at the point in the reactor where the Doppler effect is to be measured. A calibrated, servo-controlled, fine autorod (FAR) is used to maintain the reactor critical with either the Doppler sample or the reference in place in the reactor. The average FAR position is electronically determined and the difference of these autorod positions gives the reactivity worth of the Doppler sample relative to the reference. The reactivity change as a function of Doppler sample temperature is obtained by repeating the sample-reference oscillation procedure for various Doppler sample temperatures.

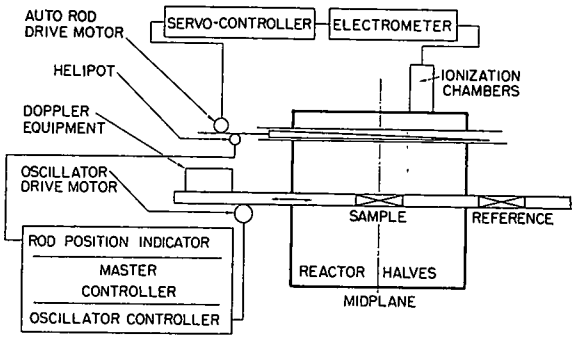

FIG. II-24-1. Double-Ended Doppler-Oscillator Drawer. *ANL Neg. No. 116-416.*

Doppler Equipment

DOUBLE-ENDED DESIGN: ASSEMBLY 6

The Assembly 6 experiments utilized the Doppler equipment pictorially represented in Fig. II-24-1. The Doppler-oscillator drawer, running through both reactor halves, was substituted for the normal central matrix drawers of the reactor. This drawer was attached to a train arrangement which periodically oscillated the Doppler and reference samples to a position at the reactor midplane. The drawer construction was such that when either sample was at the midplane, the other sample was entirely outside the critical reactor. The remainder of the drawer in line with the sample positions was loaded to be as nearly identical to the normal core drawer loading as was consistent with the requirement of maintaining a maximum of a few in-hours reactivity swing as the Doppler and reference samples were oscillated. The oscillator platform also held the associated equipment for heating the sample and monitoring its temperature, and the vacuum system used to inhibit heat losses from the heated sample. In addition, a forced-air system was used to cool the Doppler capsule and to prevent heat transfer from the capsule to the reactor. Temperature-controlled air was passed completely through the drawer, passing over the Doppler and reference samples, and discharging from the end of the oscillator drawer.

SINGLE-ENDED DESIGN: ASSEMBLY 6A

The Assembly 6A experiments utilized the Doppler equipment pictorially represented in Fig. II-24-2.

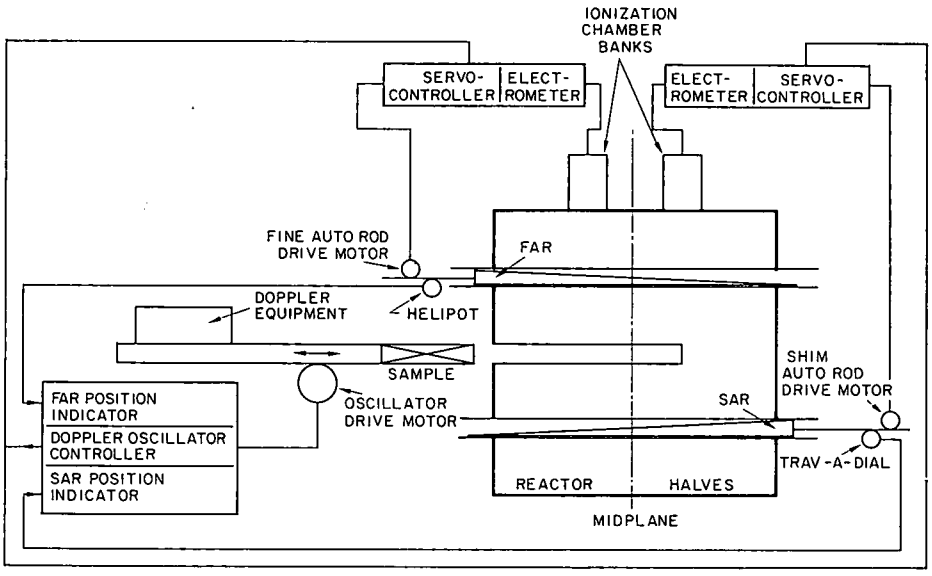

FIG. II-24-2. Single-Ended Doppler Oscillator Drawer. *ANL Neg. No. 116-922.*

TABLE II-24-I. NATURAL UO_2 DOPPLER-EFFECT MEASUREMENTS IN ZPR-6 ASSEMBLIES 6 AND 6A

ZPR-6 Assembly	Reactivity Change,[a] Ih/kg-U/Sample Temperature,[b] °K		
6 with sodium	−0.132/505	−0.266/811	−0.353/1081
6A with sodium	−0.137/514		
6A without sodium	−0.075/488	−0.131/722	−0.196/1050

[a] $\sigma \approx 0.002$ Ih/kg-U.
[b] Data normalized to 0.000 Ih/kg-U at 293°K.

The Doppler-oscillator drawer completely penetrated one reactor-half and extended approximately one-half of the sample length into the other reactor-half. The Doppler sample was placed at the front of the drawer while the remainder of the drawer was empty except for electrical and air-cooling connections to the sample. When the drawer was fully inserted, the Doppler sample was at the reactor center; when fully withdrawn, the drawer position in the reactor was left voided. A shim autorod (SAR), as shown in Fig. II-24-2, was used to balance the reactivity swings between the sample-in and sample-out positions. The SAR had two operating modes: autorod and fixed-shim. As the oscillator was traversed, the SAR was switched to autorod mode and maintained the reactor critical. When the oscillator drawer arrived at the fully-inserted or fully-withdrawn positions, the SAR was switched to the fixed shim mode and sought pre-determined shim positions that maintained a nominally zero sample-reference reactivity difference as measured with the FAR with the sample at room temperature. These shim positions were maintained constant throughout the Doppler measurement procedure. The sample vacuum, heating, and temperature monitoring systems were self-contained on the oscillator drive mechanism. The FAR was used to measure the reactivity changes as in the double-ended design. A counter-flow, forced-air system was utilized to cool the Doppler capsule and to prevent heat transfer to the reactor. The temperature-controlled air was passed through the drawer, over the Doppler sample, and then discharged back through the drawer using a concentric piping system.

EXPERIMENTAL DETAILS

The Doppler sample used in these experiments was natural UO_2 (N1) nominally 1 in. in diam by 12 in. long, and weighing 1.26629 kg. The weight of uranium was 1.11687 kg of which 99.28 w/o was ^{238}U.

The Doppler measurement performed in Assembly 6 was done with a ¼ in. stainless steel filter inserted between the sample and the surrounding reactor core. This filter, combined with the effective ¼ in. built-in stainless steel filter associated with the double-ended Doppler-oscillator drawer, provided an equivalent ½ in. stainless steel filter region around the Doppler sample. The purpose of such a filter region, as described in Ref. 6, was to reduce the hot-cold resonance interaction effect. The measurements performed in Assembly 6A however did not use the additional ¼ in. filter because this measurement was for reference to pin-type configurations and it would not be practical in genera to insert such a filter in pin-type configurations. The single-ended design also had an effective ¼ in. built-in stainless steel filter.

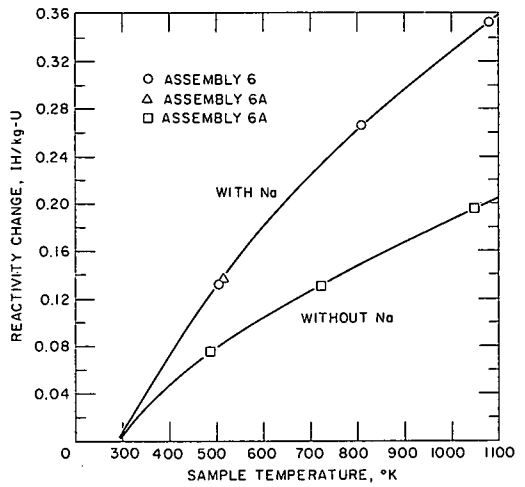

FIG. II-24-3. Natural UO_2 Doppler-Effect Measurements in ZPR-6 Assemblies 6 and 6A. *ANL Neg. No. 116-921.*

EXPERIMENTAL RESULTS

A tabulation of the uranium Doppler-effect data is given in Table II-24-I. The Assembly 6 results[7] for the ^{238}U Doppler-effect are also given for purposes of comparison with the Assembly 6A results. The data are also plotted in Fig. II-24-3. The expansion reactivity effect for natural UO_2 has been shown not to be significant, so no corrections to the experimental data are necessary.

CONCLUSIONS

The hardening of the reactor spectrum associated with sodium voiding in Assembly 6A substantially reduces the uranium Doppler effect in comparison with corresponding measurements made in Assembly 6 with no sodium voiding. Over the range 600 to 1100°K there is an approximately constant 43 % reduction, and below 600°K there is a proportionally smaller reduction.

The data taken in Assembly 6A, with sodium, is in good agreement with corresponding Assembly 6 data taken approximately two years before. This agreement indicates the reproducibility of Doppler-effect measurements using quite different experimental apparatus and also after having disassembled and then having reassembled the same reactor core.

REFERENCES

1. R. A. Karam, W. R. Robinson, G. S. Stanford and G. K. Rusch, *ZPR-6 Assembly 6A, A 4000-Liter UO_2 Fast Core*, Applied Physics Division Annual Report, July 1, 1969 to June 30, 1970, ANL-7710. pp. 175–183.
2. R. A. Karam, L. R. Dates, W. Y. Kato, J. E. Marshall, T. Nakamura and G. K. Rusch, *A 4000-Liter Uranium Oxide Fast Core, Assembly 6 of ZPR-6*, Reactor Physics Division Annual Report, July 1, 1967 to June 30, 1968, ANL-7410, pp. 75–80.
3. R. A. Lewis, K. D. Dance, J. F. Meyer and E. F. Groh, *The Variable Temperature Rodded Zone (VTRZ) Project*, Applied Physics Division Annual Report, July 1, 1969 to June 30, 1970, ANL-7710, pp. 189–196.
4. T. J. Yule, E. F. Bennett and I. K. Olson, *Measured Neutron Spectra in ZPR-6 Assembly 6A, ZPR-9 Assembly 25, and ZPR-9 Assembly 26, FTR-3*, Applied Physics Division Annual Report, July 1, 1969 to June 30, 1970, ANL-7710, pp. 183–189.
5. J. W. Daughtry, E. F. Groh and C. E. Till, *Doppler Effect Measurements to 2000°K in ZPR-9*, Reactor Physics Division Annual Report, July 1, 1967 to June 30, 1968, ANL-7410, pp. 103–108.
6. R. A. Lewis and T. W. Johnson, *Sensitivity of Small-Sample Doppler-Effect Measurements to Environment*, Reactor Physics Division Annual Report, July 1, 1967 to June 30, 1968, ANL-7410, pp. 96–103.
7. J. W. Daughtry and R. A. Lewis, *Uranium Doppler Measurements in ZPR-6 and -9 Oxide Cores*, Reactor Physics Division Annual Report, July 1, 1968 to June 30, 1969, ANL-7610, pp. 193–197.

II-25. Initial Plate-Rod Heterogeneity Measurements—LMFBR Demonstration Reactor Critical Experimental Program

R. A. LEWIS, L. G. LESAGE, C. E. TILL, J. E. MARSHALL, E. M. BOHN, M. SALVATORES* and G. S. STANFORD

A. INTRODUCTION

This report describes a set of measurements carried out in ZPR-6 Assembly 7 (see Paper II-11) to evaluate the effect on measured core physics parameters of the onfigurational heterogeneity differences between the ıormal plate-form ZPR fast critical assemblies and rodded assemblies typical of a UO_2-PuO_2 fueled LMFBR. These measurements were the first of a series of plate-rod heterogeneity measurements planned for the ANL LMFBR Demonstration Reactor Critical Experiments Program[1] currently underway on ZPR-6 Assembly 7 and ZPPR Assemblies 2 and 3. In these initial measurements, selected physics parameters were measured at the center of a special 10.9 x 10.9 x 24 in. rodded zone built into the center of Assembly 7 and

* Comitato Nazionale per L'Energia Nucleare, Casaccia, Italy.

compared with central measurements in the regular uniform plate structure of Assembly 7. Four types of plate-rod comparison measurements were made in Assembly 7:

1. Central in-cell sodium-voiding reactivity worth measurements,
2. Central reactivity worths of small samples of various materials,
3. Intra-cell $^{238}U/^{239}Pu$ capture-to-fission ratios and $^{238}U/^{239}Pu$ and $^{235}U/^{239}Pu$ fission ratios,
4. Direct measurement of the reactivity differences between compositionally matched 10.9 in. sq. x 24 in. central plate and rodded zones.

B. Special Zones

The plate-rod comparison measurements reported here were made at the center of three special zones built into the center of Assembly 7:

1. *Reference Rodded Zone (10.9 x 10.9 x 24 in.)*
   This zone consisted of 50 calandria cans (2 x 2 x 12 in. each) loaded into the 25 central matrix tubes of each half of the reactor; that is, the zone encompassed a region 5 matrix tubes square extending 12 in. deep on each side of the midplane.
2. *Small Rodded Zone (6.5 x 6.5 x 24 in.)*
   This zone consisted of 18 calandria cans loaded into the central 9 matrix tubes of each reactor half. The small rodded zone was used to test the spectral equilibration in the reference rodded zone by comparing central material reactivity worths in the two zone sizes as described in Section C.
3. *Matched Plate Zone (10.9 x 10.9 x 24 in.)*
   This zone was identical to the regular Assembly 7 drawer pattern except that the plate materials within the volume of the reference rodded zone were carefully chosen to closely match the composition of the reference rodded zone.

Figure II-25-1 shows the dimensions of a calandria can typical of those used in these experiments. The cans (Type F) were constructed of 304 L stainless steel and were nominally full of sodium. The sodium loading of the cans was chosen to match Assembly 7.

Each calandria can was loaded with 32, nominally 15 w/o Pu, UO_2-PuO_2 fuel rods. Figure II-25-2 shows the dimensions of a typical fuel rod. These were also designed to match the Assembly 7 composition.

Figure II-25-3 shows the calandria cans and rods compared with a plate fuel drawer.

C. Spectral Equilibration Check for the Rodded Zone

Although the rodded zone was very closely matched in homogenized composition to the Assembly 7 plate core, the differences between the rodded and plate

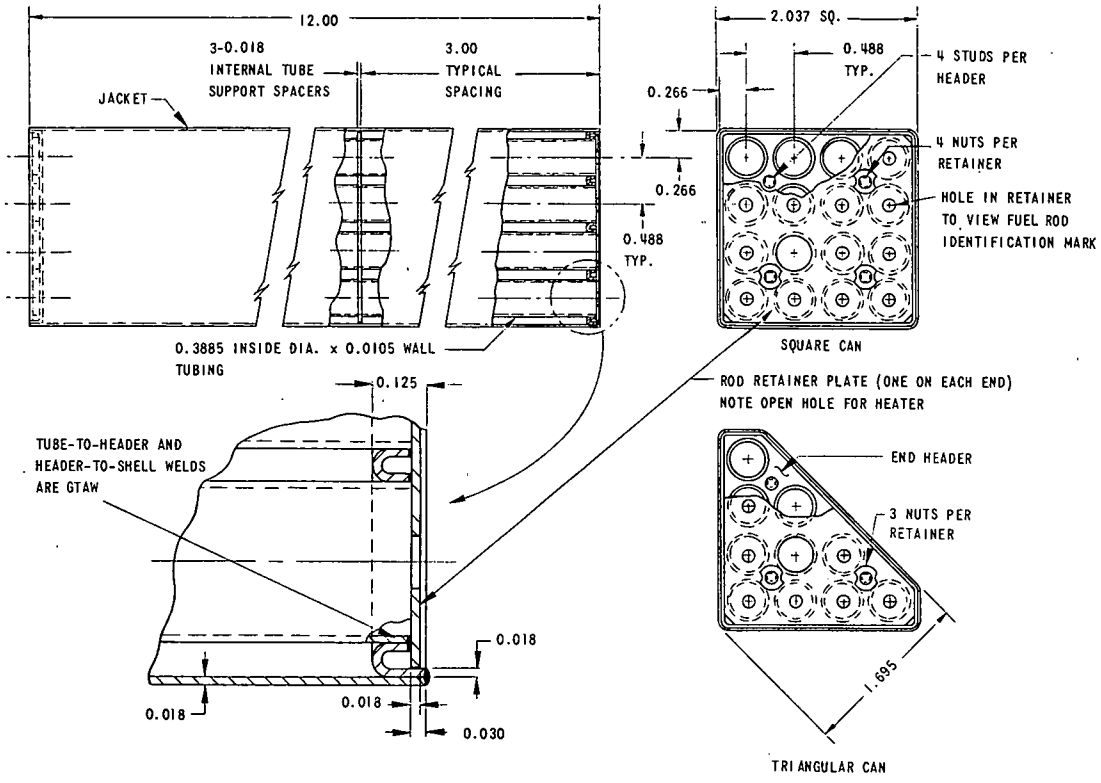

Fig. II-25-1. Square Calandria Cans (All Dimensions in Inches). *ANL Neg. No. 116-430.*

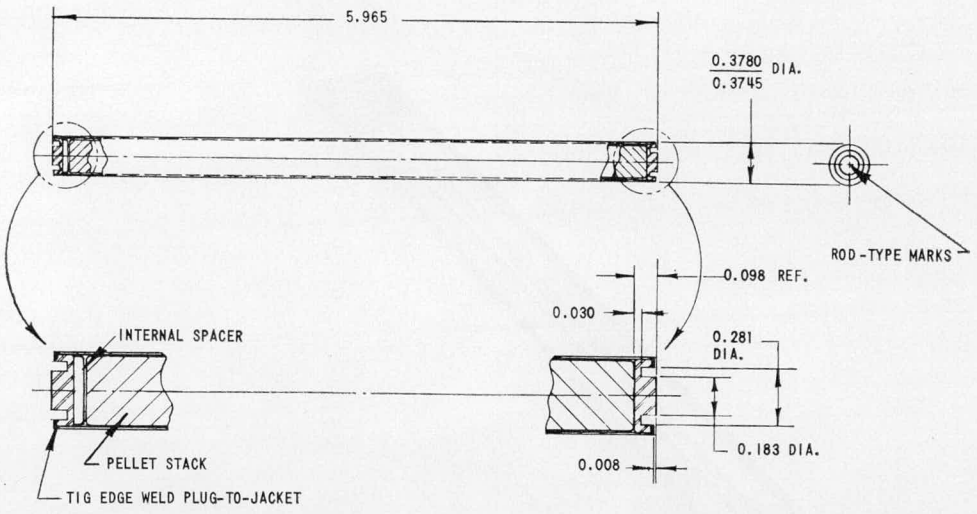

NOTES:

1. THE FINISHED RODS MUST BE STRAIGHT WITHIN 2 mils OVER THEIR LENGTH.
2. THE FINISHED RODS MUST PASS THROUGH A 0.3810-in. DIA x 6.5 in. LONG CYLINDRICAL GAGE BY GRAVITY FORCE ONLY.

FIG. II-25-2. Fuel Rod (All Dimensions in Inches). *ANL Neg. No. 116-431.*

configurations give rise to effective cross section differences; the rodded configuration has much less nuclear heterogeneity and thus less fast fission and more low-energy absorption than in the plate case. As a result, there is a question as to whether the 10.9 x 10.9 x 24 in. reference rodded zone was large enough to make the neutron and adjoint spectra at the core center asymptotic to those in a large similarly-rodded core. In an attempt to answer this question empirically, central reactivity worths of selected materials were compared between the reference rodded zone and the smaller 6.5 x 6.5 x 24 in. rodded zone; the same material samples were used in the two cases. The materials chosen for the comparison were selected for their relative sensitivity to real and adjoint flux spectrum changes.

Table II-25-I summarizes the material worth comparison. All measurements were made with nominally ⅞ in. diam x 2 in. long samples in the ZPR-6 radial sample changer. The sample changer was positioned so that the sample spans the central drawer. A detailed description of the actual samples used is given in Section E of this report. Reactivity measurements utilized the ZPR-6 autorod.

Table II-25-I also shows the corresponding calculated central worths and calculated (normalized) perturbation denominators. These calculations were based on ENDF/B-1 cross sections processed through MC² and spatially-weighted using the CALHET escape probability routine. The ARC 1D diffusion theory perturbation (STP006) package was used to generate the numbers.

If the spectra were asymptotic in all cases and if the calculated cross sections were reasonably correct, the measured and calculated ratios in Table II-25-I should in all cases be exactly equal to the inverse perturbation denominator ratios given in Table II-25-I. With the exception of the apparently anomalous depleted uranium measurement in the small rodded zone, there is no measurable difference between the reference rodded zone results and the results for the small rodded zone; this is consistent with the calculated values. Experimentally, the relatively constant value for the ratio of the worths in the 5 x 5 zone to those in the 3 x 3 zone implies that the spectra in these zones are nearly the same. This is evidence that the spectra in either of the zones is close to its asymptotic value for the rodded composition. The good agreement between the measured weighted-average reactivity worth ratios among the three cases (5 x 5, 3 x 3, and plate) and the calculated perturbation denominator ratios for these cases is evidence that the calculations are correctly predicting the rodded zones. The calculations also predict a nearly asymptotic spectrum at the center of the rodded zones.

D. Central In-Cell Sodium-Voiding Measurements

Two types of in-cell sodium removal reactivity measurements—central-oscillator measurements and gross zone-voiding measurements—were carried out in the reference rodded zone and in the regular Assembly 7 plate cell. These measurements were specifically aimed at the in-cell sodium worth in contrast to the approximately cell-average-spectrum sodium worth obtained

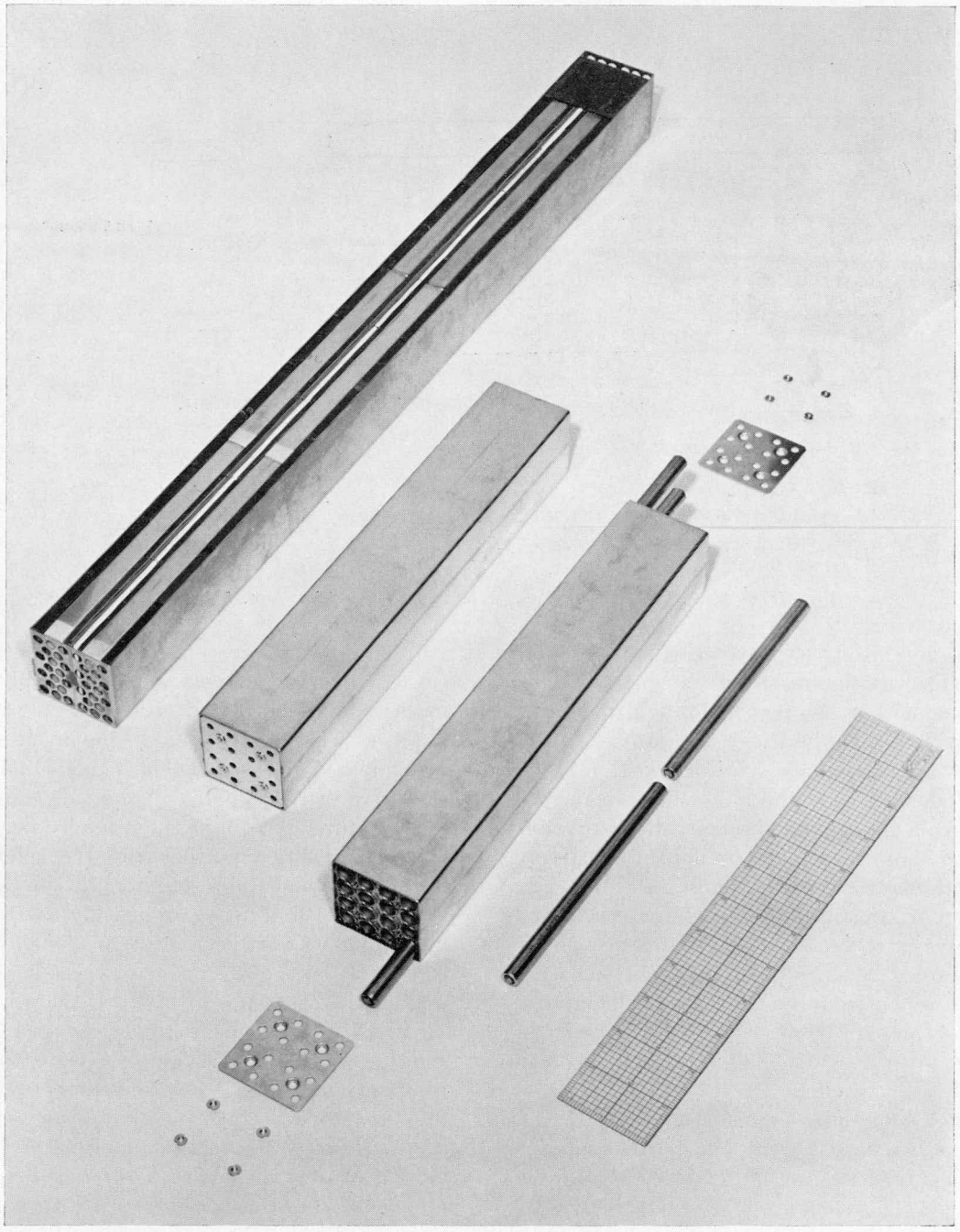

FIG. II-25-3. Typical Plate-Type Fuel Drawer, Calandria Cans and Oxide Fuel Rods. *ANL Neg. No. 116-3.*

from the central small-sample sodium worth measurements discussed in Sections C and E of this report.

The central-oscillator in-cell sodium-removal measurement in the reference rodded zone was carried out using three 2 x 2 x 12 in. calandria cans—one nominally full of sodium (Type F), one half-empty of sodium axially (that is, 6 in. voided and 6 in. sodium—Type SF), and the other completely empty of sodium (Type V). Each can was mounted in a special secondary container that could be mounted in the sample position of the axial oscillator drawer. The oscillator drawer was installed so that it could be extended through both reactor halves in the central matrix tube. The measurement was carried out in steps as follows:

a. A set of 32 UO_2-PuO_2 fuel rods was selected.
b. The specially-mounted sodium-filled calandria can, loaded with the selected set of 32 rods, was mounted in the axial oscillator.
c. The reactor was taken critical and, using the ZPR-6 autorod, the reactivity difference was

TABLE II-25-I. Rodded Zone Size Effects

Material	Measured Central Worths					Calculated Central Worths				
	Ih/kg[a]			Ratios		Ih/kg[a]			Ratios	
	Plate[b]	3 x 3[c]	5 x 5[d]	$\frac{5 \times 5}{\text{Plate}}$	$\frac{5 \times 5}{3 \times 3}$	Plate	3 x 3	5 x 5	$\frac{5 \times 5}{\text{Plate}}$	$\frac{5 \times 5}{3 \times 3}$
Sodium	4.7 ± 0.5	5.9 ± 0.3	5.4 ± 0.3	1.2 ± 0.1	0.92 ± 0.07	5.01	4.99	4.95	0.988	0.992
Carbon	12.2 ± 0.2	13.2 ± 0.3	12.5 ± 0.3	1.02 ± 0.2	0.95 ± 0.02	13.16	13.12	13.22	1.005	1.008
304 SS	5.0 ± 0.1	4.5 ± 0.1	4.6 ± 0.1	0.90 ± 0.03	1.02 ± 0.03	5.62	5.48	5.39	0.959	0.984
Depleted Uranium[e]	9.5 ± 0.3	10.3 ± 0.3	9.0 ± 0.2	0.95 ± 0.04	0.87 ± 0.04	13.89	13.17	12.93	0.931	0.982
Plutonium[f]	−157.9 ± 0.9	−154.8 ± 0.6	−153.8 ± 0.6	0.975 ± 0.007	0.992 ± 0.007	−193.6	−190.6	−188.2	0.972	0.987
Perturbation Denominator[g]						1.562×10^3	1.590×10^3	1.612×10^3	0.968[h]	0.986[h]

[a] Worth of removing material.
[b] Regular Assembly 7.
[c] Small rodded zone (6.5 in. square x 24 in.)
[d] Reference rodded zone (10.9 in. square x 24 in.).
[e] Sample is by weight: ^{235}U 0.22, ^{238}U 99.78.
[f] Sample is by weight: ^{239}Pu 97.75, ^{240}Pu 1.00, ^{241}Pu 0.05, Al 1.20.
[g] Normalized to $\sum_i \chi_i \phi_i^* = 1$ and $\sum_i \nu_i \phi_i \Sigma_{f_i} = 1$ at center.
[h] Inverse ratio.

measured between (1) the reactor with the calandria can centered axially in the core and (2) the reactivity of the reactor with a reference portion of the oscillator at the core center (calandria can out of core). An oscillation technique, of the type used for the ZPR Doppler measurements, was used.

d. The reactor was shut down, the sodium-filled calandria can was removed, the selected set of fuel rods was transferred to the empty calandria can, and the empty can was mounted in the axial oscillator.
e. Step c was repeated for the sodium-voided calandria can. The voided can was centered axially in the core for the measurement.
f. The final result consists of the difference of the reactivity differences (sample-to-void) measured in steps c and e.
g. Steps b through f were repeated using the half-voided calandria can. In this case, however, the 6 in. voided section was centered axially in the core and the reference sodium-filled case was taken with this same axial sample positioning.

The gross-voiding in-cell sodium-removal measurement in the reference rodded zone was carried out by comparing the reactivity of the reactor with the reference rodded zone to the reactivity of the reactor with the central 18 calandria cans (that is, 3 tubes x 3 tubes, 12 in. into each half) replaced by calandria cans half-empty of sodium (that is, 6 in. with no sodium and 6 in. with sodium, Type SF) in the axial direction. The voided ends of the replacement calandria cans were placed next to the reactor midplane. The fuel rods were the same in the sodium-in and sodium-out cases. The measurement was carried out in steps as follows:

a. The reference rodded zone was loaded into Assembly 7.
b. The reactor was taken critical, the boron rods fully removed, the fueled rods fully inserted except for one rod, and criticality maintained with the autorod.
c. Using the fueled rod and autorod calibrations, the total excess reactivity of the core, with all control elements in their most reactive state, was calculated.
d. The reactor was shutdown and the central 18 calandria cans were replaced with 18 calandria cans half-voided of sodium axially. The voided ends of the replacement cans were placed toward the center of the reactor. The UO_2-PuO_2 fuel rods from the sodium-filled cans were placed in the half-voided cans in the identical positions they had in the sodium filled cans.
e. Steps b and c were repeated.
f. The final result consists of the difference in the total excess reactivity calculations in steps c and e corrected for ^{241}Pu decay and for small differences in core average temperature between the sodium-in and sodium-out case.

Small corrections, of the order of the reactivity measurement uncertainties, were also made to both types of voiding measurements for the reactivity worth of the stainless steel mass differences between the sodium-filled and empty calandria cans used in the measurements.

Table II-25-II summarizes the results of the two types of in-rod-cell sodium-voiding measurements. For reference, Table II-25-II also contains the in-plate-cell sodium-voiding measurements[2] (see Paper II-11) using the same two techniques as were used in the rodded zone, and the best currently available calculations of the rod and plate cell voiding reactivities. The central oscillator measurement in the regular plate environment of Assembly 7 was carried out as described above for the rodded zone, except that the measurement was performed on a 2 x 2 x 2 in. box, containing core plates

TABLE II-25-II. Central In-Cell Sodium-Voiding Measurements

Experiment Type	Reference Rodded Zone		Plate Core		Measured Ratio Rod/Plate (A/B)	Calculated Ratio Rod/Plate
	Void Size and Position	(A) Worth of Removing Na, Ih/kg (1σ)	Void Size and Position	(B) Worth of Removing Na, Ih/kg (1σ)		
Oscillator measurement: one unit-cell voided	2.2 x 2.2 x 12 ± 6 in. from midplane	6.72 ± 0.07	2.2 x 2.2 x 2 ± 1 in. from midplane	6.7 ± 0.2	1.00 ± 0.03	0.976
	2.2 x 2.2 x 6 in.	6.8 ± 0.2	—	—	—	—
Gross voiding measurement: nine unit-cells voided	6.5 x 6.5 x 12 ± 6 in. from midplane	6.4 ± 0.6	6.5 x 6.5 x 12 ± 6 in. from midplane	6.9 ± 0.3	0.93 ± 0.06	—

mounted in the axial oscillator; full and empty sodium cans were replaced in the box. The gross (3 tube x 3 tube x 6 in. into each half) sodium voiding measurement was performed as for the rodded case with empty sodium cans replacing full sodium cans in the front 6 in. of the central nine drawers of each reactor half. The calculations are based on ARC 1D diffusion perturbation calculations employing ENDF/B-1 MC²-generated cross sections, space-weighted using the CALHET escape probability technique.

The results in Table II-25-II show no measurable difference in the in-cell sodium voiding reactivity worth in the plate and rod cells to the 3–5 % precision of these measurements. This is in agreement with the 2½ % plate-rod difference predicted by calculation. Although there are undoubtedly cancelling effects, the net plate-rod heterogeneity effect on the in-cell sodium worth for this plate arrangement is small, surely less than 5 %, and very close to the calculation.

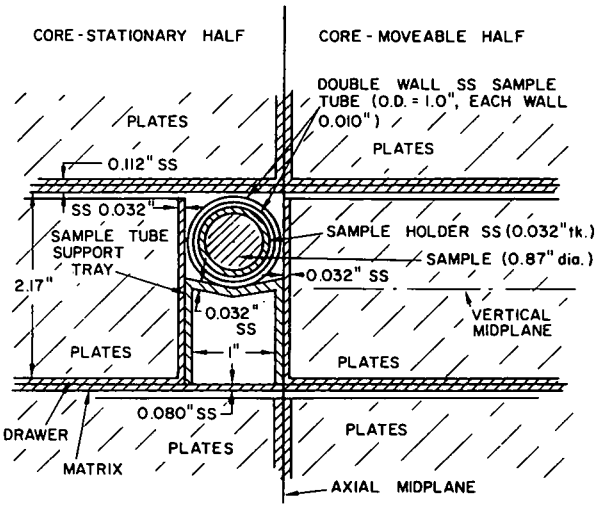

FIG. II-25-4. Vertical Section of ZPR-6 Assembly 7, Showing Arrangement of the Sample and Radial Sample-Changer Tube in the Assembly. *ANL Neg. No. 116-1033.*

E. CENTRAL SMALL-SAMPLE REACTIVITY WORTHS

Small-sample reactivity worths of various materials (scatterers, absorbers, fissioners, etc.) and reaction rate measurements (*c/f* ratios, *f/f* ratios, etc.) are routinely used in ZPR physics studies to provide spectral (real and adjoint) indices. Small-sample reactivity worths measured in the reference rodded zone are discussed in this section together with a comparison with calculations and measured worths of the same samples in the regular Assembly 7 plate core. Reaction rate measurements in the rodded zone are discussed in the next section.

The small-sample central reactivity worth measurements in the reference rodded zone were carried out using the ZPR-6 radial sample changer. The individual samples are 2 in. long and ½ or ⅞ in. in diam. In general, the mass of material in a particular sample is chosen as a compromise between minimizing the mass, so as to minimize the perturbation of the reactor spectra caused by the sample, and providing sufficient mass to give enough of a reactivity signal to permit ~5 % measurement precision in a few minutes of operating time; that is, the samples are "small" but, in general, not infinitely-dilute. The radial sample changer operates by pneumatically oscillating the samples in and out of the core inside of a 1 in. diam tube that is inserted radially by pushing the calandria cans (or drawers) in the middle horizontal row of the core stationary half back 1 in. as shown in Fig. II-25-4. For central measurements, the end of the sample changer tube is positioned so as to place the 2 in. length of the inserted sample across the 2 in. width of the central tube.

Table II-25-III summarizes the central small-sample reactivity measurements made in the reference rodded zone. Measurements made in the center of the regular Assembly 7 plate zone[3] are shown for reference. The calculated values in Table II-25-III are ARC 1D diffusion perturbation calculations using cross sections generated from ENDF/B-1 and MC², and spatially-weighted for the rod and plate cells using the CALHET escape probability technique. That is, core average cross sections were used for the sample cross sections and no attempt was made to derive accurate effective cross sections for the individual samples. Thus, the calculated ratios may be expected to be more accurate than the absolute calculated values.

The measured results for sodium in Table II-25-III are questionable and are currently under study. The data from which the rodded zone value of 5.4 ± 0.3 Ih/kg and the plate core value of 4.7 ± 0.5 Ih/kg were derived have been carefully examined and there is nothing obviously wrong with the data; the quoted 1σ statistical uncertainties are based on directly observed fluctuations in the oscillation-autorod data taken for each sample. However, a subsequent remeasurement of the sodium sample in the plate core gave a result of 6.2 ± 0.3 Ih/kg. Although no specific problem can be identified with the measurements, the discrepancy between the two plate core measurements cannot be explained analytically at this point, so the sodium measurement must be considered suspect. Several other central material reactivity worths were remeasured in the plate core and these all showed very close agreement with the original measurements.

The results of Table II-25-III support the intuitive feeling that a measurement like the small-sample reactivity worth measurement, which essentially sees the cell-average (the 2 in. sample spans the plate or rod

TABLE II-25-III. COMPARISON OF CENTRAL SMALL-SAMPLE MATERIAL REACTIVITY WORTH MEASUREMENTS IN THE REFERENCE RODDED ZONE AND THE REGULAR ASSEMBLY 7 PLATE CORE

Sample	Sample Weight, g	Measured Worth of Removing Sample (1σ)			Calculated Worth Removing Sample		
		(A) Reference Rodded Zone, Ih/kg	(B) Regular Plate Core, Ih/kg	(A/B) Rod/Plate Ratio	(C) Reference Rodded Zone, Ih/kg	(D) Regular Plate Core, Ih/kg	(C/D) Rod/Plate Ratio
Pu[a]	9.956	−153.8 ± 0.6	−157.9 ± 0.9	0.975 ± 0.007	−188.2	−193.6	0.972
Enriched U[b]	3.084	−120 ± 2	−124 ± 4	0.97 ± 0.02	−162.4	−168.4	0.964
Depleted U[c]	25.988	9.0 ± 0.2	9.5 ± 0.3	0.95 ± 0.04	12.9	13.9	0.931
Ta	8.698	55 ± 1	58 ± 2	0.95 ± 0.04	71.5	79.7	0.897
Boron[d]	0.555	590 ± 10	570 ± 10	1.04 ± 0.03	721.	774.	0.932
Na	17.044	5.4 ± 0.3[e]	4.7 ± 0.5[e]	1.2 ± 0.1[e]	4.95	5.01	0.988
C	33.441	12.5 ± 0.3	12.2 ± 0.2	1.02 ± 0.02	13.2	13.2	1.00
Fe	33.277	4.0 ± 0.3	4.3 ± 0.2	0.9 ± 0.1	5.01	5.25	0.954
Ni	37.916	6.1 ± 0.2	6.5 ± 0.2	0.94 ± 0.04	5.40	5.39	1.00
Cr	26.999	4.0 ± 0.4	4.5 ± 0.4	0.9 ± 0.01	6.98	7.33	0.952
304 SS	34.506	4.6 ± 0.1	5.0 ± 0.1	0.90 ± 0.03	5.39	5.62	0.959
			Weighted Average = 0.98 ± 0.02			Average = 0.959[f]	

[a] Composition of sample by w/o: ^{239}Pu 97.75, ^{240}Pu 1.00, ^{241}Pu 0.05, Al 1.20.
[b] Composition of sample by w/o: ^{235}U 93.24, ^{238}U 5.41, ^{234}U 0.91, ^{236}U 0.44.
[c] Composition of sample by w/o: ^{235}U 0.22, ^{238}U 99.78.
[d] Composition of sample by w/o: ^{10}B 19.88, ^{11}B 80.12.
[e] These data are in question (see text).
[f] Calculated inverse perturbation denominator measurement gives 0.968.

cell) real and adjoint spectra, will be much less sensitive to the localized effects of plate-rod in-cell heterogeneity differences than an in-cell measurement like those of Sections D and G of this report. If the calculated perturbation denominator differences are accounted for, the results of Table II-25-III indicate that within 2–4% precision there are no measurable differences, at least for this rather typical plate cell, between central small-sample reactivity worth measurements in the plate or rodded environments.

F. INTRA-CELL ^{238}U/^{239}Pu AND ^{238}U/^{235}U CAPTURE-TO-FISSION RATIOS AND ^{238}U/^{239}Pu, ^{235}U/^{239}Pu, AND ^{238}U/^{235}U FISSION RATIOS

Intra-cell absolute capture and fission reaction rate measurements in the center of the reference rodded zone were made using small ^{239}Pu, ^{235}U, and ^{238}U foils in order to look for spatial effects within the rodded cell and to provide a basis for deriving measured cell-average reaction rate ratios for comparison with corresponding plate-core cell-average measurements.

A single foil-irradiation run was carried out in the reference rodded zone. Two of the 50 calandria cans in the reference rodded zone contained foils. Figure II-25-5 shows the foil locations.

The overall objective was to measure the average reaction rates within the UO_2-PuO_2 fuel rods. Thus, the most obvious and desirable thing is to place unclad uranium and plutonium foils between pellets within the UO_2-PuO_2 fuel rods. Although special equipment to permit close approximations to such direct measurements in the rodded configuration is currently being fabricated, the equipment was not available at the time of these measurements. It was not possible to work inside a UO_2-PuO_2 rod and it was necessary to use available aluminum-clad plutonium foils. As the best available approximation to the desired in-rod measurements, ^{238}U-^{239}Pu-^{238}U and ^{238}U-^{235}U-^{238}U foil packets ("P" and "U" foil packets in Fig. II-25-5) were placed between the ends of the 6 in. UO_2-PuO_2 fuel rods in selected tubes of the central calandria can as shown in Fig. II-25-5. Thus the foils were separated from the adjacent UO_2-PuO_2 pellets by the 100 mil thick stainless steel fuel rod end caps.

In order to provide a basis for an empirical correction to the measured reaction rates between rods ("P" and "U" locations) to give the desired reaction rates within the rods, a special subsidiary set of measurements was performed using 16% enriched UO_2 fuel rods. The enriched UO_2 rods used were selected from an inventory of rods that were designed to match the reactivity worth of the UO_2-PuO_2 fuel rods. Using the UO_2 rods it is possible to place bare ^{238}U and ^{235}U foils inside the rods; the axial-ratio setup is shown in Fig. II-25-5 as Calandria B, "T" foil packet. The general technique

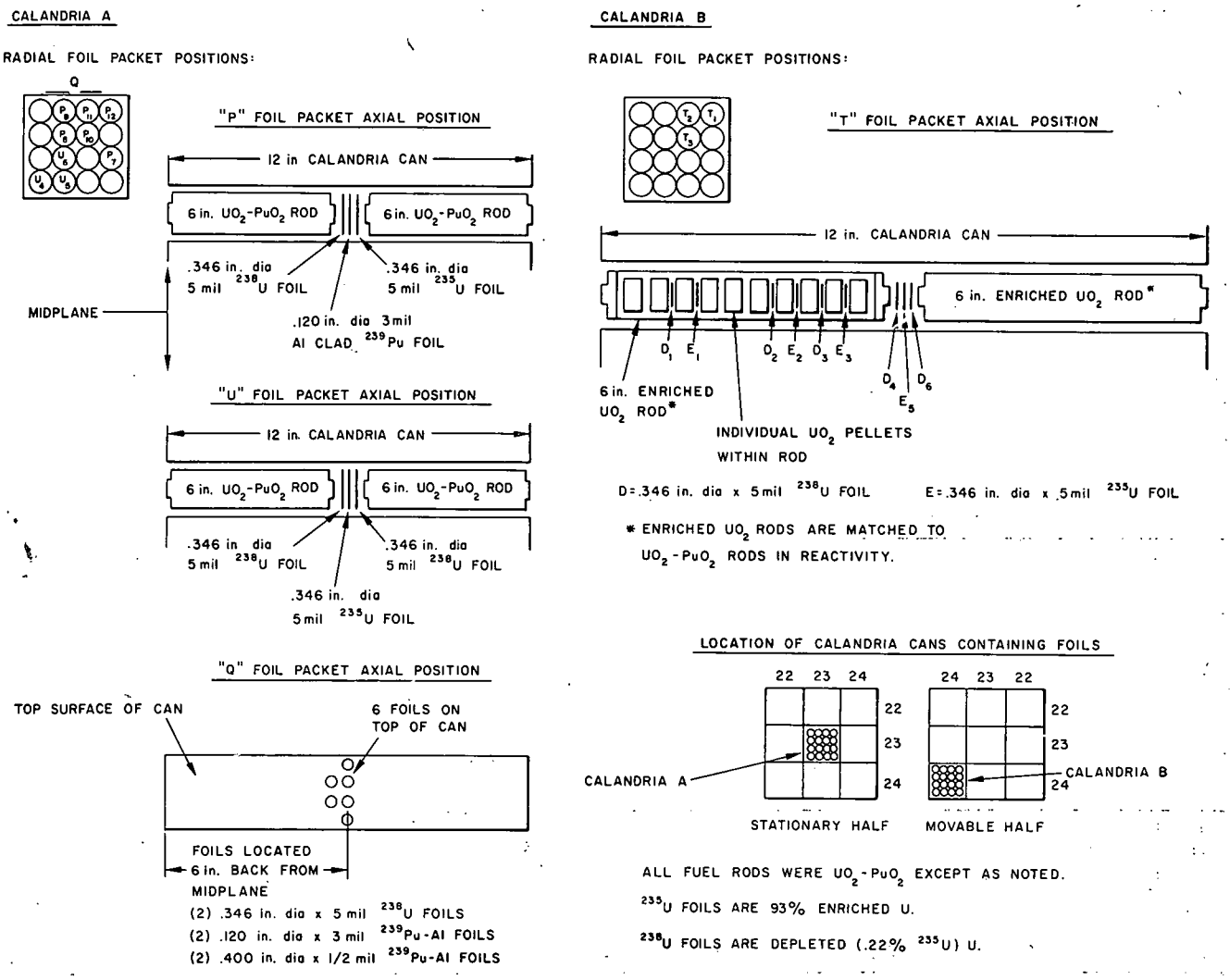

FIG. II-25-5. Foil Positions for Measurement in Rodded Zone. *ANL Neg. No. 116-1065.*

used to derive the ^{238}U and ^{235}U axial ratios was as follows:

1. All the counting results for the calandria foils were extrapolated to the center of the reactor by making axial cosine corrections and radial J_0 corrections.
2. It was observed that the extrapolated results for the "T," "U," and "P" foil packets were in good agreement with each other for captures in ^{238}U, and that the ^{238}U fission rates were the same for the "T" and "U" packets, but the ^{238}U fission rate was ~1.6 % lower in the "P" packet. This difference is ascribed to the fact that the 127 mg ^{235}U foils in the "T" and "U" packets had approximately ten times as much fissile material as the plutonium foils in the "P" packets, leading to increased high-energy flux. (A recent transport theory calculation gives qualitative support to this postulate—predicting, in fact, a greater effect than was observed.) Consequently, in analyzing the experimental results, the ^{238}U fission rates observed in the "T" and "U" packets were reduced by 1.6 %.
3. From the extrapolated T_1, T_2, and T_3 data, the ratio of in-rod to between-rod reaction rates was obtained for ^{235}U fission, ^{238}U fission, and ^{238}U capture, for each of the three rods. The three ratios for each material were then averaged to obtain one ratio for ^{235}U fission, one for ^{238}U fission, and one for ^{238}U capture for use in calculating the reaction rates occurring inside the pins from the between-the-pin foils in the UO_2-PuO_2 and UO_2 rods (Fig. II-25-5). The assumption was made that the ratio for ^{235}U fission was applicable to ^{239}Pu fission. The ratios are presented in Table II-25-IV.
4. Three in-rod to between-rod ratios for ^{238}U capture, three for ^{238}U fissions, and three for ^{235}U fission were obtained at the core center position based on the extrapolation of the T_1, T_2, and T_3 data.

The sets of three ratios were individually averaged to obtain one ^{238}U capture ratio, one ^{238}U fission ratio, and one ^{235}U fission ratio. The ^{238}U capture and fission ratios were then used to correct ^{238}U capture and fission data for the UO_2-PuO_2 rod case, and the ^{235}U fission ratio was used to correct ^{239}Pu fission data in the UO_2-PuO_2 rod case. The ratios are summarized in Table II-25-IV.

The details of the techniques used for counting the activated foils and reducing the data to absolute reaction rates have been discussed elsewhere[4] (also, see Paper II-16). For the absolute calibration of the fission foils, ^{235}U, ^{238}U, and ^{239}Pu fission chambers, with foils on their faces, were located near (but not in) the rodded zone and the fission rates in the chambers were determined during the foil irradiation run. In order to calibrate the $^{238}U/^{239}Pu$ c/f measurement and to further calibrate the $^{235}U/^{239}Pu$ measurement, an irradiation of a set of appropriate foils was made on a rotating wheel in the Argonne Thermal Source Reactor thermal column simultaneously with the foil irradiation in ZPR-6.

As a third calibration method, some of the ^{238}U and plutonium foils which were at the fission-chamber faces were radiochemically analyzed after they had been counted, yielding absolute values for ^{238}U fission, ^{238}U capture, and ^{239}Pu fission.

The data from the "P" and "U" foil packet (extrapolated to the core center and multiplied by the appropriate in-pin to between-pin ratio) were used to obtain the in-rod reaction rate ratios. The individual "P" and "U" foil packet results are shown in Table II-25-V. Table II-25-V shows evidence of a slightly softer neutron spectrum between calandria cans than within calandria cans. This is expected as a result of the relatively greater amount of sodium and stainless steel between nearest-neighbor fuel rods in adjacent calandria cans as compared with between nearest-neighbor fuel rods within calandria cans. This small amount of rodded cell non-uniformity is a consequence of calandria can fabrication compromises and the ZPR matrix structure.

In order to derive cell-averaged reaction rate ratios, the reaction rate data from the "P" and "U" packets, corrected as described above, were handled as follows:

1. The reaction rate data from packets P_7, P_9, P_{11}, and U_5 (Fig. II-25-5) were averaged to obtain

TABLE II-25-IV. In-Rod to Between-Rod Reaction Rate Ratios at the Core Center

Foil Packet (Fig. II-25-5)	$^{235}U_{fission}$[a]	$^{238}U_{fission}$[b]	$^{238}U_{capture}$
T_1	0.9818	1.0271	0.8066
T_2	0.9842	1.0312	0.9088
T_3	0.9832	1.0295	0.9050
Average	0.9831	1.0292	0.9068
Uncertainty (1σ) in average	±0.2%	±0.2%	±0.2%

[a] This is actually the overall fission rate ratio for 93% enriched uranium.

[b] This is actually the overall fission rate ratio for depleted uranium (0.22% ^{235}U).

TABLE II-25-V. Rodded-Zone Reaction-Rate Ratios for Typical Pin Locations[a]

Pin Position in Calandria Can	Pin[b]	f^{25}/f^{49}	f^{28}/f^{49}	c^{28}/f^{49}	f^{28}/f^{25}	c^{28}/f^{25}	c^{28}/f^{28}
Corner	T_1	—	—	—	0.02325	0.1366	5.882
	U_4	—	—	—	0.02332	0.1376	5.907
	P_{12}	—	0.02448	0.1445	—	—	5.903
	Average[c]	1.052	0.02449	0.1446	0.02331	0.1375	5.905
Middle-Outer	T_2	—	—	—	0.02368	0.1353	5.720
	U_5	—	—	—	0.02343	0.1356	5.793
	P_7	—	0.02455	0.1442	—	—	5.872
	P_9	—	0.02495	0.1440	—	—	5.769
	P_{12}	—	0.02468	0.1419	—	—	5.749
	Average[c]	1.055	0.02472	0.1433	0.02346	0.1358	5.795
Central	T_3	—	—	—	0.02360	0.1340	5.683
	U_6	—	—	—	0.02365	0.1352	5.723
	P_8	—	0.02475	0.1421	—	—	5.740
	P_{10}	—	0.02495	0.1414	—	—	5.667
	Average[c]	1.053	0.02485	0.1419	0.02364	0.1348	5.710

[a] All ratios are on a per-atom basis.

[b] For pin locations, see Fig. II-25-5.

[c] For each pin position, the values labeled "Average" are ratios of the average reaction rates for that position (not the average of the ratios).

values that can be considered typical of the rods in the middle group of outer calandria can tubes (8 such tubes in a can).

2. Reaction rate data from packets P_8, P_{10}, and U_6 were averaged to obtain values that can be considered typical of the inside group of calandria can tubes (4 such tubes in a can).
3. Reaction rate data from packets P_{12} and U_4 were averaged to obtain values that can be considered typical of tubes in the corners of the calandria cans (4 such tubes in a can).
4. The reaction rate data were cell-averaged by weighting the data by the number of fuel rods in the cell of each type. Finally, the cell-averaged reaction-rate ratios were obtained by taking the appropriate ratios of the reaction-rate data.

Table II-25-VI summarizes the cell-averaged ratios for the center of the rodded zone and compares these values with cell-averaged central ratios measured in the Assembly 7 plate zone (see Paper II-16). Table II-25-VI also contains calculated rod and plate central cell-average ratios. The calculations are based on ARC 1D diffusion calculations using cross sections generated from ENDF/B-1 via MC² with CALHET space-weighting within the cell.

Two general conclusions may be drawn from the measured reaction rate ratio data of Table II-25-VI:

1. Within statistics, there are no measurable differences in the cell-average ^{235}U and ^{239}Pu fission rates and cell-average ^{238}U capture rate between the plate cell and the rodded cell.
2. The cell-average ^{238}U fission rate in the rodded cell is significantly greater, about 6%, than the cell-average ^{238}U fission rate in the plate cell.

The first of these two experimental conclusions is predicted by the calculations summarized in Table II-25-VI; the second conclusion is not predicted by calculation. A comparison of the measured and calculated values in Table II-25-VI for the rodded cell shows that, compared with ^{235}U fission, ^{239}Pu fission is calculated about 9% low, and ^{238}U capture is calculated about right. These observations are in essentially exact agreement with the results of the null-zone measurements in ZPR-3 Assembly 55 and ZPR-9 Assembly 24[4] and are consistent with recent hypotheses concerning errors in ENDF/B ^{238}U inelastic cross sections.

TABLE II-25-VI. Comparison of Core-Center Cell-Average[a] Reaction Rate Ratios in the Reference Rodded Zone and the Assembly 7 Plate Core

Ratio	Measured Values (per atom basis)			Calculated		
	Reference Rodded Zone	Assembly 7 Plate Core ($1\sigma = \pm 2\%$)	Rodded / Plate	Rodded Zone	Plate Core	Rodded / Plate
f^{25}/f^{49}	1.054	1.065	0.990	1.146	1.1505	0.996
f^{28}/f^{49}	0.02470	0.02338	1.056	0.02342	0.02305	1.016
c^{28}/f^{49}	0.1433	0.1430	1.002	0.1642	0.1641	1.001
f^{28}/f^{25}	0.02347	0.02202	1.066	0.02044	0.02004	1.020
c^{28}/f^{25}	0.1360	0.1343	1.013	0.1433	0.1426	1.005

[a] Cell refers to region defined by a single 2.17 in. square matrix tube; in the rodded case this is a complete calandria can and in the plate case this is a complete fuel drawer.

G. Direct Plate-Rod Zone Reactivity Comparison

Introduction

In this experiment the reactivity difference between Assembly 7 with the central 10.9 x 10.9 x 24 in. rodded zone and with the compositionally-matched plate zone was measured. The objective was to measure the reactivity effect of the configurational differences between the plate and rodded cell-structures without the complicating effects of simultaneous compositional differences. Ideally, the two zones would be exactly matched in smeared composition so that the measurement would unambiguously measure only the configurational effect. As a practical matter, however, some compositional mismatches were permitted; the reasons for this were:

1. The nominal weights and compositions of the individual pieces used in the plate and rod zones are fixed so that, while it is possible to come very close to a compositional match by carefully selecting plates, rods, and calandria cans, it is not possible to exactly match smeared (average) cell compositions.
2. The precision in the knowledge of the composition of the plate and rod pieces is limited by the finite amount of analytical work (chemical and isotopic data) done in characterizing the pieces. It is useless to try to match compositions to better than the inherent compositional uncertainties.
3. Because the various materials present have vastly differing reactivity worths per unit mass, a small fraction of the total number of materials present effectively determine the possible precision of composition matching in the reactivity sense. It is useless to work out accurate compositional matching for any individual material beyond the point where the increased accuracy will reduce the overall reactivity uncertainty between the zones when all materials are considered.

Technique Used for Material Matching Between the Plate and Rodded Zones

Both the rodded zone and the matched plate zone were built into the center of Assembly 7 as described in

Section B of this memo. The only difference between the "matched plate zone" and the regular Assembly 7 plate arrangement and cell composition was that the plates in the "matched" zone were more carefully selected to match the material masses of the rodded zone than were the plates in the regular Assembly 7 drawers; the differences between the material weights in the "matched" plate zone and in the regular Assembly 7 drawers was small.

The rodded zone and the matched plate zone were 10.9 x 10.9 x 24 in.; that is, they were five regular ZPR matrix tubes wide by five tubes high and extended the length of one 12 in. calandria can into each reactor half. The rodded zone was formed from the matched plate zone by the following steps (the actual sequence used differed from the one given but was equivalent to it):

1. Start with the matched plate zone loaded into regular ZPR 33 in. stainless steel front drawers without positioning tabs (30 in. of core and 3 in. of depleted uranium axial blanket) and 12 in. stainless steel boat type back drawers. The boats are small drawers 12 x 2 x ½ in. high and 20 mil thick containing 10 in. of depleted uranium axial blanket.
2. Remove the front 12 in. of plate material from each of the 25 affected drawers. Move the remaining 18 in. of core plate and 3 in. of depleted uranium materials to the front of the drawer. Load the boat materials into the rear 12 in. of the front drawers. Then remove the boats.
3. Push each 33 in. front drawer back 12 in. into the matrix tube.
4. Insert loaded calandria cans into the front 12 in. of each matrix tube.
5. Insert the molybdenum strips (to match the molybdenum in the Pu-U-Mo fuel plates) between the calandria cans and the matrix tubes.

Note that because of the change in position of the front drawers and the removal of the axial blanket boats the amount of stainless steel as a function of axial position changes between the matched plate and rodded zone configurations not only in the 24 in. zone itself, but also in the 31 in. axial sections adjacent to the zone. These changes must be accounted for in the calculation of the plate-to-rod mass defect reactivity effect.

The actual matching of the compositions of the plate and rod zones, the calculation of mass defects, and the calculation of the reactivity effect of these defects was based on a scheme by which the affected volume of Assembly 7 was conceptually divided into 350 matching units; each unit was one matrix tube square and 6 in. long. Thus, there were 7 matching units per matrix tube per reactor half, 100 matching units in the actual plate-rod zone and 125 matching units in each of the two adjacent axial regions. Compositional matching was attempted within these units but not on any smaller volume. It was felt that these units were sufficiently small because the significant changes in material position, within the matrix tube, between the plate and rod zones occur almost entirely near the core center where the worth gradients are small.

The mass of each constituent material and its uncertainty was evaluated for each of the 350 matching units separately for the rodded and matched-plate zones. Within the 100 matching units comprising the actual plate-rod zone, all materials differed to some extent between the plate and rodded cases. Within the 250 axial matching units only the stainless steel mass changed between the plate and rodded cases. It was found that the distributions of plate-to-rod mass defects for all materials among the 100 central zone matching units were essentially uniform; similarly, the distribution of stainless steel mass defects were essentially uniform over the 250 axial units.

METHOD OF CALCULATING THE PLATE-TO-ROD ZONE MASS DEFECT REACTIVITY CORRECTION AND ITS PRECISION

Basic Method of Calculation

Let

$g_{m,j,Plt}$ ≡ the best available estimate of the mass of material m in composition matching unit j of the plate zone,

$g_{m,j,Rd}$ ≡ the best available estimate of the mass of material m in composition matching unit j of the rodded zone,

$\sigma_{g_{m,j,Plt}}$ ≡ the best available estimate of the standard deviation of $g_{m,j,Plt}$ (based on ½ the 67.5% confidence interval),

$\sigma_{g_{m,j,Rd}}$ ≡ the best available estimate of the standard deviation of $g_{m,j,Rd}$ (based on ½ the 67.5% confidence interval).

The composition matching units were described in Part 2 of this section. There was a total of 350 composition matching units, 100 in the actual plate-rod zone and 125 in each of the two adjacent axial zones; that is, j = 1 to 350. The materials involved in the composition matching were the following: sodium, molybdenum, iron, nickel, chromium, manganese, ^{235}U, $^{234+236+238}U$, oxygen, ^{238}Pu, ^{239}Pu, ^{240}Pu, ^{241}Pu, ^{242}Pu, and the total plutonium, uranium, and SS304 impurities.

The rodded zone is taken as the reference for the mass defect calculation and the mass defect for material m in composition matching unit j is defined by

$$\Delta g_{m,j} \equiv g_{m,j,Rd} - g_{m,j,Plt} \qquad (1$$

and

$$\sigma_{\Delta g_{m,j}} \equiv [\sigma^2_{g_{m,j,Rd}} + \sigma^2_{g_{m,j,Plt}}]^{1/2}. \qquad (2)$$

Since the rodded zone is taken as the reference, all mass defects are attributable to an incorrect loading of the matched plate zone; a positive mass defect indicates that the loading of the matched plate zone is lower than that of the rodded zone. Thus, in evaluating the reactivity effect of the mass defects, what is required is the reactivity correction to the matched plate zone corresponding to conceptual mass adjustments to the matched plate zone that would bring it into equality with the rodded zone. Therefore, the appropriate material reactivity worths with which to weight the existing mass defects are the measured Assembly 7 plate in-cell central worths (see Paper II-19) of the addition of the equalizing materials corrected to the position of the mass defect.

The reactivity to be added (algebraically) to the reactivity of the matched plate zone in order to correct for $\Delta g_{m,j}$ is

$$\Delta\rho_{m,j} = \rho_{m,j,Plt}\Delta g_{m,j} \qquad (3)$$

and

$$\sigma_{\Delta\rho_{m,j}} = [(\rho_{m,j,Plt}\ \sigma_{\Delta g_{m,j}})^2 + (\Delta g_{m,j}\ \sigma_{\rho_{m,j,Plt}})^2]^{1/2}, \qquad (4)$$

where

$\rho_{m,j,Plt}$ ≡ best available estimate of the reactivity worth of adding unit mass of material m in composition matching unit j within the plate cell of the plate zone,

$\sigma_{\rho_{m,j,Plt}}$ ≡ best estimate of the standard deviation of $\rho_{m,j,Plt}$,

$\Delta\rho_{m,j}$ ≡ reactivity correction to the matched plate zone to correct for the mass defect in material m in composition matching unit j,

$\sigma_{\Delta\rho_{m,j}}$ ≡ standard deviation in $\Delta\rho_{m,j}$.

The overall reactivity correction for mass defects in all materials in all composition matching units is

$$\Delta\rho \equiv \sum_{m=1}^{\substack{all\\materials}} \sum_{j=1}^{350} \Delta\rho_{m,j} \qquad (5)$$

and

$$\sigma_{\Delta\rho} \equiv \left[\sum_{m=1}^{\substack{all\\materials}} \sum_{j=1}^{350} \sigma^2_{\Delta\rho}\right]^{1/2}. \qquad (6)$$

Modifications to the Basic Method of Calculation

The method of calculating the plate zone reactivity correction and its uncertainty described in the preceding section represents the basic method used in the analysis of this experiment. However, in the actual application of the method, certain characteristics of the situation in the experiment were used to simplify the calculation and to reduce the large amount of data handling involved. These modifications in the calculational method are described here. It is not believed that these simplifications significantly affect the accuracy or precision of the experiment.

First of all, $\Delta g_{m,j}$ is zero for all materials except iron, nickel, chromium, and manganese for all composition matching units outside of the actual plate-rod zone; that is,

$$\Delta g_{m,j} = 0$$

for $m \equiv$ iron, nickel, chromium, or manganese and for j not in the central 100 composition matching units. This last is true because everything except the stainless steel in the drawer (and boat) is identical between the plate and rod zone cases in the two (125 composition matching units each) axial zones adjacent to the plate-rod zone.

Secondly, the spatial distributions of mass defects for all materials in the actual plate-rod zone (central 100 compsotion matching units) and for iron, nickel, chromiun, and manganese in the adjacent axial regions are very nearly uniform. Because of this nearly uniform mass defect distribution, very little accuracy is lost in the calculation of the reactivity correction if, instead of multiplying the mass defect for each material and composition matching unit by the appropriate reactivity worth, and summing, as in Eqs. (3) and (4), the mass defects for each material are first summed over selected subregions of the problem, then multiplied by the average reactivity worth of the material over the subregion, and, finally, summed over all materials and subregions. Thus, instead of Eqs. (3) through (6), we take two subregions in the problem: namely, the central zone (composed of the central 100 composition-matching units) (CZ) and the combined adjacent axial regions (composed of the 250 axial composition-matching units) (AR).

SUMMARY OF THE CALCULATION OF THE MATCHED PLATE ZONE REACTIVITY CORRECTION FOR ALL MATERIALS AND ALL REGIONS

Table II-25-VII summarizes the mass data for all materials in the experiment. Table II-25-VII is based on the measured material weights and the estimated mean compositions of the constituent materials. The molybdenum was added to the rodded zone in the form of thin strips slipped into the vertical spaces between the calandria cans and the matrix tubes.

The central plate-core reactivity worths used for the various materials in the experiment are summarized in Table II-25-VIII. The table also summarizes the average-to-center material reactivity worth ratios that were used.

Table II-25-IX summarizes the results of the matched

TABLE II-25-VII. ROD ZONE AND MATCHED PLATE ZONE MASS DEFECTS

Material	Region	Total Region Weights		
		(A) Rodded Zone,[a] kg	(B) Matched Plate Zone, kg	(A − B) Mass Defect, kg
Total Pu	Central Zone	18.8944	18.9032	−0.0088
^{238}Pu		0.00954	0.0108	−0.00126
^{239}Pu		16.3233	16.3312	−0.0079
^{240}Pu		2.193	2.189	0.004
^{241}Pu		0.3308	0.3324	−0.0016
^{242}Pu		0.0378	0.0398	−0.0020
$^{239+241}$Pu		16.6541	16.6636	−0.0095
Total U		107.50	107.13	0.37
^{235}U		0.243	0.230	0.013
^{238}U (includes 234 and 236)		107.27	106.90	0.37
Oxygen		16.917	16.647	0.270
Mo		1.684	1.676	0.008
Na		16.494	16.511	−0.017
Total SS 304 + Fe		50.034	46.684	3.350
Fe (includes all other than Ni, Cr, and Mn)		35.174	36.722	−1.548
Ni		4.908	3.360	1.548
Cr		9.306	6.196	3.110
Mn		0.645	0.406	0.239
Total Pu and U Impurities (^{241}Am, Th, etc.)		0.175	0.126	0.049
Total SS 304 + Fe	Axial Regions			
Fe (includes all other than Ni, Cr, and Mn)		10.549	3.152	7.397
Ni		1.364	0.426	0.938
Cr		2.773	.817	1.956
Mn		0.239	0.0067	0.172

[a] Total PuO_2-UO_2 rod core weight for the actual 1600 rods used

$$= 143.4840 \text{ kg} \begin{cases} 96 \text{ pins from Lot-4} = 8.6139 \text{ kg } PuO_2\text{-}UO_2 \\ 1504 \text{ pins from Lot-6} = 134.8701 \text{ kg } PuO_2\text{-}UO_2 \end{cases}$$

plate zone reactivity correction calculation for the overall experiment.

SUMMARY OF THE CALCULATION OF THE CONTRIBUTIONS TO THE UNCERTAINTY IN THE MATCHED-PLATE ZONE REACTIVITY CORRECTION FROM ALL MATERIALS AND REGIONS OF THE EXPERIMENT

The calculated contributions from each material and region of the experiment to the uncertainty in the overall matched-plate zone reactivity correction are summarized in Table II-25-X.

EXPERIMENTAL RESULTS OF THE PLATE-TO-ROD REACTIVITY DIFFERENCE MEASUREMENT AND COMPARISON WITH CALCULATIONS

The measured reactivity difference between the matched plate zone and the rodded zone was 68.7 ± 1.0 Ih (1σ) (reactivity measurement uncertainty only); that is, the plate zone is more reactive than the rodd zone. The measurement was carried out in steps follows:

a. The rodded zone was loaded into Assembly 7 as described previously in this report. It should be

TABLE II-25-VIII. CENTRAL MATERIAL REACTIVITY WORTHS AND AVERAGE-TO-CENTER MATERIAL WORTH RATIOS

Region	Material	(C) Central Worth, Ih/kg (1σ)	Source[a]	(D) Average-to-Center Worth Ratio	Source
Central zone	^{239}Pu	171.5 ± 3.9	In-cell measurement	0.813	Least squares fit of radial and axial traverse data in plate core.
	^{240}Pu	17.5 ± 1.8	Calculation	0.813	
	^{241}Pu	275.3 ± 28	Calculation	0.813	
	^{242}Pu	10.6 ± 1.1	Calculation	0.813	
	^{235}U	133.3 ± 3.1	Plate core measurement	0.759	
	^{238}U	−9827 ± 0.317	Plate core measurement	0.759	
	O	−11.4 ± 1.3	Inferred from Fe_2O_3 and U_3O_8 measurements	0.685	
	Mo	−15.4 ± 0.1	Plate core measurement	0.685	
	Na	−6.04 ± 0.16	Average of in-cell and in-calandria measurement	0.641	
	Fe	−4.73 ± 0.20	In-cell measurement	0.685	
	Ni	−6.85 ± 0.25	In-cell measurement	0.685	
	Cr	−5.03 ± 0.25	In-cell measurement	0.685	
	Mn	−10.0 ± 1.0	Calculation	0.685	
Combined axial regions	Fe	−4.73 ± 0.20	In-cell measurement	−0.063[b]	Least squares fit as above plus cosine^2 distribution into blankets.
	Ni	−6.85 ± 0.25	In-cell measurement	−0.063	
	Cr	−5.03 ± 0.25	In-cell measurement	−0.063	
	Mn	−10.0 ± 1.0	Calculation	−0.063	

[a] For all purely calculated central worths a 1σ imprecision of 10% was assumed. Note that experimental worth data were available for all of the significant mass defects.

[b] Stainless steel 304 worth changes from (−) to (+) with the addition of stainless steel as traverse passes from core into blanket.

noted that Assembly 7 had been modified slightly just prior to this plate-rod zone $\Delta\rho$ measurement by replacing 150 kg-fissile Pu-U-Mo fuel plates at the extreme periphery of the core with 150 kg-fissile Pu-Al fuel plates. Subsequent central material worth measurements were made to measure any change in the perturbation denominator of the core resulting from this fuel change; as expected, no change in the perturbation denominator was found.

b. The assembly was made critical with normal cooling-air flow. After waiting for the equiilbrium core temperature profile, the parameters of the critical configuration were recorded; that is, reactor power, all boron rods out, all fueled rods full-in except one partially out, movable-stationary reactor-half corner separations, fine autorod (FAR) critical position, and the temperature profiles.

c. Based on the measured reactivity calibrations of the single fueled rod that was partially out and of the FAR, the total excess reactivity of the assembly with the rodded zone and all control elements in their most reactive positions, $\Delta\rho$ rod, was calculated.

d. The assembly was shutdown and the rodded zone replaced by the matched plate zone using a loading sequence backwards from the plate-to-rod loading sequence described previously in this report.

e. The assembly was brought to critical again with the movable-stationary reactor-half corner separations matched as closely as possible to the rodded

TABLE II-25-IX. PLATE-ROD ZONE EXPERIMENT—MATCHED PLATE ZONE REACTIVITY CORRECTION

Region	Material	Reactivity Correction,[a] Ih
Central zone	Pu	−1.42
	U	−1.44
	O	−2.11
	Mo	−0.085
	Na	+0.066
	Fe (+ all impurities)	+4.85
	Ni	−7.28
	Cr	−10.73
	Mn	−1.64
Combined axial regions	Fe (+ all impurities)	+2.20
	Ni	+0.40
	Cr	+0.63
	Mn	+0.11
		Total −16.4

[a] (A − B)CD from Tables II-25-VII and II-25-VIII.

TABLE II-25-X. SUMMARY OF THE RESULTS OF THE CALCULATION OF THE CONTRIBUTIONS TO THE UNCERTAINTY IN THE MATCHED-PLATE ZONE REACTIVITY CORRECTION

Material, m	Central Zone (CZ) rms Total $\sigma_{\Delta\rho_{m,CZ}}$ Ih	Axial Regions (AR) rms Total $\sigma_{\Delta\rho_{m,AR}}$ Ih	All Regions $\sigma_{\Delta\rho_m}$ (rms Sum) Ih
^{238}Pu	(<0.14)[a]	—	(<0.14)[a]
^{239}Pu	2.23	—	2.23
^{240}Pu	0.05	—	0.05
^{241}Pu	0.31	—	0.31
^{242}Pu	0.01	—	0.01
Pu total (rms)	2.25	—	2.25
^{235}U	0.26	0.00	0.26
$^{238+}$U[b]	1.64	0.00	1.65
U total (rms)	1.66	0.00	1.66
Mo	0.01	—	0.01
O	0.77	—	0.77
Na	0.01	—	0.01
Fe + all impurities	0.36	1.10	1.16
Ni	0.45	0.21	0.50
Cr	0.85	0.31	0.90
Mn	0.25	0.06	0.26
$\sigma^{k}_{\Delta\rho_{region}}$	3.08	1.16	3.29
$\sigma_{\Delta\rho}$	—	—	3.29

[a] Not included in rms totals.
[b] $^{238+}U = {}^{238}U + {}^{234}U + {}^{236}U$.

TABLE II-25-XI. MEASURED AND CALCULATED REACTIVITY DIFFERENCE BETWEEN THE COMPOSITIONALLY-MATCHED PLATE AND RODDED ZONES (10.9 x 10.9 x 24 in.) IN ASSEMBLY 7

	Reactivity Difference (Plate-Rod)		
	$\Delta\rho$ As-Built,[a] Ih (1σ)	$\Delta\rho$ Composition Mismatch Correction,[b] Ih (1σ)	$\Delta\rho$ Compositional Match, Ih (1σ)
Measured	68.7 ± 1.0	−16.4 ± 3.3	52.3 ± 3.4
Calculated	—	—	50.9

[a] Uncertainty is reactivity measurement uncertainty only.
[b] Uncertainty in the correction includes the effects of uncertainty in the reactivity worth of materials and of uncertainties as to how much material was present.

case. Using the same cooling-air flow and reactor power as for the rodded case, the same data as described in (b) above were recorded; in this case, two fueled rods were full-out and one partially out.

f. As for the rodded case, the total excess reactivity of the assembly with the matched-plate zone and all control elements in their most reactive positions, $\Delta\rho$ plate was calculated using rod calibrations, assuming all control elements were in their most reactive positions.
g. The plate-to-rod reactivity difference was calculated as $\Delta\rho_{plate} - \Delta\rho_{rod}$ with corrections for the measured difference between average core temperatures in the rod and plate cases (using a previously measured temperature coefficient) and for the ^{241}Pu decay in the two days between the rod and plate mesaurement. The temperature correction was 1.2 ± 0.1 Ih (1σ) and the ^{241}Pu correction was 0.8 ± 0.2 Ih (1σ).
h. The estimated uncertainty in the measurement (1σ = 1 Ih) is the combination of estimates of the uncertainties in the reactor-half closure reproducibility, rod calibrations, temperature correctoins, and ^{241}Pu correction. The half closure uncertainty dominates.

In order to derive a number for the "measured" reactivity difference between compositionally-matched plate and rod zones it is necessary to adjust the directly measured value by the reactivity correction from Table II-25-IX with its uncertainty from Table II-25-X; that is, −16.4 ± 3.3 Ih (1σ). Thus the best available "measured" plate-to-rod reactivity difference for comparison with calculation is (52.3 ± 3.4) Ih (1σ).

The best currently available calculated value for the expected plate-to-rod reactivity difference for the configuration of this experiment is 50.9 Ih. The plate zone is calculated to be more reactive because the fuel lumping gives relatively more fast fission and relatively less low-energy absorption than the rods. The homogeneous cross-sections were generated from ENDF/B-1 using MC[2]. Corrections were then made in the resonance range, using equivalence theory, to get effective in-plate and in-rod ^{238}U capture, ^{238}U fission, and ^{239}Pu fission cross sections; these cross sections were then cell-averaged using CALHET. The calculation used ARC 1D diffusion perturbation theory and individual runs were made to get the perturbed calculation.

Table II-25-XI compares the mesaured and calculated plate-to-rod zone reactivity difference.

REFERENCES

1. W. G. Davey and C. E. Till, *The Demonstration Reactor Benchmark Critical Assemblies Program*, Trans. Amer. Nucl. Soc. **12**, 696 (1969).
2. R. A. Lewis, *Comparison of Measurements of Sodium-Void Coefficients in Plates and Pins*, Reactor Development Program Progress Report, ANL-7776, pp. 5–6 (1971).
3. E. M. Bohn, *Central Reactivity Worths Measured in ZPR-6*

Assembly 7, Reactor Development Program Progress Report, ANL-7783, pp. 13–15 (1971).
4. C. E. Till, J. M. Gasidlo, E. F. Groh, L. G. LeSage, W. R. Robinson and G. S. Stanford, *Null-Reactivity Measurements of Capture/Fission Ratio in ^{235}U and ^{239}Pu*, Nucl. Sci. Eng. **40**, 132 (1970).

II-26. The Variable Temperature Rodded Zone (VTRZ) Project

K. D. Dance, J. F. Meyer, E. F. Groh and D. M. Smith

The VTRZ is an approximately 360 liter heatable zone (6 ft long and 20 in. in diam split axially into two 3 ft zones), capable of operation at temperatures up to 550°C. It is to be installed in the ZPR-6 critical facility. The VTRZ project was initiated in 1967 for the purpose of designing, developing, and fabricating the necessary equipment for the VTRZ. The VTRZ equipment will permit integral physics measurements to be made in environments typical of the temperature condition and fuel configuraion of Liquid Metal Fast Breeder Reactors (LMFBRs).

A description of the conceptual design of the VTRZ and of the basic VTRZ experimental program is contained in Ref. 1. References 2 and 3 contain descriptions

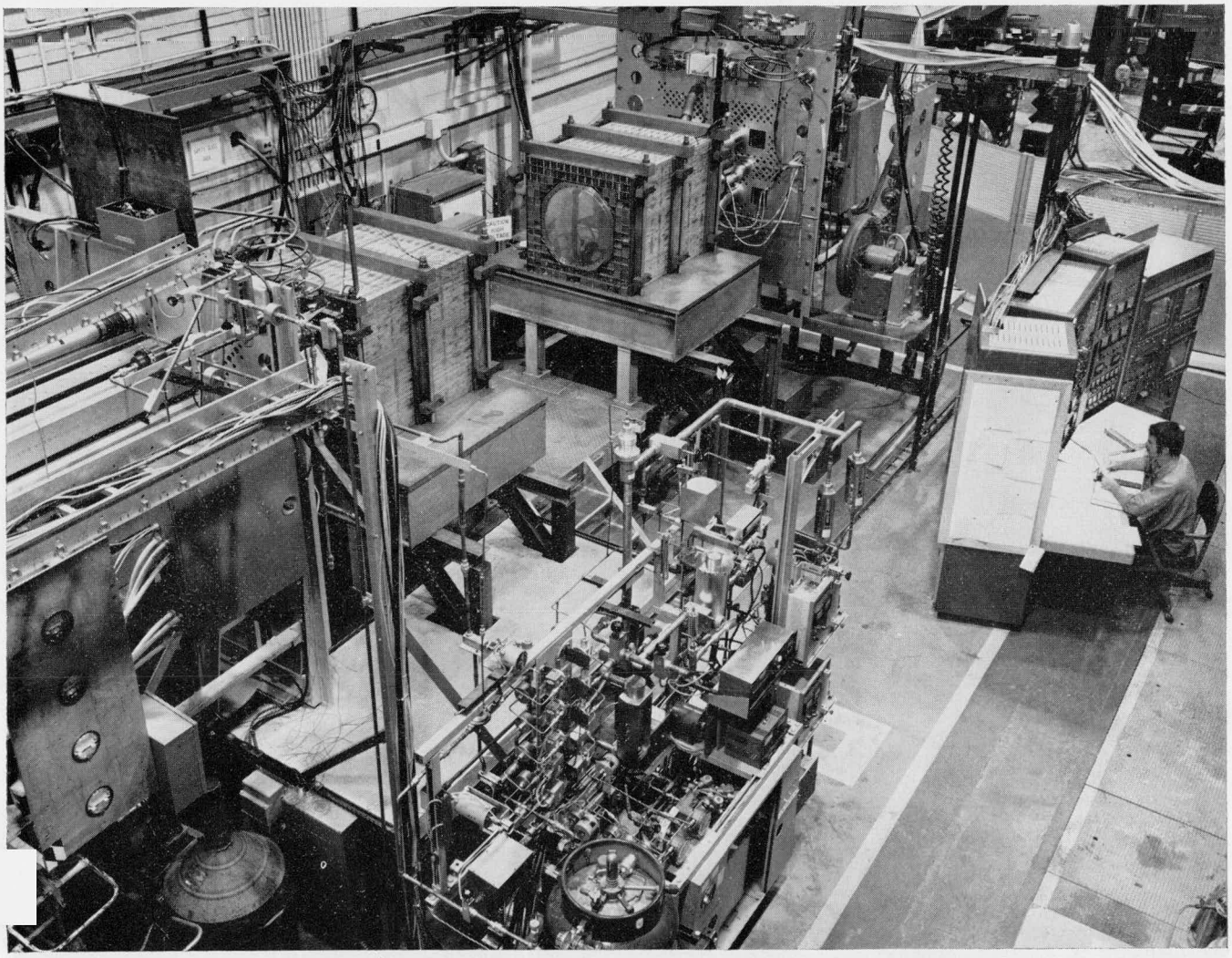

Fig. II-26-1. VTRZ Installed in Out-of-Pile Installation. *ANL Neg. No. 116-853.*

of the progress of the project during the 1968–1969 and the 1969–1970 periods, respectively. This paper is a progress report for the VTRZ Project during the period July 1970 to June 1971.

Progress of the VTRZ Project from July 1, 1970 to June 30, 1971

The principal accomplishments of the VTRZ Project during this period may be summarized as follows:

1. Completion of the AEC review of the VTRZ Final Safety Analysis Report.
2. Preparation of the VTRZ Quality Assurance Installation Phase Program.
3. Completion of the procurement of the VTRZ Heatable Zone Facility and the VTRZ fuel rods.
4. Completion of the out-of-pile installation of the VTRZ Heatable Zone Facility.
5. Initiation of the out-of-pile installation phase testing program.

AEC safety review

The VTRZ Final Safety Analysis Report[4] (FSAR) and the accompanying VTRZ-ZPR-6 Operating Limits document were submitted for AEC review and approval on April 1, 1970. Several design changes, required as a result of the AEC review, were incorporated into the VTRZ system and formal approval of the VTRZ safety documents was obtained in October 1970.

VTRZ qaulity assurance program

The overall VTRZ Quality Assurance Program was approved by the AEC in October of 1969. This document contained the detailed Quality Assurance plans for the design and development phase and the procurement phase. Only brief outlines of the Quality Assurance (QA) plans for the installation phase and the operations and maintenance phase were given in the original VTRZ QA Program. A detailed VTRZ Installation Phase Quality Assurance Plan was prepared

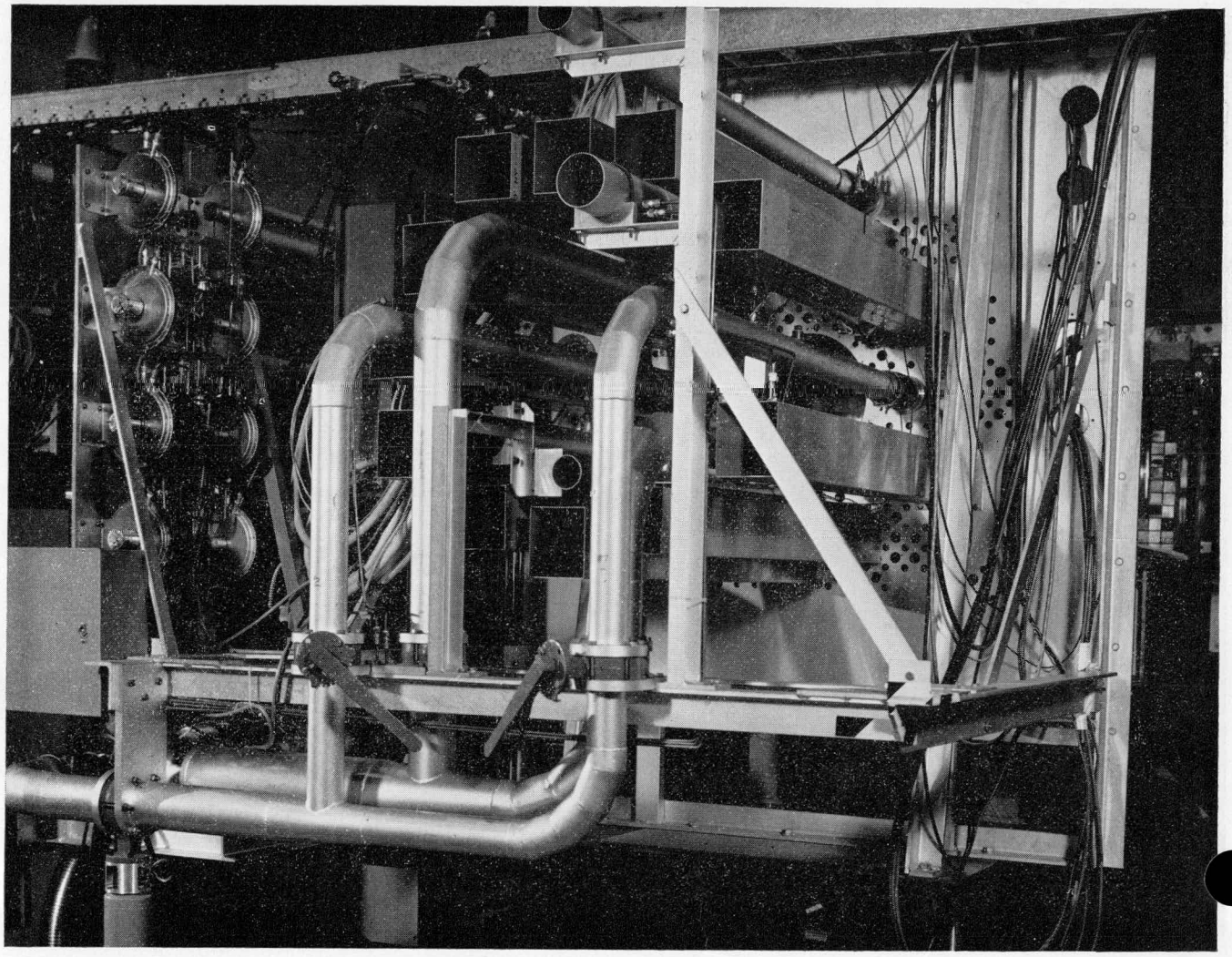

Fig. II-26-2. Reactor Table Mockup. *ANL Neg. No. 116-854.*

and submitted to the AEC in November 1970. A detailed Quality Assurance Plan for the Operation and Maintenance Phase will be prepared prior to initiation of VTRZ operation in ZPR-6.

The VTRZ Project was audited by ANL Quality Assurance Management (QAM) in November 1970. The final report on the QAM audit findings was issued in January 1971. VTRZ responses to QAM recommendations were submitted to QAM in March 1971.

VTRZ PROCUREMENT

Procurement of all VTRZ equipment has been the primary task during the past fiscal year. Procurement has included preparation of detailed manufacturing and QA plans, monitoring of all fabrication in ANL Central Shops and Electronics and purchasing of commercial items. Procurement during the past fiscal year has been concerned primarily with the VTRZ Heatable Zone Facility equipment. All VTRZ calandria can procurement was started in 1969 and as of June 30, 1970, all UO_2 fuel rods were procured. All fuel rod procurement was completed June 30, 1971, with final delivery of all PuO_2-UO_2 fuel rods. Procurement of all Heatable Zone Facility equipment was started in June 1970 and completed in March 1971.

Fabrication of Heatable Zone Facility components included: construction of the heatable inner barrel assemblies, the welded outer matrix structures and the air cooling system; welding, brazing and leak checking of all argon loop components; purchasing of all electrical power equipment; and fabrication of all monitoring and control instrumentation. The mechanical construction of the barrels and matrix structures was accomplished in ANL Central Shops under very strict QA procedures. All phases of the mechanical construction in Central Shops was monitored by VTRZ project personnel. The fabrication of the argon loop equipment was accomplished using certified Central Shops welders

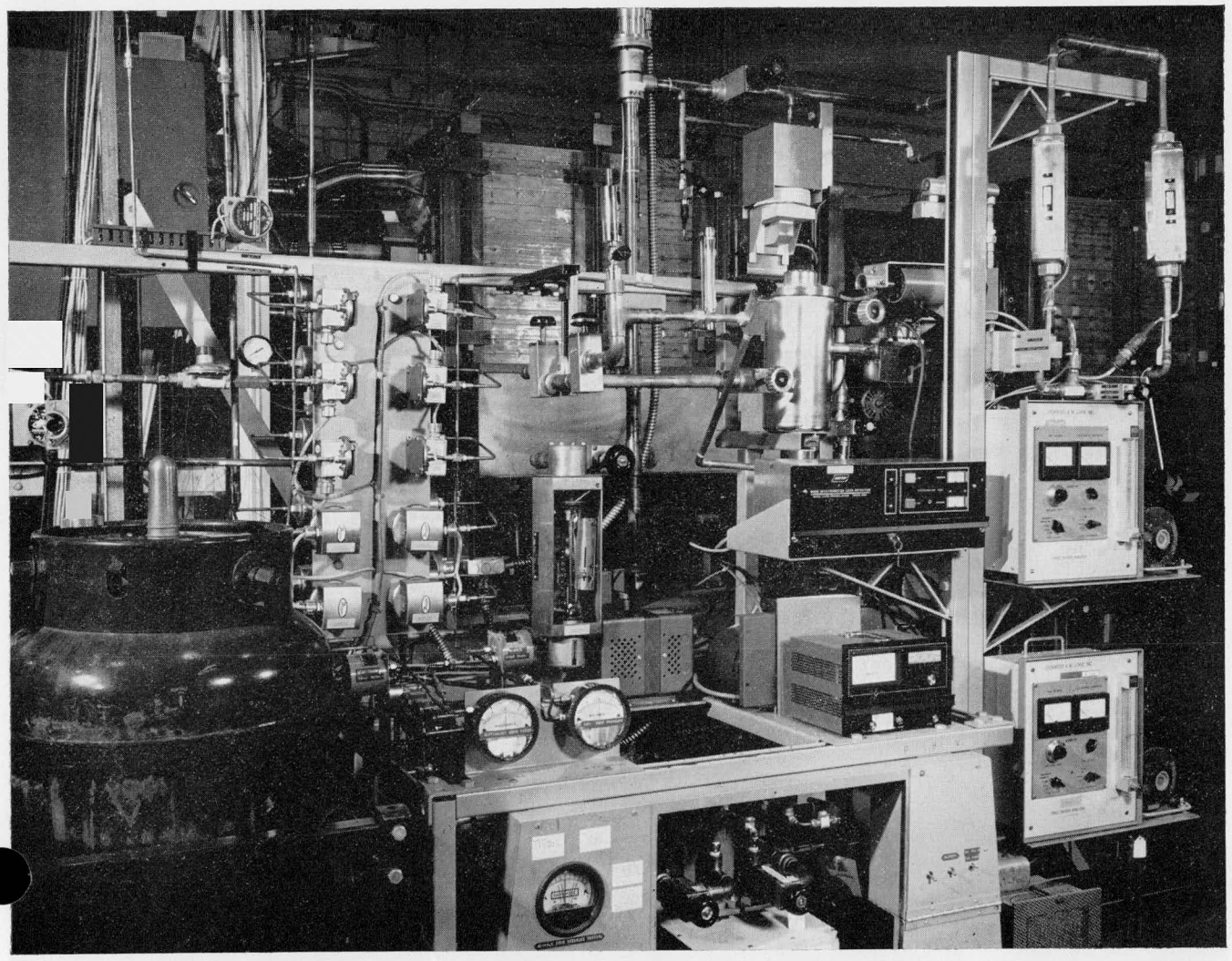

FIG. II-26-3. VTRZ Argon Loop Equipment. *ANL Neg. No. 116-855.*

working under the direct supervision of VTRZ project personnel. All instrumentation fabrication was prepared by the ANL Electronics Division following the manufacturing and QA plans prepared by VTRZ personnel.

OUT-OF-PILE INSTALLATION

The VTRZ Heatable Zone Facility has been assembled in an out-of-pile installation to permit testing of all components prior to their use in the ZPR-6 critical assembly. The out-of-pile installation includes a mockup of the basic ZPR-6 assembly and will permit testing of all functions of the VTRZ exclusive of the actual neutronics. For example, full scale heatups of the inner barrel with actual sodium-filled calandria cans containing depleted UO_2 pins will be conducted in the out-of-pile assembly.

Work on the out-of-pile installation was started in November 1970 with the start of construction of the reactor table mockup. The reactor table mockup was completed in March 1971. The reactor table mockup (see Figs. II-26-1 and II-26-2) does not duplicate all reactor components, but it does duplicate all items essential to determining any possible problems in the final in-pile VTRZ installation. The air cooling system, the mounting plates to be used in the final reactor installation, and control rod mockups are included in the out-of-pile facility. The movable half reactor table mockup is also mounted on wheels to allow the duplication of table movement, including scrams.

Installation of all electrical power equipment was completed in the period from February to April 1971. Most wires for the electrical power equipment were cut to a length appropriate for use in the final in-pile installation in order to facilitate moving from the out-of-pile setup to the final in-pile installation.

Installation of the argon loop equipment, shown in Fig. II-26-3, and the instrumentation equipment, shown in Fig. II-26-4, was completed in the period from February to June 1971. The installation included com-

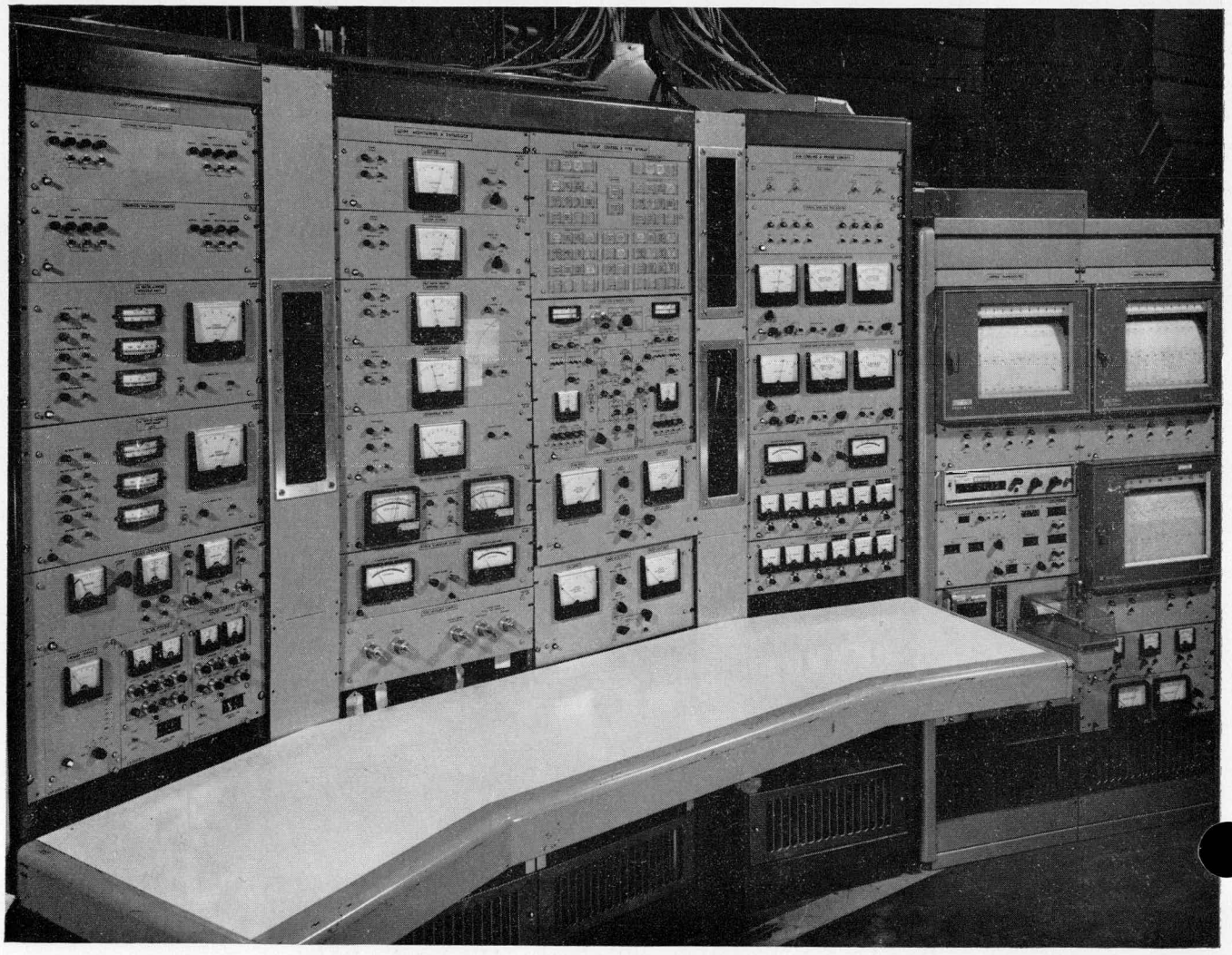

FIG. II-26-4. VTRZ Instrumentation Equipment. *ANL Neg. No. 116-856.*

ponent checkout of all parts. The inner barrel and outer matrix assemblies were assembled and installed, after extensive load testing, on the reactor table mockup in May and June of 1971 (see Fig. II-26-5).

INSTALLATION PHASE TESTING

An extensive out-of-pile testing program was started in April 1971. The testing program is designed to check the system performance of all components prior to installation of the VTRZ into ZPR-6. The testing will include both unheated VTRZ operation and heated (to 550°C) operation. Actual heatable calandria cans loaded with depleted UO_2 pins will be used in the heatup tests.

The out-of-pile testing began with load tests of the welded outer matrix structures and the ball mounts holding the heatable inner barrel in place in the room temperature outer matrix structure. The tests proved the ability of all components to safely support their full design load. The load testing was conducted during the months of April and May 1971.

The electrical power supply system was completely performance-tested in the months of May and June 1971. The initial electrical power system tests uncovered certain performance failures in the basic supply units and certain inadequacies in the power monitoring equipment. System design changes were made to correct these deficiencies and the system was successfully performance-tested.

The argon loop flow system and associated instrumentation testing was begun in June 1971 and will be completed in the months of July and August prior to the first heatup scheduled for September 1971.

OUTLOOK FOR JULY 1, 1971 THROUGH JUNE 30, 1972

Current schedules call for completion of unheated VTRZ out-of-pile tests by September 1971. Heated out-of-pile tests are scheduled for completion by January 1972.

Operation and maintenance manuals for the VTRZ

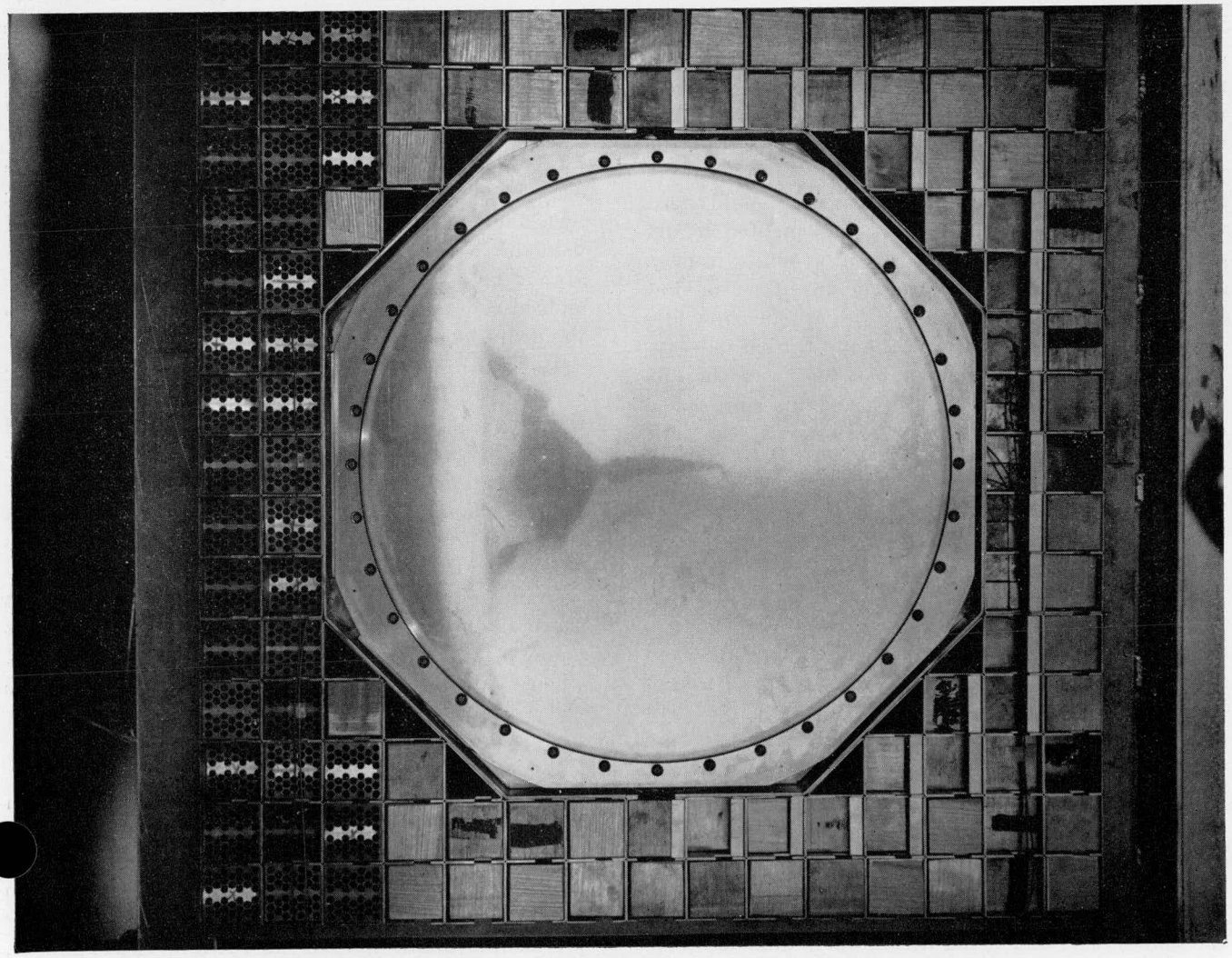

FIG. II-26-5. VTRZ Outer Matrix and Inner Barrel Assemblies. *ANL Neg. No. 116-857.*

Heatable Zone Facility are to be prepared by February 1972.

Installation of VTRZ into ZPR-6 is scheduled to begin in January 1972 and be completed by April 1972. The first heated measurements using ^{235}U are to commence in April 1972, and continue through the remainder of the fiscal year.

References

1. R. A. Lewis, F. H. Martens and C. E. Till, *The Variable Temperature Rodded Zone Project*, Reactor Physics Division Annual Report, July 1, 1967 to June 30, 1968, ANL-7410, pp. 124–125.
2. R. A. Lewis, K. D. Dance, J. F. Meyer and T. W. Johnson, *The Variable Temperature Rodded Zone (VTRZ) Program*, Reactor Physics Division Annual Report, July 1, 1968 to June 30, 1969, ANL-7610, pp. 137–143.
3. R. A. Lewis, K. D. Dance, J. F. Meyer and E. F. Groh, *The Variable Temperature Rodded Zone (VTRZ) Project*, Applied Physics Division Annual Report, July 1, 1969 to June 30, 1970, ANL-7710, pp. 189–196.
4. R. A. Lewis, K. D. Dance, J. F. Meyer and E. M. Bohn, *Variable Temperature Rodded Zone Project Final Safety Analysis Report*, ANL-7638 (1970).

II-27. Noise Effects in Rod Drop Analysis

E. F. Bennett and I. K. Olson

Introduction

The time-profile of reactor flux in response to a sudden change in multiplication contains sufficient information to permit the determination of both initial and final subcriticality. This fact is the basis of several particular methods for determining subcriticality from the profiles. Figure II-27-1 is a typical flux profile in response to a sudden rod drop. The oldest and most widely used of these methods is implemented by recording three numbers—the pre-drop flux (from a steady state), the flux just after the drop (measured at a time long compared with the prompt neutron lifetime but short compared with the most rapidly decaying delayed neutron precursor half life), and the flux asymptotically after the drop. If these fluxes are called ϕ_1, ϕ_2, and ϕ_3, respectively, point-kinetics analysis leads to the result

$$\frac{\phi_2 - \phi_3}{\phi_1} = \frac{\rho_2 - \rho_1}{\rho_2 + \beta(1 - \rho_2)} \frac{\beta}{\rho_2} \tag{1}$$

$$\frac{\phi_3}{\phi_1} = \frac{\rho_1}{\rho_2}, \tag{2}$$

where $\rho = 1 - k$. Equations 1 and 2 may be solved simultaneously for ρ_1, which will then be a function of the quantities $(\phi_2 - \phi_3)/\phi_1$ and ϕ_3/ϕ_1 only. The definition of ϕ_1 and of ϕ_2 is clear—they are simply average values over intervals of time over which the profile is unchanging and consequently they are not dependent on the interval chosen. The definition of ϕ_3 cannot be made specific without defining the time, τ_1, when averaging commences and the time, τ_2, when it terminates. Only when the interval $\tau_2 - \tau_1$ is short enough and the values of τ_1 and τ_2 fall within the prompt-jump restriction mentioned can we use Eqs. 1 and 2 and solve for ρ algebraically. For arbitrary values of τ_1 and τ_2 we may, however, write

$$\rho_1 = \text{REACT}\left[\frac{\phi_2(\tau_1, \tau_2) - \phi_3}{\phi_1}, \frac{\phi_3}{\phi_1}\right]. \tag{3}$$

REACT is a unique function of arguments but must be evaluated by a computer in the conventional manner; by changing ρ_1 (and ρ_2 through Eq. 2) until the observed value of $(\phi_2 - \phi_3)/\phi_1$ and ϕ_3/ϕ_1 are reached. This can always be done to the limits of computing accuracy and, in consequence, there is no practical objection to the definition of REACT as given in Eq. 3.

If one is in possession of a computer algorithm corresponding to Eq. 3, there is no longer need to restrict the values of τ_1 and τ_2 as must be done if Eqs. 1 and 2 are to apply. In fact, where one must deal with a practical experimental situation and is faced with a considerable noise scatter in the profile, noise acts as a constraint to the definition of the interval. As it turns out, if one defines τ_1 safely after the drop (about 0.5 sec) and τ_2 to be about 25 sec, one has achieved about the best obtainable measurement precision; the exact value of τ_2 is somewhat sensitive to subcriticality. Choice of τ_2 less than or greater than its optimum value will worsen the precision obtainable.

Effects of Noise

We have raised the question of noise in the profile in regard to the choice of time intervals for the determination of the average ϕ_2. It is very desirable to h a model for random flux noise which can be applied to the method of analysis and can be made the basis for precision estimates in each subcriticality measurement.

This program can, in fact, be carried out and one requires only two parameters—the detector efficiency defined as the ratio of neutron detection rate to pile fission rate and the power calibration defined as the fission rate at 1% subcritical. These parameters can both be measured without too much difficulty and are sufficient to determine the precision of any measurement of subcriticality by rod-drop profile analysis.

The measurement method based on Eq. 3 is only one of several methods which have been proposed,[1] although it is the oldest. Since three flux points are sufficient to determine subcriticality, more will also suffice, and in Ref 1 a different approach is used in which finely sampled profiles are analyzed by fitting procedures over long intervals of time before and after the drop. These methods have certain advantages and disadvantages relative to the three-point method (it seems reasonable to call the method based on Eq. 3 or Eqs. 1 and 2 with restriction on τ, a three point method). They are, at least in some versions, very flexible and will present reactivity versus time from a flux profile versus time. Any change whatsoever in reactivity can be accommodated by this scheme and the restriction to rapid multiplication change, necessary for the three point rod-drop method, does not appear.

If random-noise effects were not a consideration, there would be no reason to use other than inverse kinetics. However, noise does constitute a large effect upon the profile as seen, for example, in Fig. II-27-1. One can find a basis for certain misgivings concerning the numerical details of an inverse kinetics approach, or any approach involving a fitting procedure. These misgivings are present even for random-detection noise and are exacerbated by the true noise existing in reactors which tends to fluctuate in a way in which correlations appear over adjacent time intervals. This tendency for fluctuations to persist in time will influence an analysis of profiles based upon fitting a function to a measured profile of flux versus time. The correct way of assigning an error to a fit, for example, must take into account the correlations associated with the noise. The three-point method, because of its simplicity, can accommodate noise rather easily. Noise, even including a general pile-noise component reflecting the nonstationary nature of the rod-drop problem, can be derived in terms of detector efficiency and power calibration for a single integral over the flux. By use of single integrals only, the problem of interpreting errors resulting from a fitting procedure is avoided.

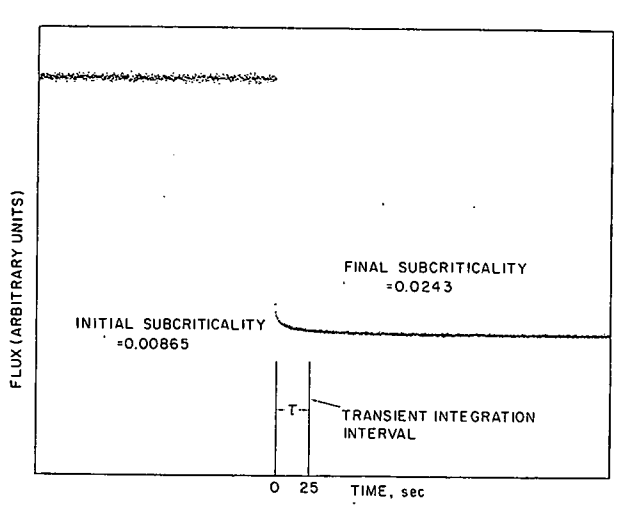

FIG. II-27-1. Experimental Rod Drop Flux Profile for an FTR-EMC Core on ZPR-9. *ANL Neg. No. 116-860.*

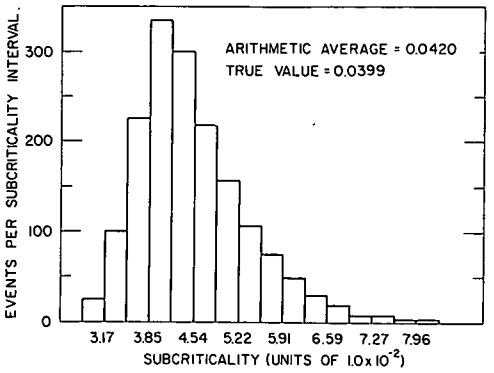

FIG. II-27-2. Distribution of the Values of Initial Subcriticality for a Simulated Rod Drop with Noise Added. *ANL Neg. No. 116-929.*

A study of subcriticality measurements using the extended three point method of Eq. 3 was made using unpublished results based upon the Fast Test Reactor-Engineering Mock-up Core (FTR-EMC) series. The results were compared with an inverse kinetics analysis, both as to the value of subcriticality measured and the scatter in results. No statistically significant discrepancy was observed for initial subcriticalities less than about 2.5%. Results for subcriticality derived using either method agreed well.

The scatter observed for the three-point method was predicted well by the known efficiency and power calibration. These conclusions are illustrated by the results of a computer simulation of noise-perturbed rod drops shown in Figs. II-27-2 and II-27-3 and indicate that care should be exercised in treating the results of rod drop experiments made under practical, experimental conditions. These conditions are especially severe for the FTR-EMC cores at high subcriticality. Figure II-27-2 is the frequency of occurrence of a particular value of initial subcriticality (as determined by the three-point method) from an ensemble of about 1700 randomly-perturbed profiles simulating a rod drop from $\rho = 0.04$ to $\rho = 0.05$. Parameters corresponding to an FTR-EMC core were used. At these far subcritical values of multiplication, there is no need to include a

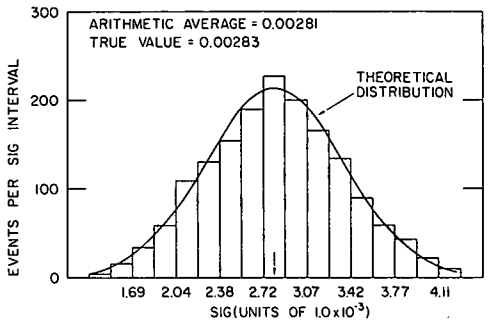

FIG. II-27-3. Distribution of the Values of SIG for the Simulated Rod Drop. *ANL Neg. No. 116-928.*

pile component in the noise, and rod drop profiles were simulated on the basis of random scatter in detection only. Notice that the distribution in initial subcriticality is skewed, and in fact the mean value of the ensemble is about 5% higher than the true value of 0.04. The true value is not exactly predicted; an uncertainty in the rod drop time relative to the basic sampling interval results in an error of about one part in four hundred, which is typical. It would not be proper to use the mean of a series of runs to define the subcriticality for this core.

Figure II-27-3 is a distribution of the fluctuations in the quantity $(\phi_2 - \phi_3)/\phi_1$ (referred to as SIG) which is of direct interest in the three point method and is used in the analysis via Eq. 3. It is clear that the dominant source of errors in SIG is the error in the value of $(\phi_2 - \phi_3)$ which is the difference of two nearly equal quantities. One would expect the distribution of fluctuations of $(\phi_2 - \phi_3)$ to be Gaussian since both ϕ_2 and ϕ_3 are simple integrals over the profile. The expected error for this drop as derived from the known power calibration and detector efficiency was used to predict the width of a Gaussian which is also plotted on Fig. II-27-3. The computed Gaussian is seen to represent, to the limits of statistics in the ensemble, the observed scatter in SIG. Since the distribution in SIG is Gaussian, its average is an unbiased estimator and does, in fact, lead to the true value (within finite-ensemble error limits) for initial subcriticality when used in Eq. 3.

CONCLUSION

The precision obtainable in rod drop measurements of initial subcriticality varies inversely as the square root of the total spontaneous fission neutron source (mostly ^{240}Pu) for plutonium-fueled assemblies, and also depends on detector efficiency. The spontaneous fission source existing in fuel used in the FTR-EMC core series allows a certain level of precision. This level is marginal relative to requirements and the random-scatter effects that accompany measurements are frequently large.

Different analyses of profiles agree well with each other, at least for subcriticalities less than about 2.5%, and there is no evidence within this range for systematic errors which can be attributed to the presence of noise in the profile. The statistical precision that is assignable to a particular drop analysis depends on many factors including initial and final subcriticality and detector efficiency and power calibration. This precision can be ascertained directly without restrictions on the noise source using a version of three-point analysis. The ability to determine precision in any measurement under general assumptions of the noise source and to combine the results of repeated identical drops without bias are advantages of the three-point analysis which may, depending upon the circumstances and requirements of the experiments, favor its use over the more general inverse kinetics.

REFERENCE

1. S. G. Carpenter and R. W. Goin, *Rod Drop Measurements of Subcriticality,* Applied Physics Division Annual Report, July 1, 1969, to June 30, 1970, ANL-7710, p. 206.

II-28. A Theoretical Formulation of Analysis of Deterministic Errors in Inverse-Kinetics Measurements of Reactivity in Subcritical Systems

D. H. SHAFTMAN

I. INTRODUCTION

One general procedure of estimating the reactivity of a given subcritical configuration is to perturb the system to a subcritical state with a different reactivity, measure the resulting time-dependent neutron count rate from a neutron detector at a fixed location, and analyze the data to infer the time-dependent reactivity. This measurement is referred to commonly as a "rod-drop measurement" although the perturbation mig involve a withdrawal of fuel, or an insertion of conti rods, or perhaps even an increase in reactivity. A neutron source is required, although this "external" source

might be inherent to the system, e.g., spontaneous fission neutrons from ^{240}Pu present in plutonium-fueled systems.

In typical statics-multiplication measurements of subcritical reactivity, neutron count rates are measured in the quasi-equilibrium initial state and in some other reference state. A third datum is the reactivity of the reference state or the change in reactivity from the initial state to the reference state. From these three independent datum points an estimate of the reactivity of the initial state is obtained. Features of the rod-drop measurement are that no reference value of reactivity is needed as input, and also that the inferred driving reactivity is quite insensitive to the value assumed for the mean prompt neutron lifetime in the basic kinetics equations.

The method of analysis of the rod-drop data generally is referred to as an "inverse-kinetics" analysis; indeed, normally the composite of measurement and analysis is identified as an "inverse-kinetics method".

In the development of the typical statics-multiplication methods and inverse-kinetics methods, a simplified point-kinetics model is used wherein all kinetics parameters other than reactivity are assumed to be unaffected by the perturbation. Further, the count rate is assumed to be inversely proportional to the reactivity, or to Δk_{eff}, depending upon the particular kinetics model. For the point-kinetics model where reactivity is the essential parameter, however, it is sufficient for accuracy of the statics-multiplication method that the ratio $Q\Lambda$/count-rate be proportional to the reactivity; indeed this is the defining model of that statics-multiplication model. Here, Q is the effective external neutron source, and Λ is the mean prompt-neutron generation time. Equivalently, when Δk_{eff} is the essential parameter, the defining model is that $Q\ell$/count-rate is proportional to Δk_{eff}, where ℓ is the mean prompt-neutron lifetime. In the sections following, implications of the deviation of this ratio from proportionality to Δk_{eff} are discussed. Error formulas are developed.

The focus of the present paper is a theoretical formulation of analysis of error in the estimates of reactivity due to the approximations of simplified point-kinetics. The error analysis is not extended here to the effects of statistical fluctuations in neutron detection and of reactor noise. The work is one aspect of a multi-faceted program of analysis and experiment concerning inverse-kinetics measurements in the various programs of "critical" experiments on zero-power fast-reactor systems at Argonne National Laboratory. This particular study has been meshed with studies by other theoreticians and experimenters.

The space-time neutron kinetics computer program QX1[1] has been used to simulate rod-drop measurements in systems resembling certain ZPR-9 fast-reactor loadings. In these systems, as in the ZPR-9, neutron detectors were positioned far out in the reflector. As discussed in Sections IV and V of this paper, there are several approximations of simplified point-kinetics for which corrections should be made. In some rod-drop measurements, the most important corrections to simplified point-kinetics have opposite signs, thereby tending to reduce the net error in use of point-kinetics. This type of error cancellation has been observed in the QX1 simulations pertaining to rod-drop measurements in the ZPR-9 program. It should be noted, however, that QX1 is limited to problems where the systems have one space dimension, and so the actual 3-space-dimension asymmetries of loading, rod drops, and detector location and local material environment could not be modeled.

In other systems, and with other choices for the reactivity perturbation and of neutron detection, it is conceivable that the principal errors of simplified point-kinetics might act in the same direction, and larger errors in reactivity estimates then would result.

II. Additional Remarks on Inverse-Kinetics (IK) Methods

Inverse-kinetics methods may be viewed as determinants of time-dependent sub-prompt-critical multiplication where the total effective neutron source is the sum of the effective external source and the time-dependent effective source of delayed neutrons. The time scale of the multiplication is Λ or ℓ, depending upon whether reactivity or Δk_{eff} is the parameter sought. To a good approximation, in these measurements the time derivative of the neutron count rate may be set equal to zero, and formulas analogous to statics-multiplication may be developed to describe this dynamic multiplication. If the neutron count rate and the ratio of the total effective source to the pre-drop external source are known at three non-trivially different time points, simplified point-kinetics yields three equations which may be solved for estimates of the reactivities of the initial and final states. An example is a 3-point method, discussed in Sections III and IV, in which two points are the time-asymptotic mean count rates in the initial and final states and the third point is the prompt-drop count rate immediately after a very rapid reactivity perturbation. More generally, a third datum point could be the time-integrated (or time-averaged) count rate over a longer time interval starting shortly after the rod drop (see Papers II-27 and II-29). Indeed, in principle only after-drop data need be used, as discussed in Paper II-29. However, the reactivity estimates obtained from this analysis of after-drop data appear to be quite sensitive to effects of statistical

fluctuations, and the method is yet to be proved to be useful for practical systems as now formulated (see Paper II-29).

To attempt to minimize errors due to statistical fluctuations, some IK methods process data of count rate to obtain aggregates of values of certain kinetics parameters from which least-squares analysis derives best values. In the IK method developed by Carpenter and Goin[2] a set of values is obtained of sub-prompt-critical multiplication of the after-drop source, and a least-squares analysis yields a best value of the parameter

$$\frac{\beta_{eff}}{\Delta k_{eff} - \beta_{eff} k_{eff}}$$

in the after-drop system. The method of Cohn[3] (also see Paper II-31) evaluates Δk_{eff} as a function of time and performs a weighted-least-squares analysis to find best constant values of the effective source and Δk_{eff} in the after-drop system. In the IK method of Carpenter and Goin, and also that of Cohn, the data emphasized are the time-asymptotic pre-drop and post-drop mean count rates plus the count rate in the time period starting soon after the completion of the drop, since in this portion of the after-drop time record there is the largest deviation from the two asymptotic states. Also, the IK method of Bennett emphasizes that portion of the after-drop time record (see Paper II-27). If the rod drop is well approximated as a step-function in time, these IK methods then have as an essentially common basis a particular 3-point method where the intermediate point is the count rate immediately after the rod drop. This method is discussed next.

III. Reference 3-Point Method of Simplified Point-Kinetics

Sections I and II provide the background and motivation for an inverse-kinetics method where the reactivity perturbation is well represented as a step-function in time and the neutron count rate is measured at the three "points": (time-mean) asymptotic count rate in each of the pre-drop and post-drop states; and the count rate immediately after completion of the rod drop. Let these count rates be denoted by R_0, R_2, and R_1, respectively, at the fixed detector position $\mathbf{r}_0$. In the model in which the asymptotic count rates are inversely proportional to Δk_{eff}, using the prompt-drop approximation, ignoring terms involving time derivatives, and assuming constancy of the β_{eff_i}, the equations

$$\overline{\Delta k_0} = \frac{\beta_{eff}}{1 - \beta_{eff}} \frac{1 - \frac{R_1}{R_0}}{1 - \frac{R_1}{R_2}} \tag{1}$$

$$\overline{\Delta k_2} = \frac{R_0}{R_2} \overline{\Delta k_0} \tag{2}$$

provide estimates of Δk_{eff} for the initial state ($\overline{\Delta k_0}$) and final state ($\overline{\Delta k_2}$), where $\Delta k \equiv k_{eff} - 1$.

The prompt-drop relationship used is

$$\frac{R_1}{R_0} = \frac{\overline{\Delta k_0} - \overline{k_0}\,\beta_{eff}}{\overline{\Delta k_2} - \overline{k_2}\,\beta_{eff}} .$$

IV. A Modified 3-Point Method

The reference 3-point IK method summarized in Section III is based on a model of simplified point-kinetics where the count rate is proportional to the multiplied source, with a time-invariant factor of proportionality. However, typically this factor is different in the initial and final states because of changes in the energy spectrum and the space variation of the neutron flux. If it proved to be a good approximation to assume that the factor was time-invariant after the rod drop, straightforward modifications of the simplified point-kinetics and hence of the various IK methods would be feasible. The space-time kinetics program QX1 has been applied to computer simulations of rod-drop experiments in fast-reactor systems approximating systems studied in the ZPR-9 facility, in the limitation to one space dimension. Neither statistical fluctuations nor reactor noise was included. Analysis of the computer outputs for a variety of cases indicated that the QX1 parameters ρ ("reactivity"), β_{eff}, and Λ were essentially constant once the (rapid) rod-drop was completed. This supplies motivation for a modified 3-point IK method detailed below. Additional study is needed for other configurations and for two or more space dimensions to establish the ranges of validity and usefulness of this near-constancy of the parameters after the drop.

Using the terminology of the QX1 program,[1] and assuming G neutron energy groups, let the neutron flux $\phi(\mathbf{r},t) \equiv [\phi_1(\mathbf{r},t), \cdots, \phi_G(\mathbf{r},t)]$ be written as the product of an "amplitude function," $N(t)$, and a "shape function" $\psi(\mathbf{r},t) \equiv [\psi_1(\mathbf{r},t), \cdots, \psi_G(\mathbf{r},t)]$. The QX1 time-dependent normalization of $\psi(\mathbf{r},t)$ is that

$$\sum_{g=1}^{G} \int_{all\ space} \psi_{0g}^*(\mathbf{r}) \frac{1}{v_g} \psi_g(\mathbf{r},t)\, d\mathbf{r} \equiv 1 ,$$

where

$$\psi^*(\mathbf{r},0-) \equiv [\psi_{01}^*(\mathbf{r}), \cdots, \psi_{0G}(\mathbf{r})]$$

is the normalized dominant λ-mode adjoint flux eigenfunction in the pre-drop configuration.

Let Σ_g be the group-g effective cross section of t neutron detector for neutron counting at the space position $\mathbf{r}_0$. Assume that the rod drop is very rapid and that after the rod drop is completed the QX1 values of

ρ, β_{eff}, Λ, the effective external source density Q, and also $\sum_{g=1}^{G} \psi_g(\mathbf{r}_0,t)\Sigma_g$ are all time-invariant. The symbol β will be used to represent β_{eff}; the subindex 0 or 2 refers to the pre-drop or after-drop state. Then, within the model of the prompt-drop approximation, and ignoring time derivatives, the QX1 values of Δk_{eff} are given by

$$\Delta k_{0c} = \frac{\beta_0^*}{1-\beta_0^*} \frac{1 - \frac{R_1}{R_0}\left[\frac{\beta_2}{\beta_0^*} R_{02}\right]}{1 - \frac{R_1}{R_2}\left[\frac{1-\beta_2}{1-\beta_0^*}\right]} \tag{3}$$

$$\Delta k_{2c} = \frac{1}{R_{02}} \frac{R_0}{R_2} \Delta k_{0c}. \tag{4}$$

In Eqs. (3) and (4), $\beta_0^* \equiv [Q_0/Q_2]\beta_0$, where Q_0 and Q_2 are the effective external neutron sources in the pre-drop and after-drop systems. The factor $1/R_{02}$ adjusts the pre-drop count rate so as to make it properly comparable with the time-asymptotic post-drop count rate. Note that Eq. (3) includes additional corrections to relate the effective external sources and β_0 when the prompt-drop count rate is used as the third point. The parameter R_{02} is defined by

$$R_{02} \equiv \frac{Q_0}{Q_2} \frac{\ell_0}{\ell_2} \frac{\sum_{g=1}^{G} \psi_g(\mathbf{r}_0, 0-)\,\Sigma_g}{\sum_{g=1}^{G} \psi_g(\mathbf{r}_0, \infty)\,\Sigma_g}.$$

The initial reactivity is defined in QX1 to be the λ-mode reactivity. The final reactivity is not. A comparison of the λ-mode reactivity and the QX1 reactivity has been made for one case involving a change in k_{eff} from 0.98 to 0.96. The QX1 reactivity agreed with the λ-mode value to within one percentage point.

It is interesting that the ratio, Q_0/Q_2, of the effective external sources enters directly only to higher order in the determination of Δk_{2c}, provided

$$1 - \frac{R_1}{R_2}\left[\frac{1-\beta_2}{1-\beta_0^*}\right] \approx 1 - \frac{R_1}{R_2}.$$

The ratio appears as a first-order factor in the determination of Δk_{0c}. Thus, for example, in the artificial case where at time zero the only change is to halve the intensity of the external source, interpretation of the resulting count rate by Eqs. (1) and (2) would give the grossly erroneous result that $\overline{\Delta k_0} \approx \frac{1}{2}\,\Delta k_{0c}$; but $\overline{\Delta k_2} \approx \Delta k_{2c} = \Delta k_{0c}$.

V. Errors in Reactivity Estimations in Equations (1) and (2)

Relative to the QX1 reactivity, the errors inherent in the use of simplified point-kinetics may be determined by comparing $\overline{\Delta k_0}$ with Δk_{0c}, and $\overline{\Delta k_2}$ with Δk_{2c}:

$$\frac{\overline{\Delta k_0}}{\Delta k_{0c}} = \frac{Q_2}{Q_0} \frac{1-\beta_0^*}{1-\beta_0} \frac{1 - \frac{R_1}{R_0}}{1 - \frac{R_1}{R_0}\left[\frac{\beta_2}{\beta_0^*} R_{02}\right]} \frac{1 - \frac{R_1}{R_2}\left[\frac{1-\beta_2}{1-\beta_0^*}\right]}{1 - \frac{R_1}{R_2}} \tag{5}$$

$$\frac{\overline{\Delta k_2}}{\Delta k_{2c}} = R_{02} \frac{\overline{\Delta k_0}}{\Delta k_{0c}}. \tag{6}$$

If the perturbation involves little or no change in Q, then, unless R_1/R_2 is very close to unity, Eq. (5) may be simplified to

$$\frac{\overline{\Delta k_0}}{\Delta k_{0c}} \approx \frac{Q_2}{Q_0} \frac{1 - \frac{R_1}{R_0}}{1 - \frac{R_1}{R_0}\left[\frac{\beta_2}{\beta_0^*} R_{02}\right]}. \tag{5'}$$

Consider now the implications of Eqs. (5) and (6) for perturbations where the change in Q is negligible. The factor R_{02} is a composite of corrections for changes in various parameters from the initial state to the final state. Study of FTR-3-like configurations with the QX1 program has indicated that when the detector was located far from the reactor core some corrections tended to counteract others, so that R_{02} was closer to unity. It is conceivable that for other configurations or details of the experiment the principal corrections might be in the same direction. For such cases R_{02} might be significantly different from unity, and so might be $(\beta_2/\beta_0^*)R_{02}$. When $R_{02} \approx 1$, it might happen that $R_{02} < 1$ and $(\beta_2/\beta_0^*)R_{02} > 1$; in that event $(\overline{\Delta k_0}/\Delta k_{0c}) > 1$ and yet possibly $(\overline{\Delta k_2}/\Delta k_{2c}) < 1$. Typically, however, β_2/β_0^* is much closer to unity than is R_{02}, and $R_{02} - 1$ and $(\beta_2/\beta_0^*)R_{02} - 1$ have the same algebraic sign. In these cases, if Δk_{0c} is overestimated in magnitude then so is Δk_{2c}, and the fractional overestimate of Δk_{2c} is larger. Similarly, if the magnitude of Δk_{0c} is underestimated, then the fractional underestimate in the magnitude of Δk_{2c} is larger.

In some experiments, the principal interest might be in the value of the change in reactivity rather than in the reactivity of the initial configuration or of the final configuration. From Eqs. (5) and (6)

$$\frac{\overline{\Delta k_2} - \overline{\Delta k_0}}{\Delta k_{2c} - \Delta k_{0c}} = \left[\frac{R_{02}\,\Delta k_{2c} - \Delta k_{0c}}{\Delta k_{2c} - \Delta k_{0c}}\right] \frac{\overline{\Delta k_0}}{\Delta k_{0c}}. \tag{7}$$

If $R_{02} > 1$ and also $(\beta_2/\beta_0^*)R_{02} > 1$, then

$$\frac{\overline{\Delta k_2} - \overline{\Delta k_0}}{\Delta k_{2c} - \Delta k_{0c}} > \max\left\{\frac{\overline{\Delta k_0}}{\Delta k_{0c}}, \frac{\overline{\Delta k_2}}{\Delta k_{2c}}\right\} = \frac{\overline{\Delta k_2}}{\Delta k_{2c}} > 1.$$

If $R_{02} < 1$ and also $(\beta_2/\beta_0^*)R_{02} < 1$, then

$$\frac{\overline{\Delta k_2} - \overline{\Delta k_0}}{\Delta k_{2c} - \Delta k_{0c}} < \min\left\{\frac{\overline{\Delta k_0}}{\Delta k_{0c}}, \frac{\overline{\Delta k_2}}{\Delta k_{2c}}\right\} < 1 .$$

VI. Error Amplifications in the 3-Point Method

By waiting long enough to establish quasi-equilibrium conditions, and by averaging over long enough time periods, values of R_0 and R_2 may be found with negligible error. However, the prompt-drop count rate is subject to a number of influences. Taking the partial differences of Δk_{0c} and Δk_{2c} with respect to R_1 in Eqs. (3) and (5), to first order:

$$\frac{\delta(\Delta k_{0c})}{\Delta k_{0c}} = \frac{\dfrac{1-\beta_2}{1-\beta_0^*}\dfrac{R_1}{R_2} - \left[\dfrac{\beta_2}{\beta_0^*} R_{02}\right]\dfrac{R_1}{R_0}}{\left[1 - \dfrac{1-\beta_2}{1-\beta_0^*}\dfrac{R_1}{R_2}\right]\left[1 - \left(\dfrac{\beta_2}{\beta_0^*} R_{02}\right)\dfrac{R_1}{R_0}\right]} \frac{\delta R_1}{R_1} \qquad (8)$$

$$\frac{\delta(\Delta k_{2c})}{\Delta k_{2c}} = \frac{\delta(\Delta k_{0c})}{\Delta k_{0c}} . \qquad (9)$$

Analogously, to first order:

$$\frac{\delta(\overline{\Delta k_0})}{\overline{\Delta k_0}} = \frac{\dfrac{R_1}{R_2} - \dfrac{R_1}{R_0}}{\left[1 - \dfrac{R_1}{R_2}\right]\left[1 - \dfrac{R_1}{R_0}\right]} \frac{\delta R_1}{R_1} \qquad (10)$$

$$\frac{\delta(\overline{\Delta k_2})}{\overline{\Delta k_2}} = \frac{\delta(\overline{\Delta k_0})}{\overline{\Delta k_0}} . \qquad (11)$$

When $(R_1/R_0) \approx 1$ or $(R_1/R_2) \approx 1$, a small fractional error in R_1 is amplified to much larger fractional errors in Δk. The degree of amplification depends on how $\delta R_1/R_1$ varies with the value of R_1.

A second type of error amplification appears in Eqs. (5) and (6), namely, in the failure to account for the errors of simplified point-kinetics. When $(R_1/R_0) \approx 1$, deviation of $(\beta_2/\beta_0^*)R_{02}$ from unity leads to greatly amplified fractional errors in Δk. As observed by Carpenter,[4] however, the ratio $\overline{\Delta k_0}/\Delta k_{0c}$ might be relatively insensitive to changes in R_1/R_0. This may be seen in the situation where $Q_2 = Q_0$ and

$$\frac{\beta_2}{\beta_0^*} R_{02} \approx 1 + C\left[1 - \frac{R_1}{R_0}\right], \quad \text{with } |C| \ll 1.$$

If also

$$\frac{1 - \dfrac{R_1}{R_2}\left[\dfrac{1-\beta_2}{1-\beta_0^*}\right]}{1 - \dfrac{R_1}{R_2}} \approx 1,$$

Eq. (5) implies that

$$\frac{\overline{\Delta k_0}}{\Delta k_{0c}} \approx \frac{1 - \dfrac{R_1}{R_0}}{1 - \dfrac{R_1}{R_0}\left[\dfrac{\beta_2}{\beta_0^*} R_{02}\right]} \approx \frac{1}{1 - C\dfrac{R_1}{R_0}} \approx 1 + C\frac{R_1}{R_0},$$

and so $\overline{\Delta k_0}/\Delta k_{0c}$ would vary much less than R_1/R_0. Nevertheless, error amplification is obvious, for then

$$\frac{1 - \dfrac{\overline{\Delta k_0}}{\Delta k_{0c}}}{1 - \dfrac{\beta_2}{\beta_0^*} R_{02}} \approx \frac{\dfrac{R_1}{R_0}}{1 - \dfrac{R_1}{R_0}}$$

VII. Summary

Two types of errors in single rod-drop measurements of subcriticality have been discussed and formulas of deterministic error analysis have been presented to elucidate

1. errors arising from use of a model of simplified point-kinetics, and error amplification;
2. amplification of error in the prompt-drop count rate, R_1.

There is an essential unifying structure of various IK methods. This structure is shown clearly in the 3-point IK method that utilizes the values of count rates, R_0 and R_2, in the quasi-equilibrium initial and final states, plus the prompt-drop count rate, R_1. Unpublished work by the author has demonstrated specifically that the error analysis exemplified by Eqs. (5) and (6) for the described 3-point method applies well to the Carpenter-Goin IK method.[2] The method of Bennett (see Paper II-27) is a 3-point method also. It is a reasonable conjecture that the method of Cohn[3] (see also Paper II-31) may be subjected to a similar error analysis.

The reference 3-point method is more sensitive to error in R_1 than are IK methods that utilize count-rate data at many different time points. Even for this second type of error, the error analysis for the reference 3-point method may be usefully applied to some other IK methods. Unpublished work by the author has shown that the method of Bennett is basically similar except that the corresponding value of R_1 is obtained as a weighted means of extrapolated values.

References

1. D. A. Meneley, K. O. Ott, and E. S. Weiner, *Fast-Reactor Kinetics—The QX1 Code*, ANL-7769 (1971).
2. S. G. Carpenter and R. W. Goin, *Rod-Drop Measurements of Subcriticality*, Applied Physics Division Annual Report, July 1, 1969, to June 30, 1970, ANL-7710, pp. 206–209.
3. C. E. Cohn, *Experience with Subcriticality Determinations by Rod Drop in the FTR-3 Critical Experiments*. Trans. Am. Nucl. Soc. **14**, 1971, p. 29.
4. S. G. Carpenter, Argonne National Laboratory (private communication).

II-29. Inverse-Kinetics Analysis with Implicit Compensation for Approximations of Point-Kinetics

D. H. Shaftman

Introduction

Paper II-28 discusses certain deterministic errors in inverse-kinetics measurements of reactivity in subcritical systems. One category of error is the use of a simplified point-kinetics model without corrections for the effects of changes in the space and energy distribution of the neutron flux in the perturbed system. It is emphasized in Paper II-28 that a small deviation from unity in a composite correction factor $(\beta_2/\beta_0{}^*)R_{02}$ typically results in amplified errors in the Δk estimates obtained from simplified point-kinetics equations. Therefore, there is an incentive to develop an inverse-kinetics (IK) method that implicitly makes corrections for these errors of simplified point-kinetics. Alternatively, from other measurements and from reactor physics calculations, correction factors could be inferred.

The IK method described in this paper analyzes the after-drop count rate in a rod-drop experiment to obtain the reactivity of the final state. No independent knowledge is needed of the values of β_2/β_0, ℓ_0/ℓ_2 (or Λ_0/Λ_2), and changes in the QX1 shape function of the neutron flux. Indeed, this IK method supplies a value for the composite factor needed to adjust the predrop count rate, R_0, so as to make it properly comparable with the after-drop data (see Paper II-28). However, to obtain the reactivity of the initial state, the ratio of effective external sources, Q_0/Q_2, is needed.

A computer program has been prepared to test the method in the presence of statistical fluctuations in count-rate data.[1] A limited computer simulation of sets of "noisy runs" has indicated that, in the present (least-squares) formulation, reactivity estimates inferred might be quite sensitive to the fluctuations, and especially fluctuations in the count-rate data at times close to $t = 0$. It should be considered, therefore, that the purpose of this paper is to describe the principles of the method. Its usefulness for practical application to a broad range of rod-drop measurements in systems of interest is yet to be established.

Deterministic Neutron-Kinetics Equations for the After-Drop Count Rate in Subcritical Multiplying Systems

Consider a quasi-equilibrium, subcritical multiplying stem with a constant external neutron source. Assume that at time zero step-function changes are made and that the final state is subcritical with different reactivity. Assume multigroup diffusion theory with G neutron-energy groups and m groups of delayed-neutron precursors. Let the space-time neutron flux be written as the product $\phi \equiv N(t)\psi(\mathbf{r},t)$, where $N(t)$ is an "amplitude function" and $\psi(\mathbf{r},t) \equiv [\psi_1(\mathbf{r},t), \cdots, \psi_G(\mathbf{r},t)]$ is a "shape function". In this model, the amplitude function is defined as the real solution of QX1-type point-kinetics equations in the after-drop system (see Ref. 2):

$$\frac{dN(t)}{dt} = \frac{\rho^* - \beta}{\Lambda} N(t) + \sum_{i=1}^{m} \lambda_i \eta_i(t) + Q \qquad (1)$$

$$\frac{d\eta_i(t)}{dt} = \frac{\beta_i}{\Lambda} N(t) - \lambda_i \eta_i, \qquad 1 \leqq i \leqq m. \qquad (2)$$

Let $R(t) \equiv N(t) \sum_{g=1}^{G} \psi_g(\mathbf{r}_1,t)\Sigma_g$ be a neutron counting rate with detection at space position $\mathbf{r}_1$, for times $t > 0$. In Eqs. (1) and (2), ρ^* is the reactivity (QX1), Q is the effective neutron source, and the β_i's are the effective values of the precursor-group β's of the after-drop system. Assume that at all times $t > 0$ all of these parameters and also $\sum_{g=1}^{G} \psi_g(\mathbf{r}_1,t)\Sigma_g$ are time invariant. Approximate $dN(t)/dt$ by zero.

With the indexing 0 (zero) and 2 (two) to represent the quasi-equilibrium pre-drop state and post-drop state, respectively, the solution of Eq. (2) is

$$\eta_i(t) = \exp(-\lambda_i t) \cdot \left[\eta_{i_0} + \frac{\beta_{i_2}}{\Lambda_2} \int_{0+}^{t} du \exp(\lambda_i u) N(u)\right], \qquad (3)$$

where

$$\eta_{i0} = \frac{1}{\lambda_i} \frac{\beta_{i_0}}{\Lambda_0} N_0, \qquad N_0 \equiv N(0-).$$

Substituting Eq. (3) into Eq. (1) and multiplying by $\sum_{g=1}^{G} \psi_g(\mathbf{r}_1,0+)\Sigma_g$,

$$0 = \left[\frac{\rho_2^* - \beta_2}{\Lambda_2}\right] R(t) + \frac{\beta_2}{\Lambda_2}\left[\frac{\beta_0}{\beta_2}\frac{1}{S_{02}} R_0\right] \sum_{i=1}^{m} \frac{\beta_{i_0}}{\beta_0} \exp(-\lambda_i t) + \frac{\beta_2}{\Lambda_2} \sum_{i=1}^{m} \lambda_i \frac{\beta_{i_2}}{\beta_2} \exp(-\lambda_i t) \int_{0+}^{t} du \exp(\lambda_i u) R(u) \qquad (4)$$
$$+ Q_2 \sum_{g=1}^{G} \psi_g(\mathbf{r}_1,0+)\Sigma_g.$$

In Eq. (4), $R_0 \equiv N_0 \sum_{g=1}^{G} \psi_g(\mathbf{r}_1,0-)$ is the (assumed-constant) count rate at $\mathbf{r}_1$ for times $t < 0$, and

$$S_{02} \equiv \frac{\Lambda_0}{\Lambda_2} \frac{\sum_{g=1}^{G} \psi_g(\mathbf{r}_1,0-)\Sigma_g}{\sum_{g=1}^{G} \psi_g(\mathbf{r}_1,0+)\Sigma_g}.$$

Note that $(\beta_2/\beta_0)S_{02} = (k_2/k_0)(\beta_2/\beta_0^*)R_{02}$. (See Paper II-28.)

Equation (4) may be abbreviated:

$$0 = X_1R(t) + X_2F(t) + X_3G(t) + X_4, \quad (5)$$

where

$$X_1 \equiv \frac{\rho_2^* - \beta_2}{\Lambda_2}$$

$$X_2 \equiv \frac{\beta_2}{\Lambda_2}\left(\frac{\beta_0}{\beta_2}\frac{1}{S_{02}}R_0\right)$$

$$X_3 \equiv \frac{\beta_2}{\Lambda_2}$$

$$X_4 \equiv Q_2\sum_{g=1}^{G}\psi_g(\mathrm{r}_1,0+)\Sigma_g$$

$$F(t) \equiv \sum_{i=1}^{m}\frac{\beta_{i_0}}{\beta_0}\exp(-\lambda_i t)$$

and

$$G(t) \equiv \sum_{i=1}^{m}\lambda_i\frac{\beta_{i_2}}{\beta_2}\exp(-\lambda_i t)\int_{0+}^{t} du\exp(\lambda_i u)R(u).$$

Given data of R_0 and of $R(t)$ for $t > 0$, and input values of the λ_i, β_{i0}/β_0, and β_{i2}/β_2, evaluate Eq. (5) at four different values of t to get a set of four linear algebraic equations in the four unknowns X_1, X_2, X_3, and X_4. Equation (5) is homogeneous and so the X_j are determined only to within a scalar multiple. However, ratios of parameters are unambiguous:

$$\frac{\rho_2^* - \beta_2}{\beta_2} = \frac{X_1}{X_3} \quad \text{and} \quad \frac{\beta_0}{\beta_2}\frac{1}{S_{02}}R_0 = \frac{X_2}{X_3}. \quad (6)$$

With appropriate definitions of the parameters, Eqs. (1) and (2) apply also to the pre-drop system, yielding

$$\frac{\rho_0^*}{\beta_0} = -\frac{1}{\beta_0}\frac{Q_0\Lambda_0\sum_{g=1}^{G}\psi_g(\mathrm{r}_1,0-)\Sigma_g}{R_0} = -\frac{Q_0}{Q_2}\frac{X_4}{X_2}. \quad (7)$$

Even if Q_0/Q_2 is unknown, $\rho_2^*/\beta_2 = (X_1/X_3) + 1$ is known. If also Q_0/Q_2 is known, then $\rho_0^*/\beta_0 = -(Q_0/Q_2)(X_4/X_3)$ is obtained.

Calculation of Reactivities in Non-Deterministic Systems

The parameters X_1 to X_4 could be evaluated also from the four linear algebraic equations obtained by integrating Eq. (5) over four time intervals $[t_1,t_2]$, $[t_3,t_4]$, $[t_5,t_6]$, and $[t_7,t_8]$, following the rod drop:

$$\begin{aligned} 0 &= X_1\int_{t_j}^{t_{j+1}} du\,R(u) \\ &+ X_2\sum_{i=1}^{m}\frac{1}{\lambda_i}\frac{\beta_{i_0}}{\beta_0}[\exp(-\lambda_i t_j) - \exp(-\lambda_i t_{j+1})] \\ &+ X_3\sum_{i=1}^{m}\lambda_i\frac{\beta_{i_2}}{\beta_2}\int_{t_j}^{t_{j+1}} du\exp(-\lambda_i u)\int_{0+}^{u} dv\exp(\lambda_i v)R(v) \\ &+ X_4(t_{j+1} - t_j). \end{aligned} \quad (8)$$

Using integration by parts, the third term on the right hand side of Eq. (8) can be reduced to a function of simple convolution integrals of the form of $G(t)$, defined above. Further, applying integration by parts to the convolution integrals one obtains an equation involving integrals of the form

$$\int du\,R(u) \quad \text{and} \quad \int du\exp(\lambda_i[u - t])\int_a^u dv\,R(v).$$

In the presence of statistical fluctuations in the time record of count rate, the smoothing characteristics of time integration exemplified by Eq. (8) offer an alternative solution. More generally, least-squares techniques could be applied to evaluate the X_j, using either Eq. (5) or Eq. (8) as the basis.

References

1. S. G. Carpenter, Argonne National Laboratory (private communication). C. E. Cohn, Argonne National Laboratory (private communication).
2. D. A. Meneley, K. O. Ott and E. S. Wiener, *Fast-Reactor Kinetics—The QX1 Code*, ANL-7769 (1971).

II-30. An Analysis of Subcritical Reactivity Measurements Using Pulsed-Neutron Techniques

W. Y. Kato and D. A. Meneley

Introduction

It is important to be able to measure the subcriticality of fast reactors when the system is \$20 to \$30 subcritical. This is so because at the beginning of life of a core it is necessary to have about \$25 excess reactivity bui into the system, and this must be held down by shim rods at startup. When refueling becomes necessary, it must be done with the shim rods inserted and the sys-

tem subcritical by \$20 to \$30. In order to accomplish refueling in a safe manner it is important to know the subcriticality of the system accurately at the end of life of the core.

The subcriticality of both thermal and fast reactors has been determined by such techniques as rod drop, inverse kinetics, and source multiplication which basically depend on observing delayed neutron effects, and those techniques which observe the decay of prompt fission chains.[1-3] The latter experiments fall broadly into two categories: the Rossi-alpha type where one observes the decay of fission chains which arise from neutrons of spontaneous fission, external source, or cosmic-ray origin, and the pulsed-neutron type where one observes the decay of prompt neutrons which have been produced by a neutron burst or pulse from an external source. Noise measurements, such as the cross power spectral density[2] measurements which observe the break frequency of the transfer function, fall in the former category. Both categories depend on the existence of a fundamental mode (attainment of equilibrium spectrum) during the decay process when measurements are attempted when the reactor is far subcritical. Both categories also assume the linearity of alpha [$\alpha = (\rho - \beta)/\Lambda$ where ρ is the reactivity, β the total effective delayed neutron fraction, and Λ the neutron generation time] with reactivity.

Description of Analysis

In the case of fast reactors, questions have been raised regarding the existence of a fundamental mode far subcritical.[4] In order to obtain a better understanding of subcritical reactivity measurements of fast systems we have used the principles outlined by Preskitt et al.[3] and carried out a series of numerical calculations simulating a pulsed-neutron experiment similar to the work of Brickstock et al.[5] The calculations were done using the recently developed one-dimensional, multigroup diffusion, space-dependent kinetics code, QX1.[6] The code determines the prompt-decay mode as defined by Preskitt et al.[3] and is capable of identifying the domain in which no single decay mode exists.

Two fast reactor configurations which had substantially different neutron lifetimes were investigated. One configuration simulated the FTR-3[7] reactor core in one dimension with a ring of boron safety rods between the outer core and the nickel reflector as shown in Fig. II-30-1. The second core simulated a reactor (FFTF-FMC core) having the boron safety rods in a region between the inner and outer cores instead of in the reflector as shown in Fig. II-30-2. The atom densities used in the calculations for the core and reflector regions for typical cases for the two configurations are given in Table II-30-I. The same volume fractions were maintained for the fuel, coolant and structural materials for the various regions for the two cases. Only the boron ring was moved from between the outer core and reflector in the first case to between the inner and outer cores in the second case. The subcriticality of the two

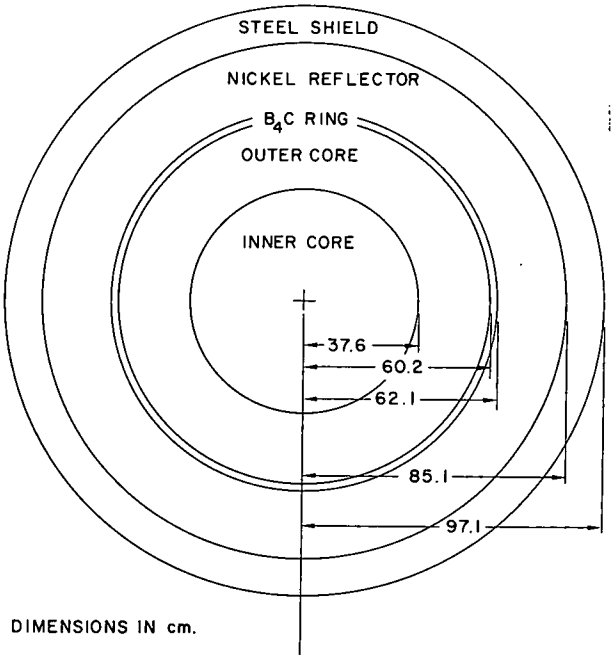

Fig. II-30-1. Reactor Configuration with Boron Ring between Outer Core and Reflector. *ANL Neg. No. 116-1060.*

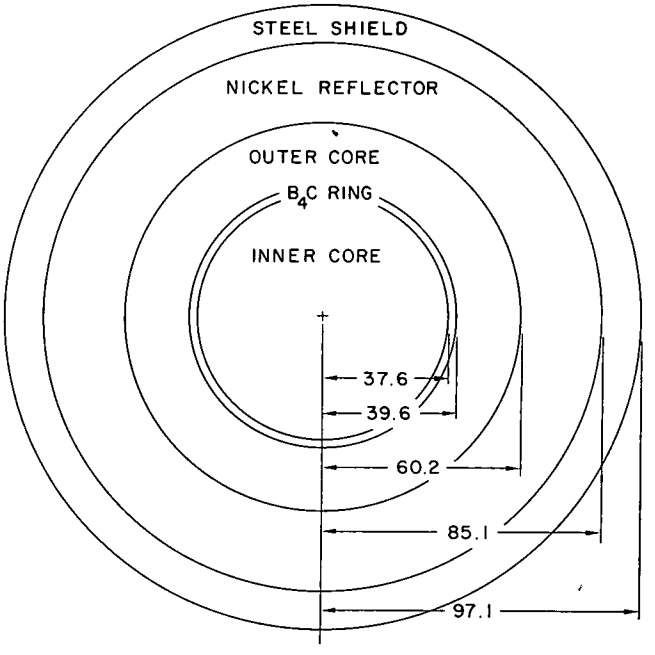

Fig. II-30-2. Reactor Configuration with Boron Ring between Inner and Outer Core. *ANL Neg. No. 116-1061.*

TABLE II-30-I. ATOM DENSITIES, 10^{22} atoms/cc

	^{239}Pu	^{240}Pu	^{241}Pu	^{238}U	^{235}U	O	C	Fe	Ni	Cr	Mn	Mo	Na	^{10}B
Reactor with Boron Ring between Inner and Outer Core														
Inner core	0.1134	0.00825	0.00111	0.4234	0.000943	1.1306	0.003026	1.3066	0.1551	0.3250	0.02386	0.01172	1.0432	
B_4C safety rod							5.7527	1.1320	0.1553	0.3254	0.0239	0.00105	0.4126	1.0601
Outer core	0.1731	0.0175	0.00245	0.5635	0.00125	1.2717	0.1069	1.5907	0.1507	0.3159	0.0232	0.04412	0.8701	
Nickel reflector								0.8720	4.8072	0.2432			0.6754	
Steel shield								3.9849	0.5372	1.1258			0.6754	
Reactor with Boron Ring between Outer Core and Reflector														
Inner core	0.09832	0.00825	0.00111	0.4385	0.000943	1.1306	0.003026	1.3066	0.1551	0.3250	0.02386	0.01172	1.0432	
Outer core	0.1500	0.0175	0.00245	0.5865	0.00125	1.2717	0.1069	1.5907	0.1507	0.3159	0.0232	0.04412	0.8701	
B_4C safety rod							5.7527	1.1320	0.1553	0.3254	0.02389	0.00105	0.4126	1.0601
Nickel reflector								0.8720	4.8072	0.2432			0.6754	
Steel shield								3.9849	0.5372	1.1258			0.6754	

systems was varied by modifying the ^{239}Pu and ^{238}U atom densities.

Three types of numerical calculations with a ten-energy group structure were made using the QX1 code for each of the two reactor configurations to determine alpha as a function of subcriticality: (1) a solution of the homogeneous (source free) diffusion equation; (2) a solution of the inhomogeneous equation with a source term representing the spontaneous fission neutrons from ^{240}Pu; and (3) a solution of the inhomogeneous equation in a dynamic mode, an alpha/velocity type solution at many time intervals with an external 1-μsec width pulsed neutron source. Ten-group cross sections which had been obtained using the MC^2 code and the ENDF/B microscopic cross section library were used in the calculations.

Alpha for the two static cases was calculated using the relationship $\alpha = (\rho - \beta)/\Lambda$. These alphas are designated as the static alphas without source and with source. The dynamic alpha was obtained by calculating the time derivative of a ^{235}U fission reaction rate $\Sigma_f(E)$-$\phi(t,E)$ within the range of an almost constant logarithmic slope. The ^{235}U fission rate was chosen to simulate the use of a fission detector in an actual measurement. Provided an asymptotic prompt-decay mode exists, the result of the latter type of calculation is equivalent to that obtained by Murley[8] in calculating the neutron lifetime for a critical system.

RESULTS

A typical reaction rate decay curve for the reactor system which has the boron carbide safety rods in the outer core region and is about \$20 subcritical is shown in Fig. II-30-3. The reaction rates and alpha as a function of time are plotted for two different positions in the reactor. It can be seen that it takes about eighty microseconds after the neutron pulse before a quasi-equilibrium condition is reached. This quasi-equilibrium was obtained with a 1 μsec wide neutron pulse of approximately 6×10^{11} neutron/sec intensity introduced at the center of the core. This can be compared with the 10^{10} and 10^{11} neutrons/sec source intensities which can be obtained from conventional Cockroft-Walton type D-T reaction sources. In this calculation there was a background source due to the spontaneous fission of ^{240}Pu and the background reaction rate due to this source is also shown in Fig. II-30-3. The initial pulsed source intensity must be sufficiently greater than the background source in order to attain a quasi-equilibrium condition. In Fig. II-30-4 is shown the reaction rate decay curve for the case when the system was only about \$2 subcritical. Because of the smaller value of alpha the fundamental mode persists for a greater length of time. The values of alpha as a function of time are also plotted in the two curves.

The results of the alpha calculations as a function of subcriticality for the two reactor configurations are shown in Fig. II-30-5. The upper three curves represent the alphas calculated from the reactor configuration where the safety rods are in the outer core. The static alphas obtained from the source free (homogeneous solution) calculation represents the usual assumption of linearity made for pulsed neutron experiments to measure the subcriticality of a system. This calculation in effect assumes that the spectrum is invariant for various degrees of subcriticality. The solid circles represent static alphas obtained by including the spontaneous fission source from ^{240}Pu as a source term in the calculation. The triangles represent the dynamic alpha values, alpha being the parameter that is measured in a pulsed neutron type or Rossi alpha type experiment.

Fig. II-30-6 shows the alpha calculations plotted in

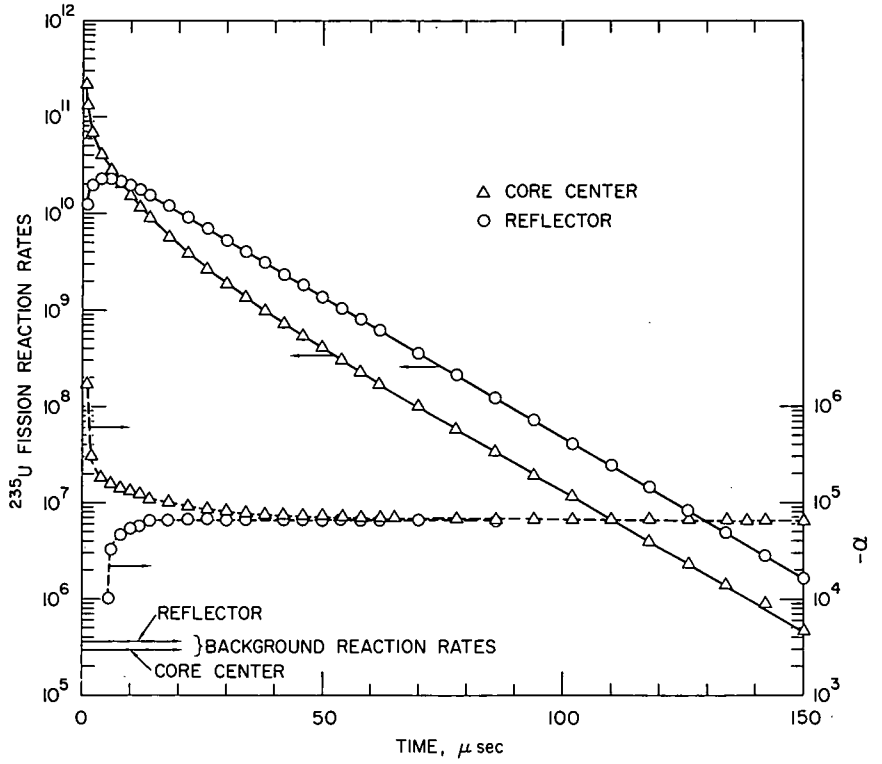

FIG. II-30-3. Reaction Rate and Alpha Versus Time. The Reactor Is \$20 Subcritical. *ANL Neg. No. 116-1046.*

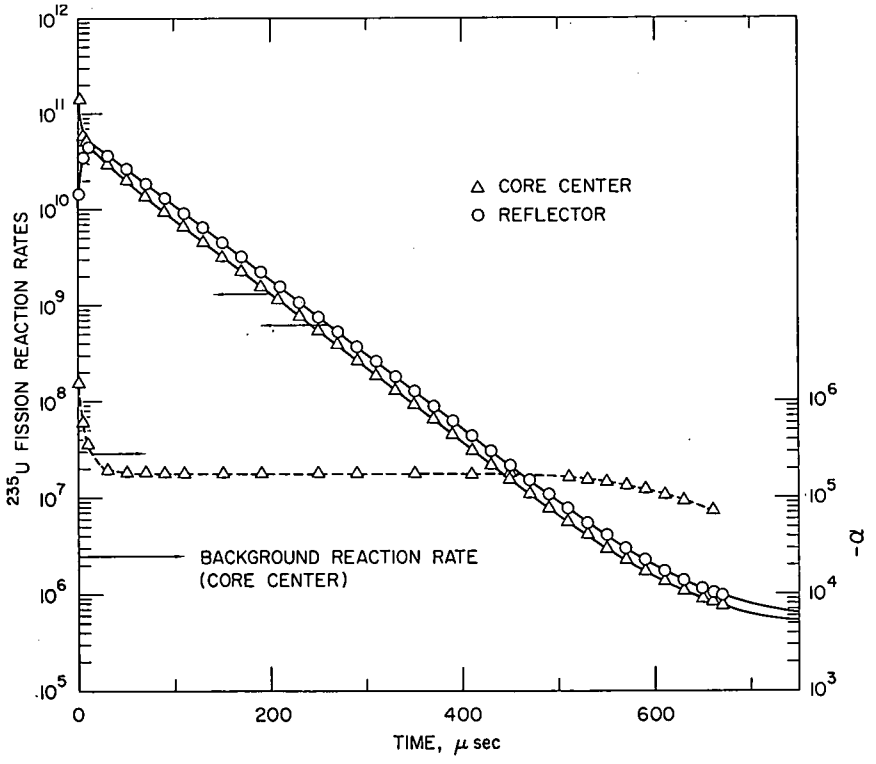

FIG. II-30-4. Reaction Rate and Alpha Versus Time. The Reactor Is \$2.3 Subcritical. *ANL Neg. No. 116-1047.*

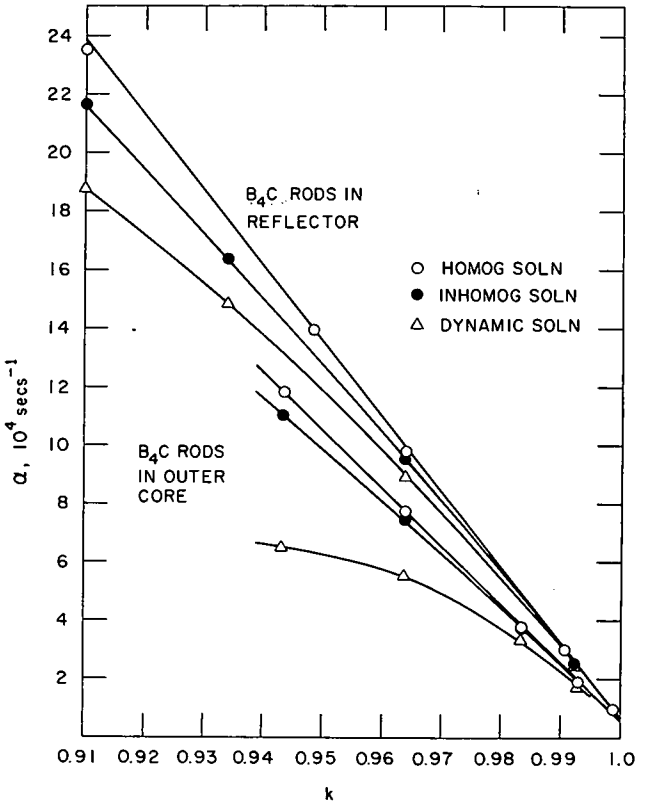

FIG. II-30-5. Alpha Versus Reactivity. *ANL Neg. No. 116-836.*

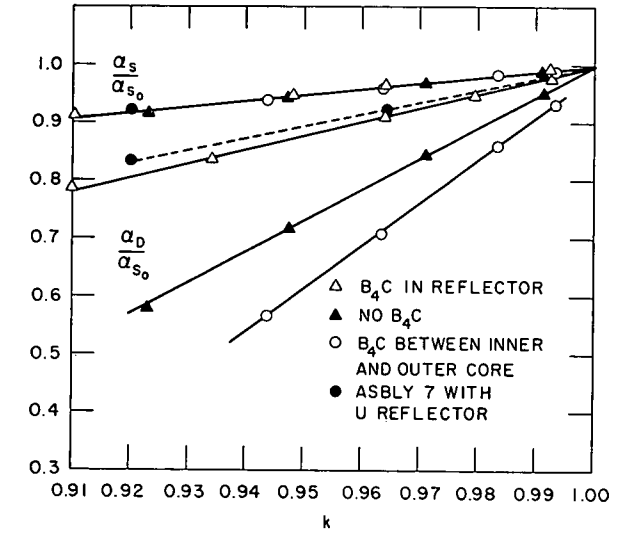

FIG. II-30-6. Alpha Ratios Versus Reactivity. *ANL Neg. No. 116-1062.*

a different manner. The ratios of the dynamic alpha to the static alpha without source have been plotted for four different reactor configurations. In addition to the two reactor configurations previously mentioned, results of calculations for the case with no B_4 safety rods and a case for an assembly with a uranium reflector (ZPR-6 Assembly 7)[9] are also plotted.

Conclusions

The conclusions which can be drawn from the results are:

(1) With this model a spectrum which is in quasi-equilibrium is found in the reactor as far as \$25 subcritical.

(2) With increasing degrees of subcriticality the quasi-equilibrium spectrum of the prompt-neutron decay undergoes spectral distortion, becomes progressively softer in the core, and is substantially different from that calculated at critical or from an inhomogeneous statics calculation. The neutron lifetime, therefore, increases substantially for the softer spectrum of the dynamic case because of the 1/v weighting.

(3) There is less spectral distortion of the quasi-equilibrium spectrum for cores having a uranium or other heavy element reflector which does not degrade the spectrum appreciably.

(4) In the nickel reflected systems the dynamic alpha departs increasingly from linearity for greater degrees of subcriticality. In order to measure the subcriticality of fast systems using the pulsed neutron or other techniques which observe the decay of prompt-fission chains, it is necessary to know the functional relationship between alpha and reactivity as noted by Preskitt et al.[3] for thermal systems. Some of the other techniques which also observe the decay of prompt fissions and which have the same difficulty are: Rossi alpha, noise analysis methods which measure the roll-off or break frequency, and the cross power spectral density method which measures the quantity β/ℓ.

References

1. G. R. Keepin, *Physics of Nuclear Reactors*, (Addison Wesley Publishing Co., Inc., Reading, Massachusetts, 1965).
2. R. E. Uhrig, *Random Noise Techniques in Nuclear Reactor Systems*, (Ronald Press Company, New York, 1970).
3. C. A. Preskitt et al., *Interpretation of Pulsed-Source Experiments in the Peach Bottom HTGR*, Nucl. Sci. Eng. **29**, 283 (1967).
4. F. Storrer and M. Stievenart, *Contribution to the Theory of the Pulsed Neutron Technique Applied to Fast Multiplying Systems*, EUR-593 (1964).
5. A. Brickstock, A. R. Davies and I. C. Smith, *A Time-Dependent Multigroup Diffusion Code with Automatic Resonance Self-Shielding of Cross Sections*, Proc Conference on Application of Computing Methods to Reactor Prol lems, ANL-7050, 413 (1965).
6. K. O. Ott and D. A. Meneley, *Accuracy of the Quasistatic Treatment of Spatial Reactor Kinetics*, Nucl. Sci. Eng. **36**, 402 (1969).

7. J. W. Daughtry et al., *Experimental Results from the FTR-3 Critical Assembly Program*, Trans. Am. Nucl. Soc. **14**, (1971).
8. T. E. Murley, *Calculating the Prompt-Neutron Lifetime in Fast Reactors*, Trans. Am. Nucl. Soc. **10**(1), 268 (1967).
9. L. E. LeSage, E. M. Bohn, J. E. Marshall, R. A. Karam, C. E. Till, R. A. Lewis and M. Salvatores, *Initial Experimental Results from ZPR-6 Assembly 7, The Single Zone Demonstration Reactor Benchmark Assembly*, Trans. Am. Nucl. Soc. **14**, 17 (1971).

II-31. Subcriticality Determination by Rod Drop in the FTR-3 Critical Experiments

C. E. Cohn

Introduction

The rod drop method has been used to perform a large number of subcriticality measurements on various core configurations for the Fast Test Reactor (FTR)-3 critical experiment program. In the process, advances have been made in the theory and practice of these measurements.

Such a measurement starts with the reactor at equilibrium in its most reactive subcritical configuration. Reactivity is rapidly removed by scramming one or more rods. The neutron flux is monitored by an on-line digital computer[1] until equilibrium is approximately reestablished.

The resulting flux record is processed by an inverse kinetics algorithm to yield a reactivity record. In doing this a value must be assumed for the neutron source in the assembly that is being multiplied to yield the observed flux level. The validity of that source guess is checked by observing the reactivity record after rod motion stops. The actual reactivity is constant at that time so the reactivity record should also be constant. Therefore, the inverse kinetics calculation is repeated to search for a source value yielding a reactivity record that is most nearly constant. The final result is obtained from an average over the reactivity record preceding the drop.

In effect, the ratio of count rates before and at long times after the drop gives the ratio of multiplications before and after the drop. The source value then allows the correct scale factors to be put on the multiplications, thus yielding the reactivities.

The source search is complicated by the statistical fluctuations in flux. As a result of these the source value finally selected contains an error. This difficulty is aggravated at greater subcriticalities where the effect of the delayed neutrons is relatively smaller. Figure II-31-1 gives an insight into this problem. Here are calculated flux traces from three instantaneous rod drops that have the multiplication but that start from widely different subcriticalities. The three traces are distinguishable only by slight differences in the delayed neutron decay right after the drop. That decay is all the information available for determination of the source value.

As compared with some other methods of subcriticality measurement, such as noise, multiplication, or pulsed neutrons, the rod drop method does work with somewhat thin information. On the other hand, it does not depend on a reference measurement at or near critical and requires fewer assumptions about the kinetics of the assembly or the invariance of certain quantities.

Source-Search Scheme

The algorithm used for the source search must have adequate discrimination in the presence of statistical

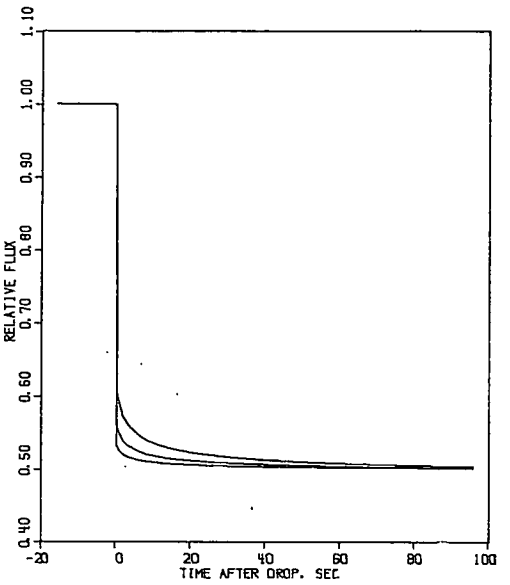

Fig. II-31-1. Calculated Flux Traces from Three Instantaneous Rod Drops. The Upper Curve Is a Drop from −0.5% k to −1%, the Middle Curve Is a Drop from −1% to −2% and the Lower Curve Is a Drop from −2% to −4%. *ANL Neg. No. 116-749.*

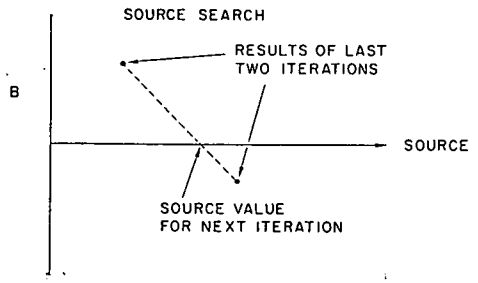

FIG. II-31-2. Source-Search Scheme. *ANL Neg. No. 116-753.*

fluctuations and must be free from bias. In the scheme chosen the function $\Delta k(t) = A + BF(t)$ is fitted to the calculated reactivity after the drop. A source value is sought such that the amplitude B of the time dependent part $F(t)$ is zero. Two different forms have been used for $F(t)$. Our earlier work used a simple straight line $F(t) = t$ while we are currently using a sum of decaying exponentials $F(t) = e^{-0.013t} + 8.05e^{-0.031t} + 7.14e^{-0.136t} + 13.31e^{-0.344t}$. The sum of exponentials is a better approximation to the actual shape of the reactivity curves and does give about 25 % better precision in the result.

Figure II-31-2 shows how the search actually proceeds. A straight line in source-amplitude space is drawn between the results of the last two iterations. The source value at which that line crosses the source axis is used for the next iteration.

An error in the amplitude is estimated by the usual least squares method. The search is terminated when the amplitudes of the last two iterations differ by less than one percent of this error. The procedure requires two starting source values. One of these is taken as zero, while the other is derived from a subcriticality guess supplied by the operator.

Some source search schemes used by other workers have been tried and discarded because of various difficulties. One of these searched for the source value that gave a minimum in the sum of squares of deviations of the reactivity after the drop about an average. This lacked sensitivity. The other scheme fit a straight line to reactivity after the drop versus inverse flux and derived a correction to the source value from the slope of that line. This introduced a bias resulting from the correlations between the fluctuations in flux and the resulting fluctuations in reactivity.

Simulation Studies

Some computer simulations have been done to study the properties of the technique. For these, noisefree flux profiles were developed by a point reactor direct kinetics algorithm.[2] These flux profiles were perturbed by noise simulated by pseudorandom Gaussian variates. The rms amplitude of these variates was made to correspond to the counting statistics obtained in actual measurements, that is, of the order of 100,000 counts/sec at one percent subcritical. However, the lack of correlation between variates corresponded to the somewhat unrealistic situation of detection noise rather than reactor noise predominating.

In these simulations 2200 flux points were taken as in the actual measurements with 100 flux points occurring before the start of the rod drop. The rods were assumed to drop linearly in 0.2 sec. For each configuration the process was replicated 100 times.

The conclusions resulting from these simulations were as follows:

Application of the rod drop code to noise free flux profiles returned the correct subcriticality to four significant figures. For the noisy cases, magnitudes of drop greater than one-half percent made little difference in precision for either one percent or two percent subcriticality, while smaller drop magnitudes gave poorer precision. Furthermore, the flux must be followed for at least 100 sec after the drop to obtain optimum precision. On the other hand, the time between the end of the rod drop and the start of the reactivity fit did not seem too critical. Delays of as much as one second had little effect. Finally, the sum of exponentials fit gave about 25 % better precision than the straight-line fit.

Instrumentation

The actual measurements had been done at first using existing reactor instrumentation to obtain flux data. This consisted of a boron-loaded ion chamber mounted on the matrix structure and connected to a current amplifier in the control room. The output of the current amplifier went to a voltage-to-frequency converter, and the output of the converter was counted in a data scaler attached to a digital computer. The scaler was read and reset at time intervals determined by a crystal-controlled time mark generator. In the process, a number of deficiencies of that instrumentation became evident. The ion chamber, being mounted on the matrix structure, was unduly subject to microphonic disturbances from the rod scrams. To alleviate that, it was replaced by a bank of four chambers mounted just over the matrix but isolated from it.

With the current amplifier remote from the chamber, significant amounts of 60-Hz hum were induced by ground loops at its input. To alleviate that, a new current amplifier was constructed with remote range switching capabilities. It was placed directly adjacent to the chambers. This greatly reduced hum pickup by eliminating ground loops and transmitting the signal to the control room at a low impedance level. However, some hum still remained. This was handled by making

the data scaler readout coherent with the ac line. That is, the time mark generator was removed. The readout control pulses were obtained by scaling the output of a Schmitt trigger with ac input. Each scaler reading then represented an integral over one or more complete cycles of the hum, cancelling out the hum contribution. Most of the later measurements have used a sampling interval of $\frac{1}{15}$ sec. By comparison of measurements with different sampling times, it was established that no error is introduced by a sampling time as long as this.

The performance of this bank of ionization chambers was compared with the performance of an in-core glass scintillator of the type used for noise measurements (see Paper II-32). There was a high degree of correlation, from 30 to 70%, between the flux readings in the two detectors. This indicated that the fluctuations in the output of the two detectors arose primarily from reactor noise rather than from detection statistics. This implied that further increases in detection efficiency would not be profitable in improving the precision of the rod drop measurements. Furthermore, the in-core scintillation detector was quite severely perturbed by microphonics.

Results

A large number of rod drop measurements were made in the course of the FTR-3 program. For each subcritical configuration, flux readings were taken from seven different detectors distributed throughout the assembly. These flux readings can be considered as indicators of multiplication and can be compared with subcriticality as indicated by the rod drops. Figure II-31-3 shows such a comparison for one detector which was located in the axial reflector about half way between the center and the edge of the core. Here the abscissa is the subcriticality in inhours measured by rod drop. The ordinate is the inverse of the detector reading in arbitrary units. The straight line is a weighted least squares fit constrained to go through the origin. If the rod drop measurements were perfect indicators of subcriticality, and if the detector readings were perfect indicators of multiplication all points would lie on the line. The degree of agreement seen here was apparently limited to just this one detector. Figure II-31-4 shows considerably poorer agreement for a detector located in the radial reflector at the mid-plane. The agreements for the other detectors lay in between these extremes. It may be noted that the deviations are not systematic. They are believed to arise from changes in detector efficiency resulting from configuration changes.

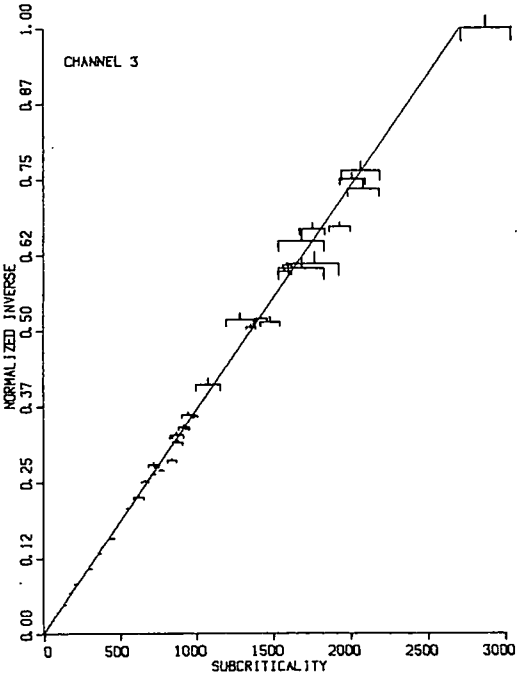

Fig. II-31-3. Comparison between Rod-Drop and Multiplication Measurements Showing Good Agreement. *ANL Neg. No. 116-751.*

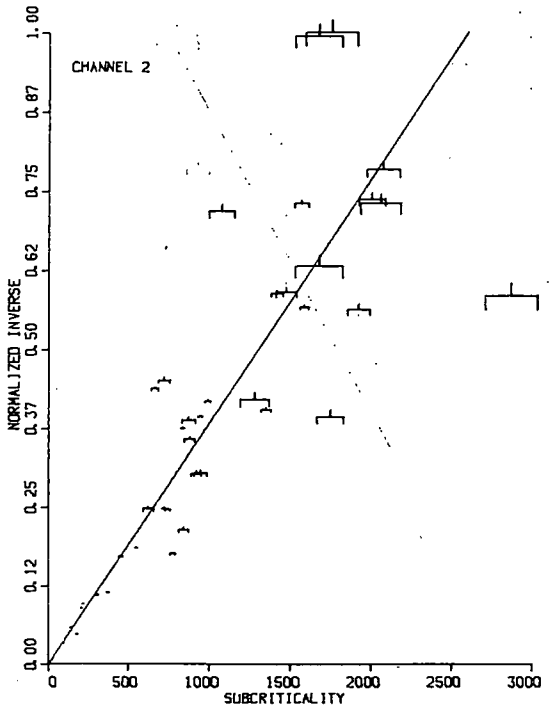

Fig. II-31-4. Comparison between Rod-Drop and Multiplication Measurements Showing Poor Agreement. *ANL Neg. No. 116-748.*

Figure II-31-5 shows the same plot for the detector that was used for the rod drops. Note that the rod drops, unlike multiplication, do not require detector efficiency to be constant with respect to a reference measurement. They only require constant detector efficiency through the rod drop itself.

For each point of these graphs, the error bar indicates

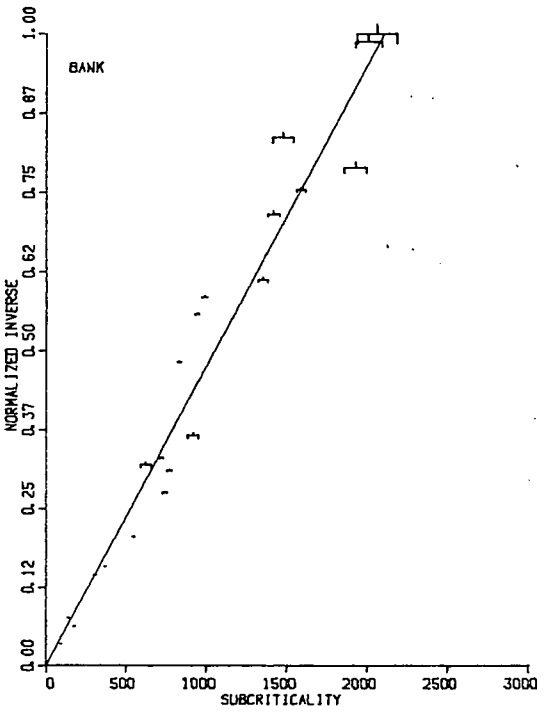

FIG. II-31-5. Comparison between Rod-Drop Measurements and Multiplication Measurements Taken with the Same Detector Used for the Rod-Drop Measurements. *ANL Neg. No. 116-750.*

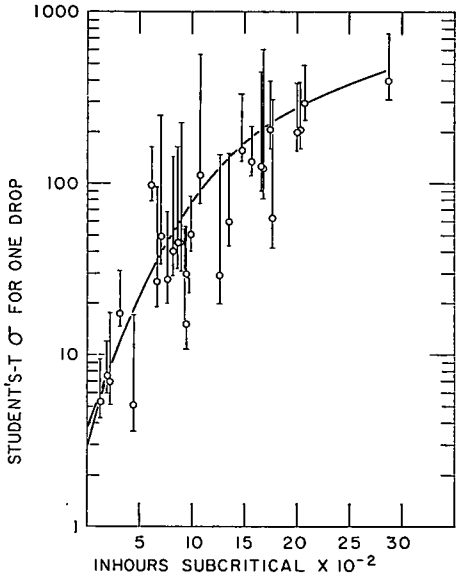

FIG. II-31-6. Error in Inhours in a Rod-Drop Measurement as a Function of Initial Subcriticality. *ANL Neg. No. 116-754.*

an estimate of the error on the rod-drop subcriticality. The straight-line fit was weighted in accordance with these errors. Figure II-31-6 shows how the errors were obtained. For various configurations six or more drops were made. From these the standard deviation of a single measurement was estimated by Student's-T. The error bars shown are the uncertainties of the estimates. The curve is an eyeball fit and was used to estimate the error for runs where a number of drops were not taken. These errors are of the same order of magnitude as those reported by others.[3]

As a further check on the validity of the inverse kinetics technique, some positive reactivity insertions were done and the inverse kinetics results were compared with period measurements reduced by the Hurlimann-Schmid technique.[4] These insertions started at equilibrium at about 14 inhours subcritical and ended from 6 to 16 inhours supercritical. Very good agreement was obtained between the two methods. Good agreement between period and inverse kinetics results has also been our experience in uranium assemblies.

There is a fundamental difficulty in the interpretation of period measurements in plutonium assemblies. This difficulty is not present when the inherent source is negligible. Where a source is present, a reactor on an asymptotic period has flux behavior given by $n(t) = Ae^{Bt} - C$, i.e., a rising exponential minus a constant. The constant arises from the source. There are three parameters to be determined, namely A, B and C. This expression may be expanded in Taylor's series to give $n(t) = A - C + ABt + \mathcal{O}(t^2)$. Where the period is slow and the total measuring time short, the higher order terms will be small and the flux will be almost a straight line. That situation will be indeterminate because three parameters are to be fit while a straight line gives information about only two. Without a source, obviously, the third parameter is not present so there is no indeterminacy. In measurements with a source, the only information available is in the higher order terms, that is, in the curvature of the flux trace. To maximize this information, a period measurement should be run for a long enough time to cover as wide a range of flux magnitudes as possible.

REFERENCES

1. C. E. Cohn, *Automated Data Analysis and Control for Critical Facilities*, Proc. Symposium on Use of Computers in Analysis of Experimental Data and the Control of Nuclear Facilities, Argonne National Laboratory, Argonne, Illinois, May 4–6, 1966, AEC Symposium Series 10, CONF-660527, pp. 49–66.
2. J. J. Kaganove, *Numerical Solution of the One-Group, Space-Independent Reactor Kinetics Equations for Neutron Density Given the Excess Reactivity*, ANL-6132 (1960).
3. S. G. Carpenter and R. W. Goin, *Rod-Drop Measurements of Subcriticality*, Applied Physics Division Annual Report, July 1, 1969, to June 30, 1970, ANL-7710, pp. 206–209.
4. T. Hurlimann and P. Schmid, *"Determination of the Stable Reactor Period in the Presence of a Neutron Source*, Nukleonik **5**, 236 (1963) (Translation in ANL-TRANS-282, February 1966).

II-32. Subcriticality Determination by Noise Techniques in the FTR Engineering-Mockup Critical-Experiment Program

C. E. Cohn

Noise methods have been applied to the measurement of subcriticality in the Fast Test Reactor (FTR) Engineering Mockup critical-experiment program (see Paper II-1) as a cross-check on subcriticality measurements by rod drop.[1] Initial efforts used the two-detector cross-power spectral density (CPSD) method.[2]

Equipment for these measurements included, as high-efficiency neutron detectors, two Nuclear Enterprises NE-905 glass scintillators, each 1½ in. diam and 1 in. thick containing about 4.7 g of ^{6}Li. Each photomultiplier output enters a General Radio 1925-9707 multifilter, which allows selection of one of thirty ⅓-octave bands with center frequencies from 100 to 80,000 Hz. Both filters are set to the same frequency. Their outputs enter the two inputs of an analog multiplier. The multiplier output is integrated by a voltage-to-frequency converter having two pulse outputs, one active on positive excursions of the multiplier output and the other active on negative excursions. These outputs are counted in two separate scalers, and the difference between the scaler readings indicates the CPSD.

The system is calibrated by exposure of one scintillator to white noise in the form of a ^{60}Co source. Both multifilter inputs are connected to one detector output, and measurements are taken as described above. For each band, the reading taken on a reactor run is divided by the white-noise reading, calibrating out equipment frequency response.

With this equipment it was found possible to measure roll-off frequencies to 1 or 2% in one hour, from near critical down to 2% subcritical. However, the CPSD method gave unsatisfactory results apparently because of departures from point kinetics in the reactor behavior. Near critical, observed roll-off frequency was up to 10% greater with the detectors in the center of the core than with the detectors in the reflector. Furthermore, measured subcriticalities disagreed sharply with rod-drop results, being low by as much as 30% of the latter.

Another method was developed and has given results agreeing with rod-drop measurements within 0.1% Δk. Like the methods of Seifritz[3] and Albrecht,[4] it measures coherence between signals from two neutron detectors, but unlike their methods it uses the same equipment as for the CPSD measurements. While the CPSD at a given frequency is indicated by the difference between the two above mentioned scaler readings, the coherence is indicated by their ratio. This ratio is given by

$$R = \frac{\int_0^\infty \int_0^\infty xyP(x,y)\,dx\,dy + \int_\infty^0 \int_\infty^0 xyP(x,y)\,dx\,dy}{\int_0^\infty \int_\infty^0 xyP(x,y)\,dx\,dy + \int_\infty^0 \int_0^\infty xyP(x,y)\,dx\,dy}$$

where $P(x,y)$ is the bivariate Gaussian probability density function

$$P(x,y) = \frac{1}{2\pi\sqrt{1-\gamma^2}} \cdot \exp\left[\frac{1}{2(1-\gamma^2)}(x^2 - 2\gamma xy + y^2)\right]$$

(in standard measure). Here γ is the coherence or correlation which ranges from zero with no correlation to unity with complete correlation. Integrating, we obtain[5]

$$R = \frac{\frac{2}{\pi}(\gamma(\sin^{-1}\gamma) + \sqrt{1-\gamma^2}) + \gamma}{\frac{2}{\pi}(\gamma(\sin^{-1}\gamma) + \sqrt{1-\gamma^2}) - \gamma}$$

The value of γ corresponding to a measured R is determined from this formula.

With coherence determined, subcriticality in dollars is given by

$$\$ = (1 + \$_1)\sqrt{\left(\frac{\gamma_1}{1-\gamma_1}\right)\left(\frac{1-\gamma_2}{\gamma_2}\right)} - 1,$$

where γ_2 is the coherence observed in the subcritical state, γ_1 is the coherence observed at the near-critical reference and $\$_1$ is the subcriticality of the reference. (This is a variant of a previous formula[3] that was restricted to a critical reference.) Results are not sensitive to detector location; good results have been obtained with the detectors either in the center of the core or in the axial reflector. The coherence measurements are made at the lowest multifilter frequency; that is, 100 Hz.

References

1. C. E. Cohn, *Experience with Subcriticality Determination by Rod Drop in the FTR-3 Critical Experiments*, Trans. Am. Nucl. Soc. **14**, 29 (1971).
2. T. Nomura, S. Gotoh and K. Yamaki, *Reactivity Measurements by the Two-Detector Cross-Correlation Method and*

Supercritical Reactor-Noise Analysis, Conference on Neutron Noise, Waves and Pulse Propagation, University of Florida, Gainesville, Florida, February 14–16, 1966; AEC Symposium Series 9, May 1967, CONF-660206.
3. W. Seifritz, *The Polarity Correlation of Reactor Noise in the Frequency Domain*, Nuclear Applications and Technology **7**, 513–522 (1969).
4. G. M. Hess and R. W. Albrecht, *Polarity Spectral Analysis Reactivity Errors*, Trans. Am. Nucl. Soc. **12**, 738 (1969).
5. Dr. Nicola Pacilio, CNEN, Italy (private communication).

II-33. Inverse Kinetics Techniques Applied to ZPPR Fast Critical Assemblies

R. W. Goin, S. G. Carpenter, J. M. Gasidlo and R. E. Kaiser

Introduction

Inverse kinetics techniques are involved either directly or indirectly in many of the experiments and operational measurements at ZPPR. Some of these are small reactivity perturbation measurements, Doppler effect measurements, importance measurements, control rod calibrations, autorod calibrations, temperature coefficient determinations, subcriticality determinations, safety rod scram-time determinations and safety rod worths. The introduction of the ZPPR on-line computer and data acquisition system[1] has made possible the accumulation of necessary data, and provides the computing power for the application of these techniques.

Basic Inverse Kinetics Algorithms

The inverse solution of the point-kinetic equation with an external neutron source in use at ZPPR is based upon the algorithm developed by Kaganove[2] for the case of no external source and extended by Gasidlo[3] to include an external source. This algorithm has been programmed for the ZPPR SEL 840 MP on-line computer and serves as the basis for the evaluation of several types of experimental data as discussed below.

The point kinetics equation, with an external source is

$$\frac{dn(t)}{dt} = [k(t)(1-\beta) - 1]\frac{n(t)}{\ell} + \sum_{j=1}^{M} \lambda_j C_j(t) + S, \tag{1}$$

where

$k(t) \equiv$ system multiplication
$\beta \equiv$ total effective delayed neutron fraction
$\ell \equiv$ prompt neutron lifetime
$\lambda_j \equiv$ decay constant for the jth delayed neutron precursor $(1 \le j \le m)$
$C_j(t) \equiv$ concentration of the jth delayed neutron precursor $(1 \le j \le m)$
$S \equiv$ the effective external neutron source.

The delayed neutron precursor concentration for the jth delayed neutron group is described by

$$\frac{dC_j(t)}{dt} = \frac{k(t)n(t)\beta_j}{\ell} - \lambda_j C_j(t), \qquad (1 \le j \le m), \tag{2}$$

where

$\beta_j \equiv$ the delayed neutron fraction of the jth group

and

$$\beta = \sum_{j=1}^{M} \beta_j .$$

By defining a new variable

$$A_j(t) = \frac{\ell \lambda_j C_j(t)}{n(t)}, \tag{3}$$

Eqs. (1) and (2) can be rewritten to solve for $k(t)$ in terms of the power history:

$$k(t) = \frac{\alpha(t)\ell + 1}{(1-\beta)} - \frac{1}{(1-\beta)} \sum_{j=1}^{M} A_j(t) - \frac{S\ell}{(1-\beta)n(t)} \tag{4}$$

and

$$\frac{dA_j(t)}{dt} = k(t)\lambda_j\beta_j - [\lambda_j + \alpha(t)]A_j(t), \quad (1 \le j \le m), \tag{5}$$

where

$\alpha(t) = \frac{1}{n(t)}\frac{dn(t)}{dt} \equiv$ the instantaneous inverse period.

The solution to the inhomogeneous differential equations (5) is

$$A_j(t) = A_j(0)e^{-[\lambda_j + \alpha(t)]t} + \int_0^t e^{-[\lambda_j + \alpha(t)]s} k(s)\beta_j\lambda_j ds. \tag{6}$$

The integral in Eq. (6) can be solved by parts fo. discrete time steps and the result substituted into Eq. (4) to solve for $k(t)$, time step by time step. The result is

$$\delta_i = \frac{\ell(\alpha_i - \alpha_{i-1}) + S\ell\left(\frac{1}{\phi_{i-1}} - \frac{1}{\phi_i}\right) - \sum_{j=1}^{M}\left[\frac{\lambda_j\beta_j k_{i-1}E_{i,j}}{(\lambda_j + \alpha_i)} - A_{j,i-1}E_{i,j}\right]}{1 - \beta + \sum_{j=1}^{M}\frac{\lambda_j\beta_j}{(\lambda_j + \alpha_i)}\left[1 - \frac{E_{i,j}}{\Delta t(\lambda_j + \alpha_i)}\right]}, \tag{7}$$

where the subscript i denotes the ith time step,

$$E_{i,j} = 1 - e^{-(\lambda_j + \alpha_i)\Delta t}$$

$\delta_i \equiv$ change in k during time step i

so

$$k_i = k_{i-1} + \delta_i .$$

The precursor concentrations at time step i are given by

$$A_{j,i} = A_{j,i-1}e^{-(\lambda_j+\alpha_i)\Delta t} + \frac{\beta_j\lambda_j}{(\lambda_j + \alpha_i)} \cdot\left[k_{i-1}E_{i,j} + \delta_i\left(1 - \frac{E_{i,j}}{\Delta t(\lambda_j + \alpha_i)}\right)\right]. \tag{8}$$

In this derivation, the assumption is made that the reactivity is a linear function over a time interval, and that the power (countrate) behaves exponentially over the time interval.

Equations (7) and (8) form the basis for the algorithms used at ZPPR.

The initial conditions are that the system is in a steady state; that is, the reactor has been at a constant power for a sufficiently long time that all delayed neutron precursor concentrations have reached equilibrium.

The value of the source term, S, (or the product $S\ell$) in Eq. (4) is required for each reactor configuration. The effective source is obtained by doing effectively a subcriticality determination using the method described later. A source term measurement is made at each operational power scale by stabilizing the reactor at the top of the power scale and then scramming rods which are worth ~0.50 or 0.75$. The subcriticality determination technique is then used to obtain the effective source term for use in any other inverse kinetics applications on that configuration.

Perturbation Samples and Rod Calibration

The data required for the evaluation of small reactivity samples are the power history and the position of the sample, starting with the reactor in a steady state and recording the power while driving the sample in and out of the reactor several times. Reactivity as a unction of position (and time) is then obtained from nverse kinetics. The resulting reactivity history is then fitted to a polynomial in time and position, from zero to third order in time and from first to eighth order in position.[4] The polynomial fit in time provides the reactivity drift correction which is subtracted from the reactivity history.

The sample is usually stopped at least at its "in" position and its "out" position for several seconds. The drift-corrected reactivities are averaged over all points where the sample was not moving and the uncertainty is obtained from the deviation of the individual values about the average. If the sample is stopped at positions between the "in" and "out" positions a reactivity traverse is obtained.

If the sample is moved continuously between the "in" and "out" position, an "on-the-fly" reactivity traverse is obtained by averaging the drift-corrected reactivity over some interval of travel, e.g., one cell width. The uncertainties of these on-the-fly reactivities are computed as the product of the statistical uncertainties of the stationary values and the ratio of the square root of the integrated time at each position. After the average drift-corrected reactivities are obtained, along with the associated statistical uncertainties, the empty capsule and sample holder reactivities (which are measured separately) are subtracted and the result normalized to zero at some point out of the reactor and tabulated and plotted.

A Doppler effect measurement is handled in essentially the same manner. In this case, instead of an empty capsule and sample holder being measured separately, the Doppler capsule at a reference temperature is driven in and out of the reactor. The reference-temperature drift-corrected reactivity traverse is subtracted from that obtained with the sample heated to various temperatures to obtain the Doppler effect.

Autorod and control rod calibrations are done by oscillating the rod through its full length of travel several times and obtaining the drift-corrected reactivity as a function of position. In this case, the polynomial in position is used to provide a continuous calibration curve.

The accuracy of this technique for determining the reactivity worth of a sample in ZPPR is typically ~0.003 Ih for measurements at a reactor power of 40 W and a total integrated time at each position of 30 min. This is just the statistical uncertainty in an individual central-worth-type measurement and does reflect systematic uncertainties, such as those occurring in sample mass or composition. A typical plot of drift-corrected reactivity as a function of sample position is shown in Fig. II-33-1.

The technique described above has been programmed

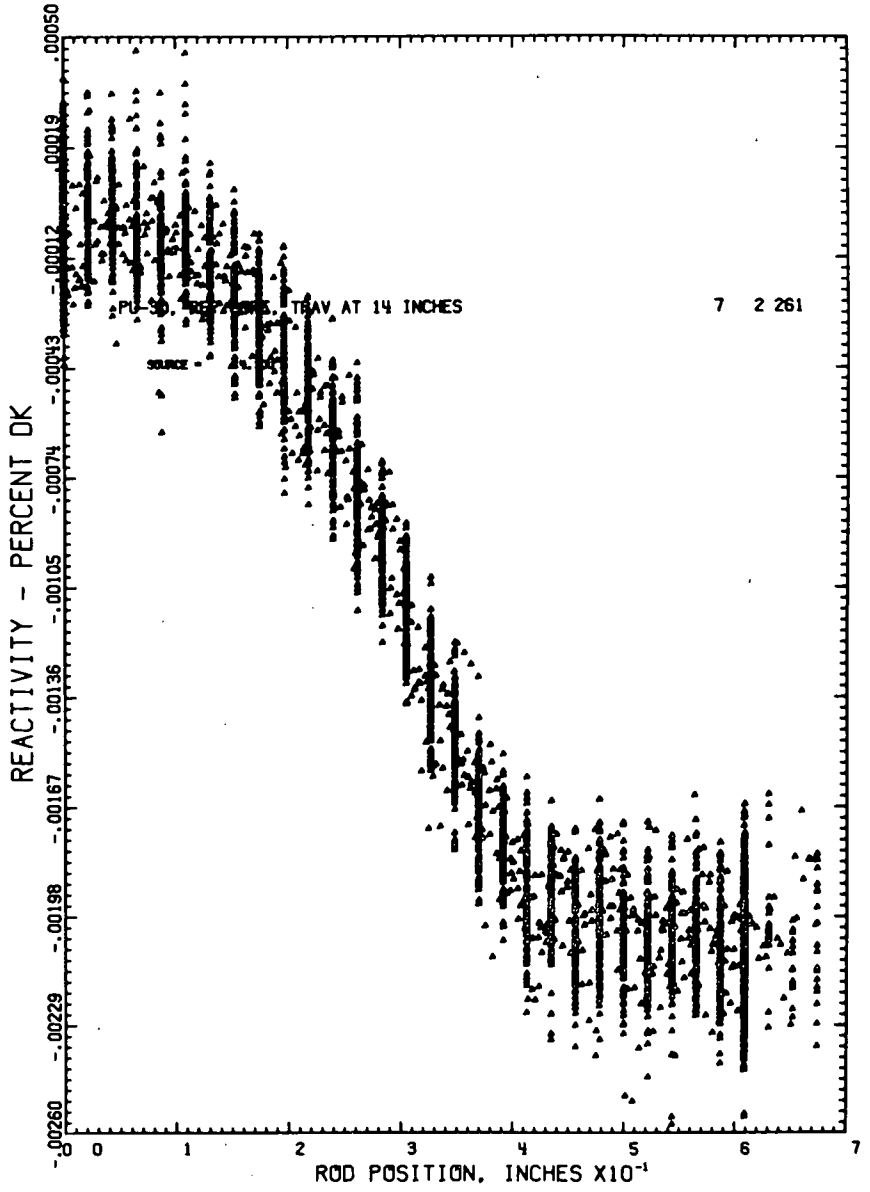

FIG. II-33-1. Pu-30 IK Output. *ANL 103-A11954.*

on the SEL 840 MP on-line computer at ZPPR as IVCAL, which provides as output the drift-corrected reactivity for each sample position desired, with the associated uncertainty. An auxiliary program called SMOOTH performs a linear interpolation to obtain the reactivity values at the exact positions desired. A second auxiliary program, BORE, computes the worth per unit mass of the empty capsule and subtracts the empty sample holder and empty capsule from each sample measurement. A third auxiliary program provides the reactivity per unit sample mass in a printed form suitable for reporting, provides card images for subsequent use, and plots the reactivity traverse. The final output, sample worth as a function of position, is shown in Fig. II-33-2.

SUBCRITICALITY DETERMINATION

The subcriticality of a reactor system which has a relatively large source of uniformly distributed neutrons can be determined to a fair degree of accuracy to below $20 subcritical using inverse kinetics techniques.[6]

The method in use at ZPPR basically involves slightly rearranging the kinetics equation in a form giving powe (as a function of time) as a linear function of the de layed neutron precursor concentration integral (also a function of time).

$$n(t) = \frac{\ell\dot{n}(t) - \ell S}{k(t)(1-\beta) - 1} - \frac{\ell \sum \lambda_j C_j(t)}{k(t)(1-\beta) - 1}. \quad (9)$$

Immediately after a step change, $k(t)$ is constant, $k(t) = k_f$, so Eq. 9 assumes the form

$$n(t) = A + BZ(t), \quad (10)$$

where

$$Z(t) = \ell \sum \lambda_j C_j(t)$$

$$A = \frac{\dot{n}(t)\ell - S\ell}{k_f(1-\beta) - 1}$$

and

$$B = \frac{1}{k_f(1-\beta) - 1}.$$

In a system where $S \gg \dot{n}(t)$, (which is the case in a plutonium system such as ZPPR), the constant A reduces to

$$A = -\frac{S\ell}{k_f(1-\beta) - 1}. \quad (11)$$

Thus, by first evaluating the power history of a step change using inverse kinetics with an initial guess for S (such as $S = 0$), a first prediction of the delayed neutron precursor history is determined. Using a least squares fit to a straight line, the coefficients A and B are determined, which provide a prediction of S, because

$$S\ell = A/B. \quad (12)$$

This prediction (which is usually within one percent of the asymptotic value) is then used in a second evaluation of the power history which provides an improved delayed neutron precursor history, and so on. A third iteration does not provide any further improvement (i.e., change) in the predicted value of S.

The values A and B provide the k of the system before the step change—from the steady-state condition on the inverse kinetics equation $k(0) = -S/[(1-\beta)n(0)]$ and the k after the step change (k_f)

$$k_f = \frac{\beta - \frac{1}{B}}{1-\beta}. \quad (13)$$

Statistical uncertainties of the predicted values of k are obtained from the uncertainties on A and B established from the least squares fitting technique. Tests of this technique on actual reactor data have only gone down to ~$5 subcritical. Tests of data produced from a direct kinetics code, where a rod movement was realistically simulated and random noise superimposed, showed that reactivities down to $27 subcritical were predicted to within 6%. Further tests are being conducted at this writing.

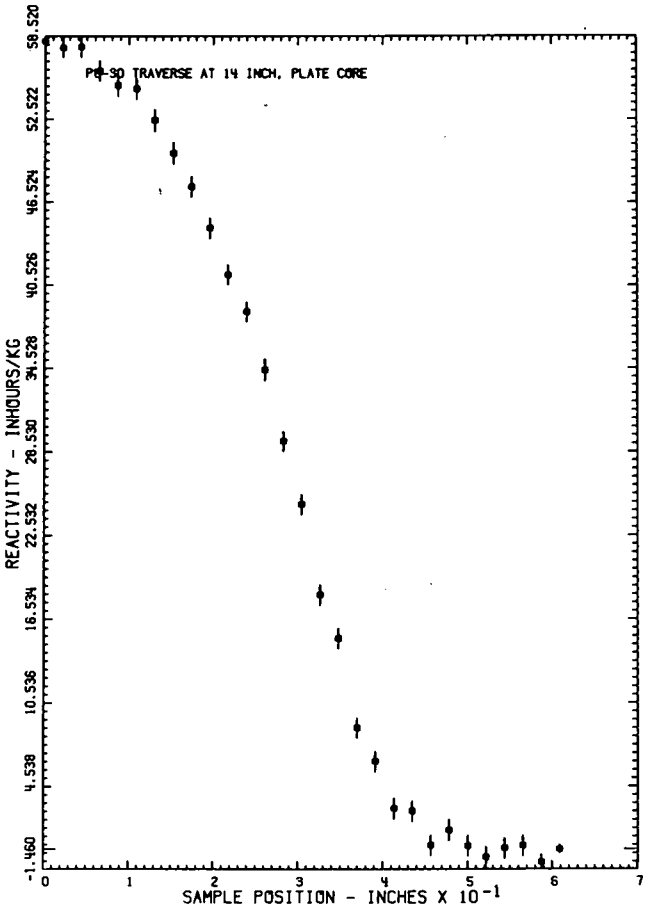

FIG. II-33-2. Pu-30 Ream Output. *ANL-103-A11962.*

The accuracy of this technique depends upon several assumptions[5] and the experiment must be planned with them in mind. For example, the source effectiveness (or the detector efficiency) should not change during the run. That is, the fraction of neutrons impinging upon the detector should not change, and the spectrum of the impinging neutrons should not change. In addition, the reactor should not be perturbed in such a way that the effective delayed neutron parameters or the prompt neutron lifetime are affected by the step change. The experimental restrictions are discussed in detail in Ref. 5.

IMPORTANCE MEASUREMENTS

The variation of source importance with position is based upon the determination of $k(t)$ from the power history as a ^{252}Cf neutron source is moved through the reactor.[6] Equation (4) can be written for this measure-

ment as

$$k(t) = \frac{\alpha(t) + 1}{1 - \beta} - \frac{1}{1 - \beta}\sum_{j=1}^{M} A_j(t) - \frac{S\ell}{(1 - \beta)n(t)} - \frac{S_s(r)\ell}{(1 - \beta)n(t)} + k_s(r)\,, \tag{14}$$

where

$k_s(r) \equiv$ the effect of the ^{252}Cf sample and holder as a function of position

$S_s(r) \equiv$ the effective source as a function of source position

$$S_s(r) = \frac{S\phi_s^*(r)}{\bar{\phi}_f^*}\,, \tag{15}$$

where

$\phi_s^*(r) \equiv$ source importance

$\bar{\phi}_f^* \equiv$ average fission importance.

By doing essentially a central worth measurement (as described previously) of a ^{252}Cf sample at two different power levels, $S_s(r)$ can be solved for. For each measurement, the inverse kinetics solution can be written

$$k_A(t,r) = k(t) - \frac{S_s(r)\ell}{(1 - \beta)n(t)} + k_s(r)\,, \tag{16}$$

where

$k_s(r) \equiv$ the worth of the moving sample and holder

$k(t) \equiv$ the k of the system which is constant except for drift, and can be described by a polynomial.

The measurements at the two different power levels are done identically, that is, the source travels at the same speed and is left in the same stationary position for the same length of time. Then the inverse kinetics solutions for the two runs may be subtracted, resulting in

$$k_A(p,t) - k_A^h(p,t) = \frac{S_s(p) + S}{n(t)} - \frac{S_s(p) + S}{n^h(t)} + g(t)\,, \tag{17}$$

where $g(t)$ is a composite drift function and the superscript h indicates the low power run.

Let

$$X(p,t) = k_A(p,t) - k_A^h(p,t)$$

and

$$R(t) = \frac{1}{n(t)} - \frac{1}{n^h(t)}$$

whence

$$X(p,t) = [S_s(p) + S]*R(t) + g(t). \tag{18}$$

If there are discrete positions points, a least squares technique can be applied. If the sample is driven continuously, the k as a function of position can be averaged over some position interval as in the case of the on-the-fly traverse to provide discrete position points.

Let the number of position points be N. At any specific position point j

$$X_j(t) = (S_{sj} + S)R(t) + g(t), \tag{19}$$

where $X_j(t)$ is defined only for the times t when the sample is at position p. This results in N equations to define the entire time span: these may be combined to give

$$X(p_1, p_2, \cdots, p_N, t) = S'_{S1}R(t_{p1}) + S'_{S2}R(t_{p2}) + \cdots + S'_{SN}R(t_{pN}) + a + bt + ct^2 + dt^3, \tag{20}$$

where the drift function $g(t)$ has been represented by a third-order polynomial in time and $S'_{si} = S_{si} + S$.

Dividing this relation by $R(t)$ results in

$$\frac{X(p_i,t)}{R(t)} = S'_{s1} + S'_{s2} + \cdots + S'_{sN} + a\frac{1}{R(t)} + b\frac{t}{R(t)} + c\frac{t^2}{R(t)} + d\frac{t^3}{R(t)}\,. \tag{21}$$

The values of S_{s1} and the coefficients of the drift polynomial can be obtained from a least-squares fit to the above relation.

An additional assumption is that S_{pN} (the value of S with the source sample at its outermost position) is zero. This implies that $S'_{pN} = S$. The importance traverse is then obtained by subtracting S_{pN} from each of the S_{pi}. Very good results have been obtained with this technique. Preliminary evaluation of radial importance measurements at various axial positions agree in absolute magnitude with a central axial traverse measurement.

Operational Measurements

Some of the parameters necessary for normal reactor operations are control rod calibrations, safety rod worths, safety rod scram time, reactor temperature coefficient and the half-closure gap worth.

The safety rod worth (or shutdown margin) is obtained by scramming the rods, either individually or one at a time, and following the power history from before the first rod drop until after the last rod drop with

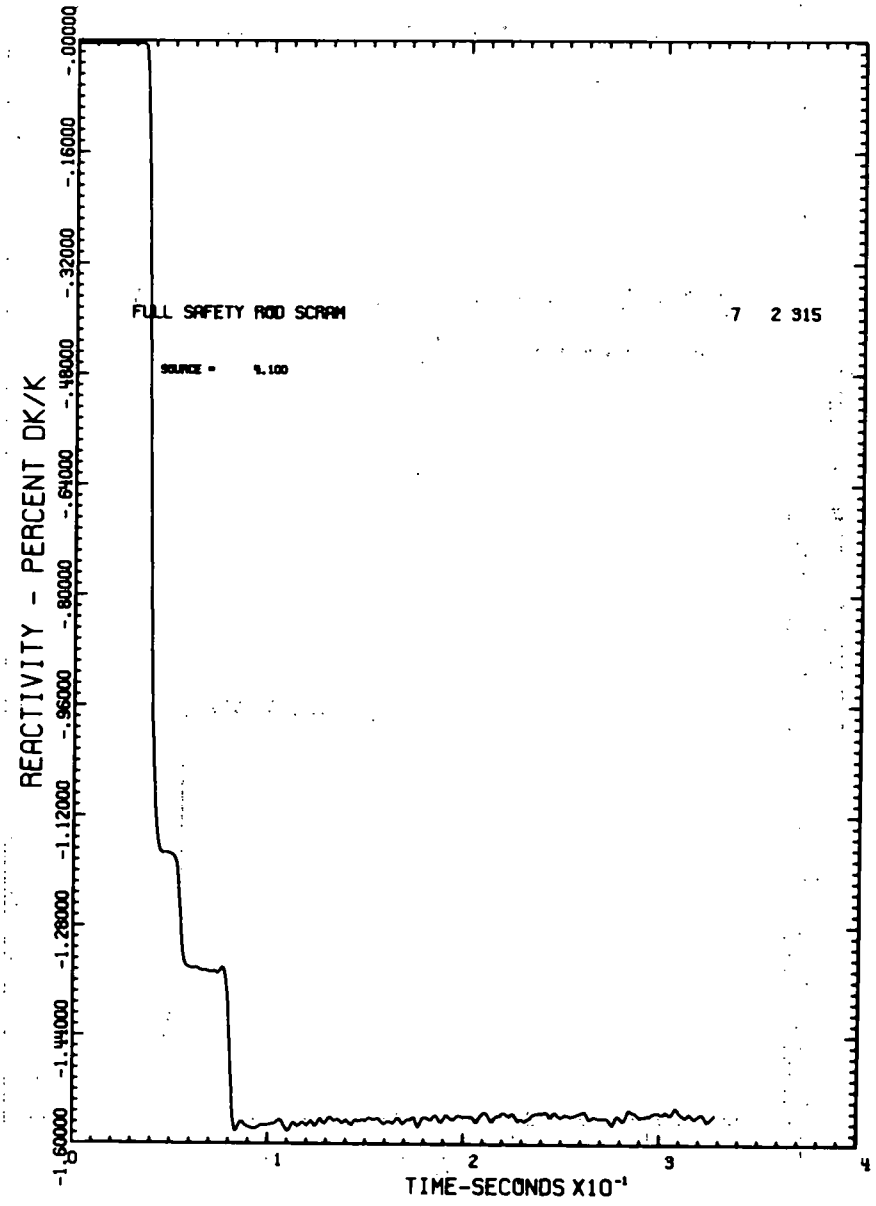

FIG. II-33-3. All Safety Rods Scrammed Simultaneously. *ANL-103-A11959.*

inverse kinetics. The calculated reactivity before and after each rod drop provides the individual rod worth. The total safety rod worth is obtained by scramming all of the safety rods simultaneously, or by summing the worths of individual rods. An example of the reactivity trace obtained by scramming all of the safety rods nearly simultaneously is shown in Fig. II-33-3.

The safety rod scram times (that is, the time required for a rod to complete its insertion from the time the scram was initiated) are measured on a periodic basis as part of the weekly checkout procedure. The most convenient method of checking scram times has proven to be that which uses the inverse kinetics technique. The integrated power is sampled every 0.01 sec, and the rods are scrammed approximately at 1 sec intervals. The inverse kinetics evaluation of the resulting power history provides a reactivity trace from which the time from initiation of the scram to the seating of the rod can be determined to within ~10 ms. If a safety rod does not move freely, it will show clearly on this reactivity trace. Figure II-33-4 shows the characteristic reactivity behavior of the safety rods when scrammed, clearly indicating the rod "bounce" after the drop. An expanded reactivity trace for one rod, as shown in Fig. II-33-5, is used for ascertaining scram time and freedom of movement.

The reactor temperature coefficient is obtained by stabilizing the reactor at some power (e.g., 30 to 40 W)

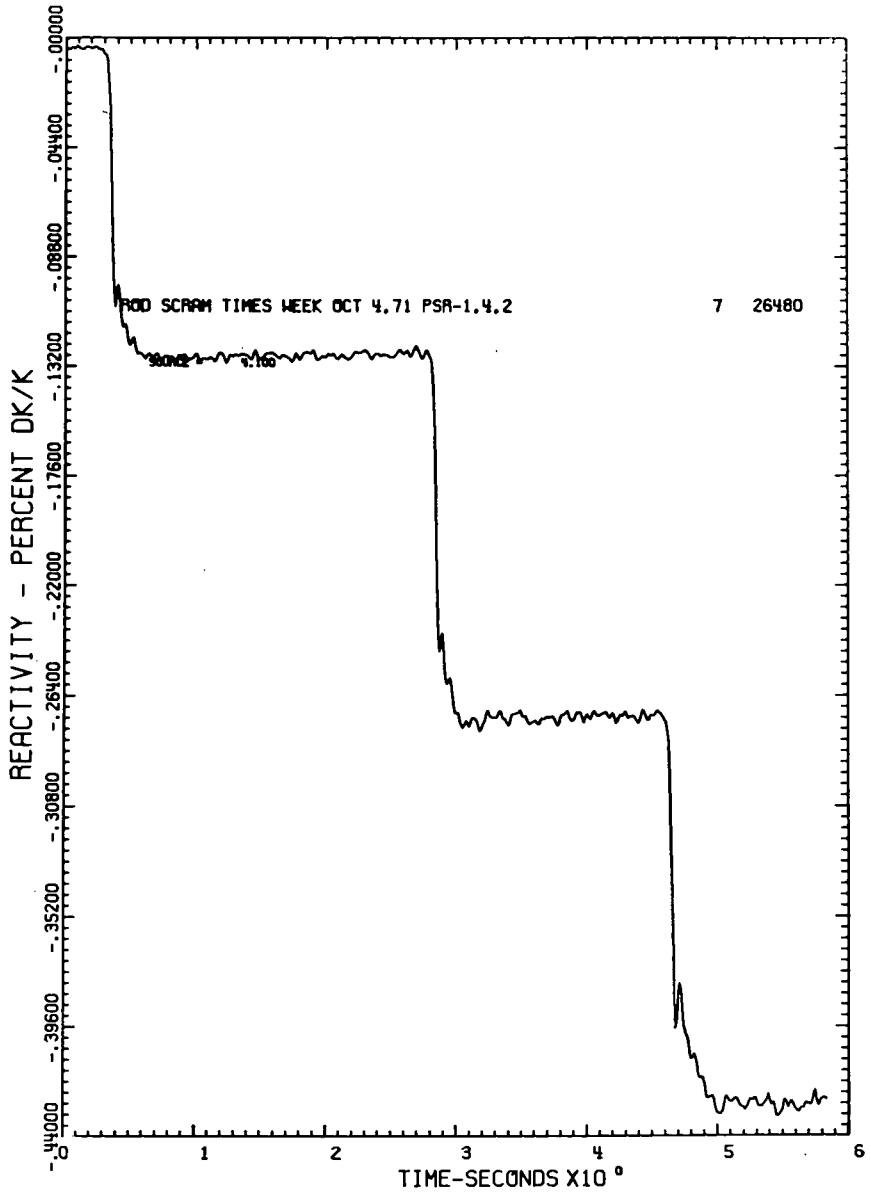

FIG. II-33-4. Scram Time (3 Rods). *ANL-103-A11956*.

and then recording the power history and turning off the cooling air to the reactor. The power history is recorded for 30 to 45 min and the reactor temperature is recorded at 5 min intervals. The temperature range covered is typically ~2°C. The reactivity history as a function of time is correlated with the temperature history as a function of time to provide a temperature coefficient of reactivity over the temperature range observed.

The half-closure gap worth is required for estimating uncertainties in any half-closure experiment. This is determined by following the power history while the halves are scrammed apart. Figure II-33-6 shows the reactivity trace for ~5 sec after the scram. After approximately 4 sec, the countrate is down to ~1 % of full scale, but the halves travel at 0.5 in./sec. A typical gap worth is 0.73 Ih/mil for the first half inch of reactor-half travel.

CONCLUSION

Inverse kinetics techniques have proven to be extremely valuable in a variety of experimental and operational measurements at ZPPR. The availablility of the SEL 840 MP on-line computer and data acquisition system has provided the capability of acquiring and storing power history and sample position data necessary for the application of these techniques, a the computing power required for the evaluation these data. The application of these techniques has provided more information from a given experiment than was possible before, as well as extending the range of accuracy of a given experiment.

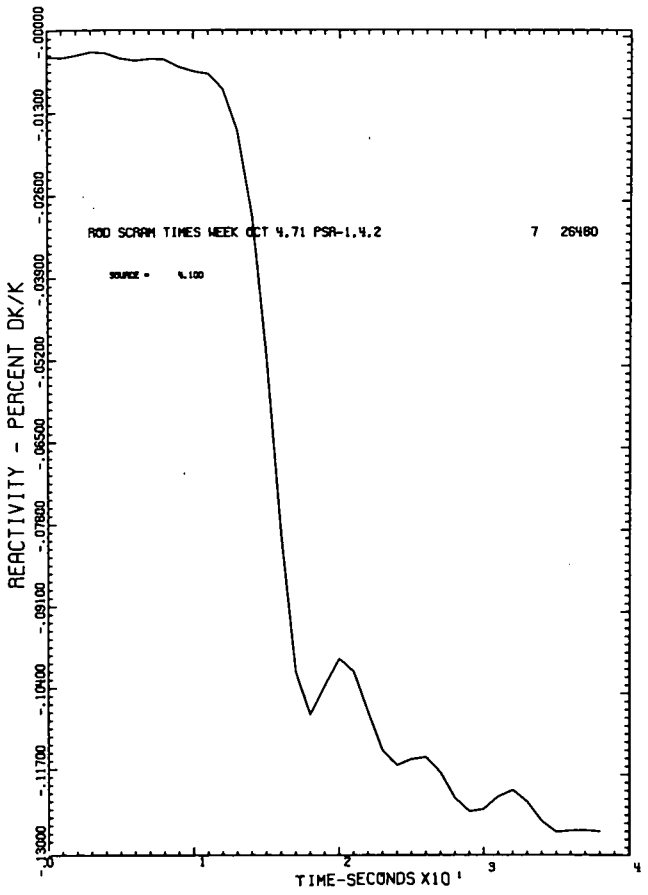

FIG. II-33-5. Scram Time (1 Rod). *ANL-103-A11958.*

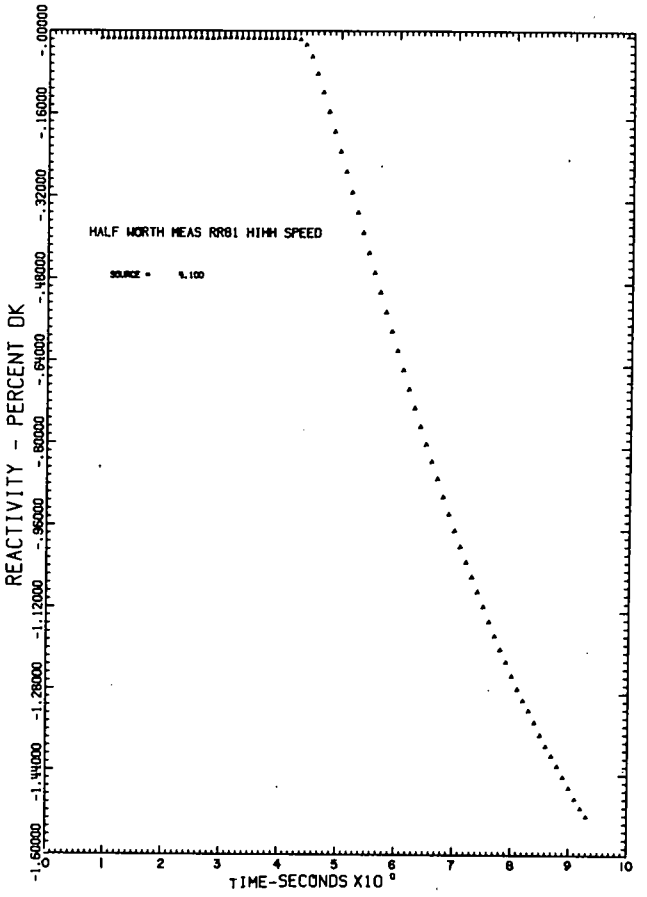

FIG. II-33-6. Gap Worth. *ANL-103-A11961.*

REFERENCES

1. R. W. Goin, C. L. Beck, J. E. Hutton and A. L. Hess, *On-line Computer System for the Zero Power Plutonium Reactor (ZPPR)*, Reactor Physics Division Annual Report, July 1, 1968 to June 30, 1969, ANL-7610, p. 371.
2. J. J. Kaganove, ANL-AMD Applications Program Library Report *Program R-102, Inverse Kinetics*, (1964).
3. J. M. Gasidlo, Argonne National Laboratory (private communication).
4. R. W. Goin and C. L. Beck, *Critical Reactivity Measurement Technique at the Zero Power Plutonium Reactor (ZPPR)*, Applied Physics Division Annual Report, July 1, 1969 to June 30, 1970, ANL-7710, pp. 274–276.
5. S. G. Carpenter and R. W. Goin, *Rod Drop Measurements of Subcriticality*, Applied Physics Division Annual Report, July 1, 1969 to June 30, 1971, ANL-7710, pp. 206–209.
6. R. J. Tuttle, *Neutron-Importance Measurements in the Advanced Epithermal Thorium Reactor (AETR) Critical Experiments*, Nuc. Sci. Eng. **21**, 451–462 (1965).

II-34. Measurement and Analysis of Space Dependent Parameters in a Demonstration Plant Benchmark Critical

R. E. KAISER, W. G. DAVEY, P. I. AMUNDSON, A. L. HESS, R. J. FORRESTER, B. NEWMARK* and C. L. BECK

INTRODUCTION

ZPPR Assembly 2 is a demonstration plant benchmark critical, designed in cognizance of the general design features envisioned by the major LMFBR contractors.[1] The experimental program has been developed by Argonne with appropriate consideration of contractor requirements in order to most effectively answer the problems encountered by those contractors in their early design phase.

Assembly 2 is a large two-zone core, with an enrich-

* Westinghouse Electric Corp., Pittsburgh, Pennsylvania.

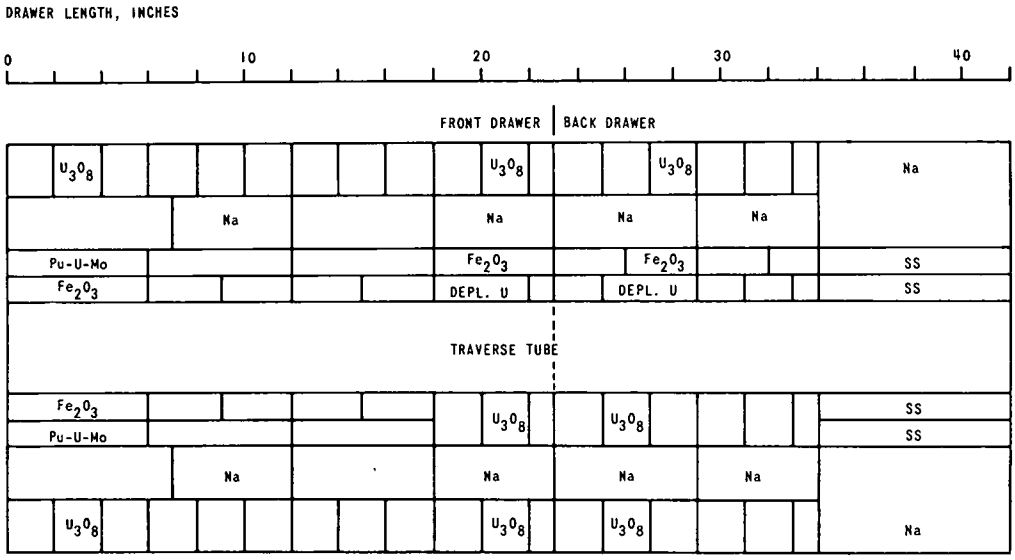

DRAWER LOADING TO ACCOMMODATE AXIAL TRAVERSE TUBE IN INNER CORE OF ZPPR ASSEMBLY 2

FIG. II-34-1. Drawer Loadings for Axial Counter Traverses in ZPPR Assembly 2. *ANL-ID-103-A11989.*

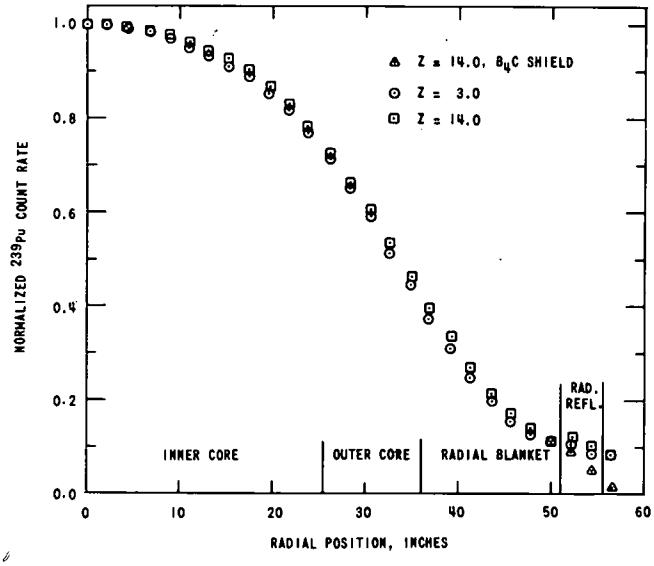

FIG. II-34-2. Results of Room Return Experiment with ^{239}Pu Counter Traverse. *ANL-ID-103-A11651.*

ment ratio (outer zone/inner zone) of 1.5. Spatial dependence of reaction rates and reactivity worths of fuel, coolant, and structural materials—and their comparison with calculation—are thus of considerable interest.

REACTION RATE TRAVERSES

A series of radial count-rate traverses was performed at each of three axial positions, 3.036, 14.036 and 22.036 in. from the reactor midplane. In addition, axial traverses were run along the radial centerline in order to normalize the different sets of radial data. The counters included ^{235}U, ^{238}U, ^{239}Pu and ^{240}Pu fission chambers and a ^{10}B (n,α) counter. The cylindrical fission chambers have an active length of 2.173 in., one matrix tube width, and an o.d. of about 0.4 in. The ^{10}B counter is a dual counter with the isotopes deposited on flat plates along the center of the cylinder.

The radial traverse tube was installed using "tunnel elements" of each of the reactor materials, which had holes for that specific purpose, thereby avoiding the introduction of extra void space near the traverse tube. The axial traverse tube was installed in the center of a drawer as shown in Fig. II-34-1. Although some additional void space was unavoidable in the axial measurement, an effort was made to keep the tube environment characteristic of the unperturbed core.

A determination of the effect of room-return on radial traverse data in the reflector and in the outer portion of the radial blanket was conducted using the ^{239}P fission counter in the 14-in. position. A one-inch-thi layer of B_4C was loaded around the outside of the reflector in the vicinity of the traverse tube, extending

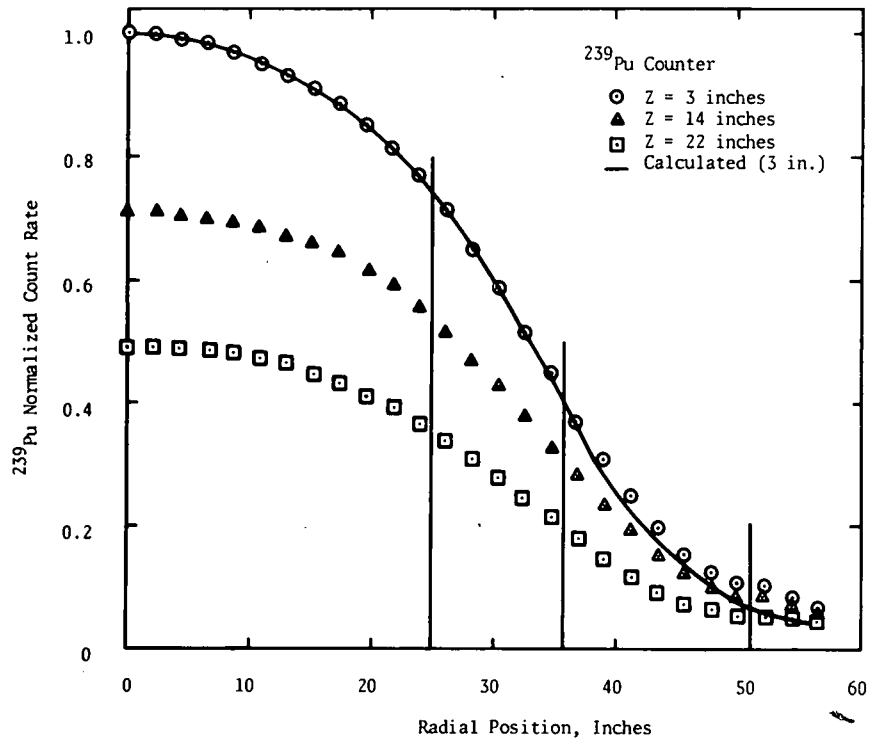

FIG. II-34-3. Radial Counter Traverses for ^{239}Pu in ZPPR Assembly 2. *ANL-ID-103-A11817.*

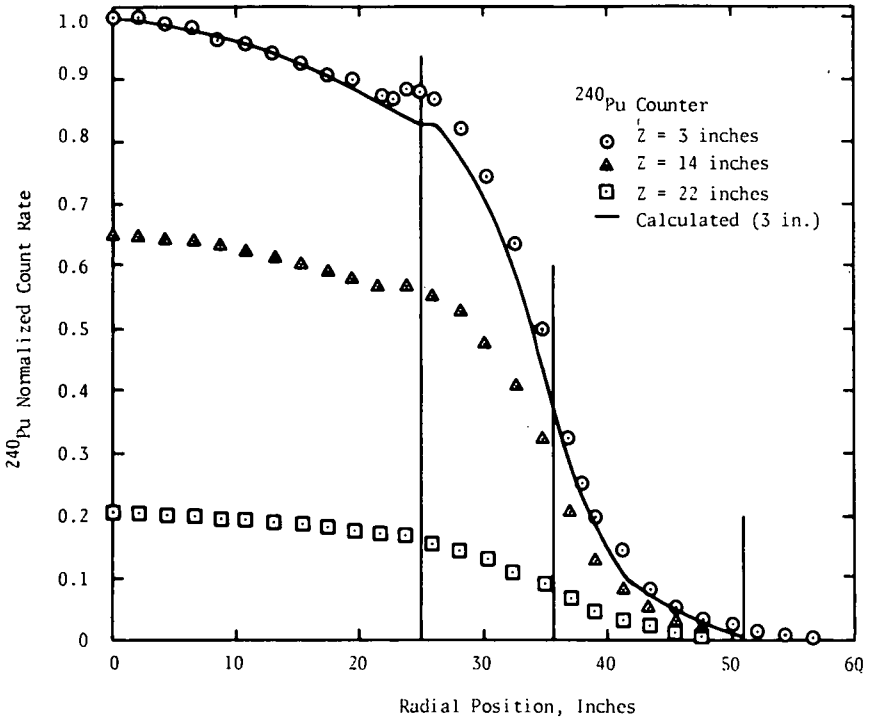

FIG. II-34-4. Radial Counter Traverses for ^{240}Pu in ZPPR Assembly 2. *ANL-ID-103-A11812.*

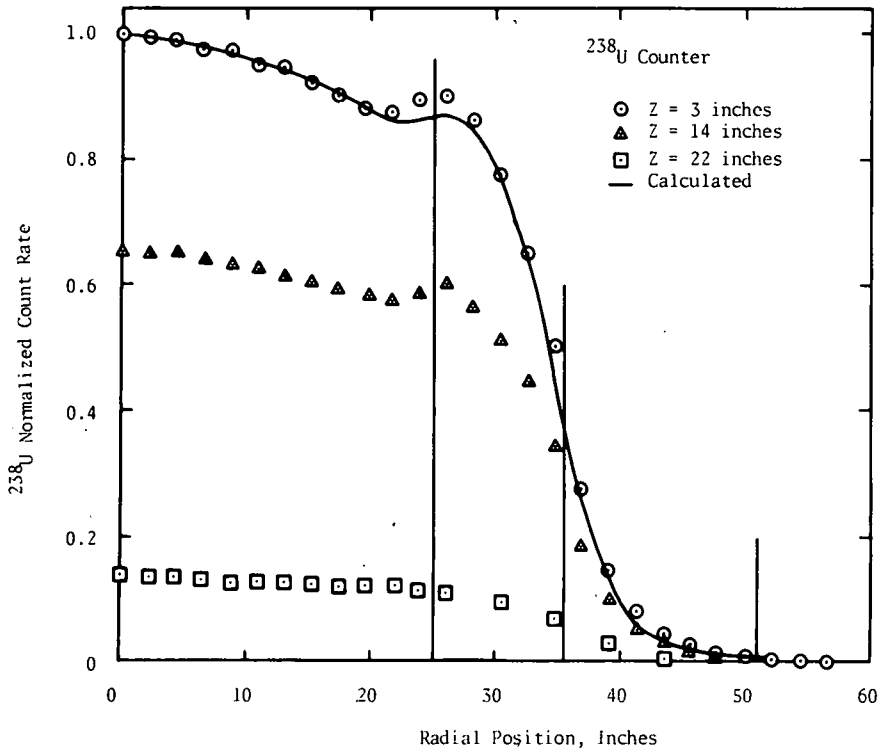

FIG. II-34-5. Radial Counter Traverses for ^{238}U in ZPPR Assembly 2. *ANL-ID-103-A11813.*

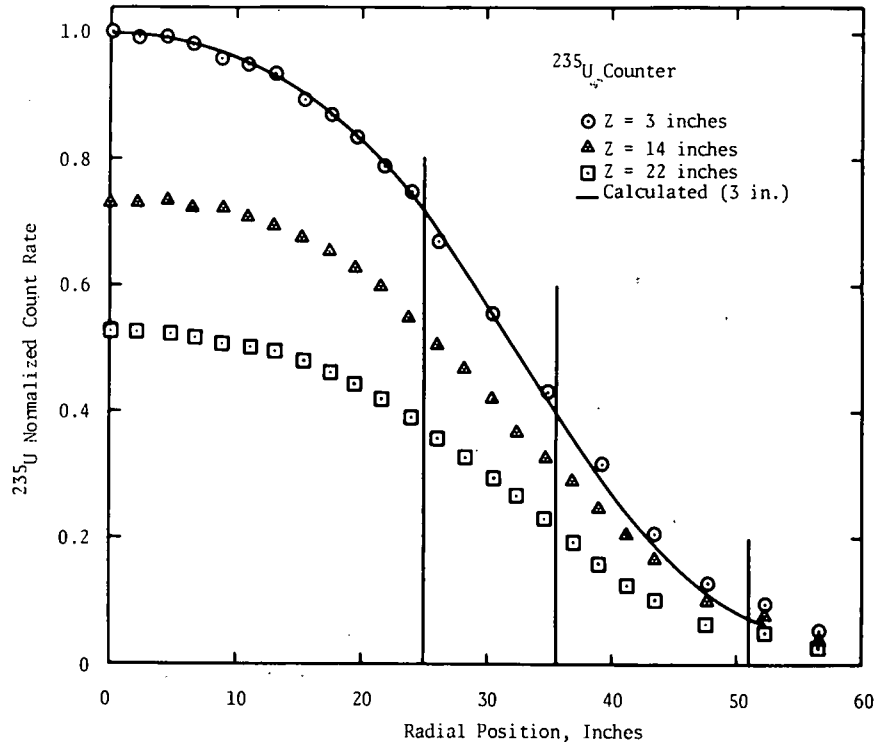

FIG. II-34-6. Radial Counter Traverses for ^{235}U in ZPPR Assembly 2. *ANL-ID-103-A11793.*

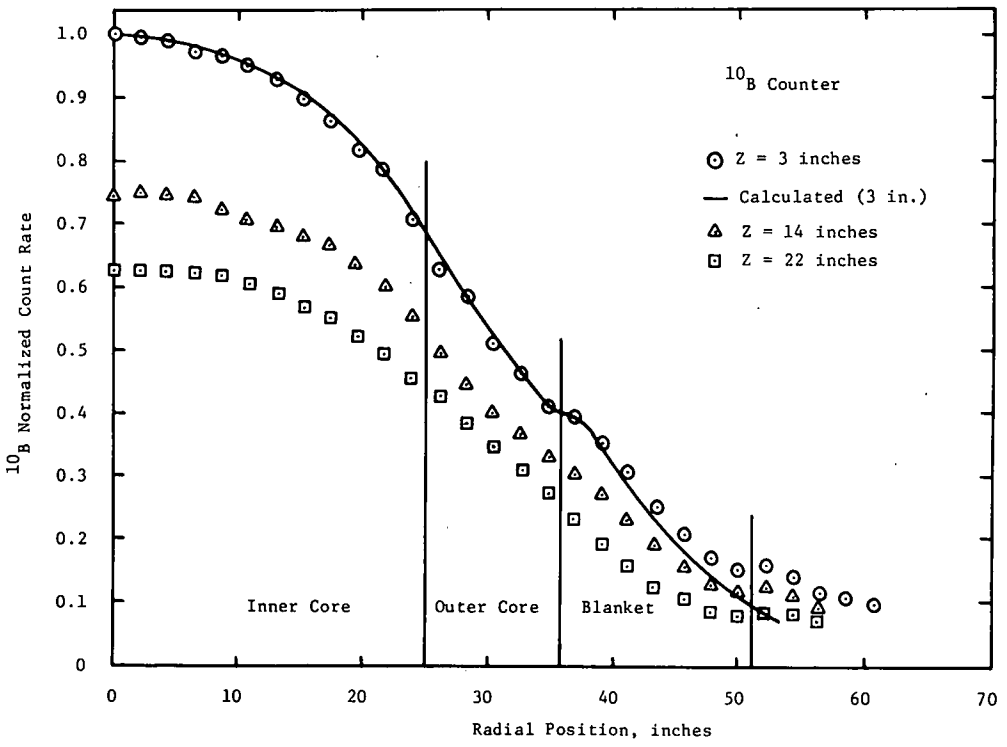

FIG. II-34-7. Radial Counter Traverses for ^{10}B in ZPPR Assembly 2. *ANL-ID-103-A11984.*

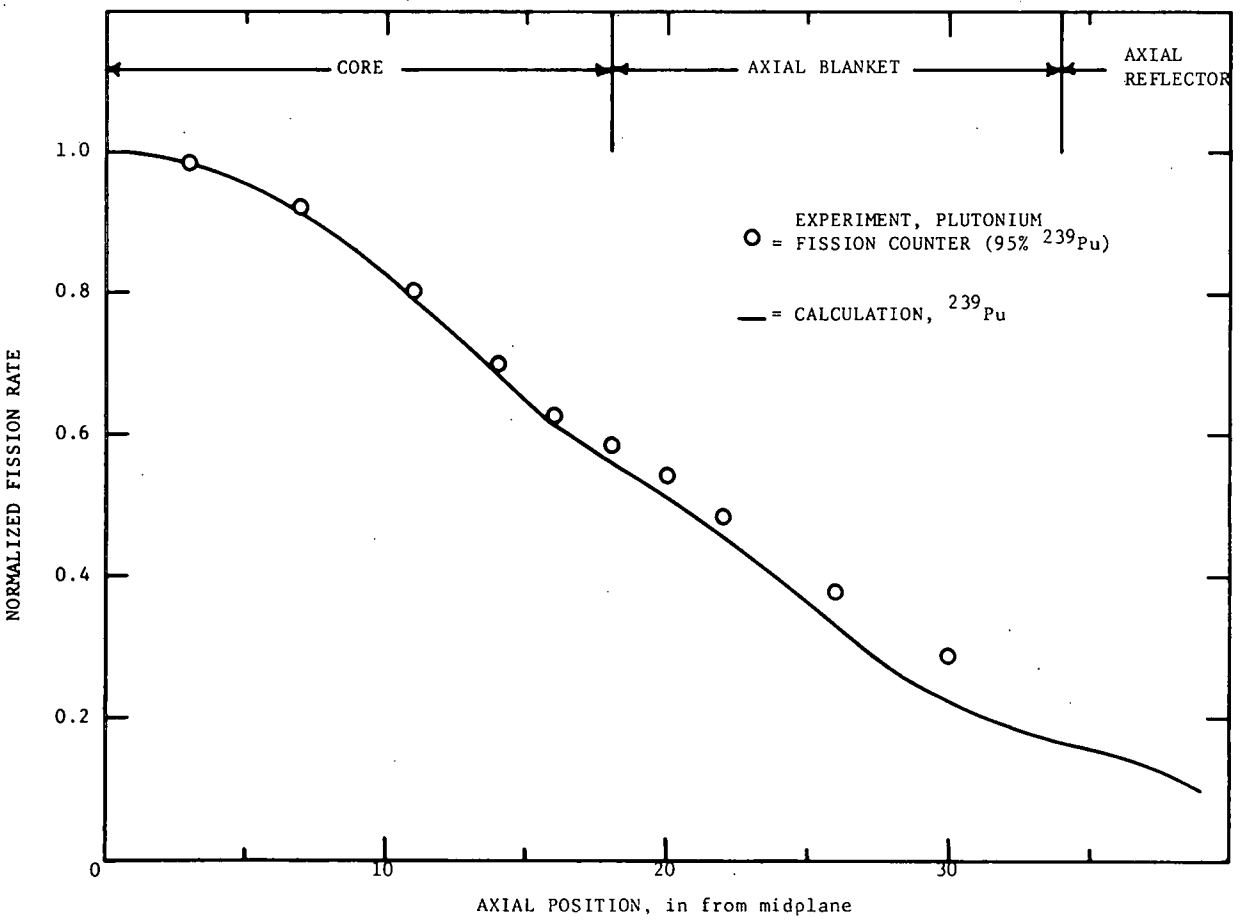

FIG. II-34-8. Comparison of Calculated and Experimental ^{239}Pu Axial Fission-Rate Profile. *ANL-ID-103-11802.*

at least 7 in. in all directions. This caused a significant decrease in the count-rates at the end of the traverse as shown in Fig. II-34-2. The results of this test indicate that significant room return is seen in the outer 4 to 6 in. of the traverse, and that the fissile reaction rate distribution data in the reflector must be considered in light of these results for analytical comparison purposes.

Analysis of the reaction rate experiment was performed using 2-D diffusion calculations[2] with CALHET[3] weighted cross sections for each reactor zone. Spacings were arranged so that the mesh points in the calculation fell exactly along the traverse positions. The comparisons at $z = 3$ in. are presented in Figs. II-34-3 through II-34-7, for the different isotopes. Comparisons with calculation are seen to be quite good, and tend to remain so for the $z = 14$ and 22 in. positions. The axial results are shown in Figs. II-34-8

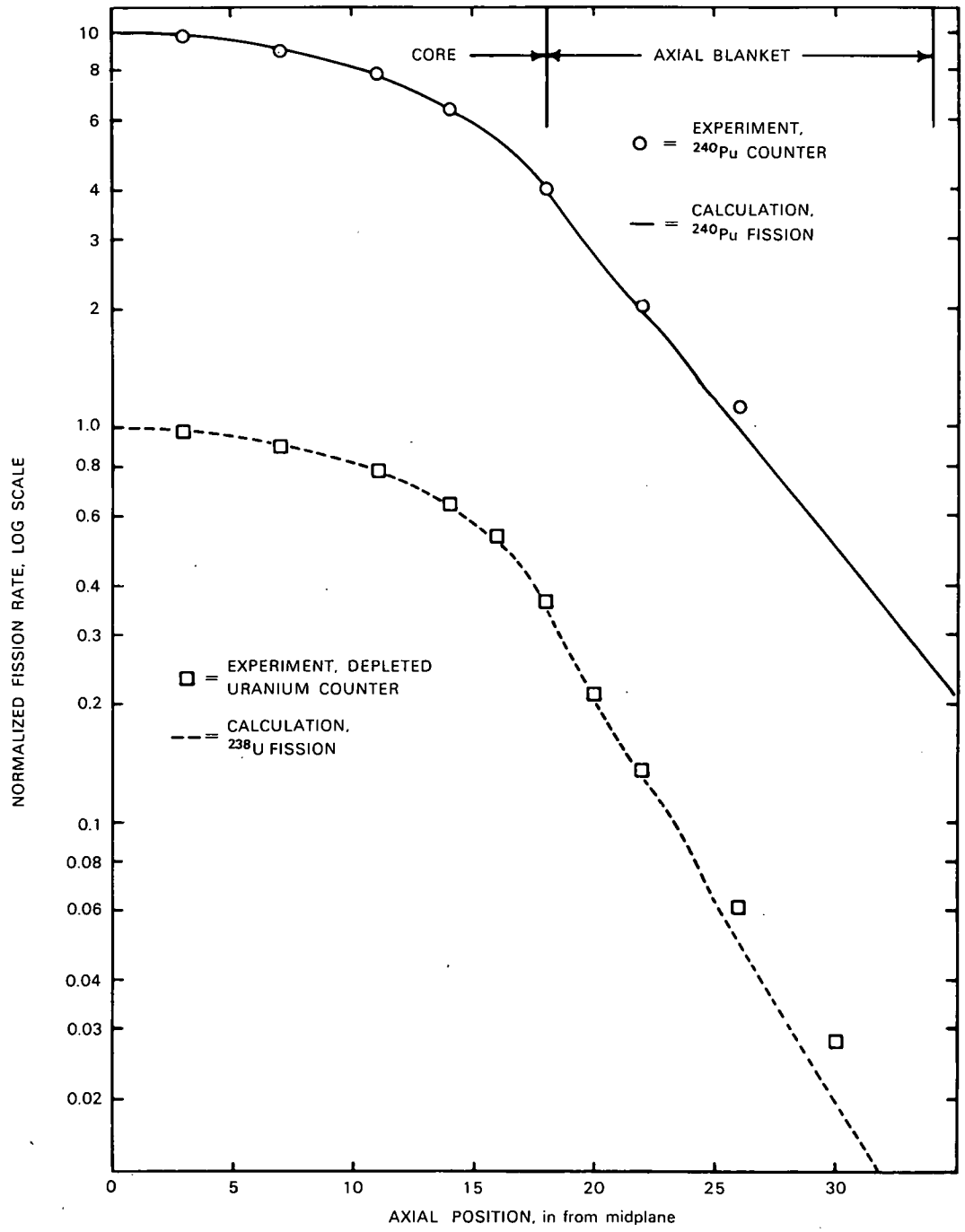

FIG. II-34-9. Comparison of Calculated and Experimental ^{238}U and ^{240}Pu Axial Fission-Rate Profiles. *ANL-ID-103-A11792.*

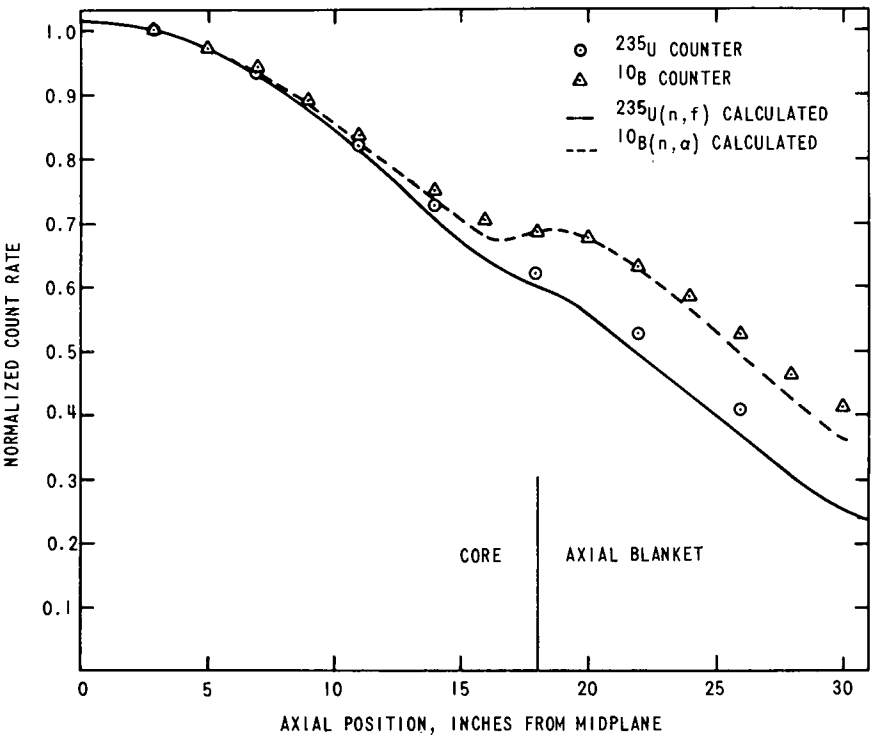

FIG. II-34-10. Comparison of Calculated and Experimental ^{235}U and ^{10}B Axial Reaction-Rate Profiles. *ANL-ID-103-A11985.*

through II-34-10, and indicate a slightly greater discrepancy between calculated and measured values in the axial blanket, although the comparison in the core and the first few inches of blanket is quite good. All radial and axial traverse data are presented in Tables II-34-I through II-34-VI.

Fission Ratios

Fission ratios were measured at the center of the inner core using spherical, back-to-back chambers containing deposition foils of the respective isotopes. The results of these measurements are shown in Table II-34-VII relative to ^{235}U. The traverse counter data described previously were then normalized to the central fission ratios and the fission ratio as a function of position obtained. This process was facilitated by the fact that the traverse counters are of extremely high isotopic purity, sufficient to preclude the need for corrections to the count-rates due to impurity isotopes.

The ratios $^{238}U/^{235}U$ and $^{239}Pu/^{235}U$ were determined as a function of core radius, at the 3 in. axial position, and the results are listed in Table II-34-VIII. The increased hardening of the spectrum in the outer core is readily apparent, especially in the $^{238}U/^{235}U$ ratio, which increases by about 40% in the outer core over the central value.

Small-Sample Reactivity Measurements

A large number of small-sample reactivity measurements were made in the $z = 3$ in. radial traverse position, and select samples of key materials have been run as radial traverses or central (i.e., $r = 0$) measurements in the radial traverse positions at $z = 11.036$, 14.036 and 22.036 in. in the same traverse tube and core configuration as the counter traverses. The inverse kinetics technique was used in all of these measurements, including the traverses. Central measurements were made by oscillating the sample between two positions, in and out, with continuous motion between positions. The traverses were obtained by inserting 10 sec pauses every 2.173 in. (one matrix tube width) during the motion between the in and out positions. The reactivity as a function of time was then obtained from the power history, and corrections for reactor drift were applied as described in Paper II-33.

The samples used were 2.173 in. long and up to 0.40 in. diam, with masses and compositions as given in Paper II-37. The positioning of the samples at the beginning of a run is accurate to about $\pm 1/16$ in., and the repeatability during oscillation is about ± 0.01 in. Measurements of the empty sample carrier, dummy capsules, and samples were made, and the empty carrier and dummy capsule data were combined to give a cap-

TABLE II-34-I. Normalized Radial ^{239}Pu Counter Traverses in ZPPR Assembly 2

Radius, in.	z = 3 in.		z = 14 in.		z = 22 in.	
	Normalized Count-rate	Error, %	Normalized Count-rate	Error, %	Normalized Count-rate	Error, %
0.000	1.000	<0.8	1.000	<0.8	1.000	<1.0
2.173	1.002		1.000		0.999	
4.346	0.994		0.990		0.994	
6.519	0.984		0.984		0.986	
8.692	0.969		0.974		0.975	
10.865	0.950		0.961		0.955	
13.038	0.933		0.947		0.934	
15.211	0.912		0.930		0.910	
17.384	0.888		0.905		0.873	
19.557	0.855		0.868		0.838	
21.730	0.818		0.832		0.795	
23.903	0.769		0.781		0.742	
26.076	0.713		0.726		0.685	
28.249	0.651		0.661		0.627	
30.422	0.588		0.604		0.567	
32.595	0.515		0.534		0.502	
34.768	0.448		0.463		0.442	
36.941	0.371		0.396		0.370	
39.114	0.309		0.335		0.300	
41.287	0.249		0.271		0.242	
43.460	0.198		0.215		0.193	
45.633	0.157		0.173		0.155	
47.806	0.125		0.141		0.130	
49.979	0.108		0.121		0.115	
52.152	0.106		0.122		0.118	
54.325	0.0858		0.103		0.107	
56.498	0.0814		0.0838		0.0964	

TABLE II-34-II. Normalized Radial ^{240}Pu Counter Traverses in ZPPR Assembly 2

Radius, in.	z = 3 in.		z = 14 in.		z = 22 in.	
	Normalized Count-rate	Error, %	Normalized Count-rate	Error, %	Normalized Count-rate	Error, %
0.000	1.000	<0.7	1.000	<1.0	1.000	<0.9
2.173	1.000		0.995		0.995	
4.346	0.989		0.985		0.987	
6.519	0.984		0.975		0.983	
8.692	0.962		0.967		0.977	
10.865	0.958		0.956		0.958	
13.038	0.942		0.934		0.943	
15.211	0.926		0.918		0.924	
17.384	0.909		0.889		0.909	
19.557	0.900		0.871		0.890	
21.730	0.877		0.851		0.875	
22.816	0.871		—		—	
23.903	0.883		0.816		0.876	
24.979	0.879		—		—	
26.076	0.868		0.775		0.852	
28.249	0.821		0.715		0.811	
30.422	0.741		0.644		0.733	
32.595	0.638		0.557		0.629	
34.768	0.498		0.461		0.497	
36.941	0.322		0.347		0.317	
38.027	0.255		—		—	
39.114	0.200		0.250		0.197	
41.287	0.144		0.178		0.126	
43.460	0.0833		0.124		0.0820	
45.633	0.0547		0.0868		0.0553	
47.806	0.0372	1.0	0.0606		0.0361	
49.979	0.0246	1.4	0.0435		0.0246	
52.152	0.0158	1.7	0.0303	1.1	0.0170	1.2
54.325	0.00985	2.2	0.0212	1.3	0.0106	1.6
56.498	0.00718	2.6	0.0168	1.5	0.00790	1.8

TABLE II-34-III. Normalized Radial ^{238}U Counter Traverses in ZPPR Assembly 2

Radius, in.	z = 3 in.		z = 14 in.		z = 22 in.	
	Normalized Countrate	Error, %	Normalized Countrate	Error, %	Normalized Countrate	Error, %
0.000	1.000	<0.9	1.000	<0.9	1.000	<3.5
2.173	0.992		0.990		0.984, 1.001	
4.346	0.993		0.992		0.965, 0.982	
6.519	0.974		0.975		0.945, 0.960	
8.692	0.972		0.966		0.938, 0.930	
10.865	0.947		0.955		0.945, 0.938	
13.038	0.944		0.938		0.925, 0.942	
15.211	0.920		0.924		0.934, 0.885	
17.384	0.898		0.906		0.901, 0.873	
19.557	0.879		0.886		0.896, 0.898	
21.730	0.876		0.879		0.865, 0.883	
23.903	0.896		0.905		0.840, 0.848	
26.076	0.906		0.914		0.815	
28.249	0.862		0.859		0.782	
30.422	0.777		0.790		0.704	<4.5
32.595	0.651		0.675		0.599	
34.768	0.502		0.528		0.498	
36.941	0.279		0.292		0.344	
39.114	0.148		0.154		0.238	
41.287	0.0821		0.0874		0.148	
43.460	0.0480		0.0511		0.0974	
45.633	0.0281		0.0304		0.0634	
47.806	0.0174		0.0184		0.0414	
49.979	0.0102		0.0113		0.0255	
52.152	0.00581	1.1	0.00635	1.1	0.0156	
54.325	0.00284	1.5	0.00327	1.5	0.00858	6.0
56.498	0.00170	1.7	0.00197	1.7	0.00531	7.7

TABLE II-34-IV. Normalized Radial ^{235}U Counter Traverses in ZPPR Assembly 2

Radius, in.	z = 3 in.		z = 14 in.		z = 22 in.	
	Normalized Countrate	Error, %	Normalized Countrate	Error, %	Normalized Countrate	Error, %
0.000	1.000	<0.8	1.000	<0.8	1.000	<1.0
2.173	0.988		1.002		0.996	
4.346	0.997		1.002		0.991	
6.519	0.980		0.987		0.982	
8.692	0.959		0.985		0.974	
10.865	0.952		0.962		0.962	
13.038	0.936		0.944		0.941	
15.211	0.896		0.926		0.909	
17.384	0.871		0.894		0.875	
19.557	0.833		0.858		0.843	
21.730	0.787		0.818		0.796	
23.903	0.740		0.749		0.744	
26.076	0.670		0.691		0.682	
28.249	—		0.641		0.627	
30.422	0.556		0.575		0.563	
32.595	—		0.511		0.506	
34.768	0.431		0.454		0.446	
36.941	—		0.402		0.375	
39.114	0.318		0.340		0.305	
41.287	—		0.282		0.245	
43.460	0.208		0.225		0.193	
45.633	—		0.178		0.153	
47.806	0.129		0.140		0.123	
49.979	—		0.115		0.104	
52.152	0.098		0.108		0.101	
54.325	—		0.0881		0.0941	
56.498	0.057		0.0681		0.0711	

TABLE II-34-V. Normalized Radial ^{10}B Counter Traverses in ZPPR Assembly 2

Radius, in.	z = 3 in.		z = 14 in.		z = 22 in.	
	Normalized Count-rate	Error, %	Normalized Count-rate	Error, %	Normalized Count-rate	Error, %
0.000	1.000	<0.8	1.000	<0.6	1.000	<1.0
2.173	0.995		1.002		0.999	
4.346	0.989		1.000		0.997	
6.519	0.973		0.995		0.986	
8.692	0.965		0.972		0.982	
10.865	0.947		0.947		0.961	
13.038	0.923		0.931		0.932	
15.211	0.902		0.909		0.905	
17.384	0.861		0.894		0.881	
19.557	0.813		0.854		0.832	
21.730	0.787		0.801		0.788	
23.903	0.706		0.741		0.727	
26.076	0.629		0.664		0.672	
28.249	0.582		0.598		0.612	
30.422	0.509		0.536		0.552	
32.595	0.461		0.485		0.494	
34.768	0.412		0.442		0.437	
36.941	0.397		0.404		0.369	
39.114	0.356		0.364		0.305	
41.287	0.305		0.312		0.254	
43.460	0.257		0.259		0.205	
45.633	0.209		0.212		0.167	
47.806	0.171		0.177		0.140	
49.979	0.155		0.157		0.127	
52.152	0.159		0.166		0.136	
54.325	0.140		0.152		0.132	
56.498	0.114	↓	0.128	↓	0.120	↓

TABLE II-34-VII. Results of Inner Core Fission Ratio Measurements Relative to ^{235}U in ZPPR Assembly 2

Isotope Ratio	Fission Ratio		
	Measured	Calculated	C/E
$^{233}U/^{235}U$	1.446 ± 0.022	1.384	0.957
$^{234}U/^{235}U$	0.1492 ± 0.0023	0.1309	0.878
$^{236}U/^{235}U$	0.0443 ± 0.0007	0.4043	0.912
$^{238}U/^{235}U$	0.0201 ± 0.0004	0.0187	0.929
$^{239}Pu/^{235}U$	0.9372 ± 0.0142	0.8616	0.919
$^{240}Pu/^{235}U$	0.1704 ± 0.0026	0.1584	0.929

TABLE II-34-VIII. Fission Ratios as a Function of Radial Position, 3 In. Back from the Interface in ZPPR Assembly 2

Region	Radius, cm	Pu-239 / U-235	U-238 / U-235
Inner core		0.9372 ± 2.1%	0.0201 ± 2.1%
	5.519	0.9502	0.0201
	11.039	0.9340	0.0200
	16.558	0.9401	0.0199
	22.078	0.9465	0.0203
	27.597	0.9350	0.0200
	33.116	0.9338	0.0202
	38.636	0.9542	0.0206
	44.155	0.9559	0.0207
	49.675	0.9616	0.0212
	55.194	0.9743	0.0224
	60.714	0.9690	0.0242
Outer core	66.233	0.9980	0.0272
	77.323	0.9913	0.0281
	88.311	0.9759	0.0234
Radial blanket	99.350	0.9088	0.0093
	110.388	0.8969	0.0047
	121.427	0.9107	0.0027 ± 2.2%
Radial reflector	132.466	1.0131	0.0012 ± 2.8%
	143.505	1.3467	0.0006 ± 4.4%

TABLE II-34-VI. Axial Counter Traverse Data from ZPPR Assembly 2

Dist. from Interface, in.	^{235}U		^{240}Pu		^{239}Pu		^{238}U		^{10}B	
	Norm. Count	Error,[a] ±%	Norm. Count	Error,[a] ±%	Norm. Count	Error,[a] ±%	Norm. Count	Error,[a] ±%	Norm. Count	Error,[a] ±%
3.036	1.000	—	1.000	—	1.000	—	1.000	—	1.000	—
7.036	0.938	<0.5	0.913	<0.4	0.937	<0.5	0.912	<0.4	0.939	<0.4
11.036	0.823	<0.5	0.787	<0.5	0.816	<0.5	0.788	<0.4	0.835	<0.4
14.036	0.732	<0.5	0.651	<0.4	0.711	<0.4	0.656	<0.4	0.750	<0.4
16.036	—	—	—	—	0.637	<0.5	0.538	<0.5	0.705	<0.4
18.036	0.621	<0.6	0.403	<0.5	0.595	<0.5	0.369	<0.5	0.687	<0.4
20.036	—	—	—	—	0.553	<0.5	0.215	<0.5	0.676	<0.4
22.036	0.528	<0.5	0.205	<0.6	0.495	<0.5	0.137	<0.5	0.631	<0.4
26.036	0.406	<0.6	0.114	<0.6	0.386	<0.5	0.0617	<0.8	0.526	<0.5
30.036	—	—	—	—	0.294	<0.6	0.0286	<1.0	0.412	<0.5

[a] Only statistical counting errors are considered (one standard deviation).

sule worth in $\Delta k/k$ per gram. This information was then used to account for slight fluctuations in capsule weight for the various samples. The sodium sample and its dummy were treated separately, since this particular sample is larger than the standard size. The Na-4 sample was 6 in. long and 0.4 in. diam so as to provide a sufficient reactivity signal while not requiring a larger traverse tube.

The results of the central measurements at the three inch axial position are presented in Paper II-37, and the worth as a function of position for ^{239}Pu, ^{238}U, ^{10}B, sodium, and tantalum are given in Figs. II-34-11

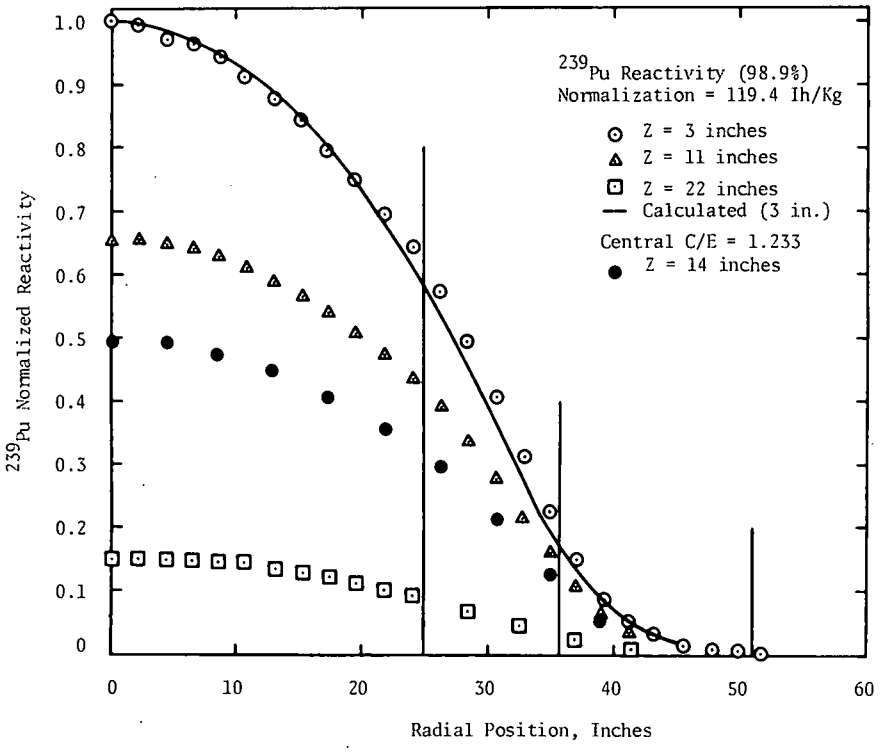

FIG. II-34-11. Radial Worth Distributions for ^{239}Pu in ZPPR Assembly 2. *ANL-ID-103-A11988.*

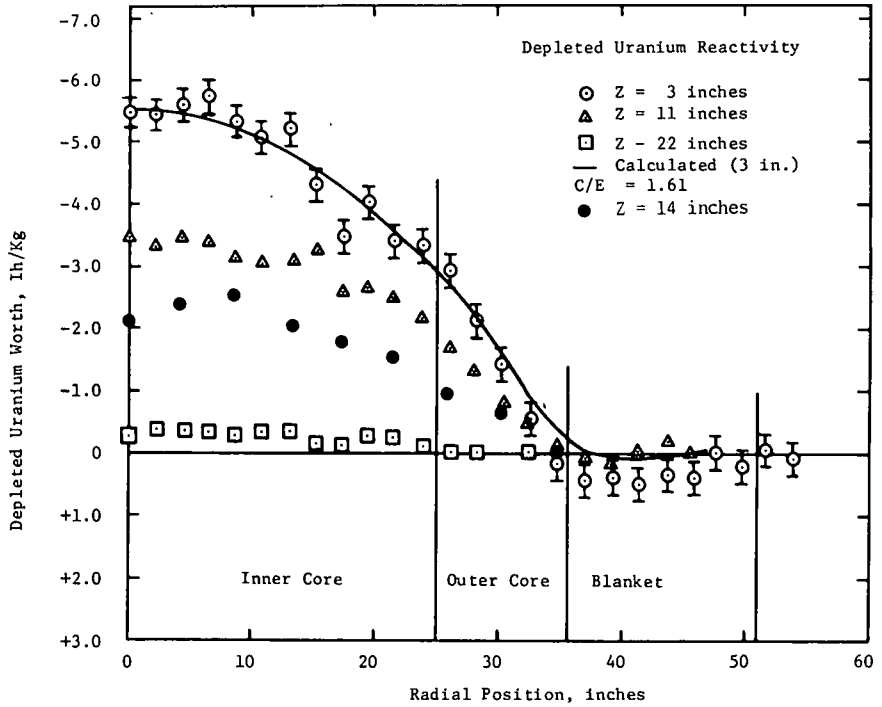

FIG. II-34-12. Radial Worth Distributions for ^{238}U in ZPPR Assembly 2. *ANL-ID-103-A11986.*

through II-34-15. The calculated curves are included for the data at the 3 in. position, and indicate good comparison insofar as the shape of the curve is concerned, but the substantial central worth discrepancy is still present. The calculations were based on 2D diffusion calculations of the fluxes and adjoints, as in the case of the reaction rate traverses, and the worths were determined from 2D diffusion perturbation calcula-

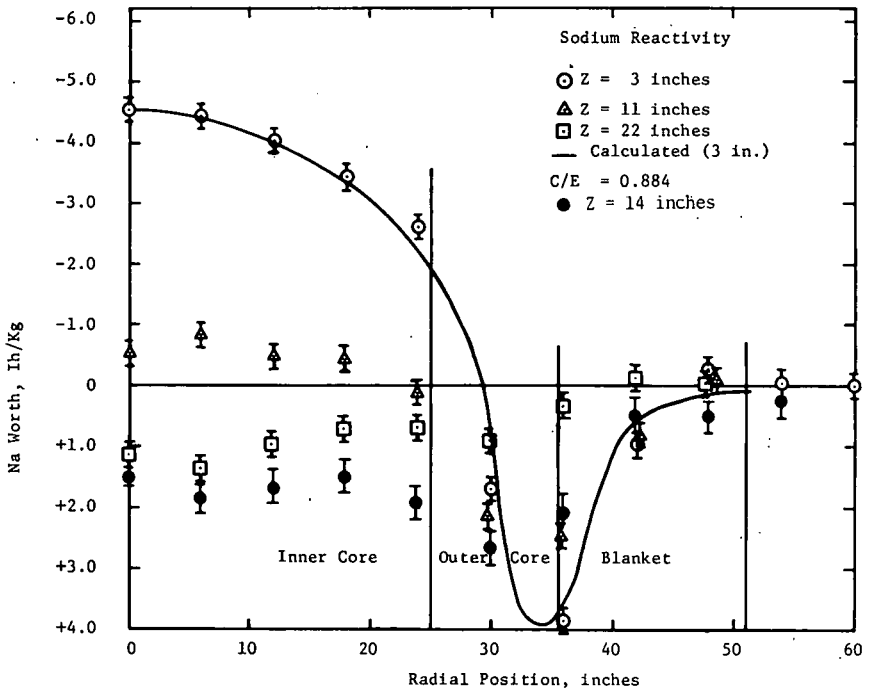

FIG. II-34-13. Radial Worth Distributions for Sodium in ZPPR Assembly 2. *ANL-ID-103-A11982.*

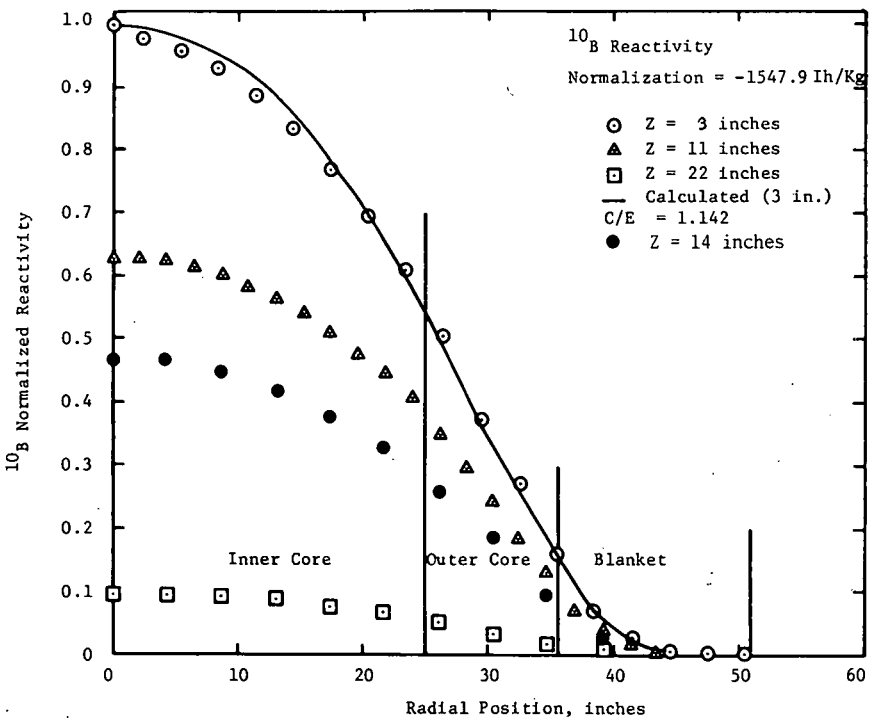

FIG. II-34-14. Radial Worth Distributions for ^{10}B in ZPPR Assembly 2. *ANL-ID-103-A11987.*

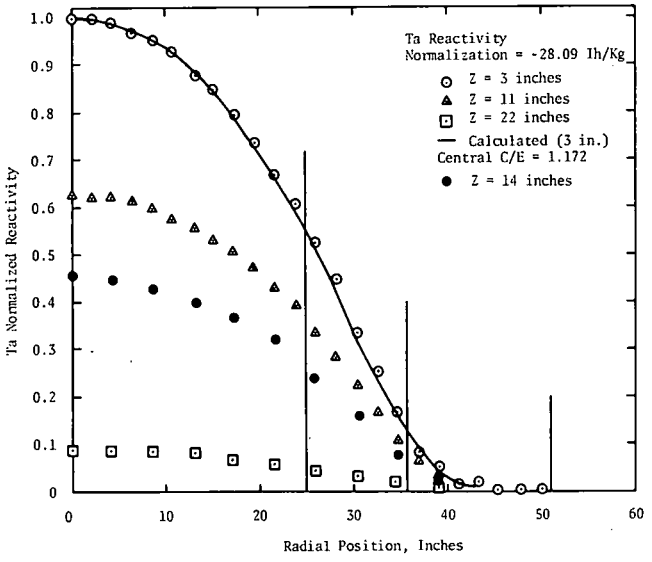

FIG. II-34-15. Radial Worth Distributions for Ta in ZPPR Assembly 2. *ANL-ID-103-A11983.*

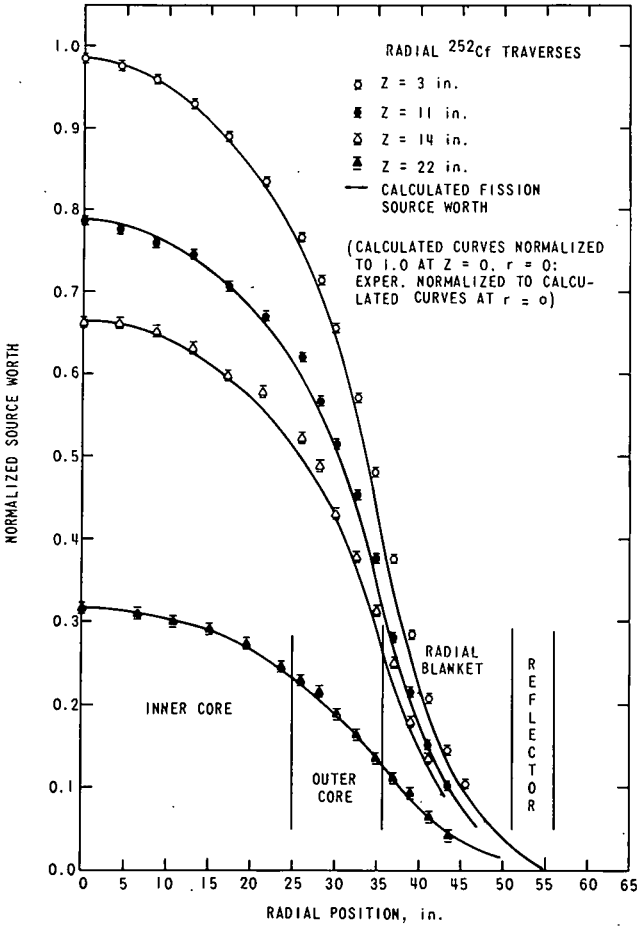

FIG. II-34-16. Radial Worth Distributions for a ^{252}Cf Neutron Source in ZPPR Assembly 2. *ANL-ID-103-B11001.*

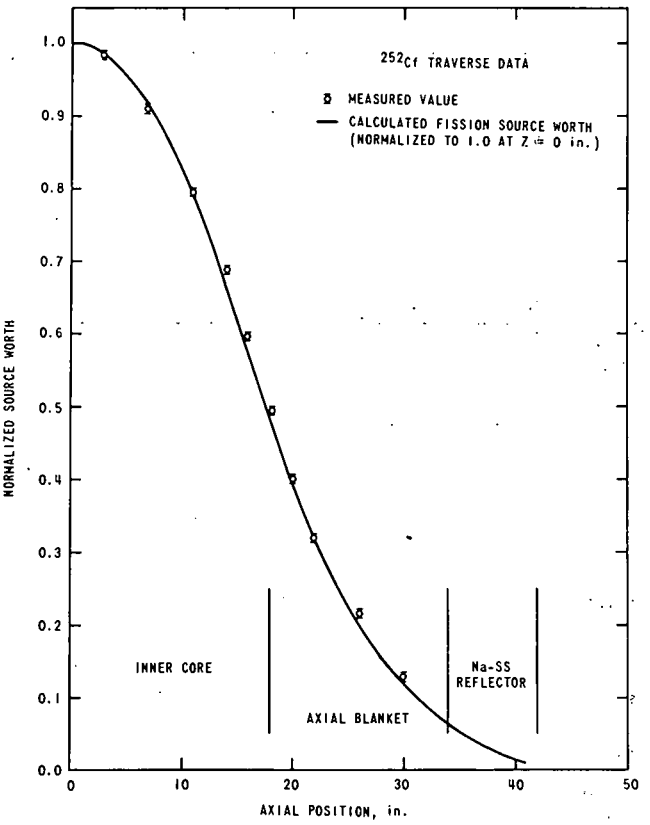

FIG. II-34-17. Axial Worth Distributions for a ^{252}Cf Neutron Source in ZPPR Assembly 2. *ANL-ID-103-B11000.*

tions, using inhour conversion factors described in Paper II-45.

Reactivity traverses were also run with a ^{252}Cf source in a standard perturbation-sample capsule, in each of the axial positions where other reactivity samples were run. The measurements were done at low power (10–20 W) and again at ten times that power, where the source worth was small, to provide a dummy measurement. An axial traverse was also run to provide normalization of the radial traverses, since they are power-dependent. The radial and axial results are illustrated in Figs. II-34-16 and II-34-17, respectively. The calculations shown on these two figures represent the product, summed over energy groups, of the adjoint flux and the pointwise fission source as obtained from two-dimensional diffusion theory. The calculated curves are all normalized to 1.0 at the core center ($r = 0$, $z = 0$). The axial measurements are normalized to the calculations at $z = 3$ in., and each of the measured radial traverses is normalized to its calculated curve at $r = 0$ in. The normalization of the radial data is, however, identical to that for the axial data with the exception of the 14-in. traverse position. This can be seen from the comparison between experiment and calculation for the axial traverse.

TABLE II-34-IX. Source-Constant Comparisons between Radial and Axial ^{252}Cf Traverses

Axial Position, in.	Source-Constant	
	Radial Center Point[a]	Axial
3	—	1.97 ± 0.006
11	1.59 ± 0.005	1.59 ± 0.009
14	1.32 ± 0.005	1.37 ± 0.009
22	0.63 ± 0.005	0.64 ± 0.009

[a] 3-in. measurement performed with different detector efficiency; therefore Q is not available.

The worth of a neutron source in a reactor is given by

$$\Delta k = \frac{S\ell\epsilon}{n} = \frac{Q}{n},$$

where S is in neutrons/sec, ℓ is the neutron lifetime, ϵ represents detector efficiency, and n is the neutron density. The quantity Q then represents an effective source term which is power independent. A comparison of Q as obtained from the axial ^{252}Cf traverse and from the center points of the radial traverses is given in Table II-34-IX, and indicates good consistency between the measurements. All of the radial measurements appear slightly high near the inner core/outer core boundary and in the outer core, but otherwise the comparison of shapes is quite accurate.

Conclusions

All of the experiments performed in ZPPR Assembly 2 involving reaction rate and/or reactivity distributions appear to be consistent with 2D diffusion theory analysis insofar as the shapes of the distributions are concerned. It would appear that within core regions this is especially true, both in axial and radial directions. Some small discrepancies were noted in the calculations through the axial blanket, and in the outer core for the ^{252}Cf traverse data. None of the discrepancies are large enough to suggest any serious problem in reaction rate or reactivity distributions, although the central worth discrepancies are still present as seen in the normalizations of the reactivity curves.

References

1. R. E. Kaiser and R. J. Norris, *Critical Mass Evaluation in ZPPR Assembly 2, a Demonstration Reactor Benchmark Assembly*, Applied Physics Division Annual Report, July 1, 1969, to June 30, 1970, ANL-7710, pp. 140–146.
2. B. J. Toppel, Ed., *The Argonne Reactor Computation System* ANL-7332 (1967).
3. F. L. Fillmore and L. D. Felton, *The CALHET-2 Heterogeneous Perturbation Theory Code and Application to ZPR-3-48*, AI-69-13 (1969).

II-35. Critical Mass Evaluation for the Final Plate Version of ZPPR Assembly 2 and Comparison of Reference Loadings

R. E. Kaiser, A. L. Hess and R. J. Norris

Introduction

Assembly 2 in the Zero Power Plutonium Reactor (ZPPR) is a simplified representation of the current designs considered for the 300–500 MWe demonstration liquid metal fast breeder reactor (LMFBR). The program of experiments on ZPPR-2, keyed to obtain information necessary in the design of the demonstration reactor, has been underway since early 1970. In the course of the experiments, four different reference configurations have been established to determine the clean critical mass for a basic benchmark design of a cylindrical core with inner and outer zones of equal volume. The initial approach to critical yielded a reference configuration (Loading No. 21) with a 52% inner/48% outer zone volume split. The second reference configuration, Loading No. 47, was the original 50/50 representation based on the initial drawer-material loading patterns. Subsequently, the drawer loading patterns were modified and the third configuration (Loading No. 77) was a 50/50 core-zone loading with a slightly higher inner core sodium density. These first three configurations all had control rods in the inner core which were spiked with extra columns of plutonium. The final reference configuration for the plate version of Assembly 2 was Loading No. 90, a 50/50 core-zone split based on the modified composition but with no spiked control rods.

Descriptions of the first two configurations (Loadings No. 21 and 47) and the evaluation of their just-critical fuel masses, are given in Ref. 1. In this paper we will describe the Loadings 77 and 90 configurations, discuss the corrections to establish the critical masses, and intercompare the results from the three 50/50 configurations. The design and results from Loading 90

have been adopted to generate a benchmark model for testing of cross sections; this model is given in Paper II-50.

Assembly Design

The basic core-zone composition in Assembly 2 (with 32%-equivalent PuO_2-UO_2, 40% sodium, 19% stainless steel and 9% void) simulates that of typical power LMFBR designs and matches in composition both the standard rodded-zone experiments and the Variable Temperature Rodded Zone (VTRZ)[2] experiments designed for the fast critical facilities. A core length of 36-in. was selected and a volume of around 1250 liters per zone was expected, with the plutonium enrichment in the outer zone relative to the inner zone set at 1.5:1.

Surrounding the core are 16-in.-thick radial and 18-in.-thick axial blankets of compositions simulating sodium-cooled UO_2 blankets. The radial blanket in turn is enclosed by a 4-in.-thick steel reflector. Behind the axial blanket in Half 1 of the reactor is an 8-in. axial reflector of equal volume fractions of sodium and stainless steel. Because of material limitations, the Half 2 axial reflector was made of 5-in.-thick solid steel.

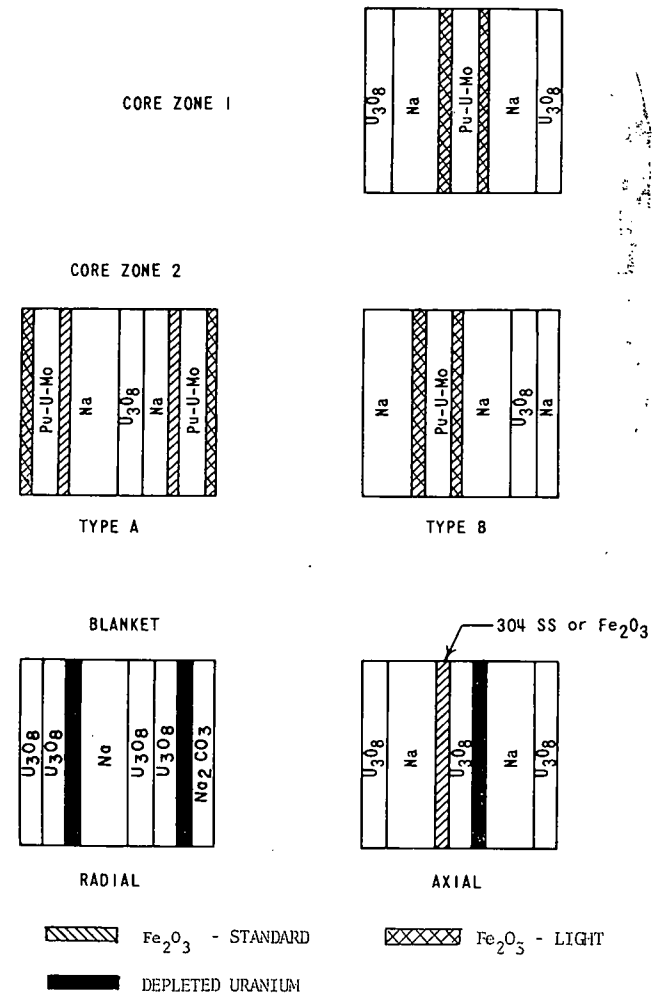

Fig. II-35-1. ZPPR Assembly 2 Drawer Loadings. *ANL Neg. No. 116-945.*

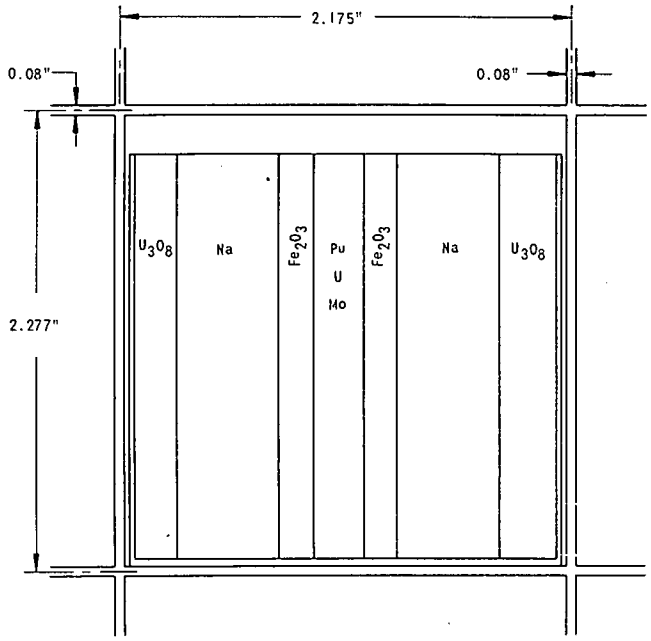

Fig. II-35-2. ZPPR Matrix Configuration with Assembly 2 Inner Core Drawer Loading. *ANL Neg. No. 116-946.*

Regional Drawer Loadings

Figure II-35-1 shows the basic material drawer loading patterns used in the core and blanket regions of Assembly 2. The overall cells for each region include the drawer and matrix tube as illustrated for the inner core in Fig. II-35-2. The unit-matrix dimensions in Fig. II-35-2 (2.175 x 2.277 in.) are based on the overall loaded assembly dimensions and are revisions from the nominal tube dimensions (2.173 x 2.273 in.) upon which previous specifications[1] were based. Consequently, dimensions and compositions given in Ref. 1 require complementary adjustments.

The core zones also included movable fuel-loaded drawers (for reactor control) with different steel and sodium contents and in some cases spiking with extra fuel plates. In addition, the reactor safety rods (poison rods normally withdrawn) were provided with ½-in.-wide steel guide tubes which were adjacent to narrow (1½-in. wide) core drawers, thus giving some core matrix units with altered sodium and steel contents. Table II-35-I lists the material densities for the various core drawers.

The radial blanket drawer loadings were based on the single cell pattern shown in Fig. II-35-1; however, to enable the higher core sodium density, ½-in. columns of sodium in the outer blanket regions were replaced

TABLE II-35-I. Compositions of Core Sections, Radial Blankets, and Radial Reflector in Front Drawers of Final Plate Version of ZPPR Assembly 2 (Loading 75-On)

Region Drawer Type:	Inner Core Standard	Inner Core with Rod Guide	Inner Core Control	Inner Core Spiked Control	Outer Core A (2 cols. Pu-U-Mo)	Outer Core B (1 col. Pu-U-Mo)	Outer Core B with Rod Guide	Inner Radial Blanket in Front Drawers	Outer Radial Blanket in Front Drawers	Radial Reflector (in matrix)
Section length, cm. (per reactor half)	45.811	45.811	45.847	45.847	45.811	45.811	45.811	58.511	58.511	96.52
	Average Composition,[a] 10^{22} atoms cm^3									
^{239}Pu	0.08437	0.08250	0.08244	0.16686	0.16893	0.08446	0.08250			
^{240}Pu	0.01117	0.01092	0.01091	0.02209	0.02237	0.01118	0.01092			
^{241}Pu[b]	0.00154	0.00147	0.00147	0.00300	0.00307	0.00153	0.00147			
^{242}Pu	0.00018	0.00018	0.00017	0.00036	0.00037	0.00018	0.00018			
^{238}Pu	0.00006	0.00005	0.00005	0.00011	0.00011	0.00006	0.00005			
^{241}Am[b]	0.00029	0.00028	0.00028	0.00057	0.00058	0.00029	0.00028			
^{235}U	0.00123	0.00122	0.00122	0.00140	0.00142	0.00088	0.00087	0.00244	0.00244	
^{238}U	0.55515	0.54938	0.54896	0.63047	0.63687	0.39741	0.39143	1.10457	1.10456	
Na	0.88611	0.44306	0.88543	0.63960	0.63954	1.08521	0.64269	0.63912	0.60021	
O	1.31252	1.31251	1.12057	1.17038	1.45095	0.89178	0.89178	2.00424	2.00438	
Fe	1.25739	1.22230	1.41129	1.80972	1.56711	1.19601	1.30168	0.69594	0.75534	7.15610
Cr	0.26994	0.25870	0.35173	0.37449	0.25193	0.25238	0.28194	0.20005	0.21738	0.12052
Ni	0.12200	0.11639	0.15989	0.17134	0.11589	0.11602	0.12797	0.09003	0.09864	0.05133
Mn	0.02092	0.02052	0.02719	0.02882	0.02016	0.02020	0.02221	0.01541	0.01725	0.05981
Si	0.01308	0.01140	0.01563	0.01674	0.01128	0.01132	0.01251	0.00894	0.00966	0.00503
Mo	0.02306	0.02273	0.02304	0.04465	0.04471	0.02313	0.02278	0.00143	0.00147	0.00118
Cu	0.00189	0.00204	0.00254	0.00268	0.00203	0.00203	0.00218	0.00169	0.00181	0.00126
C	0.00294	0.00307	0.00400	0.00400	0.00233	0.00233	0.00307	0.10111	0.10117	0.05575
Al	0.00034	0.00025	0.00035	0.00044	0.00043	0.00044	0.00034	0.00021	0.00027	
P	0.00050	0.00053	0.00065	0.00065	0.00041	0.00041	0.00053	0.00041	0.00041	0.00016
S	0.00017	0.00019	0.00028	0.00028	0.00014	0.00014	0.00019	0.00014	0.00014	0.00249
H								0.00083	0.00083	

[a] Excludes impurities (mostly light elements) in fuel plates, equal to about 0.4 w/o of ^{239}Pu content.
[b] As of Loading 90 reference date, 10-9-70.

with double ¼-in. columns, thus creating inner and outer radial blanket zones of different compositions and also a difference in the blanket loadings in the front 23 in. and back 11 in. Table II-35-I includes the radial blanket compositions in the front drawers, and Table II-35-II lists the back drawer radial blanket compositions.

The axial blankets behind the core zones were based on a two-drawer cell as indicated in Fig. II-35-1. However, the blanket loadings behind the inner core included steel shims on the drawer bottoms, and in both zones there were composition perturbations due to control rods and safety rod channels. The average axial blanket compositions in Table II-35-II include the effects of all the drawer variations. The spring gap cited in Table II-35-II represents the spring, the back piece of the front drawer, and the front piece of the back drawer.

The loadings of axial reflector behind the radial and axial blanket regions in Half No. 1 (cell pattern not shown) basically simulated a half-steel, half-sodium region. With the loadings of different types of steel, shims, and the other core perturbations, there arose three axial reflector subregions in Half 1 with the compositions indicated in Table II-35-II. Similarly, three subregions were obtained in the all-steel Half 2 axial reflector. Table II-35-I contains the radial reflector composition.

Reference Critical Configurations

Initial Critical Configuration

ZPPR Assembly 2 first went critical on March 4, 1970 and the clean reference configuration, Loading No. 21, was run on March 12. Kaiser and Norris[1] have shown the interface diagram for Loading 21 which had a total core volume of 2506 liters split 52/48 into the inner and outer zones. The loaded fuel mass was 1067.3 kg (^{239}Pu + ^{241}Pu).

Original Equal-Zone Configuration

The first reference equal-zone configuration, Loading No. 47 run on April 16, 1970, had a total core volume

TABLE II-35-II. COMPOSITIONS OF AXIAL BLANKET AND REFLECTOR REGIONS IN REFERENCE LOADING 90 OF FINAL PLATE VERSION OF ZPPR ASSEMBLY 2

Axial Region:	Inner Radial Blanket in Back Drawers	Outer Radial Blanket in Back Drawers	Average Axial Blanket of Inner Core [a,b]	Average Axial Blanket of Outer Core[a,b]	Spring Gap between Front and Back Drawers	Half No. 1 Axial Reflector			Half No. 2 Axial Reflector		
						Average behind Inner Core[a]	Average behind Outer Core[a]	Behind Radial Blanket Regions	Average behind Inner Core[a]	Average behind Outer Core[a]	Behind Radial Blanket Regions
Section Length, cm:	27.940	27.940	40.640[b]	40.640[b]	0.735	20.320	20.320	20.320	12.700	12.700	12.700
	Composition, 10^{22} atoms/cm^3										
^{235}U	0.00246	0.00246	0.00156	0.00156	—	—	—	—	—	—	—
^{238}U	1.11688	1.11688	0.70356	0.70570	—	—	—	—	—	—	—
Na	0.64126	0.58818	0.87386	0.88084	—	0.88891	0.89766	0.89985	—	—	—
O	2.03209	2.03209	1.38946	1.40083	—	—	—	—	—	—	—
Fe	0.68479	0.75154	1.07508	0.93550	2.11333	3.17508	3.03278	4.03694	7.31947	7.24109	7.25594
Cr	0.19725	0.21668	0.28351	0.24180	0.43927	0.89182	0.85066	0.19944	0.20448	0.15377	0.14877
Ni	0.08925	0.09897	0.12753	0.10954	0.15030	0.40205	0.38434	0.08976	0.08832	0.06618	0.06392
Mn	0.01643	0.01782	0.02297	0.02054	0.02792	0.08272	0.08039	0.04078	0.06461	0.06203	0.06179
Si	0.00877	0.00968	0.01410	0.01116	0.01689	0.04795	0.04505	0.00872	0.01000	0.00655	0.00627
Mo	0.00142	0.00147	0.00143	0.00142	0.00230	0.00142	0.00142	0.00142	0.00129	0.00129	0.00128
Cu	0.00169	0.00181	0.00174	0.00173	0.00300	0.00171	0.00171	0.00171	0.00142	0.00142	0.00141
C	0.10163	0.10163	0.00359	0.00296	0.02840	0.01399	0.01336	0.02901	0.05595	0.05595	0.05613
Al	0.00018	0.00027	0.00024	0.00024	0.00010	0.00020	0.00021	0.00021	—	—	—
P	0.00041	0.00041	0.00065	0.00056	0.00097	0.00288	0.00279	0.00102	0.00174	0.00164	0.00162
S	0.00014	0.00014	0.00022	0.00018	0.00038	0.00063	0.00060	0.00132	0.00252	0.00251	0.00252
H	0.00084	0.00084	—	—	—	—	—	—	—	—	—

[a] Average for whole region includes perturbations from control drawers and safety-rod channels.
[b] For total 5-in. section in front drawers plus 11-in. section in back drawers, excluding spring gap.

of 2382 liters. Reference 1 also describes this configuration. A review of the records for loading 47, however, have given a loaded-mass value of 1017.87 kg (^{239}Pu + ^{241}Pu) and a corrected critical mass of 1016.8 ± 1.0 kg, both revisions of the Ref. 1 quotations.

MODIFIED EQUAL-ZONE CONFIGURATION WITH SPIKED CONTROL RODS

The sodium density in the inner core of the first 50/50 configuration was less than desired. In order to obtain a better match with pin-calandria compositions, drawer loadings were modified to use only ½ in. sodium cans in the core regions, the axial blanket, and the inner portions of the radial blanket. Thus in the modified equal-zone version, the radial blanket is divided into two sub-regions with different sodium and steel contents. The reduction of sodium cladding in the inner core entailed a plate/calandria mismatch in steel content; this was countered by adding 1/16 in. steel rims at the bottom of the inner core drawers.

The modified composition equal-zone reference, Loading 77, was established June 22, 1970 and had core-zone outlines identical with those of the previous reference (Loading 47). Figure II-35-3 shows the interface pattern for Loading 77, which had a loaded fuel mass of 1017.7 kg of (^{239}Pu + ^{241}Pu). With the unit matrix dimensions in Fig. II-35-2 and the Table II-35-I compositions, the interface diagram defines an *xy* model for the as-built, modified 50/50 reference configuration (uncorrected). Figures II-35-4 and II-35-5 give the *rz* geometry for an equivalent volume, smooth cylindrical representation of the uncorrected as-built system. With all control rods in and at an average core temperature of 24.9°C, the excess reactivity of the as-built system was about 0.064 % $\Delta k/k$. Table II-35-III gives the average compositions (including the perturbations of control drawers and safety-rod channels) for the as-built core zones of Loading 77; also in the table is a composition for an inner core were it without fuel spikes in the control rods. The blanket and reflector region compositions in Table II-35-II are specifically for the later reference (Loading 90), but are reasonably close for use with a Loading 77 model.

FINAL EQUAL-ZONE CONFIGURATION, NO SPIKED CONTROL RODS

The third reference core for the equal-zone configuration, Loading 90, was established on October 9, 1970.

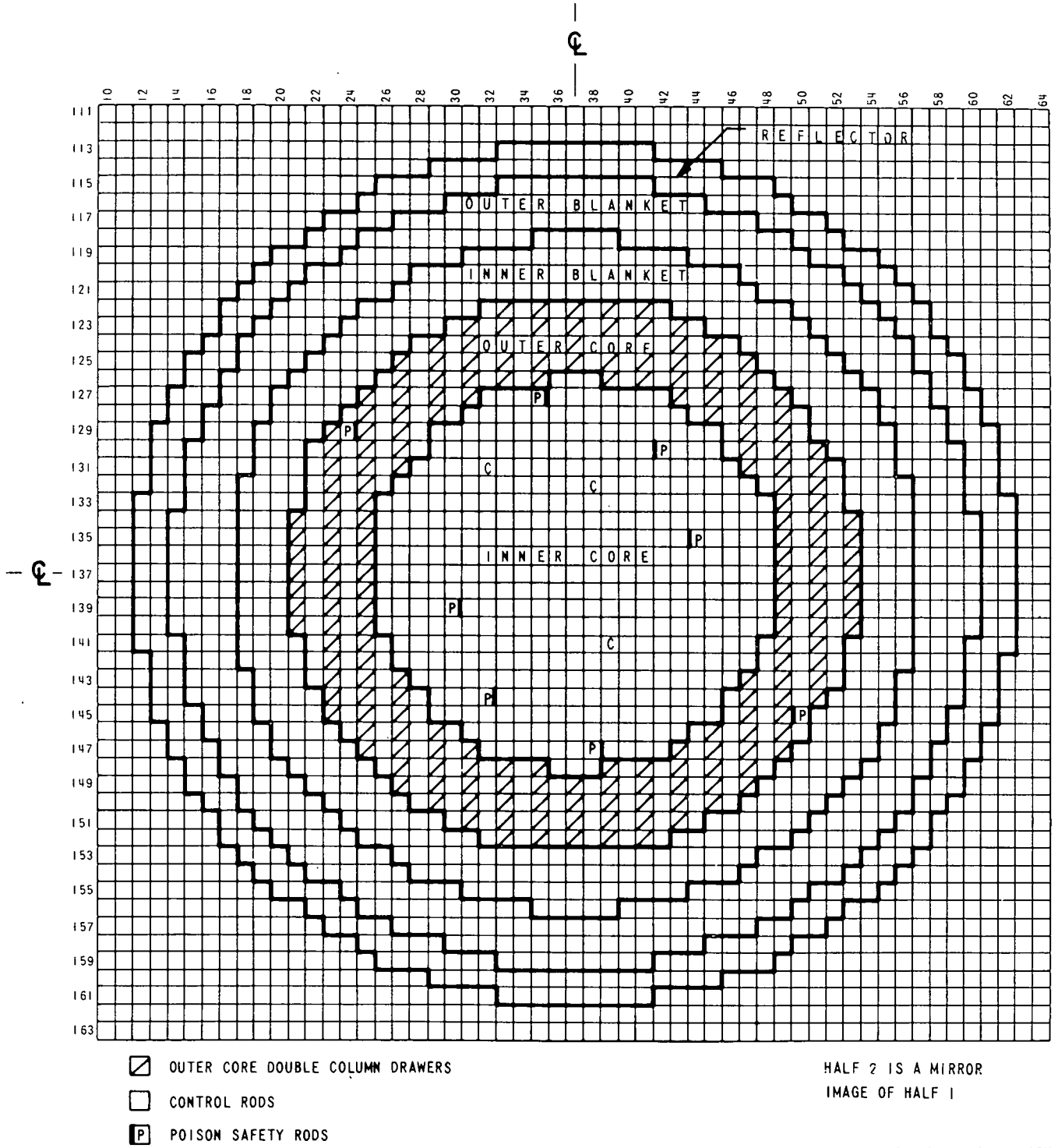

FIG. II-35-3. Interface Diagram for Loading 77 of ZPPR Assembly 2, the Modified Equal-Zone Reference Configuration. *ANL-ID-103-A11603.*

The changes involved in this instance were the installation of shim control rods (in ½ in. safety channels) and the resulting removal of the spiked control drawers. The result was an expansion for criticality to 1194.4 liters per zone and a total loaded mass of 1030.52 ± 1.0 kg ($^{239}Pu + ^{241}Pu$). Figure II-35-6 is the interfac diagram of this reference final plate-version of ZPPI Assembly 2. It should be noted that the control rod positions and some safety rod locations are no longer mirror images in Half No. 2.

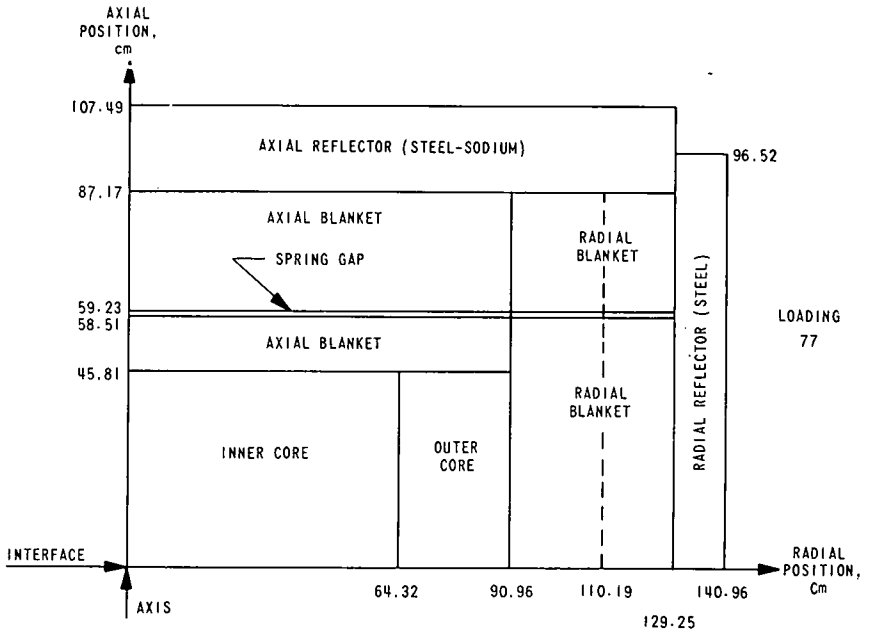

FIG. II-35-4. Cylindrical Representation for the As-built Modified Equal-Zone Configuration of ZPPR Assembly 2, Half 1. *ANL Neg. No. 116-947.*

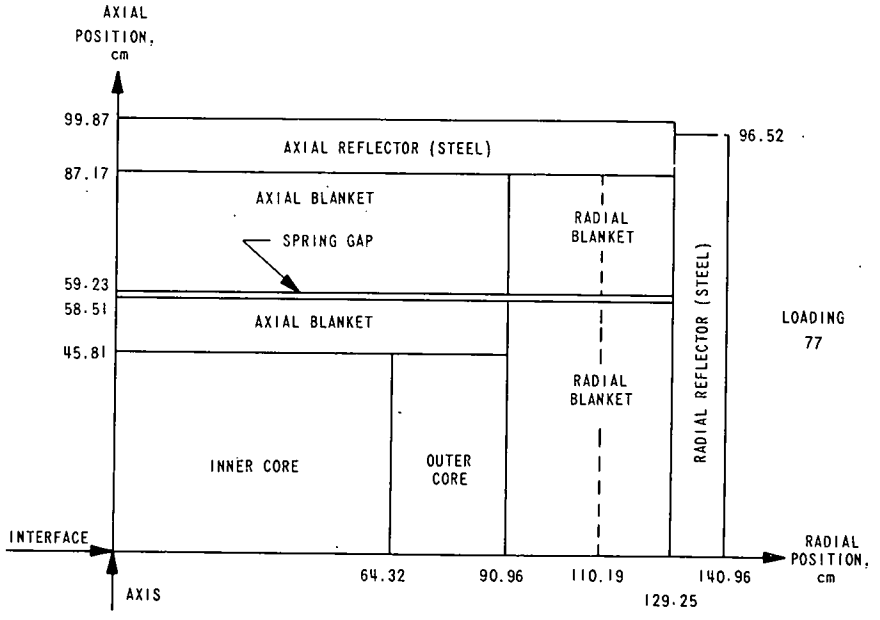

FIG. II-35-5. Cylindrical Representation for the As-Built Modified Equal-Zone Configuration ZPPR Assembly 2, Half 2. *ANL Neg. No. 116-948.*

The Fig. II-35-6 pattern with the Fig. II-35-2 cell dimensions and the Table II-35-I data define an *xy* model for the as-built Loading 90 with an excess reactivity of about 0.062% $\Delta k/k$ for the core at an average operature of 25.3°C. Figures II-35-7 and II-35-8 give *rz* geometry for the as-built Loading 90 represented as a smooth cylinder with region volumes equivalent to actual volumes (no corrections). Table II-35-III includes the average core zone compositions and Tables II-35-I and II-35-II contain the compositions for the blanket and reflector regions.

CRITICAL MASS CORRECTIONS

To derive the critical mass, or the just-critical smooth cylindrical model with uniform region compositions (averages of materials in heterogeneous cells) from the as-built configuration requires corrections for certain model/as-built differences. The corrections

TABLE II-35-III. AVERAGE CORE-ZONE COMPOSITIONS FOR REFERENCE CONFIGURATIONS OF FINAL PLATE VERSION OF ZPPR ASSEMBLY 2

Material	Average Composition,[a] 10^{22} atoms/cm^3				
	Loading No. 77			Loading No. 90	
	As-built Inner Core	Inner Core without Control-Rod Spiking	Outer Core	Inner Core	Outer Core
^{239}Pu	0.08453	0.08433	0.12680	0.08433	0.12741
^{240}Pu	0.01120	0.01117	0.01679	0.01117	0.01687
^{241}Pu[b]	0.00157	0.00156	0.00234	0.00154	0.00232
^{242}Pu	0.00018	0.00018	0.00027	0.00018	0.00028
^{238}Pu	0.00006	0.00006	0.00009	0.00006	0.00009
^{241}Am[b]	0.00026	0.00026	0.00040	0.00029	0.00044
^{235}U	0.00123	0.00123	0.00115	0.00123	0.00115
^{238}U	0.55522	0.55502	0.51546	0.55503	0.51915
Na	0.87897	0.87957	0.85966	0.87964	0.85643
O	1.31122	1.31109	1.16688	1.31158	1.17613
Fe	1.25899	1.25801	1.38251	1.25763	1.38521
Cr	0.27043	0.27037	0.25230	0.27018	0.25229
Ni	0.12223	0.12220	0.11601	0.12210	0.11601
Mn	0.02097	0.02096	0.02019	0.02095	0.02020
Si	0.01308	0.01307	0.01130	0.01307	0.01130
Mo	0.02311	0.02306	0.03394	0.02306	0.03410
Cu	0.00190	0.00190	0.00203	0.00190	0.00203
C	0.00295	0.00295	0.00233	0.00295	0.00233
Al	0.00034	0.00034	0.00043	0.00034	0.00043
P	0.00050	0.00050	0.00041	0.00050	0.00041
S	0.00017	0.00017	0.00014	0.00017	0.00014

[a] Excludes impurities (mostly light elements) in fuel plates equal to about 0.4% of the ^{239}Pu weight.

[b] As of reference dates 6/22/70 for Loading 77 and 10/9/70 for Loading 90.

account for the interface gap, the stepped core outline, spiking of control rods, the excess reactivity in the control rods, the source subcriticality, and referral to a standard core temperature. For comparison of critical masses of different configurations, an accounting of the ^{241}Pu decay is also required.

INTERFACE GAP CORRECTION

Measurements[1] with feeler gauges have indicated an average separation of 2.5 mils between the reactor halves upon closure. In the equal-zone core, a separation worth of 0.73 Ih/mil was derived from a table scram, giving a gap correction of 1.82 Ih. No additional correction was determined for the effect of homogenizing the stainless steel drawer fronts, as this may be considered part of the overall heterogeneity correction.

CORE-EDGE SMOOTHING CORRECTION

Calculated curves of ^{239}Pu worth versus radius, normalized to the drawer worths at the radial boundaries of the inner and outer core zones, provided approximate curves of drawer worth versus radius in the vicinity of the boundaries. The as-built configuration xy details are input to a computer code which does a geometric accounting of the fuel "transferred" from outside to inside the core-zone equivalent-area circle and determines the worth of the "transfers" using the worth versus radius curve. In each case the smoothing effect was quite small because of the core size and the fact that the loading pattern was devised to give the best possible representation of a circle.

EXCESS REACTIVITY AND SPIKED RODS

After a reasonable temperature stabilization period, positions of all control rods are determined at a steady power during the reactor run for each reference configuration. Later rod calibrations then determine the extra reactivity available were the rods to be completely inserted. The additional worth of a spiked rod as opposed to a standard rod was determined as the difference in calibrated rod worth before and after spiking, which was 38.7 Ih/rod for the rods in matrix units 132-31 and 232-31 of Loading 77.

SOURCE SUBCRITICALITY

The spontaneous fission of ^{240}Pu provides a built-in source in a plutonium-fueled assembly, so that at steady-state low powers the reactor will be subcritical by an amount

$$\Delta k = -\frac{S\ell}{n} = -\frac{Q}{CR},$$

where S is the volumetric source strength, ℓ is the neutron lifetime, and n the neutron density, and where $Q = S\ell\epsilon$, ϵ being the detector efficiency, and CR is the detector countrate. The constant Q is evaluated experimentally, which then provides for the evaluation of the degree of subcriticality during the reference run. The correction is obviously power dependent, and may thus vary in significance between different references.

TEMPERATURE CORRECTIONS

Temperature-drift experiments[1] with the reactor air cooling absent provided an average core temperature coefficient of reactivity of -2.9 ± 0.2 Ih/°C. Average temperatures were derived from a selection of core thermocouples in each reference configuration, and the worth difference from a standardized temperature of 22°C was found using the coefficient.

^{241}Pu DECAY EFFECTS

The radioactive decay of ^{241}Pu, with a half-life of 13.2 years, is sufficient to cause a noticeable change in the excess reactivity of a given reference configuration.

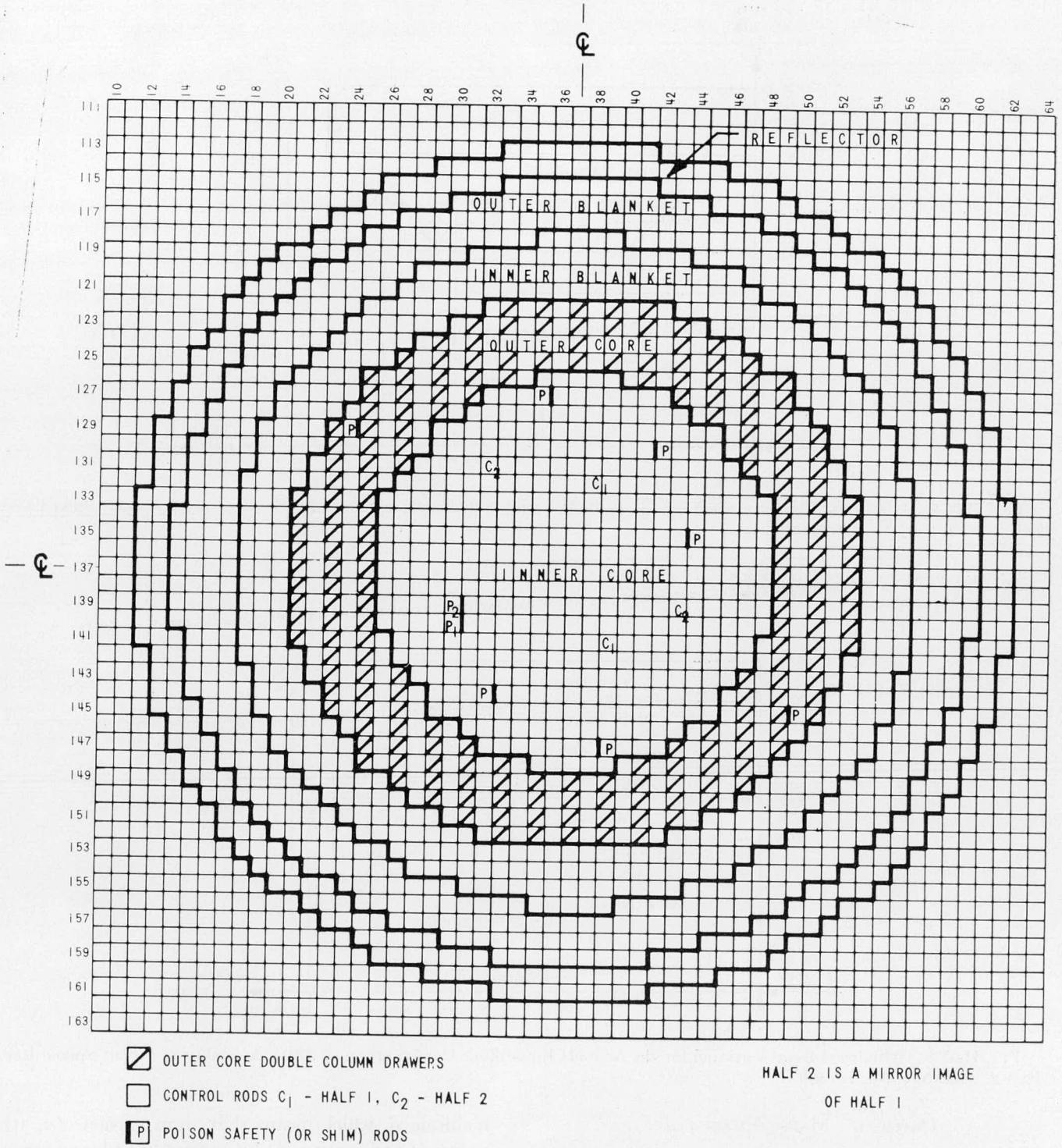

FIG. II-35-6. Interface Diagram for Loading 90 of ZPPR Assembly 2, the Equal-Zone Reference Configuration with No Spiked Rods. *ANL-ID-103-A11604.*

Comparison of runs with identical loadings indicates that the loss of reactivity due to this effect is about 0.35 Ih/day, which requires that any comparison between reference cores dated several days (or weeks) apart must consider this effect. It must be noted that the atom densities for ^{241}Pu and ^{241}Am in Table II-35-I are for the date of the Loading 90 reference run, and the values for Loading 77 need a 109-day adjustment

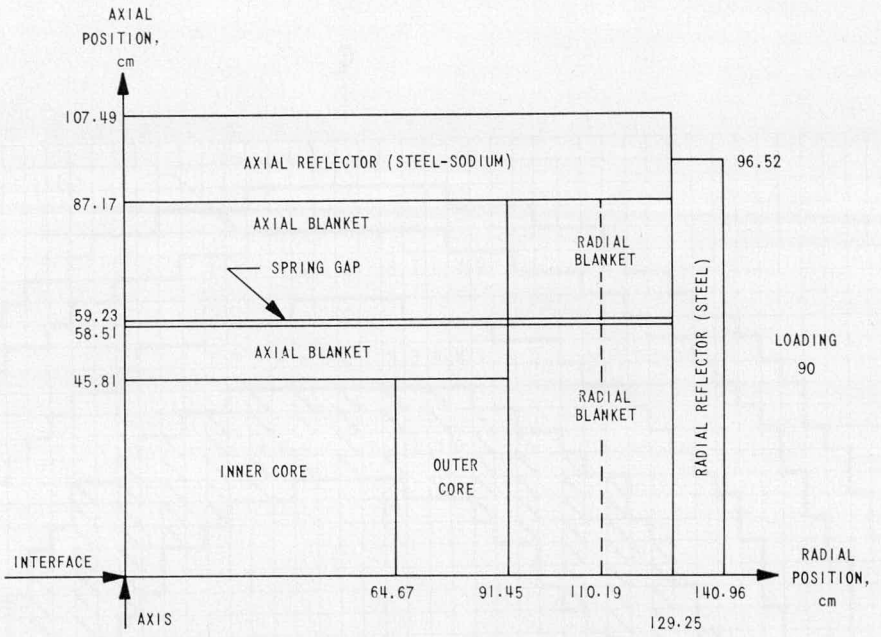

FIG. II-35-7. Cylindrical Representation for the As-built Equal Zone Configuration of ZPPR Assembly 2 without Spiked Rods Half 1. *ANL Neg. No. 116-949.*

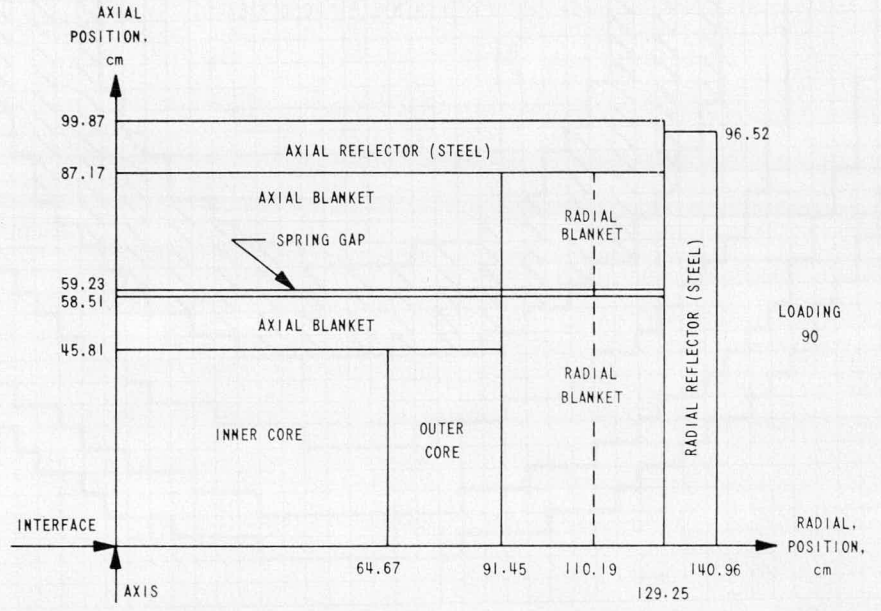

FIG. II-35-8. Cylindrical Representation for the As-built Equal-Zone Configuration of ZPPR Assembly 2 without Spiked Rods, Half 2. *ANL Neg. No. 116-950.*

CRITICAL MASS EVALUATION

The corrected critical masses for the Loadings 77 and 90 reference cores in Assembly 2 were obtained from the corrections described above by expressing the reactivity effect of each correction in terms of edge fuel worths. The relationship between reactivity change and a compensating change in mass is complicated due to the two-zone nature of the core. A relationship was derived with a stipulation that equal zone volumes be maintained, which means that an expansion of r_o (the radius of the outer core) be accompanied by an expansion of r_i (the radius of the inner core). With this requirement, the addition of reactivity caused by expan sion of r_o is balanced to a large extent by the expansion of r_i . Thus the increment of mass needed to compensate for a given amount of reactivity will be much larger when the equal-zone requirement is maintained. The effect of boundary interaction is also evident in the

large (~50 kg) mass change in going from a 52/48 volume ratio to a 50/50 volume ratio in the first two reference critical loadings.

Experiments in the original equal-zone configuration (Loading 47 or similar) provided worths of 16 4 ± 0.5 and 9.03 ± 0.5 Ih for types A (2-columns Pu-U-Mo) and B (1 column Pu-U-Mo) outer core drawers, respectively, replacing radial blanket drawers at the core blanket boundary. Similarly, at the inner/outer core boundary, inner core drawers replacing outer core drawers were found to be worth −25.78 ± 0.5 and −3.06 ± 0.5 Ih for outer core types A and B drawers, respectively.

For a replacement of an A and a B type outer core drawer (total of 1.50 kg ^{239}Pu) with two inner core drawers (1.00 kg) coupled with replacing four radial blanket drawers with two each of types A and B outer core drawers (3.00 kg), the net worth would be 22.0 ± 1.0 Ih. The combination is an equal increase in both core zones (2 drawers/zone) with a net fuel change of +2.50 kg ^{239}Pu. Thus the desired fuel-mass/reactivity correlation (for small equal-volume increments in core-zone size) is +8.8 ± 0.4 Ih/kg of contained ^{239}Pu.

Table II-35-IV lists the reactivity corrections required to the as-built Loadings 77 and 90 configurations and the equivalent mass adjustments. The total mass adjustments added to the as-built mass loadings,

TABLE II-35-IV. Corrections to As-Built Configurations to Derive Critical Masses for the Nos. 77 and 90 Equal-Zone Core Loadings of ZPPR Assembly 2

	Loading No. 77 (Reference Date 6/22/70)		Loading No. 90 (Reference Date 10/9/70)	
	Effect Worth,[a] Ih	Equivalent Mass Correction,[b] kg	Effect Worth,[a] Ih	Equivalent Mass Correction[b], kg
Effect to be corrected				
Excess reactivity in control rods	69.43	−7.88	65.93	−7.48
Control rod spiking				
Spike fuel removal	—	−1.00	—	—
Removal worth	−77.42	+8.79	—	—
Core-edge smoothing				
IC/OC boundary	−0.03	<0.01	−0.03	<0.01
OC/RB boundary	+0.04	<0.01	+0.04	<0.01
Interface gap worth	1.82	−0.21	1.82	−0.21
Source subcriticality	−5.34	+0.61	−4.08	+0.46
Temperature correction (to 22°C)	8.47	−0.96	9.51	−1.08
Critical mass evaluation				
As-loaded mass, kg (^{239}Pu + ^{241}Pu)	1017.68 ± 1.0		1030.52 ± 1.0	
Total mass correction, kg	−0.65 ± 0.10		−8.31 ± 0.85	
Corrected critical mass, kg (^{239}Pu + ^{241}Pu) (heterogeneous cylindrical reactor at 22°C as of reference date)	1017.03 ± 1.0		1022.21 ± 1.31	
Corrected core radii, cm (heterogeneous, smooth-cylinder, k = unity model)				
Inner core	64.34		64.42	
Outer core	90.99		91.10	

[a] Worth defined as reactivity advantage of equivalent-volume smooth cylindrical representation with no source over as-built configuration with steady-power rod situations. Thus, a positive worth requires a removal of fuel to obtain a just-critical representation.

[b] $\Delta\rho/\Delta m$ = 8.81 Ih/kg for net equal-volume increments to th core zones.

[c] Uncertainties on the corrections are rms averages of the approximate uncertainties of the components. Total uncertainty on the critical mass is based on the manufacturer's specifications for compositions (1% in ^{241}Pu, 0.1% in ^{239}Pu).

TABLE II-35-V. Corrected Fissile Material Inventory in the Core and Blanket Regions of the Equal Zone Configurations of ZPPR Assembly 2, Loading 77

Isotope	Mass,[a] kg				
	Inner Core	Outer Core	Radial Blanket	Axial Blanket	Total
^{239}Pu	398.78	599.62	—	—	998.40
^{241}Pu	7.46	11.16	—	—	18.62
^{235}U (fuel)	2.48	3.72	—	—	6.20
^{235}U (U_3O_8)	3.22	1.61	43.93	12.85	61.61
Totals	411.94	616.11	43.93	12.85	1084.83

[a] Based on the reactor configurations after the critical mass corrections have been applied.

TABLE II-35-VI. Corrected Fissile Material Inventory in the Core and Blanket Regions of the Equal Zone Configuration of ZPPR Assembly 2, Loading 90

Isotope	Mass,[a] kg				
	Inner Core	Outer Core	Radial Blanket	Axial Blanket	Total
^{239}Pu	399.77	604.00	—	—	1003.77
^{241}Pu	7.36	11.07	—	—	18.43
^{235}U (fuel)	2.49	3.75	—	—	6.24
^{235}U (U_3O_8)	3.23	1.62	43.38	12.89	61.12
Totals	412.85	620.44	43.38	12.89	1089.56

[a] Based on the reactor configurations after the critical mass corrections have been applied.

TABLE II-35-VII. Corrected Critical Masses for the Equal-Zone Reference Cores of ZPPR Assembly 2 Including ^{241}Pu Decay Adjustment

Reference Loading No.	Day of Year	Δt, Days	$\Delta\rho$,[a] Ih	Δm,[b] kg $^{(239+241)}$Pu	Corrected Mass, kg $^{(239+241)}$Pu	
					at Ref. Date	at Day 106/70
47	106/70	0	0	0	1016.8 ± 1.0	1016.8 ± 1.0
77	173/70	67	−23.4 ± 2.3	−2.6 ± 0.3	1017.0 ± 1.0	1014.4 ± 1.0
90	282/70	176	−61.6 ± 6.2	−7.0 ± 0.7	1022.2 ± 1.3	1015.2 ± 1.5

[a] Assumes 0.35 ± 0.04 Ih/day lost due to ^{241}Pu decay.
[b] $\Delta\rho/\Delta m$ = 8.81 Ih/kg.

determined from exact inventory records, then gives the just-critical masses listed in the table. The adjusted core-zone radii in Table II-35-IV, to give smooth cylindrical models which were just critical, were derived from the corrected critical mass values and the fuel atom densities listed in Table II-35-III for the core zones (with no rod spiking).

The inventories of total fissile mass (kg of ^{235}U plus ^{239}Pu and ^{241}Pu) for Loadings 77 and 90 with the critical mass adjustments are recorded in Tables II-35-V and II-35-VI. The mass of fissile material is given by isotope, plate type, and reactor zone; in addition, the totals for the entire reactor are given.

Comparison of Reference Loadings with Equal-Volume Core Zones

A comparison of the corrected critical masses for the three equal-zone references is presented in Table II-35-VII. Each of the cores has been adjusted to the same date (the date of Loading 47) by correcting for the reactivity loss due to ^{241}Pu decay. The value used for the rate of loss of reactivity was 0.35 Ih/day, which is based on observed reactivity losses during the five-week shutdown for annual cell integrity tests. This value compares with a calculated value of 0.25 Ih/day, which is somewhat suspect because of the uncertainties in the cross section data for ^{241}Pu and ^{241}Am. The rather large corrections in mass due to ^{241}Pu decay are the result of the requirement that equal zone volumes be maintained, as discussed previously, and do not indicate the actual loss of 7 kg of fissile material in 176 days.

Conclusions

The results in Table II-35-VII show a high degree of consistency, indicating that the sodium loading change did not have a major reactivity effect, and that the technique for correction for spiked rods was quite accurate. The mass uncertainty arising from the probable error in the combined reactivity corrections, due to various physical adjustments to obtain a smooth model, are seen to be of the same order as the uncertainty due to the isotopic analysis of the fuel. It is observed that the requirement in a two-zone core system for equal zone volume increments to compensate for reactivity changes entails a more than double total-core volume increment over a simple increment to the outer zone alone.

References

1. R. E. Kaiser and R. J. Norris, *Critical Mass Evaluations in ZPPR Assembly 2, a Demonstration Reactor Benchmark Assembly*, Applied Physics Division Annual Report, July 1, 1969, to June 30, 1970, ANL-7710, pp. 140–146.
2. R. A. Lewis, K. D. Dance, J. F. Meyer and E. F. Groh, *The Variable Temperature Rodded Zone (VTRZ) Project*, Applied Physics Division Annual Report, July 1, 1969, to June 30, 1970, ANL-7710, pp. 189–196.

II-36. Effects of Sodium Voiding on Reactor Parameters in the Demonstration Plant Benchmark Critical

A. P. Olson, W. G. Davey, R. E. Kaiser, J. C. Young, R. J. Norris and A. L. Hess

Benchmark critical experiments are being performed on ZPPR Assembly 2 in support of the initial design phases of the LMFBR demonstration plants.[1] ZPPR Assembly 2 is a 2400-liter simulated plutonium-oxide-fueled system containing a two-zoned core characterized by equal-volume zones and an outer-to-inner core enrichment ratio of 1.5.[2] As part of this program, a series of sodium-voiding measurements have been

made and compared with corresponding analytical determinations.

The sodium-voiding experiment ranged from the removal of less than 0.2 kg of sodium from the central core drawer of the split-type assembly to the voiding of 61.4 kg of sodium from a central 93-drawer zone. The reactivity effects caused by the progressive removal of sodium from the central core region are given in Table II-36-I. The effect caused by the voiding in the single drawer was determined by oscillating the drawer in and out of the assembly and analyzing the resulting power history by the inverse kinetics technique. For the multi-drawer zones, the worths were determined from the associated critical rod positions relative to that of the reference unvoided configuration. The control rod calibration remained constant for voided zones up to 93 matrices.

Analysis of the sodium-voiding experiments was carried out within the ARC system via the 2D diffusion-perturbation modules. Neutron cross sections in 27 groups were obtained from ENDF/B VERSION I (1968) data as described in Ref. 2. These cross sections were generated by the MC² fundamental-mode code, in which it was assumed that the reactor zone of interest was sufficiently large to attain an equilibrium spectrum. However, reaction rate and worth data taken within the largest voided zone indicated that only a small portion of that zone had attained an equilibrium spectrum. Hence, neither of the two cross section types available (100% sodium in or 100% sodium out) were strictly applicable. Nevertheless, first order perturbation theory (FOP) calculations using both cross section types generally agreed to within 2% as shown in Table II-36-I. Consequently the lack of spectral equilibration did not introduce an appreciable error in the calculations. Table II-36-I also shows reactivity worths from direct k-calculations and from exact first-order perturbation theory (EFOP) calculations.

The central sodium void coefficient is the difference between two opposing effects of similar magnitude: the removal term is only 1.4% larger than the scattering source term. Consequently, the central coefficient is very sensitive to small errors in the adjoint spectrum and the sodium cross sections. In the largest voided zone, the leakage term accounts for 35% of the sodium void coefficient, but the calculated/experimental (C/E) ratio is about the same as at the center. This constancy implies that the leakage term was calculated with accuracy similar to that for the combined spectral terms.

An "inverse" voiding experiment was conducted at the center of the 93-drawer voided zone. The experiment consisted of inserting two ½ x 2 x 6 in. sodium-filled cans in the front of a drawer in matrix position 137-37 ($r = 0$). The measured reactivity due to sodium was -6.40 ± 0.49 Ih/kg for 0.163 kg of sodium added.

TABLE II-36-I. Sodium Void Worths in ZPPR-2

Number of Voided Drawers	Axial Depth Voided per Half, cm	Sodium Mass Removed, kg	Reactivity Worth, Ih (998.49 Ih = 1% $\Delta k/k$)						
			Experiment	Best Calculation	C/E	Exact First-Order Perturbation	Calculated Reactivity Difference	FOP from Unvoided Configuration	
								Sodium Only	All[a]
1	15.33								
	(Half 1 only)	0.169	0.822 ± 0.06	0.624	0.76			0.623	0.625
	30.57	0.660	2.5 ± 0.8	1.733	0.71			1.733	1.754
9	15.33	2.969	14.6 ± 0.8	11.18	0.77			11.18	11.22
	30.57	5.942	17.0 ± 0.8	14.20	0.84	14.20	13.5 ± 2.0	14.72	14.89
21	15.33	6.908						26.09	26.18
	30.57	13.866	45.4 ± 0.8	33.56	0.74	33.56	32.7 ± 2.0	30.93	31.37
45	30.57	29.714	95.2 ± .0.8	—	—				
69	30.57	45.562	147.0 ± 0.8	—	—				
93	15.33	30.59						110.8	111.4
	30.57	61.410	198.1 ± 0.8	152.8	0.77	152.8	147.8 ± 2.0	137.9	138.4
	45.81	91.42						82.8	84.8

[a] Cross sections from separate, fully-voided MC² calculation. It includes the effect of sodium voiding on other isotopic cross sections, calculated assuming that the voided region is large enough to have an equilibrium spectrum.

TABLE II-36-II. Comparison of FTR-Voiding Experiments in Plate Core with Voiding Worths Derived from Small-Sample Traverses

Experimental Step	Drawers Voided in Step per Half	Sodium Removed in Step, kg	Measured Step Worth in FTR Exps, Ih	Step Worth on basis of Radial and Axial Sodium Traverses[a]	Cumulative Results		
					Zone Drawers per Half	Summation of Step Worth, Ih	
						FTR	Traverses[a]
1	1	0.660	2.5 ± 0.5	2.09 ± 0.13	1	2.5 ± 0.5	2.09 ± 0.13
2 (includes Step 1)	9 (includes center)	5.942	17.0 ± 0.8	18.76 ± 1.18	9	17.0 ± 0.8	18.76 ± 1.18
3	12	7.924	28.4 ± 0.8	24.81 ± 1.56	21	45.4 ± 0.8	43.57 ± 2.75
4	24	15.848	49.8 ± 0.8	48.70 ± 3.07	45	95.2 ± 0.8	92.27 ± 5.82
5	24	15.848	51.8 ± 0.8	47.21 ± 2.98	69	147.0 ± 0.8	139.48 ± 8.80
6	24	15.848	51.1 ± 0.8	45.57 ± 2.88	93	198.1 ± 0.8	185.0 ± 11.7

[a] Uncertainty in derived worths is based on probable error in central worth of 6 in. x ⅜ in. diam. sodium sample.

TABLE II-36-III. Fission Ratio Comparison in the Voided and Unvoided Cores of ZPPR Assembly 2

	$^{238}U/^{235}U$			$^{239}Pu/^{235}U$		
	Unvoided	Voided	% Change	Unvoided	Voided	% Change
Experiment	0.0201 ± 0.0004	0.0242 ± 0.0004	+20.5	0.9372 ± 0.0142	0.9676 ± 0.0141	+3.2
Calculation	0.01883	0.02232	+18.5	0.8631	0.9052	+4.9
C/E	0.9368 ± 0.02	0.9216 ± 0.02	—	0.9209 ± 0.015	0.9355 ± 0.015	—

The ratio of sodium worth in the 93-drawer voided zone to that in the unvoided zone for a similar experiment was measured to be 1.32, and calculated as 1.23, for a C/E of 0.93.

Radial and axial sodium worth profiles were measured using a small sample of ⅜-in. diam by 6 in. length. Calculated worth profiles were used to smoothly fit the experimental data points. Numerical integration of the smooth fits to the experimental data points gave excellent agreement with the experimentally determined worths for voided zones, as shown in Table II-36-II.

It is a curious fact that the experimental worth in Ih/kg of sodium is constant to within experimental error from 21 to 93 voided drawers per half. The exact FOP calculations for the worth per kg of sodium actually *increase* by 3% from 21 to 93 voided drawers. From the point-wise perturbation worth calculations (per unit volume), one would expect about a 6% drop in the worth of sodium at the outer edge of the 93-drawer voided zone compared with the outer edge of the 21-drawer voided zone. The effect which compensates for this is the enhancement of the worth of the sodium near the center of the voided zone, due to hardening of the spectrum within the voided zone as the zone increases in size. As previously discussed when dealing with the "inverse" voiding experiment, this worth enhancement ratio of 1.23 is not negligible, and it appears to be calculated quite well. We note that only a fraction of the worth enhancement ratio of 1.23 need be invoked in order to correlate with the calculated increase in sodium worth from 21 to 93 voided drawers.

Table II-36-III contains a comparison of calculated and measured fission ratios in the 93-drawer voided zone and in the unvoided core. The measurements were performed using back-to-back fission chambers mounted at core center, 7.62 cm from the axial mid-plane. The ratios were determined from analyzer-integrated countrates with a correction applied which accounts for extrapolation of the counts/channel from the lower discriminator to zero pulse height. The quoted errors include contributions from counting statistics, statistical errors in foil compositions, and in foil weights.

From Table II-36-III, it can be seen that the neutron spectrum becomes significantly harder in the voided zone than in the unvoided core, from the increase in the $^{238}U/^{235}U$ fission ratio. The spectral hardening effect as indicated by the change in fission ratios is calculated very well.

In summary, one concludes that:

1. The reactivity worth of sodium near the center of ZPPR-2 is not calculated accurately, the ra of calculation and experiment (C/E) being a proximately 0.8.
2. By contrast, the fractional *changes* in some parameters can be predicted with accuracy; these include

changes in the perturbation worth of sodium in voided and unvoided zones, and changes in fission ratios at the center of zones.

3. Up to the maximum size of central zone voided, the specific worth of sodium shows a remarkable constancy. This appears to be due to compensation of leakage effects by the increased worth of centrally-located sodium as the zone size increases; the magnitude is consistent with measured (and calculated) changes in sodium worth in the voided and unvoided conditions.
   This constancy is not expected for even larger zone sizes where leakage becomes even greater, but experimental tests of this, while planned, have not yet been performed.
4. Over the range of zone sizes investigated, the integrated experimental small-sample worths are in excellent agreement with the zone voiding worths.

References

1. C. E. Till and W. G. Davey, *The Demonstration Reactor Benchmark Critical Assemblies Program*, Trans. Am. Nucl. Soc. **13**, 293 (1970).
2. A. P. Olson and N. C. Paik, *Heterogeneity and Criticality Studies on the Zero Power Plutonium Reactor (ZPPR) Assembly 2, a Demonstration Reactor Benchmark Critical*, Applied Physics Division Annual Report, July 1, 1969 to June 30, 1970, ANL-7710, pp. 146–155.

II-37. Demonstration Plant Benchmark Central Reactivity Measurements

C. L. Beck, W. G. Davey, R. E. Kaiser, R. J. Norris and P. I. Amundson

Introduction

An extensive series of measurements were performed in ZPPR Assembly 2[1] to determine the worth of small cylindrical and annular samples at the center of the reactor. Table II-37-I contains a description of the reactivity samples used for this series of measurements. A selection of isotopic abundances was provided for the plutonium, uranium, and boron samples to allow for isotopic worth separation. The isotopic analysis information is presented in Tables II-37-II through II-37-IV. Sample diameters and annular thicknesses were varied to allow sample size corrections to be calculated.

All sample worths were determined as the change in reactivity between an "in" and "out" position. The samples were oscillated between the two positions through a traverse tube located 3.04 in. from the interface. An autorod kept the reactor at steady power while the sample was traversed, and the autorod position was converted to a relative reactivity for the determination of the sample worth.

Reactor Configuration

The reactor configuration was the same as outlined in the description of Assembly 2 in Ref. 1, except that a low worth autorod was installed in the movable half nd the sample changer and traverse assembly were ıstalled in the fixed half of the reactor. Slight adjustments in the total number of fuel drawers in the reactor were required to maintain criticality; however, the core composition remained unchanged.

Experimental Equipment

The experimental setup requires a traverse tube to be inserted through the reactor along a diameter 3.036 in. from the midplane. A sample carrier, push rod and follower rod (Fig. II-37-1) are placed in the traverse tube. A remotely operated sample changer is used to remove and insert samples when the sample carrier is positioned at the full out position. The sample carrier is oscillated between an in and out position by a stepping-motor-driven screw drive coupled to the push rod. The center of the sample carrier is positioned at the axial center line of the reactor by aligning a mark on the follower rod with the outer surface of the reactor matrix assembly.

The ZPPR autorod system is an automatic device for monitoring the neutron flux level and maintaining this level constant through insertion and removal of a tantalum blade. As presently designed, it consists of an AC motor driving a rotating ball nut which in turn drives a ball screw into and out of the reactor. Attached to the end of the ball screw is the tapered tantalum blade. This system is used to maintain a constant power level in the reactor after a near stable level has already been achieved by manual manipulation of the control rods.

Experimental Method

The autorod is calibrated using inverse kinetics to convert the power history to a reactivity worth calibration curve. To avoid problems of non-linearity in the autorod calibration curve, autorod positions were con-

TABLE II-37-I. DESCRIPTIONS OF ZPR REACTIVITY SAMPLES

Sample I.D.	Geometry	Dimensions, in.			Sample[a] Mass, g	Capsule Mass, g	Melt No. or Composition	Dummy No.
		Length	O.D.	Wall Thickness				
Pu-8	Annular	2.173	0.390	0.005	3.0347	10.3397	R-524	D-1–D-4
Pu-10	Annular	2.173	0.390	0.015	8.8478	10.7480	R-524	D-1–D-4
Pu-12	Annular	2.173	0.390	0.025	14.2288	10.5230	R-524	D-1–D-4
Pu-14	Annular	2.173	0.390	0.005	3.0217	10.7499	R-528	D-1–D-4
Pu-16	Annular	2.173	0.390	0.015	8.2391	10.6543	R-528	D-1–D-4
Pu-18	Annular	2.173	0.390	0.025	13.7749	10.6661	R-528	D-1–D-4
Pu-20	Annular	2.173	0.390	0.005	3.5115	10.7129	R-529	D-1–D-4
Pu-22	Annular	2.173	0.390	0.015	8.3384	10.2920	R-529	D-1–D-4
Pu-24	Annular	2.173	0.390	0.025	13.2560	10.7758	R-529	D-1–D-4
Pu-26	Cylinder	2.173	0.100	—	4.4518	11.0206	R-530	D-5–D-8
Pu-28	Cylinder	2.173	0.200	—	16.8639	10.9648	R-530	D-9–D-12
Pu-30	Cylinder	2.173	0.300	—	38.0907	11.6003	R-530	D-13–D-16
Pu-32	Cylinder	2.173	0.100	—	3.9173	11.1206	R-524	D-5–D-8
Pu-34	Cylinder	2.173	0.200	—	17.0474	10.9585	R-524	D-9–D-12
Pu-36	Cylinder	2.173	0.300	—	38.6469	11.6688	R-524	D-13–D-16
Pu-38	Cylinder	2.173	0.100	—	4.2427	10.6110	R-528	D-5–D-8
Pu-40	Cylinder	2.173	0.200	—	16.9529	11.1659	R-528	D-9–D-12
Pu-42	Cylinder	2.173	0.300	—	38.1472	11.5960	R-528	D-13–D-16
Pu-44	Cylinder	2.173	0.100	—	4.4337	10.7633	R-529	D-5–D-8
Pu-46	Cylinder	2.173	0.200	—	17.0297	11.2653	R-529	D-9–D-12
Pu-48	Cylinder	2.173	0.300	—	38.4081	11.5649	R-529	D-13–D-16
U-2	Cylinder	2.173	0.100	—	4.7931	11.0646	212E-2	D-5–D-8
U-4	Cylinder	2.173	0.200	—	21.0999	11.2499	212E-2	D-9–D-12
U-6	Cylinder	2.173	0.300	—	46.8887	11.4626	212E-2	D-13–D-16
U-8	Annular	2.173	0.390	0.005	3.9375	10.6693	212E-2	D-1–D-4
U-10	Annular	2.173	0.390	0.015	11.1751	10.1261	212E-2	D-1–D-4
U-12	Annular	2.173	0.390	0.025	18.4611	10.5669	212E-2	D-1–D-4
Du-2	Cylinder	2.173	0.100	—	5.1962	11.089	D-1R	D-5–D-8
Du-4	Cylinder	2.173	0.200	—	21.0243	11.213	D-1R	D-9–D-12
Du-6	Cylinder	2.173	0.300	—	47.4269	11.417	D-1R	D-13–D-16
Du-8	Annular	2.173	0.390	0.020	14.9410	10.2976	D-1R	D-1–D-4
ZPR-3-1	Cylinder	2.002	0.420	—	85.76	—	0.21 w/o U-235	—
ZPR-3-2	Cylinder	2.004	0.200	—	19.63	—	99.79 w/o U-238	—
U-235	Cylinder	2.002	0.020	—	19.63	—	93.16 w/o U-235	—
Na-4	Cylinder	6.000	0.424	—	12.724	26.928	From EBR-II coolant lines	D-45
B-1	Cylinder	2.174	0.401	—	4.1928	10.521	Enriched	D-1–D-4
B-2	Cylinder	2.172	0.181	—	0.7529	12.386	Enriched	D-17–D-20
B-3	Cylinder	2.173	0.097	—	0.2619	11.965	Enriched	D-21–D-24
B-4	Cylinder	2.713	0.052	—	0.0738	11.250	Enriched	D-25–D-28
B-5	Annular	2.173	0.400	0.040	1.8370	17.233	Enriched	D-37–D-40
B-6	Annular	2.173	0.401	0.020	0.9562	17.947	Enriched	D-33–D-36
B-7	Annular	2.173	0.400	0.0094	0.4968	20.776	Enriched	D-29–D-32
B-8	Cylinder	2.167	0.400	—	2.3447	10.631	Natural Group I	D-1–D-4
B-9	Cylinder	2.172	0.181	—	0.4834	12.710	Natural Group I	D-17–D-20
B-10	Cylinder	2.172	0.097	—	0.1785	12.047	Natural Group I	D-21–D-24
SS-1	Cylinder	2.173	0.390	—	33.635	10.347	SS-304	D-1–D-4
Fe-1	Cylinder	2.172	0.389	—	33.277	10.611	99.99% pure	D-1–D-4
Fe_2O_3-2	Cylinder	2.169	0.401	—	5.2648	10.624	99.999% pure	D-1–D-4
Ta-1	Cylinder	2.174	0.389	—	70.504	10.678	99.9% pure	D-1–D-4
Ta-2	Cylinder	2.173	0.200	—	18.647	11.124		D-9–D-12
Ta-3	Cylinder	2.173	0.100	—	4.681	10.614		D-5–D-8
Ta-4	Annular	2.174	0.378	0.021	13.859	10.597		D-1–D-4
Ta-5	Annular	2.175	0.378	0.011	5.893	10.320		D-1–D-4

TABLE II-37-I. *Continued*

Sample I.D.	Geometry	Dimensions, in.			Sample[a] Mass, g	Capsule Mass, g	Melt No. or Composition	Dummy No.
		Length	O.D.	Wall Thickness				
Mo-1	Cylinder	2.173	0.390	—	43.398	10.688	99.95% pure	D-1-D-4
Mo-2	Cylinder	2.173	0.200	—	11.392	10.740		D-9-D-12
Mo-3	Annular	2.173	0.376	0.0195	7.564	10.545		D-1-D-4
Mo-4	Annular	2.169	0.376	0.010	3.701	10.647		D-1-D-4
Nb-1	Cylinder	2.174	0.390	—	36.370	10.585	99.82% pure	D-1-D-4
Nb-2	Cylinder	2.174	0.200	—	9.581	11.107		D-9-D-12
Nb-3	Annular	2.174	0.377	0.020	6.938	10.525		D-1-D-4
Nb-4	Annular	2.172	0.377	0.010	3.272	10.709		D-1-D-4
W-1	Cylinder	2.174	0.376	—	75.555	10.684	99.5% pure	D-1-D-4
W-2	Cylinder	2.173	0.249	—	33.430	11.569		D-13-D-16
W-3	Annular	2.173	0.400	0.0091	6.933	10.698		D-1-D-4
W-4	Annular	2.173	0.392	0.018	14.796	10.631		D-1-D-4
Ni-1	Cylinder	2.173	0.390	—	37.916	10.691	99.995% pure	D-1-D-4
Mn-1	Cylinder	2.173	0.3986	—	18.010	10.343	99.99% pure	D-1-D-4
Cr-3	Cylinder	2.173	0.375	—	26.999	10.644	99.996% pure	D-1-D-4
V-1	Cylinder	2.174	0.390	—	25.980	10.712	99.987% pure	D-1-D-4
C-1	Cylinder	2.174	0.391	—	8.027	10.672	reactor grade 10 ppm ash	D-1-D-4
Ti-1	Cylinder	2.174	0.390	—	19.232	10.660	99.6% pure	D-1-D-4
Poly-1	Cylinder	2.173	0.390	—	4.024	10.567		D-1-D-4
Poly-2	Cylinder	2.172	0.2005	—	1.062	11.303		D-9-D-12
Poly-3	Cylinder	2.172	0.102	—	0.269	10.959		D-5-D-8
Al-1	Cylinder	2.173	0.390	—	11.437	10.559	99.995% pure	D-1-D-4
Al_2O_3-1	Cylinder	2.169	0.4005	—	3.171	10.602	99.999% pure	D-1-D-4
Al_2O_3-3	Cylinder	2.174	0.376	—	15.061	10.359		D-1-D-4
Zr-1	Cylinder	2.174	0.390	—	27.635	10.648	99.989% pure	D-1-D-4

[a] Uncertainty in qouted masses is ±2.0 mg. Sample masses must be adjusted by given purity fractions to give isotopic masses. All 10 boron samples, plus Fe_2O_3-2, Mn-1, and Al_2O_3-1 are powder samples.

TABLE II-37-II. PLUTONIUM SAMPLE ANALYSIS

	Melt Number			
	R-524	R-528	R-529	R-530
Major Elements, w/o				
Pu[a]	98.96	98.39	97.67	98.26
Al[b]	1.10	1.27	1.20	0.95
Isotopic Composition of Pu,[d] w/o				
Pu-238	0.005	0.002	0.191	
Pu-239	86.273	73.502	40.964	98.926
Pu-240	11.461	22.033	42.258	1.023
Pu-241	2.084	3.841	12.090	0.049
Pu-242	0.178	0.625	4.688	0.002
Am-241	0.134	0.264	0.946	
Gas Analysis,[b] ppm				
H	1	4	2	4
O	72	224	340	167
N	84	54	35	17
Minor Elements,[c] ppm				
Fe	150	100	100	1700
Ni	50	10	50	10000
Cr	10	10	5	1100
Y	400	200	1000	200
C	380	230	230	

[a] ±0.30%.
[b] ±5.00%.
[c] Factor of 2.
[d] ±0.01%.

TABLE II-37-III. URANIUM SAMPLE ANALYSIS

Isotopic Composition	Melt Number			
	212 E-2		D-1R	
	w/o	Std. Error	w/o	Std. Error
Mass No.				
234	0.945160	0.001574	0.000708	0.000029
235	93.192047	0.010260	0.213179	0.000788
236	0.258504	0.000865	0.004528	0.000188
238	5.604275	0.010872	99.781570	0.000808
Gas Analysis, ppm	(±5%)			
H		7	18	
O		324	363	
N		30	43	
Minor Elements, ppm	(Est. Accuracy—factor of two)			
Ag		(0.5)	1	
Al		10	60	
As		L 100	L 100	
B		0.1	0.1	
Be		L 0.2	L 0.2	
Bi		L 2	L 2	
C		151		
Ca		L 50	L 50	
Cd		110	L 10	
Co		L 10	L 10	
Cr		60	3	
Cu		2	50	
Fe		100	100	
K		L 100	L 100	
Li		L 5	L 5	
Mg		10	20	
Mn		6	150	
Mo		8	L 5	
Na		2	3	
Ni		200	10	
P		60	40	
Pb		2	2	
Sb		L 10	L 10	
Sn		L 2	2	
Ti		L 100	L 100	
Zr		L 100	L 100	

Note: Symbol meaning: L: less than; ( ): accuracy uncertain.

TABLE II-37-IV. BORON SAMPLE ANALYSIS

	Enriched	Natural Group I	Natural Group II[a]
Isotopic Composition of Boron, w/o			
B^{10}	92.19	18.42	18.72
B^{11}	7.81	81.58	81.28
Major Element, w/o			
Boron	94.50	82.24	91.00

[a] Not used at the 3.04 in. position.

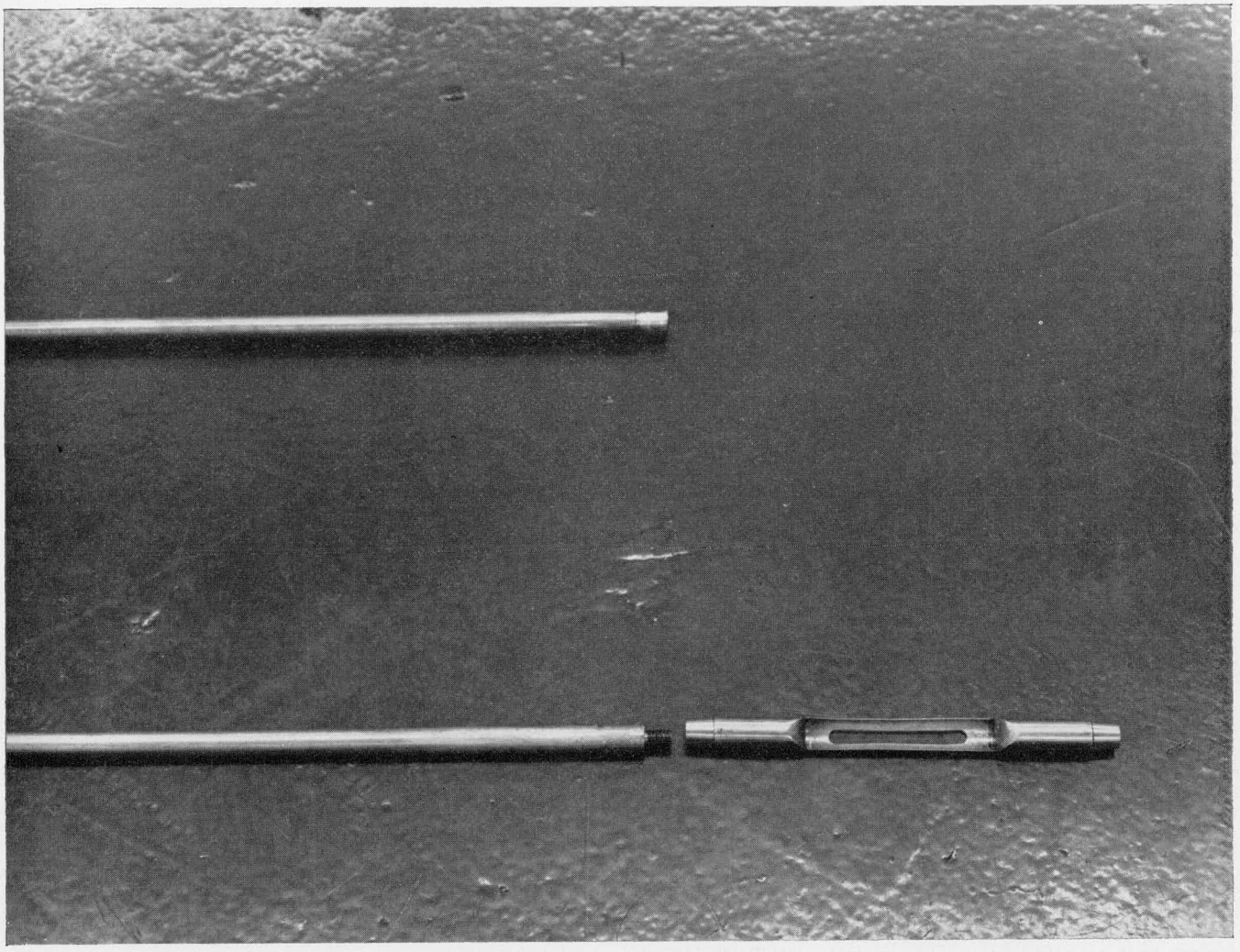

FIG. II-37-1. Push Rod, Empty Carrier and Follower Rod of the Automatic Sample Changer and Traverse Mechanism. *ANL-103-A11891.*

verted to relative reactivity prior to evaluating the sample worth.

A reactivity worth is determined for the sample and the traverse mechanism using the standard reactivity evaluation techniques[2] in use at ZPPR which account for reactor drift during the measurement. To account for the encapsulating material and traverse mechanism, a series of reactivity measurements were run for empty capsules and for the empty carrier. A linear least squares fit was done on the reactivity worth of the capsules and empty carrier versus the capsule weight. The standard deviation of the values about the fitted line provides an error estimate for this series of experiments, and all error values listed in Tables II-37-V and II-37-VI are based on this standard deviation weighted by the ratios of the square roots of the integrated power. The capsule weight for each sample as obtained from Table II-37-I was substituted into the fitted equation to obtain the reactivity correction due to the capsule and traverse mechanism. The samples were oscillated a minimum of three times in and out of the reactor for each sample, with the sample being held stationary at each turn-around-point for 120–130 sec. The "in" position is at the axial centerline and the "out" position is at 4 in. outside the radial reflector. Initial positioning of the traverse mechanism is accurate to 0.06 in. and repositioning during the experiment is accurate to 0.01 in.

RESULTS

The reactivity worths determined from this series of experiments is presented in Table II-37-VI for scattering and absorption samples, and in Table II-37-V for the fissile and fertile materials. These worths are as measured, with no corrections for sample size effects,

TABLE II-37-V. SMALL-SAMPLE REACTIVITY WORTHS FOR FISSILE AND FERTILE MATERIALS MEASURED ON THE AXIAL CENTERLINE, 3 in. FROM THE INTERFACE IN ZPPR ASSEMBLY 2

Sample I.D.	Composition Type	Sample Mass, g	Specific Worth,[a] Ih/kg
Pu-8	11% ^{240}Pu	3.0347	106.26 ± 1.06
Pu-10		8.8478	106.61 ± 0.42
Pu-12		14.2288	106.46 ± 0.43
Pu-14	22% ^{240}Pu	3.0217	92.17 ± 1.22
Pu-16		8.2391	93.72 ± 0.54
Pu-18		13.7749	94.55 ± 0.45
Pu-20	42% ^{240}Pu	3.5115	72.66 ± 1.05
Pu-22		8.3384	72.30 ± 0.44
Pu-24		13.2560	72.97 ± 0.46
Pu-26	1% ^{240}Pu	4.4518	117.06 ± 0.83
Pu-28		16.8639	116.72 ± 0.37
Pu-30		38.0907	119.04 ± 0.10
Pu-32	11% ^{240}Pu	3.9173	107.65 ± 1.58
Pu-34		17.0474	108.80 ± 0.36
Pu-36		38.6469	109.40 ± 0.16
Pu-38	22% ^{240}Pu	4.2427	95.40 ± 1.04
Pu-40		16.9529	97.08 ± 0.36
Pu-42		38.1472	98.37 ± 0.12
Pu-44	42% ^{240}Pu	4.4337	73.76 ± 0.83
Pu-46		17.0297	75.30 ± 0.36
Pu-48		38.4081	76.48 ± 0.16
Du-2	Depleted U	5.1962	−6.33 ± 1.19
Du-4		21.0243	−6.33 ± 0.29
Du-6		47.4269	−6.12 ± 0.13
ZPR-3-2[b]		19.63	−5.53 ± 0.33
ZPR-3-1[b]		85.76	−5.59 ± 0.07
U-235[b]	Enriched U	19.63	87.38 ± 0.30

[a] Worth per kg of sample mass.

[b] Special samples with no capsules; refer to Table II-37-I for description.

no separation of isotopic information, and no correction for impurities. The values are for Ih per kilogram of sample weight. The conversion factor of 1015.67 Ih/% $\Delta k/k$ was used to obtain the final results.

REFERENCES

1. R. E. Kaiser and R. J. Norris, *Critical Mass Evaluation in ZPPR Assembly 2, a Demonstration Reactor Benchmark Assembly*, Applied Physics Division Annual Report, July 1, 1969, to June 30, 1970, ANL-7710, pp. 140–146.
2. R. W. Goin and C. L. Beck, *Critical Reactivity Measurement Techniques at the Zero Power Plutonium Reactor (ZPPR)*, Applied Physics Division Annual Report, July 1, 1969, to June 30, 1970, ANL-7710, pp. 274–276.

TABLE II-37-VI. SMALL-SAMPLE REACTIVITY WORTHS MEASURED ON THE AXIAL CENTERLINE, 3 in. FROM THE INTERFACE IN ZPPR ASSEMBLY 2
(*A* ≡ *annular sample*)

Sample I.D.		Sample Mass, g	Specific Worth,[a] Ih/kg
B-1 (enriched)		4.193	−1547.94 ± 2.43
B-2	"	0.753	−1765.61 ± 8.21
B-3	"	0.262	−1885.53 ± 23.58
B-4	"	0.074	−2009.32 ± 63.44
B-5	" A	1.837	−1726.47 ± 1.75
B-6	" A	0.956	−1870.87 ± 6.46
B-7	" A	0.497	−1915.03 ± 12.43
B-8 (natural)		2.345	−360.49 ± 1.89
B-9	"	0.483	−358.02 ± 9.01
B-10	"	0.179	−378.96 ± 17.99
Ta-1		70.504	−27.28 ± 0.09
Ta-2		18.647	−30.43 ± 0.33
Ta-3		4.681	−36.73 ± 1.32
Ta-4	A	13.859	−37.10 ± 0.44
Ta-5	A	5.893	−41.78 ± 1.05
SS-1		33.635	−3.58 ± 0.18
Fe-1		33.277	−3.06 ± 0.10
Fe_2O_3-2		5.265	−3.90 ± 1.17
Mo-1		43.398	−10.96 ± 0.14
Mo-2		11.392	−12.55 ± 0.54
Mo-3	A	7.564	−12.77 ± 0.82
Mo-4	A	3.701	−10.04 ± 1.67
Nb-1		36.370	−15.64 ± 0.17
Nb-2		9.581	−17.03 ± 0.64
Nb-3	A	6.938	−19.37 ± 0.89
Nb-4	A	3.272	−20.64 ± 1.89
W-1		75.555	−10.48 ± 0.05
W-2		33.430	−11.33 ± 0.81
W-3	A	6.933	−15.76 ± 0.89
W-4	A	14.796	−12.63 ± 0.30
Ni-1		37.916	−4.62 ± 0.16
Mn-1		18.010	−7.41 ± 0.33
Cr-3		26.999	−3.29 ± 0.22
V-1		25.980	−3.59 ± 0.24
C-1		8.027	−11.05 ± 0.77
Ti-1		19.232	−3.42 ± 0.32
Poly-1		4.024	222.77 ± 1.54
Poly-2		1.062	172.24 ± 5.81
Poly-3		0.269	159.34 ± 22.97
Al-1		11.437	−5.82 ± 0.54
Al_2O_3-1		3.171	−10.44 ± 1.95
Al_2O_3-3		15.061	−6.47 ± 0.41
Zr-1		27.635	−3.93 ± 0.16
Na-4		12.724	−5.02 ± 0.34

[a] Worth per kg of sample mass.

II-38. Calculated Size Effects for Reactivity Perturbation Samples in ZPPR

P. J. Collins* and R. G. Palmer

Introduction

The reactivity worths of most materials of interest to the LMFBR program have been measured in ZPPR Assembly 2 as a function of position. The measurements are conveniently made by oscillating small samples into and out of the reactor through a traverse tube. Most measurements have been made with cylindrical or annular samples. Since adequate analytical methods are not available for treating this complex situation in general, the worths of many of the important materials were measured near to the center of the reactor over a range of sample sizes, thus providing a test of calculational methods (see Paper II-37).

As a preliminary method for calculating sample size effects, a simple multigroup collision probability code, SARCASM, has been developed. The code treats self-multiplication, absorption and multiple scattering within a finite small sample on a broad group basis. The code has several limitations; firstly, the effect of the sample on the reactor is treated only to first order and secondly, because of the restriction to broad groups, materials with strong resonances present problems. The data used in SARCASM must be appropriately resonance shielded and the shielding is duplicated, in the broad group sense, in the code. The resonance shielding problem is accentuated for a material, for example ^{238}U, which is also present in the reactor. For a number of materials of interest, however, the method gives a good account of the experimental results.

The SARCASM Code

For a uniform isotropic flux ϕ at the surface of the sample, the number of primary collisions in group i at position $\mathbf{r}$ is

$$N_i^{(1)}(\mathbf{r})d\mathbf{r} = \Sigma_{ti}\phi_i P_i(\mathbf{r})\, d\mathbf{r}, \qquad (1)$$

where Σ_t is the macroscopic total cross section and $P(\mathbf{r})$ is the escape probability from $\mathbf{r}$. The total number of primary collisions in the sample of volume V, in group i, is

$$N_i^{(1)} = \Sigma_{ti}\phi_i V P_{0i}, \qquad (2)$$

with P_{0i} the average escape probability.

The number of secondary neutrons produced in the mple by scattering and fission which escape to the reactor, in group i, is

$$N_{i\,esc}^{(2)} = \sum_j \phi_j (\Sigma_{scj\to i} + \chi_i (\nu\Sigma_f)_j) \int P_j(\mathbf{r}) P_i(\mathbf{r})\, d\mathbf{r}. \qquad (3)$$

If the spatial distribution of secondary neutrons is assumed to be flat, this becomes

$$N_{i\,esc}^{(2)} = \sum_j \phi_j (\Sigma_{scj\to i} + \chi_i(\nu\Sigma_f)_j) P_{0j} P_{0i} V. \qquad (4)$$

Under the same assumption, the number of neutrons which escape to the reactor after two collisions in the sample, $N_{i\,esc}^{(3)}$, may be readily calculated and so on. Using the unperturbed adjoint, ϕ^*, at the sample position, the following expression is evaluated:

$$N(\text{sample}) = \frac{1}{V}\sum_i \phi_i^* (N_{i\,esc}^{(2)} + N_{i\,esc}^{(3)} + \cdots - N_i^{(1)}), \qquad (5)$$

where the summation over the order-of-scattering index is continued to convergence. In the limit of zero sample size, this reduces to the standard first order perturbation theory numerator, $N(\text{FOP})$. The code calculates a correction factor to multiply the full FOP worth from

$$f = N(\text{sample})/N(\text{FOP}). \qquad (6)$$

For infinite slab geometry, two options are available in the code: the spatial distribution of the secondary source may be taken to be flat or the detailed distribution may be used as in Eq. (3) (with higher order sources assumed to be flat). For the range of sample sizes used in the ZPPR measurements, the use of a flat secondary distribution has been found to lead to negligible error. The two options are compared in Table

TABLE II-38-I. Comparison of Flat and Exact Secondary Distributions

Material	Atom Density, 10^{24} atoms/cm^3	Slab Thickness, mm	Sample Size Correction Factor, f	
			Exact Secondary Distribution	Flat Secondary Distribution
^{239}Pu	0.048	5	1.1909	1.1919
		20	2.1415	2.1704
		40	5.2579	5.4694
^{10}B	0.060	5	0.7039	0.7041
		20	0.4612	0.4624
		40	0.3333	0.3361
^{12}C	0.072	5	0.9448	0.9448
		20	0.8127	0.8117
		40	0.6284	0.6226

*UKAEA, Winfrith, Dorchester, Dorset, England.

II-38-I for ^{239}Pu, ^{10}B and ^{12}C. The thicknesses for slabs, with mean chords equal to those of the ZPPR samples, range up to about 5 mm. The flat secondary distribution is assumed in cylindrical and annular geometry. In these cases, collision probability routines developed by Nicholson[1] are incorporated into the code. A similar method, for slab geometry, has been described by Karam.[2]

TABLE II-38-II. CENTRAL REACTIVITY WORTHS FOR PLUTONIUM SAMPLES

Sample Number	Sample Description,[a] Composition, Geometry, Mass of Pu	Sample Size Correction	Calculated Worth, C, Ih/kg of Pu	Experimental Worth, E,[b,c] Ih/kg of Pu	C/E[c]
Pu-26	R-530, Cyl., 4.374g	1.0194	139.37	119.09 ± 0.97	1.170 ± 0.010
Pu-28	" Cyl., 16.571g	1.0390	142.05	118.75 ± 0.36	1.196 ± 0.004
Pu-30	" Cyl., 37.428g	1.0587	144.75	121.09 ± 0.08	1.195 ± 0.001
Pu-8	R-524, Ann., 3.003g	1.0053	125.47	107.32 ± 1.17	1.169 ± 0.013
Pu-10	" Ann., 8.756g	1.0125	126.37	107.66 ± 0.49	1.174 ± 0.005
Pu-12	" Ann., 14.081g	1.0188	127.16	107.52 ± 0.30	1.183 ± 0.003
Pu-32	" Cyl., 3.877g	1.0198	127.28	108.73 ± 1.56	1.171 ± 0.017
Pu-34	" Cyl., 16.870g	1.0396	129.75	109.89 ± 0.35	1.181 ± 0.004
Pu-36	" Cyl., 38.245g	1.0595	132.24	110.50 ± 0.16	1.196 ± 0.002
Pu-14	R-528, Ann., 2.973g	1.0054	112.77	93.61 ± 1.43	1.205 ± 0.018
Pu-16	" Ann., 8.107g	1.0126	113.57	95.18 ± 0.74	1.193 ± 0.009
Pu-18	" Ann., 13.553g	1.0189	114.28	96.03 ± 0.44	1.190 ± 0.005
Pu-38	" Cyl., 4.174g	1.0201	114.41	96.89 ± 0.84	1.181 ± 0.010
Pu-40	" Cyl., 16.680g	1.0400	116.65	98.60 ± 0.36	1.183 ± 0.004
Pu-42	" Cyl., 37.533g	1.0597	118.86	99.91 ± 0.11	1.190 ± 0.001
Pu-20	R-529, Ann., 3.430g	1.0051	88.26	74.33 ± 1.23	1.187 ± 0.020
Pu-22	" Ann., 8.144g	1.0117	88.84	73.95 ± 0.42	1.201 ± 0.007
Pu-24	" Ann., 12.947g	1.0175	89.35	74.64 ± 0.46	1.197 ± 0.007
Pu-44	" Cyl., 4.330g	1.0193	89.50	75.46 ± 0.98	1.186 ± 0.015
Pu-46	" Cyl., 16.633g	1.0377	91.12	77.03 ± 0.36	1.183 ± 0.006
Pu-48	" Cyl., 37.513g	1.0559	92.72	78.24 ± 0.16	1.185 ± 0.002

[a] Detailed isotopic compositions and dimensions are given in Paper II-37.
[b] 1% $\Delta k/k$ = 1015.7 Ih.
[c] The errors quoted are due to statistics only. The data should be regarded as preliminary.

TABLE II-38-III. CENTRAL REACTIVITY WORTHS FOR ENRICHED BORON AND TANTALUM SAMPLES

Material	Sample Number	Sample Description,[a] Geometry, Mass (^{10}B or Ta)	Sample Size Correction	Calculated Worth, C, Ih/kg	Experimental Worth, E,[b,c] Ih/kg	C/E[c]
Enriched boron	B-1	Cyl., 3.653g	0.7740	−2044	−1775 ± 3	1.151 ± 0.002
	B-2	Cyl., 0.656g	0.8800	−2324	−2025 ± 9	1.148 ± 0.005
	B-3	Cyl., 0.228g	0.9143	−2415	−2163 ± 27	1.116 ± 0.014
	B-4	Cyl., 0.064g	0.9505	−2510	−2305 ± 73	1.089 ± 0.035
	B-5	Ann., 1.600g	0.8657	−2286	−1980 ± 2	1.154 ± 0.001
	B-6	Ann., 0.833g	0.9177	−2424	−2146 ± 7	1.129 ± 0.004
	B-7	Ann., 0.433g	0.9510	−2512	−2197 ± 14	1.143 ± 0.007
Tantalum	Ta-1	Cyl., 70.504g	0.5874	−31.82	−27.28 ± 0.09	1.166 ± 0.004
	Ta-2	Cyl., 18.647g	0.6482	−35.11	−30.43 ± 0.33	1.154 ± 0.013
	Ta-3	Cyl., 4.681g	0.7157	−38.77	−36.73 ± 1.32	1.055 ± 0.038
	Ta-4	Ann., 13.859g	0.7701	−41.71	−37.10 ± 0.44	1.124 ± 0.014
	Ta-5	Ann., 5.893g	0.8391	−45.45	−41.78 ± 1.05	1.088 ± 0.028

[a] Detailed isotopic compositions and dimensions are given in Paper II-37.
[b] 1% $\Delta k/k$ = 1015.7 Ih.
[c] The errors quoted are due to statistics only. The data should be regarded as preliminary.

TABLE II-38-IV. CENTRAL REACTIVITY WORTHS FOR SCATTERING AND INTERMEDIATE ABSORBING SAMPLES

Material	Sample Number	Sample Description,[a] Geometry, Mass	Sample Size Correction	Calculated Worth, C, Ih/kg	Experimental Worth, E,[b,c] Ih/kg	C/E[c]
Polyethylene	Poly-1	Cyl., 19.232g	1.583	302.5	222.8 ± 1.5	1.358 ± 0.009
	Poly-2	Cyl., 4.024g	1.338	255.7	172.2 ± 5.8	1.485 ± 0.050
	Poly-3	Cyl., 1.062g	1.178	225.1	159.3 ± 23.0	1.413 ± 0.204
Sodium	Na-4	Cyl., 12.724g	0.9947	−4.005	−4.67 ± 0.27	0.86 ± 0.005
Carbon	C-1	Cyl., 8.027g	0.9391	−10.151	−11.05 ± 0.77	0.92 ± 0.06
Iron	Fe-1	Cyl., 33.277g	0.9830	−3.612	−3.06 ± 0.10	1.18 ± 0.04
Chromium	Cr-3	Cyl., 26.999g	0.9803	−5.101	−3.29 ± 0.22	1.55 ± 0.11
Nickel	Ni-1	Cyl., 37.916g	0.9853	−4.034	−4.62 ± 0.16	0.87 ± 0.03

[a] Detailed isotopic compositions and dimensions are given in Paper II-37.
[b] 1% $\Delta k/g$ = 1015.7 Ih.
[c] The errors quoted are due to statistics only. The data should be regarded as preliminary.

RESULTS

The preliminary analysis for a number of the ZPPR samples is given in Tables II-38-II through II-38-IV. First order perturbation theory worths were obtained from an *rz* model of the reactor using ENDF/B VERSION 1 data in 27 groups. The fluxes and adjoints at the sample position were input to SARCASM for calculation of the size corrections. The consistency of the ratio of calculated-to-experimental worths, C/E, for a given material, taking into account the experimental uncertainties, is a test of the sample size calculation. The experimental results are still in the process of refinement and subject to possible later modification.

The plutonium samples, in Table II-38-II, fall into four sets with different isotopic compositions. For a given composition the values of C/E agree to within two standard deviations of the statistical uncertainty for almost all samples. Table II-38-III includes results for strongly absorbing samples of boron and tantalum for which rather large size corrections are necessary. Shielded data for each tantalum sample were obtained from an MC² calculation. The sample size correction given in the table includes this shielding factor. Results for materials for which scattering effects are important are given in Table II-38-IV. The polyethylene samples provide a sensitive test of the method since the size corrections are large. A data set for hydrogen was constructed for the SARCASM code since these data were not available in the ENDF/B library. For polyethylene, good agreement with experiment is obtained for the variation with sample size. However, the worths of scattering materials are very sensitive to the energy dependence of the adjoint flux. The size corrections for other materials in the table must be regarded as provisional since, for these, only one sample size has been studied.

In summary, the simple method of calculating sample size effects adopted in the SARCASM code gives good agreement with experiment for several of the more important materials. The approximations inherent in the code do not appear to lead to serious errors within the accuracy achievable in the ZPPR measurements. A more refined method, however, will be necessary for an adequate treatment of strong resonant absorbing materials such as ^{238}U.

REFERENCES

1. R. B. Nicholson, *Self Shielding of Annular and Solid Cylinders*, Reactor Physics Division Annual Report, July 1, 1969 to June 30, 1970, ANL-7710, pp. 443–445.
2. R. A. Karam, K. D. Dance, T. Nakamura and J. E. Marshall, *Analysis of Central Reactivity Worths in Fast Critical Assemblies*, Nucl. Sci. Eng. **40**, 414 (1970).

II-39. Evaluation of Experimental Uncertainties on Small-Sample Reactivity Measurements in ZPPR Assembly 2

S. G. CARPENTER and R. E. KAISER

INTRODUCTION

The small sample reactivity measurements in ZPPR are made using inverse kinetics directly or an autorod which has been calibrated by inverse kinetics. In both cases the sample or the rod is repeatedly cycled while the power level is monitored and recorded by integrat-

ing over short time intervals (~0.5 sec). This history is then used to determine the reactivity as a function of sample or autorod position and time. The worth is found as a function of position by performing a least squares fit to the data while allowing a third order reactor reactivity drift in time (see Paper II-33).

There are a number of ways in which uncertainties can enter the results which have been investigated. For the present discussion no errors in the class of "mistakes" will be considered. These would include noise pickup in chambers, gamma background not compensated against, cable and chamber noise pickup, bad position or time readouts, non-linear power channels, etc.

Input Data Uncertainty

The first class of uncertainty arises from the input data which are calculated or taken from other measurements. These include β_{eff}, ℓ, a_is, λ_is and the effective neutron source S.

The value of β_{eff} is taken from a calculation of the core. It depends on the assumed β for the fissionable materials (mostly ^{238}U and ^{239}Pu), the assumed delayed neutron spectrum and the calculated distribution and magnitude of fission rates for each isotope as well as the spatial and energy distributions of the adjoint flux. Several parts of the intermediate data can be experimentally checked, such as the relative fission rates and spatial distributions. This has been done in ZPPR Assembly 2 and the calculation is substantially correct (see Paper II-34). The spatial distribution of fission neutron importance has also been compared with experiment and it is also substantially correct. The main areas of concern are β for each isotope, the delayed neutron spectrum, and the energy-dependent importance. Fortunately the measurement of the worth of a small sample is not sensitive to β_{eff}. As an example, a central measurement of a sample which was determined to be 1.3299¢ with the normal input for ZPPR Assembly 2 was recalculated from the power history after increasing β_{eff} by 10%. The result was 1.3305¢. This would indicate that within the generally quoted accuracies and the possible error in β_{eff} there is no uncertainty in the measured value due to a β_{eff} uncertainty. The results are about the same percent different for other small samples.

The same conclusion is arrived at for a lifetime uncertainty. The calculated value is more sensitive to changes in cross sections and calculational methods. The measured value[1] of β/ℓ was very close to the calculated value, 5782 ± 125 sec^{-1} versus 5701 sec^{-1}, so that there is little chance that ℓ is uncertain by as much as a factor of two. Nevertheless when the lifetime is increased by a factor of two, the result for the 1.3¢ sample changes only in the fifth significant figure. No significant error is introduced by an uncertainty in ℓ.

The value of S is determined from experiment (see Paper II-33). The reproducibility is generally quoted to better than 2%. There may be a systematic error which is also of this magnitude as the result is also somewhat dependent on input data. It is not expected that the error could be as large as 10%. But again, for this change the resulting change in the experimental value of a 1.3¢ sample is in the fifth significant figure when the measurement is made at several hundred watts. When done at a lower power, the change becomes larger.

The remaining constants are the a_i, λ_i set. The procedure in obtaining them is to assume the constants for each isotope as well as the energy spectrum for each group, and to combine them with spatial reactor calculational results for fission rates and adjoint flux distributions. The resulting values of a_i (effective) sum to unity and the λ_i values are unchanged. It is possible[2] to experimentally determine if the correct ratio of delayed neutrons from ^{238}U and ^{239}Pu has been obtained if it is assumed that the constants for each isotope are correct. For ZPPR Assembly 2 the measured ratio is within the experimental error of about 2%. Also of interest is the fact that the central ^{238}U to ^{239}Pu fission ratio is calculated to within the experimental uncertainty as well as the full reactor ratio of fissions. About 47% of the delayed neutron worth comes from ^{238}U. If this fraction is increased or decreased by 10% (to 57% or 37%) the worth of the 1.33¢ sample is changed by about 0.07¢. The largest effect is this last one which will limit the accuracy of these measurements to about 1%.

In summary, the experimental accuracy does not rely on input from reactor calculations since either the experimental value is insensitive to any modification of input caused by the calculation or the input can be checked for consistency experimentally. The limiting accuracy arises from correct assignment of the a_is. For ZPPR Assembly 2, 1% would seem like a reasonable systematic error due to uncertainties in the input data.

Statistical Uncertainties

Because of the random nature of the interactions in the core and detector an uncertainty exists in the small sample reactivity measurements. For many samples, this is larger than the known systematic uncertainties discussed in the last section. Because most measurements are repeated over several oscillations, it is possible to obtain estimates of the statistical fluctuations and compare the results with theory as well as to observe certain malfunctions in equipment once the expected variation has been determined.

As an example of the magnitude of the statistics, a series of measurements has been taken in which the

autorod position was averaged over a period of 100 sec for each sample position (in and out), and the sample worth was determined from

$$D_k = (-1)^k[\rho_k - \tfrac{1}{2}(\rho_{k-1} + \rho_{k+1})],$$

where ρ_k is the average autorod position with the sample either in or out. Data were taken at the rate of 100 points/sec for the autorod averaging. This averaging technique cancels linear reactor drift for each D_k, and cancels quadratic drifts over a series of D_ks. The technique that was used in the ZPPR measurements employed six measurements of ρ_k, and thus four values of D_k. The error in individual values of the measured reactivity, D_k, was determined from

$$\sigma_{D_k} = \sqrt{\frac{\sum_i (D_k^i - \bar{D}_k)^2}{N-1}},$$

and the error in $\bar{D}_k$, the average value, was determined[3] as

$$\sigma_{\bar{D}_k} = \sigma_{D_k}\sqrt{\frac{8}{3N}}.$$

The derivation of the above formula assumes $N \gg 1$, which is not rigorously true for only four differences. The effect of this assumption has been investigated, and the $\sqrt{8/3N}$ formulation was found to give a value that is conservative by about 10 percent, i.e., a larger value for $\sigma_{\bar{D}_k}$. The use of this evaluation takes into account the fact that the D_k values are not independent measurements, but are partially correlated.

Most of the measurements were performed at a power of 90 W giving a total integrated power of 15 W-h per sample. A selected group of samples was then repeated at 610 W, giving an integrated power of 101.7 W-h per sample. The accuracy of the measurement should thus improve by the square root of the ratio of the integrated powers, or a factor of 2.60.

The expected uncertainty for a large set of samples was found by averaging the uncertainties of each of the sample worths measured under a given set of conditions. This procedure helped to eliminate the statistical variations in $\sigma_{\bar{D}_k}$ which were encountered. For the 90 W runs, 112 separate measurements (Table II-39-I) of $\sigma_{\bar{D}_k}$ were averaged to give $\overline{\sigma_{90}} = (5.04 \pm 0.23) \times 10^{-8}\ \Delta k/k$. At

TABLE II-39-I. Statistical Uncertainties for 90 W Reactivity Measurements[a]

Reactor Run No.	$\sigma_{\bar{D}_k}$, 10^{-8}	Reactor Run No.	$\sigma_{\bar{D}_k}$, 10^{-8}	Reactor Run No.	$\sigma_{\bar{D}_k}$, 10^{-8}	Reactor Run No.	$\sigma_{\bar{D}_k}$, 10^{-8}
154	4.8432		2.7838	174	1.6079		6.9162
	4.2442		7.8521		6.2772		3.1706
	3.8532		5.1967		7.1675		7.1498
					2.5101		3.3952
155	7.2119	171	7.3131		3.9075		1.0984
	2.5269		5.7480		3.5591		1.4035
	4.2696		2.9499				4.3780
	2.7574		7.4889	175	10.0005		2.4152
	8.4532		3.5876		8.9733		7.9106
	4.5338		2.3701				7.4358
	3.3201			179	7.1982		1.9331
	1.3934	172	5.8435		4.5768		1.9111
	7.5066		1.9271		4.5740		1.6484
			8.5096		7.7558		0.7493
156	5.3110		5.2531		2.4311		6.0826
	5.5900		9.1922		4.8912		6.1148
	3.8898		3.7164				
	8.5120		2.4208	180	6.5055	182	0.6620
	4.1716		3.7149		4.9649		6.2434
	4.5314		7.0718		3.3580		
	5.1948		9.1326		4.4765	195	6.3921
	9.0942				4.1267		4.1098
		173	3.9267		2.5605		
158	4.2575		5.1114		6.2431	196	7.5327
	4.6794		7.9299		7.4096		
			6.6343		6.4042	200	5.9949
159	3.9184		8.6598		4.2075		
	1.6990		8.0061		5.3668		
	2.7027		3.5151		2.6236		
	2.8542		7.3499		12.8313		
	6.1215		1.4374		3.7171		
	2.7688		5.7655				
	2.4174		5.7069	181	9.1627		
	4.8931				7.1821		

[a] $\overline{\sigma_{90}} = (5.04 \pm 0.23) \times 10^{-8}$.

TABLE II-39-II. Statistical Uncertainties for 650 W Reactivity Measurements[a]

Reactor Run No.	$\sigma_{\bar{D}_k}$, 10^{-8}
184	1.0319
	1.4346
	3.8224
	2.1055
	0.8815
	5.0437
	1.6274

[a] $\overline{\sigma_{650}} = (2.28 \pm 0.63) \times 10^{-8}$.

the 610 W power level, seven samples (Table II-39-II) were included in the average, which gave $\overline{\sigma_{610}} = (2.28 \pm 0.63) \times 10^{-8}\ \Delta k/k$. In both cases the first two measurements in each run were discarded, as the errors were always high due to reactor drift. Since the comparison between powers is based on reactor noise as the predominant source of error, non-linear reactor drift or other systematic errors would make the comparison invalid. The measured increase in accuracy amounted to a factor of 2.21 ± 0.62 instead of the predicted 2.60, but this may still include some drift effect and is considered acceptable. Also, the uncertainties are calculated from the individual D_ks and thus do not contain a second order drift correction. Thus any second order drift that was present would tend to reduce the gain in accuracy expected from a given increase in power.

The magnitude of the average uncertainty ($5.04 \pm 0.23 \times 10^{-8}$ at 90 W) compares favorably with the theoretical error due to reactor noise in a square wave oscillator experiment, as calculated by the method of Frisch and Littler[4]. The expression for the error is

$$\Delta = \left[\frac{1 + r\rho A^2(\omega)}{2rN_f T A^2(\omega)}\right]^{1/2},$$

where

$\Delta \equiv$ expected error in Δk_{eff}

$r \equiv$ detector efficiency $\equiv \left[\frac{\text{reactions/sec in detector}}{\text{fissions/sec in reactor}}\right]$

$N_f \equiv$ core fission rate

$A(\omega) \equiv$ reactor transfer function, a function of k_{eff}

$\rho \equiv \frac{\overline{\nu(\nu-1)}}{\bar{\nu}^2} \approx 0.8$

$T \equiv$ cycle time.

The above equation can be rearranged and expressed in terms of reactor power, P (watts) as

$$\Delta = \frac{1.1 \times 10^{-5}}{(PT)^{1/2}}\left(1 + \frac{1}{r\rho A^2(\omega)}\right)^{1/2}.$$

The ZPPR Assembly 2 measurements were performed at a power of 90 W, with a six-minute cycle time and a detector efficiency of 4.6×10^{-6} (10^{-7} amps at 58 W). The cycle includes 600 sec of actual measuring time—100 sec at each of three "in" and three "out" positions. Using a value of $A^2(\omega) = (4.6/0.0033)^2 = 1.94 \times 10^6$, the error equation becomes

$$\Delta = \frac{1.1 \times 10^{-5}}{(PT)^{1/2}}(1.14)^{1/2} = \frac{1.17 \times 10^{-5}}{(PT)^{1/2}},$$

which gives a theoretical estimate of the error of 5.03×10^{-8} for the ZPPR experiments at 90 W. It is worth noting that an improved detector efficiency could only reduce the $(1.14)^{1/2}$ value to 1. The reactor noise is large compared with the chamber noise.

Use of a calibrated autorod to perform the experiments should not add a significant error. If, under certain circumstances, the autorod is found to contribute a significant error, inverse kinetics measurements, based on the power history during the oscillations, would be preferable.

If the reactor is run at 100 W and the sample measurement uses 1000 sec, a 1 % uncertainty is obtained for a 0.1¢ sample. The systematic error would then predominate, although relative values could still be improved.

Conclusions

It has been possible to make small sample central reactivity measurements in ZPPR Assembly 2 with uncertainties of about 1 % in reasonable counting times for samples of 0.1¢ or greater reactivities. For a short period of time after the halves close (~½ h) the drift rate of reactor reactivity is high enough to reduce the accuracy for small samples using the present drift rate corrections. For large (>1¢) samples, no wait is necessary. Ratios of worths can be expected not to be limited to the 1 % systematic error if measurements are made at the same powers so the uncertainties in S cause compensating errors.

Uncertainties due to the point kinetics assumptions are possible but have not been evident in spatial distribution measurements which compare well in shape with calculations. More work in this area is required to determine what limit in accuracy is imposed from this cause.

References

1. W. K. Lehto, Argonne National Laboratory (private communication).
2. S. G. Carpenter and S. Ramchandran, *β_{eff} Ratio Measurements*, Reactor Physics Division Annual Report, July 1968 to June 30, 1969, ANL-7610, pp. 212–215.
3. E. F. Bennett and R. L. Long, *Precision Limits in the Measurement of Small Reactivity Changes*, Nucl. Sci. Eng. **17**, 425 (1963).
4. O. R. Frisch and D. J. Littler, *Pile Modulation and Statistical Fluctuation in Piles*, Phil. Mag., Vol. 45 (1954).

II-40. Gamma Ray Dose Measurements in the ZPPR Demonstration Benchmark

G. G. Simons and T. S. Huntsman

Introduction

Thermoluminescent dosimeters (TLD) have been widely used in the field of health physics; however, they have not been routinely used in measuring absorbed gamma ray doses in reactor-type environments. Potentially, TLD materials offer the experimentalist a powerful tool for providing detailed information pertinent to gamma ray heating at every critical location in a fast reactor. The dosimeter capsules can be made small enough so that intricate studies within a single matrix drawer in a zero power critical assembly, such as ZPPR, can be completed. Coarse dose mappings throughout the core, blanket, reflector and shield may also be made.

Gamma ray dose measurements, both across single lattice cells and for axial and radial dose traverses, have been completed inside ZPR-3 critical assemblies. The results are reported in Refs. 1–3. Two types of solid extruded 1 x 6 mm TLD rods containing approximately 13 mg of lithium fluoride were used. One type was composed of natural lithium containing 92.5 % ^{7}Li and 7.5 % ^{6}Li; the other type was enriched to 99.993 % ^{7}Li. The TLD rods were encased in stainless steel.

ZPPR-2 Dose Traverse

A traverse measurement of absorbed dose was completed at a few axial and radial positions in ZPPR-2. The dosimeter capsules used consisted of 1 in. long x ⅛ in. diam (0.035-in. wall) stainless steel sleeves each containing three ^{7}LiF extruded TLD rods. As-loaded sleeves in Drawers 137-41, 137-47, 137-52 and 137-57 are shown in Fig. II-40-1. The resulting data (see Table II-40-I) are presented in terms of instrument readout in nanocoulombs (nc) and dose (rads) relative to the stainless steel jacket around the TLD. Conversion from nc to rads was completed using a calibrated ^{60}Co source.

Plutonium-239 foils, located 2.75 in. from the interface but near the vertical centerline of matrix drawer 139-37, and the TLD rods were exposed simultaneously for a nominal 892 Wh. The ^{239}Pu(n,f) reaction rate was $1.018 \times 10^{8} \pm 1.3$ % reactions/g/W-h.[4] The absolute foil reaction rates at the radial positions which contained TLD rods can be derived from the above reaction rate and the ^{239}Pu counter traverse for the reference core loading given in Paper III-35. The standard deviation for the batch of TLD rods was 5.8 %. Thus, using an average readout of three rods per capsule, the standard deviation of the reported instrument readouts will be

TABLE II-40-I. Absorbed Dose Measurements in ZPPR-2 Using Stainless Steel Encapsulated ^{7}LiF TLD Rods

Capsule Tag	Matrix Drawer	Axial Position From Core C_L, in.	TLD Readout,[a] nc	Dose Relative to Steel,[b] Rad
L	137-41	0	243.3	2082
M		3	249.9	2123
N		7	209.2	1841
O		11	202.1	1789
P		14	153.6	1423
Q		16	142.7	1339
R		18	99.1	988
S		20	53.8	569
T		22	37.6	404
U		26	24.7	270
V		30	16.1	180
A	137-47	0	215.1	1883
B		3	203.6	1799
C		7	188.6	1726
D		11	163.1	1496
E		14	140.1	1318
F		16	122.9	1177
G		18	78.0	808
H		20	39.7	427
I		22	29.2	316
J		26	20.7	228
K		30	12.2	139
W	137-52	0	149.3	1391
X		3	149.2	1381
Y		7	137.5	1297
Z		11	119.0	1151
1		14	93.8	941
2		16	80.9	837
3		18	49.9	528
4		20	25.5	279
5		22	18.6	207
6		26	12.1	138
7		30	7.9	92
8	137-57	0	14.9	167
9		3	15.6	175
10		7	13.7	155
11		11	12.2	140
12		14	10.1	116
13		16	9.13	106
14		18	7.71	89
15		20	6.98	82
16		22	5.75	68
17		26	4.01	48
18		30	2.62	32

[a] Standard deviation = ±3.5%.

[b] Standard deviation dependent on gamma ray spectra ≥3.5%.

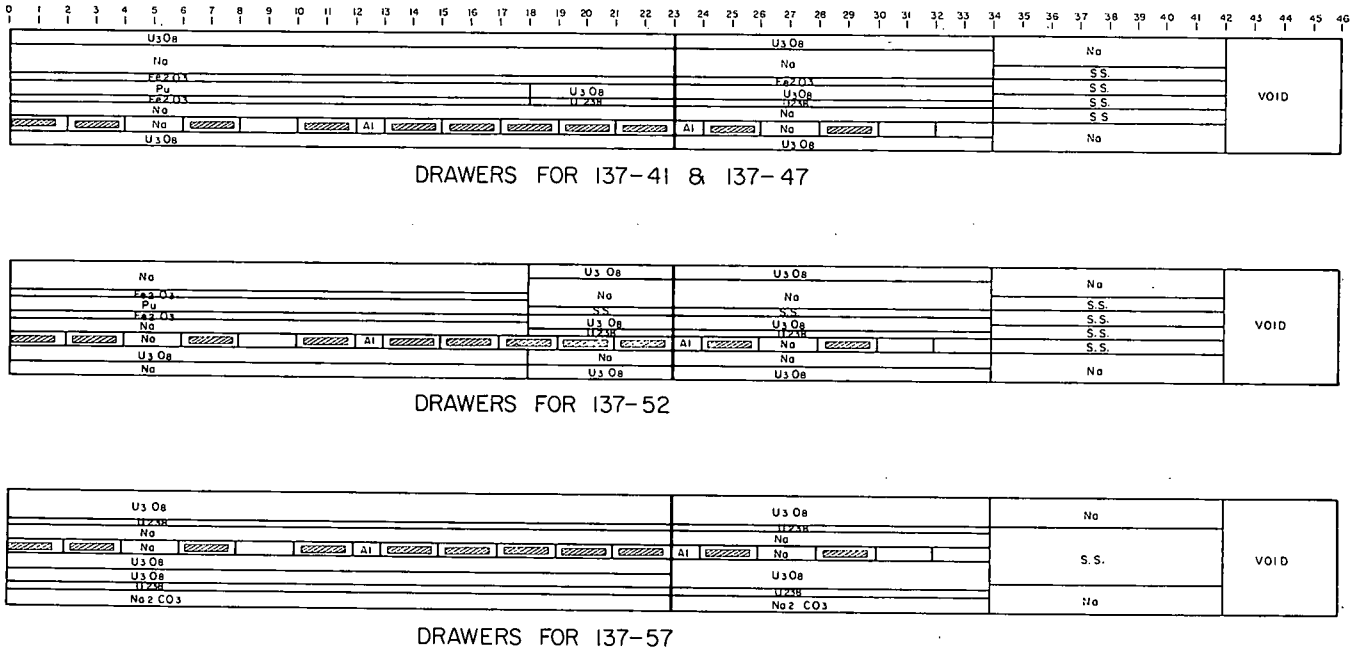

FIG. II-40-1. TLD Capsules Positioned on Top of the ZPPR Matrix Drawers for the ZPPR-2 Reference Core Dose Traverse Measurements. *ANL-ID-103-A11878.*

3.5%. However, the reported doses will have a larger error, depending on the variation of the W parameter (discussed in Paper III-29) between the calibration source energy (1.25 MeV) and the gamma ray spectra in the reactor.

REFERENCES

1. G. G. Simons, *Thermoluminescent Dosimetry Applied to Gamma Ray Dose Measurements in Critical Assemblies,* Applied Physics Division Annual Report, July 1, 1969 to June 30, 1970, ANL-7710, pp. 289–294.
2. G. G. Simons, *Thermoluminescent Dosimeter Measurements in ZPR-3 Assemblies 61 and 62,* Reactor Development Program Progress Report, ANL-7753, October 1970, pp. 23–24.
3. G. G. Simons, *Thermoluminescent Dosimeter Measurements in ZPR-3 Assembly 63A,* Reactor Development Program Progress Report, ANL-7798, March 1971, pp. 95–96.
4. D. W. Maddison, Argonne National Laboratory (private communication).

II-41. Demonstration Benchmark Control Rod Measurement Program—Part I: Measurements

S. G. CARPENTER, J. T. HITCHCOCK, R. W. GOIN and J. C. YOUNG

INTRODUCTION

The materials which are proposed for LMFBR control are tantalum and boron. In order to provide some Zero Power Plutonium Reactor (ZPPR) experimental data on these materials before constructing Assembly 3, which will be more representative of a core with control rods and control channels, a series of experiments has been run using Assembly 2. The experiments were designed to provide a series of increasingly complicated tests against which to compare basic cross sections and design methods.

The simplest reactivity measurements were those of small samples of various dimensions at the center of the core. These ranged from nearly infinitely dilute to several inches in the shortest dimensions. Selected small sample reactivities were then measured as a function of position in the core. The axial length was increased so that single control rods of small area were formed and their worths as a function of insertion and radial position were obtained.

The final part of the ZPPR Assembly 2 control rod program was the measurement of reactivity and other

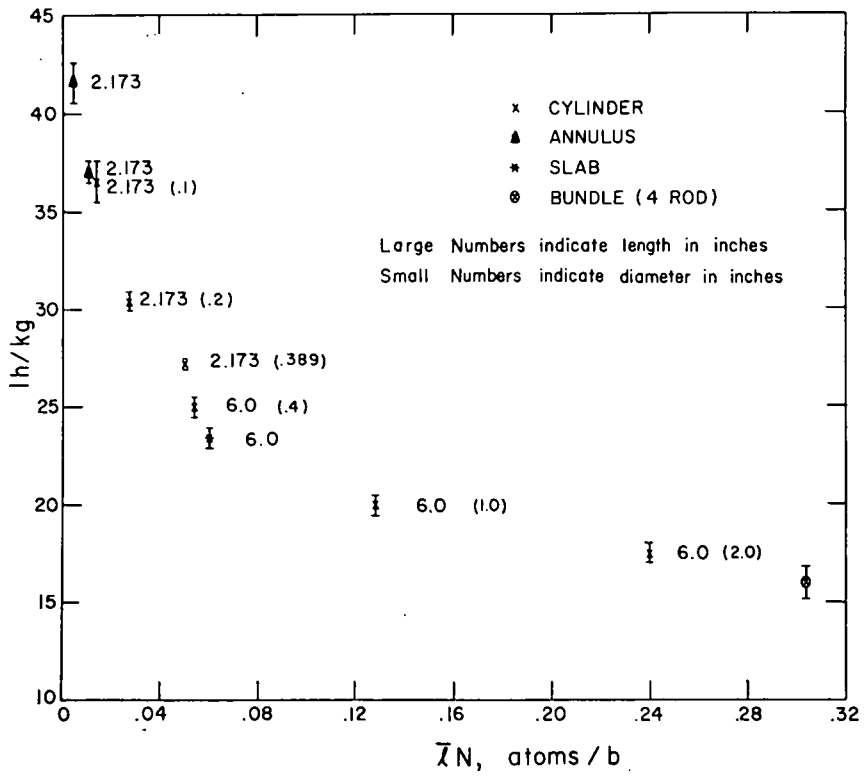

FIG. II-41-1. Specific Worth as a Function of $\bar{l}N$ for Ta Samples of Various Shapes. *ANL-ID-103-A11771.*

effects resulting from the insertion of simulated power-reactor control rods. These "mockup" rods had a cross-sectional area of 2 × 2 matrix positions and were of full or half height (36 in.). Both tantalum and natural B_4C rods were constructed, with and without sodium. Single rod effects and the interaction effects of pairs of rods were studied. All reactivity worths of rods were made in the subcritical state without any change in the core loadings or dimensions. For the measurement of power and small sample reactivity perturbations caused by the mockup rods, the reactor was returned to critical.

Sample Size Effects

At the core center (radial center, 3.036 in. off center axially) the worths of a series of samples of varying self-shielding were measured. Figure II-41-1 shows a summary of these results for tantalum. The worth in inhours per kilogram is plotted as a function of the mean cord length times the atom density. The length and diameter of the samples, as well as the uncertainty in the measurements, are indicated in the figure. Corrections were made for the fact that certain samples did not have their centers located at the same point. The point indicated for the four-rod bundle (discussed later in the mockup rod section) was obtained by assuming that the ratio of the worths between the 36-in. long by 2-in. diam rod and the 36-in. long bundle was the same as it would have been for 6-in. long samples. The various sample shapes would not be expected to fall exactly on a smooth curve but should be quite close.

A similar experiment has been reported in Core 17 of the Epithermal Critical Experiments Laboratory (ECEL), Atomics International.[1] The latter data include clusters of pins and indicate that they lie on the same curve as that for single cylinders. The points in Fig. II-41-1 are intended to cover the complete range from infinitely dilute to the size contemplated for power reactors and is expected to apply to a wide range of shapes.

Small Sample Worth Distributions

Since the calculated worth distributions are not a strong function of sample size, only a few distributions were measured to determine the spatial worth distributions for boron and tantalum. Figure II-41-2 shows a typical radial map for sample B-5. It is a 1.8 g enriched boron annular sample. Other results also shown on the curve will be discussed later. Much more data of this type are available, some of which are mentioned in Paper II-34. Seven different boron samples were used and, to within experimental uncertainties, the ratios of worths in each of two outer core positions to that in the center of the core are the same. For example, the 4.2 g

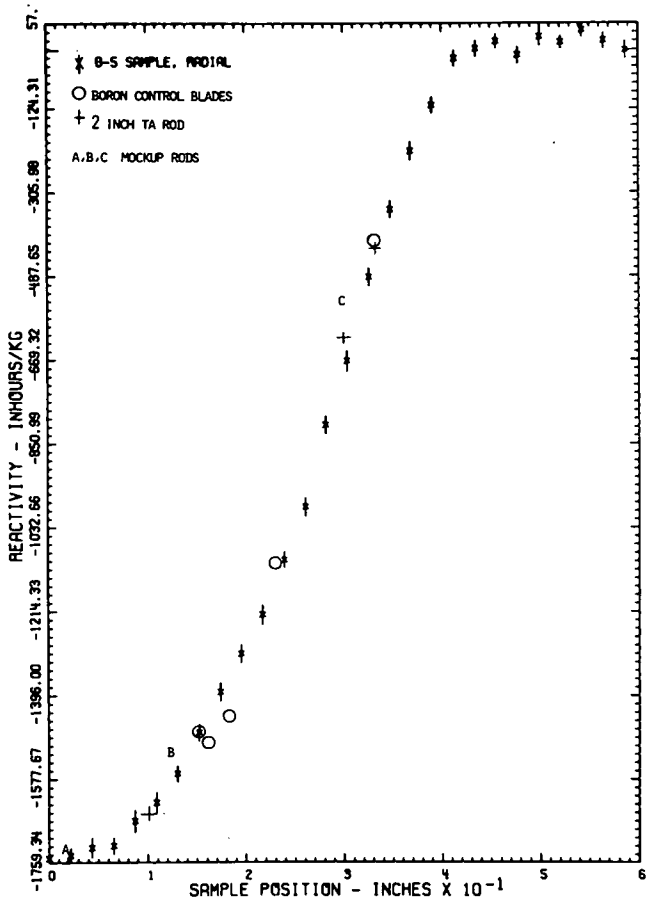

FIG. II-41-2. Specific Worth of B-5 Sample as a Function of Radius, Showing Mockup Rods and B_4C Blades. *ANL-ID-103-11779.*

enriched boron cylindrical sample gives ratios of 0.357 and 0.271, while the largest annulus has ratios of 0.358 and 0.274. The tantalum values are not as consistent. Radial distributions are also available at other axial positions. The shapes demonstrate little change.

Axial shapes were also measured for 6-in. long samples at two radial locations. The axial shapes of the tantalum ¼ x 2 x 6 in., tantalum 0.4 in., tantalum 1 in. and B-1 samples in the inner core and the boron ¼ x 2 x 6 in. sample in the outer core were the same within experimental error. The three other samples (tantalum 2 in. in the inner and outer core, and boron ¼ x 2 x 6 in. in the inner core) were not identical but very similar. Figure II-41-3 shows the results for the 0.4-in. diam, 6-in. long tantalum sample. The zero point is that for a sample extending from 0 to 6 in. in an empty drawer. The drawer location is noted on the figure.

SINGLE DRAWER RODS

The detailed worth curves were measured for half length rods of both control materials. The tantalum rod was 2 in. in diam and the boron rods were blades of enriched boron carbide 2 in. high and ¼ in. thick. Figure II-41-4 shows the results of all these measurements normalized to 10, fully inserted to the core center. In each case about 52% of the worth was in the first half core height. In spite of the varying radial location shown in the graph and the fact that both poison materials are included, the shapes are again nearly the same. Also included on the curve is a calculated value for tantalum at the core center.

The total worths have been normalized at the smallest radii for each element and plotted on Fig. II-41-2, which illustrates the small sample boron radial traverse. To a good approximation, the relative rod worths as a function of position can be determined from the small sample distribution. It is expected that the worth of the rods at any position in the core could be approximated from a central measured worth and the small sample curve. Using Fig. II-41-1, one may find the relative value of differently shaped rods; thereby it is hoped that from the various measurements good estimates can be made of the worth of any sized boron or tantalum rod at any position in the core and at any insertion.

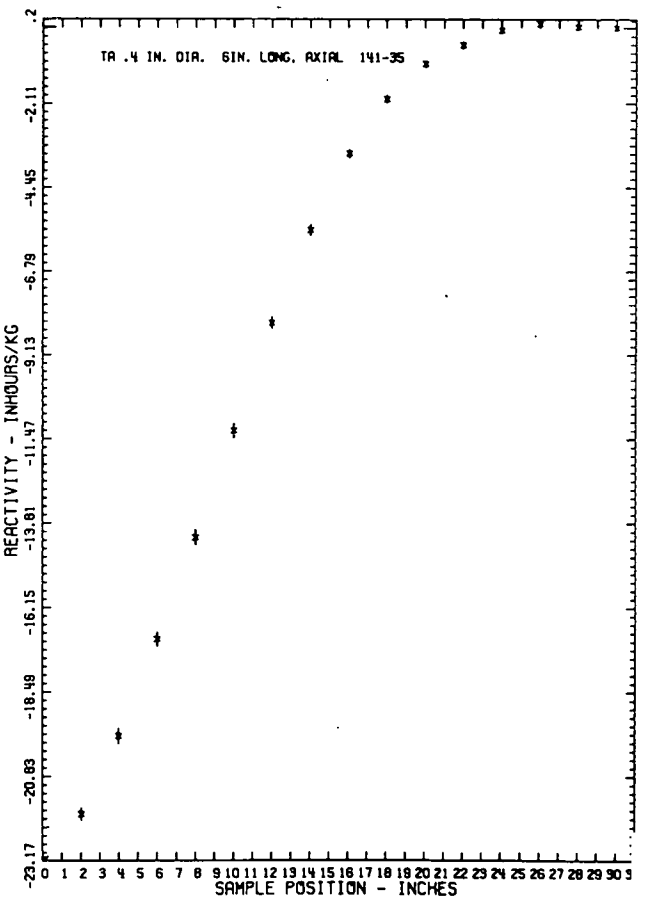

FIG. II-41-3. Specific Worth as a Function of Axial Position for a 0.4 in. Diam Ta Rod Position 0 = Fully Inserted Rod. *ANL-ID-103-A11778.*

Mockup Rod Worths

Figure II-41-5 shows the loading of the drawers which make up the mockup rods. Eight drawers are used for each full rod, four in each half. In addition to these rods, two others were used which were different in that the sodium plates were replaced by empty cans.

Figure II-41-6 indicates the locations used for the measurements. Two positions in the inner core and one (C) in the outer core were used for the full height rods. The center of the center position is slightly different from the core center. In each measurement of the rod worth, no other changes were made in the core outside of the mockup rod. Multiple rod drops[2] were performed for each reactor condition and from these the effective source was determined. From these sources the subcriticality for each reactor condition was found from a multiplication measurement using the equilibrium power. The measurements included those in the normal core, each rod in the various positions, a void in each position, and sodium plates in Position C. Differences were taken to provide the values shown in Table II-41-I. The results have been corrected for ^{241}Pu decay and core temperature. The uncertainty in the worth of the sodium for Rod 1 in Position C is large because of the three-week time difference between the void and rod worth measurement and the uncertainty in the ^{241}Pu decay correction.

Again the relative worths in the three positions are nearly the same for tantalum and boron. Figure II-41-2 also includes the relative worths of the mockup rods in comparison with the small boron sample traverse. The sodium worth is small compared with the total rod worth. The worth of the core drawers is the difference between the values in the first and the last sections of Table II-41-I.

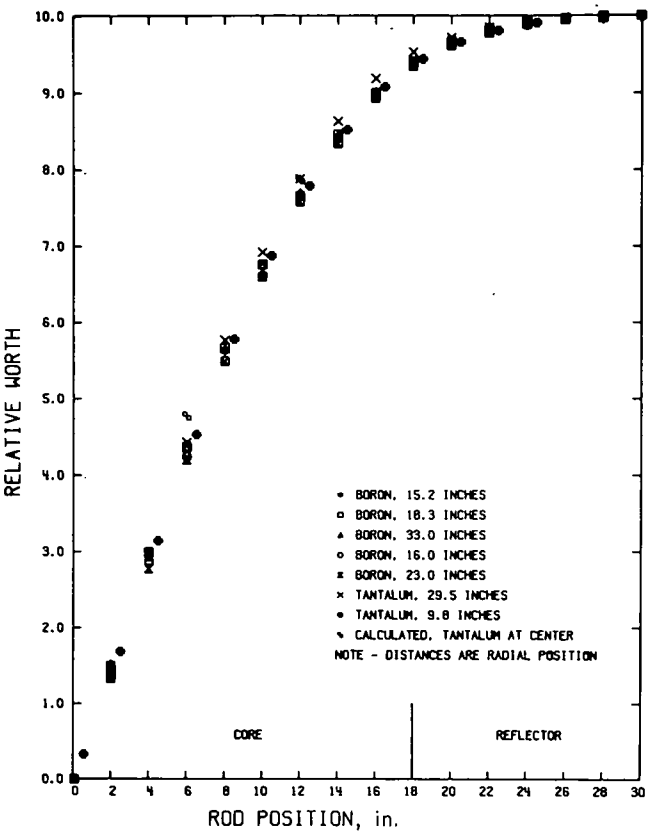

Fig. II-41-4. Normalized Rod Worths. *ANL-ID-103-A11776.*

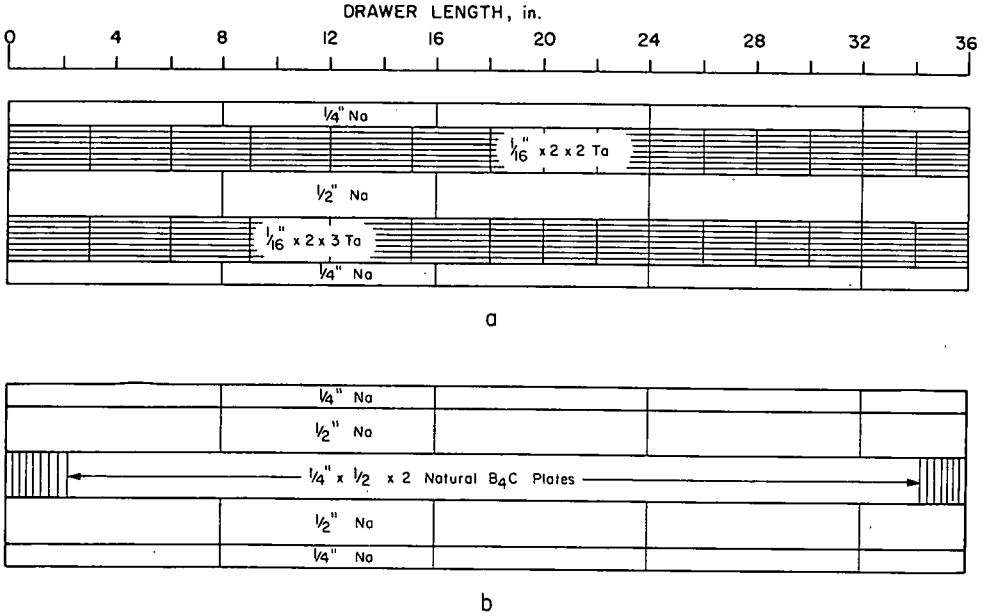

Fig. II-41-5. Drawer Loadings for Mockup Rods: a) Ta-Na Drawer, Rod Type 1; b) B-Na Drawer, Rod Type 2. *ANL Neg. No. 116-904.*

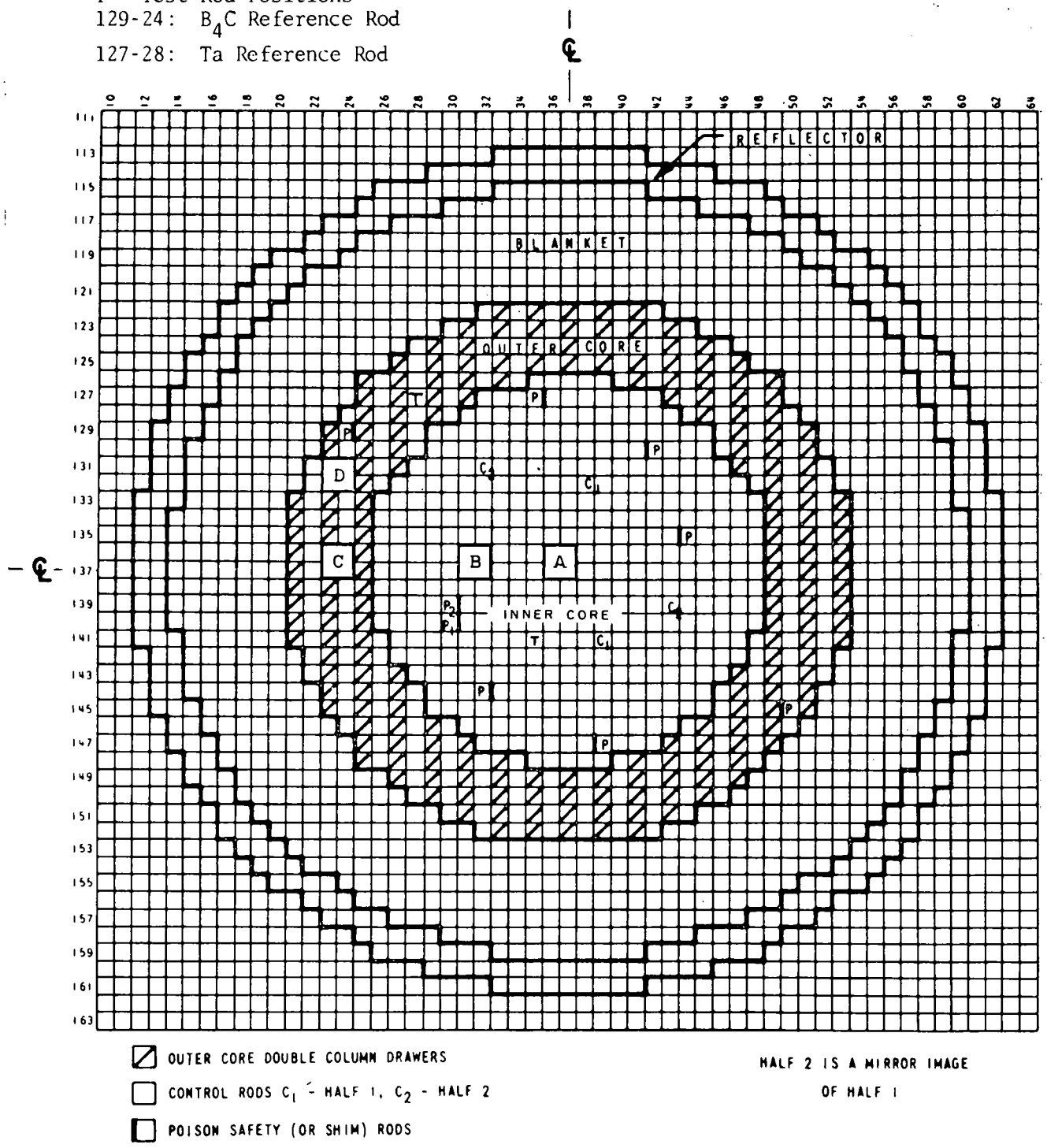

ASSEMBLY 2 - REFERENCE LOADING
WITH EQUAL ZONE VOLUMES
AND NO SPIKED CONTROL RODS

FIG. II-41-6. Mockup and Reference Rod Positions for Control Element Experiments. *ANL-ID-103-A11775.*

To investigate the effect of changing the material distribution within the rod, two experiments were done in Position A with the sodium filled rods. In the tantalum rod, the three inner plates of each of the two tantalum rows in each drawer were moved to the center. In the boron drawer the single column was split in half and separated with ½ in. of sodium. This left the outer tantalum positions the same but move the outer boron out ¼ in. The reactivities were remeasured. The difference between the two tantalum rods was 0.000 ± 0.009 dollars and between the two boron rods 0.033 ± 0.009 dollars, with the new rod being worth more. The latter value is in the direction expected since the rod was actually larger, even though it was comprised of the same material and located in the same drawer.

Effects of Mockup Rods

The effect on various quantities due to the insertion of the mockup rods at the core center was measured.

TABLE II-41-I. Worth of Mockup Control Rods of Full Core Height

Position	Rod 1, Ta + Na	Rod 3, Ta	Sodium in Rod 1	Rod 2, B_4C + Na	Rod 4, B_4C	Sodium in Rod 2
Worth Relative to Void, $\Delta k/\beta_{eff}$[a]						
A	−2.45 ±0.04	−2.40 ±0.04	−0.05 ±0.01	−2.47 ±0.04	−2.44 ±0.04	−0.03 ±0.01
B	−2.13 ±0.04			−2.15 ±0.04		
C	−0.726 ±0.006	−0.717 ±0.003	−0.009 ±0.006	−0.730 ±0.003	−0.742 ±0.003	+0.012 ±0.003
Worth Relative to Drawers of Sodium Plates, $\Delta k/\beta_{eff}$						
A[b]	−2.49 ±0.04	−2.44 ±0.04	−0.05 ±0.01	−2.51 ±0.04	−2.48 ±0.04	−0.03 ±0.01
C	−0.893 ±0.006	−0.884 ±0.003	−0.009 ±0.006	−0.896 ±0.003	−0.909 ±0.003	+0.013 ±0.003
Worth Relative to Core, $\Delta k/\beta_{eff}$						
A	−3.31 ±0.04	−3.26 ±0.04	−0.05 ±0.01	−3.33 ±0.04	−3.30 ±0.04	−0.03 ±0.01
B	−2.90 ±0.04			−2.92 ±0.04		
C	−1.475 ±0.006	−1.465 ±0.006	−0.010 ±0.006	−1.478 ±0.006	−1.491 ±0.006	+0.013 ±0.003

[a] β_{eff} = 0.003180 from calculation; the entries are independent of β_{eff}.

[b] The reactivity of sodium drawers in position A was derived from a single drawer measurement at the center of the core.

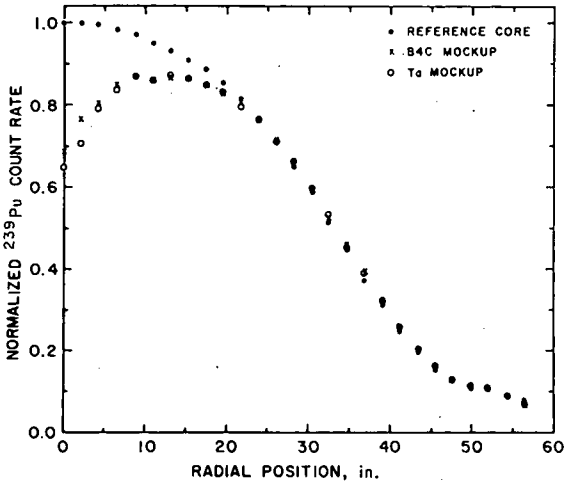

Fig. II-41-7. Normalized Radial Pu-239 Fission Counter Traverses in Reference Core and with B_4C and Ta Mockup Drawers. *ANL-ID-103-A11774.*

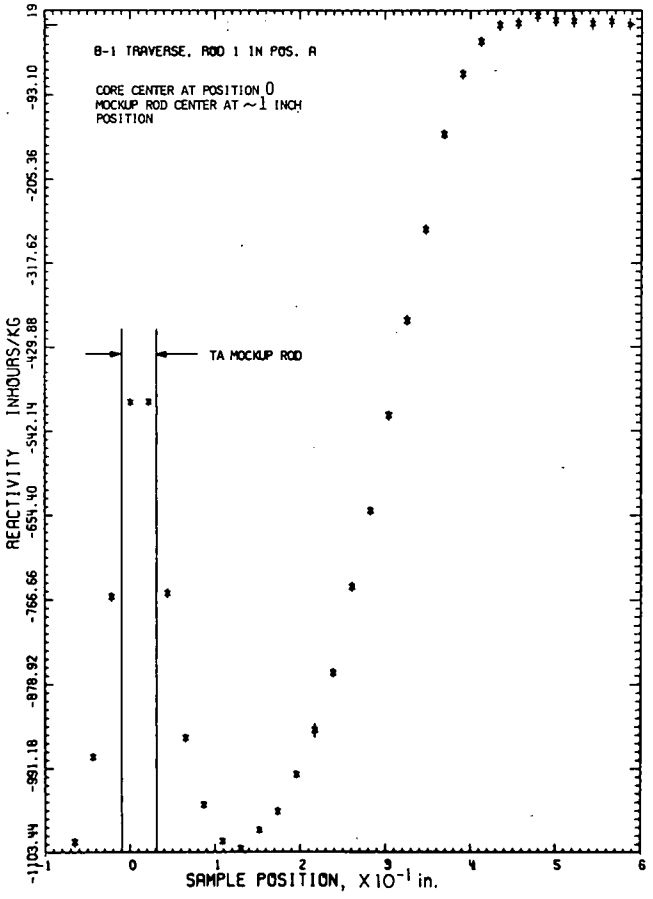

Fig. II-41-8. ^{10}B Reactivity Worth Near Ta Mockup Rod, ZPPR-2. *ANL-ID-103-A11777.*

Tantalum capture and ^{239}Pu fission rates are given in Paper II-43. Thermoluminescent dosimetry measurements of gamma distributions were also measured. The method used is described in Paper III-29. Figure II-41-7

TABLE II-41-II. SHADOWING EFFECT OF MOCKUP CONTROL RODS AT HALF CORE HEIGHT

Configuration	Worth Relative to Void, $\Delta k/\beta_{eff}$
Rod 2 Position C	$W_C = -0.381 \pm 0.003$
Rod 2 Position D	$W_D = -0.245 \pm 0.003$
Rod 2 Positions C and D	$W_{CD} = -0.597 \pm 0.003$
Shadowing effect of Rod 2 in positions C and D	$W_C + W_D - W_{CD} = -0.029 \pm 0.006$
Rod 1 Position A	$W_A = -1.29 \pm 0.02$
Rod 1 Position B	$W_B = -1.13 \pm 0.02$
Rod 1 Positions A and B	$W_{AB} = -2.29 \pm 0.04$
Shadowing effect of Rod 1 in positions A and B	$W_A + W_B - W_{AB} = -0.13 \pm 0.05$

TABLE II-41-III. EFFECT OF MASSIVE CONTROL RODS ON TANTALUM AND B_4C REFERENCE ROD WORTHS, (EXPERIMENTAL VALUES OF $\Delta k/\beta_{eff}$[a])

Full Core-Height Rods: Types and Positions	Worth of Half Core-Height Ta Ref.	Worth of Half Core-Height B_4C Ref.
1, 2, 3, or 4 in A	-0.245 ± 0.006	-0.151 ± 0.006
Void in A	-0.211 ± 0.003	-0.135 ± 0.003
Void in B	-0.208 ± 0.003	-0.129 ± 0.003
1 or 2 in B	-0.211 ± 0.006	-0.116 ± 0.006
1, 2, 3, or 4 in C	-0.195 ± 0.003	-0.107 ± 0.003
Void or Na in C	-0.204 ± 0.003	-0.123 ± 0.003
Normal Core	-0.195 ± 0.003	-0.123 ± 0.003

[a] $\beta_{eff} = 0.00318$.

shows the change in the ^{239}Pu fission distribution produced by Rod 1 and Rod 2 in the core center (Position A). The curves are normalized to the same total power. In order to make these measurements, the fuel loading was increased to return to a critical condition. For this case, where the rod worths are equal, the tantalum rod reduces the fission rate to a greater extent inside the rod (the first two points) but the difference is very small outside the rods. Similar data were obtained for $^{10}B(n,\alpha)$ around the boron center rod.

In the same manner, the radial worths of small samples of boron and tantalum were determined with both types of rods at the center in order to show the region over which rod interactions would be expected. Again, the shapes for both the boron and tantalum samples were quite similar around both rods with only slight differences in the central dips. The result for a boron traverse around the tantalum rod is shown in Fig. II-41-8. The effect of the rod being off center by 1 in. is easily seen in both the position of the dip and the fact that the peak at the negative position will be higher.

Two interaction measurements were also done with the mockup rods. In this case, however, they were only of half core height. Table II-41-II shows the individual and combined worth as well as the difference of these two values. These values were obtained with no fuel added to the normal core. The tantalum rod was used in the inner core Positions A and B and the boron rod in the outer core Positions C and D. The expected magnitude can be estimated for the A–B position from the tantalum reactivity traverse made through the Position A tantalum mockup rod. The change in the tantalum worth from the unperturbed case is about 13 % for both the small sample and the rod at the B position. The distance between Positions C and D is about the same as that between A and B, and the reduction in the worth of rod D is fractionally about the same as that in Rod B.

In addition, the change in the worth of a half-core-length rod of both tantalum and boron near the outer edge of the core was measured for each reactor change. The position of these two reference rods is shown in Fig. II-41-6. Table II-41-III presents a summary of the various results. The trend is as expected. A rod in Position A increases the edge worths as does the removal of fuel. When Position C is reached, the close reference rod is reduced in worth while the other remains unchanged.

REFERENCES

1. Annual Technical Progress Report, *LMFBR Physics Programs GFY 1970, AI-AEC-12969.*
2. S. G. Carpenter and R. W. Goin, *Rod Drop Measurements of Subcriticality,* Applied Physics Division Annual Report, July 1, 1969 to June 30, 1970, ANL-7710, pp. 206–209.

II-42. Demonstration Benchmark Control Rod Measurements—Part II: Analysis

J. P. Plummer, R. G. Palmer, G. L. Grasseschi and B. Newmark*

Introduction

A number of experiments were performed in ZPPR Assembly 2 to obtain general data on the performance of absorbing control rods in a typical dilute fast reactor. The power reactor control rods were simulated in ZPPR by arrangements of sodium plates and boron carbide or tantalum plates in a four drawer bundle. The control rod configurations and a description of the experiments are presented in detail in Paper II-41.

This paper describes the analysis that has been performed on the control rod studies and compares the measured and calculated results. The analysis varied in sophistication from diffusion theory calculations on homogeneous models of the control rods to discrete ordinate transport calculations on a detailed heterogeneous arrangement of boron carbide and sodium plates.

Calculational Procedures

The basic cross section library used in the calculational studies was the 27 group set generated by MC² from the ENDF/B VERSION 1 data and spatially averaged over the various cell types in the reactor by the integral transport perturbation theory code CALHET-3. For reasons of economy, it was deemed necessary to perform many of the calculations in only 7 groups, the cross sections for which were derived by collapsing the 27 group cross sections using region-dependent spectra. Resonance self-shielded group cross sections for the tantalum plates, with and without sodium, were obtained by additional MC² calculations performed in the fine group mode using the normal core homogeneous 66 fine group fluxes as the envelope spectrum. Since the ^{11}B isotope was not available in the ENDF/B library, the ^{11}B in the natural boron of the B_4C rods was simulated by extra carbon in the ratio of 1.24 ^{11}B atoms to one ^{12}C atom. This ratio was based on a comparison of the relative scattering cross sections of ^{11}B and ^{12}C.

Generally, the rod worths were calculated using the 2D diffusion module of the ARC system. The materials in the four drawer bundles were assumed to be distributed homogeneously over the volume of the drawer. Table II-42-I gives the atomic densities used in the calculations. The worths of the rod configurations were calculated as $(k_{nr} - k_r)/\beta_{eff}$ where k_r and k_{nr} are the eigenvalues with and without the absorbing rods, respectively. Some of the control rod measurements were made relative to void but, because of the inherent difficulties associated with calculating voids by diffusion theory, the calculations were made relative to sodium or normal core material. The uncertainty in the worths of the rods due to convergence considerations has been estimated conservatively at 1¢.

Results

Table II-42-II presents the calculated worths of centrally located full-core-height rods of boron and tantalum. Measured values are implicit in the calculate/experimental (C/E) values shown. Since the central axis of the core occurred along the center of a drawer, rather than along a cornerline, the centerline of the four drawer bundles occurred at $r = 4$ cm. However, the correction factor for comparison with the exact-central control rod calculations was estimated to be much less than the experimental error. The worth of a centrally located 2-in.-diam axial rod was also calculated and is shown in Table II-42-II. In the experiment, the rod was located at $r = 26.5$ cm and so first order perturbation theory was invoked to obtain a correction factor to apply to the calculated result so that it could be compared with experiment. For purposes of comparison, the results for a one dimensional radial model using the 1DX code are shown in the table. A single value of B^2, obtained from MC², was used to simulate leakage in the axial direction. All the calculated results in Table II-42-II are based upon a 27 group treatment.

Figure II-42-1 shows the rod worth shape on withdrawal of the 2 in. radially-central tantalum rod. This is based on *rz* calculations of rod worth for various de-

TABLE II-42-I. Homogenized Atom Densities for the Tantalum and Boron Carbide Mockup Control Rods

Material	Homogenized Atom Density, 10^{24} atoms/cm³	
	B_4C	Tantalum
Na	0.012864	0.008423
Fe	0.009877	0.008964
Cr	0.002709	0.002458
Ni	0.001394	0.001266
Mn	0.000199	0.000183
Mo	0.000007	0.000006
Ta	—	0.022154
^{10}B	0.004038	—
^{11}B	0.016374	—
C	0.005294	—

* Westinghouse Electric Corp., Pittsburgh, Pennsylvania.

TABLE II-42-II. Diffusion Theory, Cylindrical Geometry, Calculated Central B_4C and Tantalum Rod Worths Relative Both to Inner Core (IC) Material and to Sodium—Comparison with Experiment

Rod	1DX, dollars	C/E	2D Diff.,[a] dollars	C/E
2 in. diam Ta	1.07 (Rel. to Na)	1.07 ± 0.02	1.13 (Rel. to Na)	1.13 ± 0.02[b]
4-drawer Ta				
a) Normal	3.26 (Rel. to IC)	0.985 ± 0.012	3.37 (Rel. to IC)	1.02 ± 0.01
	2.45 (Rel. to Na)	0.984 ± 0.016	2.69 (Rel. to Na)	1.08 ± 0.02
b) Na-voided	Not calculated	—	3.33 (Rel. to IC)	1.02 ± 0.01
			2.65 (Rel. to Na)	1.09 ± 0.02
4-drawer B_4C	3.24 (Rel. to IC)	0.973 ± 0.012	3.34 (Rel. to IC)	1.00 ± 0.01
	2.40 (Rel. to Na)	0.956 ± 0.015	2.65 (Rel. to Na)	1.06 ± 0.02

[a] k for the unpoisoned system is 0.98140.

[b] The experimental value is relative to void.

Note: In the experiments, the 4-drawer bundles are approximately 4 cm off center, and the 2 in. tantalum rod is 26.5 cm off center. A calculated correction factor has been applied to the calculated 2 in. rod worths, but is considered negligible in the case of the 4-drawer bundles.

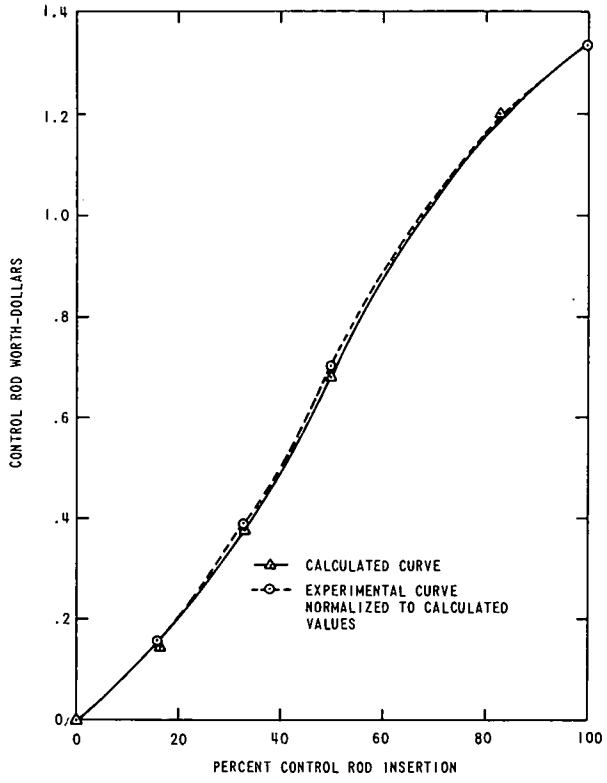

Fig. II-42-1. Rod Worth versus Percent Rod Insertion for 2 in. Central Tantalum Rod. *ANL Neg. No. 103-A11948.*

grees of insertion by the $k_1 - k_2$ difference technique. The experimental points are also shown and agree quite well with the calculated curve.

Results for off-radial-center control rods, as calculated by *xy* geometry diffusion theory, are presented in Table II-42-III. The *xy* calculations were all done in the 7-group structure, and the results are all for full-core-height rods relative to core material. Rod positions A, B, C, and D are shown in Fig. II-41-6. Rod interaction effects were also calculated by comparing the sum of the worths of individual rods at two positions with their combined worths. These results are shown in Table II-42-IV. Because of the inventory limitations on the absorber materials, the rod interaction experiments could be performed only with half-core-length rods. The unavailability of a 3-dimensional computer code precluded any calculations of off-center half rods, so full-core-height calculations had to be used. Another difficulty arose from the fact that all the experimental worths for the rod interaction studies were relative to void while the calculated worths, for the reasons mentioned under Calculational Procedures, were relative to core material.

TABLE II-42-III. Worth of Full-Core-Height Mockup Control Rods, Including Interaction Effects: Calculation (7 Group, *XY* Geometry, 2D-DIFF) versus Experiment
(*All results relative to core material*)

Rod(s)	$\Delta k/\beta_{eff}$		
	Experiment, dollars	Calculation, dollars	C/E
B_4C at A	3.33 ± 0.04	3.24	0.97 ± 0.01
Ta at A	3.31 ± 0.04	3.30	1.00 ± 0.01
B_4C at B	2.92 ± 0.04	2.87	0.98 ± 0.01
Ta at B	2.90 ± 0.04	2.92	1.01 ± 0.01
B_4C at C	1.48 ± 0.01	1.47	0.99 ± 0.01
Ta at C	1.48 ± 0.01	1.47	0.99 ± 0.01
B_4C at D	1.09 ± 0.02[a]	1.11	1.02 ± 0.02
Ta at A & B	6.03 ± 0.09[a]	5.82	0.97 ± 0.02
B_4C at C & D	2.51 ± 0.02[a]	2.27	0.90 ± 0.0

[a] Calculated from experimental results for worth relative to void for half core-height rods, assuming half core-height worth = 0.52 × full core-height worth, and using the measured worths of drawers of core material relative to void.

Discussion

There are many possible sources of error in the calculations, some of which, like the inability to calculate off-center half-height rods, have already been mentioned. Budget limitations forced the use of some less exact calculational techniques, producing inaccuracies in the rod worths which could be estimated quantitatively. Following is a discussion of some of these approximations.

The mesh spacing used in the *xy* calculations was one interval per drawer except for the drawers containing the control rod material and the immediate neighboring drawer on each side where the spacing was halved. A calculation was made for the normal system (no control rods) in which the mesh spacing was everywhere two intervals per drawer. This resulted in an eigenvalue only 0.05 % lower than a similar calculation with the one-interval-per-drawer spacing.

In order to compare the 7-group cross sections with the 27-group set, the worth relative to inner-core material of the central four-drawer tantalum bundle was calculated in *rz* geometry in both 7 and 27 groups. The 27-group worth was higher by 0.98 %.

The *xy* model enabled an estimate to be made of the effect of the circularization of the region interfaces, which is necessary to the cylindrical model. A 1D radial calculation was done using the same region and group-dependent DB^2 values to simulate axial leakage as were used in the *xy* calculations. The 0.06 % difference in the values of k_{eff} obtained (the *xy* result was higher) indicates that the effect of circularizing the region interface is slight.

Test calculations were made to make sure that the *xy* calculations were in substantial agreement with the *rz* calculations in those cases where tests could be made, i.e., unperturbed cores and cores with radially central rods. In the 7-group structure, an *rz* calculation for an unpoisoned core yielded a value of k_{eff} that was 0.4 % lower than the corresponding *xy* calculation.

The 2D transport code DOT was used to look at two more approximations: (1) the use of diffusion theory in control rod calculations, and (2) the homogenization of the contents of the 4-drawer control rod bundles. The model was a slightly idealized version of Loading 90 in which the small assymmetries were ignored and the configuration was represented in *xy* geometry by one quadrant with mirror boundary conditions for the bottom and left. The B_4C rod was represented by two models: (1) the homogenized B_4C composition, smeared over the entire drawer, and (2) a 0.5 by 2.0 in B_4C plate surrounded throughout the rest of the drawer by homogenized sodium and stainless steel. The rod worth for both models was calculated by DOT (S8) and by the 2D diffusion module of the ARC system. A breakdown of diffusion theory was evidenced by the fact that the heterogeneous rod worth was greater than that of the homogeneous rod, according to diffusion theory. Comparing the diffusion theory worth for the smeared rod with the transport theory worth for the same smeared rod gave a transport correction of −7.6 %. This compared quite well with a value of −6.7 % obtained previously from 1D diffusion and transport calculations in 27 groups. Then, comparing the DOT values for the worth of the smeared rod and the non-smeared rod gave a further heterogeneity correction of −2.7 %. It should be noted that all these calculations were done using cross sections collapsed to 7 groups by the code CCSX. However, option 4[1] was used to collapse the transport cross section for the ensuing diffusion theory calculations while option 2 (straight flux weighting) was used for the DOT cross sections.

TABLE II-42-IV. Mockup Control Rod Interaction Effects: Experiment (Half-Core-Height Rods) versus Calculation
(Full-core-height rods, interaction effect divided by 2)

Rods	Experiment: $\left[\Delta k_{(c)}^{(a)} + \Delta k_{(d)}^{(b)} - \Delta k_{(cd)}^{(ab)}\right] / \beta_{eff}$, dollars	Calculation: $\left[\Delta k_{(c)}^{(a)} + \Delta k_{(d)}^{(b)} - \Delta k_{(cd)}^{(ab)}\right] / 2\beta_{eff}$, dollars
Ta at A & B	0.13 ± 0.05	0.20
B_4C at C & D	0.03 ± 0.01	0.15

Note: $\beta_{eff} = 0.00322$.

The results shown in Tables II-42-II through II-42-IV are not corrected for any of the effects discussed in this section. If correction factors are applied for the three most significant approximations—that is, smearing the rods, using diffusion theory, and collapsing to 7 groups (in the case of the *xy* calculations)—the C/E ratios for the four drawer B_4C and tantalum bundles drop to the range 0.88 to 0.93 in contrast to the C/E ratios of 1.15 to 1.25 found for small samples.

Reference

1. A. Travelli, *A New Formulation of Multigroup Microscopic Cross Sections*, Reactor Physics Division Annual Report, July 1, 1967 to June 30, 1968, ANL-7410, pp. 413–421.

II-43. Tantalum Capture and Plutonium Fission Rates Around Control-Rod Mockups in ZPPR Assembly 2

D. W. Maddison

Control-rod mockups for boron and tantalum loaded rods have been investigated in ZPPR Assembly 2 (see Papers II-41 and II-42). Foil irradiations were done in these configurations to determine the reaction rates in and around the rods for $^{239}Pu(n,f)$ and also $^{181}Ta(n,\gamma)$ for the tantalum loaded rod.

The plutonium fission rate distribution was done primarily to determine the effect of the control rod at nearby locations. The tantalum capture distribution was designed to provide information on the extent of gamma-ray heating that would take place in the control rod.

The control-rod mockups consisted of four drawers, drawer 136-37 being the upper right drawer of the group. The relative rates for $^{239}Pu(n,f)$ are shown in Fig. II-43-1 for the two types of control rods, with ar-

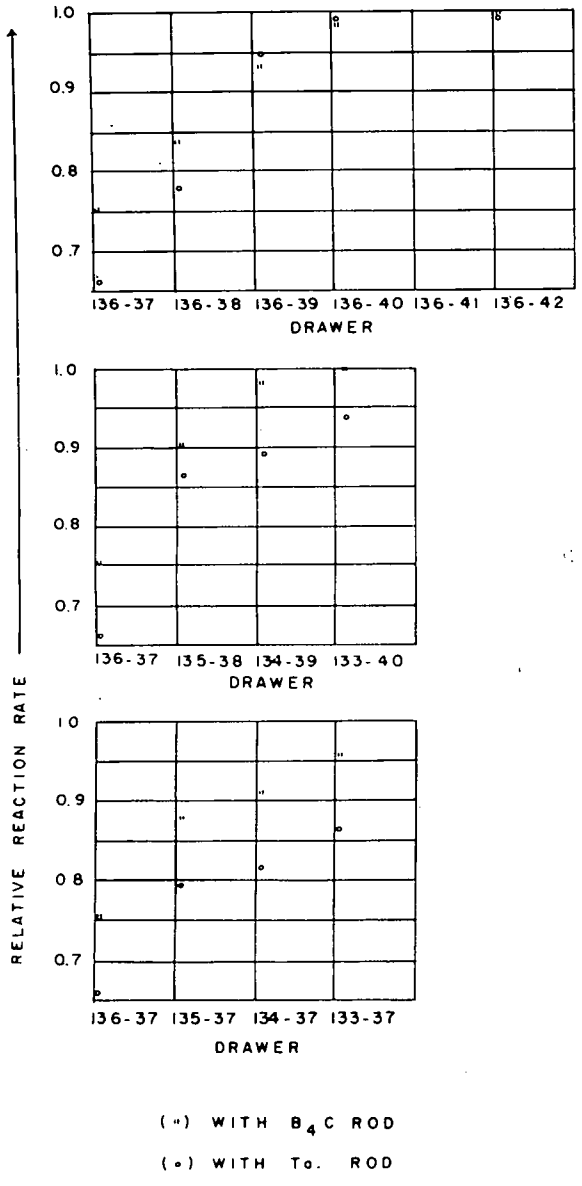

Fig. II-43-1. $^{239}Pu(n,f)$ Reaction Rates Around Control-Rod Mockups.

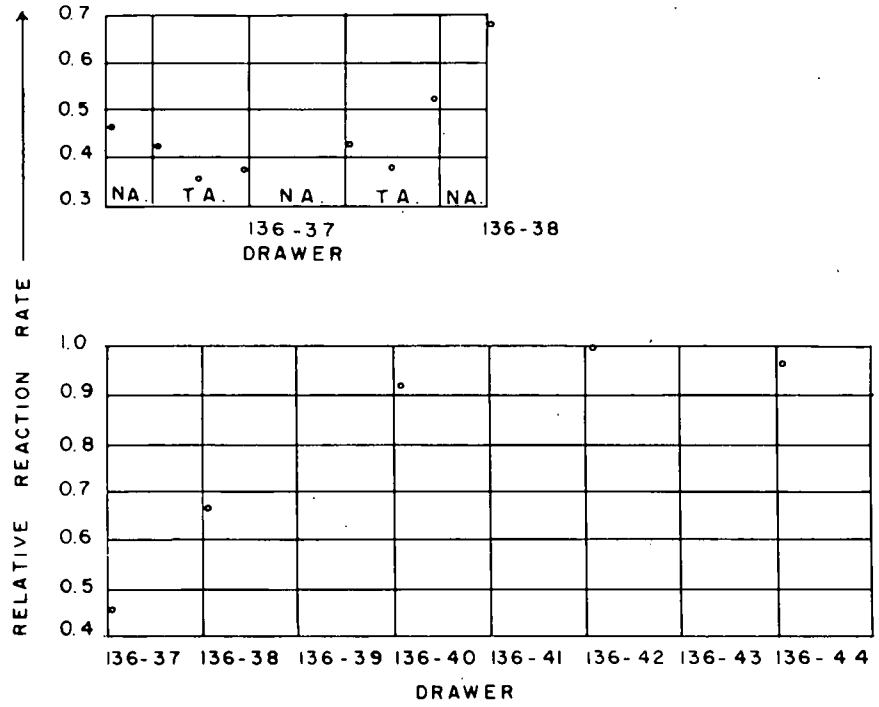

FIG. II-43-2. $^{181}Ta(n,\gamma)$ Reaction Rate in and Around Tantalum Control-Rod Mockup.

bitrary normalization at the highest values. The errors range from 1.8 to 4.0 % for the tantalum rod data, and from 0.85 to 1.60 % for the boron rod data. Figure II-43-2 presents the $^{181}Ta(n,\gamma)$ results around the tantalum rod and within one of the four drawers of the rod. The errors associated with the tantalum activation data range from 1.2 to 2.5 %. It should be noted that tunneled tantalum plates, 0.0625 in. thick, were used in six positions to accommodate the foils in the drawer.

II-44. Reactivity Doppler Measurements in ZPPR Assembly 2

R. E. KAISER, J. M. GASIDLO and W. G. DAVEY

INTRODUCTION

An extensive program of reactivity Doppler measurements has been planned for ZPPR Assembly 2,[1] involving pin-calandria zones and the normal plate core, and including measurements in sodium voided configurations. During the period of this report, results have been obtained for natural UO_2 and PuO_2 samples at the center of the normal plate core and in a central, 93-drawer sodium-voided zone. The measurement technique was developed at Argonne National Laboratory.[2,3] and involved the oscillation of a heated sample in and out of a cold reactor. Although the standard oscillation experiment has traditionally used a calibrated auto-rod to determine reactivity worth, some tests were run in this sequence of experiments to evaluate the feasibility of inverse kinetics measurements of Doppler reactivity.

EXPERIMENTAL EQUIPMENT

The equipment used in reactivity Doppler measurements in ZPPR is basically the same as that used on Argonne's other zero power reactors, with certain modifications. The principal difference in the ZPPR system is the dual-heater temperature control system. This system, described in detail in Paper No. III-32, was designed to eliminate variations in reactor temperature as the sample is heated. This is accomplished by applying about 150–200 W of heat at all sample temperatures, and automatically adjusting the proportion of total heater power between sample and auxiliary heaters. Auxiliary heater power is controlled by thermistors

placed in the primary coolant path downstream from the sample. The ZPPR system was designed to use the same samples as are used in ZPR-6 and -9, which are usually 12 in. long and 1 in. in diameter.

The Doppler oscillator rod is constructed in sections, and can be assembled to penetrate the reactor either axially or radially with the same drive mechanism used for both. Cell air is pulled through the Doppler rod for cooling, and returned to the reactor cooling system where it is filtered and cooled with the exhaust air from the reactor. Vacuum system, heaters, and drive system controls can all be operated remotely from the reactor control room. Data acquisition is handled by the SEL 840 computer for autorod experiments as well as inverse kinetics runs, and the experimenter controls the computer from the control room teletype in either case.

Autorod Measurements

Measurements were performed using axial penetration of the oscillator rod, 2.173 in. above the exact center of the inner core, with the sample centered at the reactor interface when at the "in" position. Total length of the oscillation was 53 in., sufficient to completely remove the sample from the axial reflector with 5 in. to spare. Balancing of the reactivity swing caused by Doppler rod motion was accomplished by loading ⅛ x 1 x 2 in. pieces of depleted uranium and aluminum (for the natural UO_2 sample) in covered trays which extended along the length of the rod, as shown in Fig. II-44-1. Balancing for the PuO_2 sample was accomplished in the same manner, except that the materials used were enriched uranium and aluminum.

The worth of the oscillation was determined, as described by Bennet and Long,[4] from the equation

$$D_k = (-1)^{k+1} [\rho_k - \tfrac{1}{2} (\rho_{k+1} + \rho_{k-1})], \qquad (1)$$

where D_k is the difference in worth between "in" and "out" positions of the Doppler rod. The quantity ρ_k represents the reactivity at the kth end point of the oscillation, as determined from the average autorod position while the Doppler sample is stationary. If an even number of differences is used, this procedure will eliminate linear and quadratic reactivity drifts. From 12 to 16 values of D_k were obtained for each sample temperature, and the standard deviation of the average D_k was obtained as described by Bennet and Long.[4]

Total sample worths, at ambient temperature, were obtained by measuring the reactivity effect of replacing the UO_2 (or PuO_2) sample by a dummy capsule, while maintaining the same balance tray loadings as were used with the respective Doppler capsules. The dummy measurements were performed by inverse kinetics for the UO_2 balance loading because the worth of the autorod was too small to follow the reactivity swin

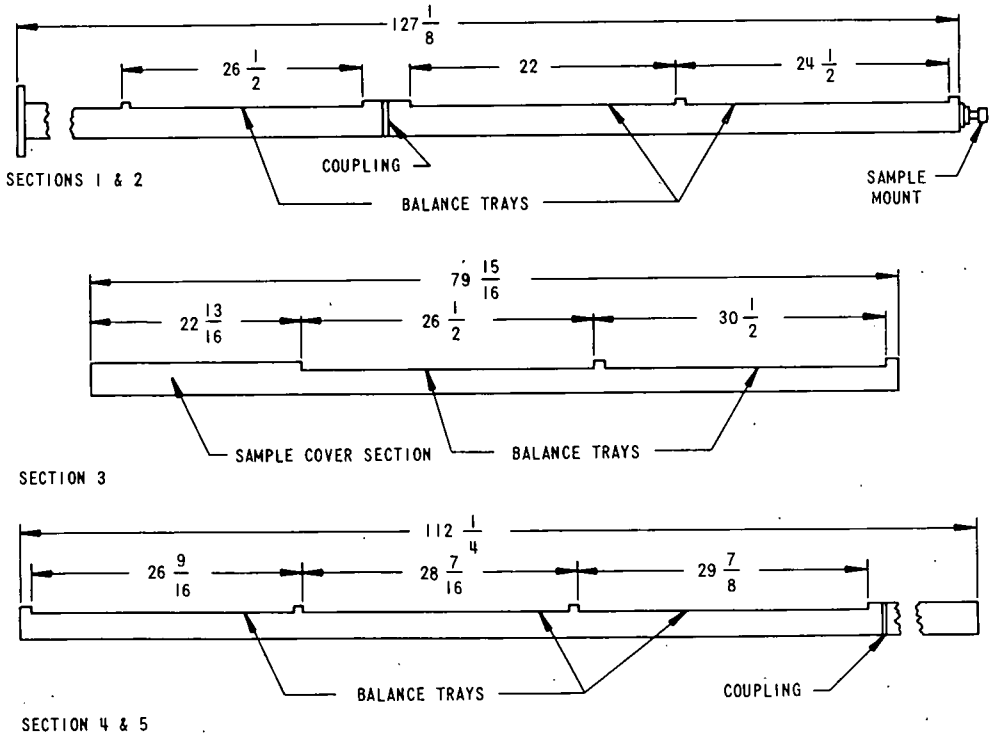

Fig. II-44-1. ZPPR Doppler Rod Schematic-Axial Penetration. *ANL-103-A11906.*

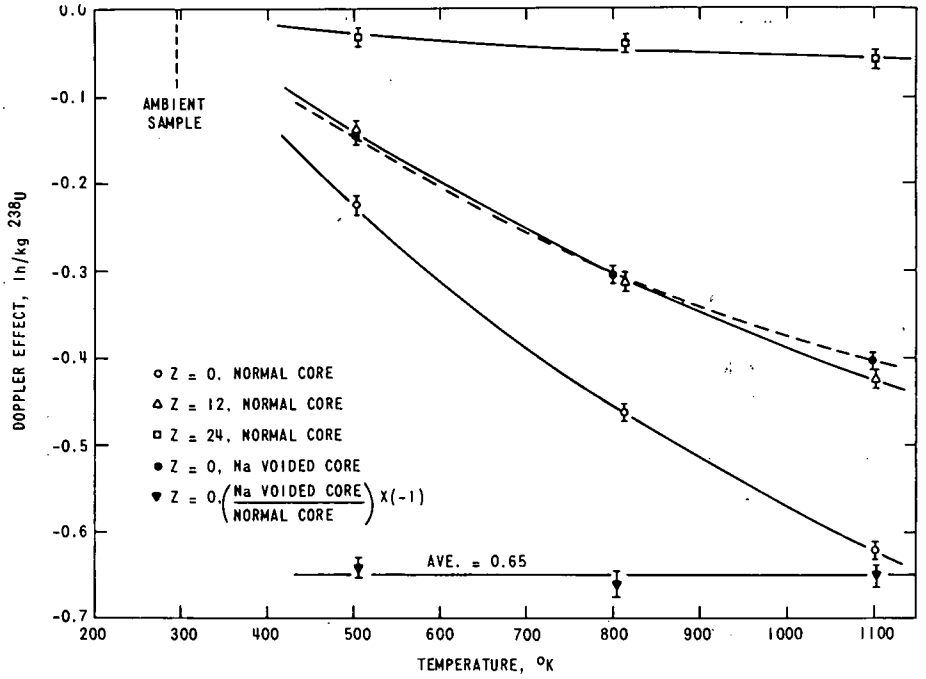

FIG. II-44-2. Natural UO_2 Doppler Results in the ZPPR Assembly 2 Plate Cores. *ANL-103-A11904.*

during the oscillation of the dummy capsule. The measurement of the worth of the PuO_2 sample was determined from critical rod positions because of safety considerations involving large, positive worth samples.

The initial autorod experiments were run with a six-minute cycle time: 40 sec travel time, 20 sec wait for transients to die out, and a 5 min integration of autorod position. Tests were run using shorter integration times or shorter wait times, but no significant variations in the results were seen. A four-minute cycle (40 sec travel, 40 sec wait, 160 sec integrate) was used in the remaining experiments because it gave a more efficient use of reactor time.

The results of the natural UO_2 measurements in the normal and sodium voided plate cores are shown graphically in Fig. II-44-2. The 12-in. long UO_2 sample was measured at three different positions in the normal core, (1) at the reactor interface, $z = 0$ (-6 to $+6$), (2) at $z = 12$ in. ($+6$ to $+18$), and (3) at $z = 24$ in. ($+18$ to $+30$). The U-238 Doppler effect drops off rapidly as the sample moves axially outward, with a reduction in magnitude of better than a factor of 10 in going from core center to the first 12 in. of the axial blanket. The comparison between the central measurements in the normal and the sodium-voided cores is also shown in Fig. II-44-2, and indicates a uniform reduction of about 35% in the magnitude of the Doppler effect upon removal of the sodium. Tables II-44-I and II-44-II present the Doppler effect data and total sample worths for the natural UO_2 sample in the normal and the sodium-voided cores.

TABLE II-44-I. DOPPLER EFFECT AND TOTAL SAMPLE WORTH FOR NATURAL UO_2 AT DIFFERENT AXIAL POSITIONS IN THE NORMAL PLATE CORE OF ZPPR ASSEMBLY 2

Temp, °K	Ih/kg ^{238}U		
	$z = 0$ (-6 to $+6$)	$z = 12$ ($+6$ to $+18$)	$z = 24$ ($+18$ to $+30$)
503	-0.224 ± 0.008	-0.140 ± 0.011	-0.032 ± 0.009
814	-0.462 ± 0.009	-0.312 ± 0.010	-0.039 ± 0.009
1102	-0.622 ± 0.009	-0.423 ± 0.010	-0.060 ± 0.010
Sample (300)	-6.61 ± 0.02	-2.68 ± 0.11[a]	-0.43 ± 0.11[a]

[a] Obtained from inverse kinetics traverse data.

TABLE II-44-II. COMPARISON OF NATURAL UO_2 DOPPLER EFFECT IN THE NORMAL AND SODIUM-VOIDED PLATE CORES OF ZPPR ASSEMBLY 2

Nominal Temp., °K	Ih/kg ^{238}U		
	Na-Voided Core	Normal Core	Ratio V/N
500	-0.144 ± 0.009	-0.224 ± 0.008	0.641 ± 0.012
800	-0.306 ± 0.012	-0.462 ± 0.009	0.661 ± 0.015
1100	-0.406 ± 0.011	-0.622 ± 0.009	0.653 ± 0.014
Sample (300)	-6.44 ± 0.02	-6.61 ± 0.02	0.974 ± 0.028

The plutonium oxide sample was run at core center in both the normal and sodium-voided cores, with the results shown in Fig. II-44-3. The base temperature of

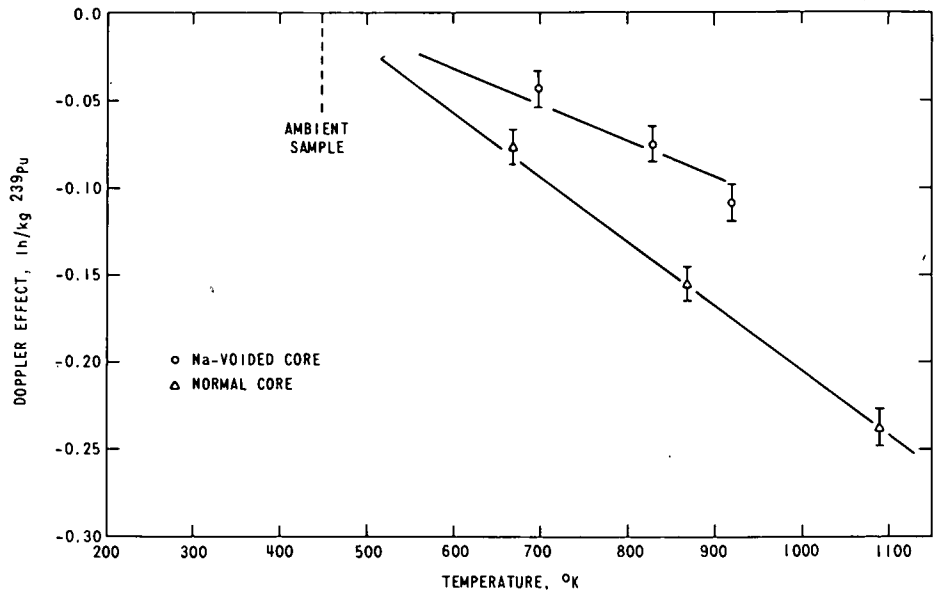

FIG. II-44-3. PuO_2 Doppler Results in the ZPPR Assembly 2 Plate Cores, $Z = 0$. *ANL-103-A11903.*

TABLE II-44-III. COMPARISON OF PuO_2 DOPPLER EFFECT IN THE NORMAL AND SODIUM-VOIDED PLATE CORES OF ZPPR ASSEMBLY 2

Voided Core Temp., °K	Ih/kg Pu[a]		Normal Core Temp., °K
	Na-Voided Core	Normal Core	
700	−0.044 ± 0.011	−0.077 ± 0.010	670
830	−0.076 ± 0.010	−0.155 ± 0.009	870
920	−0.109 ± 0.011	−0.238 ± 0.009	1090
Sample (300)	+103.2 ± 0.8	+107.3 ± 0.8	Sample (300)

[a] Data are not corrected for expansion effects.

the PuO_2 sample was about 445°K due to alpha decay heating effects. During the experiment in the sodium-voided core, severe out-gassing of the sample occurred, and the resulting partial loss of vacuum limited the maximum temperature to 920°K. As this was the first time this particular sample had been run, the problem was not unexpected. The subsequent experiment in the normal plate core, performed with the same sample, encountered only minor out-gassing problems which slowed the experiment somewhat, but did not limit the maximum temperature. The data, including the specific temperatures involved, are presented in Table II-44-III.

In a core such as ZPPR-2, with a height of only 36 in., the 12 in. long Doppler sample will expand into a significant flux gradient as it is heated. The worth of this effect for the UO_2 sample has been estimated to be positive, and less than one percent of the effect at 1100°K. For the PuO_2 sample the effect is negative, and may be as much as 20% of the measured effect at 1100°K. In addition, there is the problem of change in internal multiplication in the PuO_2 sample. This effect has not yet been accurately assessed, principally due to a lack of precise data on the expansion characteristics of the sample.

INVERSE KINETICS MEASUREMENTS

The inverse kinetics technique, which has been used for rod calibrations and small-sample perturbation measurements, was tested in some of the runs in the plate core Doppler experiments. The method has two potential advantages: (1) no autorod need be installed, so that core perturbation is minimized—especially in a pin-calandria zone, and (2) the possibility of obtaining Doppler effect traverse data while the sample is in motion. In order to justify using the inverse kinetics measurements, it is necessary to demonstrate that the results obtained are consistent, within experimental errors, with data obtained using the calibrated autorod. For this reason, several of the runs performed with the autorod were repeated by inverse kinetics, as shown in Table II-44-IV. The results appear to be consistent, but with a tendency for the autorod measurement to be slightly higher. This would indicate the possibility of a small systematic error in one or both of the measurements as discussed below.

Data for the Doppler effect in the 12 in. sample, shown in Fig. II-44-4 as a function of sample position, is obtained as a matter of course from the inver kinetics measurements as the sample oscillates betwe the "in" and "out" positions. The data include the ef fects of the long sample moving through the axial flux gradients, and so do not represent a true differential

curve. Investigations into the feasibility of obtaining a true differential curve from these data are currently in progress. The single-position measurements for UO_2 in the normal core are shown in Fig. II-44-4, along with the inverse kinetics traverse data, illustrating the excellent agreement between the two techniques.

TABLE II-44-IV. COMPARISON OF AUTOROD AND INVERSE KINETICS DOPPLER MEASUREMENTS

Measurement	Ih/kg	
	Autorod	Inverse Kinetics
Nat. UO_2 in Na-Voided Core, 300–1100°K	−0.406 ± 0.011	−0.397 ± 0.007
PuO_2 in Normal Core, 300–1100°K	−0.238 ± 0.009	−0.251 ± 0.010
Nat. UO_2 Sample, Normal Core		
300–500°K	−0.224 ± 0.008	−0.210 ± 0.008
300–800°K	−0.462 ± 0.009	−0.450 ± 0.008
300–1100°K	−0.622 ± 0.009	−0.594 ± 0.008

Data similar to those shown in Fig. II-44-4 were also obtained for the PuO_2 sample. However, in the case of PuO_2, the measured effect was negative at the center and became positive as the sample moved out of the reactor in the axial direction. The cross-over point occurred with the center of the 12 in. sample 8 in. from the interface, and the maximum positive worth occurred where the sample straddled the core/axial blanket boundary, 18 in. from the interface. The interpretation of the data is complicated by three factors: (1) axial expansion of the sample into a flux gradient, (2) changes in internal multiplication, and (3) the length of the sample (12 in.) with respect to reactor dimensions. After an approximate correction for axial expansion, a significant negative effect remains at the core center, sufficient to indicate that the Doppler effect itself may be negative, even after corrections for internal multipli-

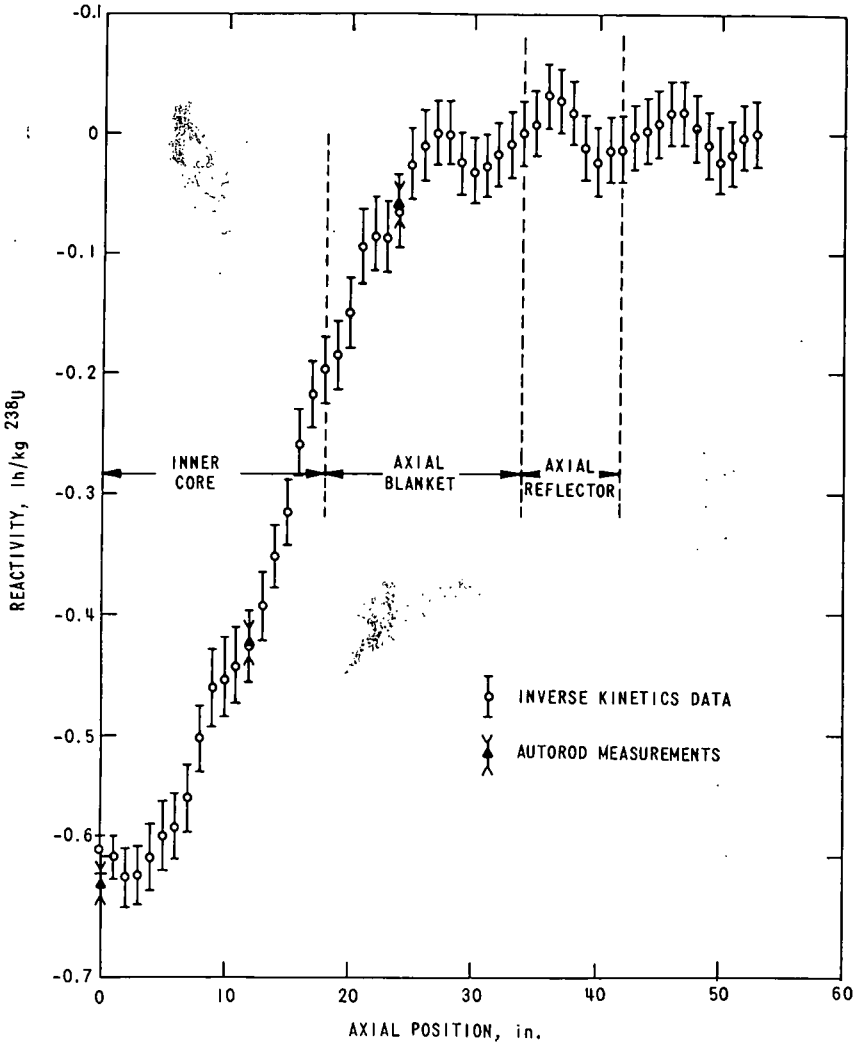

FIG. II-44-4. Natural UO_2 Doppler Effect as a Function of Axial Position in ZPPR Assembly 2. *ANL-103-A11905.*

cation effects are made. This conclusion must be qualified, however, until a better understanding of the axial traverse data is obtained, which would explain the change in sign of the measured effect as a function of axial position.

Evaluation of Uncertainties

The evaluation of uncertainties which arise due to the statistical nature of the data is quite straightforward, and represents a minimum achievable error. For the inverse kinetics measurements, this error was typically about 0.003 Ih, and for the autorod measurements about 0.004 to 0.007 Ih. These values, however, do not include any possible systematic errors that may arise, such as autorod calibration error, reactor drift, etc. There are several possible sources of such errors, although the equipment is designed to eliminate most of them.

Reactivity drift due to changes in the reactor temperature distribution have caused problems in all reactivity measurements and calibrations on ZPPR. Analytical corrections have been developed for correcting these data, but it is as yet uncertain whether or not these methods are accurate enough over the extended duration of a Doppler measurement. In subsequent experiments, additional data will be obtained during periods of high drift rate or rapidly changing drift rate to permit an assessment of the accuracy of the drift corrections.

Further complications resulting from reactor drift would develop if the changes in reactor temperature were sufficient to cause significant changes in the rate of heat loss from the oscillator rod to the reactor. This would cause changes in the temperature of the balance material downstream from the sample, thus altering the reactivity profile of the rod. Due to the relatively small magnitude of the reactor temperature fluctuations, and the fact that the Doppler cooling air is heated, this is probably not a significant problem. The problem of heat loss from the oscillator rod affecting the reactor is believed to have been solved by the dual-flow cooling system described in Paper No. III-32. No changes in reactor temperature were observed when the Doppler sample was heated.

Calibration data constitute a potential source of error in autorod measurements, especially when the size of the measured quantity is small. The autorod was calibrated using continuous motion between the limit switches and following the reactor power history with inverse kinetics. Data were obtained over a period of 40 min at a power of 400 W and a third order drift correction was applied.

The calibration of the autorod, as well as the inverse kinetics measurements, are subject to the uncertainties in the delayed neutron parameters and the lifetime. The effects of these uncertainties are assumed to be quite small as explained in Paper No. II-39. As a result of consideration of the estimated magnitudes of these errors along with previous experience with Doppler measurements on ZPR-3 and other reactivity measurements on ZPPR, a systematic uncertainty of 0.005 Ih has been assigned to all of the measurements reported here, and added algebraically to the statistical uncertainty of each individual measurement.

Conclusions

The results of the Doppler experiments in the inner plate core of Assembly 2, the first such experiments performed in ZPPR, were quite satisfactory. The mechanical heat transfer and data acquisition systems all functioned smoothly, and the experimental techniques, in general, were quite reliable.

As expected, the ^{238}U Doppler effect was negative, and showed a significant reduction in magnitude when the sodium was voided. The measured effect of PuO_2 was also strongly negative, but changes in internal multiplication and axial expansion into a significant flux gradient present in the 36-in. high ZPPR-2 core contribute much of this effect. These effects are yet to be evaluated with confidence, but it is anticipated that the corrections might not account for the entire negative reactivity change, thus resulting in a slightly negative Doppler effect for PuO_2 at the center of the core.

References

1. R. E. Kaiser and R. J. Norris, *Critical Mass Evaluation in ZPPR Assembly 2, a Demonstration Reactor Benchmark Assembly*, Applied Physics Division Annual Report, July 1, 1969 to June 30, 1970, ANL-7710, pp. 140–146.
2. J. M. Gasidlo, *Results of Recent Doppler Experiments in ZPR-3*, Proc. International Conference on Fast Critical Experiments and Their Analysis, ANL-7320, 345 (1966).
3. C. E. Till, R. A. Lewis and R. N. Hwang, *ZPR-6 Doppler Measurements and Comparison with Theory*, Proc. International Conference on Fast Critical Experiments and Their Analysis, ANL-7320, 319 (1966).
4. E. F. Bennett and R. L. Long, *Precision Limitations in the Measurement of Small Reactivity Changes*, Nucl. Sci. Eng. **17**, 425–432 (1963).

II-45. Kinetics Parameters for ZPPR Assembly 2

A. P. Olson, R. E. Kaiser and G. L. Grasseschi

In order to establish recommended values of the kinetics parameters for use in the reduction of experimental data for ZPPR Assembly 2,[1] a series of calculations varying in sophistication has been performed ranging from 1D diffusion to 2D transport. Reflected in these calculations are the differences arising from improved calculational models and from changes in the reactor configuration. The resulting kinetics parameters are summarized in Tables II-45-I and II-45-II.

The first calculation of β, very preliminary in nature, was made using approximate reactor dimensions and compositions. At that time, better information did not exist because the assembly had not yet been loaded in ZPPR. 22-group neutron cross sections from ANL Set 224 were utilized by the MACH1 Code[2] in a 1D spherical geometry calculation for a two-zone equal-volume core of 2566 liters. Results of this calculation are given in column 2 of Table II-45-I.

Detailed descriptions of several loadings of ZPPR Assembly 2 are given in Ref. 1. The calculational model for all three loadings consisted of circularized cylinders having slightly differing compositions and dimensions.

Neutron cross sections were obtained from MC^2 [3] in 27-group form as described in Ref. 4. Uranium and plutonium isotopic cross sections were heterogeneously self-shielded, and all broad group cross sections were spatially flux-weighted to account for flux advantage/disadvantage factors in the unit cells. Diffusion theory flux calculations were made with the DARC2D[5] module of the ARC system, whereas S_4 transport theory real and adjoint scalar fluxes were derived by DOT. All 2D calculations of β used the PARC2D[6] module of the ARC system.

Finally, the best available calculation is for Loading 90 (column 8 of Table II-45-I). Improved heterogeneously self-shielded cross sections were obtained for ^{238}U, ^{239}Pu, ^{240}Pu and ^{241}Pu in the two core zones, and heterogeneously self-shielded cross sections were also obtained for ^{238}U in the radial and axial blankets. In

TABLE II-45-I. Descriptions of Calculational Models, with Calculated Kinetics Parameters for ZPPR-2

Reactor Configuration	2566 liter Core 50/50	2372 liter Core 50/50 Loading 74, ¼ in. Na in I.C.			2376 liter Core 50/50 Loading 77, ½ in. Na in I.C.		2407 liter Core 50/50 Loading 90
Flux Code	MACH 1 (1D)	DARC2D	DARC2D	DOT (2D Transport)	DARC2D	DOT (2D Transport)	DARC2D
β Code	MACH 1	PERT-V[b]	PARC2D	PARC2D	PARC2D	PARC2D	PARC2D
ℓ_p, 10^{-7} sec	4.9500	5.5561	5.4671	5.4553	5.5963	5.5780	5.5400
β	0.0031718	0.0032258	0.0032593 ± 0.0000100	0.0032487 ± 0.0000100	0.0032412 ± 0.0000100	0.0032332 ± 0.0000100	0.0032136 ± 0.0000100
Ih/%$\Delta k/k$	1026.82	997.90	994.11	997.57 998.52[a]	995.96 996.70[a]	998.26 998.96[a]	998.14 998.49[a]
$\beta \times$ Ih/%$\Delta k/k$	3.257	3.219	3.240	3.241 3.243[a]	3.228 3.230[a]	3.228 3.230[a]	3.207 3.209[a]
β Data	Keepin,[7] Fast Fission, Tables 4-7, 4-14	Keepin,[7] β_i/β Table 4-7 (Fast) n/F, Table 4-14 (Thermal)	Keepin,[7] Fast Fission, Table 4-7				
Data	Keepin,[7] Fast Fission, Table 4-7	Keepin,[7] Fast Fission, $24\lambda_i$, Table 4-7	$6\lambda_i$	$6\lambda_i$, $24\lambda_i$, Table 4-7			

[a] Uses $24\lambda_i$-values, Keepin,[7] Table 4-7 (Fast Fission).

[b] See Ref. 8.

TABLE II-45-II. CALCULATED EFFECTIVE KINETICS PARAMETERS FOR ZPPR ASSEMBLY 2

Group, i		β_i	λ_i, sec^{-1}
1	^{235}U	2.6337-6	0.0127
2		1.5407-5	0.0317
3		1.3389-5	0.115
4		2.9587-5	0.311
5		9.2901-6	1.40
6		1.8932-6	3.87
7	^{238}U	1.8544-5	0.0132
8		2.0136-4	0.0321
9		2.3501-4	0.139
10		5.7268-4	0.358
11		3.3200-4	1.41
12		1.1067-4	4.02
13	^{239}Pu	5.5837-5	0.0129
14		4.2438-4	0.0311
15		3.2393-4	0.134
16		5.0072-4	0.331
17		1.5723-4	1.26
18		5.3216-5	3.21
19	^{240}Pu	1.8780-6	0.0129
20		1.6538-5	0.0313
21		1.1121-5	0.135
22		2.1958-5	0.333
23		8.2953-6	1.36
24		1.6730-6	4.04
25	^{241}Pu	3.4770-6	0.0129
26		2.6431-5	0.0311
27		2.0174-5	0.134
28		3.1185-5	0.331
29		9.7925-6	1.26
30		3.3144-6	3.21

β_{eff} (total) = 0.0032136 ± 0.0000100; $\ell_p = 5.540 \times 10^{-7}$ sec; Ih/%$\Delta k/k$ = 998.49.

addition, the blanket cross sections were spatially self-shielded by flux-weighting across the unit cells via the CALHET-3 code.

The differences between the various sets of effective parameters are significant only between 1D and 2D calculations. The 2D calculations appear to be necessary for kinetics parameter generation for such a large, multi-zone reactor configuration.

Data were taken from Keepin[7] (Table 4-7) for ^{235}U, ^{238}U, ^{239}Pu and ^{240}Pu. For ^{241}Pu, the data of Table 4-14[7] were used to estimate the fast fission value of n/F, the absolute total delayed-neutron yield per fission, as follows:

$$(n/F)^{241}_{fast} \approx (n/F)^{241}_{thermal} \times \frac{(n/F)^{239}_{fast}}{(n/F)^{239}_{thermal}} = 0.0159 .$$

Similarly, for the average total neutron-yield per fission,

$$\bar{\nu}^{241}_{fast} \approx \bar{\nu}^{241}_{thermal} \times \frac{\bar{\nu}^{239}_{fast}}{\bar{\nu}^{239}_{thermal}} = 3.38 ;$$

hence we obtain

$$\beta^{241}_{fast} \equiv \frac{(n/F)^{241}_{fast}}{\bar{\nu}^{241}_{fast}} \approx 0.0047 \pm 0.0005 .$$

The above uncertainty in β^{241}_{fast} is the same as that quoted by Keepin[7] for $\beta^{241}_{thermal}$; it probably should be even larger. This uncertainty leads to an uncertainty in β of ±0.0000100, or about ⅓ %.

REFERENCES

1. R. E. Kaiser and R. J. Norris, *Critical Mass Evaluation in ZPPR Assembly 2, a Demonstration Reactor Benchmark Assembly*, Applied Physics Division Annual Report, July 1, 1969 to June 30, 1970, ANL-7710, pp. 140–146.
2. D. A. Meneley, L. C. Kvitek and D. M. O'Shea, *MACH1, A One-Dimensional, Diffusion Theory Package*, ANL-7223 (1966).
3. B. J. Toppel, A. L. Rago and D. M. O'Shea, *MC², A Code to Calculate Multigroup Cross Sections*, ANL-7318 (1967).
4. Arne P. Olson and Nam Chin Paik, *Heterogeneity and Criticality Studies on the Zero Power Plutonium Reactor (ZPPR) Assembly 2, a Demonstration Reactor Benchmark Critical*, Applied Physics Division Annual Report, July 1, 1969 to June 30, 1970, ANL-7710, pp. 146–155.
5. T. A. Daly, G. K. Leaf and A. S. Kennedy, *The ARC System Two-Dimensional Diffusion Theory Capability, DARC2D*, ANL-7716 (to be published).
6. T. A. Daly, D. A. Schoengold, D. E. Neal and G. K. Leaf, *The ARC System Two-Dimensional Adjunct Calculations*, ANL-7720 (to be published).
7. G. R. Keepin, *Physics of Nuclear Kinetics*, (Addison-Wesley Publishing Co., Inc., Reading, Massachusetts, 1965).
8. R. W. Hardie and W. W. Little, Jr., *PERT-V, A Two-Dimensional Perturbation Code for Fast Reactor Analysis*, BNWL-1162 (1969).

II-46. Measured Reaction Rates in ZPR-3 Assemblies 60, 61, and 62 Using Foils

D. W. Maddison

The ZPR-3 Assemblies 60, 61, and 62 were a set of critical assemblies dealing with EBR-II.[1] Reaction rate measurements were made in several cell positions at three locations in each assembly; one near the core center, one on the core side of the core-blanket interface, and the third on the blanket side of the interface. The measurements described here were done with 1.27 cm diam foils. Other measurements with large foil pieces were also made.[2]

Figure II-46-I indicates the foil placements in the three assemblies. The foil packets consisted of 1.27 cm diam foils with thicknesses varying from 0.0025 to 0.025 cm. Each packet contained the following foils: 2 each of ^{238}U and ^{235}U, and one each of aluminum, tungsten, gold, indium and nickel. The results of these measurements have been reported in recent ANL publications.[3,4] Tables II-46-I through II-46-III give the various relative reaction rates for these assemblies with arbitrary normalization to highest values. Average relative errors are as follows: Au(n,γ), 0.6 %; In(n,n),

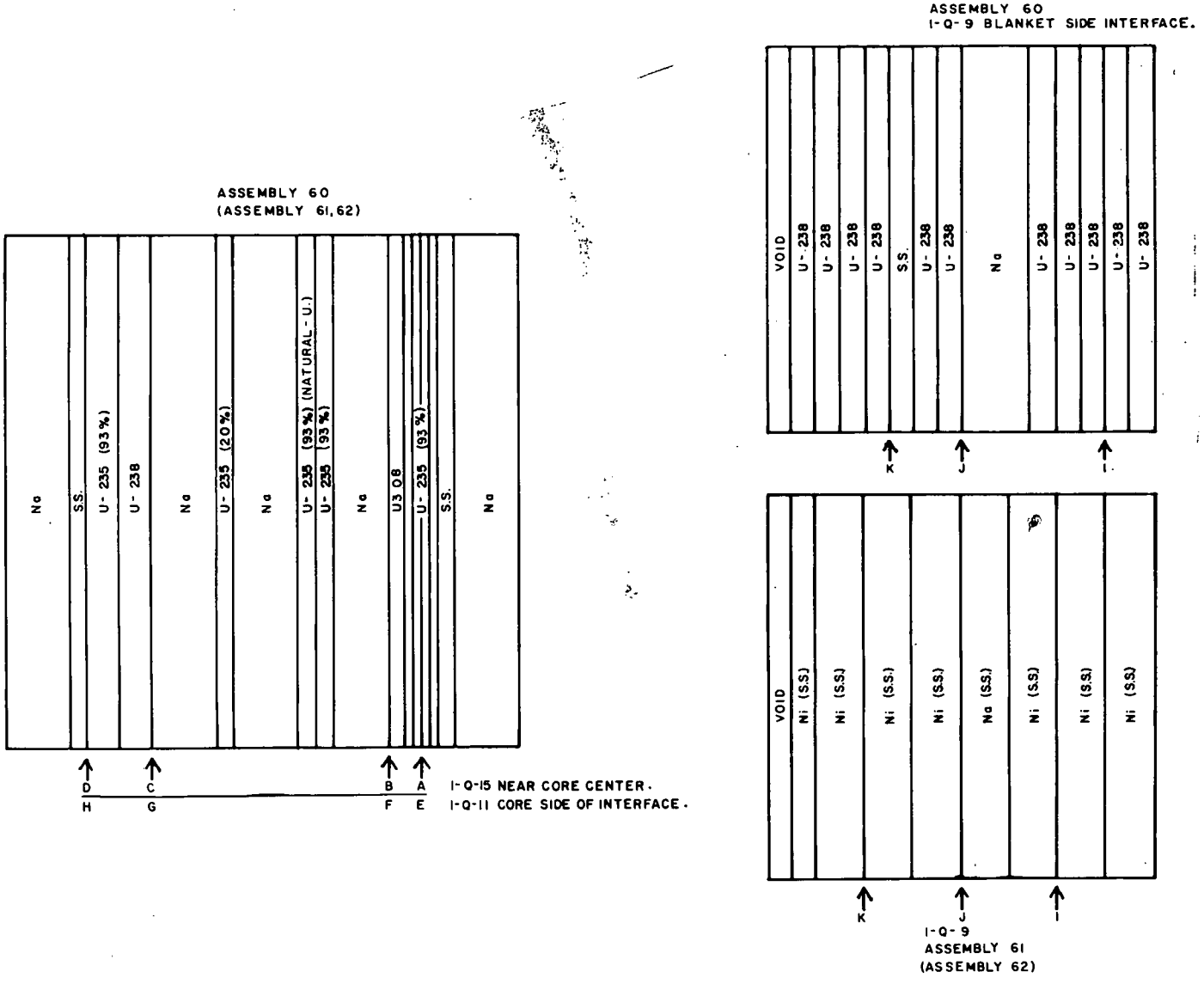

FIG. II-46-1. Foil Packet Locations in ZPR-3 Assemblies 60, 61 and 62. *ANL-ID-103-A11896.*

TABLE II-46-I. ZPR-3 Assembly 60 Reaction Rates

Position	U-235 (n,f)	U-238 (n,f)	U-238 (n,γ)	Al-27 (n,α)	Ni-58 (n,p)	Au-197 (n,γ)	W-186 (n,γ)	In-115 (n,n')	In-115 (n,γ)
A	1.000	1.000	1.000	1.000	1.000	0.972	1.000	1.000	1.000
B	0.987	0.927	0.992	0.867	0.910	1.000	0.994	0.926	0.998
C	0.967	0.870	0.970	0.897	0.877	0.980	0.971	0.903	0.993
D	0.967	0.938	0.959	0.880	0.929	0.962	0.970	0.946	0.988
E	0.660	0.600	0.665	0.600	0.608	0.690	0.711	0.571	0.691
F	0.659	0.530	0.656	0.521	0.532	0.695	0.720	0.508	0.670
G	0.589	0.438	0.609	0.399	0.437	0.668	0.690	0.419	0.652
H	0.582	0.426	0.595	0.361	0.430	0.644	0.687	0.408	0.621
I	0.358	0.088	0.427	0.106	0.085	0.518	0.499	0.098	0.445
J	0.319	0.068	0.401	0.072	0.063	0.487	0.466	0.070	0.403
K	0.295	0.055	0.375	—	0.049	0.466	0.455	0.060	0.380

TABLE II-46-II. ZPR-3 Assembly 61 Reaction Rates

Position	U-235 (n,f)	U-238 (n,f)	U-238 (n,γ)	Al-27 (n,α)	Ni-58 (n,p)	Au-197 (n,γ)	W-186 (n,γ)	In-115 (n,n')	In-115 (n,γ)
A	0.967	1.000	0.319	1.000	1.000	0.135	0.062	1.000	0.203
B	0.940	0.909	0.320	0.801	0.895	0.135	0.061	0.920	0.203
C	0.926	0.889	0.311	0.799	0.866	0.134	0.061	0.897	0.205
D	0.924	0.926	0.321	0.920	0.952	0.124	0.059	0.980	0.202
E	0.665	0.601	0.239	0.597	0.636	0.123	0.058	0.628	0.174
F	0.655	0.650	0.241	0.516	0.546	0.135	0.068	0.574	0.188
G	0.651	0.459	0.239	0.415	0.455	0.159	0.078	0.503	0.201
H	0.692	0.474	0.322	0.377	0.465	0.209	0.148	0.497	0.251
I	0.999	0.102	1.000	0.097	0.060	0.950	0.947	0.102	0.946
J	1.000	0.096	0.981	0.100	0.052	0.996	0.997	0.082	1.000
K	0.973	0.069	0.973	0.053	0.036	1.000	1.000	0.076	0.987

TABLE II-46-III. ZPR-3 Assembly 62 Reaction Rates

Position	U-235 (n,f)	U-238 (n,f)	U-238 (n,γ)	Al-27 (n,α)	Ni-58 (n,p)	Au-197 (n,γ)	W-186 (n,γ)	In-115 (n,n')	In-115 (n,γ)
A	0.978	0.972	0.572	1.000	1.000	0.276	0.134	1.000	0.504
B	0.967	0.951	0.571	0.942	0.930	0.281	0.139	0.828	0.468
C	0.991	0.815	0.550	0.889	0.897	0.282	0.135	0.869	0.472
D	1.000	1.000	0.561	0.950	0.957	0.271	0.135	0.877	0.475
E	0.730	0.635	0.386	0.656	0.619	0.238	0.118	0.571	0.346
F	0.700	0.529	0.387	0.556	0.545	0.257	0.130	0.539	0.403
G	0.662	0.450	0.383	0.438	0.459	0.279	0.144	0.440	0.407
H	0.675	0.448	0.480	0.495	0.467	0.347	0.226	0.437	0.444
I	0.765	0.092	0.980	0.100	0.070	0.944	0.921	0.115	0.953
J	0.759	0.076	1.000	0.075	0.064	0.978	0.958	0.097	0.961
K	0.728	0.067	0.983	0.057	0.049	1.000	1.000	0.073	1.000

0.6–3.5 %; In(n,γ), 1.0–2.5 %; W(n,γ), 1.0 %; Ni(n,p), 1.0–4.0 %; Al(n,α), 3–12 %; ^{238}U(n,f), 1.0–8.0 %; ^{238}U(n,γ), 0.5–1.4 %; ^{235}U(n,f), 0.6–1.5 %.

There are significant differences in each of these assemblies. For those reactions that are particularly sensitive to lower energy neutrons, ^{235}U(n,f), ^{238}U(n,γ), Au(n,γ), W(n,γ) and In(n,γ), the highest reaction rates occurred in the central core region for Assembly 60 (^{238}U blanket) and near the core-blanket interface for the nickel and steel reflected Assemblies 61 and 62. The high-energy neutron-sensitive reaction rates, however, changed very little from assembly to assembly. The ^{238}U(n,f) reaction-rate distribution was essentially the same for Assemblies 60 and 61, but showed a small shift in the steel reflected assembly.

Since all these reactions are sensitive to neutron over a wide range of energies, and usually in a non-uniform manner, caution must be exercised in forming conclusions from these reaction-rate distributions. In spite of the very large gold resonance at 5 eV, earlier

investigations indicated that in the central core region of some previous ZPR-3 assemblies, 95% of the gold captures were due to the higher energy resonances.

References

1. W. P. Keeney, R. O. Vosburgh, J. M. Gasidlo and D. Meneghetti, *The EBR-II Critical Assemblies—ZPR-3 Assemblies 60, 61, 62*, Applied Physics Division Annual Report, July 1, 1969 to June 30, 1970, ANL-7710, pp. 137–140.
2. N. D. Dudey, R. R. Heinrich, R. J. Popek, R. P. Larsen and R. D. Oldham, *Activation-rate Measurements in the ZPR-3 Mockup Critical Experiments*, ANL-7781 (1971).
3. D. W. Maddison, Argonne National Laboratory Reactor Development Progress Report, ANL-7737 (1970), p. 27.
4. D. W. Maddison, Argonne National Laboratory Reactor Development Progress Report, ANL-7765 (1970), p. 20.

II-47. Neutron Spectra in ZPR-3 Assemblies 62 and 63B

G. G. Simons and R. J. Forrester

Introduction

Fast neutron spectrum measurements, using small proton-recoil proportional counters, have been completed inside the ANL uranium- or plutonium-fueled critical assemblies. This technique, initiated at ANL by Bennett,[1] allows the measurement of a differential flux with sufficient detail to permit meaningful comparison between the experimental flux and smoothed ultrafine MC[2] fundamental-mode calculations and either spatially dependent fine or broadgroup transport or diffusion theory calculations. Systematic errors in these measured spectra can be minimized provided proper counters, associated electronics, data acquisition, gamma ray discrimination, and data reduction are used.

Recently designed high-count-rate electronics and the availability of small counters allow completion of "in-core" measurements at typically less than 2% subcritical.[2] Spectra measured at this level of subcriticality can be compared directly to calculations obtained for a critical assembly. Therefore, meaningful measurements of recoil proton spectra can be completed at all essential locations within either a uranium- or a plutonium-fueled critical assembly over a nominal energy range of 1 keV to 2 MeV.

Methods of analysis for these data have been developed for both cylindrical[3] and spherical[4] chambers using analytic expressions to describe distortions within the chambers. Experimentally determined response functions are also becoming available.[5]

Spectrometer System Operation

The spectrometer system used in this work consisted of two stainless steel cylindrical proportional counters, two Larson preamplifiers, high-count-rate electronics, and an on-line (8K, 18 bit) Data Machines 622 computer. A report is being prepared which describes the detailed design and operation of this spectrometer.[2]

Figure II-47-I shows the detector drawers containing both the hydrogen- and the methane-filled counters plus their preamplifiers. As shown, each counter was encased in a 0.04-in.-thick lead sleeve to reduce the number of low energy photons reaching the detector walls. The voids directly behind the preamplifiers contained characteristic reactor materials (see next section). By removing the drawer ends, it was possible to position the center of the active volumes 1 in. from the center line of these small cores. Thus the counter tips were extended into a 2 x 4 in. void in either matrix positions 2-P-16, 2-P-11 or 2-P-9.

A 10-atm total pressure, predominately hydrogen-filled counter 0.375 in. in diameter was used to obtain proton-recoil spectra from about 1 to 160 keV for matrix positions 1-P-11 and 1-P-9. For matrix location 1-P-16, the energy range was from about 2 to 160 keV. Data were obtained within the hydrogen counter using four or five voltage settings of either 3350, 3650, 3950, and 4250 or 3350, 3650, 3950, 4250 and 4500 V. Data acquisition times for each high-voltage setting varied from 40 to 90 min, depending upon the count rate within each neutron energy interval. The severe gamma-ray background and the low neutron flux below 2 keV resulted in omission of neutron data below 2 keV (the 4500 V data) for the central matrix position of 1-P-16.

An 8.2-atm total pressure, predominately methane-filled 0.625-in. diam counter was used from about 100 keV to above 2 MeV. High voltage settings of 3000, 3250 and 3400 V were required. Run times were from 45 to 60 min each.

The 60 keV energy overlap between data obtained with the two counters ensured that the data from both counters were properly normalized. Also, an approximately 50% overlap existed for each of the hydrogen- and methane-filled counter data sets. This overlap

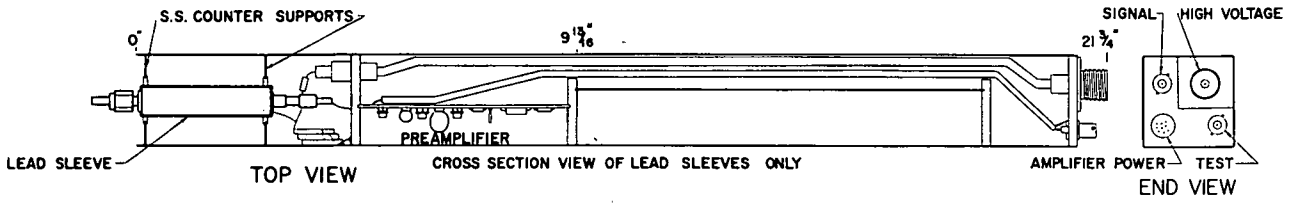

METHANE GAS FILLED PROTON RECOIL PROPORTIONAL COUNTER LOADED IN A MATRIX DRAWER

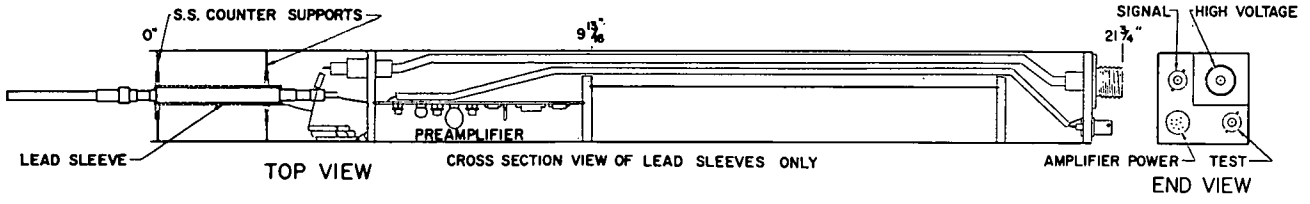

HYDROGEN GAS FILLED PROTON RECOIL PROPORTIONAL COUNTER LOADED IN A MATRIX DRAWER

FIG. II-47-1. Proton Recoil Proportional Counter Detector Assemblies. *ANL-ID-108-A11472.*

between data sets was important since it allowed assessment of operation of the system over the complete neutron energy range as well as verification that the gamma-ray induced events were properly removed.

Distortions in proton-recoil data resulting from both pulse-pile-up and preamplifier saturating overload pulses were diminished by utilizing specially designed electronics. The Larson preamplifier was designed specifically for proton-recoil proportional counter spectrometers.[8] This solid-state, charge-sensitive preamplifier has a 20 V output swing which operates under overloaded conditions without saturating.

Figure II-47-2 shows a block diagram of the high-count-rate electronics. This system was operated in a dual-parameter, gamma-ray discrimination mode with an 18 bit, 8K Data Machines 622 on-line computer. Proper operation of this spectrometer at count rates exceeding 30,000 cps for the methane-filled counter and 10,000 cps for the hydrogen-filled counter was verified in the Argonne Fast Source Reactor (AFSR). The maximum possible count-rate limit has not been determined for the system. The upper limit will be set by the saturation-inducing events in the hydrogen counter.

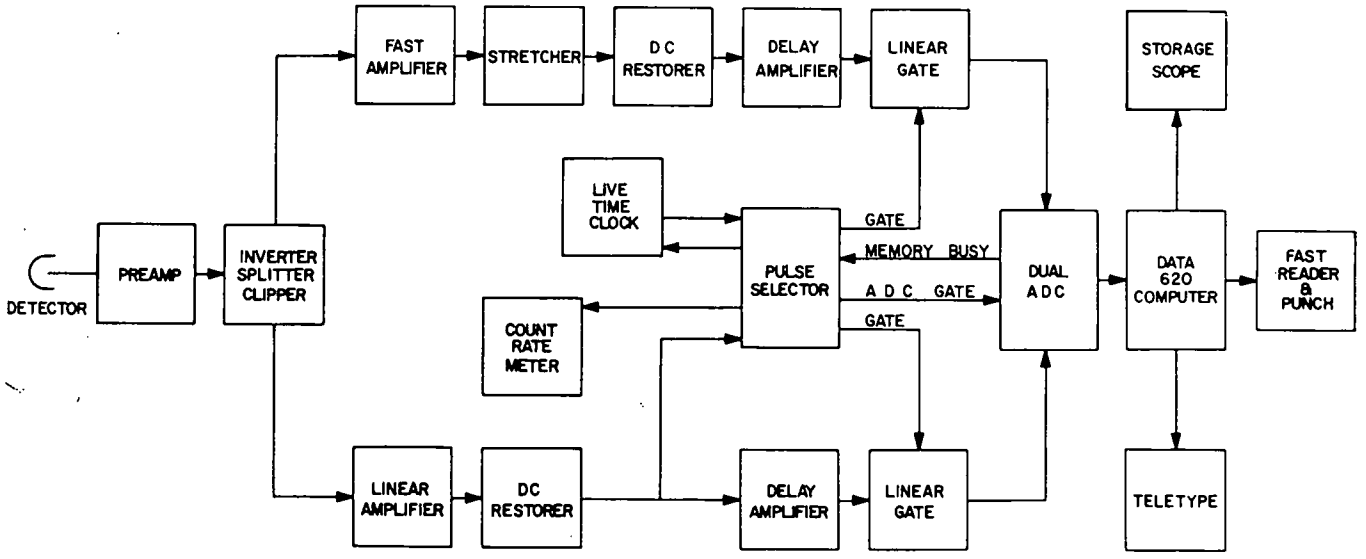

FIG. II-47-2. Proton Recoil Proportional Counter High Countrate Electronics. *ANL-ID-108-11989.*

Both the hydrogen- and the methane-filled counters were calibrated in the Argonne Fast Source Reactor thermal column just prior to each neutron spectrum measurement. This was a standard calibration procedure which used the monoenergetic protons from the $^{14}N(n,p)^{14}C$ reaction induced by thermal neutrons in the nitrogen gas within the detector chambers to determine a relationship between gas multiplication A and voltage V for each counter. The calibration data were reduced on the Data Machines 622 computer. The code performed a least-squares fit to the straight-line relation $(\ln A)/V^x$ versus V, where x is a variable parameter chosen to minimize the sum of the squared errors associated with the fit.

During data acquisition, a precision reference pulser was used to determine recoil proton keV per channel based on settings obtained during calibration.

A recurring ambiguity exists when nitrogen is used to calibrate the hydrogen detector.[6,7] Protons from the $^{14}N(n,p)^{14}C$ reaction are much more energetic (615 keV) than the protons which were measured with the hydrogen counter in a critical assembly (1 to 160 keV). The long track length pulses tend to be clipped by the pulse shaping linear amplifier. (This factor was previously determined experimentally.[7]) Thus this systematic bias must be accounted for. Analyses of these data were completed by performing a linear 5% transformation of the keV per channel values obtained during calibration of the hydrogen counter. Following nonuniform electric field and carbon recoil corrections on the proton spectra measured with the methane-filled chamber, the 3000 V data (taken with the methane-filled chamber) and the 3350 V data (taken with the hydrogen-filled chamber) exhibited good overlap. A possible solution associated with detector calibration would be to calibrate the chambers in filtered beams using materials having known resonances over the energy region of interest.

Neutron Spectra Measured

Detailed measurements (0.048 lethargy width) of the spatially dependent fast-neutron spectra were completed on the ZPR-3/EBR-II series of critical assemblies (Nos. 61, 62 and 63B). These measurements were used to determine the effect of the steel and nickel reflectors on the spatial neutron flux and to evaluate the precision associated with the calculational techniques.

The spectra measured in ZPR-3 Assembly 61—the nickel rich assembly—in matrix positions 1-P-16, 1-P-11 and 1-P-9 were reported in Ref. 9. Critical loading diagrams and reactor compositions for Assemblies 62 and 63B are given in Refs. 10 and 11, respectively.

ZPR-3 Assembly 62

Three neutron spectra were measured in ZPR-3 Assembly 62—the steel-rich assembly—in matrix positions 1-P-16, 1-P-11 and 1-P-9. Materials loaded into the counter drawers for each position are shown in Fig. II-47-3. These measurements were completed using the same detectors, high voltage settings, and instrument gain settings as those used for the previously reported Assembly 61 measurements. The detectors were recalibrated and separate gamma-ray backgrounds were measured for these data.

The central spectrum (Fig. II-47-4) is very similar to that of Assembly 61. Near the core/reflector interface (1-P-11) dips exist from the sodium, oxygen, iron and chromium scattering resonances (Fig. II-47-5). The reflector spectrum (Fig. II-47-6) shows the structure expected from the iron scattering resonances near 30 keV and between 150 and 220 keV. It is interesting that

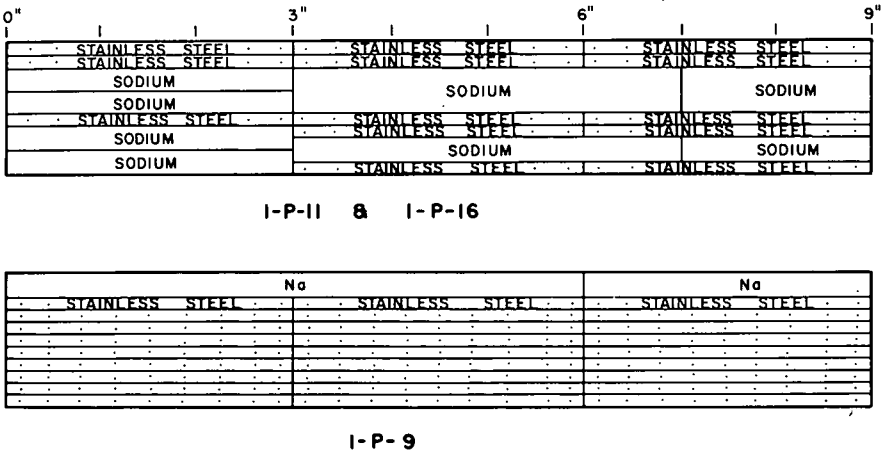

Fig. II-47-3. Characteristic Reactor Materials Loaded into the Counter Drawers during the Spectra Measurements in ZPR-3/62. *ANL-ID-103-A2120.*

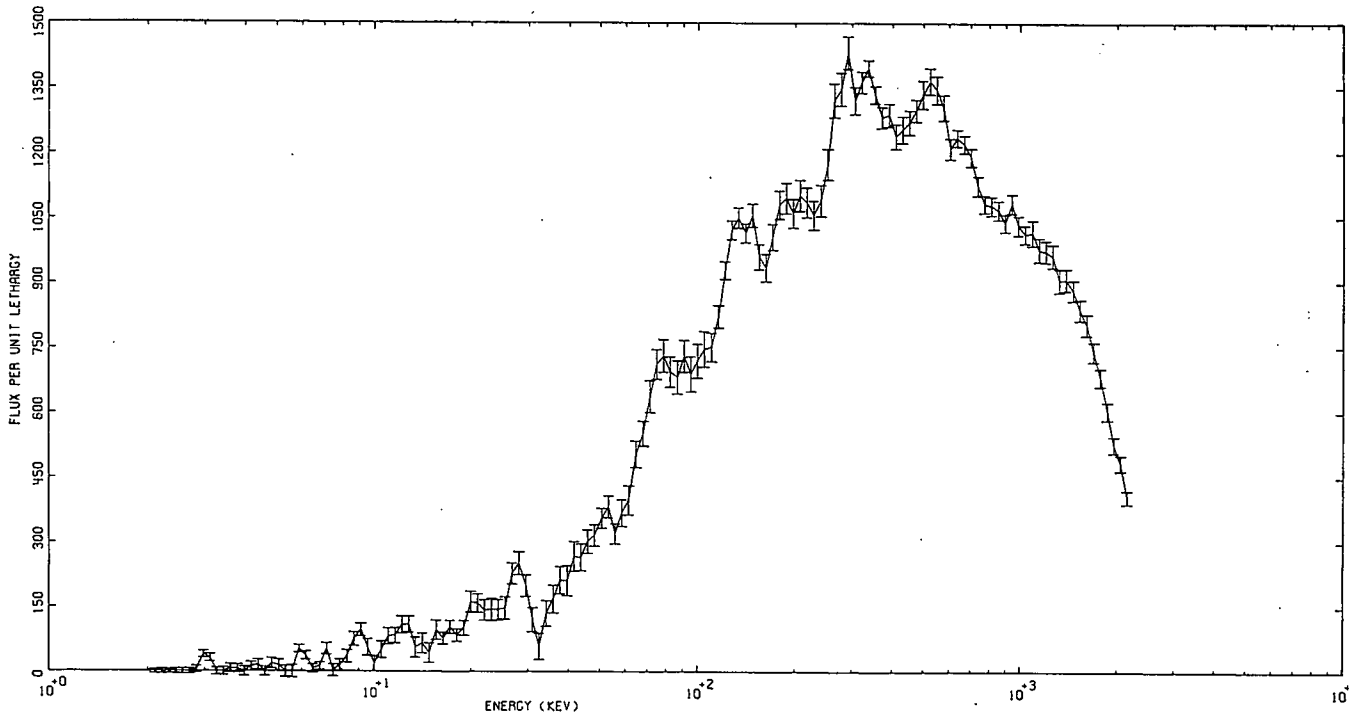

FIG. II-47-4. Central Spectrum in ZPR-3 Assembly 62. *ANL-ID-103-A2147.*

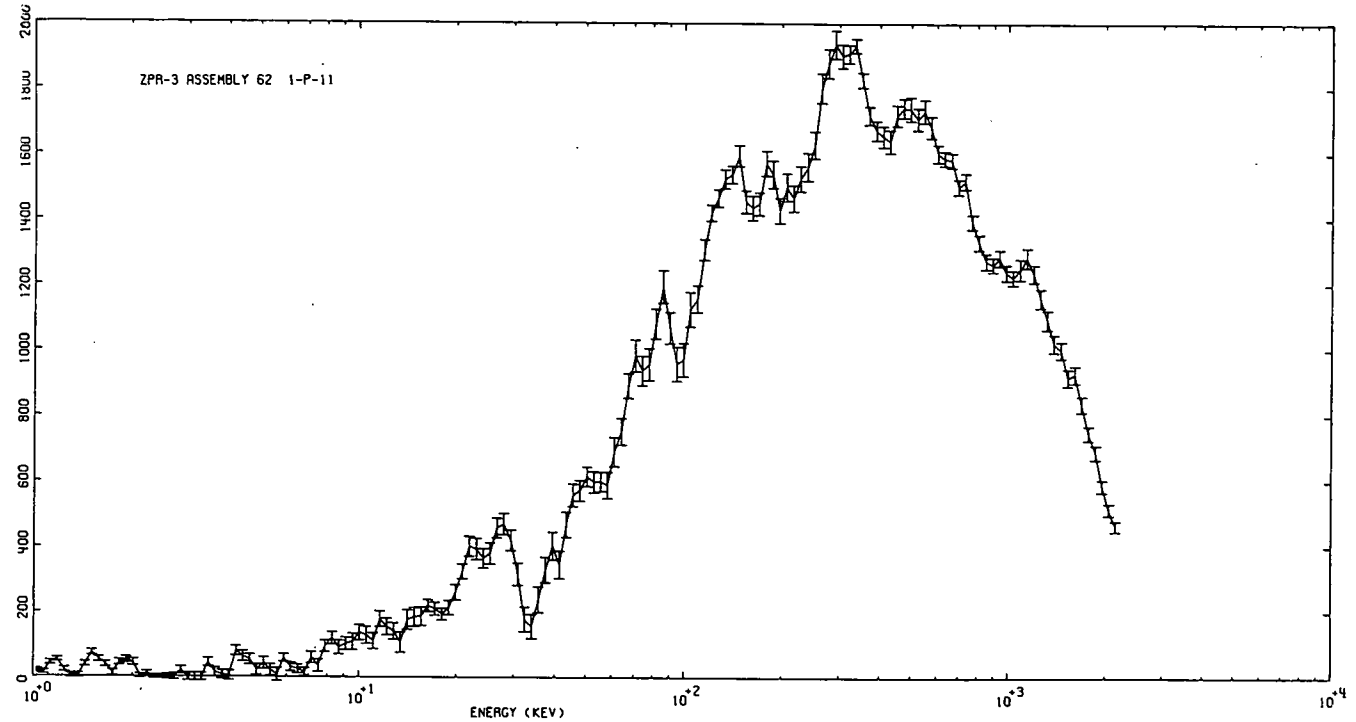

FIG. II-47-5. Spectrum in Location 1-P-11 of ZPR-3 Assembly 62. *ANL-ID-103-A2145.*

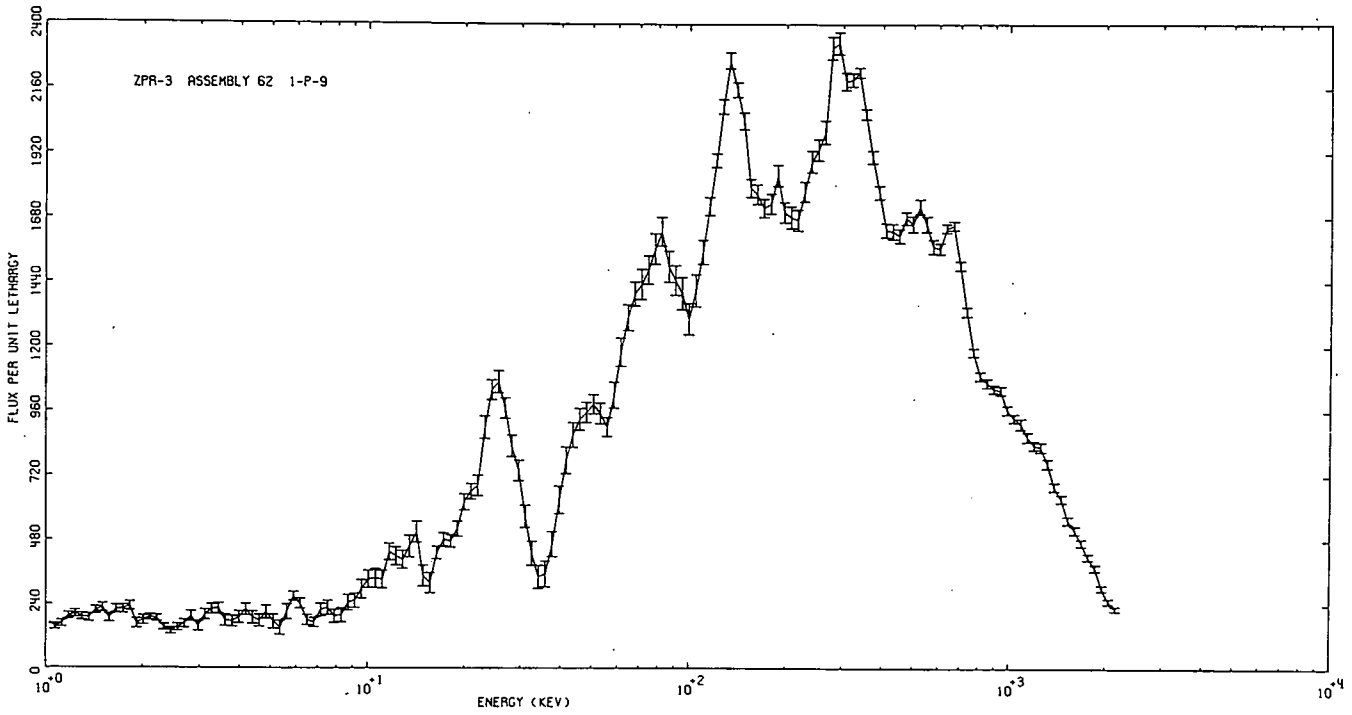

FIG. II-47-6. Spectrum in Location 1-P-9 of ZPR-3 Assembly 62. *ANL-ID-108-A2144.*

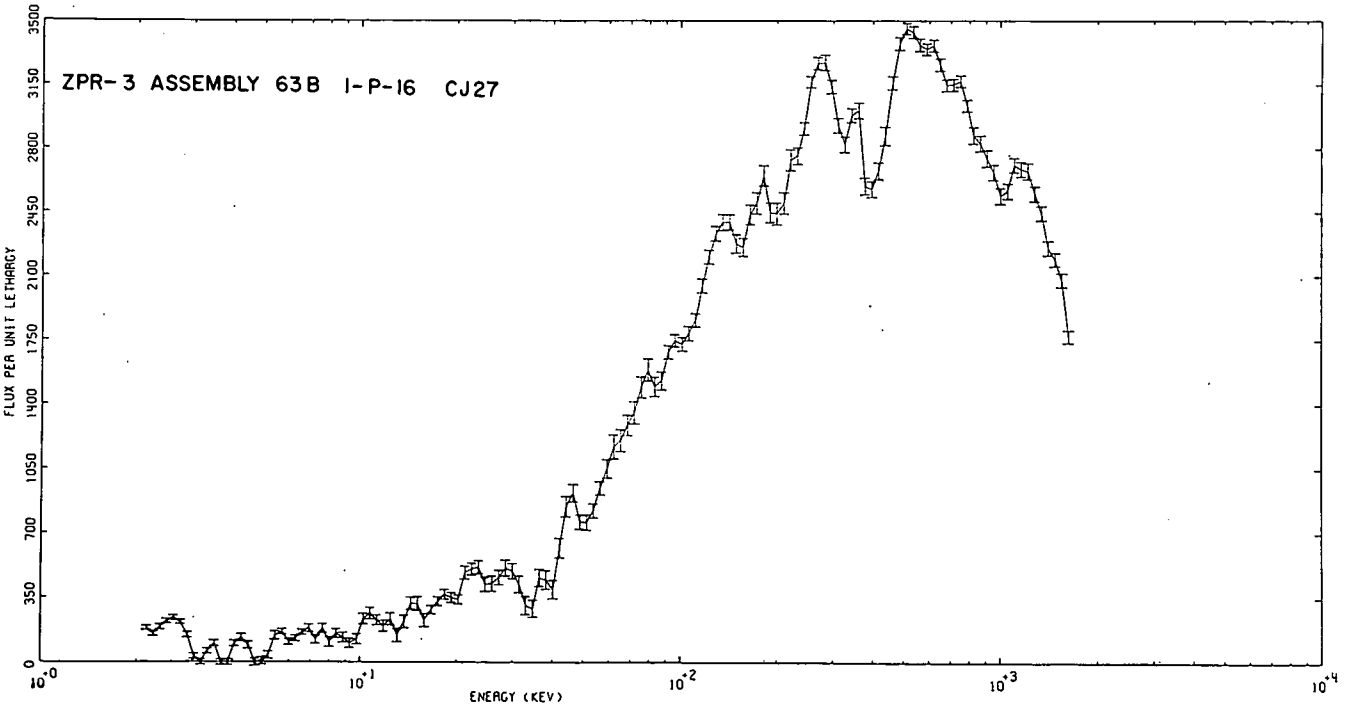

FIG. II-47-7. Central Spectrum in ZPR-3 Assembly 63B. *ANL-ID-108-A11766.*

the iron resonances between 75 and 90 keV are not visible. Chromium scattering causes flux depressions at about 50 and 100 keV.

ZPR-3 ASSEMBLY 63B

The spectrum measured at the center of Assembly 63B exhibits structure similar to that found in Assemblies 61 and 62. Near the oxygen resonance regions the flux depression is greater since this assembly contained clustered oxide-fueled subassemblies (Fig. II-47-7).

The precision of this measurement is less than that associated with the spectra of Assemblies 61 and 62. This measurement was completed without calibrating the chambers since the AFSR reactor was inoperable. Thus systematic errors due to use of an approximate calibration may exist in this spectrum.

References

1. E. F. Bennett, *Fast Neutron Spectroscopy by Proton-Recoil Proportional Counting*, Nucl. Sci. Eng. **27**, 16 (1967).
2. J. M. Larson and G. G. Simons, *Applied Fast Neutron Spectroscopy Using Proton-Recoil Proportional Counters*, ANL-7862 (to be published).
3. E. F. Bennett and T. J. Yule, *Techniques and Analyses of Fast Reactor Neutron Spectroscopy with Proton-Recoil Proportional Counters*, ANL-7763 (1971).
4. A. M. Broomfield and M. D. Carter, *Proton Recoil Counter Techniques in ZEBRA*, AEEW-M905 (1969).
5. J. C. Young, G. M. Borgonovi and K. L. Crosbie, *Fast Reactor Spectrum Measurements*, Gulf-RT-10421 (1970).
6. E. F. Bennett, Argonne National Laboratory (private communication).
7. J. M. Stevenson, J. M. Gasidlo, V. C. Rogers, G. G. Simons and R. O. Vosburgh, *Experimental Results for ZPR-3 Assemblies 58 and 59*, ANL-7695 (1970).
8. J. M. Larson, *A Wide-Band Charge-Sensitive Preamplifier for Proton-Recoil Proportional Counting*, ANL-7517 (1969).
9. G. G. Simons, *Fast Neutron Spectrum Measurements in the Zero Power Plutonium Reactor (ZPPR) and ZPR-3 Critical Assemblies*, Applied Physics Division Annual Report, July 19, 1969 to June 30, 1970, ANL-7710, pp. 157–165.
10. W. P. Keeney, R. O. Vosburgh and D. Meneghetti, *Mockup Critical Experiments*, Reactor Development Program Progress Report, ANL-7737, 27–28 (1970).
11. W. P. Keeney, R. O. Vosburgh and D. Meneghetti, *Mockup Critical Experiments*, Reactor Development Program Progress Report, ANL-7765, 14–20 (1970).

II-48. ZPR-3 Assembly 63, A Heterogeneously Loaded, Steel Reflected EBR-II Critical Assembly

W. P. Keeney, R. O. Vosburgh, J. M. Gasidlo and D. Meneghetti*

Introduction

After completing the first three cores of the current series of criticals in support of the EBR-II Program,[1] the remaining time allocated for the operation of ZPR-3 was utilized in an investigation of a heterogeneous critical with three arrangements of simulated EBR-II subassemblies.[2] These three arrangements were designed to obtain the maximum data for analytical comparison on the widest range of simulated core loadings.

The first of the three assemblies, 63A, was designed to obtain radial reaction rate distributions and gamma dose rate distributions in a heterogeneous core which contained all of the simulated EBR-II subassemblies of a postulated EBR-II loading. The spatial arrangement of these subassemblies within the core followed a pattern which was logical for EBR-II and was modified only to obtain criticality by the substitution of full for partial simulated ^{235}U driver subassemblies. The constraint was a critical system with a fixed core outline.

Assembly 63B, with a central zone of simulated 37-pin uranium-plutonium oxide subassemblies, was designed to obtain the central neutron spectrum in addition to the radial reaction rate traverses for analytical comparisons.

The final core modification, Assembly 63C, was a compromise because of the limited available time for use of the ZPR-3 facility. By grouping the two types of simulated uranium-plutonium oxide subassemblies on opposite flats of the quasi-hexagonal core, it was possible simultaneously to obtain traverse data for the two oxide composition loadings when abutted against the radial steel-reflector.

Design of Assembly 63

CORE REGION

The cross-sectional area of the ZPR-3 matrix tubes, 4.75 in.,[2] was ideally suited to simulate EBR-II subas-

* EBR-II Project, Argonne National Laboratory.

TABLE II-48-I. ASSEMBLY 63: AVERAGE COMPOSITIONS OF SIMULATED EBR-II SUBASSEMBLIES IN THE CORE REGION, 10^{24} atoms/cm^3

Material	Simulated Subassembly[a]						
	Partial Driver	Full Driver	37 Pin Oxide	19 Pin Oxide	Control and Safety—EBR-II	Control and Safety—ZPR-3	Structural
^{235}U	0.003404	0.006912	0.004472	0.002236	0.004722	0.004717	—
^{238}U	0.003858	0.006248	0.0003189	0.0001594	0.004898	0.002495	—
$^{239+241}Pu$	—	—	0.001067	0.001067	—	—	—
$^{240+242}Pu$	—	—	0.0000508	0.0000508	—	—	—
Na	0.01043	0.01043	0.008343	0.006602	0.01251	0.01251	0.004176
O	—	—	0.01334	0.008003	—	—	—
Fe	0.01988	0.01218	0.01968	0.02973	0.01152	0.01573	0.04579
Cr	0.004946	0.003029	0.002599	0.006018	0.002867	0.003912	0.01139
Ni	0.002164	0.001326	0.001137	0.002633	0.001255	0.001712	0.004984
Mn	0.0002064	0.0001265	0.0001085	0.0002513	0.0001197	0.0001633	0.0004756
Si	0.0002397	0.0001485	0.0001273	0.0002950	0.0001403	0.0001916	0.0005582

[a] The core region is 13.06 in. in length, with 6.03 in. in Half 2, and 7.03 in. in Half 1.

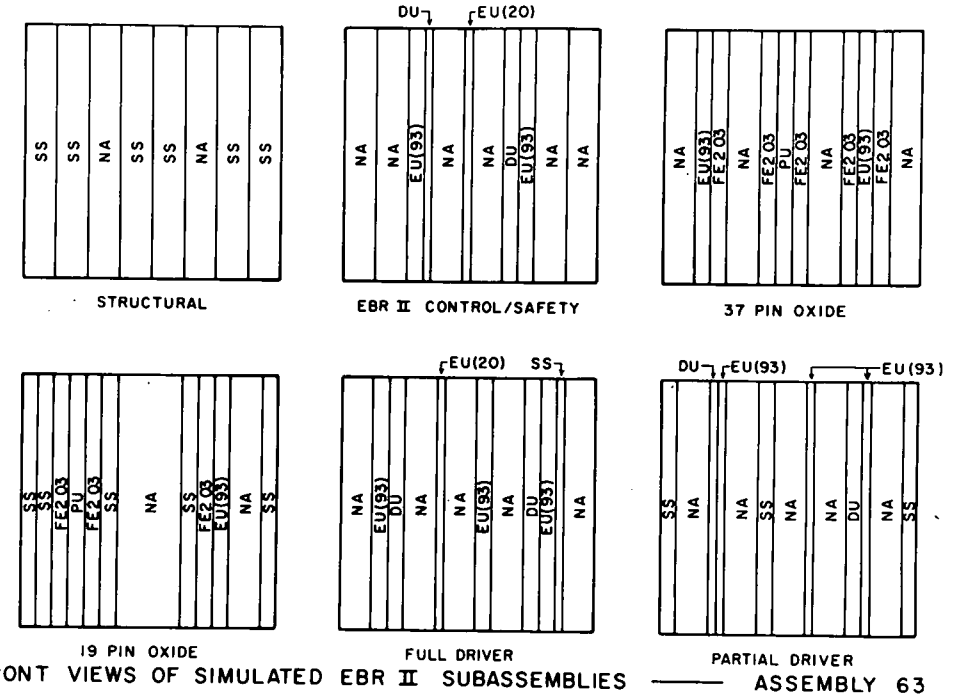

FIG. II-48-1. Front Views of Simulated EBR-II Subassemblies, Assembly 63. *ANL-ID-103-B11002.*

semblies on a one-to-one basis. The compositions listed in Table II-48-I are those chosen by the EBR-II Project from the various loadings possible on ZPR-3. It should be noted that the ZPR-3 control/safety drawers are loaded as a modification of the EBR-II control/safety simulated drawers. The effective core length, including the interface of the opposing drawer, is 13.06 in. As in the previous assemblies in this EBR-II series,[1] the core was divided with 6.03 in. in the movable half and 7.03 in. in the fixed half of ZPR-3. The quasi-hexagonal assembly geometry was retained. The axial center of the critical was then 0.53 in. back from the interface in the fixed half of ZPR-3. Front views of each type of simulated EBR-II subassembly are shown in Fig. II-48-1. In all of the drawer loading figures, "DU" signifies depleted uranium and "EU", enriched uranium, the enrichment being indicated in parentheses.

AXIAL REFLECTORS, GAPS, RADIAL REFLECTOR AND RADIAL BLANKET

External to the core region all of the zone heights and compositions of the previous EBR-II critical (As-

TABLE II-48-II. ASSEMBLY 63: AVERAGE COMPOSITIONS OF ZONES EXTERNAL TO CORE REGION, 10^{24} atoms/cm^3

Element	R1	R2	R3	R4	R5	R6	R7	
	Upper Gap	Upper Reflector	Lower Gap	Lower Reflector	SS Radial Reflector	Axial End of SS Radial Reflector	Radial Blanket	
							Half 1	Half 2
^{235}U							0.000055	0.000054
^{238}U							0.026505	0.026548
Na	0.01480	0.01029	0.01199	0.00898	0.00205	0.00203	0.00457	0.00455
Fe	0.01844	0.02802	0.02332	0.03175	0.04900	0.04982	0.00964	0.00963
Cr	0.00480	0.00762	0.00622	0.00881	0.01348	0.01337	0.00254	0.00253
Ni	0.00209	0.00331	0.00271	0.00382	0.00578	0.00581	0.00111	0.00110
Mn	0.000260	0.000501	0.000379	0.000626	0.000977	0.000835	0.000146	0.000145
Si	0.00015	0.00012	0.00014	0.00007	0.000388	0.000265	0.00007	0.00007
Mo	0.00001	0.00003	0.00002	0.00004	0.00007	0.00004	—	—

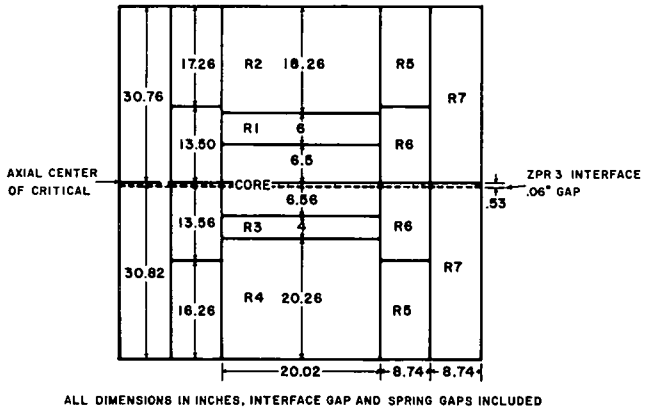

FIG. II-48-2. Assembly 63, Horizontal Section. *ANL-ID-103-A11853.*

sembly 62) were retained.[1] The compositions of each zone are listed in Table II-48-II. A horizontal section of the assembly is shown in Fig. II-48-2.

ASSEMBLY 63A

Each half of Assembly 63A was loaded with nine 19-pin simulated oxide, nine 37-pin simulated oxide, six simulated structural and fourteen simulated EBR-II control/safety subassemblies. The ZPR-3 control and safety drawers are included in the EBR-II control/safety count. These were loaded in the locations shown in Fig. II-48-3. The remaining core locations were loaded with partial drivers. These partial drivers were then replaced, in a preferred order, with full drivers until criticality was reached. A tabulation of the loading is obtained in Table II-48-III corresponding to Fig. II-48-3, the reference configuration.

The loading convention for the partial drivers, which were loaded as "half drawers" in column 16, was that matrix position J-16 contained 0.4492 kg ^{235}U and position V-16 contained 0.8984 kg ^{235}U. The "half drawers" representing full drivers that were loaded in matrix positions in columns numbered less than 16 contained 0.9788 kg ^{235}U and columns numbered greater than 16 contained 1.7631 kg ^{235}U. Pairs of half drawers in the same row then represented a full reflector and a full core drawer.

The β values in Table II-48-IV, supplied by the EBR-II Project from a 29 group, homogenized, cylindrical diffusion calculation, were utilized to obtain the control rod calibration from which the k of the reference core was determined to be 1.00068 $\pm$ 0.00003.

ASSEMBLY 63B

Assembly 63B was loaded with the twenty-one central simulated 37 pin oxide, six simulated structural, and the equivalent of twelve simulated EBR-II control and safety subassemblies as shown in Fig. II-48-4. The remaining core positions were loaded with partial drivers which were changed to full drivers to approach critical. The loading convention for the "half drawers" was identical to that of Assembly 63A. The tabulated loading of the reference core, corresponding to Fig. II-48-4, is given in Table II-48-III. The reference configuration, Fig. II-48-4, was determined to have a k of 1.00082 $\pm$ 0.00003.

The β values of Table II-48-V for this core were taken from an EBR-II Project calculation utilizing the 29-group cross section set in a cylindrical diffusion calculation in which the central oxide cluster was taken as one zone and the surrounding core drawers were homogenized into an annulus.

ASSEMBLY 63C

Assembly 63C was loaded with eight of each type c simulated oxide drawers on opposite flats of the quas hexagon, as shown in Fig. II-48-5. The approach to critical was again made by exchanging full drivers for

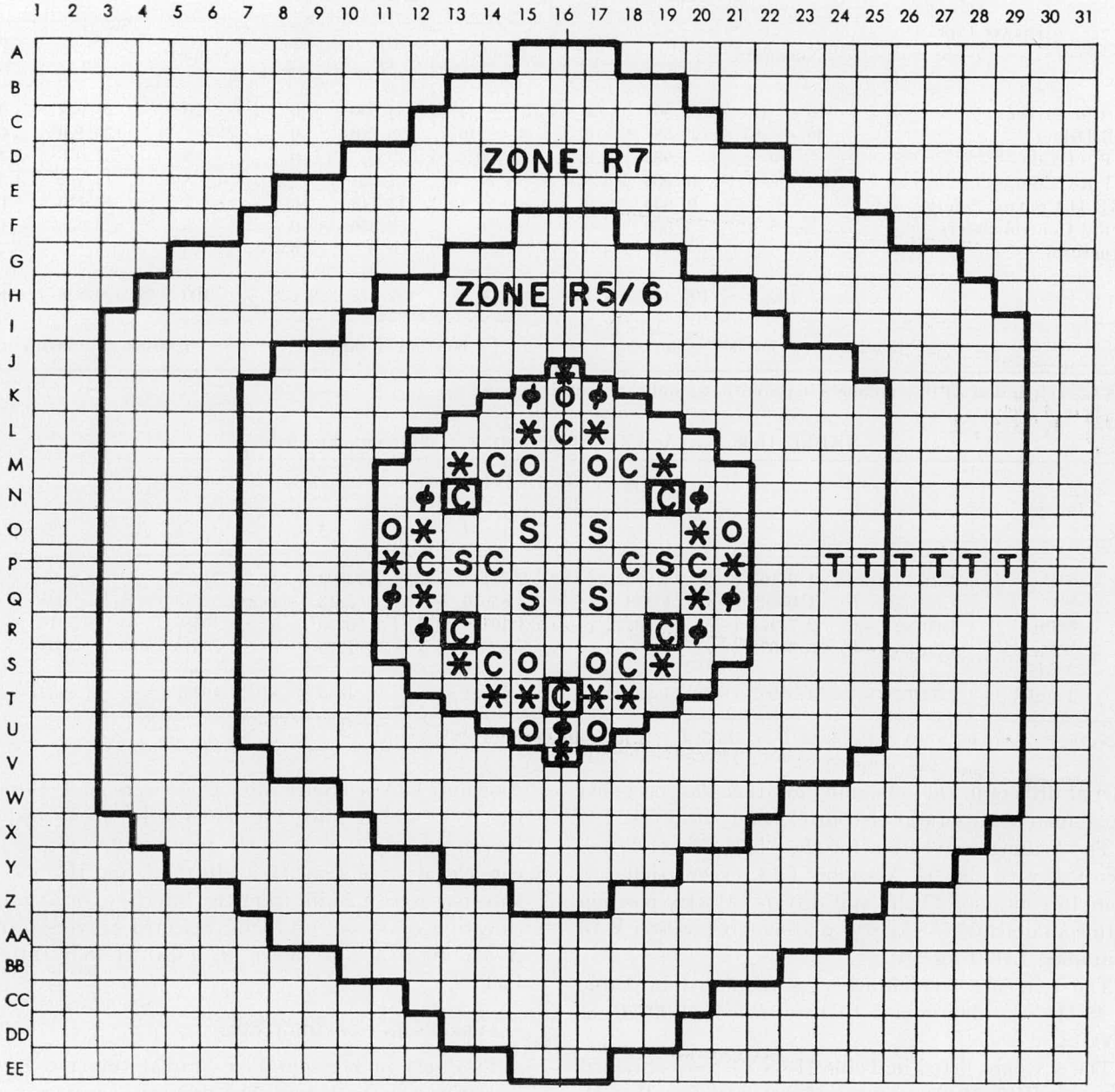

FIG. II-48-3. Assembly 63A, Reference Core. *ANL-ID-103-A2158.*

TABLE II-48-III. Fissile Loadings and Reactivity of Reference Loadings in Assembly 63

Drawer Type	63A			63B			63C		
	Number[a]	^{235}U, kg	^{239}Pu, kg	Number[a]	^{235}U, kg	^{239}Pu, kg	Number[a]	^{235}U, kg	^{239}Pu, kg
Partial Driver	16 + (1)	22.909	0	24 + (1)	33.690	0	20	26.952	0
Full Driver	39 + (6)	123.387	0	30 + (6)	98.710	0	39 + (7)	126.129	0
19 Pin Oxide	9	7.983	3.874	0	0	0	8	7.096	3.443
37 Pin Oxide	9	15.966	3.874	21	37.254	9.038	8	14.192	3.443
EBR-II Control/Safety	9	16.859	0	7	13.113	0	7	13.113	0
ZPR-3 Control/Safety	5	9.356	0	5	9.356	0	5	9.356	0
Structural	6	0	0	6	0	0	6	0	0
Total	100	196.460	7.748	100	192.123	9.038	100	196.838	6.886
k_{eff}	1.00068 ± 0.00003			1.00082 ± 0.00003			1.00350 ± 0.00015		

[a] In each half of ZPR-3, numbers in parentheses indicate half drawer pairs.

TABLE II-48-IV. Assembly 63A: Delayed Neutron Fractions

Isotope	Group Effective Delayed Neutron Fractions						
	1	2	3	4	5	6	Total
^{235}U	2.21412 (−4)	1.24107 (−3)	1.09541 (−3)	2.37144 (−3)	7.45809 (−4)	1.51493 (−4)	5.82664 (−3)
^{238}U	9.58035 (−6)	1.00962 (−4)	1.19386 (−4)	2.85936 (−4)	1.65813 (−4)	5.52713 (−5)	7.36950 (−4)
^{239}Pu	3.69782 (−6)	2.72471 (−5)	2.10192 (−5)	3.19180 (−5)	1.00230 (−5)	3.40589 (−6)	9.73110 (−5)
^{240}Pu	6.50288 (−8)	6.34031 (−7)	4.45912 (−7)	8.12860 (−7)	2.97275 (−7)	6.73513 (−8)	2.32246 (−6)
Total	2.34755 (−4)	1.36992 (−3)	1.23626 (−3)	2.69011 (−3)	9.21943 (−4)	2.10237 (−4)	6.66322 (−3)

Note: $\beta_{eff} = 6.66 \times 10^{-3}$; Ih/% $\Delta k/k = 446.5$; $\ell = 3.16 \times 10^{-7}$ sec.

partial drivers in the remaining locations not occupied by simulated structural or control/safety drawers.

The loading convention for the "half drawers" was identical with that of Assembly 63A, except that column 16 contained "half" full drivers. Matrix position J-16 contained 0.9788 kg ^{235}U and matrix position V-16 contained 1.7631 kg ^{235}U.

The reference configuration as tabulated in Table II-48-III was determined to have a k of 1.00350 ± 0.00015.

The β values listed in Table II-48-VI were obtained from an EBR-II Project calculation utilizing the 29-group cross section set in a homogeneous, two-zone, cylindrical, diffusion calculation in which the interior drawers were homogenized to form a central region and the two peripheral oxide regions were homogenized into an outer annulus together with the other simulated elements in corresponding peripheral locations.

Experimental Program

traverses in assembly 63a

Three sets of horizontal or "radial traverses" were done with ^{235}U, ^{238}U, and ^{10}B traverse counters in the Assembly 63A reference core. These were made through the P, L, and H rows, Fig. II-48-4. In the P row, the traverse was 0.50 in. from the reactor interface, or at a core elevation of $Z = 0.0$ in. In the L and H rows, the traverses were 1.25 in. from the interface, or at a core elevation of $Z = +0.75$ in. Selected traverses from Assembly 63A are shown in Figs. II-48-6 through II-48-8.

traverses in assembly 63b

Two sets of horizontal or "radial traverses" were done through the P row. The first set of traverses was done through the P row of the reference core, Fig. II-48-4, with a full driver replacing the partial driver in matrix position T-18. The ^{235}U and ^{238}U traverses are graphed in Figs. II-48-9 and II-48-10. The second set of traverses was done in a modified reference core in which a simulated structural subassembly was inserted in the P-16 matrix position (the core center) and simulated full drivers were inserted in the P-13 and 19 matrix positions. The L-14 position contained a partial driver. For comparison with the unmodified core the same reaction rate traverses are graphed in Figs. II-48-11 and II-48-12.

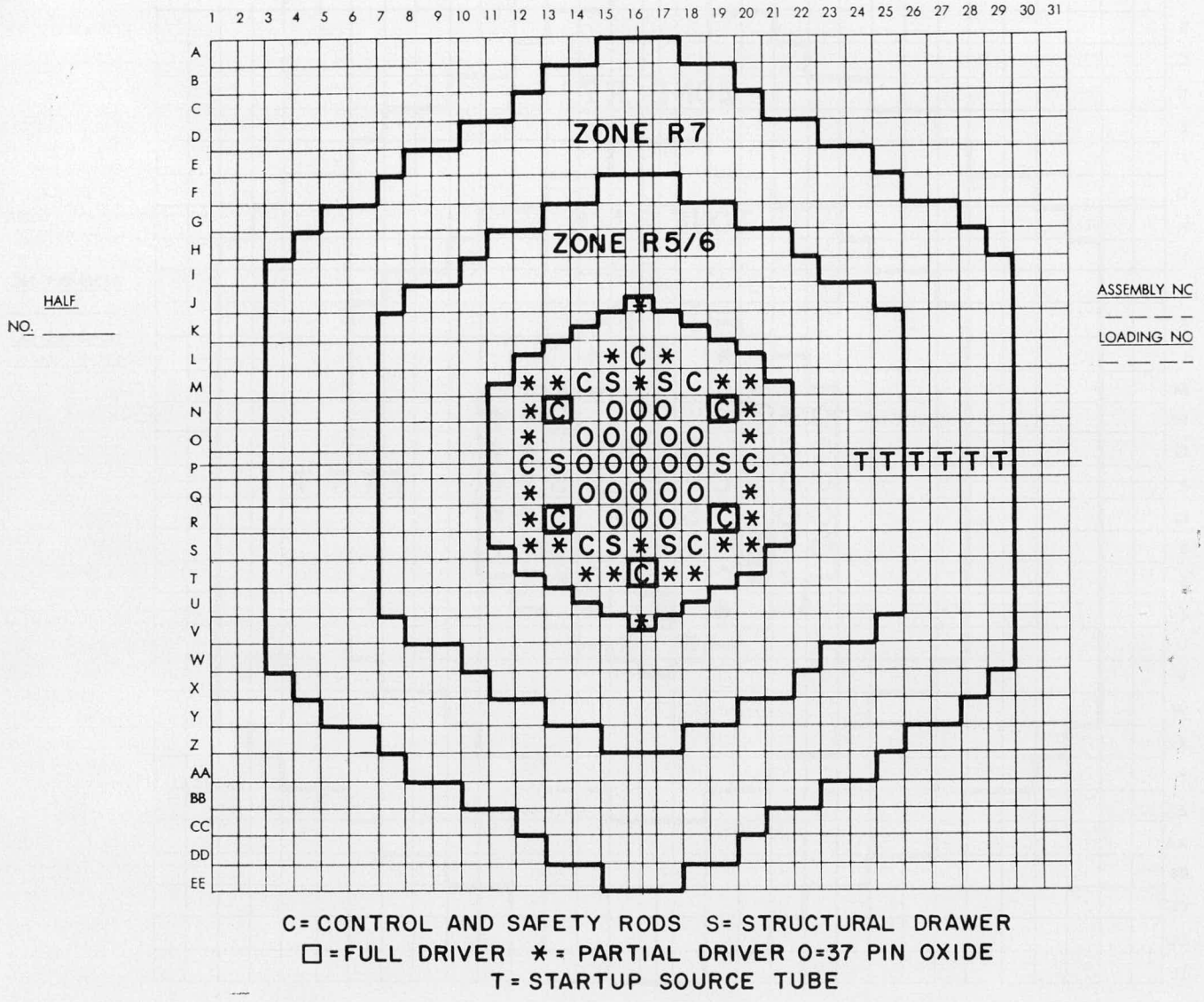

FIG. II-48-4. Assembly 63B, Reference Core. *ANL-ID-103-A2207*.

TABLE II-48-V. ASSEMBLY 63B: DELAYED NEUTRON FRACTIONS

Isotope	Group Effective Delayed Neutron Fractions						
	1	2	3	4	5	6	Total
^{235}U	2.14960 (−4)	1.20491 (−3)	1.06349 (−3)	2.30233 (−3)	7.24075 (−4)	1.47078 (−4)	5.65684 (−3)
^{238}U	7.21218 (−6)	7.60053 (−5)	8.98748 (−5)	2.13862 (−4)	1.24826 (−4)	4.16087 (−5)	5.54783 (−4)
^{239}Pu	7.44895 (−6)	5.48870 (−5)	4.23414 (−5)	6.42962 (−5)	2.01906 (−5)	6.86087 (−6)	1.96025 (−4)
^{240}Pu	1.43834 (−7)	1.40239 (−6)	9.86293 (−7)	1.79793 (−6)	6.57529 (−7)	1.48971 (−7)	5.13694 (−6)
Total	2.29765 (−4)	1.33720 (−3)	1.19669 (−3)	2.58368 (−3)	8.69749 (−4)	1.95696 (−4)	6.41278 (−3)

Note: $\beta_{eff} = 6.41 \times 10^{-3}$; Ih/% $\Delta k/k = 458.2$; $\ell = 3.16 \times 10^{-7}$ sec.

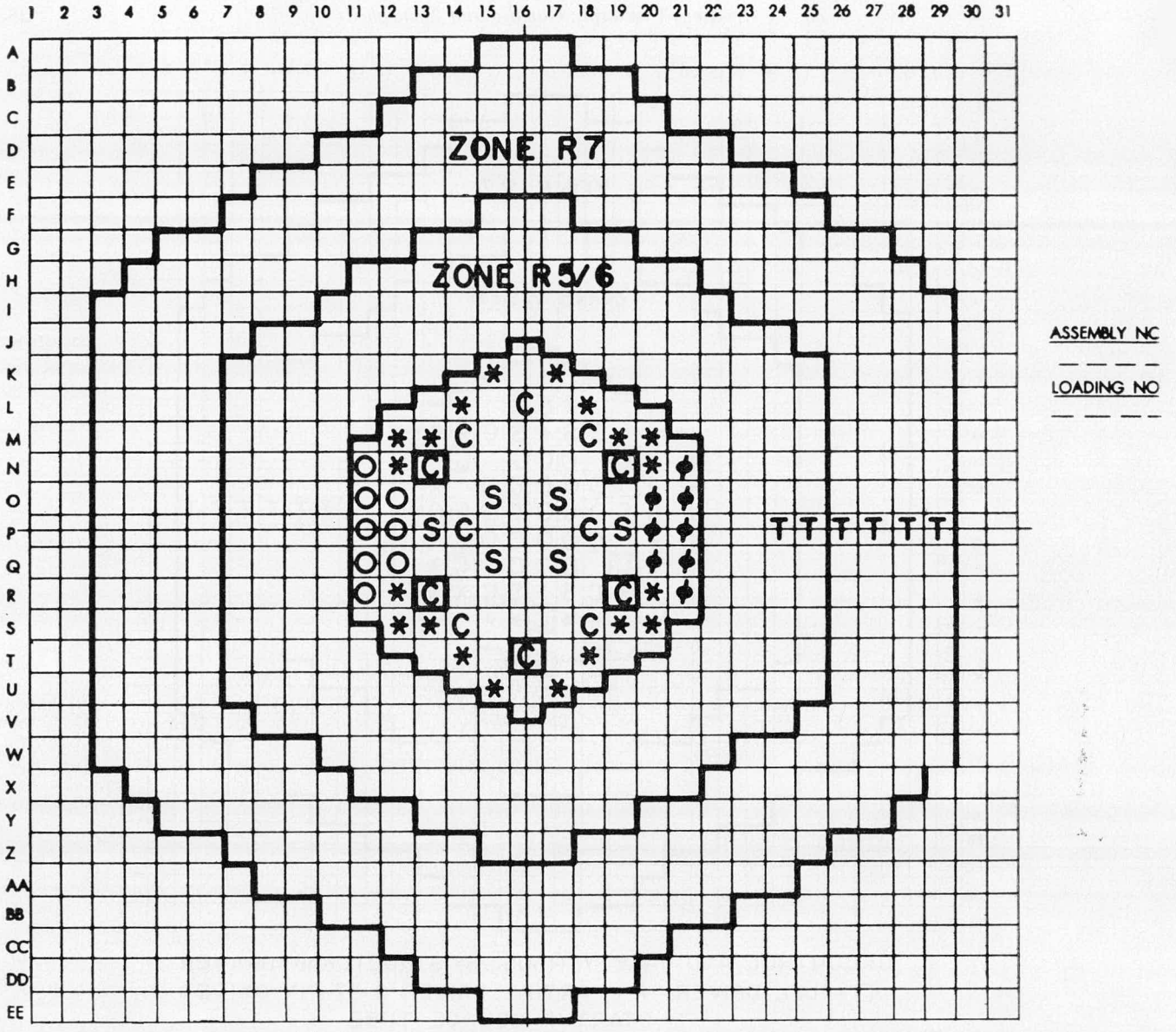

FIG. II-48-5. Assembly 63C, Reference Core. *ANL-ID-103-A2208.*

TABLE II-48-VI. ASSEMBLY 63C: DELAYED NEUTRON FRACTIONS

Isotope	Group Effective Delayed Neutron Fractions						
	1	2	3	4	5	6	Total
^{235}U	2.24540 (−4)	1.25861 (−3)	1.11088 (−3)	2.40494 (−3)	7.56346 (−4)	1.53633 (−4)	5.90895 (−3)
^{238}U	1.01729 (−5)	1.07208 (−4)	1.26770 (−4)	3.03624 (−4)	1.76070 (−4)	5.86902 (−5)	7.82536 (−4)
^{239}Pu	2.35409 (−6)	1.73459 (−5)	1.33812 (−5)	2.03195 (−5)	6.38083 (−6)	2.16824 (−6)	6.19498 (−5)
^{240}Pu	4.01919 (−8)	3.91871 (−7)	2.75602 (−7)	5.02399 (−7)	1.83735 (−7)	4.16274 (−8)	1.43543 (−6)
Total	2.37108 (−4)	1.38355 (−3)	1.25131 (−3)	2.72939 (−3)	9.38981 (−4)	2.14533 (−4)	6.75488 (−3)

Note: $\beta_{eff} = 6.75 \times 10^{-3}$; Ih/% $\Delta k/k = 441.8$; $\ell = 3.16 \times 10^{-7}$ sec.

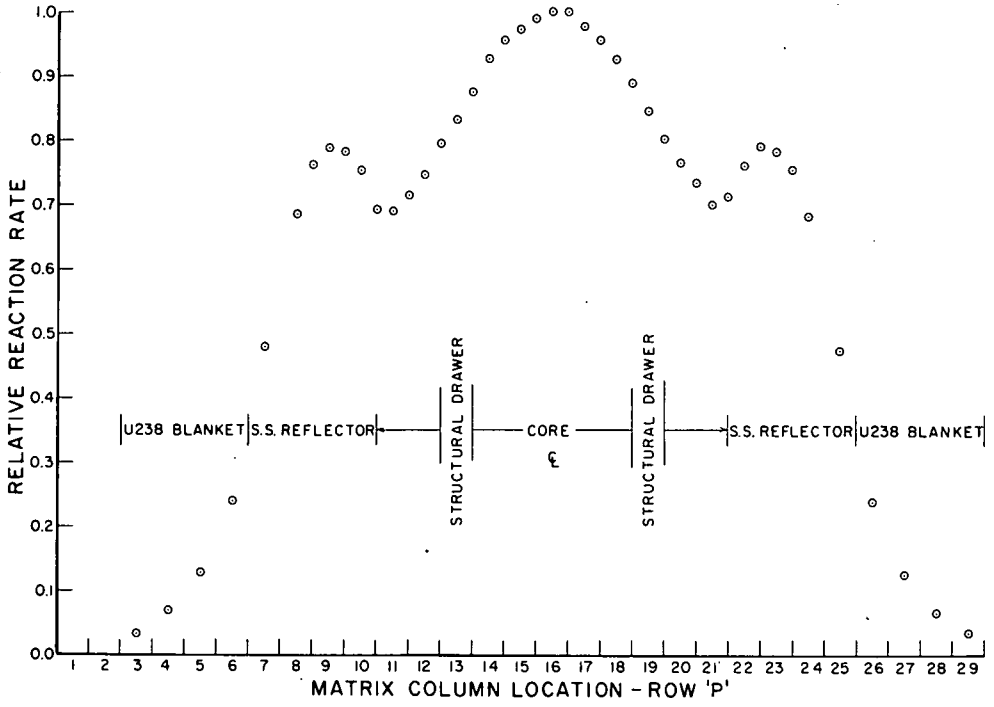

FIG. II-48-6. Assembly 63A, ^{235}U Radial Reaction Rate Traverse in P Row. *ANL-ID-103-A2165*.

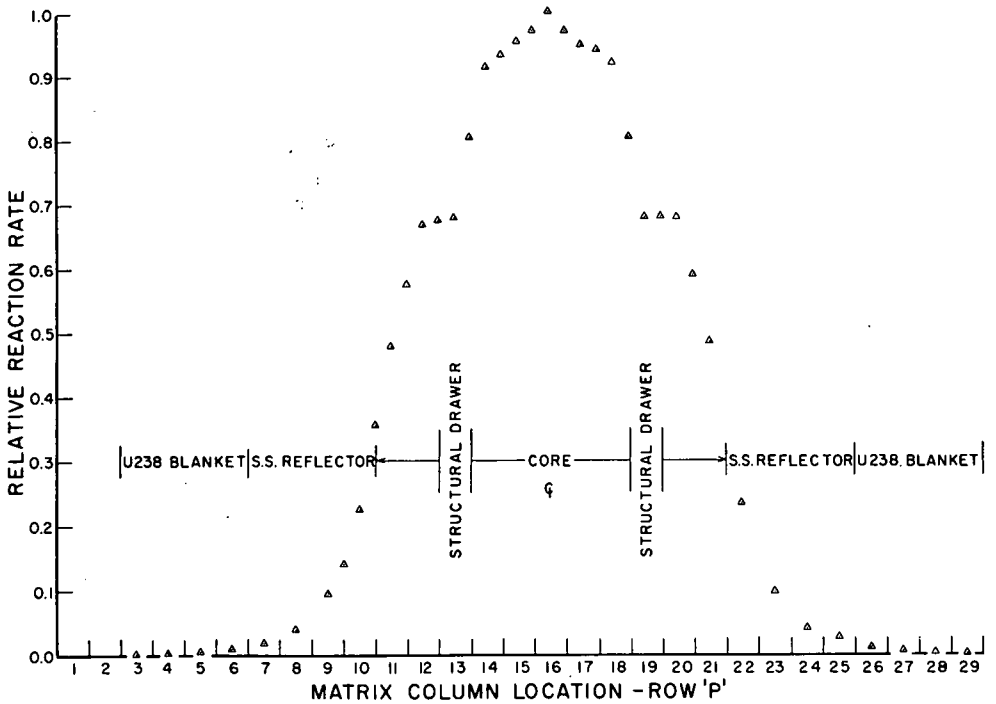

FIG. II-48-7. Assembly 63A, ^{238}U Radial Reaction Rate Traverse in P Row. *ANL-ID-103-A2166*.

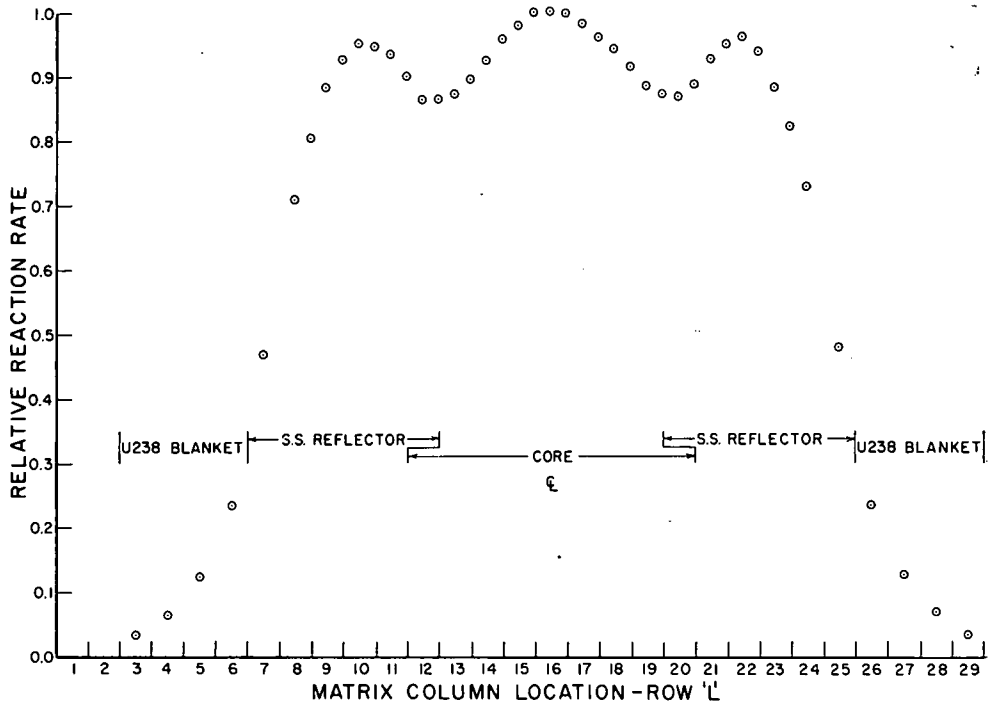

FIG. II-48-8. Assembly 63A, ^{235}U Radial Reaction Rate Traverse in L Row. *ANL-ID-103-A2167*.

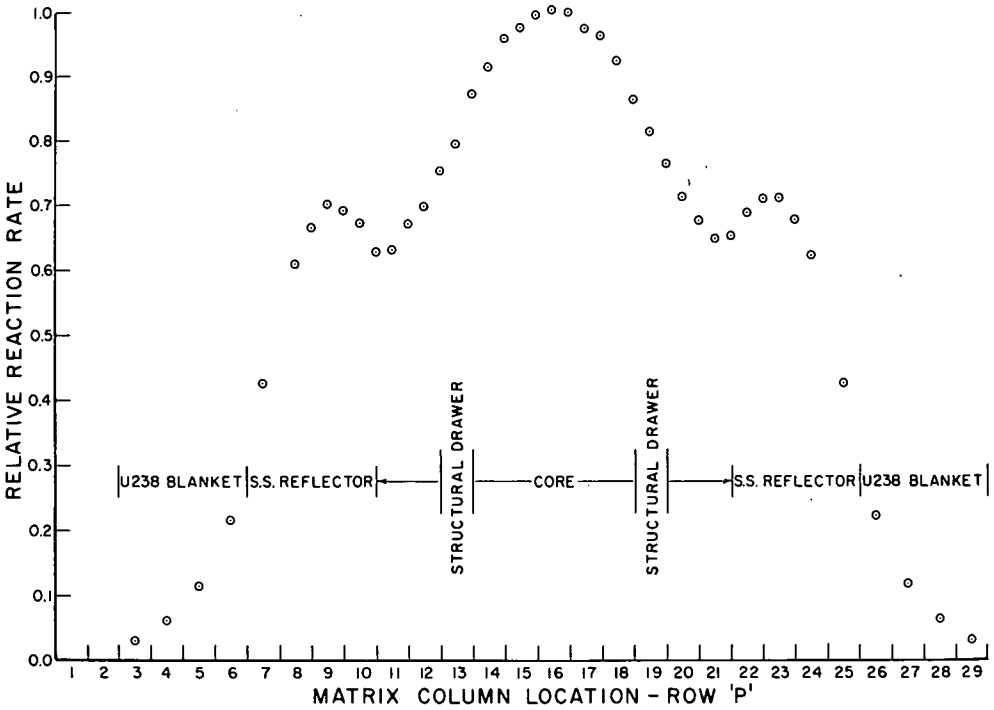

FIG. II-48-9. Assembly 63B, ^{235}U Radial Reaction Rate Traverse in P Row. *ANL-ID-103-A2214*.

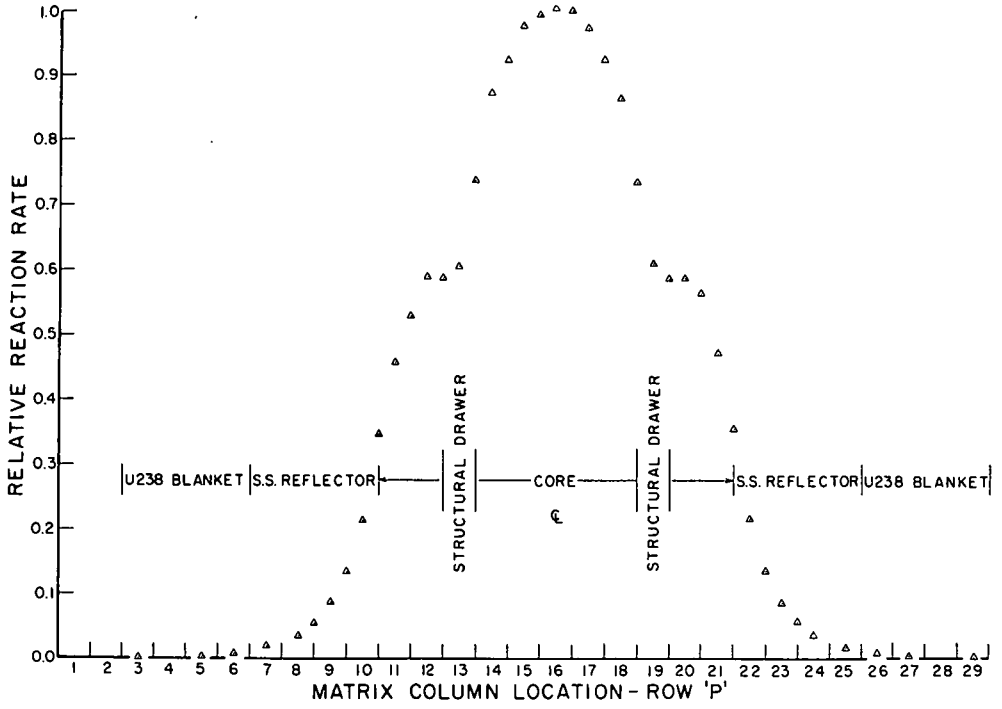

FIG. II-48-10. Assembly 63B, ^{238}U Radial Reaction Rate Traverse in P Row. *ANL-ID-103-A2210.*

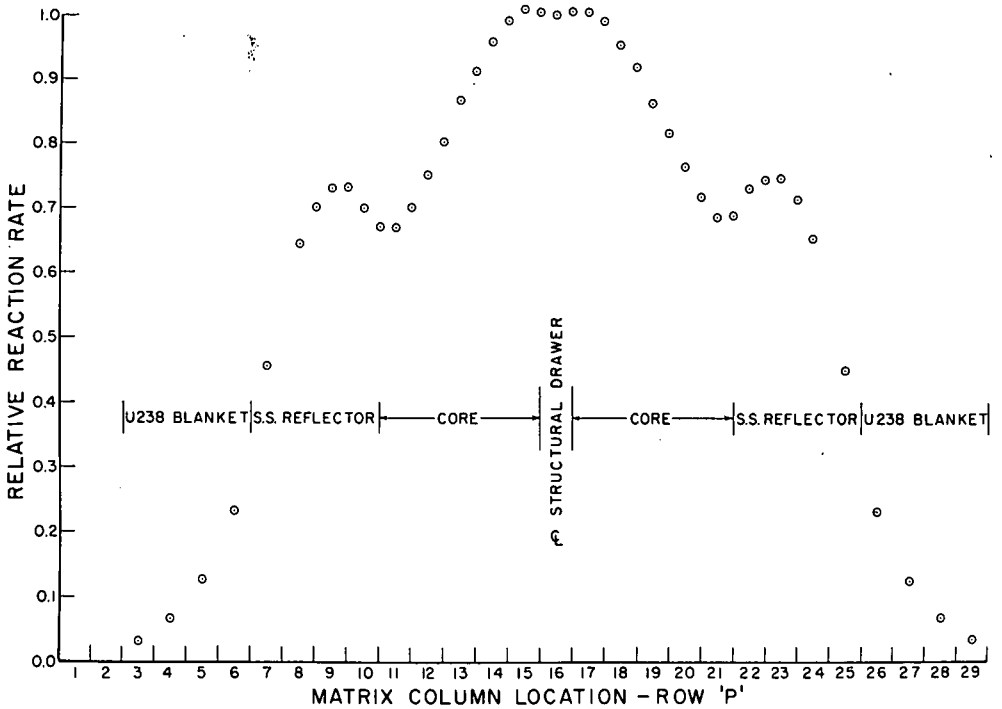

FIG. II-48-11. Assembly 63B, Modified Reference Core, ^{235}U Radial Reaction Rate Traverse in P Row. *ANL-ID-103-A2212.*

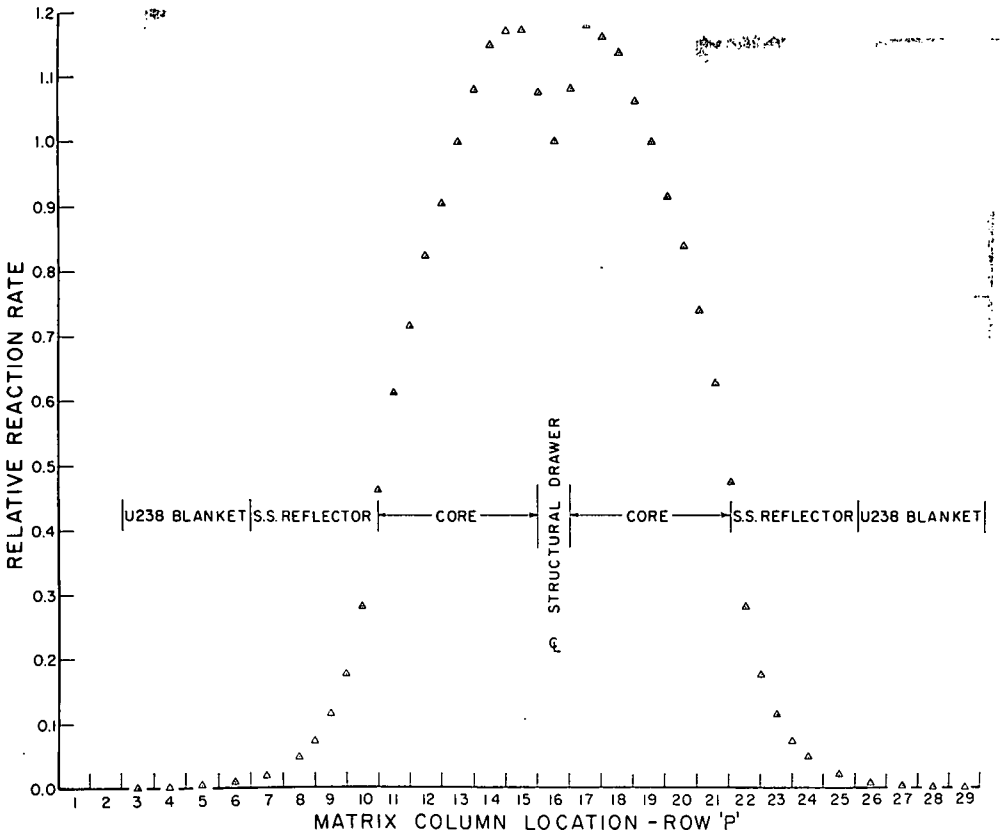

FIG. II-48-12. Assembly 63B, Modified Reference Core, ^{238}U Radial Reaction Rate Traverse in P Row. *ANL-ID-103-A2211.*

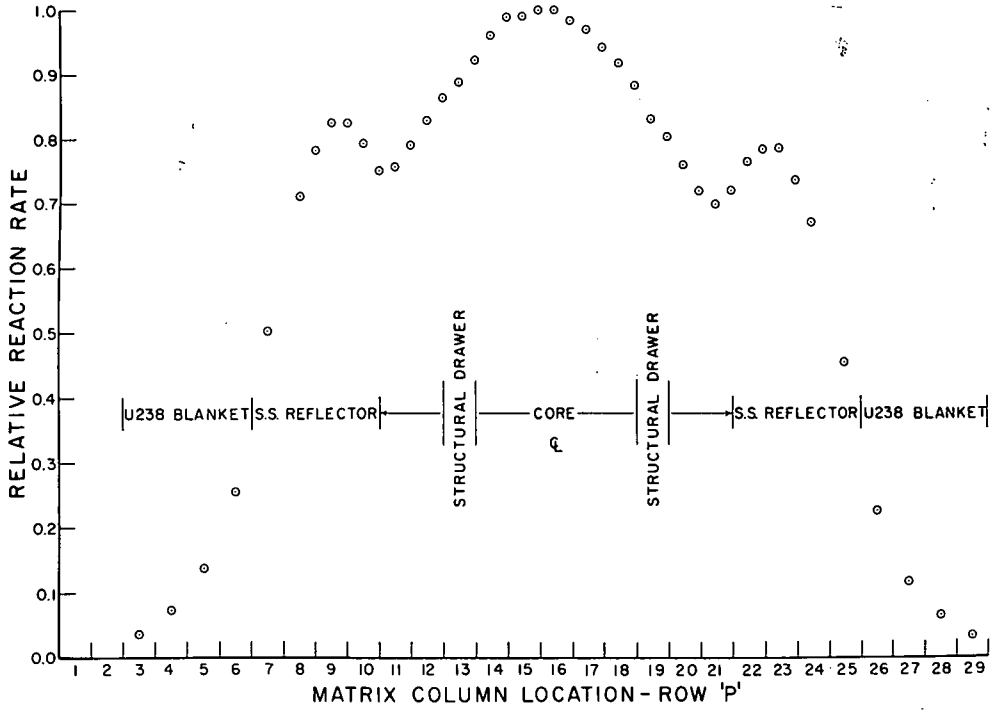

FIG. II-48-13. Assembly 63C, ^{235}U Radial Reaction Rate Traverse in P Row. *ANL-ID-103-A2217.*

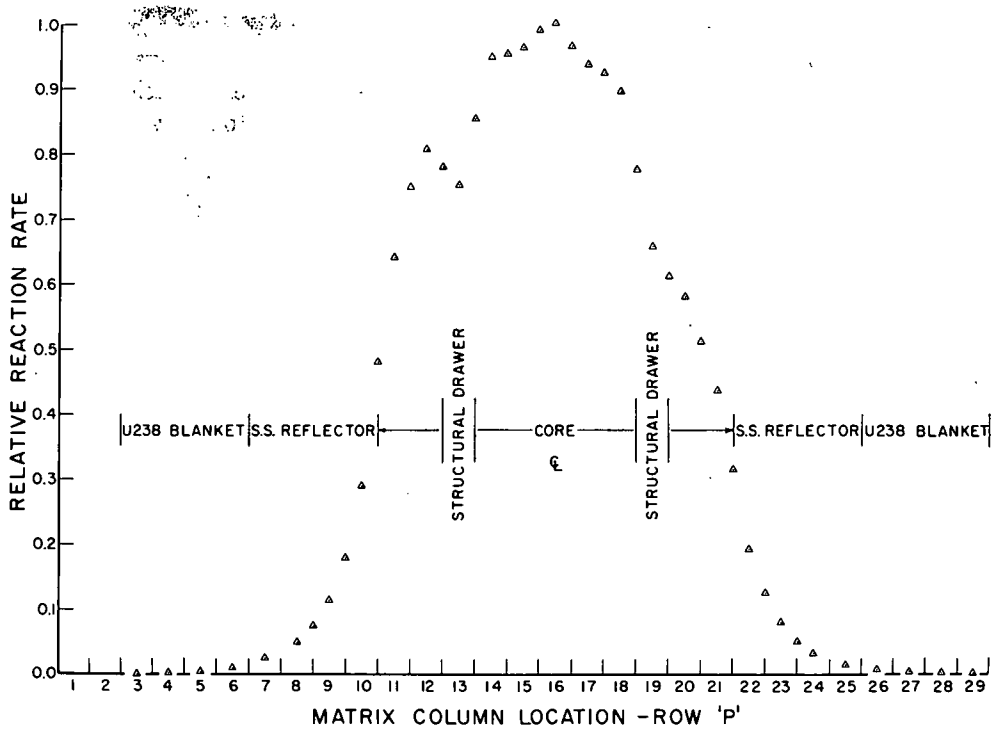

FIG. II-48-14. Assembly 63C, ^{238}U Radial Reaction Rate Traverse in P Row. *ANL-ID-103-A2216.*

TRAVERSES IN ASSEMBLY 63C

One set of horizontal or "radial traverses" was made in the Assembly 63C reference core. The only modification was the extraction of the scource tube to occupy the 26-through-31 matrix column positions and the insertion of the traverse in the P row. The ^{235}U and ^{238}U reaction rate traverses are graphed in Figs. II-48-13 and II-48-14.

REFERENCES

1. W. P. Keeney, R. O. Vosburgh, J. M. Gasidlo and D. Meneghetti, *The EBR-II Critical Assemblies—ZPR-3 Assemblies 60, 61, and 62*, Applied Physics Division Annual Report, July 1, 1969, to June 30, 1970, ANL-7710, pp. 137–140.
2. L. J. Koch, W. B. Loewenstein and H. O. Monson, *Addendum to Hazard Summary Report, Experimental Breeder Reactor-II (EBR-II)*, ANL-5719 (Addendum) (1962).

II-49. Further Analyses of Plutonium-Fueled ZPR-3 Benchmark Criticals Using ENDF/B VERSION I

A. L. HESS and R. G. PALMER

INTRODUCTION

The ZPR-3 Assemblies 48, 48B, 49, 50, 53, 54, 58 and 59 were a series of eight simple, plutonium-fueled physics studies. The cores, ranging in volume from 90 to 450 liters, were all constructed from a basic one-drawer unit cell with simple variations, including the substitution of void for sodium (change of Core 48 to Core 49), graphite for void (49-to-50 transition) and the decrease in uranium content by replacement with graphite (the series 50, 53 and 58). The reflector materials were also varied (54 and 59 had steel and lead reflectors, respectively). Such simple changes provided analytical benchmarks for studying how errors in material cross sections contribute to discrepancies in the calculations of critical size, spectral indices, and reactivity coefficients. The single-drawer-cell core construction simplifies the evaluation of heterogeneity effects, and the high graphite contents in these cores provided well-degraded spectra. Thus, these assemblies provide integral data useful for evaluating the calculational methods and nuclear-data compilations to be employed in the design of fast-breeder demonstration reactors.

A program of postanalyses using cross sections based on ENDF/B VERSION I has been completed for these eight "benchmark" systems. Included in the analytical program were investigations of the effects of heterogeneity on calculated k-values and fission ratios; the results of these aspects of the studies have been reported earlier.[1] This write-up presents the results of the completion of the study during this year, giving comparisons of best calculated fission ratios and reactivity coefficients with measurements, and discussing problems with the models and methods utilized. As a reference for these discussions, the reader is urged to review Ref. 1.

The analyses were carried out primarily with modules of the Argonne Reactor Computation (ARC) system[2] starting with the preparation of multigroup cross sections with MC².[3] The MC² library used was generated entirely from VERSION I of ENDF/B (1968 edition), a file of microscopic data now superseded. Because VERSION I is thought to be deficient, the results of this study should not be construed as definitive data tests of ENDF/B, but more so an examination of some of the experimental and computational problems associated with data testing. These studies also form the groundwork for establishing analytical techniques to be used in testing of later versions of ENDF/B and provide comparative values for evaluating the effects of the changes made to the data files.

Methods of Analysis

The course of the analysis used for this study, as described in detail in Ref. 1, can be summarized as follows:

1) The ARC epithermal cross section module (MC²) was used to generate 30-group cross section sets for the various regions of the eight assemblies. An MC² case was run for each different core cell and blanket cell assuming a homogeneous dispersion of materials; included at infinitesimal densities were materials involved in fission ratio and reactivity coefficient measurements. Then, separate MC² runs in the heterogeneous mode were made for each unique fuel or fertile plate situation in a cell to give appropriate resonance-shielded cross sections.

2) Spatial averagings of cross sections over the core cells were carried out using the code CALHET-2,[4] an integral-transport theory formulation for calculating flux distributions in slab geometry. For the fuel and fertile isotopes, the input cross sections were those generated with the heterogeneous MC² cases, and the cross sections for other materials came out of the homogeneous MC² cases. The output cross sections from CALHET-2 for each core cell thus accounted completely for cell heterogeneity, both the resonance shielding and spatial-flux-variation aspects.

3) The ARC one dimensional diffusion theory module was employed to study the effects of heterogeneity on calculations of k-effective, fission ratios and reactivity coefficients. Spherical-model problems were run for each assembly using the homogeneous-MC², heterogeneous-MC² and CALHET-weighted cross section sets in the core. A spherical transport-theory calculation (S_8) was also obtained for each assembly.

4) The 2-D diffusion capability in ARC was adopted to calculate the best value for k-effective, after adding the transport correction, to be given for these assemblies using ENDF/B VERSION I-based cross sections. Only CALHET-weighted cross sections were used in the core regions of these cases, with the rz model established from the as-built assembly (with minor adjustments for geometric irregularities but no heterogeneity adjustments).

5) The first order perturbation theory code PERT-V[5] was used to calculate central reactivity coefficients and relative fission rates. Conversion routines written in Idaho allow direct use of the ARC 2-D real and adjoint flux data sets by PERT-V. The fluxes used for each assembly (from the rz problems cited in step 4 above) thus had spectra representative of the environment in the cell-plate structure around the material-worth samples and the fission chambers. However, the cross sections used for the sample materials and fission-chamber platings were taken from the homogeneous-MC² problems to provide average resonance shielding representing the sample or fissile-foil material uniformly dispersed in minute concentration across the core cell.

The results of the analyses through step 4 have been reported in Ref. 1. The step 5 results are presented herein along with details of the calculational models, comparison of one- and two-dimensional calculations, and the over-all conclusions from the study.

Description of Assemblies and Calculational Models

Figures II-49-1 and II-49-2 indicate the core cells used and the general features of the eight cylindrical assembly loadings. Detailed specifications of the plate components of the cells can be found in the report on Assembly 48 by Broomfield et al.[6] The average regional compositions used in the assembly calculational models are given in Tables II-49-I and II-49-II, and Table II-49-III lists the dimensions and mesh specifications for the models.

Specifications for the two-dimensional rz models are based on the as-built, heterogeneous-structure critical configurations as described in experimental reports[6–10]

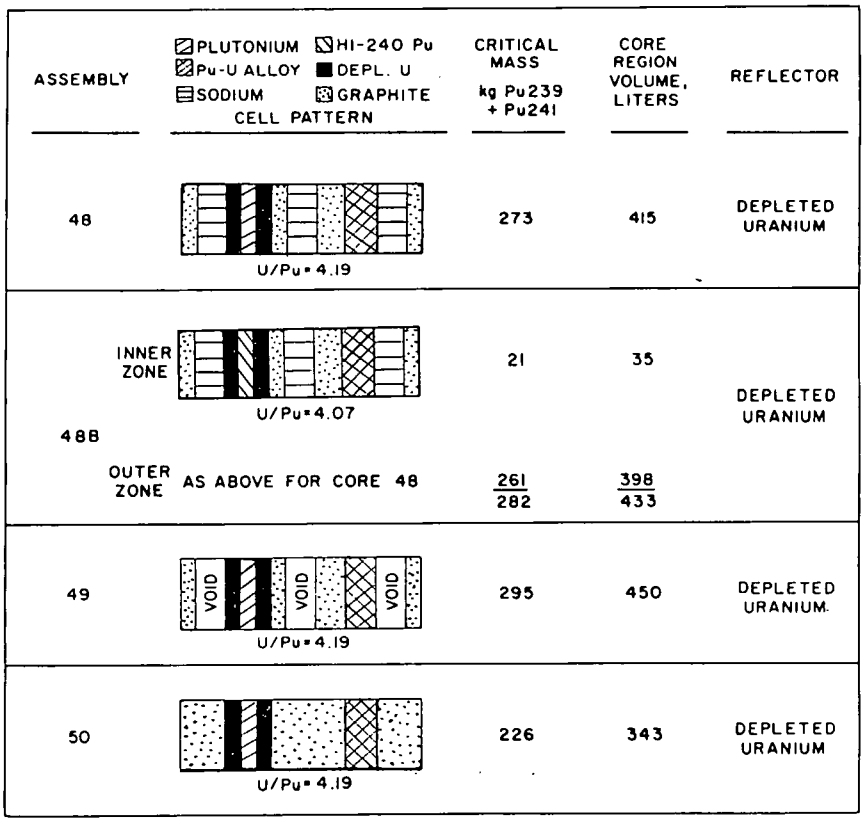

FIG. II-49-1. Description of Assemblies 48, 48B, 49 and 50. *ANL Neg. No. 116-955 T-1.*

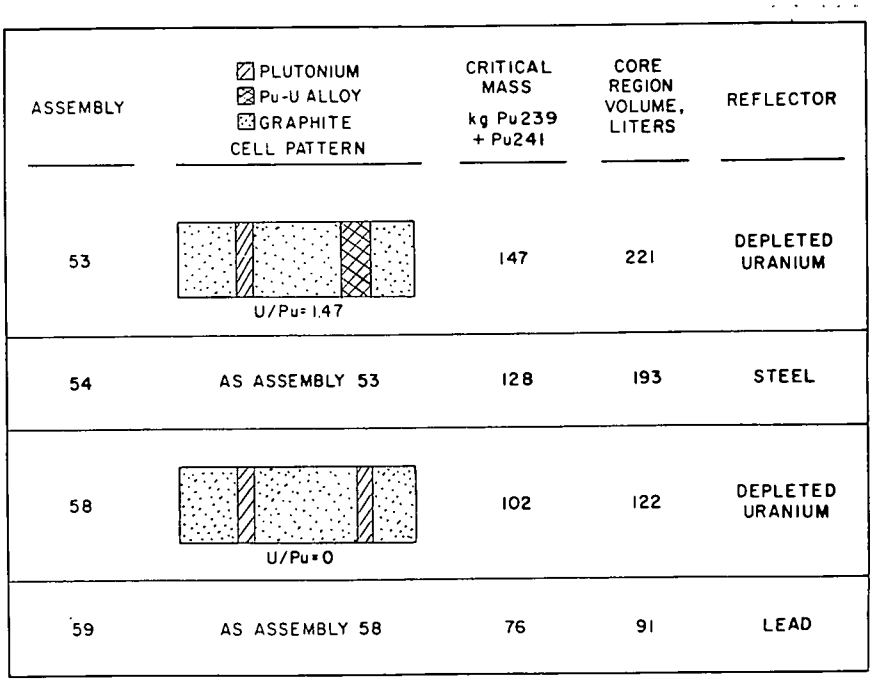

FIG. II-49-2. Description of Assemblies 53, 54, 58 and 59. *ANL Neg. No. 116-954 T-1.*

TABLE II-49-I. Compositions Used in Core Regions of Calculational Models of Eight ZPR-3 Plutonium Benchmark Criticals

Materials	Homogenized Core Compositions, 10^{21} atoms/cm^3						
	Core 48, and Outer Zone of Core 48B	Inner Zone of Core 48B	Core 49	Core 50	Cores 53 and 54	Core 58	Core 59
Contributions from Plutonium Plates							
^{239}Pu	1.0609	0.8520	1.0609	1.0609	1.0609	2.1024	2.1030
^{240}Pu	0.0506	0.2556	0.0506	0.0506	0.0551	0.1001	0.1003
^{241}Pu	0.0048	0.0532	0.0048	0.0047	0.0049	0.0058	0.0056
Contributions from Pu-U Alloy Plates							
^{239}Pu	0.5846	0.5846	0.5846	0.5846	0.5917	—	—
^{240}Pu	0.0553	0.0553	0.0553	0.0553	0.0560	—	—
^{241}Pu	0.0063	0.0063	0.0063	0.0063	0.0065	—	—
^{238}U	2.5799	2.5799	2.5799	2.5799	2.6104	—	—
^{238}U from Depleted U	4.8248	4.8248	4.8248	4.8248	—	—	—
Others in Fuel & Fertile Plates							
^{242}Pu	0.0004	0.0075	0.0004	0.0004	0.0002	0.0001	0.0001
^{235}U	0.0161	0.0161	0.0161	0.0161	0.0065	—	—
Diluents and Structure							
Na	6.2302	6.2302	—	—	—	—	—
C	20.7660	20.7660	20.7660	45.9400	55.8100	59.0700	59.0200
Fe	10.1800	10.2200	10.0800	7.3000	7.4740	7.6890	7.7170
Cr	2.5310	2.5430	2.5080	1.8160	1.8590	1.9120	1.9190
Ni	1.1190	1.1130	1.1210	0.7960	0.8140	0.9280	0.8750
Mn	0.1060	0.1060	0.1050	0.0760	0.0780	0.0798	0.0801
Mo	0.2057	0.2057	0.2050	0.2057	0.2082	—	—
Al	0.2342	0.2434	0.2332	0.1992	0.2020	0.3067	0.3111

on the assemblies. The core radius for each model was defined as that of the circular cylinder of volume equivalent to the as-built core volume with minor adjustments for the differences of the simple model from the complex actual system; the adjustments account for effects such as:

(1) the drawer front interface between the halves of the reactor

(2) the irregular, stepped radial outline of the core

(3) spiking of the control drawers with extra fuel

(4) the excess reactivity of the system available with the control drawers fully inserted

(5) referring to a standard, homogeneous reactor temperature.

For all the models, no adjustment has been made for the effect of cell heterogeneity, and thus the influence of plate structure must be accounted for in the generation of group-averaged cross sections.

The largest uncertainty in the cylindrical models comes from the core-edge irregularity correction, which accounts for the "transfer" of fuel in the protruding edges of the as-built core radial periphery to inside the boundary of an equivalent-volume circular cylinder. Except as noted below, the corrections were evaluated using a formulation involving the gradient of fuel worth at the core edge and geometric analysis of the amount and displacement of fuel occurring in the "transfer"; initially, an approximate manual analysis was used, but this was replaced with an exact, computerized geometric accounting.

As seen in Fig. II-49-1, the core cells for Assemblies 48, 48B, 49 and 50 utilized the same contents of uranium and plutonium, but had variations in plutonium isotopic makeup, sodium content and graphite content. The core-edge corrections on these initial four systems ranged from 108 to 161 inhours. Overall, the uncertainties in critical 2-D models amount to about $\pm 0.1\%$ $\Delta k/k$.

The core cell for Assemblies 53 (with a uranium blanket) and 54 (with a steel blanket) is shown in Fig. II-49-2; relative to the core 50 cell, 10 v/o uranium was replaced by graphite. The two-dimensional models used in the analyses are as reported by Kaiser et al.,[9] and include corrections for excess reactivity and for the interface gap. There were no spiked control rods, and the effects of smoothing the core outline was found to be negligible using the computerized correction formulation. However, it is possible that for both systems the edge-smoothing correction is underestimated appreciably and a proper adjustment requires comparative two-dimensional (xy) and one-dimensional (infinite cylinder)

TABLE II-49-II. Compositions Used in Blanket Regions of Calculations on Eight ZPR-3 Plutonium Benchmark Criticals

Model, Region	Average Composition, 10^{21} atoms/cm³					
	Material	Assemblies 48, 48B, 49 and 50	Assembly 53	Assembly 54	Assembly 58	Assembly 59
2-D model, radial blanket	^{235}U	0.083	0.083	—	0.086	—
	^{238}U	39.880	39.770	—	38.710	—
	Fe	4.540	4.541	75.214	4.540	4.540
	Cr	1.129	1.129	1.152	1.129	1.129
	Ni	0.494	0.494	0.494	0.494	0.494
	Mn	0.047	0.047	0.562	0.047	0.047
	Al	0.055	0.056	0.056	0.055	0.055
	Pb	—	—	—	—	28.240
	C	—	—	0.564	—	—
2-D model, axial blanket	^{235}U	0.082	0.083	—	0.086	—
	^{238}U	39.330	39.770	—	39.050	—
	Fe	5.633	5.758	76.404	5.593	5.593
	Cr	1.401	1.433	1.456	1.391	1.391
	Ni	0.613	0.627	0.627	0.609	0.609
	Mn	0.059	0.059	0.574	0.058	0.058
	Al	0.069	0.071	0.071	0.068	0.068
	Pb	—	—	—	—	28.160
	C	—	—	0.564	—	—
Spherical model, blanket	^{235}U	0.083	0.083	—	0.086	—
	^{238}U	39.690	39.770	—	38.820	—
	Fe	4.925	4.847	75.360	4.903	4.903
	Cr	1.225	1.205	1.205	1.219	1.219
	Ni	0.536	0.528	0.528	0.534	0.534
	Mn	0.051	0.500	0.565	0.051	0.051
	Al	0.060	0.059	0.059	0.060	0.060
	Pb	—	—	—	—	28.200
	C	—	—	0.564	—	—

diffusion theory calculations which have not been carried out here. Accordingly, a larger uncertainty, on the order of $\pm 0.3\,\% \Delta k/k$, should be assigned to these models.

The cell pattern for the Assembly 58 and Assembly 59 cores, also shown in Fig. II-49-2, was the simplest of the series with only plutonium and graphite plates. Assembly 58 had uranium in the radial and axial blankets, but Assembly 59, with lead blankets, was completed devoid of uranium. The cylindrical models reported for the two systems by Stevenson et al.[10] include corrections only for excess reactivity and the interface gap. In Assembly 58 the core radial outline was almost square and the core-edge correction code was not considered appropriate for this case. Instead, the cylindrical Assembly 58 model for our analyses was derived using a two-dimensional xy diffusion-theory calculation based on the as-built loading pattern to provide an axial buckling, and then a radius-search in a one-dimensional cylindrical calculation converging on the same buckling value. The correction obtained for the core 58 radius was equivalent to $-0.55\,\% k$ in reactivity. No correction for edge irregularity was applied on the Assembly 59 2-D model used in our analysis because the as-built outline was more circular and the effect was thought to be small based on the effects reported for Assemblies 53 and 54. However, the Core-59 model cannot be considered more accurate than about $\pm 0.3\,\% k$.

The spherical models defined in Tables II-49-I through II-49-III were derived directly from the cylindrical models using core shape factors as recommended by Davey.[11] The blanket composition for the 2-D models in Assemblies 48, 48B, 49 and 50 is that computed as the average blanket composition for Assembly 48 (average of radial and axial regions weighted by core-boundary areas). The blanket compositions for the other four spherical models are likewise averages of the 2-D radial and axial regions.

Comparison of One- and Two-Dimensional Diffusion Theory Calculations

The k-values given by 2-D diffusion theory using the cylindrical models are listed in the second line of Table

TABLE II-49-III. Geometries and Mesh Structures Used in Calculations on Eight ZPR-3 Plutonium Benchmark Criticals

		Assembly							
		48	48B		49	50	53	54	58	59
			Inner Core	Outer Core						
2-D model radial specifications (for quadrant)	Outer Radii, cm									
	Core, axial blanket	41.59	19.00	42.44	43.30	37.82	33.94	31.76	27.319	23.83
	Inner radial blanket	52.66		53.532	54.392	48.91	45.01	43.00	33.319	38.68
	Outer radial blanket	76.06		76.06	76.06	76.06	68.50	68.50	58.35	58.34
	Mesh Intervals									
	Core, axial blanket	19	9	10	20	19	19	19	18	16
	Inner radial blanket	5		5	5	5	6	5	4	8
	Outer radial blanket	6		6	5	6	6	6	6	6
2-D model axial specifications (for quadrant)	Axial length, cm									
	Core	38.176	15.27	22.906	38.176	38.176	30.48	30.48	25.48	25.48
	Inner axial blanket	10.16		10.16	10.16	10.16	10.16	10.16	5.00	10.16
	Outer axial blanket	20.37		20.32	20.32	20.32	20.32	20.32	25.48	20.32
	Mesh Intervals									
	Core	19	9	10	20	19	19	19	18	18
	Inner axial blanket	5		5	5	5	6	5	4	6
	Outer axial blanket	6		6	6	6	6	6	6	6
Spherical model specifications	Outer Radii, cm									
	Core	45.27	20.22	45.84	46.43	42.45	36.95	35.31	30.17	27.34
	Inner blanket	55.27		55.84	56.43	52.45	46.95	45.31	40.17	37.34
	Outer blanket	75.27		75.84	76.43	72.45	66.95	65.31	60.17	60.17
	Mesh Intervals									
	Core	90	40	50	90	90	75	75	60	60
	Inner blanket	15		15	15	15	15	15	15	15
	Outer blanket	20		20	20	20	20	20	20	20

Note: Inner and outer blankets in each section of same composition, different mesh structure.

TABLE II-49-IV. Results of Two-Dimensional Diffusion-Theory Calculations and Evaluation of One-Dimensional Models

	Assembly							
	48	48B	49	50	53	54	58	59
Shape factor used	0.9366	0.9339	0.9323	0.9339	0.9579	0.9546	0.9627	0.9416
k-eff of rz, 2-D calculation	0.9884	0.9895	0.9795	0.9936	1.0127	1.0005	1.0148	1.0078
k-eff of 1-D calculation	0.9885	0.9891	0.9766	0.9949	1.0190	0.9848	1.0191	0.9898
Discrepancy of 1-D model, $\Delta k/k$	+0.0001	−0.0004	−0.0030	+0.0012	+0.0062	−0.0157	+0.0042	−0.0179
Edge-worth factor F in $\Delta M/M = F\,\Delta k/k$	6.05	6.2	6	6.35	7.23	4.56	3.42	2.90
1-D discrepancy equivalence in $\Delta M/M$	0.0006	−0.0025	−0.0180	+0.0076	+0.0448	−0.0716	+0.0144	−0.0519
Adjusted shape factor	0.9360	0.9364	0.9503	0.9263	0.9131	1.026	0.9483	0.9935

II-49-IV as a comparison with the 1-D k-values in the next line. The spherical models used in the one-dimensional diffusion-theory calculations were only approximate as they served for the studies of heterogeneity effects. However, the comparison here of k-value results between 1-D and 2-D calculations is useful to judge the validity of the shape factors used. In the table, the 1-D versus 2-D discrepancy in k for each assembly is related through the core fuel-edge worth factors to a discrepancy in volume, and an "adjusted" shape factor is thereby obtained.

For most of the uranium-blanketed cores, the shape

factor adjustments are relatively minor, probably because of accurate spherical-model evaluations from past analyses or because of the adequacy of the Davey formulation.[3] However, the anomalously high adjustments needed for the Assemblies 54 and 59 shape factors, to give agreement between 1-D and 2-D calculations, indicate that other corrections are required for the spherical models of these assemblies. The total discrepancy in each of these two cases is probably a combination of the error resulting from use of a shape factor for a uranium blanket and an error from use of an insufficient reflector thickness in the spherical model. The 30 cm and 32.83 cm, respectively, for the Assemblies 54 and 59 1-D models probably do not represent the proper translation of the reflector thicknesses in the 2-D models. These calculations suggest that 30 cm of steel or lead do not constitute an effectively "infinite" blanket as is the case for ^{238}U. Further studies of blanket effectiveness and shape factors for intermediate-element reflectors are needed to determine more exact spherical models for Assemblies 54 and 59. Also, studies of the large discrepancy observed between 1-D and 2-D results for Assembly 53 are needed.

Comparison of Measured Fission Ratios with Values from 2-D Diffusion Calculations

The spectra given at the central mesh points of the cylindrical-model diffusion calculations were used to calculate the fission ratios considered to be the best representation given by ENDF/B VERSION I data with all the heterogeneity effects included. Cross sections for the ratio constituents were those given by the homogeneous MC[2]. Table II-49-V compares the calculated ratios with the experimental values for the assemblies where measurements were made. It is seen that the discrepancies of the calculations from the measurements for particular ratios is fairly consistent between assemblies; this would not be the case for the threshold-fissile isotopes had the heterogeneity effects not been included.[1]

No strongly significant trends are indicated in the calculated-to-experiment (C/E) ratios according to core composition or spectral character, but generally it may be noted that the calculated spectra are too soft, or that the low-energy ^{235}U fission cross sections are too high.

Comparison of Central Reactivity Coefficient Measurements with Values from Two-Dimensional Perturbation Theory

Table II-49-VI compares the central worths of ^{239}Pu, ^{235}U, and ^{10}B, calculated using the perturbation theory code PERT-V, with the experimentally determined values. The values given for the measurements are for the individual isotopes after adjusting for the minor constituents of other isotopes and correcting for finite-sample effects in the experimental samples; overall, the uncertainty for the measured values is ±5%. The experiments in all cases involved small, 2-in. long cylindrical or annular samples situated at the center of a 2-in. cubical void at the core center.

TABLE II-49-V. Final Values of Fission Ratios, Calculated Using Central Spectra from Two-Dimensional Diffusion Theory Calculations, Compared with Measurements

Fission Ratio Relative to U-235	Assembly					
	48	48B	49	50	53	59
U-238						
Experiment	0.0307	0.0297	0.0345	0.0251	0.0254	0.0325
Calculated	0.02903	0.0278	0.0324	0.0237	0.0239	0.0293
C/E	0.946	0.936	0.938	0.945	0.942	0.902
U-236						
Experiment	0.067	0.066	0.075	0.054	0.0533	0.068
Calculated	0.0627		0.070	0.0503	0.0508	0.0624
C/E	0.936		0.934	0.932	0.954	0.918
U-234						
Experiment	0.204	0.198	0.228	0.158	0.1466	0.183
Calculated	0.1833	0.177	0.206	0.139	0.1327	0.1587
C/E	0.898	0.894	0.904	0.878	0.905	0.867
Pu-240						
Experiment	0.243	0.229			0.174	0.207
Calculated	0.2154	0.2085	0.240	0.166	0.158	0.1869
C/E	0.886	0.911			0.911	0.903
Pu-239						
Experiment	0.976	0.964	0.986	0.903	0.928	0.942
Calculated	0.907	0.902	0.934	0.839	0.822	0.830
C/E	0.929	0.936	0.947	0.929	0.885	0.881
U-233						
Experiment	1.480	1.439	1.454	1.412	1.454	1.466
Calculated	1.412	1.409	1.429	1.371	1.366	1.385
C/E	0.954	0.976	0.983	0.971	0.939	0.945

The calculations gave the worths of the isotopes along radial and axial traverses through the core center, and the values selected for comparison with measurements were the worths integrated over the first two radial and axial mesh points as a simulation of the region involved in the measurements. A code option for using a k of unity in the perturbation equations was specified to correspond with the measurements at criticality.

Most of the deviations of the calculated worths exhibit the same patterns as have been observed in the analyses of other plutonium criticals, the C/E ratios ranging between 1.2 and 1.3. The notable exceptions are the ^{235}U worths calculated for Assemblies 58 and 59

TABLE II-49-VI. Comparison of Measured Central Reactivity Coefficients with Best Values Calculated Using Two-Dimensional Perturbation Theory

		Assembly							
		48	48B	49	50	53	54	58	59
Calculated Ih/%k		985	968	974	970	992	1073	1008	1048
Pu-239 worth, Ih/kg	Experiment	442	437	399	536	678	750	879	1084
	Calculated	558	535	495	699	907	1072	1089	1358
	C/E	1.26	1.22	1.24	1.30	1.34	1.43	1.24	1.25
U-235 worth, Ih/kg	Experiment	335	335	297	443	516	564	597	747
	Calculated	430	417	379	560	640	749	611	759
	C/E	1.28	1.24	1.28	1.26	1.24	1.33	1.02	1.02
B-10 worth, Ih/kg	Experiment	−9220	−8920	−7140	−17000	−38000	−41100	−55300	−68600
	Calculated	−11416	−10888	−8464	−22256	−45682	−54070	−68014	−83830
	C/E	1.24	1.22	1.18	1.31	1.20	1.32	1.23	1.22

(calculations agreeing with measurements) and the 43%-high ^{239}Pu worth calculated for Assembly 54.

The discrepancies of the calculated ^{239}Pu and ^{235}U worths in Assembly 48 (26 and 28% higher than measurements) agree to about 2% with results observed before by Hess[12] in the analyses using homogeneously-shielded cross sections based on ENDF/B VERSION I. Thus, the effects of cell heterogeneity does not significantly influence the worth calculations for these two fissile isotopes. However, the calculated ^{10}B worth using the "heterogeneous" real and adjoint spectra of the 2-D Assembly 48 calculation is about 15% greater than the worth given by a homogeneous analysis[12]; this reflects the spectrum softening produced by the heterogeneous shielding of resonances.

Conclusions

Four major conclusions were drawn from the overall program of analyses on these eight assemblies, including the studies of calculated heterogeneity effects and the comparison of measured and calculated parameters.

(1) There is a clear need to adequately account for the heterogeneous structure in the highly moderated critical assemblies, such as have been studied, not only the evaluate the effect on criticality, but also to represent the proper environment for fission ratio experiments and material worth measurements.

(2) The well-known "reactivity discrepancy", that is, the deviation of calculated central worths of materials from measured values by about +20 to +30%, is again observed in these studies. It does not appear that cell-heterogeneity effects are entirely responsible for these discrepancies (for example, by influence on the perturbation-denominator calculation) but the softening of the spectra due to heterogeneous shielding does affect such low-energy indices as the central worth of ^{10}B. Nor does the calculation of delayed-neutron and reactivity-conversion factors seem to cause the discrepancy, as indicated by the consistency of C/E values between the uranium-blanketed and the steel and lead reflected cores.

(3) As data tests of ENDF/B VERSION I, the analyses with these eight benchmarks have reaffirmed general trends noted in analyses with other benchmark systems. Increasing contents of ^{238}U tend to depress k values, and increased moderation of plutonium-fueled systems results in higher k values. The low-energy alpha for ^{239}Pu in VERSION I is known to be too low and there is integral evidence of this in the strong upward trend in k obtained with these small, highly moderated cores. The consistently lower-than-measured values of fission ratios (relative to ^{235}U) found in the study may indicate calculated spectra which are too soft or excessive fission cross sections for ^{235}U at low energies.

(4) Although the assemblies studied were simple and the differences between them (sole changes in contents of ^{238}U, carbon or sodium) should accentuate the effects of errors in particular material cross sections, the cores were relatively small and the analyses thereby were subject to greater uncertainties. The larger corrections for core-edge irregularity and transport effect, and the more pronounced influence of the reflector on the core-center spectrum mean that more sophisticated analytical methods are required if these assemblies are to be used reliably as benchmark tests of cross sections.

References

1. A. L. Hess, R. G. Palmer and J. M. Stevenson, *A Post-analytical Study of Eight ZPR-3 Benchmark Criticals Using ENDF/B Data*, Applied Physics Division Annual Report, July 1, 1969 to June 30, 1970, ANL-7710, p. 224.

2. B. L. Toppel, Editor, *The Argonne Reactor Computation (ARC) System*, ANL-7332 (1967).
3. B. J. Toppel, A. L. Rago and D. M. O'Shea, *MC²*, *A Code to Calculate Multigroup Cross Sections*, ANL-7318 (1967).
4. F. L. Fillmore and L. D. Felton, *The CALHET Heterogeneous Perturbation-Theory Code and Application to ZPR-3-48*, AI-67-91 (1967).
5. R. W. Hardie and W. W. Little, *PERT-V, A Two-Dimensional Perturbation Code for Fast Reactor Analysis*, BNWL-1162 (1969).
6. A. M. Broomfield, A. L. Hess, P. I. Amundson, Q. L. Baird, E. F. Bennett, W. G. Davey, J. M. Gasidlo, W. P. Keeney, J. K. Long and R. L. McVean, *ZPR-3 Assemblies 48, 48A, and 48B; The Study of a Dilute Plutonium-fueled Assembly and its Variants*, ANL-7759 (1970).
7. Reactor Development Program Progress Report, July 1967, ANL-7357.
8. L. Mountford and R. O. Vosburgh, *ZPR-3 Assembly 50—Benchmark Core Containing a Graphite Substitution for Sodium*, Reactor Physics Division Annual Report, July 1, 1968 to June 30, 1969, ANL-7610, pp. 77-84.
9. R. E. Kaiser, J. M. Gasidlo, W. K. Lehto, L. A. Mountford, J. E. Powell, N. A. Hill, R. O. Vosburgh and J. M. Stevenson, *ZPR-3 Assemblies 53 and 54—Continuation of Studies of Basic Physics Cores—Depleted Uranium Blanket and Iron Reflected Versions*, Reactor Physics Division Annual Report, July 1, 1968 to June 30, 1969, ANL-7610, pp. 84-94.
10. J. M. Stevenson, J. M. Gasidlo, V. C. Rogers, G. G. Simons and R. O. Vosburgh, *Experimental Results for ZPR-3 Assemblies 58 and 59*, ANL-7695 (1970).
11. W. G. Davey, *An Analysis of 23 ZPR-3 Fast Reactor Critical Experiments*, Nucl. Sci. Eng. **19**, 259-273 (1964).
12. A. L. Hess, *Review of CSEWG Data Testing of ENDF/B with Analyses of ZPR-3 Assemblies 48 and 11*, Reactor Physics Division Annual Report, July 1, 1968 to June 30, 1969, ANL-7610, p. 222.

II-50. Prescription of a Benchmark Model of ZPPR Assembly 2 for Data Testing of ENDF/B

A. L. Hess and R. G. Palmer

Introduction

As participants in efforts of the national Cross Section Evaluation Working Group (CSEWG) to establish an evaluated nuclear data file (ENDF/B) for reactor calculations, the authors have in the past drawn up specifications[1] for several benchmark models of fast-reactor criticals for data testing. The largest previous model was ZPR-3 Assembly 48 with a core volume of 450 liters. In continuing participation, and to enable data testing on a system relevant to the designs of large fast power reactors, a benchmark prescription of ZPPR Assembly 2 was formulated and submitted to CSEWG. This report gives the details of a prescribed calculational model which was based on Loading 90, an equal-core zone reference configuration of ZPPR Assembly 2. The corrections and approximations to the as-built loading to derive the model are explained below. Included are descriptions of the drawer cells used to construct the various assembly regions in order to illustrate the heterogeneity aspects of consequence to proper data testing.

Because of the nature of the Assembly 2 core, with an inner zone plus an outer zone of higher plutonium density, the benchmark model is necessarily a two-dimensional (*rz*) representation. Also, it was decided that the determination of the heterogeneity effects should be part of the data testing and no adjustments have been applied to the model herein to effect an equivalent homogeneous system.

Compositions for Assembly Regions

Figure II-50-1 shows the cylindrical representation of ZPPR Assembly 2. Average compositions for the regions illustrated, listed in Tables II-50-I and II-50-II, were derived from the as-built specifications given in Paper II-35 for Loading 90. The radial dimensions for the core zones in Fig. II-50-1 are those given in Paper II-35 for the critical mass of Loading 90 after applying corrections as cited below.

The reference as-built loading contained equal volumes in the inner and outer core zones. The inner core zone was composed of a repetition of a one-drawer unit cell; the outer core zone utilized a two-drawer cell. Both inner and outer core zones contained some partial core drawers, with ½-in. wide void channels (for poison rods) alongside, and the inner core contained movable control drawers. The average core-zone compositions in Table II-50-I are not the unit cell compositions, but include the perturbations (in sodium and steel densities) from the void channels and control drawers averaged over the total zone. The axial-region compositions in Table II-50-II also include the effects of the void channels and control drawers. Furthermore, the compositions of the radial blanket

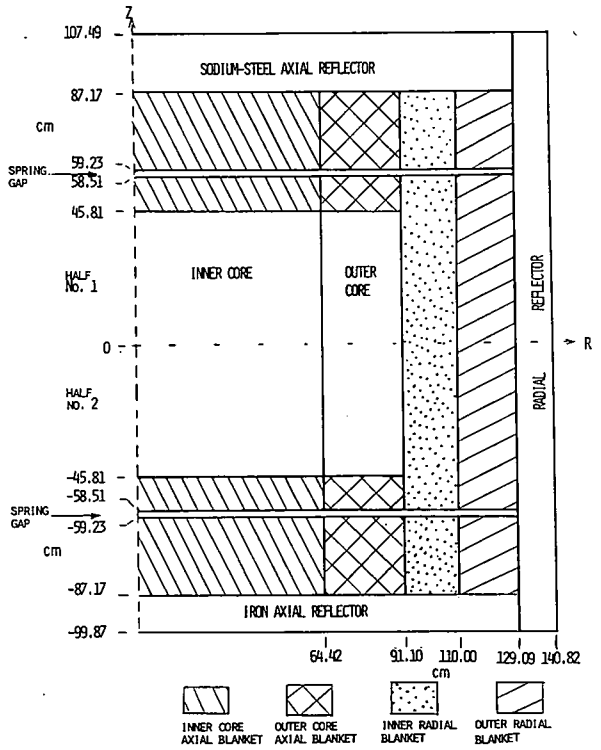

FIG. II-50-1. Benchmark Model of ZPPR Assembly 2. *ANL-ID-103-A11998.*

TABLE II-50-I. AVERAGE COMPOSITIONS OF CORE AND RADIAL BLANKET REGIONS OF ZPPR ASSEMBLY 2, LOADING 90

Material	Region Compositions, 10^{22} atoms/cm³				
	Inner Core Zone	Outer Core Zone	Inner Radial Blanket	Outer Radial Blanket	Radial Reflector
^{239}Pu	0.08433	0.12741	—	—	—
^{240}Pu	0.01117	0.01687	—	—	—
^{241}Pu	0.00154	0.00232	—	—	—
^{242}Pu	0.00018	0.00028	—	—	—
^{238}Pu	0.00006	0.00009	—	—	—
^{241}Am	0.00029	0.00044	—	—	—
^{235}U	0.00123	0.00115	0.0024	0.0024	—
^{238}U	0.55549[a]	0.51980[a]	1.1085	1.1085	—
C	0.0030	0.0023	0.1013	0.1013	0.0558
O	1.3116	1.1761	2.0132	2.0133	—
Na	0.8796	0.8564	0.6398	0.5963	—
Al	0.0003	0.0004	0.0002	0.0003	—
Fe	1.2576	1.3852	0.6923	0.7541	7.1561
Cr	0.2702	0.2523	0.1991	0.2172	0.1205
Ni	0.1221	0.1160	0.0898	0.0987	0.0513
Mn	0.0209	0.0202	0.0157	0.0174	0.0598
Cu	0.0019	0.0020	0.0017	0.0018	0.0013
Mo	0.0231	0.0341	0.0014	0.0015	0.0012
Si[b]	0.0137	0.0118	0.0094	0.0102	0.0091
H	—	—	0.0008	0.0008	—

[a] Includes impurities in fuel plates.
[b] Includes minor concentrations of phosphorus and sulfur.

regions and axial reflector regions are averages over two or three subregions.

DIMENSIONS FOR A HETEROGENEOUS-REGION MODEL HAVING $k = 1$

The radial dimensions for the core zones in Fig. II-50-1 have been adjusted to give a model with $k = 1$ and with equal volumes in both zones. The adjustments account for a number of corrections to the as-built loading:

1. for the partial insertion of control rods,
2. for the subcriticality at operating power,
3. for the gap between the halves of the reactor,
4. for a uniform temperature representation (average of 22.0° C).

There were no control drawers spiked with extra fuel in this loading, and the effect of smoothing the radial outlines of the inner and outer core was estimated to be negligible. A correction for the heterogeneity of the core and blanket unit cells was *not* applied, and thus, the effects of heterogeneity must be included in the generation of the multigroup cross sections for each region.

The total adjustment to the as-built ^{239}Pu + ^{241}Pu loading to derive the just-critical model was -8.5 ± 0.9 kg, and with equal volume reductions in the inner and outer core zones, gave the core radii shown in Fig. II-50-1. The radial blanket and reflector radii were adjusted to obtain the same thicknesses as in the as-built case. Overall, the loading uncertainty is about

TABLE II-50-II. AVERAGE COMPOSITIONS OF AXIAL BLANKET REGIONS OF ZPPR ASSEMBLY 2, LOADING 90

Material	Region Composition, 10^{22} atoms/cm³				
	Axial Blankets of Inner Core	Axial Blankets of Outer Core	Spring Gaps	Sodium-Steel Axial Reflector (Half No. 1)	Iron Axial Reflector (Half No. 2)
^{235}U	0.0016	0.0016	—	—	—
^{238}U	0.7036	0.7057	—	—	—
C	0.0036	0.0030	0.0284	0.0214	0.0557
O	1.3895	1.4008	—	—	—
Na	0.8739	0.8808	—	0.8966	—
Al	0.0002	0.0002	0.0001	0.0002	—
Fe	1.0751	0.9355	2.1133	3.5713	7.2681
Cr	0.2835	0.2418	0.4393	0.5347	0.1639
Ni	0.1275	0.1095	0.1503	0.2412	0.0706
Mn	0.0230	0.0205	0.0279	0.0611	0.0623
Cu	0.0017	0.0017	0.0030	0.0017	0.0014
Mo	0.0014	0.0014	0.0023	0.0014	0.0013
Si[a]	0.0150	0.0119	0.0182	0.0305	0.0114

[a] Includes minor concentrations of phosphorus and sulfur.

±1.5 kg of $^{239}Pu + {}^{241}Pu$ (out of 1024 kg); this gives an uncertainty of about ±0.0006 $\Delta k/k$ for the model.

Assembly Heterogeneity Description

UNIT CELL DESCRIPTIONS

The outer dimensions of the ZPPR matrix tubes, determined from the total lattice dimensions, were 5.5245 cm wide and 5.7839 cm high. The drawers inserted into the tubes had an inside cross section of 2-in. square for the loading of the various reactor-material plates. Thus, the total cell could be represented as a 2 x 2 in. loading area of plates inside a structural box as illustrated in Fig. II-50-2. The arrangements of the plate columns used in the core and blanket drawers of the modified plate version of ZPPR Assembly 2 (as for Loading 90) are shown in Fig. II-50-3.

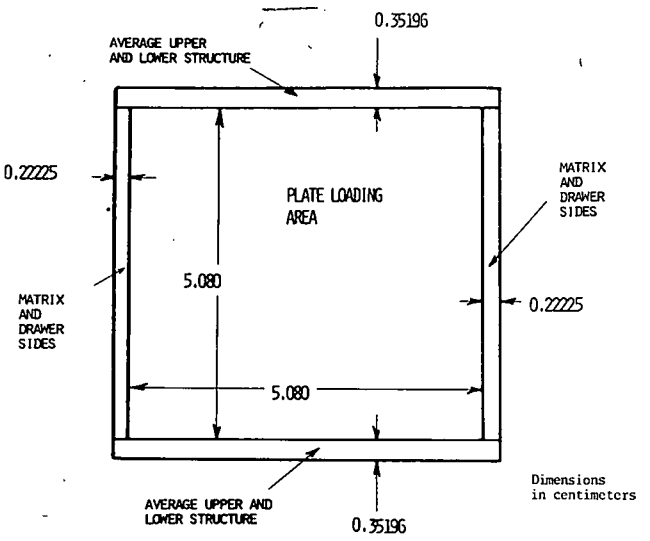

FIG. II-50-2. Geometry of ZPPR Unit-Matrix Cells. *ANL-ID-103-A11997.*

MATERIAL COLUMN SPECIFICATIONS

Tables II-50-III and II-50-IV give average widths and compositions for the plate columns used in the core and blanket drawers. For the canned materials (fuel, sodium, and Na_2CO_3) a nominal thickness of 0.015 in. was chosen for the steel cladding, and the remainder of the column width (¼ in. or ½ in.) was assumed to be occupied by the fuel, sodium, or Na_2CO_3-plate core. For all of the column materials, the densities were derived assuming the assigned widths, a height of 2 in., and a length of 18.036 in. (column length plus thickness of drawer front). Table II-50-IV includes the composition for the side structure of the cell (drawer plus matrix) homogenized over the true widths of the matrix wall plus drawer side plus slack. Compositions for the upper and lower regions of the cells as indicated in Fig. II-50-2 are given in Table II-50-V. These include the drawer front and bottom, matrix, edges and ends of the claddings, and in some cases shims on the bottom of the plate loadings.

REGION CELL REPRESENTATIONS

Tables II-50-III and II-50-IV include a letter designation at the top for each of the different types of material columns. For cell calculations to be used in determining heterogeneously-averaged cross sections, the overall cell for each region can be viewed as a stack of vertical columns (5.08 cm high by 5.5245 cm total width) sandwiched between horizontal upper and lower plates of structure; the cell descriptions so conceived are as follows.

Inner Core Cell

The plate-loading pattern for core zone 1 is shown at the top in Fig. II-50-3. Using the notations for column lablels as given in Tables II-50-III and II-50-IV,

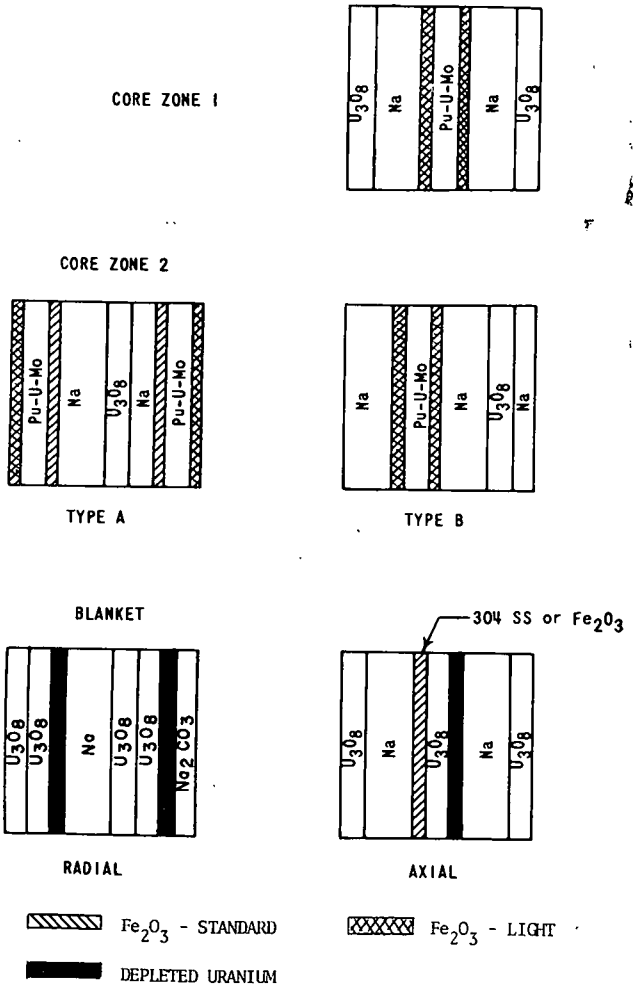

FIG. II-50-3. Cell-Loading Patterns for ZPPR Assembly 2. *ANL-ID-103-A11999.*

TABLE II-50-III. SPECIFICATIONS OF FUEL, FERTILE, AND IRON OXIDE CONSTITUENTS OF CORE AND BLANKET CELLS

Cell Component	Cores of Pu-U-Mo Alloy Plates	¼-in. Thick U_3O_8 Columns	½-in. Thick U_3O_8 Columns	⅛-in. Thick Depleted U Columns	Standard Fe_2O_3 Columns	Light Fe_2O_3 Columns
Label	A	B	C	D	E	F
Thickness, cm	0.5588	0.6350	1.2700	0.3175	0.3175	0.3175
Material	Atom Densities, 10^{22}/cm³					
^{238}Pu	0.0006	—	—	—	—	—
^{239}Pu	0.9501	—	—	—	—	—
^{240}Pu	0.1258	—	—	—	—	—
^{241}Pu	0.0176	—	—	—	—	—
^{242}Pu	0.0021	—	—	—	—	—
^{241}Am	0.0018	—	—	—	—	—
^{235}U	0.0060	0.0034	0.0035	0.0103	—	—
^{238}U	2.6988	1.5646	1.6189	4.5778	—	—
Mo	0.2436	—	—	—	—	—
O	—	4.1691	4.2901	—	5.5404	4.6632
Fe	—	—	—	—	3.6869	3.1735

TABLE II-50-IV. SPECIFICATIONS OF SODIUM, SODIUM CARBONATE, CLADDING AND REACTOR STRUCTURE CONSTITUENTS OF CORE AND BLANKET CELLS

Cell Component	Cores of ¼-in. Na Columns	Cores of ½-in. Na Columns	Cores of ¼-in. Na_2CO_3 Columns	Cladding of Fuel, Na and Na_2CO_3 Plates	⅛-in.-Thick Stainless Steel Column	Structure Side Wall, Matrix and Drawer
Label	G	H	I	J	K	L
Thickness, cm	0.5588	1.1938	0.5588	0.0381	0.3175	0.22225
Material	Atom Density, 10^{22}/cm³					
Na	2.2302	2.3300	2.2291	—	—	—
C	—	—	1.1140	—	0.0270	0.0162
O	—	—	3.3438	—	—	—
Fe	—	—	—	5.5936	5.8032	3.5911
Cr	—	—	—	1.6276	1.6146	1.0303
Ni	—	—	—	0.8189	0.7303	0.4510
Mn	—	—	—	0.1176	0.1584	0.0875
Si[a]	—	—	—	0.0778	0.0981	0.0501
Mo	—	—	—	0.0043	—	0.0086
Cu	—	—	—	0.0093	—	0.0096
Al (H)	—	—	(0.0094)	0.0067	—	—

[a] Includes minor concentrations of sulfur and phosphorus.

the vertical constituents of the cell (including the side structure of the matrix and drawers) are as follows:

L B J H J F J A J F J H J B L.

Column 2 of Table II-50-V gives the upper and lower structure atom densities for these drawers (which had steel shims on the bottom).

Outer Core Cell

As shown in the middle of Fig. II-50-3, the outer core cell was actually a two-drawer cell with three columns of fuel (giving a 1.5 ratio of fuel density of the outer zone relative to the inner zone). For simplicity, it is represented here as two cells, A and B: outer core A, with upper/lower structure shown in column 3 of Table II-50-V,

L F J A J E J H J B J G J E J A J F L;

outer core B, with upper/lower structure shown in column 4 of Table II-50-V,

L J H J F J A J F J H J B J G J L.

Radial Blanket Cell

The loading pattern at the bottom left in Fig. II-50-3 was that used in the front 23 in. (to the spring gap) in each half of the inner radial blanket. The column notations for these regions would thus be

L C D J H J B B D J I J L.

For the back 11 in. of the inner radial blanket (beyond the spring gap in each half of the assembly) the U_3O_8 was all in the form of ½-in. thick plates, giving the pattern of vertical constituents as

L C D J H J C D J I J L.

The upper/lower structure composition in column 5 of Table II-50-V applies to the overall average cell (full 34-in. length in each assembly half) of the inner radial blanket.

The outer radial blanket contained double columns of ¼-in. thick sodium in place of the ½-in. thick sodium above, giving the pattern for the front 23 in. as

L C D J G J J G J B B D J I J L,

and for the back 11 in. as

L C D J G J J G J C D J I J L.

Axial Blanket Cell

As indicated in Fig. II-50-3, a two-drawer cell was used for the axial blanket regions, the difference between the two drawers being a column (⅛ in.) of steel in place of a column of Fe_2O_3. Thus for the Fe_2O_3 loaded drawer, the pattern of vertical components would be

L B J H J E B D J H J B L,

and the steel loaded drawer pattern would be

L B J H J K B D J H J B L.

The axial blanket behind the inner core contained steel shims at the bottom of the drawers, giving a high-density upper/lower structure region as indicated in column 6 of Table II-50-V.

The last column of Table II-50-V lists the upper/lower structure composition for the cell of the axial blankets behind the outer core.

Radial and Axial Reflectors

No cell descriptions are given here for the reflector regions because their remote locations imply insignificant heterogeneity effects on reactor parameters. Homogeneous compositions, as in Table II-50-II, should be assumed.

TABLE II-50-V. Compositions of Upper and Lower Cell Structure

Material	Average Compositions of Upper and Lower Structural[a] Regions for Core and Blanket Cells, 10^{22} atoms/cm³					
	Cell for Inner Core	Cell for Outer Core A	Cell for Outer Core B	Cell for Inner Radial Blanket	Cell for Axial Blanket of Inner Core	Cell for Axial Blanket of Outer Core
Fe	3.9436	2.8733	2.8801	2.4899	3.6611	3.5240
Cr	1.1337	0.8237	0.8268	0.7141	1.0693	0.7347
Ni	0.4960	0.3643	0.3482	0.3128	0.4703	0.3259
Mn	0.0860	0.0680	0.0683	0.0551	0.0814	0.0621
Si[b]	0.0607	0.0335	0.0338	0.0330	0.0580	0.0332
Mo	0.0054	0.0050	0.0055	0.0060	0.0059	0.0059
Cu	0.0072	0.0074	0.0074	0.0065	0.0068	0.0068
Al	0.0008	0.0009	0.0009	0.0003	0.0007	0.0007
C	0.0148	0.0097	0.0097	0.0096	0.0144	0.0094

[a] Region dimensions as illustrated in Fig. II-50-2.
[b] Includes minor concentrations of phosphorus and sulfur.

Recommendations

The inclusion of all the cell descriptions is not to suggest that calculations are needed for each case to generate cell-averaged cross sections for all regions, but rather to point out the variances typically encountered in the construction of the critical assemblies and to show why the region compositions differ. One cell calculation each for the radial and axial blankets, with the patterns shown at the bottom of Fig. II-50-3, should be sufficient to obtain multigroup sets for use in all blanket and reflector regions. Another acceptable simplification would be to merge together the claddings and cores for such plates as sodium, fuel, and Na_2CO_3.

It should also be mentioned that the homogenized compositions of the cell descriptions cited above will not agree exactly with the average region compositions given in Tables II-50-I and II-50-II because the column densities presented in Tables II-50-III and II-50-IV are averages of several lengths of plates, whereas the different regions involved variations of column plate-length patterns. Also, as indicated earlier, the core and axial blanket regions contain void channels and extra drawer steel homogenized into their compositions.

It can be appreciated that the inclusion of the heterogeneity aspects into the data testing requires extensive extra effort and computer time. As a shortcut, using only homogeneously shielded cross sections in all of the model regions would provide a k-value which then could be corrected for the heterogeneity effect. This correction, the advantage of the as-built system due to the cell plate structure, need only be calculated by one of the CSEWG data-testing participants for use by all participants. We suggest that a correction

value of 1.2% $\Delta k/k$, as determined by Olson[2] using ENDF/B VERSION I data, may be applicable regardless of the changes in the later versions of ENDF/B. However, the use of homogeneous cross sections in the diffusion calculations would give real and adjoint spectra which are not representative of the environment for fission-ratio and material-worth experiments.

REFERENCES

1. W. G. Davey and A. L. Hess, *Prescriptions of Fast Critical Benchmarks for Integral Testing of ENDF/B*, Reactor Physics Division Annual Report, July 1, 1968 to June 30, 1969, ANL-7610, pp. 220–221.
2. A. P. Olson, Applied Physics Division (private communication).

II-51. Calculations for Fast Reactor Benchmarks with ENDF/B Data

E. M. PENNINGTON

INTRODUCTION

Calculations were performed for fast reactor benchmark assemblies according to specifications[1] supplied to members of the Cross Section Evaluation Working Group. Table II-51-I gives the atomic number densities for the constituents of these assemblies. For the original VERSION-II calculations, the basic cross section data were taken from ENDF/B tapes 201, 202, 203 and 204, which were distributed by the National Neutron Cross Section Center in the summer of 1970. The data were processed through the codes DAMMET,[2] ETOE,[3] and MERMC2[4] to produce a library for the IBM-360 version of the MC² multigroup cross section code.[5] In some cases errors in the original tapes were corrected using the CRECT[2] code.

The MC² problems were run using a 26 broad-group structure from 10 MeV down to 22.6 eV in which each group had a lethargy width of 0.5 and was subdivided into two fine groups and 60 ultra-fine groups. The consistent P_1 approximation was used in the cores with a search on B^2 to give a k_{eff} of unity, while the ordinary P_1 approximation with $B^2 = 0$ was used in the reflectors. Both core and reflector regions were treated as homogeneous. The problems were run in the ultra-fine group mode with materials having mass numbers less than 100 generally being treated as elastic scattering Legendre materials. For the Godiva and Jezebel cores, which have no light materials, the ordinary P_1; fine-group approximation was used. The fission spectrum used belonged to the isotope in the mixture undergoing most fissions.

The output MC² cross sections served as input to the specified[1] transport- or diffusion-theory approximations in spherical geometry for the calculation of k_{eff}, fluxes, and adjoint fluxes. The one-dimensional transport or diffusion paths in the ARC system[6] were followed. An ARC editing routine provided reaction rates at the core center using the calculated fluxes In the transport of diffusion calculations it was necessary to use the fission spectrum for the principal fissionable material in the core in both core and reflector because of an ARC system restriction. Information relating to the input for the criticality calculations is presented in Table II-51-II.

Perturbation calculations were performed following the diffusion theory perturbation path in the ARC system[6] to determine material central worths, effective delayed neutron fractions, and prompt neutron lifetimes. The real and adjoint fluxes from the transport or diffusion runs were used along with the MC² cross sections in these calculations. The delayed neutron data involved in computing delayed-neutron-dependent quantities were those of Keepin.[7]

Because of the low k_{eff} values obtained by the various laboratories with the original Version-II ENDF/B data, a task force meeting was held at Brookhaven National Laboratory in February 1971 to consider remedial action. It was decided to adjust cross sections of important materials within experimental error limits to give better agreement with integral experiments. A table of factors was provided to be used for computing new broad group cross sections by multiplying the original VERSION-II cross sections by these factors. The changes involved increases in the fission cross sections of ^{239}Pu, ^{235}U and ^{238}U over certain energy ranges, and a decrease in the capture cross section of ^{238}U. Table II-51-III lists the multiplicative factors which were supplied for each group. Some changes were made in the broad group fission spectra of the assemblies as well. The ARC system has provisions which enable one to rerun the transport or diffu ion problems while making the required data modifications in the same computer run.

New versions of ^{235}U, ^{238}U and ^{239}Pu in the ENDF/B

TABLE II-51-I. Atomic Number Densities for Benchmark Assemblies, 10^{24} atoms/cm^3

Material	ZPR-3-48		ZEBRA-3		JEZEBEL	GODIVA
	Core	Blanket	Core	Blanket	Core	Core
^{234}U	—	—	—	—	—	0.000492
^{235}U	0.000016	0.000083	0.000228	0.000301	—	0.045000
^{238}U	0.007405	0.039976	0.031560	0.040990	—	0.002498
^{239}Pu	0.001645	—	0.003465	—	0.037050	—
^{240}Pu	0.000107	—	0.000183	—	0.001751	—
^{241}Pu	0.000011	—	0.000016	—	0.000117	—
C	0.020770	—	—	—	—	—
Na	0.006231	—	—	—	—	—
Fe	0.010180	0.004925	0.004559	0.003496	—	—
Cr	0.002531	0.001196	0.000818	0.000913	—	—
Ni	0.001119	0.000536	0.000321	0.000360	—	—
Mn	0.000106	0.000051	—	—	—	—
Mo	0.000206	—	—	—	—	—
Al	0.000233	0.000060	—	—	—	—
Cu	—	—	0.004794	—	—	—

Material	ZPR-3-6F		VERA-1B		ZPR-3-56B	
	Core	Blanket	Core	Blanket	Core	Blanket
^{234}U	0.000069	—	0.000092	—	—	—
^{235}U	0.006727	0.000089	0.007349	0.000250	0.000014	—
^{238}U	0.007576	0.040026	0.000469	0.034400	0.006195	—
^{239}Pu	—	—	—	—	0.001358	—
^{240}Pu	—	—	—	—	0.000181	—
C	—	—	0.057540	—	0.001030	—
O	—	—	—	—	0.015000	—
Na	—	—	—	—	0.008669	0.007879
Fe	0.007712	0.004539	0.006283	0.006464	0.013700	0.007824
Cr	0.001918	0.001129	0.001635	0.001682	0.002500	0.001941
Ni	0.000839	0.000494	0.000689	0.000708	0.001090	0.042261
Mn	0.000080	0.000047	—	—	0.000220	0.000300
Mo	—	—	—	—	0.000343	—
Al	0.019019	0.001359	—	—	—	—
H	—	—	0.000058	—	—	—

TABLE II-51-II. Specifications for Criticality Calculations

Assembly	Method	Radii, cm		Mesh Intervals	
		Core	Blanket	Core	Blanket
ZPR-3-48	Diff.	46.46	76.46	30	20
ZEBRA-3	S_8	23.67	54.17	40	30
JEZEBEL	S_{16}	6.385	—	40	—
)DIVA	S_{16}	8.741	—	40	—
'R-3-6F	S_8	22.995	53.495	40	30
vERA-1B	S_8	19.138	58.588	40	40
ZPR-3-56B	S_4	52.72	87.06	40	20

TABLE II-51-III. Multiplication Factors for Broad Group Modifications to ENDF/B Cross Sections

Group	E_L, MeV	σ_f^{49}	σ_f^{28}	σ_γ^{28}	σ_f^{25}
1	6.065	1.06	1.08	—	1.08
2	3.679	1.06	1.08	—	1.08
3	2.231	1.06	1.08	—	1.08
4	1.353	1.00	1.08	—	—
5	0.8209	1.00	1.08	0.95	—
6	0.4979	1.07	1.08	0.95	—
7	0.3020	1.02	—	0.95	—
8	0.1832	1.02	—	0.95	—
9	0.1111	1.03	—	0.95	—
10	0.06738	1.05	—	—	—
11	0.04087	1.06	—	—	—
12	0.02479	1.08	—	—	—
13	0.01503	1.09	—	—	—
14	0.00912	1.10	—	—	—

TABLE II-51-IV. k_{eff} AND CORE BUCKLINGS FOR THE BENCHMARK ASSEMBLIES

Assembly	k_{eff}			B^2, cm^{-2}	
	V-II	BGM	PM	V-II	PM
ZPR-3-48	0.9614[a]	0.9939	—	0.002295	—
ZEBRA-3	0.9490	—	0.9917	0.007493	0.008412
JEZEBEL	0.9887	—	—	0.08789	—
GODIVA	1.0012	—	—	0.06573	—
ZPR-3-6F	0.9926	1.0079	1.0091	0.006261	0.006354
VERA-1B	0.9893	1.0000	0.9990	0.009845	0.009861
ZPR-3-56B	—	—	0.9989[b]	—	0.001857

[a] An S_4 transport theory calculation gave $k_{eff} = 0.9680$ for ZPR-3-48.

[b] 0.9989 = 1.0044 (from S_4) − 0.0157 (geometry correction) + 0.0102 (heterogeneity correction) as per specifications.[1]

data were processed through RIGEL[8] (which replaces DAMMET), ETOE[3] and MERMC2[4] so that a library for MC² was produced containing the original VERSION-II data and the three new materials. Some of the benchmark assemblies were rerun following the MC², transport, and perturbation paths in the ARC system using the three new materials and the original VERSION-II data for the other materials.

RESULTS

Table II-51-IV presents k_{eff} from the transport- or diffusion-theory calculations for the assemblies which were run with the original Version-II data (V-II), the broad-group-modified data (BGM), and the data modified by Pitterle (PM). Broad group bucklings for the cores from the MC² output are also given. Various results using the V-II and the BGM data were previously reported in Ref. 9.

Central fluxes, normalized to a sum of 100, are given in Table II-51-V. These were computed in the transport or diffusion calculations based on the V-II data,

TABLE II-51-V. CENTRAL FLUXES FOR BENCHMARK ASSEMBLIES

Group	E_L, MeV	ZPR-3-48	ZEBRA-3	JEZEBEL	GODIVA	ZPR-3-6F	VERA-1B	ZPR-3-56B
1	6.065	0.4349	0.5390	2.4038	1.4490	0.5968	0.6343	0.3569
2	3.679	1.7632	2.0129	9.0748	6.5053	2.7410	3.1025	1.4640
3	2.231	3.8653	3.7190	15.900	13.637	6.4488	7.6010	3.5640
4	1.353	5.8870	4.8331	18.365	17.910	9.6247	12.152	5.0526
5	0.8209	7.5246	8.2224	17.264	17.952	12.411	12.875	6.0154
6	0.4979	9.8457	15.330	13.887	15.832	16.661	12.389	10.973
7	0.3020	11.576	18.378	10.149	12.107	16.758	11.298	10.110
8	0.1832	10.999	15.932	6.2424	7.3613	13.480	9.5823	12.431
9	0.1111	10.252	11.899	3.4313	3.9450	9.2541	7.9331	12.247
10	0.06738	8.6547	8.6348	1.7620	1.9216	5.8305	6.2944	10.043
11	0.04087	7.0949	5.5806	0.8553	0.8502	3.6497	4.9164	7.5965
12	0.02479	5.1991	2.5930	0.3849	0.3352	1.4130	3.5453	5.0281
13	0.01503	5.0925	1.6138	0.1643	0.1213	0.8486	2.7709	5.4592
14	0.00912	3.9391	0.4883	0.0695	0.0458	0.2008	1.9640	3.7156
15	0.00553	2.4996	0.1517	0.0279	0.0174	0.0519	1.2624	2.0310
16	0.00335	1.6394	0.0514	0.0110	0.0059	0.0218	0.8148	1.2146
17	0.00203	0.7499	0.0137	0.0045	0.0021	0.0056	0.4669	0.4426
18	0.00123	1.3160	0.0053	0.0020	0.0008	0.0017	0.2366	1.0811
19	0.000749	0.8148	0.0015	0.0008	0.0003	0.0005	0.1027	0.6472
20	0.000454	0.4697	0.0005	0.0003	0.0001	0.0002	0.0386	0.3295
21	0.000275	0.2253	0.0002	0.0001	—	0.0001	0.0137	0.1232
22	0.000167	0.0976	—	0.0001	—	—	0.0041	0.0501
23	0.000101	0.0411	—	—	—	—	0.0014	0.0183
24	0.0000614	0.0146	—	—	—	—	0.0006	0.0052
25	0.0000373	0.0027	—	—	—	—	0.0002	0.0007
26	0.0000226	0.0007	—	—	—	—	0.0001	0.0001
27	0.0	0.0005	—	—	—	—	0.0001	0.0001
1–6	—	29.321	34.656	76.895	73.286	48.483	48.753	27.426
7–13	—	58.868	64.631	22.989	26.642	51.234	46.341	62.915
14–27	—	11.811	0.713	0.116	0.072	0.283	4.906	9.659

format were provided by T. Pitterle* and were distributed by the National Neutron Cross Section Center to CSEWG in the spring of 1971 on tape 700. These

* Westinghouse Advanced Reactor Division, Westinghouse Electric Corporation.

TABLE II-51-VI. ONE-GROUP CROSS SECTIONS AT CORE CENTERS, b

Isotope	Cross Section	ZPR-3-48		ZEBRA-3		GODIVA	ZPR-3-56B	ZPR-3-6F			VERA-1B		
		V-II	BGM	V-II	PM	V-II	PM	V-II	BGM	PM	V-II	BGM	PM
^{233}U	(n,γ)	0.3190	—	0.1692	—	0.08652	—	0.1392	0.1393	—	0.1753	0.1754	—
	(n,f)	2.819	—	2.162	—	1.963	—	2.079	2.080	—	2.302	2.303	—
^{235}U	(n,γ)	0.5480	0.5444	0.2807	0.2744	0.1312	0.5064	0.2222	0.2224	0.2217	0.3130	0.3135	0.3145
	(n,f)	1.958	1.957	1.411	1.396	1.252	1.848	1.343	1.352	1.340	1.538	1.550	1.539
^{238}U	(n,γ)	0.2762	0.2711	0.1687	0.1549	0.1079	0.2590	0.1462	0.1413	0.1354	0.2013	0.1976	0.1952
	(n,f)	0.05854	0.06373	0.05597	0.05855	0.1942	0.05410	0.09468	0.1024	0.09947	0.1134	0.1226	0.1195
^{239}Pu	(n,γ)	0.4302	0.4264	0.1574	0.1723	0.06224	0.4144	0.1192	0.1193	—	0.2128	0.2124	—
	(n,f)	1.794	1.857	1.592	1.639	1.706	1.805	1.627	1.681	—	1.699	1.757	—
^{240}Pu	(n,γ)	0.4014	0.3986	0.1962	0.1920	0.1115	0.3593	0.1637	0.1638	—	0.2276	0.2280	—
	(n,f)	0.4475	0.4490	0.4824	0.4839	1.022	0.4093	0.6654	0.6647	—	0.7005	0.7001	—

TABLE II-51-VII. ACTIVATION RATIOS AT CORE CENTERS

Ratio	ZPR-3-48			ZEBRA-3		
	V-II	BGM	Expt.	V-II	PM	Expt.
$\sigma_f^{28}/\sigma_f^{25}$	0.02990	0.03257	0.0307 ± 0.0004	0.03966	0.04194	0.0461 ± 0.0008
$\sigma_\gamma^{28}/\sigma_f^{25}$	0.1411	0.1385	0.138 ± 0.004	0.1195	0.1109	—
$\sigma_f^{49}/\sigma_f^{25}$	0.9164	0.9490	0.976 ± 0.010	1.128	1.174	1.190 ± 0.014
$\sigma_f^{23}/\sigma_f^{25}$	1.440	—	1.480 ± 0.015	1.532	—	1.542 ± 0.019
$\sigma_f^{40}/\sigma_f^{25}$	0.2286	0.2295	0.243 ± 0.002	0.3418	0.3466	0.373 ± 0.005

Ratio	GODIVA		ZPR-3-6F			
	V-II	Expt.	V-II	BGM	PM	Expt.
$\sigma_f^{28}/\sigma_f^{25}$	0.1551	0.156 ± 0.005	0.07053	0.07576	0.07422	0.078 ± 0.002
$\sigma_\gamma^{28}/\sigma_f^{25}$	0.08613	—	0.1089	0.1045	0.1010	0.104 ± 0.003
$\sigma_f^{49}/\sigma_f^{25}$	1.363	1.42 ± 0.02	1.212	1.244	—	1.22 ± 0.03
$\sigma_f^{23}/\sigma_f^{25}$	1.567	1.63 ± 0.10	1.549	1.538	—	1.53 ± 0.03
$\sigma_f^{40}/\sigma_f^{25}$	—	—	0.4957	0.4916	—	0.53 ± 0.02

Ratio	VERA-1B				ZPR-3-56B	
	V-II	BGM	PM	Expt.	PM	Expt.
$\sigma_f^{28}/\sigma_f^{25}$	0.0737	0.07912	0.07764	0.067 ± 0.001	0.02928	0.0308 ± 0.0003
$\sigma_\gamma^{28}/\sigma_f^{25}$	0.1309	0.1275	0.1268	0.131 ± 0.006	0.1402	—
$\sigma_f^{49}/\sigma_f^{25}$	1.104	1.134	—	1.070 ± 0.026	0.9768	1.028 ± 0.010
$\sigma_f^{23}/\sigma_f^{25}$	1.496	1.486	—	1.433 ± 0.047	—	—
$\sigma_f^{40}/\sigma_f^{25}$	0.4554	0.4517	—	0.40 ± 0.03	0.2215	0.282 ± 0.003

except for ZPR-3-56B for which the PM data were used.

Table II-51-VI gives one group cross sections at the re center from the transport or diffusion problems r ^{233}U, ^{235}U, ^{238}U, ^{239}Pu and ^{240}Pu. The cross sections nvolved have the shielding of the core mixture for the actual core constituents, and are at infinite dilution otherwise. Activation ratios at the core center are presented in Table II-51-VII, and are compared with experimental values.

Calculated and experimental worths are compared in Table II-51-VIII.

Delayed neutron fractions and prompt neutron lifetimes are presented in Table II-51-IX. The computed

TABLE II-51-VIII. Central Worths for Benchmark Assemblies, 10^{-5} $\Delta k/k$-mole

Material	ZPR-3-48		ZEBRA-3			ZPR-3-6F		
	V-II	Expt.	V-II	PM	Expt.	V-II	PM	Expt.
^{235}U	106.2	79.3 ± 0.9	287.8	252.5	197 ± 4	162.5	154.8	137 ± 5
^{238}U	−7.640	−5.9 ± 0.1	−14.98	−12.84	−9.9 ± 0.4	1.647	2.380	1.5 ± 0.5
^{239}Pu	136.9	106.1 ± 0.9	440.6	405.4	318 ± 8	277.5[a]	—	251 ± 12[a]
^{240}Pu	23.01	19.4 ± 5.0	—	—	—			
^{10}B	−100.6	−89.1 ± 0.9	−128.6	—	−105 ± 5	−93.76	—	−86 ± 5
^{12}C	−0.2001	−0.05 ± 0.03	−3.874	—	−3.9 ± 0.2	—	—	—
Al	−0.5220	−0.42 ± 0.03	—	—	—	0.2173	0.09280	0.23 ± 0.35
Mn	−2.116	−1.18 ± 0.04	—	—	—	−0.3533	−0.5521	−0.65 ± 0.24
Cr	−1.014	−0.49 ± 0.04	—	—	—	−1.250	−1.356	−0.55 ± 0.19
Fe	−0.9647	−0.69 ± 0.04	—	—	—	−0.9715	−1.085	−0.9 ± 0.3
Ni	−1.757	−1.07 ± 0.04	—	—	—	−3.295	−3.380	−1.7 ± 0.5

Material	VERA-1B			GODIVA		ZPR-3-56B	
	V-II	PM	Expt.	V-II	Expt.	PM	Expt.
^{235}U	239.4	230.9	221 ± 3	1004	983 ± 7	80.99	78.3 ± 2.2
^{238}U	12.13	12.13	7.5 ± 0.3	144.7	160 ± 2	−5.806	−4.95 ± 0.22
^{239}Pu	423.3	—	387 ± 5	1905	1881 ± 13	109.8	100.5 ± 2.0
^{240}Pu	—	—	—	1107	1122 ± 130	—	—
^{10}B	−267.2	—	−237 ± 50	—	—	—	—
^{12}C	7.213	6.785	5.95 ± 0.12	—	—	−0.5707	−0.338 ± 0.034
^{23}Na	—	—	—	—	—	−0.4164	−0.232 ± 0.109
Cr	2.641	2.255	—	—	—	−0.8367	−0.749 ± 0.073
Fe	2.512	2.152	—	—	—	−0.7991	−0.776 ± 0.029
Ni	−1.047	−1.142	—	—	—	−1.474	−1.115 ± 0.037
Steel[b]	2.252	1.908	2.1 ± 0.3	—	—	—	—
^{197}Au	−44.09	—	−26 ± 1	−63.64	−49 ± 2	—	—

[a] 95.5% ^{239}Pu, 4.5% ^{240}Pu.
[b] Steel is 73% Fe, 19% Cr, 8% Ni.

TABLE II-51-IX. Delayed Neutron Fractions and Prompt Neutron Lifetimes

Assembly	β_{eff}		ℓ, sec	
	V-II	PM	VI-II	PM
ZPR-3-48	0.003398	—	2.737×10^{-7}	—
ZEBRA-3	0.004159	0.004192	6.025×10^{-8}	6.081×10^{-8}
GODIVA	0.006607	—	5.987×10^{-9}	—
ZPR-3-6F	0.007220	0.007206	7.284×10^{-8}	7.325×10^{-8}
VERA-1B	0.007477	0.007433	1.000×10^{-7}	1.003×10^{-7}
ZPR-3-56B	—	0.003139	—	2.021×10^{-6}

quantities are not highly accurate since the only prompt fission spectrum involved is that of the principal fissionable material in the core.

Discussion

The original Version-II cross sections produced values of k_{eff} which are considerably low, especially for the ^{239}Pu fueled assemblies. This suggested that Version-II cross sections for important materials such as ^{239}Pu, ^{238}U and ^{235}U are not sufficiently accurate. The broad-group modifications proposed by the ENDF/B task force led to better k_{eff} values, as did the Pitterle modifications on tape 700. Since changes in basic data within limits of experimental error can make rather large differences in integral quantities, it is not possible to compile sufficiently accurate data for reactor calculations by evaluating experimental differential data without reference to results of integral experiments. However, integral results must be used with caution as they depend on many energy-dependent cross sections. Various cross section changes could combine to give about the same changes in integral quantities. The improvements in k_{eff} resulting from using either the broad-group modified or the Pitterle modified data are largely attributable to a decrease in the capture cross sections of ^{238}U and increases in the fission cross sections of ^{239}Pu and ^{238}U.

It should be pointed out that not all differences b tween experimental and computed quantities can be attributed to inaccurate cross sections. The transformation of the actual heterogeneous three-dimensional

benchmark assemblies to homogeneous spherical geometry can introduce some error. Also the computational methods have some defects such as the use of only one fission spectrum for core and blanket, and the approximate treatment of elastic slowing-down by heavy materials in MC². There is room for future work both in data compilation with better consideration of integral results and in improvement of calculational methods.

References

1. W. G. Davey and A. L. Hess, Argonne National Laboratory, *Additional Fast Reactor Benchmarks for Phase II-Data Testing of ENDF/B*, memo distributed to members of the CSEWG, February 21, 1969; also see H. Alter, Atomics International, *Additional Fast Reactor Benchmarks*, memo distributed to CSEWG members, April 7, 1971.
2. National Neutron Cross Section Center, *Description of the ENDF/B Processing Codes CHECKER, CRECT, DAMMET, PLOTFB and Retrieval Subroutines*, BNL-13582 (ENDF-110), (September 1967). (Revised April 1969.)
3. D. M. Green and T. A. Pitterle, *ETOE, A Program for ENDF/B to MC² Data Conversion*, APDA-219 (ENDF-120), June 1968.
4. E. M. Pennington, J. C. Gajniak, A. B. Cohen and W. Bohl, *Service Routines for the Multigroup Cross-Section Code MC²*, ANL-7654 (1970).
5. B. J. Toppel, A. L. Rago and D. M. O'Shea, *MC²*, *A Code to Calculate Multigroup Cross Sections*, ANL-7318 (1967).
6. B. J. Toppel, Ed., *The Argonne Reactor Computation (ARC) System*, ANL-7332 (1967).
7. G. R. Keepin, *Physics of Nuclear Kinetics*, (Addison-Wesley Publishing Company, Inc., Reading, Massachusetts, 1965).
8. D. E. Cullen, Brookhaven National Laboratory, *Program RIGEL*, Draft of a report distributed to CSEWG members, April 13, 1970.
9. E. M. Pennington, *Calculations for Fast Reactor Benchmarks with Version-II ENDF/B Data*, Proc. Third Conference on Neutron Cross Sections and Technology, University of Tennessee, Knoxville, March 15–17, 1971. CONF-710301, Vol. 1, pp. 51–57.

II-52. Sensitivity Studies of the Effect of Uncertainty in the $^{238}U(n,\gamma)$ and in the $^{239}Pu(n,f)$ and (n,γ) Cross Sections

H. H. Hummel

A paper bearing the above title has been published[1] and a somewhat more complete version was issued as an ANL report.[2]

A spherical model of a large LMFBR with two enrichment zones in the core was used to determine variations in k, breeding ratio, sodium void effect, and ^{238}U Doppler effect associated with assumed uncertainties in the $^{238}U(n,\gamma)$ and in the $^{239}Pu(n,f)$ and (n,γ) cross sections.

The assumed variations for the $^{238}U(n,\gamma)$ cross section were of the order of $\pm 15\,\%$ for energies below 100 keV and $\pm 10\,\%$ for energies from 100 keV to 1 MeV, which is probably somewhat pessimistic. In the unresolved resonance region up to 25 keV the cross section variation was assumed to correspond to a variation in the p-wave strength function. Total variations found in the reactor parameters for extreme variations in the $^{238}U(n,\gamma)$ cross section were about 3 % in k, 0.10 in breeding ratio, 5 % of the total-core sodium voiding effect which was 2.7 % k, and 20 % in the ^{238}U Doppler effect.

For $^{239}Pu(n,f)$ and (n,γ) cross sections a number of measurements have recently become available for energies below 30 keV tabulated in common energy intervals, thereby facilitiating comparison. It was assumed that variations among these measurements represented reasonable uncertainty limits. The tabulated values were used directly to produce variations in reactor characteristics, except that a common self-shielding correction was applied for energies below 5 keV. For variations in $^{239}Pu(n,f)$ cross sections, holding $\alpha = \sigma(n,\gamma)/\sigma(n,f)$ constant, extreme variations in the following parameters were found: about 1 % in k, 0.004 in breeding ratio, 3 % in ^{238}U Doppler effect, and 12 % in sodium void effect. For α variations with the $^{239}Pu(n,f)$ cross section held constant, the extreme variations were about 0.8 % in k, 0.05 in breeding ratio, 11 % in sodium void effect, and 12 % in ^{238}U Doppler effect.

For $^{239}Pu(n,f)$ cross sections above 30 keV, with α held constant, a variation of about 15 % was made between 40 keV and 1 MeV, corresponding to the difference between the White[3] and Poenitz[4] (preliminary) ^{235}U fission cross sections used as a standard. This was considered to be a representative uncertainty. It produced a variation of about 3 % in k, 10 % in sodium void effect, and insignificant changes in the other quantities. A variation of 20 % in α above 30 keV produced a change of 0.02 in breeding ratio and minor changes in the other quantities.

The variations in parameters quoted above are based on adjustment to critical by enrichment variation following a cross section variation. Other methods of adjusting to critical did not change the results greatly.

Although not all possible cross section uncertainties have been studied, it is believed that those considered here are the most important ones. It is obvious that uncertainties in k and in breeding ratio are still far too large, with cross sections of both ^{238}U and ^{239}Pu being important contributors. While much progress has been made in the α measurement of ^{239}Pu in the last several years, the lack of agreement among various measurements still constitutes a problem. There has been a large reduction in uncertainty in sodium void effect calculations recently because of the improvement in knowledge of both $\sigma(n,f)$ and α of ^{239}Pu below 30 keV.

References

1. H. H. Hummel, *Sensitivity Studies of the Effect of Uncertainty in the $^{238}U(n,\gamma)$ and in the $^{239}Pu(n,f)$ and (n,γ) Cross Sections*, Proc. Third Conference on Neutron Cross Sections and Technology, March 15–17, 1971, University of Tennessee, Knoxville, Tennessee, CONF-710301, Vol. I., pp. 65–71.
2. H. H. Hummel, *Sensitivity Studies of the Effect of Uncertainty in the $^{238}U(n,\gamma)$ and in the $^{239}Pu(n,f)$ and (n,γ) Cross Sections*, ANL-7851 (August 1971).
3. P. H. White, *Measurements of the ^{235}U Neutron Fission Cross Sections in the Energy Range 0.14 MeV*, J. Nucl. Energy **19**, 325 (1965).
4. W. P. Poenitz, *Measurement of the ^{235}U Fission Cross Section in the keV Energy Range*, Proc. Conference on Neutron Cross Sections and Technology, Washington, D. C., March 1968, Vol. I, p. 503.

II-53. Comparisons of ENDF/B VERSIONS I, II and II-Modified

R. A. Karam, W. R. Robinson, M. Salvatores* and C. E. Till

Introduction

ZPR-6 Assembly 6A, a uranium benchmark critical, and ZPR-6 Assembly 7, a plutonium benchmark critical, were chosen for comparison of ENDF/B VERSIONS I, II and II-Modified. Assemblies 6A and 7 had essentially the same composition in diluent materials and had the same unit-cell structure; the main difference between the two assemblies was that Assembly 7 simulated a typical LMFBR $(Pu\text{-}U)O_2$ composition and Assembly 6A simulated a UO_2 composition. The material composition, the unit-cell structure, and other details pertinent to the assemblies can be found in Paper II-11.

MC² Calculations

Three MC² calculations (consistent B-1) were performed to generate three 27-group cross sections sets for the homogeneous composition of ZPR-6 Assembly 7. This assembly is a Demonstration Plant Benchmark Critical fueled with plutonium. ENDF/B-VERSION I data were used in one calculation; ENDF/B-VERSION II data were used in the second; and in the third, ENDF/B-VERSION II data were used for all isotopes except iron, nickel and chromium (stainless steel). In the third case, the data for iron, nickel and chromium came from the ENDF/B-VERSION I file. The second and third MC² calculations were made in order to evaluate the effects on the critical parameters of including the 665 resolved resonances of iron, nickel and chromium in ENDF/B-VERSION II.

For ZPR-6 Assembly 6A, the uranium-fueled Demonstration Plant Benchmark Critical, two MC² calculations were performed: (1) ENDF/B-VERSION I data were used for all isotopes and (2) ENDF/B-VERSION II data were used for all isotopes except stainless steel. The data for stainless steel in the second problem were taken from the ENDF/B-VERSION I file.

ENDF/B-VERSION II Modification

Tests of ENDF/B-VERSION II on the benchmark criticals gave k_{eff} predictions in the range 0.95 to 0.97. The Cross Section Evaluation Working Group (CSEWG) recommended the following tentative modifications at the broad group (0.5 Δu) level:

1. increase σ_f^{235} in the first three groups by 8%,
2. increase σ_f^{238} in the first six groups by 8%,
3. decrease σ_c^{238} in groups 5–9 by 5%,
4. multiply σ_f^{239} in groups 1–14 by the following factors:

Group	Factor
1	1.06
2	1.06
3	1.06
4	1.00
5	1.00

* Comitato Nazionale per L'Energia Nucleare, Casaccia, Italy.

TABLE II-53-I. k COMPARISONS ENDF/B-I, -II, AND -II MODIFIED[a]

	Assembly 7				Assembly 6A		
	Version-I	Version-II with Version-I SS	Version-II	Version-II Modified	Version-I	Version-II with Version-I SS	Version-II Modified with Version-I SS
2-D Homogeneous Cylinder	0.9616	—	—	—	0.9818	—	—
1-D Homogeneous Sphere	0.9616	0.9469	0.9469	0.9768	0.9818	0.9698	0.9781

[a] Heterogeneities are not accounted for in any manner.

TABLE II-53-II. REACTION RATIOS

	Assembly 7				Assembly 6A		
	ENDF/B-I	ENDF/B-II with Version-I SS	ENDF/B-II	ENDF/B-II Modified	ENDF/B-I	ENDF/B-II with Version-I SS	ENDF/B-II Modified with Version-I SS
U_f^{235}/Pu_f^{239}	1.140	1.136	1.140	1.100	1.079	1.080	1.042
U_f^{238}/Pu_f^{239}	0.0235	0.0224	0.0230	0.0240	0.0234	0.0226	0.0233
U_c^{238}/Pu_f^{239}	0.1664	0.1688	0.1667	0.1583	0.1615	0.1609	0.1530

Group	Factor
6	1.07
7	1.02
8	1.02
9	1.03
10	1.05
11	1.06
12	1.08
13	1.09
14	1.10

In all cases, the corresponding change in σ_{tr} was incorporated.

k CALCULATIONS

The MC², ENDF/B-VERSION I, homogeneous cross sections were used to calculate k_{eff} of the as-built assemblies with a 2-D diffusion code.[1] The k_{eff} from the 2-D calculation was then used in a 1-D spherical calculation and the radius of the sphere which gave the same k_{eff} as the 2-D calculation k_{eff} was determined. This spherical radius was then held constant in the calculation of the spherical k_{eff}, using the MC²-generated ENDF/B VERSION II and the broad-group-modified ENDF/B VERSION II cross sections. Table II-53-I summarizes the results. The modification of ENDF/B-VERSION II is seen to increase the k_{eff} of Assembly 7, a plutonium-fueled system, and the k_{eff} of Assembly 6A, a uranium-fueled system, by 3% and 83%, respectively.

REACTION RATIOS

The reaction ratios with the various sets are given in Table II-53-II. These ratios were computed for samples at the center of each sphere using the homogeneous sets.

THE CAPTURE-TO-FISSION RATIO α

The capture-to-fission ratio of ^{239}Pu and ^{235}U in Assemblies 7 and 6A respectively were calculated for samples at the center of each assembly using the various sets. Table II-53-III summarizes the results.

CENTRAL REACTIVITY WORTHS

The reactivity worths were calculated for a few samples at the center of each core with the various cross section sets using first-order perturbation theory. The results are summarized in Table II-53-IV.

NEUTRON SPECTRUM

A comparison of the neutron spectra obtained with the various sets is shown in Table II-53-V.

TABLE II-53-III. THE CAPTURE-TO-FISSION RATIO COMPARISON

Assembly 7, α^{239}			Assembly 6A, α^{235}		
ENDF/B-I	ENDF/B-II	ENDF/B-II Modified	ENDF/B-I	ENDF/B-II with Version-I SS	ENDF/B-II Modified with Version-I SS
0.2446	0.2798	0.2753	0.2823	0.2828	0.2841

TABLE II-53-IV. CENTRAL REACTIVITY WORTH COMPARISON, Ih/kg[a]

Sample	Assembly 6A			Assembly 7			
	ENDF/B-I	ENDF/B-II with Version-I SS	ENDF/B-II Modified with Version-I SS	ENDF/B-I	ENDF/B-II with Version-I SS	ENDF/B-II	ENDF/B-II Modified
^{235}U	48.99	+48.53	+48.71	172.0	172.0	169.9	166.78
^{239}Pu	62.69	+63.32	63.41	202.9	201.5	198.9	204.33
^{10}B	−1189.79	−1178.32	−1095.2	−3470	−3342	−3450	−3211
Ta	−19.95	−19.77	−19.91	−66.81	−64.2	−68.0	−67.99
Na	+0.100	+0.136	0.0107	−6.21	−6.94	−6.06	−7.11
^{238}U	−4.42	−4.41	−4.33	−12.83	−12.48	−12.48	−12.31

[a] 1% $\Delta k/k$ in Assembly 6A = 458 Ih; 1% $\Delta k/k$ in Assembly 7 = 1035 Ih.

TABLE II-53-V. SPECTRUM COMPARISON WITH THE VARIOUS SETS

Group	Lower Energy Level, keV	Assembly 6A			Assembly 7		
		ENDF/B Version-I	ENDF/B-II with Version-I SS	ENDF/B-II Modified with Version-I SS	ENDF/B Version-I	ENDF/B Version-II	ENDF/B Version-II Modified
1	6065.0	0.200	0.216	0.215	0.289	0.297	0.296
2	3679.0	0.982	1.021	1.017	1.168	1.199	1.202
3	2231.0	2.726	2.756	2.738	2.850	2.952	2.953
4	1353.0	4.112	4.266	4.243	3.994	4.254	4.263
5	820.8	5.237	5.409	5.398	4.945	5.086	5.110
6	497.9	10.272	10.469	10.456	9.618	9.518	9.543
7	302.0	9.669	9.711	9.705	9.098	9.175	9.205
8	183.2	12.658	12.609	12.615	11.927	11.644	11.692
9	111.1	11.887	11.805	11.823	11.297	12.047	12.101
10	67.38	10.668	10.556	10.569	10.288	10.240	10.262
11	40.87	8.661	8.528	8.539	8.532	8.062	8.060
12	24.79	6.671	6.588	6.593	5.830	5.582	5.567
13	15.03	5.899	5.826	5.838	5.256	6.474	6.429
14	9.119	3.992	3.930	3.935	4.412	4.655	4.601
15	5.531	2.221	2.194	2.197	2.599	2.632	2.602
16	3.355	1.277	1.263	1.264	1.569	1.604	1.585
17	2.035	0.452	0.454	0.454	0.563	0.592	0.585
18	1.234	1.203	1.191	1.192	1.615	1.670	1.651
19	0.749	0.691	0.686	0.687	1.063	1.128	1.115
20	0.454	0.330	0.328	0.328	0.617	0.669	0.661
21	0.275	0.122	0.121	0.121	0.264	0.291	0.288
22	0.101	0.064	0.067	0.067	0.182	0.204	0.202
23	0.037	0.005	0.006	0.007	0.021	0.024	0.024
24	0.014	—	—	—	0.0007	0.0009	0.0009
25	0.005	—	—	—	—	—	—
26	0.0006	—	—	—	—	—	—
27	—	—	—	—	—	—	—

MC² TIME REQUIREMENT

The time requirements for the MC² problems on the IBM-360-75 are compared in Table II-53-VI.

SUMMARY

For Assembly 7 the predicted k_{eff} with the modified ENDF/B-II set was 3% more reactive than that obtained with ENDF/B-II and 1.5% more reactive than that obtained with ENDF/B-I. For Assembly 6A the predicted k_{eff} with the modified ENDF/B-II set was 0.83% more reactive than that obtained with ENDF/B-II and 0.37% less than that obtained with ENDF/B-I. The heterogeneity effects for Assemblies 7 and 6A are estimated to be 1.35% $\Delta k/k$, respectively (see Paper II-11).

The use of the modified ENDF/B-II set resulted in a 3.5 to 4 % decrease in $^{235}U/^{239}Pu$ fission ratios relative to ENDF/B-II and ENDF/B-I sets. An increase of the same magnitude was obtained for the $^{238}U/^{238}Pu$ fission ratio. The ratio of capture in ^{238}U to fission in ^{239}Pu decreased by 5 %. These changes are in the general direction of agreement with measurement (see Paper II-11).

The ^{235}U capture-to-fission ratio in Assembly 6A was essentially the same with all sets. There was a significant change ($\sim$5 %) in α^{239} between ENDF/B-I and ENDF/B-II. The change in α between ENDF/B-II and modified ENDF/B-II was only 1.5 %.

The central reactivity worths with all sets were approximately the same.

The neutron spectrum obtained with ENDF/B-VERSION II is similar to that obtained with ENDF/B-VERSION II Modified. Both spectra are harder in the high-energy groups and softer in the lower-energy groups than that obtained with ENDF/B-VERSION I.

TABLE II-53-VI. MC² Time Requirements for ZPR-6 Assemblies 6A and 7 using ENDF/B-I and -II and Combinations Thereof

Assembly	ENDF/B-I, min	ENDF/B-II, min	ENDF/B-II with SS from ENDF/B-I, min
6A	26	—	30
7	40	92	55

The effect of including the 665 resonances of iron, nickel, and chromium in ENDF/B-VERSION II on k_{eff}, the reaction ratios, the central reactivity worths, and on the capture-to-fission ratio is not large enough for normal purposes to justify the increase in computation time associated with using stainless steel of VERSION II.

Reference

1. B. J. Toppel, *The Argonne Reactor Computation (ARC) System*, Anl-7332 (1967).

II-54. A Study of Methods of Cross Section Error Identification Utilizing Integral Data from Fast Critical Assemblies

K. O. Ott,* R. B. Pond and J. M. Kallfelz†

Introduction

In Ref. 1 a general discussion concerning cross section data adjustment philosophies utilizing integral data from fast critical assemblies was presented. Despite the assumption that cross section information is contained in the deviations between theoretical and experimental integral results, considerable disagreement about the best method of extracting this information persists. The study in Ref. 1 also outlined the four fitting procedures which encompass the current data adjustment philosophies.

The present paper (see also Ref. 2) summarizes a uniform comparison of these four cross section data adjustment procedures and further investigates each procedure as a function of the uncertainty in the experimental integral data and the uncertainty in the theoretical microscopic cross section data. A simulation of fifty critical assemblies in a one-group, zero-dimensional model was used as a basis to investigate the adjustment procedures.

A description of this work, including some numerical results and conclusions, has been published in Ref. 2.

The Adjustment Procedures

The four adjustment procedures described in Ref. 1 lead to the following system of equations characterized by the free parameter γ:

$$\sum_{k'}^{K} h_{kk'} u_{k'} = b_k \qquad (1)$$

with

$$h_{kk'} = \sum_{n}^{N} \frac{H_{kn} H_{k'n}}{(s_n^\rho)^2} + \gamma \frac{\delta_{kk'}}{(s_k^\sigma)^2}$$

$$b_k = -\sum_{n}^{N} \frac{H_{kn}}{(s_n^\rho)^2} \Delta\rho_n ,$$

where

s_n^ρ is the average reactivity error of the nth integral experiment,
s_k^σ is the error in the theoretical kth cross section,
u_k is the kth cross section change to be found by the fitting procedure,

* Purdue University, Lafayette, Indiana.
† Georgia Institute of Technology, Atlanta, Georgia.

$\Delta\rho_n$ is the difference between the experimental and the theoretically predicted reactivities,

H_{kn} is the sensitivity of the criticality in the nth integral experiment with respect to the theoretical kth cross section change, u_k^{th}.

Letting $h^{kk'}$ denote the inverse of $h_{kk'}$, the solution of Eq. (1) is given by

$$u_k = \sum_{k'}^{K} b_{k'} h^{kk'} . \tag{2}$$

The specification of γ is as follows:

1. Procedure No. 1 ($\gamma = 0$) is the no-constraint procedure, which is the weighted least square fit of the measured and the calculated experimental reactivities.
2. Procedure No. 2 ($\gamma = 1$) is the combined-fit procedure, which is the weighted least square fit of both the reactivities and the cross sections.
3. Procedure No. 3 ($\gamma = 1/\Lambda$) is the fixed-square-fit procedure, which is the weighted least square fit of the cross sections subject to the constraint

$$\frac{1}{N}\sum_{n}^{N} (1/s_n^{\rho})^2 \left[\sum_{k}^{K} H_{kn} u_k(\Lambda) + \Delta\rho_n\right]^2 = 1 .$$

4. Procedure No. 4 ($\gamma = \Lambda'/\beta^2$) is the ellipsoidal-constraint fit, which is the weighted least square fit of the reactivities subject to the constraint

$$\sum_{k}^{K} [u_k^2(\Lambda')/(\beta s_k^{\sigma})^2] = 1$$

if the result of the unconstrained fit (Procedure No. 1) is outside the constraint ellipsoid.

In Procedure Nos. 3 and 4 above, Λ and Λ' are Lagrange multipliers introduced in the weighted least square minimum principal. The multipliers are determined by iterating either Λ or Λ' in the fit until the respective constraint conditions are met.

In principal γ ranges between 0 and ∞. The specific value of γ emphasizes either a bias toward the integral experiments or toward the cross section data. For the extreme $\gamma = \infty (\beta = 0)$, $u_k = 0$, i.e., no adjustment in the cross sections is allowed.

Procedure No. 4 is extremely useful as a universal adjustment procedure to investigate systematically the effect of γ in the fitting procedure since it provides a measure of the bias toward integral or differential experiments in terms of the size of the constraint ellipsoid. As a result of this feature, there are values of β such that $\gamma = 0$, 1, and $1/\Lambda$, and hence Procedure Nos. 1–3 correspond to specific values of β in Procedure No. 4. The maximum size of the constraint ellipsoid (β_{max}) corresponds to $\gamma = 0$. The increase of β beyond β_{max} does not change the fit, i.e., for $\beta \geq \beta_{max}$, $\gamma = 0$.

Cross Section Identification

The error identification achieved by a fitting procedure can be described by a figure-of-merit defined as

$$f(\beta) = \frac{\sum_{k}^{K'} (1/s_k^{\sigma})^2 \left| u_k - u_k^{\text{th}} \right|}{\sum_{k}^{K'} (1/s_k^{\sigma})^2 \left| u_k^{\text{th}} \right|} , \tag{3}$$

where $1 \leq K' \leq K$ and $0 \leq \beta \leq \beta_{max}$. It is this figure-of-merit which indicates accumulative cross section identification for different adjustment procedures and also the sensitivity of the adjustment procedures to uncertainties in the integral data (s_n^{ρ}) and in the cross section data (s_k^{σ}).

Error Identification of the Adjustment Procedures

Figure-of-merit as a function of β

The error identification is practically independent of s_n^{ρ} for small βs ($\beta \lesssim 1.75$) and becomes increasingly dependent on s_n^{ρ} for larger βs. Between $1.75 \lesssim \beta \lesssim 2.25$ the error identification passes through a minimum as β approaches β_{max}. For very small s_n^{ρ} (0.01 %) the minimum may be identical with $f(\beta_{max})$. Generally for s_n^{ρ} in the range 0.1 to 0.3 %, the fixed-square fit (Procedure No. 3) is located near the minimum while the combined-fit (Procedure No. 2) is located between the fixed-square and the no-constraint fits (Procedure Nos. 3 and 1). Since Procedure Nos. 1–3 generally correspond to relatively large β values, the error identification is strongly improved by increased accuracy of the integral data.

Systematic errors in s_n^{ρ}

In the fitting procedure the term $\Delta\rho_n$ is the difference between the experimental and the theoretically predicted reactivities. The average reactivity error in the experimental value includes for the nth integral experiment a systematic, $\delta\rho^{syst}$, and a statistical, $\delta\rho^{stat}$, component. To find out how the different adjustment procedures behave for a wide range of systematic errors, the average criticality constants were shifted by letting $\delta\rho^{syst}$ vary from -2 % to $+2$ % while the statistical error $\delta\rho^{stat}$ (the straggling about the average criticality constant) was held at 0.1 %. In the adjustment procedure only the statistical error ($s_n^{\rho} = \delta\rho_n^{stat}$) was used. The systematic error was not considered in the adjustment procedure in accordance with the fact that practically neither its size nor its sign is known.

The results of this investigation for the different adjustment procedures showed that the cross section identification (figure-of-merit) is considerably less sensitive to $\delta\rho^{syst}$ for a given $\delta\rho^{stat}$ than is $f(\beta)$ to $\delta\rho^{stat}$

for $\delta\rho^{syst} = 0.0$. The fact that minor modifications of the microscopic data may significantly shift the average criticality constant can be considered as an explanation of the insensitivity of the adjustment procedures to systematic errors. The systematic error in the reactivity may therefore be practically disregarded and only the comparatively small statistical error influences the cross section error identification. It is essentially the reduction of the straggling which yields accurate error identification. To a first approximation one may delete the systematic errors and work in the adjustment procedures only with the nonsystematic and statistical components.

UNCERTAINTY IN s_k^σ

The uncertainty of the errors in the microscopic data was introduced into the fitting procedures by multiplying the values of s_k^σ by a constant α^σ. A value of $\alpha^\sigma > 1$ describes an overestimate of the s_k^σ errors and $\alpha^\sigma < 1$ an underestimate.

The no-constraint and the fixed-square procedures (Procedure Nos. 1 and 3) are by definition of the procedures independent of α^σ. In the combined-fit (Procedure No. 2), the error identification does change but it is a relatively slowly varying function of α^σ.

UNCERTAINTY IN s_n^ρ

The uncertainty of the errors in the integral measurements was introduced into the fitting procedures by multiplying the values of s_n^ρ by a constant α^ρ. A value of $\alpha^\rho > 1$ describes an overestimate of the s_n^ρ errors and $\alpha^\rho < 1$ an underestimate.

The no-constraint and the ellipsoidal-constraint procedures (Procedure Nos. 1 and 4) are by definition of the procedures independent of α^ρ. The error identification does change for the combined-and the fixed-square fits (Procedure Nos. 2 and 3) as a function of α^ρ. Generally, however, the combined-fit is less sensitive to α^ρ than the fixed-square fit is to α^ρ. The reason that this is true concerns the relative position of the two procedures on the β scale and the shape of the minimum of $f(\beta)$. As indicated earlier, the fixed-square fit is located near the minimum and the combined fit is located on the wing. Generally the minimum is fairly sharp and the wing fairly flat. On the β scale, a change in β therefore changes the error identification $[f(\beta)]$ more rapidly for the fixed square fit than for the combined fit.

Conclusions

Although the no-constraint fit (Procedure No. 1) is independent of uncertainties in either s_k^σ or s_n^ρ, the cross section error identification is not particularly good except for a very small value of the average reactivity error in the integral data. The fixed-square procedure (Procedure No. 3) is independent of the uncertainty in s_k^σ while the combined-fit procedure (Procedure No. 2) is not independent of the uncertainties in either s_k^σ or s_n^ρ. Even though the no-constraint and the fixed-square fits are better under certain circumstances, the combined-fit procedure seems to be preferable for general usage for the following reason. Probably the most inaccurate entries in a fitting procedure are the uncertainties in both the microscopic data and the integral measurements and, as shown above, only the combined-fit procedure is relatively insensitive to the accuracy of either of the assumed errors.

References

1. K. O. Ott, R. B. Pond and J. M. Kallfelz, *A Study of Methods of Cross Section Error Identification Utilizing Integral Data from Fast Critical Assemblies,* Applied Physics Division Annual Report, July 1, 1969, to June 30, 1970, ANL-7710, pp. 227–230.
2. K. O. Ott, R. B. Pond and J. M. Kallfelz, *A Study of Methods of Cross-Section Error Identification Utilizing Integral Data from Fast Critical Assemblies,* Proc. Third Conference on Neutron Cross Sections and Technology, March 15–17, 1971, Knoxville, Tennessee, Conf-710301 (Vol. 1), pp. 25–31.

II-55. ^{239}Pu Self-Shielding Factors as a Function of σ_p Based on ENDF/B VERSION I Data

M. Salvatores* and K. D. Dance

Broad group self-shielding factors for the capture and ssion cross sections of ^{239}Pu were generated in both the unresolved and resolved resonance energy range. The calculations were made for a 27-broad-group structure consisting of 21 groups of lethargy width 0.5 followed by four groups of lethargy width 1.0, one group of lethargy width 2.0, and a thermal group. In the unresolved resonance energy range (groups 11 through 21)

* Comitato Nazionale per L'Energia Nucleare, Casaccia, Italy.

self-shielding factors, f_x^g, were defined as

$$f_x^g = \left[\int_g \sigma_x^\infty(E)dE\right]^{-1} \frac{\int_g \frac{\sigma_x(E)dE}{\sigma_p^{eq} + \sigma_R(E)}}{\int_g \frac{dE}{\sigma_p^{eq} + \sigma_R(E)}}, \quad (1)$$

where the integrations are over the energy interval corresponding to group g, x refers to the capture or fission process, σ_x^∞ is the infinite dilution cross section for process x, σ_R is the total resonance cross section, σ_p^{eq} is the equivalent potential scattering cross section. In the evaluation of the integrals of Eq. (1), the effects of overlapping resonances (both inter- and intra-sequence effects) were taken into account using the formulation of Hwang.[1] A code[2] written according to Hwang's method was used to generate resonance self-shielding factors for many values of σ_p^{eq} in the range of practical interest for calculation of fast reactors.

In the resolved resonance energy range (groups 21 through 25), where the narrow resonance approximation is less applicable to the resonances of ^{239}Pu, the self-shielding factors were defined as

$$f_x^g = \left[\int_g \sigma_x^\infty(E)dE\right]^{-1} \frac{\int_g \sigma_x(E)\phi(E)dE}{\int_g \phi(E)dE}. \quad (2)$$

The calculation of the flux $\phi(E)$ and the integrations indicated in Eq. (2) were performed with the resonance absorption code RABBLE.[3] The direct integration of the Boltzmann equation over the resolved resonance energy range was performed for an infinite homogeneous medium and different calculations were made corresponding to many values of the equivalent potential scattering cross section of the medium.

The resonance parameters of ENDF/B VERSION I were used for all the calculations. The unresolved resonance parameters are summarized in Table II-55-I and Fig. II-55-1. In Table II-55-II the smooth cross sections to be used in connection with ENDF/B resolved resonance parameters are given. The smooth cross section values are included in the final broad

TABLE II-55-I. ENDF/B VERSION 1 UNRESOLVED RESONANCE S-WAVE PARAMETERS FOR ^{239}Pu

	$J = 0$	$J = 1$
$\overline{D}$ (eV)	8.78	3.12
Γ_n (eV)$^{1/2}$	0.00094	0.000334
Γ_γ (eV)	0.0387	0.0387
Γ_f (eV)	2.8	see Fig. II-55-1
ν_f	2	1
μ	1	1
g_j	0.25	0.75
Nuclear radius	0.905×10^{-12} b$^{-1/2}$	

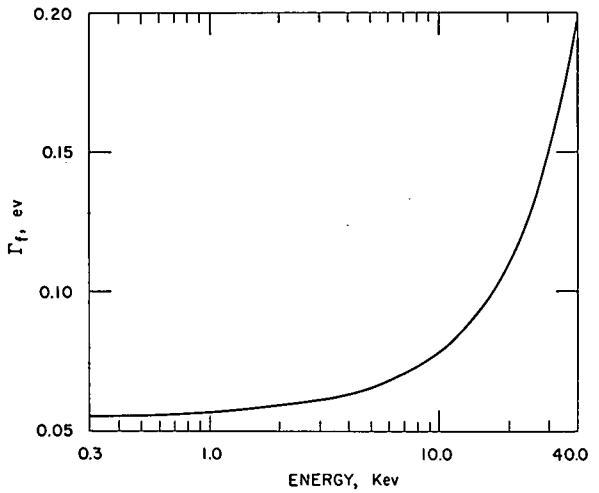

FIG. II-55-1. Fission Width, Γ_f, for $\ell = 0$, $J = 1$ State of ^{239}Pu. *ANL Neg. No. 116-1077.*

TABLE II-55-II. ^{239}Pu SMOOTH CROSS-SECTIONS FOR RESOLVED RESONANCE ENERGY RANGE, b

Energy Range, eV	Fission	Capture
454–275	−1.5596	−1.4229
275–0	1.94	0.226

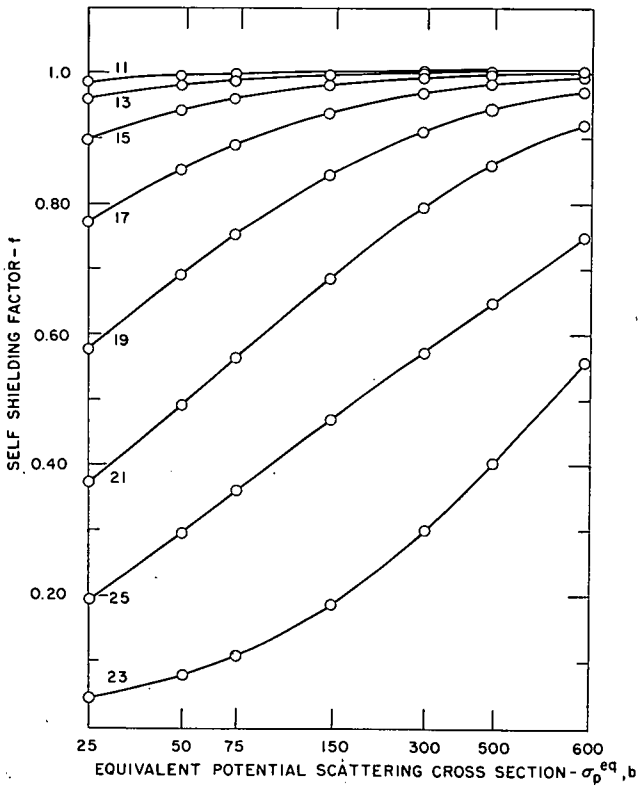

FIG. II-55-2.' ^{239}Pu Capture Self-Shielding Factors Versus σ_p for Broad Group Energy Structure. *ANL Neg. No. 116-1076.*

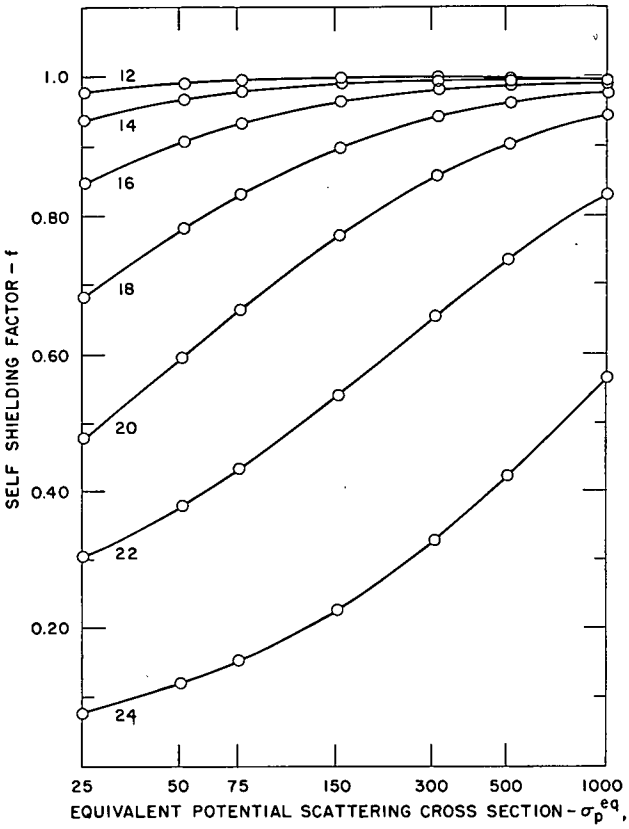

FIG. II-55-3. ^{239}Pu Capture Self-Shielding Factors Versus σ_p for Broad Group Energy Structure. *ANL Neg. No. 116-1074.*

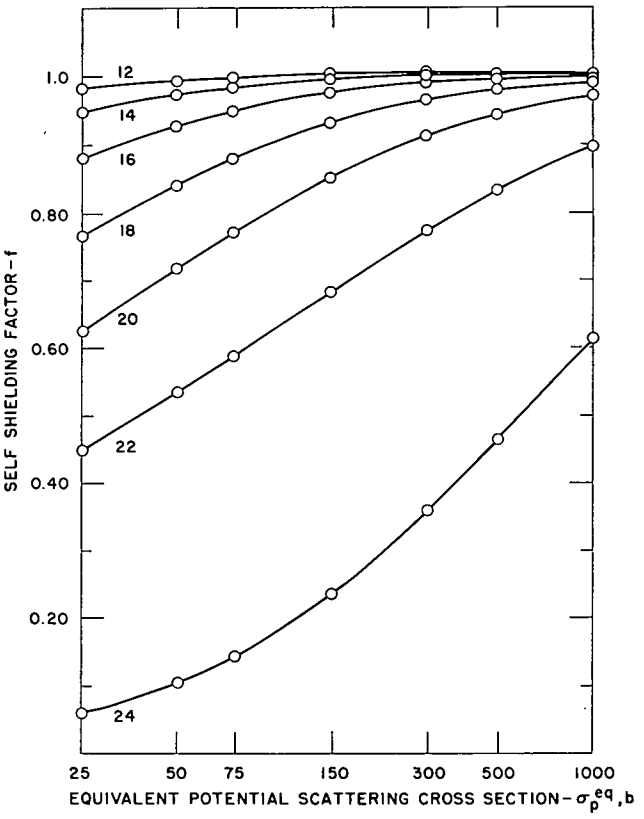

FIG. II-55-5. ^{239}Pu Fission Self-Shielding Factors Versus σ_p for Broad Group Energy Structure. *ANL Neg. No. 116-1075.*

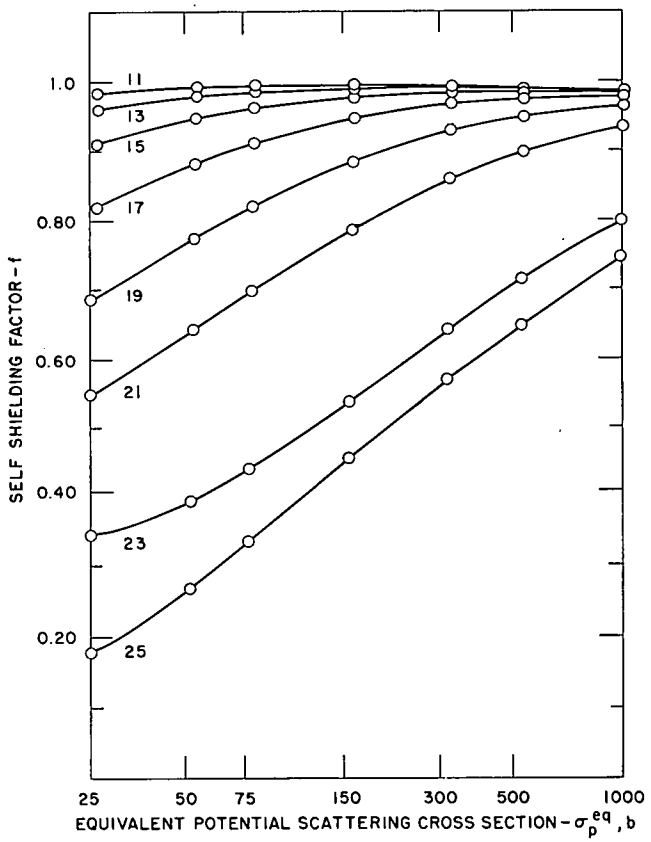

FIG. II-55-4. ^{239}Pu Fission Self-Shielding Factors Versus σ for Broad Group Energy Structure. *ANL Neg. No. 116-1078.*

TABLE II-55-III. INFINITE DILUTION CROSS SECTIONS FOR ^{239}Pu.

Energy Group	$\sigma^{\infty}_{capture}$	$\sigma^{\infty}_{fission}$
11	0.1888	0.9000
12	0.3110	1.0908
13	0.4958	1.3564
14	0.7502	1.7206
15	1.1045	2.2419
16	1.6036	2.9276
17	2.2857	3.8546
18	3.2133	5.0984
19	4.4347	6.7145
20	6.0619	8.8127
21	8.2179	11.5368
22	15.737	22.584
23	36.571	43.931
24	39.223	51.587
25	44.523	68.097

group self-shielding factors. The broad group self-shielding factors obtained with the above procedure were least squares fitted to obtain fitting parameters for use in connection with equivalence theory.[4]

Curves of the self-shielding factors for capture and fission as a function of σ_p are shown in Figs. II-55-2 through II-55-5.

Table II-55-III gives the infinite dilution broad-group cross sections obtained using the procedures outlined above with σ_p^{eq} approaching infinity.

In a previous work,[5] analogous self-shielding fitting parameters were derived for ^{235}U and ^{238}U. With the necessary adjustments due to the different broad-group energy structure, the ^{239}Pu, ^{238}U and ^{235}U fitting parameters were used in extensive heterogeneity resonance self-shielding effect calculations in both ZPR-6 Assemblies 6A and 7 (see Papers II-11 and II-16). The fitting coefficients made a consistent comparison of Assemblies 6A and 7 possible without repeated MC² calculations.

References

1. R. N. Hwang, *Doppler Effect Calculations with Interference Corrections*, Nucl. Sci. Eng. **21**, 423 (1965).
2. R. N. Hwang, Argonne National Laboratory (private communication).
3. P. H. Kier and A. A. Robba, *RABBLE, A Program for Computation of Resonance Absorption in Multiregion Reactor Cells*, ANL-7326 (1967).
4. K. D. Dance, *An Equivalence—Theory Capture Cross Section for Plate-Type Cells*, Reactor Physics Division Annual Report, July 1, 1967 to June 30, 1968, ANL-7410 pp. 433–435.
5. K. D. Dance, R. A. Karam, J. E. Marshall and R. B. Pond, *Analysis of Central Reactivity Worths Incorporating Resonance Self-Shielding,* Reactor Physics Division Annual Report, July 1, 1968 to June 30, 1969, ANL-7610 pp. 165–170.

II-56. Two-Dimensional Fast-Reactor Disassembly Calculations with Space-Time Kinetics

E. L. Fuller, D. A. Meneley, T. A. Daly, W. T. Sha, A. J. Lindeman and G. K. Leaf

Introduction

In fast-reactor disassembly analysis,[1,2] it is commonly assumed that both power density and material reactivity worth distribution are constant throughout an excursion. It is further assumed that reactivity changes due to material motion can be calculated by perturbation theory. AX-1[(3)] was the first attempt to remove these assumptions; reactivity changes due to material motion were calculated periodically during an excursion by neutron transport theory. However, AX-1 is limited to one space dimension and does not account for reactivity feedback other than that due to material motion or delayed neutron precursors. In this paper, the results of calculations made with a two-dimensional model[4,5] are presented. The model has been discussed in detail in Ref. 5. This model can treat transients initiated by such mechanisms as coolant voiding, predisassembly motion of fuel and/or structural material, and control rod motion. Furthermore, reactivity feedbacks due to such effects as Doppler broadening of ^{238}U resonances and thermal expansion of various reactor materials are considered. Most importantly, though, the model has the capability of describing material motion during disassembly. Consequently, the reactivity effects of fuel motion can be directly assessed.

The model consists of five segments: a two-dimensional, space-time multigroup diffusion theory calculation; a two-dimensional, hydrodynamics model; an energy balance; an energy-density-dependent equation of state; and a transformation algorithm between Eulerian and Lagrangian coordinates. The neutronics equations are solved in the Eulerian coordinate system; the hydrodynamics, energy balance, and equation of state are solved in the Lagrangian coordinate system. The transformation between the two systems occurs through material volume fractions, power density, temperatures, and precursor concentrations. As a result, complete flexibility of material location in the reactor is obtained. The neutronics calculations are on an Eulerian mesh to avoid the accumulation of truncation errors that would occur if the calculations were made on the Lagrangian mesh. The hydrodynamic calculations are on a Lagrangian mesh to properly account for nonrigid boundaries and interfaces between fluids wit different thermodynamic properties. Some accumula tion of truncation error is tolerated so that these effects can be properly treated. If the truncation error due to

mesh distortion becomes too large, however, it can be eliminated by the rezoning process.[6]

Numerical Results

The transients described below are highly simplified in the sense that they were chosen for comparison of the point and spatial kinetics models, rather than to represent realistic accident situations. Secondly, they were chosen so that differences between point and spatial kinetics were expected to be small, so that possible anomalous behavior of the spatial kinetics code (which is in its testing phase) could be detected more easily.

The reactor configuration analyzed is shown in Fig. II-56-1. The dimensions are typical of an oxide-fueled LMFBR with full-power rating of 2400 MWt. Fuel, sodium, and stainless steel volume fractions in the core are 0.42, 0.37, and 0.21, respectively. The reactor is represented by a 280-interval spatial mesh grid and four energy groups; the error in initial criticality relative to an 1120-interval grid and twenty-six energy groups is approximately 0.5% $\delta k/k$. The four group structure was selected so that two energy groups were in the resonance absorption range. It is recognized that greater energy detail will be required for actual analysis work; however, four groups were considered adequate for purposes of model comparison.

Three different models are used to analyze this system. The spatial kinetics and disassembly model described above is compared with the point kinetics model in which the flux shape function is constant; the two models are otherwise identical. The third model used is the VENUS disassembly code. This code includes a point kinetics solution; however, the reactivity coefficients which are input may be calculated from eigenvalue differences using static flux codes, so that the model is not strictly point kinetics.

The accident-initiating mechanism is removal of sodium uniformly over the core in 0.020 seconds. The reactivity ramp rate is approximately \$150 per second ($\beta = 0.0034$). Negative feedback arises from increased resonance absorption as fuel temperature increases and from motion of fuel during disassembly. The Doppler feedback with sodium in the core, expressed as the coefficient Tdk/dT, is -0.008. This value was obtained from two static eigenvalue calculations with uniform core fuel temperatures of 1400 and 2900°K, respectively.

The first series of calculations was carried out from initial conditions approximating those in a system ;t prior to disassembly following a rapid reactivity ;ertion. The fuel temperature was taken to be uniform throughout the core at 2900°K, and the power was set at 8.64×10^5 MW, or 360 times full operating power.

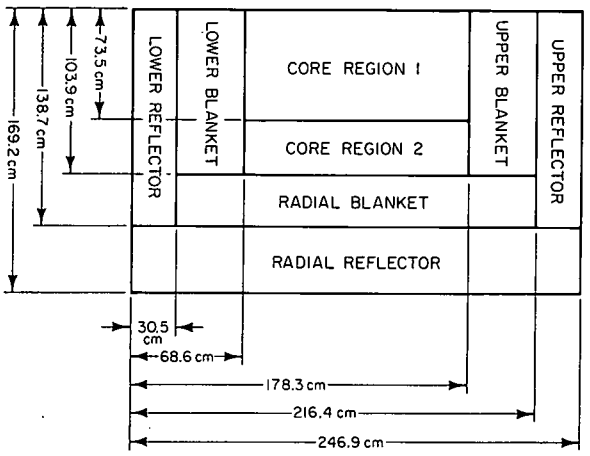

Fig. II-56-1. Reactor Configuration. *ANL Neg. No. 116-833.*

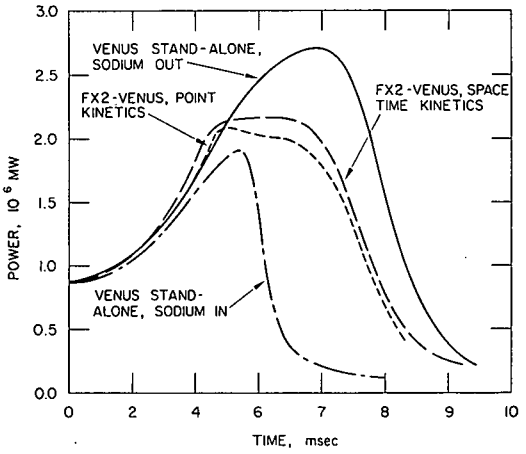

Fig. II-56-2. Total Reactor Power from High-Temperature Initial Conditions. *ANL Neg. No. 116-828.*

The sodium-out equation of state was specified in the disassembly model. Reactivity tables for the VENUS code were generated using the FX2 code option at the initial state of the reactor. The power, reactivity, and total energy are plotted in Figs. II-56-2 through II-56-4. Referring to the pairs of curves marked "FX2-VENUS," it can be seen that the point kinetics model gives very similar results to the spatial kinetics model in this case. The differences are attributable to spectral changes caused by the fuel temperature rise which are not accounted for in the point model.

The curves marked "VENUS STAND ALONE, SODIUM IN" show the results of the standard VENUS code with $Tdk/dT = -0.008$ and sodium-in equation of state. The energy yield is much lower in this case, mainly because of the rapid disassembly following generation of high pressures. The curves marked "VENUS STAND ALONE, SODIUM OUT" show the effects of changing to the sodium-out equation of

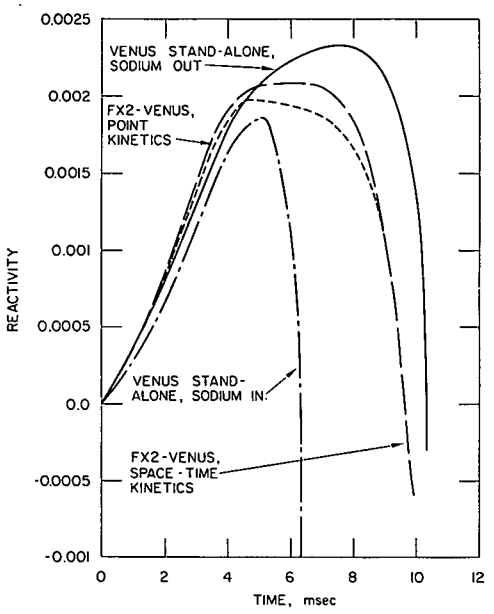

FIG. II-56-3. Reactivity from High-Temperature Initial Conditions. *ANL Neg. No. 116-835.*

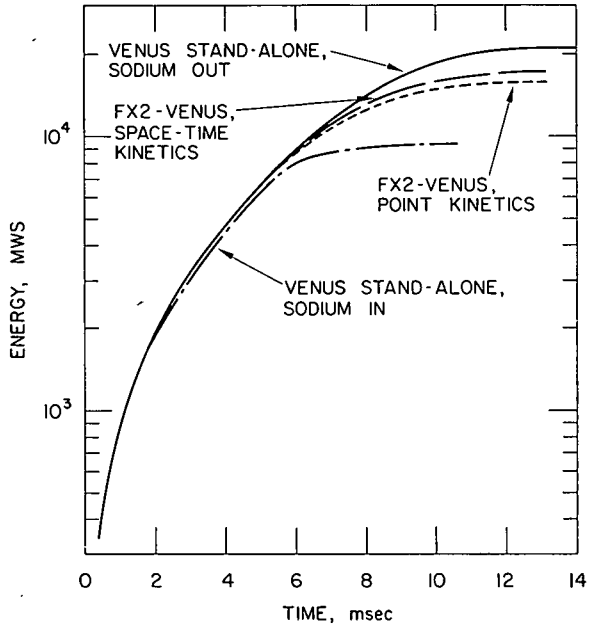

FIG. II-56-4. Energy Yield from High-Temperature Initial Conditions. *ANL Neg. No. 116-830.*

state and $Tdk/dT = -0.004$, roughly equal to the Doppler coefficient for sodium-out conditions. This second case gives a higher energy yield than FX2-VENUS because the correct Doppler coefficient is somewhere between the sodium-in and sodium-out values. Note that the disassembly rates (as indicated by the negative reactivity slopes in Fig. II-56-3 are not remarkably different for the three cases using the sodium-out equation of state. This indicates that disassembly reactivity feedback calculation using a reactivity table (as does VENUS) does not lead to gross error, at least for the small fuel motions which occurred in these runs. This is, however, a question which deserves further detailed investigation to establish the generality of this observation.

The second series of calculations was the same as the first except that the initial power was 2400 MWth and the initial core fuel temperature was 1400°K. The power, reactivity, and energy plots are shown in Figs. II-56-5 through II-56-7. Referring to the pairs of curves marked "FX2-VENUS", it can be seen that the effect on the energy yield of the spectral shift during the excursion is more pronounced than in the previous case. This is due to the fact that the reactivity is near prompt critical, and so a small error in reactivity can

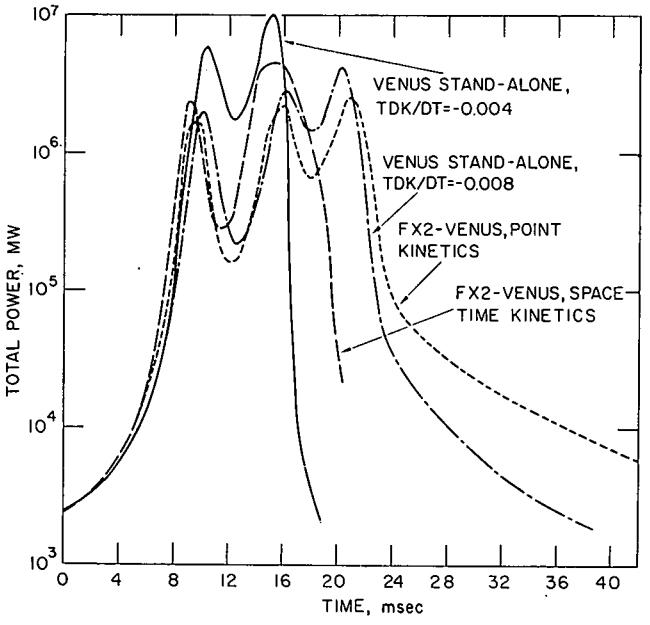

FIG. II-56-5. Total Reactor Power from Normal Operating Initial Conditions. *ANL NEG. No. 116-827.*

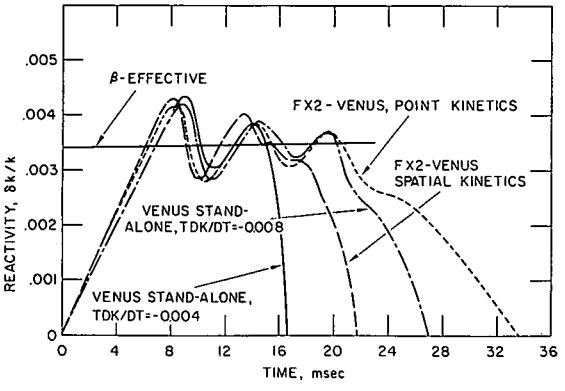

FIG. II-56-6. Reactivity from Normal Operating Initial Conditions. *ANL Neg. No. 116-834.*

lead to a larger error in the prompt reactivity, $(\rho - \beta)$. The true energy yield is ~30 % higher than is predicted by the point kinetics version of FX2-VENUS. The pairs of curves marked "VENUS STAND ALONE" indicate the influence of the Doppler coefficient on the transient behavior. (The sodium-out equation of state and reactivity table were used in both cases.)

The insertion ramp rate used in the VENUS calculation was somewhat low in this case, so that the super-prompt critical portion of the transient is initiated somewhat later. The low Doppler coefficient case with VENUS overestimates the energy yield by 50 %. The VENUS case with $Tdk/dT = -0.008$ results in an energy yield very close to the correct value, by fortuitous cancellation. The energy accumulated up to 18 msec. was approximately 0.65 of the space-time value; however, a third power peak occurred in the VENUS case which supplied the additional energy. There is, obviously, no guarantee that such cancellation will occur in all cases.

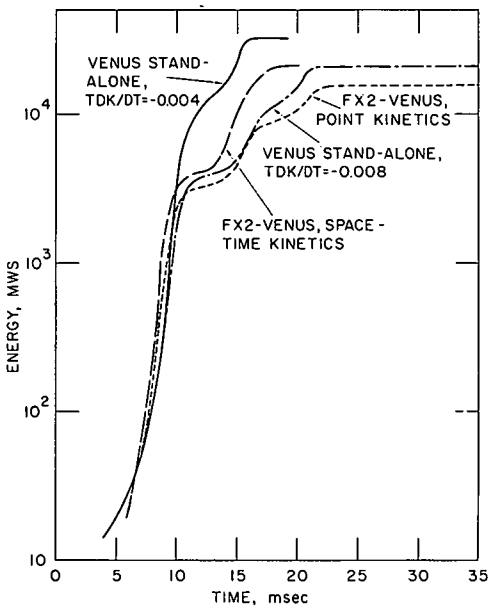

FIG. II-56-7. Energy Yield from Normal Operating Initial Conditions. *ANL Neg. No. 116-829.*

Discussion and Conclusions

Investigation of errors introduced by approximations to neutron kinetics behavior is now possible in a two-dimensional model. The cases described here do not constitute an adequate test of these approximations in any sense. The main point which can be made is that the results indicate that the FX2-VENUS code is fairly well tested, so that a study of two-dimensional spatial effects can begin. Further verification of the model will be carried out whenever an independent calculation is possible. One case which can provide insight is a zero-Doppler problem starting from a very high power. This problem would provide an indication of the point at which the reactivity-table approximation breaks down.

The energy yields of accidents computed using the FX2-VENUS space-time model tend to be higher than those computed using the true point-kinetics model. (In this context the term "true point kinetics," refers to the model employing the initial flux-shape function throughout the transient.) Virtually all analysts, however, apply a point kinetics model with coefficients calculated for conditions which are representative of the conditions expected during the transient. For example, the Doppler coefficient usually is calculated by static eigenvalue differences using cross sections at two temperatures. Presuming that the analyst preselects these conditions properly, such procedures should give results which are closer to the correct result than those obtained from the true point-kinetics model. Obviously, no firm statement can be made concerning the errors introduced by these models; however, no assurance can be given that the results are conservative unless very extreme assumptions are made. In such cases, the remaining question is whether or not the design penalties which result from this conservatism are acceptable.

Finally, it is hoped that the FX2-VENUS code and planned extensions to include transient heat transfer models will provide verification and guidance for the use of simpler models for routine safety studies, and thereby increase confidence in their predictions.

References

1. N. Hirakawa, *MARS—A Two Dimensional Excursion Code,* APDA-198 (1967).
2. W. T. Sha and T. H. Hughes, *VENUS—A Two Dimensional Coupled Neutronics-Hydrodynamics Fast Reactor Power Excursion Computer Program,* ANL-7701 (1971).
3. D. Okrent, J. M. Cook, D. Satkus, R. B. Lazarus and M. B. Wells, *AX-1, A Computer Program for Coupled Neutronics-Hydrodynamics Calculations on the IBM-704,* ANL-5977 (1959).
4. D. A. Meneley, G. K. Leaf, A. J. Lindeman, T. A. Daley and W. T. Sha, *A Kinetics Model for Fast Reactor Analysis in Two Dimensions,* Symposium on Dynamics of Nuclear Systems, March 23–25, 1970, Tucson, Arizona.
5. W. T. Sha, T. A. Daly, A. J. Lindeman, E. L. Fuller, D. A. Meneley and G. K. Leaf, *Two-Dimensional Fast-Reactor Disassembly Analysis with Space-Time Kinetics,* Proc. ANS-AEC Conference on New Developments in Reactor Mathematics and Applications, March 29–31, 1971, Idaho Falls, Idaho, CONF-710302 (Vol. 1), p. 128.
6. P. L. Browne, *REZONE; A Proposal for Accomplishing Rezoning in Two Dimensional Lagrangian Hydrodynamics Problems,* LA-3455-MS, TID-4500 (1966).

II-57. Conservative Analytical Estimates of the Consequences of Failure Propagation in a Hypothetical Accident for a Ceramic-Fueled LMFBR

P. J. Persiani and M. Stevenson*

Introduction

This study is an exercise in developing a design basis accident resulting from conservative estimates of the consequences of failure propagation in a hypothetical accident for a ceramic-fueled LMFBR. The initiating event leading to such an accident is chosen to be a sodium-vapor explosion occurring in a single assembly with consequent damage propagation to adjacent assemblies.

The initial expulsion of sodium from the first subassembly may be assumed to occur from a full or partial coolant flow blockage due to:

1. Fuel element failure within a fuel assembly with debris restricting the coolant passage (either inlet or outlet),
2. Malfunction of experiments in test assemblies relating to coolant flow testing,
3. High-burnup fuel-element failure with subsequent fission gas release and sodium ejection.

These events may not directly result in extensive damage to the assembly. However, if sodium does reenter the assembly after some fraction of the cladding and fuel become molten, then a fuel-coolant interaction may create a pressure pulse causing damage to the assembly. The deformation may be such that it mechanically interacts with and perturbs the normal operating conditions of adjacent assemblies. The resultant physical condition of the fuel in these adjacent assemblies may then lead to further failure events. Reactivity effects due to fuel redistribution and sodium voiding in the initial single assembly malfunction may occur simultaneously with damage and voiding in the adjacent assemblies.

The consequences of the above initiating event and its potential for leading to a design basis accident is the subject matter of this study.

There are several qualifications which must be considered as an integral part of this paper. In order to attain the conditions usually associated with design-basis pressure loadings, it was found necessary to hypothesize a failure in the action of the protective system. In most of the cases studied conditions were such that several different scram signals could have been generated in a time period adequate for safety devices to be activated.

Although attempts were made to include a degree of realism into the initiating conditions, this correspondence should not be attached to the subsequent steps. For example, a reactor designed to accommodate stainless steel structural swelling would have assembly spacings much greater than those in a tight-core design. It should be expected then that the consequences of a mechanical interaction between assemblies would be less severe in an open-core design concept.

In a tight-core design concept, the collective interaction of the assemblies can more or less be made to "bow" in a predetermined manner, assuming that all mechanical constraints have been identified. This is a difficult problem. In the open-core design the collective spatial deflections of the assemblies under thermally induced forces are also difficult to assess. Therefore, at present it is not clear how to take into account the bowing effect on the failure propagation of a malfunctioning assembly under severely changing thermal conditions.

The above consideration, along with the limited experimental data relevant to the physical models used in the analysis, introduces a high degree of uncertainty at each step in the chain of events. Therefore, throughout the analysis assumptions and decisions were made to emphasize the more pessimistic conditions.

Accident Progression

A flow chart delineating possible sequence of events in the progression of an accident is included in Fig. II-57-1. Of the several possible chains, three primary paths were adopted for this phase of the study. These are briefly:

1. The six adjacent assemblies are not structurally deformed, but a slow power transient results from the initial reactivity effects caused by the slumping of the fuel in the voided subassembly.
2. The deformation of six adjacent assemblies leads to instantaneous cladding rupture by impact followed by voiding of coolant through fission gas release. These six assemblies may then collapse through fuel melting into a more reactive configuration.
3. The deformation of six adjacent assemblies is accompanied by a severe coolant flow reduction a subsequent voiding by heating. Collapse of t fuel may then follow the sodium film dryout.

The assumed severe pressure pulse due to a fuel-

* Babcock and Wilcox Co., Lynchburg, Virginia.

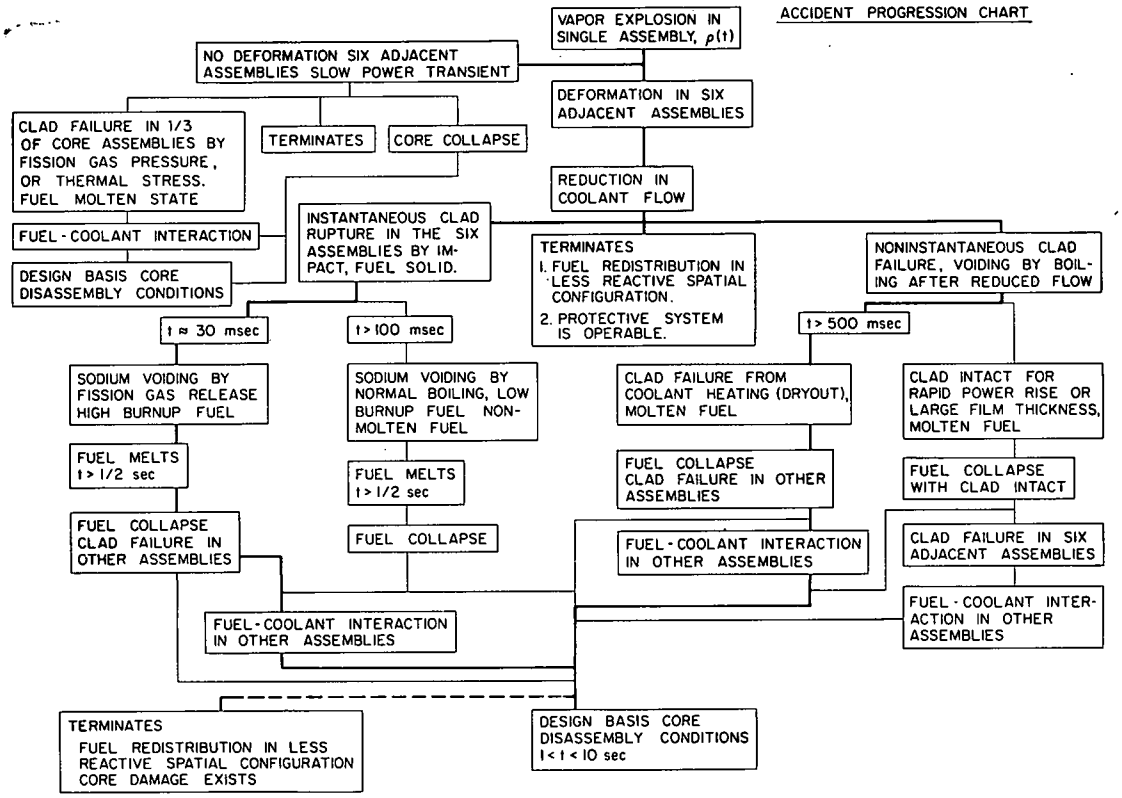

FIG. II-57-1. Accident Progression Chart. *ANL Neg. No. 116-885.*

coolant interaction in a single malfunctioning assembly may have a negligible mechanical effect on the six adjacent assemblies; however, the potential for large deformations of the assembly can walls and fuel pins does exist. This deformation may directly cause a local or full-assembly flow reduction in these six assemblies or it may create cladding ruptures leading to fission gas release from the failed pins and a subsequent severe flow reduction. It is unlikely that the damage and/or flow reduction will be identical in these six assemblies, particularly if they are of different types (fuel or experimental) or of different burnup histories. However, it is difficult to predict the noncoherence of the damage and to assure that in all cases the damage will not be near-coherent. Thus, the direction taken in the initial analyses was to assume that the six adjacent assemblies were identical and that the damage to the assemblies was coherent, with the effects of possible noncoherence assessed in later analyses.

In any event, the flow reduction in these six adjacent assemblies may be severe enough that coolant voiding begins within a fraction of a second if sufficient fission gas is released from failed pins or in about one second if a negligible amount of fission gas is released. If the coolant does not reenter these assemblies for several seconds following voiding, a situation which is likely if the flow reduction is partial or if the coolant does not completely void the lower half of the core, then cladding and fuel melting may result. Sufficient cladding and fuel melting near the core axial midplane may lead to a fuel pin collapse, since in most LMFBR designs the fuel pins are not supported at the top.

Several reactivity effects are associated with this accident progression. The initial malfunctioning assembly may have contributed a positive or negative reactivity through either coolant expulsion or fuel movement. The expulsion of coolant in the six adjacent assemblies will have a reactivity effect which may be positive or negative depending on the local void coefficients and the extent to which they are voided. However, the dominant effect will generally be that of fuel collapse since the expulsion may contribute a strong positive reactivity. The power transient resulting from these reactivity effects, particularly fuel collapse, may lead to further core damage and possibly a core disassembly, provided enough positive reactivity is available.

During the fuel collapse phase of the accident, the reactor power level will rise and fuel temperature conditions may develop for which cladding failures occur in core assemblies where the coolant flow has not been disturbed. If a fraction of the fuel in these assemblies is

in a molten state, then a fuel-coolant interaction may take place. The resultant rapid voiding in these regions would add to the positive reactivity insertion. The magnitude and rate of this additional reactivity will depend on the model assumed for the interaction.

Cladding failures may occur in the upper-half segment of the fuel elements. The localized interaction would initially void the upper region of the core where the sodium reactivity effect is negative. If some fuel material is ejected into the coolant and carried along by the sodium, then again the voiding reactivity effect becomes less positive.

It should also be expected that cladding ruptures would occur in fuel elements with nonmolten fuel. The rupture could result particularly in cladding materials whose physical strength properties have been compromised by high fluence associated with extensive burnup. Dynamic thermally induced fuel swelling pressure and perhaps thermal stresses imposed on the highly embrittled cladding could result in an instantaneous structural rupture. If fission gas is released instantaneously, it should be expected that the sodium would void immediately. Depending on the structural condition of the oxide fuel, it is possible that some particulate fuel material would be forced out by the fission gas into the coolant region and be carried out of the high worth core region along with the ejection of the sodium.

Experimental data relating to fuel redistribution in a fuel-coolant interaction or fuel pin cladding failure is at present inadequate for constructing reasonably realistic analytical models. Therefore the pessimistic assumption adopted for this study is that a fuel-coolant interaction is accompanied by a positive reactivity effect. However, some cases are studied where an attempt is made to simulate some fuel movement into a less reactive distribution by reducing the positive sodium-voiding reactivity effect.

Methods of Analysis

Accidents in which propagation of failure proceeds from assembly to assembly through mechanical damage, thermal-hydraulic effects, or a combination of both are difficult to model analytically in the absence of experimental data on the specific mechanism of propagation. Analysis of specific events such as a single channel flow blockage and the resulting coolant voiding, the pressure pulse resulting from a fuel-coolant interaction, the resulting mechanical deformation of a single assembly wall, or the melt-through of an assembly wall due to contact with molten fuel, can be separately modeled and calculated within some margin of uncertainty. However, an adequate coupling of all of these mechanisms in a complete calculational package including all of the corresponding reactivity effects is not possible at the present time. In order to investigate the consequences of failure propagation leading to a more extensive core incident, it was necessary to utilize a computer code in which the reactivity effects and the power transient could be calculated as completely as possible. Of the safety related computer programs available, the MELT-II code[1] appeared as the most readily usable to partially satisfy the objectives of the transient calculation for this study.

The MELT-II code couples a two-dimensional multichannel thermal analysis with a corresponding multichannel reactivity history for reactor transient and accident calculations. An average fuel pin in a number of thermal regions (channels) corresponding to annular rings in the core is analyzed with regard to calculating radial and axial temperature distributions in the pin and the axial temperature distribution in the coolant subchannel corresponding to that pin. Average temperatures in the pin are used to determine feedbacks due to fuel compaction, Doppler effect, and fuel/cladding thermal expansion. The core average coolant temperature is used to determine a coolant density (expansion) feedback effect. In many accident situations the reactivity effect from coolant voiding is extremely important, and three voiding models are included in MELT-II. The first of these is a slug ejection model based on the BLOW code,[3] the second is a simple slug ejection model in which the driving pressure is from fission gas release, and the third is a simple slug ejection model in which the driving pressure is from an assumed fuel-coolant interaction. An option allowing voiding to proceed according to an input time function is also available. A fuel collapse model (see Ref. 2) is included in which the point of collapse is calculated according to the condition of the fuel pin at a given axial location. All of the fuel above that axial position is then assumed to fall under gravitational acceleration. A number of trip conditions for the voiding models and for the fuel collapse model may be set according to input values. Reactivity effects due to voiding and fuel movement are calculated using input two-dimensional worth distributions. In addition, an external driving reactivity may be input through a time table.

In all calculations in this first phase of the study, the physical, nuclear, and thermal parameters were those used by the Pacific Northwest Laboratory (PNL) for their safety analysis work.[4] The core description for the MELT-II runs used in this study was also the same as that used in the PNL work. Six thermal regions or channels were used with the first channel corresponding to the center assembly, the second channel to the ring of six assemblies adjacent to the center assembly, and so forth, with the sixth channel corresponding to the sixth and last ring of core assemblies.

An explicit modeling of the initiating events for the failure propagation accident was not attempted in this study. Rather the approach used was to assume that a single assembly event may occur, such as a pressure pulse from a fuel-coolant interaction, which can compromise the integrity of the adjacent assemblies and that the event itself may involve a reactivity effect. The latter possibility was included by estimating a range of reactivities which might result from a single assembly event, and four cases within this range were used in parametric studies involving the thermal mechanical effects from the single assembly event. The assumed four reactivity case histories are: (1) an \$0.50 insertion at a \$2.50/sec rate, assumed to possibly arise from voiding the single assembly followed by a fuel collapse in that assembly; (2) a \$0.20 step insertion possibly arising from voiding the assembly concurrent with a slight fuel compaction; (3) a net zero reactivity insertion; and (4) a −\$0.30 step insertion assumed to arise from voiding the assembly concurrent with ejecting from the assembly a certain fraction of the fuel.

INSTANTANEOUS CLADDING RUPTURE

As stated in the preceding section, three primary paths for the accident progression were investigated. The first of these, that of immediate cladding ruptures in the six adjacent assemblies, leading to fission gas release and subsequent rapid voiding, was modeled by assuming that the voiding began at the initial time and that the core and axial reflectors were voided within 20 msec. This is extremely pessimistic in the sense that even with some fission gas release from high burnup assembly cladding ruptures, the gas release would be slow enough that the most immediate effects would be to reduce the coolant flow and to cause local voiding due to the fission gas itself. The consequent effect would be to enhance the possibility of heating the coolant to the point that normal boiling or voiding would begin. However, the assumed rapid voiding provides an upper limit on this effect.

NONINSTANTANEOUS CLADDING FAILURES

The second case, that of extensive deformation (crushing) in the adjacent assemblies, was modeled by assuming that flow in these assemblies was reduced to 20% of its normal value and that the coolant was heated until it reached a normal boiling temperature plus 100°K superheat. A slug ejection voiding rate (450 cm/sec) corresponding to the 100°K superheat was used for this situation. Initially this rate of ejection was used for both the upper and lower void interfaces, but in later cases the lower slug ejection rate used was much slower (100 cm/sec and 20 cm/sec). This is perhaps more realistic since for this partial flow situation the lower liquid slug would tend to move much slower because of the hydraulic head at the inlet. Further, it is quite possible that liquid coolant would remain for some time in the lowest portion of the core in which the heating rate is low. In these voiding cases, any axial segment of an assembly (or channel) was assumed to be insulated at the time that segment was voided, although variations were run to determine the effect of cooling the pins through the coolant film on the pin surface which might remain after voiding had occurred.

NO MECHANICAL DEFORMATION TO ADJACENT ASSEMBLIES

The third case considered was that of no deformation to adjacent assemblies. This simply involved calculating the power transient resulting from the initial reactivity effect (in the first two reactivity cases) from the malfunctioning assembly. The purpose of this was to determine if failures in other assemblies throughout the reactor might occur due to the power transient itself.

FUEL COLLAPSE CONSIDERATIONS

Fuel collapse was calculated in all cases with the gravity collapse model outlined above. Collapse was assumed to begin in a pin in which approximately 50% of the fuel at any axial segment was molten. This is perhaps overly conservative since the remaining solid fuel might retain enough structural integrity to support the pin until a greater percentage of the pin was molten. The exact time of the beginning of collapse, however, is not extremely important since it affects primarily the starting time scale of events and not the ultimate consequences. It should be pointed out that collapse begins in segments of the pin which have been voided, and, in these cases, the cladding will be molten well before the beginning of collapse.

FUEL CLADDING CRITERION

The fuel-coolant interaction or instantaneous fission gas release criterion used in this analysis was influenced in part by the fuel-element-lifetime model constructed by Bump[5] in his development of the SWELL code. The code is designed to estimate when cladding of an LMFBR mixed-oxide element may fail under normal and off-normal power or thermal conditions. The basic approach used is the empirically developed function which relates the fuel-swelling induced pressure on the cladding to the pressure of the fission gas retained in the fuel. The changes in the fission gas pressure are directly related to the changes in the thermal conditions of the fuel.

The correlation established with the available experimental data seems to indicate that cladding failure is to be expected when a fuel over-temperature (overpower or over-coolant temperature) condition of 25 to

50% exists. Although a generalization of the related data is difficult to discern, the cladding damage appears to be consistent with the condition that the fuel pin central region temperature is about 40°C above the melting point of 3040°K. This condition was assumed in the study to indicate cladding damage and consequent fuel-coolant interaction or instantaneous fission gas release.

There are several reasons that make the correlation of cladding damage to fuel burnup conditions and cladding fluence somewhat unclear:

1. The conductivity of the fuel (and hence temperature distribution) as a function of irradiation time is not known.
2. The extent of the reduction of the strength properties of the structural cladding material is difficult to relate to the fluence history under operating conditions.
3. The structural integrity of the observed stainless steel swelling is inadequately understood and therefore has not been included in fuel-element studies.

These uncertainties make a more detailed analysis of fuel failure propagation unrealistic. Therefore, in scoping a design basis nuclear incident, large margins of uncertainties are reflected by adopting pessimistic sequences of events, all with a high level of vagueness as to specific models. These margins of uncertainties can be minimized only with the generation of extensive experimental data.

GENERAL REMARKS

Attempts were made in a few cases to estimate the effects of noncoherence of events on the ultimate consequences. The noncoherence was modeled in two ways. First, in some cases, fuel collapse was assumed to begin with slightly different percentages of molten fuel in the six assemblies adjacent to the malfunctioning assembly. This could correspond to either varying degrees of structural integrity in these assemblies, different fuel melting temperatures, or perhaps to slightly different power densities in these assemblies. In some flow reduction cases, noncoherence was also introduced by assuming different values of the reduced flow, in particular, 10, 15, and 20% in three pairs of the six assemblies.

Results

As outlined above, the number of cases investigated in this part of the study was extensive. For this reason, two cases which essentially span all other cases will be discussed in detail.

INSTANTANEOUS CLADDING RUPTURE

The first case (Case IA) is that in which a \$0.50 reactivity insertion at a \$2.50/sec rate is introduced simultaneously with the beginning of rapid voiding in the row of assemblies (Channel 2) adjacent to the center assembly because of cladding rupture and expulsion of sodium by escaping fission gas. This case provides in one sense an upper limit of the cases studied in that the reactor power remains high (a factor of two to three times normal power) until fuel collapse begins.

In Table II-57-I are listed the secular sequence of events for four alternate paths to either the termination of the incident or the design basis core disassembly conditions. The Case I series of steps follows the heavy-shaded line from the instantaneous clad failure as shown in the Accident Progression Chart (Fig. II-57-1). The variations within this case are mainly to explore the effect that fuel-coolant interaction or sodium voiding in other core assemblies would have on the design basis accident. Case IA assumes that after fuel collapse has started in Channel 2 (1.7 sec after the initiating event), the core disassembly conditions are obtained by the positive feedback of further fuel collapse only. The design basis disassembly condition was chosen to occur at about 1.84 sec with a net reactivity input of about \$0.986 and at a rate of \$16/sec.

A simulated fuel-coolant interaction is included in Case IB. An attempt was made to introduce a more probable conjecture that only some of the fuel elements (say one-third) in the other channels undergo cladding rupture at one instant in the accident. The cladding rupture in these channels are assumed to occur instantaneously with a consequent fuel-coolant interaction of fission gas release voiding the channel of its coolant. The criterion used to trip this event was discussed in the Fuel Cladding Damage section. It appears that the power and therefore the fuel temperature conditions for sodium ejection will occur in Channels 3 and 5 within 3 msec of each other. The core disassembly conditions are then reached some 3 msec after cladding failures occur in Channel 5. It appears that this sequence of steps yields the more severe disassembly conditions, with net positive reactivity insertion being about \$0.09 above prompt critical and with an insertion rate of \$60/sec. The major component is the \$49/sec ramp due to the sodium being ejected by either the fuel-coolant interaction or fission gas release or some combination of both phenomena.

The last two cases listed are essentially slight variations of the latter event. The purpose of Case IC is an attempt to explore the effects of voiding from the upper half section of the core. The effect of some fuel being ejected along with the sodium is investigated in Cas ID. As expected, these last two events tend to reduc the positive sodium-voiding effect of Case IB with a slightly altered time sequence. The ramp rate and net positive reactivity at core disassembly conditions are

TABLE II-57-I. INSTANTANEOUS CLADDING RUPTURE

Time	Remarks	
0	a. Reactivity ramp insertion $d\rho/dt$ = \$2.50/sec, due to sodium ejection and fuel collapse in single assembly malfunction. b. Voiding starts in six adjacent assemblies (Channel 2) at midplane due to fission product gas release. Voiding rate, ~2500 cm/sec. c. Coolant flow rate essentially not disturbed throughout remainder of core.	ρ_{max} = \$0.50
20 msec	Power peaks to ~100 MW.	ρ_{net} = \$0.49
30 msec	Voiding completes in Channel 2. Power, ~500 MW. Doppler effective in power reduction.	ρ_{net} = \$0.36
200 msec	Power peaks to ~1400 MW. Input reactivity complete.	$\rho_{input,\ max}$ = \$0.50 ρ_{net} = \$0.70
1.7 sec	Fuel collapse starts in Channel 2. Power, ~800 MW.	ρ_{net} = \$0.26
	CASE IA. NO FUEL-COOLANT INTERACTION IN OTHER CORE ASSEMBLIES	
<1.84 sec	Fuel collapse starts in Channel 3.	
	Core Disassembly Conditions	
1.84 sec	Fuel collapse and total positive reactivity insertion, $d\rho/dt$ = \$16/sec	ρ_{net} = \$0.986
	CASE IB. FUEL-COOLANT INTERACTION (Sodium Ejection Starts from Core Axial Center Region)	
1.825 sec	One-third fuel element failures in Channel 3. Ejection of sodium only. Voiding rate, 2500 cm/sec.	
1.828 sec	One-third fuel element failures in Channel 5. Ejection of sodium only. Voiding rate, 2500 cm/sec.	
	Core Disassembly Conditions	
1.831 sec	Total positive reactivity insertion, $d\rho/dt$ = \$60/sec. Fuel collapse \$11/sec. Sodium ejection, \$49/sec.	ρ_{net} = \$1.09
	CASE IC. FUEL-COOLANT INTERACTION (Sodium Ejection Starts from Core Upper Axial Region)	
1.821 sec	One-third fuel element failures in Channel 3. Ejection of sodium only. Voiding rate, 2500 cm/sec. Fuel collapse reactivity, $d\rho/dt$ = \$11/sec.	ρ_{net} = \$0.99
1.825 sec	One-third fuel element failures in Channel 5. Ejection of sodium only. Voiding rate, 2500 cm/sec. Fuel collapse reactivity, $d\rho/dt$ = \$11/sec. Sodium ejection reactivity, $d\rho/dt$ = \$16/sec.	ρ_{net} = \$1.03
	Core Disassembly Conditions	
1.831 sec	Total positive reactivity insertion, $d\rho/dt$ = \$26/sec. Fuel collapse $d\rho/dt$ = \$11/sec. Sodium ejection, $d\rho/dt$ = \$15/sec.	ρ_{net}= \$0.99
	CASE ID. FUEL COOLANT INTERACTION (Sodium with Fuel Ejection Starts from Core Axial Center Region)	
1.825 sec	One-third fuel element failures in Channel 3. Ejection of sodium and fuel (simulation) assumed as 30% of molten fuel in 15 cm central section. Voiding rate, 2500 cm/sec.	
1.830 sec	One-third fuel element failures in Channel 5. Ejection of sodium and fuel (simulation) assumed as 30% of molten fuel in 15 cm central section. Voiding rate, 2500 cm/sec. Fuel collapse, $d\rho/dt$ = \$11/sec. Sodium and fuel ejection, $d\rho/dt$ = \$28/sec.	ρ_{net} = \$1.06
	Core Disassembly Condition	
1.832 sec	Total positive reactivity insertion, $d\rho/dt$ = \$35/sec. Fuel collapse, $d\rho/dt$ = \$11/sec. Sodium and fuel ejection, $d\rho/dt$ = \$25/sec.	ρ_{net} = \$1.03

$26/sec and $0.99; and $35/sec and $1.03 for Cases IC and ID respectively.

NONINSTANTANEOUS CLADDING FAILURES

The second case (Case II) is that in which a step insertion of $-0.30 is introduced simultaneously with a flow reduction to 20% in Channel 2. This case is significant in that the power transient would not be detected by a 20% overpower scram trip until after fuel collapse had begun. A value of the lower void interface velocity of 20 cm/sec was found to yield a more pessimistic set of circumstances. Voiding began at about 25–30 cm above the core axial midplane, and with the above value for lower void velocity, fuel collapse began about 10 cm above the midplane. With higher downward voiding speeds, fuel collapse was found to begin only slightly above the midplane. This higher collapse initiation position led to a higher collapse reactivity addition rate since for the first 10 cm of downward movement fuel was not moving into the lower half of the core.

The chain of events for two variations of this problem is listed in Table II-57-II. As indicated in the Accident Progression Chart (Fig. II-57-1), there is an expected time delay between the onset of the mechanical deformation with a partial flow blockage and cladding failure.

As anticipated, the characteristic time leading to a fuel collapse situation for this class of accident is lengthened to 6.7 sec compared with 1.7 sec as in the Case I series accidents.

In Case IIA, it is assumed that the fuel-coolant interaction event does not occur. The computations indicate that core disassembly conditions are to be expected 200 msec after fuel collapse starts in Channel 2. It appears that the onset of fuel melting in Channels 3, 4, and 5 is delayed long enough by the coolant flow in these channels that the fuel collapse does not contribute to the positive reactivity ramp of $12/sec from Channel 2.

Cladding failure followed by sodium ejection from either the fuel-coolant interaction or the fission gas release mechanism is considered in the alternate Case IIB. Consequently, the core disassembly conditions are established some 4 msec sooner but with a total positive ramp of $42/sec and a net reactivity of $0.07 above prompt critical.

TABLE II-57-II. NONINSTANTANEOUS CLADDING FAILURES

Time	Remarks	
0	Negative reactivity step insertion $\rho(0) = \$-0.30$ due to assumed instantaneous ejection of fuel and sodium in single assembly malfunction.	
1 msec	a. Partial flow reduction in six adjacent assemblies, coolant flow rate reduced to 20% of critical flow. b. Coolant flow not disturbed throughout remainder of core assemblies.	
1.22 sec	Voiding starts in six adjacent assemblies (Channel 2) in the upper axial core region. Upward rate of voiding, 450 cm/sec. Downward rate of voiding, 20 cm/sec. Power, 250 MW.	$\rho_{net} = \$0.26$
6.2 sec	Fuel melting starts in Channel 2. Power, 357 MW. Doppler effective in reducing power.	$\rho_{net} = \$-0.04$
6.3 sec	Voiding completes in Channel 2. Power 355 MW.	$\rho_{net} = \$-0.05$
6.7 sec	Fuel collapse starts in Channel 2. Power, 355 MW.	$\rho_{net} = \$-0.05$
	CASE IIA. NO FUEL COOLANT INTERACTION	
6.889 sec	Fuel melting starts in Channels 3, 4, and 5. Total positive reactivity insertion, $d\rho/dt$ = $12/sec.	$\rho_{net} = \$0.97$
	Core Disassembly Condition	
6.898 sec	Fuel collapse and total positive reactivity insertion, $d\rho/dt$ = $12/sec.	$\rho_{net} = \$0.97$
	CASE IIB. FUEL-COOLANT INTERACTION (Sodium and Fuel Ejection Simulated)	
6.889 sec	Fuel melting starts in Channels 3, 4, and 5. Total positive reactivity insertion, $d\rho/dt$ = $12/sec.	$\rho_{net} = \$0.97$
6.892 sec	One-third fuel element failures in Channels 3 and 5. Ejection of sodium and fuel simulated. Fuel collapse reactivity, $d\rho/dt$ = $12/sec. Sodium and fuel ejection reactivity, $d\rho/dt$ = $30/sec.	$\rho_{net} = \$1.03$
	Core Disassembly Condition	
6.894 sec	Total positive reactivity insertion, $d\rho/dt$ = $42/sec. Fuel collapse $d\rho/dt$ = $12/sec. Sodium and fuel ejection, $d\rho/dt$ = $30/sec.	$\rho_{net} = \$1.07$

CASE III—NO DEFORMATION IN ADJACENT ASSEMBLIES

As mentioned previously, a problem was studied in which the initial malfunctioning assembly introduced only a reactivity effect with no accompanying deformation of the adjacent assemblies. The resulting power transients for the two reactivity cases calculated (a \$0.50 insertion at \$2.50/sec and a \$0.20 step insertion) were relatively mild. In the first of these two, some cladding failures could possibly have occurred after about 5 sec from the time of initiation, but, in the second case, fuel failure was not likely within 10 sec after initiation, at which point the problem was stopped. Although it is perhaps possible that the reactivity contributed by a single malfunctioning assembly could initiate a relatively slow transient in which fuel failures could occur and lead to a disassembly condition, the probability of these events occurring combined with the probability of no protective action is extremely low. Further, this accident is bounded in consequences by the other accidents investigated in this study.

INTERMEDIATE CASES

A number of other problems were studies involving the four initiating reactivity cases and the two primary paths discussed above. Results for these problems were generally the same as for Cases I and II, although the time sequence of events varied from problem to problem. All of these cases terminated with the core in a disassembly condition with the exception of a problem intermediate to Cases I and II above. For this problem, the initiating events were a \$0.30 step reactivity insertion combined with the initiation of rapid voiding in Channel 2. Disassembly conditions were not reached since the fuel collapse reactivity became negative before sufficient energy had been generated to cause further fuel failure or disassembly conditions to be reached.

FUEL COLLAPSE VARIATIONS

The fuel collapse model used for the previous problems is in several ways limited. For example, it is unlikely that fuel pins can fall completely unimpeded in their motion. The fuel collapse in Refs. 1 and 2 allows the use of a frictional term such that the collapsing fuel is accelerated by gravity until it reaches a terminal velocity. Two problems were studied in which this option was used with a terminal velocity of 10 cm/sec and 100 cm/sec, respectively. With the 10 cm/sec terminal velocity, the transient was essentially controlled by the Doppler feedback. The collapse reactivity addition rate was low, and the reactor power rise was relatively slow.

Sufficient fuel was moving into the lower half of the core to cause the collapse reactivity to become negative before further fuel failure or disassembly conditions could be met. With the 100 cm/sec terminal velocity, the accident sequence was about the same as for the corresponding case without a frictional effect. Although in this case the peak fuel collapse reactivity rate was lowered by about 30%, the power rise was sufficient to lead to conditions for further fuel failures or disassembly. These results indicate that for this particular accident situation, simply slowing the fuel collapse can prevent reaching disassembly conditions despite the fact that the peak collapse reactivity may be constant.

It is difficult to assess the magnitude of forces resisting fuel collapse, although several effects may contribute. Certainly liquid viscosity will tend to slow the flow of molten fuel and this effect can be assessed if a reasonable model of the flow configuration can be developed. More difficult to assess are such forces as pressures created by fission gas release as more fuel becomes molten or by fuel vapor pressure from the extremely hot fuel in the initial collapse region.

It should be expected that if more sophisticated models including these effects were developed, the probability of localized fuel collapse leading to disassembly, as considered in this study, could be considerably reduced.

THE EFFECT OF NONCOHERENT FUEL COLLAPSE

As mentioned in the preceding section, an attempt was made to determine the effect of noncoherence of events in the six assemblies (Channel 2) adjacent to the malfunctioning assembly. A calculation was made of a case corresponding to Case I but in which collapse was initiated with a variation in the collapse initiation criterion. Specifically, in three pairs of the six assemblies, the collapse initiation temperatures in the fuel node monitored were set at 2950, 3040, and 3050°K (a melting temperature of 3040°K was used). The result of this was to decrease the effective reactivity addition from fuel collapse such that the transient was terminated without reaching further fuel failure or disassembly conditions. This occurred since the first of the three pairs of assemblies to begin collapsing had collapsed approximately 20 cm and was contributing a negative collapse reactivity before the second pair began collapsing.

A case was calculated corresponding to Case II but in which noncoherence was introduced by reducing the flow to 10, 15, and 20% respectively in the three pairs of assemblies in Channel 2. The results for this problem were much the same as for the collapse initiation noncoherence problem discussed above. Again, the transient was terminated due to a negative collapse reactivity from the first pair of assemblies to begin collapsing.

These results indicate that a relatively modest deviation from complete coherence of fuel collapse in these six assemblies may preclude reaching disassembly conditions. It is difficult to specifically identify the validity of all sources of noncoherence, but the effect is to either lessen the severity of the accident or to lessen the probability of its occurrence.

Discussion

A general comment consistent with the results of this study is that failure propagation leading to further core damage may proceed via several paths. Since the objective of this study was to explore core disassembly conditions in order to set design criteria, minimal effort was applied to explore the alternate end condition (see Fig. II-57-1, Accident Progression Chart) of terminating the accident without a violent core disassembly. To establish a case for this event would require more experimental data than are available in order both to better define the physical condition of the core and to develop less pessimistic analytical models.

To accomplish this, detailed and specific data must be generated on:

1. Fuel and clad thermal conductivity as a function of burnup,
2. Physical properties and the structural integrity of the fuel and clad material at several levels of irradiation,
3. Fuel and clad behavior under thermally induced stresses at high burnup and fluences,
4. The spatial distribution of fuel material in overtemperature conditions,
5. Fuel coolant interaction mechanisms,
6. Fuel collapse mechanisms.

This partial listing of required data should be obtained under conditions similar to those anticipated in an LMFBR power reactor. Furthermore, it is inadequate to rely mainly on integral type experiments for modeling mechanisms that are to be included in a total systems analysis program.

The uncertainties in physical and neutronic data are important; however, these are often secondary in magnitude compared with the lack of knowledge concerning specific events in the accident sequence. For example, pressure pulses from molten fuel-coolant interactions severe enough to grossly deform surrounding assemblies have not been experimentally verified. Similarly, there are uncertainties associated with the nature of sodium voiding, fission gas release, and fuel collapse. These uncertainties are reflected in pessimistic models which in turn give pessimistic solutions. The result is an analysis which dampens the effect of the uncertainties by overestimating the consequences of each event.

In the absence of more data and better models, a determined effort was made to reflect a reasonable level of pessimism at each step in the sequence of events. For example, the assumption that only one-third of the cladding failed in other channels was influenced by the one-third batch loading program usually planned for LMFBR studies. One assumes here that if an assembly of fuel elements is under conditions for malfunction, then a reasonable pessimistic conjecture is that a good fraction of that batch may also undergo damage and this could occur at any stage of burnup. The upper bound of the pessimistic assumption would be to assume that the whole channel of assemblies would be damaged simultaneously.

The most adverse design basis disassembly conditions of the problems studied are those associated with Case IB in which the sodium-voiding effect added a \$49/sec ramp to the fuel collapse ramp of \$11/sec. However, if one assumes that some fuel is ejected with the sodium (Cases ID and IIB), then the total \$42/sec ramp for this case could be used as an acceptable initiating condition for the design basis core disassembly.

References

1. A. E. Walter, A. Padilla, Jr. and R. J. Shields, *MELT-II, A Two-Dimensional Neutronics-Heat Transfer Code for Fast Breeder Safety Analysis*, BNWL-1320 (to be published).
2. P. J. Persiani, A. Watanabe, U. Wolff, S. Grifoni and B. Warman, *Some Considerations on the Meltdown Problem for FARET*, ANL-6935 (1964); see also, *Preliminary Considerations on the Safety Analysis of FARET*, Trans. Am. Nucl. Soc. **7**(1), 501 (1964).
3. E. G. Schlectendahl, *Die Ejektion von Natriü aus Reaktorkühlkanälen Nukleonik* **10**, 270 (1967).
4. D. E. Simpson, A. E. Waltan and A. Padilla, Battelle Northwest Laboratory (private communication).
5. T. R. Bump, *Mechanical and Thermal Analysis of Cylindrical Fuel Elements During Off-Normal Conditions After Extended Burnup*, Nucl. Appl Tech. **9**, 301 (1970).

II-58. Comparison of Filter Effects in the Design of the Fuel Element Failure Propagation Loop (FEFPL)

A. E. McArthy

Calculations have been made to study the effects of changes in filters on neutron fluxes and power distributions in the design of the Fuel Element Failure Propagation Loop. The loop is to be irradiated in the Engineering Test Reactor (ETR). Several problems were solved in investigating the effects of different combinations in the borated filter region (Region 6) and the cadmium filter region (Region 10). One dimensional transport theory in the ARC system[1] was employed for calculations, using cross section set 201.

In the cylindrical geometry used for the calculational model, the volume of the assembly containing 19 fuel

TABLE II-58-I. FEFPL Calculation Configuration

Region No.	Material	Outer Radius, cm	Volume Fraction	Atom Density, 10^{24}		Region No.	Material	Outer Radius, cm	Volume Fraction	Atom Density, 10^{24}	
1	Fuel cylinder of irradiated assem.	1.72								Ni	0.00647
									0.211		
							Helium				
	UO_2		0.44	^{235}U	0.006991	10	Filter	6.67			
				^{238}U	0.001914		Cadmium		1.0	Cd	0.0464
				O	0.01782						
	Sodium		0.42	Na	0.01034	11	Water	7.14	1.0	H	0.0656
	Steel		0.166	Fe	0.009844					O	0.0328
				Cr	0.003071						
				Ni	0.001361	12	Flow shroud	7.30			
2		1.872	1.0	Fe	0.059		Aluminum		1.0	Al	0.0602
				Cr	0.0185						
				Ni	0.0082	13	Water	7.62	1.0	H	0.0656
3		3.332	1.0	Na	0.02461					O	0.0328
4	Flow dividers and helium	3.814				14	ETR core	43.50			
							Water		0.4955	O	0.01625
	Steel		0.685	Fe	0.0406					H	0.0325
				Cr	0.01267		Aluminum		0.4339	Al	0.0261
				Ni	0.005614		Steel		0.03855	Zr	0.000656
	Helium		0.315				Zirconium		0.0155	Fe	0.00229
							Nickel		0.0135	Cr	0.000713
5	Sodium	4.106	1.0	Na	0.02461		^{235}U		0.00265	Ni	0.001546
							^{238}U		0.0002	^{235}U	0.0001267
6	Filter	4.398					B(Nat.)		0.0002	^{238}U	0.00000956
	Steel		0.936	Fe	0.0552					B(N)	0.0000210
				Cr	0.0173						
				Ni	0.00768	15	Beryllium ref.	54.93			
	Boron (at.)		0.064	B	0.008811		Water		0.0642	H	0.004094
										O	0.002047
7	Sodium	5.117	1.0	Na	0.02461		Aluminum		0.0444	Al	0.00267
							Beryllium		0.8932	Be	0.1104
8	Primary vessel and helium	5.878				16	Aluminum ref.	70.17			
	Steel		0.789	Fe	0.0463		Water		0.1233	H	0.008088
				Cr	0.0145					O	0.004044
				Ni	0.00643		Aluminum		0.8586	Al	0.05169
	Helium		0.216				Steel		0.0142	Fe	0.000842
9	Secondary vessel and helium	6.596								Cr	0.0002627
										Ni	0.0001164
	Steel		0.789	Fe	0.0468		Uranium		0.00005	^{235}U	0.00000239
				Cr	0.0146						

elements of UO_2 (the central element plus 6 and 12 elements in the next two rings) with associated sodium and steel formed the central region in four of the problems. Other adjoining cylindrical annuli of the irradiated assembly consisted of sodium, flow dividers, filters, and containment vessels. The configuration comprised a total of 16 regions with ETR core material, the beryllium reflector, and the aluminum reflector forming Regions 14, 15, and 16, respectively. The central fuel cylinder region was homogenized. The UO_2 was 88.5% of theoretical density and the uranium was 78.5% enriched. Table II-58-I lists the materials, volume fractions, compositions, atom densities, and radii of the regions. The od of each fuel element, including the 15 mil steel cladding, was 0.23 in. The small amount of helium in regions 4, 8 and 9 was not included in the input of atom densities.

Data for the fuel elements, region compositions, radii of assemblies, ETR core material, and outside regions were obtained from Refs. 2 and 3.

A borated (2 w/o natural boron in steel) filter region twice as thick as that listed in Table II-58-I, and with steel replacing cadmium in Region 10, yielded about the same maximum-to-average fission power (1.18) in the test assembly as did the Table II-58-I configuration. The thicker borated filter region plus cadmium in Region 10 resulted in only a small decrease in the value of the maximum-to-average power ratio (1.18 to 1.16) but produced a large decrease in the power generated in a test assembly fuel element (from 9.5 kW/ft for the configuration in Table II-58-I and 9.1 kW/ft for the case with the thick borated filter region and no cadmium, to 8.2 kW/ft). With sodium replacing the borated steel in Region 6, the cadmium filter produced a maximum-to-average value of 1.23, with an average power of 11.8 kW/ft generated in a fuel element in the test assembly.

TABLE II-58-II. FEFPL Calculation Configuration
(*Central regions*)

Region No.	Material	Outer Radius, cm	Volume Fraction	Atom Density, 10^{24}
1	Fuel element	0.2921		
	UO_2		0.71386	^{235}U 0.014279
				^{238}U 0.001075
				O 0.0307
	Steel		0.28614	Fe 0.016882
				Cr 0.0052936
				Ni 0.002346
2	Fuel elements + sodium	1.00605		
	UO_2		0.41766	^{235}U 0.007635
				^{238}U 0.001347
				O 0.01796
	Steel		0.1674	Fe 0.009877
				Cr 0.0030969
				Ni 0.0013727
	Sodium		0.41494	Na 0.010212
3	Fuel elements + sodium	1.72		
	UO_2		0.39778	^{235}U 0.006330
				^{238}U 0.002224
				O 0.01710
	Steel		0.15945	Fe 0.0094076
				Cr 0.0029498
				Ni 0.0013075
	Sodium		0.44277	Na 0.010897

A calculation was made using the Table II-58-I configuration data except that the central region was replaced by three regions. The new regions consisted of a central region of one fuel element and Regions 2 and 3 containing 6 and 12 fuel elements, respectively. Table II-58-II lists the data for these three regions. The uranium in the central element was 93% enriched. The elements in Region 2 contained 85% enriched uranium and the uranium in Region 3 was 74% enriched. The results of the calculation using these three enrichments in the fuel elements of the assembly being irradiated showed a radial maximum-to-average fission rate of 1.6 and an average power of 9.32 kW/ft in each of the 19 fuel elements.

Calculations including only the cadmium filter (sodium in the borated filter region) gave a maximum-to-average fission rate of 1.5 and an average power of 11.5 kW/ft in each of the 19 fuel elements.

Further analyses were made of the effects of filters and enrichment combinations in the Fuel Element Failure Propagation Loop design. The geometry, calculational methods, and fuel elements in the irradiated assembly were the same as those described above. Calculations were made with 7, 19, and 37 fuel elements in the irradiated assembly. One fuel element was in Region 1 with 6, 12, and 18 fuel elements in Regions 2, 3, and 4, respectively. In each of the calculations results were found for the following cases: inclusion of both filters, inclusion of no filters, inclusion of a cadmium filter only, inclusion of only the borated steel filter (2 w/o natural boron in steel), and inclusion of a cadmium filter located in the boron filter position (the remainder of the boron filter region having been replaced by sodium). When the boron filter was not used it was replaced with sodium, and when the cadmium was not used it was replaced with steel.

The central fuel element was always 93% enriched and the uranium in Region 2 was 78% enriched in the

TABLE II-58-III. FEFPL CALCULATION CONFIGURATION

Region No.	Material	Outer Radius, cm	Volume Fraction	Atom Density, 10^{24}		Region No.	Material	Outer Radius, cm	Volume Fraction	Atom Density, 10^{24}	
1	Fuel region	0.434				10	Sodium	5.117	1.0	Na	0.02461
	UO_2		0.3430	^{235}U	0.00686						
				^{238}U	0.000516	11	Primary vessel and helium	5.878			
				O	0.01475		Steel		0.789	Fe	0.0463
	Sodium		0.5197	Na	0.01279					Cr	0.0145
	Steel		0.1373	Fe	0.008142					Ni	0.00643
				Cr	0.002540		Helium		0.216		
				Ni	0.001126						
2	Fuel region	1.12				12	Secondary vessel and helium	6.596			
	UO_2		0.3631	^{235}U	0.006403		Steel		0.789	Fe	0.0468
				^{238}U	0.001406					Cr	0.0146
				O	0.01561					Ni	0.00647
	Sodium		0.4914	Na	0.01209		Helium		0.211		
	Steel		0.1455	Fe	0.008628						
				Cr	0.002692	13	Filter	6.67			
				Ni	0.001193		Cadmium		1.0	Cd	0.0464
3	Fuel region	1.78									
	UO_2		0.4045	^{235}U	0.006089	14	Water	7.14	1.0	H	0.0656
				^{238}U	0.002610					O	0.0328
				O	0.01739						
	Sodium		0.4334	Na	0.01067	15	Flow shroud	7.30			
	Steel		0.1621	Fe	0.009613		Aluminum		1.0	Al	0.0602
				Cr	0.002999						
				Ni	0.001329	16	Water	7.62	1.0	H	0.0656
										O	0.0328
4	Fuel region	2.44									
	UO_2		0.4169	^{235}U	0.004931	17	ETR core	43.50			
				^{238}U	0.004034		Water		0.4955	O	0.01625
				O	0.01793					H	0.0325
	Sodium		0.416	Na	0.01024		Aluminum		0.4339	Al	0.0261
	Steel		0.1671	Fe	0.00990		Steel		0.03855	Zr	0.000656
				Cr	0.003091		Zirconium		0.0155	Fe	0.00229
				Ni	0.001370		Nickel		0.0135	Cr	0.000713
							^{235}U		0.00265	Ni	0.001546
5	Steel	2.592	1.0	Fe	0.059		^{238}U		0.0002	^{235}U	0.0001267
				Cr	0.0185		B (Nat.)		0.000154	^{238}U	0.00000956
				Ni	0.0082					B(n)	0.0000210
6	Sodium	3.332	1.0	Na	0.02461	18	Beryllium ref.	54.93			
							Water		0.0624	H	0.004094
7	Flow dividers and helium	3.814								O	0.002047
	Steel		0.685	Fe	0.0406		Aluminum		0.0444	Al	0.00267
				Cr	0.01267		Beryllium		0.8932	Be	0.1104
				Ni	0.005614	19	Aluminum ref.	70.17			
	Helium		0.315				Water		0.1233	H	0.008088
										O	0.004044
8	Sodium	4.106	1.0	Na	0.02461						
							Aluminum		0.8586	Al	0.05169
9	Filter	4.398					Steel		0.0142	Fe	0.000842
	Steel		0.936	Fe	0.0552					Cr	0.0002627
				Cr	0.0173					Ni	0.0001164
				Ni	0.00768		Uranium		0.00005	^{235}U	0.00000239
	Boron (Nat.)		0.064	B	0.008811						

TABLE II-58-IV. RATIO OF RADIAL MAXIMUM-TO-AVERAGE POWER IN THE IRRADIATED FEFPL ASSEMBLY

Filter	Number of Fuel Elements in Irradiated Assembly		
	7	19	37
Cd and B	1.06	1.13	1.12
None	1.38	1.71	1.90
B	1.12	1.23	1.25
Cd	1.08	1.17	1.17
Cd in inside filter position	1.07	1.14	1.14

TABLE II-58-V. AVERAGE POWER IN A FUEL ELEMENT OF THE IRRADIATED ASSEMBLY, *kW/ft*

Filter	Number of Fuel Elements in Irradiated Assembly		
	7	19	37
Cd and B	12.2	8.79	6.85
None	34.6	22.0	15.8
B	15.2	10.7	8.17
Cd	15.8	11.0	8.34
Cd in inside filter position	15.1	10.6	8.14

7-fuel-element calculations. For the 19-fuel-element calculations the uranium in the region of 6 fuel elements had an enrichment of 80% and in the region with 12 fuel elements an enrichment of 65%. Calculations involving 37 fuel elements had enrichments of 82%, 70%, and 55% in the regions of 6, 12, and 18 fuel elements, respectively. Table II-58-III lists the materials, volume fractions, compositions, atom densities, and radii of the regions. These values are for the 37 element case, and include both filters and uranium enrichments of the irradiated assembly for this case.

Table II-58-IV lists the ratio of the radial maximum-to-average power in the irradiated assembly for the different filter situations and the average power in a fuel element of the irradiated assembly is given in Table II-58-V.

Additional calculations were made using the configuration specified in Table II-58-III with 19 fuel elements in the irradiated assembly and no filters. The values for the radial maximum-to-average fission power in the test assembly were 1.54, 1.38, 1.33, and 1.55 for uranium enrichments in Region 3 of 0.4333, 0.3250, 0.2167, and 0.160, respectively. The values for the average power generated in a fuel element were 19.4, 17.9, 16.3, and 15.3 kW/ft, respectively.

For an enrichment of 85% in Region 2 (5% more than in the above calculations) and enrichments of 0.3250 and 0.160 in Region 3, the radial maximum-to-average fission power ratios in the assembly were 1.37 and 1.61 and the average powers generated in a fuel element were 18.1 and 15.5 kW/ft, respectively.

A final calculation for 19 fuel elements in the irradiated assembly and with no filters gave radial maximum-average fission power ratio in the test assembly of 1.30 and an average power generated in a fuel element of 16.6 kW/ft. In this calculation the uranium in Region 2 had an enrichment of 0.694 and in Region 3 an enrichment of 0.265. The average power in each element of Region 1 was 15.9 kW/ft, in the elements of Region 2, 16.9 kW/ft, and in the elements of Region 3, 16.5 kW/ft.

REFERENCES

1. B. J. Toppel, Ed., *The Argonne Reactor Computation (ARC) System*, ANL-7332 (1967).
2. E. W. Barts, Argonne National Laboratory (private communication).
3. J. C. Carter, Argonne National Laboratory (private communication).

II-59. Gamma-Ray Dose Rates from Radioactive Sodium and Fission Products in the Fuel Element Failure Propagation Loop (FEFPL)

A. E. MCARTHY

To assist in the design of the Fuel Element Failure Propagation Loop (FEFPL), calculations have been made to estimate the dose rates due to gamma rays from the radioactive sodium and fission products contained in the loop after irradiation at the center of the Engineering Test Reactor (ETR). An array of 19 fuel elements located at the center of FEFPL and contained in a cylinder of radius 1.96 cm was considered in the calculation. The loop included the neutron filter, containment vessels, sodium, and an outside aluminun wall. The UO_2 of each fuel element had a radius o 0.10 in. and the outside diameter of each element, including the steel cladding, was 0.230 in. A cross section of the loop is shown in Fig. II-59-1.

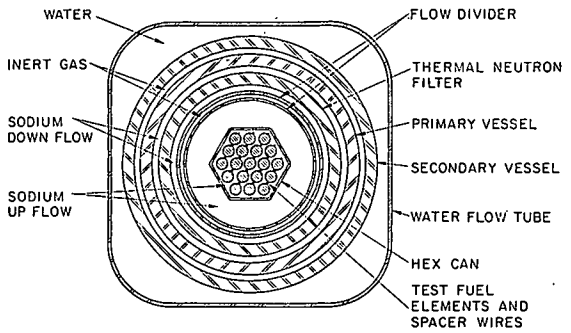

FIG. II-59-1. Cross Section of Fuel Element Failure Propagation Loop for Testing in ETR Core. *ANL Neg. No. 900-1056.*

Dose rates due to fission products were found at a point 1 cm from the outside surface of the loop at the midplane and 1 cm above the top of the loop on the axial centerline. The dose rate 1 cm above the top of the loop was calculated for the fission products contained in the 91.44-cm-long source cylinder and also for the condition where all fission products were assumed to be uniformly distributed in the total coolant volume. The dose rate due to sodium activity was found for a point 1 cm above the top of the loop (143 cm above the top sodium surface) on the axial centerline. For this determination, and in the calculation for the fission products uniformly distributed in the coolant, the total volume of coolant was assumed to be in a cylinder with its top surface at the same level as the top of the sodium in the loop. The cylinder was assumed to have a radius of 6 in.

Dose Rates from Activity of Fission Products

Fission product source values for decay gamma rays (MeV/fission) were based on values listed in Ref. 1. For conservatism, equilibrium fission products were assumed and 6 h of cooling were included. Calculations were made for three energy groups and conservative attenuation coefficients were used for the energies represented in each group. The fission power in the loop was determined by the total UO_2 volume in the 19 elements (352.1 cm^3) and an assumed power density of 2000 W/cm^3 of UO_2 (an average of 12.4 kW/ft). All fission product dose rates can be increased in proportion to any increase in power density.

The gamma-ray flux for each source energy group was calculated by the upper limit formula[2] for the axial centerline at the end of a cylinder. An average source density was determined for each group by assuming the total fissions in the 19 fuel elements to be uniformly distributed in the source cylinder having a radius of 1.96 cm and a length of 91.44 cm. In calculating the flux 1 cm above the top of the loop with the fission products contained in the source cylinder, a 510.5 cm thickness of sodium with a density of 0.82 g/cm^3 was considered to be the shield above the source.

The formula given in Ref. 2 for midplane flux calculations was used to find the group fluxes 1 cm outside the loop at the midplane, with thicknesses of the materials in the loop regions outside the source cylinder serving as shielding.

In all cases the calculated fluxes were converted to dose rates using the conversion factors given in Ref. 3. Table II-59-I lists the source values used for the fission product delayed gamma rays and includes 6 h of cooling.

The dose rate due to gamma rays from fission products in the source cylinder was calculated for a dose point 1 cm outside the loop in the loop midplane. This dose rate was calculated to be 2.5×10^6 R/h. The dose rate from this same source at a point 1 cm above the loop on the axial centerline was about 2 mR/h. The dose rate from fission product activity at a point 1 cm above the loop on the axial centerline, with all fission products uniformly distributed in the coolant and all the coolant in the assumed cylinder, was calculated to be 2.8×10^4 R/h.

Dose Rates from Sodium Activity

Equilibrium activity of the sodium in the loop with 6 h of cooling was used in the dose rate calculations. After five days of irradiation the sodium reached over

TABLE II-59-I. Fission Product Source Values

Energy Group	Source Cylinder Average Source Density, MeV/cm^3-sec	Source Uniformly Distributed in Coolant, MeV/cm^3-sec
1	1.34×10^{13}	1.6×10^{11}
2	5.7×10^{12}	6.7×10^{10}
3	4.2×10^{10}	5.0×10^{8}

TABLE II-59-II. Neutron Fluxes for Sodium Activity Calculations

Group	Inside Neutron Filter, n/cm^2-sec	Outside Neutron Filter, n/cm^2-sec
3	1.2×10^{14}	1.0×10^{14}
4	1.9×10^{14}	1.5×10^{14}
5	1.9×10^{14}	1.7×10^{14}
6	1.2×10^{14}	1.2×10^{14}
7	9.3×10^{13}	1.0×10^{14}
8	8.3×10^{13}	9.0×10^{13}
9	6.5×10^{13}	7.3×10^{13}
10	3.5×10^{13}	4.3×10^{13}
11	3.1×10^{13}	3.8×10^{13}
12	2.6×10^{13}	3.5×10^{13}
13	3.0×10^{13}	3.4×10^{13}
14	3.0×10^{12}	2.2×10^{13}
15	3.0×10^{12}	2.6×10^{13}
16	—	7.0×10^{13}

99 % of its equilibrium activity. Uniform mixing of the sodium in the loop was assumed, and the saturated activity was calculated by finding the total neutron capture rate by sodium in all energy groups (absorptions/sec) in the volume of sodium in the activating flux region and dividing by the total sodium volume circulating in the loop (6.74×10^4 cm^3). Any increase in the total sodium volume would cause a proportional decrease in the calculated dose rates.

Multigroup neutron fluxes were obtained by calculations using the SNARG-1D and SNARG-2D codes of the ARC system.[4,5] The midplane flux distributions were calculated for 16 energy groups for a configuration including the ETR core and inserted loop. The cadmium filter had a thickness of 35 mils.

Fluxes used in the sodium activity calculations were derived from calculations for the seven-fuel-element test assembly. Flux values for the 19 element assembly should not be sufficiently different to produce a significant error in the calculated sodium activity. A conservative average value for each of the 16 group fluxes at the midplane was estimated and used in the activity calculations. The volume of sodium in the 3 ft long fuel element region was used as the irradiated sodium volume. The sodium volume inside the filter in this region was 3142 cm^3 and the volume outside was 897 cm^3. Group fluxes used in the activity calculations are listed in Table II-59-II. Neutron absorptions by sodium in groups 1 and 2 are insignificant and these fluxes are not shown. The sodium absorption cross sections and the 16 group energy limits are given in Ref. 3.

The saturated activity of the sodium in the loop was calculated to be 1.8×10^{10} dis/cm^3-sec or 0.48 Ci/cm^3. This activity gives a gamma-ray source value for the flux calculation of 2.5×10^{10} MeV/cm^3-sec for the 1.38 MeV photon, and 4.9×10^{10} MeV/cm^3-sec for the 2.76 MeV photon. The sodium throughout the loop was assumed to be at a temperature of 550°C and have an atom density of 2.147×10^{22} atoms/cm^3.

The dose rate due to sodium activity at a point 1 cm above the top of the loop with all of the sodium in the assumed cylinder was calculated to be 7.9×10^3 R/h and includes 6 h of decay.

Possible errors in the sodium absorption cross sections could result in the calculated activity being too low. However, the calculational model used in determining the dose rate is believed to be conservative. The dose rate should be no more than 30 % higher than the calculated value.

References

1. N. E. Halden, M. R. Mendelson and T. E. Dudley, *Total Gamma Energy Release Due to Thermal Neutron Fission in U-235*, Nucl. Sci. Eng. **30**, 461 (1967).
2. T. Rockwell III, Ed., *Reactor Shielding Design Manual*, USAEC Report TID-7004, 1956, p. 360 and p. 402.
3. Reactor Physics Constants, ANL-5800, 2nd Edition (1963), p. 657 and pp. 568–574.
4. G. J. Duffy, H. Greenspan, S. D. Sparck, J. V. Zapatka and M. K. Bulter, *SNARG-ID, A One-dimensional, Discrete-ordinate, Transport-theory Program for the CDC-3600*, ANL-7221 (1966).
5. J. C. Carter, Argonne National Laboratory (private communication).

Section III

Experimental Techniques and Facilities

Measured integral reactor physics parameters are necessary for either direct introduction into reactor design calculations or for comparison with values obtained analytically using basic microscopic cross section data. In the latter case the objective is to verify either the cross section data or the calculational techniques. Reactor integral parameters are obtained using special measurement techniques in exponential or critical facilities. The papers presented in this section deal largely with the development of such special techniques, facilities, and radiation detection devices. Included also are papers which describe specially developed equipment useful in obtaining microscopic nuclear data.

III-1. Improved Fast Neutron Time-of-Flight System

A. B. Smith, P. Guenther and A. Engfer

An improved fast neutron time-of-flight system for scattering studies has been designed, constructed, and made operational. An impression of the scope of this new system can be gained from the illustration of Fig. III-1-1. A neutron burst is produced near the center of the system using the pulsed beam of the Fast Neutron Generator and the reactions ^{7}Li(p,n) or D(d,n). The duration of the burst is in the range of 1 to 2 nsec and at a repetition rate in the interval 0.2 to 2.0 MHz. Scattering samples of the order of a centimeter in size are placed at the center focus of the collimator system, about 15 cm distant from the neutron source. Neutrons scattered from these samples are concurrently observed in 10 detectors placed at flight paths defined by the collimator system. The range of scattering angles is -125 to $+160$ deg and the flight paths are variable from 2 to 7 m. Each collimator floats on an air-cushion permitting individual angular adjustment of each flight path. The collimator construction is graded to provide optimum shielding and the system is precisely aligned to well-define the flight path to the sample. The precision is such that no support shielding, such as

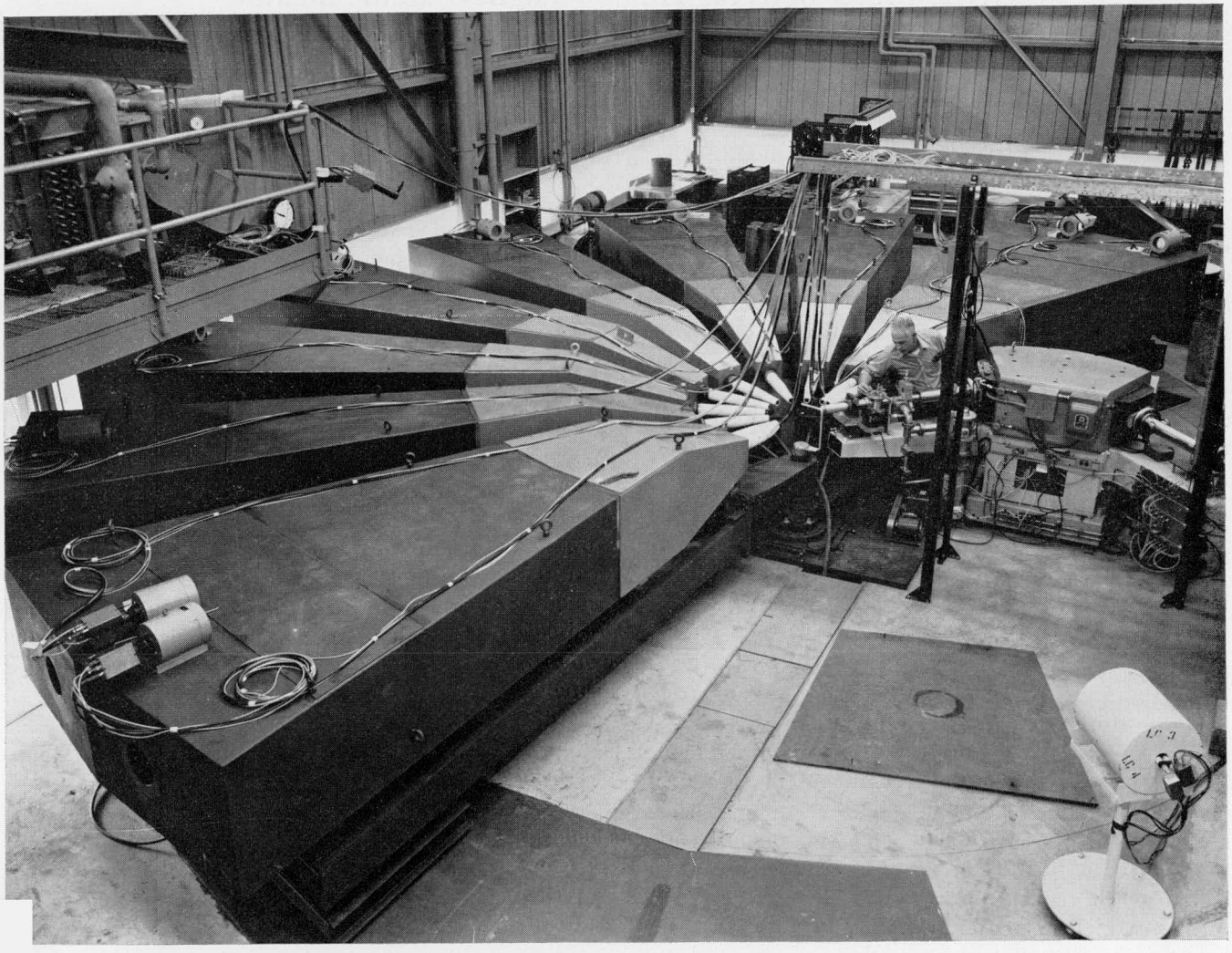

Fig. III-1-1. Photograph of the Ten-Channel Time-of-Flight System. The Scale of the Apparatus can be Judged from the Human Figure. *ANL Neg. No. 116-886.*

shadow bars or cones, is required. Neutron source monitoring is by both time-of-flight proton recoil systems and long counters.

The ten detectors are connected to a special interface system feeding into a devoted on-line computer which handles data acquisition and preliminary processing. Interestingly, this computer is neither large nor particularly modern, yet has proven ample for the purpose and has demonstrated a very good degree of reliability. The data acquisition software is complimented by off-line data reduction programs which rapidly reduce the measured time-of-flight information to cross sections, using a small digital computing system. The cross section information is available during the progress of the experimental measurements. Furthermore, the data are arranged in such a manner as to flow to the large central computing facility where corrections for multiple scattering perturbations are carried out using Monte-Carlo procedures.

Initial performance of the system has been very encouraging. A number of measurements have been completed with scattered neutron resolutions of about 0.5 nsec/m. An entire angular distribution, inclusive of elastic events and prominent inelastic groups, can be obtained in the order of an hour with a very good signal-to-background ratio. The system is very likely unique in both the quality of the data and in overall efficiency.

III-2. Multi-Detector Time-of-Flight System Software

P. Guenther

Introduction

The Applied Nuclear Physics Section's multi-detector time-of-flight (TOF) system for the measurement of elastic and inelastic neutron scattering has been in operation for many years. The adaptation of this system to the new Fast Neutron Generator (FNG) facility required extensive changes due to: a) higher neutron energies, b) new reference standards, c) increased number of detectors, and d) the acquisition of new and more powerful computers capable of handling much of the data processing previously submitted to the Applied Mathematics Division's central facility. Though essentially entirely new in both hardware and software, the principle of operation remains generally as described in Ref. 1. In this paper, both on- and off-line software for the new system is outlined.

On-Line Acquisition Code

The purpose of the on-line acquisition code is to analyze, store, record and display the 3-parameter response of the TOF detector array and to provide certain interactive control functions. The code is operational in the CDC-160A digital computers being used for this purpose. Though older, the computers are sufficiently fast for the task and have a demonstrated high degree of reliability.

Since a high degree of reliability is vital, the program retains output features such as display, printer and FORTRAN-compatible magnetic tape dumps, and interactive typewriter messages, and remains operative for data acquisition with a single 8K 160A computer and magnetic tape unit. This was possible through the extensive use of task-sharing subroutine programming. The actual code requires less than one tenth of the core, the remainder being available for the storage and the output of data received from as many as 14 TOF detectors.

Off-Line Data Analysis Code

The off-line data analysis code replaces RP121. Its purpose is to reduce the measured TOF spectra to differential scattering cross sections relative to standard known cross-sections. The program is divided into 3 major tasks.

1. The description of the efficiency of each of the TOF detectors as an analytical function of incident energy,
2. The normalization of the efficiencies to the specific experimental count rates and the computation of the scattered neutron angular distributions from measured data,
3. The correction of the angular distributions for multiple scattering within the sample using a Monte Carlo procedure.

In the above task format the code consists of 3 separately executable subprograms. As both tasks (1) and (2) use the results of task (3), an iterative procedure is employed: a first-pass computation ignores the corrections and produces an input for task 3. The output of (3) is then reentered into tasks (1) and (2). Experience has shown that this second pass produces results consistent with experimental accuracy. Further-

more, not every energy requires a separate Monte Carlo calculation and generally a moderately spaced energy mesh suffices. The above procedures are executed on an SEL 840 machine (16K, 24 bit) with the advantages of: a) a much simplified debugging of the code, b) greater accessibility and turn-around for production work, and c) the possibility of man-machine interaction for better supervision of the data analysis. For convenience most input parameters are expressed as expansions of the independent variables energy and angle. The basis functions are chosen to give good descriptions of the various parameters from one sample to the next.

The essential computations of the above tasks are illustrated as follows. The count rate at detector k due to neutrons of incident energy E_0 striking sample S is given by

$$N_K^S(E_0,\bar{\theta}) = \epsilon_k(E^S)\eta^S \frac{d\sigma^S}{d\Omega}(E_0,\bar{\theta})C^S(E_0)K^S(E_0,\bar{\theta}), \quad (1)$$

where $\epsilon_k(E^S)$ is the efficiency of detector k at the detected neutron energy E^S, η^S is the atomic density of sample S, $(d\sigma^S(E_0,\bar{\theta})/d\Omega)$ is the differential scattering cross section of sample S (elastic or inelastic) at E_0 and average scattering angle $\bar{\theta}$. $C^S(E_0)$ accounts for flux attenuation and must be considered over an effective scattering volume:

$$C^S(E_0) = \int_{sample} \phi(E_0,\mathbf{r}) \exp\left[-\eta^S\sigma_T(E_0)\ell\right] d\mathbf{r}. \quad (2)$$

$K^S(E_0,\bar{\theta})$ is the Monte Carlo correction factor derived in task 3 in the form

$$K^S(E_0,\bar{\theta}) = \sum_\ell C_\ell(E_0)P_\ell(\cos\bar{\theta}). \quad (3)$$

From the measurements and calculations N_k^S, ϵ_k, C^S and K^S are determined and thence the desired differential scattering cross sections $d\sigma/d\Omega$.

The above illustrates the successful use of a small computer system for an extensive data processing task. A true assessment of processing efficiency cannot be limited to bits, bytes, and memory cycles, but must include the overall human effort. Anyone who has struggled with the inscrutable perversity of large scale computer operating systems should enjoy the simplicity and accessibility of the small computer.

Reference

1. A. Smith, P. Guenther, R. Larson, C. Nelson, P. Walker and J. F. Whalen, *Multi-Angle Fast Neutron Time-of-Flight Systems*, Nucl. Instr. Methods **50**, 277 (1967).

III-3. Total Cross Section Measurements Using Time-of-Flight Methods on the Fast Neutron Generator (FNG)

J. F. Whalen and A. B. Smith

An experimental setup for total cross section measurements on the Fast Neutron Generator (FNG) has been designed and tested. A sample changer under the control of the 840 MP computer was designed and constructed for inserting and removing various samples from the neutron flux incident on a scintillating detector system. The detector was shielded with a standard time-of-flight (TOF) collimating tank but the flux monitor was used in an open geometry. A pulsed beam TOF method of data accumulation for both detector and monitor was used in order to reduce background and secondary neutron group contamination. Each σ_T measurement was the result of four separate time spectra: a monitor and detector spectrum with the sample in and a similar pair with the sample out. The transmission was determined from the ratio of the normalized integrated detector counts and the corre-

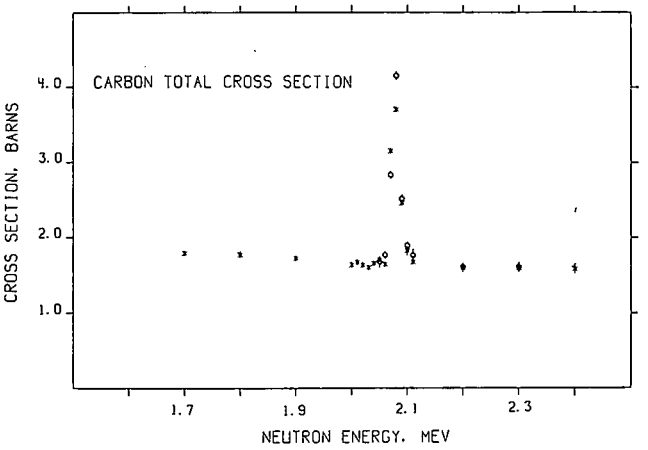

Fig. III-3-1. Illustrative Carbon Total Cross-Section Results. The Two Different Sets of Data Points Denote Measurements Made Traversing the Resonance in Opposite Energy Directions. *ANL Neg. No. 116-841.*

sponding σ_T calculated using the appropriate sample constant.

The new setup was tested by measuring σ_T for carbon over the prominent resonance at 2.08 MeV. The results are shown in Fig. III-3-1: two sets of data are displayed to demonstrate the long term stability of the apparatus by passing over the resonance twice in opposite directions. The resonance peak is not as high as other reported measurements[1] (4.2 b compared with 5.1 b) but this could be the result of the target thickness which was ~5 keV or about ½ the resonance width. The region immediately on either side of the resonance follows the ENDF values extremely well.[2]

REFERENCES

1. S. Cierjacks, *Measurements and Analysis of the Total Neutron Cross Section of Carbon from 0.5 to 30 MeV*, Proc. Conference on Neutron Standards and Flux Normalization, October 21–23, Argonne National Laboratory, Argonne, Illinois. AEC Symposium Series #23, pp. 190–200.
2. Evaluated Neutron Data File-B, National Neutron Cross Section Center, Brookhaven National Laboratory (1970).

III-4. Modification of the Peripheral Configuration for On-Line and Off-Line Fast Neutron Generator (FNG) Computer Systems

J. F. WHALEN

The peripheral configuration of the shared computer system has been augmented by a Control Data 405 card reader and two Control Data 606 magnetic tape units. These three high-speed devices have greatly reduced the normal data processing time not only by the inherent speed of the devices but also by increased reliability. In addition it permits the dedicated assignment of the original magnetic tape units to the ZPR on-line computer system.

Two additional electronic modules have been designed and constructed to expand the input-output capabilities of the on-line computer system. One module contains six computer addressable flip-flops with relay drivers or high speed logic level outputs. These can be used for controlling external devices from the computer such as sample changes, beam gates, etc. The second module contains six level shifters and inverters so that external electronic signals can be inserted into the computer interface at compatible levels and polarities.

III-5. Installation of Apparatus for Measurement of $(n,n'\gamma)$ Cross Sections at the Fast Neutron Generator (FNG) Facility

D. L. SMITH

Apparatus for measurements of gamma-ray production associated with inelastic neutron scattering has been installed at the Fast Neutron Generator (FNG) facility. While the experimental procedures are similar to those applied previously at the 3 MeV Van de Graaff facility, several modifications have been made to enhance the capabilities of the new system.[1]

A new beam target assembly permits access of a gamma ray detector to all scattering angles between 45 and 135 deg in the laboratory system. Lithium metal is evaporated on 1 in. diam by approximately 0.010 in. thick tantalum or tungsten disks which in turn are placed at the top of a stationary 1 in. diam snout whose axis is the beam line. The entire snout assembly is lined with tantalum sheet to reduce background. The beam is slightly diffused by a 60-cycle magnetic deflector to improve target heat dissipation and the target disks are cooled by an air jet. This target configuration has demonstrated the ability to withstand more than 20 W of average beam power for periods of several hours without serious reduction in neutron production.

Lithium-drifted germanium detectors and sodium iodide scintillation detectors will be employed for inelastic gamma ray measurements. Careful shielding from direct target neutrons and gamma rays is required to enhance the yield of detected inelastic gamma rays

relative to background events and to protect the detectors from permanent damage. Unfortunately, the distance from the sample to the gamma ray detector increases as shielding is added with a resulting r^{-2} decline in detection efficiency. Measurements were made to determine a shielding configuration which would be adequate for studies at neutron energies ≤ 5 MeV. Good results were obtained with a shield consisting of a lead shadow bar followed by a tapered stack of lithium-loaded polyethylene blocks with a center collimator hole and an imbedded lead pig surrounding the detector. The detector is placed about one meter from the sample. This configuration will be incorporated in the construction of a permanent shield.

The detector and shielding are supported by a welded steel cart with casters which rolls about a pivot bolted to the laboratory floor. Samples to be irradiated are supported by a slender shaft attached to the pivot assembly on the axis of rotation.

A technique for relating inelastic gamma-ray production cross sections to the relatively well known $^{235}U(n,f)$ and $^{238}U(n,f)$ fission cross sections is being investigated as an approach for avoiding the uncertainties associated with the use of the conventional normalization standard which is the cross section for production of the 845-keV gamma ray in the $^{56}Fe(n,n'\gamma)$ reaction.[2] A low-mass methane gas ionization chamber has been constructed for use as a fission counter.[3] This counter can be placed between the target and the sample to monitor the primary neutron flux.

Timing signals for time-of-flight analysis are generated by a zero-crossing discriminator which detects signals induced in a pickoff tube by beam pulses. This tube is situated near the target to minimize time walk with beam energy. Time-of-flight and pulse-height data are stored simultaneously using the FNG group SEL-840 MP computer on-line data acquisition system.[4] A version of the on-line operating code CONSP provides the necessary control software.[4]

An organic liquid scintillator is utilized as the detector for a separate time-of-flight spectrometer which monitors the neutron and gamma-ray bursts from the target and provides a means for relative normalization of a set of exposures conducted at a fixed energy (e.g., in angular distribution measurements).

The facility described here is currently being used for studies of the $^{23}Na(n,n'\gamma)$ and $^{7}Li(n,n'\gamma)$ reactions.

References

1. D. L. Smith, *Fast Neutron Inelastic Gamma Ray Studies of Arsenic and Sodium*, Applied Physics Division Annual Report, July 1, 1969 to June 30, 1970, ANL-7710, pp. 15–24.
2. M. T. McEllistrem, *Nuclear Research with Low Energy Accelerators*, J. B. Marion and D. M. Van Patter, Ed. (Academic Press, New York, 1967), pp. 167–194.
3. R. W. Lamphere, *Fast Neutron Physics, Part I*, J. B. Marion and J. L. Fowler, Ed. (Interscience Publishers, Inc., New York, 1960), pp. 449–506.
4. J. Whalen, P. Guenther and W. Poenitz, *On-Line and Interactive Computer System*, Applied Physics Division Annual Report, July 1, 1969 to June 30, 1970, ANL-7710, pp. 273–274.

III-6. Facility for Measurement of Delayed Neutron Spectra

S. A. Cox

A knowledge of the yield and energy spectra of delayed neutron emission is important for understanding the kinetic behavior of critical and subcritical systems. There has been considerable effort expended in recent years to determine the yield of delayed neutron emission. However, except for some measurements at Karlsruhe, Germany,[1] there have been no published spectra measurements since the measurements of Batchelor and Hyder.[2] The present facility is intended to provide spectral information from delayed neutron emission following fission induced by neutrons in the 2 to 6 MeV range.

The neutrons are detected by a high pressure ^{3}He counter which has an energy resolution of $\sim$7 % for 1 MeV neutrons. A pneumatic air cylinder shuttle carries the sample to the monoenergetic neutron source for irradiation. After a preset irradiation time the sample is carried to the detector. In order to enhance the delayed neutron activity of the several periods, the irradiation and counting times are varied. The activity of the various periods can be further enhanced by including a decay time between the end of the irradiation time and the start of the counting time. Thus the sequence would be (1) irradiation for time $T1$, (2) decay for time $T2$, (3) counting from start of time $T3$. This sequence is repeated many times so that the resultant measurement represents an equilibrium condition. With the sequence as described above the measured yield of a particular delayed neutron group would be

$$Y = \frac{A\, T\tfrac{1}{2}(1 - e^{-\lambda T1})(1 - e^{-\lambda T3})e^{-\lambda T2}}{T(1 - e^{-\lambda T})}$$

where

$T\frac{1}{2}$ ≡ half life of the delayed neutron group
λ ≡ decay constant of the delayed neutron group
T ≡ total cycle time = $T1 + T2 + T3$
A ≡ normalization constant.

After sufficient data with various combinations of the times $T1$, $T2$, and $T3$ are collected the spectra corresponding to the various delayed neutron periods can be sorted out in a manner similar to solving a set of simultaneous equations.

References

1. Gunter Fieg, *Messung der Spektren Verzögerter Spaltneutronen von ^{235}U, ^{238}U, ^{239}Pu mit Protonenrückstoss Proportional Zählrohnen*, Dissertation, University of Karlsruhe.
2. R. Batchelor and H. P. McK. Hyder, *The Energy of Delayed Neutrons from Fission*, J. Nucl. Energy **3**, 7 (1956).

III-7. Black Neutron Detector

W. P. Poenitz

There is a continuing need for neutron detectors with a nearly constant efficiency over a large energy range. The "Grey Neutron Detector" designed for flux measurements in neutron cross section experiments[1-3] has a flat and smooth efficiency from 0 to about 1–2 MeV. However, above this energy, the efficiency is strongly dependent on the knowledge of the leakage of neutrons out of the detector and the γ-absorption within this detector system. Thus, there is a need for a flat-efficiency detector for the MeV energy range. Such a detector has been designed.

The detector consists of a sphere, cube, or cylinder of scintillator material. The neutron beam enters the detector system through a channel which terminates in approximately the center of the detector. The scintillation light of the recoil protons and carbon nuclei is detected with several photomultipliers. Whereas a conventional recoil scintillation detector yields a continuous spectrum from zero to the primary energy, the present detector adds up the energies from successive collisions and is expected to yield a peak pulse equal to the primary energy. The advantage of such an adding device is appreciable. Extrapolation to zero pulse height can be carried out with high accuracy because the number of small pulses is very small if the detector system is sufficiently large. In Fig. III-7-1 a schematic comparison is made between the conventional recoil detector and the present device.

An actual system used in testing the design idea consisted of a cylindrical plastic scintillator 7 in. in diam and 12 in. high. The neutron beam entrance channel was 1 in. in diam and 6 in. deep. These dimensions assured a small primary leakage and a large probability for successive collisions. Three multipliers were used to view the scintillation light with a two-out-of-three coincidence to reduce the photomultiplier noise effects. Typical energy spectra obtained with 1.0 and 5.4 MeV neutrons are shown in Fig. III-7-2. The background was subtracted by using the time-of-flight method. The time resolution of the detector was essentially given by the time-of-flight uncertainty for the first collision, a FWHM of 6–8 nsec was observed.

The probability of a first collision was about 94% for 5 MeV neutrons and better than 99% for 1 MeV neutrons. Most of the neutrons collide several times, as may be concluded from the energy spectra shown in Fig. III-7-2. Thus, the efficiency of the detector was expected to be approximately equal to the first collision probability. Such high efficiency suggests that the detector was reasonably insensitive to cross section parameters. In order to check for this expectation the yield ratio for the second and first neutron group of the $^{7}Li(p,n)^{7}Be$, $^{7*}Be$ reaction was measured in the energy range from 2.0 to 2.1 MeV. The cross sections for the production of neutrons from the $^{7}Li(p,n)$ reaction are known to vary smoothly in this energy range. The neutron scattering process on carbon shows a resonance at about 2.07 MeV which causes a change of the cross section by a factor of 3. Carbon is a major component in the scintillator used. The change of its cross section should influence the detector efficiency when it is less than 100%. The results are shown in Fig. III-7-3. Some deviation from a smooth variation of the yield ratio can be noticed, though all values lie within error bars (about 2%) of a smooth yield ratio. However, this measurement supports the hope that the non-smoothness of the efficiency above 2 MeV will be very small. A Monte Carlo calculation of the efficiency of the detector has been initiated.

Many applications of this detector are suggested by its special features. The major advantage appears to

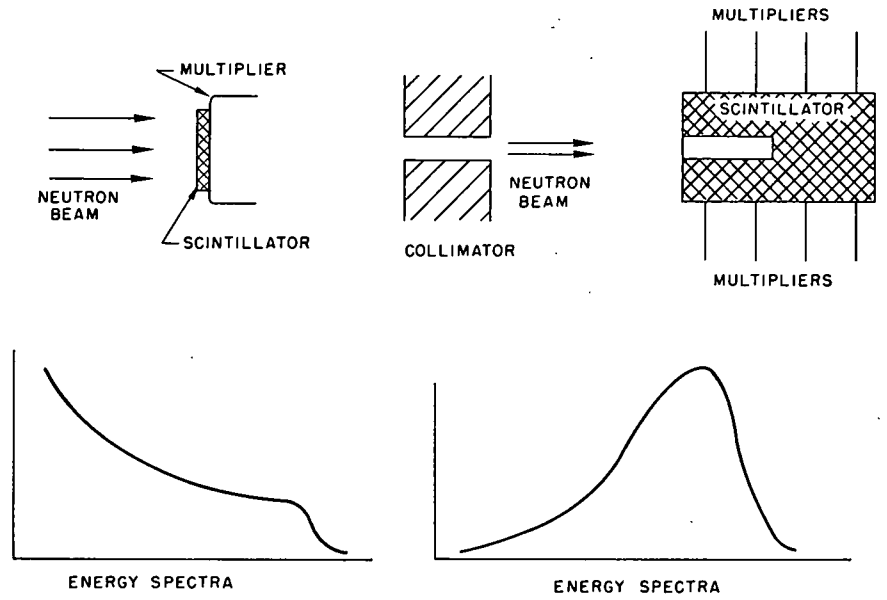

FIG. III-7-1. Schematic Comparison of Conventional Recoil Scintillation Detector and the Present System. *ANL Neg. No. 116-911.*

be that it is, in first order, independent of the cross sections involved, and that the low energy pulses in the energy spectra are infrequent. These features should allow the application of the detector for accurate absolute neutron flux measurements. The range in which the detector can be favorably employed for absolute flux measurements can be extended by using larger sizes and shorter channels as well as a scintillator with a higher hydrogen density.

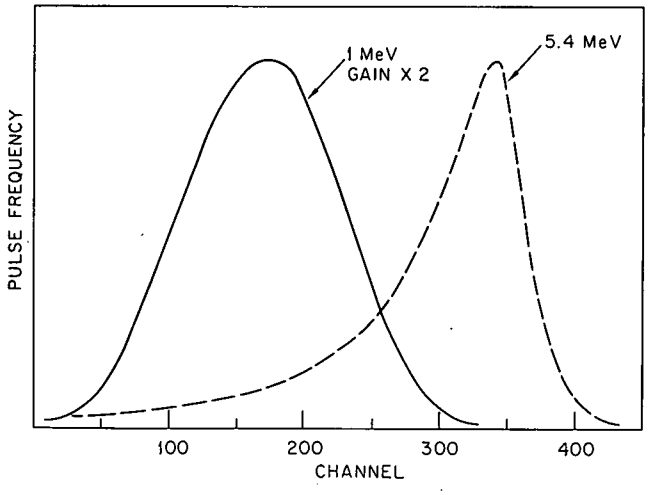

FIG. III-7-2. Energy Spectra for 1.0 an 5.4 MeV Neutrons. *ANL Neg. No. 116-912.*

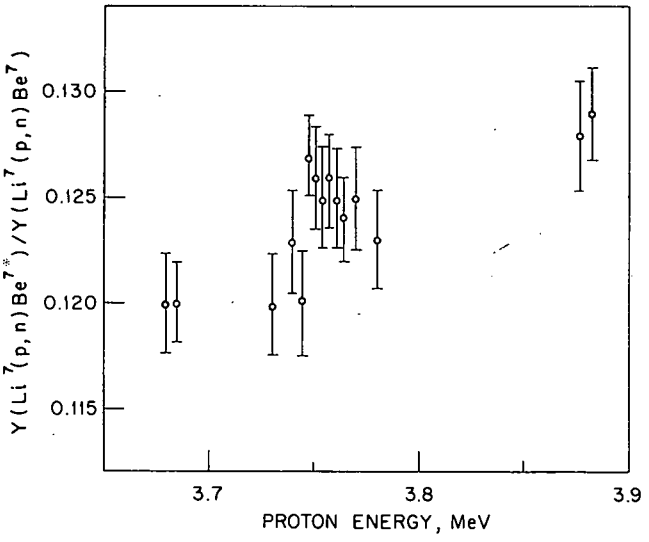

FIG. III-7-3. Yield Ratio of the Second Neutron Group in the Reaction $^7Li(p,n)^7Be$. *ANL Neg. No. 116-910.*

REFERENCES

1. W. P. Poenitz and E. Wattecamps, *A Grey Neutron Detector for Flux Measurements in the Intermediate Energy Range*, EANDC-33 "U", 102 (1963).
2. W. P. Poenitz, *A Grey Neutron Detector for the Intermediate Energy Region*, Nucl. Instr. Methods **58**, 39 (1968).
3. W. P. Poenitz, *Experimental Determination of the Efficiency of the Grey Neutron Detector*, Nucl. Instr. Methods **72**, 120 (1969).

III-8. Neutron Energy Spectrum Measurements in Large, Slightly Subcritical Assemblies by the TOF Method

E. Bennett, C. Cohn, A. De Volpi,* R. Doerner,* Raymond Gold, K. Porges, J. L. Snelgrove and B. Zolotar

A great variety of experiments using short bursts of neutrons in scattering, absorbing and fissionable media, generally referred to as "pulsed neutron" work, has been reported over a period of more than 20 years. The aim of much of the earlier work was the general one of developing, or improving, theoretical descriptions of the underlying processes in terms of measured observables. More recently, a number of facilities providing strong repetitive neutron bursts have been devoted to the specific task of the precise measurement of neutron energy spectra generated in burst-stimulated assemblies by the time-of-flight (TOF) method. With clean assemblies of simple geometry, such spectrum measurements can be compared with calculations based on cross section sets such as ENDF/B, and thus provide a valuable tool for the resolution of certain discrepancies. On the other hand, measurements made with more complex, realistic mock-ups of fast reactor cores are of considerable direct interest in connection with the prediction of various aspects of reactor performance. The TOF facility now nearing completion at ANL is an installation of the latter type.

The measurement of fast reactor neutron energy spectra has also been pursued by other methods, some of which have been developed at ANL to a high state of sophistication. However, it has been recognized for some time that no single method can adequately cover the wide range of energies represented in fast reactor spectra. Thus, proton recoil proportional counter spectrometry is intrinsically limited to the energy range from about 1 keV to 2 MeV. In the high MeV region, a variety of schemes have been applied with varying success, but generally with modest energy resolution. A new method, capable in principle of effecting some improvements within this difficult energy regime, is discussed in Paper III-12. Below 1 keV, only the TOF method can be applied. It may be averred, however, that the spectrum measured by burst-stimulation of a subcritical assembly differs from the spectrum one would find in the same assembly at criticality, and that the inference of the critical spectrum from the burst response spectrum may encounter, in some cases, certain theoretical difficulties. In principle, the critical spectrum below 1 keV can also be measured by means of a chopper, but practically this would require a neutron flux level many orders of magnitude higher than the level available from a critical assembly. Similarly, the burst-stimulated TOF spectrum above 1 MeV becomes difficult to determine with practically feasible flight paths and detectors.

A TOF system for burst-stimulated assembly neutron energy spectrum measurement has three main components: (a) a strong source of short neutron bursts, usually provided by an accelerator whose target is located on a snout projecting well into the assembly so as to irradiate it effectively with neutrons; (b) the assembly, including control instrumentation, shielding etc., (c) a re-entrant channel to the center of the assembly, facing an evacuated flight tube of 50–200 m length, at whose far end one or several fast-responding, precisely calibrated neutron detectors are installed. The accelerator is adjusted to provide pulses of 0.05 to 2 μsec length, at typical repetition rates of 0.5 to 5 kHz; each such pulse starts a clock oscillator and the signal from the neutron detector stops the clock, whence the flight time can be directly stored in a digital memory. The flight time distribution is thus gradually accumulated in a running time which may vary from several hours to days.

While this data acquisition scheme is very straightforward, the extraction of the neutron energy distribution from the raw data involves a highly complex processing program, requiring a number of ancillary measurements. The difficulty of this effort is illustrated by a detailed enumeration of processing steps:

(1) Correction for limited acquisition capability (preemption of acquisition by early arrivals or "spectrum transmission" effect) and for various electronic dead-time effects.

(2) Subtraction of detector gamma background; subtraction of random neutron background and time-correlated neutron background. The latter must generally be measured in a separate run during which the flight tube is blocked by a scattering plug. Other backgrounds can be dealt with through concurrent measurements.

(3) Deconvolution of the effect of the assembly die away and finite duration of the burst, in conjunction with the transformation from flight time to neutron energy. Deconvolution is likewise required for detectors

* Reactor Analysis and Safety Division, Argonne National Laboratory.

whose response has a widely distributed time delay (such as large boron-loaded liquid scintillators). Both of these time distributions must be known with sufficient precision through ancillary measurements and tend to be energy-dependent.

(4) The resultant delta function detector response distribution is now adjusted for the energy dependence of detection efficiency, which yields the TOF neutron energy distribution of the burst-stimulated assembly.

(5) A correction, small for energies below 1 MeV but large and increasingly uncertain in the MeV region, must be applied for the re-entrant channel effect. Both semi-empirical and purely theoretical formulations for this correction have been proposed.

(6) By applying a transformation, the resultant burst-response spectrum allows the inference of the steady-state critical neutron energy distribution at the core center (the feasibility of this step may be somewhat questionable in certain cases, as mentioned above).

This list of processing steps clearly shows the need for statistical precision of a high order, not only in the TOF acquisition but also in the ancillary data. The deconvolution process is subject to the cumulative errors of iteration or matrix inversion. Deconvolution becomes more uncertain with increasing ratio of dieaway period to neutron flight time and therefore with increasing neutron energy, decreasing flight path, and increasing assembly size and reactivity; likewise, the theoretical basis of deconvolution is challenged by assembly configurations which feature a dieaway with a weak fundamental mode.

The practical design of an experimental facility thus must take a number of conflicting requirements into account, to which, for the specific case of the ANL installation, one important further requirement is added: since other commitments of the ZPR-6 assembly (which forms part of the TOF system) militate against inaccessibility intervals of more than a few days, TOF data acquisition is limited *a priori* to a certain maximum core activation, proportional to burst source strength and running time. This limitation precludes the choice of extremely strong neutron bursts and long flight tubes, espoused in a number of existing TOF systems as the most straightforward means of alleviating the deconvolution problem. Accordingly, the ANL facility was designed to use a proton (or deuteron) accelerator which provides neutron bursts through (p,n) or (d,n) reactions; for back-up, an electron LINAC of modest energy (20 MeV) is also available. These sources, while providing a burst strength which keeps core activation within permissible levels over a few hours running time, also avoid certain problems resulting from the high gamma radiation intensity generated by high-current LINAC sources developing 80–100 MeV, which have been used in similar installations elsewhere. At the same time, the maximum flight path of the ANL facility was chosen to be 100 m. Other details of the ANL TOF system are described in Paper III-9.

The cores which will be studied by means of this system will include some relatively large configurations, featuring dieaway periods of the order of 20 μsec; for comparison, it may be noted that the 100 m flight time of a 1 MeV neutron amounts of 7.3 μsec. The successful determination of neutron spectra generated by such assemblies with the described system evidently depends very strongly on the deconvolution procedure. At present a number of such unfolding schemes, based on somewhat different reasoning, are in use. The problem requires further study, particularly with regard to the effect of the energy dependence of the dieaway; consequently, a modest experimental program which will provide a set of "template" measurements of well-distributed neutron spectra, obtained with identical detectors and widely differing flight paths, has been planned, in collaboration with Gulf General Atomic (GGA). Deconvolution of these measurements should reveal, in particular, the effect of data statistical error on processed result error.

To extract the maximum information for a given amount of core activation calls for emphasis on concurrent rather than sequential measurement. Detection devices which are designed to allow concurrent measurement of dieaway and gamma background are described in Paper III-10. In order to permit simultaneous acquisition from a number of detection channels, including multiple acquisition in certain channels (i.e. registration of more than the first detected neutron or other event), a processing facility using CAMAC interfaces had been provided. The CAMAC unit is described in Paper III-11.

A neutron detection system which offers very high detection efficiency, together with acceptable time response dispersion, was chosen for initial deployment: four ^{10}B-loaded liquid scintillator vials of 600 cm^2 combined area and 2.5 cm depth, each coupled to a photomultiplier of type RCA-4525. The dependence of detection efficiency, as well as detection delay distribution, on incident neutron energy is being determined by means of monoenergetic neutrons generated in suitable thin targets (see Paper III-13). The energy range covered by this work extends from 5 keV to 5 MeV. A continuous energy calibration over the full range, 100 eV through 5 MeV, will be obtained by intercomparison with another detector, incorporating a ^{6}Li-loaded glass scintillator, whose response will be determined by measuring it in a known spectrum provided by GGA. In this calibration another standard detector, a ^{3}He high-pressure gas scintillator, will also be used. For this latter

detector, efficiency can be expected to follow quite closely the rather well-known cross section, whereas the detection efficiencies of ^{6}Li and ^{10}B-loaded scintillators deviate strongly from the absorption cross sections of these respective nuclides as the latter fall to a level comparable with scattering cross sections of other nuclides present in the scintillator.

An important aspect of the optimum operation of the ANL system, in which, as described above, neutron bursts are generated by heavy charged particle reactions, is the total neutron yield, as well as energy and angular distribution, resulting from thick targets suitable for incorporation in the restricted space available for the target snout structure. As such yields have been measured only up to 3 MeV, a series of measurements with beryllium and lithium targets, and with both protons and deuterons of up to 7.5 MeV energy, have been started; preliminary results are reported in Paper III-14.

III-9. ZPR-6 Time-of-Flight Neutron Spectrum Measurement Facility

J. L. Snelgrove and R. C. Doerner*

A facility is being installed to permit neutron spectrum measurements by the time-of-flight (TOF) technique to be made on LMFBR type assemblies in ZPR-6. In concept, bursts of charged particles are accelerated onto suitable neutron-producing targets located in or near the central core zone of the assembly. A re-entrant hole oriented 90 deg from the charged-particle entrant hole is used to extract neutrons from the assembly and introduce them into an evacuated flight tube leading to detector stations located at 50 and 100 m from the reactor cell. The layout of the facility is shown in Fig. III-9-1.

Neutron Source System

The neutron source system consists of a charged-particle accelerator, a charged-particle beam transport system, and a neutron-producing target. Protons or deuterons can be accelerated to energies of up to 8 MeV by the Fast Neutron Generator (FNG).[1] Beam currents of up to 1 mA during the pulse can be provided by a new ion source to be installed in the FNG, providing average currents on target of a few microamperes with the pulse widths and repetition rates planned. The beam enters the transport system, shown schematically in Fig. III-9-2, where it is energy analyzed and steered by the 90 deg magnet (B1) and focused on an aperture (A). The centerline of the FNG and the plane of B1 are 168 cm lower than the centerline of the ZPR-6 core; hence, a pair of 30 deg, double focusing, mass-energy product 12, bending magnets (B2, B3) are provided to raise the beam. In addition to the focusing action of the bending magnets, a pair of quadrupole doublets (Q1, Q2) are required to produce the desired beam spot on target. As an aid in aligning and focusing the beam, three quartz plates (V1–V3) viewed remotely by closed circuit television may be inserted into the beam.

The neutron-producing target will consist of either thick natural lithium contained by a copper backing or a thick beryllium disk (see Paper III-14). The target is located at the end of the target probe (Fig. III-9-3) which is inserted into a 5.5 cm square side-entry channel in the ZPR-6 matrix. The target is cooled by circulating liquid Freon 113 behind the target disk. The target disk forms the bottom of a Faraday cup for measuring the beam current, and hence the beam power, on target. A sealed stainless steel sheath is provided around the target drift tube in the matrix as a backup barrier against any leakage of contaminants from the reactor into the source vacuum system.

The source line is evacuated to a pressure between 10^{-5} and 10^{-6} torr by the vacuum pumps shown in Fig. III-9-2 as well as by those connected to the FNG. A series of vacuum gate valves (G1–G7) is used for vacuum control, and more importantly, to provide containment upon the occurrence of an abnormal condition in the reactor cell. Since the source tube must penetrate the 1.2 m thick cell wall, a pair of fast-acting electro-pneumatically operated gate valves (G2, G3) which are designed (as a pair) to withstand the same blast and temperature-pressure conditions as the cell wall[2] is provided. Valves G1 and G6 act to isolate the transport room section of the source tube from all vacuum pumps as a further safeguard against the release of contaminants. The interlock and control systems for these valves are described later.

Personnel shielding from the fast neutrons and gamma rays produced along the source tube by scat-

* Reactor Analysis and Safety Division, Argonne National Laboratory.

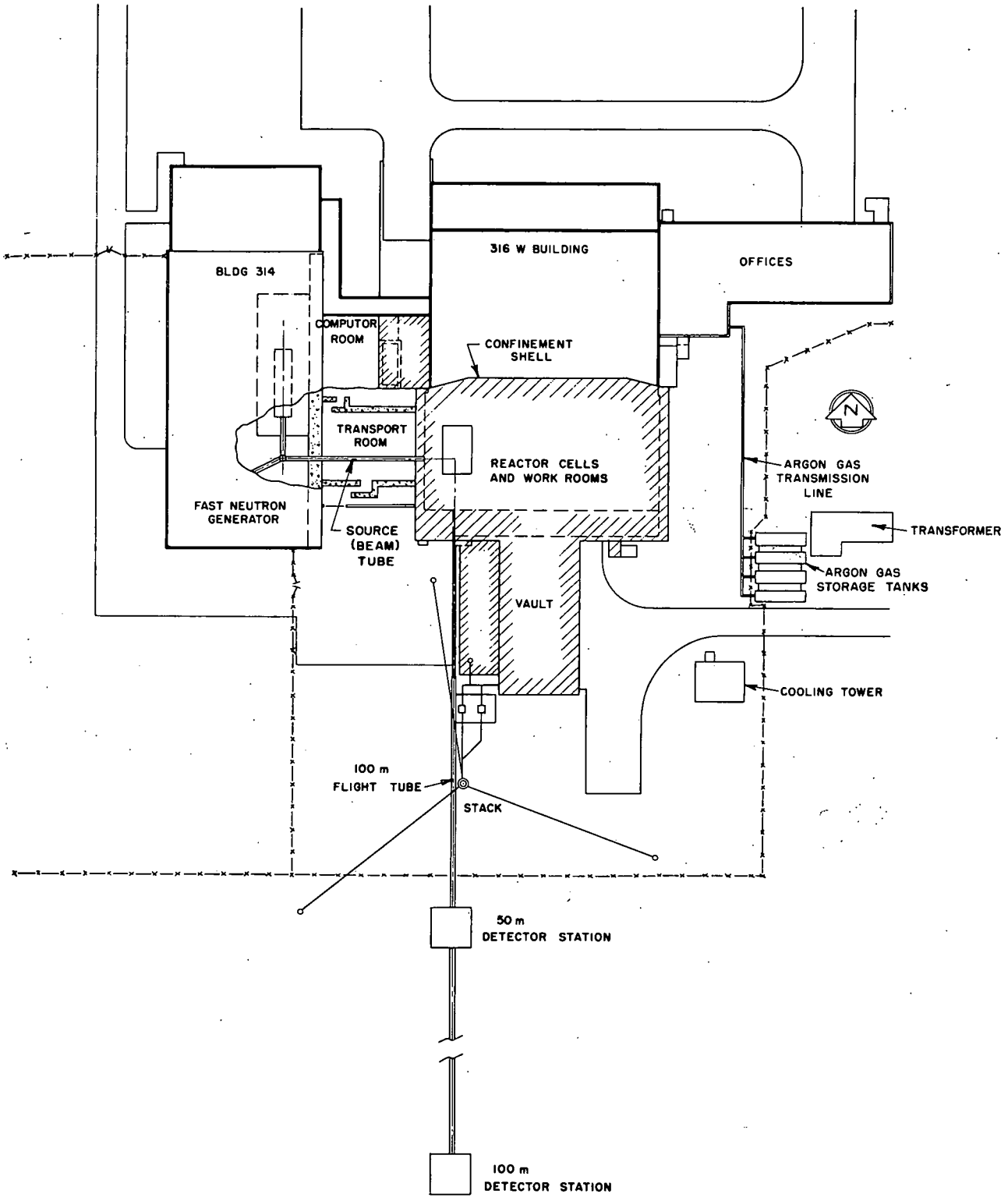

FIG. III-9-1.Layout of the ZPR-6 Time-of-Flight Neutron Spectrum Measurement Facility. *ANL Neg. No. 116-944.*

ered charged particles is provided by a tunnel of stacked concrete blocks along the entire length of the transport room. The shielding is as massive as the available room would allow due to the anticipated use of a stronger source in the future. Labryinths are provided to allow easy access to either side of the tunnel. The 1 m space between the steel confinement shell and concrete cell wall contains no shielding at present, but

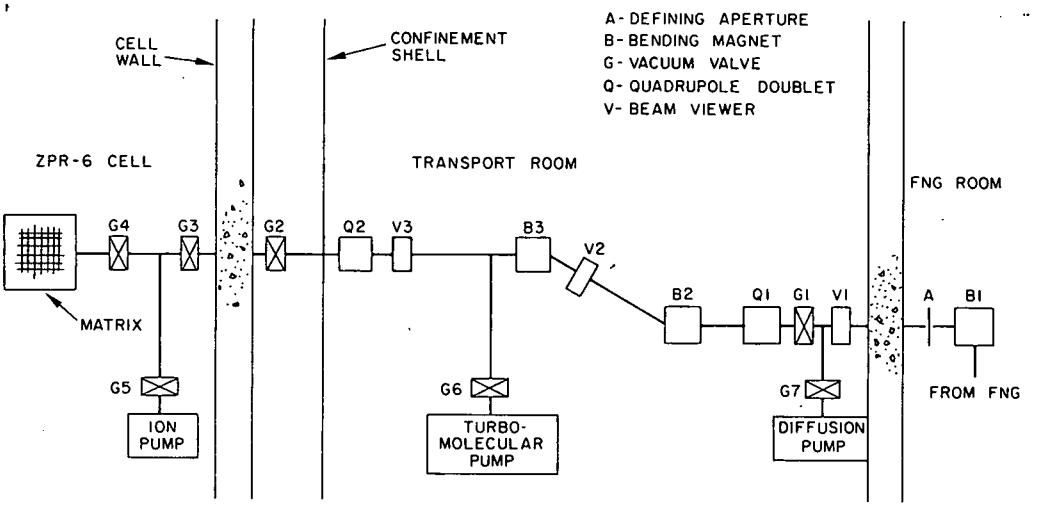

FIG. II-9-2. Schematic Diagram of the Time-of-Flight Neutron Source System. *ANL Neg. No. 116-941.*

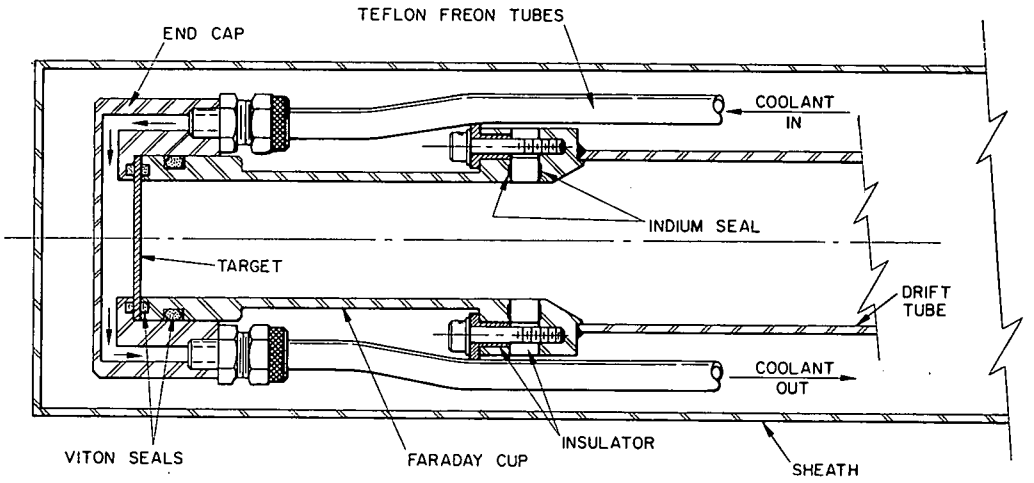

FIG. III-9-3. Neutron-Producing Target Probe. *ANL Neg. No. 116-943.*

design studies have been made for shielding in this area should it be found necessary.

NEUTRON FLIGHT SYSTEM

A schematic of the neutron flight tube is shown in Fig. III-9-4. A leakage path for neutrons from the point of interest in the core is provided by voiding the back section of the central matrix tube (or tubes) to form the re-entrant hole. Most of the neutron flight path consists of sections of pipe evacuated to pressures between 10^{-3} and 5×10^{-2} torr. In order to accommodate the large detector array (33 cm diagonal dimension) necessary for the high detection efficiency required in the ZPR-6 measurements (see Paper III-8), the pipe sections have a 13 cm i.d. between C1 and G10, a 29 cm i.d. between G10 and C2, a 59 cm i.d. between C2 and W4, and a 90 cm i.d. between 50 and 100 m. Each section of pipe is terminated by thin molybdenum end windows (W1–W4); 50 μ thickness being used for W1–W3 (13 cm diam) and 250 μ thickness being used for W4 (41 cm diam). Molybdenum was chosen rather than the more commonly used mylar for its added strength in the large window and for its substantially lower average scattering cross section (which is magnified by the decreased thickness necessary for equal strength in the smaller windows). For measurements at 100 m a section of pipe is inserted at 50 m and the window and detector are moved to 100 m. Vacuum control is effected through the use of valves G8–G14. As in the case of the source line, gate valves G8 and G9 provide cell containment and gate valve G10 isolates the confinement shell volume from the external drift tube. The concrete block detector stations at 50 and 100 m are heated and air conditioned to provide a stable environment for the detectors and associated electronics.

Neutron beam collimation is provided by a series of collimators C1–C3 and the cell wall penetration. Pres-

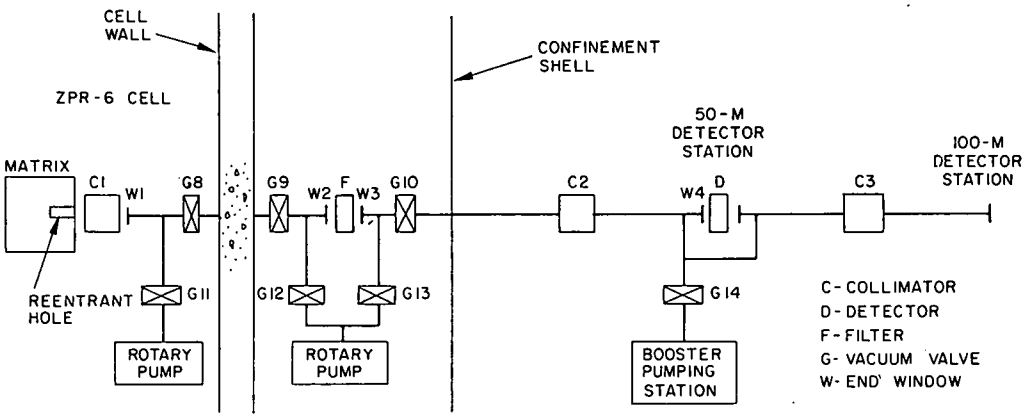

FIG. III-9-4. Schematic Diagram of the Time-of-Flight Neutron Flight System. *ANL Neg. No. 116-942.*

ent plans call for the collimators (fabrication has not begun) to be made of a material such as borated polyethylene. All will accommodate the largest solid angle allowed by the flight tube diameters, with inserts being used for smaller solid angles (smaller detectors and/or smaller spot viewed at the bottom of the re-entrant hole). Collimator C1 plus the detector actually define the solid angle, while collimators C2 and C3 function as anti-scattering baffles. Collimators C2 and C3 are contained in removable sections of the flight tube.

The air gap in the flight path between G9 and G10 is provided to facilitate the insertion of various neutron and gamma-ray filters and to make possible neutron measurements at short flight paths (see Paper III-12). Various filters are necessary during both spectrum and background accumulations. A thin boron or a thin lithium hydride filter is used during spectrum measurements to remove those low energy neutrons from the beam whose flight times are so long as to overlap the flight time of fast neutrons from the next burst. During background measurements [at least until a concurrent background determination can be made (see Paper III-10)], thick filters such as polyethylene and lead must be inserted into the beam to remove the neutrons and the gamma rays, respectively. A remotely operated mechanism for inserting the filters will be provided.

INTERLOCK AND CONTROL SYSTEM

An extensive interlock and control system has been designed to permit the safe and efficient performance of time-of-flight neutron spectrum measurements. The cell-valve interlock system provides those automatic functions necessary to supplement actions of the reactor operators in maintaining cell containment. Such parameters as cell temperature and pressure, cell-valve pneumatic system pressures, source and drift tube vacuums, and reactor control power and table position are monitored, and a value outside the "normal" range results in the immediate closing of the appropriate valves. The interlock system is based on the principle of redundancy, and redundant pneumatic systems are supplied for the cell-valves.

The FNG interlock and personnel warning system is designed basically to provide for automatic protection of personnel. Access door interlocks are provided at all entry points into potentially high radiation areas, and beam scram buttons are located at strategic points. Combination fast neutron and gamma-ray monitors consisting of Pilot B scintillator coupled to photomultiplier tubes are located in normally occupied areas adjacent to exclusion areas. High level trips in the FNG beam interlock chain will be set at appropriate settings to prevent excessive radiation exposure. The FNG interlock system also functions to protect the valves and target from beam burning by monitoring valve gate position, beam current on target, and target cooling. Any abnormal condition will result in the insertion of two independent beam stopping devices into the source tube. The personnel warning system is designed to give audible and visual warning that a charged particle beam can be, or is being, introduced into an exclusion area. The control system serves to monitor and operate those portions of the TOF system not directly related to containment or personnel safety.

PRESENT STATUS OF THE TOF FACILITY

At the present time most of the major components of the source and flight systems have been installed and partially tested. Major design work has yet to be completed for neutron collimators and filters. The interlock and control system is in the final stage of fabrication and will require an extensive installation and testing effort. A continuation of the primary neutron detection system calibration (see Paper III-10) as well as

work on related on-line detection systems (see Paper III-13) will be required. Initial testing of the complete facility is expected to begin early in 1972 with the ZPR-6 reactor in a "halves-apart" (probably unloaded) configuration. Thereafter, initial neutron spectrum measurements will be initiated at the earliest time that ZPR-6 scheduling will allow.

REFERENCES

1. S. A. Cox, *The Fast Neutron Generator (FNG) Facility*, Reactor Physics Division Annual Report, July 1, 1969 to June 30, 1970, ANL-7710, pp. 265–266.
2. W. Y. Kato, G. K. Rusch, L. R. Dates, C. E. Till, A. Ancarani, J. Van Doorninck, C. L. Cheever and E. M. Bohn, *Final Safety Analysis Report on the Use of Plutonium in ZPR-6 and -9*, ANL-7442, 138 (1970).

III-10. On-Line Detection Systems for the Time-of-Flight Neutron Spectrum Measurement Facility

K. PORGES, RAYMOND GOLD and J. L. SNELGROVE

INTRODUCTION

The ANL time-of-flight (TOF) neutron measurement facility, described in Papers III-8 and III-9, includes major components which have other scheduled commitments. Neutron spectrum measurements must therefore be carried out in such a way as to extract a maximum amount of information per unit of assembly activation (as well as per unit time).

As described in Paper III-8, processing of the neutron energy spectrum from the raw TOF acquisition requires a number of precise ancillary measurements; specifically, various backgrounds and "dieaway". Some of these measurements are usually made sequentially, partly because acquisition capability of available electronics may be limited and partly to compensate for characteristics of available detectors by varying fluence conditions. In view of the time and core activation limitation, a high-capacity acquisition system was provided for the ANL system, and a number of special detection devices as well as electronic processing techniques have been designed to allow the acquisition of virtually all processing parameters concurrently with the TOF acquisition. These devices are briefly described in this paper—first the channels used for dieaway measurement, and then those used for background measurement. The main TOF detection system has already been described in Paper III-8.

IN-CORE FISSION CHAMBERS

The "dieaway" shape is customarily measured by in-core fission chambers. With chambers of conventional design, this entails a separate run at reduced burst strength to avoid overloading; even so, the initial part of the burst profile may be rendered unreadable through gamma event pileup (particularly when an electron accelerator is used to generate the burst). In view of the energy dependence of dieaway shape, it is expedient to use at least two different chambers, say one incorporating ^{235}U-coated foils and the other ^{238}U-coated foils. Various considerations apply to the best location of the chambers; however it is clear that a location which samples the same neutron population that is viewed by the flight tube detectors considerably simplifies interpretation. Accordingly, a double fission chamber was designed to fit into the standard modular drawer of the assembly, and is intended to be located at the bottom of the re-entrant channel. In that location, pileup effects must be expected to be particularly severe. However, it is possible to reduce pileup effects by making chamber dimensions, such as plate spacing, as small as possible. On one hand this reduces the average amount of ionization deposited within the chamber by the lightly ionizing Compton recoil electrons in comparison with heavily ionizing fission fragments; on the other hand the collection time is evidently inversely proportional to the plate spacing. In practice it is expedient to make plate spacing of the order of 1 mm and then adjust the gas pressure so as to optimize the fission-to-gamma background and fission-to-amplifier input noise signal strength ratio. The effect of pulse length on pileup may be judged from the following consideration: suppose that the channel discriminator is biased to accept sixfold pileup of average gamma events in the chamber. Then quasi-rectangular pulses of 20 nsec width will result in a pileup detection probability of 3.6% at a random gamma event rate of 10^8/sec, whereas 40 nsec pulses, which ordinarily would still be considered very short for a fission chamber, increase the background detection probability to 16%. While these are only crude estimates, the illustrate the need for the shortest possible collectio time, if such chambers are to be useful in on-line dieaway acquisition.

The double fission chamber, shown in Fig. III-10-1, was accordingly designed with millimeter plate spacing;

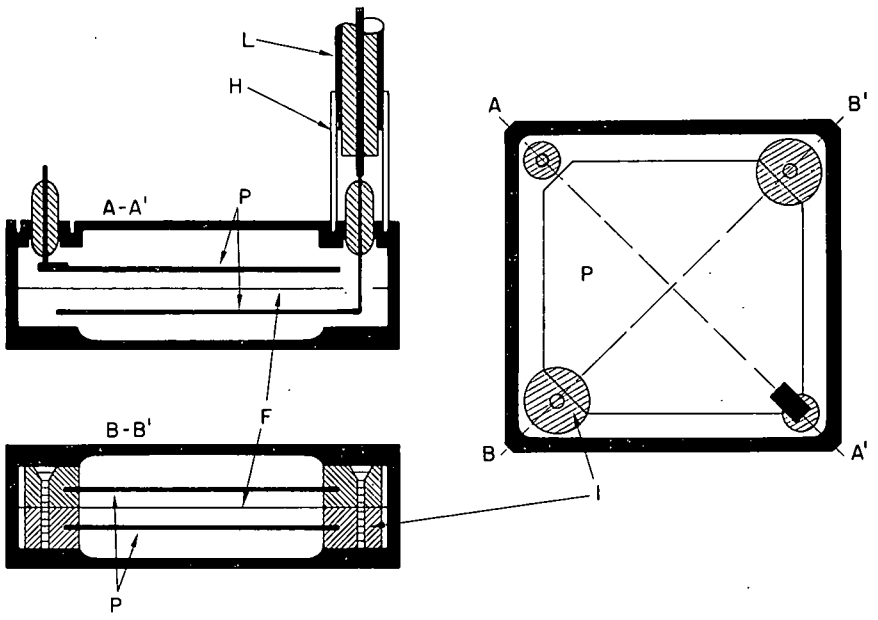

FIG. III-10-1. Double Fission Chamber. Two Diagonal Cuts are shown, A-A′ and B-B′. Plates P are Soldered into Signal (Plus High Voltage) Leads at one Corner A and Clamped in Slotted Ceramic Washers I at both Corners B. Fissionable Coatings are Applied to Two 0.004 in. Thick Aluminum Plates F, Grounded, and Clamped Back-to-Back between Washers I. Solid Copper-Sheated Signal Transmission Lines L are Attached to Ceramic Feedthrough Insulators through Sleeves H Attached to the Chamber Body. *ANL Neg. No. 116-1059.*

at the same time the coated area diameter was made relatively large (32 mm) so that the chamber could sample the whole bottom of the channel. To avoid biasing the neutron spectrum, the amount of structural stainless steel was minimized, while the chamber shell was designed to hold 3 atm over-pressure. With pure methane filling, a collection time of 12 to 15 nsec—hence pulse length well within 20 nsec—is obtained at 1.8 kV. Accordingly the insulation is designed for 2.5 kV and the plates are clamped in split ceramic washers.

To maintain a rise-time of the order of 5 nsec and minimize attenuation as well as noise pickup, the chamber signal output is conveyed to two 200 MHz amplifiers via solid-sheathed, 0.25 in. o.d., teflon-insulated transmission lines. The use of such semi-flexible lines in lieu of braided cable for various core instrumentation systems would seem to be generally advantageous (and particularly useful when in-core temperatures up to a few hundred degrees Centigrade are encountered). Performance data necessarily await initial tests of the TOF system.

Background Measurements

A difficult TOF problem arises from the presence of burst-correlated background effects. In particular, a ıbstantial correlated neutron background is observed ı some existing TOF installations. This effect is found to be associated with neutrons reaching the detector along paths at least partly external to the flight tube and can therefore be measured by plugging the latter with a scatterer located near the assembly. Since the plug transmits gamma radiation in the flight channel, a single background run subsequent to the data run can, in principle, determine all backgrounds. To scale the subtraction, it is expedient to choose burst intervals somewhat longer than the arrival time at the detector of the slowest neutrons created in the burst and assign the interval between this arrival time and the next burst to quasi-continuous background acquisition.

Neutrons which reach the detector via scattering but originate in a burst must necessarily leak through the containment and shielding surrounding the assembly and/or accelerator. Noting, in this connection, that the shielding structure of ZPR-6 appears to be considerably heavier than shields provided in some other installations, one may reasonably expect a correspondingly weaker correlated neutron background which might then be reduced to insignificance with some additional collimation and shielding. The continuous neutron background, due to delayed neutrons, spontaneous fission, and local (cosmic radiation and environmental) neutrons, can be subtracted as described above, by a background acquisition which is interleaved with the burst acquisition.

Background gamma radiation also features a burst-correlated component, consisting of a delayed replica of the dieaway and a tail due to fast-decaying isomeric levels activated in the core. In principle, gamma background need not interfere with neutron acquisition if a neutron detector with sufficiently strong gamma rejection capability (yet high neutron detection efficiency over the wide energy range of interest) can be devised.

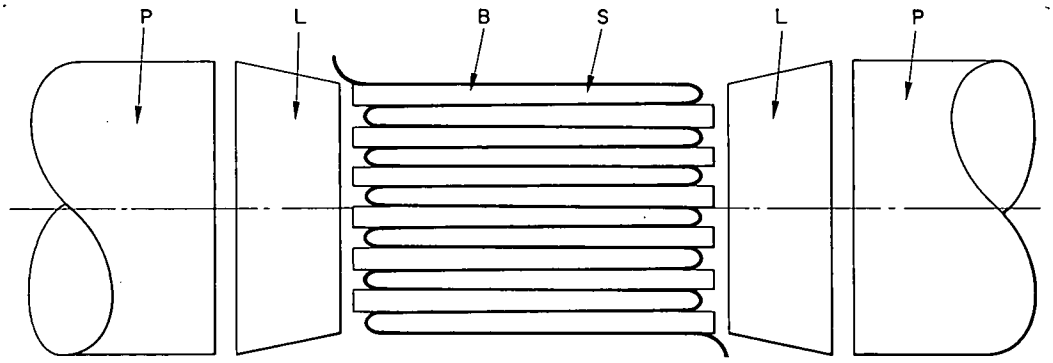

FIG. III-10-2. Gamma Detector. S, Plastic Scintillator Slab (20 Each, 0.100 in. Thick); B, Light Baffle (Aluminized Mylar, 0.002 in. Thick); L, Light Pipe (UVT Acrylic); P, Photomultiplier (RCA-8575, 2 in. Diam.). In the Drawing, Photomultipliers, Light Pipes and Detector are Slightly Separated, for Clarity; in the Assembled Package, These Components are Optically Coupled with Dow Silicone Grease and Closely Spaced through Clamping in a Frame. *ANL Neg. No. 116-1058.*

At present such a detector does not exist. A certain degree of gamma rejection is available in liquid scintillators by use of electronic pulse shape discrimination. However, differences in pulse shape for liquid organic scintillators which satisfy the neutron detection efficiency requirement are rather small, while the number of photoelectrons released by the average neutron interaction in the scintillator is only modest. Consequently, shape discrimination is subject to considerable statistical broadening which results in the rejection of a significant number of valid (neutron-generated) events when the channel is adjusted to reject gamma events to a high degree, or conversely, acceptance of a significant gamma background with substantially full neutron acceptance. (The latter *modus operandi* is preferable, since neutron rejection tends to vary with neutron energy and thus would otherwise bias the spectrum.) A shape analyzer of advanced design, provided for the ANL TOF system, has been tested extensively with different scintillators, photomultipliers, and sources. Efforts are continuing to improve the performance of this system, especially through procurement of improved scintillators; however, a number of remaining problems, such as the long-term stability of the channel and the correction of the acquisition for certain dead-time effects introduced by electronic processing, can be solved only through direct experience in actual TOF measurements. While this may require separate background acquisition runs—at least in initial measurements—another channel, described below, which rejects neutrons to a high degree, has been designed to acquire pure gamma background *concurrently*, thus providing information through which remaining gamma background in the acquisition channel can be cleanly subtracted.

This detector, shown in Fig. III-10-2, consists of a stack of plastic scintillator slabs facing the flight tube. Alternate slabs are coupled to one of the two lateral photomultipliers and slabs are mutually optically isolated through a ribbon of aluminum-coated Mylar which is wound through the stack as depicted in the figure. Slab and Mylar foil thickness are designed to correspond to the range of an 8 MeV recoil proton, which is also equivalent to the nominal range of a 40 keV electron. The bulk of Compton electrons released in the stack through gamma radiation will therefore generate light in at least two slabs, whereas all but an insignificant fraction of input neutrons release light in a single slab only. A fast coincidence requirement between photomultipliers thus produces a high degree of discrimination against neutron-generated events, as well as against photomultiplier noise. Since the plastic scintillator has a light decay of the order of nanoseconds, a coincidence resolving time of 5 nsec is practical. Preliminary trials of this system with a ^{60}Co source and an americium-beryllium neutron source demonstrated a neutron discrimination of about 2×10^3 at 60 to 80% gamma detection efficiency.

The fabricated detector has a depth of 2.5 cm and an effective area of 60 cm^2, compared with the main detectors of combined area of about 600 cm^2 at the same depth. Installed about 1 m behind the main detection system, the slab detector will not interfere with neutron detection. The relative gamma signal strength of slab and main detectors can be assayed by a single run with scattering plug inserted, and checked at any time with a gamma source. If correlated neutron background can be sufficiently reduced, as discussed above, all necessary acquisitions can thereafter be done concurrently.

It may be added that a multislab detector of the type described can, in principle, be operated also in anticoincidence mode, thus rejecting gamma events while retaining neutron events. This unfortunately also retains photomultiplier noise, and thus calls for a higher bias. However, the strong light attentuation resulting from transmission along the narrow (0.10 in.) slab militates against such a high bias, as a very substantial fraction of detections release only one or two photoelectrons.

III-11. CAMAC Crate Controllers for the SEL-840MP and DDP-24 Computers

C. E. Cohn and S. J. Rudnick*

CAMAC[1] crate controllers have been built for the Systems SEL-840MP and Honeywell DDP-24 computers. The former is intended for use with the time-of-flight experiments, while the latter is intended for use in conjunction with foil-counting equipment. These controllers are highly flexible and efficient without excessive hardware complication and include some of the special features of a previous Argonne design.[2]

On the SEL-840MP, a command (CEU) instruction is used to set up CAMAC operations. Its command word carries all bits needed to specify station number (N), sub-address (A) and function (F). These bits are saved in flip-flop registers until altered by a subsequent command word. If the specified CAMAC function is a control command (F8 = 1) a dataway operation is initiated immediately. The events in the dataway operation are timed by clock pulses supplied by the computer at a frequency of two per 1.75 μsec memory cycle.

On the DDP-24, the Output Control Pulse (OCP) instruction is used to set up CAMAC operations. Its 15-bit address field specifies N, A and F. A one in the high-order address bit identifies an OCP as being CAMAC-directed, as no other OCP carries that bit. The N, A and F bits are saved in flip-flop registers until altered by a subsequent CAMAC OCP. If the specified CAMAC function is a control command a dataway operation is again initiated immediately. The events in the dataway operation occur at 1-μsec intervals as timed by the 1-MHz computer clock. For both computers the CAMAC-specified minima for the duration of each phase are comfortably exceeded without delaying the computer.

For both computers, the possibility of dataway operations directed to more than one module is provided by a 23-bit N register which is activated whenever the N field of a CAMAC command is zero. CEU or OCP instructions can control the initialize (Z), clear (C), and inhibit (I) signals. Z is also developed whenever the computer is cleared.

* Electronics Division, Argonne National Laboratory.

A dataway write operation is set up by a CEU or OCP specifying a write function (F16 = 1, F8 = 0). The actual operation is later initiated by an output instruction. The data from the computer are strobed into a data register connected to the write (W) lines, and a dataway operation is begun. Similarly, a read operation is set up by a read function (F16 = F8 = 0). A dataway operation is initiated by an input instruction, and the computer acquires data from the read (R) lines at S1 strobe time. An immediate ready response is given to the computer on every CAMAC-directed command, input, or output instruction.

During each dataway operation the status response (Q) line is interrogated at S1 time. The result may later be examined by a test or sense instruction. On the SEL-840MP, provisions are made to initiate a dataway control operation and then test the Q line, all with one test (TEU) instruction.

On the SEL-840MP, any look-at-me (L) signal initiates a computer interrupt at one level. The station number of the module initiating the L signal is entered in a special L register, and the remaining L lines are locked out until the interrupt has been serviced. If two L signals arrive simultaneously, the higher-numbered module takes priority. The interrupt-servicing routine reads the L register as one of its first operations, and uses the result to branch to the routine that services the module originating the interrupt. This saves time by making it unnecessary to query a number of modules to determine the interrupt origin. The DDP-24, on the other hand, has enough interrupt levels available so that each L line can be connected to a separate level.

References

1. *CAMAC—A Modular Instrumentation System for Data Handling*, EUR-4100E (March 1969).
2. J. J. Eichholz, F. R. Lenkszus and M. G. Strauss, *Versatile CAMAC Crate Controller for Computer-Based Data Acquisition Systems*, IEEE Trans. Nucl. Sci. **NS-18**(1), 292 (February 1971).

III-12. Pulsed-Neutron Time-of-Flight Measurements at Short Flight Paths in a Zero Power Reactor

Raymond Gold, K. G. Porges and J. L. Snelgrove

Existence and Uniqueness of Leakage Spectra

Measurement of neutron spectra have been attempted by the pulsed neutron critical assembly time-of-flight (TOF) method at a number of Laboratories. In the data analysis of such TOF experiments, a diverse variety of assumptions have been introduced.[1] Consequently, experimental results depend crucially upon these assumptions. Hence, quantitative TOF measurements of leakage spectra are not possible unless the validity of such assumptions is tested and any limitation of the method thereby defined.

Fortunately the TOF method is amenable to introspection. One need only change the time-dependent excitation function driving the sub-critical assembly and examine the resulting effect upon the neutron spectrum. As large a change in excitation function as possible should be introduced, within the bounds and convenience of experimental capabilities. Comparison of two or more of these spectral measurements will provide conclusive evidence for or against the existence and uniqueness of a single neutron leakage spectrum that is characteristic of the given critical assembly.* Moreover, the adequacy and accuracy of data analysis, as well as any simplifying assumptions so entailed, are simultaneously tested by this process. From still another viewpoint, one can anticipate that this procedure will eventually define an upper energy limit of the domain of validity of the TOF measurements.

High Energy TOF Measurements

Given a neutron detector of fast response, high energy TOF neutron experiments may be feasible using reduced flight paths. Measurements made as close as 8–10 m would be extremely advantageous in view of anticipated intensity problems. These measurements would require a good detector response to high energy neutrons, but negligible response to low energy neutrons and gamma-rays. Such a detector has recently evolved from a ^{3}He gas scintillator which has been developed for low energy TOF experiments.[2] With a high pressure filling of ^{4}He instead of ^{3}He, this detection system provides a very fast high energy response (rise time $\sim$3 nsec) and possesses virtually no sensitivity below a few hundred keV (see Paper III-15).

* The relation between this "hopefully" unique leakage spectrum and the in-core equilibrium spectrum attained at power (in the same critical assembly) will not be considered here.

A preliminary, albeit naive, description of the data analysis for in-close TOF experiments with this detector is considered below. As with other TOF measurements, it is imperative that one test the validity of experimental results by introducing more than one excitation function, as has already been described above.

Let $M(t)$ be the time dependent response of a detector placed at a distance L from a pulsed critical assembly. Furthermore, let $P(E,t)$ be the neutron population function of energy E and time t. Hence neutrons of energy E will be detected at a time which is delayed by the time-of-flight τ, given by

$$\tau^2 = \frac{A}{E}, \tag{1a}$$

$$A = \frac{M_0 L^2}{2}, \tag{1b}$$

where M_0 is the neutron rest mass. Consequently, the neutron population $P(E,t-\tau)$ gives rise to the observed response $M(t)$ for the TOF detector at a distance L.

If $\sigma(E)$ is the detector reaction cross section per nucleon and N the total number of nuclei in the sensitive volume of the detector, then

$$M(t) = N \int_{A/t^2}^{\infty} P(\xi,t-\tau)\sigma(\xi)\, d\xi. \tag{2}$$

The lower limit in Eq. (2) implies that neutrons detected at a time t (after the pulse) must possess energies greater than that required by the flight time, i.e. $\xi \geq A/t^2$.

Expanding the neutron population $P(\xi,t-\tau)$ in a Taylor series about τ, one has

$$P(\xi,t-\tau) = P(\xi,0) + \left.\frac{\partial P}{\partial t}\right|_{t=\tau} (t-\tau) + \cdots. \tag{3}$$

Let us assume that a value of t exists, say t_0, such that for all $t \leq t_0$, the neutron population is stationary, that is,

$$P(\xi,t-\tau) \approx P(\xi,0), \qquad t \leq t_0 \tag{4}$$

for all possible neutron energies ξ. We will subsequently return to an examination of this assumption. Using Eq. (4) in Eq. (2),

$$M(t) = N \int_{A/t^2}^{\infty} P(\xi,0)\sigma(\xi)\, d\xi, \qquad t \leq t_0. \tag{5}$$

Differentiation yields

$$\frac{dM}{dt} = \frac{2N}{t} E\, P(E,0)\sigma(E). \qquad (6)$$

Since $P(E,0)$ can be identified as the leakage neutron spectrum, Eq. (6) provides

$$P(E,0) = \frac{1}{2NE\sigma(E)} \left\{ t \frac{dM}{dt} \right\}; \qquad (7)$$

that is, the desired leakage spectrum is related to the derivative of the experimental data (a not unusual relation) and E is defined by Eqs. (1a, b), viz. $E = A/t^2$.

The validity of this treatment depends on the stationary assumption introduced in Eq. (4). Neglect of higher order expansion terms implies that the change in neutron population is small compared with the population itself, in the region $t \leq t_0$. This assumption is obviously not true for very early neutron generations in pulsed neutron TOF experiments. However, given some degree of flexibility in selecting excitation functions, it may well be possible to drive critical assemblies so that the neutron population is approximately stationary in a time interval, $t_i \leq t \leq t_0$. (Here $t_i > 0$ is the time required for the neutron population to reach a stationary value.) Under such conditions, one could attempt to unfold Eq. (2) directly for the interval $t_i \leq t \leq t_0$. On the other hand, if t_i is small (i.e. $t_i \ll t_0$), higher order correction terms for Eq. (6) may suffice.

References

1. B. A. Zolotar, *Analysis of Time-of-Flight Measurements*, Applied Physics Division Annual Report July 1, 1969 to June 30, 1970, ANL-7710, pp. 197–200.
2. R. Gold and D. M. Smith, *^{3}He Gas Scintillator for Time-of-Flight Neutron Measurements*, Applied Physics Division Annual Report July 1, 1969 to June 30, 1970, ANL-7710, pp. 321–323.

III-13. Detector Efficiency Calibration With Monoenergetic Neutrons

K. Porges, I. Olson, Raymond Gold and J. Snelgrove

One of the critical pieces of information required for the conversion of time-of-flight (TOF) data into neutron energy distributions is the energy dependence of detector response. As discussed in Paper III-8 the ANL TOF system is designed to cover a range from 50–100 eV through 1–2 MeV, with the highest available detection efficiency. To provide an energy calibration of adequate precision and detail over this range is clearly a difficult and time-consuming undertaking.

The detectors which best satisfy the indicated requirement of high efficiency over a wide energy range, together with the requirement of fast response, are lithium or boron-loaded scintillators. The large cross section of ^{10}B or ^{6}Li in the eV region tends to make the detection efficiency follow the loading up to 1 to 10 keV, where cross sections of other nuclides present in the scintillator or supporting structure become comparable. In particular, strong resonances (e.g., ^{23}Na) can, in principle, result in a dip or cusp of the detection efficiency. For that reason, quartz vials are preferable to glass vials for liquid scintillators. A number of detectors of similar construction, arranged in a group, will likewise exhibit an energy response slightly different from that of a single detector. Thus a convincing final calibration can only be made with the detectors actually installed in the TOF facility, either by providing a known spectrum or by interchanging a "standard" detector of known response with the detector which is to be calibrated in the same spectrum. This can further be supplemented by Monte Carlo calculations of the detector response and/or standard detector response and with reruns with a number of computed spectra derived from relatively simple structures of clean materials.

Since the ZPR-6 critical assembly incorporated in the ANL TOF facility is committed to other programs, such extensive calibrations, actually carried out at a number of similar installations, would be impractical at ANL. Instead, the calibration, now in progress, is being sought in three steps: (a) calibration of a number of detectors by means of monoenergetic neutrons using $A(p,n)B$ reactions (where $A \equiv$ target nuclide and $B \equiv$ nuclide resulting from the reaction) with the Fast Neutron Generator (FNG); (b) intercalibration of several detectors using the Gulf Radiation Technology facility; (c) a final intercomparison of detectors in the course of actual measurements for which certain provisions have been made. In this report, the problems arising in connection with (p,n) reaction neutrons are specifically considered, with particular emphasis on the use of scandium targets.

In a detector calibration with $A(p,n)B$ neutrons the

proton energy and current delivered to the target are readily measured with very good precision, while the detector counts are equally readily accumulated over a fixed time. In principle, the number of neutrons incident on the detector can be computed from the kinematics of the reaction, threshold energy, target thickness and reaction cross section. While some of these required parameters may be available, target thickness is generally difficult to infer or measure with the required precision, and may well change during the run. A second method is to compare runs made with the detector and runs made with some standard detector in clearly defined geometry. For example, a well-calibrated activation bath has been used in 4π geometry (surrounding a target snout), as briefly described in Paper III-14. Even if vanadium rather than manganese is used in such a bath, however, this procedure is clearly very time-consuming when a large number of calibrations is required.

A widely used means of securing a detector calibration is to substitute a standard detector at every energy point. Most frequently, Hanson-McKibben "long counters" are used for that purpose. Since long counters are designed to respond with nearly uniform efficiency over a wide range of neutron energies, an approximate calibration is readily effected; however, in attempting to make the calibration more precise, one finds that the efficiency of standard long counters tends to decline in the MeV region and is somewhat uncertain elsewhere. Monte Carlo calculations as well as measurements of counter efficiency have been reported but do not agree. Even over a limited energy range, however, one must be careful to shield against room return, to which these counters are unavoidably sensitive. To intercept an effectively monoenergetic neutron beam, a standard long counter of 12 in. diam must be placed at a considerable distance from the target; on the other hand, the ratio of room return neutrons to target neutrons increases with this distance.

Another frequently used means of calibration is a fission chamber of parallel plate construction. The precisely defined response time of such chambers allows discrimination against room return by nanosecond coincidence gating; neutron energy dependence of the fission chamber efficiency can be inferred from the well-known fission cross section. In practice, however, the small area and weak intrinsic efficiency of such fission chambers calls for a location close to the target, with consequent strong sensitivity to small errors in the precise geometry, target spot size and neutron energy/angle distribution.

Over a limited neutron energy range, a very precise calibration is possible, in principle, through associated particle detection and coincidence, the associated particle being the recoiling product nucleus B in the $A(p,n)B$ reaction. The chief difficulty in making this method practical is the very low count rate due to the geometric restriction of two small solid angles as well as the requirement of a target thin enough to allow the recoil particle to escape.

Yet another calibration method depends on inference of the number of neutrons which have been emitted over a certain measurement interval from a subsequent determination of induced target activity. If no interfering activities are present in the target or backing, detector efficiency can be directly computed from the total number of target reactions and the kinematics relations, discussed below. To make the scheme practical, one further requires a reasonably strong (p,n) cross section, while the induced activity should have a suitably short half-life and result in emission of readily detected particles or radiation. If the decay scheme is precisely known and the activity counter can be calibrated, the detector efficiency can be placed on an absolute scale.

A critical comparison of the different schemes described above reveals the last-mentioned method to have the strongest potential for precision, provided a suitable target nuclide can be found. The various conditions which must be satisfied restrict the choice to a small number of relatively light nuclei, of which ^{45}Sc has the most favorable combination of properties. The 3 h positron emitter, ^{45}Ti, is readily counted; ^{45}Sc has no other isotopes and features a high melting point, allowing fabrication of stable, clean targets by electron beam evaporation on a tantalum substrate (from which no (p,n) reactions result at proton energies within a few MeV of the scandium threshold). A property of ^{45}Sc which is particularly useful for calibration purposes is the relatively large mass, resulting in favorable kinematics as discussed below, or, in practical terms, small energy dispersion with angle and a low "single energy" (SE) threshold. Thus, monoenergetic neutrons can be delivered at less than 10 keV to a detector subtending an appreciable solid angle at the target. While extensive kinematics computations and tables are available for ^{45}Sc, it may be useful to provide here a brief discussion of energy and angular distributions resulting from the basic kinematic relation (non-relativistic)

$$z = \cos\theta \pm (x^2 - 1 + \cos^2\theta)^{1/2}, \tag{1}$$

where

$$z^2 = E_n/hE_p\,, \tag{2}$$

$$x^2 = g(E_p - E_t)/hE_p\,, \tag{3}$$

$$g = m_A m_B/(m_A + m_p)(m_B + m_n), \tag{4}$$

$$h = m_p m_n/(m_p + m_A)^2, \tag{5}$$

$$E_t = -Q(m_A + m_p)/m_A\,. \tag{6}$$

In these definitions A and B denote, as above, target and product nuclei while subscripts p and n refer to proton and neutron, respectively; m denotes mass, $E \equiv$ energy, and $-Q \equiv$ reaction threshold in the center of mass system. Eq (1) is plotted in Fig. III-13-1; the vertical distance between heavy lines in that figure bounds all values of z which are intercepted by a solid angle on the beam axis having half-aperture θ. The value of θ chosen for this illustration is rather large; for a small solid angle the lower bound lies close to the upper bound, whence there is an appreciable region between $x = \sin\theta$ and $x = 1$, where two neutron energy groups appear. $x = 1$ is defined as the "single energy" (SE) threshold.

For ^{45}Sc the mass scaling constant g is evidently quite close to unity while the constant h is very small, with the result that x begins to exceed unity at proton energies E_p' quite close to the reaction threshold $E_t(E_p' - E_t \sim 5 \times 10^{-4} E_t)$. Beyond that point, only the + sign in Eq (1) applies, neutron emission rapidly approaches isotropy, and the dispersion in energy of neutrons incident on the detector resulting from finite detector aperture decreases rapidly (as $1/x$).

The number of neutrons, dn, emitted into the differential solid angle $d\Omega = d\mu/2$, $\mu = \cos\theta$, is readily found from the kinematics,

$$dn = \frac{nd\mu}{2} \frac{[\mu + \sqrt{x^2 - 1 + \mu^2}]^2}{x\sqrt{x^2 - 1 + \mu^2}}, \qquad (7)$$

where

$$n = Nw\sigma it/eA,$$

where $i \equiv$ proton current, $t \equiv$ duration of measurement, $\sigma \equiv A(p,n)B$ cross section at incident proton energy E_p, $A \equiv$ atomic weight of target nucleus, $e \equiv 1.6 \times 10^{-19}$ C, $N = 6.02 \times 10^{23}$, and $w \equiv$ target thickness in g/cm. The fraction of neutrons, $\Delta n/n$, delivered to the detector* within half-aperture θ is readily found by integration,

$$\frac{\Delta n}{n} = \frac{1}{2}\left(1 + \frac{\sin^2\theta}{x} - \cos\theta\sqrt{1 - \frac{\sin^2\theta}{x}}\right). \qquad (8)$$

Note that Eq (8) applies only above the SE threshold defined by $x = 1$; at that threshold, a cosine distribution ($\Delta n/n = \sin^2\theta$) obtains, i.e., all neutrons are emitted into the forward hemisphere. For large values of x (reached by scandium targets at proton energies ›se to threshold, as discussed above) Eq (8) can be panded in the form

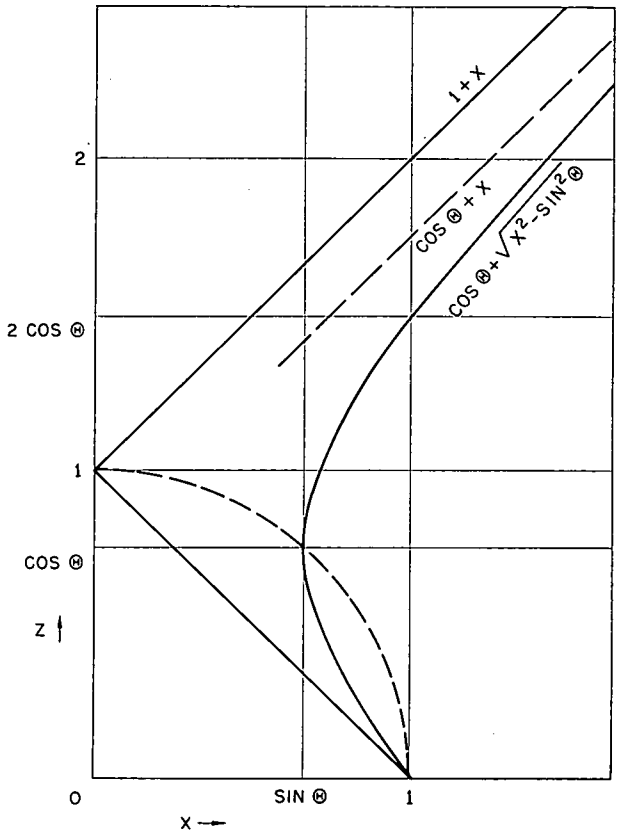

FIG. III-13-1. Universal Kinematic Relation between Proton and Neutron Velocities in (p,n) Reactions. Quantities Plotted are Defined in the Text, Eqs. (1) through (6). Vertical Distance Bounded by Heavy Lines is Proportional to the Range of Neutron Velocities Delivered within a Solid Angle of Half-Aperture θ, Aligned on the Proton Velocity Vector (a Rather Large Aperture is Shown, for Illustration). At High Proton Velocities, $x \gg 1$, the Neutron Velocity Lower Bound Approaches $x + \cos\theta$. *ANL Neg. No. 116-1072.*

$$\frac{\Delta n}{n} = \frac{1 - \cos\theta}{2} + \frac{\sin^2\theta}{2x}\left[1 + \frac{\cos\theta}{2x} + \frac{\cos\theta\sin^2\theta}{8x^3} + \cdots\right], \qquad (8')$$

which indeed describes an isotropic distribution with a small, rapidly decreasing correction term. As a consequence, the fraction of generated neutrons which reaches the detector is virtually constant over most of the energy range embraced by the calibration.

To calibrate a detector with nominally monoenergetic neutrons, it is necessary to limit the subtended solid angle in order to keep the energy spread within a certain bound. It is readily seen that the energy distribution resulting from the detector aperture is uniform:

$$dn(z)/n = z\,dz/2x, \qquad (9)$$

whence

$$dn(E_n)/n = \frac{dE_n}{4}[ghE_p(E_p - E_t)]^{-1/2}. \qquad (10)$$

* Angular distribution due to resonances in the compound nucleus is neglected in this discussion.

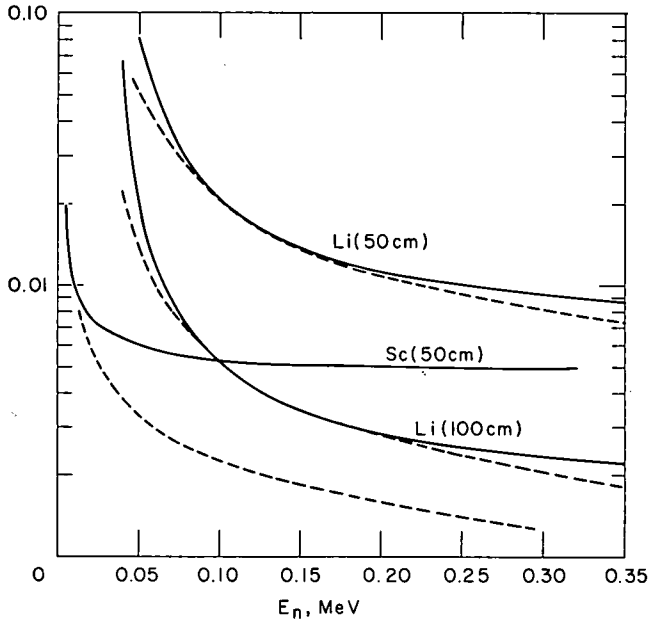

FIG. III-13-2. Fractional Neutron Yield and Energy Resolution of Scandium and Lithium Targets for 13 cm Diam. Detectors, 50 and 100 cm on Beam Axis from a Point Target. Solid Lines: Fractional Yield, Eq (8); Broken Lines: Energy Resolution $(E_{max} - E_{min})/E_{max}$. Note Almost Constant Yield for the Scandium Target, Indicating Quasi-Isotropic Angular Distribution. *ANL Neg. No. 116-1071.*

Now let $r = 2\Delta z/z = \Delta E_n/E_n$ represent the energy bound, say $r = 0.01$; then the corresponding half-aperture cosine becomes

$$\cos\theta = [(x+1)(1-r)^2 - (x-1)]/2(1-r) \quad (11)$$

and the fraction of neutrons accepted by the detector is readily seen to be

$$\Delta n/n = (x+1)^2 \frac{r}{2x}\left(1 - \frac{r}{2}\right). \quad (12)$$

Eq. 12 demonstrates the interesting fact that for a geometry which secures a certain acceptable energy spread r of neutrons incident on the detector, a heavier mass (large x) target such as scandium actually produces a higher fractional input $\Delta n/n$ than a lighter target, even though the light target tends to concentrate neutrons in the forward hemisphere (in contrast to the virtually isotropic emission pattern of the heavier target).

As a practical illustration, the fractional neutron yield $\Delta n/n$ and energy resolution $\Delta E_n/E_n = (E_{nmax} - E_{nmin})/E_{nmax}$ pertaining to a 5 in. diam detector of shallow depth, located at 50 and at 100 cm from scandium or lithium targets, has been plotted in Fig. III-13-2. It is apparent from this plot that a required resolution of 1 % can be obtained at a distance of 50 cm from a scandium target over virtually the full useful energy range of 10 to 350 keV depicted, whereas the lithium target at the same distance exhibits acceptable energy definition only above 220 keV. In an actual calibration, to be sure, the accelerator energy spread and target thickness effect tend to increase the resolution considerably near 10 keV; the accelerator for example introduces several keV spread through klystron bunching. The cross section, determining the actual neutron yield, fluctuates strongly for ^{45}Sc owing to the level structure of the compound nucleus ^{46}Ti, but runs considerably smoother (and higher) for ^{6}Li.

In the practical execution of calibration measurements, the presence of machine gamma and neutron background requires TOF acquisition with machine operation in bunched mode. A gamma flash is always obtained from Coulomb excitation in the tantalum target backing; in addition, stray neutron and proton interactions, etc., result in quasi-constant neutron as well as gamma backgrounds. With readily available electronic processing systems having a few hundred psec time resolution and a machine bunching width of a few nsec, the initial gamma flash is very easily separated from the (p,n) neutron group (recalling that the 50 cm flight time of 250 keV neutrons amounts to 72 nsec). At the same time, the quasi-continuous background is readily subtracted from the TOF spectrum and low energy neutron groups resulting from excited states can likewise be identified. Thus a highly precise means of detector calibration at discrete energies from 10 keV to 2 or more MeV is available through the use of scandium targets and a high-current, sharply bunched proton accelerator such as the ANL FNG. Since the ^{45}Ti decay scheme is rather precisely known while the target counting equipment (a 2π beta proportional counter or a NaI-Tl crystal) is readily calibrated on an absolute basis, the detector calibration can be made absolute as well as relative with very good accuracy once the angular distribution of emitted neutrons has been determined. Detectors which have been calibrated in this way and whose performance has been stabilized can serve a useful purpose in the approximate, but rapid, calibration of neutron sources of reasonably well-known spectra (e.g., fission sources).

III-14. Thick Target Neutron Yields of Lithium and Beryllium Targets Bombarded with Protons and Deuterons

K. Porges, J. L. Snelgrove, Raymond Gold, A. DeVolpi, R. J. Armani and C. E. Cohn

The total neutron yield from thick targets irradiated with charged particles is a matter of some interest in experiments where intense sources of neutrons, particularly short neutron bursts, are required. While the principal aim is often to secure the highest possible neutron yield, other factors such as energy and angular distributions of emitted neutrons may also be important considerations. From known thin target cross sections, as well as older compilations and surveys,[1-4] it appears that target nuclides which produce the best neutron yields under proton or deuteron irradiation include ^{2}H, ^{3}H, ^{7}Li, ^{9}Be and ^{12}C. Of these, the highest potential yields are available from beryllium and lithium. These nuclides are also readily fabricated into targets suitable for insertion into the ZPR-6 assembly in the TOF neutron spectrum measurement system described in Papers III-8 through III-11. In that system, the choice of target and bombarding particle which provide the largest neutron burst yield is somewhat dependent on the beam transport, limited at present to deuteron energies less than the maximum available from the Fast Neutron Generator (FNG). To determine whether redesign of certain beam transport components would be warranted, thick target neutron yield measurements of beryllium and lithium targets for energies up to 7.5 MeV were initiated after a literature survey disclosed that such measurements were not available. For Li(p,n)Be, the cross section is relatively well known as a function of proton energy; hence the thick target yield can be computed with the further aid of dE/dx data.[5] Moreover, the neutron energy distribution observed at a given angle can be computed similarly, on the basis of the reasonable assumption that scattering and straggling effects can be neglected for protons. Similar cross sections for the other reactions surveyed are, however, not available over the energy range of interest.

A preliminary investigation of the total yield was made with a vanadium bath. A thick target located at the end of a slender snout was inserted into a reentrant hole in the bath whose contents were continuously circulated through an on-line counter. The overall detection efficiency of this system can be determined by replacing the target snout with a standard source. Bath transmission of the relatively strong neutron component above 5 MeV is probably the greatest uncertainty attached to these preliminary measurements, shown in Figs. III-14-1 and III-14-2. Corrections evi-

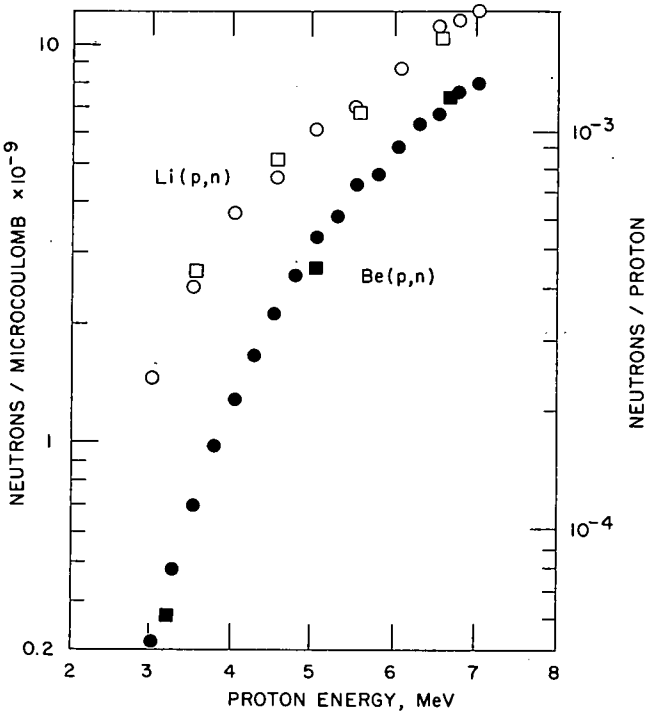

Fig. III-14-1. Thick Target Yields of Beryllium and Lithium Targets, Proton Irradiation. *ANL Neg. No. 116-1073.*

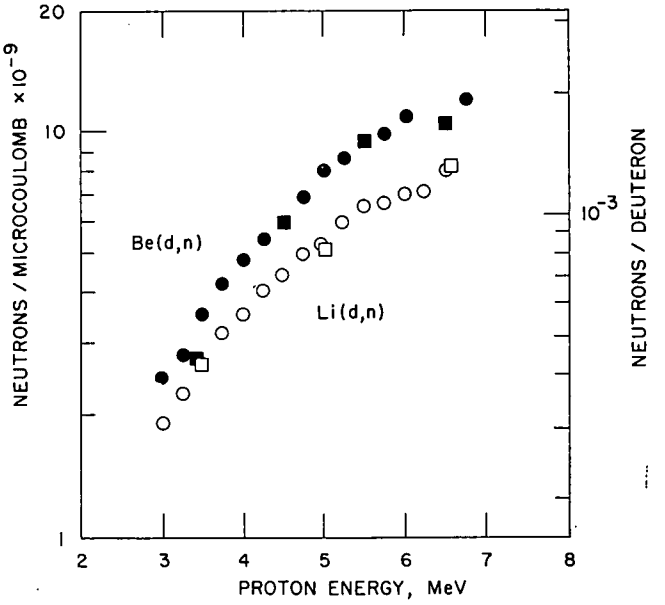

Fig. III-14-2. Thick Target Yields of Beryllium and Lithium Targets, Deuteron Irradiation. Curves Have Been Scaled to the Activation Bath Measurements, Shown as Squares. *ANL Neg. No. 116-1070.*

dently require knowledge of the energy distribution of the emitted neutrons. The figures also show a considerably larger number of points obtained by means of a large wax castle surrounding the target; a group of BF_3 counters inserted into the moderator stack yielded a strong counting rate, but the calibration of this system with standard sources again is somewhat uncertain due to relatively important neutron angle and energy distribution effects.

A measurement of the energy distribution as a function of angle was thus initiated, using TOF processing of events detected in a high-pressure ^{4}He scintillator described in Paper III-15. Five angles, 0, 40, 80, 120, and 150 deg, were chosen. For incident neutron energies below 0.5 MeV the detection efficiency of the gas scintillator begins to deviate from the adjusted ^{4}He scattering cross section and goes to zero as the energy of helium recoils is reduced below the channel threshold. Therefore, similar measurements were also made with a ^{6}Li-loaded glass scintillator whose response function rises at low energies. A further set of measurements is planned with a ^{3}He gas scintillator. A very precise calibration, described in Paper III-13, of the energy response of these various detectors (which are also used in the TOF measurement) is currently in progress.

The spectra thus computed from the data by folding in detection efficiencies are still only relative, whereas absolute yields are required for the determination of the best choice of particle and target. Consequently, Solid State Track Recorder (SSTR)[6] detection systems have been deployed to determine the absolute neutron flux at the five reference angles listed above, using *Makrofol* SSTR and asymptotically thick ^{238}U and ^{232}Th source foils. The ANL automatic track scanning system[7,8] was used for absolute counting of fission tracks released in exposures over fixed time intervals during which the proton current was accurately integrated. The computer code SIGBAR[9] will be used to calculate the convolution integral of the neutron energy spectrum observed at a certain angle and the fission cross section of the source foil, yielding a number which will provide an absolute scale for each detector spectrum measurement by comparison with the SSTR track count. Use of two different source foils, ^{238}U and ^{232}Th, permits a cross-check through data redundancy.

The final step is an integration over the measured neutron spectrum, fit of a Legendre polynomial series to the plot of integrated neutron emission per unit solid angle versus cosine of the angle of observation, and finally an integration over 4π. The data thus obtained will not only give the total neutron yield as a function of bombarding energy, but also provide a picture of the angular and energy distribution of these neutrons, a matter of importance in connection with the choice of the optimum entrance depth of the target into the subcritical assembly.

References

1. E. Amaldi, *The Production and Slowing Down of Neutrons*, Handbuch der Physik, (Springer-Verlag, Inc., New York, 1959), Vol. XXXVIII/2.
2. J. Marion and J. Fowler, *Fast Neutron Physics*, (Interscience Publishers, New York, 1963), Vol. I.
3. G. Vlasov, Neutronen, (State Publ. Corp. DDR, Berlin/Leipzig, 1965); also, B. Rybakov and V. Sidorov, *Fast Neutron Spectroscopy*, Supplement No. 6 of the Soviet Journal of Atomic Energy, 1958.
4. B. Feld, *Intense Neutron Sources from Accelerated Charged Particles*, A12-6, Advance Technology Corp. (NDA), White Plains, New York, 1953.
5. W. Aron, B. Hoffman and F. Williams, *Range/Energy Curves*, AECU-663, UCRL (1951); also, M. Rich and R. Madey, *Range/Energy Tables*, UCRL-2301 (1954).
6. R. Gold, R. J. Armani and J. H. Roberts, *Absolute Fission Rate Measurements with Solid-State Track Recorders*, Nucl. Sci. Eng. **34**, 13 (1968).
7. C. E. Cohn and R. Gold, *A Computer-Controlled Microscope for Automatic Scanning of Solid-State Nuclear Track Recorders*, Rev. Sci. Instr. (to be published).
8. R. Gold and C. E. Cohn, *Analysis of Automatic Fission Track Scanning in Solid State Nuclear Track Recorders*, Rev. Sci. Instr. (to be published).
9. R. Gold and I. K. Olson, *SIGBAR—A Program for Computing Average Fission Cross Sections in Fast Neutron Spectra*, Reactor Physics Division Annual Report, July 1968 to June 1969, ANL 7610, p. 535.

III-15. High Pressure ^{4}He Gas Scintillator for MeV Neutron Time-of-Flight Measurements

Raymond Gold, K. G. Porges and J. L. Snelgrove

The advantages of a ^{3}He gas scintillator in pulsed critical assembly time-of-flight (TOF) measurements have already been discussed.[1] For recent neutron yield measurements (see Paper III-14), the versatility of this detection system has been extended by utilizing high pressure fillings of ordinary helium,* i.e. ^{4}He. In this manner the gas scintillator serves as a ^{4}He recoil detector for high energy neutrons, with virtually no

* Small admixtures of xenon are also introduced to enhance scintillation light output.

sensitivity below a few hundred keV. Hence the ^{4}He recoil gas scintillator compliments the 1/v sensitivity attained with ^{3}He fillings. Fast response and low gamma sensitivity are common advantages which accrue for either mode of operation of the gas scintillator.[1]

Typical TOF spectra measured with the ^{4}He recoil gas scintillator using the Fast Neutron Generator (FNG) facility are shown in Figs. III-15-1 and III-15-2. Figure III-15-1 depicts data obtained from the ^{7}Li(d,n) reaction at 7.5 MeV, while Fig. III-15-2 presents data from the ^{9}Be(d,n) reaction at 7.5 MeV. Both spectra were obtained at 0 deg (i.e. in the forward direction) with a 2 m flight path. The gas scintillator

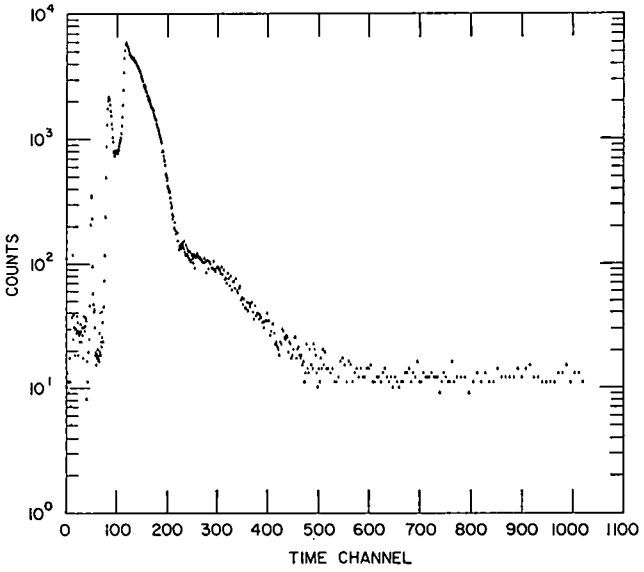

FIG. III-15-1. ^{4}He Recoil Gas Scintillator Time-of-Flight Neutron Spectrum from the ^{7}Li(d,n) Reaction at 7.5 MeV. Data were Obtained with a 2 *m* Flight Path at 0 Deg Using a Time Width of 0.989 ns per Channel. *ANL Neg. No. 116-875.*

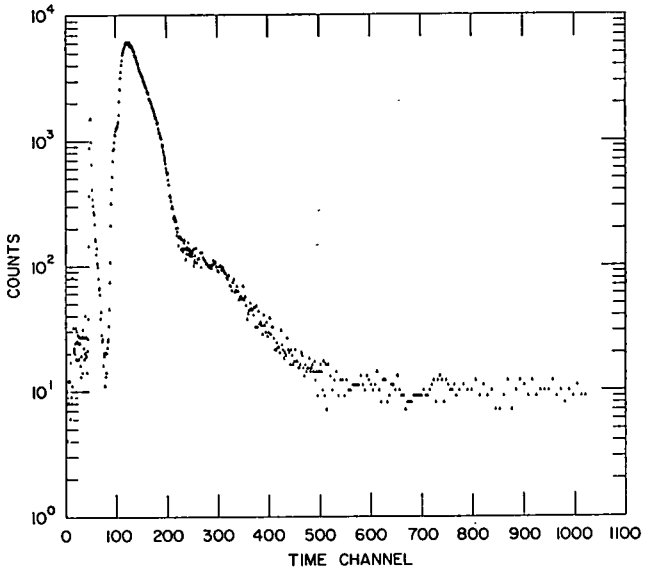

FIG. III-15-2. ^{4}He Recoil Gas Scintillator Time-of-Flight Neutron Spectrum from the ^{9}Be(d,n) Reaction at 7.5 MeV, Data were Obtained with a 2 m Flight Path at 0 Deg Using a Time Width of 0.989 ns per Channel. *ANL Neg. No. 116-876.*

was filled with a mixture of approximately 25 psi xenon and 500 psi ^{4}He. The corresponding neutron energy range covered is roughly 0.5–20.0 MeV. The presence of structure in these high energy TOF spectra is evident. Time resolution of these measurements is roughly 4 ns (FWHM) as estimated from the gamma flash peak in the neighborhood of channel 50.

REFERENCE

1. Raymond Gold and Dale M. Smith, *^{3}He Gas Scintillator for Time-of-Flight Neutron Measurements.* Applied Physics Division Annual Report, July 1, 1969 to June 30, 1970, ANL-7710, pp. 321–323.

III-16. Improved Computer Method for Polarity Cross Correlation

C. E. COHN

INTRODUCTION

A polarity-correlation noise-analysis system has been implemented on the SEL-840 computer. It is similar in many respects to the system developed by Lehto,[1] but has some improved features. Like the Lehto system, it takes as a point of departure a system that was previously implemented by the author[2] on a DDP-24 computer.

DATA ACQUISITION

As in the Lehto system, the polarity data are formed in discriminators using integrated circuit comparators. The polarity bits are collected in a word-forming buffer whose logic is based on the DDP-24 system. The main difference from that system is the organization of the bits as transmitted to the computer. In the DDP-24 system, one word at a time was transmitted to the com-

puter, containing 12 data bits from one detector interlaced with 12 data bits from the other detector. However, the present system transmits two words at a time to the computer via the block transfer control. One word contains 24 bits of data from one detector while the second word contains the contemporaneous 24 data bits from the other detector. Thus, data words from the two detectors alternate in memory. The buffer was implemented with RTL logic, with a sampling interval of 0.5 μsec.

The buffer interface also makes provision for monitoring the discriminator bias and correcting the correlogram for it. The principle of polarity correlation assumes that the discriminator threshold corresponds to the mean level of Gaussian noise, so that zero and one bits are equiprobable. If the discriminator setting deviates from this level, the correlogram must be corrected. (The first-order correction is a constant term.)[3] Use of the computer to keep track of the frequencies of zero and one bits in the data would be prohibitive in computation time. Therefore, that accounting is done externally via three pulse outputs from the buffer.

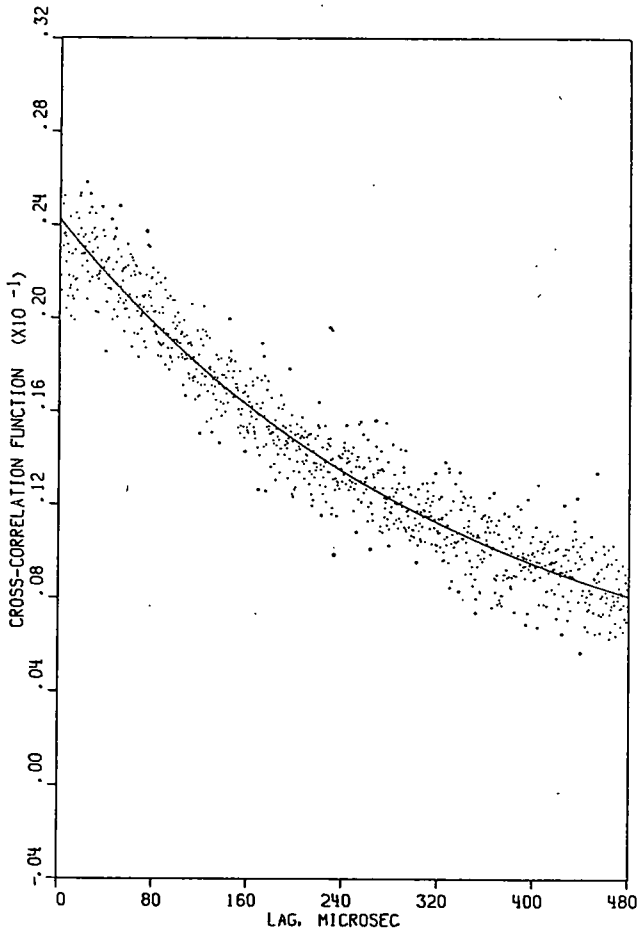

FIG. III-16-1. Typical Polarity Correlogram from ZPR-9. *ANL Neg. No. 116-752.*

One of these outputs delivers continuous clock pulses at the sampling rate, while the other two deliver those clock pulses gated with the polarity data from each detector. That is, a pulse is transmitted when the sampled polarity bit is a one, and no pulse is transmitted when the polarity bit is a zero.

These pulses are counted in three of the 24-bit binary general-purpose data scalers attached to the SEL-840. These scalers are read out and reset periodically by the computer. The hookup is arranged so that the three scalers start and stop counting simultaneously.

The scaler data are used in two ways by the computer. During a setup mode that precedes actual data taking, a bias pointer is displayed on the CRT screen. This is a line segment with its origin at the center of the screen. Its x-component is proportional to the bias in the data from one detector (i.e., the excess of ones over half the total samplings) while the y-component is proportional to the bias from the second detector. The experimenter manually adjusts the discriminators to shrink the pointer to a minimum.

During data taking, the computer reads the scalers after the calculation of every 24*th* correlogram point. The data are saved for later correction of the results and are also used to produce a bias pointer that is superimposed on the display of the developing correlogram. Through this, the experimenter may check for discriminator drift or detector malfunction.

Data Processing

As in the Lehto system, the lagged products are taken one word of bits at a time by use of the exclusive-or instruction. However, the bits resulting from the use of this instruction are not counted by programming. Instead, hardware provisions were made to do this counting more rapidly. These provisions consist of a 24-bit shift register and a 24-bit binary scaler included in the buffer interface chasis. After the exclusive-or instruction is executed, an accumulator-output-to-peripheral (AOP) instruction dumps the result into the shift register. Then, independent of the computer, the word is shifted out of the register, and the one-bits that come through are counted in the scaler. After all lagged products for a given correlogram point have been done, the scaler is read and reset.

Unlike the Lehto system, time is not taken to invert the data words from one counter before taking the lagged products. As a result, the scaler contents are equal to a quantity given by the correct sum subtracted from the maximum possible count (i.e., 24 times the number of exclusive-or operations). Account is taken of this in processing the data.

A loop cycle for retrieving and positioning the data words, performing the exclusive-or operation and dump-

ing the result to the shift register takes an average of 16 memory cycles or 28 μsec, corresponding to two-thirds cycle or 1.17 μsec per bit pair, plus overhead. This is a major improvement over the DDP-24 system, which took 2 cycles or 10 μsec per bit pair plus considerably more overhead. The present scheme increases in efficiency as the computer word length increases, since the various steps take no longer time for a longer word than for a shorter word.

An important refinement in this system is that only one lag point is calculated from each string of data. That is, a new string of data is read in for the calculation of another lag point. That is done to improve the statistical properties of the correlogram. Dragt[4] has pointed out that adjacent correlogram points taken from the same data string are themselves correlated. This can lead to difficulty in the interpretation of least-squares fits. With this system, on the other hand, all correlogram points are statistically independent and each contributes unique information.* For this reason, the correlogram is calculated at every lag point instead of at just certain lag points as was done on the DDP-24. (This type of operation would have been prohibitive on the DDP-24 due to overhead considerations.) After all lag points for one data string have been calculated, the display of the correlogram on the CRT is updated.

Operating in this way does not slow the process markedly, since read-in time for a bit pair is only 13% of the calculation time. The reading is done on a cycle-steal basis. Two data areas are provided in memory, one being filled while the other is being processed.

Figure III-16-1 shows a typical correlation function. This was obtained from the FTR-3 assembly on the ZPR-9 fast critical. The measurement was made near critical. The plastic scintillators used as detectors for the previous system were replaced with Nuclear Enterprises NE105 glass scintillators. These were each 1½ in. in diam and 1 in. long and contained about 4.5 g of ^{7}Li. The measurement shown was done near critical and took approximately one hour. The results were fitted to a single decaying exponential plus a constant, yielding a time constant of 335 ± 11 μsec. Measurements were also attempted in various further subcritical states. Such operation, however, was marginal because the lower event rate in the detectors did not cause enough pulse pile up to produce the Gaussian signal required for polarity correlation. Furthermore, as pointed out by Lehto and Goin[5] polarity correlation apparently does not make as efficient use of the data as full-amplitude cross-correlation measurements.

* The scaler system described by Lehto also has this desirable property.

REFERENCES

1. W. K. Lehto, *Zero Power Plutonium Reactor (ZPPR) Assembly 2 Noise Studies*, Applied Physics Division Annual Report, July 1, 1969 to June 30, 1970, ANL-7710, pp. 155–156.
2. C. E. Cohn, *Reactor-Noise Studies with an On-Line Digital Computer*, Nuclear Appl. **6**, 391 (1969).
3. W. Heins, A. van den Bos and B. P. Th. Veltman, *On the Polarity Correlation of Non-Zero Mean Gaussian Variables*, Report No. 65-2, Cooperation Centre for Measurement and Control, Department of Applied Physics, Technological University, Delft, Netherlands (July 1965).
4. J. B. Dragt, *Reactor Noise: A Study of Neutronic Fluctuations in Low-Power Nuclear Reactors, with Special Emphasis on Accurate Time-Domain Analysis*, RCN-101, 170–171 (1968).
5. W. K. Lehto and R. W. Goin, *The Effects of S/N Ratio on the Results of Polarity Correlation Experiments*, Applied Physics Division Annual Report, July 1, 1969 to June 30, 1970, ANL-7710, pp. 451–452.

III-17. A Polarity Correlation System for Fast Reactor Noise Studies

W. K. LEHTO, J. M. LARSON, R. W. GOIN and J. E. HUTTON

SUMMARY

A system consisting of a detector signal amplifier, polarity sampler and associated gating circuitry has been designed and tested in a fast reactor application to do noise studies by polarity correlation techniques. System versatility and accurate signal processing were emphasized. Noise studies and reactivity measurements have been done with this equipment utilizing the cross correlation and low frequency coherence techniques.

INTRODUCTION

Reactor transfer functions, decay constants, and reactivity have, until recently, been measured by full-amplitude analysis of a properly derived analog signal or by various pulse counting techniques. The most attractive method has been the cross power spectral density (CPSD) technique[1,2] which involves filtering, multiplication, and integration of two detector outputs to derive a quantity proportional to the correlated

signal power per unit bandwidth. The equivalent experiment in the time domain requires digitizing the analog signals and multiplying the resulting time series point by point. The process is repeated with one signal delayed with respect to the other, for various delay times, to generate the cross correlation function. Shape analysis of these functions yields kinetic information about the reactor and its components.

More recently, similar two-detector experiments have been done by polarity-sampling techniques[3-5] to derive the kinetic information. Polarity sampling involves the coarse quantization of an analog signal into two bits, representing the positive and negative states. Averaging consists of totaling the occurrences of like bits and dividing by the total number of samples to get a quantity $R(t)$. This is equivalent to conducting an "exclusive-or" operation on the time series of bits, summing the outputs, and dividing by the total number of samples. The correlation (coherence) is then given by[5,6]

$$\rho(t) = \sin\left[\frac{\pi}{2} R(t)\right].$$

The polarity cross correlation function is calculated by delaying one time series as in the full amplitude experiment and averaging. The result is equivalent to the cross correlation function calculated by conventional methods; this method has the advantages of simplicity, requires less equipment, and permits a considerable reduction in computer time. On the negative side, reducing the level of quantization also reduces precision and available dynamic range, the limit being one decade in a two-bit quantization scheme.[7,8]

Seifritz has applied polarity sampling techniques to band pass filtered detector signals to measure the frequency coherence function given by

$$\rho(\omega) = \left[\frac{\phi_{xy}(\omega)}{\phi_{xx}(\omega)\phi_{yy}(\omega)}\right]^{1/2}.$$

The ϕs are the one and two detector spectral densities as indicated by the subscripts.

A variation of this experiment was developed by Seifritz[5] to measure reactivities in fast reactors. The signals from the detectors were low-pass filtered, and the reactivity-related amplitude of the low frequency coherence function was sampled by the polarity-correlation technique.

Application of these polarity-sampling and calculational techniques places different requirements on the equipment and its quality. For instance, to attain the required delays of several to hundreds of microseconds in a fast reactor experiment, it is impractical to use delay lines in the calculation of the polarity-correlation function. The delays, "exclusive-or," and summing, are more efficiently done with an on-line computer. For the frequency coherence function and reactivity measurements, the computer is unnecessary since the measurements can be done by replacing the computer with an "ex-or" gate and scaler.

The requirements placed on the instrumentation are the most severe for the low-frequency coherence function measurement. Any interference such as line hum appearing in both channels would contribute to the correlation coefficient and yield biased results. The presence of line interference is not as severe in the other two polarity correlation experiments, particularly in fast-reactor applications. Any such interference is well removed from the frequencies of interest and is easily separated in the frequency coherence function measurement. In the correlation measurement the time scale is usually short enough so that bias from low-frequency interference appears as a constant that can be corrected for. In spite of this, even the smallest amount of bias is undesirable and considerable care is required in instrument design.

At Argonne National Laboratory, a system has been designed and tested in a fast-reactor application to do the three polarity correlation experiments. The systems of Cohn and Seifritz have been used as a point of departure for the design of a preamplifier, main-amplifier, polarity sampler, sign comparator, and computer interface. An improved polarity correlation algorithm has also been written which utilizes the "ex-or" instructions of the Zero Power Plutonium Reactor's on-line SEL 840 computer. Particular attention has been given to elimination of any common-mode nonreactor noise and to system versatility.

System Description

The system is shown schematically in Fig. III-17-1. The preamplifiers are current sensitive. The detectors used in the critical-facility program are photomultipliers viewing plastic scintillators. The differential amplifiers have a variable gain of 10 to 1000 with high common-mode rejection, and have high pass (3 Hz) and adjustable low pass (159 Hz to ~100 kc) filters at their inputs. These filters are used for the low-frequency-coherence-function reactivity measurements, which require limited-bandwidth signals,[5] that is $\lambda_i \ll \omega \ll 0.1\ \alpha_c[(1 - \$)^2 + Q_{max}]^{1/5}$, where α_c is the prompt neutron decay constant at delayed critical, \$ is the reactivity in dollars, and Q_{max} is the ratio of correlated to uncorrelated noise contributions. The discriminators, exclusive-or circuit, and shift registers are made up of commercially available integrated circuits and logic elements. The discriminator thresholds of the polarity sampler are normally set at zero volts and are connected so that their outputs go positive when

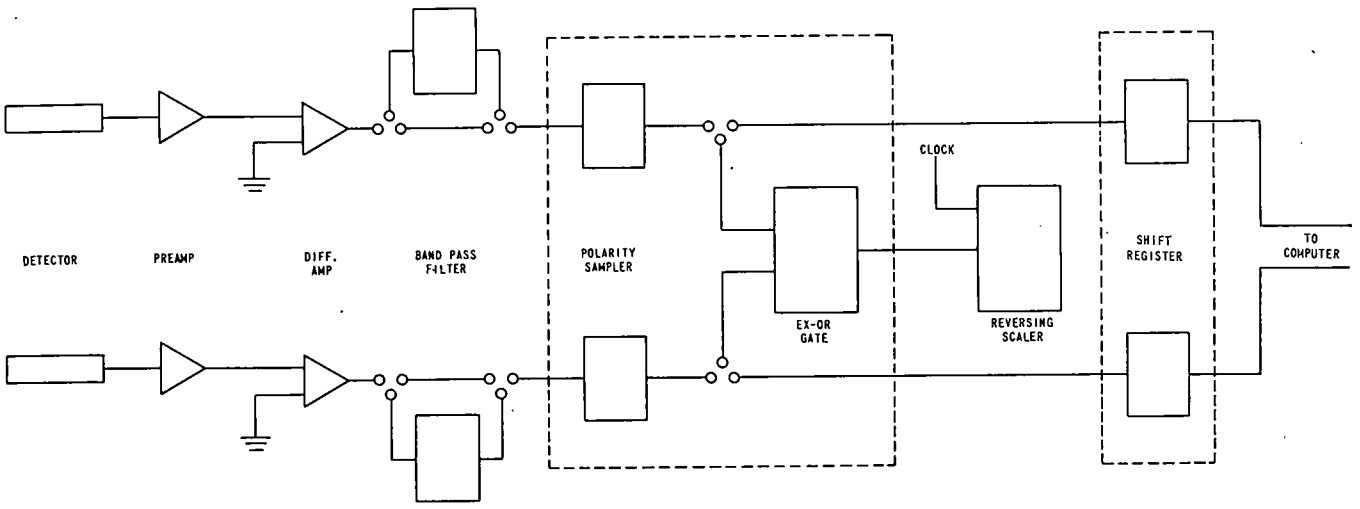

FIG. III-17-1. Schematic of Polarity Correlation Equipment. *ANL-ID-103-A11724.*

the input signal exceeds the threshold in the positive direction. The exclusive-or circuit is driven by the polarity samplers and its output goes positive only when the state of both inputs is the same and is zero when the two inputs are different.

The "ex-or" output is used to instruct the reversing scaler to count clock pulses up or down depending on the phase of the inputs. The "ex-or" gate and reversing scaler are used in reactivity measurements by the low-frequency-coherence function method. They would also be used in the frequency coherence function measurements along with band-pass filters.*

The correlation functions are calculated on line using the shift registers to input data to the computer.

INSTRUMENTATION

The preamplifier is shown schematically in Fig. III-17-2. The circuit is a current-sensitive configuration and uses a field-effect transistor, Q_1, in the first stage. Transistors Q_2 and Q_3 are cascode connected. Transistor Q_4 is a current source whose output impedance, in parallel with the output impedance of Q_4, and the input impedance of Q_5, comprise the collector load impedance of Q_3. Transistor Q_5 is an emitter follower that drives the complimentary emitter follower consisting of Q_6 and Q_7. The gain of the amplifier is determined by feedback resistor R_f, and may be expressed as $E_0 = i_{in}R_f$. Capacitor C_f provides high frequency roll-off.

Zener diodes CR-1 and CR-2 are used in the bias network of Q_3 and Q_4 to prevent stages Q_3 and Q_4 from amplifying 60 Hz hum that may be present on the ±24 V supply lines.

* The system as built has not yet been equipped with band-pass filters, but could be if the need should arise. The frequency coherence function measurement is mentioned for completeness and the capability does exist with the addition of the filters.

The preamplifier has a differential output with respect to ground that is derived at the connector side of R_1 and R_2.

The output of the preamplifier drives the differential band-limiting amplifier shown schematically in Fig. III-17-3. This amplifer has a differential input stage that is used to reject common-mode 60 Hz hum that may be picked up on the cables that connect the preamplifier to the band limiting amplifier. The differential input stage is comprised of transistors Q_1 and Q_2, whose outputs drive the unity gain differential amplifier A-1. Gain stages A-2 and A-3 are feedback amplifiers having a combined gain of 1000 maximum, with provisions for fine and coarse gain control.

The upper roll-off frequency of the band limiting amplifier is determined by the feedback capacitance shunted around amplifer stage A-3. This capacitance is switch controlled so that the upper 3 dB roll off frequency can be varied from 15.9 kHz to 159 Hz in five steps. A sixth switch position removes all feedback capacitance providing an upper 3 dB bandwidth in excess of 90 kHz.

The amplifier has a fixed low-frequency roll-off at approximately 3 Hz. The polarity sampling circuit shown in Fig. III-17-4 is comprised of an input discriminator section and a logic gating section. The input discriminator section uses type 741 operational amplifiers to limit the input signal and to set the bias levels for the 710 discriminators. The outputs of the discriminators drive TTL logic gates that are connected in a fashion that exclusive-ors the outputs of the x and y discriminators.

SHIFT REGISTER AND COMPUTER I/O SYSTEM

The shift register and I/O system are shown schematically in Fig. III-17-5. The data from the discrimi-

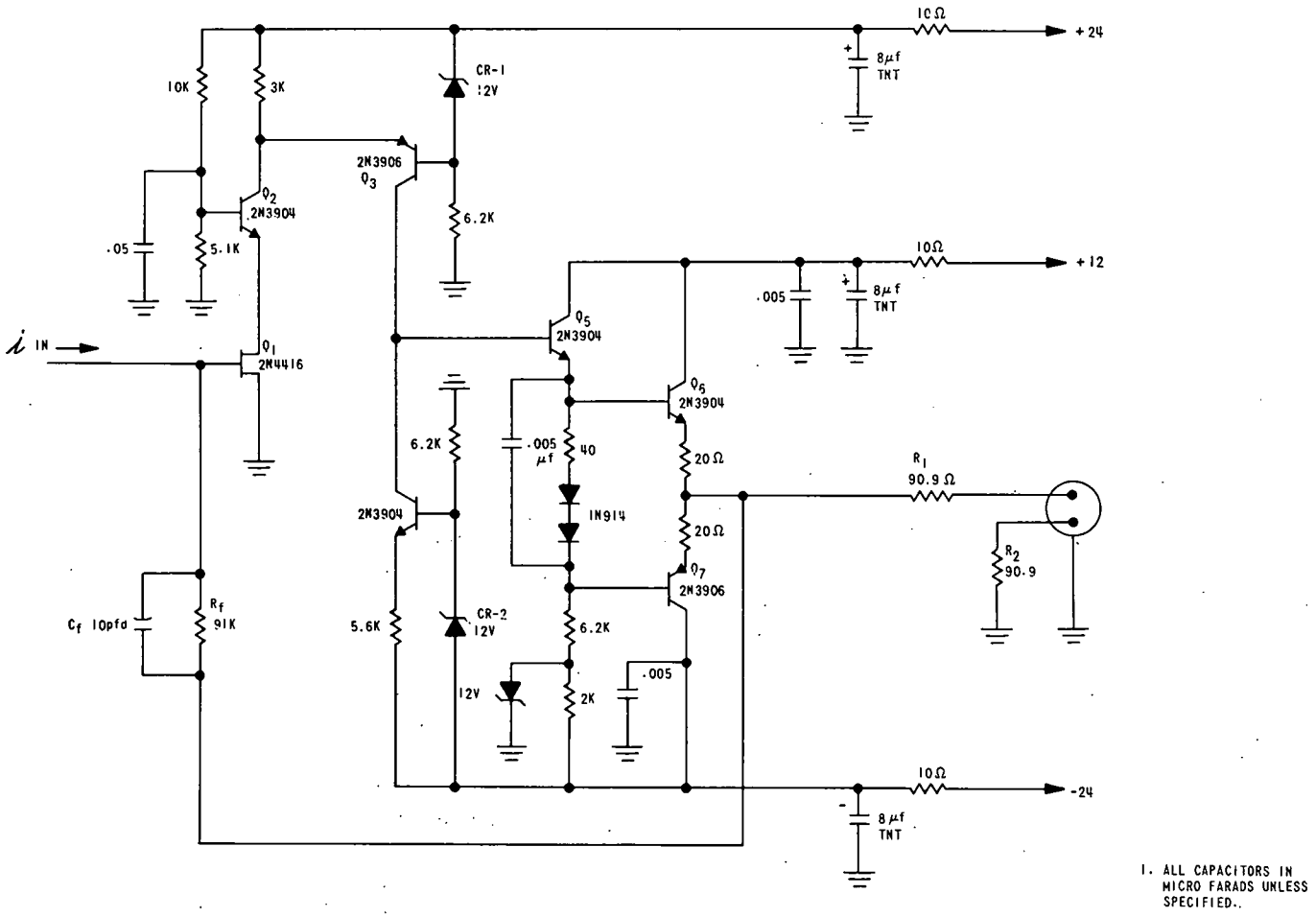

FIG. III-17-2. Schematic of the Charge Sensitive Preamplifier. *ANL-ID-103-A11725.*

nators are collected in two 24-bit shift registers in a single module. The data are then transmitted through a remote computer I/O terminal designed for collecting experimental data.

Data from each trigger circuit are gated into one of the shift registers in the shift register module by a variable frequency clock. At every 24*th* clock pulse, a computer input channel is enabled and the data in shifter register 1 are read into the computer in parallel. The signal that these data have been accepted is used to gate shift register 2 to the computer. The entire reading cycle (~20 μsec) is completed before the next clock pulse arrives, ensuring uninterrupted collection of data.

In addition to storing data, shift register 1 is used to time the computer input as follows:

The signal that the computer has read the data in shift register 1 is used to set the first bit of that register to 0 and the remaining bits to 1. Twenty-four clock pulses later this 0 bit is shifted out of the register into a flip flop in the remote I/O terminal, which enables the computer input channel and restarts the read cycle.

Figure III-17-5 also shows the details of the timing and control logic. All logic elements and control lines with the exception of the shift registers are an integral part of the remote I/O system. The I/O system is also used to provide a synchronized 500 Hz square wave to the shift registers for system and computer checkout.

PROGRAMMING TECHNIQUES FOR POLARITY NOISE CORRELATION

The programming techniques used here take advantage of some of the hardware features of the SEL 840 MP computer. Specifically, the hardware exclusive-or instruction is used to obtain the correlation function 24 bits at a time, and the three index registers are used to speed the counting of the correlated and uncorrelated bits.

Briefly, the procedure involves accumulating x plus y words of data from each counter, where x is the number of bits desired for accumulation in one pass divided by 24, and y is the number of delays needed, divided by 24. For discussion purposes, assume that x is 1 and we want

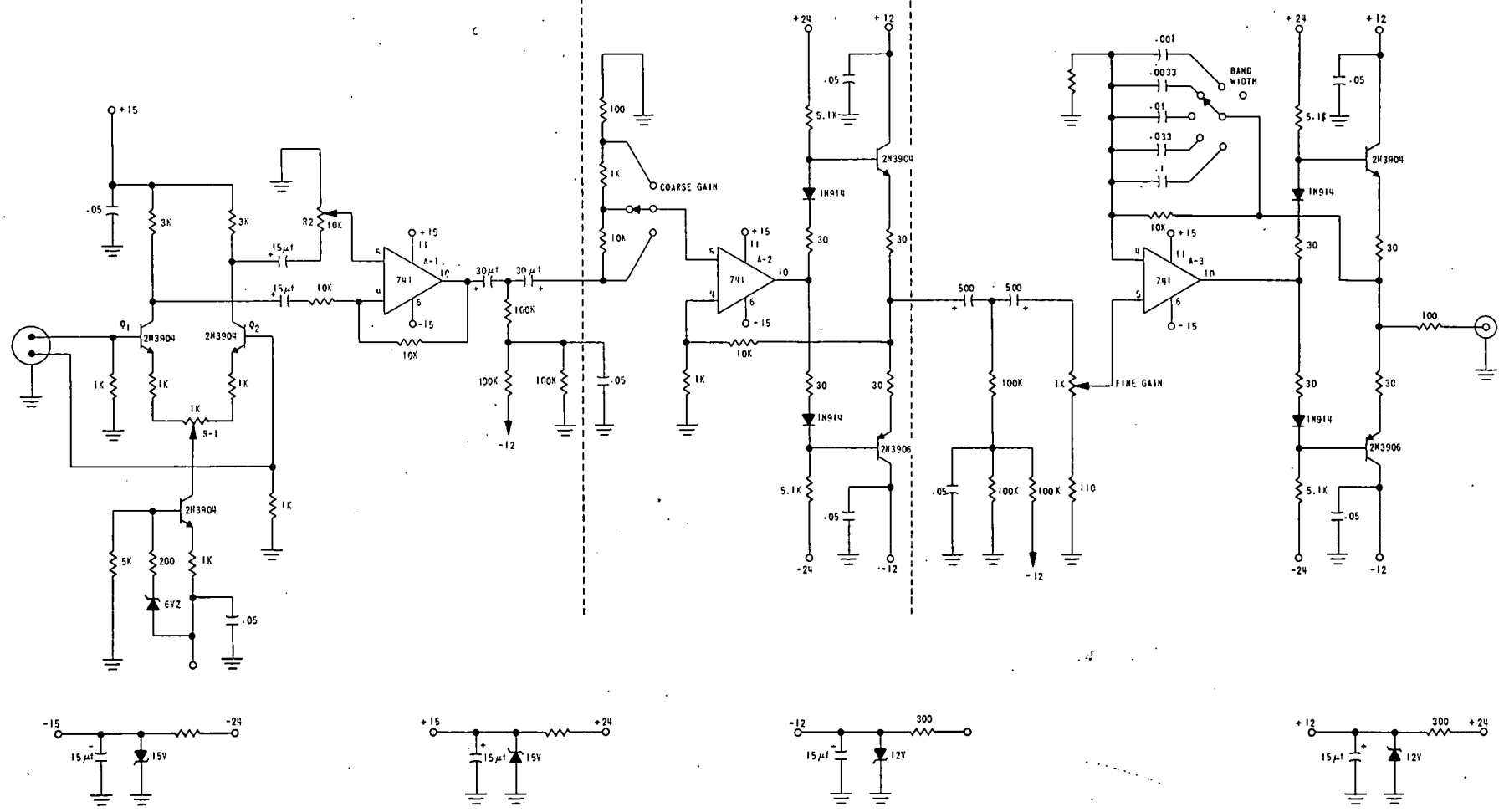

FIG. III-17-3. Main Amplifier Schematic. *ANL-ID-103-A11726.*

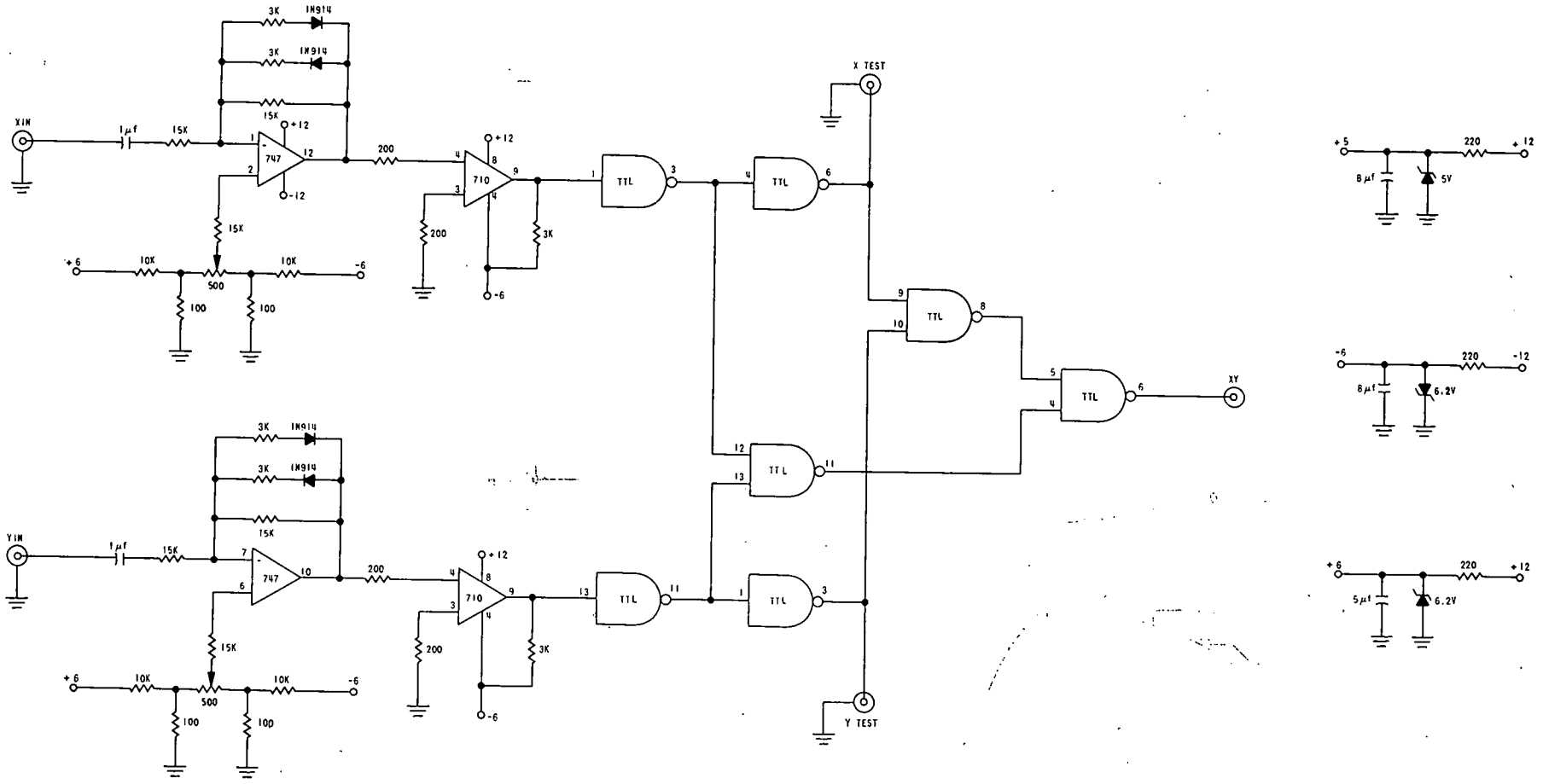

FIG. III-17-4. Polarity Sampler and Exclusive-Or Gate. *ANL-ID-103-A11727.*

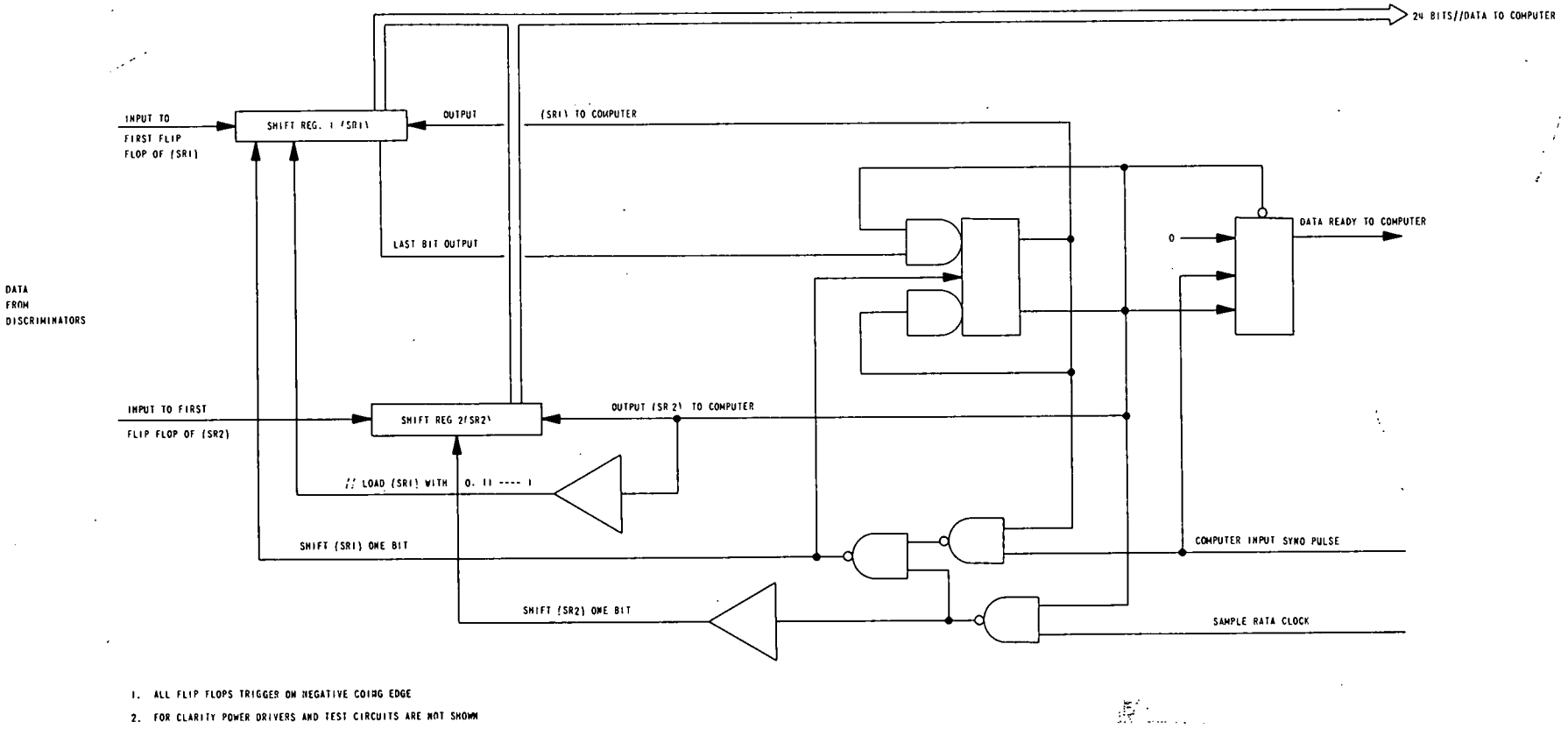

1. ALL FLIP FLOPS TRIGGER ON NEGATIVE GOING EDGE
2. FOR CLARITY POWER DRIVERS AND TEST CIRCUITS ARE NOT SHOWN

FIG. III-17-5. Computer Input-Output System. *ANL-ID-103-A11728.*

to have 24 delays. Two words are then inputed from each counter.

To determine the cross correlation function, the first word from counter number one is inverted (i.e., one bits are made zero bits and zero bits are made one bits); then the first and second words from the counter number two are loaded into the "A" and "B" hardware accumulators, respectively. Next, the inverted first word from counter number one is "exclusive-or"ed with the contents of the "A" accumulator leaving ones for correlation and zeros for noncorrelation for delay time $\tau = 0$. This bit pattern is stored in a product table; the "A" accumulator is restored to the first word from counter number two; a full-logic left shift of one bit is done (which brings the high order bit from the "B" accumulator into the low order bit of the "A" accumulator; the contents of "A" are stored in memory, and the inverted first word from counter number one is "exclusive-or"ed with the "A" accumulator. This gives the correlation for $\tau = 1$, which is stored in the product table. The "A" accumulator is restored, a full-logic shift is repeated, and so on. This procedure continues until 24 shifts and exclusive-ors have been accomplished.

Summing the bits is accomplished by use of a 256 word table that contains the sum of +1 for all the one bits and −1 for all the zero bits of the octal address of each word of the table (with the beginning of the table at location 0). The first word of the table is −8, the second word is −7, etc., and the last word is +8. To find the correlation, the word in the product table is split into three eight-bit parts which are transferred to index registers, from which they point to the word in the table that contains the sum of those eight bits. The three values are added to a sum table (one entry for each delay time τ), which is passed to a FORTRAN subroutine for print and display.

To complete the cross correlation, the reverse of the above procedure is applied. That is, the first word from counter number two is inverted, the two words from counter one are loaded into the "A" and "B" accumulators, and the same procedure is followed.

Autocorrelation follows the same pattern except that the inverted first word is "exclusive-or"ed with itself for $\tau = 0$, etc.

This technique requires ~8 μsec per bit per number of delays for cross correlation, and half that for autocorrelation.

In addition to cross- and autocorrelation programs that obtain the correlation function for all delay times between 0 and 23, and between 0 and 95, another program is in use that obtains the values for $\tau = 0$, 1, 3, 6, 10, etc. up to 300. This program is designed to take data on an interrupt basis so that while the process of correlating one batch of data is being carried out, the next batch of data is being taken.

Applications

The polarity correlation system has been tested in a fast reactor application in the Zero Power Plutonium Reactor, Assembly 2. Measurements of the correlation functions at critical and at several subcritical levels have been made. In addition, reactivity measurements have been made by the low-frequency coherence-function method. Satisfactory results have been obtained in these measurements.

The system is currently being integrated into the ZPPR experimental system and will be used as a supplemental reactivity measurement method in support of the LMFBR program.

References

1. W. Seifritz, D. Stegeman and D. Vath, *Neutron Noise, Waves and Pulse Propagation*, Conf. 660206, USAEC Symposium Series 9 (1967), p. 195.
2. T. Nomura, S. Gotoh and K. Yamaki, ibid., p. 217.
3. J. B. Dragt, ibid., p. 591.
4. C. E. Cohn, *Reactor-Noise Studies with an On-Line Digital Computer*, Nucl. Appl. Tech. **6**, 391 (1969).
5. W. Seifritz, *The Polarity Correlation of Reactor Noise in the Frequency Domain*, Nucl. Appl. Tech. **7**, 513 (1969).
6. N. Pacilio, *Reactor-Noise Analysis: The Covariance Method via Polarity Detection*, Nucl. Sci. Eng. **35**, 249 (1969).
7. P. D. Welch. *A Direct Digital Method of Power Spectrum Estimations*, IBM J. Res. Dev., Sec. 5 (1961).
8. R. C. Kryter, Oak Ridge National Laboratory (private communication).

III-18. Real-Time Counting Techniques for Determining Absolute Fission Rates and Reaction Rate Distributions in Zero Power Critical Assemblies

A. B. Long

I. Introduction

Reaction rate measurements within fast critical assemblies form a fundamental part of any experimental reactor program. Current techniques employed in these measurements include foil activations, thermoluminescent dosimetry, track recording, and the use of counters. Each of these techniques has specific applications and also has inherent advantages and disadvantages when compared with the other techniques. This report will limit itself to a discussion of the experimental methods used to accumulate and analyze reaction rates measured by counters in ZPR-6 and ZPR-9.

Counters provide the only means for real-time accumulation of data and are, therefore, the only technique suitable for time-dependent applications. They also afford the experimenter the opportunity to interact directly with the accumulation of data. Through the use of suitable experimental equipment, it is possible to accumulate and analyze the data at the time of its acquisition so that the experimenter can judge the quality of the results and make decisions affecting further acquisition of data.

II. Description of the Experimental Equipment

A. Fission Detectors

Fission rate measurements are made with Kirn-type counters.[1] These detectors are cylindrical gas-flow counters with parallel-plate configuration. Currently, a large counter with a diameter of 5.3 cm and a length of 2.5 cm is used for absolute measurements, and a smaller counter having a diameter of 2.5 cm and a length of 1.5 cm is used for traverse measurements. In both counters the fissionable material is deposited on a polished metallic disk that serves as both the front of the detector and the cathode. Another disk which serves as the anode is located at a distance of 0.5 to 0.7 cm from the source and is positioned coaxially and parallel to the source. With a bias of 100 V between the two plates and an inert atmosphere of 90% argon and 10% methane within the detector, good separation is obtained between the pulse heights produced by fission fragments and those produced by alphas and background gammas and neutrons. The reader is referred to Ref. 1 for a more detailed description of the counter.

Fission rates of different materials can be measured by one Kirn counter simply by interchanging source disks. These sources consist of fissionable material electrolytically deposited on a 3.88 cm^2 area in the case of the larger Kirn counters and on a 2.85 cm^2 area in the case of the smaller (traverse) Kirn counters. In order to reduce the energy lost by fission fragments emitted along paths that are nearly parallel to the source disk, the source disks are made of highly polished stainless steel and the fissionable material is deposited to a thickness of only 20 $\mu g/cm^2$.

Currently, high purity sources of ^{235}U, ^{238}U, ^{239}Pu and ^{240}Pu are available for fission counting in either size Kirn counter. Using these isotopic concentrations and knowing the half-life of each isotope plus its branching ratio, the masses of the foils are derived from absolute alpha counting. Uncertainties in the masses will be due to counting errors, errors in the half-lives of the isotopes and uncertainties in the isotopic determinations. The effect of these uncertainties upon absolute fission-rate measurements is considered in Section III-A of this report.

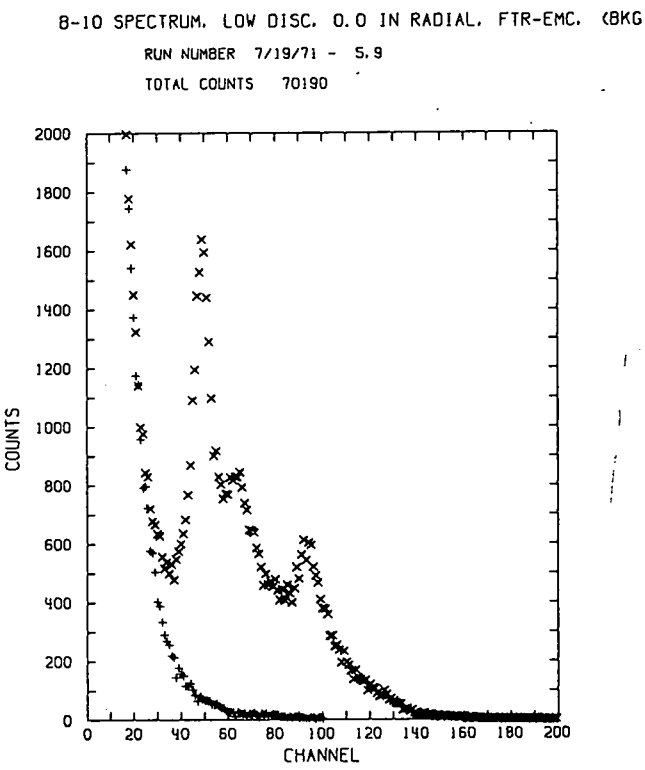

Fig. III-18-1. Typical ^{10}B and Background Spectra Recorded in a Fast Critical Assembly. *ANL Neg. No. 116-1027 T-1.*

B. ^{10}B ALPHA DETECTORS

Capture rates in ^{10}B are measured with a back-to-back cylindrical gas-flow proportional counter designed by L. S. Beller.[2] The detector is 5.6 cm long and has a diameter of 1.3 cm. It is divided along its length to form two half-cylinders; one-half contains a deposit of ^{10}B on a source plate and the other half contains a blank plate. The source and blank are placed on opposite sides of the divider wall and they cover an area 5.3 cm long by 1.0 cm wide. The reader is referred to Ref. 2 for a more detailed description of the counter.

The boron is 96.5% ^{10}B and 3.5% ^{11}B deposited to a thickness of approximately 15 $\mu g/cm^2$. The absolute boron mass has not been determined. The blank half of the detector is used to correct the ^{10}B data for gamma and neutron background. To date, the best ratio of signal-to-background in a zero-power critical assembly has been obtained with an applied bias of 500 V and a gas flow of 90% argon and 10% CO_2 (see Paper III-20). A typical ^{10}B and background spectrum recorded in a zero power critical assembly is shown in Fig. III-18-1.

C. ELECTRONICS

A schematic diagram of the electronics used to record count-rate and pulse-height information is shown in Fig. III-18-2. The bias supply (high voltage) and preamplifier are conventional units. The amplifier is an Ortec Model 486 combination amplifier and single-channel analyzer. This unit offers the advantage of a fixed dead-time for pulses of all sizes because the dead-time is generated for 1.8 μsec after the peak of the pulse is detected. As a result, accurate dead-time corrections can be made for count rates obtained from the output of this single-channel analyzer.

In order to correct for background and pulse-pile-up errors, the pulse height spectrum from the counters is recorded using a Northern Scientific analog-to-digital converter in conjunction with an SEL-840 computer. Only those pulses whose height exceeds the lower level discriminator are recorded through the requirement of a coincidence between the amplifier and the single-channel analyzer signals. A delay amplifier is required to adjust the timing requirements for this coincidence. No dead-time correction is made for these pulse-height data since it is only used in a relative sense to correct the absolute count rates obtained from the single channel analyzer.

D. TRAVERSE EQUIPMENT

Traverses are made within critical assemblies by moving a detector through a hole at the appropriate location within the assembly. For radial traverses, the current practice is to introduce a 2.8 cm diam hole extending from the outer edge of the matrix along row 23 in the stationary half to the desired depth in the core; special plates are used. The counter is then placed at the end of a long tube and is traversed through the hole using the radial sample changer mechanism. Axial traverses are performed by removing the normal reactor drawer at the appropriate position and inserting a special "L"-shaped drawer; this special drawer has a 2.5 x 2.6 cm axial hole at one corner extending along the entire length. The counter is placed in a small movable drawer which fits into the 2.6 cm square hole in the "L"-shaped drawer; the counter can be moved to any position along the length of the "L" drawer using a servo motor.

The choise of materials to be loaded around the radial or axial traverse hole is determined by the spe-

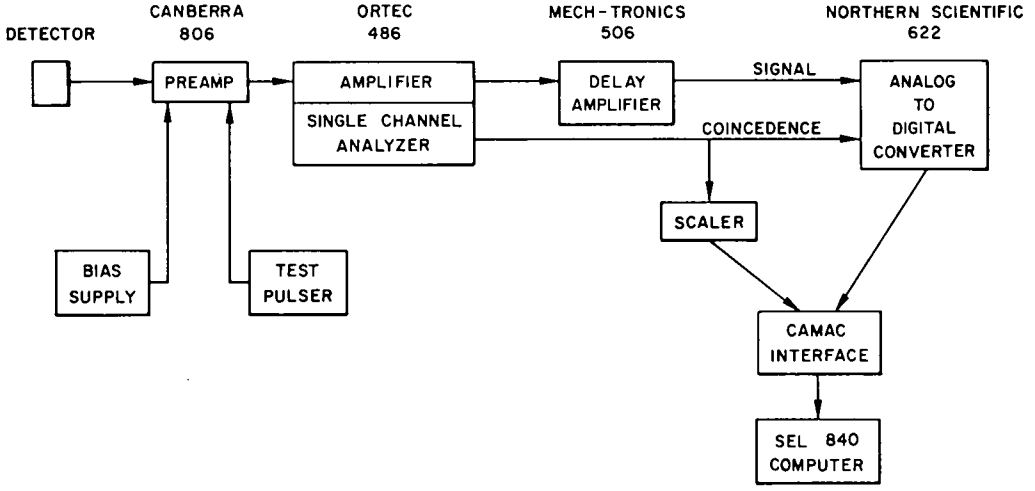

FIG. III-18-2. Schematic Diagram of One Channel of Electronics Used to Record Count Rate and Pulse Height Data. *ANL Neg. No. 116-1024.*

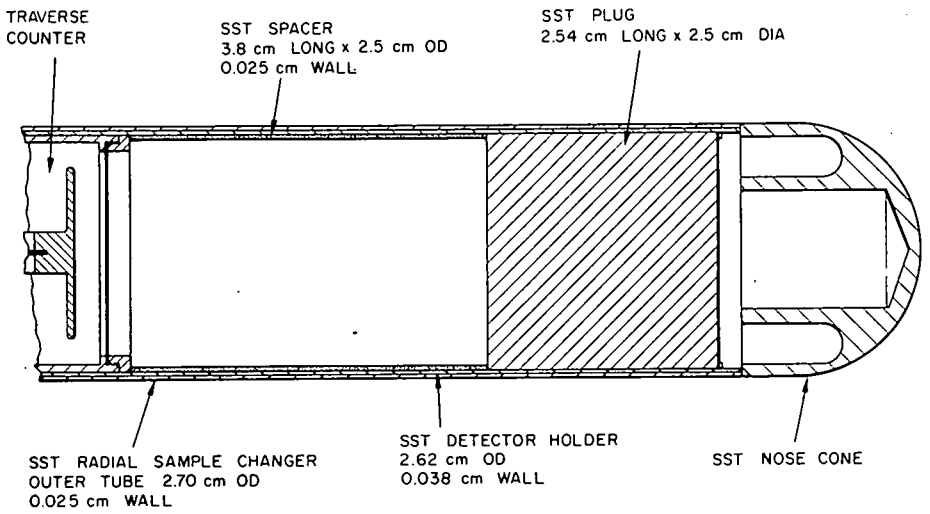

FIG. III-18-3. Cutaway Diagram of Front End of Radial Traverse Tube with Fission Counter and Stainless Steel Plug Present. *ANL Neg. No. 116-1025.*

cific experiment which is being performed. However, the immediate configuration of stainless steel around the detector due to the detector holder will be unchanged from one measurement to the next and is shown in Fig. III-18-3.

III. Analytical Techniques used in the Processing of Counter Data from Zero Power Critical Assemblies

A. Determination of Absolute Fission Rates

It is possible to determine absolute fission rates from counting and pulse-height distribution data obtained from Kirn counters. Section II of this paper describes the experimental equipment used to measure count-rate data and how to correct it for dead-time. From these corrected count-rate data, the absolute fission rate may be extracted if corrections can be made for background, detector efficiency, and if the absolute mass of the foil is known.

Consider first the corrections for background and for detector efficiency. Kirn states in Ref. 1 that the efficiency of a counter of his design is 99.9 % for fission events if the foil is only 20 $\mu g/cm^2$. The small loss in efficiency is due to the few events in which the fission fragments are emitted parallel to the foil surface and not enough ionization is produced within the chamber to be detected as a fission event. As the angle of emission with respect to the foil surface becomes larger, energy lost by the fragment also increases. There xists, therefore, a small solid angle of emission for vhich the fragment is either not detected at all or, if it is detected, it falls into the background. Theoretical calculations of this low-energy tail have been performed for detectors having much less efficient con-

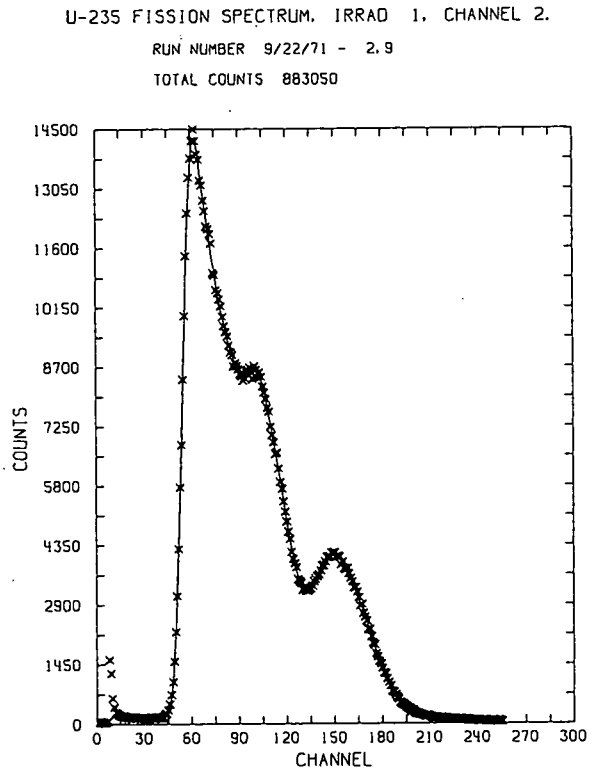

FIG. III-18-4. ^{235}U Fission Spectrum Recorded by a Kirn Counter in a Fast Critical Assembly. *ANL Neg. No. 116-1026 T-1.*

figurations than the Kirn counter; these calculations are in good agreement with experimental results.[3] Thus, it is felt that the shape of the low-energy tail which is present in Kirn counter measurements (see Fig. III-18-4) can be accurately predicted.

The correction for the low-energy tail is performed by a computer code which fits a third-order polynomial

curve to the data points that fall around the minimum count. The number of points fitted is equal to 20% of the channels between channel zero and the channel in which the first peak occurs (12 channels were fitted in the example shown in Fig. III-18-4). The minimum value of this curve, *CTVL*, and the channel in which it occurs, *CHVL*, are determined by the code. The number of fissions which produce events below the valley channel, *CHVL*, is set equal to the product of *CTVL* and *CHVL*. The tail correction factor, *TCF*, used to correct absolute count-rate data is then given by

$$TCF = \frac{TCABVL + CTVL \times CHVL}{TOTAL}, \quad (1)$$

where

TOTAL ≡ the total number of counts recorded in the fission spectrum

TCABVL ≡ the total number of counts recorded in the fission spectrum above the valley channel

CHVL ≡ the channel in which the fitted curve has a minimum

CTVL ≡ the value of the fitted curve at the minimum.

Due to the presence of some background events in the counts recorded for the valley channel, the estimate for the number of fissions in the low-energy tail is probably too large. However, since this number is generally less than 0.5% of the total fissions, the error is small when compared with other uncertainties. An experimental error for the tail correction factor is calculated assuming that there is no uncertainty in the valley channel, and that the other quantities in Eq. 1 are independent and have statistical errors equal to the square root of their values. This error is given by

$$\sigma^2_{TCF} = \frac{1}{TOTAL^2} \cdot (TCABVL + CHVL^2 \times CTVL + TCF^2 \times TOTAL). \quad (2)$$

The other source of uncertainty in the determination of absolute fission rates is the uncertainty in the absolute mass of the fission foil. Typical uncertainties in foil mass run as high as 2% for ^{235}U foils and as low as 0.4% for ^{239}Pu foils. These errors reflect counting errors, uncertainties in half-life and branching ratios, and errors in isotopic analysis; they do not include any indication of systematic errors. Fortunately, most absolute fission rates are reported relative to another absolute fission rate. For such ratios of two absolute measurements, small common errors in tail correction techniques, detector efficiency and foil mass cancel out.

B. ACCUMULATION AND ANALYSIS OF REACTION RATE DATA FROM ZERO POWER CRITICAL ASSEMBLIES

The computer code TRVS has been developed to accumulate, display, and analyze reaction-rate distribution data making use of the SEL-840 computer associated with the zero power critical assemblies. This code is one of the sub-modules in the integrated system for on-line computer acquisition of data from ZPR-6 and ZPR-9 (see Paper III-19).

Counter data are accumulated as a function of detector positions within the reactor by making use of the electronics discussed in Section II-C and the on-line peripheral scalers which are interfaced with the computer. Any combination of the following three options may be selected for accumulating these data:

1. Record only one scaler [SCAL(I)].
2. Correct the count rates in one scaler [SCAL(I)] with those recorded in another scaler [SCAL(J)].
3. Normalize the results of one or two scalers with the value of a third scaler [SCAL(K)].

These options may be expressed by one equation where, depending on the option selected, scaler J may be present or replaced by zero and scaler K may be present or replaced by a one:

$$[\mathrm{SCAL}(I) - \mathrm{SCAL}(J)]/\mathrm{SCAL}(K). \quad (3)$$

Following the accumulation of data by the selected peripheral scalers, TRVS is called to store this information plus the position of the detector during the measurement. The data which have been accumulated at different positions up to this time are all presented on a visual graphic display unit. If previous measurements have been made at the present detector location, a comparison of the results with the present data is made to check for reproducibility. After evaluating these results the experimenter can decide upon his next measurement.

Upon completion of the traverse, the results are corrected for dead-time and, if appropriate, for background in the tail. This last correction is only applicable to Kirn counter fission rate measurements and can be avoided if relative counting is acceptable. To avoid the correction, the lower level discriminator of the single channel analyzer must be set above background. However, since this tends to place the discriminator in a region of relatively high count-rate where a small drift would produce noticeable error, and because it destroys the possibility of absolute counting, the current policy has been to take fission counter data with the discriminator set just below the valley as shown in Fig. III-18-4. The data are then corrected by TRVS for the tail background by recording pulse height spectra at a number of different positions along the

traverse. These spectra are analyzed to determine the correction factors and in turn entered into TRVS. The code fits a straight line to them as a function of detector position and then corrects the counter data for the background tail as a function of position.

IV. Systematic Errors Associated with Experimental Measurements of Reaction Rates by Counters

During the FTR-3 Phase B Critical Experiments Program carried out on ZPR-9, a series of measurements were made to determine the systematic errors introduced by neutron streaming and counter perturbations on measured reaction rate distributions.[4] In those measurements the effect of neutron streaming down the traverse tube (approximate cross section, 6 cm^2) was investigated by placing a 2.5 cm long by 2.5 cm diam. stainless steel plug 3.8 cm in front of the fission detector. Stainless steel of this thickness had an attenuation of approximately 0.6 for the mean energy neutrons in the assembly. The effect of the plug on the measured $^{239}Pu(n,f)$ and $^{238}U(n,f)$ fission rate distributions was masked by the statistical uncertainty of the data. Consequently, the effects of streaming for this size traverse tube appears to be less than 7 %. The effect of the finite size of the counter on the measured reaction rates (i.e., the difference between the neutron spectrum at the counter position with and without the counter and traverse hole) was investigated by performing $^{238}U(n,f)$ foil irradiations between plates along the same path as the counter was traversed, except that neither the traverse hole nor the counter was present. Of the principle reaction rates in a ZPR plate mockup of an LMFBR core, ^{238}U fast fission is most strongly spatially dependent within the plate cell. The $^{238}U(n,f)$ counter was not able to resolve any of the fine structure in the fission rates due to the heterogeneous drawer loading; however, the foils clearly measured this structure. The results indicate that at least in the case of $^{238}U(n,f)$ reaction rate measurements, the user of the counter data must be aware that the counter data represent average special response over a significant volume of the drawer. For this reason the user must be careful when comparing calculated reaction rate distributions with distributions measured either by foils or by counters.

The reader is referred to Paper II-7 for a description of the procedures used to calculate reaction rate distribution for the FTR-3 Phase B Critical Experiments Program. In addition, a $^{239}Pu(n,f)$ foil irradiation is being planned for the current FTR-EMC experimental program. This will closely duplicate counter measurements which have already been performed. A comparison of these two measurements will yield more information about the effects of streaming and counter perturbations.

References

1. Frederick S. Kirn, *Neutron Detection With an Absolute Fission Counter*, Symposium on Neutron Detectors, Dosimetry and Standardization, Harwell, England (1962).
2. L. S. Beller, *Detection for $^{10}B(n,\alpha)$-to-Fission Ratio Measurements*, Applied Physics Division Annual Report, July 1, 1969, to June 30, 1970, ANL-7710, p. 288.
3. E. M. Bohn and A. B. Long, *Spectrum Analysis for a Silicon Fission-Fragment Detector*, Applied Physics Division Annual Report, July 1, 1969, to June 30, 1970, ANL-7710, p. 318.
4. A. B. Long and C. D. Swanson, *Measured Reaction Rate Distributions in ZPR-9 Assembly 26, FTR-3*, Applied Physics Division Annual Report, July 1, 1969, to June 30, 1970, ANL-7710, p. 65.

III-19. Integrated System for On-Line Computer Acquisition of Data from ZPR-6 and ZPR-9

A. B. Long

Introduction

An integrated system for on-line computer acquisition of experimental data utilizing an SEL-840 Computer has been developed to facilitate accumulation of data simultaneously from the ANL ZPR-6 and ZPR-9 zero-power critical facilities. The system operates in a "real time mode," which means that the computer keeps accurate track of time and is able, where necessary, to precisely control the duration of time for which a peripheral device accumulates data. The system also performs "time swapping" among as many as three different control terminals. A control terminal may be used to control the integrated system and to perform limited data input and output. The term "time swapping" is used to indicate that the central processor will execute a short program requested by one control terminal and then proceed to the requirements of the next control terminal. The frequency with which this

"time swapping" occurs is determined by the requirements of the various control terminals; however, none of the data processing programs accessible within the integrated system require more than a few minutes for execution, so that access to the computer from any control terminal will not be delayed significantly. The integrated system consists of a master control program module and many submodules written in Assembly Language and Fortran. The control module resides permanently within the core and it serves as the basic unit for control of the peripheral data accumulation devices, for control of the program submodules, and for storage and retrieval of all data. On the other hand, the program submodules are stored on the disc unit and are only brought into the computer when needed for a specific calculation or the accumulation of data by a particular peripheral device. Once the program module has completed its task it returns control to the master control module and exits, leaving the computer free for a different use. When the master control module ascertains that a given peripheral device that is accumulating data (e.g., a scaler) has run for the desired length of time, it will read the data from the device and store it in a dedicated location.

By using one master program control module and many submodules it is possible to have a larger or more flexible system for acquisition and analysis of data. In addition, since the control module is able to run the peripheral data accumulation devices independent of other computer operations, it is possible for one submodule to be analyzing data while the peripheral devices are recording data under command of the control module.

Master Program Control Module

The master program control module performs three functions which are described separately in the following:

REAL TIME OPERATION OF DATA ACCUMULATION PERIPHERALS

The real time control of the peripheral data recording devices is done by the control module on an interrupt basis. Once every one-tenth of a second the highest-priority computer interrupt is generated. This interrupt causes the control module to check each peripheral data accumulation device in turn to see if it has run for the desired length of time. If it has, the appropriate action is taken at that instant to read the data from the device, restart the unit if another iteration is required, or to stop the unit if all data acquisition is finished. The interrupt routine is then ended and the computer returns to whatever it was doing before the interrupt occurred. The whole sequence occurs in much less than a millescond.

Control of Access to the Computer from the Different Control Teriminals and Handling of the Program Submodules

In addition to checking the peripheral data accumulation devices during each interrupt, the control module also checks to determine if any control terminal has requested to be acknowledged. If such a request is made, the request is recognized during the interrupt routine and then when the computer is free the control terminal is acknowledged. Once acknowledged, the operator at that control terminal may request the control module to call in any one of the submodules. Control of the computer is then transferred to this submodule until it has finished performing its task. Following completion of the task, the control module again regains control and checks to determine if any of the other control terminals have requested to be acknowledged before returning to check the original terminal. For this reason each control terminal has equal access to the computer on a time-swapping basis. Throughout the whole process, the real-time control of the peripheral data recording devices continues on an interrupt basis.

STORAGE AND RETRIEVAL OF DATA

In order to permit different types of data to be intermixed and stored in one device, a standard storage and retrieval routine, INOT, was developed. This routine was incorporated into the control module and is therefore always in residence within the core. It can be called by any of the submodules or directly by the operator. Once called, it permits the operator to select the disc, magnetic tape, or paper tape as the device in which the data is to be stored or from which it is to be retrieved.

Each set of data recorded by the integrated system is composed of two records. The first record consists of sixty-four words of integer data used to identify and describe the second record. The first five words which uniquely define each data set consist respectively of the month, date, year on which the data was recorded, the number of the data set taken on that day, and the reactor on which the data were taken. The second record contains the actual data; its length, structure, and format are defined by specific words in the identification record. All the data are stored in binary form which saves both storage space and translation time and simplifies the process of intermixing integer, floating point, and double-precision values.

Before a data set is stored on either the disc or mag netic tape, the identification of all data sets previously stored on that unit are compared with the identification of the new data set. If an existing data set is found

with the same identification numbers, the storage is terminated until the identification numbers of the new data set are changed. This procedure assures that each data set in a given storage unit is uniquely defined and thereby retrieveable through the designation of its identification numbers.

As an additional safety precaution different magnetic tape transports and different sections of the disc unit are assigned to the different reactors by the control module. A given control terminal must initially be assigned to a specific reactor and from then on the operator at that terminal will have access only to the storage areas allocated to that reactor. Furthermore, all data stored from the assigned control terminal will automatically bear the appropriate reactor identification number. Before any data can be retrieved by the assigned control terminal, the reactor identification number for that data set will be compared to see that it agrees with the reactor number to which the terminal is assigned.

Program Submodules

GENERAL COMMENTS

A program submodule is designed to perform a specific function. When the operator needs this function to be performed he requests the master program control module to call in the appropriate submodule from the disc. Control of the computer is then transferred to that submodule until it has finished its task. This section contains a brief description of the submodules which have been or are in the process or being implemented.

Basically each of the submodules is involved with acquiring and/or analyzing data which have been recorded on-line from the reactors. The peripheral data acquisition devices that are currently used by the integrated system are:

1. Four 100 MHz, 24-bit scalers (CAMAC interface). These are used for fission or capture-rate measurements.
2. Four 10 MHz, 24-bit scalers. These are used for scaling the outputs of the voltage-to-frequency converters used in flux level or noise measurements.
3. Four 10 MHz, 24-bit reversible scalers. These are used for rod position indicators.
4. Two 1024 channel analog-to-digital converters (CAMAC interface). These are used for recording pulse-height spectra from counters.
5. One thirty channel thermocouple interface (CAMAC interface). This unit has not yet been installed; however, it will be used to determine the reactor core temperature for the purpose of reactivity connections.

All of these devices are controlled in a real-time sense by the master program control module. Once they are started by a submodule they will run independently or on an interrupt basis until the control module determines that they have run for the required length of time and the required number of iterations. During such operation the computer is free to perform some other function.

NOIS—ACCUMULATION AND ANALYSIS OF NOISE DATA BY THE COHN OR ALBRECHT METHODS

This submodule is designed to acquire and to analyze noise data from both Cohn[1] and Albrecht[2] type noise detectors. Initially the module is called to start data acquisition for up to thirty one-minute counting periods. Once the scalers have been started, the control module regains command of the computer until the counting period is finished.

Following the acquisition of data, this submodule determines the coherence of the noise data directly from a scaler value in the case of Albrecht's method and by interpolation from a table of coherence versus the ratio of two scalers in the case of Cohn's method. If the coherence is for a subcritical reactor configuration, the code then uses the measured values for the critical and subcritical coherence to determine the subcriticality of the reactor expressed in inhours. These data are corrected for core temperature and the results can be stored for comparison with additional measurements. The statistical error associated with the results is determined from the standard deviation of the coherence values derived from the different one minute counts.

RDR1 AND RDR2—ACCUMULATION AND ANALYSIS OF ROD-DROP DATA

The acquisition and analysis of subcriticality data by the rod-drop technique is performed by two separate submodules because of the limitation in memory size. The submodule RDR1 is used to acquire data from as many as three independent flux channels: a flux channel provides a pulse frequency proportional to flux level. Up to 2150 flux data points may be recorded for each flux channel and the counting time for these points can be choosen to be any multiple of 0.1 sec. The operator has complete control of when data collection begins and when it ends. Before starting collection, he may initiate a test command which records and prints out one datum point from each flux channel as a test that the channel is operating. Then during the actual collection of data, RDR1 prints out the last data point recorded from each flux channel every fifteen seconds. Finally, after data collection is complete the operator has the option to store the data

from each flux channel on disc, magnetic tape, or paper tape.

The analysis of the rod-drop data is done by the submodule RDR2. The operator specifies the identification numbers and storage location of the delayed neutron data set and the rod-drop data set to be used in the calculations. The submodule then performs the inverse kinetics analysis using the algorithm developed by Cohn.[3] The resulting initial and final subcriticality are connected for the core temperature and can be stored for comparison with additional measurements.

RCA1 AND RCA2—ACCUMULATION AND ANALYSIS OF ROD CALIBRATION DATA

The acquisition and analysis of rod calibration data are performed by two separate submodules, RCA1 and RCA2. The submodule RCA1 is similar to RDR1 except that flux data are recorded from one channel as a function of rod position or time. In this case only 1000 data points may be recorded; however, each datum point consists of the flux level and the rod position or the time. The counting time for these points can be choosen to be any multiple of 0.1 sec. The operator has complete control of when data collection begins and when it ends; the operator also is free to start and stop rod motion at any time during data collection. Following this, the operator may store the data on disc, magnetic tape, or paper tape.

The analysis of the rod calibration data is performed by RCA2 in a manner analogous to the analysis of rod drop data by RDR2. However, in this case the rod worth as a function of position or time is generated for the operator.

SCAL—ACCUMULATION OF SCALER COUNTS

The accumulation of count rate data by the four CAMAC scalers is controlled by the submodule SCAL. The operator may select any combination of these four scalers and start them simultaneously. The counting time can be any multiple of 0.1 sec and up to nine repetitions may be specified. Once the scalers are started, the control module regains command of the computer until the counting period for a given scaler is finished. Upon completion of its counting, a scaler will recall SCAL when the computer is free. The total counts for each repetition will be printed out and then the average count rate will be calculated from these counts, along with its error.

TRVS—ACCUMULATION AND ANALYSIS OF FISSION OR CAPTURE RATE DISTRIBUTIONS USING A MOVABLE COUNTER

The submodule TRVS was developed to accumulate, display, and correct reaction rate distribution data obtained from a movable counter. After the count rate data have been accumulated at a given reactor position by SCAL, the submodule TRVS is called to correct and store these data. Any combination of the following three options may be selected:

1. Record only one scaler
2. Correct the count rate of one scaler with that of another scaler
3. Normalize the results of one or two scalers with the value of a third scaler.

All data collected are graphically displayed, and if data were previously recorded at the current position a comparison is made to check for reproducibility. The cumulative results are then stored on disc and computer control is returned to the control module until the next traverse point is recorded.

Upon completion of the traverse, all data points may be corrected for alpha and neutron background as a function of position. The final results are then listed and can be stored as a data set on disc, magnetic tape, or paper tape.

ADCA—ACCUMULATION AND ANALYSIS OF PULSE-HEIGHT DATA

The submodule ADCA was originally developed to read, display, list, and store pulse-height spectra recorded by most types of multi-channel analyzers. In addition, provision was made to calculate the "tail-connection factor" used in absolute fission rate measurements (see Paper III-18) from certain pulse-height data. Currently, this submodule is undergoing revision to allow it to initiate the accumulation of pulse-height data on-line by the two 1024 channel ADCs which have just been acquired.

LLPT—LINEAR OR SEMI-LOGARITHMIC PLOTTING OF PULSE-HEIGHT DATA

The submodule LLPT is used to plot pulse-height spectra stored on disc, magnetic tape, or paper tape in the standard data set format by ADCA. Plotting is done on the calcomp plotter. The operator may select a linear or semi-logarithmic scale. One or more spectra may be plotted on the same graph using symbols or a straight line between points.

PLANS FOR ADDITIONAL SUBMODULES

Because of the modular structure of the integrated system, additional submodules may be easily added when new computer activities are required. At the present time programming is being planned for submodules to record and analyze:

1. Sample worth measurements
2. Doppler measurements
3. Excess reactivity
4. Alpha-impactor spectra.

These planned submodules will take advantage of

existing scalers, ADCs, and temperature recorders that are already interfaced with the computer.

REFERENCES

1. C. E. Cohn, *Experience with Subcriticality Determination by Noise Techniques in the FTR Engineering-Mockup Critical-Experiments Program*, Trans. Am. Nucl. Soc. **14**, 861 (1971).
2. G. M. Hess and R. W. Albrecht, *Polarity Spectral Analysis Reactivity Errors*, Trans. Am. Nucl. Soc. **12**, 738 (1969).
3. C. E. Cohn, *Experiences with Subcriticality Determination by Rod-Drop in the FTR-3 Critical Experiments*, Trans. Am. Nucl. Soc. **14**, 29 (1971).

III-20. Technique Improvements in the Use of Boron Chambers for Reaction Rate Measurements

T. J. YULE and E. F. BENNETT

INTRODUCTION

The boron reaction rate is one of the important spectral indexes in physics studies of fast reactors. The development of techniques for measuring boron reaction rates began more than three decades ago.[1] However, the adaptation of techniques which are suitable for thermal reactor environments to fast reactor studies has not been adequately investigated.

The boron reaction rate is usually determined by measuring the ionization created in a gas-filled counter by the reaction

$$n + {}^{10}\mathrm{B} \rightarrow {}^{4}\mathrm{He} + {}^{7}\mathrm{Li} + Q, \qquad (1)$$

where Q is 2.34 or 2.78 MeV. The lower Q value is associated with disintegrations leading to the first excited state of ^{7}Li at 0.44 MeV, while the higher value is associated with decays to the ground state. Boron may be present in a chamber either as a constituent of the counter gas (most frequently as BF_3) or in the form of a solid radiator in contact with the counter gas. The relative advantages and disadvantages of each type of chamber for fast reactor measurements are considered.

BF_3 COUNTERS

The desirable features of a BF_3 counter are its rather simple construction, the small slope of the plateau (number of pulses at low amplitude in the pulse-height distribution relative to the total number) and the precision with which the amount of boron (the pressure of the filling) can be determined. Technique developments have aimed at modifying the electrical characteristics of a counter so as to obtain the best plateau while at the same time limiting the sensitive volume to a well-defined region. For a counter operated as an ionization chamber, the above goals are easily realized. However, for most fast-reactor applications, noise considerations limit the useful operating region to the proportional mode. For operation in this mode, it is more difficult to establish a well-defined sensitive volume and maintain a plateau with a small slope. The problem is one of determining the best method of introducing a central wire into the counter body so that the electric field along the wire is uniform and the field lines are directed radially outward everywhere. Small changes in the electric field along the wire worsen the response significantly because multiplication is a sensitive function of the field. If the field lines are bowed at the ends of the counter, the electrical volume of the counter (the volume in which an electron will reach the multiplication region near the central wire) is different from the mechanical volume. If these volume changes are not known, an uncertainty is introduced in the determination of the absolute boron reaction rate. Typically, the sensitive region is defined by the use of guard electrodes or field tubes which are maintained at the same potential as the anode and extend about one cathode radius into the counter from the end high-voltage seals.[1] Figure III-20-1 shows the pulse-height distribution from a small counter constructed in this fashion when it is placed in a thermal flux. The counter has a sensitive length of 2.000 in., a cathode diameter of 0.625 in. and is filled with one atm enriched BF_3. The upturn in the distribution at low energy is introduced by the detection of fast electrons produced by gamma interactions in the wall material. Most of the low pulse-height events result from (n,α) reactions taking place near the end of the sensitive region, where the multiplication is low, or outside the sensitive region with one of the reaction products entering the sensitive region and depositing only a portion of its energy. If such a counter is to be useful for absolute counting, corrections for events emanating from the ends and for the difference between the mechanical and electrical volume have to be made. The counter chosen as an example is rather small, but intensity and spatial resolution considerations limit one to small counters.

More sophisticated techniques have been used to

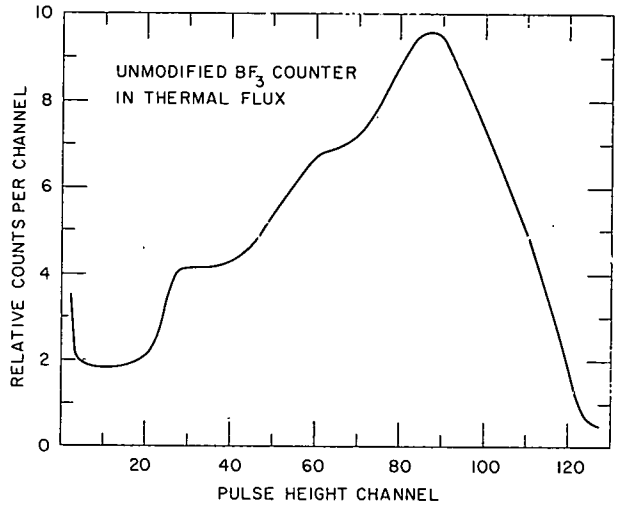

FIG. III-20-1. Pulse-Height Spectrum from a BF_3 Counter in a Thermal Flux. *ANL Neg. No. 116-884 T-1.*

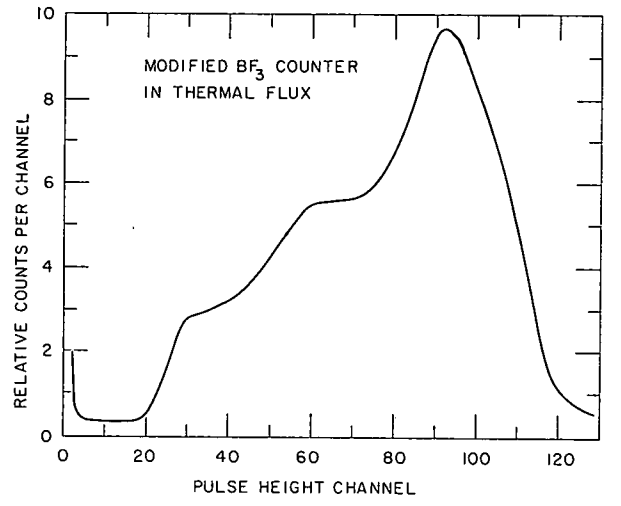

FIG. III-20-2. Pulse-Height Spectrum from a BF_3 Counter with Modified Ends in a Thermal Flux. *ANL Neg. No. 116-883 T-1.*

shape the electric field and define the sensitive volume. An early technique was the placement of two disks of semiconducting material at the ends of the sensitive volume to establish a field that has the same radial variation as the field in the central region of the counter.[1] With this design events from outside the sensitive region are prevented from entering this region. Proportional counters have also been constructed with intermediate potential electrodes to shape the field.[2] Both of these techniques are only well suited to inconveniently large counters, if their use is directed to incore measurements. Recently, a simple method has been found to produce cylindrical counters with well-defined sensitive volumes and with reduced end-associated distortion.[3] The method was discovered during a careful investigation of the effect on proton-recoil proportional-counter response functions of the distortion of internal field lines near the ends of the sensitive region. It was found that the response of a counter may be significantly improved by decreasing the diameter of the cathode over the end region. Because the modification is so simple, it may be applied to any size counter. A close to optimum choice for boron counters is for the cathode diameter over the end region to be one-half the value over the central region when the field tube diameter is ten times the anode diameter. Decreasing the end size also has the beneficial effect that fewer end-originating events enter the sensitive region. Furthermore, because the sensitive region is well defined, analytical track-length probability functions can be used to correct for the effect.[4] The biggest uncertainties in the determination of the influence of end events are introduced by uncertainties in the range-energy and energy-loss data for alpha particles and lithium ions in BF_3. Figure III-20-2 shows the response of the same sized BF_3 counter described previously and with the same filling, but having the end modification. The significant lessening in the number of low pulse-height events with the attendant improvement in the plateau is readily apparent. Less than 2% of the events produce pulse heights that fall below channel twenty. Thus, this simple technique permits the construction of small counters with good response.

The response of a BF_3 counter in a fast flux will be somewhat poorer than that in a thermal flux because of the detection of boron and fluorine recoils from elastic neutron scattering. How well the boron reaction rate can be determined with BF_3 counters is a function of the neutron spectrum. Figure III-20-3 shows the response of the same modified BF_3 counter in the central spectrum of ZPR-6 Assembly 7—a large LMFBR single-core-zone critical assembly fueled with plutonium (see Paper II-11). The increase in the relative number of low-energy events is introduced by the detection of the recoils. (The fast electrons from gamma interactions extend only over the first few channels.) The dashed line is a calculation of the recoil distribution. In the calculation, the measured neutron spectral shape for this core was normalized to reproduce the measured boron reaction rate. The normalized neutron spectrum, together with measured elastic scattering cross sections, were then used to obtain the resulting energy distribution of the recoils. The uncertainities in the cross sections are rather large and no attempt was made to include differences in W (average energy to create an ion pair) for alphas, lithium ions, and boron and fluorine recoils.[5] The dot-dashed line results from subtracting out the recoil contribution. The resulting distribution is quite similar to that observed in a thermal flux. In general, the harder the neutron spectrum, the greater will be the influence of the recoil distribution on the response

of the counter. There is no way of removing the recoil contribution to the pulse-height distribution by electronic techniques, such as rise-time discrimination or by making measurements with different ^{10}B enrichments, since the ^{10}B and ^{11}B elastic scattering cross sections are considerably different.[6]

Even with the somewhat worsened response, a BF_3 counter can be used to determine reaction rates in a fast reactor. Only events beyond the valley (about channel 23 on Fig. III-20-3) are summed to determine a relative reaction rate. The advantage of using a modified end counter (one for which the number of boron reaction product events producing low pulse heights is small) is apparent. The absolute boron reaction rate may be determined by matching the fast spectrum response to a thermal response and obtaining the contribution to the distribution from events below the cutoff. Since changes in the kinetic energy of the reaction products introduced by differences in the incident neutron energy for thermal and fast spectra are small for a typical fast reactor spectrum, the fast spectrum response with the recoil contribution subtracted out is almost identical with the thermal response.

A different problem associated with the use of BF_3 counters in a fast reactor is that oftentimes their sensitivity is too high. For example, the boron counter described previously contains about 5 mg of ^{10}B in the sensitive region, whereas count-rate considerations indicate that about $\frac{1}{50}$ of that amount would be more satisfactory. If the sensitivity is reduced by significantly reducing the pressure or size, wall-and-end effects become important and the plateau deteriorates rapidly. One possible solution may be to use a high atomic-weight buffer gas such as krypton which would allow a small amount of boron to be in the sensitive region while still keeping the track lengths short and thus maintaining good counter response. A high atomic-weight gas is needed to prevent significant worsening of the response from its recoil distribution. Because the maximum recoil energy $E_{r\,max}$ a nucleus of atomic weight A can receive in an elastic collision is

$$E_{r\,max} = E_n \frac{4A}{(A+1)^2}, \qquad (2)$$

where E_n is the incident neutron energy, the heavy-gas recoils will only be in the first few channels of the pulse-height distribution.

Solid Radiator Counters

Boron reaction rates can also be measured with solid radiator counters. These counters may be small in size and have low sensitivity. One reason solid radiator chambers have been popular in thermal reactor instrumentation is that it is possible to provide gamma compensation by using an identical chamber without the radiator. In a similar fashion, the influence of elastic scattering recoils from the counter gas, when the counter is placed in a fast flux, may be subtracted out by using a blank chamber. A disadvantage of a solid radiator chamber is that if absolute reaction rates are to be determined, it is necessary to calibrate the counter since it is not possible to directly determine very accurately the amount of boron in the radiator.

Small back-to-back proportional counters have been developed for boron reaction-rate measurements.[7] Each counter is a half cylinder. The boron solid radiator, which is typically about 15 $\mu g/cm^2$ is deposited on one

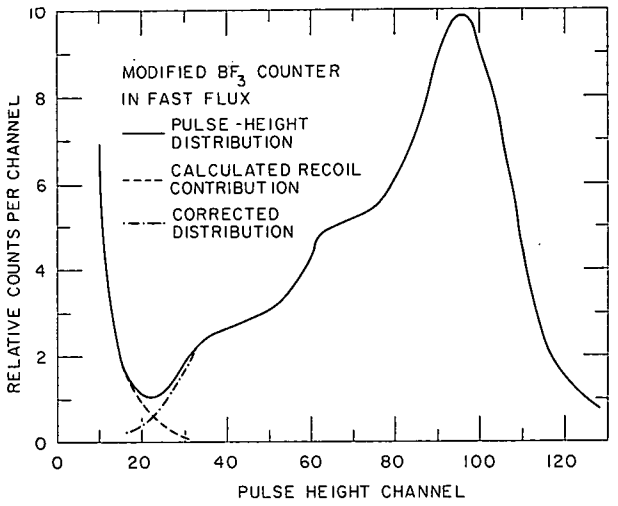

Fig. III-20-3. Pulse-Height Spectrum from a BF_3 Counter with Modified Ends in a Fast Flux. The Dashed Line is a Calculation of the Elastic Scattering Recoil Distribution. The Dot-Dashed Line Results from Subtracting out the Recoil Contribution to the Spectrum. *ANL Neg. No. 116-877.*

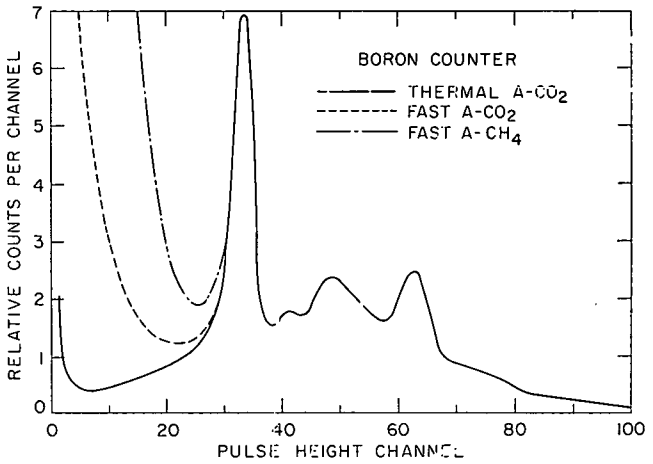

Fig. III-20-4. Pulse-Height Spectra from a Back-to-Back Boron Counter in a Thermal Neutron Flux and in a Fast Neutron Flux for an Argon-Carbon-Dioxide Flow Gas Mixture and an Argon-Methane Mixture. *ANL Neg. No. 116-962.*

side of the central plane. The other counter is a blank. Both counters are operated as flow counters.

The response for a solid radiator chamber in a thermal flux is shown as a solid line in Fig. III-20-4. The flow gas was a mixture of argon and 2% carbon dioxide. The peak between channels 30 and 40 is produced by ^{7}Li recoils. Because the track lengths of these recoils are short compared with the counter dimensions and because the average energy loss in the boron film is small, the pulse-height distribution shows a well-defined peak. The alpha particles, whose track lengths are comparable to the counter dimensions, produce a pulse-height distribution that is spread out because of track-length truncations by the walls and multiplication differences depending on track orientation. The upturn in the distribution below channel 5 results from the gamma ray sensitivity of the counter. The plateau for this type counter is somewhat worse than that for a comparable sized BF_3 counter.

When the counter is placed in a fast flux, the pulse-height distribution contains a contribution from the elastic scattering recoil distribution of components of the flow gas. Figure III-20-4 shows pulse-height distributions in a fast flux for two different flow gases—a mixture of argon and 10% methane (P-10) and a mixture of argon and 2% carbon dioxide. The fast neutron environment was that near the front of a block of depleted uranium with a natural uranium front face.[8] The block (a Snell block) was driven by thermal neutrons obtained from the leakage face of a thermal reactor. The neutron spectrum within the block is similar to that in a fast reactor. However, the relative number of high energy neutrons is less in the Snell block compared with a representative fast-reactor central neutron spectrum. Above the low side of the ^{7}Li-recoil peak the responses in a fast flux for both gas fillings are almost identical with the response in a thermal flux. Below this point the dependence of the shapes of the pulse-height distributions on the flow gas is evident. Proton recoils dominate the recoil distribution at lower energies for the P-10 gas because of the large elastic scattering cross section of hydrogen and the ability of the proton recoil to assume the full neutron energy. The response with the argon-carbon-dioxide mixture is significantly better for reaction rate determinations. Although the need to avoid any light component in the flow gas should be apparent, the pulse-height distributions for the two gas mixtures are shown here to emphasize the point.

The capabilities of BF_3 counters and solid radiator counters to provide relative boron reaction rates are about the same. Even though the recoil contribution to the pulse-height distribution can be subtracted from data taken with a solid-radiator chamber, changes in gain and differences in the characteristics of the boron and blank chambers introduce as much uncertainty in the determination of the reaction rate as using a thermal response to correct for the recoil contribution when a BF_3 counter is used. To make absolute measurements one would have to calibrate the solid radiator chamber using, for example, a BF_3 chamber as the standard. The calibration would best be made in a fast neutron environment similar to that in a fast reactor. Differences in the relative amount of perturbation of the neutron field introduced by differences in construction of the BF_3 and solid-radiator chambers cannot be assumed to be the same for fast and thermal fluxes. Experience with plate chambers to provide relative boron reaction rates is described elsewhere (see Paper II-3).

Conclusion

The advantages and disadvantages of using BF_3 counters and solid-radiator counters for determining boron reaction rates in fast reactors have been indicated. Both counters are capable of comparable accuracy for relative measurements. However, the BF_3 counter has some inherent advantages for absolute determinations. At the present time too high a sensitivity of BF_3 counters has limited their use in fast reactor studies.

References

1. B. B. Rossi and H. H. Staub, *Ionization Chambers and Counters* (McGraw-Hill Book Co., Inc., New York, 1949), Chap. 8.
2. A. Spernol and B. Denecke, *Precise Absolute Measurement of the Activity of Tritium II*, Inter. J. Appl. Rad. Isot. **15,** 195 (1963).
3. E. F. Bennett and T. J. Yule, *Response Functions for Proton-Recoil Proportional Counter Spectrometer*, Nucl. Instr. Methods **98,** 393 (1972).
4. N. L. Snidow and H. D. Warren, *Wall Effect Corrections in Proportional Counter Spectrometers*, Nucl. Instr. Methods **51,** 109 (1967).
5. I. T. Myers, *Ionization*; F. H. Attix and W. C. Roesch, Eds., *Radiation Dosimetry*, (Academic Press, New York, 1968) 2nd Ed., Vol. I, pp. 317–330.
6. F. P. Mooring, J. E. Monahan and C. M. Huddleston, *Neutron Cross Sections of the Boron Isotopes for Energies Between 10 and 500 keV*, Nucl. Phys. **82,** 16 (1966).
7. L. S. Beller, *Detector for $B^{10}(n,\alpha)$-to-Fission Ratio Measurements*, Reactor Physics Division Annual Report, July 1, 1969, to June 30, 1970, ANL-7710, p. 288.
8. E. F. Bennett and T. J. Yule, *Fast Neutron Spectra in Uranium Metal*, Reactor Physics Division Annual Repor' July 1, 1968 to June 30, 1969, ANL-7610, pp. 215–216.

III-21. Measurement of Fast Neutron Flux with a Lithium-Drifted Germanium Detector

D. L. Smith

Introduction

Lithium drifted germanium [Ge(Li)] detectors are used extensively for gamma ray measurements because in many applications the excellent energy resolution obtainable with these detectors more than compensates for their relatively low efficiency. The characteristic pulse height spectra observed in fast neutron bombardment of Ge(Li) detectors have been investigated and various fast neutron cross sections for germanium have been reported.[1-3] The available information indicates that Ge(Li) detectors might prove useful for measurements of neutron flux. This possibility was explored during the past year and the findings are reported here.

Concept

If a Ge(Li) detector is bombarded by neutrons with sufficient energy to excite low-lying states of the germanium isotopes, lines are observed in the pulse-height spectra which can be identified mainly as the full-energy peaks of gamma rays produced by the $(n,n'\gamma)$ process. Recoil of bombarded germanium atoms is responsible for the observed broadening of these lines with increased neutron energy.

When the neutron bombarding energy exceeds 694 keV, a very prominent line is observed in the spectrum at a pulse-height equivalent of 694 keV of gamma-ray energy. This line corresponds to excitation of the 0^+ first excited state in ^{72}Ge by inelastic scattering and its subsequent decay to the ground-state by the unique mode of emitting a $0^+ \rightarrow 0^+$ conversion electron with a 0.3 μsec half-life. The prominence of this line is explained by the fact that most of these internal conversion electrons lose all of their energy to ionization within the detector whereas the inelastic gamma rays which generate the other full-energy lines in the spectrum are much less likely to deposit all of their energy within the detector. The net yield (background subtracted) of events in the 694 keV peak is directly proportional to the integrated neutron flux. Neutron flux measurements with a calibrated Ge(Li) detector seems feasible for monoenergetic beams or beams with known energy distributions.

Experimental Measurements

Figure III-21-1 is a schematic diagram of the apparatus set up to calibrate a 4.2 cm² planar Ge(Li) detector

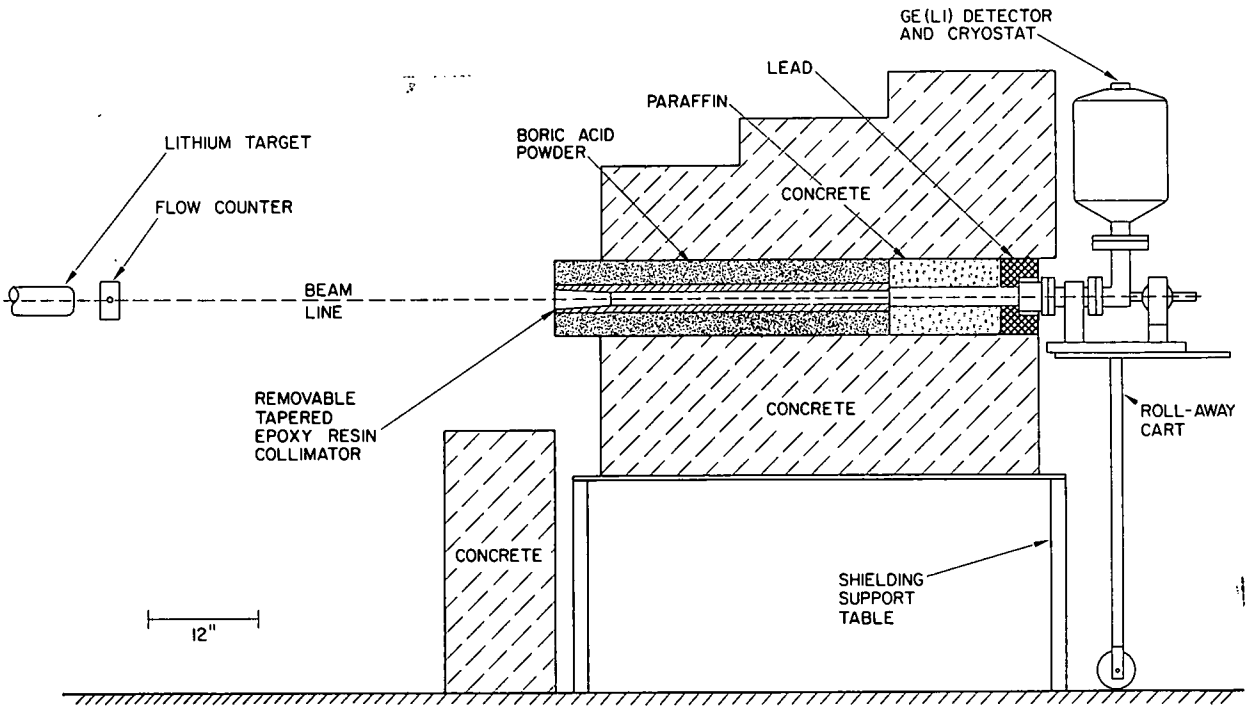

Fig. III-21-1. Schematic Diagram of Apparatus Used in Calibrating a Ge(Li) Detector for Neutron Flux Measurements. *ANL Neg. No. 116-622 Rev. 1.*

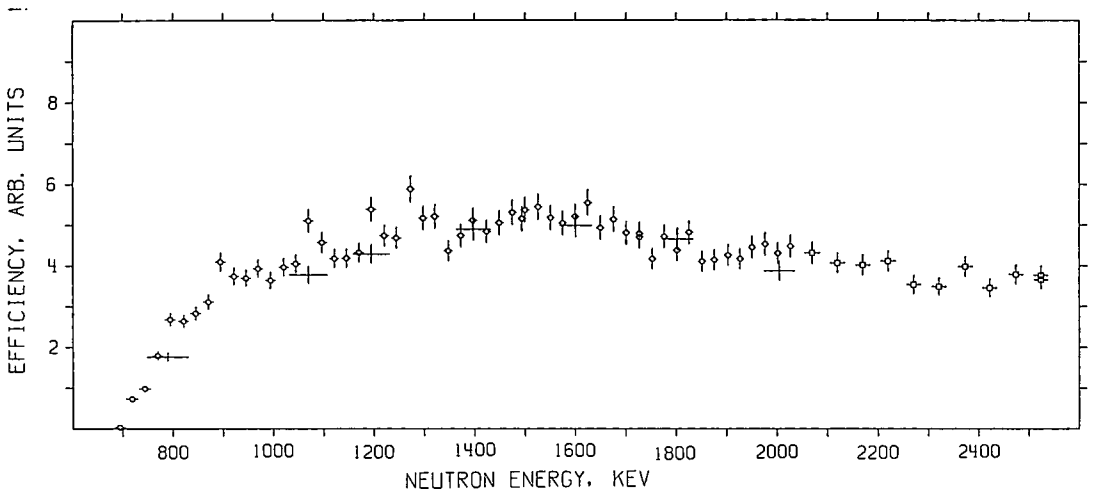

FIG. III-21-2. Relative Efficiency of a 4.2 cm² Planar Ge(Li) Detector for Neutron Flux Measurements by Means of the ^{72}Ge 794-keV Internal Conversion Electron Transition. The Three Different Data Point Symbols Distinguish Measurements Made with Different Neutron Energy Resolutions. *ANL Neg. No. 116-789.*

for neutron flux measurement via detection of ^{72}Ge 694-keV internal conversion electrons. It was decided to calibrate relative to the ^{235}U(n,f) cross section by using a low mass fission counter. Systematic background errors were minimized by placing the fission counter very close to the target and carefully shielding the Ge(Li) detector. Monoenergetic neutron beams were generated via the ^{7}Li$(p,n)^{7}$Be reaction by bombarding targets of lithium metal on a tantalum cup with direct current proton beams from the Fast Neutron Generator. The germanium detector viewed the neutron source at zero degrees through a tapered collimator. The 0.3 μsec half life of the 694-keV state in ^{72}Ge precluded background reduction by time-of-flight techniques so it was necessary to rely on shielding. Measurements were made at each energy with the collimator hole entirely plugged to determine leakage through the shield. Corrections were applied to the data for neutrons from bare tantalum cups and for second group neutrons from the ^{7}Li$(p,n)^{7}$Be*.

The uranium foil used in the fission counter was calibrated from chemical and mass analysis data and measurement of the alpha activity. The evaluated ^{235}U(n,f) cross sections prepared by W. Hart were used in the present work.[4] The solid angle subtended by the germanium detector was calculated from the target distance of 103.7 in. and the front face area of the detector. This solid angle was not limited by the collimator and amounted to 5.1×10^{-5} sr.

RESULTS

The measured relative efficiency data is presented in Fig. III-21-2. The structure below 1300 keV agrees with the observations of Lister and Smith.[2] Less structure is observed at higher neutron energies, which is favorable for the proposed application. The calculated absolute efficiency (ratio of detected events to incident neutrons) for the Ge(Li) detector used was 0.13% at 1900 keV. The following qualitative observations were also made during the course of this work.

1. The efficiency of the Ge(Li) detector was monitored by detecting gamma rays from a ^{137}Cs source placed near the detector in a fixed position and was found to be stable with time and insensitive to applied detector bias voltage.

2. The detector did not suffer noticeable deterioration in performance during the experiment as a result of fast neutron bombardment.

REFERENCES

1. C. Chasman, K. W. Jones and R. A. Ristinen, *Fast Neutron Bombardment of a Lithium-Drifted Germanium Gamma-Ray Detector*, Nucl. Instr. Methods **37**, 1 (1965).
2. D. Lister and A. B. Smith, *Fast-Neutron Scattering from Germanium*, Phys. Rev. **183**, 954 (1969).
3. K. C. Chung, *$(n,n'\gamma)$ Reactions as a Tool for Nuclear Spectroscopy Near A = 70 and A = 27*, Thesis (1969), University of Kentucky, Lexington, Kentucky. University Microfilms Order No. 70-16, 965.
4. W. Hart, *Revised Fission Cross Section Evaluations for the Energy Range 1 keV to 15 MeV*, Authority Health and Safety Branch Report No. AHSB(S) R 169, United Kingdom Atomic Energy Authority, United Kingdom (1969).

III-22. Comparison of Absolute Fission and Capture Rates Measured with Foils and Fission Chambers

R. O. Vosburgh, D. W. Maddison and R. J. Forrester

Activated foil spectrum analysis at ZPPR is done by an automated system employing Ge(Li) detectors. This system is described in Ref. 1. Calibration of the Ge(Li) detectors employs standard sources to obtain efficiency versus energy curves.[2] The ZPPR spectrum analysis technique does not entail gross counting but depends on counting specific peaks in determining the activity of a foil. This implies that the decay scheme, yield data and branching ratios must be known for the isotope in question. An alternate method, employing simultaneous irradiation of a counting foil and an absolute fission chamber, can be used to calibrate the foil counting system.

TABLE III-22-I. Foil/Chamber Comparisons

Experiment	Foil	Chamber	Ratio, Foil/Chamber
^{238}U (n,γ) foil versus ^{235}U (n,f) chamber (in AFSR thermal column)	1.12×10^5 captures/gm-sec	23.03 fiss/gm-sec $\Rightarrow 1.10 \times 10^5$ captures/gm-sec	1.018
^{239}Pu (n,f) foil versus ^{239}Pu (n,f) chamber (in ZPPR Core 2)	3.13×10^6 fissions/gm-sec	3.20×10^6 fissions/gm-sec	0.978

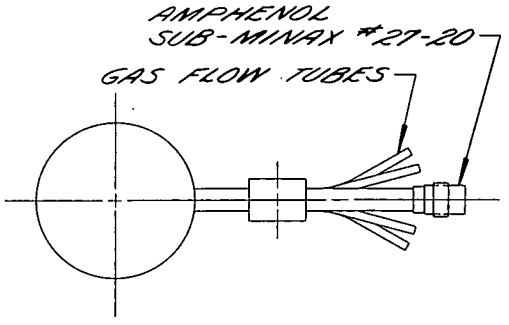

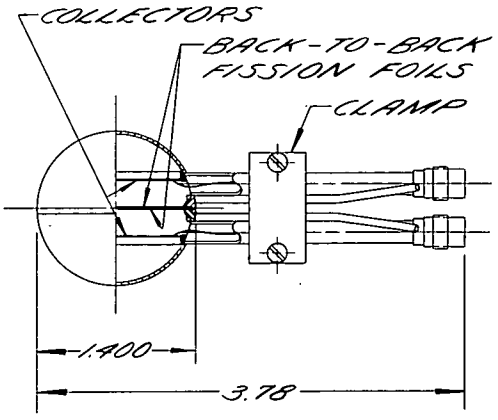

Fig. III-22-2. Spherical Back-to-Back Fissiion Chambers. *ANL-ID-103-11688.*

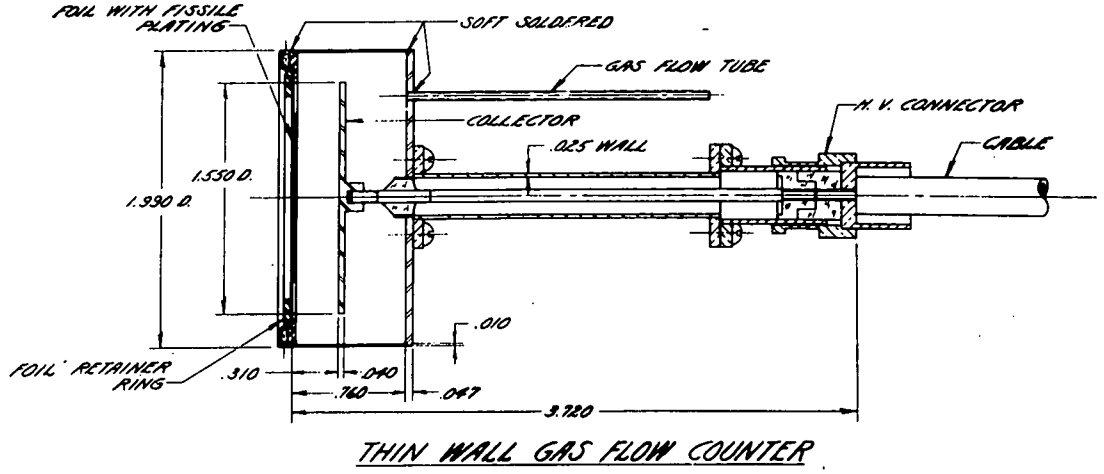

Fig. III-22-1. Thin Wall Gas Flow Counter. *ANL-ID-103-9162.*

TABLE III-22-II. DATA FOR CONVERSION OF $^{235}U(n,f)$ TO $^{238}U(n,\gamma)$

Quantity	Value
σ_{f25}	587.4 b
g_{f25}[a] at 20°C	0.9781
σ_{c28}	2.73 b
g_{c28}[a] at 20°C	1.002

[a] The Westcott g factor.

Note: This gives a calculated value of $\sigma_{c8}/\sigma_{f5} = 4.761 \times 10^{-5}$.

If a foil and an absolute fission chamber containing the same principle isotope are irradiated in identical flux, then both should yield the same reaction rates upon analysis. If the fission chamber is indeed absolute and the nucleur data used in the foil counting reduction process are assumed accurate, then the spectrum analysis detector efficiency can be determined. Conversely, if the efficiency of the analysis systems is known accurately, this method provides a check on the nucleur data used in the foil data reduction technique.

Preliminary measurements include (a) ^{238}U foil with a ^{235}U fission chamber in the Argonne Fast Source Reactor (AFSR) thermal column, and (b) a ^{239}Pu foil with a ^{239}Pu fission chamber in the fast spectrum of ZPPR Core 2. The chamber used in the AFSR thermal column is shown in Fig. III-22-1; the chamber used in AFSR is shown in Fig. III-22-2. Both fission chambers are gas-flow, parallel-plate type, with the latter being the standard back-to-back chamber used in fission ratio measurements in ZPPR.

Results of the preliminary measurements are given in Table III-22-I. The data used to derive the capture rate of ^{238}U from the ^{235}U fission chamber measurement are given in Table III-22-II. The error associated with both the foil and chamber measurement is 1.5%. Further comparisons between foil and fission chamber reaction rates in both thermal and fast neutron fluences are planned.

REFERENCES

1. D. W. Maddison and L. S. Beller, *"Characteristics and Capabilities of Automated Counting Facilities for the Zero Power Plutonium Reactor (ZPPR)*, Reactor Physics Division Annual Report, July 1, 1968 to June 30, 1969, ANL-7610, pp. 379-381.
2. L. S. Beller and D. W. Maddison, *Precision Efficiency Calibration Procedures for Ge(Li) Detectors*, Reactor Physics Division Annual Report, July 1, 1969 to June 30, 1970, ANL-7710, pp. 283-285.

III-23. Miscellaneous Electronic Techniques

C. E. COHN

INTRODUCTION

In the course of work on the Applied Physics Division programs, three useful electronic techniques were developed.

OSCILLOSCOPE TEST METHOD FOR LOGIC ELEMENTS[1]

A very revealing test on digital logic elements may be performed with the aid of an oscilloscope. The method consists in applying to the element input a sawtooth waveform running between the logic-0 and logic-1 levels, derived from the oscilloscope's time base. The output of the element is connected to the oscilloscope's signal input. In that manner, the dc transfer characteristic of the element is displayed on the screen, allowing the dc noise margins and other switching properties to be examined.

Any oscilloscope is suitable that has a dc amplifier for the signal and allows a sawtooth voltage from the time base to be taken externally.* That sawtooth must be processed by suitable external circuitry to bring it to the right voltage range. The sweep is set to an auto-triggering or free-running mode. It should be run at a moderate speed, in the milli-second range, to insure that the pattern seen is representative of the element's dc characteristic unperturbed by speedup capacitors, storage delays, or other dynamic effects.

For testing a gate or inverter, the processed sawtooth is applied to one of the inputs. The remaining inputs are connected to a logic-1 voltage for an AND or NAND gate, or to a logic-0 voltage for an OR or NOR gate, so the sawtooth will not be inhibited from switching the gate. The pattern should be observed both with and without a load corresponding to the maximum fanout connected to the gate output.

The cross-coupled gates that form a flip-flop may also be tested by this method if the flip-flop has set and reset inputs. One of the dc inputs is activate preventing its associated gate from inhibiting switching

* Care should be taken to ascertain that the oscilloscope's sawtooth output does not carry any extraneous transients that could damage the element under test.

of the other gate. The sawtooth is applied to the other dc input, and the desired pattern will be found at one of the outputs.

Figure III-23-1 was obtained with this scheme applied to a discrete-component NAND gate in the Honeywell-CCD "S-PAC" series, having logic levels of 0 and −6 V. A Tektronix 545 oscilloscope was used with a Type O operational-amplifier plug-in. The 140 V positive sweep output from the oscilloscope was attenuated by a factor of −20 in one of the operational amplifiers in the plug-in. The resulting 7 V negative sawtooth, shown in Fig. III-23-1a, was applied to the gate input.

Figure III-23-1b shows the output of the gate with no load, while Fig. III-23-1c shows the output with a load equivalent to maximum fanout. It can be readily seen that the gate's specified noise margin of 1½ V is amply met under both conditions.

A Solid-State Improvement on the VR Tube

The familiar VR tube, used in much vacuum-tube equipment, is not nearly a perfect constant-voltage element. Modern solid-state components having greatly improved properties can provide a low-cost substitute for this device. This makes possible a gain in performance for older but still useful equipment.

The simple Zener diode does not qualify as an improvement on the VR tube since the regulation of the Zener is no better and its noise production is considerably worse. Furthermore, Zeners with the necessary voltage and power ratings are inordinately expensive.

However, considerably improved performance may be had from the "amplified Zener" circuit shown in Fig. III-23-2. Here the Zener diode Z passes only the base current of the common-emitter power transistor T, so it need handle only a small fraction of the total circuit power. Voltage fluctuations appear substantially unattenuated across the emitter-base junction of the transistor, varying the collector current so as to compensate the fluctuations. Since a given change in collector current is accompanied by a much smaller change in Zener current, the effective impedance of the Zener is greatly lowered.

In the practical circuit, Z is a low-power Zener diode of the appropriate voltage. (The Sarkes-Tarzian VR series of low-cost Zeners covers the voltage range of VR tubes.) T is a power transistor (NPN shown) with adequate ratings (e.g., Motorola MJ400). The capacitor across the Zener filters out its noise. (Capacitors of this size cannot be used with VR tubes because they give rise to oscillations.)[2]

The transistor base current is low enough that a typical Zener diode will operate very close to its knee, in a region of rather unfavorable characteristics. Therefore, the resistor R is provided to increase the Zener

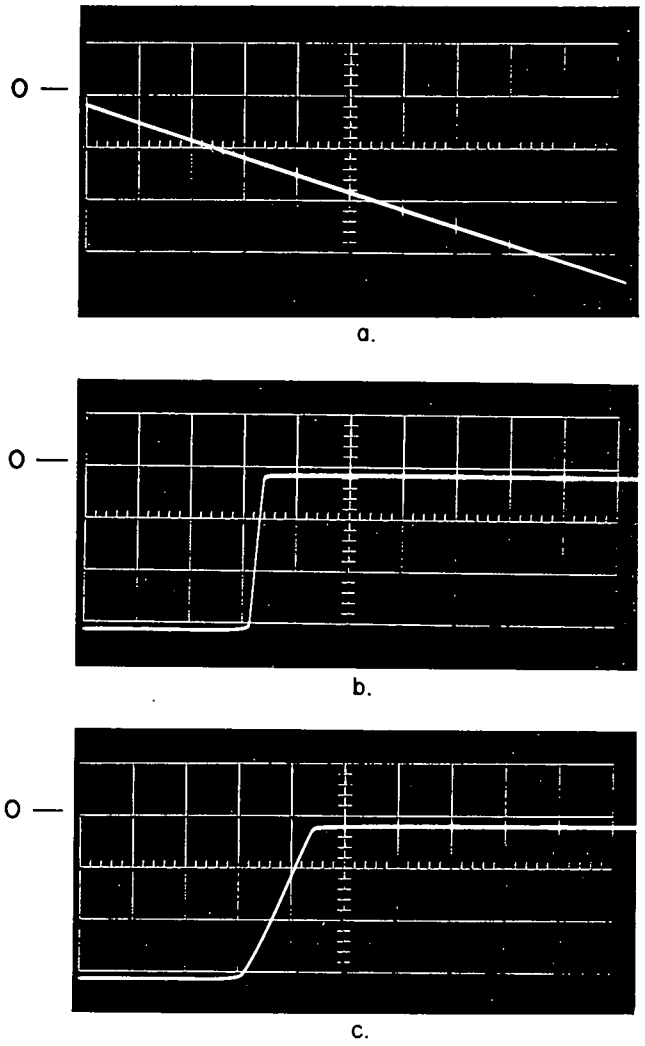

Fig. III-23-1. a. Sawtooth Applied to Input of Gate under Test. b. Gate Output with no Load. c. Gate Output with Load Equivalent to Maximum Fanout. All Traces have 2v/div Vertically and 1 ms/div Horizontally. *ANL Neg. No. 116-229.*

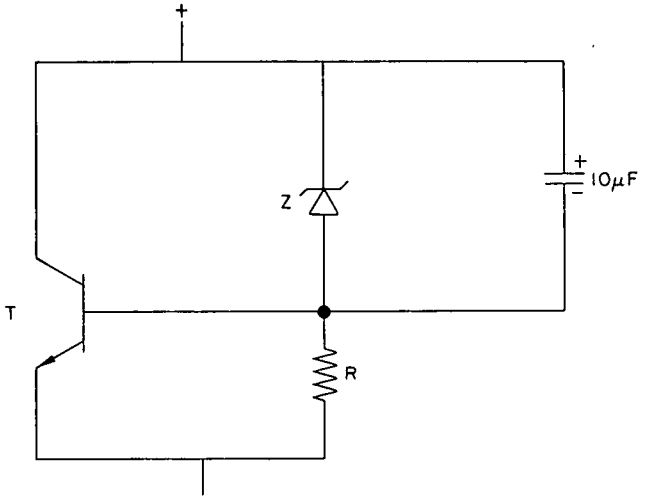

Fig. III-23-2. Solid-State Constant-Voltage Circuit. *ANL Neg. No. 116-598.*

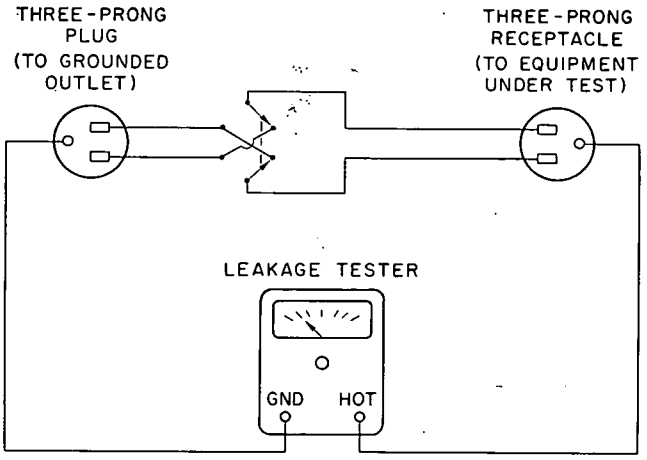

FIG. III-23-3. Leakage-Current Test Circuit. *ANL Neg. No. 116-646.*

current to a more reasonable level. Its value is not critical; a few hundred ohms is typical for the Sarkes-Tarzian Zeners operating with silicon NPN power transistors.

Application of this circuit to a typical regulated power supply reduced output ripple from 5 mV to much less than 1 mV including noise.

DETECTING FAULTS IN GROUNDED EQUIPMENT

The now-familiar three-prong ac line plug and receptacle combination removed the hazard of equipment ground faults. By the same token, though, substantial fault currents can flow undetected. Such currents can degrade the operation of sensitive equipment, produce a shock hazard if an ungrounded outlet should happen to be used, and indicate impending failure of the equipment. Therefore, it is good preventive maintenance to check equipment periodically for ground faults. This can be easily done with a leakage-current tester used in the arrangement shown in Fig. III-23-3.

Here the plug is inserted into a well-grounded three-prong outlet, while the receptacle supplies power to the equipment under test, which is isolated from ground. The leakage-current tester then reads the current flowing through the ground wire. Readings should be taken with the DPDT toggle switch in both positions, since some faults might appear only when a particular side of the line is hot.

REFERENCES

1. C. E. Cohn, *Oscilloscope Test Method for Logic Elements*, Rev. Sci. Instr. **42**, 881 (1971).
2. W. C. Elmore and M. Sands, *Electronics* (McGraw-Hill Book Co., Inc., New York, 1949) pp. 368–369.

III-24. Computerized Accounting System for ZPPR, ZPR-6 and ZPR-9 Non-Fissile Material Inventory

A. B. LONG

A computerized accounting system has been developed to maintain an up-to-date and unified inventory of all non-fissile materials (plates and rods) used in the Applied Physics (AP) Division critical facilities in Illinois and Idaho. The system permits rapid and accurate assessments of the quantity, description, and location (in storage in Illinois, in storage in Idaho, in ZPR-6, etc.) of all materials and, therefore, greatly facilitates the planning and coordination of experiments on the three AP critical facilities.

The accounting system involves storing all non-fissile reactor materials in controlled inventory areas both at ZPPR (Idaho) and ZPR-6 and ZPR-9 (Illinois) when these materials are not being used in the critical assemblies. A standard size storage bin and a uniform technique for packing the materials within the bins has also been adopted so that the quantity of plate material can be determined from the number of fully packed bins and the amount of material in the remaining partially packed bin.

Whenever a material is removed from or returned to a controlled inventory area, the transaction is recorded. Included in this record are the following pieces of information:

1. A four-letter code name which specifies the type of material involved in the transaction. Those materials which look physically alike have been color-coded to permit personnel to distinguish each type.
2. The length, height and width of the material expressed in dimensions which are multiples of $\frac{1}{64}$ in.
3. The number of pieces of this size material which are involved in the transaction. This number may be expressed either as a piece count or it

may be expressed in units or partial units of the standard storage bin.
4. A four-letter code name which specifies the area from which the material came or from which it is being taken.
5. A four-letter code name which specifies the inventory area into which the material is being brought or to which it is going.
6. The initials of the person responsible for the transaction.
7. The date of the transaction.

Periodically the transaction records are collected from all inventory areas and transcribed to cards which are then processed by a computer code on the SEL-840. The code reads the past summary of the inventory from magnetic tape and stores the information on the disc so that the summary for each material is directly accessible from the computer. The code then processes the transaction records, making the appropriate changes in the inventory summaries stored on the disc. Following this, the new inventory for each of the inventory areas and each of the critical assemblies is listed. Finally, the code reads the updated inventory summaries from the disc and stores them after the previous inventory summaries on the magnetic tape. Throughout the procedures, the computer checks to see that the total inventory for a given size material is equal to the sum of the inventories for that material in each of the separate storage and user areas. If a discrepancy should be detected, the code could be rerun starting again with the previous inventory summaries. This procedure ensures that no computer-related errors develop in the inventory records.

As a result of establishing controlled inventory areas and of routinely using the computer to process the transaction records, it has been possible to maintain an accurate inventory of the non-fissile materials associated with the zero power critical assemblies.

III-25. Developments in Analysis of Fast Neutron Data

A. De Volpi

The fast neutron hodoscope is a transient fuel movement detection system installed at TREAT reactor. Development of the hodoscope was carried out for the reactor safety program. One of the development phases which has required extensive use of the Applied Physics Division computer facilities is the analysis of the output data.

In the early stages of the hodoscope a series of pictures ("hodographs") were produced on microfilm through the DD80 facilities of the CDC-3600. To develop dynamic presentations the hodographs will ultimately be presented on the CRT display coupled to a PDP-11 computer.

In the course of data evaluation it has been found for certain transients that the hodograph data representation was inadequate. In some cases, highly nonlinear deficiencies of the detection system destroyed the value of important features of the pictures; in other cases, the fuel movements were too small for recognition by crude visual rendition.

As a result of these limitations, a plotting capability has been programmed for the Applied Physics Division SEL-840 computers. The first step in the procedure was to render the CDC-3600 data into a compact form on 7-track magnetic tape. By suppressing redundant data, the computed results were compressed into 11

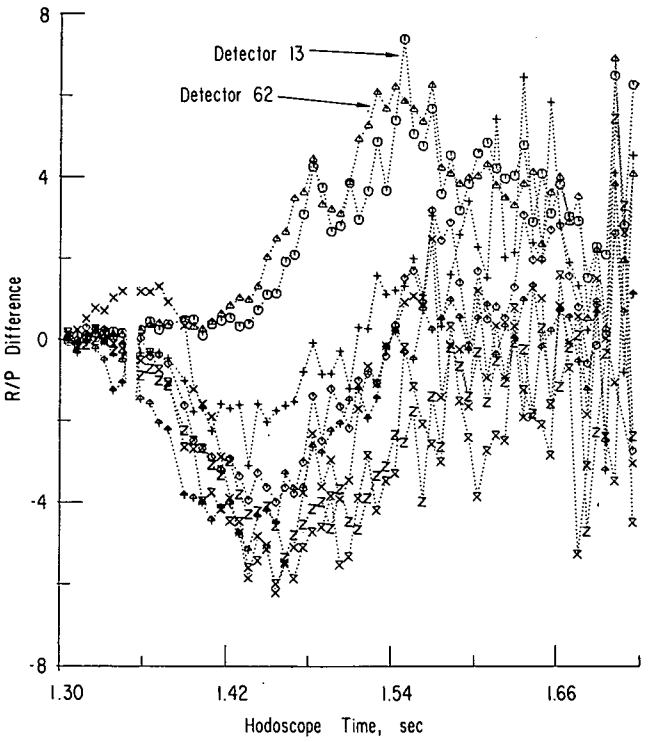

Fig. III-25-1. Example of Normalized Detector Response to Fuel Motion during TREAT Transient 1317. *ANL Neg. No. 116-901.*

words for each cycle of the transient, equivalent to one record. Magnetic tape read time was thus reduced to about 1½ sec per cycle.

The program designed in Fortran IV for the SEL-840 is called TIMEPLOT. It reads the magnetic tape input data, converts the data to suitable form, and with other controls delivers a plot of the time history of an array of detectors. Figure III-25-1 is an example.

Axes and labeling information can be read in either by card or teletype. From an array of 334 detectors, up to 11 can be chosen for simultaneous plotting using the standard symbol table.

Various tests are included in the program to exclude spurious data from being plotted. Plots in linear or semi-log scales may be called. Several data points (or records) may be averaged together into a single plotted point to reduce the symbol plotting density. It is possible to interconnect the symbols with an interpolation option. Most of the plotting options are controllable through front panel sense switches. Unattended overnight plotting is possible through automatic card feed-in of the control parameters and automatic rewind and manipulation of the magnetic tape.

A major feature of the program is the ability to store data up to a central point and then to apply that data in normalizing the remaining portions of the transient. This procedure produces an efficiency normalization and also is effective in removing most of the consequences of the non-linear deficiencies. The resulting plots, such as Fig. III-25-1, may be arranged in any combination of rows or columns. The data in Fig. III-25-1 represent part of the outcome of a high power transient (1317) in which the fuel cladding did not fail. Thus the various deflections observable are a record of the fuel motion within the single pin. In this example, the fuel initially expanded upward past the top rows (detectors 13 and 62). While some of these inside movements may be noticed in the hodographs, the quantitative details of the fuel passage and oscillation cannot be determined without these timeplots.

III-26. Improving the Efficiency of Computer Output Operations Using Direct-Memory-Access Channels

C. E. Cohn

Introduction

The discs and magnetic tapes attached to our SEL-840 computers are connected through direct-memory-access (DMA)* channels. In theory, DMA is supposed to increase throughput by overlapping input/output with computation. However, certain aspects of the simple software system supplied by the manufacturer prevented these benefits from being realized in practice. The existing routines were altered to make available the full power of the DMA for output operations.

In the simple operating system used with the SEL-840 computers, programs communicate with peripherals by calls to input/output subroutines. Each such call passes the starting address of a data buffer area in memory and a count of words to be transmitted. The routine passes these parameters to the DMA channel and then commands the peripheral to initiate the input or output operation under DMA control. At this point, no further central-processor action is required to keep the operation going. Thus, in principle the subroutine could immediately return to the calling program, allowing the latter to go on with its tasks while the input or output operation proceeds automatically, pre-empting an occasional memory cycle for data transfer. For a variety of reasons, though, this efficient procedure is not feasible.

For output operations, one reason is the possibility that the calling program, in entering data into its buffer area for the next output operation, will overwrite the data for the current operation before it has been transmitted to the peripheral. The existing subroutines prevent that by deferring the return to the calling program until the output operation is complete. Clearly, such deferral nullifies the value of the DMA, making the system throughput no better than that using just ordinary programmed data transfers.

The usefulness of the DMA may be realized at the cost of a small amount of core by providing the output subroutine with its own internal buffer area. The data to be output are moved to this buffer before output is commenced, and the DMA channel is addressed to it. Then there is no need for the contents of the calling program's buffer, so control may return directly to the calling program, which may modify the contents of its buffer immediately. The desired overlap of computa-

* Called "Block Transfer Control" (BTC) in SEL-840 nomenclature.

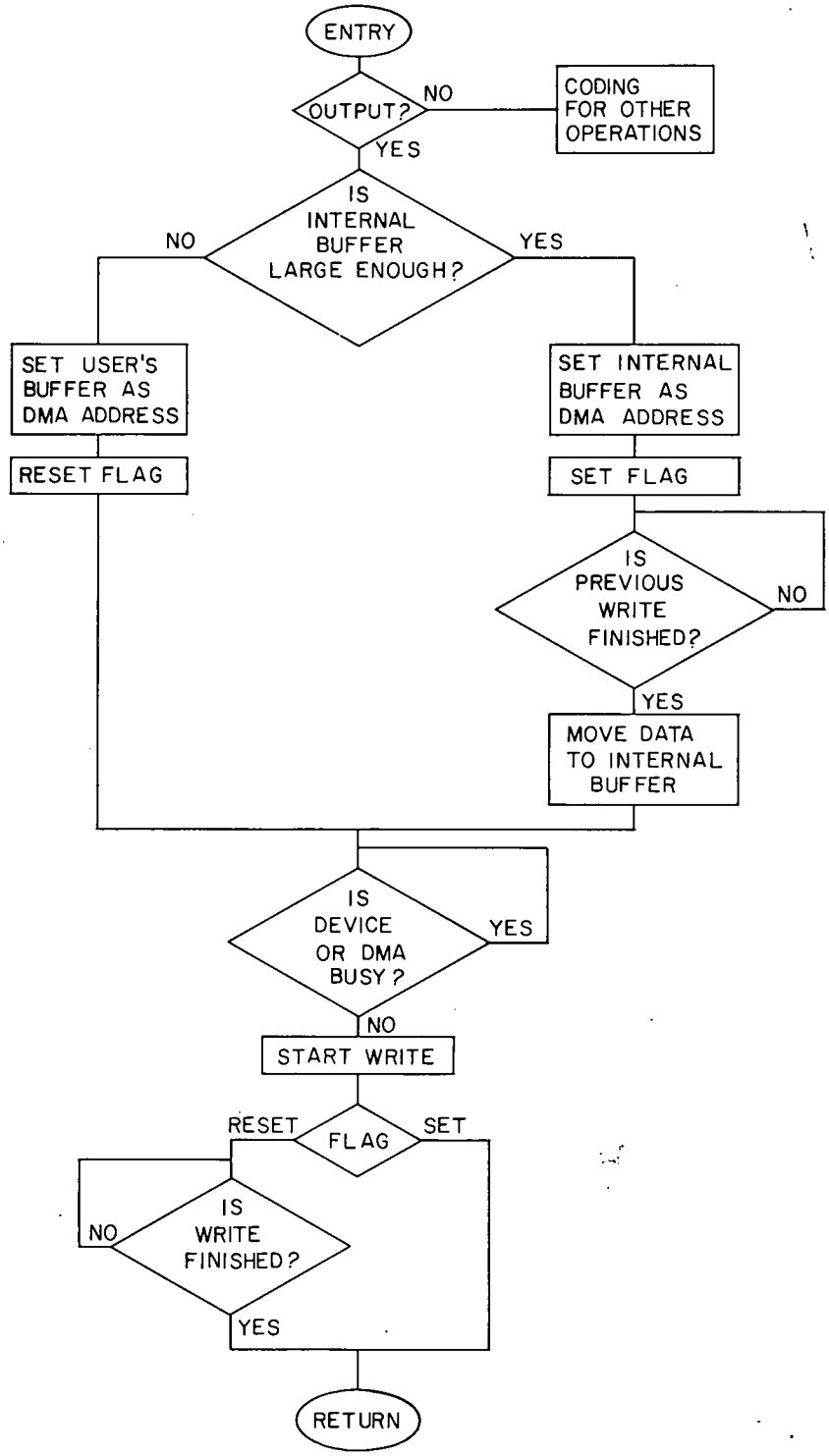

FIG. III-26-1. Output Routine for a Device that Does *Not* Check Parity after Writing (e.g. Disc). *ANL Neg. No. 116-593.*

tion and output is thus achieved. The time required to move the data to the internal buffer is normally a small fraction of the time required for the whole output operation, and thus does not detract appreciably from the gain in throughput.

It is clearly wasteful of core to provide a buffer area large enough for any conceivable requirement. Rather, the area should be just large enough for the record length most commonly employed, with longer records being handled the old way. A buffer was pro-

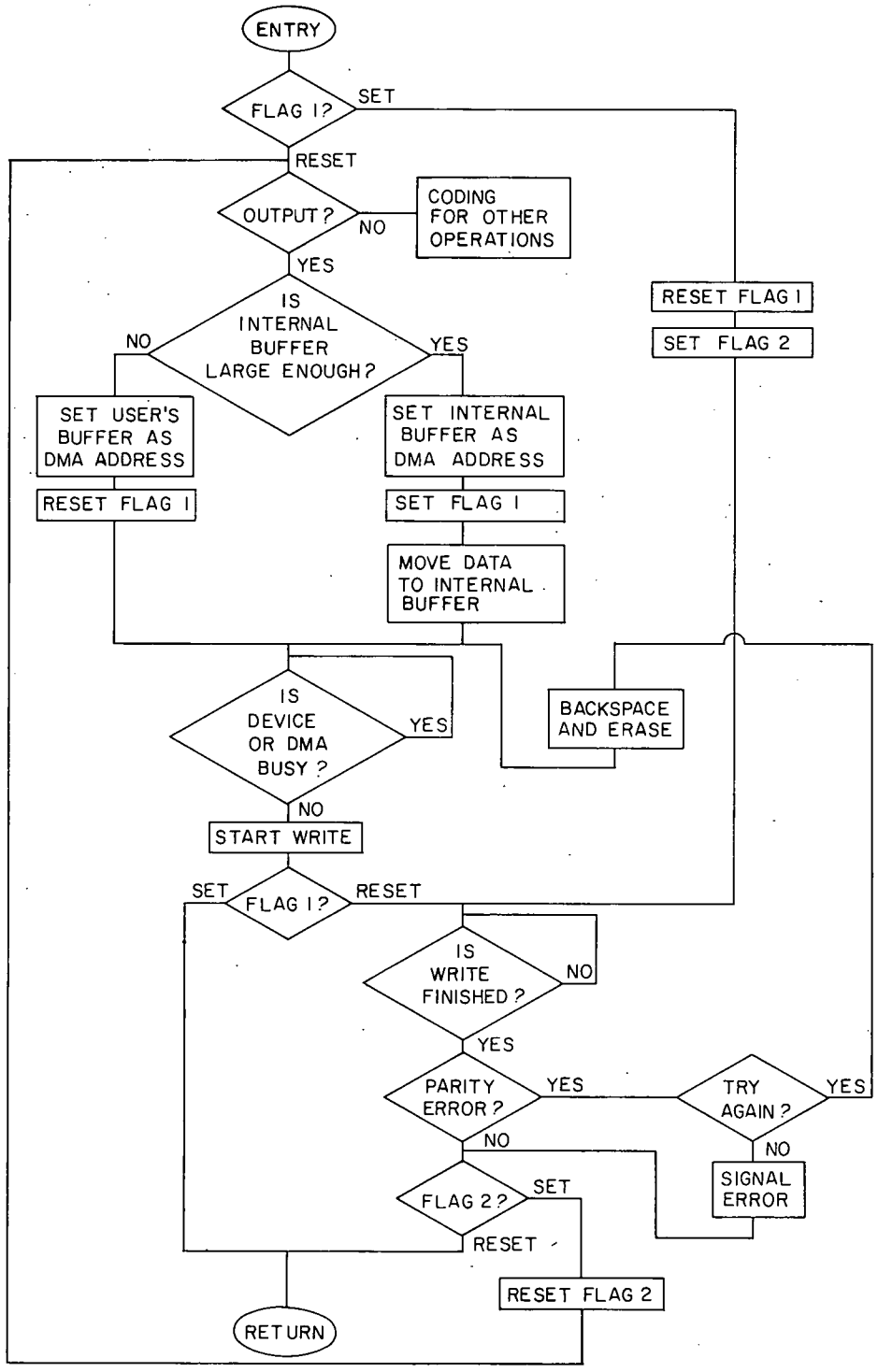

FIG. III-26-2. Output Routine for a Device that *Does* Check Parity after Writing (e.g. Magnetic Tape). *ANL Neg. No. 116-594.*

vided only large enough for a card image on the magnetic tape and one sector on the disc.

DISC OPERATIONS

Figure III-26-1 shows the flowchart for the disc subroutine operating in this way. On entry, the subroutine examines the word count to see if its internal buffer will accommodate the record. If so, the DMA channel is addressed to the internal buffer and a flag is set. Prior to actually moving data, the routine must wait until any previous write operation has completed in order to avoid disturbing the existing internal buffer

contents before they have been transmitted. If the internal buffer will not accommodate the record, the DMA channel is addressed to the calling program's buffer and the flag is reset. After a check that the peripheral and channel are available, the output operation is initiated. Then, if the flag is set, return to the calling program is immediate; but if the flag is reset, return is deferred until the output operation is complete.

Magnetic-Tape Operations

Some peripherals require a check on the correctness of data transmission after an output operation is complete. (Parity checking of magnetic tape is typical.) This is another reason why conventional routines defer the return. However, that deferral can be avoided if the parity check is postponed until the next time the subroutine is entered. Figure III-26.2 shows how that is done in the magnetic tape subroutine.

On entry, if FLAG1 is reset, a decision is made as before whether or not the internal buffer can accommodate the data to be transferred. The channel address and FLAG1 are formed accordingly. (It is not necessary here to check for completion of a previous write operation before moving data to the internal buffer because the program would not reach this point anyway if a previous operation were still in progress.)

If the peripheral and channel are available, the output operation is started. If FLAG1 is set, the return to the calling program is immediate. On the other hand, if FLAG1 is reset, the routine waits until the write operation is complete and then performs the parity check. If no error is found, the routine returns to the calling program. If an error is detected, the routine makes another attempt in the usual way.

On a subsequent entry, FLAG1 being set indicates that a postponed parity check is the first order of business. The routine then resets FLAG1, sets FLAG2, ascertains that the previous write operation has completed, and checks the parity. If no error is found, the routine resets FLAG2 and goes back to set up the next operation. If an error is detected, further write attempts may be made, as the data that were to be written remain undisturbed in the internal buffer.

Input Considerations

Comparable exploitation of DMA for input is considerably more complicated. Obviously, an input subroutine cannot return control to a calling program until the data needed by the latter are in hand. Therefore, input and computation can be overlapped only if the input routine continually reads one record ahead. This would require quite involved programming to handle correctly various situations such as backspace, rewind, end of file, and arbitrary sequences of reading and writing. Furthermore, the disc and tape routines handle a number of logical files and physical transports respectively, and so would need an internal buffer area for each, greatly increasing the drain on core space. For this system, then it seemed a reasonable compromise to overlap computation with output but to forego overlapping with input.

III-27. Ge(Li) Detector Calibration and Data Correction for Small Source-to-Detector Distances and Absolute Standard Source Comparisons

D. W. Maddison

The technique of precision efficiency calibration of Ge(Li) detectors for the ZPPR gamma-ray counting system[1] has been described in Ref. 2. Further investigation and refinement of technique has reduced the relative error of the efficiencies between the Ge(Li) detectors of this system to less than ±0.3 %. The absolute error, based upon the absolute calibrations of the standard sources, has been reduced to ±1.25 %. To achieve these results, careful attention has been paid to the geometrical relationships of the source and detector. Typical geometry places the sources about 1.8 cm above the Ge(Li) detector, or about 1 cm above the cryostat. At these small distances, the finite thickness of the source, its diameter, and the reproducibility of the source position are of major importance. The standard sources used for calibration are very thin (0.00025 cm), but the diameters are about 0.3 cm. The foil samples normally counted are 0.013 cm thick and have diameters from 0.8 to 1.3 cm. One must have available appropriate information in order to accurately determine the activities of these foils. For our particular Ge(Li) detectors (~30 cm^3), the efficiency changes 0.16 % for each 0.0025 cm vertical displacement from the standard position. Since the vertical reproducibility of the sample changer is ±0.004 cm for the vertical position, the calibration of ±0.3 %

appears to be due primarily to this factor. The horizontal sensitivity of the efficiency is 0.006 % for each 0.0025 cm. Since the horizontal reproducibility is ±0.03 cm, this effect can be ignored. The sample diameter, however, must be appropriately accounted for as well as the finite foil thickness.

To obtain the correct activity results, assuming uniform distribution of the activity through the foil, gamma ray attenuation must be calculated, particularly for uranium foils and low energy gamma rays. A correction must also be applied for prompt gamma-ray coincidences. Consider two gamma rays: gamma 1 followed promptly by gamma 2, as in the case of ^{60}Co. If the photo-peak of gamma 1 is of interest, one must consider the results of prompt coincidence with gamma 2. The total efficiency for the detection of gamma 2, however, must be considered since any detection of gamma 2 in prompt coincidence with the total-energy event of gamma 1 will remove the resulting detector output from the gamma 1 photo-peak area. The same argument of course holds for the gamma 2 photo-peak. At small source-to-detector distances these coincidence losses are not small. For our particular installation, the losses for ^{60}Co prompt coincidence amount to 3.5 to 4.6 %, depending on the particular detector used. Appropriate decay scheme information must, therefore, be available to make a proper assessment of the foil activities of interest.

The absolute activity determinations are tied directly to the absolute standard source calibrations. We have a set of standard sources from the International Atomic Energy Agency (IAEA), but these sources are too high in activity, and are not completely defined geometrically to make them useful in direct calibration of the detectors. We have obtained our own sources for calibration from an independent manufacturer and have made exhaustive comparisons with the IAEA standards, usually using a large NaI detector at large source-to-detector distances. Comparisons have also been made with some National Bureau of Standards (NBS) sources (^{60}Co, ^{137}Cs, and ^{54}Mn). The results of these comparisons are excellent. The cross comparisons of the IAEA and NBS standards, by way of our own standard sources, have given results within the quoted errors (1.0–1.5 %) for these standards, and in the case of ^{137}Cs, the results were essentially identical (±0.2 %). Because of the complex equipment involved to perform accurate calibration of source strengths, we intend to continue to use standards from outside suppliers such as NBS and IAEA. It would be desirable, however, to have standard sources with better precision (±0.5 %) available.

References

1. D. W. Maddison and L. S. Beller, *Characteristics and Capabilities of Automated Counting Facilities for the Zero Power Plutonium Reactor (ZPPR)*, Reactor Physics Division Annual Report, July 1, 1968 to June 30, 1969, ANL-7610, pp. 379–381.
2. D. W. Maddison and L. S. Beller, *Precision Efficiency Calibration Procedures for Ge(Li) Detectors*, Applied Physics Division Annual Report, July 1, 1969 to June 30, 1970, ANL-7710, pp. 283–285.

III-28. Analysis of Automatic Fission Track Scanning Data

Raymond Gold and C. E. Cohn

Fission rate measurements with solid-state track recorders (SSTR) have already been placed on a precise absolute basis with manual scanning.[1] A major inconvenience of the SSTR method is the manual counting of fission tracks, which is expensive, tedious, and time consuming. This drawback is clearly manifested in precision measurements, where counting statistics require observation of large numbers of tracks for adequate precision.[1] Elimination of the human element is highly desirable in precise measurements, since this would permit the introduction of quantitative standards for track recognition. Such standards would obviate personal bias in manual track counting, which may otherwise perturb results. Consequently, considerable interest exists in the automation of this task.

A computer controlled microscope has been developed[2,3] and applied in automatic scanning of fission tracks in SSTR. Through a rigorous treatment of automatic scanning data it has been possible, for the first time, to attain precision and absolute accuracy rivaling that of manual scanning.[4] The unique ability of the computer-controlled microscope to measure track area distributions permits introduction of a novel concept; namely, the differential track area probability distribution, which enables invariant background subtraction. Experimental error introduced by this background subtraction process is small.

In Makrofol polycarbonate resin, the track area distribution $P(x)$ is found to be well represented by a Breit-Wigner resonance curve

$$P(x) = \frac{a}{(x - c)^2 + \frac{b^2}{4}}, \quad (1)$$

while the background $B(x)$ is well represented by a decreasing exponential function

$$B(x) = \beta e^{-\gamma x}. \quad (2)$$

The observed distribution from a given specimen is fit to the sum $B(x) + P(x)$. Resulting parameter estimates (a, b, c, β and γ) are used to refine the background subtraction.

The general validity of the paralyzable counter model[5] for the accurate description of track overlap or pile-up has been established. The track density, ρ_0, observed in automatic track scanning can be expressed in terms of the true fission density, ρ, by the fundamental transcendental relation

$$\rho_0 = \eta\rho \exp(-\alpha\eta\rho). \quad (3)$$

Here α is the characteristic pile-up area and η is the optical efficiency for automatic track scanning; that is, the combined efficiency of both track registration and track etching.

Absolute calibration of this system has been successfully executed for Makrofol SSTR with a known spontaneous fission source. A series of Makrofol SSTRs were given various exposures and the observed track densities were fitted to Eq. 3. The coefficients of the paralyzable counter model so obtained are $\eta = 0.9804$ and $\alpha = 2.758 \times 10^{-6}$ cm^2, with error $\sim$1 part in 10^5 being negligible relative to counting statistics. The domain of validity of this model lies in the region $\rho_0 \lesssim 10^5$ tracks/cm^2.

The overall relative error in the number of fissions, F, obtained by automatic scanning can be written as

$$\frac{\sigma(F)}{F} = \frac{\phi(\omega)}{T} + \frac{\sigma(f)}{f}, \quad (4)$$

where $\sigma(f)/f$ is the relative error of the absolute fission rate of the calibration source, T is the number of observed tracks, and $\phi(\omega)$ represents the function

$$\phi(\omega) = \frac{1 - 2\omega e^{-\omega}}{(1 - \omega)^2} \quad (5)$$

of the dimensionless argument $\omega = \alpha\eta\rho$. The dependence of automatic scanning error upon pileup arises through the function $\phi(\omega)$. On this basis, it was found that manual and automatic fission track scanning errors do not differ significantly. This conclusion can be inferred directly from Fig. III-28-1, which presents a comparison of manual and automatic fission track counting errors as a function of observed tracks T.

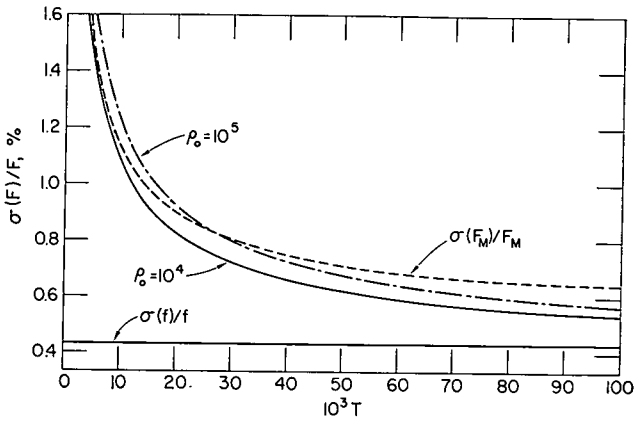

FIG. III-28-1. Overall Relative Errors in Automatic Scanning, $\sigma(F)/F$, as a Function of Observed Tracks, T, for Track Densities $\rho_0 = 10^4$ and 10^5. The $\sigma(F_M)/F_M$ Curve Depicts the Corresponding Manual Track Scanning Relative Error as a Function of (Manually) Observed Tracks T. The Constant Relative Error Denoted by $\sigma(f)/f$ Represents the Present Limiting Accuracy of Both Manual and Automatic Scanning and Corresponds to the Emission Rate Uncertainty of the ^{244}Cm Spontaneous Fission Source: *ANL Neg. No. 116-683.*

Limitations due to effects of nonuniformity in fission track density have been estimated. Extension of these precise capabilities to mica solid-state track recorders has been attempted. In contrast with Makrofol, unresolved difficulties have been encountered in the automatic scanning of mica.

REFERENCES

1. R. Gold, R. J. Armani and J. H. Roberts, *Absolute Fission Rate Measurements with Solid-State Track Recorders*, Nucl. Sci. Eng. **34**, 13–32 (1968).
2. C. E. Cohn, R. Gold and T. W. Pienias, *A Computer-Controlled Microscope for Scanning Fission Track Plates*, Reactor Physics Division Annual Report, July 1, 1968 to June 30, 1969, ANL-7610, pp. 396–399.
3. C. E. Cohn, R. Gold and T. W. Pienias, *A Computer-Controlled Microscope for Scanning Fission Track Plates*, Trans. Am. Nucl. Soc. **12**, 68 (1969).
4. R. Gold and C. E. Cohn, *Analysis of Automatic Fission Track Scanning Data*, Trans. Am. Nucl. Soc. **14**, 500 (1971).
5. C. E. Cohn, *Effect of Dead Time on Counting Errors*, Nucl. Instr. Methods **41**, 338–340 (1966).

III-29. Energy Response Calculations for Encapsulated ^{7}LiF Thermoluminescent Dosimeters

G. G. Simons

Introduction

An evaluation of the utility of using ^{7}LiF thermoluminescent dosimeter (TLD) rods (1 x 6 mm) to measure gamma ray absorbed doses in ZPPR resulted in the adoption of a general ionization theory which removed the cavity size restriction characteristic of the Bragg-Gray type cavity ionization theories.[1] It is therefore theoretically possible to relate the absorbed dose in a solid-state TLD cavity to the absorbed dose in the wall material irrespective of the cavity size, atomic number of the cavity material, or the composition of the wall. The general ionization theory can be applied in the design of a dosimeter capsule to achieve a gamma-ray sensitive device which has a good energy response. The energy response can also be estimated for any capsule provided electron equilibrium is established in the sleeve and the gamma-ray spectrum is known. Based on this theory, it is possible to estimate the magnitude of systematic errors inherent in dose measurements made within the critical assembly, provided TLD rods encased in different sleeve materials are calibrated with a standard ^{60}Co source and then exposed to fast-reactor type gamma-ray spectra.

Theory

If the composition of the TLD and the sleeve possess identical gamma-ray absorption coefficients as well as the same atomic stopping power for electrons, a matched cavity condition would exist. Under these conditions, the absorbed dose in the cavity would equal the absorbed dose in the sleeve. In practice, the matched cavity concept cannot be used in designing dosimeters for measurements in criticals. Hence, it is necessary to evaluate the wall effect for each type of sleeve material. The response of the TLD cavity relative to a TLD for which there is no wall effect is given by

$$W = \frac{(\mu_{en}/\rho)_z}{(\mu_{en}/\rho)_c} {}_Bf_z(T_0),$$

where the subscripts c and z refer to the TLD cavity and sleeve material respectively, $\mu_{en}\rho$ is the mass energy absorption coefficient, and ${}_Bf_z(T_0)$ is the mass stopping power ratio for a cavity relative to the sleeve based on the general ionization theory. Relative to the Spencer-Attix prescription for small cavities, ${}_Bf_z(T_0)$ is[1]

$$\begin{aligned} {}_Bf_z(T_0) = {} & \frac{(Z/A)_c}{(Z/A)_z} \\ & \cdot \left\{ 1 + \frac{d}{T_0} \left[\int_\Delta^{T_0} R_z(T_0, T) \left(\frac{B_c(T)}{B_z(T)} - 1 \right) dT \right. \right. \\ & \left. + \Delta R_z(T_0, \Delta) \left(\frac{B_c(\Delta)}{B_z(\Delta)} - 1 \right) \right] \\ & \left. + (1 - d) \left[\frac{(\mu_{en}/\rho)_c (Z/A)_z}{(\mu_{en}/\rho)_z (Z/A)_c} - 1 \right] \right\}, \end{aligned}$$

where T_0 is the initial energy of the electron, Δ is the electron energy for which a secondary electron would lose all of its energy at the location of formation, $R_z(T_0, T)$ is the ratio of the total electron fluence to the primary electron fluence at an energy T, $B_m(T)$ is the stopping power number per electron for $m = c$ or z, Z is the atomic number, and A is the atomic mass. The weighting factor d is given by

$$d = \int_0^g e^{-\beta x} dx \Big/ \int_0^g dx$$

where β is the effective mass absorption coefficient for electrons having the maximum energy present in the wall or cavity and g is the mean chord length of electrons traversing the cavity.

TABLE III-29-I. Mass Stopping Power Ratios Relative to LiF for Selected Materials

T_0, MeV	${}_Bf_z$			
	Teflon	Aluminum	Iron	Tantalum
	Laurence Theory			
0.15	0.9644	0.8366	0.3149	0.0635
0.25	0.9664	0.9356	0.6594	0.1568
0.4	0.9714	0.9644	0.9288	0.3905
0.6	0.9767	0.9748	0.9957	0.6784
1.00	0.9844	0.9828	1.0413	1.0365
1.50	0.9931	0.9925	1.0585	1.2018
2.00	0.9974	0.9928	1.0652	1.2514
	Spencer-Attix Theory			
0.327	0.966	0.961	0.861	—
0.754	0.980	0.994	1.027	—
1.308	0.993	1.028	1.073	—

Results

Approximate values of ${}_Pf_z(T_0)$ for teflon, aluminum, iron and tantalum sleeve materials relative to LiF based

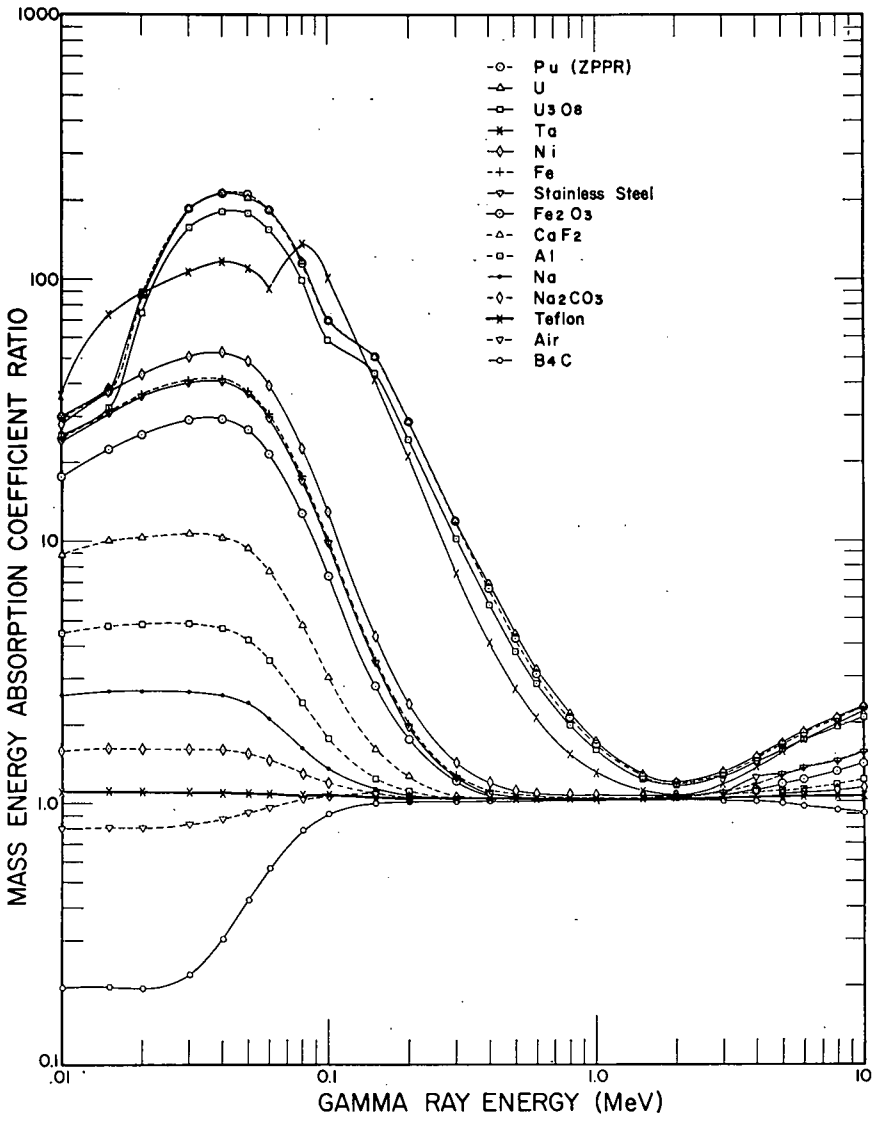

FIG. III-29-1. Mass Energy Absorption Coefficient Ratios of Selected Materials Relative to LiF. *ANL-ID-103-A11870.*

on both the Laurence and Spencer-Attix theories[2] are listed in Table III-29-I. Figure III-29-1 shows the energy dependence of several mass energy absorption coefficient ratios relative to LiF. These tabulated and plotted quantities can be used to evaluate the energy response of the dosimeter capsule.

Gamma-ray induced excitation in dosimeter capsules containing extruded ^{7}LiF rod cavities and different sleeve materials were measured. Several capsule types were irradiated in three gamma ray fields. Each field had a different characteristic spectrum. The TLD thermoluminescence (TL) variation as a function of sleeve type, sleeve wall thickness, and gamma ray energy were recorded. These experiments tested the sensitivity of the measured TL upon the capsule configuration and exposure environment. They also allowed a preliminary evaluation of the ability to predict the change in TL for different sleeves using the general ionization theory.

Table III-29-II lists the various materials, sleeve wall thicknesses, and gamma-ray sources used along with the resulting relative TL values. All of the TL values shown in Table III-29-II are reported relative to the 0.894 g/cm^2 teflon sleeve. It may be concluded from these data that when TLD rods with standard deviations of at least 5.8 % were used, the TL readouts were the same for individual sleeve materials, independent of the wall thickness selected for this study for each of the gamma-ray sources. Some of the TL values did vary between sources. It must be noted that these results do not show that the TL values are independent of sleeve thickness in general. That is, the minimum wall thickness in each case was generally at least one-half the range of the most energetic electrons

TABLE III-29-II. Relative ^7LiF Response for Selected Sleeves and Gamma Ray Sources

Sleeve Type	Sleeve Diameter, in.	Sleeve Wall Thickness		TLD Response Relative to 0.894 g/cm² Teflon Sleeve			
		in.	g/cm²	^{226}Ra	^{60}Co	ZPPR-2	
						Loading 157	Loading 158
Air	∞	∞	∞	—	1.064 ± 0.090	—	—
B_4C	⅛ in. plate	0.125	0.762	—	0.990 ± 0.084		
Teflon	0.250	0.098	0.548	1.008 ± 0.086	1.015 ± 0.086	0.993 ± 0.084	0.896 ± 0.076
	0.375	0.160	0.894	1.000 ± 0.085	1.000 ± 0.085	1.000 ± 0.085	1.000 ± 0.085
Al	0.1875	0.066	0.453	1.029 ± 0.087	1.057 ± 0.089	—	—
	0.250	0.098	0.672	1.044 ± 0.089	1.035 ± 0.088	—	—
	0.3125	0.129	0.885	1.007 ± 0.085	1.008 ± 0.086	—	—
			Av:	1.027 ± 0.087	1.035 ± 0.088		
SS[a]	0.09375	0.020	0.400	1.104 ± 0.094	1.063 ± 0.090	1.027 ± 0.087	0.978 ± 0.083
	0.125	0.035	0.700	1.052 ± 0.089	1.027 ± 0.087	1.125 ± 0.096	1.038 ± 0.088
	0.1875	0.066	1.320	1.012 ± 0.086	1.057 ± 0.089	—	—
	0.250	0.098	1.959	1.025 ± 0.087	1.039 ± 0.088	1.067 ± 0.091	0.913 ± 0.078
	0.3125	0.129	2.579	1.007 ± 0.085	1.040 ± 0.088	—	—
			Av:	1.040 ± 0.088	1.045 ± 0.089	1.073 ± 0.091	0.976 ± 0.083
Ta	0.1875	0.074	3.120	1.128 ± 0.096	1.285 ± 0.109	1.624 ± 0.138	1.531 ± 0.130

[a] Type 304 stainless steel.

TABLE III-29-III. Theoretical and Experimental Ratios of the Effect of Sleeve Material on the Cavity Excitation

Sleeve Material	F		TL_z/TL_{Teflon}
	Laurence	Spencer-Attix (Δ = 81.8)	
Aluminum	1.004	1.041	1.033 ± 0.088
Iron	1.037	1.055	1.045 ± 0.089
Tantalum	1.289	—	1.285 ± 0.109

generated in the wall by the incident gamma rays. Moreover, the maximum sleeve thicknesses were not great enough to significantly attenuate the major ^{60}Co or ^{226}Ra gamma rays. This type of experiment will be performed again using TLDs with nominal standard deviations of 3%. These data may show variations as a function of the sleeve wall thickness.

A preliminary evaluation of the general ionization theory was made using the data in Table III-29-II. The response of a TLD in a capsule of wall material z relative to a TLD in a wall material y is

$$F = \frac{(\mu_{en}/\rho)_z \; {}_B f_z(T_0)}{(\mu_{en}/\rho)_y \; {}_B f_y(T_0)} .$$

Thus the ratio of the TLD readouts for different sleeve materials should also equal F. Calculated F values were compared with the measured TL ratios of TL_z/TL_{Teflon} (see Table III-29-III).

The experimental results are in agreement with the calculated F values for all three materials. It should be noted that the accuracy in the tantalum F value is worse than for either iron or aluminum since the nuclear parameters used to calculate ${}_B f_z$ for tantalum were not as precise.

The utility of using stainless steel encased TLD dosimeters in ZPPR is reported in Paper II-40.

References

1. T. E. Burlin, *A General Theory of Cavity Ionization*, Brit. J. Radiol. **39**, 727–734 (1966).
2. NCRP, *Stopping Powers for Use With Cavity Chambers*, National Committee on Radiation Protection and Measurements, NBS Handbook 79 (1961).

III-30. Evaluation of Thermoluminescent Materials and Techniques for Determining Gamma Heating in Fast Reactors

T. J. Yule

Introduction

If cooling requirements are to be correctly assessed and thermal stresses adequately predicted in the design of an LMFBR, it is necessary to be able to determine the amount of energy that will be deposited in various regions of the reactor by gamma-ray interactions. Gamma heating measurements in the ZPRs allow one to determine the adequacy of calculational techniques and gamma-production cross section libraries and also provide gamma heating profiles for a particular design and for regions not amenable to calculation.

Numerous devices have been developed for gamma-ray dosimetry[1]: cavity ionization chambers, scintillation detectors, chemical dosimeters, solid-state integrating dosimeters, solid-state electrical-conductivity dosimeters, photographic emulsions and calorimeters. However, the particular environment of a fast reactor and operational considerations limit the number of choices. Measurements must be made in a mixed neutron-gamma radiation field in moderate fluences and in a variety of materials in which the gamma spectrum and neutron spectrum span broad energy ranges. It is also desirable to perform simultaneous measurements in a number of locations with probes that introduce a minimum amount of perturbation. This report considers only one particular type of solid-state integrating dosimeter—the thermoluminescent dosimeter (TLD). At the present time this type of dosimeter seems most promising for gamma-heating measurements because, of its small size, good sensitivity, broad dose range, low neutron sensitivity and advanced state of development.

The principle of operation of a TLD is rather straightforward. The TLD material contains a number of room-temperature stable electron or hole traps which are filled when ionizing radiation creates free electrons or holes. To read out the dosimeter the material is heated, returning the electrons to the conduction band. The transitions from the conduction band to the valence band result in emission of visible wavelength radiation; the number and intensity are related to the material's exposure.

Extensive developments in TLD materials and techniques in the last ten years have produced a system that is applicable to a wide range of exposure conditions and one that is being increasingly employed for dosimetry.[2] However, there are two special areas of concern in the application of TLD techniques to measuring gamma heating in fast reactors—the neutron sensitivity of the TLD material and the relationship between the TLD response and the heating in the particular material under consideration. Any TLD material shows some neutron sensitivity because recoil ions from elastic scattering, gamma rays from neutron capture or other reaction products create ionization in the material. Since we are only interested in measuring gamma heating, neutron induced contributions to the TLD signal must be corrected for. With respect to the second area of concern, the relationship between the TLD response and heating in the material around the TLD is a function of the composition of the TLD and of the surrounding medium, size of the TLD and the gamma spectrum. A simple relationship independent of gamma-ray energy exists only if the TLD material and surrounding medium are the same. Since the gamma spectra are usually unknown and since it is usually impossible to have both materials the same, it is important to choose a TLD material which introduces the least amount of uncertainty in the determination of gamma heating.

TLD techniques have been applied to reactor studies and to other mixed environments, such as those encountered in weapons testing. Stanford and Johnson used CaF_2:Mn powder to measure gamma heating in a thermal critical facility.[3] Consideration was given to the two areas mentioned above. LiF powder was used to measure gamma heating[4] as a function of position in a single cell at the center of Zebra-6. There have been a number of measurements with CaF_2:Mn hot-pressed chips to measure gamma doses near nuclear rockets (see, for example, Ref. 5). Gibson and Stuetzer have attempted to determine the neutron sensitivities of various solid-state integrating gamma dosimeters and to evaluate these devices for gamma dosimetry in a nuclear reactor environment.[6,7] Wingate, Tochilin and Goldstein have done a careful investigation of the response of LiF to neutrons and charged particles.[8] LiF has been used for dose mappings, single-cell dose heterogeneity and blanket-reflector and reflector-core interface studies for the EBR-II series of ZPR-3 critical assemblies.[9] An evaluation of ^{7}LiF for gamma ray dose measurements in ZPPR appears in Paper II-40.

Relation between Absorbed Dose in the Medium and Absorbed Dose in the Dosimeter Material

Because of the importance of accurate measurements of absorbed dose in relating the effects of ionizing radiation on physical, chemical and biological systems, a considerable effort has gone into establishing the relation between the absorbed dose in the medium, ${}_mE_z$, and the absorbed dose in the dosimeter material, ${}_mE_d$. Since the earliest radiation dosimeters were gas-filled chambers, attention was first centered in relating the absorbed dose in the gas (the product of the number of ion pairs formed per unit mass, ${}_mJ$, and the average energy, W, necessary to form an ion pair) to the absorbed dose in the medium. Gray[10,11] derived the well known Bragg-Gray equation,

$$ {}_mE_z = \frac{1}{f}\,{}_mE_d = \frac{1}{f}\,W_m J, \qquad (1) $$

where f is the ratio of the mass stopping power of the gas to that of the wall for directly ionizing particles. Bragg[12] had earlier indicated the relationship in a qualitative way.

Gray's derivation assumed that (1) the electron spectrum in the medium is not affected by the cavity, (2) the influence of gamma-ray interactions with the cavity material is negligible, and (3) the electrons lose energy continuously in interacting with the cavity material. For convenience Gray assumed that the mass stopping power ratio for electrons was independent of energy. Laurence[13] explicitly took into account the energy dependence and averaged the mass stopping power ratio over the equilibrium electron spectrum. However, even with this modification, the agreement between the predictions of cavity ionization theory and experiment was often poor. Pressure, cavity-size and wall-material effects not predicted by the theory were realized. Burch[14] and Spencer and Attix[15] included discrete energy losses by electrons and were able to improve the agreement. However, since the first two assumptions were still made, the theories were applicable only to cavities with dimensions considerably smaller than the electron ranges in the cavity material. This condition is not difficult to attain with gas-filled cavities, but is quite difficult to attain with solid- and liquid-state detectors. Burlin[16] proposed modifications to the Spencer-Attix theory which remove the restriction on the size of the cavity. The predictions of this more general theory have been compared with experimental results from solid-state dosimeters covering the complete range of both cavity size and atomic number of the surrounding medium.[17] In general, good agreement was found. A detailed description of cavity-chamber theory is contained in Ref. 18.

Although it is useful to realize the rather high degree of sophistication that cavity-ionization theory has attained, for our purposes certain simplifying assumptions may be made which make its predictions rather apparent. Since the reactor environment contains a gamma spectrum which extends over a broad energy range (and which is usually not known), we are interested in the behavior of f as a function of energy. The ratio of cavity size to electron range moves from one extreme for low gamma-ray energies at which the size of the cavity is large compared with the range of the electrons to the other extreme at high gamma-ray energies at which the size of the cavity is small compared with the range of the electrons. In the two regions the interaction of gamma rays with matter are dominated by different processes—at low energies (below a few hundred keV) the photoelectric effect dominates while at high energies the Compton effect is more important. At low energies the energy absorbed per unit mass of material is simply

$$ {}_mE = NT_\gamma \mu_{en}/\rho, \qquad (2) $$

where N is the gamma fluence, T_γ is the gamma energy and μ_{en}/ρ is the mass energy-absorption coefficient. Since N and T_γ are the same for the cavity and surrounding material, the relation between the absorbed dose in the surrounding material and that in the cavity material is

$$ {}_mE_z = \frac{(\mu_{en}/\rho)_z}{(\mu_{en}/\rho)_d}\,{}_mE_d. \qquad (3) $$

For the photoelectric effect, the photoelectron has almost the same energy as the incident gamma-ray, and for the above expression to hold it is assumed that a photoelectron created in the cavity (surrounding material) deposits all its energy in the cavity (surrounding material). At high gamma-ray energies the absorbed dose in each region will be proportional to the mass stopping power for the material in the region, averaged over the equilibrium electron distribution. For Compton scattering there is a distribution of electron energies, but a suitable averaging is performed[16] if one simply chooses the average electron energy, $\bar{T}$, given by [19]

$$ \bar{T} = T_i\,(\sigma_a/\sigma), \qquad (4) $$

where T_i is the incident gamma-ray energy, σ_a is the absorption cross section, and σ is the total cross section (scattering plus absorption) and takes the value of the mass stopping power at that energy.[16] For solid-state dosimeters the inclusion of the discrete nature of electron energy losses is of little consequence. The Burlin cavity ionization theory alluded to earlier links

the low and high energy domains in a reasonable (although inexact) way.

As a specific example consider the surrounding medium to be iron and the solid-state dosimeter to be either LiF or CaF_2:Mn—the two most popular TLD materials. Figure III-30-1 shows the ratio of the mass energy-absorption coefficients[19] at the incident gamma-ray energy and mass stopping powers[20,21] at the average Compton energies. The large values of the ratio of the mass energy-absorption coefficients at low energies arise because the photoelectric cross section[19] is proportional to Z^4. At higher energies there is not much variation and the values are close to unity. This is to be expected since the Compton cross section[19] is proportion to Z and the mass is approximately proportional to Z. The ideal dosimeter should have a ratio that is independent of energy. In practice the effective Z of the dosimeter and surrounding material should be kept as close as possible.

Figures III-30-2 and III-30-3 show $1/f$ for a LiF-Fe and a CaF_2:Mn-Fe system, respectively. The curves are obtained from the curves shown in Fig. III-30-1 with the dashed lines indicating the behavior in the transition region for a reasonable size dosimeter as predicted by the Burlin theory of cavity ionization.

Since the gamma-ray energy spectrum is usually not known in a reactor and since there can be a sizeable spectral dependence if the dosimeter and surrounding material are not matched, it is important in ascertaining the accuracy of gamma-heating measurements to investigate this effect for representative fast-reactor gamma-ray spectra. Figure III-30-4 shows calculated gamma spectra for various regions (core, blanket and reflector) in a typical fast-breeder demonstration plant design.[22] The calculations were done with twenty energy

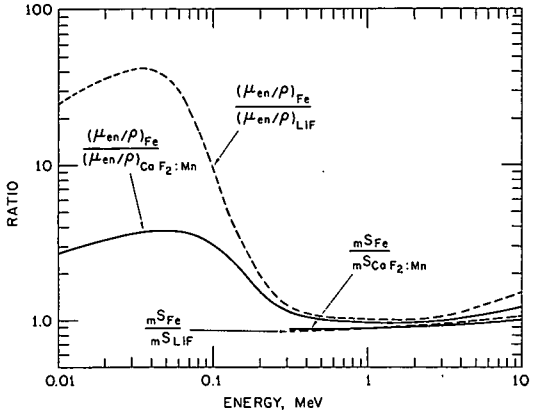

FIG. III-30-1. Ratios of the Mass Energy-Absorption Coefficients of Iron to LiF and to CaF_2:Mn as a Function of Energy and Ratios of the Mass Stopping Powers Calculated at the Average Energy of the Compton Electrons of Iron to LiF and to CaF_2:Mn as a Function of Energy. *ANL Neg. No. 116-1020.*

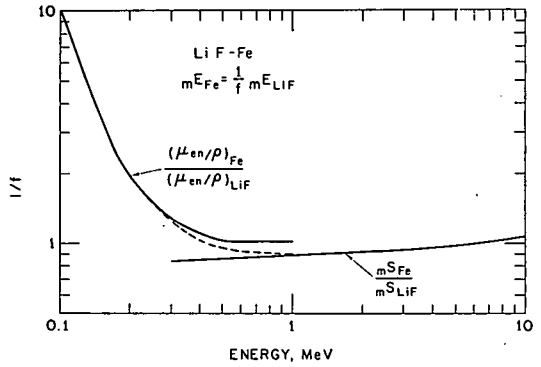

FIG. III-30-2. Variation of $1/f$ as a function of Energy for a LiF Dosimeter Surrounded by Iron. At Low Energies the Curve is Equal to the Ratio of the Mass Energy Absorption Coefficients of Iron to LiF and at High Energies is Equal to the Ratio of the Mass Stopping Powers Calculated at the Average Energy of the Compton Electrons of Iron to LiF. The Dashed Line Indicates the Behavior in the Transition Region Predicted by Burlin's Cavity Ionization Theory. *ANL Neg. No. 116-1021.*

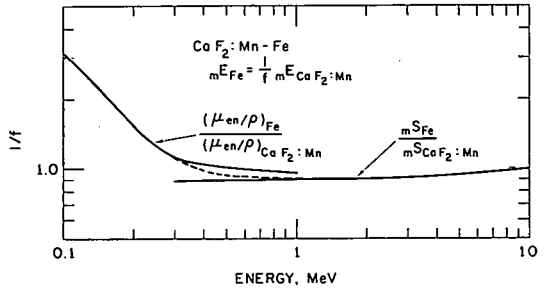

FIG. III-30-3. Variation of $1/f$ as a Function of Energy for a CaF_2:Mn Dosimeter Surrounded by Iron. At Low Energies the Curve is Equal to the Ratio of the Mass Energy Absorption Coefficients of Iron to CaF_2:Mn and at High Energies is Equal to the Ratio of the Mass Stopping Powers Calculated at the Average Energy of the Compton Electrons of Iron to CaF_2:Mn. The Dashed Line Indicates the Behavior in the Transition Region Predicted by Burlin's Cavity Ionization Theory. *ANL Neg. 116-1019.*

groups; the smooth lines on the figure simply smooth out the calculated histograms. Certain simplifying assumptions were made. The gamma source from fission was assumed to have the same spectral shape as that accompanying the fission of ^{235}U with thermal neutrons, irrespective of the fissioning isotope. Furthermore, the material in each cell was homogenized, which leads to some difficulty in interpreting the low-energy part of the spectrum. At low energies the photoelectric effect is important. Since the atomic numbers of the materials in a cell are quite different, one can expect the low-energy part of the spectrum to show some variation throughout the cell. It can be noted from the figure that in regions such as the core and blanket, which have a large amount of high-Z material, the low-energy peak is located at about 0.5 MeV; however, in

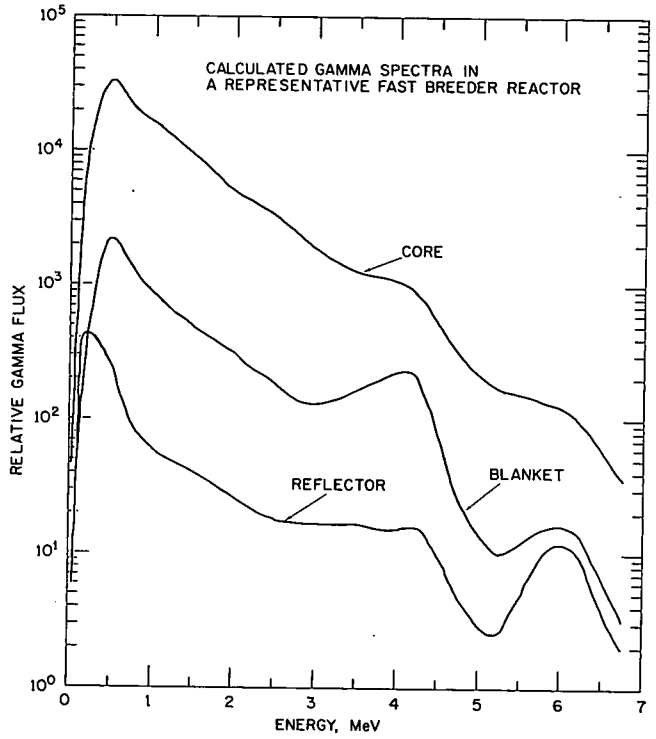

FIG. III-30-4. Calculated Gamma Spectra in the Core, Blanket, and Reflector of a Typical Fast Breeder Demonstration Reactor Design. *ANL Neg. No. 116-1014.*

the reflector, which contains mostly stainless steel and sodium, the low-energy peak is shifted to lower energies—a region where the spectral dependence of the dosimeter becomes important.

If we require that the amount of material around the dosimeter (the material for which gamma heating is to be measured) is such that electron equilibrium is established, a suitable thickness is about 1 g/cm², which corresponds to the range of a 2 MeV electron. To determine the effects of spectral sensitivity of the dosimeter, the spectral-weighted average of $1/f$ is given by

$$\frac{\bar{1}}{f} = \frac{\Sigma\phi_i(1/f_i)\,\exp\,[-(\mu/\rho)_i t]}{\Sigma\phi_i\,\exp\,[-(\mu/\rho)_i t]} \qquad (5)$$

where ϕ_i is the gamma flux in group i and $1/f_i$ is the value of $1/f$ at the average group energy, $(\mu/\rho)_i$ is the mass attenuation coefficient at the average group energy for the material around the dosimeter and t is the thickness of the material. The exponential term is included to take into account (to first approximation) attenuation of the gamma spectrum by material around the dosimeter. Table III-30-I contains average values of $1/f$ for the three spectra shown in Fig. III-30-4 for LiF-Fe and CaF_2:Mn-Fe systems. With a LiF-Fe system the spectral sensitivity can introduce a 30% difference between the measured and true doses if a single average $1/f$ value is used for all reactor regions; with a CaF_2:Mn-Fe system, the difference amounts to 15%. Almost all of the difference between average $1/f$ values for the core, blanket or reflector is associated with the shift of the gamma peak in the reflector region to lower energies—a region in which the spectral sensitivity of the dosimeters is important. It is interesting to note that the region where there is a maximum effect is one of moderate average Z, the reflector. In a high-Z region, even though there is a gross mismatch of the average Z of the region and that of the dosimeter, the high photoelectric cross section has led to the attenuation of the low-energy flux and thus the influence of the low-energy region on the average $1/f$ value is small.

Neutron Sensitivities of TLD Materials

Any TLD material may be expected to show some neutron sensitivity. Thermal neutrons create ionization in the material either through charge-particle reactions such as the $^6Li(n,\alpha)^3H$ in the LiF dosimeter or through gamma-producing reactions such as $^{25}Mn(n,\gamma)^{26}Mn$ in the CaF_2:Mn dosimeter. Fast neutrons will create ionization by producing heavy-ion recoils through elastic scattering. The heavy ions not only lose their energy in excitation and ionization of the lattice ions but also in producing displacements of the lattice ions and lattice vibrations. Since the number of thermal neutrons in a fast reactor is insignificant, we will mainly consider fast neutron sensitivities of TLD materials.

Neutron sensitivities have been investigated for LiF[7,8,23,24,25,26] CaF_2:Mn[7,27,28,29] and BeO[30]. The experimental determination is not straightforward because the neutrons are always accompanied by gamma rays and oftentimes the gamma field dominates the response.[7,8] Furthermore, the neutron response is influenced by the material around the dosimeter and care has not always been taken in determining this contribution to the response. In general, the agreement between various determinations has been poor. Several rather interesting phenomena associated with neutron stimulation of TLD materials have been observed. LiF exposed to thermal neutrons has a different shaped glow curve than that resulting from gamma irradiation.[8,26] As an aside, it may be noted that for BeO dosimeters readout by observing thermally stimulated

TABLE III-30-I. Spectrum Averaged Values of $1/f$ for a Dosimeter Surrounded with Iron in Various Regions of a Fast Breeder Reactor

Region	LiF-Fe	CaF_2:Mn-Fe
Core	0.987	0.958
Blanket	0.978	0.954
Reflector	1.283	1.102

exoelectron emission, a relation has been found between peak location and linear energy transfer (LET) of the ionizing particles; this phenomenon is being investigated for dosimetric application.[31] Another interesting effect was the observation by one group that the combined thermoluminescent response of ^{7}LiF dosimeters exposed in a gamma field only, and in a fast neutron field only, was greater than the response of a single dosimeter exposed to both gamma and fast neutrons.[23] They hypothesized that the gamma response was reduced as a result of trap emptying by fast-neutron irradiation. It was later found that the results were spurious, being associated with the encapsulation process.[24,25] With moderate neutron fluences the responses are additive; with high fluences it is possible to reduce the sensitivity by a combination of permanent and temporary damage.[33]

The only comprehensive study of neutron sensitivity was that made for LiF and the findings will be reviewed.[8] These results also indicate what might be expected for other TLD materials. Figure III-30-5 shows the measured and calculated neutron sensitivity of ^{7}LiF (>99.9 % ^{7}Li) as a function of neutron energy. The calculation assumes that only elastic scattering is important. The slopes of the calculated and measured curves are similar; however, the measured values are lower by an order of magnitude and the calculated peak does not appear in the measurement. The lower measured values can be explained by the LET dependence of the response. Figure III-30-6 shows the relative dose response versus the LET of charged particles. The LET of electrons is usually about 1 keV/μ, whereas

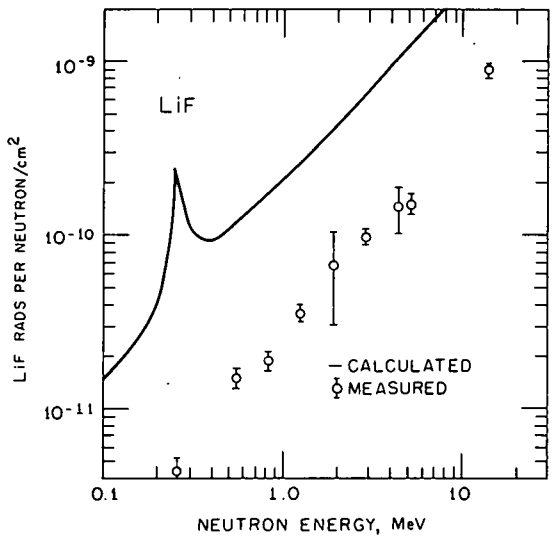

Fig. III-30-5. Dose Per Unit Neutron Fluence for ^{7}LiF as a Function of Neutron Energy. The Curve is the Calculated Response and the Points are Measured Values. The Figure is from Ref. 8. *ANL Neg. No. 116-1017.*

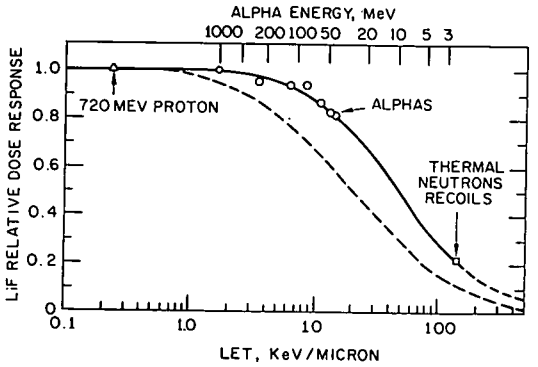

Fig. III-30-6. Relative Dose Response of LiF Versus the Linear Energy Transfer. The Point Labeled Thermal Neutron Recoils Results from the ^{6}Li$(n,\alpha)^3$H Reaction. The Dashed Line is a Calculated Curve for Anthracene. The Figure is from Ref. 8. *ANL Neg. No. 116-1015.*

that for recoils have initial values of several hundred keV/μ. The relative efficiency of LiF for recoils compared with that for electrons (generated by gamma interactions) might be 10 % or less. This same type of LET dependence is seen in photographic films, phosphate glass rods and organic phosphors such as anthracene. The dashed line in Fig. III-30-6 is a prediction for anthracene. One expects a variation with LET because of the dependence of the probability for recombination on ionization density and thus LET. Furthermore, since for a given energy, low LET particles have considerably longer track lengths than high LET particles, the number of available activator sites will be higher for low LET particles and this might be expected to influence the relative response. It should also be noted that care must be taken in extrapolating to lower energies a curve through the measured values of the sensitivity as a function of energy, because at lower energies it is increasingly difficult for the recoils to lose energy by ionization and excitation. The energy is lost by elastic collisions resulting in lattice-ion displacements and lattice vibrations, and thus free electrons or holes are not created.[34,35]

Figure III-30-7 shows the measured and calculated neutron sensitivity of CaF_2:Mn as a function of neutron energy. The calculation assumes that only elastic scattering is important in depositing energy. The scattering is assumed to be isotropic in the center of mass. Cross sections were obtained from Ref. 36. The individual contributions to the calculated response from fluorine recoils and from calcium recoils are shown. Because the lighter fluorine recoil can assume more of the incident neutron energy, its contribution dominates. The measured values represented by circles were obtained with monoenergetic neutrons.[7] The data are questionable because of problems with subtraction of gamma background. The same group measured neu-

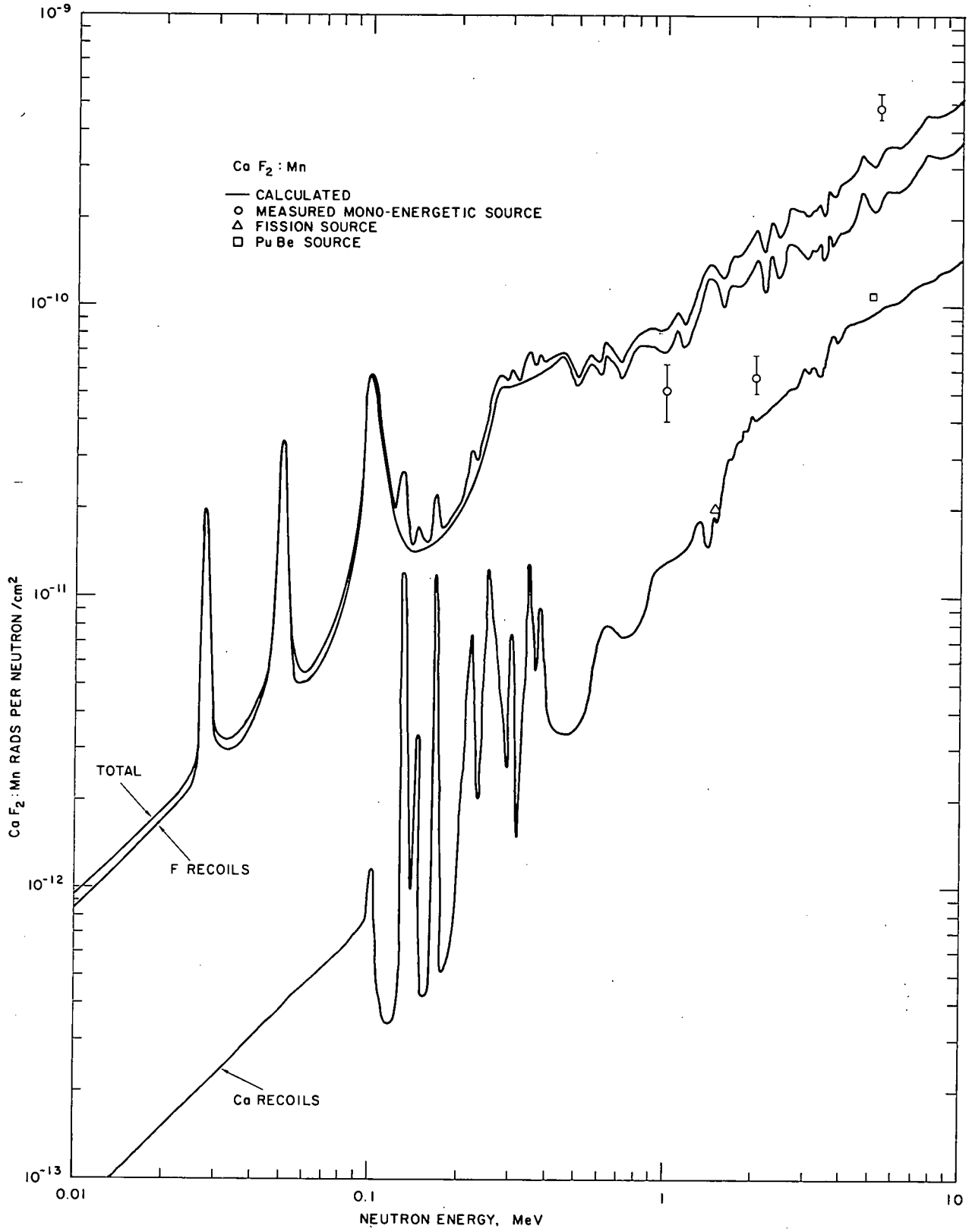

FIG. III-30-7. Dose Per Unit Neutron Fluence for CaF_2:Mn as a Function of Neutron Energy. The Upper Curve is the Calculated Response and the Two Lower Curves Show the Contribution of Fluorine Recoils and Calcium Recoils. The Circles Represent Measured Values with Monoenergetic Neutron beams,[7] the Square is the Measured Value with a Pu-Be Source and is Shown at the Average Neutron Energy of the Source[27] and the Triangle Represents the Measured Value in the Fission Spectrum of the Oak Ridge Fast Burst Reactor and is Shown at the Average Neutron Energy.[28] *ANL Neg. No. 116-1016.*

tron sensitivities of LiF and quoted values 10–20 times greater than those reported in Ref. 8. The high values are inconsistent with the results of integral experiments. The point (square) at about 5 MeV was obtained with a plutonium-beryllium neutron source.[27] A detailed description of the experiment is lacking. The point (triangle) at about 1.5 MeV represents an exposure to fission neutrons at the Oak Ridge National Laboratory Fast Burst Reactor.[28] A measurement under the same conditions with LiF yielded a result consistent with the data shown in Fig. 5. It is clear that additional integral measurements, as well as monoenergetic source measurements are needed for CaF_2:Mn.

In order to ascertain the extent of the uncertainty in a gamma-heating determination introduced by the neutron sensitivity of the TLD, it is necessary to consider the relative influences on the response of the gamma and neutron fields existing in a typical fast reactor. Recently, extensive reaction-rate measurements and gamma-heating rates in stainless steel (^{7}LiF was the TLD) were made for an engineering mockup of the Fast Flux Test Reactor.[37] The relative neutron spectrum is known from proton-recoil measurements[38] and calculations. Normalization may be obtained by requiring agreement with measured fission rates. The percentage neutron contribution to the TLD signal is probably most significant in a region near the center of the core (the neutron spectrum is also best known in this region). The spectrum was normalized to produce the measured ^{235}U fission rate during the TLD exposure. The measured neutron sensitivity of ^{7}LiF (Fig. III-30-5) was used to determine the contribution due to the neutrons. Figure III-30-8 shows the dose contributed by the neutrons as a function of neutron group (each group is ½ lethargy unit wide). A cutoff of 100 keV was used. This energy is near the lower limit of the measured neutron sensitivity. The sensitivity is dropping off rapidly and the results are little affected by the value of this cutoff as long as it is below a few hundred keV. The neutron contribution to the signal amounted to 10%. If one assumes that the relative sensitivity of CaF_2:Mn as a function of LET is the same as that for LiF (Fig. III-30-6) and reduces the calculated neutron sensitivity by the appropriate amount the neutron contribution to the TLD signal would be 5% if CaF_2:Mn had been the dosimeter. Measurements in a fission spectrum show that CaF_2:Mn is half as sensitive to fast neutrons as ^{7}LiF, thus confirming that such reduction is reasonable.[28]

Concluding Remarks

The usefulness of TLD methods for gamma-heating determinations in fast reactors is to some extent compromised by the spectral dependence of the response and by the neutron sensitivity. It is important to realize the extent of these effects if meaningful results are to be obtained. The origins of these effects have been outlined and their extent indicated for particular dosimeter-surrounding material systems in representative fast-reactor environments. The need for continued experimentation and analysis was indicated. It should be realized that the most popular TLD materials at the present time were chosen because of their very high sensitivity and closeness to tissue response. These same TLD materials are not necessarily the most appropriate for gamma-heating measurements in fast reactors where high sensitivity is not as important and where one is interested in having a matched dosimeter-surrounding medium where the surrounding medium usually has a significantly higher average Z than tissue.

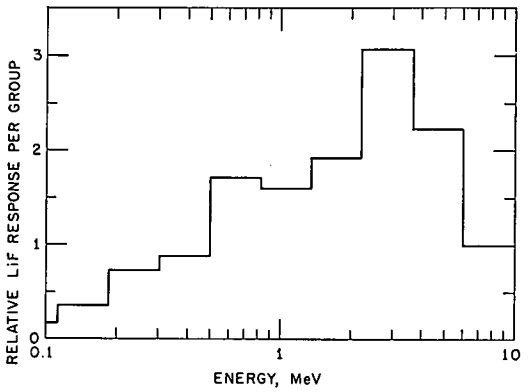

Fig. III-30-8. Group-Averaged Relative Contributions to the LiF-Fe System Response for the Fast Flux Test Reactor Spectrum. *ANL Neg. No. 116-1018.*

References

1. F. H. Attix and W. C. Roesch, Eds., *Radiation Dosimetry*, (Academic Press, New York, 1966) 2nd Ed., Vol. II.
2. J. R. Cameron, N. Suntharalingam and G. N. Kenney, *Thermoluminescent Dosimetry*, (The University of Wisconsin Press, Madison, 1968).
3. G. S. Stanford and T. W. Johnson, *Determination of Gamma-ray Heating in a Critical Facility by Thermoluminescent Dosimetry*, ANL-7373 (1968).
4. J. Adamson, R. M. Absalom, A. B. Baker, G. Ingram, S. K. I. Pattenden and J. M. Stevenson, *ZEBRA 6: Dilute Plutonium-fueled Assembly*, Proc. Intern. Conference on Fast Critical Experiments and Their Analysis, October 10–13, 1966, Argonne, Illinois, ANL-7320, pp. 216–230.
5. D. J. Hill and W. D. Rankin, *Comparison of Experimentally Measured and Calculated Radiation Environment Internal to the PAX R-1 Reactor*, Trans. Am. Nucl. Soc. **13,** 12 (1970).
6. N. N. Gibson and M. Stuetzer, *An Evaluation of Gamma Dosimetry in a Nuclear Reactor Environment*, NDL-TR-108 (1968).
7. M. Stuetzer and N. N. Gibson, *Neutron Sensitivities of Various Gamma Dosimeters*, NDL-TM-52 (1968).
8. C. L. Wingate, E. Tochilin and N. Goldstein, *Response of*

Lithium Fluoride to Neutrons and Charged Particles, F. H. Attix, Ed., Proc. Intern. Conference on Luminescence Dosimetry, Stanford University, 1965 (USAEC Division of Technical Information, 1967) pp. 421–434.
9. G. G. Simons, *Thermoluminescent Dosimetry Applied to Gamma Ray Dose Measurements in Critical Assemblies*, Applied Physics Division Annual Report, July 1, 1969 to June 30, 1970, ANL-7710, pp. 289–294.
10. L. H. Gray, *The Absorption of Penetrating Radiation*, Proc. Roy. Soc. **A122**, 647 (1929).
11. L. H. Gray, *An Ionization Method for the Absolute Measurement of Gamma-ray Energy*, Proc. Roy. Soc. **A156**, 578 (1936).
12. W. H. Bragg, *Studies in Radioactivity*, (Macmillan, New York, 1912).
13. G. C. Laurence, *The Measurement of Extra Hard X-rays and Gamma-rays in Roentgens*, Can. J. Res. **A15**, 67 (1937).
14. P. R. J. Burch, *Cavity Ion Chamber Theory*, Radiation Res. **4**, 361 (1955).
15. L. V. Spencer and F. H. Attix, *A Theory of Cavity Ionization*, Radiation Res. **3**, 239 (1955).
16. T. E. Burlin, *A General Theory of Cavity Ionization*, Brit. J. Radiol. **39**, 727 (1966).
17. F. K. Chan and T. E. Burlin, *An Experimental Examination of a General Cavity Theory Using a Solid State Dosimeter*, Brit. J. Radiol. **43**, 54 (1970).
18. T. E. Burlin, *Cavity-Chamber Theory*, F. N. Attix and W. C. Roesch, Eds., *Radiation Dosimetry*, (Academic Press, New York, 1968) 2nd Ed., Vol. I, pp. 331–392.
19. R. D. Evans, *X-ray and γ-ray Interactions*, F. N. Attix and W. C. Roesch, Eds., *Radiation Dosimetry*, (Academic Press, New York, 1968) 2nd Ed., Vol. I, pp. 93–155.
20. M. J. Berger and S. M. Seltzer, *Tables of Energy Losses and Ranges of Electrons and Positrons*, NASA SP-3012 (1964).
21. M. J. Berger and S. M. Seltzer, *Additional Stopping Power and Range Tables for Protons, Mesons, and Electrons*, NASA SP-3036 (1966).
22. J. T. Madell and L. B. Miller, Argonne National Laboratory, (private communication).
23. B. G. Oltman, J. Kastner, P. Tedeschi and J. N. Beggs, *The Effect of Fast Neutron Exposure on the ^{7}LiF Thermoluminescent Response to Gamma-rays*, Health Phys. **13**, 918 (1967).
24. N. Goldstein, W. G. Miller and P. F. Rago, *Additivity of Neutron and γ-ray Exposures for TLD Dosimeters*, Health Phys. **18**, 157 (1970).
25. R. H. Wallace, P. L. Ziemer, J. Kastner and B. G. Oltman, *The Relationship Between Encapsulation and Apparent Fast Neutron-Induced Fading in TLD*, Health Phys. **20**, 221 (1971).
26. A. R. Reddy, K. Ayyangar and G. L. Brownell, *Thermoluminescence Response of LiF to Reactor Neutrons*, Radiation Res. **40**, 552 (1969).
27. J. S. Handloser, *Thermoluminescent Dosimeter as the Gamma Component of Nuclear Accident Dosimeter*, Proc. Intern. Conference on Personnel Dosimetry for Radiation Accidents, I.A.E.A., Vienna, 1965, pp. 115–126.
28. E. Tochilin, *Thermoluminescent Dosimetry for Shielding Studies in a Reactor Environment*, Trans. Am. Nucl. Soc. **13**, 420 (1970).
29. K. J. Puite, *Thermoluminescent Sensitivity of CaF_2:Mn in a Mixed Neutron-Gamma Field*, Health Phys. **20**, 437 (1971).
30. E. Tochilin, N. Goldstein and W. G. Miller, *Beryllium Oxide as a Thermoluminescent Dosimeter*, Health Phys. **16**, 1 (1969).
31. E. M. Robinson and M. Oberhofer, *A Sensitive Ceramic BeO-TSEE-Dosimeter*, Health Phys. **18**, 434 (1970).
32. K. Becker, J. S. Cheka and M. Oberhofer, *Thermally Stimulated Exoelectron Emission, Thermoluminescence and Impurities in LiF and BeO*, Health Phys. **19**, 391 (,1970).
33. M. J. Marrone and F. H. Attix, *Damage Effects in CaF_2:Mn and LiF Thermoluminescent Dosimeters*, Health Phys. **10**, 431 (1964).
34. G. H. Kinchin and R. S. Pease, *The Mechanism of the Irradiation Disordering of Alloys*, J. Nucl. Energy **1**, 200 (1955).
35. G. J. Dienes and G. H. Vineyard, *Radiation Effects in Solids*, R. E. Marshak, Ed., *Interscience Monographs in Physics and Astronomony*, (Interscience Publications, New York, 1957) Vol. II.
36. Neutron Cross Sections, BNL-325, 2nd Ed. (1960).
37. G. G. Simons and G. S. Standford, Argonne National Laboratory (private communication).
38. T. J. Yule and E. F Bennett, *Measured Neutron Spectra in a Number of Uranium- and Plutonium-Fueled Reactor Assemblies*, Nucl. Sci. Eng. **46**, 236 (1971).

III-31. A Precision Remote Controlled Electrometer for Reactor Power Measurements

J. M. Larson

Introduction

Various reactor experiments are performed at the ZPPR facility where the reactor power is measured by using a neutron sensitive ionization chamber and an electrometer. Because of the wide variety of measurements made at the facility, a precision, fast responding, low drift electrometer is required so that the same electrometer can be used for a variety of applications and experiments.

Commercially available electrometers that have been used in the past have, in general, had limited frequency response, excessive drift or noise, poor linearity, or a combination of the above. Because of these problems and the fact that other requirements, such as remote gain selection and zeroing, exist at the ZPPR facilit it was decided to develop an electrometer that w better suited for the particular requirements at ZPPR.

In general, an electrometer was needed that would meet the following specifications:

(1) Current ranges from 10^{-5} to 10^{-10} amps full scale by range resistor change in 6 steps. Output voltage of 10 V full scale on each range.

(2) Input offset current of 10^{-13} amp maximum.

(3) Output 10 to 90 % response time of 5 milliseconds or less on gain ranges of 10^{-5} through 10^{-7} amps, and 30 milliseconds or less on gain ranges of 10^{-8} through 10^{-10} amps—this output response to be obtained with input capacities as high as 1000 pfd.

(4) Integral non-linearity less than 0.025 % of full scale for outputs from 5 to 100 % of full output.

(5) Output drift less than 0.025 % per 24 h at constant temperature. Short term drift less than 0.01 %, and drift due to temperature changes to be less than 0.01 %/°C.

(6) Remote gain selection and remote zeroing.

(7) Provision for remote gain control by computer.

Basic Circuit

Because of the need for remote zeroing, the over-all electrometer was designed in two sections as shown in Fig. III-31-1.

The first section contains the electrometer amplifier and is located in the reactor cell. The second section contains a terminating amplifier and driver that has provision for gain and dc zero adjustment. The second section is located at the control room and is driven by the remote electrometer via shielded differential lines.

The gain ranges of the electrometer are determined by the shunt feedback resistors around the electrometer amplifier. These resistors are selected by reed relays which are controlled remotely by the range selection circuitry of the terminating amplifier unit. Gain and zero offset adjustments are made at the terminating amplifier by the variable resistors shown in the feedback and offset circuitry of the output driving amplifier.

The range selection circuitry of the terminating amplifier unit has a three line binary input so that the electrometer's gain ranges can also be selected remotely by computer control.

Detailed Circuit Description

The circuit diagram of the remote electrometer unit is shown in Fig. III-31-2. The electrometer amplifier is comprised of an Intech A-127 operational amplifier and transistors Q_3 and Q_4. Transistors Q_3 and Q_4 are

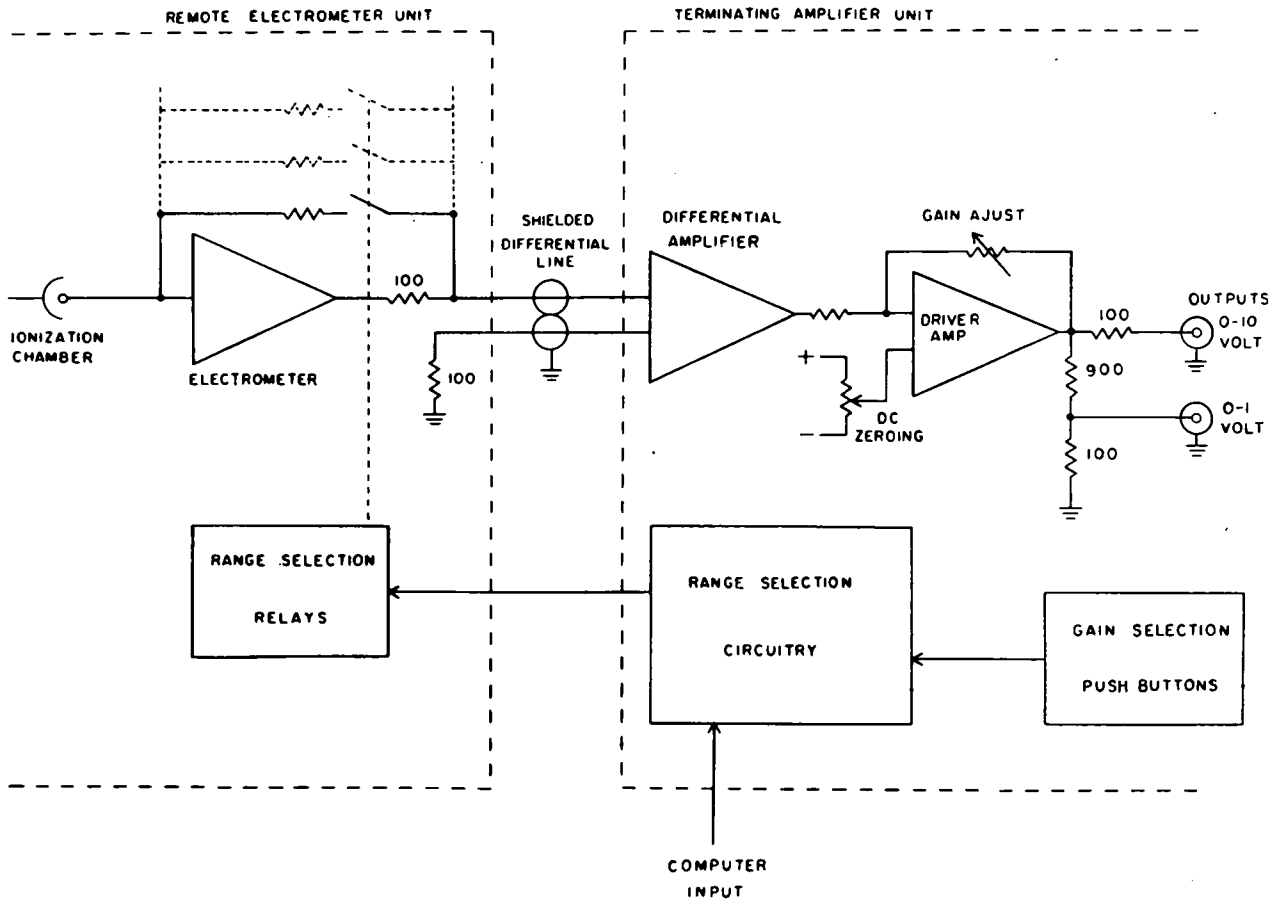

Fig. III-31-1. Block Diagram of the Overall Electrometer System. *ANL-ID-103-A11897.*

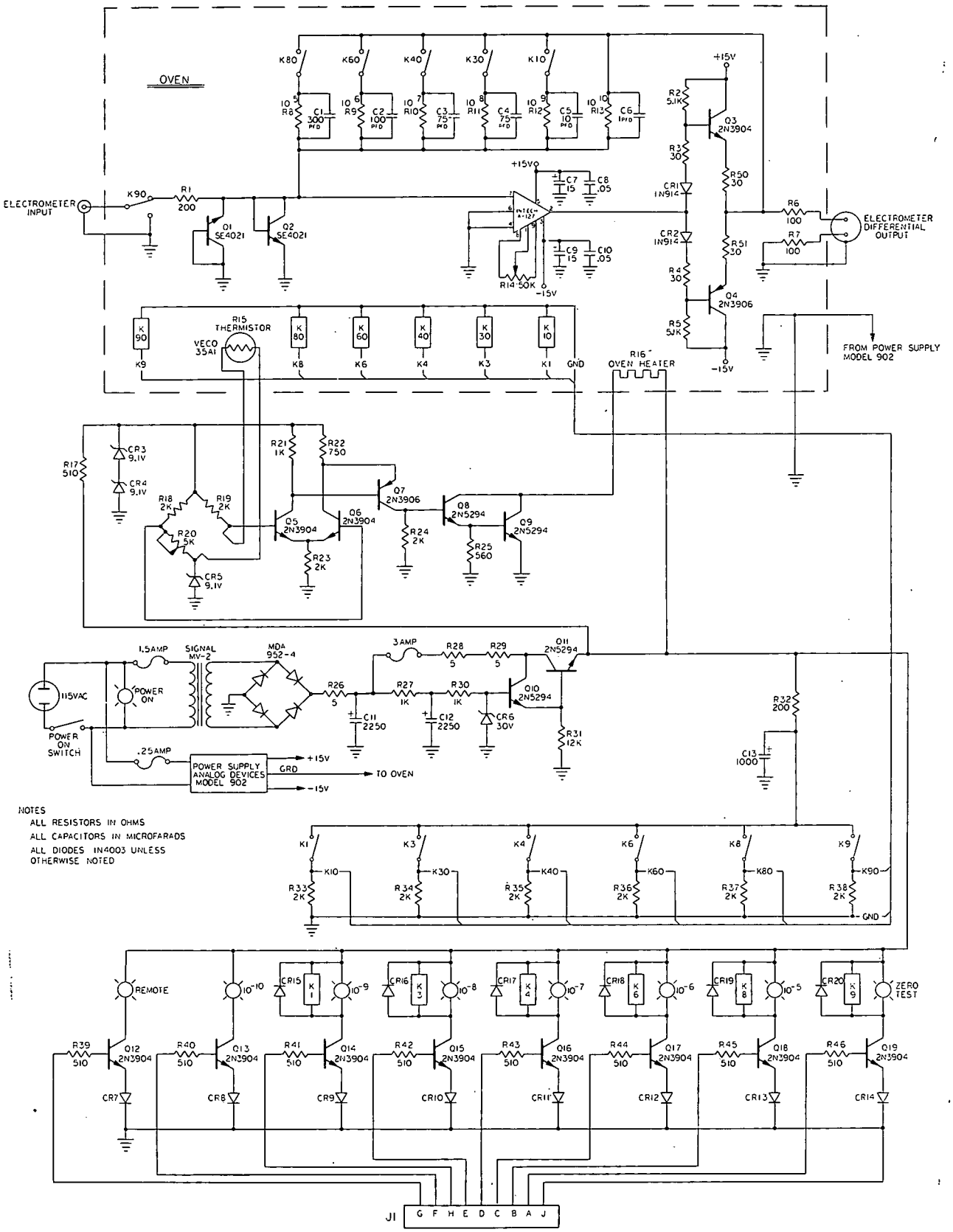

FIG. III-31-2. Schematic Diagram of Remote Electrometer. *ANL-103-A11820 Rev. 1.*

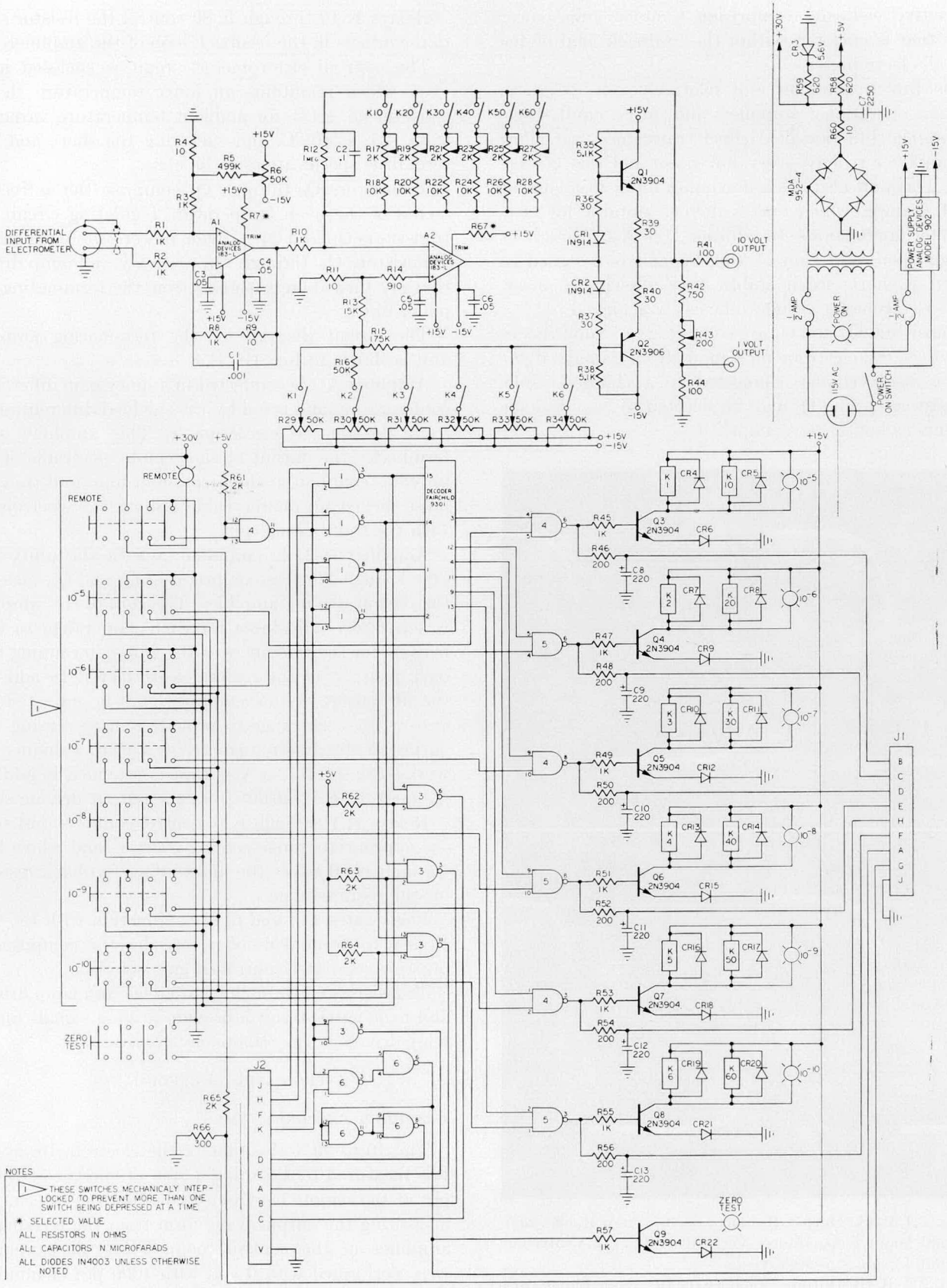

FIG. III-31-3. Schematic Diagram of Terminating Amplifier Unit. *ANL-103-A11821 Rev. 1.*

the active elements comprising a unity gain power stage that is enclosed within the feedback loop of the over-all electrometer.

The Intech amplifier is a relatively new design in modular operational amplifiers and, in its input stage, uses special junction field effect transistors that allow the amplifier to have very low noise and low voltage drift. This unit also has a maximum input bias current of 10^{-13} amps, which makes it very suitable for electrometer applications. In addition, the A-127 amplifier has an open loop gain of 100,000 and is designed so that it is short circuit stable, thus allowing a linear, stable electrometer design to be easily achieved.

Transistors Q_1 and Q_2 are connected as clamp diodes to protect the electrometer's input from damage if the unit is inadvertently connected to a charged cable. Transistors Q_1 and Q_2 may be selected to have leakage currents as low as 10^{-14} amps.

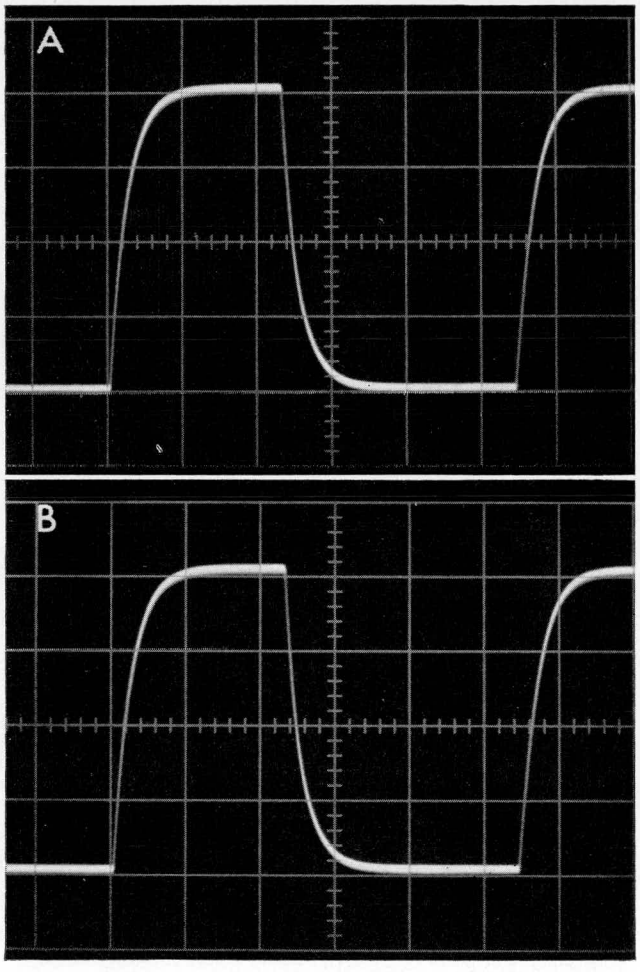

FIG. III-31-4A. Output Response on 10^{-5} Amp Range. Zero External Input Capacitance. Vertical Scale = 2 V/division. Horizontal Scale = 5 ms/division.

FIG. III-31-4B. Output Response on 10^{-5} Amp Range. 1000 pfd External Input Capacitance. Vertical Scale = 2 V/division. Horizontal Scale = 5 ms/division.

Relays K-10 through K-80 control the resistor selection contacts in the feedback loop of the amplifier.

The over-all electrometer circuit is enclosed in an oven which maintains an inner temperature that is constant to $\pm 1\%$ for ambient temperature variations from $(25 \pm 10)^\circ C$, thus allowing the short and long term drift specifications to be met.

Transistors Q_5 through Q_9 comprise the active elements of the oven temperature regulating circuit and transistors Q_{10} and Q_{11} provide power supply regulation. Transistors Q_{12} through Q_{19} are relay and lamp drivers that are turned on by signals from the terminating maplifier unit.

The circuit diagram of the terminating amplifier unit is shown in Fig. III-31-3.

Amplifier A-1 is connected in a unity gain differential configuration and is fed by the shielded differential line from the remote electrometer. This amplifier stage terminates the output of the remote electrometer and provides common mode rejection of hum and transient noise picked up on the cable linking the electrometer with the terminating unit.

Amplifier A-2, in conjunction with the unity gain driver stage which is comprised of Q_1 and Q_2, make up the output driving amplifier. The gain of this amplifier is separately adjustable for each gain range to compensate for the tolerances of the gain determining feedback resistors of the remote electrometer. In addition, the dc output of this amplifier may be adjusted separately for each range to provide remote zeroing. The output of the driver stage drives a 10-to-1 divider network so that a 0 to 1 V output is provided in addition to the 0 to 10 V output from the output driving stage.

Relays K-1 through K-6, control contacts that select the appropriate range-zeroing resistors and relays K-10 through K-60 select the appropriate feedback resistors for the required gain.

Logic gates 1, 3 and 6, in conjunction with the 9301 Binary to decimal decoder, decodes the computer inputs for computer controlled gain selection.

Transistors Q_3 through Q_9 are relay and lamp drivers, and logic gates 4 and 5 provide driving signals for the relay drivers in the remote electrometer unit.

Operating Performance

Measured Response Times

The 10 to 90% rise time of the electrometer system was measured by injecting a step of current at the input of the remote electrometer in the reactor cell, then measuring the output wave form from the terminating amplifier in the control room. These measurements were performed with 0 and with 1000 pfd of input capacity added to the input of the electrometer to simulate the expected extremes of input capacity that might

be met in actual use. Photographs of the electrometer's response are shown in Figs. III-31-4 and III-31-5 for the 10^{-5} and 10^{-10} amp ranges, respectively. In each case there is essentially no significant increase in rise time when the electrometer's input is loaded with 1000 pfd of external capacity.

NOISE

The noise generated by the electrometer is very low, approximately 5 mV peak to peak with zero external input capacity on the 10^{-10} range, and 30 mV peak to peak with 1000 pfd external on that range. The low noise generated by the unit is due almost entirely to the noise characteristics of the junction FETs used in the input of the A-127 amplifier.

Photographs of output noise on the 10^{-10} range with 0 and with 1000 pfd of input capacity are shown in Fig. III-31-6.

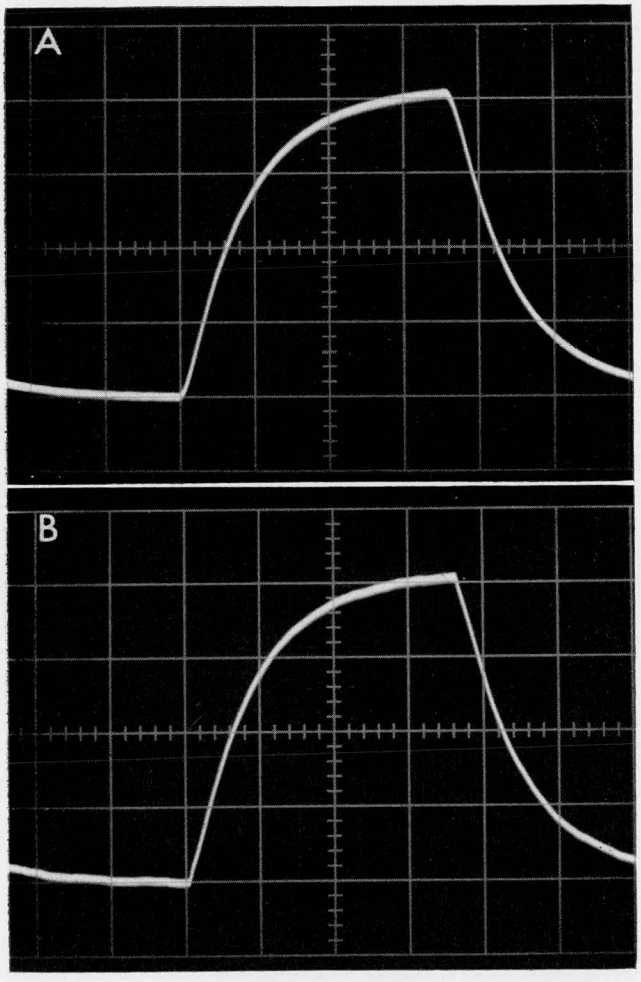

FIG. III-31-5A. Output Response on 10^{-10} Amp Range. Zero xternal Input Capacitance. Vertical Scale = 2 V/division. Horizontal Scale = 20 ms/division.

FIG. III-31-5B. Output Response on 10^{-10} Amp Range. 1000 pfd External Input Capacitance. Vertical Scale = 2 V/division. Horizontal Scale = 20 ms/division.

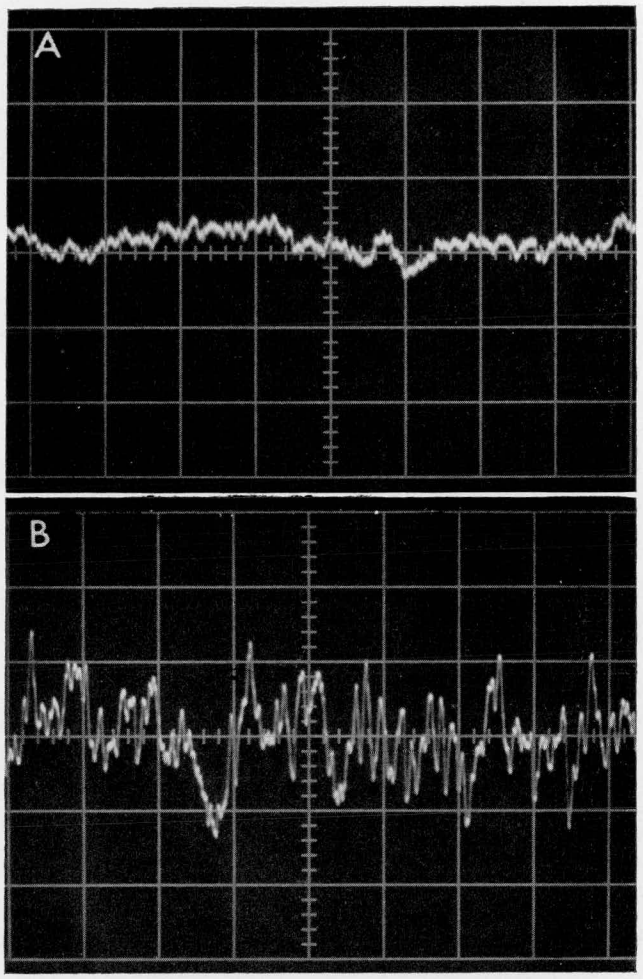

FIG. III-31-6A. Electrometer Output Noise on 10^{-10} Range with Zero External Input Capacitance. Output Voltage = 10 V for 10^{-10} Amp Input. Vertical Scale = 5 mV/division. Horizontal Scale = 10 ms/division.

FIG. III-31-6B. Electrometer Output Noise on 10^{-10} Range with 1000 pfd External Input Capacitance. Output Voltage = 10 V for 10^{-10} Amp Input. Vertical Scale = 10 mV/division. Horizontal Scale = 10 ms/division.

DRIFT AND LINEARITY

The measured short and long term dc output drift of the unit is less than 0.01 % of full scale.

The integral non-linearity was measured at 0.025 % maximum which was the limit of the measuring apparatus.

CONSTRUCTION

A photograph of the remote electrometer and the terminating amplifier unit is shown in Fig. III-31-7. Both units are designed with standard 19 in. panels for rack or cabinet mounting. The zeroing potentiom-

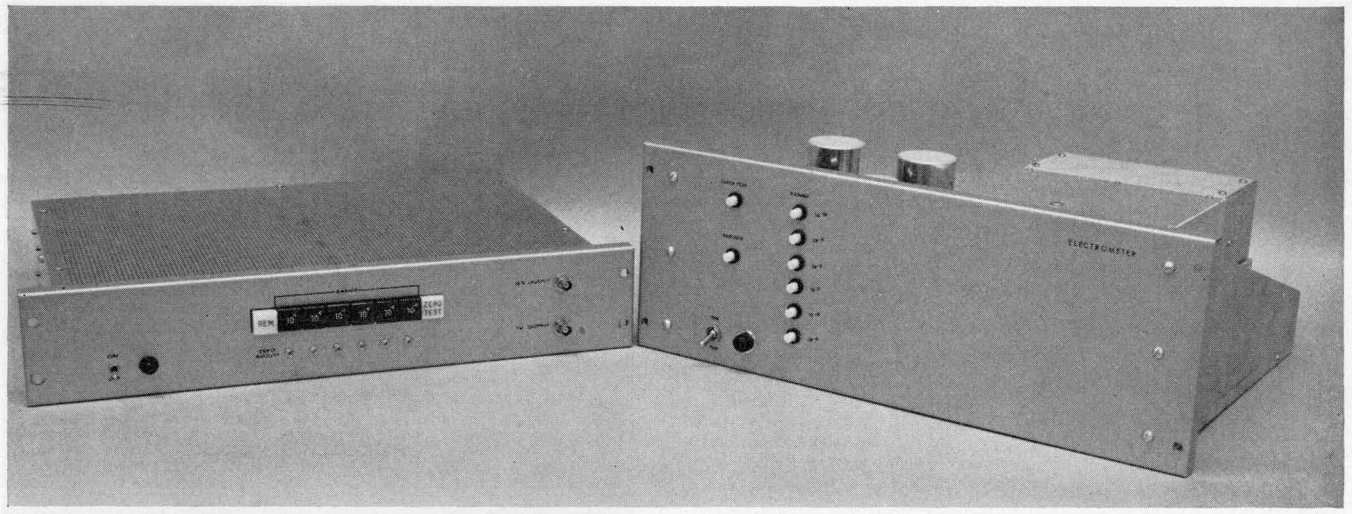

FIG. III-31-7. Photograph of Remote Electrometer and Terminating Amplifier Units. *ANL-ID-103-A11902.*

eters of the terminating amplifier are panel mounted below their respective range selection push buttons and the push buttons are internally lighted to indicate the particular range selected. Indicator lights are also mounted on the panel of the remote electrometer to indicate the gain range in which the unit is operating.

III-32. Effectiveness of the Dual Heater Temperature Control System in the ZPPR Reactivity Doppler Mechanism

J. M. GASIDLO, R. E. KAISER, D. P. PRUETT and J. C. YOUNG

INTRODUCTION

The heat lost from a ZPPR Doppler sample at elevated temperatures is removed from the reactor by air-cooling the sample. In the past, very high coolant air flow rates were necessary to reduce to negligibly small values systematic reactivity effects caused by the heat loss. This meant the use of high-pressure air compressors with the attendant refrigerators, dryers, and finally a temperature regulating stage. The system described herein eliminates the entire expensive high pressure cooling air system by using a low pressure blower in conjunction with a dual heater system which is balanced to provide constant heat loss to the reactor system at all Doppler sample temperatures.

DESIGN CONCEPT

The Doppler sample in use at ZPPR is of the same basic design which has been developed in the Applied Physics Division at Argonne.[1,2] An element consists of oxide pellets contained in a sealed tube with the sample heater wound around the outside of the tube. The Doppler capsule consists of the element supported in a small vacuum-tight silvered tube. The individual components and an assembled capsule are shown in Fig. III-32-1. The Doppler capsule is mounted in an oscillator rod which provides the necessary vacuum and electrical connections for the element, paths for the sample cooling air, and trays for balance material to minimize reactivity swings when the rod is oscillated. The rod oscillates in the reactor through a guide tube and additional cooling air is passed between the rod and guide tube to reduce heat transfer from the rod to the reactor.

The ZPPR Doppler equipment mounted in the reactor for an experiment is shown schematically in Fig. III-32-2. The Doppler capsule cooling air enters the rod at the drive end and exhausts from the far end of the rod, beyond the airflow seal. With this design, the two air flow paths are never mixed and the impedance of each path is essentially constant for all rod positions. Therefore, the cooling air flow rate down each path constant for all rod positions.

Cooling air flow is provided by a small axial fan blower which delivers from 20 to 80 CFM at a constant pressure difference of 2.5 psi. This provides a total flow

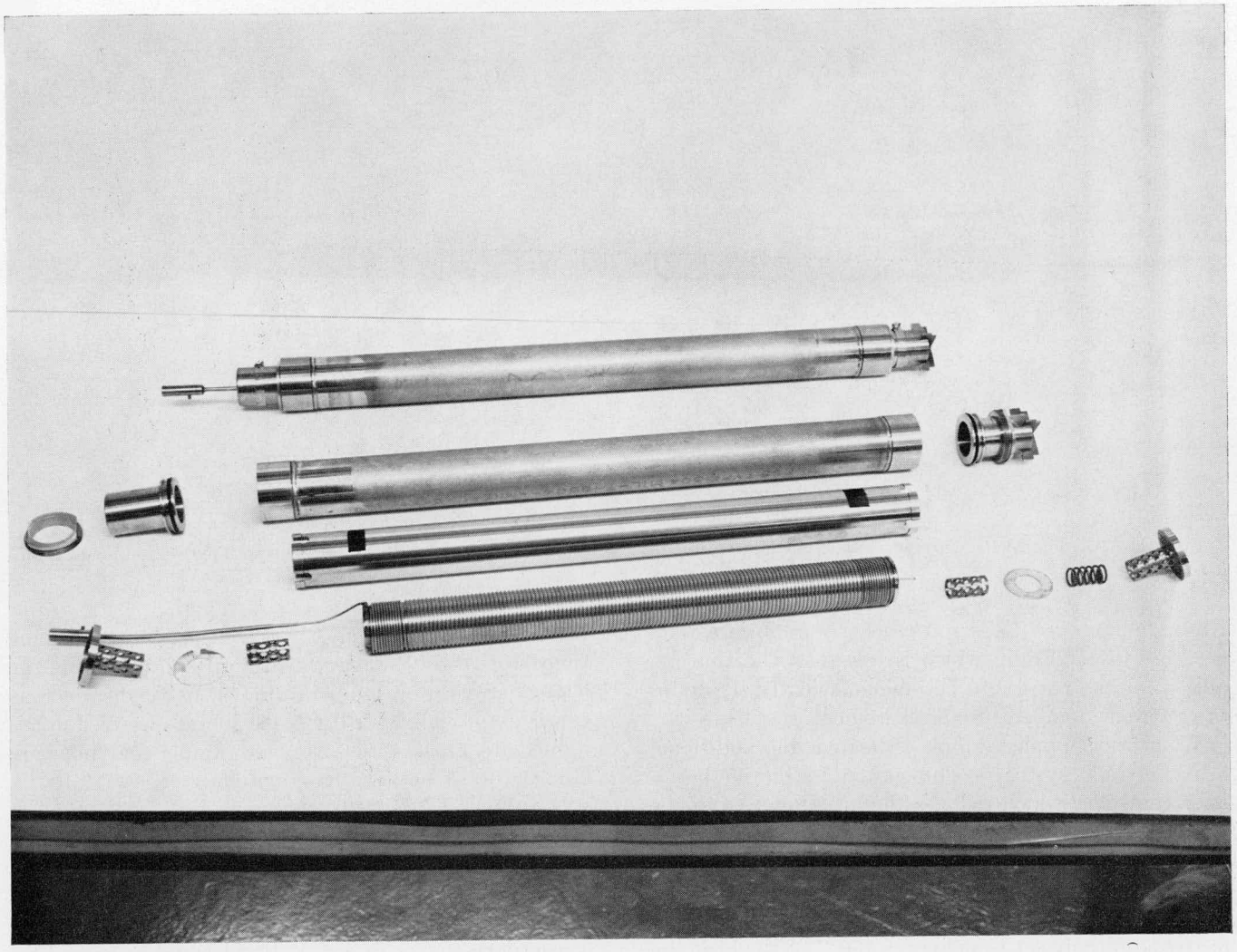

FIG. III-32-1. Individual Components and an Assembled ZPPR Reactivity Doppler Capsule. *ANL-103-A11731.*

rate down each path of ~25 CFM. By using the blower to pull cell air through the rod and exhausting the air from the blower directly into the cell temperature control system, the cell acts as a very large source of temperature-controlled air (68 ± 0.25°F) and the Doppler sample is not affected by the heat input of the blower.

In the past, such a low coolant air flow rate would have been insufficient. The significant difference in the new system which allows the use of such low flow rates is the addition of the auxiliary heater which is wound around the Doppler capsule. This is shown in Fig. III-32-3.

When an experiment is being performed, the blower is turned on and the auxiliary heater is set to deliver ~150% of the heat the Doppler capsule will lose at the highest sample temperature. The thermistor mounted on the end of the Doppler capsule in the cooling air path is used as a sensor for the auxiliary heater con-

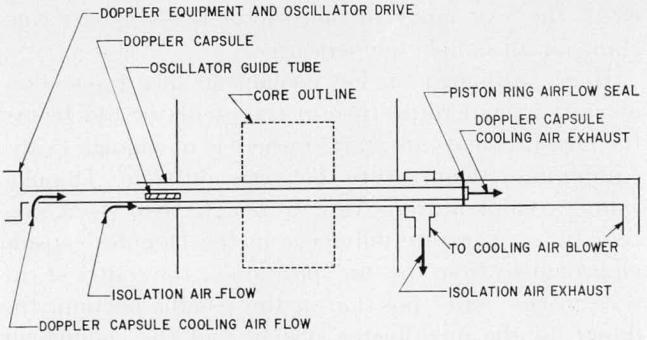

FIG. III-32-2. Schematic of the ZPPR Reactivity Doppler Mechanism Mounted in the Reactor. *ANL-103-A11967.*

troller which maintains the air at constant temperature at that point. Since constant temperature cell air is flowing through the rod at a constant rate, heat input to the system is constant. With such low air flow rates, there is a 15°C rise in the cooling air temperature.

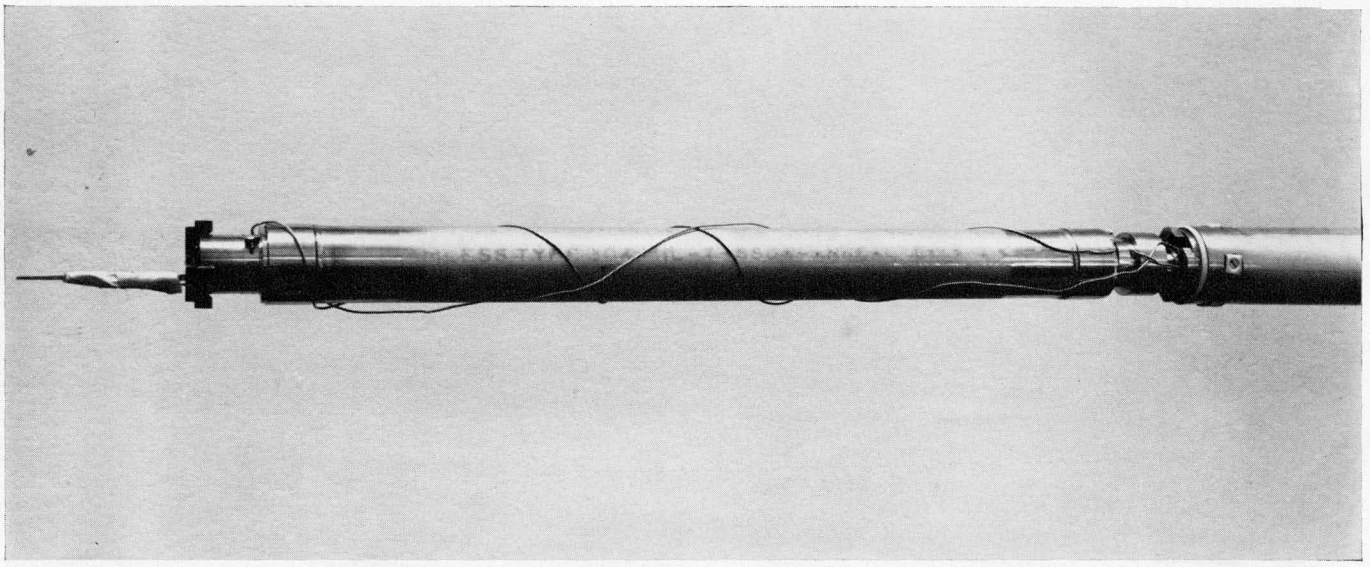

FIG. III-32-3. The ZPPR Doppler Capsule Mounted on the Oscillator Rod with Auxiliary Heater and Thermistor Lead. *ANL-103-A11928.*

Normally, the oscillator rod reaches equilibrium temperature in ~30 min, which is less than the time required for the reactor to become sufficiently stable for the reference temperature measurement.

When the Doppler sample is heated, the additional heat loss to the system is compensated for by the thermistor controller which reduces the heat input from the auxiliary heater. Since the sample heat loss is to the Doppler capsule and the auxiliary heater is wound around the capsule, the two heat sources affect the system as a single heat source. Since the auxiliary heater is initially set to deliver ~150% of the heat the sample will lose at its highest temperature, and the thermistor sensor has a very large temperature coefficient, the heat input to the reactor is essentially constant for all sample temperatures.

Hence, although the low coolant air flow rates allow an initial temperature rise in the oscillator rod before the measurements are started, there is no change in the equilibrium temperature between different Doppler sample temperatures. Also, although there is a systematic temperature difference in the Doppler capsule environment from the "in" position at the center of the core to the "out" position in the reactor plenum, the design of the dual-heater system and the cooling air paths forces this difference to be the same for all sample temperatures and hence it does not affect the experimental results.

System Performance and Tests

Tests have been performed to measure both the interaction of the heating system with the reactor and the variation of total heat input with sample temperature. The interaction effect was measured by oscillating the rod with the auxiliary heater off and observing the change in reactor temperature when the heater was turned on. A change of 0.4 ± 0.1°C was observed in the immediate area of the Doppler sample and nowhere else. A total reactor interaction effect of $\sim 1 \times 10^{-8}\ k$ was estimated for a 10% change in heat input. Such a change in heat input would also result in a temperature change in the oscillator rod balance material in the cooling path downstream from the dual-heater. Using the results of the ZPPR experiments (see Paper II-44), a reactivity change of $\sim 5 \times 10^{-8}\ k$ could be caused by a 10% change in total heat input from the dual heater system.

Total heat input from both heaters was determined for a number of sample temperatures and experiments by measuring the voltage and current for each heater. All results were compared with the value for the auxiliary heater at reference sample temperatures. For low sample temperatures, the sample heater controller was set to overshoot very slightly and the sample cooled slowly by ~1% of the difference from the reference temperature. At intermediate sample temperatures, the thermal inertia of the sample resulted in long term oscillations of ~2% peak-to-peak in sample temperature. Data for these runs were recorded periodically for several cycles to determine the average heat input by the heaters and thus the heat loss rate to the reactor system. The temperature variations were so small that no corresponding variations could be found in the reactivity signal. The heat input from the sample heater was almost constant at the highest sample temperatures, but again the data were recorded periodically to

obtain an average over the entire high temperature portion of the experiment.

The measured average total heat input from both of the heaters was within the precision of the meters, that is, $\sim \pm 3\%$. This means that the balanced dual-heater system holds systematic reactivity effects caused by heat loss from the sample to no more than $\pm 2 \times 10^{-8}$ k.

Conclusions

A simple and inexpensive cooling air temperature control system has been developed for the ZPPR reactivity Doppler experiments which holds systematic reactivity effects to $\pm 2 \times 10^{-8}$ k. This is completely adequate for the wide range of experiments normally performed in the ZPPR.

If it were necessary for a special experiment, the systematic temperature effects could be reduced to 10^{-9} k by the use of more expensive control equipment.

References

1. G. J. Fischer, D. A., Meneley, R. N. Hwang, E. F. Groh and C. E. Till, *Doppler Effect Measurements in Plutonium-Fueled Fast Power Breeder Reactor Spectra*, Nuc. Sci. Eng. **25**, 37–46 (1966).
2. C. E. Till, R. A. Lewis and E. F. Groh, *Doppler Effect Measurements on a Dilute Carbide Fast Assembly - ZPR-6 Assembly 4Z*, Reactor Physics Division Annual Report, July 1, 1965 to June 30, 1966, ANL-7210, pp. 129–137.

III-33. Zero Power Plutonium Reactor (ZPPR) Roof Filter Test Experience

P. B. McCarthy, R. G. Matlock and R. L. Cheever

The filtration containment for ZPPR is provided by a large (50 ft diam) sand filter backed up with high efficiency particulate (HEPA) filters. This is a unique reactor containment system but utilizes common techniques for filtering airborne radioactive particulates. Periodic in-place efficiency tests are required to determine filtration efficiency and to detect any deterioration which may be occurring. A system for testing the ZPPR sand filter had been developed and two tests, performed a year apart, have been conducted. The sand filter, with gravel above and below the sand, is the roof for the reactor cell. This is covered with a structure called the top hat which contains 285 HEPA filters. A cross section of the top of the reactor cell, the gravel sand roof, and the top hat are shown in Fig. III-33-1.

Description of Roof and Test Equipment

As shown in Fig. III-33-1, thick layers of gravel are placed above and below the sand layers. The sand is held from dropping through the gravel with 26 mesh wire screen (0.021 in. wide square hole size), which is layed on top of the gravel. The gravel and sand roof is held on top of the circular reactor cell with 1⅞ in. diam catenary cables on 15 in. center lines in a square pattern. The gravel and wire screen act as a support for the sand layers and also hold the sand in place in case high velocity gas were to pass through the filter. The sand is the principal filtering medium, with practically no filtering benefits coming from the gravel.

The lower layer is 50 ft in diam and 12 in. thick and the upper layer is 62.5 ft in diam and 18 in. thick. The step was placed in the filter to preclude the possibility of channeling up along the wall but because of the step, the velocity of the test aerosol changes. As shown in Fig. III-33-2, the percent penetration of the test aerosol is quite sensitive to the superficial velocity (velocity assuming no area is occupied by sand).

The tests to determine percent penetration through the sand filter were run using dioctylphathalate (DOP) as the test aerosol. This aerosol is used in testing HEPA filters and is commonly called smoke since it has the appearance of smoke. It is discussed in RDT Standard F 3-34. In order to obtain a velocity of aerosol across the sand filter which would result in a penetration sufficient to read with particulate detection units a 100 HP fan was used to pump 15,000 cfm of air into the bottom of the sand filter. Eight standard DOP generators, also described in RDT F 3-34, were used to produce 49.2 μg/liter of DOP. The DOP was injected into the 15,000 cfm air stream, and the air and DOP passed through two 24 in. diam hoses to the roof.

The DOP concentration was measured just before it reached the sand filter and again in the discharge from the sand filter. Two TDA-2C smoke detectors made by Air Techniques Inc. were used to measure smoke concentration. One unit had minor scale divisions to 0.0002% and the other unit had minor scale divisions to 0.002%.

Test Results and Conclusions

At the 5 fpm minimum superficial velocity of aerosol through the sand filter the pressure drop was 9.9 in H_2O. Other pressure drops in the system brought the

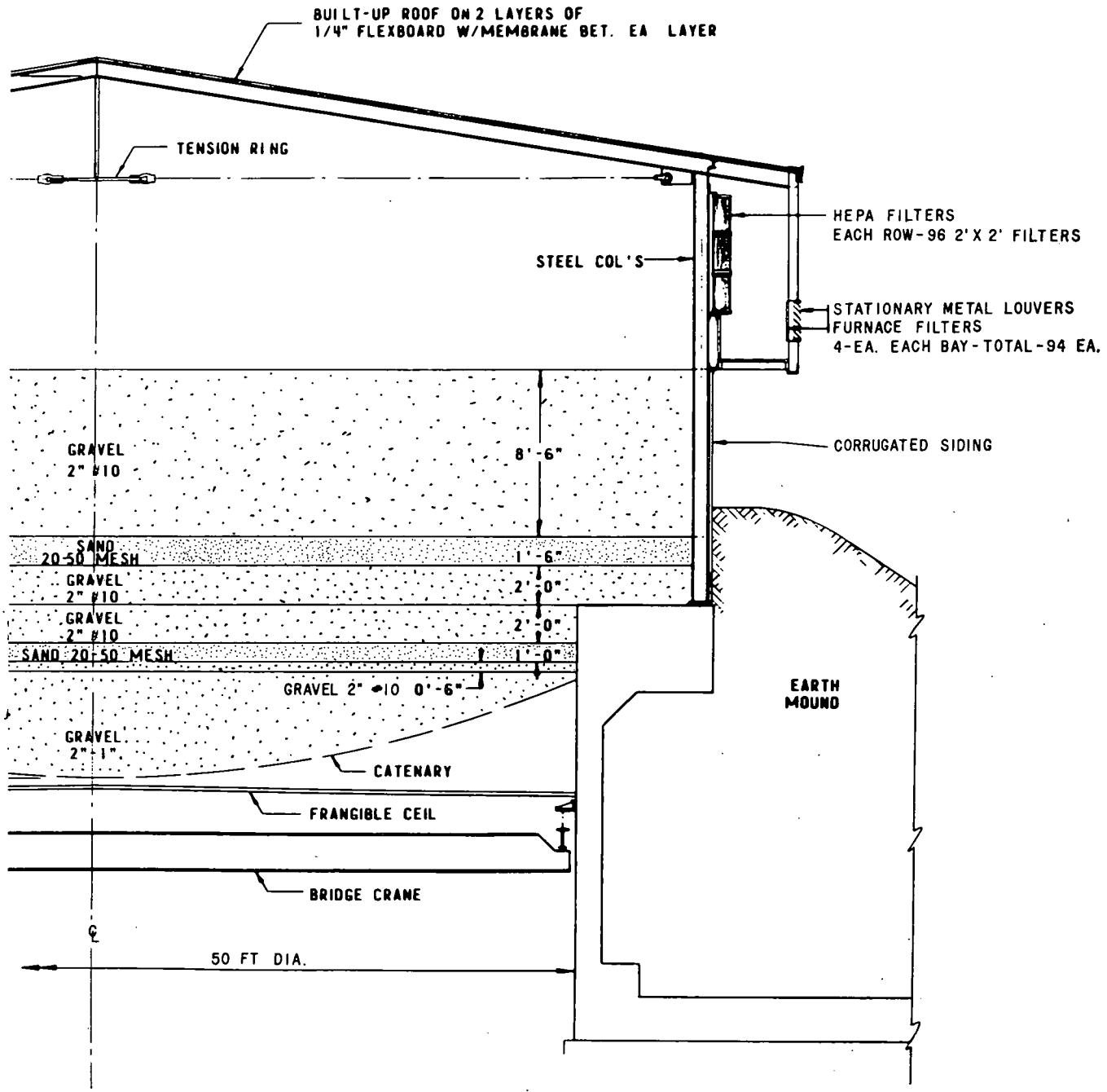

FIG. III-33-1. ZPPR Roof Cross Section. *ANL-ID-108-A11898*.

discharge head at the fan to 19 in. H_2O. The superficial velocity in the lower layer of sand was 7.8 fpm. The laboratory test results plotted in Fig. III-33-2 show a penetration of 0.0014% at 5 fpm and 0.004% at 7.8 fpm. Inplace tests on the ZPPR roof showed an average penetration of 0.0025 ± 0.0005% in both the 1970 and 1971 tests. Figure III-33-2 presents the laboratory test results and the ZPPR field test results.

Penetration data from in-place testing of the ZPPR roof with DOP aerosol has been shown to agree with penetration results in laboratory tests. Therefore, ZPPR roof DOP penetration can be correlated to plutonium aerosol penetration data obtained in laboratory tests.

The in-place tests showed that the ZPPR roof sand filter was in good condition and that it was not deteriorating. The tests require a considerable amount of equipment and testing time, but in view of the importance of the containment, the effort is justified.

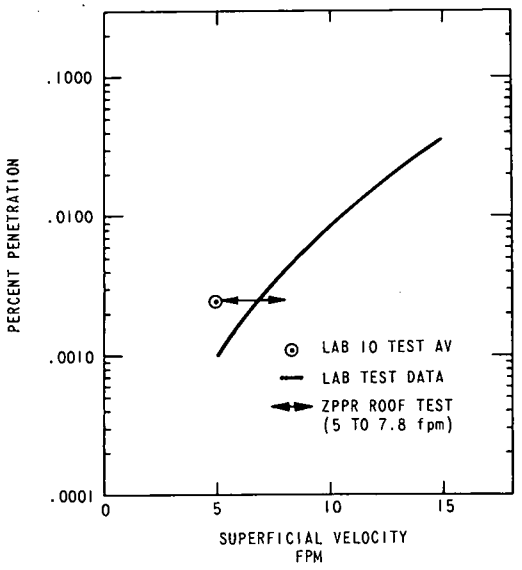

FIG. III-33-2. DOP Penetration Tests. *ANL-ID-103-A11899.*

III-34. Relocating the Argonne Fast Source Reactor (AFSR)

R. O. VOSBURGH, R. G. MATLOCK, P. B. MCCARTHY and R. N. CURRAN*

INTRODUCTION

The Argonne Fast Source Reactor is a compact reactor used as a source of both fast and thermal neutrons. It consists of a right circular cylindrical core, 4½ in. in diam by 4½ in. high, and contains 21½ kg of 93% enriched uranium clad in 304 SS. The core is entirely surrounded by a depleted uranium blanket, also right circular, 20½ in. in diam by 20½ in. high. The reactor has a 4 x 4 x 6 ft thermal column, various penetrations to the blanket and core, and a fast column. The core and blanket are surrounded by a nominally 4½ ft thick, high-density concerete biological shield. The reactor is air cooled and can operate continuously at about 900 W within the 120°C maximum temperature limitation. A detailed description of the reactor is provided in Ref. 1 and 2.

AFSR provides neutrons in both the thermal and fast energy ranges for laboratory experiments. It has been used for technique development, such as proton recoil spectrometer, Rossi-α measurements, foil irradiation calibrations, fission chamber and detector comparions and calibrations.

The AFSR had operated at the ANL West Area of the National Reactor Testing Station (Idaho) since 1959. During the planning of the ZPPR Facility in the ANL East Area, it was recognized that better utilization of AFSR could be realized at this new facility. A room was designed and a new biological shield installed for AFSR during construction of ZPPR. The reactor and associated components were moved from the ANL West Area to the ZPPR Facility in late 1970.

RELOCATION

The disassembly, moving, and reassembly at the new site of the reactor components was accomplished by ANL personnel. Each component was removed and shipped to the new site where it was inspected, necessary maintenance performed, and then installed.

The core was loaded into three separate approved birdcages and shipped for storage in the Laboratory and Office Building storage vault in the ANL East Area. Following the pre-startup checkout of the reactor, the core was removed from storage for inspection. Several blemishes on the core cladding were discovered at this time. It was decided that the blemishes did not constitute an operational hazard and the fuel plus cladding was to be used "as is". A periodic inspection of the core cladding is in effect to continue surveillance of the blemishes.

The AFSR blanket (2100 kg of depleted uranium)

* EBR-2 Project, Argonne National Laboratory.

TABLE III-34-I. DIMENSIONS OF EXPERIMENTAL FACILITIES

Experimental Facility & Description	Dimensions
Core (Including 304 SS Cladding)	Diam: 4.51 in. Height: 4.68 in.
Glory Hole Horizontal axis of hole intercepts axis of core 0.15 in. above center of core. Center point of hole is 66⅛ ± 1/16 in. from the face of shield (Glory Hole #1), and is 66 1/16 ± 1/16 in. through Glory Hole #2.	Effective Inside Diam: 0.514 in. (with thimble)
Grazing Hole Horizontal axis of hole passes axis of core at a distance of 3.875 in. and lies 1.277 in. below center of core. Minimum blanket thickness between grazing hole and core is 0.984 in. Center point of grazing hole is 66⅛ ± 1/16 in. from face of shield through Grazing Hole #1 and 66 1/16 ± 1/16 in. through Grazing Hole #2.	Diam: 1.078 in.
Beam Hole Horizontal axis of hole intercepts axis of core 0.015 in. above center of core. Hole itself terminated in blanket 2.852 in. from axis of core. Minimum blanket thickness between beam hole and core is 0.500 in. The beam hole liner prevents insertion of anything farther than 4 in. from inner end of hole.	Diam: 2.218 in. Effective Inside Diam: 2.150 in. (with liner)
Graphite Thermal Column The blanket cavity is embedded 15¼ in. into the end of the thermal column. Minimum thickness of graphite between the first hole and the reactor is 8¾ in. Between the second hole and the reactor is 2 ft 8¾ in. of graphite. The holes have been reamed to 2½ in. Stringers can be removed along the axis of the thermal column to accept equipment up to 16 x 16 in. Center of the thermal column is 66 ± ¼ in. from either shield face in either hole.	Height: 4 ft Width: 4 ft Length: 6 ft 2½ in. max. 4 ft 9 in. min.
Miscellaneous Rossi alpha at delayed critical. Prompt neutron lifetime (assuming β effective = 0.0068). Operational core loading. Estimated critical mass. Coolant flow.	 3.65×10^5 sec^{-1} 1.86×10^{-8} sec 21.665 kg U (enriched) 21.25 kg U (enriched) ~78 cfm

was checked for dimensions prior to shipment. Upon receipt at the ZPPR/AFSR facility the dimensions were measured again to assure that no deformation occurred in handling the blanket. Such deformation could conceivably cause a change in reactivity of the system.

The relocation left AFSR essentially unchanged except for the improvement modifications discussed below.

MODIFICATIONS

The concrete shield has been modified in two significant ways. At the original site the shield was poured on top of the foundation. Measurements indicated undesirable radiation streaming at the shield/foundation interface, and additional shielding around the base was required. Taking this into account, the new shield/foundation interface is located two feet below floor level. Measurements of radiation levels with the new shields showed that streaming has been eliminated.

The second modification made to the shield was the replacement of the stepped beam hole plug with a four foot square hole and a rollaway concrete plug. This is called the *fast column* and is shown in Fig. III-34-1.

The fast column modification was included in the design in anticipation of a future use where, for instance, matrix tubes of the critical assembly type can be mounted in place of the rollaway plug. This would allow studies on subcritical configurations using AFSR as a fast neutron source.

The AFSR core is of a split design with the bottom ⅖ of the fissile material and depleted uranium plug attached to a pneumatic ram. At AFSR in the West Area, this ram had a total stroke of 43 in. (the lower 37 in. of travel are at a nominal 18 in./min and the last 6 in. of travel are regulated by a two speed screw jack). The pneumatic ram portion of the safety plug has been modified in the relocated AFSR. The lower portion of core is mounted on a pneumatic ram whose total stroke is 8 in. The entire 8 in. movement is regulated by a two speed screw jack. The short stroke pneumatic ram is mounted, in turn, on a movable drive plate. The drive plate can be lowered 35 in., positioning the lower portion of the core in the pit area for inspection or maintenance.

Minor modifications include items such as installing a new linear channel, a new log-period chart recorder, changing the lamp power supply to 24Vdc, modifying the slow shutdown circuit and eliminating the separate dc power key switch. These modifications were included either for improving operational characteristics or up dating the system components.

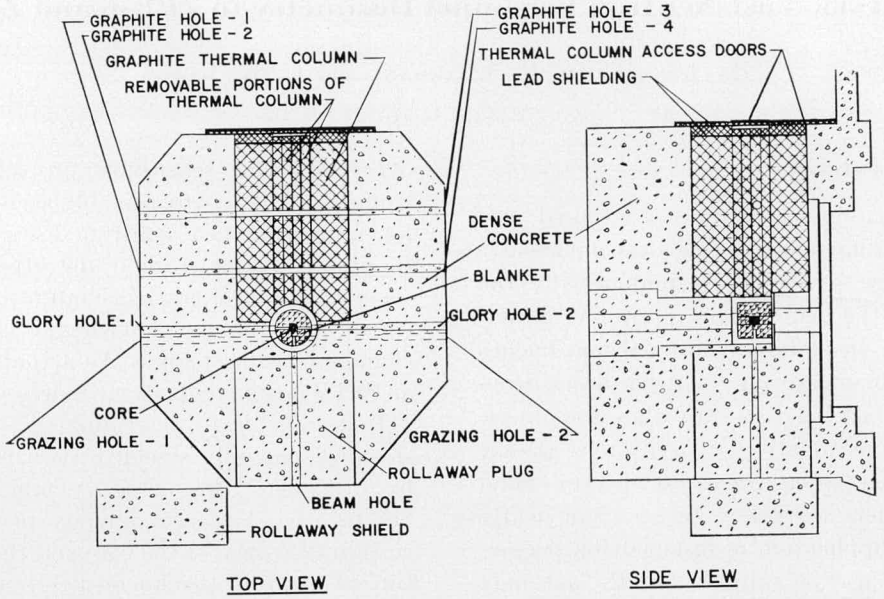

EXPERIMENTAL FACILITIES
AFSR

FIG. III-34-1. Experimental Facilities, AFSR. *ANL-ID-103-6201.*

TABLE III-34-II. AVAILABLE FLUXES

Position	Flux Characteristics: Cadmium Ratio for				One Watt-Hour Gives the Following Number of Fissions per Gram of				One-Watt Power Level Gives the Following Fluxes, $n/cm^2/sec$
	B^{10}	$\frac{\sigma_f^{28}}{\sigma_f^{25}}$	$\frac{\sigma_f^{24}}{\sigma_f^{25}}$	$\frac{\sigma_f^{49}}{\sigma_f^{25}}$	^{235}U	^{238}U	$U_{enriched}$	^{239}Pu	
Center of Glory Hole		0.147		1.26	6.0×10^9	8.8×10^8	5.6×10^9	7.6×10^9	5.0×10^8
Center of grazing hole		0.050		1.27	1.8×10^9	9.0×10^7	1.7×10^9	2.4×10^9	1.5×10^8
Inner end of beam hole[a]		0.059	0.39	1.27	2.3×10^9	1.4×10^8	2.2×10^9	2.8×10^9	2.0×10^8
Inner end of beam hole liner	1.17	0.027	0.31	1.51	1.0×10^9	2.75×10^7	9.4×10^8	1.5×10^9	8.0×10^7
Center of graphite hole #1	34						8.2×10^9	1.1×10^{10}	1.5×10^6
Center of graphite hole #2	~800			1.28			1.0×10^9	1.4×10^9	1.9×10^5
Beamhole	Beams available 1 foot out from face of reactor shield.								1.0×10^4
Grazing hole									1.8×10^3
Glory Hole									1.3×10^3
Vertical cooling duct									3.3×10^3

[a] Not normally accessible.

INFORMATION FOR EXPERIMENTERS

This section contains reactor characteristics, descriptions of physical penetrations, and information of interest to potential users of the AFSR.

A view of the reactor depicting the available experimental facilities is shown in Fig. III-34-1. A physical description of each of these facilities is given in Table III-34-I. The neutron fluxes available in each of these penetrations are given in Table III-34-II.

REFERENCES

1. G. S. Brunson, *Design and Hazards Report for the Argonne Fast Source Reactor*, ANL-6024 (1959).
2. R. G. Matlock and R. O. Vosburgh, *Addendum to the Design and Hazards Report for the Argonne Fast Source Reactor ANL-6024*, (to be published).

III-35. Fast Neutron Personnel Dosimetry in ZPR-6 and ZPR-9

Raymond Gold, R. J. Armani and G. K. Rusch

Introduction

In order to adequately record dose of exposed personnel, radiation dosimeters must possess sufficiently high sensitivity. Low sensitivity is undoubtedly the major limitation of the fast neutron personnel dosimeters in present use. In fact, conventional film badges are not suitable for measuring neutron doses from ZPR-6 and -9 type fast reactors since they are almost completely insensitive, relative to allowable weekly doses, to typical fast reactor neutron spectra. Solid State Track Recorders (SSTR)[1] possess sufficiently high sensitivity for application in fast neutron personnel dosimetry. The use of suitable SSTRs not only overcomes this sensitivity problem, but provides a gamma insensitive, reasonably accurate, simple method for measuring fast neutron doses to personnel from these cores. Small SSTR detection packages can be easily assembled (with asymptotically thick sources) which are just as convienient as pocket ionization chambers or film badges. An actual photograph of such an SSTR dosimeter package is presented in Fig. III-35-1.

It is possible to determine the doses received from shielded, partially shielded, or bare fast reactor cores by utilizing a dosimeter assembly consisting of two SSTRs each having a unique spectral response. Two constants typical of the core and the SSTRs along with the spectrum of the shielded core and the spectrum of

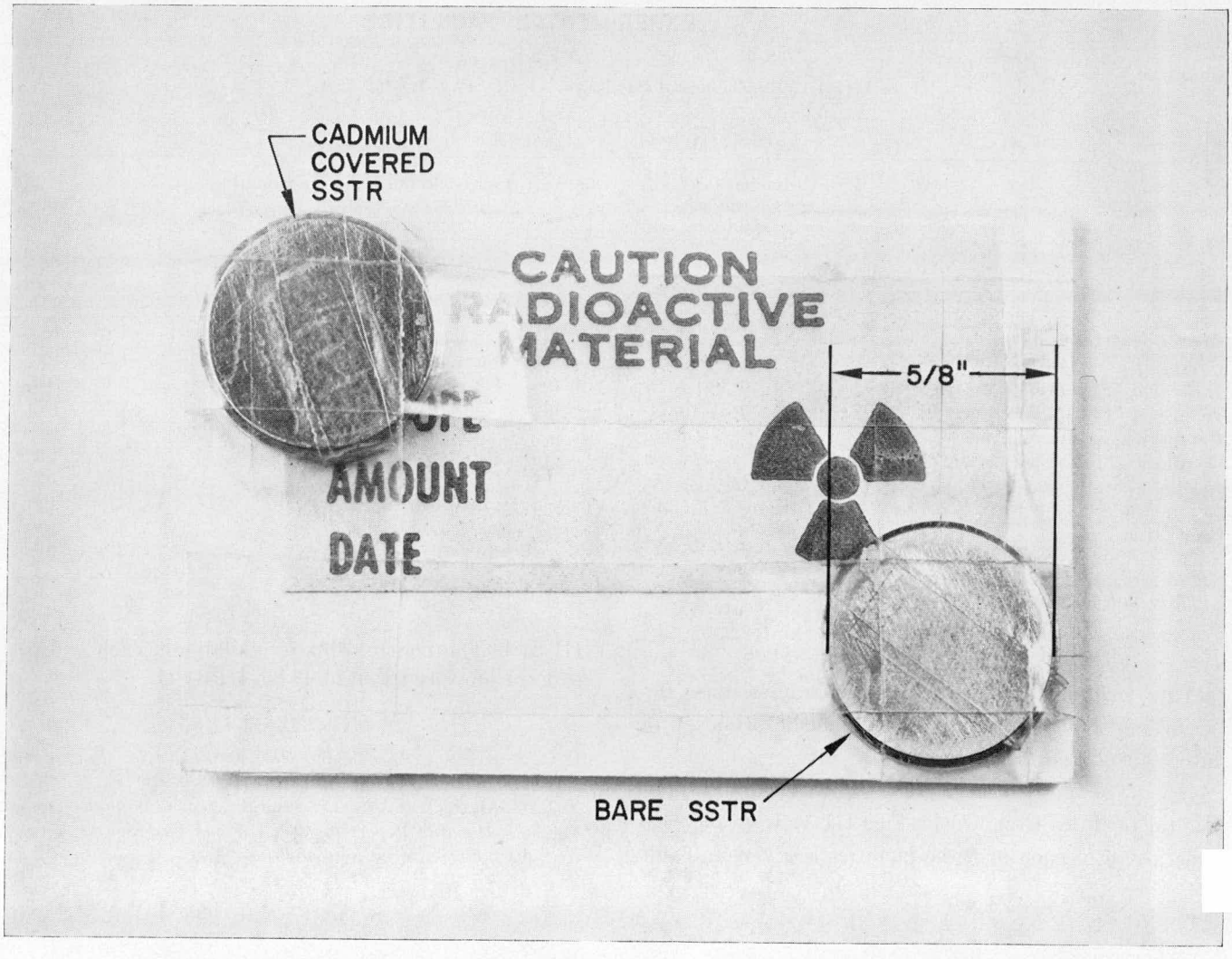

Fig. III-35-1. SSTR Fast Neutron Personnel Dosimeter Used in ZPR-6 and ZPR-9. *ANL Neg. No. 116-919.*

the bare core, provide all of the information required to translate SSTR derived data to dose information. The constants are readily obtained by exposing an SSTR dosimeter package to the neutron flux from the bare core and another to the neutron flux from the shielded core. The spectra may be obtained from calculations or from measurements.

In the case of ZPR-6 and -9, it appears that combinations of two spectra adequately describe the fields encountered, for dosimetry purposes. For situations where two spectra cannot be combined to adequately describe a resultant field, it may be necessary to determine the spectrum of each unique component and to employ an additional SSTR with a suitable, unique spectral response for each such contributing component. Approximations may, however, be useful to reduce the number of SSTRs required for complex fields.

Although the treatment presented herein is in principle sufficiently general to encompass the use of SSTRs containing various types of fissionable material and the use of various shielding materials to modify the spectral response of an SSTR, this discussion will be restricted to dosimeters employing bare ^{235}U foils and cadmium covered ^{235}U foils. Extension of the treatment to more general systems or systems containing additional unique components is not difficult. Accuracy of the dose information is dependent upon the accuracy of the ^{235}U fission cross section, the accuracies of the spectral information, the RBE (Relative Biological Effectiveness)[3] curve, and the counting statistics of the SSTR data. It is considerably better than anything presently available.

It should not be assumed that the data analysis described below is in any way unique. In fact, two alternative and equally adequate treatments were simultaneously advanced.[2] The treatment chosen for presentation below is the analysis which has been actively used for fast neutron personnel dosimetry in ZPR-6 and ZPR-9.

Analysis of SSTR Data

In fast neutron personnel exposures, one can generally assume the existence of a source of energetic neutrons. Shielding provides both attenuation and moderation of these energetic source neutrons. In addition, neutrons that undergo a sufficient number of scattering events will eventually be thermalized (i.e. so-called room return). An adequate assessment of neutron dose can therefore be obtained by arbitrarily decomposing the neutron flux into three components: namely, fast (or source) neutrons, intermediate (or moderated) neutrons, and thermal neutrons. These three flux components will be designated by ϕ_f, ϕ_i, and ϕ_{th}, respectively. In the ZPR-6 or ZPR-9 environment, ϕ_f would be the neutron spectrum arising from unshielded core faces, whereas ϕ_i corresponds to the neutron spectrum from fully shielded faces of the critical assembly.

Let ϕ_f, ϕ_i and ϕ_{th} be unit normalized. The dose rate per unit flux, D_f, D_i, and D_{th}, corresponding to these three components can be written as

$$D_f = \int R(E)\phi_f(E)dE, \tag{1a}$$

$$D_i = \int R(E)\phi_i(E)dE, \tag{1b}$$

and

$$D_{th} = R_{th}, \tag{1c}$$

where $R(E)$ is the well-known energy dependent Snyder dose equivalent function for neutrons.[3] The total neutron dose rate can accordingly be written as the linear superposition

$$D = I_f D_f + I_i D_i + I_{th} D_{th}, \tag{2}$$

where I_f, I_i, and I_{th} are the corresponding absolute intensities of ϕ_f, ϕ_i, and ϕ_{th}, respectively. These absolute intensities can be determined from bare and cadmium covered SSTR exposures. Hence the fast neutron dose can be ascertained provided the spectral dependence of the fast and intermediate neutron components is known (i.e. measured or calculated).

Let T_B and T_{cd} be the bare and cadmium covered SSTR track density (tracks/cm^2), respectively. The fission rate per atom for the bare and cadmium covered exposures is given by

$$F_B = T_B/(tS_\infty) \tag{3a}$$

and

$$F_{cd} = T_{cd}/(tS_\infty), \tag{3b}$$

respectively. Here S_∞ is the known asymptotic sensitivity (atoms/cm^2)$^{(1)}$ and t is the time duration of the exposure.

Both the fast and intermediate flux components contribute to cadmium covered track density, T_{cd}. Let α_i and α_f represent the relative contributions of the intermediate and fast components to T_{cd}. Then

$$T^f_{cd} = \alpha_f T_{cd} \tag{4a}$$

and

$$T^i_{cd} = \alpha_i T_{cd}, \tag{4b}$$

where

$$\alpha_i + \alpha_f = 1. \tag{4c}$$

Here T^f_{cd} is that part of T_{cd} due to the fast component and T^i_{cd} is that part of T_{cd} due to the intermediate component.

The cadmium ratio

$$\mathrm{CR} = T_B/T_{cd} \tag{5}$$

can be used as a spectral index to infer the degree of moderation, i.e., the relative contributions of the fast and intermediate components. Two calibration exposures are required, one in the fast (source) flux ϕ_f and the other in a fully moderated flux, i.e., with ϕ_i only. Let $(\mathrm{CR})_f$ and $(\mathrm{CR})_i$ denote the cadmium ratios arising with the spectra ϕ_f and ϕ_i, respectively. In terms of these calibrations, a simple linear interpolation model implies

$$\alpha_f = \frac{(\mathrm{CR})_i - (\mathrm{CR})}{(\mathrm{CR})_i - (\mathrm{CR})_f}. \tag{6}$$

Applying the very same decomposition to the cadmium covered fission rate, F_{cd}, one can write

$$F^f_{cd} = I_f \int \sigma_f(E)\phi_f(E)dE = I_f\langle\sigma_f\rangle_f \tag{7a}$$

and

$$F^i_{cd} = I_i \int \sigma_f(E)\phi_i(E)dE = I_i\langle\sigma_f\rangle_i, \tag{7b}$$

where $\langle\sigma_f\rangle_f$ and $\langle\sigma_f\rangle_i$ are the average fission cross sections in the fast and intermediate neutron spectra, respectively.

Equations (3) through (7) can be used to express the absolute intensities I_f and I_i in terms of the SSTR measurements. One finds

$$I_f = \frac{F^f_{cd}}{\langle\sigma_f\rangle_f} = \frac{\alpha_f T_{cd}}{tS\infty\langle\sigma_f\rangle_i} \tag{8}$$

and

$$I_i = \frac{F^i_{cd}}{\langle\sigma_f\rangle_i} = \frac{\alpha_i T_{cd}}{tS\infty\langle\sigma_f\rangle_i} \tag{9}$$

The thermal neutron intensity, I_{th}, can be found from the difference of the bare and cadmium covered exposures. One has

$$I_{th} = \frac{F_B - F_{cd}}{\sigma_{th}} = \frac{T_B - T_{cd}}{tS\infty\sigma_{th}}$$

where σ_{th} is the thermal fission cross section of the asymptotically thick SSTR source.

References

1. R. Gold, R. Armani and J. Roberts, *Absolute Fission Rate Measurements with Solid State Track Recorders*, Nucl. Sci. Eng. **34**, 13–32 (1968).
2. G. K. Rusch, R. J. Armani and R. Gold, Argonne National Laboratory (private communication).
3. *Engineering Compendium on Radiation Shielding*, Vol. I, Shielding Fundamentals and Methods, p. 18 (Springer-Verlag, New York, Inc., 1968).

III-36. Fast Neutron Dosimetry Study of the Movable Personnel Shields in ZPR-9 Assembly 27

Raymond Gold, R. J. Armani and A. DeVolpi

Increased personnel radiation dose resulting from the advent of plutonium loaded cores is of concern in the general operation of the ZPR critical facilities. To quantitatively ascertain the personnel radiation hazard of the ZPR environment, a limited set of measurements has been conducted with the movable personnel shields in ZPR-9 Assembly 27. As such, these measurements provide:

1. An operating guide for current ZPR exposure levels,
2. An evaluation, albeit crude, of the personnel shields,
3. A guide to the design of improved shielding which can reduce personnel exposure by a factor of 10 to 100.

The movable personnel shields are composed of 6 in. of Benelex, 1 in. of steel, ¾ in. of lead, and ¼ in. of boral. Three separate movable shields (2 ft wide by 6 ft high by 8 in. thick) can be suspended to shield the face of each core.

Solid State Track Recorder (SSTR)[1] measurements (with asymptotically thick ^{235}U sources) were carried out at a distance of 8 in. from the core face to determine the fast neutron dose rate as a function of gap distance between two such movable shields, as depicted in Fig. III-36-1. Such a geometry is typically encountered in critical facility work, e.g., loading and unloading operations. Fast neutron dose measurements with SSTR are described in Paper III-35. Exposures were carried out when the ZPR-9 facility was not in use, that is, either overnight or on weekends.

Dose rate results as a function of half-gap distanc X are presented in Fig. III-36-2. (The backside co face was completely shielded for these measurements.) The experimental error (~10 %) displayed in Fig. III-36-2 is due to track counting statistics. Total experi-

mental error, including systematic effects, has been estimated as nominally 20%. In the simple linear interpolation model, which has been used here, the dose rate $\dot{D}$(mR/hr) is given by*

$$\dot{D} = [0.0587 + 0.8403\alpha_f]T_{cd} + 2.04 \times 10^{-4}T_{th}, \quad (1)$$

where T_{cd} and $T_{th} = T_B - T_{cd}$ are the cadmium covered and bare minus cadmium covered tracks/cm^2-hr. In terms of boundary data measurements in ZPR-9 Assembly 27, the relative weight parameter α_f is given by

$$\alpha_f = 0.0383[27.5 - \mathrm{CR}], \quad (2)$$

where CR is the cadmium covered ratio, CR $= T_B/T_{cd}$.

It can be seen that the dose rate $\dot{D}$ rises quite rapidly and increases by more than two orders of magnitude as the half-gap distance is increased to only $X = 2$ in. After attaining a maximum in the neighborhood of $X = 4$ in., $\dot{D}$ falls off monotonically with increasing X. It is evident that a non-negligible dose buildup occurs due to scattering from the sides of the movable shields. This effect can be roughly evaluated by assuming that the direct dose rate $\dot{D}_d$ is proportioned to the exposed solid angle (the constant of proportionality is determined from measurements carried out at large X, where the scattered component is negligible). In this manner, one finds

$$\dot{D}_d = 209.5 \tan^{-1}\left\{\frac{4.5X}{[1360 + X^2]^{1/2}}\right\}. \quad (3)$$

The smooth curve in Fig. III-36-2 represents the direct dose rate $\dot{D}_d$, obtained according to Eq. (3). For the 8 in. core detector distance investigated here, the scattered dose clearly dominates over the region of interest, i.e., $X < 6$ in.

Guide to the Design of Improved Personnel Shielding

The dose data obtained from ZPR-9 Assembly 27 provide a design framework for improved personnel shielding. As a constraint we shall accept the existing personnel shields and will attempt to introduce relatively inexpensive modifications. Consequently, an improved shielding arrangement could consist of three elements:

1. The reactor face normally covered by the movable shields.
2. The reactor face under loading operation will also be covered by the movable shields, except for a gap of about 3½ to 4 in. along the particular vertical slot being fueled.
3. Within this vertical slot, a special adjustable filler shield which will reduce the source beam to an area of about 3 x 3 in. (see Fig. III-36-3).

With the aid of Fig. III-36-2, the additional protec-

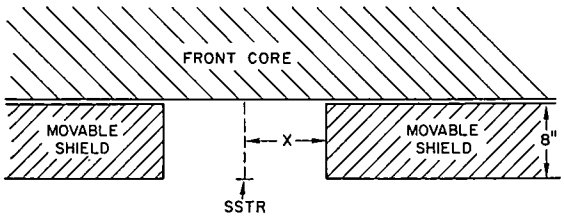

Fig. III-36-1. Location of SSTR for Dose Measurements in ZPR-9 Assembly 27. X is Half of the Gap Distance between Two Adjacent Movable Shields. *ANL Neg. No. 116-874.*

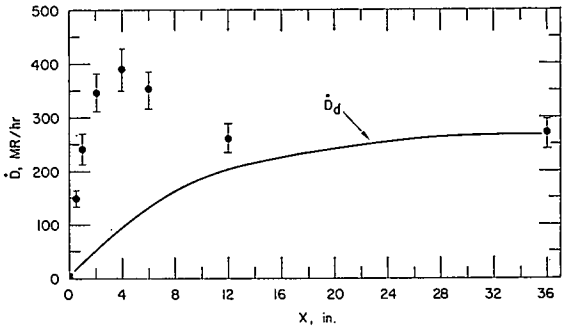

Fig. III-36-2. Dose Rate $\dot{D}$ as a Function of Half-Gap Distance X. The Smooth Curve, $\dot{D}_d$, is the Estimated Direct Dose Rate According to Eq. 3. *ANL Neg. No. 116-873.*

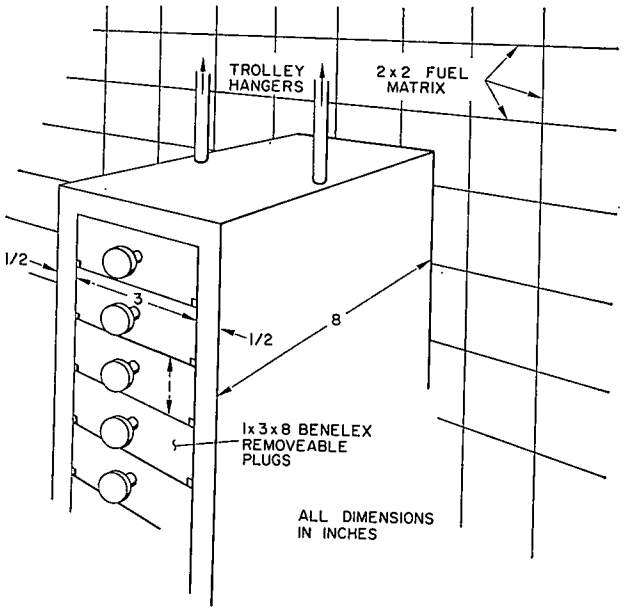

Fig. III-36-3. Special Adjustable Filler Shield Providing a 3 x 8 in. Gap for Fuel Loading Operations. *ANL Neg. No. 116-906.*

* It should be noted that $\dot{D}$ is a "point" dose rate and, as such, does not account for any perturbations which may be introduced by the presence of a human body.

tion to be achieved with a 3 x 3 in. slot opening can be estimated. With personnel shields removed from both core faces the radiation dose rate is evaluated at about 290 mR/hr. With the backside core face shielded and with the front side closed so that the movable shields are only 3 in. apart, the radiation level along the slot is about 300 mR/hr. The fact that the dose rate in the middle of a 3 in. gap is greater than the dose rate in the complete absence of shields is accounted for by the inscattering and buildup of fast neutrons, as shown in Fig. III-36-2. Were it not for this inscattered component, the dose would be only about 40 mR/hr.

To estimate the effect of reducing the vertical dimensions of the gap to achieve the 3 x 3 in. square hole shown in Fig. III-36-3, one can again assume that the inscattering effect will dominate. Thus, the point dose, as measured by the SSTR, will still be about 300 mR/hr in front of a 3 x 3 in. hole, as it is with the 3 in. gap fully open in the vertical direction. In fact, we should estimate it as increased to roughly (300/270) × 300 or about 333 mR/hr. This does not imply that a person loading fuel at a 3 x 3 in. gap would receive an exposure of 333 mR/hr versus 270 mR/hr without any shielding. The actual exposure would be reduced by one or two orders of magnitude for the following three reasons:

1. The previous dose rates given in Fig. III-36-2 are point dose rates. Since there is only a 3 x 3 in. gap, the net whole body exposure to this collimated beam must be reduced in accordance with typical body area, which is approximately 750 in.^{2} Thus, the whole body exposure would only be about 1.2 % of the 333 mR/hr or 4 mR/hr. The exposure measured with zero half-gap was 3 mR/hr, which should be added to the 4 mR/hr direct dose to give a total of 7 mR/hr.
2. The dose arising from exposure to the 3 x 3 in. hole is likely to focus primarily on the hands, arms, and head of the worker. The allowable exposures to such organs are greater by a factor of two or three compared with whole body irradiation, which affects blood-forming organs and gonads.
3. The effective time duration of exposure, on a practical basis, is likely to be considerably less with a 3 x 3 in. gap than with no shielding, since it is the time integral which prevails. More specifically, when a person is on the loading platform, his entire visit contributes to dose accumulation. However, when there is a 3 x 3 in. slot supplying the dominant field, only the time spent immediately in front of the slot can lead to a significant accumulation; all other positions are relatively safe. This shortening of exposure time can readily lead to a significant reduction in exposed dose.

Accordingly, a reduction factor of 10 to 100 in dose to individuals loading fuel is estimated with the additional protection of a 3 x 3 in. slot. The upper limit would be the dose accumulated at the rate of 3 mR/hr when all movable shields are in position. The construction of such a slot filler is indicated in Fig. III-36-3. It consists of a support of 3½ to 4 in. width which has shelves filled with removable shielding plugs of 1 in. height and 3 in. width. The support is moved to the vertical column loading position, and then the existing movable shields are placed immediately adjacent, perhaps coupled tightly or clasped together. Hangers similar to those used for the existing movable shields can be used to support the frame. The thickness is, of course, the same as the movable shields—8 in. Each of the removable plugs slides on a shelf. Removal of three plugs is required to provide access to any given matrix tray.

The slot filler plugs can probably be made of Benelex or masonite capped with cadmium or boral on both ends. To minimize exposure due to horizonatal movements of the filler shield, fuel should be loaded completely according to columns as much as possible. In addition, the outside of the filler shield should be marked with the fuel loading matrix image in order to facilitate location of the proper fuel drawers. Since it may be possible to move this filler shield by crane to the opposite reactor face and to other positions on one face, then only one such insert need be fabricated per critical assembly; otherwise, it could be useful to have two or four such adjustable filler shields.

Reference

1. R. Gold, R. J. Armani and J. H. Roberts, *Absolute Fission Rate Measurements with Solid State Track Recorders*, Nucl. Sci. Eng. **34**, 13 (1968).

Section IV

Reactor Computation Methods and Theory

To a large degree, the quality of reactor design and performance depends upon the quality of the conceptual models and their portrayal in accurate mathematical representation, and upon the quality and efficiency of computational methods. A priori, the continuous development and refinement of theory and computational methods leads to the design of more dependable, safer, and better performing reactors. It is with this intent that the studies described in this section were undertaken.

IV-1. Implementation Strategy for the MC²-2 Code

B. J. TOPPEL

The new code, MC²-2, now being implemented on the IBM/360 model 75 computer, is intended to provide accurate multigroup cross sections for a wide range of applications including critical experiment analysis, core calculations, and, to a somewhat lesser extent, shielding applications. The coding effort stresses computational economy, although accuracy is the primary objective. In addition, the code is planned so that approximate cross sections may be rapidly generated by relaxing the rigor of the basic algorithms.

MC²-2 will be responsive to essentially all of the comments received from LMFBR contractor laboratories as well as other laboratories and universities in the U.S., and will comply with the standards set forth by the de facto Committee on Computer Code Coordination which was convened at the request of the Division of Reactor Development and Technology. Considerable effort is being expended to develop a product which can be implemented as simply as possible on other computers. The code is fully variably dimensioned and makes use of standardized I/O subroutines to accomplish block data transfer between main core and peripheral storage. To the fullest extent possible standard Fortran is being used to ease conversion to other computers.

As part of the MC²-2 coding effort, a new variably dimensioned ENDF/B processing package is being implemented to replace the ETOE[1] and MERMC2[2] codes. In addition to data format conversion, the new processing codes will take over some of the computations currently being performed by MC²[3] at each execution. One of the major changes is the fact that the library processor generates tabulated cross section data using ENDF/B supplied resolved resonance parameters for all light nuclides (mass $\lesssim 100$). During the MC²-2 execution, these light materials are then no longer recognized as having resolved resonances. Recent tests using the Version II data of ENDF/B with the numerous iron, nickel, and chromium resonances indicate that this new strategy will result in significant execution time economy. The library processor also now produces the ultra fine group ($\Delta u \approx 1/120$) cross sections from the tabulated data as compared with this function now being performed at each execution of MC². User-provided library data may also be merged with the ENDF/B data in the new library processor.

The MC²-2 code will be described below by means of comparisons with the current MC² algorithms. The reader is referred to Ref. 3 for full details concerning MC².

Figure IV-1-1 shows a schematic diagram of the energy structure of MC². A three group-structure-heirarchy is employed, namely ultra fine groups (ufg) with $\Delta u = 1/120$, fine groups (fg) with $\Delta u \approx \frac{1}{4}$ and the final broad groups (bg) with $\Delta u \approx \frac{1}{2}$ to 1. Since the Legendre coefficient data are rigidly structured in the library with a top energy of 10 MeV, only a fine group treatment is possible above 10 MeV if EMAX is chosen above 10 MeV. The top of the resolved resonance region is noted only to indicate the relative energy position of various parts of the calculation. Cross sections for the thermal group are supplied by the user.

Figure IV-1-2 shows the general flow of logic in MC². Several points should be recalled. Only the resolved resonance cross sections and Legendre elastic scattering treatment occur at the ufg level. All other cross sections, in particular the inelastic and $(n,2n)$ cross sections, are evaluated at a fg detail. The fg inelastic treatment which produces artificial discontinuities in the spectrum is one of the areas in MC² known to be inadequate. An inconsistency also exists in MC² in that the resolved resonance cross sections do not correctly influence the ufg spectrum; therefore the resonance cross sections require a broad group collapsing treatment distinct from that of the other types of cross sections in the problem. MC² evaluates the ufg resolved resonance cross sections by performing an integration over each ufg, namely

$$\bar{\sigma}_{c_j} = \frac{\int_j \frac{\sigma_c(E)}{\Sigma_t(E)}\, dE}{\int_j \frac{dE}{\Sigma_t(E)}}. \tag{1}$$

This integration is very time consuming when the problem contains a large number of resolved resonances. In particular, the Version II data of ENDF/B with the many resolved resonances of iron, nickel and chromium result in very long running times in MC².

Figure IV-1-3 shows schematically the energy structure of the new MC²-2 code. In MC²-2 there are only two group-

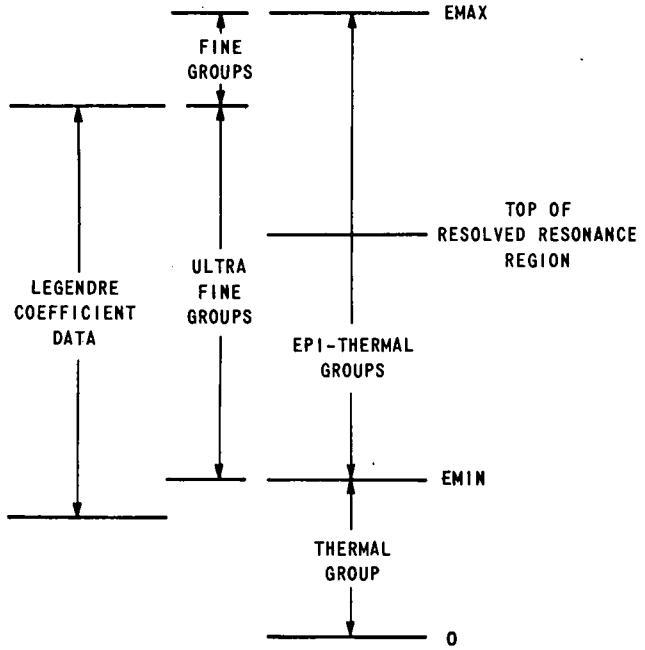

FIG. IV-1-1. Schematic Diagram of the MC² Energy Structure. *ANL Neg. No. 112-6995.*

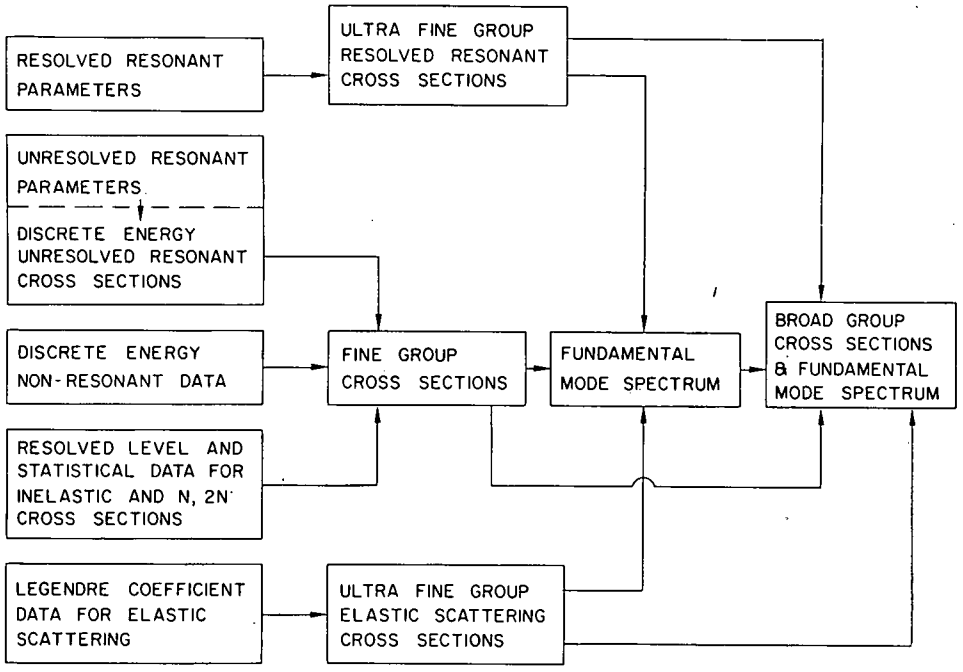

FIG. IV-1-2. Logic Flow Diagram of MC². *ANL Neg. No. 116-850.*

structures: ufg and bg. In MC² a multigroup treatment is used throughout whereas MC²-2 is divided into a multigroup (MG) spectrum calculation at the higher energies and a continuous slowing down (CSD) spectrum calculation[4,5] at lower energies.

The CSD formalism, presented in detail in Refs. 4 and 5, is briefly outlined below for purposes of orientation. We will restrict the following discussion to the case of isotropic elastic scattering, although the code incorporates the algorithms appropriate to anisotropic elastic scattering in the general P_n or B_n representations.[5]

In a homogeneous medium with isotropic elastic scattering, the neutron balance equation can be written as

$$\Sigma(u)\phi(u) = S(u) + \sum_i \int_{u-\epsilon_i}^{u} du' \Sigma_{s_i}(u')\phi(u') \frac{e^{u'-u}}{1-\alpha_i}, \tag{2}$$

where the source term $S(u)$ is made up of contributions due to fission, inelastic and $(n,2n)$ scattering, and inhomogeneous sources. The summation is over all isotopes present and

$$\epsilon_i = \ln \frac{1}{\alpha_i}, \tag{3}$$

where

$$\alpha_i = \left(\frac{A_i - 1}{A_i + 1}\right)^2. \tag{4}$$

The elastic slowing down density, which is the rate at which neutrons are elastically moderated above a given lethargy, is defined as

$$q(u) = \sum_i \int_{u-\epsilon_i}^{u} du' \Sigma_{s_i}(u')\phi(u') \int_{u}^{u'+\epsilon_i} du'' \frac{e^{u'-u''}}{1-\alpha_i}. \tag{5}$$

Equations (2) and (5) may be combined to obtain

$$\frac{dq(u)}{du} = S(u) - \Sigma_{ne}\phi(u), \tag{6}$$

where

$$\Sigma_{ne} = \Sigma - \Sigma_s .$$

An approved Goertzel-Grueling approximation[6] is made by assuming a slowly varying total collision density

$$F(u') = \Sigma(u')\phi(u') \approx F(u) + (u' - u)\frac{dF(u)}{du}, \qquad u \geq u' \geq u - \epsilon_i . \tag{8}$$

The use of Eq. (8) with Eqs. (5) and (6) yields

$$\frac{dq(u)}{du} = -\frac{\Sigma_{ne}(u)}{M(u)} q(u) + \frac{\hat{\xi}(u)\Sigma(u)}{M(u)} S(u), \tag{9}$$

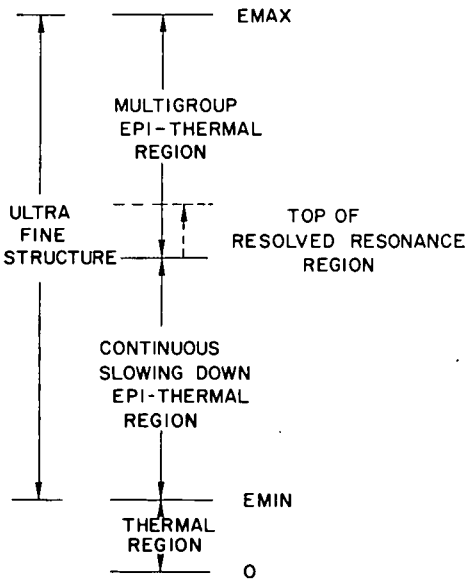

FIG. IV-1-3. Schematic Diagram of the MC²-2 Energy Structure. *ANL Neg. No. 116-851.*

where

$$M(u) = \hat{\xi}(u)\,\Sigma_s(u) + \hat{\gamma}(u)\,\Sigma_{ne}(u) \tag{10}$$

and

$$\phi(u) = \frac{q(u) + \dfrac{\bar{a}(u)}{\bar{e}(u)}\,S(u)}{M(u)}. \tag{11}$$

The composite moderating parameters $\hat{\xi}$ and $\hat{\gamma}$ consist of weighted moments of the slowing down kernel over the scattering interval ($\ln 1/\alpha_i$) of the individual elements of the mixture. The definitions of the various moderating parameters $\hat{\xi}$, $\hat{\gamma}$, $\bar{a}$, $\bar{e}$, etc. are given in Refs. 4 and 5. As an example,

$$\bar{a}(u) = \sum_i \int_{u-\epsilon_i}^{u} du' \,\frac{\Sigma_{s_i}(u)}{\Sigma(u')}\,(u' - u)\left[\frac{e^{u'-u} - \alpha_i}{1 - \alpha_i}\right]. \tag{12}$$

As indicated in Fig. IV-1-3, the energy interface between the two regions is variable at user option. It should be emphasized that in the CSD calculation, only elastic scattering is treated continuously while the inelastic and $(n,2n)$ scattering are still treated with scattering matrices on a ufg basis. Inelastic and $(n,2n)$ fg scattering matrices are generated in MC², whereas in MC²-2 the large dimensions which would be required for ufg scattering matrices necessitates employing a strategy wherein the inelastic and $(n,2n)$ sources are accumulated into the receptor groups as the spectrum is generated, rather than generating and storing ufg inelastic scattering matrices.

The variable CSD-MG interface permits an all CSD spectrum calculation as an option. It is expected that the CSD treatment will rival the MG treatment for accuracy and will be more efficient.

As in the case of MC², the cross sections for the thermal region will be user-supplied since MC²-2 is still basically a fast reactor epithermal cross section code.

Figure IV-1-4 shows the logic flow through MC²-2. The new code differs significantly from MC² in that the resonance effects are now taken into account by first solving the slowing down equations for the "asymptotic" neutron slowing down density ignoring narrow resonances. Then the resonance reaction rate is computed for each resonance, starting with the highest energy resonance, using the narrow resonance approximation and the flux resulting from the asymptotic slowing down density, but attenuated due to absorption in higher energy resonances. The equations outlining the method used given below are based on the results in Ref. 7.

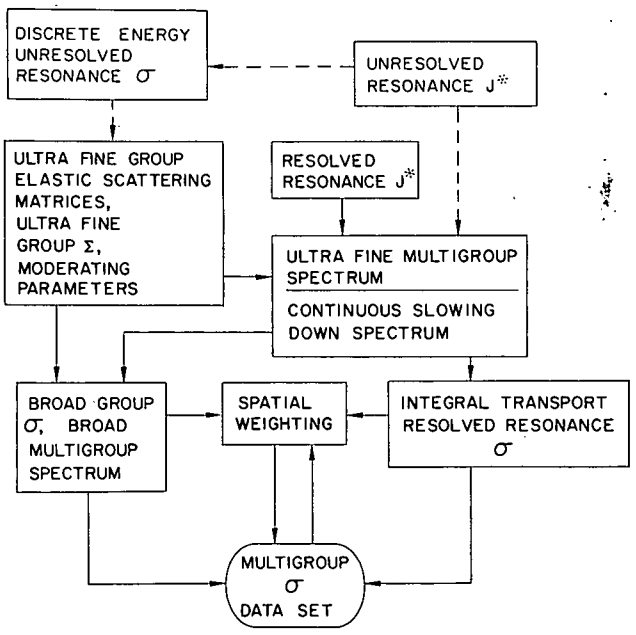

FIG. IV-1-4. Logic Flow Diagram of MC²-2. *ANL Neg. No. 116-852.*

In the resolved resonance region the asymptotic slowing down density

$$q_{as}(u) = q_{as}(u_0) \exp\left[-\int_{u_0}^{u} du' \frac{\Sigma_{ne}(u')}{M(u')}\right], \qquad u > u_0, \tag{13}$$

where Σ_{ne} and M are defined for the mixture exclusive of the narrow resonances. M is defined by Eq. (10).

The flux, as given earlier, is defined as

$$\phi(u) = \frac{q(u)}{M}, \tag{14}$$

which applies either to the asymptotic or attenuated quantities.

The narrow resonance approximation for the flux in the vicinity of resonance r at u_r is

$$\phi(u) = \frac{\Sigma(u_r)}{\Sigma(u_r) + N_r\sigma_r(u) + \sum_{r' \neq r} N_{r'}\sigma_{r'}(u)} \phi_{as}(u) Q_r, \tag{15}$$

where the attentuation factor Q_r accounts for the effect of absorption in lower lethargy resonances; Σ is the total cross section exclusive of narrow resonances; N_r and σ_r are the atomic density and total cross section, respectively, of the isotope having the resonance r.

The absorption rate in the resonance r is approximated by

$$A_r = \int_{\Delta u} du\, N_r\sigma_{a_r}(u)\phi(u) \approx \frac{\Gamma_{f,r} + \Gamma_{c,r}}{E_r} J^* \frac{q_{as}(u_r)}{M(u_r)} Q_r. \tag{16}$$

The attenuation of the slowing down density across a resonance is computed from

$$q(u_r + \Delta u) = q(u_r - \Delta u) - A_r = q_{as}(u_r)Q_r(1 - p_r), \tag{17}$$

where

$$P_r = \frac{A_r}{q_{as}(u_r)Q_r} \tag{18}$$

and

$$Q_r = \prod_{r'} (1 - p_{r'}), \qquad u_{r'} < u_r. \tag{19}$$

The attenuated slowing down density is related to the asymptotic slowing down density by

$$q(u) = q_{as}(u) \prod_{r} (1 - p_r), \qquad u_r < u. \tag{20}$$

In Eq. (16), J* is a generalized J integral including interference and overlap effects for either single or multilevel representations of the resonances. J* may be written as

$$J^* = J + H, \tag{21}$$

where J is the integral relating to the isolated resonance r[8] and H is an overlap correction term.[9] In the code, the number of overlapping neighboring resonances involved in the evaluation of H will be set through calculational experience. Initially four neighboring resonances on each side of resonance r are being included. The integral J can be written in a generalized form[10] to include interference scattering and multi-level representations:

$$\begin{aligned} J(\beta_r,\theta_r,a_r,b_r) &= \frac{1}{2}\int_{-\infty}^{\infty} \frac{\psi(\theta_r,x_r) + b_r\chi(\theta_r,x_r)}{\beta_r + a_r\chi(\theta_r,x_r) + \psi(\theta_r,x_r)}\, dx_r \\ &= J(\beta_r,\theta_r,0,0) + I(\beta_r,\theta_r,a_r) - b_rM(\beta_r,\theta_r,a_r), \end{aligned} \tag{22}$$

where

$$I(\beta_r,\theta_r,a_r) = a_r^2 \int_0^{\infty} \frac{\chi_r^2}{(\beta_r + \psi_r)^2 - (a_r\chi_r)^2} \cdot \frac{\psi_r}{\beta_r + \psi_r}\, dx_r \tag{23}$$

$$M(\beta_r,\theta_r,a_r) = a_r \int_0^{\infty} \frac{\chi_r^2}{(\beta_r + \psi_r)^2 - (a_r\chi_r)^2}\, dx_r. \tag{24}$$

For single level resonances $b_r = 0$ while for multilevel resonances b_r is defined in terms of the parameters of the Adler-Adler representation.[11] The resonance integrals are obtained using a very fast 13 point Gauss-Jacobi quadrature.

For unresolved resonances, two options will be available as implied by the dashed lines in Fig. IV-1-4. Either the J^* integrals will be used as outlined above to attenuate an asymptotic slowing down density, or alternatively ufg unresolved resonance cross sections will be generated as in the present MC² approach. In the former case, the CSD-MG interface will lie above the unresolved energy region, while for the latter approach, the unresolved resonance region may be included in the MG portion of the spectrum. As for the resolved resonances, the unresolved J^* will include interference scattering and overlapping effects due to neighboring resonances. As in MC², an average over a chi-squared distribution will be used to evaluate the average resonance parameters at each of the unresolved resonance energy values. An option is included to omit the self-overlap calculation which is the most time consuming part of the unresolved resonance region calculation.

For the spectrum calculation, the user may select a P_1, B_1, consistent P_1 or consistent B_1 option. The code uses an extended transport approximation to incorporate higher order anisotropic and transport effects.[5,12,13] As an example, consider the case of the consistent P_ℓ equations with $\ell = 0, 1, 2, \ldots, N$; if we ignore the ϕ_{N+1} in the $\ell = N$ equation, assume that no source terms are present for $\ell \geq 2$, and assume that, for the scattering integrals

$$\sum_i \int_{u-\epsilon_i}^{u} du' \, \Sigma_{s_i}^{\ell}(u' \to u)\phi_\ell(B,u) \approx \Sigma_s^{\ell}(u)\phi_\ell(B,u), \qquad \ell \geq 2, \tag{25}$$

the $N + 1$ equations can be reduced to the two equations

$$\eta\phi_1(B,u) + \Sigma(u)\phi_0(B,u) = S_0 + \sum_i \int_{u-\epsilon_i}^{u} du'\Sigma_{s_i}^{0}(u' \to u)\phi_0(B,u') \tag{26}$$

$$\frac{1}{3}\eta\phi_0(B,u) + H_{1,N}(B,u)\phi_1(B,u) = S_1 + \sum_i \int_{u-\epsilon_i}^{u} du'\Sigma_{s_i}^{1}(u' \to u)\phi_1(B,u'), \tag{27}$$

where the higher order transport and anisotropic scattering effects are reflected in $H_{1,N}$ which is given by the contained fraction representation

$$H_{\ell,N} = b_{\ell-1} + \cfrac{a_\ell}{b_\ell + \cfrac{a_{\ell+1}}{b_{\ell+1} + \cfrac{a_{\ell+2}}{b_{\ell+2}\cdots}}}. \tag{28}$$

The continued fraction (28) terminates at b_{N-1}, where

$$\begin{aligned} b_0 &= \Sigma(u) \\ b_\ell &= \Sigma(u) - \Sigma_s^{\ell+1}(u), \qquad 1 \leq \ell \leq N-1 \\ a_\ell &= -\frac{\ell+1}{2\ell+1}\cdot\frac{\ell+1}{2(\ell+1)+1}\eta^2, \qquad 1 \leq \ell \leq N-1 \\ \eta &= iB. \end{aligned} \tag{29}$$

The higher order angular flux components are constructed recursively using

$$\phi_\ell(B,u) = -\frac{\dfrac{\ell}{2\ell+1}\eta\phi_{\ell-1}(B,u)}{H_{\ell,N}(B,u)}. \tag{30}$$

The ϕ_ℓ are used in producing the $\ell = 2, 3, \cdots$ broad group scattering matrices.

The P_0 and P_1 elastic scattering matrices are generated using an improved algorithm as compared with that used in MC² in that the variation across the source group is now accounted for explicitly; in MC² a simple average ove each end of the source group is used. In addition, a heavy mass approximation[14] has been incorporated to reduc calculational time for isotopes of mass sufficiently large to scatter down at most three ufg. A transport approximation, available on option, will produce less accurate scattering matrices and moderating parameters at a reduced computation cost.

As mentioned earlier, inelastic and $(n,2n)$ scattering are treated at an ufg detail. The algorithm also takes account of the energy angle correlation[15,16] in MC²-2, although this was not done in MC². The $(n,2n)$ scattering will routinely use the ENDF/B scattering laws owing to the excessive running times required to calculate the scattering rigorously. However, the rigorous treatment is included in the code and may be invoked for generating standard reference $(n,2n)$ data.

In cases in which the user deems the narrow resonance approximation to be inadequate, he may elect to re-evaluate the broad-group resolved resonance cross sections using an integral transport[17] type algorithm. The strategy being taken is that broad-group resolved resonance cross sections may, at the option of the user, be overwritten by values based on the integral transport approach over a selected energy range. Thus, for example, the user may choose to recompute resonance cross sections only from 300 eV to thermal, and retain the narrow resonance approximation derived values for the higher energy cross sections.

For heterogeneous configurations such as those encountered in the critical experiments program, the integral-attenuation factor formalism is applied for each unique self-shielded material,[18] and heterogeneous cross sections are developed for spatial weighting as the last step in the cross section preparation.[19] The spatial weighting may be per-

TABLE IV-1-I. COMPARISON OF MC² AND MC²-2 CAPABILITIES

MC²	MC²-2
Single level Breit-Wigner	Single level Breit-Wigner or Adler-Adler multi-level
Narrow resonance approximation	Narrow resonance approximation or integral transport (RABBLE) treatment
Two region pin or plate cells	ZPR plate heterogeneity explicitly included
Tabulated data not included in Σ_t	Tabulated data included in Σ_t
Expensive integration for resolved resonance cross sections	Fast J integral calculation
Resolved resonance cross sections inconsistently used in spectrum calculation	Resolved resonance J integrals used as spectrum attenuation factors
s and p wave resonances used[a]	s, p and d wave resonances used[b]
Self-overlap effect not calculated for unresolved resonances	Self-overlap effect included for unresolved resonances
Γ_f and Γ_n treated differently in unresolved integrations[a]	Γ_f and Γ_n treated consistently in unresolved calculation[b]
Ultra fine, fine and broad groups	Ultra fine and broad groups
Fixed ultra fine group width	User selected ultra fine group width
Fine group $\sigma_{inel}(j \rightarrow k)$, $\sigma_{n,2n}(j \rightarrow k)$	Ultra fine group $\sigma_{inel}(j \rightarrow k)$, $\sigma_{n,2n}(j \rightarrow k)$
One spectrum for $(n,2n)$ product neutrons	Separate spectrum for each $(n,2n)$ product neutron
Elastic scattering assumed linear across source group	Variation across source group treated for elastic scattering
Energy independent buckling and no external sources	Group dependent buckling and external sources
Single fission spectrum vector used	Isotope dependent fission spectra vectors or matrices used
Fine group averaging performed at each execution	Ultra fine group averaging done once in library preparation
All resonance calculations performed at each execution	Light element resonances handled once in library preparation
P_0 and P_1 elastic scattering matrices generated	Higher order P_ℓ elastic scattering matrices generated
All multigroup	Multigroup-continuous slowing down or all continuous slowing down
P_1, consistent P_1, consistent B_1 fundamental mode options	P_1, B_1, consistent P_1, consistent B_1 extended transport approximation fundamental mode options
Broad group cross sections strictly applicable for problem mixture	Broad group cross sections applicable for range of mixtures
No data saved for restart[a]	Any interface data set saved at user option[b]
Contains a number of approximations and inconsistencies, and limited in application	Intended to provide high precision results over a wide range of applications, to serve as a standard for design calculations

[a] Pre-ARC System version of MC².
[b] Included in ARC system version of MC².

TABLE IV-1-II. MC²-2 Code Areas

Code Area	Description
1. Primary Library Preparation (ETØE-2)	Reads binary ENDF/B data, one or more existing MC²-2 libraries, and BCD user data such as temperature and ufg width and produces primary MC²-2 library. Combines the functions of ETØE and MERMC2
2. User Library Preparation	Reads primary MC²-2 library data and BCD user data such as isotope names, private cross section data, number of primary library ufgs per user library ufg, and user library energy limits, and produces a user MC²-2 library in the same format as the primary MC²-2 library.
3. Run Time Library Processor	Reads MC²-2 library and processed BCD user data (from area 4) such as problem energy limits, problem isotope names, and produces a run time library. May also collapse primary ufg data to coarser data.
4. Problem BCD Input Processor	Reads and processes BCD user data such as atom densities, temperatures, isotope names, broad group structure, heterogeneity information, and order of extended transport approximation.
5. Unresolved Resonance Calculation	Prepares ufg σ_c and σ_f or unresolved resonance integrals for problem mixture and for each different heterogeneity material.
6. Resolved Resonance Calculation	Prepares resonance integrals for each resolved resonance for the mixture and for each different heterogeneity material.
7. Elastic Scattering Matrices, Moderating Parameters and Macroscopic Cross Section Preparation	Prepares homogenized ufg macroscopic cross sections, elastic scattering matrices, and moderating parameters for CSD calculation.
8. UFG Spectrum Calculation	Calculates ufg real spectrum by combining multigroup and CSD treatments and obtains a critical buckling. Options are P_1, B_1, consistent P_1, and consistent B_1 extended transport. Calculates broad group resonance cross sections.
9. Broad Group Cross Section	Prepares broad group cross sections using ufg spectrum and ufg cross section data.
10. Broad Group Spectrum Calculation	Calculates broad group fundamental mode real and adjoint spectra and obtains a critical buckling.
11. RABBLE Calculations	Prepares broad group resolved resonance cross sections using an integral transport approach for the problem mixture and for each different heterogeneity material for cases in which area 6 algorithms are inadequate.
12. Spatial Weighting Calculation	Calculates spatial fluxes and spatially weights broad group cross sections to account for plate heterogeneities.

formed, at user option, using conventional S_n transport theory to generate the spatial spectrum, or by employing a weighting spectrum derived with the use of the collision probability concept in integral transport theory.[20]

The broad-group collapsing algorithms[21] provide cross sections which have some validity in compositions close to but not identical with the composition used to produce the original spectrum.

By way of summary, Table IV-1-I compares the MC² and MC²-2 capabilities. A number of capabilities included in MC²-2 which are also available in the ARC system[21,22] version of MC² are noted by the superscript b.

The code has been partitioned into twelve areas or modules. Table IV-1-II lists the code areas and gives a brief description of the function of each area.

The flow through the code will be controlled by path driver modules which will link to the various code areas a required for the problem at hand. The modular approach permits easy storage of the various partial results and facilitates reruns utilizing earlier data. Each of the code areas has specified upper and lower interface data sets through which the various code areas communicate.

Code testing is currently underway in areas 1, 2, 5, 6 7, and 8, and programming is proceeding in other areas of

the code. It is hoped that the code can be relased early in 1972 to selected LMFBR contractor laboratories for outside testing.

General distribution of the code will be accomplished through the Argonne Code Center after the code has been thoroughly tested by the user community.

References

1. D. M. Green and T. A. Pitterle, *ETØE, A Program for ENDF/B to MC² Data Conversion*, APDA-219 (ENDF-120), (1968).
2. E. M. Pennington, J. C. Gajniak, A. B. Cohen and W. Bohl, *Service Routines for the Multigroup Cross Section Code, MC²*, ANL 7654 (1970).
3. B. J. Toppel, A. L. Rago and D. M. O'Shea, *MC², A Code to Calculate Multigroup Cross Sections*, ANL-7318 (1967).
4. W. M. Stacey, Jr., *Continuous Slowing Down Theory Applied to Fast Reactor Assemblies*, Nucl. Sci. Eng. **41**, 381 (1970)
5. W. M. Stacey, Jr., *Continuous Slowing Down Theory for Anisotropic Elastic Neutron Moderation in the P_N and B_N Representations*, Nucl. Sci. Eng. **41**, 457 (1970).
6. G. Goertzel and E. Greuling, *An Approximate Method for Treating Neutron Slowing Down*, Nucl. Sci. Eng. **7**, 69 (1960).
7. W. M. Stacey, Jr., *Resolved Narrow Resonance Reaction Rates in Fast Reactor Mixtures*, Nucl. Sci. Eng. **41**, 455 (1970).
8. L. Dressner, *Resonance Absorption in Nuclear Reactors*, (Pergamon Press, Inc., New York, 1960).
9. R. N. Hwang, *Doppler Effect Calculations with Interference Corrections*, Nucl. Sci. Eng. **21**, 523 (1965).
10. R. N. Hwang, Argonne National Laboratory (private communication).
11. D. B. Adler and F. T. Adler, *Neutron Cross Sections in Fissile Elements*, Proc. Conference on Breeding, Economics and Safety in Large Fast Power Reactors, October 7–10, 1963, ANL-6792, p. 695.
12. C. N. Kelber, H. Henryson, II, E. M. Pennington and W. Stacey, Jr., *Higher Order Transport Approximations for MC²-2*, Applied Physics Division Annual Report, July 1, 1969 to June 30, 1970, ANL-7710, pp. 381–387.
13. G. I. Bell, G. E. Hansen and H. A. Sandmeier, *Multitable Treatments of Anisotropic Scattering in S_N Multigroup Transport Calculations*, Nucl. Sci. Eng. **28**, 376 (1967).
14. H. Henryson, II, *Multigroup Elastic Scattering Cross Sections for Heavy Elements*, Nucl. Sci. Eng. **43**, 235 (1971).
15. M. Segev, *Inelastic Matrices in Multigroup Calculations*, Applied Physics Division Annual Report, July 1, 1969 to June 30, 1970 ANL-7710, pp. 374–381.
16. M. Segev, *Group Transfer Matrices and Their Relation to Basic Cross Section Data*, Nucl. Sci. Eng. **45**, 369 (1971)
17. P. H. Kier and A. A. Robba, *RABBLE, A Program for Computation of Resonance Absorption in Multiregion Reactor Cells*, ANL 7326 (1967).
18. W. M. Stacey, Jr. and B. A. Zolotar, *Heterogeneous Resonance Absorption Within the Attenuation Factor Formalism*, Applied Physics Division Annual Report, July 1, 1969 to June 30, 1970, ANL-7710, pp. 373–374.
19. R. Palmer and B. Zolotar, *Heterogeneity Algorithms for MC²-2*, Applied Physics Division Annual Report, July 1, 1969 to June 30, 1970, ANL-7710, pp. 393–395.
20. F. Storrer, A. Khairallah, M. Cadilhac and P. Benoist, *Heterogeneity Calculation for Fast Reactors by a Perturbation Method*, Nucl. Sci. Eng. **24**, 153 (1966).
21. A. Travelli, *A New Formulation of Multigroup Microscopic Cross Sections*, Reactor Physics Division Annual Report, July 1, 1967 to June 30, 1968, ANL-7410, pp. 413–421.
22. B. J. Toppel, Ed., *The Argonne Reactor Computation (ARC) System*, ANL-7332 (1967).
23. L. C. Just, H. Henryson, II, A. S. Kennedy, S. D. Sparck, B. J. Toppel and P. M. Walker, *The System Aspects and Interface Data Sets of the Argonne Reactor Computation (ARC) System*, ANL-7711 (1971).

IV-2. Improvements in the Variably Dimensioned MC² Capability of the Argonne Reactor Computation (ARC) System

C. G. Stenberg

The execution of the variably dimensioned MC² capability in the ARC system[1] has been routinely used to generate multigroup cross sections. The modifications that have been made in this capability include a recoding effort in the unresolved resonance calculation and a correction in the calculation that generates the inelastic and $(n,2n)$ scattering matrices.

Modification Made in the Unresolved Resonance Region

The release of Version II neutron cross section data[2,3] has resulted in the generation of a new MC² library.[3] During the past year Argonne users have had the option of performing MC² calculations using neutron data from either an MC² library[4] generated from revised Version I data or an MC² library[3,5] generated from Version II data. The execu-

tion of MC² problems using the MC² library containing Version II data has resulted in a large increase in computer memory required, especially in the unresolved and resolved resonance module CSC001.[6] The large increase arose from the fact that certain arrays in the unresolved resonance region, namely the arrays containing the average radiation widths, average spacings, average fission widths, and average neutron widths, can now exhibit energy dependence. These arrays can require a large amount of storage space in the BPOINTER[7] container array. Each of these four arrays has a dimension D in double precision words, equal to

$$D = MNLS*MNJS*MNI*NOI*MNP, \tag{1}$$

where

1. *MNLS* is the maximum number of angular momentum states for any given material in the problem
2. *MNJS* is the maximum number of channel spins for the largest angular momentum state for any given material in the problem
3. *MNI* is the maximum number of isotopes for any given material in the problem
4. *NOI* is the number of materials in the problem
5. *MNP* is the maximum number of unresolved energy points for any given material in the problem.

These arrays can become quite large when there are many materials in the problem and when Version II data for materials like molybdenum and/or niobium are included. This may be seen by referring to Table IV-2-I which is a listing of a current MC² library. The library contains 60 Version II materials,[3,5] 19 revised Version I materials from a 77 material library[4] currently available, and 3 revised Version II materials.[5] The following are given in Table IV-2-I:

1. *MAT*, the ENDF/B material identification number
2. The identification in a left-adjusted A-6 format
3. The presence or absence of elastic scattering Legendre coefficient data
4. *NRES*, the number of resolved resonances
5. *NI*, the number of isotopes for a material
6. *NP*, the number of unresolved energy points
7. *NLS*, the number of angular momentum states
8. *NJS*, the number of channel spins for the largest angular momentum state.

The unresolved resonance calculation in module CSC001 has been recoded so that only one material at a time is processed, rather than all of the materials at once, as had been the case. This recoding effectively reduces the dimension in Eq. (1) by the factor *NOI* and all other quantities (*MNLS*, *MNJS*, *MNI*, and *MNP*) now refer to the specific material being processed rather than to the largest dimensioned material in the problem. No changes or modifications have been made in the algorithms or computational capability in this module.

Two large MC² calculations have been run using Version II data as a test of the code changes. Timing data and core requirements are presented in Tables IV-2-II and IV-2-III. Problem A was an ultrafine group calculation, homogeneous in composition, with an energy range from 10 MeV to 0.68 eV, having 66 fine energy groups and 27 broad energy groups. Twenty Version II materials were included and the elastic scattering of nine of these materials were analyzed using a Legendre treatment.[8] Problem B was identical to Problem A with the exception that Version I data were used for chromium, iron, and nickel. Problem A, containing 1528 resolved resonances, was run using the newly coded resonance module CSC001 and the other current ARC production MC² modules. Problem A used only the main computer core. Problem B, containing 863 resolved resonances, used the present ARC production MC² modules and required use of the large core storage (IBM 2361) in addition to the main computer memory.

Table IV-2-II displays the time spent in the various areas in module CSC001 for the execution of problems A and B. The most noticeable fact is the very long execution time taken for both problems because each has a large number of resolved resonances. The much longer execution time in the calculational area of the unresolved and resolved resonances (e.g., areas 4 and 5 of problem A) is due entirely to the fact that this problem has so many more resolved resonances. The number of resolved resonances affects both areas 4 and 5. The only additional overhead time that problem A requires over problem B is the trivial 13.3 seconds in area 6. This was the time spent requesting pointers and sifting and purging the BPOINTER container array for each of the materials in the problem. This was done in order to provide the proper size arrays for the processing of one material at a time in the unresolved resonance calculations.

Table IV-2-III shows a profile of the two MC² calculations. After finishing the unresolved and resolved resonance calculations in module CSC001, both problems should require the same calculational time for modules CSC002 and CSC003.[6] Problem A required an additional 608 seconds in these two modules because the 9 large buffers required

TABLE IV-2-I. 82-MATERIAL MC² LIBRARY INCLUDING 60 VERSION II MATERIALS

MAT	MC² Material Identification	Legendre Data	Resolved Resonances, NRES	Isotopes per Material, NI	Unresolved Energy Points, NP	Angular Momentum States, NLS	Channel Spins for Largest Angular Momentum State, NJS
1041	U-2322	No	0	—	—	—	—
1043	U-2342	No	21	1	15	2	2
1046	U-2362	No	15	1	15	2	2
1050	PU2382	No	14	1	3	2	2
1055	PU2422	No	21	1	15	2	2
1102	U-2352	No	89	1	25	2	4
1103	U-2382	No	250	1	15	2	2
1104	PU2392	No	89	1	30	2	3
1105	PU2402	No	201	1	11	2	2
1117	TH2322	No	229	1	15	2	2
1009	B-10 2	Yes	0	—	—	—	—
1013	O-16 2	Yes	0	—	—	—	—
1014	MG 2	Yes	0	—	—	—	—
1015	AL27 2	Yes	0	—	—	—	—
1016	TI 2	Yes	0	—	—	—	—
1017	V 2	Yes	0	—	—	—	—
1019	MN55 2	No	27	—	—	—	—
1085	CU63 2	Yes	28	—	—	—	—
1086	CU65 2	Yes	20	—	—	—	—
1087	CU 2	Yes	48	—	—	—	—
1140	C-12 2	Yes	0	—	—	—	—
1111	MO 2	Yes	46	7	All 15	All 2	2, 2, 4, 2, 4, 2, 2
1112	NB 2	Yes	218	1	15	3	6
1121	CR 2	Yes	183	—	—	—	—
1122	FE 2	Yes	188	—	—	—	—
1123	NI 2	Yes	294	—	—	—	—
1026	XE1352	No	0	—	—	—	—
1027	SM1492	No	30	1	15	2	4
1028	EU1512	No	28	1	15	2	4
1029	EU1532	No	21	1	15	2	4
1030	GD 2	No	29	—	—	—	—
1031	DY1642	No	2	1	15	2	2
1032	LU1752	No	17	1	15	2	4
1033	LU1762	No	21	1	15	2	4
1035	TA1812	No	78	1	15	2	4
1037	AU1972	No	63	1	15	2	4
1048	NP2372	No	33	1	2	1	1
1056	AM2412	No	19	1	2	1	1
1057	AM2432	No	12	1	15	1	1
1058	CM2442	No	15	1	3	2	2
1060	W-1822	No	6	1	15	2	2
1061	W-1832	No	16	1	15	2	3
1062	W-1842	No	17	1	15	2	2
1063	W-1862	No	5	1	15	2	2
1083	RE1852	No	30	1	15	2	4
1084	RE1872	No	25	1	15	2	4
1088	He 2	No	0	—	—	—	—
1120	D 2	No	0	—	—	—	—
1007	BE-9 2	Yes	0	—	—	—	—
1042	U3FP12	No	0	—	—	—	—
1045	U5FP12	No	0	—	—	—	—
1052	P9FP12	No	0	—	—	—	—
1066	U3FP22	No	0	—	—	—	—
1067	U3FP32	No	0	—	—	—	—
1068	U5FP22	No	0	—	—	—	—
1069	U5FP32	No	0	—	—	—	—
1070	P9FP22	No	0	—	—	—	—
1071	P9FP32	No	0	—	—	—	—
1106	PU2412	No	44	1	23	2	4

TABLE IV-2-I. *Continued*

MAT	MC² Material Identification	Legendre Data	Resolved Resonances, NRES	Isotopes per Material, NI	Unresolved Energy Points, NP	Angular Momentum States, NLS	Channel Spins for Largest Angular Momentum State, NJS
1059	NA23 2	Yes	3	—	—	—	—
1020	FE	Yes	0	—	—	—	—
1047	U 238	No	209	1	15	2	2
1051	PU239	No	89	1	16	1	2
1018	CR	Yes	0	—	—	—	—
1021	NI	Yes	0	—	—	—	—
1054	PU241	No	0	—	—	—	—
1005	LI 6	No	0	—	—	—	—
1006	LI 7	No	0	—	—	—	—
1012	N 14	Yes	0	—	—	—	—
1053	PU240	No	41	1	14	2	2
1059	NA 23	Yes	3	—	—	—	—
1044	U 235	No	89	—	—	—	—
1022	ZR	Yes	83	—	—	—	—
1054	PU241R	No	57	1	25	2	4
1044	U235	No	118	1	23	2	4
1047	U238	Yes	239	1	9	2	2
1051	PU239	No	87	1	20	2	3
1053	PU240M	No	41	1	14	2	2
1047	U 238I	No	209	1	15	2	2
102	U-235R	No	89	1	38	2	4
103	U-238R	No	412	1	15	2	2
104	PU239R	No	89	1	43	2	3

TABLE IV-2-II. Time Spent in Various Areas of Module CSC001 for Problems A and B

Area in Module	Problem A	Problem B
1. Interrogate MC² library for problem, sec	1.6	2.1
2. Read and reorder resolved resonances, sec	28.8	22.0
3. Initialize quantities and read W table, sec	1.0	1.0
4. Unresolved resonance calculation, sec	436.7	252.3
5. Resolved resonance calculation, sec	5020.0	2910.0
6. Print out ultrafine group resolved resonance macroscopic cross sections, sifting and purging container array, and write container array onto disk, sec	35.9	22.6
Total time spent in module CSC001, sec	5524.0	3210.0

for transferring elastic scattering matrices from computer memory to disk and back to computer memory had to be reduced to one-fourth their normal size in order that the problem could be contained in the main computer core. This emphatically illustrates the need for efficient buffering of data, especially when large amounts of data are involved, and the cost in computing time when inefficient buffering is encountered. It should be noted that before the modification to module CSC001, neither problem A nor B could have been contained only in main core memory even with a reduction in the Legendre data buffer size.

Correction in the Calculation of Scattering Matrices

In the MC² capability in the ARC system, the inelastic and $(n,2n)$ scattering matrices are computed by using the nuclear evaporation model above the region of the resolved levels. The energy distribution for emitted neutrons is represented by

$$N(E) = Ee^{-E/T},$$

where T is the appropriate nuclear temperature.[8] The fourth file of the MC² library contains tabulated nuclear tem-

TABLE IV-2-III. PROFILE OF TWO MC² PROBLEMS USING VERSION II NEUTRON CROSS SECTION DATA

Profile	Problem A	Problem B
Number of resolved resonances in problem	1528	863
MC² capability used	Present ARC production MC² capability with new coded module CSC001	Present ARC production MC² capability
Core size utilized: (double precision words)		
Main computer core	98,000	84,000
Large core storage	0	135,000
Other options invoked	Reduce the size of 9 buffers used in processing the Legendre materials	—
Time in seconds spent in module CSI001	2	2
Time in seconds spent in module CSC001	5524	3210
Time in seconds spent in CSC002 and CSC003	2025	1417

peratures as a function of energy. Subroutine INSCAT[8] calculates $\langle T^m \rangle_j$, the average temperature for material m and for fine energy group j. The normalized secondary neutron-scattering probability is given by

$$P^m_{j\to k} = \frac{\int_{E_k}^{E_{k+1}} E e^{-E/\langle T^m\rangle_j}\, dE}{\sum_{k=j}^{n} \int_{E_k}^{E_{k+1}} E e^{-E/\langle T^m\rangle_j}\, dE}, \tag{2}$$

where j is the index of the source fine group, k is the index of the receptor fine group, and E_{k+1} and E_k are the upper and lower energy boundaries, respectively, for energy group k. The sum of the denominator is over all groups of energy less than or equal to that of group j. Until recently the evaluation of the integrals of Eq. (2)

$$\int_{E_k}^{E_{k+1}} E e^{-D/\langle T^m\rangle_j}\, dE = (\langle T^m\rangle_j)^2 \left[e^{-E_k/\langle T^m\rangle_j} \left(\frac{E_k}{\langle T^m\rangle_j} + 1 \right) - e^{-E_{k+1}/\langle T^m\rangle_j} \left(\frac{E_{k+1}}{\langle T^m\rangle_j} + 1 \right) \right] \tag{3}$$

began with the source group $j = 1$ (highest energy fine group in the problem) and worked down to the lowest energy source group, i.e., the group which contains the threshold energy for statistical inelastic or $(n,2n)$ data. The code checked to determine if the in-group scattering were equal to zero for source group j and, if so, scattering into other receptor groups were not calculated for source group j.

This procedure can create an error in calculating $P^m_{j\to k}$ for the lowest energy source group. For this source group, the average value of the temperature, $\langle T^m \rangle_j$, can be quite small because the threshold energy for inelastic or $(n,2n)$ scattering may be just slightly below E_{k+1}. The arguments of the exponentials in Eq. (3) may therefore be very large for the in-group scattering and the exponential routine returns a zero if x becomes too large in exp $(-x)$. Thus the in-group scattering may be identically zero. In this case, no other elements of the scattering probability matrix are calculated for this source group. Scattering to lower groups does not involve the large negative exponent and hence should be non-negligible.

The MC² capability in the ARC system has been changed so that all elements of the scattering probability matrix that are energetically possible will be calculated. Any element of this matrix that is less than 10^{-50} will be set equal to zero so that computer underflow errors will be avoided when computing the microscopic and macroscopic homogenized inelastic and $(n,2n)$ scattering matrices using the scattering probability matrix.

REFERENCES

1. C. G. Stenberg and H. Henryson, II, *MC² Capability in the Argonne Reactor Computation (ARC) System* Reactor Physics Division Annual Report, July 1, 1969 to June 30, 1970, ANL-7710, pp. 367–371.
2. M. K. Drake, Ed., *Data Formats and Procedures for the ENDF Neutron Cross Section Library*, BNL-50274(T-601), (1970).

3. E. M. Pennington and J. P. Regis, *Developments Relating to the ENDF/B Project*, Reactor Physics Division Annual Report, July 1, 1969 to June 30, 1970, ANL-7710, pp. 50–52.
4. E. M. Pennington, J. C. Gajniak and A. B. Cohen, *Developments Relating to the ENDF/B Project*, Reactor Physics Division Annual Report, July 1, 1968 to June 30, 1969, ANL-7610, pp. 40–43.
5. E. M. Pennington, Argonne National Laboratory (private communication).
6. C. G. Stenberg and A. L. Rago, *Capabilities of MC² in the Argonne Reactor Computation (ARC) System*, Reactor Physics Division Annual Report, July 1, 1968 to June 30, 1969, ANL-7610, pp. 469–471.
7. L. C. Just, H. Henryson, II, A. S. Kennedy, S. D. Sparck, B. J. Toppel and P. M. Walker, *The System Aspects and Interface Data Sets of the Argonne Reactor Computation (ARC) System*, ANL-7711, pp. 79–134 (1971).
8. B. J. Toppel, A. L. Rago and D. M. O'Shea, *MC²*, *A Code to Calculate Multigroup Cross Sections*, ANL-7318 (1967).

IV-3. ETOE-2, A Program for Conversion of ENDF/B to MC²-2

C. G. Stenberg

The ETOE-2 (ENDF/B to MC²-2) code under development is a processing code that generates a library for the MC²-2[1] code. ETOE-2 is being written entirely in FORTRAN-IV and is variably dimensioned using the facilities of the subprogram package BPOINTER[2] which manages variably dimensioned arrays. The code will conform to the recommendations set forth by the Computer Code Coordination Committee, namely that a code should execute within 50,000 words of computer memory and all unformatted input/output should be handled by block data transfer. Block data transfer is a scheme for transferring records of data between computer core and peripheral storage devices with the data being read or written as a block with a single subscripted array structure. The intent of block data transfer is to increase input/output efficiency.

The ETOE-2 code accepts as input a binary alternate mode Evaluated Nuclear Data File/B (ENDF/B) tape[3] in which the data are arranged in the hierarchy of file (i.e., class of data such as resonance parameter, tabulated data, Legendre coefficients for elastic scattering, inelastic scattering, etc.), material, and reaction type. This binary alternate mode ENDF/B tape is produced by the program RIGEL[4] (replacement for the DAMMET[5] program) which has as input a binary coded decimal (BCD), standard mode (i.e., hierarchy of material, file, and reaction type) ENDF/B tape as received from the National Neutron Cross Section Center. It should be noted that the binary alternate mode ENDF/B tape that is used as input to ETOE-2 has binary records of data containing more than one subscripted list structure so the ENDF/B tapes do not have records compatible with the concept of block data transfer.

Table IV-3-I lists the titles and contents of the eight files which constitute the MC²-2 library generated by the ETOE-2 code. The main flow diagram presented in Fig. IV-3-1 displays the processing of the first five files of the ENDF/B data as obtained from the RIGEL program and the construction of the eight files of the MC²-2 library.

The administrative file contains user-supplied dependent specification data (e.g., material names, highest energy point in the library, group lethargy width for all energy groups in the library, highest order permitted for extended transport approximation, etc.), material identification data, resolved resonance control information, and inelastic and $(n,2n)$ distribution control information. This file's information is accumulated through the processing of the user supplied card input data and files 2, 3, and 5 of the binary alternate ENDF/B data. Hence this first file of the MC²-2 library is the last file of the library to be written.

The function table file contains a tabulated representation of the real and imaginary parts of the complex error function, $W(x,y)$, both on coarse and fine mesh intervals over specified ranges, tabulated values of the exponential integral E_3, and tabulated first flight escape and transmission probabilities. The ETOE-2 code will provide the following options: calculating these tabulated functions and generating a function table file, reading the function table from a peripheral storage device to generate this library file, or omitting the function table file from the MC²-2 library.

Almost all of the data in the unresolved and resolved resonance files of the MC²-2 library are simply a reorderin and restructuring of the data presented in file 2 ENDF/B data. A user-supplied parameter in ETOE-2 is a limiting mass number which is used in conjunction with the continuous slowing down (CSD) approach[6] for the spectrum calculation in the MC²-2 code. For all masses greater than the limiting mass number, the unresolved and resolved

TABLE IV-3-I. The Eight Files of the MC²-2 Library

File Number	Title	Contents
1.	Administrative	Specifications, material identification parameters, resolved resonance control information, and inelastic and $(n,2n)$ distribution control information
2.	Function table	Tabulated real and imaginary parts of the complex error function $W(x,y)$, tabulated exponential integral E_3, and tabulated first flight escape and transmission probabilities
3.	Unresolved resonance data	Unresolved resonance isotope control data, unresolved spin state and energy data, and statistical unresolved resonance data
4.	Resolved resonance data	Resolved resonance isotope control data. Resolved resonance parameters are present in the form of single-level or multilevel Breit-Wigner parameters or Adler-Adler multilevel parameters
5.	Smooth (tabulated) data	Coefficients for the calculation of $\nu(E)$, the number of neutrons per fission, and ultrafine group averaged cross sections for the following reactions: elastic scattering, fission, (n,γ), (n,p), (n,d), (n,H^3), (n,He^3), (n,α), and total cross section
6.	Inelastic and $(n,2n)$ distributions	Ultrafine group averaged cross sections for each resolved scattering level and ultrafine group averaged temperature data for the following: inelastic excitation temperature for the continuum and temperatures associated with the statistical calculation of $(n,2n)$ scattering for each partial energy distribution
7.	Fission spectra data	Ultrafine group averaged parameters in the generalized fission spectrum
8.	Legendre data	Legendre coefficients specified at ultrafine group boundaries; standard zero, first, and second order T matrix elements; "incomplete" T matrix elements; and mass dependent constants used in calculation of continuous slowing down moderating parameters

resonance parameters and associated resonance data will appear in the unresolved and resolved resonance file of the MC²-2 library. Also for these masses, which have resonance parameters given, tabulated values of the potential scattering cross section over the entire resonance region will be generated and added to the smooth non-resonant tabulated elastic scattering data of file 3 ENDF/B data. For masses less than the limiting mass number no unresolved or resolved resonance parameters or associated resonance parameters will appear in the unresolved and resolved resonance files of the MC²-2 library. Instead, tabulated values of the scattering cross section, which includes potential scattering and capture cross sections will be generated from the resonance parameters and added to their appropriate counterparts of file 3 ENDF/B data. Tabulated scattering and capture cross sections generated from resolved resonance parameters will be formed using one of the following options: a single-level Breit-Wigner representation for zero temperature,[7] a Doppler broadened single-level Breit-Wigner representation,[7] or an Adler-Adler multilevel treatment without Doppler broadening.[3] The desired number of tabulated scattering and capture cross sections per resonance is a user input option to ETOE-2. Tabulated scattering and capture cross sections generated from unresolved resonance parameters will be calculated using a single level Breit-Wigner representation for an isolated resonance with the provision for Doppler broadening. It is assumed that the limiting mass number will never be set high enough to exclude a fissionable material from the unresolved or resolved resonance file of the MC²-2 library. Therefore no provision for generating tabulated fission cross sections from resonance parameters has been made.

The smooth tabulated non-resonance data file consists of ultrafine group averaged cross sections. These cross sections are formed by averaging the tabulated energy-cross section pairs from file 3 ENDF/B data over ultrafine groups for the following reactions: elastic scattering, fission, (n,γ), (n,p), (n,d), (n,H^3), (n,He^3), (n,α), and total cross section. Before ultrafine group averaging takes place for elastic scattering and capture data, the tabulated scattering and capture cross sections calculated, when appropriate, from resonance parameters are added to their respective le 3 ENDF/B data. Part of the user input to ETOE-2 are the maximum and minimum MC²-2 library energy limits s well as the ultrafine group lethargy width.

The file containing inelastic and $(n,2n)$ distributions consists of ultrafine group averaged cross sections and temperature data. In a manner similar to file 3, cross sections are formed by averaging the tabulated energy-cross section pairs from file 3 ENDF/B data over ultrafine groups for the following reactions: total inelastic, $(n,2n)$ scatter-

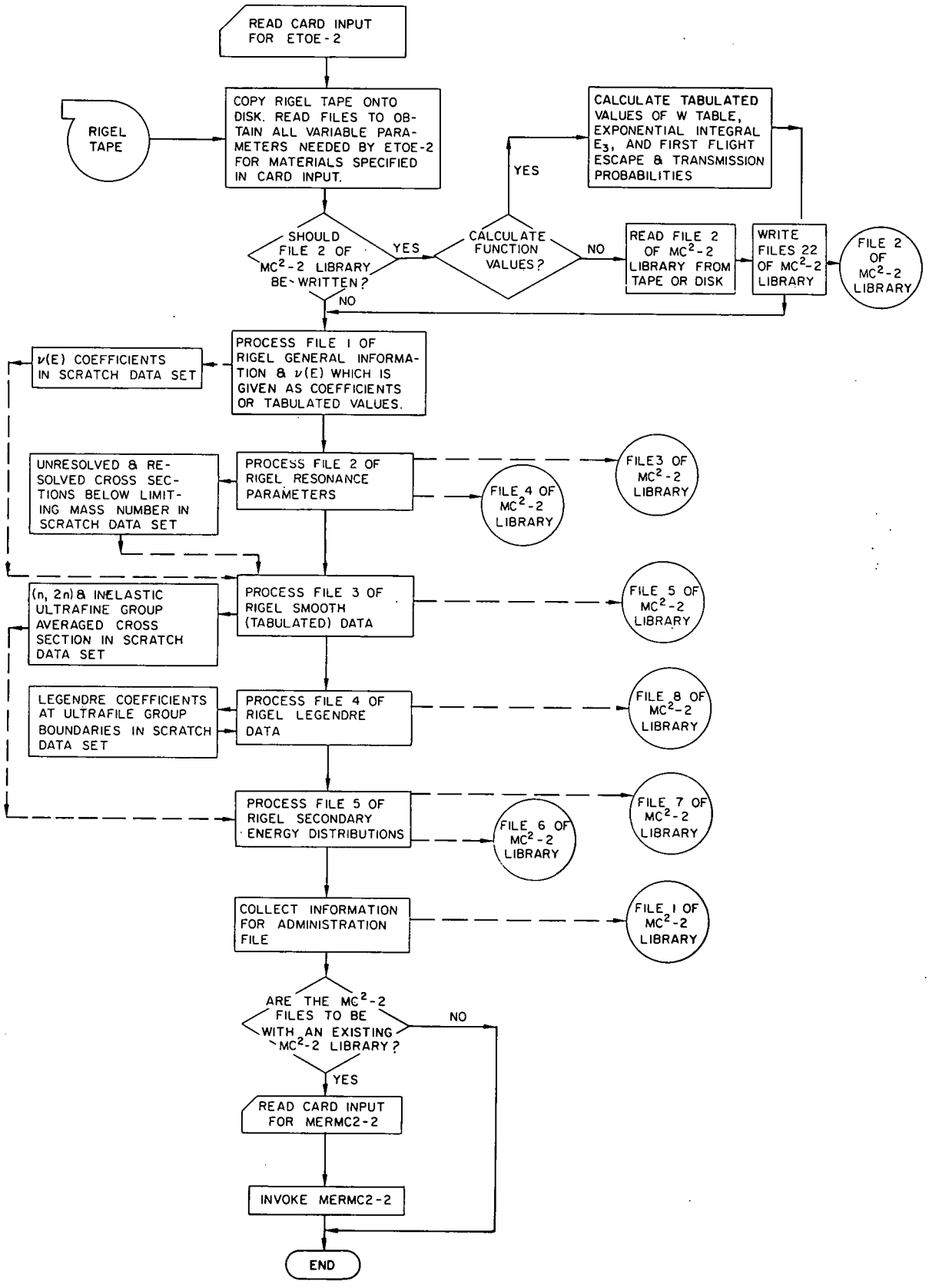

FIG. IV-3-1. Main Flow Diagram for ETOE-2. *ANL Neg. No. 116-849.*

ing, and inelastic excitation cross sections for each resolved scattering level. Ultrafine group averaged temperature data are calculated from ENDF/B file 5 tabulated energy-temperature pairs for the following: inelastic excitation temperature for the continuum and the temperatures associated with statistical calculation of $(n,2n)$ scattering for each partial energy distribution.

The fission spectra data file contains ultrafine group-averaged parameters from the generalized fission spectrum. The generalized fission spectrum is represented by

$$\chi(E) = \alpha(E)\frac{E}{\tau(E)^2}e^{-E/\tau(E)} + (1-\alpha(E))\sqrt{\frac{4E}{\pi\beta(E)^3}}e^{-E/\beta(E)},$$

where $\alpha(E)$, $\beta(E)$, and $\tau(E)$ are given in file 5 of ENDF/B as tabulated functions of incident neutron energy E. The ETOE-2 code calculates the ultrafine group averaged values of $\alpha(E)$, $\beta(E)$, and $\tau(E)$ for the MC²-2 library file.

The Legendre data file contains Legendre coefficients specified at ultrafine group energy boundaries for elastically scattered neutrons. File 4 of ENDF/B provides angular distribution data either in the form of Legendre polynomial coefficients or as tabulated probability distributions. The ETOE-2 code calculates Legendre coefficients when ENDF/B data are in the form of tabulated probability distributions. The Legendre coefficients at ultrafine group boundaries are then formed by interpolating the ENDF/B values. The maximum order expansion coefficient permitted in the MC²-2 library is a user-specified option to ETOE-2. The Legendre data file also contains mass dependent constants used in the calculation of continuous slowing down moderating parameters as well as the zero, first and second order T matrix elements.[8,9] The zero and first order T matrix elements are calculated by a recursive method[7] in order to circumvent a precision problem encountered while integrating products of high order Legendre polynomials. The second order T matrix elements are calculated by integrating products of Legendre polynomials since the second order T matrix elements are required only for low order Legendre polynomials.

Presently the ETOE-2 program is approximately 80 % coded. As areas and segments are coded, preliminary testing using ENDF/B data will be performed and files 2 through 8 of the MC²-2 library will be constructed. Files 2, 3, 4, 5 and 8 of the MC²-2 library have been created using selected materials for the purpose of performing active testing of various areas of the MC²-2 code (see Paper IV-1).

The ETOE-2 code produces a binary MC²-2 library for each of the binary alternate ENDF/B tapes supplied to it. Part of the ETOE-2 code package will consist of a capability for merging partial MC²-2 libraries in order to form one complete library. This facility will be similar to the existing MERMC2[10] code that is now used to merge and add new data to existing MC²[11] library tapes.

References

1. B. J. Toppel, *Plans for the New MC² Code, MC²-2*, Reactor Physics Division Annual Report, July 1, 1969 to June 30, 1970 ANL-7710, pp. 371–373.
2. L. C. Just, H. Henryson, II, A. S. Kennedy, S. D. Sparck, B. J. Toppel and P. M. Walker, *The System Aspects and Interface Data Sets of the Argonne Reactor Computation (ARC) System*, ANL-7711, pp. 79–134 (1971).
3. M. K. Drake, Ed., *Data Formats and Procedures for the ENDF Neutron Cross Section Library*, BNL-50274 (T-601), (1970).
4. D. E. Cullen, Brookhaven National Laboratory (private communication).
5. National Neutron Cross Section Center, *"Description of the ENDF/B Processing Codes CHECKER, CRECT, DAMMET, PLOTFB, and Retrieval Subroutines*, BNL-13582 (ENDF-110), (September 1967) (Revised April 1969).
6. W. M. Stacey, Jr. *Continuous Slowing-Down Theory for the Elastic Moderation of Neutrons*, Reactor Physics Division Annual Report, July 1, 1969 to June 30, 1970, ANL-7710, pp. 404–407.
7. D. M. Green and T. A. Pitterle, *ETOE, A Program for ENDF/B to MC2 Data Conversion*, APDA-219 (ENDF-120), (1968).
8. H. Henryson, II, C. G. Stenberg and B. J. Toppel, *Calculation of Elastic Scattering Matrices*, Reactor Physics Division Annual Report July 1, 1969 to June 30, 1970, ANL-7710, pp. 395–403.
9. H. Amster, *Heavy Moderator Approximations in Neutron Transport Theory*, J. Appl. Phys. **29**(4), 623–627 (1958).
10. E. M. Pennington, J. C. Gajniak, A. B. Cohen and W. Bohl, *Service Routines for the Multigroup Cross-Section Code MC²*, ANL-7654 (1970).
11. B. J. Toppel, A. L. Rago and D. M. O'Shea, *MC², A Code to Calculate Multigroup Cross Sections*, ANL-7318 (1967).

IV-4. Modifications of the ARC System and Adaptation to the Current IBM Operating System

W. L. Woodruff

Numerous modifications have been made in the standard paths, catalogued procedures, and computational modules of the ARC System. Some modifications are the result of efforts to extend and improve the ARC System, while others have been necessary to adapt the ARC System to a new IBM operating system (OS360, IBM Release-19). Some minor coding "bugs" have also been encountered as user experience has accumulated.

With the implementation of OS360, IBM Release-19, it was necessary to make the ARC System compatible with this new operating system. The conversion consisted mainly of upgrading the ARC System Fortran I/O package with the new IBM I/O package of Release-19 and of changes in the Job Control Language (JCL) of the catalogued procedures used by the ARC System.

Under Release-19 the spanning of logical records in a variably blocked sequential data set is now handled by OS360, whereas before (with Release-17) the function was handled by Fortran. In order to obtain the span support it is now necessary to specify the subparameter RECFM=VBS in the data control block (DCB) of the JCL for each sequential binary data set. The meaning of the subparameter LRECL in the DCB for such data sets has also changed from the previous usage. LRECL must now be set to either the length of the largest physical record contained in a given data set or to LRECL=X if the variable length records might exceed 32,756 bytes. Thus, the JCL of the ARC System catalogued procedures has been modified to use the subparameters RECFM=VBS and LRECL=X in the DCB parameter for all sequential binary data sets.

The ARC System Fortran I/O package was re-link edited to include the Release-19 version of the IBM I/O package. The IBM macro IHCFIOSM for Release-19, invoked by the routine IHCFIOSH, was modified in an identical fashion to that previously described for the Release-17 version.[1] The ARC System routine ARCIBCOM was not changed. These modifications to the ARC System catalogued procedures and I/O package were tested prior to implementation with satisfactory results.

The introduction of the new release of OS360, however, did create some further difficulties for the ARC System. ARC System modules which pass parameters can no longer have a dummy MAIN(1) program when compiled under Release-19. The dummy MAIN program usually does little more than call the actual driver subprogram and provide an entry point for the module. Since the current operating system does not require the use of a MAIN program, the use of a MAIN program has been eliminated. The driver subprogram with the parameter list to be passed is now designated as subroutine MAIN to preserve the use of ENTRY MAIN in the overlay structure of the module. This lack of a MAIN program for a load module has produced one minor difficulty. Direct access data sets OPENed by a module are CLOSEd by OS360 only if RETURN is from a MAIN program in the module. Although the ARC System makes very limited use of direct access data sets (currently only one module), all buffers allocated to OPEN data sets should be released as part of the cleanup procedure needed prior to a LINK to another module. To circumvent this problem, a Fortran callable assembler language routine has been written which CLOSEs all direct access data sets before a RETURN is made from the module.

The current operating system also now imposes a 50,000 line limit on printed output, and jobs whose printing would exceed this limit must be directed to tape for peripheral processing. This new practice has uncovered a problem in the cleanup procedure used in many of the standard paths and in some of the computational modules. The procedure consisted of a CLOSE or REWIND of all OPEN sequential data sets before a LINK to another module. This releases buffer allocations for OPEN data sets and prevents possible core-fragmentation difficulties in LOADing the next module to be executed. With the printed output directed to a tape unit, the REWIND or CLOSE also produces a physical rewind of the tape, and data generated by a module is overwritten by data generated by a subsequent module. REWINDs of the data set allocated for printing have now been removed from all paths and modules.

As part of a general upgrading of the ARC System standard paths, a uniform cleanup procedure has been adopted which consists of calls to the subroutine PRCLOZ after the execution of each of the module in a path.[2] The su routine PRCLOZ avoids a REWIND of the data set for printing while still providing a cleanup of all other OPE data sets. The buffers for printing are shared by all modules LINKed in a path. Default options have now been assigned in many of the standard paths, and a path-dependent BCD data set is required only if other than the default options are desired.

A standard path and catalogued procedure has been written for the two-dimensional transport theory capability of the ARC System[3] (see Paper IV-5). The capability is currently available for user testing.

Modifications have been made to the one and two-dimensional diffusion theory modules (NUC002, NUC004)[4] and (NUC005, NUC006)[5] which allow the user to supply an adjoint flux guess in the execution of a combined real and adjoint computation. A subroutine FLXIN was added which tests for and reads the user's guess. If no adjoint flux guess is supplied by the user, the latest real flux is used, as was the case before the modifications. The microscopic and macroscopic cross-section group collapse modules (AJC007 and AJC008)[6] have also been modified to allow the use of the dynamic storage allocation routine BPOINTER[1] and to provide the capability of specifying BPOINTER container array sizes in the BCD code-dependent data set A.COL.[1] These modules can be invoked in the standard path STP004.[2]

REFERENCES

1. L. C. Just, H. Henryson, II, A. S. Kennedy, S. D. Sparck, B. J. Toppel and P. M. Walker, *The System Aspects and Interface Data Sets of the Argonne Reactor Computation (ARC) System*, ANL-7711 (1971).
2. W. L. Woodruff, H. Henryson, II, J. Hoover, P. H. Kier and C. G. Stenberg, *The ARC Systems Standard Paths*, ANL-7712 (1971).
3. R. H. Thompson, G. K. Leaf, L. T. Bryant, D. Schoengold and H. Greenspan, *The ARC System Two-dimensional Transport Theory Capability*, ANL-7718 (to be published).
4. D. E. Neal, G. K. Leaf and A. S. Kennedy, *The ARC System One-dimensional Diffusion Theory Capability, DARC1D*, ANL-7715 (1971).
5. T. A. Daly, A. S. Kennedy and G. K. Leaf, *The ARC System Two-dimensional Diffusion Theory Capability, DARC2D*, ANL-7716 (to be published).
6. E. A. Kovalsky, J. Zapatka, H. Henryson, II, J. Hoover and P. M. Walker, *The ARC System Cross-Section Homogenization and Modification Capabilities*, ANL-7714 (1971).

IV-5. Two-Dimensional Transport Theory Capabilities in the ARC System

H. GREENSPAN, R. H. THOMPSON* and W. L. WOODRUFF

Two-dimensional Transport Theory computational capability has been implemented in the ARC system. The standard path STP011 links ARC system modules NUI001,[1] NUI002,[2] NUI006,[1] NUC001,[1] NUC008,[3] AJC002,[4] and NUE002[3] for this purpose.

NUC008 is the module which contains the algorithms for the solution of the 2-D Discrete Ordinate (S_n) approximation to the multigroup transport equations, for a variety of problem conditions.

The code allows either isotropic or linear anisotropic scattering. Fission fractions may be incident-energy dependent (fission matrix) or not. Homogeneous or inhomogeneous problems can be solved. In the inhomogeneous problems, volume and surface sources are treated. The volume sources are restricted to be isotropic. Anisotropy is allowed for in the surface sources.

Regular (real) or adjoint solutions and the corresponding k_{eff} are obtained in the homogeneous case. Also, the dimensions of a specified set of regions, material concentrations, and inverse period may be varied to achieve a specified k_{eff} in criticality searches.

The module has a built-in set of directions and weights for orders $n = 2, 4, 6, 8, 12, 16$; however, the user may specify his own set of directions and weights. At the user's option, the program will provide group skipping and a coarse mesh rebalancing to help convergence. Streaming corrections and density factors may be specified by the region.

The geometries treated are xy and rz. The boundary conditions can be either free, reflective or periodic. A white (isotropic return) boundary condition is available for the right boundary in rz geometry.

At the user's option the code generates a restart data set. This enables the user to proceed from that point in the problem where the restart has been generated. In addition to the flux and some other characteristic parameters, the restart data set contains pointers to locations of arrays and thus makes it unnecessary to reconstruct them.

Separate input fluxes (not from restart) may also be used to start a calculation.

* Applied Mathematics Division, Argonne National Laboratory.

The edits available include print-outs of normalized fluxes, fission and external sources, power, total removal, scattering and balances. On request, a neutron inventory may be invoked which computes, for specified isotopes, materials, and/or compositions, at each point, region, area, zone or total reactor, for specified groups, the following reaction rates: (n,γ), (n,α), (n,p), fission, total elastic removal, inelastic removal, $(n,2n)$ removal, total removal, power, power density, maximum-to-average power density, and/or the following source ratios: fission, $(n,2n)$, and scattering. In addition, total or regional leakage rates and breeding and conversion rates may be calculated.

Test problems have been run with the 2-D transport module. These have been run in xy and rz geometries for the homogeneous cases. The calculated k_{eff} values compare to any desired accuracy with the k_{eff} as computed with SNARG-2D[5] for the same problem. Also tested were the search options on dimension and on material concentration. The restart and initial flux input were also tested and made operative.

REFERENCES

1. E. A. Kovalsky, J. Zapatka, H. Henryson, II, J. Hoover and P. M. Walker, *The ARC System Cross Section Homogenization and Modification Capabilities*, ANL-7714 (1971).
2. E. A. Kovalsky and D. E. Neal, *The ARC System Neutronics Input Processor*, ANL-7713 (1971).
3. R. H. Thompson, G. K. Leaf, L. T. Bryant, D. Schoengold and H. Greenspan, *The ARC System Two-dimensional Transport Theory Capability*, ANL-7718 (to be published).
4. T. A. Daly, D. E. Neal, D. A. Schoengold and G. K. Leaf, *The ARC System Two-dimensional Adjunct Calculations*, ANL-7720 (to be published).
5. G. J. Duffy, H. Greenspan, S. D. Sparck, J. V. Zapatka and M. K. Butler, *SNARG-2D, A Two-dimensional, Discrete-ordinate Transport-theory Program for the CDC-3600*, ANL-7426 (1968).

IV-6. User Experience With the ARC System

H. HENRYSON, II and B. J. TOPPEL

The increasing size and complexity of codes for reactor calculations has led many laboratories to the development of automated modular computational systems. In addition to the work in the United States at Knolls Atomic Power Laboratory,[1] Argonne National Laboratory,[2] and the Savannah River Laboratory,[3] France, Germany, England, Japan and Norway have pursued work in this field. The recommendations of the Committee on Computer Code Coordination to the Advisory Committee on Reactor Physics have stressed the need for compatibility with future modular systems. The Argonne Reactor Computation (ARC) System at Argonne National Laboratory, on which work began in 1965, has successfully accomplished many of the goals of a large modular system by providing a practical and efficient environment for reactor physics production and development work.

In the development of the ARC System, use was made of the extensive data management facilities of the IBM ØS/360. At Argonne's Idaho and Illinois sites, the ARC system provides the basic environment for reactor computations. The system has also operated on a number of IBM/360 configurations in the U.S., and has been modified to successfully execute on the CDC 6400, 6600, and 7600 computers.[4] Although the ARC system was designed about the special needs of reactor calculations, the system aspects are of use in any field where calculations are modular in nature and each calculation may require the entire computer memory as well as many files of interface data.

TABLE IV-6-I. ARC SYSTEM STANDARD PATH MODULES

1. STP001 (PATH1D, PATHSH) 1D-Diffusion
2. STP002 (PTR1D) 1D-Transport
3. STP003 (PDIF2D, PD2DSH) 2D-Diffusion
4. STP004 Burnup Diffusion
5. STP005 (MCSQRE) Multigroup Cross-sections
6. STP006 (PERT1D) 1D-Diffusion Perturbation
7. STP007 (PERT2D) 2D-Diffusion Perturbation
8. STP008 2D-Spatial Synthesis
9. STP009 General Neutronics
10. STP010 ENDF/B to MC²
11. STP011 2D-Transport

TABLE IV-6-II. SAMPLE ARC SYSTEM INPUT FOR 1-D DIFFUSION CALCULATION

```
//INPUT1D JOB (FXXXXX,10,3),NAME,MSGLEVEL=1,CLASS=
               A,REGION=(760K,1000K)
ACCOUNTING CARD
/*SETUP DEVICE=2314,ID=DISK23
//EXEC ARCSPOO1,MICRVOL=DISK23,MICRXS1='XSISO.FILE1',
//             MICRXS2='XISO.FILE2'
//SYSIN DD *
BLOCK=OLD
DATASET=XS.ISO
BLOCK=STPOO1
DATASET=A.PDIF1D
01          4       0       0       0
DATASET=A.DIF1D
01              SAMPLE 1-D DIFFUSION PROBLEM. PROBLEM 1
01                  0       0       0       3       25
02                          0               1.0
03                100       1
DATASET=A.NIP
01              SAMPLE 1-D DIFFUSION PROBLEM. PROBLEM 1
03                 30       0       0
04                  3       4
05          XUO.4692
06      GODIVAO.0           8.71                    40
14              CORE  U235 0.045447    U238          0.00256
15       CORE  GODIVA
BLOCK=STPOO1
MODIFY=A.NIP
01              SAMPLE 1-D DIFFUSION PROBLEM. PROBLEM 2
04                  3       2
05=DELETE
MODIFY=A.DIF1D
01              SAMPLE 1-D DIFFUSION PROBLEM. PROBLEM 2
01                  0       0       0       3       25
/*
```

The computing needs of the reactor community may be broadly classified in terms of three types of users: (1) production users; (2) users interested in linking existing capabilities in non-standard ways; and (3) users developing new capabilities. The ARC system provides an efficient environment for the three classes of users.

PRODUCTION USERS

In its present context a production user may be considered one who is not directly concerned with the fact that he is using a modular system. Rather, his concerns are with invoking a "standard" capability (for example, 1-D neutronics calculations) in as simple a manner as possible, with the ease of preparing and modifying input data, and with the ability to retrieve interface data from prior calculations. For such users the ARC system provides a number of "standard paths" which may be considered as a library of stand-alone codes with standardized input specifications. In Table IV-6-I a list of ARC system standard paths is presented. An example of the input deck required to run the 1-D diffusion theory path is given in Table IV-6-II. This example illustrates a number of points characteristic of all standard paths in the ARC system. Input data are divided into blocks which are referenced by the standard path and processed sequentially by ARC system routines. In the example of Table IV-6-II, BLØCK=ØLD flags the interface data sets which have been generated previously by an execution of either the same or a different path in the ARC system. BLØCK=STP001 contains BCD data required for the particular execution. Within each block of data a number of keywords provide the system routines with information regarding the processing of these data. For example, DATASET= indicates that the following data are used to create a new interface file, whereas MØDIFY= indicates that the named file already exists but should be modified using the data in this subblock. The structuring of data in this format, along with the variety of keywords available,[5] has proved an extremely flexible and easy-to-use convention for ARC system users. The user need not be concerned with the burden of specifying anything except

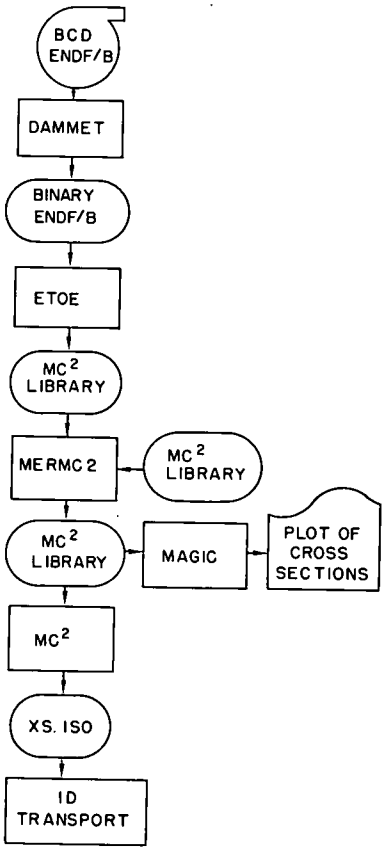

FIG. IV-6-1. Sample ARC System Path. *ANL Neg. No. 116-1069.*

TABLE IV-6-III. INPUT FOR SAMPLE ARC SYSTEM PATH

```
BLOCK=OLD
DATASET=ENDFBCD2
DATASET=WTABLE
DATASET=MCSQRE2
BLOCK=STP002
DATASET=A.INPTR1
..... INPUT DATA .....
DATASET=A.PRT1D
..... INPUT DATA .....
DATASET=A.NIP
..... INPUT DATA .....
BLOCK=STP010
NOSORT=A.DAMMET
..... INPUT DATA .....
NOSORT=A.ETOE
..... INPUT DATA .....
NOSORT=A.MERMC2
..... INPUT DATA .....
NOSORT=A.MAGIC
..... INPUT DATA .....
BLOCK=STP005
DATASET=A.XSSPC
..... INPUT DATA .....
```

```
C     SAMPLE ARC SYSTEM PATH DESIGNED TO READ ENDF/B TAPE, CREATE
C     MC**2 LIBRARY, PLOT SELECTED CROSS SECTION DATA FROM MC**2
C     LIBRARY, EXECUTE MC**2 PROBLEM TO CREATE BROAD GROUP CROSS
C     SECTIONS AND EXECUTE ONE-DIMENSIONAL TRANSPORT CALCULATION
C
C     MODULES AND PATHS INVOKED BY THIS PATH
C
C         STP002      (1-D TRANSPORT STANDARD PATH)
C                     NUI001  (INHOMG)
C                     NUI002  (GNIP)
C                     NUI005  (1-D TRANSPORT SPECIFICATIONS)
C                     NUI006  (RUN TIME CROSS SECTION MODIFICATIONS)
C                     NUC001  (HOMOG)
C                     NUC003  (SNARC1D)
C                     NUE001  (OUTMAN1D)
C                     AJC001  (INVENT1D)
C         STP005      (MC**2)
C                     CSI001  (INPUT)
C                     CSC001  (RESXEC)
C                     CSC002  (SCSFM)
C                     CSC003  (BCSFM)
C         STP010      (ENDF/B MANAGEMENT)
C                     CSI002  (CHECKER)
C                     CSI003  (CRECT)
C                     CSI004  (DAMMET)
C                     CSI005  (ETOE)
C                     CSI006  (MERMC2)
C         CSI008      (MAGIC)
C
C     SET UP DATASET NAME GLOSSARY
C
      DOUBLE PRECISION DSNAME(90)
      DATA DSNAME/
     18HA.CHECK ,8HA.CRECT ,8HA.DAMMET,8HA.ETOE  ,8HA.INPTR1,
     28HA.INVENT,8HA.MERMC2,8HA.NIP   ,8HA.OUTMAN,8HA.PRT1D ,
     38HA.STP010,8HA.XSSPC ,8HB.HOMOG ,8HBC      ,8HENDFBCD1,
     48HENDFBCD2,8HENDFBCD3,8HENDFBIN1,8HES.D1D  ,8HES.D1SH ,
     58HFA.D1   ,8HFA.D1A  ,8HFM.FLUX ,8HFR.D1   ,8HFR.D1A  ,
     68HFR.PN   ,8HFSA.D1  ,8HFSR.D1  ,8HGEOM    ,8HGEOM.P  ,
     78HJA.D1   ,8HJR.D1   ,8HMCSQRE1 ,8HMCSQRE2 ,8HMCSQRE3 ,
     88HSCR001  ,8HSCR002  ,8HSCR003  ,8HSP.CICN ,8HSP.CRIT ,
     98HSP.T1NEW,8HSP.T1OLD,8HTHRM.LIB,8HWTABLE  ,8HXS.C.ANI,
     A8HXS.C.AUX,8HXS.C.MIN,8HXS.PNTR1,8HXS.C.RES,8HXS.C.SMT,
     B8HXS.C.UFG,8HXS.ENDF ,8HXS.ENDF3,8HXS.FLUX ,8HXS.I.INP,
     C8HXS.I.RES,8HXS.INSCT,8HXS.ISO  ,8HXS.ISO2 ,8HXS.PNTR ,
     D16*8HDUMMY
     E8HXS.M.ANI,8HXS.M.AUX,8HXS.M.MIN,8HXS.C.MI1,8HXS.PNTR2,
     F8HXS.SCRCH,8HXS.SCR1 ,8HXS.SCR2 ,8HXS.SCR3 ,8HXS.SORS ,
     G8HXS.THERM,8HXS.UNRES,8HA.MAGIC ,8H$       /
C
C     INITIALIZE ARC SYSTEM ROUTINES
C
      CALL SYSTEM(DSNAME)

C     CREATE MC**2 LIBRARY FILES FROM INPUT ENDF/B FILE BY INVOKING
C     THE STANDARD PATH STP010
C
C     REQUIRED BCD INPUT OBTAINED FROM DATA BLOCK STP010 MAY INCLUDE
C     THE DATASETS A.CHECK,A.CRECT,A.DAMMET,A.ETOE,A.MAGIC,A.MERMC2,
C     AND A.STP010
C
      CALL LINK(8HSTP010  )
C
C     PLOT SELECTED DATA FROM MC**2 FILES BY INVOKING THE MODULE CSI008
C
C     REQUIRED BCD INPUT IS DATASET A.MAGIC WHICH HAS ALREADY BEEN
C     PROCESSED FROM DATA BLOCK STP010
C
      CALL LINK(8HCSI008  )
C
C     CREATE BROAD GROUP CROSS SECTION SET USING THE MC**2 STANDARD
C     PATH AND THE LIBRARY DATA CREATED ABOVE BY STP010
C
C     REQUIRED BCD INPUT OBTAINED FROM DATA BLOCK STP005 WHICH
C     CONTAINS THE DATASET A.XSSPC
C
      CALL LINK(8HSTP005  )
C
C     USING BROAD GROUP CROSS SECTIONS DO 1-D TRANSPORT CALCULATION
C
C     REQUIRED BCD INPUT OBTAINED FROM DATA BLOCK STP002 WHICH MAY
C     CONTAIN THE DATASETS A.INPTR1,A.INVENT,A.NIP,A.OUTMAN,A.PRT1D
C
      CALL LINK(8HSTP002  )
C
C     IF DIFFUSION THEORY CALCULATION WERE REQUIRED INSTEAD OF
C     TRANSPORT CALCULATION, REPLACE THE STATEMENT CALL LINK(8HSTP002  )
C     WITH THE STATEMENT CALL LINK(8HSTP001  ) AND REPLACE REQUIRED
C     BCD DATASETS A.INPTR1 AND A.PRT1D WITH A.DIF1D AND A.PDIF1D
C
      STOP
      END
```

FIG. IV-6-2. Coding of Sample ARC System Path. *ANL Neg. Nos. 116-1067 and 116-1068.*

the most rudimentary job control language in preparing his job. Rather, his major responsibility lies in specifying his input data. In this regard the user reaps the advantages of a modular system since the same input data sets are used by a number of standard paths. Thus, the changes in input required in going from a 1-D diffusion theory calculation to a 1-D transport theory calculation, exclude the information common to both; e.g., geometry, composition and search specifications. The example given in Table IV-6-II also illustrates the users ability to modify his input data, thus permitting a number of problems to be executed in sequence. A further benefit to the user of the ARC system has been the ease of saving alphanumeric or binary data from a given run for use in restarting a later run of the same or a different path.

Non-Standard Path Users

The large number of alternative ways of linking a large collection of modules make it impossible to predict all of the complex interactions a user might wish to specify in writing an ARC system path. Consequently, the user often finds that, although the modules are available to do his job, a standard path has not yet been written to link the modules in the order he requires. The ARC system provides an extremely flexible and simple means of manipulating modules at the user's discretion. By following a small number of ARC system conventions, it is possible for a user to access the complete library of modules (and standard paths) with a Fortran program. An example of such a use is illustrated in Fig. IV-6-1. The user wishes to calculate broad group cross sections from ENDF/B data using the multigroup code MC², plot selected data, and then use the cross sections in a 1-D S_N calculation. An investigation of Table IV-6-I shows that, although standard paths exist to perform the preparation of an MC² library, the MC² calculation, and the S_N calculation, a single path is not available to perform the whole calculation. Furthermore, although a module is available to plot data from the MC² library (c.f., Table IV-6-V), it is not available in any of the standard paths. In Fig. IV-6-2 the nine-statement Fortran program required to execute this "non-standard" path is shown. The example illustrates the ease of accessing any of the modules available in the ARC system. The input data required by such a path follow the same conventions illustrated in the example of Table IV-6-II, and an example is provided in Table IV-6-III.

TABLE IV-6-IV. Neutronics Calculation Modules

1.	NUI001 (INHØMG) Cross-section Homogenization Specifications
2.	NUI002 (GNIP) Code Independent Specifications
3.	NUI005 1D-Transport Specifications
4.	NUI006 Run-time Microscopic Cross-section Modifications
5.	NUC001 (HØMØG) Cross-section Homogenization
6.	NUC002 (DIF1D) 1D-Diffusion External Source and K Calculation
7.	NUC003 (SNARC1D) 1D-Transport
8.	NUC004 (D1DSH) 1D-Diffusion Search
9.	NUC005 (DIF2D) 2D-Diffusion External Source and K Calculation
10.	NUC006 (D2DSH) 2D-Diffusion Search
11.	NUC007 Material-composition Homogenization
12.	NUC008 2D-Transport
13.	NUE001 (OUTMAN1D) 1D-Neutronics Output Manipulation
14.	NUE002 2D-Transport Output Edit

TABLE IV-6-V. Cross Section Preparation Modules

1.	CSI001	Epithermal Cross-section Specifications
2.	CSI002	ENDF/B Data Checker
3.	CSI003	ENDF/B Data Corrector
4.	CSI004	ENDF/B Format Converter
5.	CSI005	ENDF/B to MC² Format Converter
6.	CSI006	Merger for MC² Libraries
7.	CSI007	Delayed Neutron Data Preparation
8.	CSI008	Plotter for MC² Libraries
9.	CSC001	Resonance Cross-sections
10.	CSC002	Nonresonant Cross-sections and Fundamental Mode Spectrum
11.	CSC003	Broad-group Cross-sections and Fundamental Mode Spectrum
12.	CSE001	Cross-section Data Set Editor

TABLE IV-6-VI. ADJUNCT CALCULATIONS MODULES

1. AJC001 (INVENT1D) 1D-Neutron Inventory
2. AJC002 (INVENT2D) 2D-Neutron Inventory
3. AJC003 (PRT1D) 1D-Diffusion Perturbation
4. AJC004 (PRT2D) 2D-Diffusion Perturbation
5. AJC005 (SYN1D) Spatial Synthesis
6. AJC006 (CPGEØM) Geometry Dataset Writer
7. AJC007 Microscopic Cross-section Group Collapse
8. AJC008 Macroscopic Cross-section Group Collapse

TABLE IV-6-VII. FUEL-CYCLE AND DEPLETION CALCULATION MODULES

1. FCI001 Fuel Cycle Specifications
2. FCC001 Fuel Cycle

TABLE IV-6-VIII. ARC SYSTEM DOCUMENTATION

Report No.	Report Title
ANL-7711	The System Aspects and Interface Data Sets of the Argonne Reactor Computation (ARC) System
ANL-7712	The ARC System Standard Paths
ANL-7713	The ARC System Neutronics Input Processor
ANL-7714	The ARC System Cross-section Homogenization and Modification Capabilities
ANL-7715	The ARC System One-dimensional Diffusion Theory Capability, DARC1D
ANL-7716	The ARC System Two-dimensional Diffusion Theory Capability, DARC2D
ANL-7717	The ARC System One-dimensional Transport Theory Capability, SNARC1D
ANL-7718	The ARC System Two-dimensional Transport Theory Capability, SNARC2D
ANL-7719	The ARC System One-dimensional Adjunct Calculations and Edits
ANL-7720	The ARC System Two-dimensional Adjunct Calculations and Edits
ANL-7721	The ARC System Fuel Cycle Analysis Capability, REBUS
ANL-7722	The ARC System Cross-section Generation Capability, ARC-MC²
ANL-7334	SYN2D, A Flux Synthesis Program Based on a Discontinuous Trial Function Formulation
ANL-7768	The Conversion of the Argonne Reactor Computation (ARC) System to the Control Data 6000 and 7000 Series Hardware

In a manner quite similar to that given in the example above, it has been a simple matter to provide a large choice of neutronics calculations in the ARC System Fuel Cycle capability REBUS.[8] In particular, paths exist to perform the flux calculation for fuel cycle, using 2-D diffusion, 2-D synthesis, 1-D diffusion, or 1-D transport algorithms.

A list of present ARC system modules is given in Tables IV-6-IV through IV-6-VII. As the size of such an open-ended system grows, it is obvious that good documentation of all modules in the system becomes a prerequisite for efficient use of the system. Consequently, a number of volumes are being prepared (Table IV-6-VIII) which provide information on all of the system aspects, conventions, and interface data sets of the ARC system, as well as a description of both the physics and coding of ARC system modules.

METHODS DEVELOPMENT

Just as it is possible to write new paths which make use of existing computational modules, it is also possible to take advantage of existing capabilities when adding new algorithmic capability. The elimination of the necessity for programming duplication is one of the chief benefits of a modular system. In Table IV-6-IX a list is given which illustrates how various modules are utilized repeatedly for a number of different computational capabilities. Thus, the recently completed 2-D transport module is used by a standard path which links to the same input processor, cross section homogenization, and inventory modules as the 2-D diffusion theory path. Similarly, a multigroup space-time reactor disassembly dynamics capability being developed is making extensive use of the same computational modules used by the neutronics standard paths. The latter effort includes the conversion of a stand-alone hydrodynamics code, VENUS, to a modular structure. The ease of incorporating stand-alone codes into the ARC system was also demonstrated by the minor effort required to link the five ENDF/B processing codes CRECT, CHECKER, DAMMET, ETOE and MERMC2[7] into a single path.

TABLE IV-6-IX. ARC System Modules Invoked by Standard Path Modules

Standard Path Module	ARC System Modules Invoked
STP001	NUI001, NUI002, NUI006, NUC001, NUC002, NUC004, NUE001, AJC001
STP002	NUI001, NUI002, NUI005, NUI006, NUC001, NUC003, NUE001, AJC001
STP003	NUI001, NUI002, NUI006, NUC001, NUC005, NUC006, AJC002
STP004	NUI001, NUI002, NUC001, NUC005, NUC006, NUC007, FCI001, FCC001
STP005	CSI001, CSC001, CSC002, CSC003
STP006	NUI001, NUI002, NUI006, NUC001, NUC002, NUC004, NUE001, AJC001, AJC003, AJC006, CSI007
STP007	NUI001, NUI002, NUI006, NUC001, NUC005, NUC006, AJC002, AJC004, AJC006, CSI007
STP008	NUI001, NUI002, NUC001, AJC005
STP009	NUI001, NUI002, NUI006, NUC001, NUC002, NUC004, NUC005, NUC006, NUE001, AJC001, AJC002, AJC003, AJC005, AJC006, CSI007
STP010	CSI002, CSI003, CSI004, CSI005, CSI006
STP011	NUI001, NUI002, NUI006, NUC001, NUC008, NUE002, AJC002

Conclusion

In the coming years, incorporation of additional capability into the ARC system will be a continuing effort, both from internal methods development activities at ANL and from codes developed at other laboratories. The utility and capability of the system will accelerate as the algorithm repertoire of the system expands and as new and more powerful computing capability becomes available at Argonne.

New capabilities under active development which will be incorporated into the ARC system include: the new multigroup cross section capability, MC²-2; a spatially dependent cross section generating capability; a three-dimensional diffusion theory capability; a comprehensive fuel cycle analysis capability; and a 2-D safety analysis package.

In future years, as other laboratories implement linked modular code systems, it is hoped that the ARC system will be useful as an established reference system which may provide standard computational packages for reference calculations.

References

1. H. J. Kopp and D. S. Selengut, *Datatran—A Data-Handling Computer Language for a Large Modular Reactor System*, Proc. International Conference on the Utilization of Research Reactors and Reactor Mathematics and Computation, Mexico City, 1967.
2. B. J. Toppel, *The Argonne Reactor Computation (ARC) System*, ANL-7332 (1967).
3. H. C. Honeck, J. E. Suich, J. C. Jensen, C. E. Bailey and J. W. Stewart, *Joshua—A Reactor Physics Computational System*, Proc. Conference on the Effective Use of Computers in the Nuclear Industry, Knoxville, Tennessee, April 21, 1969.
4. A. J. Lindeman, L. C. Just and R. H. Lee, *The Conversion of the Argonne Reactor Computation (ARC) System to Control Data 6000 and 7000 Series Equipment*, Proc. Conference on New Developments in Reactor Mathematics and Applications, Idaho Falls, Idaho, March 29–31, 1971, Vol. 1, p. 464 (1971).
5. L. C. Just, H. Henryson, II, B. J. Toppel and A. S. Kennedy, *The System Aspects and Interface Data Sets of the Argonne Reactor Computation (ARC) System*, ANL-7711 (to be published).
6. D. A. Meneley, G. K. Leaf and P. M. Walker, *Fast Reactor Fuel Cycle Studies—Formulation and Solution Methods*, Reactor Physics Division Annual Report, July 1, 1966 to June 30, 1967, ANL-7310, pp. 493–501.
7. E. M. Pennington, J. C. Gajniak, A. B. Cohen and W. Bohl, *Service Routines for the Multigroup Cross Section Code, MC²*, ANL-7654 (1970).

IV-7. Studies of Spectral Synthesis in Spatially Dependent Fast-Reactor Dynamics

W. M. Stacey, Jr. and J. P. Regis

The idea of calculating the neutron flux spectrum by combining known trial spectra was introduced by Calame and Federighi[1] to compute spatially dependent thermal spectra. This idea was applied to calculate spatially dependent spectra in fast reactors by Storrer and Chaumont[2] and by Stacey,[3] and subsequently by others. The theory for combining trial spectra to compute space- and time-dependent spectra has been developed by Henry[4] and Stacey;[5]

and Stacey[6] has subsequently applied this method to compute time-dependent spectra in a uniform fast reactor. The purpose of this paper is to report several calculations of space- and time-dependent spectra in multi-region fast-reactor models.

Spectral synthesis equations were derived by substituting expansions for the flux and current in terms of known trial spectra ψ_n and ρ_n,

$$\phi(x,E,t) = \sum_{n=1}^{N} \phi_n(x,t)\psi_n(E), \tag{1}$$

$$J(x,E,t) = \sum_{n=1}^{N} J_n(x,t)\rho_n(E), \tag{2}$$

into the P_1 equations, weighting, and integrating over energy. The equations are then combined to eliminate the J_n, resulting in the set of equations

$$\sum_{n=1}^{N} [- \nabla\cdot D^{n'n}(x,t)\nabla\phi_n(x,t) + \Sigma^{n'n}(x,t)\phi_n(x,t) - (1-\beta)\chi^{n'}F^n(x,t)\phi(x,t) + (1/v)^{n'n}\dot{\phi}_n(x,t)] - \sum_{m=1}^{N} \lambda_m \chi_m^{n'} C_m(x,t) = 0, \qquad n' = 1, \cdots, N. \tag{3}$$

These equations have the same generic form as the multigroup diffusion equations, with the important exception that for the latter $D^{n'n} = D^{nn}\delta_{n'n}$ and $\Sigma^{n'n} = 0$, $n' < n$ for no upscatter. The associated precursor equations are

$$\beta_m \sum_{n=1}^{N} F^n(x,t)\phi_n(x,t) - \lambda_m C_m(x,t) = \dot{C}_m(x,t), \qquad m = 1, \cdots M. \tag{4}$$

The coefficients in Eqs. (3) and (4) are integrals of cross sections or fission spectra with weighting function n' and/or trial spectrum n, taken over all energy.

The RAUMZEIT code[7] has been modified to solve Eqs. (3) and (4) [the modification consisted of generalization of the code to accept $(1/v)^{n'n}$, $n' \neq n$]. Several transients in which spatial and spectral shifts were important have been calculated for multi-region fast-reactor models. The trial and weighting functions were 26-group fluxes and adjoints. For comparison, the transients were also calculated with the QX1 code, which solves the one-dimensional multigroup kinetics equations by the improved quasistatic method.[8]

One of these transients was based on a uniform slab core 350 cm thick with a 50-cm blanket on each end. The transient was initiated by linearly decreasing the boron concentration in the right 150-cm of the core, and simul-

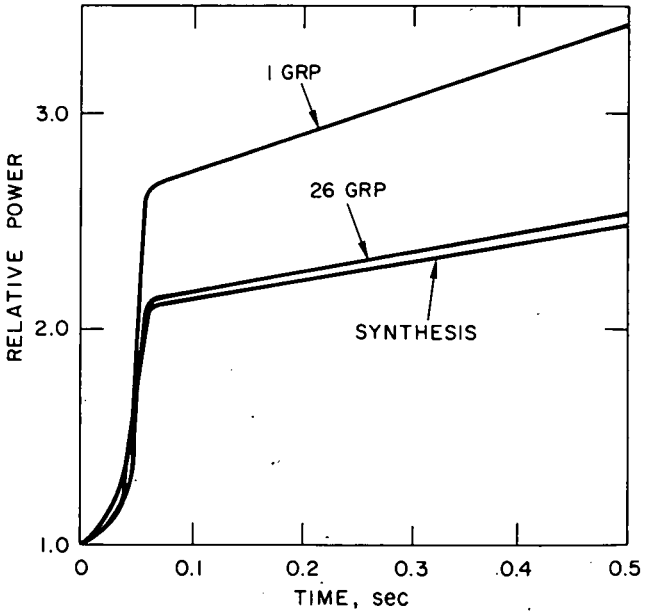

FIG. IV-7-1. Asymmetric Perturbation in Slab Reactor Model. *ANL Neg. No. 116-374.*

taneously increasing the boron concentration in the left 150-cm of the core at the same rate, for 0.06 sec. Two fundamental-mode spectra corresponding to the core composition, but with more or less boron than was in the core initially or at any time during the transient, were taken as trial spectra. A third trial spectrum was a fundamental mode spectrum characteristic of the blanket with a source characteristic of the core fundamental mode current. Weighting functions were adjoints for the same conditions.

The total power predicted by the spectral synthesis calculation is in good agreement with the QX1 result, as shown in Fig. IV-7-1. For comparison, a one-group spatially dependent calculation, with constants collapsed over the initial core spectrum, is shown (1GRP) to illustrate the importance of spectral shifts upon the calculation. A measure of the importance of spatial plus spectral effects is provided by the fact that the point kinetics solution for this transient is a constant power.

In general, it appears that spectral synthesis provides an effective and relatively simple model for treating spectral shifts in fast-reactor transient calculations. Results of other calculations have been published in the literature.[9]

References

1. G. P. Calame and F. D. Federighi, *A Variational Procedure for Determining Spatially Dependent Thermal Spectra*, Nucl. Sci. Eng. **10**, 190 (1961).
2. F. Storrer and J. M. Chaumont, *The Application of Space-Energy Synthesis to the Interpretation of Fast Multizone Critical Experiments*, Proc. International Conference on Fast Critical Experiments and Analysis, Argonne, Illinois, ANL-7320 (1967).
3. W. M. Stacey, Jr., *Modal Approximations: Theory and an Application to Reactor Physics* (MIT Press, Cambridge, Massachusetts, 1967); also *Fast Reactor Calculational Models*, Nucl. Sci. Eng. **28**, 443 (1967).
4. A. F. Henry, *Few-Group Approximations Based on a Variational Principle*, Nucl. Sci. Eng. **27**, 493 (1967).
5. W. M. Stacey, Jr., *General Multigroup and Spectral Synthesis Equations*, Nucl. Sci. Eng. **40**, 73 (1970).
6. W. M. Stacey, Jr., *Spectral Synthesis Applied to Fast-Reactor Dynamics*, Nucl. Sci. Eng. **41**, 249 (1970); also *Spectral Synthesis Methods in Fast-Reactor Dynamics*, Symposium on Dynamics of Nuclear Systems, Tucson, Arizona, March 1970 (University of Arizona Press, 1972).
7. C. H. Adams and W. M. Stacey, Jr., *RAUMZEIT—A Program to Solve Coupled Time-Dependent Neutron Diffusion Equations in One Space Dimension*, KAPL-M-6728 (1967).
8. K. O. Ott and D. A. Meneley, *Accuracy of the Quasistatic Treatment of Spatial Reactor Kinetics*, Nucl. Sci. Eng. **36**, 402 (1969).
9. W. M. Stacey, Jr., *Application of the Spectral Synthesis Method to the Analysis of Spatially Dependent Fast-Reactor Transients*, Nucl. Sci. Eng. **45**, 221 (1971).

IV-8. Studies of Spectral Flux Synthesis

H. Greenspan

The purpose for the development of synthesis techniques is to provide a means for quicker and cheaper reactor calculations for complex, multidimensional (space, energy, time) configurations than is possible by direct methods. A variety of these synthesis approximations has been developed. Recently Stacey[1] has written a complete summary (including an extensive bibliography) of what has been done in this field.

At the heart of the synthesis techniques is the representation of the multidimensional neutron distribution by a relatively small sum of products. Each factor of these products is of lower dimensionality than the original neutron distribution, and sets of these factors have been predetermined from solutions of simpler problems. The remaining sets of factors, that is, the combining functions, are to be determined. With judicious rearrangements and redefinitions, the resulting system of equations for the combining functions are made to correspond in form to direct approach (diffusion or transport theory) equations, but the system has a considerably smaller number of unknowns, and the direct method computer program is used for the solution.

The objective here is: a) To evaluate the applicability of the spectral synthesis method as formulated by Lorenzini and Robinson[2] to LMFBR design; b) To gain experience and insight in the use of the above, thus benefitting the evelopment of alternate numerical algorithms for the solution of the spectral-synthesis equations other than those sed in the direct method programs which sometimes fail in this application. Currently the evaluation a) has been carried out within the framework of diffusion theory.

Briefly, with Lorenzini and Robinson, it is assumed that the flux $\Phi(\mathbf{r},E)$ can be represented by a linear combination of the type

$$\Phi(\mathbf{r},E) = \sum_{i=1}^{N} \phi_i(\mathbf{r}) f_i(E), \tag{1}$$

where the $f_i(E)$ are known energy spectra (N linearly independent trial functions), and $\phi_i(\mathbf{r})$ are position-dependent combining coefficients. Here E represents the energy and $\mathbf{r}$ is the position vector. The problem is to determine the $\phi_i(\mathbf{r})$ and associated criticality.

The diffusion equation for a given region is

$$-D(E)\nabla^2\Phi(\mathbf{r},E) + \sigma_t(E)\Phi(\mathbf{r},E) = \frac{\chi(E)}{\lambda}\int_0^\infty \nu\sigma_f(E')\Phi(\mathbf{r},E')\,dE' + \int_0^\infty \sigma_s(E' \to E)\Phi(\mathbf{r},E')\,dE', \tag{2}$$

where D, σ_t, σ_f, σ_s are the diffusion coefficient, total, fission and scattering macroscopic cross sections respectively; χ is the fission fraction, ν is the mean number of neutrons per fission, and $\lambda = k_{eff}$. All of these, except λ, are region dependent as well as energy dependent quantities.

Inserting Eq. (1) into Eq. (2) and multiplying the resulting equation by an arbitrary set of weights $g_i(E)$, $1 \leq i \leq N$, and integrating over energy, we obtain the matrix equation

$$-\bar{D}\nabla^2\bar{\phi} + A\bar{\phi} = \frac{1}{\lambda}F\bar{\phi} + S\bar{\phi}, \tag{3}$$

where

$$\bar{D} = (D_{ij}) = \left[\int_0^\infty g_i(E)f_j(E)D(E)\,dE\right] \tag{4}$$

$$A = (A_{ij}) = \left[\int_0^\infty g_i(E)f_j(E)\sigma_t(E)\,dE\right] \tag{5}$$

$$F = (F_{ij}) = \left\{\left[\int_0^\infty g_i(E)\chi(E)\,dE\right]\left[\int_0^\infty f_j(E)\nu\sigma_f(E)\,dE\right]\right\} \tag{6}$$

$$S = (S_{ij}) = \left\{\int_0^\infty \left[g_i(E)\int_0^\infty f_j(E')\sigma_s(E' \to E)\,dE'\right]dE\right\} \tag{7}$$

and

$$\bar{\phi} = \begin{bmatrix}\phi_1\\ \phi_2\\ \vdots\\ \phi_N\end{bmatrix} \text{ is a column matrix.} \tag{8}$$

To make Eq. (3) suitable for solution on existing diffusion theory codes, further modifications are necessary. These modifications include provisions that the standard region (material) interface condition of diffusion theory be satisfied.

Having the same linearly independent set of trial functions $f_j(E)$ for all the regions is both necessary and sufficient for satisfying the continuity-of-flux condition across an interface. For the continuity-of-current condition it is sufficient that the diagonal matrix $\mathfrak{D}_\ell$ be

$$\mathfrak{D}_\ell = \text{diag}\left[\int_0^\infty f_j(E)D_\ell(E)\,dE\right] \tag{9}$$

for each region ℓ.

With the above and some rearrangements, Eq. (3) becomes (omitting the region index ℓ),

$$-\mathfrak{D}\nabla^2\bar{\phi} + \mathfrak{A}\bar{\phi} = \frac{1}{\lambda}\mathfrak{F}\bar{\phi} + \mathfrak{S}\bar{\phi}. \tag{10}$$

Here the matrices

$$\mathfrak{A} = \text{diag}\,(\mathfrak{D}\bar{D}^{-1}A) \tag{11}$$

$$\mathfrak{F} = \mathfrak{D}\bar{D}^{-1}F \tag{12}$$

$$\mathfrak{S} = \mathfrak{D}\bar{D}^{-1}\,(S\text{—non diagonal elements of A}), \tag{13}$$

$\bar{D}^{-1}$ being the inverse of matrix $\bar{D}$.

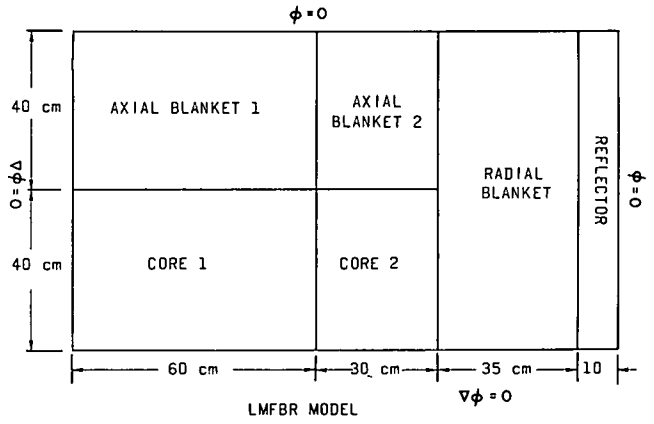

FIG. IV-8-1

TABLE IV-8-I. VOLUME FRACTIONS OF MATERIALS IN THE DESIGNATED REGIONS

	^{239}Pu	^{238}U	Na	Fe	O
Core 1	0.001086	0.006383	0.01041	0.01814	0.01494
Core 2					
a	0.001501	0.005380	0.01098	0.01807	0.01376
b	0.001501	0.005380	0	0.01807	0.01376
Axial Blnkt 1		0.008013	0.00881	0.02444	0.01603
Axial Blnkt 2					
a		0.007383	0.00950	0.02385	0.01477
b		0.007383	0	0.02385	0.01477
Radial Blnkt		0.014515	0.00660	0.01728	0.02903
Reflector			0.00440	0.06912	

Equation (10) can be solved with any diffusion program that allows full scattering matrices, and although the $\mathfrak{F}$ matrix is formulated here to appear to contain a fission matrix, it can be recast into the usual form of a fission vector. Furthermore, the multigroup problem of G groups has been transformed into an N "group" problem, $N \ll G$. However, caution is in order, because, employing the iterative procedure used for the solution in the standard diffusion program, we now have a problem for which the properties of the matrices resulting from the finite difference form of Eq. (10) may not be such as to guarantee convergence and a positive reconstructed flux [Eq. (1)].

A FORTRAN-IV program has been written to construct the quantities in Eqs. (4) through (7) and Eqs. (11) through (13), given sets of $\{f_i(E_k)\}$ and $\{g_i(E_k)\}$, $1 \leq i \leq N$; k, where $1 \leq k \leq G$, is the group index for the multigroup representation of $f(E)$, $g(E)$ and other energy dependent quantities.

Having computed the parameters for Eq. (10), the program arranges them like macroscopic cross sections in the XS.C.MIN format, which subsequently is the "cross section" input to the ARC system multigroup modules.

The reactor configuration for which calculations have been done using the described spectral-synthesis method is shown in Fig. IV-8-1. Two cases, (a, b), differing in the composition assignment for regions II and VI were studied. The compositions are shown in Table IV-8-I.

The primary cross section set was the 24 group set GEADV.[4] The trial functions f were obtained from a fundamental mode calculation code of Stacey's.[5] Simple vectors containing 1 and 0 were used for weights g. Two sets of three trial functions were computed. In the first set (TS1), spectra were obtained for Core 1, Radial Blanket, and Reflector; in the second set (TS2) spectra from Core 2, Radial Blanket, and Reflector were used.

The ARC system module DIF2D[6] was used to compute the k_{eff} for both case a and case b. The same code was also used for the 24 group problem and the few-group problems, where the 24 group set of cross sections was collapsed to 3, 4 and 8 group sets, the Core 1 spectrum being used for collapsing the cross section set

Table IV-8-II shows the results for case a, Table IV-8-III for case b; in all cases the problems converged to the value of k_{eff} with the same precision ($\epsilon = 10^{-6}$ in Δk) and the same number (30) of outer iterations.

The results shown in Table IV-8-II indicate that the spectral-synthesis method seems promising in predicting k_{eff}, although no attempt has been made to optimize the selection and the number of trial functions, and very crude

TABLE IV-8-II. k_{eff} FOR CASE a

	k_{eff}
24 group	1.05883
3 TS1	1.05880
3 group	1.07787
4 group	1.07064
8 group	1.06412

TABLE IV-8-III. k_{eff} FOR CASE b

	k_{eff}
24 group	1.05447
3 TS1	1.04665
3 TS2	1.07150
3 group	1.07446
4 group	1.06665

weights were used. With the current formulation for $\mathfrak{F}$ using the fission fraction matrix, use has been made of the DIF2D capability for handling such problems. However, when DIF2D encounters such a problem it chooses the channel-ordered iteration procedure, which is slower than the usual group ordered procedure. This and not being able to use the iteration acceleration procedures in DIF2D for these problems make the execution time unfavorable compared with ordinary group collapsing.

Revision of this $\mathfrak{F}$ matrix formulation to the vector form, and further computation of reconstructed fluxes, power distributions, and breeding ratios will permit a fuller evaluation of the spectral-synthesis method.

REFERENCES

1. W. M. Stacey, Jr., Argonne National Laboratory (private communication).
2. P. G. Lorenzini and A. H. Robinson, *Solution of the Diffusion Equation by the Spectral Synthesis Method*, Nucl. Sci. Eng. **44**, 1 (April 1971).
3. W. M. Stacey, Jr., Argonne National Laboratory (private communication).
4. W. M. Stacey, Jr., Argonne National Laboratory (private communication).
5. D. A. Meneley, Argonne National Laboratory (private communication).
6. T. A. Daly, G. K. Leaf and A. S. Kennedy, *The ARC System Two-dimensional Diffusion Theory Capability, DARC2D*, ANL-7716 (to be published).

IV-9. Synthesis Calculations in a Highly Nonseparable Fast Reactor Cell

V. LUCO

INTRODUCTION

The Merriman cell was introduced originally as one of the Benchmark[1] problems, "designed to tax capabilities of synthesis approximations." The fluxes in this cell configuration are highly nonseparable and strongly varying, and these characteristics make it indeed difficult to synthesize using just a few trial flux shapes. The original Merriman cell had a thermal spectrum; in the present study the atomic compositions have been chosen in order to obtain a faster spectrum, more representative of the type of energy spectrum to be found in an LMFBR.

The two-dimensional, multigroup, single-channel, discontinuous-trial function synthesis module of the ARC system, named SYN2D,[(2)] was used in these studies.

THE MERRIMAN FAST CONFIGURATION

The reactor configuration used in this study is a Merriman-type configuration. This type of configuration was proposed by Wachspress and Merriman[1] as a Benchmark problem "designed to tax capabilities of synthesis approxi-

mations." It has a highly nonseparable flux distribution which makes it hard to synthesize with a few basic flux shapes.

The dimensions, geometrical disposition, and boundary conditions of the configuration are shown in Fig. IV-9-1. The core regions in the lower left and upper right corners contain ^{239}Pu and ^{238}U. The rest of the cell is filled with a mixture of nickel and sodium. The compositions are shown in Table IV-9-I.

The calculations in this study were performed using six energy groups. The energy boundaries are listed in Table IV-9-II.

The cross sections used are from the 29601 cross section set, which is a six-group set obtained from an original 29-group set prepared for FFTF studies, designated in the 29001 set.[3]

The first step in the study was to obtain two-dimensional fluxes and the corresponding k_{eff} using a regular finite difference approximation to the problem. These fluxes and k_{eff} were then used as standard or "exact" values with which the different synthesis results were compared. The DIF2D neutronics module of the ARC System[4] was used

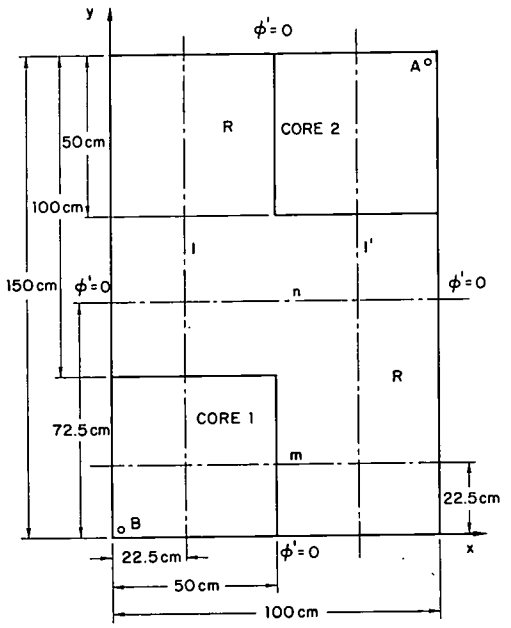

FIG. IV-9-1. Merriman Configuration. *ANL Neg. No. 116-871.*

TABLE IV-9-I. REGION COMPOSITIONS

Region	Isotope	atoms/b/cm
Core	^{239}Pu	0.00103
	^{238}U	0.00619
Reflector	Ni	0.04744
	Na	0.00653

TABLE IV-9-II. ENERGY BOUNDARIES

Group	Lower Energy Boundary
1	1.35 MeV
2	183 keV
3	24.8 keV
4	4.31 keV
5	275 eV
6	10^{-5} eV

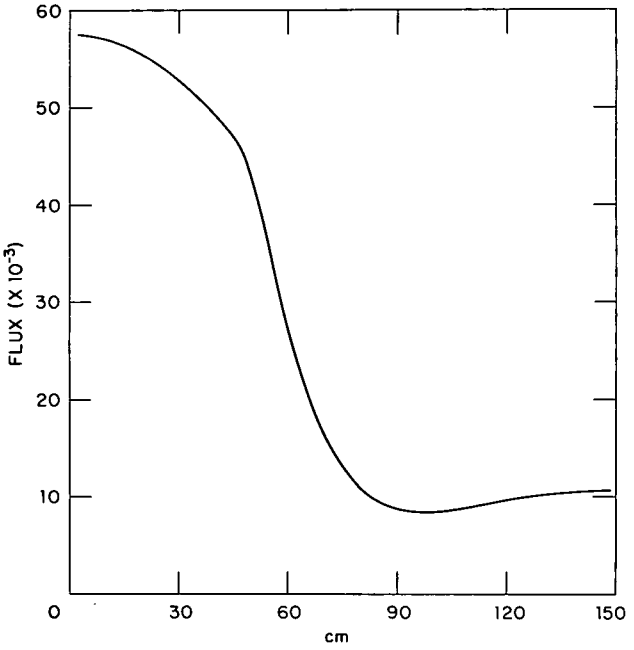

FIG. IV-9-2. Two-Dimensional Flux Profile, Group 2, along Line l, Fig. IV-9-1. *ANL Neg. No. 116-869.*

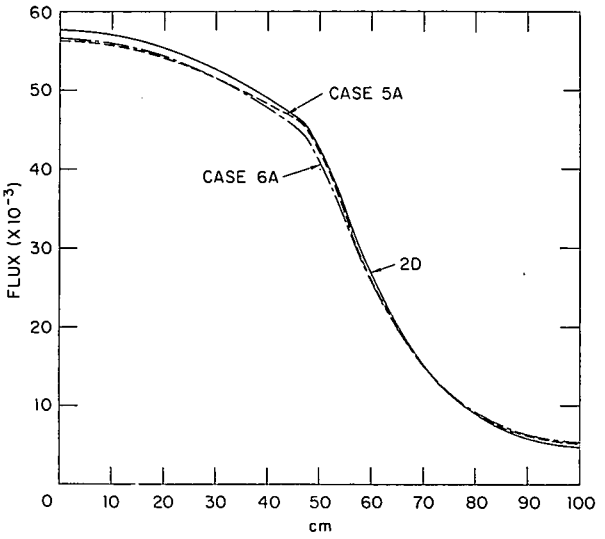

FIG. IV-9-3. Group 2 Fluxes along Line m, Fig. IV-9-1. *ANL Neg. No. 116-865.*

for this calculation with an equally spaced mesh in both x and y directions, with mesh spacing of 5 cm. One-dimensional profiles of the two-dimensional fluxes obtained along the lines l, m, and n (see Fig. IV-9-1) for energy groups 2 and 4 are plotted in Figs. IV-9-2 through IV-9-7.

Groups 2 and 4 have been singled out throughout this report for plotting and analysis simply because they represent well the two basic flux behavior patterns in the cell: one for high energy fluxes (groups 1, 2, and 3) and the other for low energy fluxes (groups 4, 5, and 6).

The fast fluxes (Figs. IV-9-2 and IV-9-4) are strongly peaked at the core regions along lines l and m having large gradients at the interfaces between core and reflector. The flux in group 4 (Figs. IV-9-5 and IV-9-6) shows a strong reflector peaking effect. The effect of the second core is quite marked along line l, producing a second flux peak in both groups shown.

The fluxes along line n (Figs. IV-9-4 and IV-9-7) are transition fluxes, and are relatively flat and low. The value of k_{eff} obtained was 1.108612 ± 0.000001.

Continuous Synthesis Calculations

The two-dimensional fluxes were synthesized by combining precomputed y-dependent trial functions $H_g(y)$ with calculated x-dependent coefficients $T_g(x)$:

$$\phi_g(x,y) = \sum_{i=1}^{M} H_{gi}(y) T_{gi}(x), \qquad g = 1, 2, \cdots, 6. \tag{1}$$

The weight functions used were either the functions $H_{gi}(y)$ themselves, or a set of adjoint fluxes $H^*_{gi}(y)$.

The calculations reported in this section were of the continuous trial function, single-channel type. In other words, the expansion [Eq. (1)] for the flux applies throughout the cell: $0 \leq x \leq 100$ cm and $0 \leq y \leq 150$ cm.

Several one-dimensional trial function and adjoint sets were generated:

Set 1: This set consisted of the one-dimensional fluxes and adjoint in a semi-infinite slab having the compositions found along line l (see Fig. IV-9-1) and its symmetric fluxes and adjoints (along line l′ in Fig. IV-9-1).

Set 2: The fluxes in this set were: a). those for a semi-infinite slab with line l compositions, with fission suppressed in CORE 1, and with an external source proportional to the fission source in CORE 2, inserted in the region extending from 100 to 150 cm, and b). its symmetric flux (along line l' in Fig. IV-9-1).

The adjoint fluxes had adjoint sources proportional to the fission cross sections in CORE 1.

Set 3: The same as Set 2, but with the fission cross section reduced to two-thirds its original value.

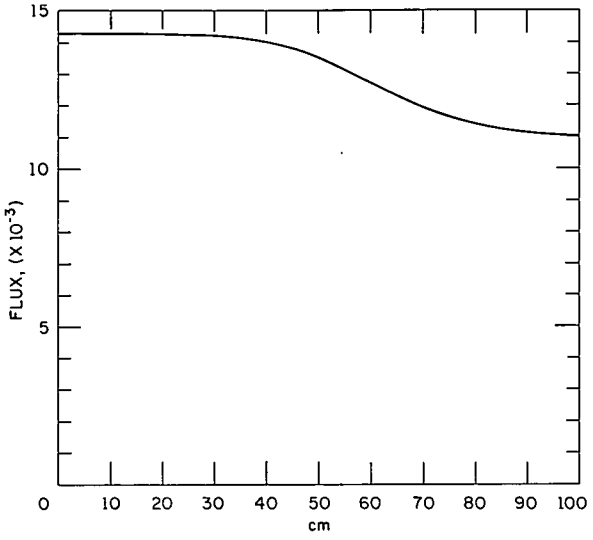

FIG. IV-9-4. Two-Dimensional Flux Profile, Group 2, along Line n, Fig. IV-9-1. *ANL Neg. No. 116-866.*

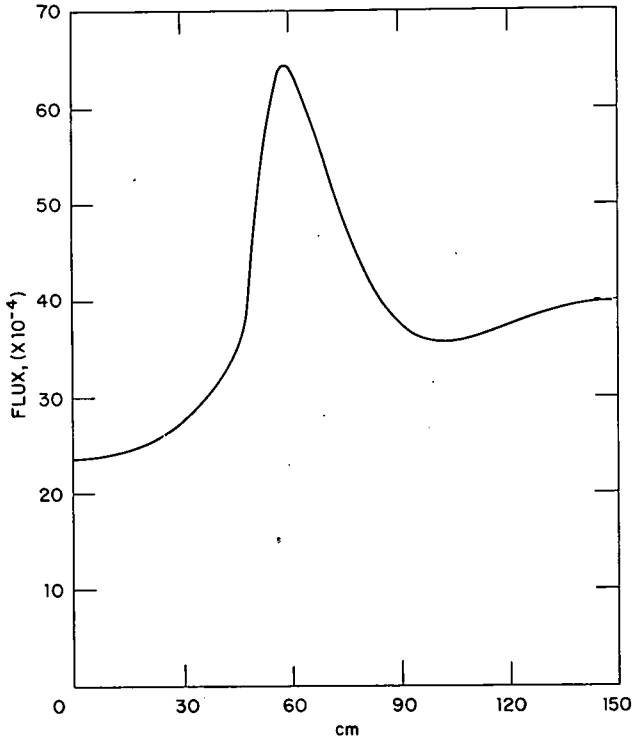

FIG. IV-9-5. Two-Dimensional Flux Profile, Group 4, along Line l, Fig. IV-9-1. *ANL Neg. No. 116-864.*

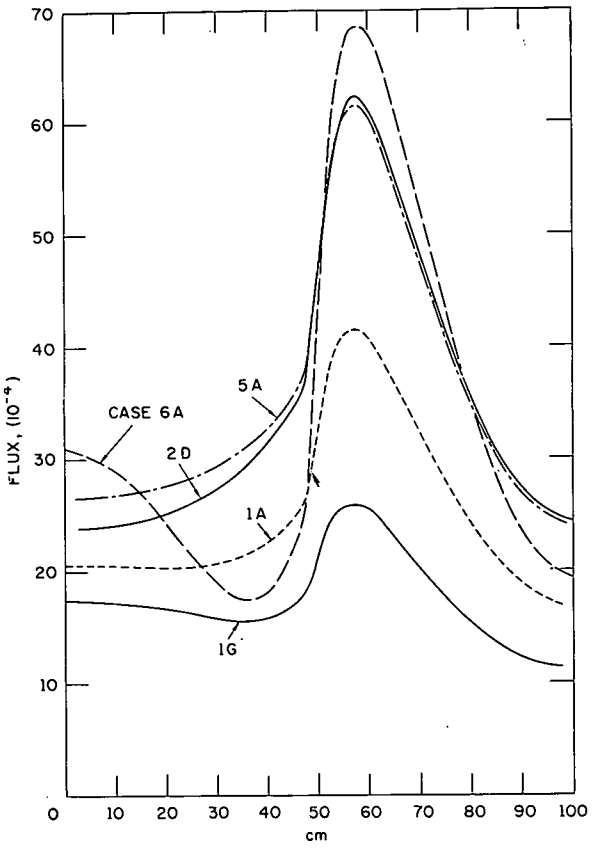

FIG. IV-9-6. Group 4 Fluxes along Line m, Fig. IV-9-1. *ANL Neg. No. 116-867.*

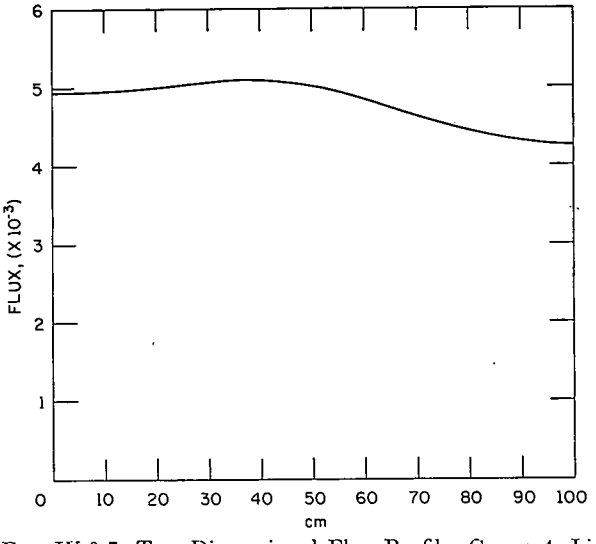

FIG. IV-9-7. Two-Dimensional Flux Profile, Group 4, Line n, Fig. IV-9-1. *ANL Neg. No. 116-863.*

Set 4: This set consisted of the fluxes and adjoints in a three-region slab. The first region extended from $y = 0$ to $y = 50$ cm and was filled with a mixture of core and reflector in equal proportions. The third region had the same composition. The second region extended from $y = 50$ cm to $y = 100$ cm and had the composition of the reflector. The fluxes for groups 2 and 4 from Sets 1, 2, and 3 along line l, Fig. IV-9-1, and those from Set 4 are plotted in Figs. IV-9-8 and IV-9-9.

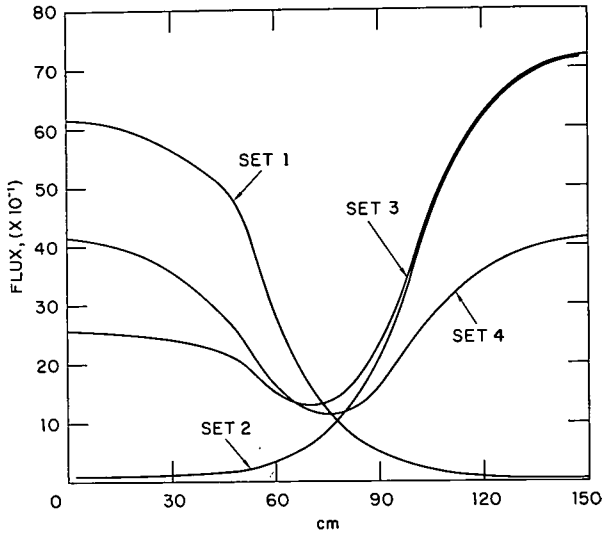

FIG. IV-9-8. Trial Functions, Group 2. For Sets 1, 2 and 3 Only the Function Corresponding to Line 1 Is Shown, Fig. IV-9-1. *ANL Neg. No. 116-868.*

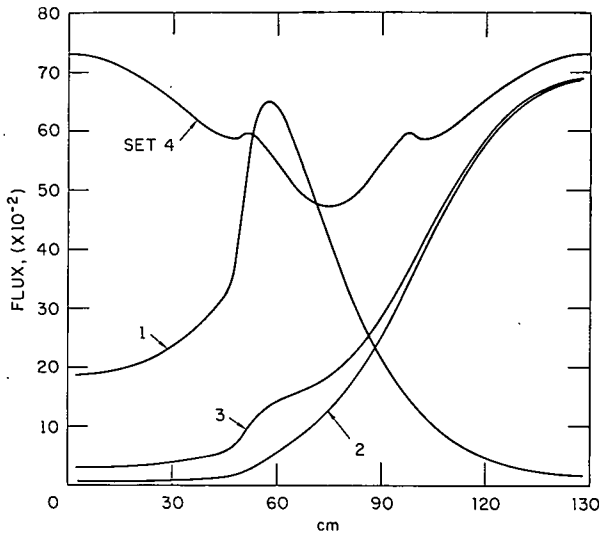

FIG. IV-9-9. Trial Functions, Group 4. For Sets 1, 2 and 3 Only the Function Corresponding to Line 1, Fig. IV-9-1 Is Shown. *ANL Neg. No. 116-870.*

TABLE IV-9-III. CONTINUOUS SYNTHESIS CASES

Case	Weighting[a]	k_{eff}	Δk	% $\Delta k/k$	Trial Function Sets
1	A	1.055753	0.052859	4.767	1
	G	1.100650	0.007962	0.718	
2	A	1.054683	0.053929	4.864	1, 4
	G	1.177284	0.068672	6.194	
3	A	1.101779	0.006833	0.616	1, 2
	G	1.096606	0.012006	1.083	
4	A	1.103428	0.005184	0.468	1, 3
	G	1.096660	0.011952	1.078	
5	A	1.107937	0.000675	0.061	1, 2, 4
	G	1.095884	0.012728	1.148	
6	A	1.108307	0.000305	0.027	1, 3, 4
	G	1.095830	0.012782	1.153	

[a] A ≡ Adjoint weighting; G ≡ Galerkin weighting.

All these one-dimensional trial functions were calculated with DIF1D, the one-dimensional multigroup diffusion module in the ARC System. The synthesis calculations were performed with the SYN2D module of the ARC System, a two-dimensional multigroup synthesis code which allows for both continuous and discontinuous trial function single-channel synthesis. The continuous trial function, single-channel synthesis results are summarized in Table IV-9-III.

Group 4 fluxes along line m are plotted in Fig. IV-9-6, for Cases 1A, 1G, and 5A, 6A (see Table IV-9-IV), together with the corresponding 2D flux profiles.

Based on these results we can make the following observations:

(1) The results are very sensitive to the type of weighting used. A change in weighting can change a very good synthesis result into a poor one as exemplified by Cases 5A, 5G, and 6A, 6G.

(2) Using adjoint weighting, it is possible to obtain very satisfactory results for both k_{eff} and flux shapes if an appropriate set of trial functions is used. "Appropriate set of trail functions," means a set with which there is the possibility of representing the actual flux with reasonable closeness. The trial function sets in Cases 5A, 5G, 6A,

TABLE IV-9-IV. SYMMETRIC INTERFACE RESULTS

Case	Order	Region 1 T.F.	Region 2 T.F.	Cyl. Error?	k_{eff}
1	1st	ψ_{11}	ψ_{12}	yes	1.40957
	2nd	ψ_4	ψ_4		
	3rd	ψ_{21}	ψ_{22}		
2	1st	ψ_{11}	ψ_{12}	no	1.14336
	2nd	ψ_4	ψ_{22}		
	3rd	ψ_{21}	ψ_4		
3	1st	ψ_{11}	ψ_4	no	1.14304
	2nd	ψ_4	ψ_{12}		
	3rd	ψ_{21}	ψ_{22}		
4	1st	ψ_{11}	ψ_{22}	no	1.16582
	2nd	ψ_4	ψ_4		
	3rd	ψ_{21}	ψ_{12}		

and 6G had this potential and in Cases 5A and 6A were actually combined to produce good fluxes (see Figs. IV-9-3 and IV-9-6), and a very good value of k_{eff}.

(3) A fairly good value of k_{eff} (or even an excellent one) can be obtained, as in Case 1, even when the set of trial functions used is not satisfactory for predicting the actual flux. The fluxes calculated in these cases are quite inaccurate, as they must be, given the insufficiency of the trial functions. These conclusions should be clear from Fig. IV-9-10 where the trial functions and the two-dimensional fluxes to be synthesized are shown together. The two trial functions in Set 1 cannot be combined to produce a reasonably close picture of the two-dimensional flux. An attempt to construct the two-dimensional flux rise from $x = 100$ cm to $x = 150$ cm by adding some amount of trial function 2 results in a very inaccurate description of the central flux peak. This is actually what happened in Cases 1A and 1G.

INTERFACE CONDITIONS/DISCONTINUOUS SYNTHESIS

The SYN2D synthesis module can handle discontinuous trial function, single-channel synthesis expansions. This, in general, means that the synthesis expansion of the flux is allowed to have discontinuities along the mixing-function coordinate only.

For the present configuration, the discontinuous trial function, single-channel approach implies that the expansion in Eq. (1) did not apply for the whole x-coordinate range. Instead, two expansions were used for the fluxes:

$$\left.\begin{aligned} \phi_g^{(1)}(x,y) &= \sum_{i=1}^{M_1} H_{gi}^{(1)}(y)T_{gi}^{(1)}(x), \qquad 0 \le x \le 50 \text{ cm} \\ \phi_g^{(2)}(x,y) &= \sum_{i=1}^{M_2} H_{gi}^{(2)}(y)T_{gi}^{(2)}(x), \qquad 50 \le x \le 100 \text{ cm} \end{aligned}\right\} g = 1,2,\cdots,6. \tag{2}$$

With these expansions one has, in general, for $x = 50$:

$$\phi_g^{(1)}(50,y) \neq \phi_g^{(2)}(50,y) \tag{3}$$

$$D_g^{(1)}(50,y)\left.\frac{\partial \phi_g^{(1)}}{\partial x}\right|_{x=50} \neq D_g^{(2)}(50,y)\left.\frac{\partial \phi^{(2)}}{\partial x}\right|_{x=50}; \tag{4}$$

that is, there are discontinuities in both fluxes and currents at $x = 50$ cm. $D_g^{(1)}$ and $D_g^{(2)}$ are the values of the diffusion coefficients on the respective sides of the material interface occurring at $x = 50$.

In developing equations to determine the functions $T_{gi}^{(k)}(x)$ by weighted residual procedures (of which the variational method is a particular case) the weighted integrals of the residuals $\epsilon_g(y)$ and $\eta_g(y)$ generated by Eqs. (3) and 4),

$$\epsilon_g(y) = \phi_g^{(1)}(50,y) - \phi_g^{(2)}(50,y) \tag{5}$$

and

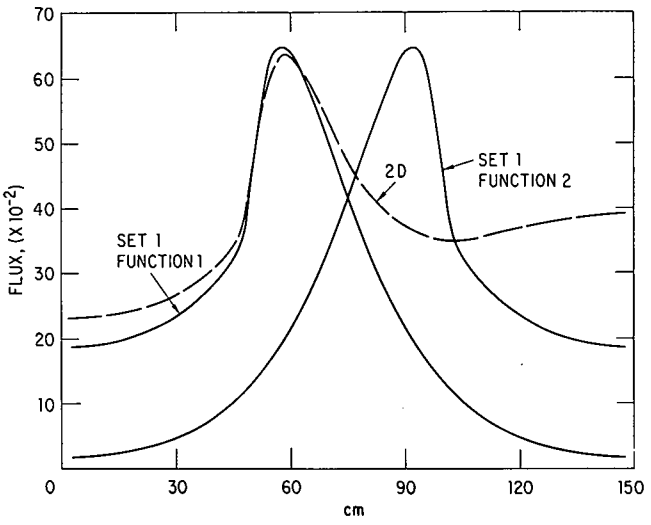

FIG. IV-9-10. Trial Functions from Set 1 and Two-Dimensional Flux Profile, Group 4, along Line 1, Fig. IV-9-1. *ANL Neg. No. 116-902 Rev.*

$$\eta_g(y) = D_g^{(1)}(50,y)\left.\frac{\partial \phi_g^{(1)}}{\partial x}\right|_{x=50} - D_g^{(2)}(50,y)\left.\frac{\partial \phi_g^{(2)}}{\partial x}\right|_{x=50} \tag{6}$$

are set equal to zero:

$$\int_0^{150} R_{gj}(y)[\phi_g^{(1)}(50,y) - \phi_g^{(2)}(50,y)]\,dy = 0, \qquad j = 1, 2, \cdots, M_1 \tag{7}$$

$$\int_0^{150} S_{gj}(y)\left[D_g^{(1)}(50,y)\left.\frac{\partial \phi_g^{(1)}}{\partial x}\right|_{x=50} - D_g^{(2)}(50,y)\left.\frac{\partial \phi_g^{(2)}}{\partial x}\right|_{x=50}\right]dy = 0, \qquad j = 1, 2, \cdots, M_2. \tag{8}$$

The weight functions $R_{gn}(y)$ and $S_{gm}(y)$ can be selected in a variety of ways. Two possible choices have been implemented in the SYN2D synthesis module:

(a)

$$\left.\begin{aligned} R_{gn}(y) &= H_{gn}^{(1)*}(y) \\ S_{gm}(y) &= H_{gm}^{(2)*}(y) \end{aligned}\right\} \text{Variational} \tag{9}$$

$$\left.\begin{aligned} R_{gn}(y) &= H_{gn}^{(1)}(y) \\ S_{gm}(y) &= H_{gm}^{(2)}(y) \end{aligned}\right\} \text{Galerkin} \tag{10}$$

(b)

$$R_{gn}(y) = S_{gn}(y) = \frac{H_{gn}^{(1)*}(y) + H_{gn}^{(2)*}(y)}{2} \qquad \text{Variational} \tag{11}$$

$$R_{gn}(y) = S_{gn}(y) = \frac{H_{gn}^{(1)}(y) + H_{gn}^{(2)}(y)}{2} \qquad \text{Galerkin.} \tag{12}$$

Whether in variational or Galerkin form, Option (a) uses one set of weight functions for the flux and another for the currents. These weight functions are either the trial functions for the flux on each side of the interface or the corresponding adjoints. The numbers of trial functions on both sides of the discontinuity interface are independent of each other.

In Option (b) the weight functions for fluxes and currents are the same. They are the average of trial fluxes on both sides of the interface in the Galerkin mode or of their corresponding adjoints in the variational mode. This, of course, implies that there are the same number, $M_1 = M_2$, of trial functions on both sides of the discontinuity and that they are paired in a certain order.

Option (a) of the interface conditions clearly differentiates between both sides of the interface, and will be known accordingly as the asymmetric interface conditions.

Option (b) does not differentiate between synthesis regions on both sides of the interface, and will henceforth be called the symmetric interface conditions.

Discontinuous Synthesis Calculations

The overall accuracy in both k_{eff} and flux shapes obtained for this reactor configuration, using the sets of trial functions previously specified in a discontinuous mode, was rather poor.

Moreover, two well-known characteristics of the results induced by the handling of discontinuities, which are undesirable, but usually small, are in this case quite large. These undesirable characteristics are:

(1) The value of k_{eff} and the flux shapes depend on the arbitrary ordering of the trial functions when using the symmetric interface conditions.

(2) Spurious asymmetries are introduced in the flux shapes when the asymmetric interface conditions are used.

Discontinuous Synthesis Calculations with Symmetric Interface Conditions

If for every trial function used in the synthesis region to the left of the interface line, $x = 50$ cm, $0 \leq y \leq 150$ cm, its symmetric is used to the right of the interface, the system of differential equations determining the mixing coefficients in both regions will be identical. This is clearly so because the coefficients of the system of differential equations are integrals of the form

$$\int_0^b H^{*(k)}(y) H^{(k)}(y) \Sigma^{(k)}(y)\, dy = C_{ij}^{(k)}, \tag{13}$$

where $k = 1, 2$ for the two regions.

If

$$H_i^{*(1)}(b - y) = H_i^{*(2)}(y) \tag{14}$$

and

$$H_j^{(1)}(b - y) = H_j^{(2)}(y)$$

where $b = 150$ cm, and if

$$\Sigma^{(1)}(b - y) = \Sigma^{(2)}(y), \tag{15}$$

one gets by simple substitution

$$\begin{aligned} C_{ij}^{(1)} &= \int_0^b H_i^{*(1)}(y) H_j^{(1)}(y) \Sigma^{(1)}(y)\, dy \\ &= \int_0^b H_i^{*(1)}(b - u) H_j^{(1)}(b - u) \Sigma^{(1)}(b - u)\, du \\ &= \int_0^b H_i^{*(2)}(u) H_j^{(2)}(u) \Sigma^{(2)}(u)\, du = C_{ij}^{(2)}. \end{aligned} \tag{16}$$

If moreover the trial functions are ordered in both regions in such a way that the pairing indicated in definitions (11) and (12) combines each function with its symmetric, it can be shown that the interface conditions generated by Eqs. (7) and (8) are[5]

$$\left.\frac{dT_{gi}^{(1)}(x)}{dx}\right|_{x=50} = 0, \qquad i = 1, 2, \cdots, M \tag{17}$$

$$\left.\frac{dT_{gi}^{(2)}(x)}{dx}\right|_{x=50} = 0, \qquad i = 1, 2, \cdots, M. \tag{18}$$

These, together with the conditions at the external boundaries

$$\left.\frac{dT_{gi}^{(1)}(x)}{dx}\right|_{x=0} = 0, \qquad i = 1, 2, \cdots, M \tag{19}$$

$$\left.\frac{dT_{gi}^{(2)}(x)}{dx}\right|_{x=150} = 0, \qquad i = 1, 2, \cdots, M, \tag{20}$$

produce mixing functions $T_{gi}^{(1)}(x)$ and $T_{gi}^{(2)}(x)$ which are constants.

The synthesized fluxes $\phi_g^{(1)}(x,y)$ and $\phi_g^{(2)}(x,y)$ [Eq. (2)], are then flat in the x-direction, and usually exhibit a sharp discontinuity at $x = 50$ cm.

This result, which will be called from now on the cylindrical effect [as each one of the fluxes $\phi_g^{(1)}(x,y)$, $\phi_g^{(2)}(x,y)$ takes on a cylindrical shape], is of course totally in error, usually manifested also in an extremely high value for k_{eff}. Its occurrence is clearly due to the combination of the symmetric reactor configuration in a Merriman-type cell, and the consequent natural choices of symmetric trial functions ordered in such a way that at the interface each function is paired with its symmetric in the next synthesis region.

It can be shown that the cylindrical effect is removed by simply reordering the trial functions in one of the synthesis regions. This is done by showing that in that case the interface conditions generated by Eqs. (7) and (8) are not equivalent to Eqs. (17) and (18).[5] However the problem with this type of interface condition in the present reactor configuration still remains because, as the following numerical results show, the value of k_{eff} is extremely sensitive to the arbitrary pairing of the trial functions at the interface.

To simplify the understanding of the results in Table IV-9-IV, the region to the left of the interface line ($x = 50$ cm, $0 \leq y \leq 150$ cm) will be called region 1 and that to the right of it will be called region 2 (see Fig. IV-9-2). Moreover the trial functions in the sets used in these cases will be individually named as follows (see above for general definitions of these sets):

Sets 1 and 2 consist of: (1) the functions calculated along line l in region 1, now called ψ_{11}, ψ_{21} respectively; and (2) the functions calculated along line l' in region 2, now called ψ_{12}, ψ_{22} respectively.

Set 4 has only one function, now called ψ_4. The pairing of trial functions shown in Case 1, Table IV-9-IV, in which each trial function is paired with its companion in the same set is the one that, as has been explained, results in the cylindrical error. As is clear from Table IV-9-IV, in the other three cases shown the ordering of trial functions in region 2 is changed, thus eliminating the cylindrical error.

Discontinuous Synthesis Calculations with Asymmetric Interface Conditions

The use of the asymmetric interface weighting as defined in Eqs. (9) and (10) introduces a spurious asymmetry in the system of synthesis equations and boundary conditions. This happens even when the sets of trial functions chosen on both sides of the discontinuity are symmetric, as in the calculations analyzed in the last section.

It is easy to see how this comes about. As in the last section, for every trial function $H_{gi}^{(1)}(y)$ used in region 1, the function

$$H_{gi}^{(2)}(y) = H_{gi}^{(1)}(b - y), \qquad b = 150 \text{ cm} \tag{14}$$

is used in region 2. As shown also in the last section, the coefficients generated by these trial functions for the corresponding mixing functions $T_i^{(1)}(x)$ and $T_i^{(2)}(x)$ in the set of synthesis differential equations are identical. In order to have a symmetric solution for the problem, it is necessary to have $T_i^{(1)}(x)$ and $T_i^{(2)}(x)$ obey the same boundary and interface conditions. But the coefficients for $T_i^{(1)}(x)$ in the continuity of flux interface conditions as defined by Eqs. (7) and (9) [or similarly by Eqs. (7) and (10)] are

$$K_{gij}^{(1)} = \int_0^b H_{gi}^{(1)}(y) R_{gj}(y)\, dy, \qquad j = 1, 2, \cdots, M. \tag{21}$$

The coefficients for $T_{gi}^{(2)}(y)$ in the same set of continuity conditions are

$$K_{gij}^{(2)} = \int_0^b H_{gi}^{(2)}(y) R_{gj}(y)\, dy, \qquad j = 1, 2, \cdots, M. \tag{22}$$

Using Eq. (14), Eq. (21) can be transformed into

$$K_{gij}^{(1)} = \int_0^b H_{gi}^{(2)}(b - u) R_{gj}(b - u)\, du. \tag{23}$$

Clearly the coefficients $K_{gij}^{(2)}$ and $K_{gij}^{(1)}$ given by Eqs. (22) and (23) will be equal only when

$$R_{gj}(y) = R_{gj}(b - y). \tag{24}$$

The weight functions defined in Eqs. (9) and (10) do not have this property in general, and consequently the interface conditions affect differently the functions $T_i^{(1)}(x)$ and $T_i^{(2)}(x)$ and the resulting fluxes are asymmetric.

As the following numerical examples show, the flux asymmetry introduced by the asymmetric interface conditions is very large in some cases. The ordering of the trial functions on both sides of the interface does not affect the re-

TABLE IV-9-V. Asymmetric Interface Results

Trial Function Sets	k_{eff}	$\phi_g(A)/\phi_g(B)$					
		g / 1	2	3	4	5	6
1, 3	1.08724	1.99	1.96	1.87	2.72	2.30	2.01
1, 2, 3	1.18705	0.52	0.54	0.45	0.15	0.32	0.48
1, 2, 4	1.14001	1.07	1.07	1.07	1.08	1.39	1.07

sults at all in this case and consequently when trial function sets are listed, the implication is that one member of the set enters the synthesis expansion in region 1 and the other enters the expansion in region 2, in any order. $\phi_g(A)/\phi_g(B)$ is the ratio of fluxes at points A and B (see Fig. IV-9-1) for group g. The results are listed in Table IV-9-V.

Conclusions

The conclusions obtained from these studies are twofold:

(1) Quite satisfactory values of k_{eff} and reasonably good fluxes can be obtained for this fast-reactor cell configuration with the continuous trial function, adjoint-weighting option of SYN2D, if an appropriate set of trial functions is used. (Appropriate in the sense that the set of trial functions has the possibility of representing the actual flux with reasonable closeness.)

(2) Both the symmetric and asymmetric modes of the discontinuous trial-function option of SYN2D yield unsatisfactory results for this configuration using the sets of discontinuous trial functions specified above. These choices of trial functions are not capricious; they are of the type normally selected for this purpose and are of the kind one would expect a user to select naturally for this kind of configuration. Using these trial functions, as has been shown, the symmetric mode produces widely different results employing the same set of trial functions in different orderings, and the asymmetric mode introduces large spurious asymmetries in the flux description.

References

1. Benchmark Problem Committee of the Mathematics and Computation Division of the American Nuclear Society, Eds., *Argonne Code Center: Benchmark Problem Book*, ANL-7416 (1968), p. 50.
2. V. Luco, G. K. Leaf and J. G. Stork, *SYN2D, A Flux Synthesis Program Based on a Discontinuous Trial Function Formulation*, ANL-7334 (1967).
3. D. Meneghetti, A. J. Ulrich, P. J. Persiani and J. C. Beitel, *Calculational Studies in Support of the Fast Flux Test Facility (FFTF) Critical Experiments in ZPR-3*, Reactor Physics Division Annual Report, July 1, 1967 to June 30, 1968, ANL-7410, p. 221.
4. T. A. Daly, G. K. Leaf and A. S. Kennedy, *The ARC System Two-Dimensional Diffusion Theory Capability, DARC2D*, ANL-7716 (to be published).
5. G. K. Leaf and J. Stork, Argonne National Laboratory (private communication).

IV-10. Single-Channel Continuous-Trial-Function Calculations in a Fast Reactor Configuration

V. Luco

Introduction

A series of two-dimensional synthesis calculations using the SYN2D module of the ARC system with continuous trial functions has been performed for a typical LMFBR configuration. The object of the calculations was to investigate the quality of the synthesis results that can be obtained in this situation for a variety of one-dimensional trial function choices.

Reactor Configuration

The reactor model chosen for this study is the reactor described in Ref. 1. This model represents a typical 1000 MWe LMFBR design. The dimensions of the reactor and its subdivision in major regions are shown in Fig. IV-10-1, where one quarter of the configuration is depicted in rz coordinates.

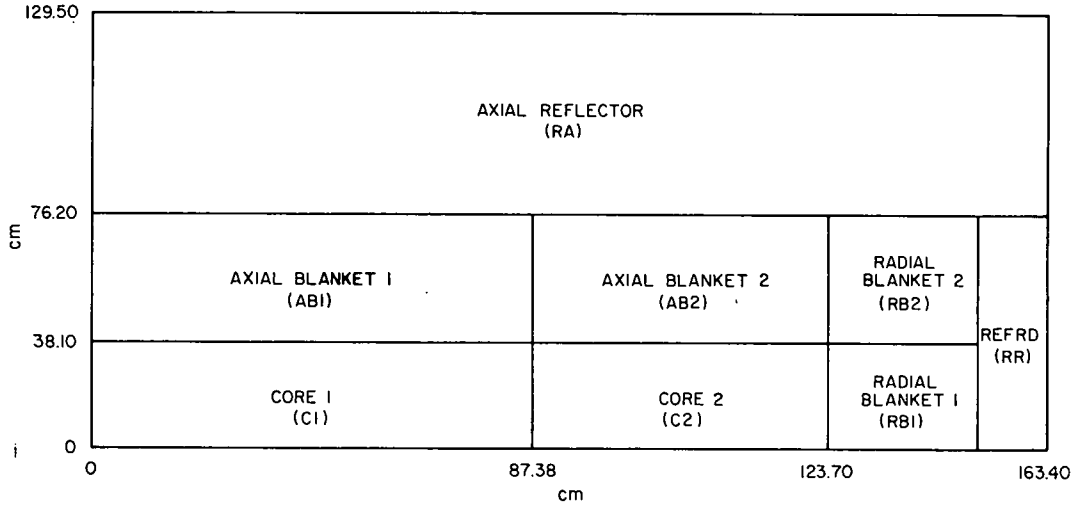

FIG. IV-10-1. Reactor Configuration. *ANL Neg. No. 116-960 T-1.*

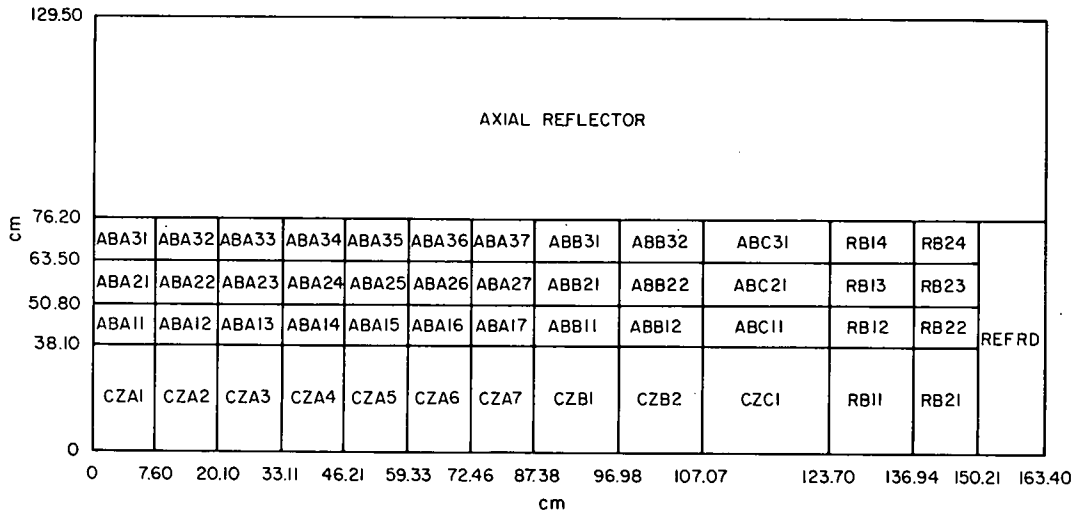

FIG. IV-10-2. Detailed Reactor Configuration. *ANL Neg. No. 116-959 T-1.*

For the neutronic calculations, both synthesis and finite-difference, the reactor isotopic compositions were specified in more detail as shown in Fig. IV-10-2 and in Tables IV-10-I and IV-10-II, where the geometrical layout of the finer region structure and its isotopic compositions are specified. Table IV-10-I gives a beginning-of-cycle (BOC) isotopic composition and Table IV-10-II gives the middle-of-cycle (MOC) composition.

The calculations in this study were performed using six energy groups whose boundaries are listed in Table IV-10-III. The cross sections used are from the Argonne 29601 cross section set, which is a six group set obtained from an original 29-group set prepared for FFTF studies, called the 29001 set.[2]

The first step in the calculations was to obtain two-dimensional fluxes and the corresponding values of k_{eff}, power fractions, and regional and total breeding ratios using a regular finite difference approximation to the problem. The values obtained were then used as standard or "exact" values against which the various synthesis results were compared. The ARC modules DIF2D[3] and INVENT,[4] which perform two-dimensional diffusion calculations and inventories respectively, were used to obtain these parameters.

Synthesis Calculations

The synthesis calculations in this study are of the single-channel continuous-trial function type; in terms of trial functions, there is only one expansion of the flux which applies over the entire axial domain. Galerkin weighting was employed throughout.

TABLE IV-10-I. BEGINNING-OF-CYCLE ISOTOPIC COMPOSITION

M1	U238	M7	O 16
M2	PU239	M8	LUFP
M3	PU240	M9	TA181
M4	PU241	M10	SS
M5	PU242	M11	NA 23
M6	U235		

CZA1	M1	0.75784E-02M2	0.83804E-03M3	0.36211E-03
CZA1	M4	0.13721E-03M5	0.48331E-04M6	0.18432E-04
CZA1	M7	0.11817E-05M8	0.27026E-03M9	0.0
CZA1	M10	0.127C9E-01M11	0.83235E-02	
CZA2	M1	0.75797E-02M2	0.83795E-03M3	0.36204E-03
CZA2	M4	0.13731E-03M5	0.48314E-04M6	0.18450E-04
CZA2	M7	0.11775E-05M8	0.26897E-03M9	0.0
CZA2	M10	0.127C9E-01M11	0.83235E-02	
CZA3	M1	0.75833E-02M2	0.83769E-03M3	0.36188E-03
CZA3	M4	0.13755E-03M5	0.48270E-04M6	0.18499E-04
CZA3	M7	0.11666E-05M8	0.26556E-03M9	0.0
CZA3	M10	0.127C9E-01M11	0.83235E-02	
CZA4	M1	0.75893E-02M2	0.83724E-03M3	0.36159E-03
CZA4	M4	0.13797E-03M5	0.48194E-04M6	0.18582E-04
CZA4	M7	0.11480E-05M8	0.25989E-03M9	0.0
CZA4	M10	0.12709E-01M11	0.83235E-02	
CZA5	M1	0.75975E-02M2	0.83654E-03M3	0.36116E-03
CZA5	M4	0.13856E-03M5	0.48082E-04M6	0.18702E-04
CZA5	M7	0.11209E-05M8	0.25191E-03M9	0.0
CZA5	M10	0.127C9E-01M11	0.83235E-02	
CZA6	M1	0.76093E-02M2	0.83543E-03M3	0.36046E-03
CZA6	M4	0.13937E-03M5	0.47915E-04M6	0.18867E-04
CZA6	M7	0.10824E-05M8	0.24148E-03M9	0.0
CZA6	M10	0.12709E-01M11	0.83235E-02	
CZA7	M1	0.76262E-02M2	0.83305E-03M3	0.35894E-03
CZA7	M4	0.14059E-03M5	0.47598E-04M6	0.19127E-04
CZA7	M7	0.10175E-05M8	0.22743E-03M9	0.0
CZA7	M10	0.127C9E-01M11	0.83235E-02	
CZB1	M1	0.70911E-02M2	0.10794E-02M3	0.49265E-03
CZB1	M4	0.19772E-03M5	0.65478E-04M6	0.18074E-04
CZB1	M7	0.85486E-C6M8	0.26360E-03M9	0.0
CZB1	M10	0.12709E-01M11	0.83235E-02	
CZB2	M1	0.71164E-02M2	0.10828E-02M3	0.49127E-03
CZB2	M4	0.20096E-03M5	0.64885E-04M6	0.18483E-04
CZB2	M7	0.76086E-C6M8	0.23335E-03M9	0.0
CZB2	M10	0.127C9E-01M11	0.83235E-02	
CZC1	M1	0.70302E-02M2	0.10704E-02M3	0.49606E-03
CZC1	M4	0.18858E-C3M5	0.67083E-04M6	0.16956E-04
CZC1	M7	0.11113E-05M8	0.23849E-03M9	0.0
CZC1	M10	0.12709E-01M11	0.83235E-02	
RB11	M1	0.11736E-01M2	0.20289E-03M3	0.57890E-05
RB11	M4	0.93495E-07M5	0.13265E-C8M6	0.30778E-04
RB11	M7	0.12518E-05M8	0.43070E-04M9	0.0
RB11	M10	0.23618E-01M11	0.38901E-02	
RB21	M1	0.11813E-01M2	0.15134E-03M3	0.31784E-05
RB21	M4	0.37344E-07M5	0.38096E-09M6	0.32127E-04
RB21	M7	0.98386E-06M8	0.18651E-04M9	0.0
RB21	M10	0.23618E-01M11	0.38901E-02	

ABA11	M1	0.10105E-01M2	0.17053E-03M3	0.60418E-05
ABA11	M4	0.10980E-C6M5	0.16767E-C8M6	0.26626E-04
ABA11	M7	0.10580E-05M8	0.40138E-04M9	0.0
ABA11	M10	0.127C9E-01M11	0.83235E-02	
ABA12	M1	0.10106E-01M2	0.16984E-03M3	0.59887E-05
ABA12	M4	0.10835E-06M5	0.16465E-08M6	0.26643E-04
ABA12	M7	0.10538E-05M8	0.39865E-04M9	0.0
ABA12	M10	0.12709E-01M11	0.83235E-02	
ABA13	M1	0.10109E-01M2	0.16803E-03M3	0.58493E-05
ABA13	M4	0.10458E-C6M5	0.15685E-C8M6	0.26690E-04
ABA13	M7	0.10426E-05M8	0.39147E-04M9	0.0
ABA13	M10	0.127C9E-01M11	0.83235E-02	
ABA14	M1	0.10113E-01M2	0.16497E-03M3	0.56177E-05
ABA14	M4	0.98424E-07M5	0.14435E-C8M6	0.26769E-04
ABA14	M7	0.10237E-05M8	0.37959E-04M9	0.0
ABA14	M10	0.127C9E-01M11	0.83235E-02	
ABA15	M1	0.10119E-01M2	0.16056E-03M3	0.52910E-05
ABA15	M4	0.89946E-C7M5	0.12763E-08M6	0.26883E-04
ABA15	M7	0.99627E-C6M8	0.36307E-04M9	0.0
ABA15	M10	0.127C9E-01M11	0.83235E-02	
ABA16	M1	0.10126E-01M2	0.15441E-03M3	0.48462E-05
ABA16	M4	0.78835E-07M5	0.10660E-08M6	0.27042E-04
ABA16	M7	0.95719E-06M8	0.34188E-04M9	0.0
ABA16	M10	0.12709E-01M11	0.83235E-C2	
ABA17	M1	0.10143E-01M2	0.14334E-03M3	0.41071E-05
ABA17	M4	0.61485E-C7M5	0.75964E-09M6	0.27329E-04
ABA17	M7	0.88726E-06M8	0.30460E-C4M9	0.0
ABA17	M10	0.12709E-01M11	0.83235E-02	
ABB11	M1	0.10165E-01M2	0.12698E-03M3	0.31276E-05
ABB11	M4	0.40825E-C7M5	0.43520E-C9M6	0.27758E-04
ABB11	M7	0.78202E-06M8	0.25360E-04M9	0.0
ABB11	M10	0.12709E-01M11	0.83235E-C2	
ABB12	M1	0.10187E-01M2	0.11032E-03M3	0.22605E-05
ABB12	M4	0.25070E-07M5	0.22461E-09M6	0.28198E-04
ABB12	M7	0.67170E-06M8	0.20969E-04M9	0.92000E-03
ABB12	M10	0.12709E-01M11	0.83235E-02	
ABC11	M1	0.10122E-01M2	0.16136E-03M3	0.41347E-05
ABC11	M4	0.60782E-07M5	0.77699E-09M6	0.26866E-04
ABC11	M7	0.98613E-06M8	0.34491E-04M9	0.0
ABC11	M10	0.12709E-01M11	0.83235E-02	
RB12	M1	0.11854E-01M2	0.11454E-03M3	0.18243E-05
RB12	M4	0.16507E-07M5	0.12622E-09M6	0.33088E-04
RB12	M7	0.72607E-06M8	0.15169E-04M9	0.0
RB12	M10	0.23618E-01M11	0.38901E-02	
RB22	M1	0.11893E-01M2	0.84732E-04M3	0.10140E-05
RB22	M4	0.67472E-C8M5	0.37952E-10M6	0.33842E-04
RB22	M7	0.56874E-06M8	0.68236E-05M9	0.0
RB22	M10	0.23618E-01M11	0.38901E-02	

TABLE IV-10-I. *Continued*

ABA21	M1	0.10189E-01M2	0.11249E-03M3	0.26851E-05
ABA21	M4	0.32359E-07M5	0.31796E-09M6	0.28130E-04
ABA21	M7	0.72976E-06M8	0.16140E-04M9	0.0
ABA21	M10	0.12709E-01M11	0.83235E-02	
ABA22	M1	0.10190E-01M2	0.11201E-03M3	0.26609E-05
ABA22	M4	0.31923E-07M5	0.31217E-09M6	0.28142E-04
ABA22	M7	0.72668E-06M8	0.16031E-04M9	0.0
ABA22	M10	0.12709E-01M11	0.83235E-02	
ABA23	M1	0.10191E-01M2	0.11073E-03M3	0.25974E-05
ABA23	M4	0.30786E-07M5	0.29720E-09M6	0.28175E-04
ABA23	M7	0.71849E-06M8	0.15744E-04M9	0.0
ABA23	M10	0.12709E-01M11	0.83235E-02	
ABA24	M1	0.10194E-01M2	0.10857E-03M3	0.24920E-05
ABA24	M4	0.28928E-07M5	0.27318E-09M6	0.28231E-04
ABA24	M7	0.70464E-06M8	0.15268E-04M9	0.0
ABA24	M10	0.12709E-01M11	0.83235E-02	
ABA25	M1	0.10198E-01M2	0.10547E-03M3	0.23428E-05
ABA25	M4	0.26369E-07M5	0.24099E-09M6	0.28311E-04
ABA25	M7	0.68447E-06M8	0.14606E-04M9	0.0
ABA25	M10	0.12709E-01M11	0.83235E-02	
ABA26	M1	0.10203E-01M2	0.10113E-03M3	0.21387E-05
ABA26	M4	0.22997E-07M5	0.20025E-09M6	0.28424E-04
ABA26	M7	0.65565E-06M8	0.13746E-04M9	0.0
ABA26	M10	0.12709E-01M11	0.83235E-02	
ABA27	M1	0.10214E-01M2	0.92346E-04M3	0.17602E-05
ABA27	M4	0.17163E-07M5	0.13484E-09M6	0.28653E-04
ABA27	M7	0.59784E-06M8	0.11923E-04M9	0.0
ABA27	M10	0.12709E-01M11	0.83235E-02	
ABB21	M1	0.10230E-01M2	0.79176E-04M3	0.12621E-05
ABB21	M4	0.10407E-07M5	0.68628E-10M6	0.29004E-04
ABB21	M7	0.50995E-06M8	0.92395E-05M9	0.0
ABB21	M10	0.12709E-01M11	0.83235E-02	
ABB22	M1	0.10244E-01M2	0.67425E-04M3	0.87389E-06
ABB22	M4	0.59867E-08M5	0.32564E-10M6	0.29319E-04
ABB22	M7	0.42707E-06M8	0.74864E-05M9	0.92000E-03
ABB22	M10	0.12709E-01M11	0.83235E-02	
ABC21	M1	0.10207E-01M2	0.99220E-04M3	0.15892E-05
ABC21	M4	0.14431E-07M5	0.11073E-09M6	0.28495E-04
ABC21	M7	0.62739E-06M8	0.12827E-04M9	0.0
ABC21	M10	0.12709E-01M11	0.83235E-02	
RB13	M1	0.11909E-01M2	0.69018E-04M3	0.67828E-06
RB13	M4	0.37410E-08M5	0.17143E-10M6	0.34268E-04
RB13	M7	0.45000E-06M8	0.62227E-05M9	0.0
RB13	M10	0.23618E-01M11	0.38901E-02	
RB23	M1	0.11936E-01M2	0.51255E-04M3	0.38602E-06
RB23	M4	0.15896E-08M5	0.54692E-11M6	0.34705E-04
RB23	M7	0.35532E-06M8	0.29638E-05M9	0.0
RB23	M10	0.23618E-01M11	0.38901E-02	
ABA31	M1	0.10242E-01M2	0.70238E-04M3	0.11130E-05
ABA31	M4	0.86508E-08M5	0.53776E-10M6	0.29195E-04
ABA31	M7	0.48191E-06M8	0.65764E-05M9	0.0
ABA31	M10	0.12709E-01M11	0.83235E-02	
ABA32	M1	0.10242E-01M2	0.69925E-04M3	0.11028E-05
ABA32	M4	0.85328E-08M5	0.52791E-10M6	0.29204E-04
ABA32	M7	0.47980E-06M8	0.65333E-05M9	0.0
ABA32	M10	0.12709E-01M11	0.83235E-02	
ABA33	M1	0.10243E-01M2	0.69095E-04M3	0.10762E-05
ABA33	M4	0.82254E-08M5	0.50248E-10M6	0.29225E-04
ABA33	M7	0.47419E-06M8	0.64201E-05M9	0.0
ABA33	M10	0.12709E-01M11	0.83235E-02	
ABA34	M1	0.10245E-01M2	0.67698E-04M3	0.10319E-05
ABA34	M4	0.77226E-08M5	0.46158E-10M6	0.29262E-04
ABA34	M7	0.46470E-06M8	0.62319E-05M9	0.0
ABA34	M10	0.12709E-01M11	0.83235E-02	
ABA35	M1	0.10247E-01M2	0.65682E-04M3	0.96900E-06
ABA35	M4	0.70271E-08M5	0.40654E-10M6	0.29315E-04
ABA35	M7	0.45084E-06M8	0.59684E-05M9	0.0
ABA35	M10	0.12709E-01M11	0.83235E-02	
ABA36	M1	0.10250E-01M2	0.62847E-04M3	0.88215E-06
ABA36	M4	0.61030E-08M5	0.33626E-10M6	0.29390E-04
ABA36	M7	0.43084E-06M8	0.56226E-05M9	0.0
ABA36	M10	0.12709E-01M11	0.83235E-02	
ABA37	M1	0.10255E-01M2	0.56491E-04M3	0.70429E-06
ABA37	M4	0.43512E-08M5	0.21331E-10M6	0.29561E-04
ABA37	M7	0.38627E-06M8	0.48007E-05M9	0.0
ABA37	M10	0.12709E-01M11	0.83235E-02	
ABB31	M1	0.10268E-01M2	0.46905E-04M3	0.47374E-06
ABB31	M4	0.23957E-08M5	0.95639E-11M6	0.29822E-04
ABB31	M7	0.31826E-06M8	0.35469E-05M9	0.0
ABB31	M10	0.12709E-01M11	0.83235E-02	
ABB32	M1	0.10277E-01M2	0.39221E-04M3	0.31466E-06
ABB32	M4	0.12926E-08M5	0.41722E-11M6	0.30034E-04
ABB32	M7	0.26009E-06M8	0.28320E-05M9	0.92000E-03
ABB32	M10	0.12709E-01M11	0.83235E-02	
ABC31	M1	0.10256E-01M2	0.57715E-04M3	0.56456E-06
ABC31	M4	0.30573E-08M5	0.13750E-10M6	0.29554E-04
ABC31	M7	0.38036E-06M8	0.49293E-05M9	0.0
ABC31	M10	0.12709E-01M11	0.83235E-02	
RB14	M1	0.11942E-01M2	0.39723E-04M3	0.23920E-06
RB14	M4	0.78545E-09M5	0.21225E-11M6	0.35016E-04
RB14	M7	0.27023E-06M8	0.25315E-05M9	0.0
RB14	M10	0.23618E-01M11	0.38901E-02	
RB24	M1	0.11953E-01M2	0.29878E-04M3	0.14211E-06
RB24	M4	0.35766E-09M5	0.74721E-12M6	0.35251E-04
RB24	M7	0.21796E-06M8	0.13042E-05M9	0.0
RB24	M10	0.23618E-01M11	0.38901E-02	
REFAX	M10	4.26485E-02M11	1.0952 E-02	
REFRD	M10	7.8857 E-02M11	1.65375E-03	

TABLE IV-10-II. Middle-of-Cycle Isotopic Composition

M1	U238	M7	O 16
M2	PU239	M8	LUFP
M3	PU240	M9	TA181
M4	PU241	M10	SS
M5	PU242	M11	NA 23
M6	U235		

CZA1	M1	0.72268D-02M2	0.87732D-03M3	0.38228D-03
CZA1	M4	0.11058D-03M5	0.54023D-04M6	0.13058D-04
CZA1	M7	0.23803D-05M8	0.58751D-03M9	0.0 D+00
CZA1	M10	0.12709D-01M11	0.83235D-02	
CZA2	M1	0.72307D-02M2	0.87714D-03M3	0.38210D-03
CZA2	M4	0.11082D-03M5	0.53978D-04M6	0.13105D-04
CZA2	M7	0.23696D-05M8	0.58383D-03M9	0.0 D+00
CZA2	M10	0.12709D-01M11	0.83235D-02	
CZA3	M1	0.72407D-02M2	0.87664D-03M3	0.38164D-03
CZA3	M4	0.11145D-03M5	0.53860D-04M6	0.13232D-04
CZA3	M7	0.23412D-05M8	0.57417D-03M9	0.0 D+00
CZA3	M10	0.12709D-01M11	0.83235D-02	
CZA4	M1	0.72573D-02M2	0.87577D-03M3	0.38084D-03
CZA4	M4	0.11250D-03M5	0.53660D-04M6	0.13444D-04
CZA4	M7	0.22934D-05M8	0.55815D-03M9	0.0 D+00
CZA4	M10	0.12709D-01M11	0.83235D-02	
CZA5	M1	0.72807D-02M2	0.87443D-03M3	0.37964D-03
CZA5	M4	0.11401D-03M5	0.53365D-04M6	0.13749D-04
CZA5	M7	0.22241D-05M8	0.53585D-03M9	0.0 D+00
CZA5	M10	0.12709D-01M11	0.83235D-02	
CZA6	M1	0.73117D-02M2	0.87228D-03M3	0.37774D-03
CZA6	M4	0.11603D-03M5	0.52932D-04M6	0.14164D-04
CZA6	M7	0.21270D-05M8	0.50700D-03M9	0.0 D+00
CZA6	M10	0.12709D-01M11	0.83235D-02	
CZA7	M1	0.73574D-02M2	0.86766D-03M3	0.37362D-03
CZA7	M4	0.11910D-03M5	0.52110D-04M6	0.14823D-04
CZA7	M7	0.19627D-05M8	0.46734D-03M9	0.0 D+00
CZA7	M10	0.12709D-01M11	0.83235D-02	
CZB1	M1	0.68689D-02M2	0.10580D-02M3	0.50307D-03
CZB1	M4	0.17133D-03M5	0.70584D-04M6	0.14604D-04
CZB1	M7	0.15873D-05M8	0.52098D-03M9	0.0 D+00
CZB1	M10	0.12709D-01M11	0.83235D-02	
CZB2	M1	0.69336D-02M2	0.10684D-02M3	0.49822D-03
CZB2	M4	0.17915D-03M5	0.68975D-04M6	0.15629D-04
CZB2	M7	0.13432D-05M8	0.44344D-03M9	1.4964 D-03
CZB2	M10	0.12709D-01M11	0.83235D-02	
CZC1	M1	0.68873D-02M2	0.10627D-02M3	0.50472D-03
CZC1	M4	0.17414D-03M5	0.70455D-04M6	0.14898D-04
CZC1	M7	0.15396D-05M8	0.49332D-03M9	0.0 D+00
CZC1	M10	0.12709D-01M11	0.83235D-02	
RB11	M1	0.11620D-01M2	0.29455D-03M3	0.97752D-05
RB11	M4	0.18926D-06M5	0.33145D-08M6	0.28462D-04
RB11	M7	0.18154D-05M8	0.65575D-04M9	0.0 D+00
RB11	M10	0.23619D-01M11	0.38902D-02	
RB21	M1	0.11756D-01M2	0.20124D-03M3	0.50488D-05
RB21	M4	0.70958D-07M5	0.97727D-09M6	0.30837D-04
RB21	M7	0.13315D-05M8	0.25584D-04M9	0.0 D+00
RB21	M10	0.23619D-01M11	0.38902D-02	

ABA11	M1	0.98658D-02M2	0.35007D-03M3	0.17292D-04
ABA11	M4	0.45742D-06M5	0.11319D-07M6	0.21840D-04
ABA11	M7	0.22527D-05M8	0.92241D-04M9	0.0 D+00
ABA11	M10	0.12709D-01M11	0.83235D-02	
ABA12	M1	0.98688D-02M2	0.34816D-03M3	0.17096D-04
ABA12	M4	0.44988D-06M5	0.11065D-07M6	0.21891D-04
ABA12	M7	0.22406D-05M8	0.91336D-04M9	0.0 D+00
ABA12	M10	0.12709D-01M11	0.83235D-02	
ABA13	M1	0.98767D-02M2	0.34310D-03M3	0.16581D-04
ABA13	M4	0.43028D-06M5	0.10410D-07M6	0.22023D-04
ABA13	M7	0.22087D-05M8	0.88964D-04M9	0.0 D+00
ABA13	M10	0.12709D-01M11	0.83235D-02	
ABA14	M1	0.98898D-02M2	0.33458D-03M3	0.15729D-04
ABA14	M4	0.39845D-06M5	0.93716D-08M6	0.22247D-04
ABA14	M7	0.21545D-05M8	0.85058D-04M9	0.0 D+00
ABA14	M10	0.12709D-01M11	0.83235D-02	
ABA15	M1	0.99085D-02M2	0.32231D-03M3	0.14537D-04
ABA15	M4	0.35516D-06M5	0.80082D-08M6	0.22577D-04
ABA15	M7	0.20758D-05M8	0.79656D-04M9	0.0 D+00
ABA15	M10	0.12709D-01M11	0.83235D-02	
ABA16	M1	0.99336D-02M2	0.30543D-03M3	0.12948D-04
ABA16	M4	0.29987D-06M5	0.63557D-08M6	0.23017D-04
ABA16	M7	0.19652D-05M8	0.72717D-04M9	0.0 D+00
ABA16	M10	0.12709D-01M11	0.83235D-02	
ABA17	M1	0.99713D-02M2	0.27914D-03M3	0.10585D-04
ABA17	M4	0.22309D-06M5	0.42454D-08M6	0.23719D-04
ABA17	M7	0.17857D-05M8	0.63278D-04M9	0.0 D+00
ABA17	M10	0.12709D-01M11	0.83235D-02	
ABB11	M1	0.10019D-01M2	0.24452D-03M3	0.77451D-05
ABB11	M4	0.14077D-06M5	0.22684D-08M6	0.24667D-04
ABB11	M7	0.15381D-05M8	0.52410D-04M9	0.0 D+00
ABB11	M10	0.12709D-01M11	0.83235D-02	
ABB12	M1	0.10071D-01M2	0.20615D-03M3	0.51542D-05
ABB12	M4	0.76969D-07M5	0.99924D-09M6	0.25729D-04
ABB12	M7	0.12658D-05M8	0.40646D-04M9	0.92000D-03
ABB12	M10	0.12709D-01M11	0.83235D-02	
ABC11	M1	0.10034D-01M2	0.23319D-03M3	0.73912D-05
ABC11	M4	0.13454D-06M5	0.21927D-08M6	0.24976D-04
ABC11	M7	0.14701D-05M8	0.48876D-04M9	0.0 D+00
ABC11	M10	0.12709D-01M11	0.83235D-02	
RB12	M1	0.11795D-01M2	0.16765D-03M3	0.33187D-05
RB12	M4	0.37660D-07M5	0.36859D-09M6	0.31705D-04
RB12	M7	0.10955D-05M8	0.21135D-04M9	0.0 D+00
RB12	M10	0.23619D-01M11	0.38902D-02	
RB22	M1	0.11863D-01M2	0.11264D-03M3	0.16303D-05
RB22	M4	0.13184D-07M5	0.90540D-10M6	0.33092D-04
RB22	M7	0.77763D-06M8	0.93033D-05M9	0.0 D+00
RB22	M10	0.23619D-01M11	0.38902D-02	

TABLE IV-10-II. *Continued*

ABA21	M1	0.10048D-01M2	0.23141D-03M3	0.80046D-05	ABA31	M4	0.40587D-07M5	0.42055D-09M6	0.27091D-04
ABA21	M4	0.14616D-04M5	0.23648D-08M6	0.24866D-04	ABA31	M7	0.10675D-05M8	0.14357D-04M9	0.0 D+00
ABA21	M7	0.15945D-05M8	0.36197D-04M9	0.0 D+00	ABA31	M10	0.12709D-01M11	0.83235D-02	
ABA21	M10	0.12709D-01M11	0.83235D-02		ABA32	M1	0.10163D-01M2	0.14097D-03M3	0.32831D-05
ABA22	M1	0.10050D-01M2	0.22997D-03M3	0.79054D-05	ABA32	M4	0.39780D-07M5	0.40939D-09M6	0.27118D-04
ABA22	M4	0.14352D-04M5	0.23073D-08M6	0.24904D-04	ABA32	M7	0.10603D-05M8	0.14195D-04M9	0.0 D+00
ABA22	M7	0.15849D-05M8	0.35810D-04M9	0.0 D+00	ABA32	M10	0.12709D-01M11	0.83235D-02	
ABA22	M10	0.12709D-01M11	0.83235D-02		ABA33	M1	0.10166D-01M2	0.13835D-03M3	0.31641D-05
ABA23	M1	0.10055D-01M2	0.22616D-03M3	0.76446D-05	ABA33	M4	0.37683D-07M5	0.38070D-09M6	0.27190D-04
ABA23	M4	0.13666D-04M5	0.21596D-08M6	0.25000D-04	ABA33	M7	0.10413D-05M8	0.13770D-04M9	0.0 D+00
ABA23	M7	0.15595D-05M8	0.34794D-04M9	0.0 D+00	ABA33	M10	0.12709D-01M11	0.83235D-02	
ABA23	M10	0.12709D-01M11	0.83235D-02		ABA34	M1	0.10172D-01M2	0.13392D-03M3	0.29665D-05
ABA24	M1	0.10063D-01M2	0.21972D-03M3	0.72126D-05	ABA34	M4	0.34279D-07M5	0.33530D-09M6	0.27312D-04
ABA24	M4	0.12552D-04M5	0.19253D-08M6	0.25175D-04	ABA34	M7	0.10087D-05M8	0.13062D-04M9	0.0 D+00
ABA24	M7	0.15162D-05M8	0.33114D-04M9	0.0 D+00	ABA34	M10	0.12709D-01M11	0.83235D-02	
ABA24	M10	0.12709D-01M11	0.83235D-02		ABA35	M1	0.10179D-01M2	0.12750D-03M3	0.26896D-05
ABA25	M1	0.10075D-01M2	0.21042D-03M3	0.66065D-05	ABA35	M4	0.29673D-07M5	0.27627D-09M6	0.27491D-04
ABA25	M4	0.11038D-04M5	0.16184D-08M6	0.25423D-04	ABA35	M7	0.96108D-06M8	0.12069D-04M9	0.0 D+00
ABA25	M7	0.14530D-05M8	0.30722D-04M9	0.0 D+00	ABA35	M10	0.12709D-01M11	0.83235D-02	
ABA25	M10	0.12709D-01M11	0.83235D-02		ABA36	M1	0.10190D-01M2	0.11866D-03M3	0.23253D-05
ABA26	M1	0.10092D-01M2	0.19761D-03M3	0.58022D-05	ABA36	M4	0.23929D-07M5	0.20695D-09M6	0.27739D-04
ABA26	M4	0.91199D-05M5	0.12505D-08M6	0.25767D-04	ABA36	M7	0.89431D-06M8	0.10762D-04M9	0.0 D+00
ABA26	M7	0.13642D-05M8	0.27718D-04M9	0.0 D+00	ABA36	M10	0.12709D-01M11	0.83235D-02	
ABA26	M10	0.12709D-01M11	0.88325D-02		ABA37	M1	0.10205D-01M2	0.10533D-03M3	0.18125D-05
ABA27	M1	0.10110D-01M2	0.17799D-03M3	0.46377D-05	ABA37	M4	0.16506D-07M5	0.12555D-09M6	0.28122D-04
ABA27	M4	0.65447D-07M5	0.79833D-09M6	0.26305D-04	ABA37	M7	0.78990D-06M8	0.89278D-05M9	0.0 D+00
ABA27	M7	0.12227D-05M8	0.23437D-04M9	0.0 D+00	ABA37	M10	0.12709D-01M11	0.83235D-02	
ABA27	M10	0.12709D-01M11	0.83235D-02		ABB31	M1	0.10224D-01M2	0.88773D-04M3	0.12373D-05
ABB21	M1	0.10147D-01M2	0.15308D-03M3	0.32857D-07	ABB31	M4	0.92728D-08M5	0.57654D-10M6	0.28620D-04
ABB21	M4	0.39066D-07M5	0.39687D-09M6	0.27016D-04	ABB31	M7	0.65134D-06M8	0.68708D-05M9	0.0 D+00
ABB21	M7	0.10318D-05M8	0.18522D-04M9	0.0 D+00	ABB31	M10	0.12709D-01M11	0.83235D-02	
ABB21	M10	0.12709D-01M11	0.83235D-02		ABB32	M1	0.10243D-01M2	0.71458D-04M3	0.74392D-06
ABB22	M1	0.10179D-01M2	0.12611D-03M3	0.20809D-05	ABB32	M4	0.42755D-08M5	0.20271D-10M6	0.29148D-04
ABB22	M4	0.19634D-07M5	0.15645D-09M6	0.27788D-04	ABB32	M7	0.50279D-06M8	0.50228D-05M9	0.92000D-03
ABB22	M7	0.82348D-06M8	0.13866D-04M9	0.92000D-03	ABB32	M10	0.12709D-01M11	0.83235D-02	
ABB22	M10	0.12709D-01M11	0.83235D-02		ABC31	M1	0.10230D-01M2	0.83146D-04M3	0.11259D-05
ABC21	M1	0.10157D-01M2	0.14457D-03M3	0.30532D-05	ABC31	M4	0.82503D-08M5	0.50677D-10M6	0.28778D-04
ABC21	M4	0.35902D-07M5	0.36427D-09M6	0.27247D-04	ABC31	M7	0.60956D-06M8	0.62629D-05M9	0.0 D+00
ABC21	M7	0.97448D-06M8	0.17088D-04M9	0.0 D+00	ABC31	M10	0.12709D-01M11	0.83235D-02	
ABC21	M10	0.12709D-01M11	0.83235D-02		RB14	M1	0.11925D-01M2	0.56321D-04M3	0.45356D-06
RB13	M1	0.11876D-01M2	0.10039D-03M3	0.12789D-05	RB14	M4	0.19871D-08M5	0.71746D-11M6	0.34502D-04
RB13	M4	0.91239D-08M5	0.54764D-10M6	0.33406D-04	RB14	M7	0.42414D-06M8	0.31618D-05M9	0.0 D+00
RB13	M7	0.69470D-06M8	0.80771D-05M9	0.0 D+00	RB14	M10	0.23619D-01M11	0.38902D-02	
RB13	M10	0.23619D-01M11	0.38902D-02		RB24	M1	0.11945D-01M2	0.38150D-04M3	0.22058D-06
RB23	M1	0.11913D-01M2	0.67538D-04M3	0.61953D-06	RB24	M4	0.68812D-09M5	0.17567D-11M6	0.34984D-04
RB23	M4	0.31349D-08M5	0.13221D-10M6	0.34244D-04	RB24	M7	0.29814D-06M8	0.17322D-05M9	0.0 D+00
RB23	M7	0.48793D-06M8	0.40146D-05M9	0.0 D+00	RB24	M10	0.23619D-01M11	0.38902D-02	
RB23	M10	0.23619D-01M11	0.38902D-02		REFAX	M10	4.26485E-02M11	1.0952 E-02	
ABA31	M1	0.10162D-01M2	0.14195D-03M3	0.33283D-05	REFRD	M10	7.8857 E-02M11	1.65375E-03	

TABLE IV-10-III. ENERGY BOUNDARIES

Group	Lower Energy Boundary
1	1.35 MeV
2	183 keV
3	24.8 keV
4	4.31 keV
5	275 eV
6	10^{-5} eV

TABLE IV-10-IV. M.O.C. k_{eff} VALUES

Calculation	Type of Calculation	k_{eff}	Δk_{eff} Error
	2D	1.003480	—
1	TF 1, 2, 3, 4, 5	1.003058	0.000422
2	TF 1, 3, 5	1.003015	0.000465
3	TF 1, 3, 4	1.002893	0.000597
4	TF 1, 2, 5	1.002840	0.000640
5	TF 1, 2, 4	1.002893	0.000597
6	TF 1, 5	1.002862	0.000618
7	TF 1	1.002476	0.001004

TABLE IV-10-V. M.O.C. SYNTHESIS RESULTS

Calc.	k_{eff}	BR	Regional Breeding Ratios					
			C1	C2	AB1	AB2	RB1	RB2
DIF2D	1.003480	1.37081	0.50449	0.28833	0.24182	0.13552	0.11885	0.05181
5 T.F.	1.003058	1.37429	0.50592	0.28708	0.27193	0.13376	0.14979	0.05583
3 T.F.	1.003015	1.38121	0.50634	0.28673	0.24187	0.13375	0.14980	0.06272
1 T.F.	1.002440	1.39521	0.50886	0.28509	0.23832	0.13604	0.14903	0.07796

Cacl.	k_{eff}	BR	Regional Power Fractions						P_{max}, arbitrary units	P_{max} Location, cm	
			C1	C2	AB1	AB2	RB1	RB2		r	z
DIF2D	1.003480	1.37081	0.5071	0.3816	0.0515	0.0235	0.0311	0.0052	0.75254	1.266	3.810
5 T.F.	1.003058	1.37429	0.5087	0.3798	0.0514	0.0233	0.0312	0.0055	0.75798	1.266	3.810
3 T.F.	1.003015	1.38121	0.5092	0.3793	0.0514	0.0234	0.0312	0.0055	0.76197	1.266	3.810
1 T.F.	1.002440	1.39521	0.5115	0.3773	0.0499	0.0249	0.0310	0.0054	0.76933	1.266	3.810

TABLE IV-10-VI. B.O.C. SYNTHESIS RESULTS

Calc.	k_{eff}	BR	Regional Breeding Ratios					
			C1	C2	AB1	AB2	RB1	RB2
DIF2D	1.042968	1.46050	0.46276	0.28740	0.27912	0.17329	0.17703	0.08090
5 T.F.	1.040214	1.42670	0.47620	0.28065	0.28636	0.16808	0.14574	0.06966

Calc.	k_{eff}	BR	Regional Power Fractions						P_{max}, arbitrary units	P_{max} Location, cm	
			C1	C2	AB1	AB2	RB1	RB2		r	z
DIF2D	1.042968	1.46050	0.4858	0.4112	0.0398	0.0238	0.0324	0.0069	0.69292	1.266	3.810
5 T.F.	1.040214	1.42670	0.4998	0.4016	0.0407	0.0233	0.0286	0.0061	0.69032	1.266	3.810

Five trial functions were used. All of them were one-dimensional radial flux shapes, obtained with the DIF1D[5] module of the ARC system, using the five different radial MOC compositions in the reactor (see Fig. IV-10-2).

Trial function 1 is the one-dimensional flux in an infinitely long cylinder with radial compositions and dimensions identical to those in the core region of the reactor, starting with CZA1, CZA2, $\cdots$, and ending with the reflector region REFRD. Trial functions 2, 3 and 4 are the one-dimensional fluxes in infinitely long cylinders with radial compositions and dimensions identical with those in the first, second and third axial blanket regions, starting with compositions ABA11, ABA21 and ABA31, respectively. Trial function 5 is a reflector trial function using only the reflector composition across the axial reflector region, in which a volume source proportional to the fission source generated in calculating trial function 4 was introduced.

Using these five trial functions, a series of synthesis calculations was performed for the MOC configuration (Table IV-10-II). Trial function number 1—the one based upon core compositions—was present in all the calculations performed. Table IV-10-IV summarizes some typical k_{eff} results obtained.

The values obtained are quite good for the calculations with five, three, and even two trial functions. The last, and surprisingly good, calculation using only one trial function shows the importance of the core contribution to k_{eff}.

The values of regional breeding ratios were calculated for the regions shown in Fig. IV-10-1. The total breeding ratios were calculated with the INVENT[4] module using the fluxes from the 2D calculation and synthesis calculations 1, 2 and 7. These values, together with the regional power fractions, peak power, peak power location, and k_{eff}, are listed in Table IV-10-V. The synthesis results, especially those using five trial functions, are remarkably accurate. The errors never exceed a few percent and generally are well under 1 %.

One more synthesis calculation was performed, using five trial functions, to test the ability of the trial functions obtained for the middle-of-cycle conditions to synthesize fluxes corresponding to an appreciably different burnup stage of the same reactor. This calculation used the same five trial functions previously described to expand the flux corresponding to the beginning-of-cycle composition given in Table IV-10-I. The results are listed in Table IV-10-VI. As expected, the accuracy obtained is clearly less in this case. Nevertheless, most of the values obtained are still within a few percent of the corresponding 2D results. Quantities such as k_{eff}, peak power, and peak power location are predicted quite well.

Conclusions

The continuous synthesis procedure using a few one-dimensional trial functions has produced remarkably accurate values of a variety of physically significant reactor parameters, for a typical two-dimensional LMFBR configuration. When the trial functions are used in a model with appreciably different compositions from the model for which they were calculated, the results, even though still acceptable are, as might be expected, of lower quality. This implies that synthesis methods could be used for fuel cycle calculations, employing trial functions computed for a single stage in the cycle.

References

1. AEC Research and Development Report, GEAP-5678 (September 1968).
2. D. Meneghetti, A. J. Ulrich, P. J. Persiani and J. C. Beitel, *Calculational Studies in Support of the Fast Flux Test Facility (FFTF) Critical Experiments in ZPR-3*, Reactor Physics Division Annual Report, July 1, 1967 to June 30, 1968, ANL-7410, p. 221.
3. T. A. Daly, G. K. Leaf and A. S. Kennedy, *The ARC System Two-Dimensional Diffusion Theory Capability, DARC2D*, ANL-7716 (to be published).
4. D. E. Neal, D. A. Schoengold, G. Jensen, G. Main, T. A. Daly, E. A. Kovalsky and G. K. Leaf, *The ARC System One-dimensional Adjunct Calculations and Edits. Part II (AJC003)*, ANL-7719 (to be published).
5. D. E. Neal, G. K. Leaf and A. S. Kennedy, *The ARC System One-dimensional Diffusion Theory Capability, DARC1D*, ANL-7715 (1971).

IV-11. Solution of the Multigroup Neutron Diffusoin Equations by Space-Energy Factorization

W. M. Stacey, Jr. and H. Henryson, II

An approximate, and computationally economical, method for solving the multigroup neutron diffusion equations has been developed and evaluated. The basis of the method is the factorization of the neutron flux into the product of a spectral function which is independent of position and a spatial function which is computed on a broad-group basis. Consistent, and implicitly coupled, equations are derived for the spectral and spatial functions, and an iterative solution routine is devised. The method is analogous to a consistent group-collapsing scheme in that there is an iteration to consistency between the fine-group spectral function and the broad-group spatial functions.

The method has been evaluated for one- and two-dimensional, 24-group LMFBR problems and for one-dimensional, 165-group LMFBR problems. For the former problems, use of as few as two broad-group shape functions yielded an approximation which was sufficiently accurate for scoping analyses, while the use of six broad-group shape functions yielded quite accurate results. Use of fifteen broad-group shape functions yielded satisfactory results in the 165-group problems. For both sets of problems, the results of the factorized calculations were more accurate than the results of few-group calculations in which the number of few groups and the number of broad-group spatial functions were identical. However, the factorization solutions required somewhat more computing time. The factorization method was also found to provide an excellent source guess for a direct multigroup solution, reducing the number of iterations required to converge the latter by 30–50 %.

The results of this work have been published in the literature.[1-4] A code, based upon the factorization method and using MC² fine-group cross sections as input, has been written to generate spatially dependent broad-group cross sections in one-dimensional geometries.

References

1. W. M. Stacey, Jr., *Solution of the Neutron Diffusion Equation by Space-Energy Factorization*, Nucl. Sci. Eng. **45**, 189 (1971).
2. W. M. Stacey, Jr. and H. Henryson, II, *Applications of Space-Energy Factorization to the Solution of Static Fast-Reactor Neutronics Problems*, Proc. National Topical Meeting on New Developments in Reactor Mathematics and Applications, Idaho Falls, March 1971 Conf. 710302.
3. W. M. Stacey, Jr., *Evaluation of Space-Energy Factorization for Two-Dimensional LMFBR Diffusion Theory Problems*, Nucl. Sci. Eng. **46**, 421 (1971).
4. W. M. Stacey, Jr. and H. Henryson, II, *Application of Space-Energy Factorization to LMFBR Diffusion Theory Calculations*, Trans. Am. Nucl. Soc. **14**, 205 (1971).

IV-12. An Efficient Method for Evaluating the $J(\beta,\theta,a,b)$ Integral

R. N. Hwang

Introduction

The integral $J(\beta_k,\theta_k,a_k,b_k)$ represents a generalized form of the usual J-integral which arises: (1) when the effect of the interference scattering cross section in the single-level formulation is included; or (2) when the multilevel formalism is used. $J(\beta_k,\theta_k,a_k,b_k)$ is defined as

$$J(\beta_k,\theta_k,a_k,b_k) = \frac{1}{2}\int_{-\infty}^{\infty} \frac{\psi(\theta_k,x_k) + b_k\chi(\theta_k,x_k)}{\beta_k + 2a_k\chi_k + \psi(\theta_k,x_k)}\, dx_k, \tag{1}$$

where the parameters are defined according to the formulation of the cross sections.[1] Physically, it is equivalent to the resonance integral of an "isolated" resonance excluding the effect of mutual self-shielding due to the neighboring resonances when the NR-approximation is assumed. In other words, it has precisely the same physical meaning as the usual J-integral.

In the single-level formulation, b_k is set equal to zero. Parameters a_k and β_k can be defined slightly differently in

the resolved and the unresolved resonance regions to be consistent with the data in the ENDF/B file. For the resolved resonance region, a_k and β_k are defined as

$$a_k = \sqrt{\beta_k g_j \frac{\Gamma_{nk}}{\Gamma_k} \frac{\sigma_{pa}}{\sigma_p}}, \tag{2}$$

where

$\beta_k = \sigma_p/\sigma_{0k}$
σ_{pa} = potential scattering cross section of the absorber under consideration, b
$\sigma_p = \Sigma_t/N$ or Σ_t^{eq}/N, b/atom.

For the unresolved energy region, parameters a_k and β_k can be defined as

$$a_k = \tfrac{1}{2} \tan 2\delta_\ell \tag{3}$$

and

$$\beta_k = \sigma_p/(\sigma_{0k} \cos 2\delta_\ell), \qquad \text{(or the equivalent } \sigma_p), \tag{4}$$

where

$$\delta_\ell = \arctan\left[\frac{j_\ell(R/\lambda\!\!\!^{-})}{n_\ell(R/\lambda\!\!\!^{-})}\right] \tag{5}$$

$$\delta_0 = R/\lambda\!\!\!^{-} \tag{6}$$

$$\delta_1 = R/\lambda\!\!\!^{-} - \arctan\,(R/\lambda\!\!\!^{-}) \tag{7}$$

$$\delta_2 = R/\lambda\!\!\!^{-} - \arctan\left[\frac{3R/\lambda\!\!\!^{-}}{3 - (R/\lambda\!\!\!^{-})^2}\right], \tag{8}$$

and j_ℓ and n_ℓ are the spherical Bessel and Neumann functions, respectively.

The resonance integral for the "isolated" resonance k is related to $J(\beta_k, \theta_k, a_k, 0)$ by

$$(RI)_k = \frac{\sigma_p}{E_{0k}} \Gamma_x c J(\beta_k, \theta_k, a_k, 0), \tag{9}$$

where

$$c = \begin{cases} 1 & \text{for resolved resonances} \\ 1/\cos 2\delta_\ell & \text{for unresolved resonances.} \end{cases}$$

In the multilevel formalism of the Adler-Adler form,[2,3] parameters are defined as follows:

$$\theta_k = \Gamma_k^{(s)}/\Delta \tag{10}$$

$$\nu_k = \Gamma_k^{(s)}/2 \tag{11}$$

$$a_k = (\tfrac{1}{2})(H_{tk}/G_{tk}) \tag{12}$$

$$\beta_k = \sigma_p \Gamma_k^{(s)}/(4\pi\lambda\!\!\!^{-2} g_j G_{tk} \sqrt{E_{0k}}) \tag{13}$$

$$b_k = H_{xk}/G_{xk}, \tag{14}$$

where the multilevel parameters are defined in Ref. 2 and obtained from ENDF/B by ETOE-2.

The corresponding resonance integral for an "isolated" resonance excluding the mutual self-shielding effect is therefore

$$(RI)_k = \frac{\sigma_p G_{xk}}{E_{0k}} \frac{\Gamma_k^{(s)}}{G_{tk}} J(\beta_k, \theta_k, a_k, b_k). \tag{15}$$

With parameters for various cases defined, the numerical technique for evaluating $J(\beta_k, \theta_k, a_k, b_k)$ will be discussed. A direct numerical integration of Eq. (1) using any algorithm is highly undesirable due to the asymmetri behavior of the χ-function. The integration must be performed on the positive as well as the negative planes of x where the integrand exhibits different behavior. However, this difficulty can be avoided and, in fact, one may take full advantage of the symmetric and the asymmetric properties of the ψ- and χ-functions by redefining $J(\beta_k, \theta_k, a_k, b_k)$ in the following way:

$$J(\beta_k,\theta_k,a_k,b_k) = J(\beta_k,\theta_k) + \int_0^\infty dx_k \sum_{n=1}^{\infty} (2a_k)^{2n} \frac{\psi\chi^{2n}}{(\beta_k+\psi)^{2n+1}} - b_k \int_0^\infty dx_k \sum_{n=1}^{\infty} (2a_k)^n \frac{\chi^{2n}}{(\beta+\psi)^{2n}}. \quad (16)$$

The two series in Eq: (16) must be uniformly convergent on physical grounds. Since $(\beta_k + 2a_k\chi + \psi)$ has the physical meaning of the total cross section, which must be positive everywhere to be meaningful, it follows that $\beta_k + \psi \geq 2a_k\chi$ everywhere. It is interesting to note that the two geometric series can be written in closed form, and $J(\beta_k,\theta_k, a_k,b_k)$ becomes

$$J(\beta_k,\theta_k,a_k,b_k) = J(\beta_k,\theta_k) + I(\beta_k,\theta_k,a_k) - b_k M(\beta_k,\theta_k,a_k), \quad (17)$$

where the I- and M-integrals are defined as

$$I(\beta_k,\theta_k,a_k) = (2a_k)^2 \int_0^\infty \frac{\chi^2}{(\beta_k+\psi)^2 - (2a_k\chi)^2} \cdot \frac{\psi}{\beta_k+\chi}\, dx_k \quad (18)$$

and

$$M(\beta_k,\theta_k,a_k) = (2a_k) \int_0^\infty \frac{\chi^2}{(\beta_k+\psi)^2 - (2a_k\chi)^2}\, dx_k. \quad (19)$$

The advantage of Eq. (17) over Eq. (1) is quite obvious. Instead of integrating over both the positive and the negative planes of x_k, the integration now is over the positive x_k only. On the other hand, there are two extra integrals to be evaluated. It should be noted that the magnitudes of $I(\beta_k,\theta_k,a_k)$ and $M(\beta_k,\theta_k,a_k)$ are generally much smaller than that of the corresponding J-integral. For instance, in the case of the single-level formulation, a cursory check indicates that the magnitude of the I-integral is generally less than 15 % of that of the corresponding J-integral for most cases of practical interest. A similar situation is also expected for the case of the multilevel formulation based on the limited data available on ^{235}U, ^{239}Pu, and ^{241}Pu. Hence, less strict error criteria are required for the I- and M-integrals.

An accurate and efficient algorithm using the Gauss-Jacobi quadrature[4] is proposed to evaluate these integrals simultaneously. In this algorithm, the J-integral is evaluated accurately to the relative error of less than 0.1 % everywhere in the region of practical interest ($10^{-5} \leq \beta$; any θ). The same number of mesh-points are used for I- and M-integrals so that the total number of calculations for the ψ- and χ-integrals are minimized. The M- and I-integrals obtained this way are less accurate, with a relative error of less than 1 %, which is believed to be sufficient for the problems of practical interest. The detailed description of this algorithm and its mathematical justification will be described in the following sections.

Technique of Rational Transformation

The proposed algorithm is directly based on the utilization of the general characteristics of the Gauss quadrature and the analytical behavior of the ψ- and χ-functions. In general, the efficiency of the Gauss quadrature depends strongly on how the integrand behaves. It is generally true that the integration is exact for a given number of mesh-points N if the integrand is of the form $\sum_{k=1}^{N} A_k x^k$ where $k \leq 2N - 1$. Clearly, the most favorable integrand for the Gauss-quadrature formulas[4] is the one which can be approximated by the polynomial $\sum_k A_k x^k$ with k as small as possible. As discussed previously,[1] the integrand of the form $[\psi(x,\theta)]/\beta + \psi(x,\theta)$ does not meet this requirement since the ψ-function quickly approaches its asymptotic series when x becomes large. As one shall see later, the integrand of the form $[\chi(\theta,x)]/\beta + \psi(\theta,x)$ is even worse since $\chi(\theta,x)$ approaches its asymptotic series faster than the corresponding $\psi(\theta,x)$. One way of resolving this problem is to divide the integrand into two parts whereby the integrand of the second integral in the asymptotic region also exhibits the form of $\sum_k A_k y^k$ with the variable of integration $y = 1/x$ as described by Ref. 5. In this paper, a new method of treating integrands of the forms

$$\left(\frac{\psi}{\beta+\psi}\right)^n, \left(\frac{\chi}{\beta+\psi}\right)^{2n}, \text{ and } \left(\frac{\chi}{\beta+\chi}\right)^{2n} \frac{\psi}{\beta+\psi}$$

is proposed. For simplicity, let $f(x)$ be the integrand under consideration. Instead of integration over x, a transformation is made so that

$$\int_0^\infty f(x)\, dx = \frac{1}{K}\int_0^1 \frac{du}{\sqrt{1-u^2}} \frac{f(u)}{(1-u^2)} = \frac{\pi/N}{K}\left\{\frac{1}{2}f(0) + \sum_{i=2}^{\frac{N-1}{2}} \frac{f(u_i)}{1-u_i^2}\right\} + R_N, \quad (20)$$

where N, the total number of points over both the positive and the negative domains of u, is taken to be an odd integer and the new variable u is related to x by

$$u^2 = \frac{K^2x^2}{1 + K^2x^2}, \tag{21}$$

and the choice of the parameter K will be discussed later.

Equation (2) represents the Gauss-Jacobi quadrature with an odd number of mesh points where the related orthogonal polynomial is the Chebyshev polynomial of first kind and

$$u_i = \cos\frac{(2i - 1)\pi}{2N} \tag{22}$$

$$R_N = \frac{\pi}{(2N)!2^{2N-1}} f^{(2N)}(\xi); \qquad 0 < \xi < 1. \tag{23}$$

The inclusion of the $u_i = 0$ point is a significant saving in computing time since $\chi(0,\theta_k) = 0$ and $\psi(0,\theta_k)$ is related to the complementary error function which can be evaluated readily using the exceedingly efficient rational approximation suggested by Hastings.[6] Thus, the total number of entries to the ψ- and χ-functions is $(N - 1)/2$. The quantity $(N - 1)/2$ will be referred to as the total number of points required for the integration of all three integrals.

The purposes of making the rational transformation are manyfold. The most obvious purpose is to take advantage of the asymptotic properties of the ψ- and χ-functions whereby

$$\lim_{u\to 1}\left\{\frac{1}{1 - u^2}\left(\frac{\chi}{\beta + \psi}\right)\right\} = \text{constant} \tag{24}$$

and

$$\lim_{u\to 1}\left\{\frac{1}{1 - u^2}\left(\frac{\chi}{\beta + \psi}\right)^{2N}\frac{\psi}{\beta + \psi}\right\} = \text{constant}\cdot\lim_{u\to 1}(1 - u^2)^N. \tag{25}$$

Hence, the asymptotic behavior of $\sum_k a/x^k$ in the x domain can be eliminated. Of even greater importance from a mathematical point of view is that the transformation amounts to the analytic continuation of the series $\sum_{k=0}^{\infty} a_k x^k$ in the x domain which does not converge in the limit of large x. The corresponding series $\sum_k \gamma_k u^k$ is believed to converge much more rapidly in the u domain $(0 \leq u \leq 1)$. By choosing the parameter K appropriately according to the analytical behavior of the ψ- and χ-functions, it was found that one may obtain an accuracy of 0.1 % for the $J(\beta_k,\theta_k,0,0)$ integral and 1 % or better for the I- and M-integrals using the same number of mesh points in the region of practical interest. The minimum number of mesh points required for the prescribed accuracy is obviously dependent on the magnitudes of β, θ, and α. For large θ, for instance, all integrals of the form defined in Eq. (17) are practically exact for a minimum of one point as ψ and χ become the natural line-shape functions. At the other extreme, a comparatively large number of mesh points is required when β and θ are both small. It was found that a total of six points is sufficient in all regions of practical interest for LMFBR applications.

Choice of K

From Eqs. (24) and (25), it is obvious that, for the case of large θ, where ψ- and χ-functions approach the natural line shapes, the method becomes most efficient. For the case of small θ, the ψ- and χ-functions will approach the natural line shape functions only if x is large. The rapidity with which the ψ- and χ-functions approach their asymptotic forms depends strongly on the magnitude of θ. Hence, the problem becomes the appropriate choice of K as a function of θ and β so that

$$f = \sum_{i=1}^{N} \alpha_i u_i^{2N} \tag{26}$$

converges rapidly in the nonasymptotic region where the ψ- and χ-functions are significantly different from their corresponding natural line shapes.

The parameter K will be chosen to satisfy the error criteria of $|\epsilon| \leq 0.1$ for J and $|\epsilon| \leq 1$ % for M- and I-integrals. Since the behavior of the integrand f and its derivatives $f^{(2n)}$ depend on the magnitudes of β and θ, it is, therefore, useful to divide the region of practical interest into three regions:

I. Fast Reactor Region $[\beta/\psi(0,\theta) \geq 0.2;\ \theta \leq 1]$

II. Lorentzian Region ($\theta > 0.5$ outside of Region I)
III. Intermediate Region (region outside of Regions I and II).

I. Fast Reactor Region [$\beta/\psi(0,\theta) \geq 0.2$, $\theta \leq 1$]

This region is extremely important for fast reactor calculations since approximately 80 % or more of the resonances under consideration fall in this region. Two special characteristics of the integrands in this region are: (1) the shapes of the integrands are generally not too different from the corresponding ψ or χ^2 in the numerators; and (2) the integrands can always be expressed in terms of the rapidly convergent series in u, namely,

$$\frac{\psi}{\beta+\psi} = \frac{\psi(x,\theta)}{\beta-\psi(0,\theta)} + \frac{\psi(x,\theta)[\psi(0,\theta)-\psi(x,\theta)]}{[\beta+\psi(0,\theta)]^2} + \frac{\psi(x,\theta)[\psi(0,\theta)-\psi(x,\theta)]^2}{[\beta+\psi(0,\theta)]^3} + \cdots . \tag{27}$$

In the nonasymptotic region where $\psi(x,\theta)$ can be approximated by the Gauss form, Eq. (27) becomes

$$\frac{\psi(x,\theta)}{\beta+\psi(x,\theta)} \approx \frac{\psi(0,\theta)}{\beta+\psi(0,\theta)} \sum_{n=0}^{\infty} (-1)^n A_n y^{2n} = \frac{\psi(0,\theta)}{\beta+\psi(0,\theta)}\left[1 + \sum_{n=1}^{\infty} B_n u^{2n}\right], \tag{28}$$

where.

$$\begin{aligned} A_0 &= 1 \\ A_1 &= 1 - \frac{1}{\beta+\psi(0,\theta)} \\ A_2 &= \frac{1}{2}\left[1 - \frac{3}{\beta+\psi(0,x)} - 2\psi(0,\theta)\left(\frac{1}{\beta+\psi(0,x)}\right)^2\right]; \text{ etc.} \end{aligned} \tag{29}$$

and

$$B_\nu = \sum_{\lambda=1}^{\nu} (-1)^\lambda C_{\lambda-1}^{\nu-1} A_\lambda \frac{\theta^2}{4K^2}$$

where

$$C_{\lambda-1}^{\nu-1} = \frac{(\nu-1)!}{(\nu-\lambda)!(\lambda-1)!}, \qquad \text{(the binomial coefficient)}.$$

It was found that the convergence of Eq. (28) is relatively insensitive to the value of K as long as $\theta/6 \leq K \leq \theta/2$. From numerical experimentation, it was found that

$$K = \theta/5 \tag{30}$$

will yield the most accurate results in the J-integral. A similar argument is also applicable to the M- and I-integrals.

II. Lorentzian Region ($\theta > 0.5$ *Outside of Region I*)

In this region, the ψ- and χ-functions will approach their asymptotic form rapidly, and the quantity $\psi/(\beta+\psi)$ approaches $1/(\beta+1+\beta x^2)$ rapidly. Hence, K may be taken to be close in value to $\sqrt{\beta/(\beta+1)}$. In this region, the accuracy of the integration is generally not sensitive to the values of K as long as $0.3\sqrt{\beta/(\beta+1)} < K \leq \sqrt{\beta/(\beta+1)}$. It was found

$$K \approx \sqrt{2\beta/(\beta+1)} \tag{31}$$

will generally give good results for J-, M-, and I-integrals.

As in the case of Region I, the proposed method is also exceedingly efficient in this region. Less than five points are required to give the prescribed accuracy.

II. Intermediate Region (*Region Outside of Regions I and II*)

Among the three regions, the proposed method is relatively least efficient in this one. Both β and θ are small in the intermediate region. It is also the region of least importance in fast reactor applications.

For the J-integral, the integrand $\psi/(\beta+\psi)$ exhibits a step function behavior with a sharp drop near

$$x = \frac{2}{\theta} \ln \left[2 + \frac{\sqrt{\pi}}{2} \frac{\theta}{\beta} \right],$$

where $\psi/(\beta + \psi)$ is approximately equal to half of the value at $x = 0$. This is quite obvious if ψ is replaced by the Gauss form. The point of inflection for $\psi/(\beta + \psi)$ is also close to this half-way point. Since the point of inflection is still small compared with $x = 7/\theta$ where $\psi(x, \theta)$ approaches $1/x^2$,[7] it is rather difficult to choose a K that will reproduce the same step function-like behavior for quantity $(1 - u^2)$.

One way of choosing K in this region is to use a reference point x_1, which represents the break point of the power series and the asymptotic series representations of $\psi/(\beta + \psi)$. The exact value of x_1 is extremely difficult to obtain. From Ref. 1 it is clear that x_1 must be approximately equal to the break point suggested by Nicholson and Grasseschi.[5] Hence, x_1 will be taken to be

$$x_1 = \frac{2}{\theta} \left[1.8971 + \ln \left(1 + 0.85 \frac{\sqrt{\pi}\,\theta}{2\beta} \right) \right]^{\frac{1}{2}} \tag{32}$$

for values of $x_1 \geq \sqrt{(\beta + 1)/\beta}$; and

$$x_1 = \left(\frac{1}{2} \left\{ \frac{4}{\theta^2} \left[1.8971 + \ln \left(1 + 0.85 \frac{\sqrt{\pi}\,\theta}{2\beta} \right) \right] + \frac{1 + \beta}{\beta} \right\} \right)^{\frac{1}{2}}. \tag{33}$$

or x_1 in Eq. (32) $< \sqrt{(\beta + 1)/\beta}$.

Define

$$u_1^2 = \frac{K^2 x_1^2}{1 + K^2 x_1^2}, \tag{34}$$

so that

$$K^2 = \left(\frac{u_1^2}{1 - u_1^2} \right) \frac{1}{x_1^2} \tag{35}$$

By numerical experimentation, it was found that, by setting $u_1 \approx 0.77$ or $1/K = 0.8292\, x_1$, good results in J-, M-, and I-integrals can be obtained for the case where Eq. (32) is valid. Better results can be obtained by letting

$$1/K = 0.8292\, x_1 \rho, \tag{36}$$

where

$$\rho = 1 + \frac{0.018(\beta - 0.00128)}{\beta + 0.00128} + \frac{0.08\beta}{\psi(0, \theta)}. \tag{37}$$

For the case where Eq. (33) is applicable, good results can be obtained by letting $u_1^2 = 0.5$ or

$$1/K = x_1. \tag{38}$$

When β becomes extremely small, the integrands are not sensitive to the Gaussian-like behavior of the ψ-function and Eq. (38) will approach the same limit defined previously for the Lorentzian region.

To give the prescribed accuracy of $|\epsilon| \leq 0.1\%$ for the J-integral and $|\epsilon| \leq 1\%$ for the M- and I-integrals, a total of six points is required in this region. It should be noted that Region III is generally very small for problems of practical interest. The cases with extremely small β are those for low-energy resonances with large neutron width. The combination of low resonance energy and large neutron width implies that θ must be reasonably large. It is extremely rare that a resonance will fall within the region $\beta \leq 10^{-3}$ and $\theta < 0.1$.

Further Economies

Under the condition that β_k is large compared with $\psi(0, \theta_k)$, $J(\beta_k, \theta_k, a_k, b_k)$ can be evaluated analytically without going through the integration routine. In fast reactor applications there are a significantly large number of resonances that satisfy this condition. It is undoubtedly a significant saving of computing time to include the analytical expressions in the proposed algorithm.

The integral $J(\beta_k, \theta_k, a_k, b_k)$ can be expressed in terms of a uniformly convergent series

$$J(\beta_k,\theta_k,a_k,b_k) = \frac{1}{2}\left\{\int_{-\infty}^{\infty}\frac{\psi(x_k,\theta_k)+b_k\chi(x_k,\theta_k)}{\beta_k+\psi(0,\theta_k)}\,dx_k + \int_{-\infty}^{\infty}dx_k\,\frac{[\psi(x_k,\theta_k)+b_k\chi(x_k,\theta_k)][\psi(0,\theta_k)-\psi(x_k,\theta_k)-2a_k\chi(x_k,\theta_k)]}{[\beta_k+\psi(0,\theta_k)]^2}+\cdots\right\} \quad (39)$$

$$= \frac{\pi/2}{[\beta_k+\psi(0,\theta_k)]}\left\{1+\frac{[\psi(0,\theta_k)-\frac{1}{2}\psi(0,\sqrt{2}\,\theta_k)]-a_kb_k\psi(0,\sqrt{2}\,\theta_k)}{[\beta_k+\psi(0,\theta_k)]}+\cdots\right\},$$

where identities given in Ref. 8 were used. It was found that, for

$$\frac{\beta_k+\psi(0,\theta_k)}{\psi(0,\theta_k)} \geq 15,$$

an accuracy of $|\epsilon| \leq 0.1\,\%$ can be obtained by keeping only the first two significant terms in Eq. (39). Thus,

$$J(\beta_k,\theta_k,0,0) \approx \frac{\pi/2}{[\beta_k+\psi(0,\theta_k)]}\left[1+\frac{\psi(0,\theta_k)-\frac{1}{2}\psi(0,\sqrt{2}\,\theta_k)}{\beta_k+\psi(0,\theta_k)}\right] \quad (40)$$

$$M(\beta_k,\theta_k,a_k) \approx \frac{\frac{\pi}{2}a_kb_k\psi(0,\sqrt{2}\,\theta_k)}{[\beta_k+\psi(0,\theta_k)]^2} \quad (41)$$

$$I(\beta_k,\theta_k,a_k) \approx 0. \quad (42)$$

Conclusion

The new algorithm using the technique of the rational transformation and the Gauss-Jacobi quadrature is believed to provide an accurate, economical, and flexible tool for evaluting the $J(\beta_k,\theta_k,a_k,b_k)$ integral. This algorithm is particularly efficient in Region I where most of the practical problems in fast reactor applications fall and in Region II where θ is relatively large. It was found that an accuracy of $|\epsilon| \leq 0.1\,\%$ for the J-integral and $|\epsilon| \leq 1.0\,\%$ for the M- and I-integrals can be obtained by using five mesh points or less (total entries of the QUICKW routine).[9] For Region III, which is less important in fast reactor applications, six mesh points are required to give the prescribed accuracies. If one relaxes the accuracy of the J-integral to $|\epsilon| \leq 0.5\,\%$ for this region, five mesh points are sufficient.

References

1. R. N. Hwang, *Preliminary Investigations of Resolved Resonance Algorithum for the New MC² Code*, Applied Physics Division Annual Report, July 1, 1969, to June 30, 1970, ANL-7710, pp. 387.
2. D. B. Adler and F. T. Adler, *Neutron Cross Sections in Fissile Elements*, Proc. Conference on Breeding, Economics, and Safety in Large Fast Reactors, ANL-6792 (1963), p. 695.
3. R. N. Hwang, *Application of Statistical Theory and Multilevel Formalism to Doppler Effect Analysis-I*, Nucl. Sci. Eng. **36**, 67–81 (1969).
4. A. H. Stroud and D. Secrest, *Gaussian Quadrature Formulas*, (Prentice-Hall, Inc., Englewood Cliffs, New Jersey, 1966).
5. R. B. Nicholson and G. Grasseschi, *A Fast Accurate Technique for Calculation of the Resonance J-Function*, Reactor Physics Division Annual Report, July, 1968 to June 30, 1969, ANL-7610, p. 499.
6. C. Hastings, Jr., *Approximations for Digital Computers*, (Princeton University Press, Princeton, New Jersey, 1955).
7. A. Reichel, *On the Evaluation of Doppler-Broadened Cross-Section Functions*, Nucl. Sci. Eng. **20**, 547 (1964).
8. R. N. Hwang, *Application of Statistical Theory and Multilevel Formalism to Doppler Effect Analysis-II*, Nucl. Sci. Eng. **36**, 82 (1969).
9. B. J. Toppel, A. L. Rago and D. M. O'Shea, *MC²*, *A Code to Calculate Multigroup Cross Sections*, ANL-7318 (1967).

IV-13. An Accurate Method for Evaluating the Overlap Term in the Unresolved Resonance Region

R. N. HWANG

INTRODUCTION

Extensive studies of the role of the resonance overlap effect in fast reactor calculations have been described in previous work.[1,2] A rather crude method was proposed for estimating the overlap effect of neighboring resonances of the same sequence in the unresolved energy region. This early method is believed to be reasonably accurate in the energy region where resonances are strongly overlapping. However, it becomes questionable in the relatively low-energy region and for the cases where the "equivalent" potential scattering cross section becomes small. These are the situations that one must face in the analysis of Doppler-effect experiments and of heterogeneity studies for fast-reactor critical assemblies. The significance of the overlap effect on the temperature dependence of the Doppler coefficient under meltdown conditions, where the extremely high temperature of the fuel pin may be accompanied by spectrum hardening due to the loss of sodium, must also be realized. Under this condition, even the well-separated ^{238}U resonances become strongly overlapping. The accurate estimation of the overlap effect is, therefore, important in fast reactor safety studies. Some preliminary results concerning this problem have been given in previous work.[3] Hence, an accurate estimation of the overlap effect is desirable.

The purpose of this report is to describe a newly developed method for estimating the overlap effect due to resonances of the same spin sequence in the unresolved energy region. Improvement on the earlier method[1,2] has been made in three general areas. First of all, the exact Doppler-broadened line-shape function $\psi(\theta,x)$ is used instead of the approximate Gaussian form used previously. Secondly, the new method is made applicable even in the relatively low-energy region and for cases where the equivalent scattering cross sections per absorbing atom, σ_p^{eq}, is small. The assumption that $[\psi(\theta,x)/\beta] > 1$, used in the previous method, has been avoided. This assumption obviously breaks down whenever $[\psi(\theta,0)/\beta] \leq 0$. Finally, the Dyson's correlation function[4] for levels is used instead of the rather crude approximation used in the previous work.[1,2] The use of the approximate correlation function described previously was found to underestimate the overlap effect in the high-energy region.[5]

The analytical and numerical foundations of the proposed method are described in detail in subsequent sections. A code has been developed to test and evaluate the merits of the proposed method. The last section describes the CHOPSUEY code and its computing time required for calculations of practical interest.

FORMULATION OF THE OVERLAP TERM

If the NR-approximation and the "nearest neighbor" approximation[1,2] are assumed, the overlap term for a given process x due to the resonances of the same sequence can be written as

$$\tilde{o}_x = \frac{1}{\langle D\rangle}\left\langle \frac{\Gamma_{xk}}{2}\int_{-\infty}^{\infty}\Omega(\delta)\,\frac{d\delta}{\langle D\rangle}\int_{-\infty}^{\infty}\frac{\psi_k}{\beta_k+\psi_k}\cdot\frac{A_{k'}\psi_{k'}dx_k}{\beta_k+\psi_k+A_{k'}\psi_{k'}}\right\rangle_{k\&k'}, \tag{1}$$

where $A_{k'}$ is the ratio of the peak cross section of resonance k' with respect to a given resonance k and $\langle D\rangle$ is the average level spacing. The brackets $\langle\ \rangle$ indicate the statistical average over the distribution functions of the resonance parameters of both the kth and k'th resonances. The correlation function $\Omega(\delta)$ is the probability that any k'th resonance will be found at a distance of $\delta = E_k - E_{k'}$ from a given resonance k. For our purpose, $\Omega(\delta)$ is taken to be Dyson's two-level correlation function[4,5]

$$\Omega(y) = 1 - \{s(y)\}^2 + \frac{\partial s(y)}{\partial(y)}\,si(y), \tag{2}$$

where

$$y = \frac{\pi\,|\,E_k - E_{k'}\,|}{\langle D\rangle} \tag{3}$$

$$s(y) = \frac{\sin|\,y\,|}{y} \tag{4}$$

and the sine integral, $si(y)$, is defined as

$$si(y) = -\int_y^\infty \frac{\sin t}{t}\, dt. \tag{5}$$

Equation (1) involves multiple integrals. A direct numerical approach is believed to be extremely time-consuming, if at all practical, for routine design calculations. Equation (1) can be simplified considerably by series expansion.

Note that the integral can be expressed as

$$\int_{-\infty}^{\infty} \frac{\psi_k}{\beta_k + \psi_k} \cdot \frac{A_{k'}\psi_{k'}}{\beta_k + \psi_k + A_{k'}\psi_{k'}}\, dx_k = \int_{-\infty}^{\infty} \frac{\psi_k}{\beta_k + \psi_k} \left\{ \frac{\psi_{k'}}{\beta_{k'} + \psi_{k'}} - \frac{A_k\psi_k\psi_{k'}}{(\beta_{k'} + \psi_{k'})^2} + \cdots \right\}, \tag{6}$$

provided the resulting integrals are uniformly convergent. The substitution of Eq. (6) into Eq. (1) gives

$$\bar{\sigma}_x = K_1 - K_2 + \cdots, \tag{7}$$

where

$$K_1 = \frac{1}{\langle D\rangle^2} \langle \Gamma_{xk} J\rangle_k \langle \Gamma_{k'} J\rangle_{k'} - L_1 \tag{8}$$

$$L_1 = \frac{1}{\langle D\rangle} \int_{-\infty}^{\infty} W\left(\frac{\delta}{\langle D\rangle}\right) \frac{d\delta}{\langle D\rangle} \int_{-\infty}^{\infty} \left\langle \frac{\Gamma_{xk}}{2} \frac{\psi_k}{\beta_k + \psi_k} \right\rangle_k \left\langle \frac{\psi_{k'}}{\beta_{k'} + \psi_{k'}} \right\rangle_{k'} dx_k \tag{9}$$

$$J = \int_0^\infty \frac{\psi_k dx_k}{\beta_k + \psi_k}; \tag{9a}$$

$$K_2 = -\frac{1}{\langle D\rangle^2} \langle \tau_{xk}\rangle_k \left\langle \frac{\Gamma_{k'}}{2} \sigma_p^{eq} \frac{\partial}{\partial \sigma_p^{eq}} J \right\rangle_{k'} - L_2 \tag{10}$$

$$L_2 = -\frac{1}{\langle D\rangle} \int_{-\infty}^{\infty} W\left(\frac{\delta}{\langle D\rangle}\right) \frac{d\delta}{\langle D\rangle} \int_{-\infty}^{\infty} \left\langle \frac{\Gamma_{xk}}{2} \left[\frac{\psi_k}{\beta_k} - \frac{\psi_k}{\beta_k + \psi_k} \right] \right\rangle_k \left\langle \frac{\Gamma_k}{2} \sigma_p^{eq} \frac{\partial}{\partial \sigma_p^{eq}} \frac{\psi_{k'}}{\beta_{k'} + \psi_{k'}} \right\rangle_k dx_k \tag{11}$$

$$\tau_{xk} = \frac{\Gamma_{xk}}{2\beta_k} \int_{-\infty}^{\infty} \frac{\psi_k^2}{\beta_k + \psi_k}\, dx_k = \frac{\pi}{2} \left\langle \frac{\Gamma_{xk}}{\beta_k} \right\rangle - \langle \Gamma_{xk} J\rangle_k \tag{12}$$

$$-\frac{\partial}{\partial \sigma_p^{eq}} \left(\frac{\psi_k}{\beta_k + \psi_k} \right) = \left[\frac{\psi_k}{\beta_k + \psi_k} - \frac{\psi_k^2}{(\beta_k + \psi_k)^2} \right] \frac{1}{\sigma_p^{eq}} \tag{13}$$

and

$$W\left(\frac{\delta}{\langle D\rangle}\right) = 1 - \Omega\left(\frac{\delta}{\langle D\rangle}\right). \tag{14}$$

For cases of practical interest, the series in Eq. (7) is uniformly convergent on physical grounds. In contrast to the series expansion used in the previous work, it is clear that the terms in Eq. (7) will converge more rapidly, even in the relatively low-energy region. In the region where the previous series expansion is valid, Eq. (7) is equivalent to the inclusion of many terms in the previous expression. In the high-energy region, both expressions become identical. The rapidity of convergence of Eq. (7) depends on the degree of the self-shielding effect of the given isotope and the ratio of the average level spacing and the Doppler width in the energy region under consideration. Note that $\langle \tau_{xk}\rangle$ defined in Eq. (12) represents the degree of self-shielding effect and is proportional to $1 - \bar{s}$, where $\bar{s}$ is the self-shielding factor

$$\langle \Gamma_{xk} J\rangle \Big/ \left\langle \frac{\Gamma_{xk}\pi}{2} \Big/ \beta_k \right\rangle.$$

In fact, for practically all problems of interest in the unresolved region, the self-shielding effect is relatively small and $\langle \tau_{xk}\rangle$ is generally much smaller than $\langle \Gamma_{xk} J\rangle_k$. From Eqs. (8), (10), and (13), it is obvious that $K_1 \gg K_2$ if the self-shielding effect is relatively weak. A similar argument can be made to show that the higher-order terms are also small. It is generally true that the resonance sequence with large average spacing will tend to have a stronger self-shielding effect in the low-energy region. It will be shown in a later section that one seldom needs to retain the higher-order terms beyond K_2 and all K_n terms become identically zero when the average spacing $\langle D\rangle$ becomes much larger than the corresponding Doppler width and the average total width.

Since the J-integral and other related integrals can be readily evaluated using the algorithm proposed in Paper

IV-12, the main task here is to evaluate the integral L_1. Once L_1 is known, L_2 can be evaluated quite readily as one will be shown.

Evaluation of L_1 and L_2

L_1 defined in Eq. (9) is still too complicated and a direct numerical approach will undoubtedly require excessive computing time. Furthermore, $W(\delta/\langle D\rangle)$ involves oscillatory functions which are highly undesirable for quadrature formulas. The problem can be resolved by the use of the Fourier transform technique.

A. Technique of Fourier Transform

Define a function $P_k(\xi)$ such that

$$P_k(\xi) = \frac{1}{\sqrt{2\pi}} \int_{-\infty}^{\infty} \frac{\psi_k e^{i\xi x_k}}{\beta_k + \psi_k}\, dx_k = F\left\{\frac{\psi_k}{\beta_k + \psi_k}\right\}. \tag{15}$$

The Fourier transform of $W(\delta/\langle D\rangle)$, say $\omega(\xi)$, is[4,5]

$$\begin{aligned} \omega(\xi) &= \frac{\langle D\rangle}{\sqrt{2\pi}}\left\{1 - \left|\frac{\langle D\rangle\xi}{\pi}\right| + \left|\frac{\langle D\rangle\xi}{2\pi}\right| \ln\left[1 + \left|\frac{\langle D\rangle\xi}{\pi}\right|\right]\right\}, \qquad \left|\frac{\langle D\rangle\xi}{2\pi}\right| \leq 1 \\ \omega(\xi) &= \frac{\langle D\rangle}{\sqrt{2\pi}}\left\{-1 + \left|\frac{\langle D\rangle\xi}{2\pi}\right| \ln\left[\frac{|\langle D\rangle\xi/\pi| + 1}{|\langle D\rangle\xi/\pi| - 1}\right]\right\}, \qquad \left|\frac{\langle D\rangle\xi}{2\pi}\right| > 1. \end{aligned} \tag{16}$$

From the convolution theorem and the Parseval theorem,[6] it can be shown quite readily that

$$L_1 = \frac{1}{2\langle D\rangle^2} \int_{-\infty}^{\infty} \sqrt{2\pi}\omega(\xi) \left\langle \Gamma_{xk} P_k\left(\frac{\Gamma_k}{2}\xi\right)\right\rangle_k \left\langle \frac{\Gamma_{k'}}{2} P_{k'}\left(\frac{\Gamma_{k'}}{2}\xi\right)\right\rangle_{k'} d\xi. \tag{17}$$

Note that the quantities inside the brackets are the statistically averaged values over the appropriate distribution functions of resonance parameters. The same subscript can be used for the two averaged quantities.

It is interesting to note that $P_k(\xi)$ is the unique solution of the following integral equation

$$\beta_k P_k(\xi) + \frac{1}{2}\int_{-\infty}^{\infty} \exp\{[-(\xi - t)^2/\theta_k^2] - |\xi - t|\} P_k(t)dt = \sqrt{\pi/2}\exp[-(\xi^2/\theta_k^2) - |\xi|], \tag{18}$$

where the function on the right-hand side is simply the Fourier transform of the ψ-function as described in Ref. 7.

Before attempting to solve these integral equations, it is important to realize some analytical characteristics of $P_k(\Gamma_k\xi/2)$. First of all, $P_k(\Gamma_k\xi/2)$ is an even function so that $P_k(\Gamma_k\xi/2) = P_k(-\Gamma_k\xi/2)$. Secondly, in the limit of large β_k, $P_k(\Gamma_k\xi/2)$ asymptotically approaches

$$P_k\left(\frac{\Gamma_k}{2}\xi\right) \cong \sqrt{\pi/2}\exp\left(-\frac{\Delta^2}{4}\xi^2 - \frac{\Gamma_k}{2}|\xi|\right)\Big/\beta_k, \tag{19}$$

where Δ is the Doppler width. Thirdly, in another extreme where Γ_k is large compared with Δ, ψ becomes Lorentzian. As a result, $P_k(\Gamma_k\xi/2)$ asymptotically approaches

$$P_k\left(\frac{\Gamma_k}{2}\xi\right) \approx \frac{\sqrt{\pi/2}}{\sqrt{\beta_k(\beta_k + 1)}} \exp\left[-\frac{\Gamma_k}{2}\sqrt{\frac{\beta_k + 1}{\beta_k}}\,\xi\right], \tag{20}$$

according to Eq. (15). Of particular academic interest is the fact that Eq. (20) yields

$$L_1 = \frac{\pi^2}{4\langle D\rangle^2}\left\langle \Gamma_{xk}\Gamma_{k'} \sqrt{\frac{1}{\beta_k(\beta_k + 1)}}\sqrt{\frac{1}{\beta_{k'}(\beta_{k'} + 1)}}\,\frac{1}{z} \cdot\left\{1 - \exp(-z)\frac{\sinh z}{z} - Ei(-z)\left(\cosh z - \frac{\sinh z}{z}\right)\right\}\right\rangle_{k\&k'}, \tag{20a}$$

where $Ei(-z)$ is the exponential integral, and

$$z = \frac{\pi}{\langle D\rangle}\left[\Gamma_k\sqrt{\frac{\beta_k + 1}{\beta_k}} + \Gamma_{k'}\sqrt{\frac{\beta_{k'} + 1}{\beta_{k'}}}\right]\Big/ 2. \tag{20b}$$

It follows that

$$K_1 = \frac{\pi^2}{4\langle D\rangle^2}\left\langle \Gamma_{xk}\sqrt{\frac{1}{\beta_k(\beta_k+1)}}\,\Gamma_{k'}\sqrt{\frac{1}{\beta_{k'}(\beta_{k'}+1)}}\,\phi_0(z)\right\rangle_{k\&k'}, \tag{20c}$$

where $\phi_0(z)$ is identical with that derived by Moldauer[8] for the correction term of the fluctuation in the reaction cross section based on a completely different physical argument. This signifies the strong analogy between these overlap correction terms.

The characteristics defined by Eqs. (19) and (20) provide some clues on how $\langle \Gamma_{xk} P_k(\Gamma_k\xi/2)\rangle$ and $\langle(\Gamma_k/2)P_k(\Gamma_k\xi/2)\rangle$ vary as functions of ξ. This information is extremely important in the subsequent construction of quadrature formulas.

With proper normalization, Eqs. (17) and (18) can be evaluated quite readily using Gauss-Hermite quadratures. Define a new variable

$$\eta = \alpha\xi, \tag{21}$$

where α is chosen to be

$$\alpha = \sqrt{(\langle D\rangle/\pi)^2 + (\Delta^2/2) + \gamma^2}$$

and

$$\gamma = \left\langle \Gamma_k\sqrt{\frac{\beta_k+1}{\beta_k}}\right\rangle. \tag{22}$$

Equation (17) becomes

$$L_1 = \frac{1}{\alpha}\frac{1}{2\langle D\rangle^2}\sum_{i=1}^{N} a_i\sqrt{2\pi}\,\omega(\eta_i/\alpha)\left\langle \Gamma_{xk}g_2(\eta_i)P_k\left(\frac{\Gamma_k\eta_i}{2\alpha}\right)\right\rangle\left\langle \frac{\Gamma_k}{2}\,g_2(\eta_i)P_k\left(\frac{\Gamma_k\eta_i}{2\alpha}\right)\right\rangle g_1(\eta_i) + R_N, \tag{23}$$

where

$$g_2(\eta_i) = \exp\left[\frac{\Delta^2\eta_i^2}{4\alpha^2}\right] \tag{24}$$

$$g_1(\eta_i) = \exp\left[\left(\frac{\langle D\rangle^2}{\pi^2\alpha^2} + \frac{\gamma^2}{\alpha^2}\right)\eta_i^2\right] \tag{25}$$

$$a_n = \frac{2^{n-1}n!\sqrt{\pi}}{n^2[H_{n-1}(\eta_n)]^2} \tag{25a}$$

$$R_N = \frac{N!\sqrt{\pi}}{2^N(2N)!}f^{(2N)}(y), \qquad -\infty < y < \infty \tag{25b}$$

and η_i is the ith zero of the Hermite polynomial $H_n(\eta)$ and $f^{(2n)}(y)$ is the $2n$th derivatives of the integrand. Here the purpose of changing the variable is to ensure that the integrand varies slowly as a function of η in order to make the Gauss-Hermite quadrature highly efficient regardless of the values of $\langle D\rangle$, Δ, Γ_k, or β_k. Similarly, the integral in Eq. (18) can be replaced by the Gauss-Hermite quadrature so that the resulting equation assumes the form of a matrix equation

$$\underline{A}\underline{P} - \underline{B}. \tag{26}$$

By normalizing each row of the matrix element of $\underline{A}$ to its diagonal element, one has

$$A_{ij} = \frac{a_j}{4\alpha}\,g_1(\eta_j)g_2(\eta_j)\Gamma_k\exp\left[\frac{\Delta^2}{2\alpha^2}\eta_i\eta_j - \frac{\Gamma_k}{2\alpha}\,|\eta_i - \eta_j|\right]\Big/ N_0, \qquad i \neq j \tag{27}$$

and

$$A_{ij} = 1, \qquad \text{for} \quad i = j, \tag{27a}$$

where

$$N_0 = g_2(\eta_i)\left[\beta_k + \frac{a_i\Gamma_k}{4\alpha}\,g_3(\eta_i)\right] \tag{28}$$

$$g_3(\eta_i) = [g_2(\eta_i)]^2 g_1(\eta_i) \tag{29}$$

$$B_i = \sqrt{\pi/2}\,\exp\left(-\frac{\Gamma_k}{2}\left|\frac{\eta_i}{\alpha}\right|\right)\Big/ N_0 . \tag{30}$$

Hence, the quantities $P_k(\Gamma_k\eta_i/2\alpha)$ needed for Eq. (23) are just the solution of a system of N equations. An efficient matrix inversion routine is needed for this purpose. The matrix $\underline{A}$ can be further simplified by partition, utilizing the symmetric properties of P_k. It should be noted that the normalization of the matrix proposed here is extremely important from a numerical point of view. This ensures that the coefficients of each linear equation will not have vanishingly small magnitudes simultaneously.

From Eqs. (23) and (18), it is clear that the Gauss-Hermite quadrature is most efficient and accurate when the Doppler width is larger than or comparable with the average spacing and the average total width. On the other hand, the Gauss-Hermite quadrature is less efficient when Δ becomes small. Under the latter condition, $P_k(\Gamma_k\xi/2)$ approaches the exponential form defined by Eq. (20). From a practical point of view, the proposed quadrature is highly desirable because it yields accurate values for cases with large Doppler width where the relative importance of the overlap effect is high. For the cases with small Doppler width where the overlap effect is less important, the accuracy of the results is less critical. It was found that a 10-point Gauss-Hermite quadrature is sufficient to give accurate results.

Since the matrix inversion of a relatively large matrix is generally time consuming, it is, therefore, desirable to optimize the proposed method to suit the routine application. The proposed method can be made more economical in two general areas:

(1) In the region where β_k is much larger than $\psi(\theta_k,0)$, the matrix inversion can be avoided completely. Under this condition, $P_k(\xi)$ can be represented accurately by the first two terms of the Neumann series solution of Eq. (18). It was found that this approximation is adequate as long as $[\beta_k + \psi(\theta_k,0)]/\psi(\theta,0)$ is larger than 2.5. For the fissile isotopes, for instance, approximately 80 % of the unresolved resonances in a typical fast-reactor problem belong to this region. Hence, a significant saving in computer time can be achieved.

(2) In the region where the matrix inversion is necessary, the symmetry properties of $P_k(\Gamma_k\eta_i/2\alpha)$ can be utilized. The matrix $\underline{A}$ can be partitioned into four submatrices of the size $N/2 \times N/2$ where N is chosen to be 10 or any even number. By further utilizing the symmetry property of the Gauss-Hermite quadrature points, it can be shown readily that only two $N/2$ x $N/2$ where N is chosen to be 10 or any even number. By further utilizing the symmetry property of the Gauss-Hermit equadrature points, it can be shown readily that only two $N/2$ x $N/2$ matrix inversions are necessary in the actual calculations. Since the computing time required for the matrix inversion varies approximately as the cube of N, a considerable saving in computer time can be achieved.

Once L_1 is evaluated, L_2 can be obtained quite readily using the results of $P_k(\Gamma_k\eta/2\alpha)$, namely

$$L_2 = -\frac{1}{2\langle D\rangle^2}\int_{-\infty}^{\infty}\sqrt{2\pi}\,\omega(\xi)\left\langle\Gamma_{xk}\left\{\sqrt{\pi/2}\,\frac{\exp\left[-(\Delta^2\xi^2/4) - (\Gamma_k|\xi|/2)\right]}{\beta_k} - P_k\left(\frac{\Gamma_k}{2}\xi\right)\right\}\right\rangle_k \cdot\left\langle\frac{\Gamma_{k'}}{2}\,\sigma_p^{(eq)}\,\frac{\partial}{\partial\sigma_p^{(eq)}}\,P_{k'}\left(\frac{\Gamma_k}{2}\xi\right)\right\rangle_k d\xi. \tag{31}$$

It is interesting to note that the only unknown in Eq. (31) is the quantity

$$\frac{\partial}{\partial\sigma_p^{(eq)}}\,P_k\left(\frac{\Gamma_k}{2}\xi\right).$$

The latter quantity can be related to $P_k(\Gamma_k\xi/2)$. Let

$$R = -\sigma_p^{(eq)}\,\frac{\partial}{\partial\sigma_p^{(eq)}}\,P\left(\frac{\Gamma_k}{2}\xi\right). \tag{32}$$

Differentiating Eq. (18) with respect to $\sigma_p^{(eq)}$ and replacing the integral by the Gauss-Hermite quadrature, one obtains a matrix equation of the form

$$\underline{AR} = \underline{V}/N_0 ,$$

and

$$V_i = P_i\exp\left[\frac{\Delta^2\eta_i}{4\alpha^2}\right]\beta_k ,$$

where P_i is simply the solution of Eq. (26) and N_0 is the normalization factor defined by Eq. (28). Hence,

TABLE IV-13-I. TIMING OF CHOPSUEY

	sec
MC² (QFJ) (no overlap)	120
Proposed algorithms (overlap included)	
Case I	47
Case II	28

$$\underline{R} = \underline{A}^{-1}\underline{V}/N_0 , \tag{33}$$

where $\underline{A}^{-1}$ has already been obtained in evaluating L_1. Thus, the second-order term can be obtained readily once the first-order term is known.

For cases where the asymptotic formula is applicable, R is simply related to the corresponding asymptotic solution of P through Eq. (32).

The same technique, in principle, can be extended to even higher-order terms. However, the evaluation of higher-order terms beyond the second order is believed to be unnecessary on physical grounds. For cases in the low-energy region where the self-shielding effect is large, the average spacing is generally much larger than the corresponding Doppler width and the natural width for all problems of practical interest. Under such conditions, all K_n terms vanish as $\omega(\xi)$ approaches the Dirac δ-function.

CHOPSUEY CODE

The CHOPSUEY code has been developed to test and evaluate the merits of the proposed method. The code uses the input and output routines of the RP-270 code written by Rago,[9] with modifications to allow for both s- and p-wave resonances. Ten quadrature points were used for both the neutron width and the fission width distributions. The fast J-integral routine developed in Paper IV-12 was incorporated.

One of the great concerns is whether the proposed method is efficient enough to be economical in routine applications. Test calculations have been made for problems with ^{239}Pu and ^{238}U using ENDF/B parameters. For fertile isotopes, computing time is generally negligible. The most severe test is believed to be the case when ^{239}Pu is in high concentration. Calculation of ^{239}Pu cross sections requires not only averaging over the fission width distribution function, but also there are as many as 30 energy points for all five spin sequences. Two cases at room temperature were considered in the test calculations.

Case 1

$$^{239}\text{Pu}: \sigma_p^{(eq)} = 71.6/\text{atm}$$
$$^{238}\text{U}: \sigma_p^{(eq)} = 40\ \text{b/atm}$$

Case 2

$$^{239}\text{Pu}: \sigma_p^{(eq)} = 300\ \text{b/atm}$$
$$^{238}\text{U}: \sigma_p^{(eq)} = 30\ \text{b/atm}.$$

It should be noted that the calculations require much less time at higher temperatures as more entries to the asymptotic region become evident. Table IV-13-I summarizes the results of the computer time required for the proposed method as compared with the time required for the old MC² routine[10] (Subroutine QFJ) without the overlap effect. The time estimates given in Table IV-13-I include the input-output time as required by the CHOPSUEY code but exclude the compilation time and wait time.

From Table IV-13-I, it is clear that the proposed method is much superior to the old subroutine not only on the theoretical ground but also in terms of the computing time. The significant improvement in the algorithm for evaluating the generalized J-integral discussed previously[6] is more than enough to compensate for the computing time required for the more rigorous treatment of the overlap effect.

REFERENCES

1. R. N. Hwang, *Doppler Effect Calculations with Interference Corrections*, Nucl. Sci. Eng. **21**, 523 (1965).
2. R. N. Hwang, *An Improved Method of Doppler-Effect Calculation for Fissile Materials in the Intermediate Energy Region*, Proc. Conference on Breeding, Economy, and Safety in Large Fast Reactors, October 7–10, 1963, Argonne, Illinois, ANL-6792, pp. 711–726.

3. R. N. Hwang and K. Ott, *Comparison and Analysis of Theoretical Doppler-Coefficient Results of Fast Reactors*, ANL-7269 (196_).
4. F. J. Dyson, *Statistical Theory of the Energy Levels of Complex Systems*, J. Math. Phys. **3**, 1966 (1962).
5. R. N. Hwang, *Application of Statistical Theory and Multilevel Formalism to Doppler Effect Analysis-II*, Nucl. Sci. Eng. **36**, 82 (1969).
6. I. N. Sneddon, *Fourier Transforms* (Mc-Graw Hill Book Co., Inc., New York, 1951).
7. R. N. Hwang, *Application of Statistical Theory and Multilevel Formalism to Doppler Effect Analysis-I*, Nucl. Sci. Eng. **36**, 67 (1969).
8. P. A. Moldauer, *Statistical Theory of Nuclear Collision Cross Sections*, Phys. Rev. **135**, No. 3B, 642 (1964).
9. A. L. Rago, Argonne National Laboratory (private communication).
10. B. J. Toppel, A. L. Rago and D. M. O'Shea, *MC²*, *A Code to Calculate Multigroup Cross Sections*, ANL-7318 (1967).

IV-14. The Effect of Wide-Scattering Resonances Upon Multigroup Cross Sections

W. M. Stacey, Jr.

The composition dependence of microscopic multigroup cross sections is sometimes accounted for in fast-reactor analysis by an approximate method of the genre proposed by Bondarenko.[1] In this method a wide-scattering resonance occurring within a group is represented by an effective constant cross section for the purpose of computing cross sections for other isotopes. The purpose of this paper is to examine the influence of this type of approximation upon microscopic narrow resonance and elastic removal cross sections.

The contribution of narrow (e.g. uranium and plutonium) resonances to multigroup cross sections depends not only upon these resonances, but also upon the composition of the medium in question. This composition dependence arises from the competition between the resonance and nonresonance "background" reactions, and from the shape of the "asymptotic" flux which weights the contribution of each resonance.

For process x ($x \equiv$ capture, fission) the group cross section is defined as

$$\bar{\sigma}_x \equiv \frac{\int_{\Delta u} \sigma_x(u)\phi(u)\,du}{\int_{\Delta u} \phi(u)\,du} = \frac{\sum_i \int_{\Delta u} \sigma_x^i(u)\phi(u)\,du}{\int_{\Delta u} \phi(u)\,du}, \tag{1}$$

where the sum is over all resonances of the sequence (isotope, quantum state) in question which fall within the group. Using the NRA and the single-level formula, Eq. (1) may be approximated by

$$\bar{\sigma}_x \approx \frac{\sum_i (\Gamma_x^i/E_0^i)\sigma_p^i \phi_{as}(u_0^i) J(\theta_i,\beta_i)}{\int_{\Delta u} \phi_{as}(u)\,du - \sum_j (\Gamma^j/E_0^j) J(\theta_j,\beta_j)\phi_{as}(u_0^i)}. \tag{2}$$

The sum in the denominator is over all resonances of all sequences within the group.

It is convenient in evaluating Eq. (2) to assume that the total "background" cross section per resonance atom (σ_p^i) is the same for all resonances in the sequence and that $\phi_{as}(u) \propto$ constant. Then Eq. (2) can be evaluated directly. Moreover, the composition dependence of $\bar{\sigma}_x$ is uniquely characterized by σ_p, which facilitates the construction of tables for rapid cross section determination such as those proposed by Bondarenko.[1]

One of the purposes of this paper is to examine the effect of the large sodium-scattering resonance ($\sigma_0 = 912$ eV) at 2.85 keV upon the average group cross section for ^{238}U and ^{239}Pu as given by Eq. (2), and to evaluate the magnitude of the resulting error inherent in the Bondarenko type cross section scheme. Resonance parameters for ^{238}U were taken from ENDF/B and ^{239}Pu parameters were constructed by a statistical ladder technique. Equation (2) was evaluated "exactly", using ϕ_{as} given by continuous slowing-down theory and an energy-dependent σ_p^i based on the value of the sodium-scattering cross section at each individual narrow resonance.

A qualitative appreciation for the effect of σ_p^i on $\bar{\sigma}_x$ can be obtained by expanding J about its infinite dilution valu

$$J(\theta_i,\beta_i) = J(\theta_i,\infty)\left[1 - \frac{2}{\pi\beta_i}\int_0^\infty \psi^2(\theta_i,x)\,dx + \cdots\right], \qquad \psi < \beta_i. \tag{3}$$

ρ_i is the ratio of σ_p^i to the peak resonance cross section. The second term in Eq. (3), the self-shielding term, becomes negligible at the peak of the sodium resonance and becomes significant in the wings, for mixtures typical of LMFBR cores. The temperature dependence of J is contained entirely in the self-shielding term.

As can be seen from Eq. (2), the effect of the sodium resonance upon ϕ_{as} also influences $\bar{\sigma}_x$.

Two plausible methods were considered in defining an average σ_p to be used over an energy group containing the sodium resonance. In the first method the sodium resonance was simply ignored. (This is consistent with an application of the Bondarenko scheme in which the same σ_p is used for all energy groups.) This would obviously overpredict the self-shielding, hence also the Doppler effect. A second method consists of averaging the sodium-scattering cross section over the group to obtain a value to be used in defining an effective σ_p for the group. This has the effect of underpredicting the self-shielding of those narrow resonances located in the wings of the sodium resonance, without changing significantly the self-shielding of those narrow resonances near the peak of the sodium resonance. Thus, this method underpredicts the self-shielding, and hence the Doppler effect.

A series of calculations has been performed to evaluate $\bar{\sigma}_c^{28}$, $\bar{\sigma}_c^{49}$, and $\bar{\sigma}_f^{49}$ for different group structures and compositions typical of LMFBR cores. Several methods were considered for averaging the sodium-scattering cross section. The typical results shown in Table IV-14-I are based upon flux weighting with $\phi \propto 1/\xi\Sigma_t$, which yielded the best results. Some appreciation for the significance of these results is obtained by considering that a half-lethargy group about the sodium resonance contributes roughly 10% to the total Doppler effect in a typical LMFBR.

The use of an averaged scattering cross section to include the effect of the sodium resonance in σ_p is clearly superior to ignoring the sodium resonance, and results in errors that are tolerable for preliminary calculations. This suggests that Bondarenko-type schemes should be used with a group-dependent σ_p which can reflect the presence of the sodium resonance.

Another major difficulty which has been encountered in using the Bondarenko scheme[1] to generate multigroup cross sections for fast reactors is in the treatment of elastic removal cross sections for mixtures containing wide scattering resonances.[2,3] This problem has been examined, and new prescriptions for elastic removal cross sections have been developed.

The microscopic elastic removal cross section for a group is, by definition,

$$\bar{\sigma}_{rem}^{-i} \equiv \frac{\int_{\epsilon_i}^{u_L} du\, K_i(u - u_L)\sigma_s^i(u)\phi(u)}{\int_{u_T}^{u_L} du\, \phi(u)}, \tag{4}$$

where u_L and u_T are the lethargies corresponding to the lower and upper energies of the group, ϵ_i is the greater of u_T or u_L minus the maximum lethargy a neutron loses from a scattering collision with isotope i, K_i is the scattering transference kernel for isotope i, σ_s^i is the microscopic scattering cross section for isotope i, and ϕ is the neutron flux.

In the Bondarenko scheme, Eq. (4) is approximated by

$$\bar{\sigma}_{rem}^i \approx \frac{\bar{\sigma}_s^i \xi_i}{u_L - u_T} b_i, \tag{5}$$

TABLE IV-14-I. Percent Errors in Group Average ^{238}U Resonance Capture Cross Section[a]

ΔE, keV	ΔU	$\bar{\sigma}_c^{28}$ (300°K)		$\frac{\bar{\sigma}_c^{28}(1000°K) - \bar{\sigma}_c^{28}(300°K)}{\bar{\sigma}_c^{28}(300°K)}$	
		1	2	1	2
3.35–3.03	0.10	−21	−1	+216	−16
3.03–2.74	0.10	−26	−4	+431	−5
2.74–2.48	0.10	−22	−1	+109	−9
2.48–2.24	0.10	−27	−4	+53	−7
3.35–2.61	0.25	−42	−8	+251	−18
3.35–2.03	0.50	−27	−8	+43	−22

[a] Method 1 ignores sodium resonance. Method 2 uses averaged scattering cross section to include sodium resonance in σ_p.

TABLE IV-14-II. Macroscopic Elastic Removal Cross Section in the Vicinity of the 27.9-keV Iron Resonance

Method	ΔE, keV	ΔU	Σ_{el}^{rem}
Exact	31.5–28.5	0.10	0.4505
A	31.5–28.5	0.10	0.4085 (−9.3%)
B	31.5–28.5	0.10	0.4043 (−10.3%)
C	31.5–28.5	0.10	0.3939 (−12.5%)
Exact	31.5–24.5	0.25	0.0788
A	31.5–24.5	0.25	0.0995 (+26.3%)
B	31.5–24.5	0.25	0.0880 (+11.7%)
C	31.5–24.5	0.25	0.0736 (−6.0%)
Exact	31.5–19.1	0.50	0.0352
A	31.5–19.1	0.50	0.0371 (+5.2%)
B	31.5–19.1	0.50	0.0335 (−4.8%)
C	31.5–19.1	0.50	0.0366 (+4.6%)

where ξ_i is the zeroth lethargy moment of K_i and b_i is a correction factor. $\bar{\sigma}_s^i$ is the average scattering cross section in the group, computed from

$$\bar{\sigma}_s^i = \frac{\int_{u_T}^{u_L} du\{\sigma_s^i(u)/[\sigma_t^i(u) + \sigma_0]\}}{\int_{u_T}^{u_L} du/[\sigma_t^i(u) + \sigma_0]}, \tag{6}$$

where σ_t^i is the total cross section for isotope i, and σ_0 is a constant which represents the total cross section due to other isotopes per atom of isotope i.

The probability that a neutron which scatters at u will have a final lethargy $u' > u_L$ depends exponentially upon $u - u_L$ through K_i. It is apparent from Eq. (4) that the precise location of a scattering resonance within a group can have a significant influence upon $\bar{\sigma}_{rem}^i$. This dependence is not accounted for in the Bondarenko scheme, save for the extra factor b_i included for this purpose. Equation (5) does not account at all for the presence of a scattering resonance in a mixture in the definition of removal cross sections for nonresonance isotopes.

An alternate expression for $\bar{\sigma}_{rem}^i$ was drived from Eq. (4) by assuming

$$\phi(u) \propto 1/\sum_i \xi_i N_i \sigma_i(u). \tag{7}$$

Using the unbroadened line shape functions ψ and χ in the resonance cross section, it was then possible to integrate Eq. (4) to obtain analytical expressions for $\bar{\sigma}_{rem}^i$. The existence and position of a scattering resonance is accounted for explicitly in the definition of the removal cross sections for both resonance and nonresonance isotopes.

Elastic removal cross sections have been computed for mixtures typical of fast-breeder reactors, for groups in the vicinity of three prominent resonances (2.85 keV sodium, 27.9 keV iron, and 1.0 MeV oxygen). In cases where the Bondarenko scheme resulted in large errors, the new prescriptions were significantly better. Results for groups near the iron resonance are given in Table IV-14-II. Method B is the Bondarenko scheme and Method C is the new prescription. Method A is similar to the Bondarenko scheme, except that the denominators in the integrals of Eq. (6) are replaced by

$$[\xi_i \sigma_t^i(u) + \sum_{j \neq i} N_j \xi_j \sigma_t / N_i].$$

A detailed description of these prescriptions, together with the results of additional calculations, has been published.[4]

References

1. I. I. Bondarenko, Ed., *Group Constants for Nuclear Reactor Calculations*, (Consultants Bureau, New York, 1964).
2. H. Küsters et al, *The Group Cross-Section Set KFK-SNEAK*, Proc. Symposium on Fast Reactor Physics, Karlsruhe, October 30–November 3, 1967, Vol. I (IAEA, Vienna, 1968), pp. 167–186.
3. H. Van Dam, *Some Remarks on Group Cross Sections for Mixtures with a Resonance-Scattering Component*, Nukleonik **11**, 298 (1969).
4. W. M. Stacey, Jr., *The Effect of Wide Scattering Resonances Upon Multigroup Cross Sections*, Nucl. Sci. Eng., **47**, 29 (1972).

IV-15. Approximate Treatments of the Effect of Anisotropy Upon Elastic Neutron Moderation

W. M. Stacey, Jr.

Anisotropy in the center-of-mass elastic scattering distribution has an important effect upon the neutron spectrum in a fast-reactor assembly. Direct computation of anisotropic elastic scattering can become involved, in some representations, and a stratagem such as the transport approximation (see, for example, Refs. 1 and 2) is frequently utilized in order to account for anisotropic effects while retaining the relative computational simplicity of the purely isotropic scattering formalism. Numerical comparisons (e.g. Ref. 3) of the transport approximation with a more rigorous treatment of anisotropic elastic scattering generally indicate that the former is a useful approximation for fast-reactor assemblies.

The purposes of this paper are to examine the transport approximation within the framework of continuous slowing-down theory and to suggest an alternate approximation which has the virtue of correctly predicting the average logarithmic energy decrement, or the first lethargy moment of the elastic slowing-down kernel. The transport approximation correctly predicts the first angular moment of the elastic scattering kernel. Thus, the alternate approximation is expected to be somewhat better than the transport approximation for space-independent problems. This expectation is borne out by numerical examples.

In continuous slowing-down theory the elastic slowing-down density in an infinite medium satisfies[2]

$$\frac{dq(u)}{du} = -\frac{\Sigma_{ne}(u)}{M(u)}\,q(u) + \frac{\epsilon(u)}{M(u)}\,S(u), \tag{1}$$

where Σ_{ne} is the nonelastic cross section, S is the source due to fission, inelastic scattering, etc., and M and ϵ characterize the moderating properties of the medium. For the Greuling-Goertzel theory[4]

$$M(u) \equiv -\sum_i N_i\sigma_i^0(u)\sum_{\ell=0}^{\infty} T_{0\ell,i}^1\,\frac{\sigma_i^\ell(u)}{\sigma_i^0(u)} - \frac{\sum_i N_i\sigma_i^0(u)\sum_{\ell=0}^{\infty} T_{0\ell,i}^2\,\frac{\sigma_i^\ell(u)}{\sigma_i^0(u)}}{\sum_i N_i\sigma_i^0(u)\sum_{\ell=0}^{\infty} T_{0\ell,i}^1\,\frac{\sigma_i^\ell(u)}{\sigma_i^0(u)}}\,\Sigma_{ne}(u), \tag{2}$$

and

$$\epsilon(u) \equiv -\sum_i N_i\sigma_i^0(u)\sum_{\ell=0}^{\infty} T_{0\ell,i}^1\,\frac{\sigma_i^\ell(u)}{\sigma_i^0(u)}. \tag{3}$$

In Eqs. (2) and (3), N_i is the concentration of isotope i, σ_i^ℓ is the ℓth Legendre moment of the angular scattering distribution in the center-of-mass system, and $T_{0\ell}^n$ are the nth order lethargy moments of the center-of-mass to laboratory system transfer functions.[5] The quantity ϵ corresponds to $\xi\Sigma_s$ for the mixture.

The basis of the transport approximation is to treat elastic scattering as if it were isotropic in the center-of-mass system, but with the cross section reduced by a multiplicative factor $(1 - \bar{\mu}_i)$, where $\bar{\mu}_i$ is the average cosine of the scattering angle in the laboratory system for isotope i, and may be constructed from

$$\bar{\mu}_i(u) = \sum_{\ell=0}^{\infty} T_{1\ell,i}^0\,\frac{\sigma_i^\ell(u)}{\sigma_i^0(u)}. \tag{4}$$

Thus, in the transport approximation, Eqs. (2) and (3) are replaced by

$$M_{tr}(u) = -\sum_i N_i\sigma_i^0(u)[1 - \bar{\mu}_i(u)]T_{00,i}^1 - \frac{\sum_i N_i\sigma_i^0(u)[1 - \bar{\mu}_i(u)]T_{00,i}^2}{\sum_i N_i\sigma_i^0(u)[1 - \bar{\mu}_i(u)]T_{00,i}^1}\,\Sigma_{ne}(u) \tag{5}$$

and

$$\epsilon_{tr}(u) = -\sum_i N_i\sigma_i^0(u)[1 - \bar{\mu}_i(u)]T_{00,i}^1. \tag{6}$$

Note that

$$-T_{00,i}^1 \equiv \xi_i \equiv 1 - \alpha_i[\ln(1/\alpha_i)]/(1 - \alpha_i)$$

and

$$-T^2_{00,i} \equiv a_i \equiv \frac{\alpha_i[\ln(1/\alpha_i)]^2}{2(1-\alpha_i)} - \xi_i$$

where

$$\alpha_i \equiv (M_i - 1)^2/(M_i + 1)^2,$$

with M_i being the atomic mass of isotope i.

The moderating properties of the medium are largely characterized by the parameter $\epsilon(\xi\Sigma_s)$, which is usually the dominant term in M. The transport approximation does not correctly predict ϵ.

With the definition

$$\bar{\beta}_i(u) \equiv -\sum_{\ell=1}^{\infty} \frac{T^1_{0\ell,i}}{T^1_{00,i}} \cdot \frac{\sigma^\ell_i(u)}{\sigma^0_i(u)}, \tag{7}$$

Eqs. (2) and (3) can be rigorously written

$$M(u) = -\sum_i N_i\sigma^0_i(u)[1-\bar{\beta}_i(u)]T^1_{00,i} - \frac{\sum_i N_i\sigma^0_i(u)[1-\bar{\beta}_i(u)]T^2_{00,i}Z_i(u)}{\sum_i N_i\sigma^0_i(u)[1-\bar{\beta}_i(u)]T^1_{00,i}}\,\Sigma_{ne}(u), \tag{8}$$

$$\epsilon(u) = -\sum_i N_i\sigma^0_i(u)[1-\bar{\beta}_i(u)]T^1_{00,i}, \tag{9}$$

with

$$Z_i(u) \equiv \frac{1 + \sum_{\ell=1}^{\infty} \frac{T^2_{0\ell,i}}{T^2_{00,i}} \frac{\sigma^\ell_i(u)}{\sigma^0_i(u)}}{1 + \sum_{\ell=1}^{\infty} \frac{T^1_{0\ell,i}}{T^1_{00,i}} \frac{\sigma^\ell_i(u)}{\sigma^0_i(u)}}. \tag{10}$$

An alternate approximation, which correctly predicts ϵ, can be constructed by using Eqs. (8) and (9) with $Z_i \equiv 1$ in Eq. (8). This amounts to treating the elastic scattering as if it were isotropic in the center-of-mass system, but with the isotopic scattering cross section reduced by the multiplicative factor $(1 - \bar{\beta}_i)$.

Equation (1) was solved for the elastic slowing-down density due to a monoenergetic source at 10 MeV for a mixture typical of proposed fast breeder reactor cores (Table IV-15-I). Solutions were obtained using (a) the exact anisotropic prescriptions of Eqs. (2) and (3); (b) the transport approximation prescriptions of Eqs. (5) and (6); (c) the alternate approximation prescriptions of Eqs. (8) and (9) with $Z_i \equiv 1$; and (d) the isotropic prescriptions obtained from Eqs. (2) and (3) by retaining only the $\ell = 0$ terms. ENDF/B angular scattering data were used.

As shown in Fig. IV-15-1, anisotropic scattering greatly reduces the elastic slowing-down density relative to the isotropic result. The transport approximation accounts for most of the anisotropic effect, but the alternate approximation is significantly superior in this respect.

The transport approximation and the alternate approximation were also used in conjunction with the improved Greuling-Goertzel prescriptions[4] for the moderating parameters M and ϵ [i.e. M and ϵ of the improved theory were evaluated as if the elastic scattering were isotropic, but with the isotropic scattering cross section reduced by $(1 - \bar{\mu}_i)$ or $(1 - \bar{\beta}_i)$]. These results, shown in Fig. IV-15-2 for a monoenergetic source at 10 MeV in the mixture of Table IV-15-I, again indicate that the transport approximation accounts for a major part of the considerable anisotropic scattering effect upon elastic neutron moderation, but that the alternate approximation is superior in this respect.

TABLE IV-15-I. COMPOSITION

Isotope	Concentration, 10^{24} atoms/cc
^{16}O	0.016
^{23}Na	0.010
^{56}Fe	0.010
^{238}U	0.010
^{239}Pu	0.001

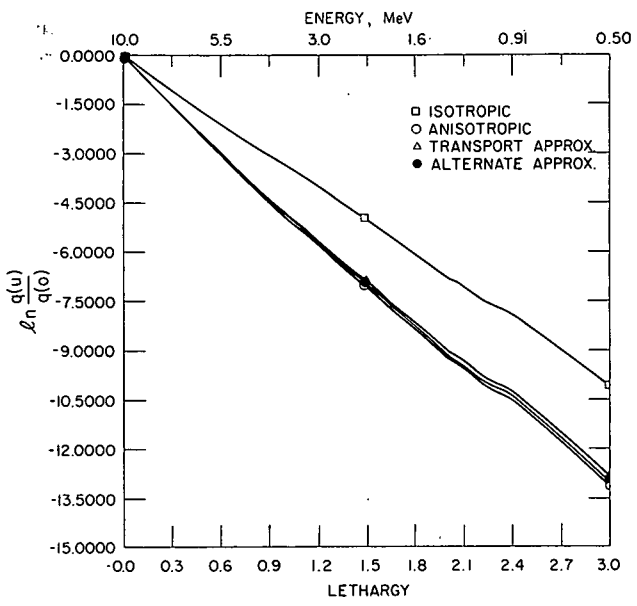

FIG. IV-15-1. Elastic Slowing-Down Density in a Fast-Reactor Core Resulting from a Monoenergetic Source at 10 MeV. Greuling-Goertzel Moderating Parameters. *ANL Neg. No. 116-378.*

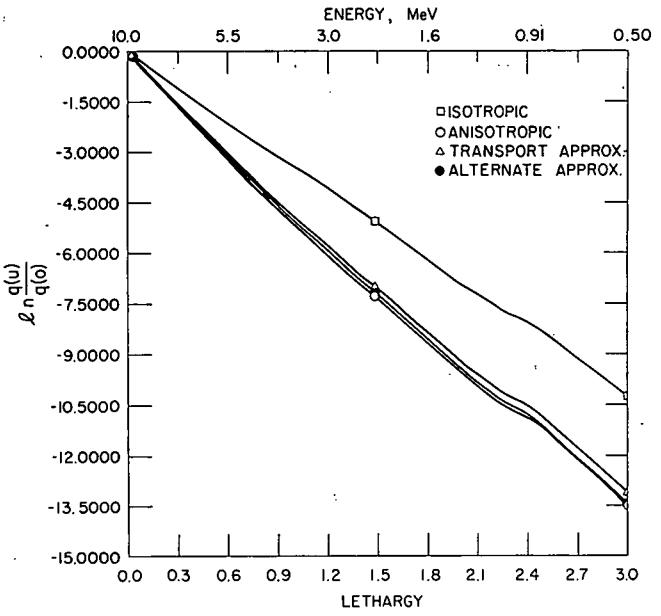

FIG. IV-15-2. Elastic Slowing-Down Density in a Fast-Reactor Core Resulting from a Monoenergetic Source at 10 MeV. Improved Greuling-Goertzel Moderating Parameters. *ANL Neg. No. 116-377.*

Because the same amount of computational effort and the same type of data are required in both cases, it seems reasonable to suggest that the alternate approximation should be used in preference to the transport approximation in space-independent calculations.* Moreover, the limited numerical results presented above suggest that either approximation may be entirely adequate for most spectrum calculations in fast-reactor mixtures.

REFERENCES

1. S. Yiftah, D. Okrent and P. A. Moldauer, *Fast Reactor Cross Sections*, (Pergamon Press, New York, 1960), Chap. 4.
2. I. I. Bondarenko, Ed., *Group Constants for Nuclear Reactor Calculations*, (Consultants Bureau, New York, 1964).
3. E. D. Pendlebury and L. H. Underhill, *The Validity of the Transport Approximations in Critical-Size and Reactivity Calculations*, Proc. Seminar on Physics of Fast and Intermediate Reactors (IAEA, Vienna, 1962), Vol. II.
4. W. M. Stacey, Jr., *The Effect of Anisotropic Scattering Upon the Elastic Moderation of Fast Neutrons*, Nucl. Sci. Eng. **44**, 194 (1971).
5. P. F. Zweifel and H. Hurwitz, Jr., *Transformation of Scattering Cross Sections*, J. Appl. Phys. **25**, 1241 (1954).
6. W. M. Stacey, Jr., *Continuous Slowing Down Theory for Anisotropic Elastic Neutron Moderation in the P_N and B_N Representations*, Nucl. Sci. Eng. **41**, 381 (1970).

* There is little motivation to use either approximation with continuous slowing-down theory, because only the first few moments of the angular scattering data need be used to evaluate the exact expressions for the moderating parameters.[4] However, there is considerable motivation to reduce the computation of higher-order contributions to transfer matrices in the conventional multigroup theory.

IV-16. Variational Field Theory

W. M. STACEY, JR.

Variational theory has been used in reactor physics in direct applications (e.g. flux synthesis, generalized perturbation theory, and the evaluation of integral parameters) and indirectly to provide a theoretical framework relating seemingly diverse methods. Such a theoretical framework frequently suggests improved approximations. This paper is concerned with the systematic development of a variational field theory and an examination of some of the consequences of such a theory.

Equations which define a "consistent" set of "boundary" conditions, and hence a field,[1] for a given set of differential equations are derived from a variational principle. The equivalence of functionals defined over an entire domain $0 \leq x \leq L$ and functionals defined over only a subdomain $0 \leq x \leq z < L$, but with a surface term added to account for the excluded subdomain, is exploited. The functional

$$J[y] = \int_0^L dx\, F[x,y(x),y'(x)], \qquad y \equiv \sum_{i=1}^{N} y_i \tag{1}$$

has as Euler equations

$$\frac{\partial F}{\partial y_j} - \frac{d}{dx}\frac{\partial F}{\partial y_j'} = 0, \qquad j = 1, \cdots, N. \tag{2}$$

The functional

$$\hat{J}[y] = \int_0^z dx\, F[x,y(x),y'(x)] - G[z,y(z)],$$

is equivalent to J, i.e. it also has Eqs. (2) as Euler equations, if G satisfies the Hamilton-Jacobi equation

$$\frac{\partial G[z,y(z)]}{\partial z} - F[z,y(z),y'(z)] + \sum_{i=1}^{N} y_i'(z)\frac{\partial G[z,y(z)]}{\partial y_j} = 0, \tag{4}$$

and if

$$\frac{\partial F[z,y(z),y'(z)]}{\partial y_j'} = \frac{\partial G[z,y(z)]}{\partial y_j}, \qquad j = 1, \cdots, N. \tag{5}$$

A boundary condition for G follows from the required equivalence of $\hat{J}$ and J at $z = L$,

$$G[L,y(L)] = 0, \tag{6}$$

and the equivalence of $\hat{J}$ and J at $z = 0$ implies that the stationary value of the functional J is just $G[0,y(0)]$.

When this theory is applied to monoenergetic neutron diffusion theory,

$$F[x,\phi,\phi'] = D(\phi')^2 + (\Sigma_a - \nu\Sigma_f)\phi^2 - 2\phi S, \tag{7}$$

and a solution is sought of the form

$$G(z,\phi) = -\alpha(z)\phi^2 + 2\beta(z)\phi + \gamma(z), \tag{8}$$

Eqs. (4) and (5) yield

$$\alpha'(z) - \frac{\alpha^2(z)}{D} = -(\Sigma_a - \nu\Sigma_f) \tag{9a}$$

$$\beta'(z) - \frac{\alpha(z)\beta(z)}{D} = -S \tag{9b}$$

$$\gamma'(z) + \frac{\beta^2(z)}{D} = 0 \tag{9c}$$

and

$$D\phi'(z) = -\alpha(z)\phi(z) + \beta(z). \tag{9c}$$

Boundary conditions at $z = 0$ are obtained for α and β, while boundary conditions at $z = L$ are obtained for γ and ϕ. Thus, one would sweep from 0 to L in evaluating Eqs. (9a) and (9b) for α and β, then sweep from L to 0 in evaluating Eqs. (9c) and (9d) for γ and ϕ. This is exactly the double-sweep method [except that Eq. (9c) is omitted] usually attributed to Stark[2] for solving the one-dimensional neutron diffusion equation. This widely used method, which is usually postulated on an ad hoc basis, follows naturally from the field theoretic formulation.

Examples from one- and two-group neutron diffusion theory have been investigated.

If, instead of $\hat{J}$, an equivalent functional is required to have the form

$$\tilde{J}[y] = -G[z,y(z)] + \int_z^L dx\, F[x,y(x),y'(x)], \tag{10}$$

and if J of Eq. (1) is a minimum principle, then G must satisfy

$$\frac{\partial G[z,y(z)]}{\partial z} + F[z,y(z),y'(z)] + \sum_{j=1}^{N} y_j'(z)\,\frac{\partial G[z,y(z)]}{\partial z} \leq 0, \tag{11}$$

and Eqs. (5), but with a minus sign on the right side of the latter.

Defining

$$\psi_j(z) \equiv -\frac{\partial G}{\partial y_j}, \qquad j = 1, \cdots, N; \qquad \psi_{N+1}(z) \equiv -\frac{\partial G}{\partial z}, \tag{12}$$

Eq. (11) may be written

$$0 = \max_{y'}\left[\psi_{N+1} + \sum_{j=1}^{N} \psi_j y_j' - F\right], \tag{13}$$

which is the Maximum Principle of Pontryagin.[3]

Rewriting Eq. (11) as

$$-\frac{dG[z,y(z)]}{dz} \geq F[z,y(z),y'(z)], \tag{14}$$

integrating over $z \leq z' \leq z + \Delta z$, and evaluating F at z, results in

$$G[z,y(z)] = \min_{y'}\{G[z + \Delta z, y(z + \Delta z)] + \Delta z F[z,y(z),y'(z)]\} \tag{15}$$

which is Bellman's Dynamic Programming algorithm.[4]

A more detailed exposition of these results has been published in the literature.[5]

References

1. I. M. Gelfand and S. V. Fomin, *Calculus of Variations*, (Prentice-Hall, Englewood Cliffs, New Jersey, 1963).
2. R. Ehrlich and H. Hurwitz, Jr., *Multigroup Methods for Neutron Diffusion Problems*, Nucleonics **12**, 23 (1954).
3. L. S. Pontryagin et al, *The Mathematical Theory of Optimal Processes*, (John Wiley (Interscience), New York 1962).
4. R. Bellman, *Dynamic Programming*, (Princeton University Press, Princeton, New Jersey 1957).
5. W. M. Stacey, Jr., *Variational Field Theory*, J. Math. Physics **12**, 2296 (1971).

IV-17. Collision Probability Methods with Anisotropic Scattering

W. M. Stacey, Jr.

Collision probability methods, which are widely used in fast-reactor calculations, are generally based upon the assumption of isotropic scattering. It is the purpose of this paper to indicate an extension to the case of anisotropic scattering.

The multigroup form of the Boltzman equation, in slab geometry, may be written

$$\begin{aligned}\mu\frac{d\psi^g}{dx}(x,\mu) + \Sigma^g(x)\psi^g(x,\mu) &= \frac{1}{2}S^g(x) + \sum_{g'\leq g}^{\infty}\sum_{\ell'=0}^{\infty}\frac{2\ell'+1}{2}P_{\ell'}(\mu)\Sigma_{s\ell'}^{g'\to g}(x)\int_{-1}^{1}d\mu' P_{\ell'}(\mu')\psi^g(x,\mu') \\ &\equiv \sum_{\ell'=0}^{\infty}\frac{2\ell'+1}{2}P_{\ell'}(\mu)Q_{\ell'}^g(x) \equiv Q^g(x,\mu).\end{aligned} \tag{1}$$

This may be formally integrated over $0 \leq x \leq L$ to obtain

$$\psi(z,\mu) = \begin{cases}\exp\left[-\int_0^z \frac{\Sigma^g(x')}{\mu}\,dx'\right]\psi^g(0,\mu) + \int_0^z dx \exp\left[-\int_x^z \frac{\Sigma^g(x')}{\mu}\,dx'\right]\frac{Q^g(x,\mu)}{\mu}, & \mu > 0 \\ \exp\left[\int_z^L \frac{\Sigma^g(x')}{\mu}\,dx'\right]\psi^g(L,\mu) - \int_z^L dx \exp\left[\int_z^x \frac{\Sigma^g(x')}{\mu}\,dx'\right]\frac{Q^g(x,\mu)}{\mu}, & \mu < 0\end{cases} \tag{2}$$

Use Eqs. (2) in the definition for the Legendre moments of the flux:

$$\begin{aligned}\phi_\ell^g(z) &\equiv \int_{-1}^{1} d\mu\, P_\ell(\mu)\psi^g(z,\mu)\\ &= \sum_{\ell'=0}^{\infty} \frac{2\ell'+1}{2}\left\{\phi_{\ell'}^g(0)\int_0^1 d\mu\, P_\ell(\mu)P_{\ell'}(\mu)\exp\left[-\int_0^z \frac{\Sigma^g(x')}{\mu}\,dx'\right]\right.\\ &\quad + \int_0^z dx\, Q_{\ell'}^g \int_0^1 d\mu\, P_\ell(\mu)P_{\ell'}(\mu)\exp\left[-\int_x^z \frac{\Sigma^g(x')}{\mu}\,dx'\right]\Big/\mu\\ &\quad + \phi_{\ell'}^g(L)\int_{-1}^0 d\mu\, P_\ell(\mu)P_{\ell'}(\mu)\exp\left[\int_z^L \frac{\Sigma^g(x')}{\mu}\,dx'\right]\\ &\quad \left.- \int_z^L dx\, Q_{\ell'}^g(x)\int_{-1}^0 d\mu\, P_\ell(\mu)P_{\ell'}(\mu)\exp\left[\int_z^x \frac{\Sigma^g(x')}{\mu}\,dx'\right]\mu\right\}, \qquad \ell = 0,1,\cdots\infty.\end{aligned} \tag{3}$$

If it is assumed that

$$\begin{aligned}\phi_\ell^g(z) &= \phi_\ell^{gi}, \qquad z_i \le z \le z_{i+1}\\ Q_\ell^g(z) &= Q_\ell^{gi}, \qquad z_i \le z \le z_{i+1}\\ \Sigma^g(z) &= \Sigma^{gi}, \qquad z_i \le z \le z_{i+1},\end{aligned} \tag{4}$$

then the integrals in Eqs. (3) may be performed analytically. (Note that this would also be true for any polynomial dependence upon z.) The resulting set of equations, truncated at $\ell,\ell' = N$, may be written

$$\Sigma^{gi}\Delta_i\phi_\ell^{gi} = Q_\ell^{gi}\Delta_i + \sum_{j=0}^{L}\sum_{\ell'=0}^{N} R_{ij}^{\ell\ell',g}\frac{Q_{\ell'}^{gj}}{\Sigma^{gj}} + \sum_{\ell'=0}^{N} U_{\ell\ell'}^{gi}\phi_{\ell'}^g(0) + \sum_{\ell'=0}^{N} V_{\ell\ell'}^{gi}\phi_{\ell'}^g(L), \qquad i = 0,\cdots,L;\ \ell = 0,\cdots,N, \tag{5}$$

where

$$\frac{2}{2\ell'+1}R_{ij}^{\ell\ell',g} \equiv \begin{cases}-[A_{\ell\ell'}(\theta_{ij}^g) - A_{\ell\ell'}(\xi_{ij}^g) - A_{\ell\ell'}(\pi_{ij}^g) + A_{\ell\ell'}(\rho_{ij}^g)], & j < i\\ [A_{\ell\ell'}(\Sigma^{gi}\Delta_i) - B_{\ell\ell'}(\Sigma^{gi}\Delta_i) - A_{\ell\ell'}(0) + B_{\ell\ell'}(0)], & j = i\\ [B_{\ell\ell'}(\theta_{ij}^g) - B_{\ell\ell'}(\xi_{ij}^g) - B_{\ell\ell'}(\pi_{ij}^g) + B_{\ell\ell'}(\rho_{ij}^g)], & j > i\end{cases} \tag{6}$$

$$\frac{2}{2\ell'+1}U_{\ell\ell'}^{gi} \equiv A_{\ell\ell'}(\theta_{i0}^g) - A_{\ell\ell'}(\pi_{i0}^g) \tag{7}$$

$$\frac{2}{2\ell'+1}V_{\ell\ell'}^{gi} \equiv B_{\ell\ell'}(\pi_{iL}^g) - B_{\ell\ell'}(\theta_{iL}^g). \tag{8}$$

The optical distances are defined in terms of Σ^{gi} and $\Delta_i \equiv z_{i+1} - z_i$:

$$\begin{aligned}\xi_{ij}^g &\equiv \sum_{k=j+1}^{i-1}\Sigma^{gk}\Delta_k, \qquad \theta_{ij}^g \equiv \xi_{ij}^g + \Sigma^{gj}\Delta_j,\\ \rho_{ij}^g &\equiv \xi_{ij}^g + \Sigma^{gi}\Delta_i, \qquad \pi_{ij}^g \equiv \xi_{ij}^g + \Sigma^{gj}\Delta_j + \Sigma^{gi}\Delta_i,\end{aligned} \tag{9}$$

where the i and j refer to the spatial intervals $i, j = 0, 1, \cdots, L$. The functions $A_{\ell\ell'}$ and $B_{\ell\ell'}$ are defined by

$$A_{\ell\ell'}(r) \equiv \int_0^1 d\mu\mu\, P_\ell(\mu)P_{\ell'}(\mu)e^{-r/\mu} \equiv \int_1^\infty dt\,\frac{P_\ell(1/t)P_{\ell'}(1/t)e^{-rt}}{t^3} \tag{10}$$

$$B_{\ell\ell'}(r) \equiv \int_{-1}^0 d\mu\mu\, P_\ell(\mu)P_{\ell'}(\mu)e^{r/\mu} \equiv -\int_1^\infty dt\,\frac{P_\ell(-1/t)P_{\ell'}(-1/t)e^{-rt}}{t^3}, \tag{11}$$

which are related to the exponential integral functions $E_n(r)$. Note that $A_{\ell\ell'}$, $B_{\ell\ell'}$ involves E_n, $n = 3, \cdots, \ell + \ell' + 3$. Furthermore, $B_{\ell\ell'} = \mp A_{\ell\ell'}$, depending upon whether $\ell + \ell'$ is even $(-)$ or odd $(+)$, and $B_{\ell\ell'} = B_{\ell'\ell}$, $A_{\ell\ell'} = A_{\ell'\ell}$.

For the special case $\ell,\ell' = 0$, Eqs. (5) reduce to the conventional collision probability equations.

The method was applied to the cell problem indicated in Table IV-17-I, which is typical of a ZPR core drawer, in order to obtain some appreciation of the importance of scattering anisotropy. Monoenergetic calculations were

TABLE IV-17-I. ONE DIMENSIONAL CELL MODEL

Region	Δx, in.	Material
1	0.32	U_3O_8
2	0.63	Na
3	0.13	Fe_2O_3
4	0.32	Pu-U-Mo
5	0.13	Fe_2O_3
6	0.63	Na
7	0.32	U_3O_8

TABLE IV-17-II. PERCENT SCALAR FLUX ERROR (RELATIVE TO $\ell = 5$) AS A FUNCTION OF SCATTERING MOMENT, ℓ'

ℓ	Region 1	2	3	4	5	6	7
	1 MeV						
0	−0.16	+1.16	+1.91	+3.00	+4.52	+5.69	+7.20
1	+0.16	+0.25	+0.17	+0.17	+0.26	+0.37	+0.60
3	+0.08	+0.08	+0.08	+0.08	+0.09	+0.09	+0.10
	5 MeV						
0	−1.40	+0.15	+1.44	+3.34	+5.90	+7.44	+9.59
1	+0.27	+0.65	+0.86	+1.08	+1.69	+1.96	+2.29
2	−0.14	−0.11	+0.00	+0.15	+0.35	+0.50	+0.76
3	+0.05	+0.02	+0.00	−0.04	+0.00	+0.02	+0.04
4	−0.02	−0.02	+0.00	+0.00	+0.00	−0.02	−0.02

made at 5 and 1 MeV, using isotropic cross sections and source distributions from a multigroup isotropic collision probability calculation (CALHET) and anisotropic cross sections from ENDF/B-I. Cell boundary conditions typical of a core-blanket interface [$\phi_\ell^\ell(0)$ and $\phi_\ell^\ell(L)$] were obtained by first making a homogenized whole-reactor calculation.

The scalar flux (ϕ_0) in each region is compared in Table IV-17-II for different approximations to the scattering anisotropy. It is seen that rather large errors result when isotropic scattering is assumed. Moreover, it seems that $\ell = 1$ or $\ell = 3$ scattering is sufficient for this class of problems. Preliminary calculations indicated that use of the transport approximation did not significantly improve the $\ell = 0$ results, in no case yielding results as good as those obtained for $\ell = 1$. This suggests that standard collision probability methods based on isotropic scattering may be questionable for fast-reactor applications, but that a relatively low-order P_ℓ approximation may suffice.

IV-18. One-Dimensional Space-Time Kinetics Benchmark Calculations

E. L. FULLER

INTRODUCTION

It is imperative to know whether or not one-dimensional space-time diffusion theory codes can indeed calculate transient behavior correctly. Not only should the total power be calculated correctly, but the flux tilt should be accurately found as well. Furthermore, the degree of sensitivity of the solution to time step size should be known. Accordingly, Stacey[1] has devised a benchmark problem to test such codes. He considered the one-dimensional slab reactor shown in Fig. IV-18-1. It is a 240 cm, 3-region thermal reactor with zero-flux boundary conditions at each end. Regions one and three are made of the same material, and are more reactive than is region 2. Hence, the steady-state flux initially has a minimum value at the center of region 2.

The group constants for this reactor are shown in Table IV-18-I. Note that the fission cross sections for regions 1 and 3 are larger than those for region 2. Nevertheless, region two produces 44% of the steady-state power, while regions 1 and 3 each produce only 28%, because region two is so much larger than the other two regions. A static calculation using these group constants yields a k_{eff} of 0.90155. The fission cross sections are divided by this value to obtain a critical system. Six precursor families are used, with $\beta = 0.0075$. The delayed data are shown in Table IV-18-II.

THERMAL REACTOR CALCULATIONS

Three types of transient are compared; a subcritical transient, a delayed supercritical transient, and a prompt supercritical transient. All are initiated by a ramp change in Σ_a^2 in region 1. For the subcritical transient, the cross

TABLE IV-18-I. Initial Two Group Constants

	Region	
	1 and 3	2
D^1, cm	1.50 + 0	1.00 + 0
D^2, cm	5.00 − 1	5.00 − 1
Σ_a^1, cm^{-1}	2.60 − 2	2.00 − 2
Σ_a^2, cm^{-1}	1.80 − 1	8.00 − 2
$\nu\Sigma_f^1$, cm^{-1}	1.00 − 2	5.00 − 3
$\nu\Sigma_f^2$, cm^{-1}	2.00 − 1	9.90 − 2
$\Sigma^{1\to2}$, cm^{-1}	1.50 − 2	1.00 − 2
χ^1	1.00 + 0	1.00 + 0
χ^2	0.00 + 0	0.00 + 0
v^1, cm/sec	1.00 + 7	1.00 + 7
v^2, cm/sec	3.00 + 5	3.00 + 5

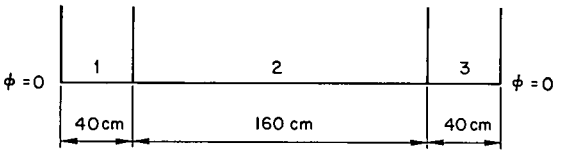

Fig. IV-18-1. Slab Reactor for One-Dimensional Kinetics Benchmark Calculations. *ANL Neg. No. 116-932.*

TABLE IV-18-II. Delayed Neutron Parameters

Family	Effective Delay Fraction	Decay Constant, sec^{-1}
1	2.50 − 4	1.24 − 2
2	1.64 − 3	3.05 − 2
3	1.47 − 3	1.11 − 1
4	2.96 − 3	3.01 − 1
4	8.60 − 4	1.14 + 0
6	3.20 − 4	3.01 + 0

section is increased by 3 % in 1.0 sec. It is linearly decreased by 1 % in 1.0 sec for the delayed supercritical transient, and by 5 % in 0.01 sec for the prompt supercritical transient.

Stacey[1] performed his calculations using RAUMZEIT.[2] We are testing two codes, the two-group code WIGLE,[3] and the multigroup code QX1,[4] which was designed for fast reactor analysis. Table IV-18-III shows the total power versus time for the subcritical transient as calculated by the three codes. The cumulative number of shape functions to each time is also given for QX1. Note that most of the shape functions are calculated during the ramp (to 1.0 sec). The times at which the shape functions are recalculated result from the use of the default values of the time-step-selection parameters. The average shape step is thus 4.5×10^{-2} sec. The WIGLE and RAUMZEIT time steps were 10^{-3} sec. The time-integrated algorithm in RAUMZEIT was used to obtain the results shown. Note that there is virtually no difference in total power among the three codes. The same holds true for the tilt effect, as shown in Table IV-18-IV.

Relative regional power is the ratio of the power in a region to the initial power in that region. The greater the deviation in one region relative to the others, the greater the change in flux shape. Note that the power decreases much more quickly in region 1 than it does in regions 2 or 3. Nevertheless, the three codes were able to properly account for the tilt without undue difficulty, giving virtually the same answers. Thus, each code properly calculated the neutronic behavior during the subcritical transient.

The power behavior during the delayed supercritical transient is demonstrated in Table IV-18-V. Recall that the transient is initiated by a 1 % ramp decrease in Σ_a^2 over a period of 1.0 sec. As is shown, the results of all three codes agree. The time step size for both WIGLE and RAUMZEIT is 10^{-3} sec. For QX1, more than half of the shape function recalculations took place during the ramp. Thus, during the ramp portion, the average shape step was 0.04 sec, as opposed to a value of 0.08 sec for the entire transient. These again result from the use of the default values of the time step selection parameters.

Table IV-18-VI shows the tilt effect for the delayed supercritical transient. It is also the same for each code. The power increases much more in region 1 than in regions 2 and 3.

TABLE IV-18-III. Total Power for Subcritical Transient

Time, sec	RAUMZEIT	WIGLE	QX1	QX1 Shape No.
0.0	1.0000	1.0000	1.0000	—
0.1	0.9299	0.9298	0.9298	7
0.2	0.8733	0.8732	0.8733	11
0.5	0.7597	0.7596	0.7597	21
1.0	0.6588	0.6588	0.6588	36
1.5	0.6432	0.6432	0.6433	41
2.0	0.6307	0.6306	0.6307	44

The prompt supercritical transient is initiated by a 5 % ramp decrease in Σ_a^2 in region 1 for 0.01 sec. This is a very severe transient—a \$300 per sec asymmetric insertion. The RAUMZEIT solution (TI algorithm) essentially agrees with WIGLE, as is indicated in Table IV-18-VII. Each uses a time step of 10^{-5} sec. The QX1 solution differs, because the transient is so severe, and the reactivity insertion is so asymmetric, that the time derivative of the shape function is relatively large, thus making error accumulation non-negligible. Even so, use of the default values of the time-step selection parameters gives quite acceptable answers. Note again that more than half of the shape function recalculations took place during the insertion. The average time step for QX1 is 9×10^{-5} sec.

The tilt effect is shown in Table IV-18-VIII. WIGLE and RAUMZEIT agree here, too. QX1, however, slightly

TABLE IV-18-IV. Relative Regional Power for Subcritical Transient

	Time, sec						
	0.0	0.1	0.2	0.5	1.0	1.5	2.0
Region 1							
RAUMZEIT	1.0000	0.8621	0.7521	0.5337	0.3453	0.3236	0.3066
WIGLE	1.0000	0.8621	0.7520	0.5336	0.3452	0.3235	0.3066
QX1	1.0000	0.8621	0.7521	0.5336	0.3452	0.3235	0.3066
Region 2							
RAUMZEIT	1.0000	0.9340	0.8805	0.7724	0.6753	0.6588	0.6455
WIGLE	1.0000	0.9339	0.8804	0.7724	0.6753	0.6587	0.6455
QX1	1.0000	0.9340	0.8805	0.7724	0.6753	0.6588	0.6455
Region 3							
RAUMZEIT	1.0000	0.9910	0.9831	0.9655	0.9463	0.9382	0.9312
WIGLE	1.0000	0.9910	0.9830	0.9655	0.9462	0.9381	0.9311
QX1	1.0000	0.9910	0.9831	0.9656	0.9463	0.9383	0.9312

TABLE IV-18-V. Total Power for Delayed Supercritical Transient

Time, sec	RAUMZEIT	WIGLE	QX1	QX1 Shape No.
0.0	1.000	1.000	1.000	—
0.1	1.028	1.028	1.028	5
0.2	1.063	1.062	1.063	7
0.5	1.205	1.205	1.205	12
1.0	1.740	1.740	1.740	26
1.5	1.959	1.959	1.959	33
2.0	2.166	2.165	2.166	37
3.0	2.606	2.605	2.606	43
4.0	3.108	3.107	3.108	48

TABLE IV-18-VI. Relative Regional Power for Delayed Supercritical Transient

	Time, sec						
	0.0	0.1	0.5	1.0	2.0	3.0	4.0
Region 1							
RAUMZEIT	1.000	1.056	1.399	2.435	3.216	4.017	4.928
WIGLE	1.000	1.056	1.399	2.435	3.215	4.016	4.927
QX1	1.000	1.056	1.398	2.435	3.216	4.017	4.928
Region 2							
RAUMZEIT	1.000	1.027	1.194	1.701	2.113	2.540	3.027
WIGLE	1.000	1.027	1.193	1.701	2.113	2.539	3.026
QX1	1.000	1.027	1.193	1.701	2.113	2.540	3.027
Region 3							
RAUMZEIT	1.000	1.004	1.029	1.107	1.199	1.299	1.417
WIGLE	1.000	1.004	1.028	1.107	1.199	1.298	1.416
QX1	1.000	1.004	1.029	1.107	1.199	1.298	1.416

TABLE IV-18-VII. Total Power for Prompt Supercritical Transient

Time, sec	RAUMZEIT	WIGLE	QX1	QX1 Shape No.
0.000	1.000	1.000	1.000	—
0.001	1.022	1.022	1.022	3
0.005	1.659	1.659	1.666	39
0.010	1.565 + 1	1.565 + 1	1.573 + 1	139
0.012	7.019 + 1	7.019 + 1	7.055 + 1	187
0.015	6.804 + 2	6.803 + 2	6.836 + 2	214
0.018	6.613 + 3	6.611 + 3	6.642 + 3	220
0.020	3.012 + 4	3.011 + 4	3.025 + 4	222

TABLE IV-18-VIII. Relative Regional Power for Prompt Supercritical Transient

	Time, sec					
	0.000	0.001	0.005	0.010	0.015	0.020
Region 1						
RAUMZEIT	1.000	1.058	2.484	3.481 + 1	1.570 + 3	6.956 + 4
WIGLE	1.000	1.058	2.484	3.481 + 1	1.570 + 3	6.954 + 4
QX1	1.000	1.068	2.507	3.497 + 1	1.577 + 3	6.986 + 4
Region 2						
RAUMZEIT	1.000	1.014	1.544	1.258 + 1	5.389 + 2	2.385 + 4
WIGLE	1.000	1.014	1.544	1.258 + 1	5.388 + 2	2.385 + 4
QX1	1.000	1.013	1.550	1.265 + 1	5.414 + 2	2.396 + 4
Region 3						
RAUMZEIT	1.000	1.000	1.017	1.342	1.486 + 1	6.181 + 2
WIGLE	1.000	1.000	1.017	1.342	1.485 + 1	6.179 + 2
QX1	1.000	0.991	1.010	1.351	1.500 + 1	6.214 + 2

overestimates the tilt, that is, it over-predicts the power in region 1, and, early in the transient, underpredicts the power in region 3.

The primary objective of this work was to determine whether or not each code could properly calculate the benchmark transients. The fact that WIGLE and RAUMZEIT strongly agree with one another implies that they are both in good working order. The fact that QX1 gives nearly the same answers implies that its solution would be improved by the calculation of more shape functions (that is, by tightening the time-step-selection parameters). Therefore this was done. By using parameters that approximately tripled the number of shape function recalculations, identical agreement with WIGLE and RAUMZEIT was obtained. However, the amount of computer time required was large.

We now turn to the secondary objective; that is, to determine the sensitivity of each solution to the time step size. Table IV-18-IX shows the total power for the prompt supercritical transient as a function of time step size. Data from RAUMZEIT for time steps larger than 10^{-4} does not appear in Stacey's writeup[1] of the solution, but it has since become clear that they are nearly the same as WIGLE, whether the TI algorithm or the AV algorithm is used. That is, a time step of 10^{-3} sec gives unsatisfactory answers in either case. The QX1 solution, on the other hand, is much less sensitive to an increase in the average shape step.

A more complete picture of time-step sensitivity is given in Fig. IV-18-2. The total power at 0.02 sec (the end of the transient) is shown for both QX1 and WIGLE. On this scale, RAUMZEIT datum points would be directly atop the WIGLE triangles. It is clearly seen that the QX1 solution is relatively insensitive to the number of shape function recalculations. However, this is only part of the story. QX1 requires much more running time than does WIGLE to achieve equivalent accuracy. For example, the WIGLE solution for a time step of 2×10^{-4} sec requires 1½ min. on the CDC-3600. QX1, for a shape step of 9×10^{-4} sec, requires 4 min. on the IBM 360-75. But, there is yet another important aspect. QX1 does every calculation as though the transient had nonlinear feedback. Thus, it repeats each amplitude function calculation (including inner product calculations at the so-called reactivity steps), although it does not repeat each shape function recalculation. The calculations with RAUMZEIT and WIGLE, on the other hand, were done in a linear manner; each time step was passed through only once. If these codes were

TABLE IV-18-IX. TOTAL POWER FOR PROMPT SUPERCRITICAL TRANSIENT AS A FUNCTION OF TIME STEP SIZE

Time, sec	Δt, sec								
	RAUMZEIT			WIGLE			QX1 (Avg. Shape Step)		
	TI, 10^{-5}	AV, 10^{-5}	TI, 10^{-4}	10^{-5}	10^{-4}	10^{-3}	9.0×10^{-5}	2.1×10^{-4}	8.7×10^{-4}
0.000	1.000	1.000	1.000	1.000	1.000	1.000	1.000	1.000	1.000
0.001	1.022	1.022	1.022	1.022	1.022	1.022	1.022	1.022	1.022
0.005	1.659	1.659	1.659	1.659	1.659	1.672	1.666	1.673	1.673
0.010	1.565 + 1	1.565 + 1	1.566 + 1	1.565 + 1	1.567 + 1	1.802 + 1	1.573 + 1	1.583 + 1	1.571 + 1
0.012	7.019 + 1	7.019 + 1	7.028 + 1	7.019 + 1	7.033 + 1	8.768 + 1	7.055 + 1	7.092 + 1	6.993 + 1
0.015	6.804 + 2	6.803 + 2	6.818 + 2	6.803 + 2	6.824 + 2	9.582 + 2	6.836 + 2	6.868 + 2	6.740 + 2
0.018	6.613 + 3	6.612 + 3	6.632 + 3	6.611 + 3	6.639 + 3	1.049 + 4	6.642 + 3	6.674 + 3	6.544 + 3
0.020	3.012 + 4	3.011 + 4	3.022 + 4	3.011 + 4	3.026 + 4	5.176 + 4	3.025 + 4	3.040 + 4	2.980 + 4

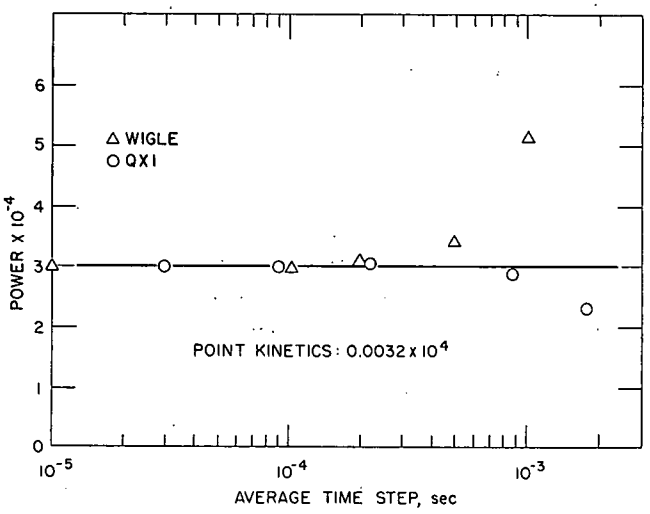

FIG. IV-18-2. Power at 0.02 sec as a Function of Time-Step Size. *ANL Neg. No. 116-930.*

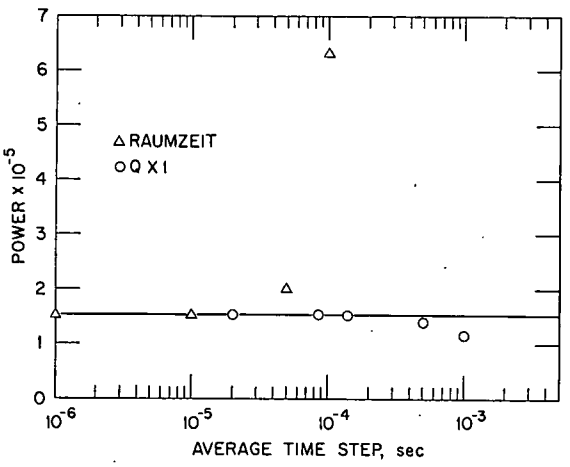

FIG. IV-18-3. Power at 0.005 sec and at Increased Neutron Velocities as a Function of Time-Step Size. *ANL Neg. No. 116-931.*

to be used in conjunction with a nonlinear feedback model, then each time step would have to be repeated at least once. It appears, however, that QX1 would still run a bit longer when doing very severe asymmetric thermal reactor transients.

THE EFFECT OF INCREASED NEUTRON VELOCITIES

It was noted above that QX1 was designed primarily for fast reactor transient analysis. Thus, it was decided to increase each neutron velocity by a factor of 100, in order to assess how QX1 and RAUMZEIT compare when doing fast reactor calculations. Note that other fast reactor characteristics, such as a smaller delayed neutron fraction and fast-reactor cross sections, were not substituted. Thus, the reactor was still loosely coupled. The cross section change was the same as that of the thermal prompt supercritical transient. The final time, however, was set at 0.005 sec, since the power increased so much faster than in the thermal reactor calculations once $\rho > \beta_{eff}$. This is because the generation time is 100 times shorter due to the increased neutron velocities.

The total power as a function of time as calculated by the two codes is given in Table IV-18-X, for several time step sizes. Note again, that the QX1 solution is much less sensitive to time step variation than is the RAUMZEIT solution. The degree of sensitivity of each is shown more clearly in Fig. IV-18-3, which displays the total power at $t = 0.005$ sec as a function of time step size. From this figure, it may be deduced that, for this problem, QX1 achieves comparable accuracy to RAUMZEIT with a shape step twenty times larger. Figure IV-18-2 indicates that, for the thermal system, comparable accuracy is achieved with an average QX1 shape step only four times larger than a WIGLE (and RAUMZEIT) step. It is obvious, then, that QX1 is indeed better suited to fast reactor transient analysis than it is for thermal reactor analysis.

TABLE IV-18-X. TOTAL POWER FOR TRANSIENT WITH INCREASED NEUTRON VELOCITIES AS A FUNCTION OF TIME STEP SIZE

Time, sec	Δt, sec								
	RAUMZEIT				QX1				
	10^{-6}	10^{-5}	5×10^{-5}	10^{-4}	2.0×10^{-5}	8.5×10^{-5}	1.4×10^{-4}	5.0×10^{-4}	1.0×10^{-3}
0.000	1.000 + 0	1.000 + 0	1.000 + 0	1.000 + 0	1.000 + 0	1.000 + 0	1.000 + 0	1.000 + 0	1.000 + 0
0.001	1.178 + 0	1.178 + 0	1.178 + 0	1.178 + 0	1.178 + 0	1.178 + 0	1.178 + 0	1.178 + 0	1.178 + 0
0.002	1.558 + 0	1.558 + 0	1.558 + 0	1.559 + 0	1.558 + 0	1.558 + 0	1.558 + 0	1.558 + 0	1.558 + 0
0.003	2.797 + 0	2.797 + 0	2.797 + 0	2.798 + 0	2.797 + 0	2.797 + 0	2.787 + 0	2.787 + 0	2.759 + 0
0.004	2.072 + 1	2.073 + 1	2.085 + 1	2.125 + 1	2.072 + 1	2.072 + 1	2.066 + 1	2.006 + 1	1.832 + 1
0.005	1.537 + 5	1.553 + 5	2.037 + 5	6.327 + 5	1.535 + 5	1.532 + 5	1.527 + 5	1.407 + 5	1.189 + 5

Substitution of fast reactor group constants in a system with the same dimensions would increase the time step advantage still further. The reason is that the number of shape functions required by QX1 depends on the degree of spatial and spectral flux distortion for a given perturbation. For fixed dimensions a fast reactor is more tightly coupled than a thermal light-water reactor. On the other hand, the time step required by a direct finite-difference method in the range near prompt critical depends on the rate of change of the total flux, which in turn depends on the neutron generation time.

DISCUSSION AND CONCLUSIONS

Based on the above calculations, it may be concluded that each code can accurately calculate reactor transients. Furthermore, thermal reactor calculations can be done very economically with both WIGLE and RAUMZEIT and nearly as economically with QX1 if one does not require "Benchmark" accuracy. It is clear that WIGLE and RAUMZEIT are more effective than QX1 for calculating linear transients in thermal reactors. It is not yet known whether they will retain their economic advantage if the transient becomes nonlinear.

QX1 makes a better showing when the velocities are increased than it does for the reference calculations, because the implicit differencing method for solving the shape function equations is not too well suited for doing thermal reactor calculations. A typical shape step for an accurate solution is very many generation times when the velocities are increased, whereas, it is not too many for the reference case. Thus, for the increased-velocity case, neutrons at any given position at any time are, by and large, not the same neutrons that were at that position at the previous time. For the reference case, on the other hand, much stronger coupling is present. Thus, a fully implicit differencing scheme is not appropriate for thermal reactor calculations with QX1, whereas it is adequate for doing fast reactor calculations.

REFERENCES

1. W. M. Stacey, Jr., *Argonne Code Center: Benchmark Problem Book*, ANL-7416, Addendum (to be published). (See Section ID.6).
2. C. H. Adams and W. M. Stacey Jr., *RAUMZEIT—A Program to Solve Coupled Time-Dependent Neutron Diffusion Equations in One Space Dimension*, KAPL-M-6728 (1967).
3. W. R. Cadwell, A. F. Henry and A. J. Vigilotti, *WIGLE—A Program for the Solution of the Two-Group Space-Time Diffusion Equations in Slab Geometry*, WAPD-TM-416 (1964).
4. D. A. Meneley, K. O. Ott and E. S. Wiener, *Fast Reactor Kinetics—The QX1 Code*, ANL-7769 (1971).
5. D. A. Meneley, K. O. Ott and E. S. Wiener, *Influence of the Shape-Function Time Derivative on Spatial Kinetics Calculations in Fast Reactors*, Trans. Am. Nucl. Soc. **11**, 225 (1968).

IV-19. The Point Kinetics Algorithm for FX2

E. L. Fuller

Introduction

The two-dimensional space-time kinetics code FX2 is based on the factorization[1-3] (quasistatic) approach to solving the time-dependent multigroup diffusion equations. That is, it is assumed that the flux shape changes much more slowly in time than does its amplitude. Consequently, the solution method contains a three-level time step structure. The largest step is the interval between shape function recalculations. Within this interval are the time points at which coefficients of the amplitude function equations are recalculated. Finally, there are time points used for integration of the amplitude function equations, i.e., the point kinetics equations. Very few shape function recalculations are needed relative to the number of amplitude function recalculations. The shape function calculations are done by a two-dimensional inhomogeneous multigroup diffusion theory calculation. The amplitude function calculations are done by the point kinetics algorithm which is described below. The algorithm is an extension of a method devised by Kaganove[4] to solve the conventional point kinetics equations. Modification of Kaganove's method is necessary to account for the effects of fuel motion that might occur during disassembly or slumping accidents. Since the hydrodynamic effects during disassembly are described on a moving mesh, the modifications to the point kinetics equations take the form of corrections to account for moving precursors.

The derivation of the algorithm will be outlined first, followed by a discussion of the input and output information required. Finally, the computational logic involved in the solution will be described.

The Point Kinetics Algorithm

Solution method

Using the definitions and notation of Ref. 3, the point kinetics equations for FX2 are:

$$\dot{N} = \left(\frac{\rho - \beta}{\Lambda} + \frac{k_0 - 1}{\Lambda k_0}\right) N + \sum_{s=1}^{m} \lambda_s \eta_s + \sum_{s=1}^{m} \lambda_s \xi_s + Q' \tag{1}$$

$$\dot{\eta}_s = \frac{\beta_s'}{\Lambda} N - (\lambda_s + \kappa_s)\eta_s, \qquad 1 \le s \le m, \tag{2}$$

where

$N \equiv$ amplitude function
$\rho \equiv$ reactivity
$\beta \equiv$ effective delayed neutron fraction
$k_0 \equiv$ eigenvalue of source-free adjoint equation (unity, unless the reactor is initially subcritical)
$\Lambda \equiv$ generation time
$Q' \equiv$ external source
$\lambda_s \equiv$ decay constant for sth precursor family
$\eta_s \equiv$ weighted integral concentration of sth precursor family
$\xi_s \equiv$ correction to concentration of the sth precursor family due to fuel motion
$\kappa_s \equiv$ loss coefficient for sth precursor family
$\beta_s' \equiv$ effective delayed neutron fraction for the sth family as calculated on the moving mesh.

The first step toward obtaining a solution is to formally integrate Eqs. (2) over the time interval $t_{j-1} \le t \le t_j$. The result is

$$\eta_s(t) = \eta_s(t_{j-1}) \exp\left\{-\int_{t_{j-1}}^{t} [\lambda_s + \kappa_s(\tau)]\, d\tau\right\} + \int_{t_{j-1}}^{t} \exp\left\{-\int_{t'}^{t} [\lambda_s + \kappa_s(\tau)]\, d\tau\right\} \frac{\beta_s'(t')}{\Lambda(t')} N(t')\, dt'. \tag{3}$$

If Eq. (3) is substituted into Eq. (1), then

$$\begin{aligned} \dot{N} = \left(\frac{\rho - \beta}{\Lambda} + \frac{k_0 - 1}{\Lambda k_0}\right) N(t) + \sum_{s=1}^{m} \lambda_s \Bigg[\eta_s(t_{j-1}) \exp\left\{-\int_{t_{j-1}}^{t} [\lambda_s + \kappa_s(\tau)]\, d\tau\right\} \\ + \int_{t_{j-1}}^{t} \exp\left\{-\int_{t'}^{t} [\lambda_s + \kappa_s(\tau)]\, d\tau\right\} \frac{\beta_s'(t')}{\Lambda(t')} N(t')\, dt' + \xi_s(t) \Bigg] + Q' \end{aligned} \tag{4}$$

Next, assume the following trial solution for $N(t)$ over the interval $t_{j-1} \leq t \leq t_j$:

$$N_K(t) = \sum_{k=0}^{K} A_k(t - t_{j-1})^k \tag{5}$$

$$\frac{dN_K}{dt} = \sum_{k=1}^{K} kA_k(t - t_{j-1})^{k-1}. \tag{6}$$

The following residual is formed when the approximate solution is put into Eq. (4):

$$R_N(t) = \frac{dN_K}{dt} - \left[\frac{\rho - \beta}{\Lambda} + \frac{k_0 - 1}{\Lambda k_0}\right] N_K(t) - \sum_{s=1}^{m} \lambda_s \left[\eta_s(t_{j-1}) \exp\left\{-\int_{t_{j-1}}^{t} [\lambda_s + \kappa_s(\tau)]\, d\tau\right\} + \int_{t_{j-1}}^{t} \exp\left\{-\int_{t'}^{t} [\lambda_s + \kappa_s(\tau)]\, d\tau\right\} \frac{\beta_s'(t')}{\Lambda(t')} N_K(t')\, dt' + \xi_s(t)\right] - Q'(t). \tag{7}$$

The parameters A_k are evaluated by the method of undetermined parameters, with subdomain weighting.[5] The time-step selection technique developed by Kaganove[4] is used to ensure a stable, accurate solution.

It is obvious that $A_0 = N_K(t_{j-1})$, so that only $A_1, \cdots, A_K$ must be evaluated over the time interval. Nested subdomains are chosen such that each begins at t_{j-1}. The largest is the full interval, the next largest the half-interval, then the quarter interval, etc., until K intervals are chosen. Unit step functions over each subdomain are the weighting functions. Mathematically, the weighting functions are written as

$$V_r(t) = U(t) - U(t - t_r), \qquad r = 1, \cdots, K, \tag{8}$$

where

$$t_r = t_{j-1} + \frac{(t_j - t_{j-1})}{2^{r-1}} = t_{j-1} + \frac{\Delta t_j}{2^{r-1}} \tag{9}$$

(thus defining $\Delta t_j \equiv t_j - t_{j-1}$). The method of undetermined parameters, concisely written as

$$\int_{t_{j-1}}^{t_j} V_r(t) R_N(t)\, dt = 0, \qquad r = 1, \cdots, K, \tag{10}$$

can then be used to obtain K algebraic equations to solve for $A_1, \cdots, A_K$.

The parameters ρ, β, Λ, ξ_s, Q', β_s' and κ_s are, in general, functions of time. Since their functional dependencies cannot, in general, be prespecified, they shall be approximated by fitting to quadratic functions over time intervals—called reactivity time steps—that are, in general, quite a bit larger than the point kinetics intervals. The functional behavior of the parameters may be written as

$$p(t) = p(t_{j-1}) + (t - t_{j-1})(a_1 + 2a_2 t_{j-1}) + a_2(t - t_{j-1})^2, \tag{11}$$

where

$$p = \frac{\rho - \beta + (k_0 - 1)/k_0}{\Lambda} \tag{12}$$

$$\xi_s(t) = \xi_s(t_{j-1}) + (t - t_{j-1})(c_{1s} + 2c_{2s}t_{j-1}) + c_{2s}(t - t_{j-1})^2 \tag{13}$$

$$\frac{\beta_s'(t)}{\Lambda(t)} = \frac{\beta_s'(t_{j-1})}{\Lambda(t_{j-1})} + (t - t_{j-1})(b_{1s} + 2b_{2s}t_{j-1}) + b_{2s}(t - t_{j-1})^2, \qquad s = 1, \cdots, m \tag{14}$$

$$Q'(t) = Q'(t_{j-1}) + (t - t_{j-1})(q_1 + 2q_2 t_{j-1}) + q_2(t - t_{j-1})^2, \tag{15}$$

where the coefficients have been evaluated at an earlier time t_{i-1} which in turn is set equal to zero, so that all times are those that have elapsed since t_{i-1}. Since κ_s is a crude function, it is approximated as the initial value over the time interval (i.e., $\bar{\kappa}_s$) to simplify evaluation of the integrals that appear in Eq. (7). When Eqs. (5), (6), and (11) through (15) are substituted into Eq. (10), with the weighting functions given by Eqs. (8) and (9), the result is

$$\sum_{k=1}^{K} R_{rk} A_k = S_{rk} \qquad r = 1, \cdots, K, \tag{16}$$

where

$$R_{rk} = \Delta t_r^k - \left[\frac{p(t_{j-1})\Delta t_r^{k+1}}{k+1} + \frac{(a_1 + 2a_2 t_{j-1})\Delta t_r^{k+2}}{k+2} + \frac{a_2 \Delta t_r^{k+3}}{k+3}\right] + \sum_{s=1}^{m}\left\{\frac{\beta_s'(t_{j-1})}{\Lambda(t_{j-1})}\frac{[\Delta t_r^{k+1} - (k+1)I_{s,k}(\Delta t_r)]}{k+1}\right.$$
$$\left. + (b_{1s} + 2b_{2s}t_{j-1})\frac{[\Delta t_r^{k+2} - (k+2)I_{s,k+1}(\Delta t_r)]}{k+2} + b_{2s}\frac{[\Delta t_r^{k+3} - (k+3)I_{s,k+2}(\Delta t_r)]}{k+3}\right\}, \tag{17}$$

$$S_{rk} = \left(p(t_{j-1})\Delta t_r + (a_1 + 2a_2 t_{j-1})\frac{\Delta t_r^2}{2} + a_2\frac{\Delta t_r^3}{3} + \sum_{s=1}^{m}\left\{\frac{\beta_s'(t_{j-1})}{\Lambda(t_{j-1})}[\Delta t_r - I_{s,0}(\Delta t_r)]\right.\right.$$
$$\left.\left. + (b_{1s} + 2b_{2s}t_{j-1})\left[\frac{\Delta t_r^2}{2} - I_{s,1}(\Delta t_r)\right] + b_{2s}\left[\frac{\Delta t_r^3}{3} - I_{s,2}(\Delta t_r)\right]\right\}\right)A_0 + \sum_{s=1}^{m}\left\{\lambda_s\left[\eta_s(t_{j-1})I_{s,0}(\Delta t_r)\right.\right.$$
$$\left.\left. + \xi_s(t_{j-1})\Delta t_r + (c_{1s} + 2c_{2s}t_{j-1})\frac{\Delta t_r^2}{2} + c_{2s}\frac{\Delta t_r^3}{3}\right]\right\}$$
$$+ \left[Q'(t_{j-1})\Delta t_r + (q_1 + 2q_2 t_{j-1})\frac{\Delta t_r^2}{2} + q_2\frac{\Delta t_r^3}{3}\right], \tag{18}$$

and the so-called I-functions are defined by

$$I_{s,k}(\Delta t) = \int_{t_{j-1}}^{t} \exp\left[-(\lambda_s + \bar{\kappa}_s)(t - t')\right](t' - t_{j-1})^k\, dt', \qquad \Delta t \equiv t - t_{j-1}. \tag{19}$$

From Eq. (19), it is evident that

$$I_{s,0}(\Delta t) = \frac{1}{\lambda_s + \bar{\kappa}_s}\{1 - \exp\left[-(\lambda_s + \bar{\kappa}_s)\Delta t\right]\}. \tag{20}$$

Using Eqs. (19) and (20), the following recursion relationship can easily be derived:

$$I_{s,m}(\Delta t) = \frac{1}{\lambda_s + \bar{\kappa}_s}[\Delta t^m - mI_{s,m-1}(\Delta t)], \qquad m \geq 1. \tag{21}$$

Finally, using Eqs. (19), (20), and (21), a very useful expression for the integral of the I-function is found:

$$\int_{t_{j-1}}^{t_r} I_{s,m}(\Delta t)\, dt = \frac{1}{m+1} I_{s,m+1}(\Delta t_r), \tag{22}$$

where

$$\Delta t_r = t_r - t_{j-1}.$$

The set of algebraic equations represented by Eq. (16) can then be solved for the parameters A_k, which are in turn substituted into Eq. (5) to obtain the amplitude function at t_j. Piecewise quadratic functions ($K = 2$) are used in FX2 because they have worked very well in QX1. And, they are very well suited to be used in conjunction with Kaganove's time-step-halving-and-doubling scheme for automatically selecting the time step size. This time-step-selection technique will now be described.

TIME STEP SELECTION

Suppose that a solution has been obtained at t_{j-1} and that Δt_j has been selected. Then, two independent solutions (sets of parameters) of the point kinetics equations are found at t_j. The first of these integrates over the whole time step, yielding a solution directly at t_j. The second solution is for only half the step, yielding a solution at $t_{j-1} + (\Delta t_j/2)$. The half-step solution is then extrapolated to t_j. It will not be the same as that determined directly, but it should be close. The degree of closeness determines whether or not the solution is acceptable.

The two values are compared by forming the error norm

$$\epsilon = \frac{|N_{ext}(t_j) - N(t_j)|}{N_{ext}(t_j)} \tag{23}$$

and comparing it with a preselected tolerable error ϵ_1. If $\epsilon < \epsilon_1$, then the amplitude function $N(t_j)$ is acceptable and the solution can be found for the next step. If, in addition, $\epsilon < C\epsilon_1$, where C is a preselected parameter less than unity (usually set to 0.1), then the next time step is estimated to be $2\Delta t_j$; otherwise, $\Delta t_{j+1} = \Delta t_j$.

If, on the other hand, $\epsilon > \epsilon_1$, the solution at t_j is not acceptable, and the time step is halved. Two independent solutions to the point kinetics equations are again found, this time for $t = t_{j-1} + (\Delta t_j/2)$ and $t = t_{j-1} + (\Delta t_j/4)$. Note that the first of these has already been determined for the original comparison and hence need not be repeated. The solutions are again compared as described above. If an acceptable value of $N[t_{j-1} + (\Delta t_j/2)]$ is found, the solution for t_j will again be attempted in the same manner. This time, however, $t = t_{j-1} + (\Delta t_j/2)$ at the lower end of the time step, so that independent solutions are formed for $t = t_{j-1} + \frac{3}{4}\Delta t_j$ and $t = t_j$.

If the value $N[t_{j-1} + (\Delta t_j/2)]$ is not acceptable, the time step is halved again and the calculation is repeated for the quarter step. Calculation continues until an acceptable solution has been obtained for $t = t_j$. The procedure then begins anew to determine $N(t_{j+1})$, etc., until the end of the reactivity step is reached.

Required Input and Output Information

The following information is needed upon entry to the point kinetics algorithm: the amplitude function $N(t_{i-1})$, the coefficients $p(t_{i-1})$, a_1, a_2, $\xi_s(t_{i-1})$, c_{1s}, c_{2s}, $[\beta_s'(t_{i-1})]/[\Lambda(t_{i-1})]$, b_{1s}, b_{2s}, $Q'(t_{i-1})$, b_{1s}, b_{2s}, $Q'(t_{i-1})$, q_1, q_2, $\bar{\kappa}_s(t_{i-1})$, and the time interval (called the reactivity step) over which these are to be used (i.e., t_{i-1} to t_i). These coefficients are evaluated by fitting to parabolas the inner products for reactivity, delayed neutron fraction, etc., from the previous two i-intervals. The functions are then extrapolated to $t = t_i$. The inner products are recalculated at $t = t_i$ after $N(t_i)$ has been found. The recomputed values are compared with the extrapolated values, and the necessary corrections are made.

Once the amplitude function is evaluated at $t = t_i$, it is used, along with $N(t_{i-1})$ and $N(t_{i-2})$, to evaluate n_1, n_2, and n_3 for use in the expression

$$\ln N(t_{i+1}) = n_1 + n_2(t_{i+1} - t_i) + n_3(t_{i+1} - t_i)^2. \tag{24}$$

This extrapolation, which takes place once an estimate of t_{i+1} has been determined, is necessary to compute the energy generated over the $(i + 1)st$ interval from the increase in fuel temperature. The estimate of $N(t_{i+1})$ obtained from Eq. (24) is, of course, later corrected by carrying out a point kinetics calculation over the interval $[t_i, t_{i+1}]$.

In addition to the amplitude function information, the quantities $\hat{a}_s^i$ and $\hat{b}_s^i$, as defined in Eq. (19) of Ref. 3, are available from the point kinetics calculation. These quantities, needed to properly update the concentrations of delayed neutron precursors, are given by the expressions

$$\hat{a}_s^i = \frac{1}{\Delta t_i}\int_{t_{i-1}}^{t_i} \exp\left\{-\int_t^{t_i} [\lambda_s + \kappa_s(\tau)]\, d\tau\right\} (t - t_{i-1})N(t)\, dt, \tag{25}$$

$$\hat{b}_s^i = \frac{1}{\Delta t_i}\int_{t_{i-1}}^{t_i} \exp\left\{-\int_t^{t_i} [\lambda_s + \kappa_s(\tau)]\, d\tau\right\} (t_i - t)N(t)\, dt. \tag{26}$$

We shall now outline the method of evaluating these quantities.

Within the time interval $[t_{i-1}, t_i]$ there are J point kinetics steps ($t_0 = t_{i-1}$ and $t_J = t_i$). Let us, therefore, evaluate the integrals by summing the components of each point kinetics step; specifically,

$$\hat{a}_s^i = \frac{1}{\Delta t_i}\sum_{j=1}^{J}\int_{t_{j-1}}^{t_j} \exp\,[-(\lambda_s + \bar{\kappa}_s)(t_i - t)](t - t_{i-1}) \sum_{k=0}^{K} A_k(t - t_{j-1})^k\, dt, \tag{27}$$

$$\hat{b}_s^i = \frac{1}{\Delta t_i}\sum_{j=1}^{J}\int_{t_{j-1}}^{t_j} \exp\,[-\lambda_s + \bar{\kappa}_s)(t_i - t)](t_i - t) \sum_{k=0}^{K} A_k(t - t_{j-1})^k\, dt. \tag{28}$$

This is necessary because $N(t)$ is a piecewise polynomial function over the interval $[t_{i-1}, t_i]$, such that its coefficients differ over each point kinetics interval. Finally, after some manipulations, it can be shown that

$$\hat{a}_s^i = \frac{1}{\Delta t_i}\sum_{j=1}^{J}\left\{\exp\,[-(\lambda_s + \bar{\kappa}_s)(t_i - t_j)] \sum_{k=0}^{K} A_k[I_{s,k+1}(\Delta t_j) + (t_{j-1} - t_{i-1})I_{s,k}(\Delta t_j)]\right\}, \tag{29}$$

$$\hat{b}_s^i = \frac{1}{\Delta t_i}\sum_{j=1}^{J}\left\{\exp\,[-(\lambda_s + \bar{\kappa}_s)(t_i - t_j)] \sum_{k=0}^{K} A_k[(t_i - t_{j-1})I_{s,k}(\Delta t_j) - I_{s,k+1}(\Delta t_j)]\right\} \tag{30}$$

Computational Logic

The logical sequence of the point kinetics solution is shown in Fig. IV-19-1. The first step is to calculate the coefficients that appear in Eqs. (11) through (15). Then, the time values are initialized, the convergence criteria are set, and the starting values of the point kinetics parameters are calculated. These parameters will be updated later according to Eqs. (11) through (15). We are now ready to solve for the A_k for the first time step.

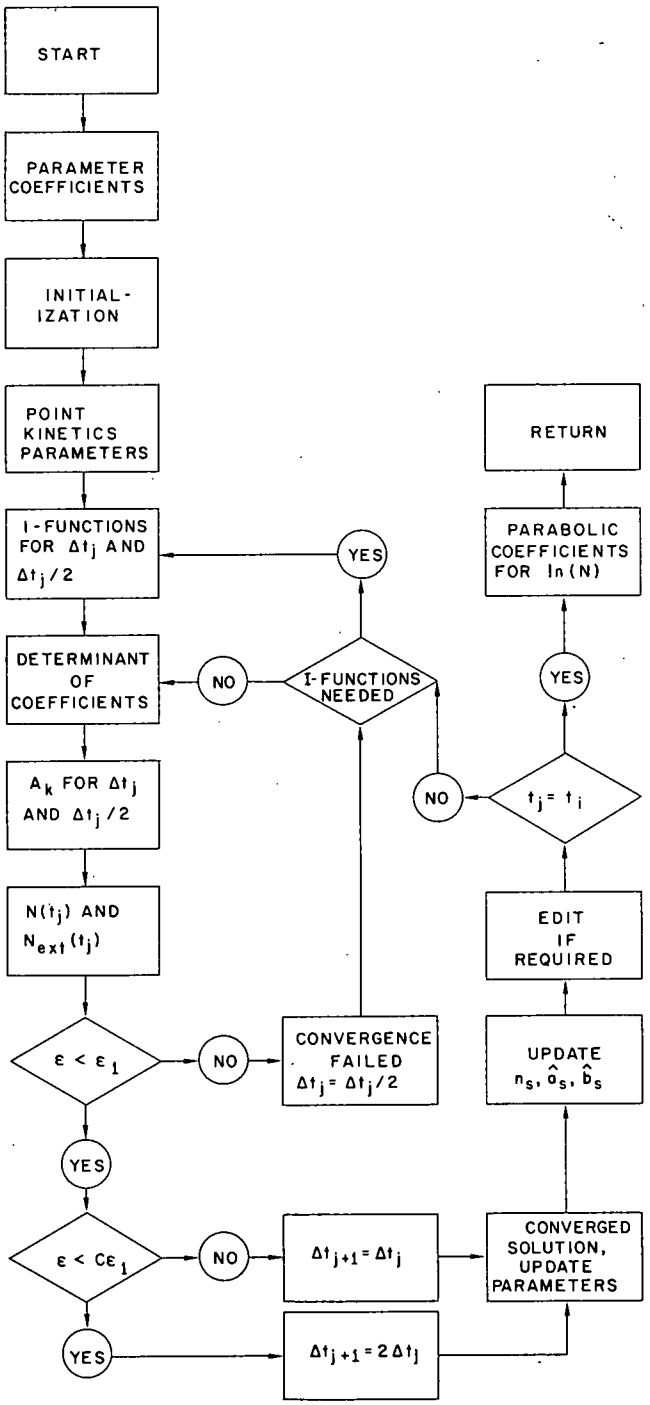

Fig. IV-19-1. Logical Sequence of Point Kinetics Solution. *ANL Neg. No. 116-817.*

We begin by calculating the I-functions needed for Δt_1 and $\Delta t_1/2$. Then we can find the coefficients R_{rk} and S_{rk} of Eq. (16) for the full step and for the half step. The determinant of coefficients is formed for each step, and solved to obtain the values of A_k for t_1 and $t_1/2$. These, in turn, are used to find $N(t_1)$ and $N_{ext}(t_1)$. If they are not close enough to each other, then the time step is halved and a solution at $t_1/2$ is attempted. If I-functions for the half-step are needed they are calculated. Otherwise, the determinants of coefficients for both the half step and the quarter step are formed and solved for the A_k.

When $\epsilon < \epsilon_1$ the solution is considered to be converged, and the next time step is selected. This next step is double the previous one if $\epsilon < 0.1\ \epsilon_1$. Otherwise, the step length remains the same. In either case the point kinetics parameters are updated to the latest time step, as are the precursor concentrations. An edit of the current information can also be made at this time. If it is necessary to calculate more I-functions for the next time step they are so calculated; otherwise, the determinants of coefficients are formed and solved for the half step and the full step.

When a converged solution has been found at $t = t_i$ (the end of the reactivity step), the parabolic coefficients for $\ln N$, needed to estimate the amplitude function behavior over the next reactivity step, are calculated. Then, the information is taken from the module to be used in other parts of the program.

References

1. A. F. Henry, *The Application of Reactor Kinetics to the Analysis of Experiments*, Nucl. Sci. Eng. **3**, 52 (1958).
2. K. O. Ott and D. A. Meneley, *Accuracy of the Quasistatic Treatment of Spatial Reactor Kinetics*, Nucl. Sci. Eng. **36**, 402 (1969).
3. D. A. Meneley, G. K. Leaf, A. J. Lindeman, T. A. Daly and W. T. Sha, *A Kinetics Model for Fast Reactor Analysis in Two Dimensions*, Symposium on Dynamics of Nuclear Systems, University of Arizona Press, Tucson, Arizona, March 23–25, 1970.
4. J. J. Kaganove, *Numerical Solution of the One-Group Space-independent Reactor Kinetics Equations for Neutron Density Given the Excess Reactivity*, ANL-6132 (1960).
5. E. L. Fuller, *Integration of the Multimode Kinetics Equations by the Method of Undetermined Parameters*, Reactor Physics Division Annual Report, July 1, 1968 to June 30, 1969, ANL-7610, pp. 528–532.

IV-20. Generalized Perturbation Methods for Sensitivity Analysis of Fast Criticals

M. Salvatores*

Introduction

In recent years the term "generalized perturbation theory" has come to indicate the theory which deals with perturbations of reactor integral characteristics, which can be expressed by means of linear or bilinear functionals of the real and/or adjoint fluxes.[1-3] If we consider a ratio, R, of these functionals, the main result of the generalized perturbation theory is to express the variation, δR, of R in terms of any cross section variation, $\delta\Sigma_x^i$, (which represents the perturbation for energy group i in the form of a linear expression),

$$\delta R/R = \sum_i a_x^i \delta\Sigma_x^i , \tag{1}$$

where x defines a type of cross section. The explicit expressions for coefficients a_x^i for the different type of functions are given in Ref. 3.

Linear expressions of the type of Eq. (1) are particularly useful when the explicit dependence of integral parameters (such as reaction rates, reactivity worths, or source worths) on nuclear group parameters is needed. A typical case is the sensitivity analysis of integral reactor parameters to nuclear cross section uncertainties. Codes were developed for the calculation of the coefficients a_x^i in diffusion theory, and for the zero-dimension (fundamental mode),[4] one-dimension,[5,6] and two-dimension[7,8] space dependent schemes. A method[9] and a code[10] were developed using an integral transport approach. In this paper the fundamental mode method and a new integral method for a heterogeneous medium will be discussed.

* Comitato Nazionale per L'Energia Nucleare, Casaccia, Italy.

Fundamental Mode Method

Let us consider the reaction rate ratio

$$R = \frac{a_1}{a_2} = \frac{\int \sigma_1 \phi dr\, dE}{\int \sigma_2 \phi dr\, dE}. \tag{2}$$

The change in R due to nuclear parameter variations in the zero-dimension approximation in multigroup notation is given by

$$\delta R/R = \sum_i \left(\frac{\phi_i \delta\sigma_{1,i}}{a_1} - \frac{\phi_i \delta\sigma_{2,i}}{a_2} \right) + \sum_i \left(\delta\chi_i \psi_i^+ + (\delta\Sigma_i^a + B_i^2 \delta D_i) \phi_i \psi_i^+ + \sum_j \delta\Sigma_{i\to j}^s (\psi_j^+ - \psi_i^+) \phi_i \right), \tag{3}$$

where ϕ_i is the solution of the linear system

$$B_i^2 D_i \phi_i + \Sigma_i^a \phi_i - \sum_j \Sigma_{j\to i}^s \phi_j = \chi_i, \qquad i = 1, 2, \cdots, \text{number of groups} \tag{4}$$

corresponding to B_i^2 values such that

$$\sum_i \nu\Sigma_{f_i} \phi_i = 1, \tag{5}$$

and the importance ψ_i^+ is the solution of the linear system

$$B_i^2 D_i \psi_i^+ + \Sigma_i^a \Psi_i^+ - \sum_j \Sigma_{i\to j}^s \psi_i^+ = S_i^+, \qquad i = 1, 2, \cdots, \text{number of groups} \tag{6}$$

where

$$S_i^+ = \frac{\sigma_{1,i}}{\sum_i \sigma_{1,i} \phi_i} - \frac{\sigma_{2,i}}{\sum_i \sigma_{2,i} \phi_i}. \tag{7}$$

$\delta\sigma_1$, $\delta\sigma_2$, $\delta\chi$, $\delta\Sigma^a$, δD and $\delta\Sigma_{i\to j}$ are pertinent both to the ratio R itself and to the system. We shall call the first term on the right of Eq. (3) the "direct" effect and the second term the "indirect" or "spectral" effect.

The CIAP-0 codes compute the quantities ϕ_i (allowing for a criticality search on B^2), ψ_i^+, $\delta R/R$, and the corresponding quantities related to the bilinear functional ratios. The normal perturbation expressions for $\delta k/k$ (i.e., the second term on the right of Eq. (3) with the substitution $\phi_i^+ \to \psi_i^+$) are also computed.

Applications

The typical application of these methods is the generation of tables of "sensitivity coefficients" for the integral quantities of interest. The quantitative or qualitative effects of any cross section uncertainty on that integral quantity can be readily evaluated from those tables. As an example, Table IV-20-I gives the sensitivity coefficients of indirect effects relative to the bilinear functional ratio represented by the ^{12}C reactivity worth. The calculation was made for ZPR-6 Assembly 7. The zero-dimensional approximation seems to be well suited for a large system such as the Demonstration Plant Benchmark Critical Assembly. As an example of the use of the coefficients of Table IV-20-I, the Cross Section Evaluation Working Group (CSEWG) recommended modifications to ENDF/B VERSION-II (see Table IV-20-II) were considered. It is possible to see that the ^{12}C reactivity worth is strongly dependent on the changes which affect the adjoint flux. However, the large effects (about 20 %) due to the variation of $\Sigma_f(^{239}Pu)$ and $\Sigma_f(^{238}U)$ are balanced by the corresponding variations of Σ_a. This is expected since the adjoint flux is characterized mainly by the energy dependence of the ratio $\nu\Sigma_f/\Sigma_a$. Changes in $\Sigma_c(^{239}Pu)$ have the effect of increasing the reactivity worth by about 3 %. In Table IV-20-III the analogous sensitivity coefficients are shown relative to the ^{10}B reactivity worth, and in Fig. IV-20-1 the absorption sensitivity coefficients are compared for the ^{10}B and ^{12}C reactivity worths. The stronger dependence of the scattering material reactivity worth on the adjoint in comparison with the pure absorber's worth is shown clearly by these results.

TABLE IV-20-I. SENSITIVITY COEFFICIENTS FOR THE CENTRAL ^{12}C REACTIVITY WORTH[a]

Group	Absorption Sensitivity Coefficients (Relative to $\delta\Sigma_a^j = 1$)			Scattering Sensitivity Coefficients (Relative to $\delta\Sigma_{j\to j+1} = 1$)			ψ Function (Sensitivity Coefficients Relative to $\delta\nu\Sigma_f^j = 1$)	ψ^+ Function (Sensitivity Coefficients Relative to $\delta\chi_j = 1$)
	Effects on ϕ^+	Effects on ϕ	Total	Effects on ϕ^+	Effects on ϕ	Total		
1	−0.50	0.13	−0.47	−0.03	0.03	0.0	0.43	−0.28
2	−4.65	0.42	−4.23	−0.01	0.65	0.64	4.21	−0.21
3	−13.00	−0.57	−13.57	−0.98	0.15	−0.83	11.80	0.12
4	−6.49	−1.02	−7.51	−0.61	−0.83	−1.44	6.37	0.15
5	−21.46	−0.23	−21.69	−0.49	0.93	0.44	23.26	0.03
6	−130.25	−2.29	−132.54	−4.34	−0.31	−4.65	44.50	0.14
7	−108.60	0.74	−107.86	−3.19	−3.43	−6.62	124.64	−0.05
8	−166.30	5.50	−160.80	−5.54	−6.64	−12.18	196.63	−0.27
9	−144.10	11.57	−132.53	−5.64	−9.02	−14.66	176.26	−0.59
10	−113.35	18.87	−94.48	−4.05	−8.82	−12.87	144.29	−1.05
11	−60.45	23.08	−37.37	−1.07	−5.28	−6.35	79.81	−1.55
12	−26.75	22.80	−3.95	0.05	−2.53	−2.48	35.95	−1.90
13	14.25	23.27	37.52	−0.28	−1.79	−2.07	−19.12	−2.11
14	31.25	17.72	48.97	−0.93	−0.89	−1.82	−41.09	−2.27
15	38.10	10.98	49.08	−1.94	0.17	−1.77	−48.67	−2.39
16	41.07	6.53	47.60	−1.52	−0.44	−1.96	−49.92	−2.35
17	15.82	2.50	18.32	−0.39	−0.07	−0.46	−18.54	−2.51
18	35.48	7.38	42.86	−1.52	−0.78	−2.30	−40.59	−2.58
19	35.95	5.38	41.33	−5.78	1.41	−4.37	−39.44	−2.85
20	33.36	2.31	35.67	−1.49	−0.26	−1.75	−31.52	−2.11
21	20.63	1.10	21.73	−3.08	0.33	−2.75	−18.67	−2.35
22	20.27	0.53	20.80	−3.66	0.30	−3.36	−15.96	−1.65
23	3.48	0.03	3.51	2.02	−1.66	0.36	−2.32	−0.71
24	0.08	0.0	0.08	−0.10	0.0	−0.10	−0.11	−1.17

[a] The group structure is based on a constant $\Delta u = 0.5$ for the first 21 groups. A constant $\Delta u = 1$ is adopted for the lower groups.

TABLE IV-20-II. CROSS SECTION EVALUATION WORKING GROUP (CSEWG) RECOMMENDED MODIFICATION TO ENDF/B VERSION-II

1. Increase σ_f^{235} in the first three groups by 8%.
2. Increase σ_f^{238} in the first 6 groups by 8%.
3. Decrease σ_c^{238} in groups 5–9 by 5%.
4. Multiply σ_f^{239} in groups 1–14 by the following factors:

Group	Factor
1	1.06
2	1.06
3	1.06
4	1.00
5	1.00
6	1.07
7	1.02
8	1.02
9	1.03
10	1.05
11	1.06
12	1.08
13	1.09
14	1.10

TABLE IV-20-III. SENSITIVITY COEFFICIENTS FOR ^{10}B REACTIVITY WORTH[a]

Group	Absorption Sensitivity Coefficients (Relative to $\delta\Sigma_a^i = 1$)			Scattering Sensitivity Coefficients (Relative to $\delta\Sigma_{j\to j+1} = 1$)			ψ Function (Sensitivity Coefficients Relative to $\delta\nu\Sigma_f^j = 1$)	ψ^+ Function (Sensitivity Coefficients Relative to $\delta\chi_j = 1$)
	Effects on ϕ^+	Effects on ϕ	Total	Effects on ϕ^+	Effects on ϕ	Total		
1	0.53	0.15	0.68	0.04	0.06	0.10	−0.45	−0.33
2	2.12	0.40	2.52	0.0	0.03	0.03	−1.92	−0.21
3	5.17	0.90	6.07	0.39	0.62	1.01	−4.69	−0.19
4	6.65	0.39	7.04	0.63	1.05	1.68	−6.53	−0.06
5	7.46	−0.81	6.65	0.17	0.57	0.74	−8.08	0.10
6	13.76	−2.71	11.05	0.46	2.38	2.84	−15.27	0.17
7	12.09	−4.83	7.26	0.36	1.59	1.95	−13.88	0.31
8	14.00	−8.49	5.51	0.47	2.22	2.69	−16.55	0.41
9	11.10	−10.20	0.90	0.43	2.06	2.49	−13.58	0.52
10	7.75	−11.24	−3.49	0.28	1.83	2.11	−9.86	0.63
11	4.18	−10.89	−6.71	0.07	1.44	1.51	−5.52	0.73
12	1.43	−9.91	−8.48	0.0	1.39	1.39	−1.92	0.83
13	−1.15	−10.39	−11.54	0.02	1.77	1.79	1.54	0.94
14	−2.90	−8.60	−11.50	0.09	1.32	1.41	3.82	1.10
15	−3.00	−5.85	−8.85	0.15	0.77	1.02	3.83	1.27
16	−2.66	−4.00	−6.66	0.10	0.31	0.41	3.24	1.44
17	−1.16	−1.55	−2.71	0.03	0.06	0.09	1.36	1.55
18	−5.36	−4.51	−9.97	0.23	0.46	0.69	6.13	1.61
19	−5.36	−3.34	−8.70	0.86	0.74	1.60	5.88	1.77
20	−5.13	−2.37	−7.50	0.23	0.38	0.61	4.85	2.17
21	−3.02	−1.18	−4.20	0.45	0.03	0.48	2.73	2.51
22	−3.41	−0.84	−3.25	0.62	0.28	0.90	2.69	2.59
23	−0.63	−0.13	−0.76	−0.37	−0.05	−0.42	0.42	3.46
24	−0.01	−0.0	−0.01	0.02	0.01	0.03	0.02	2.10

[a] The group structure is based on a constant $\Delta u = 0.5$ for the first 21 groups. A constant $\Delta u = 1$ is adopted for the lower groups

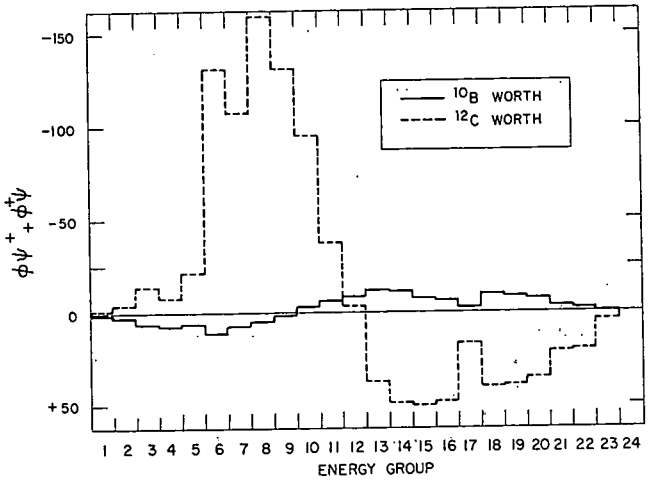

FIG. IV-20-1. Comparison of Absorption Sensitivity Coefficients for ^{10}B and ^{12}C Reactivity Worths. *ANL Neg. No. 116-928.*

SENSITIVITY ANALYSIS IN A HETEROGENEOUS MEDIUM

The functions defined in Eq. (6) may be physically defined as probabilities that a neutron of energy i be observed by a detector characterized by a "cross section" S_i^+ (see Refs. 3 and 11). If we now consider the reaction rate

$$R = \sum_{i,j} \sigma_{a_j}^i \phi_j^i V_j , \qquad \begin{cases} j = 1, 2, \cdots, \text{number of regions} \\ i = 1, 2, \cdots, \text{number of groups,} \end{cases} \tag{8}$$

defined through a cell of a critical assembly, it is possible to express again the variation of R by means of the generalized perturbation theory as a linear function of the cross section changes. That is, the sensitivity coefficient,

$$\delta R/R = \sum_{i,j} a^i_{x,j} \delta \Sigma^i_{x,j}, \tag{9}$$

will be expressed by perturbation expressions of the type

$$a^i_{x,j} = \psi^i_j \phi^i_j. \tag{10}$$

The ψ^i_j is the probability of a neutron at energy i and in region j being detected by the "detector distribution" characterized by the cross section σ^i_{dj}. In this way it will be possible to consider the effects of cross section changes on the heterogeneous flux rather than on the average flux of the cell.

In the case of an infinite repetitive heterogeneous structure it is easy, by means of a collision probability technique, to construct a set of equations [corresponding to Eq. (6)] for the probabilities ψ^{+i}_j. Each of these probabilities may be considered as the sum of two probabilities:

a) the probability of a neutron at energy i and in region j being detected directly at energy i in region j by the detector distribution with cross section σ^i_{dj}

b) the probability of a neutron at energy i and in region j being scattered to any energy k, multiplied by the probability of the neutron at energy k undergoing its next collision in region j', and then being detected.

Analytically this means that

$$\psi^{+i}_j = \sum_{k,j} \frac{\Sigma^{s,j}_{i\to k}}{\Sigma^{tot,j}_i} p^k_{jj'} \psi^{+k}_{j'} + \frac{\sigma^j_{d,j}}{\Sigma^{tot,j}_i}, \tag{11}$$

where we have introduced the probabilities $p^k_{jj'}$ of a neutron at energy k in region j experiencing its next collision in region j'. Using the importance functions given by Eq. (11) and the heterogeneous fluxes ϕ^i_j defined by means of a corresponding integral method[12] based on collision probabilities, the sensitivity coefficients of Eq. (10) will be given by

$$a^i_{A,j} = \psi^{+i}_j \phi^i_j$$

for absorption sensitivity coefficients for a $\delta \Sigma^i_{A,j}$ in region j and energy group i; and

$$a^{k\to i}_{s,j} = \phi^k_j \sum_{j'} \psi^{+i}_{j'} p^i_{j,j'}$$

for scattering sensitivity coefficients for $\delta \Sigma^{s,j}_{k\to i}$ in region j.

References

1. L. N. Usachev, *Perturbation Theory for the Breeding Ratio and for Other Number Ratios Pertaining to Various Reactor Processes*' J. Nucl. Energy, Parts A and B **18**, 571 (1964).
2. A. Gandini, *A Generalized Perturbation Method for Bi-Linear Functionals of the Real and Adjoint Neutron Fluxes*, J. Nucl. Energy **21**, 755 (1967).
3. G. P. Cecchini and M. Salvatores, *Advances in Generalized Perturbation Theory*, Nucl. Sci. Eng. **46**, 304–309 (1971).
4. G. P. Cecchini and M. Cosini, *The CIAP-0 Program*, CNEN Report RT/FI (69), 42 (1969).
5. I. Dal Bono, V. Leproni and M. Salvatores, *The CIAP-1D Code*, CNEN Report RT/FI (68), 9 (1968).
6. I. Dal Bono, V. Leproni and M. Salvatores, *The CLOBERT-1D Code*, CNEN Report RT/FI (68), 10 (1968).
7. G. P. Cecchini, *The CIAP-2D Code*, CNEN Report LFCR-9 (1967).
8. G. P. Cecchini, *The GLOBPERT-2D Code*, CNEN Report LFCR-13 (1967).
9. G. Bitelli and M. Salvatores, *Neutron Flux and Importance Distribution by Collision Method, Starting from a Generalized Source*, Nucl. Sci. Eng. **36**, 309 (1969).
10. G. Bitelli, I. Dal Bono, V. Leproni and M. Salvatores, *The DIRAC Code*, CNEN Report RT/FI (69), 18 (1970).
11. J. Lewins, *The Time-Dependent Importance of Neutrons and Precursors*, Nucl. Sci. Eng. **7**, 268 (1960).
12. F. Storrer and A. Khairallah, *Heterogeneity Calculation for Fast Reactors by a Perturbation Method*, Nucl. Sci. Eng. **24**, 154 (1966).

IV-21. Acceleration of External Source Problems in Near-Critical Systems

D. A. Meneley

Introduction

Many computer codes have the capability of solving the inhomogeneous equation which characterizes a subcritical reactor with a constant external neutron source. Most of these codes find the flux solution by iterative procedures which include acceleration techniques of various kinds. One common technique is extrapolation using factors derived from Chebyschev polynomials to reduce the error components of the flux estimate during the iterations. An estimate of the largest eigenvalue of the iteration matrix is required in this procedure, and the effectiveness of the acceleration depends strongly on the quality of this estimate. When the eigenvalue is near unity (corresponding to a nearly critical system) this estimate becomes rather uncertain, and consequently the procedure converges slowly.

A procedure for improving the convergence rate in these cases is described below. This procedure was suggested in unpublished work by D. H. Shaftman, Argonne National Laboratory. Examples are given comparing the procedure with conventional Chebyschev acceleration.

Mathematical Model

The multigroup inhomogeneous equation may be written as

$$(M - F)\phi = S, \tag{1}$$

where M represents absorption, diffusion and energy transfer, F represents the fission source, and S represents the inhomogeneous source. The flux, ϕ, is then a vector-valued function of position, subject to boundary conditions.

Equation (1) may be written:

$$\phi = (I - M^{-1}F)^{-1}u, \tag{2}$$

where

$$u = M^{-1}S.$$

Since the spectral radius of $M^{-1}F$ is less than unity, Eq. (2) may be written:

$$\phi = [I + M^{-1}F + (M^{-1}F)^2 + \cdots]u. \tag{3}$$

Expanding u in the eigenvectors ϕ_n of $M^{-1}F\phi_n = k_n\phi_n$ and substituting into Eq. (3) gives

$$\phi = \sum_{n=0}^{\infty} a_n \frac{1}{1 - k_n}\phi_n, \tag{4}$$

where a_n are the expansion coefficients of u.

The unaccelerated iterative sequence starting from zero flux may be written:

$$\phi^{(\ell)} = \sum_{n=0}^{\infty} a_n \sum_{m=0}^{\ell-1} (k_n)^m \phi_n \tag{5}$$

and

$$\phi^{(\ell)} - \phi^{(\ell-1)} = \sum_{n=0}^{\infty} a_n (k_n)^{\ell-1}\phi_n . \tag{6}$$

Multiplying Eq. (6) by

$$Q = \frac{1}{(k_0)^{\ell-1}(k - k_0)}\left[1 - (1 - k_0)\sum_{m=0}^{\ell-1}(k_0)^m\right] \tag{7}$$

and adding Eq. (5) gives

$$\phi^{(\ell)} + Q[\phi^{(\ell)} - \phi^{(\ell-1)}] = \frac{a_0}{(1 - k_0)}\phi_0 + \sum_{n=1}^{\infty} a_n[k_n{}^{\ell-1}Q + \sum_{m=0}^{\ell-1}(k_n)^m]\phi_n . \tag{8}$$

The first term on the right hand side of Eq. (7) is the first term of the solution, Eq. (4). When k_0 is near unity this term dominates the total solution. The second term represents the higher harmonics; since $(1 > k_0 > k_1 > k_2 \cdots)$ the $k_n^{\ell-1}$ terms in the summation attenuate the higher harmonics fairly rapidly as ℓ is increased. The acceleration factor Q has the effect of increasing the higher harmonic magnitudes; however, these are quite easily reduced by standard acceleration procedures.

Numerical Tests

Several cases have been run to establish the convergence characteristics of the procedure. The three steps required are:

1. Obtain the solution for the homogeneous system corresponding to the source problem.
2. For the source problem, carry out ten unaccelerated iterations starting with an initial flux guess of zero, then Do the extrapolation in the ℓth iteration according to the formula

$$\phi^{(\ell)} = \phi^{(\ell)} + Q[\phi^{(\ell)} - \phi^{(\ell-1)}]. \tag{9}$$

   The Q factor is given by Eq. (7) using the eigenvalue determined in Step 1.
3. Complete the convergence of the source problem using the usual Chebyschev acceleration.[1]

The QX1 program was modified to carry out these steps with the exception that the Q factor was applied to the ℓth iterate of the fission source rather than the flux. The results were compared with the previous version QX1 which used only Chebyschev acceleration.

Figures IV-21-1 and IV-21-2 show typical comparisons of the two methods. The reactor model used in these tests was a two enrichment zone LMFBR core of approximately 3200 liters with a core height of 61 cm. (This geometry was chosen so that the eigenvalue separation in the cylindrical QX1 problem would be relatively poor). The neutron source was calculated from the ^{240}Pu disintegration rate as a function of radius.

Figure IV-21-1 shows the convergence characteristic of the two methods with the neutron yield per fission adjusted arbitrarily to a homogeneous system eigenvalue of 0.98826. The direct Chebyschev method shows an erratic acceleration sequence resulting from its sensitivity to the estimate of the largest eigenvalue of $M^{-1}F$; 92 iterations were required to reach convergence. Normalization according to Eq. (9) results in more uniform behavior and more rapid convergence (41 iterations). Figure IV-21-2 shows the same plot except that the initial eigenvalue was adjusted to 0.99714. In this case the direct Chebyschev method fortuitously reached almost the correct source magnitude at the end of an acceleration sequence, so that it converged rapidly. A third case was run in which the initial eigenvalue was 0.99990. The direct method did not converge, but the proposed method converged in the same number of iterations as the cases shown in Figs. IV-21-1 and IV-21-2. The same general convergence behavior was shown in several other cases which were run to test the method.

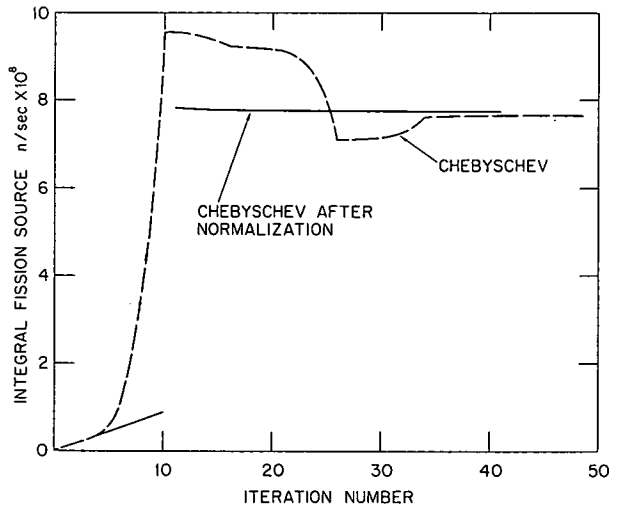

Fig. IV-21-1. Convergence Behavior of Two Acceleration Methods as Characterized by the Integrated Fission Source at Each Iteration; $K_0 = 0.98826$. *ANL Neg. No. 116-1082*

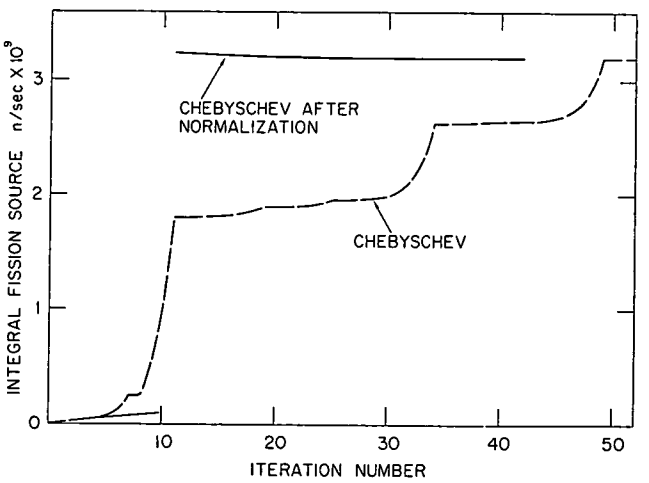

Fig. IV-21-2. Convergence Behavior for $k_0 = 0.99714$. *ANL Neg. No. 116-1081.*

Alternative Method

An alternative procedure is available which does not have the disadvantage of introducing higher harmonic contamination, but which requires more preliminary calculations. This alternative method may be useful for kinetics applications using the factorization method, since many of the subsidiary calculations must be performed for other purposes.

The source-free adjoint equation for the system given in Eq. (1) is written:

$$(M - \frac{1}{k_0} F)^T \phi^* = 0 . \tag{10}$$

This function and the real homogeneous flux, ϕ_0, are obtained first. Then the source function u of Eq. (2) is obtained by solving the equation

$$Mu = S, \tag{11}$$

which requires one outer iteration in codes such as DIF2D. Taking the inner product of ϕ^* with u determines a_0 in the expansion of u from the expression

$$\langle \phi^*, u \rangle = a_0 \langle \phi^*, \phi_0 \rangle. \tag{12}$$

The inhomogeneous problem iterative solution can then be initiated with a starting guess of

$$\phi^{(\ell=0)} = \frac{a_0}{1 - k_0} \phi_0 . \tag{13}$$

This alternate scheme has not been tested in QX1.

Reference

1. D. A. Meneley, K. O. Ott and E. S. Wiener, *Fast Reactor Kinetics—The QX1 Code*, ANL-7769 (1971).

IV-22. Application of the VIM-I Monte Carlo Code to the Analysis of ZPPR Assembly 2 Experiments

F. L. Fillmore*

Introduction

The VIM-I Monte Carlo code[1] which is being developed at AI (Atomics International) was obtained to aid in the analysis of the Fast Breeder Reactor critical experiments being performed at Argonne National Laboratory. This code is designed specifically to deal with the plate-type critical assemblies being studied and it takes advantage of the repetitive nature of the geometry of these assemblies to reduce the storage requirements for input data and to make the computing time spent in the geometry routines as short as feasible. The basic unit of geometry in VIM is the drawer, and each drawer is divided into several zones which correspond to the matrix, plates, and cans of the actual assembly. Geometry routines are also available for treating concentric homogeneous spheres and cylinders.

The VIM cross section library is based on ENDF/B VERSIONS I and II data. Each isotope in the library has its own energy grid which is tailored to meet its particular needs. Cross section data are entered for each energy point, and provision is made in the code for interpolating between points. The entire library is packed into linear arrays to conserve storage space in the computer. Resolved resonances are described by Doppler broadened pointwise data. Unresolved resonance cross sections are treated by a probability table method[2] in which the tables are based on many ladders of resonances constructed by sampling the statistical distributions for the unresolved resonance parameters. The scattering angles for anisotropic elastic scattering are obtained by sampling probability distribution

* Atomics International, a Division of North American Rockwell Corporation, Canoga Park, California.

tables which are based on the Legendre expansion coefficients of the cross section. The use of these tables in place of the Legendre coefficients results in a considerable savings in computation time.

The VIM code has certain advantages over conventional multigroup methods in the analysis of critical experiments. It permits a complete three-dimensional description of the assembly including plate heterogeneity, partially inserted control rods, etc. Adequate geometrical detail can be included to eliminate the necessity of applying correction factors to the final results. Correlated sampling and adjoint Monte Carlo techniques are being developed at AI which will enable the analysis of small sample and reactivity coefficient experiments in a more rigorous manner than is possible with conventional multigroup methods. Since the VIM cross section library is based on pointwise data, the approximations which are encountered in the construction of multigroup libraries are eliminated. The VIM library can be made as accurate as desired within the limitation of computer storage capacity, and this is no problem with the large computers now coming into use. A disadvantage of all Monte Carlo methods when applied to criticality calculations is their relatively slow convergence when compared with one- and two-dimensional multigroup methods. This comparison is much more favorable for three-dimensional calculations, and in situations where a three-dimensional calculation is considered essential, the added rigor permitted by the VIM code could make it the preferred method of analysis.

Code Modification at ANL

Since VIM was originally coded for use on the CDC-6600 computer, it was converted at ANL to run on the IBM-360/75. This conversion was complicated by the short word length of the IBM equipment. Reprogramming was required in several places to get around difficulties caused by the lack of adequate numerical precision. The dimensions of the code were also increased and the edit enlarged to accommodate problems of the size of the ZPPR critical assembly which has two core regions, three blanket regions, and two reflector regions. Extensive use was made of DISK storage for the permanent storage of the VIM cross section library and of certain output results which are subjected to detailed analysis after the Monte Carlo calculation is finished. Codes were developed to perform this analysis.

The original VIM code received from AI was designed for use with the VERSION I VIM cross section library only. When the VERSION II VIM library was obtained from AI, extensive coding changes were required to enable its use at ANL. Other revisions which were supplied by AI were also added.

Restart capability for VIM, which enables a calculation to be extended by making a second computer run, was developed at ANL. With restart capability the user can examine the results of a run of moderate length to see if they are reasonable before committing himself to a long run to obtain better convergence. The restart feature also allows a run which terminates abnormally because of computer malfunction or other abnormal condition to be restarted at a point just before the failure occurred. An option was also provided to store the initial coordinates of all source particles on tape so that fixed-source calculations using these coordinates can be done at a later time.

Monitoring of fission ratios over a central portion of the core of the critical assembly was included in the VIM code received from AI. Provision for monitoring ^{238}U absorption over this region was added at ANL as well as monitoring of multigroup flux over central portions of the inner and outer cores and of the blanket regions. Examination of results from multigroup calculations shows that the neutron spectrum is essentially independent of position over the central $\frac{1}{8}$ of the inner core. The spectrum at the radial midpoint of the outer core where spectrum measurements were made is nearly the same as the integrated spectrum over the central part of the outer core over which the spectrum is monitored.

Calculations Performed

In order to determine that the code was working properly on IBM equipment, calculations were made for ZPR-3 Assembly 48 and JEZEBEL for comparison with results obtained at AI for these assemblies. After the comparisons were seen to be satisfactory, calculations were made for ZPPR Assembly 2. Selected results from these calculations are presented in Table IV-22-I.

The heterogeneous model for ZPPR Assembly 2 is based on the equal-core volume loading number 90[3] and contains over 40,000 zones and six different drawer types. The homogeneous model was formed by homogenizing the core and blanket regions of the heterogeneous model. The experimental value of k for this loading is 1.0006. The calculated values of k using the Version-II VIM library are about 2% lower than results obtained with two-dimensional diffusion theory.[4] The discrepancy is not well understood, but may be due in part to shortcomings in the unresolved resonance probability tables that were used in the calculations. The heterogeneity effect obtained by taking

TABLE IV-22-I. VIM Monte Carlo Results

Assembly	Model	ENDF/B Cross Section Data	Number of Histories	Computer Time, min.	k	Collisions per History
ZPR-3 No. 48	Heterogeneous	VERSION I	25,600	76	1.0005 ± 0.0060[a]	40.0
ZPR-3 No. 48	Spherical	VERSION I	25,600	45	0.9689 ± 0.0070	40.4
JEZEBEL	Spherical	VERSION I	50,000	7.3	1.0047 ± 0.0043	2.19
JEZEBEL	Spherical	VERSION II	50,000	8.4	0.9900 ± 0.0040	2.27
ZPPR No. 2	Heterogeneous	VERSION I	10,000	44	0.9834 ± 0.0152	53.5
ZPPR No. 2	Heterogeneous	VERSION II	100,000	485	0.9465 ± 0.0038	54.9
ZPPR No. 2	Homogeneous	VERSION II	100,000	347	0.9322 ± 0.0038	55.1

[a] An error was found in the inelastic scattering evaporation model data after this calculation was completed. Correcting these data would reduce the value of k by about 3%.

TABLE IV-22-II. Central Reaction Rate Ratios in ZPPR Assembly 2

Quantity	Homogeneous Model	Heterogeneous Model	Experiment[a]
$^{238}U_f/^{235}U_f$	0.0209	0.0195	0.0201 ± 0.0004
$^{239}Pu_f/^{235}U_f$	0.9278	0.9201	0.9372 ± 0.0142
$^{240}Pu_f/^{235}U_f$	0.1830	0.1739	0.1704 ± 0.0026
$^{241}Pu_f/^{235}U_f$	1.345	1.385	—
$^{238}U_a/^{235}U_f$	0.1756	0.1790	—

[a] See Ref. 5

the difference between the heterogeneous and homogeneous values of k is 0.0143 ± 0.0054. This compares favorably with the value of about 0.012 obtained with multigroup methods.[4]

Central reaction rate ratios for ZPPR Assembly 2 are presented in Table IV-22-II. The calculated values are from the 100,000 history runs using the Version-II VIM library. Standard deviations for the calculated values were not computed but are estimated to be about 0.25% for ^{239}Pu and better than 1% for the rest. The two calculational models give results for the fission threshold materials ^{238}U and ^{240}Pu which differ by considerably more than the estimated standard deviations. Agreement between the results from the heterogeneous model and experiment is fairly good.

Preliminary evaluation of the calculated neutron spectra from the 100,000 history runs shows general agreement with results from two-dimensional diffusion theory calculations. However, in a few of the groups the differences are as much as two or three standard deviations. The standard deviations for groups between 1.2 keV and 3.7 MeV range from about 1 to 3.5%, while standard deviations outside this energy range are larger because only part of the neutron histories enter the high and low energy groups. The agreement with experiment is less satisfactory. This is not surprising since it is known that there are deficiencies in the ENDF/B VERSION II data upon which the VIM library is based.

References

1. L. B. Levitt and R. C. Lewis, *VIM-I, A Non-multigroup Monte Carlo Code for Analysis of Fast Critical Assemblies*, AI-AEC-12951 (1970).
2. L. B. Levitt, *The Probability Table Method for Treating Unresolved Resonances in Monte Carlo Criticality Calculations*, Trans. Am. Nucl. Soc. **14**, 648 (1971).
3. R. E. Kaiser, A. L. Hess and R. J. Norris, Argonne National Laboratory (private communication).
4. A. P. Olson, Argonne National Laboratory (private communication).
5. R. E. Kaiser, Argonne National Laboratory (private communication).

IV-23. Monte Carlo Calculations

C. N. KELBER

On January 11, 1971 a Monte Carlo Committee was formed in the Applied Physics Division, ANL, to assess the role that Monte Carlo methods and codes should play in the divisional programs, especially the critical experiment program.

The committee's attention has been focused on the development of the new code, VIM,[1] with a view towards its future use in support of the critical experiment program. This is natural because the geometric description of the systems studied by VIM is designed to permit highly detailed simulation of the critical experiments carried out in ZPR-6, ZPR-9 and ZPPR.

The committee has met several times with members of the Atomics International staff who are developing VIM and has concentrated on devising test programs to establish the validity of proposed means of simulating unresolved resonances. Priorities of various options in VIM have also been discussed with the AI staff. These priorities have been based on the following preliminary assessment of the capability of a fully developed Monte Carlo code.

A full-capability Monte Carlo code can do the following things:

(1) Compute the expected value of k_{eff}.
(2) Compute the expected flux level as desired in selected regions of energy and spatial location.
(3) Estimate the detector response corresponding to actual measurements.
(4) Estimate the perturbations introduced by small changes in specified regions (as in Doppler experiments) and predict the effect on measured parameters (such as the period).

Thus, a full-capability code is able to duplicate on the computer the experiment carried out in the critical facility. With cross sections taken directly from the ENDF/B tape, and with an accurate simulation of the experiment geometry, it is possible to pinpoint discrepancies between experiment and theory and determine the needed corrections. This is similar to the use of transport theory to correct diffusion theory, two-dimensional codes to correct one-dimensional codes, etc.

Variance reduction techniques are associated with Monte Carlo procedures because of the latter's statistical nature. In a diffusion theory calculation, for example, the result will be the same each time the same input is used. In a Monte Carlo calculation the result differs each time a quantity is estimated, from the previous estimates. The estimates are averaged to give the "expected value." The variance is an estimate of how much various estimates can be expected to differ from the "expected value." When the variance is small, the "expected value" is known with great certainty to be a good estimate of the average value that would be obtained by running the calculation for a very long time. When the variance is large, the "expected value" is a poor estimate of what one would obtain by running the calculation for a long time. Thus, variance reduction techniques are important in obtaining useful results in reasonable amounts of computing time. Because Monte Carlo procedures are analogs of the actual experiments, variance reduction techniques frequently have to be devised to suit each class of calculation. Nevertheless, there is a large body of experience to draw upon;[2,3] the important thing is to acquire the necessary expertise to know how to apply techniques that already have been developed and extend older methods to new problems.

Although Monte Carlo procedures are statistical methods, they are precise in important ways. The geometry of the actual experiment can be simulated, and the detailed energy dependence of the cross sections (as well as we know it) can be taken into account without any intervening approximations. The more typical diffusion or transport theory calculation makes approximations of varying kinds, both in simulation of geometry and energy dependence of cross sections. When, as is almost always the case, there is a discrepancy between calculation and experiment, it is necessary to find out if the intervening approximations are a major source of error. By use of Monte Carlo as a standard, the errors inherent in various methods can be assessed and thus the source of the discrepancies pinpointed. Within the LMFBR program a Monte Carlo treatment of resonance absorption and the Doppler effect has been used to assess the adequacy of transport theory methods[4] and the treatment of unresolved cross-section resonances.[5]

Because it is an analog process, the Monte Carlo method can be used to simulate two kinds of mockups: a critical experiment and an actual design. If the variance is small enough, the results form a standard for judging the adequacy of a number of methods of extrapolating from experiment to design. For example, suppose one wants to know the rod worth and power distribution associated with an off-center control rod. These alternatives could be studied:

(1) Perform a highly detailed mockup with many changes of configuration and many measurements.

(2) Perform a few highly detailed mockups and interpolate by multi-dimensional diffusion theory.

(3) Perform a "benchmark" experiment with an off-center rod simulated and use multichannel synthesis.

The first course is the most expensive and is applicable only to the specific design. The second is more useful but is difficult to use in general because of the difficulty of simulating geometry well. Thus, the interpolation might not be good for other designs. The third method is cheapest, but is one in which there is little a priori confidence. By testing the proposed synthesis against a number of Monte Carlo simulations, confidence in the method as applied to the specific problem can be established. Moreover, the same technique can be used to establish the applicability of the method to other designs. Thus, the use of Monte Carlo simulations as standards to test calculational methods extends the applicability and utility of critical experiments.

The use of Monte Carlo calculations as standards for the development of more economical but less accurate design methods is well known. A typical example is the testing of the resonance absorption code, RABBLE,[6] where Monte Carlo results[7] were used as the standard of accuracy to ascertain the accuracy of the new code.

These objectives are reasonable at this time because progress in the development of computing machines and Monte Carlo procedures[8] have progressed to the point where such procedures are competitive with two-dimensional transport theory and more economical of computing time in three dimensions.

References

1. L. B. Levitt and R. C. Lewis, *VIM-1, A Non-multigroup Monte Carlo Code for Analysis of Fast Critical Assemblies*, AI-AEC-12951 (May 15, 1970).
2. H. Greenspan, C. Kelber and D. Okrent, *Monte Carlo Methods in Reactor Computations*, Computing Methods in Reactor Physics, (Gordon and Breach, New York, N. Y., 1968) Chapter 5, pp. 365–431.
3. J. Spannier and E. M. Gelbard, *Monte Carlo Principles and Neutron Transport Problems* (Addison-Wesley Publishing Co., Reading, Mass., 1969).
4. L. B. Miller and G. H. Miley, *Some Monte Carlo Techniques for the Calculation of Doppler Coefficients*, Nucl. Sci. Eng. **40**, 438 (1970).
5. C. N. Kelber and P. H. Kier, *The Effect of Randomness on Group Cross Sections, I*, Nucl. Sci. Eng. **24**, 389 (1966); also, see *The Effect of Randomness on Group Cross Sections, II*, Nucl. Sci. Eng. **26**, 67 (1966).
6. P. H. Kier, *A Method of Calculating Mutual Shielding Between Resonances of Different Nuclides*, Trans. Am. Nucl. Soc. **8** (1), 286 (1965).
7. N. R. Candelore and R. C. Gast, *RECAP-2, A Monte Carlo Program for Estimating Epithermal Capture Rates in Rod Arrays*, WAPD-TM-427 (1964).
8. N. F. Cross and E. C. Crume, *The Use of Third Generation Computers in Monte Carlo Criticality Calculations*, Proc. Conference on the Effective Use of Computers in the Nuclear Industry, Knoxville, Tennessee, April 21–23, 1969, CONF-690401, pp. 650–658.

IV-24. Development of Computer Programs for the Statistical Generation of Fast Neutron Reaction Cross Sections

P. A. Moldauer

Recent high resolution experiments demonstrate that neutron cross sections in the fast reactor spectrum display large and rapid fluctuations about their energy averages. While it is hopeless to determine the very large numbers of parameters required to describe these fluctuations in detail, it is possible to obtain a statistical description in terms of the moments and correlation coefficients of the cross section fluctuations. Such a description is important for two reasons. First of all, by fitting statistical fluctuation parameters with theory, one obtains a better determination of optical and statistical model parameters than is available from average cross section fitting alone. This in turn improves the reliability of predicted average cross sections and fluctuations. Secondly, the statistical fluctuation parameters can be used to estimate the effect of cross section fluctuations on integral properties of reactors.

As a step in this program of utilizing cross section fluctuation information, a set of interrelated FORTRAN IV programs named STASIG have been prepared. These programs generate detailed neutron cross sections from optical and statistical model input parameters, combine and average them, and analyze their statistical properties in such a way that the results can be compared directly with similar statistical analyses of experimentally determined fluctuating cross sections.

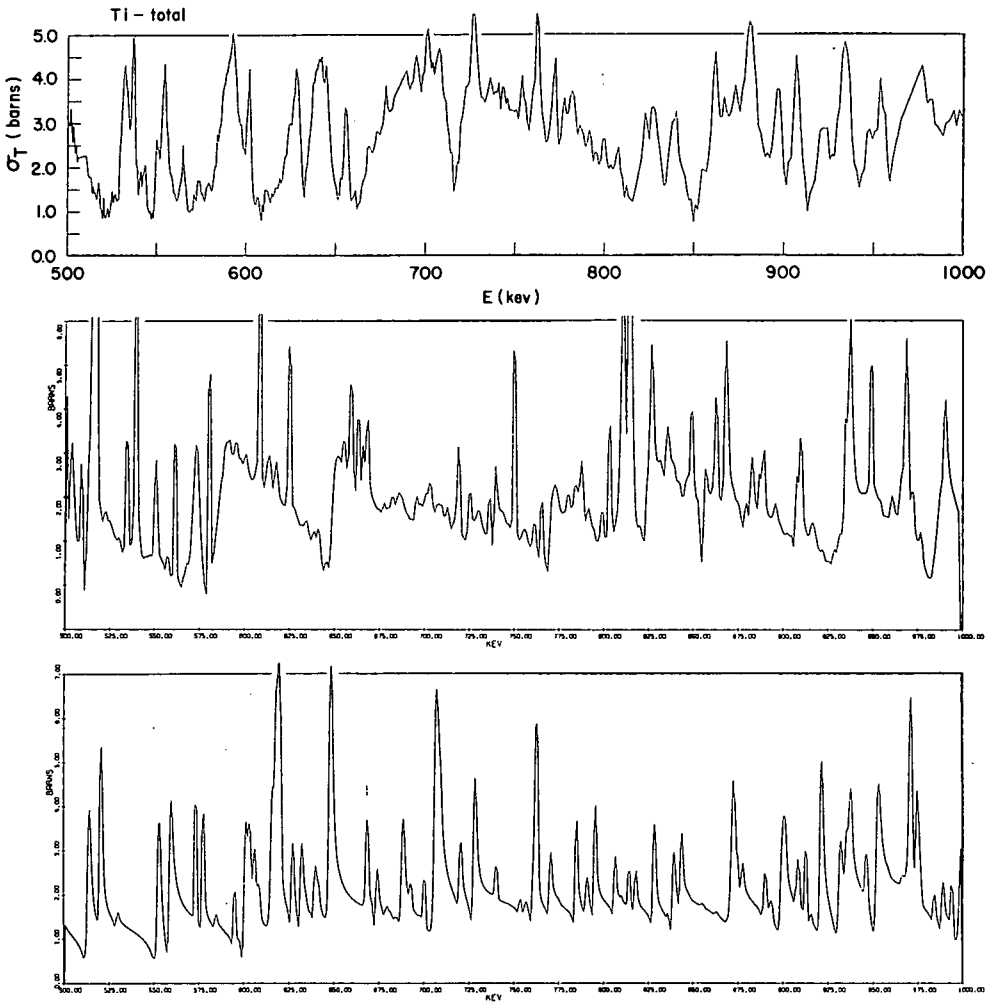

FIG. IV-24-1. Top: Experimental Total Neutron Cross Section for Titanium from 500 to 1000 keV. Middle and Bottom: Two Statistically Generated Total Cross Sections Obtained with Different Optical Model Parameters. *ANL Neg. No. 116-821.*

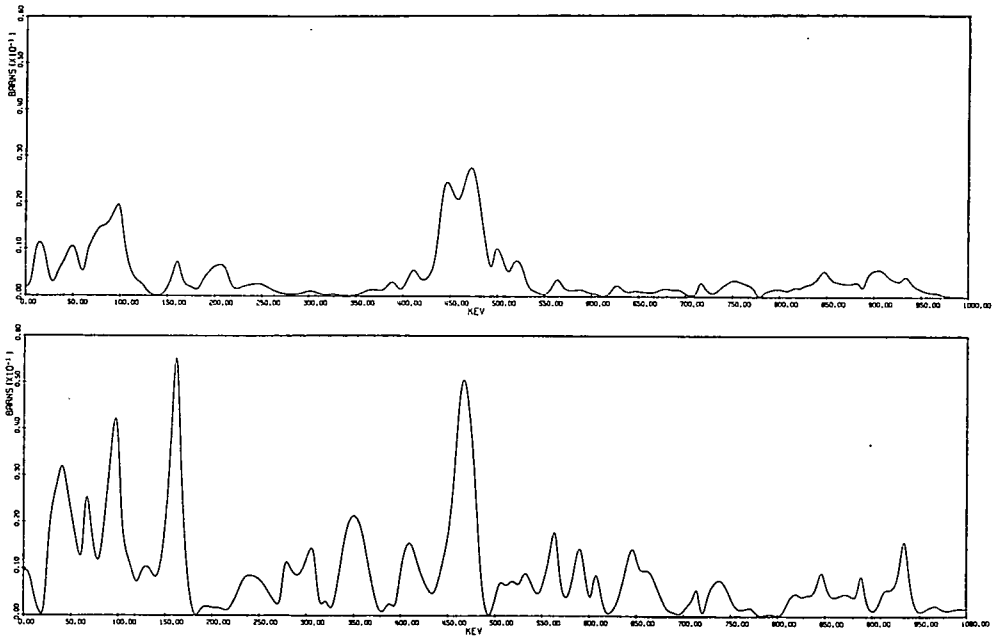

FIG. IV-24-2. Statistically Generated "Doorway State" Correlation in Two Different Reaction Channels in a 25-Channel Model. *ANL Neg. No. 116-822.*

The procedure has been applied to the statistical analysis of fast neutron scattering by iron and titanium. As an example, Fig. IV-24-1 compares the experimental total neutron cross section for titanium from 500 to 1000 keV (top curve) with two statistically generated cross sections (bottom curves). The two theoretical curves differ in the optical model parameters used, the top curve indicating more absorptions than the bottom curve. Though both of these optical models give a good account of average scattering data, they are seen to yield very different fluctuation patterns.

A second application has been to improve the theoretical understanding of average cross sections and cross section fluctuations and correlations. Figure IV-24-2 shows an example of a statistically generated correlation of the fluctuation in two independent reaction channels. The frequency of occurrence of such features, which are often described as "doorway states," can thus be predicted by the statistical theory.

Section V

Miscellaneous

This section comprises a miscellany treating a small variety of nuclear topics, none of which readily fits into the first four sections of the report.

V-1. Safety Effects of Light Water Infiltration in the Argonne Research Reactor, CP-5

C. N. KELBER

In the course of the recent rehabilitation of CP-5, a study was made of the safety problems associated with in-leakage of light water into the primary coolant (heavy water) stream from a tube rupture in the main heat exchanger.[1] The reactivity effects of the light water can be represented by a prompt positive coefficient and a delayed negative coefficient during normal operation. When the rods are pulled out (as during recovery from xenon poisoning), the effects of light water are to decrease the reactivity.

The plant is designed to render water in-leakage highly unlikely. Even in case such in-leakage occurs, the plant protection system is capable of protecting the system against rupture of many tubes in rapid succession.

The calculated effects compared well with experimental results.[2] It was calculated that the scram system offered protection against failure rates in the main heat exchanger of up to 20 tubes per second.

REFERENCES

1. C. N. Kelber, *Safety Effects of Light Water Infiltration in the Argonne Research Reactor (CP-5)*, Nucl. Sci. Eng., **47**, 127–131 (1972).
2. J. H. Talboy, E. J. Donahue, A. W. Pierce and J. J. Vronich, *Positive Reactivity from Replacement of Heavy Water by Light Water in the Coolant Channels of a Heavy Water Moderated Reactor*, Nucl. Sci. Eng. **43**, 227 (1971).

V-2. Physics Analysis for the CP-5 Fuel Study

P. J. PERSIANI and JAMES H. TALBOY*

The primary objectives of the physics analysis for a modified core loading for CP-5 were (1) to determine the core loading requirements for new fuel designs; (2) to maintain the capability of in-core experimentation; and (3) to maintain and to possibly increase the high energy component of the neutron energy spectrum for this in-core facility.

The box-type plate-element designs of the Georgia Tech Research Reactor (GTRR) and the Ames Laboratory Research Reactor (ALRR) were selected as candidates for the alternate CP-5 fuel loading. The differences between the two designs are mainly the content of the uranium-aluminum alloy and the aluminum content in the assembly. The GTRR fuel assembly consists of 16 fuel plates containing a total of 188 g of ^{235}U. The ALRR assembly is designed as a 15 fuel-plate system containing 170 g of ^{235}U. If these assemblies were to replace the 17 CP-5 tubular assemblies, the reactivity effects, $\Delta k_{eff}/k_{eff}$, would be decreased by 0.0078 for the GTRR design and 0.0328 for the ALRR-type assembly relative to the CP-5 base core. The calculated results are tabulated in Table V-2-I. The reactivity changes in CP-5 dollars ($1.00 = 0.0074) are approximately $1.00 and $4.50 for the GTRR and ALRR designs respectively. It appears, therefore, that the GTRR assembly is almost interchangeable with the current CP-5 core loading. This means that the operational and loading procedures could continue according to the present practices as far as reactivity considerations are concerned. On this basis, the GTRR-type elements were then considered as the alternate assembly design to be compared with the CP-5 fuel elements.

To maintain an in-core facility capability in the GTRR loading, one or more fuel assembly positions would have to be made available. The optimum positions were found to be in the row (or circle) of assemblies adjacent to the center assembly. Making two assembly positions available while still retaining an excess reactivity of about $28 or $k_{eff} = 1.2614$, the ^{235}U content in the GTRR design would have to be increased from 188 to 213 g per assembly. The assembly reactivity worths in the next outer row are found to differ very little from that of the assemblies adjacent to

* Research Reactor Operations Division, Argonne National Laboratory.

TABLE V-2-I. Calculated k_{eff} and Reactivity Change for GTRR and ALRR Assemblies

17-Assembly Core	CP-5 Base	GTRR Base	ALRR Base
k_{eff}	1.2614	1.2516	1.2200
Δk_{eff}	—	−0.0098	−0.0414
$\Delta k_{eff}/k_{eff}$	—	−0.0078	−0.0328

TABLE V-2-II. Calculated Relative Total Flux and Spectral Index at Three Core Positions

Core Position	Center	2nd Row	3rd Row
Relative flux	1	0.9	0.6
S.I.	1.43	1.64	2.84

the center assembly. Therefore, a 15-assembly core with assemblies removed from either the second or outer row would, in effect, not change the operating excess reactivity, and on this basis the in-core facility could be placed in either row.

However, since the experiments utilizing the in-core capability of CP-5 require a hard neutron spectrum, the position closest to the core center becomes the more desirable feature to incorporate in the alternate CP-5 core. The optimizing parameter used was the spectral index, defined as

$$\text{S.I.} = \frac{\int_0^\infty \phi(E)dE}{\int_{1ev}^\infty \phi(E)dE},$$

which is analogous to the cadmium ratio index. The computed spectral index for the various core positions are listed in Table V-2-II.

Also included in Table V-2-II are the expected flux levels, relative to the center position, at the two outer row positions. A 20 % increase in the spectral index is to be considered as the more tolerable compromise of the parameter characterizing a major feature of CP-5. It is on this basis that if the GTRR-type assembly were used, a core loading of 15 assemblies could be accomplished with two in-core facility positions available in the second row.

Additional investigations included a series of preliminary studies using several converter designs to reduce the S.I. parameter below 1.43. Using the CP-5 tubular assembly design as a base, the internal thimble was replaced by an aluminum-clad fueled element (40 g ^{235}U). An alternate design included interchanging the aluminum liner with a cadmium liner. In this manner, the cadmium liner would reduce the thermal component of the energy spectrum and the fueled thimble would partially recover the reduction in the operating excess reactivity. The results are tabulated in Table V-2-III for two cadmium alloy liners, one having a 10 % atom concentration of cadmium and the other at 100 % cadmium.

The scoping computations indicate that an appreciably enhanced hard component of the spectrum S.I. = 1.03 can be achieved with the fueled thimble and the 100 % cadmium liner. However, a reduction of 38 % in total flux is to be expected in this design. This condition could be appropriate for those irradiation experiments requiring that the effects on a measurement by the thermal neutrons relative to the high energy neutrons be minimized.

In the last column of Table V-2-III is included the effect of a simple converter design having an aluminum thimble with a 10 % cadmium liner. It appears that these conditions do not differ very much from those obtained with a fueled thimble. The advantage of the aluminum thimble design would be in not having to disturb the overall heat transport configuration of the core.

These scoping studies were made to appraise certain converter designs relative to the current CP-5 tubular-fueled elements. If the converters were placed in the second row of a 15-assembly GTRR loading, the S.I. indices would be expected to increase by about 20 %.

In summary, then, without an effort to provide a converter for an in-core facility capability, a 15-assembly GTRR-type core loading would severely compromise a major experimental capability of the CP-5 reactor.

TABLE V-2-III. Calculated Percent Excess Reactivity, Spectral Index, and Relative Total Flux for Various Converter Designs

Thimble.....	Al	Fuel	Fuel	Fuel	Al
Liner:.....	Al	Al	Cd 10%	Cd 100%	Cd 10%
% $\Delta k_{eff}/k_{eff}$	20.7	20.8	18.5	17.8	18
S.I.	1.43	1.36	1.16	1.03	1.18
Relative total flux	1.0	1.01	0.74	0.62	0.71

V-3. Analysis of Compton Continuum Measurements

RAYMOND GOLD and I. K. OLSON

The development of high-resolution (lithium-drifted) solid-state detectors for gamma-ray measurements is a significant experimental advance which has been widely applied in nuclear spectroscopy. Work with these detectors has focused on precise definition of nuclear energy levels by accurate gamma-ray-energy measurements (of photopeak response). In such investigations, only a limited number of transitions can be successfully analyzed because of the dominance of the Compton response in these detectors. Hence, these detectors cannot be used in the same manner (i.e., as photopeak detectors) for measurement of continuous gamma-ray spectra.

Although the dominance of the Compton recoil continuum in these detectors is regarded as an unwanted and troublesome complication in nuclear (energy-level) spectroscopic studies, it is precisely this response which can be exploited for continuous gamma-ray spectroscopy.[1-4] Indeed, the Compton distribution and the continuous gamma-ray spectrum are directly related by a well-defined integral equation. Consequently, the continuous gamma-ray spectrum can be determined from an unfolding calculation[5] in terms of the measured electron-recoil spectrum.

Compton-continuum measurements have been carried out with solid-state silicon detectors. In these silicon detectors, the Compton response dominated by more than two orders of magnitude in the broad energy region from 100 keV up to a few MeV. Consequently, all other photon-interaction modes can be neglected and the response kernel (or response matrix) can be calculated from first principles, provided corrections have been introduced for effects of finite detector size. It is of interest, therefore, to compare the present treatment with the work of Silk,[6,7] who has independently recognized the merit of Compton-continuum measurements.

Five computer programs: COMPSCAT, FEND, GABCO, DOSE, and COMPLOT, have been developed for the analysis and reduction of electron-recoil spectra. The relationship among these programs is depicted in Fig. V-3-1. The COMPSCAT program constructs the Compton response function (C-matrix) and uses iterative unfolding to obtain the gamma continuum from the experimental electron-recoil data. In addition, COMPSCAT provides the random error induced in the unfolded gamma spectrum. Under this option, an error matrix is constructed and iterative unfolding is again employed to obtain error estimates.

Correction of the gamma spectrum for the contribution due to gamma rays beyond the high-energy truncation point of the response matrix is carried out in the program FEND. The FEND program extrapolates the gamma continuum furnished by COMPSCAT into this high-energy region and thereby furnishes the corrected electron vector, *WP*, which can again be processed by COMPSCAT.

Program GABCO provides for correction of finite-size effects. Measurements of silicon detector response due to monoenergetic gamma rays are used in GABCO

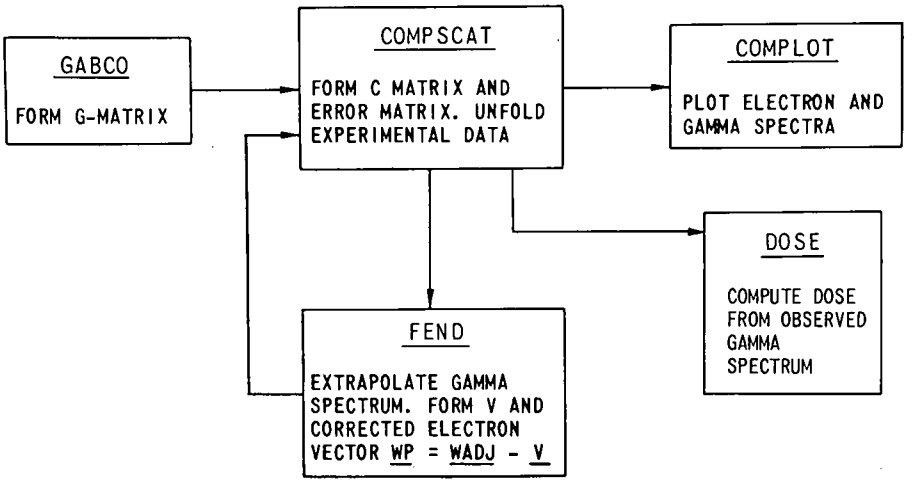

FIG. V-3-1. Block-Diagram Form of the Relationship Among the Computer Programs COMPSCAT, FEND, GABCO, DOSE and COMPLOT. *ANL. Neg. No. 118-3190 Rev. 1.*

to form the G-matrix—a matrix which describes the effects of finite detector size. The G-matrix is used, in turn, in COMPSCAT to correct the observed recoil-electron spectrum for finite-size effects.

Program DOSE applies an additional finite-size correction, the P-matrix, to gamma spectra produced by COMPSCAT. The corrected gamma continuum is then used in DOSE to calculate the (infinite medium) physical dose.

It is essential that electron and gamma spectra be available for examination and comparison at crucial stages of the data-reduction process. These requirements are satisfied by the plotting program COMPLOT. The COMPLOT program uses output from COMPSCAT to plot the desired electron or gamma spectrum.

A topical report[8] has been issued containing detailed descriptions of the computer codes COMPSCAT, FEND, GABCO, DOSE, and COMPLOT, respectively. To further illustrate the manner in which these codes function, treatment of a sample measurement is followed through all programs, and results of the data treatment for this case are given. Actual listings of these five programs are given in this report as well as computer input and output for the sample measurement.

References

1. R. Gold, *Compton Continuum Measurements for Continuous Gamma-ray Spectroscopy*, Bull. Am. Phys. Soc. **13**, 1405 (1968).
2. R. Gold, *Compton Recoil Continuum Measurements for In-core Gamma-ray Spectroscopy*, Reactor Physics Division Annual Report, July 1, 1967 to June 30, 1968, ANL-7410, pp. 373–377.
3. R. Gold, *Compton-recoil Gamma-ray Spectroscopy*, Nucl. Instr. Methods **84**, 173–194 (1970).
4. R. Gold, *Compton Recoil Measurement of Continuous Gamma Spectra*, Trans. Am. Nucl. Soc. **13**, 421 (1970).
5. R. Gold, *An Iterative Unfolding Method for Response Matrices*, ANL-6984 (1964).
6. M. G. Silk, *Iterative Unfolding of Compton Spectra*, AERE-R-5653 (1968).
7. M. G. Silk, *The Energy Spectrum of the Gamma Radiation in the Daphne Core*, J. Nucl. Energy **23**, 308 (1969).
8. R. Gold and I. K. Olson, *Analysis of Compton Continuum Measurements*, ANL-7611 (1970).

V-4. Some Comments on the Power Balance Parameters Q and ϵ as Measures of Performance for Fusion Power Reactors

P. Persiani, W. C. Lipinski* and A. J. Hatch†

I. Introduction

A survey of analytical studies of power-producing fusion reactors[1] indicates that reactor systems may require a complex of plasma-producing subsystems (containment, heating, and injection) and of energy conversion subsystems (thermal and direct). The power balance parameters used to characterize the behavior of some of these reactor systems are Q and ϵ. However, there are significant basic differences in the definitions as given by various authors. To establish a common basis for an intercomparison of these complex power systems, it has been found useful to define Q and ϵ based on a power balance of the total reactor system. The definitions are developed in Section II; limit tests and other considerations that demonstrate the generalized nature of these definitions are applied in Section III; comparison between the Q values computed from the various definitions are made in Section IV; and concluding remarks are contained in Section V.

* Reactor Analysis and Safety Division, Argonne National Laboratory.

† Physics Division, Argonne National Laboratory.

II. Definitions

The interrelationship between the subsystems of a power reactor system is shown schematically in Fig. V-4-1. The power balance equation for a reactor system may be written as the product form of the ratios of power output to power input for each of the subsystems

$$\frac{P_i}{P_c} \times \frac{P_o}{P_i} \times \frac{P_g}{P_o} \times \frac{P_c}{P_g} = 1 , \qquad (1)$$

where

$P_c \equiv$ circulating electrical power to the plasma preparation subsystem,

$P_i \equiv$ power input to the power source subsystem,

$P_0 \equiv$ power output from the power source subsystem,

$P_g \equiv$ gross electrical power output from the power conversion subsystem.

In Fig. V-4-1, the quantity $P_c - P_i$ is the power loss of the plasma preparation subsystem having an efficiency η_i ; $P_0 - P_g$ is the power loss of the conversion subsystem having an efficiency η_c ; and $P_g - P_c$ is the net electrical power output, P_e , available for external distribution. With the power multiplication factor Q

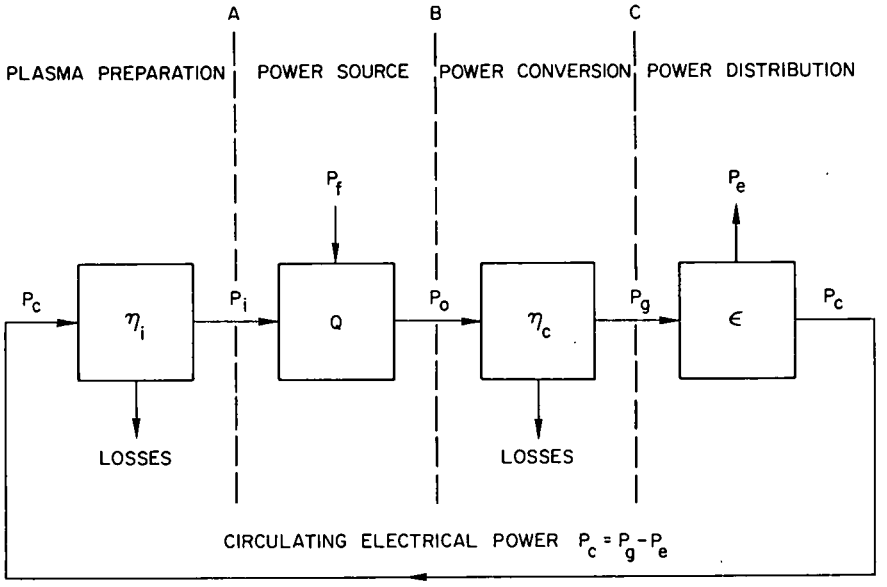

FIG. V-4-1. Basic Power Flow Diagram. *ANL Neg. No. 116-1080.*

of the power source subsystem defined as

$$Q = \frac{P_0}{P_i} \tag{2}$$

and the fractional circulating power ϵ defined as

$$\epsilon = \frac{P_c}{P_g}, \tag{3}$$

the power balance relation given by Eq. (1) may be written as

$$Q = \frac{1}{\epsilon \eta_i \eta_c}, \tag{4}$$

where $\eta_i = P_i/P_c$ and $\eta_c = P_g/P_0$.

Defining an overall system efficiency η as the product of η_i and η_c, Eq. (4) may be further reduced to

$$Q = \frac{1}{\epsilon \eta}. \tag{5}$$

The Q factor as defined in Eq. (2) is the ratio of the total reactor power output, P_0, (across interface B) to the total power input, P_i, (across interface A), where

$$P_0 = P_f + P_i, \tag{6}$$

and where P_f is the fusion power generated in the power source subsystem.

Alternatively, Q may be written in the useful form

$$Q = 1 + \frac{P_f}{P_i}. \tag{7}$$

As defined here, Q corresponds to $R + 1$ in Lawson's classic paper.[2] The parameter ϵ may also be written in the alternate useful forms

$$\epsilon = 1 - \frac{P_e}{P_g} \tag{8}$$

and

$$\epsilon = \frac{1}{1 + (P_e/P_c)}. \tag{9}$$

For the power source subsystem alone, the lower-limiting condition for $P_0 = P_i$ corresponds to $Q = 1$ in Eq. (2). If P_0 exceeds P_i (i.e., the subsystem is a power producer), then $Q > 1$ and the upper-limiting value $Q = \infty$ occurs if $P_i = 0$ (with P_0 finite). Therefore, the Q factor assumes a range of values

$$1 \leq Q \leq \infty. \tag{10}$$

As shown in Fig. V-4-1, P_g is the total power from the power conversion subsystem (across interface C), and P_c is the power flow into the plasma preparation subsystem. For a power producing system, the range of P_c is $0 \leq P_c \leq P_g$, and therefore from Eq. (3) the range of ϵ becomes

$$0 \leq \epsilon \leq 1. \tag{11}$$

The lower value corresponds to the condition that all of the gross electrical power output is available for external distribution (i.e. the circulating power is zero). The upper value corresponds to a system in which the total gross electrical power output must be circulated to maintain the system (i.e. the net electrical power output is zero). If the system is not self-sustaining, the power deficiency must be made up by an external electrical power source in order to maintain operation. Under these circumstances ϵ is greater than unity, corresponding to a negative P_e which implies an input

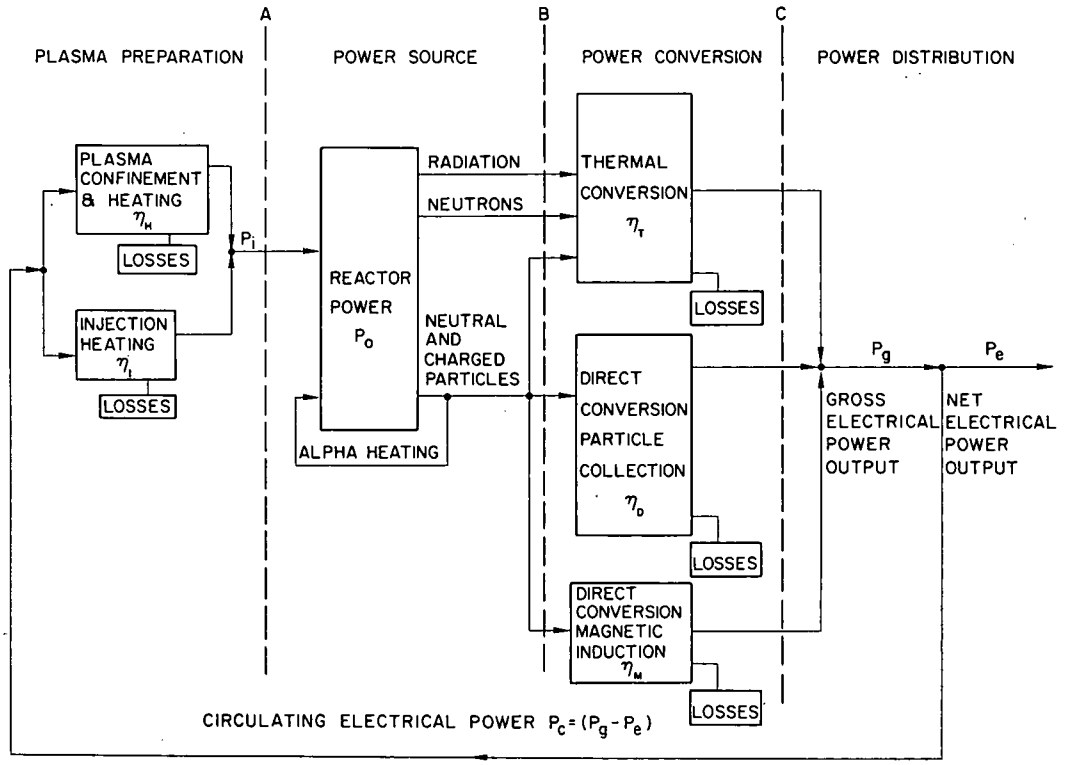

FIG. V-4-2. Typical Power Flow Diagram. *ANL Neg. No. 116-743, Rev. 2.*

power from an external system. Present experimental plasma systems operate in this range.

The significance of Eq. (4) for Q is that it incorporates ϵ and the efficiencies of the various subsystems for the entire reactor system. The relation states that for a Q value determined by the characteristics of the power source subsystem, a reduction in the fractional circulating power can be effected only by increasing the efficiencies of the power preparation and/or power conversion subsystems.

A more detailed power flow diagram of a typical fusion power reactor system[1] is shown in Fig. V-4-2.* The complete reactor system is divided into four major subsystems: plasma preparation, power source, power conversion, and power distribution. The plasma preparation subsystem is further subdivided into two minor subsystems and the energy conversion subsystem is divided into three minor subsystems as shown.

The input power, P_i, into the power source subsystem is the product of the circulating power, P_c, and the weighted efficiency, η_i, of the complex of plasma confinement and heating, and injection heating subsystems,

$$P_i = \eta_i P_c . \tag{12}$$

* Not shown explicitly in the diagram but implicit in the efficiency parameters are the power requirements of components related to plant operation such as the vacuum system, coolant pumps, magnet system, etc.

For the two plasma preparation subsystems shown in Fig. V-4-2,

$$\eta_i = f_H \eta_H + f_I \eta_I , \tag{13}$$

where f_H is the fraction of the circulating power necessary for the plasma confinement and heating subsystem having an efficiency η_H, and f_I is the fraction required to operate the injection heating subsystem having an efficiency η_I, with $f_H + f_I = 1$.

The gross electrical power output is the sum of the power converted by each of the conversion subsystems and is the product of the output power, P_0, and the overall conversion efficiency, η_c, of the complex of conversion subsystems,

$$P_g = \eta_c P_0 . \tag{14}$$

For the three power conversion subsystems shown in Fig. V-4-2,

$$\eta_c = f_T \eta_T + f_D \eta_D + f_M \eta_M , \tag{15}$$

where f_T is the fraction of the total power output, P_0, converted thermally with an efficiency η_T, f_D is the fraction converted by direct conversion with an efficiency of η_D, and f_M is the fraction converted by magnetic induction with an efficiency η_M, with $f_T + f_D + f_M = 1$.

The above treatment applied to the typical system of Fig. V-4-2 is equally applicable to even more complex

systems, with the overall system requirements still constrained by Eq. (4).

III. Limit Tests

The power balance relations derived from the above definitions are found to be consistent with limit tests for idealized systems. One such limit is obtained by considering an idealized reactor system in which all power conversion and injection subsystems are designed with 100% efficiencies, i.e. $\eta_i = \eta_c = 1$. In this limiting case, the Q factor from Eq. (4) becomes

$$\lim_{\eta_i,\eta_c \to 1} Q = \frac{1}{\epsilon}. \tag{16}$$

From Eq. (9), the Q factor in the above limit may also be written as

$$\lim_{\eta_i,\eta_c \to 1} Q = 1 + \frac{P_e}{P_c}, \tag{17}$$

which explicitly implies that for a given net electrical power output, high Q value reactor systems have relatively low circulating power requirements.

For a breakeven reactor system, that is, a zero net electrical power-producing system ($P_e = 0$), the critical Q factor, Q_{crit}, is obtained by taking the limit of Q as ϵ approaches unity,

$$\lim_{\epsilon \to 1} Q \equiv Q_{crit} = \frac{1}{\eta_i \eta_c} = \frac{1}{\eta}. \tag{18}$$

Equations (7) and (18) show the relationship between the system efficiency η and the power ratio P_f/P_i necessary to achieve a breakeven system. For an overall efficiency of $\eta = \frac{1}{3}$ as in the Lawson paper, $Q_{crit} = 3$, so that Lawson's parameter $R = P_f/P_i = 2$; that is, the fusion power source must be twice the input power for a breakeven condition.

For the combined limiting cases of 100% efficiencies and 100% fractional circulating power, the Q factor from Eq. (4) becomes

$$\lim_{\epsilon \to 1} \lim_{\eta_i,\eta_c \to 1} Q = 1. \tag{19}$$

This limiting Q value of unity represents a theoretical self-sustaining system in which the fusion power P_f approaches zero, and $P_i = P_0 = P_g = P_c$.

IV. Comparison with Other Q Definitions

Several other definitions of Q have been used in a variety of specific studies relating mostly to simple and minimum-B mirror machines. In a study of mirror systems incorporating direct conversion subsystems, Post[3] introduced the quantity Q_{EN} defined as

$$Q_{EN} = \frac{\textit{Converted nuclear power output}}{\textit{Net required input electrical power}} = \frac{P_g - \eta_D P_i}{(P_i/\eta_i) - \eta_D P_i}, \tag{20}$$

where all terms are defined in Section II. Note that the numerator of Eq. (20) represents the total converted electrical power, P_g, minus the direct-converted input power, $\eta_D P_i$; the denominator represents the total input power into the plasma preparation subsystem, P_i/η_i, minus the direct-converted input power, $\eta_D P_i$. It is significant that the subtrahends in both the numerator and denominator represent the main fraction of the circulating input power required to maintain the reactor system. In effect, Q_{EN} measures the Q for a subsystem of the total reactor system. As a result, Q_{EN} for the subsystem is greater than the Q given by Eq. (2) for the total reactor system.

A consequence of the definition of Q_{EN} is that for the limiting case in which the injection and conversion efficiencies approach unity, Q_{EN} becomes infinite independently of ϵ. This may be seen by utilizing the definitions of ϵ and P_i, given by Eqs. (3) and (12) respectively, in Eq. (20), which now becomes

$$Q_{EN} = \frac{1 - \epsilon \eta_i \eta_D}{\epsilon(1 - \eta_i \eta_D)}. \tag{21}$$

In this same limiting case, Q defined by Eq. (2) and/or Eq. (4), approaches the expected limit of $1/\epsilon$ which is consistent with the Basic Power Flow Diagram (Fig. 1) for a total reactor power system as discussed in Section III. In the limit of zero net electrical power output, the critical Q_{EN} value becomes unity independently of subsystem efficiencies.

The definition of Q_{EN} does not provide a measure which is indicative of the total plasma preparation power required to maintain the total reactor system operable. As a result there is no corresponding measure of the capital investment in equipment required to handle the total circulating power as will be discussed in Section V.

In Table I, Ref. 3, are listed the Q values for the three fuel cycle systems: (1) D-T; (2) D-D; and (3) D-^{3}He, and for each the cases A and B corresponding to different collisional loss rates. The input data for determining Q given by Eq. (2) were those used in Ref. 3. The values of ϵ computed from Eq. (3) have also been listed in Table V-4-I of this paper. Referring to Table I, Ref. 3, the values of Q_{EN} are found to exceed Q by a factor of approximately 2 to 4.

In an earlier survey study of simple mirror machines, Post[4] introduced the quantity Q defined as the ratio of total nuclear power released to the injection particle energy escaping,

$$Q_P = \frac{\textit{Reactor nuclear power output}}{\textit{Total reactor power input}} = \frac{P_f}{P_i}, \quad (22)$$

where P_f and P_i were previously defined. This definition involves only part of the power flow across interface B of Fig. V-4-2, and consequently differs from Q in Eq. (7) by an additive constant of unity. In terms of ϵ and subsystem efficiencies, Eq. (22) becomes

$$Q_P = \frac{1 - \epsilon\eta_i\eta_c}{\epsilon\eta_i\eta_c}. \quad (23)$$

The above definition of Q was used in a study of minimum-B mirror machines by Fowler and Rankin,[5] and in a review paper by Fowler.[6] Most recently, this definition was used as the figure of merit in the mirror reactor power system studies by Werner et al.[7] and Cordey[8] and in a slightly modified form by Sweetman.[9]

The difference between the Q_p of Eq. (22) and the Q of Eq. (2) is that the injection power, P_i, is not included in the accounting for the total power output. Q_p corresponds to Lawson's factor R. A consequence of the above definition is that in the limiting case of 100% injection and conversion efficiencies, Q_p approaches the value $(1 - \epsilon)/\epsilon$ which is the ratio of the net electrical power output to the circulating power. Although this may appear not to be inconsistent with the analogous limit value of Eq. (16), it does not represent the total power flow across interface B between the power and power conversion subsystem of Fig. V-4-1 or Fig. V-4-2.

In the limiting case of zero net electrical power output, the critical Q_p approaches $(1 - \eta)/\eta$, rather than $1/\eta$ as in Eq. (18). However, for a reactor system having 100% efficiencies, a self-circulating power balance (i.e. reactor output power equal to reactor input power) is more appropriately described by a Q value of unity, whereas Q_p approaches zero.

In Table V-4-I are listed the Q_p values reported in the studies of Werner et al.[7] and Cordey et al.,[8] using the definition given by Eq. (22).

TABLE V-4-I. Values of Q and ϵ for Mirror Reactors

Post[3]	D-T		D-D		D-^{3}He	
	300 keV		400 keV		400 keV	
	A	B	A	B	A	B
Q_{EN}	5.3	20.3	3.7	8.7	4.0	18.7
Q [Eq. (2)]	2.5	6.7	2.0	3.4	1.8	4.5
ϵ	0.62	0.26	0.72	0.49	0.7	0.28
Werner et al.[7]					480 keV	
					Low Q	High Q
Q_P (Ref. 7)					0.20	0.40
Q [Eq. (2)]					1.22	1.44
ϵ					0.91	0.79
Cordey et al.[8]	Min. B				Min. B	
	100 keV	300 keV			500 keV	
Q_P (Ref. 8)	2.41	1.82			0.41	
Q [Eq. (2)]	3.40	2.82			1.41	
ϵ	0.50	0.58			0.88	

V. Remarks

The operating and capital costs of the reactor systems should be expected to relate to the power parameters. To a first approximation, total power costs can be assumed to scale directly with the gross electrical power output, P_g. Therefore, the normalized capital costs are proportional to the normalized power P_g/P_e and in turn are related to ϵ through Eq. (8) as

$$\textit{Normalized Capital Costs} \propto \frac{P_g}{P_e} = \frac{1}{1 - \epsilon} \quad (24)$$

Therefore, high capital costs are to be expected for those systems having high fractional circulating power requirements.

The definitions of the power balance parameters Q and ϵ presented in this paper are applicable to complex systems involving any combination of energy conversion, plasma formation, and injection devices, and can be used as measures of performance common to all fusion reactor systems, including closed magnetic systems or open-ended magnetic systems. Some typical values of Q and ϵ listed in the survey[1] for closed systems are as follows; stellarators, $Q \sim 13$, $\epsilon = 0.22$; tokamaks, $7 \leq Q \leq 100$, $0.03 \leq \epsilon \leq 0.3$. Typical values for open-ended systems other than the mirror-machine are as follows; θ-pinch, $Q \sim 4.4$, $\epsilon = 0.36$; astron $Q \sim 8.5$, $\epsilon = 0.2$.

In summary, the power balance parameters defined in this study can be utilized to serve essentially two purposes: (1) to establish a common basis for an intercomparison of the fundamentally different approaches to a fusion power reactor system (including fusion by laser ignition); and (2) to serve eventually as feedback information to help orient and guide research and development efforts towards optimum total systems within each of the basic concepts and for different fuel cycles.

References

1. P. J. Persiani, W. C. Lipinski and A. J. Hatch, *Survey of Thermonuclear Reactor Parameters*, ANL-7807 (to be published).

2. J. D. Lawson, *Some Criteria for a Power Producing Thermonuclear Reactor*, Proc. Phys. Soc. **70**, Pt. I, No 445B, 6 (1957).
3. R. F. Post, *Mirror Systems: Fuel Cycles, Loss Reduction and Energy Recovery*, Proc. Conference on Nuclear Fusion Reactors, UKAEA, 88 (1969).
4. R. F. Post, *Critical Conditions for Self-Sustaining Reactions In the Mirror Machines*, Nucl. Fusion Suppl. Pt. I, 99 (1962).
5. T. K. Fowler and M. J. Rankin, *Fusion Balance in Mirror Machines*, J. Nucl. Energy, Pt. C **8**, 121 (1966).
6. T. K. Fowler, *Fusion Research in Open-Ended Systems*, Nucl. Fusion **9**, 3 (1969).
7. R. W. Werner et al, *Engineering and Economic Aspects of Mirror Machine Reactors with Direct Conversion*, Proc. IAEA 4th Conference on Plasma Physics and Controlled Nuclear Fusion Research, Madison, Wisconsin, 1971, Paper No. IAEA/CN-28/K-2 (to be published).
8. J. G. Cordey et al, *Efficient Recirculation of Power in Mirror Reactors*, Proc. IAEA 4th Conference on Plasma Physics and Controlled Nuclear Fusion Research, Madison, Wisconsin, 1971, Paper No. IAEA/CN-28/K-3 (to be published).
9. D. R. Sweetman, *Mirror Reactors: Some General Considerations* Proc. Conference on Nuclear Fusion Reactors, UKAEA, 112 (1969).

V-5. Nonelectrical or Off-Peak Electrical Air Conditioning

B. I. Spinrad

Introduction

The following discussion records some ideas which were generated in considering unconventional methods of coping with our energy needs in the near future. The arguments, which are entirely qualitative, are only carried so far as is needed to determine whether the concepts merit further attention.

Ecological Problems Caused by Summer Air Conditioning

The cooling of summer air is becoming commonplace in American cities. It is a delightful amenity. However, air conditioning has its disadvantages:

1. The need for air conditioning reaches its peak everywhere in a region at the same time. This strains power systems and forces older, less efficient stations for generating electricity into use. The fact that it uses electricity at peak load means that the source of power for air conditioning is operating at less than 30% efficiency in conversion of heat to work. For every calorie of cooling, three or four calories of heat are added to the environment.

2. The heat dissipated in air conditioning is added to the environment—air or water—at precisely the time when it is most sensitive to overheating; that is, when the air or water are hottest. At the electrical power station, heat is discharged either to sensitized water or to air. The ambient air temperature in the latter case is maximum, and power cycle efficiency suffers. At the point of consumption, the out-of-doors may become intolerable; this is particularly the case in downtown areas, where the heat rejected from air conditioning units may rival insolation as a local heat source.

Since three separate types of ecology—the economic ecology of the power industry, which rarely recovers its true costs in power peaks; the downtown urban ecology; and the natural ecology of air and water—all suffer from the air conditioning peak, it seems highly profitable to look for ways of avoiding it.

Air Cooling by Heat Exchange

The simplest reduction would be to utilize or create reservoirs of coldness. Subsoils average ambient temperatures over periods of years, and if cooling coils could be adequately installed, very large quantities of "cold," deposited in winter, could be withdrawn in summer (in the northern United States, subsoil temperatures rarely are above 50°F). However, except under special circumstances, it is difficult to transfer heat to or through soil.

Natural or artificial bodies of water are further accessible cold reservoirs. A simple form of air cooling can be contemplated by direct heat exchange between water reservoirs and building air. Natural waters, however, contain aquatic ecologies, which we are reluctant to disturb. Disturbance would be the result either of severly overheating an ecologically significant part, unduly thickening upper warm layers so that lower cold layers are restricted, or raising the total water system temperature uniformly and too much.

The latter result is only a possibility when quite small bodies of water are utilized. The amount of heat required to warm Lake Michigan (a potential reservoir for the cooling needs of 15–20 million people) *generally* is truly staggering; tidal slosh makes New York Bay (20–30 million people) even larger, effectively. Oceans are available to Los Angeles, Miami, etc., and large rivers and bays to most other American cities. There

are only a few metropolitan areas in America, mostly in the Southwest, where an adequate reservoir of cold water, so large as to preclude its being heated generally to an appreciable extent, does not exist.

The possibility of severely overheating an effluent does not exist either. If air temperature of 70°F is the desideratum, water effluent from cold water-hot air transfer devices (radiators in reverse) need not be higher than 70°F. That is to say, the cooling of air from 100 to 70°F can be practically achieved by raising the temperature of an appropriate amount of water from 50 to 70°F.

The possibility of drastically altering the temperature distribution in a large body of water needs more analysis, but likewise seems unlikely.

Is Cold Water Available?

I have suggested that natural bodies of cold water are adequate to absorb the excess heat of personal environmental air for the populations near them. Are they accessible? In other words, how near is "near"?

A crude answer can be gotten by examining metropolitan networks of fire hydrants. They generally take water from the city shore, back as far as the city limits go. City dimensions are 5–15 miles (Chicago: 20 x 10 miles; New York: 25 x 15 miles, with Queens Borough (the largest) about 10 x 15 miles). Thus, it seems practical to furnish a cold water service to a distance of 10–15 miles from the body of water. This would serve the cooling needs of between 75 and 90 % of the people in most metropolitan areas. In New York and Chicago, well over 50 % of the people in the metropolitan area are within a few miles of major waters.

The question of delivery might be raised. After all, a whole new piping system might have to be installed, or, at the very least, considerably more pumping power added to fire-fighting systems. However, consider the following:

1. The required water-pumping power is far less than the power installation already in service for air conditioning. As larger units, water pumps would be more efficient, and the energy wastage in transmission and transduction would likewise be far less.

2. The construction of underground water mains is very expensive in already built-up areas. However, it is a routine cost in developing new lands. In built-up areas, there is no law which says that overhead water supplies need be ugly, if we are forced to that.

3. Pumping requirements can to a degree be made more level over the day by creating a network of secondary reservoirs. A small pond, 100 ft. sq. and 10 ft. deep, can be a neighborhood recreational asset. A daily exchange of water would be sufficient to prevent its reaching temperature equilibrium with the ambient air.

The Suburbs

In less built-up areas and in suburbs the logistics of water pumping and storage are more formidable. The only supply of cold water available is that for domestic use. Although it is actually quite a bit, it is not enough; and a new capillary piping system for water would be burdensome. It seems more reasonable to consider providing a household reservoir maintained in series with domestic use. Even so, there is a discrepancy. Daily water use in a very modern, high-living-standard suburban home is rarely more than five hundred gallons, or about two tons; air conditioning requirements may run to more than 300,000 BTU/day, which would require the 20° rise of 7.5 tons of water.

Nevertheless, a 7.5-ton water storage tank is not large: a cylinder 7 ft. in diameter and 6 ft. high, a "cave" 6 x 5 x 9 ft. Such tankage can be provided under the backyard garden, or in the garage. And, at least, it can serve as a power usage leveler. The concept is to chill the stored water and to obtain cold air by blowing the air across a radiator through which cold water circulates. It would not take very sophisticated controls to:

1. Prevent the water from freezing,
2. Valve the warmed radiator-effluent water preferentially to the hot-water heater, toilets, and garden-water system,
3. Achieve variable air-cooling by adjusting air-blower speed.

It would not even take a very sophisticated analysis to learn how to use such a system in such a way that the power requirements are maximum during a low-load period. The advantages to power companies of achieving this are great enough so that they might find it economical to subsidize the installation of automatic user's equipment to achieve this end; or perhaps the gas company would be happy to repenetrate the refrigeration market, since they do *not* have a summer peak.

Other Factors of Power Use

Obtaining chilled air is by no means the only function of air conditioning. For maximum comfort, the air must be dehumidified and circulated. These functions take up about 10 % of air-conditioning power, and are assumed to be irreducible factors.

Therefore, a reduction to 10 % of present power consumption for air conditioning is the best one could expect. This would be the case if the cooling function were to be completely taken over by heat transfer from air to unrefrigerated natural water. If, however, a

significant amount of air-conditioning—say half—requires the use of refrigeration, then nevertheless, a major reduction of diurnal peak power requirement might still be achievable by use of stored chilled water.

This is nothing that is new to refrigeration manufacturers, who often try to sell the customer a smaller refrigeration unit than he thinks he wants, coupled with a refrigeration "storage" scheme. It seems desirable to sell the public on the idea that storage of "cold" is good.

Summary and Plan for Action

In urban areas, the concept of air cooling by heat transfer from warm air to cold natural water is attractive. It requires the assessment of incremental transmission costs for water, as needed for this purpose; these may be balanced against benefits of decreased power load, measured in terms of customer bills, and against benefits of decreased environmental heating. It is generally believed that large supplies of urban water are too expensive for this purpose; but I recommend that a fresh look be taken at urban use and reuse. Water used for cooling would be returned to the fresh water supply, or, alternately use of raw water systems could be reexamined.

In less built-up areas, not accessible to an adequate water reservoir network, there are advantages to power companies in spreading out the air-conditioning peak, at least diurnally. Power companies undoubtedly have a good estimate of the true cost of peak power. My guess is that this cost is high enough so that they would consider it profitable to subsidize to some degree the installation of peak-leveling, consumer equipment; chilled-water reservoir units are a conspicuous example of such equipment. Another possibility is the incorporation of the concept of peak, or demand, into the bill at a much higher relative charge than now is made. A final one is that peak-leveling, gas-consuming refrigeration equipment could couple well with a system for storage of "cold", and serve to level the annual load of both electrical and gas utilities.

V-6. Extension of the Dual Spectrum Fuel Assay Concept

C. N. Kelber

The concept of a dual spectrum facility for the assay of reactor fuel[1] has been extended to include the assay of thermal reactor fuel as well as LMFBR fuel,[2] and the problems of neutron filter choice and moderator choice have been examined. Finally an estimate was made of the resistance of the concept to errors introduced by tampering with the plutonium distribution.

The dual spectrum concept involves oscillating fuel against a standard in a hard spectrum in a dilute fast critical assembly, then softening the spectrum by introducing a moderator into the voids in the assembly, and oscillating the fuel inside various neutron absorbers or filters. The choice of moderator and of neutron filter is a set of design variables, and the objective of this work is to determine that set of design variables which yields the lowest estimated bound on the error inherent in the fuel assay, and to extend these considerations to the assay of thermal reactor fuel.

It was concluded that the filters, hafnium, boron, and cadmium, together with water or graphite moderator, offer an optimal design set. The errors in the assay of fuel were estimated to be inversely proportional to the mass content of the fuel; the resistance to tampering was found to be high.

TABLE V-6-I. Typical Errors in Mass Assay

Isotopes	Fuel Element	
	LMFBR	Thermal
All fertile	4.4 g out of 34.2 kg	20.3 g out of 27.8 kg
All fissile	1.4 g out of 4.3 kg	10 g out of 0.5 kg

The error limits for the fast fuel and thermal fuels were estimated on the basis of current critical experiment practice. These errors are presented in Table V-6-I.

References

1. C. N. Kelber, *A Dual Spectrum Concept for LMFBR Fuel Assay*, Nucl. Tech. **10**, 85 (January 1970).
2. C. N. Kelber, *Extension of the Dual Spectrum Fuel Assay Concept*, Nucl. Tech. **13**, 95 (January 1972).

Section VI

Publications

July 1, 1970 to June 30, 1971

Open Literature

1. Beller, L. S., *Small Back-to-Back Detector for Precise Comparison of Fission and (n,α) Reaction Rates*, Nucl. Instr. Methods **92**, 397–401 (1971).
2. Butler, D. K., *Modular Coding for Reactor Calculations in the United States Meeting on Modular Codes for Reactor Calculations*, Varese, Italy, December 1–3, 1970, Newsletter of the ENEA Computer Programme Library No. 11 (EACRP-A-135), p. 50 (March 1971).
3. Butler, D. K. and Meneley, D. A., *Recent Developments in Fast Reactor Kinetics*, Nucl. Safety **11**, 289–295 (July–August 1970).
4. Cohn, C. E., *Simplify Turn-On Initialization of Digital Systems*, 400 Ideas for Design. Hayden Book Co., New York, 1971, Vol. 2, pp. 237–238.
5. Corwin, W. C. and Porges, K. G., *Passive Splitters for Fast Pulse Processing*, Nucl. Instr. Methods **85**, 155 (1970).
6. Davey, W. G. and Redman, W. C., *Techniques in Fast Reactor Critical Experiments*, Gordon and Breach Science Publishers, New York, 1970.
7. Davey, W. G., *Status of Important Heavy-Element Nuclear Data above the Resonance Region*, Proc. 2nd Int. Conf. on Nuclear Data for Reactors, Helsinki, June 15–19, 1970, Vol. 2, pp. 119–135.
8. Davey, W. G., *An Evaluation of the Number of Neutrons per Fission for the Principal Plutonium, Uranium, and Thorium Isotopes*, Nucl. Sci. Eng. **44**(3), 345–371 (June 1971).
9. De Volpi, Alexander, *Neutron Escape from Water-Moderated Tanks*, J. Nucl. Energy **24**(12), 577–586 (January 1971).
10. De Volpi, Alexander, Caya, G. E., Rush, C. J. and Rudnick, S. J., *Digital Pulses Delayed with Substantially Reduced Deadtime*, Rev. Sci. Instr. **42**, 684–689 (1971).
11. De Volpi, Alexander, *Estimates of Variance and Merit Ratios from Measured Quantities of Fluctuating Origin and Inherent Correlation*, Int. J. Appl. Rad. Isotopes **22**, 103–110 (1971).
12. De Volpi, Alexander, *Deciphering and Processing Digital Photographic Data*, Proc. 9th Int. Conf. on High Speed Photography, Denver, August 2–7, 1970. Soc. Motion Picture and Television Eng., New York, 1970, pp. 58–62.
13. Dickerman, C. E., Willis, F. L., Smith, R. R., Henault, P. B., Purviance, R. T., Boland, J. F., De Volpi, Alexander, Noland, R. A., Regis, J. P., Cohen, A. B. and Walter, C. M., *TREAT Sodium Loop Experiments on Performance of Unbonded, Unirradiated EBR-II Mark I Fuel Elements*, Nucl. Eng. Design **12**(3), 381–390 (June 1970).
14. Dickerman, C. E., Robinson, L. E., Purviance, R. T., De Volpi, Alexander, Willis, F. L., Cohen, A. B. and Regis, J. P., *Power Pulse Meltdown Experiments Performed in the Mark I TREAT Sodium Loop on Clusters of 7 EBR-II Mark I Type Pins*, Nucl. Eng. Design **12**(3), 391–406 (June 1970).
15. Gold, Raymond, *Compton Recoil Gamma-Ray Spectroscopy*, Nucl. Instr. Methods **84**, 173 (1970).
16. Henryson, Herbert, *Multigroup Elastic Scattering Cross Sections for Heavy Elements*, Nucl. Sci. Eng. **43**, 235–237 (February 1971). Note.
17. Hummel, H. H. and Okrent, David, *Reactivity Coefficients in Large Fast Power Reactors*, Am. Nucl. Soc., Hinsdale, Ill., 1970.
18. Hwang, R. N. and Miller, L. B., *Conditional Variances Pertinent to Doppler Effect Studies*, Nucl. Sci. Eng. **42**, 179–190 (November 1970).
19. Karam, R. A., Marshall, J. E. and Dance, K. D., *Analysis of Heterogeneity and Sodium-Void Effects in a 2700-Liter Uranium Carbide Fast Core, ZPR-6 Assembly 5*, Nucl. Sci. Eng. **43**, 5–26 (January 1971).
20. Kelber, C. N., *A Dual Spectrum Concept for LMFBR Fuel Assay*, Nucl. Technol. **10**, 85–90 (January 1971).
21. Kelber, C. N., *An Extended Equivalence Relation*, Nucl. Sci. Eng. **42**, 257–259 (December 1970).
22. Kelber, C. N., *A Bootstrap Concept of a Safety Test Facility*, Nucl. Appl. Technol. **9**, 780–785 (December 1970).
23. Lambropoulos, P. P. and Luco, Victor, *Functionals for Discontinuous Trial Function Flux Synthesis*, J. Nucl. Energy **24**, 551–564 (December 1970).
24. Long, A. B., *Plutonium Inhalation: The Burden of Negligible Consequence*, Nucl. News **14**, 69–73 (June 1971).
25. Meadows, J. W., Smith, A. B., Whalen, J. F. and Beynon, T. D., *^{165}Ho Fast Neutron Cross Sections*, Z. Phys. **243**(2), 171–187 (1971).
26. Meadows, J. W. and Whalen, J. F., *The Total Neutron Cross Section of Lithium-7 and Carbon from 100 to 1500 keV*, Nucl. Sci. Eng. **41**, 351–356 (September 1970).
27. Moldauer, P. A., *Comment on Resonance Averaging*, Phys. Rev. **C3**, 948–949 (February 1971).
28. Okrent, David, Loewenstein, W. B., Rossin, A. D., Smith, A. B., Zolotar, B. A. and Kallfelz, J. M., *Neutron Energy Spectra for Fast Reactor Irradiation Effects*, Nucl. Appl. Technol. **9**, 454–507 (October 1970).
29. Poenitz, W. P. and Tatarczuk, J. R., *Spin Determination of Resonances in ^{165}Ho(n,γ) from Low Level Occupation Probability Ratios*, Nucl. Phys. **A151**(3), 569–578 (1970).
30. Poenitz, W. P., *Recent Experimental Data for Heavy Nuclei*, Proc. 2nd Int. Conf. on Nuclear Data for Reactors, Helsinki, June 15–19, 1970-Vol. 2, pp. 3–29.
31. Redman, W. C. and Bretscher, M. M., *Experimental Determination of the Perturbation Denominator in Fast Critical Assemblies*, Nucl. Sci. Eng. **44**(3), 450–453 (June 1971). Note.
32. Smith, A. B., *Note on the Prompt-Fission-Neutron Spectra*

of Uranium-235 and Plutonium-239, Nucl. Sci. Eng. **44**(3), 439–442 (June 1971). Note.
33. Smith, D. L., *Variation of the Intrinsic Efficiency of a Cylindrical Planar Ge(Li) Gamma-Ray Detector with Source Distance*, Nucl. Instr. Methods **94**(1). 157–163 (1971).
34. Stacey, W. M., *The Effect of Anisotropic Scattering upon the Elastic Moderation of Fast Neutrons*, Nucl. Sci. Eng. **44**, 194–203 (May 1971).
35. Stacey, W. M., *Approximate Treatments of the Effect of Anisotropy upon Elastic Neutron Moderation*, Nucl. Sci. Eng. **44**(3), 442–444 (June 1971). Note.
36. Stacey, W. M., *Xenon-Induced Spatial Power Oscillations*, Reactor Technol. **13**(3), 252–279 (Summer 1970).
37. Stacey, W. M., *Spectral Synthesis Applied to Fast-Reactor Dynamics*, Nucl. Sci. Eng. **41**, 249–258 (August 1970).
38. Stacey, W. M., *Continuous Slowing Down Theory Applied to Fast-Reactor Assemblies*, Nucl. Sci. Eng. **41**, 381–393 (September 1970).
39. Stacey, W. M., *Resolved Narrow Resonance Reaction Rates in Fast-Reactor Mixtures*, Nucl. Sci. Eng. **41**, 455–457 (September 1970). Note.
40. Stacey, W. M., *Continuous Slowing Down Theory for Anisotropic Elastic Neutron Moderation in the P_N and B_N Representations*, Nucl. Sci. Eng. **41**, 457–461 (September 1970). Note.
41. Stacey, W. M., *Calculation of Heterogeneous Fluxes and Reactivity Worths*, Nucl. Sci. Eng. **42**, 233–236 (November 1970). Note.
42. Takeuchi, Kenji and Moldauer, P. A., *Scattering Resonances and the R Function*, Phys. Rev. **C2**(3), 920–925 (September 1970).
43. Takeuchi, Kenji and Moldauer, P. A., *R-Matrix Shell-Model Calculations of Scattering and Reaction Cross Sections*, Phys. Rev. **C2**(3), 925–941 (September 1970).

Reports

1. Broomfield, A. M., Hess, A. L., Amundson, P. I., Baird, Q. L., Bennett, E. F., Davey, W. G., Gasidlo, J. M., Keeney, W. P., Long, J. K. and McVean, R. L., *ZPR-3 Assemblies 48, 48A, and 48B: The Study of a Dilute Plutonium-Fueled Assembly and its Variants*, ANL-7759 (December 1970).
2. Bryant, L. T., Duffy, G. J., Greenspan, Harold, Henryson, Herbert and Leaf, G. K., *The ARC System One-Dimensional Transport Theory Capability, SNARC1D*, ANL-7717 (January 1971).
3. Cohn, C. E., Bennett, E. F. and Yule, T. J., *Hardware and Software for Nuclear Spectroscopy on the Varian Data Machines 622/i Computer*, ANL-7704 (August 1970).
4. DeVolpi, Alexander, *International Comparison of ^{56}Mn Activity in 1968*, ANL-7642 (December 1969); *also* Metrologia **6**(2), 65 (April 1970).
5. Gold, Raymond and Olson, I. K., *Analysis of Compton Continuum Measurements*, ANL-7611 (February 1970).
6. Hess, A. L., Keeney, W. P. and McVean, R. L., *Experiments with a Series of Small, Pu-Plus-U-Fueled Fast-Reactor Criticals (FARET Mockup—ZPR-3 Assembly 46)*, ANL-7215 (January 1970).
7. Just, L. C., Henryson, Herbert, Kennedy, A. S., Sparck, S. D., Toppel, B. J., and Walker, P. M., *The System Aspects and Interface Data Sets of The Argonne Reactor Computation (ARC) System*, ANL-7711 (April 1971).
8. Kato, W. Y., Rusch, G. K., Dates, L. R., Till, C. E., Ancarani, Augusto, Vandoorninck, J. M., Cheever, C. L. and Bohn, E. M., *Final Safety Analysis Report on the Use of Plutonium in ZPR-6 and -9*, ANL-7442 (February 1970).
9. Kelber, C. N., Judd, A. M., Cinelli, Gabriel, Dickerman, C. E., Fauske, H. K., Holtz, R. E., Ivins, R. O., Lipinski, W. C., MacFarlane, D. R. Marchaterre, J. F., Miller, David, Nicholson, R. B. and Singer, R. M., *Safety Problems of Liquid-Metal-Cooled Fast Breeder Reactors*, ANL-7657 (February 1970).
10. Lipinski, W. C., Cohn, C. E., MacFarlane, D. R., Mulcahey, T. P., Okrent, David, Porges, K. G., Redman, W. C., Van Erp, J. B. and Vonderohe, R. H., *Instrumentation Systems to Protect LMFBR Core Integrity*, ANL-7793 (March 1971).
11. Olson, A. P., *RABID: An Integral Transport-Theory Code for Neutron Slowing Down in Slab Cells*, ANL-7645 (April 1970).
12. Pennington, E. M., Gajniak, J. C., Cohen, A. B. and Bohl, W. R., *Service Routines for the Multigroup Cross-Section Code MC²*, ANL-7654 (April 1970).
13. Robinson, W. R., LeSage, L. G. and Pond, R. B., *Summary of Critical-Mass Configurations, Material Concentrations, and Control-Rod Worths for ZPR-9 Zoned Fast Critical Assemblies 11–25*, ANL-7773 (March 1971).
14. Rusch, G. K., *A Code for Calculating Effluent Air Temperatures from a Sand Filter*, ANL-7687 (November 1970).
15. Smith, D. L., *Empirical Formula for Interpolation of Tabulated Photon Photoelectric Cross Sections*, ANL-7796 (March 1971).
16. Stevenson, J. M., Gasidlo, J. M., Rogers, V. C., Simons, G. G. and Vosburgh, R. O., *Experimental Results for ZPR-3 Assemblies 58 and 59*-ANL-7695 (April 1970).
17. Woodruff, W. L., *Some Improvements in Variational Flux Synthesis Methods*, ANL-7696 (May 1970).
18. Applied Physics Division Annual Report, July 1, 1969 to June 30, 1970, ANL-7710 (January 1971).

Abstracts

1. Bennett, E. F. and Yule, T. J., *Improvements in Absolute Boron Proportional Counters*, Trans. Am. Nucl. Soc. **14**(1), 415 (June 1971).
2. Carpenter, S. G., Goin, R. W., Hitchcock, J. T. and Plummer, J. P., *Control Rod Worth Measurements in the ZPPR-2 Benchmark Core*, Trans. Am. Nucl. Soc. **14**(1), 27 (June 1971).
3. Cohn, C. E., *Experience with Subcriticality Determination by Rod Drop in the FTR-3 Critical Experiments*, Trans. Am. Nucl. Soc. **14**(1), 29 (June 1971).
4. Cohn, C. E., *Improved Computer Method for Polarity Cross-Correlation*, Trans. Am. Nucl. Soc. **14**(1), 29 (June 1971).
5. Congel, F. J., Roberts, J. H., Strait, E. N., Kastner, Jacob, Oltman, B. J., Gold, Raymond and Armani, R. J., *Automatic System for Counting Etched Holes in Thin Dielectric Plastics*, Trans. Am. Nucl. Soc. **13**(2). 524 (November 1970).
6. Cox, S. A. and Hanley, P. R., *Performance of the ANL Dynamitron Tandem*, Bull. Am. Phys. Soc. **16**, 227 (February 1971).
7. Daughtry, J. W., Pond, R. B., Fleischman, R. M., Swanson, C. D., Rusch, G. K. and Kier, P. H., *The FTR-3 Critical Assembly and Experimental Program*, Trans. Am. Nucl. Soc. **14**(1), 24 (June 1971).
8. Daughtry, J. W., Long, A. B., Pond, R. B., Swanson, C. D. and Fleischman, R. M., *Reaction Rate Distributions*

and Control Rod Worths in the FTR-3 Critical Assembly, Trans. Am. Nucl. Soc. **14**(1), 25 (June 1971).

9. De Volpi, Alexander and Dickerman, C. E., *Fast Neutron Hodoscope Observation of Fuel Meltdown Experiments at TREAT: Transients 1255 and 1281*, Trans. Am. Nucl. Soc. **14**(1), 312 (June 1971).
10. De Volpi, Alexander, *Possible Systematic Discrepancies in the 2200 m/sec Fission Parameters*, Trans. Am. Nucl. Soc. **14**(1), 375 (June 1971).
11. Fuller, E. L., *One-Dimensional Thermal Reactor Kinetics Benchmark Calculations*, Trans. Am. Nucl. Soc. **14**(1), 233 (June 1971).
12. Greenspan, Harold and Carter, J. C., *A Fast Reactor Spectrum in a Thermal Core*, Trans. Am. Nucl. Soc. **14**(1), 149 (June 1971).
13. Iskenderian, H. P., *Capture-to-Fission Ratio of ^{239}Pu and ^{241}Pu*, Trans. Am. Nucl. Soc. **14**(1), 371 (June 1971).
14. Jackson, J. F. and Nicholson, R. B., *A Sensitivity Study for Fast Reactor Disassembly Calculations*, Trans. Am. Nucl. Soc. **14**(1), 356 (June 1971).
15. Kaiser, R. E., Amundson, P. I., Forrester, R. J. and Newmark, Burton, *Measurement and Analysis of Space Dependent Parameters in a Demonstration Plant Benchmark Critical*, Trans. Am. Nucl. Soc. **14**(1), 19 (June 1971).
16. Kaiser, R. E. and Gasidlo, J. M., *Measurement and Analysis of Reactivity Doppler Effects in ZPR-3 Assembly 53*, Trans. Am. Nucl. Soc. **13**(2), 710 (November 1970).
17. Kaiser, R. E., Norris, R. J., Olson, A. P. and Paik, N. C., *Predicted Characteristics with Actual Observation for the Demonstration Reactor Benchmark Assembly ZPPR-2*, Trans. Am. Nucl. Soc. **13**(2), 732 (November 1970).
18. Kaiser, R. E., Norris, R. J. and Paik, N. C., *Material Worth Measurements in the Benchmark Critical Assembly on ZPPR*, Trans. Am. Nucl. Soc. **13**(2), 734 (November 1970).
19. Karam, R. A., Stanford, G. S. and Robinson, W. R., *Anisotropic Effects in a 4000-Liter UO_2 Fast Core, ZPR-6 Assembly 6A*, Trans. Am. Nucl. Soc. **14**(1), 21 (June 1971).
20. Kelber, C. N. and McArthy, A. E., *Shielding Study for the University of Chicago Experiment in Pioneer F/G*, Trans. Am. Nucl. Soc. **14**(1), 13 (June 1971).
21. Kelber, C. N., *Extension of the Dual Spectrum Fuel Assay Concept*, Trans. Am. Nucl. Soc. **14**(1), 30 (June 1971).
22. Kelber, C. N., Banfield, T. V. and Talboy, J. H., *Safety Effects of Water Infiltration in CP-5*, Trans. Am. Nucl. Soc. **14**(1), 321 (June 1971).
23. Kelber, C. N., *Dual Spectrum Concept for LMFBR Fuel Assay*, Trans. Am. Nucl. Soc. **13**(2), 750 (November 1970).
24. Lehto, W. K., Daughtry, J. W., Pond, R. B. and Carpenter, S. G., *Fast-Reactor, Shutdown-Margin Measurements*, Trans. Am. Nucl. Soc. **14**(1), 42 (June 1971).
25. LeSage, L. G., Bohn, E. M., Marshall, J. E., Karam, R. A., Till, C. E., Lewis, R. A. and Salvatores, Massimo, *Initial Experimental Results from ZPR-6 Assembly 7, The Single-Zone Demonstration Reactor Benchmark Assembly*, Trans. Am. Nucl. Soc. **14**(1), 17 (June 1971).
26. Lewis, R. A., LeSage, L. G., Till, C. E., Marshall, J. E., Bohn, E. M., Salvatores, Massimo and Stanford, G. S., *LMFBR Demonstration Reactor Benchmark Critical Experiments Program—Initial Plate-Rod Heterogeneity Measurements*, Trans. Am. Nucl. Soc. **14**(1), 18 (June 1971).
27. Long, A. B., Bohn, E. M. and Kaiser, W. C., *Non-Perturbing Fission Counter for Use in Plate Type Critical Assemblies*, Trans. Am. Nucl. Soc. **13**(2), 762 (November 1970).
28. Luco, Victor and Woodruff, W. L., *Another Anomaly in Variational Flux Synthesis Methods*, Trans. Am. Nucl. Soc. **13**(2), 739 (November 1970).
29. Luco, Victor, *On the Eigenvalues of the Flux Synthesis Equations*, Trans. Am. Nucl. Soc. **14**(1), 203 (June 1971).
30. Ma, P. Y. and Shum, R. H., *An improved Method for Assessing Damage to the Reactor Vessel in a Fast Reactor Accident*, Trans. Am. Nucl. Soc. **13**(2), 643 (November 1970).
31. Madell, J. T., *Effect of Subassembly Clearance on Fast Reactor Performance Characteristics*, Trans. Am. Nucl. Soc. **13**(2), 777 (November 1970).
32. Madell, J. T., *Estimation of Neutronic Parameters for Preliminary Design Studies for LMFBR's*, Trans. Am. Nucl. Soc. **14**(1), 264 (June 1971).
33. McElroy, W. N., Kellogg, L. S., Armani, R. J., Tochilin, E. and Zimmer, W. H., *Selection of Fission Yields*, Trans. Am. Nucl. Soc. **13**(2), 868 (November 1970).
34. Meneghetti, David, Keeney, W. P., Vosburgh, R. O., Stenstrom, D. G., Phillips, K. E. and Gasidlo, J. M., *Depleted-Uranium, Nickel, and Steel-Reflected EBR-II Critical Assemblies on ZPR-3—Experiments and Calculations*, Trans. Am. Nucl. Soc. **13**(2), 733 (November 1970).
35. Meneghetti, David, Keeney, W. P., Vosburgh, R. O., Simons, G. G., Stenstrom, D. G., Phillips, K. E. and Gasidlo, J. M., *Experiments and Analyses of Heterogeneous Cores and Neutron Spectra in EBR-II Critical Assemblies on ZPR-3*, Trans. Am. Nucl. Soc. **14**(1), 20 (June 1971).
36. Meyer, J. F., Johnson, T. W. and Sustman, J. E., *A Sodium-Vapor Monitor*, Trans. Am. Nucl. Soc. **13**(2), 794 (November 1970).
37. Moldauer, P. A., *A Quantum-Mechanical Description of Measurements*, Bull. Am. Phys. Soc. **16**, 20 (January 1971).
38. Pond, R. B., Daughtry, J. W., Till, C. E., Groh, E. F. and Swanson, C. D., *Plutonium and ^{238}U Doppler Measurements in a Plutonium Fueled Fast Critical Assembly*, Trans. Am. Nucl. Soc. **13**(2), 710 (November 1970).
39. Redman, W. C. and Bretscher, M. M., *Experimental Determination of the Perturbation Denominator in Fast Critical Assemblies*, Trans. Am. Nucl. Soc. **13**(2), 736 (November 1970).
40. Shum, R. H. and Ma, P. Y., *An Approach for Determining the Effective Energy Release of a Fast Reactor Accident*, Trans. Am. Nucl. Soc. **13**(2), 644 (November 1970).
41. Simons, G. G., Stenstrom, D. G., Meneghetti, David and Keeney, W. P., *Gamma-Ray Dose Evaluations for the ZPR-3/EBR-II Critical Assemblies*, Trans. Am. Nucl. Soc. **13**(2), 880 (November 1970).
42. Stacey, W. M., *Studies of Spectral Synthesis in Spatially Dependent Fast-Reactor Dynamics*, Trans. Am. Nucl. Soc. **13**(2), 619 (November 1970).
43. Stacey, W. M., *Anisotropic Elastic Moderation of Neutrons*, Trans. Am. Nucl. Soc. **13**(2), 726 (November 1970).
44. Stacey, W. M., *Solution of the Neutron Diffusion Equation by Space-Energy Factorization*, Trans. Am. Nucl. Soc. **13**(2), 739 (November 1970).
45. Stacey, W. M. and Henryson, Herbert, *Application of Space-Energy Factorization to LMFBR Diffusion Theory Calculations*, Trans. Am. Nucl. Soc. **14**(1), 205 (June 1971).
46. Stacey, W. M., *Effect of the 2.85 keV ^{23}Na Resonance on*

Multigroup Narrow Resonance Cross Sections, Trans. Am. Nucl. Soc. **14**(1), 364 (June 1971).

47. Till, C. E. and Davey, W. G., *Investigation of Sodium-Voiding Reactivities and Other Safety Parameters in Fast Critical Assemblies*, Trans. Am. Nucl. Soc. **13**(2), 718 (November 1970).
48. Travelli, Armando, Ulrich, A. J. and Beitel, J. C., *Analysis of Small-Sample Boron Worth Measurements in ZPR-3/FTR-1*, Trans. Am. Nucl. Soc. **14**(1), 22 (June 1971).
49. Yule, T. J., and Bennett, E. F., *Measured Neutron Spectrum in FTR-3, a Plutonium-Fueled Fast Spectrum Reactor*, Trans. Am. Nucl. Soc. **13**(2), 687 (November 1970).